Journal of Healthcare Engineering

Advances in Feature Transformation based Medical Decision Support Systems for Health Informatics

Lead Guest Editor: Liaqat Ali
Guest Editors: Sahfqat Ullah Khan and Hafiz Tayyab Rauf

Advances in Feature Transformation based Medical Decision Support Systems for Health Informatics

Journal of Healthcare Engineering

Advances in Feature Transformation based Medical Decision Support Systems for Health Informatics

Lead Guest Editor: Liaqat Ali
Guest Editors: Sahfqat Ullah Khan and Hafiz Tayyab Rauf

Contents

Contents

Contents

Contents

Contents

Contents

Contents

Hindawi
Journal of Healthcare Engineering
Volume 2023, Article ID 9857931, 1 page
https://doi.org/10.1155/2023/9857931

Retraction

Retracted: A Method for Expanding the Training Set of White Blood Cell Images

Journal of Healthcare Engineering

Received 28 November 2023; Accepted 28 November 2023; Published 29 November 2023

This article has been retracted by Hindawi, as publisher, following an investigation undertaken by the publisher [1]. This investigation has uncovered evidence of systematic manipulation of the publication and peer-review process. We cannot, therefore, vouch for the reliability or integrity of this article.

Please note that this notice is intended solely to alert readers that the peer-review process of this article has been compromised.

Wiley and Hindawi regret that the usual quality checks did not identify these issues before publication and have since put additional measures in place to safeguard research integrity.

We wish to credit our Research Integrity and Research Publishing teams and anonymous and named external researchers and research integrity experts for contributing to this investigation.

The corresponding author, as the representative of all authors, has been given the opportunity to register their agreement or disagreement to this retraction. We have kept a record of any response received.

References

[1] Y. Su, Y. Zang, Q. Su, and L. Peng, "A Method for Expanding the Training Set of White Blood Cell Images," *Journal of Healthcare Engineering*, vol. 2022, Article ID 1267080, 11 pages, 2022.

Hindawi
Journal of Healthcare Engineering
Volume 2023, Article ID 9837045, 1 page
https://doi.org/10.1155/2023/9837045

Retraction

Retracted: Alteration of Intestinal Microbiota and Hydrogen Sulfide Metabolism in Patients with Hashimoto's Thyroiditis

Journal of Healthcare Engineering

Received 28 November 2023; Accepted 28 November 2023; Published 29 November 2023

This article has been retracted by Hindawi, as publisher, following an investigation undertaken by the publisher [1]. This investigation has uncovered evidence of systematic manipulation of the publication and peer-review process. We cannot, therefore, vouch for the reliability or integrity of this article.

Please note that this notice is intended solely to alert readers that the peer-review process of this article has been compromised.

Wiley and Hindawi regret that the usual quality checks did not identify these issues before publication and have since put additional measures in place to safeguard research integrity.

We wish to credit our Research Integrity and Research Publishing teams and anonymous and named external researchers and research integrity experts for contributing to this investigation.

The corresponding author, as the representative of all authors, has been given the opportunity to register their agreement or disagreement to this retraction. We have kept a record of any response received.

References

[1] S. Zhang, Y. Chi, H. Jin et al., "Alteration of Intestinal Microbiota and Hydrogen Sulfide Metabolism in Patients with Hashimoto's Thyroiditis," *Journal of Healthcare Engineering*, vol. 2023, Article ID 9302189, 7 pages, 2023.

Hindawi
Journal of Healthcare Engineering
Volume 2023, Article ID 9815989, 1 page
https://doi.org/10.1155/2023/9815989

Retraction

Retracted: Prediction and Analysis of Autism Spectrum Disorder Using Machine Learning Techniques

Journal of Healthcare Engineering

Received 28 November 2023; Accepted 28 November 2023; Published 29 November 2023

This article has been retracted by Hindawi, as publisher, following an investigation undertaken by the publisher [1]. This investigation has uncovered evidence of systematic manipulation of the publication and peer-review process. We cannot, therefore, vouch for the reliability or integrity of this article.

Please note that this notice is intended solely to alert readers that the peer-review process of this article has been compromised.

Wiley and Hindawi regret that the usual quality checks did not identify these issues before publication and have since put additional measures in place to safeguard research integrity.

We wish to credit our Research Integrity and Research Publishing teams and anonymous and named external researchers and research integrity experts for contributing to this investigation.

The corresponding author, as the representative of all authors, has been given the opportunity to register their agreement or disagreement to this retraction. We have kept a record of any response received.

References

[1] M. S. Qureshi, M. B. Qureshi, J. Asghar, F. Alam, and A. Aljarbouh, "Prediction and Analysis of Autism Spectrum Disorder Using Machine Learning Techniques," *Journal of Healthcare Engineering*, vol. 2023, Article ID 4853800, 10 pages, 2023.

Hindawi
Journal of Healthcare Engineering
Volume 2023, Article ID 9798461, 1 page
https://doi.org/10.1155/2023/9798461

Retraction

Retracted: Effect of the Holistic Nursing Model of Responsibility System on the Mental State of Elderly Patients with Limb Fractures Fixed by Splints in the Emergency Department

Journal of Healthcare Engineering

Received 28 November 2023; Accepted 28 November 2023; Published 29 November 2023

This article has been retracted by Hindawi, as publisher, following an investigation undertaken by the publisher [1]. This investigation has uncovered evidence of systematic manipulation of the publication and peer-review process. We cannot, therefore, vouch for the reliability or integrity of this article.

Please note that this notice is intended solely to alert readers that the peer-review process of this article has been compromised.

Wiley and Hindawi regret that the usual quality checks did not identify these issues before publication and have since put additional measures in place to safeguard research integrity.

We wish to credit our Research Integrity and Research Publishing teams and anonymous and named external researchers and research integrity experts for contributing to this investigation.

The corresponding author, as the representative of all authors, has been given the opportunity to register their agreement or disagreement to this retraction. We have kept a record of any response received.

References

[1] S. Du, Y. Hao, and Y. Jiao, "Effect of the Holistic Nursing Model of Responsibility System on the Mental State of Elderly Patients with Limb Fractures Fixed by Splints in the Emergency Department," *Journal of Healthcare Engineering*, vol. 2023, Article ID 1271606, 9 pages, 2023.

Hindawi
Journal of Healthcare Engineering
Volume 2023, Article ID 9782032, 1 page
https://doi.org/10.1155/2023/9782032

Retraction

Retracted: Higher Chronic Endometritis Incidences within Infertile Polycystic Ovary Syndrome Clinical Cases

Journal of Healthcare Engineering

Received 28 November 2023; Accepted 28 November 2023; Published 29 November 2023

This article has been retracted by Hindawi, as publisher, following an investigation undertaken by the publisher [1]. This investigation has uncovered evidence of systematic manipulation of the publication and peer-review process. We cannot, therefore, vouch for the reliability or integrity of this article.

Please note that this notice is intended solely to alert readers that the peer-review process of this article has been compromised.

Wiley and Hindawi regret that the usual quality checks did not identify these issues before publication and have since put additional measures in place to safeguard research integrity.

We wish to credit our Research Integrity and Research Publishing teams and anonymous and named external researchers and research integrity experts for contributing to this investigation.

The corresponding author, as the representative of all authors, has been given the opportunity to register their agreement or disagreement to this retraction. We have kept a record of any response received.

References

[1] S. Wang, H. Zhao, F. Li, Y. Xu, H. Bao, and D. Zhao, "Higher Chronic Endometritis Incidences within Infertile Polycystic Ovary Syndrome Clinical Cases," *Journal of Healthcare Engineering*, vol. 2022, Article ID 9748041, 6 pages, 2022.

Hindawi
Journal of Healthcare Engineering
Volume 2023, Article ID 9876973, 1 page
https://doi.org/10.1155/2023/9876973

Retraction

Retracted: Performance Evaluation of Hospital Economic Management with the Clustering Algorithm Oriented towards Electronic Health Management

Journal of Healthcare Engineering

Received 10 October 2023; Accepted 10 October 2023; Published 11 October 2023

This article has been retracted by Hindawi following an investigation undertaken by the publisher [1]. This investigation has uncovered evidence of one or more of the following indicators of systematic manipulation of the publication process:

(1) Discrepancies in scope
(2) Discrepancies in the description of the research reported
(3) Discrepancies between the availability of data and the research described
(4) Inappropriate citations
(5) Incoherent, meaningless and/or irrelevant content included in the article
(6) Peer-review manipulation

The presence of these indicators undermines our confidence in the integrity of the article's content and we cannot, therefore, vouch for its reliability. Please note that this notice is intended solely to alert readers that the content of this article is unreliable. We have not investigated whether authors were aware of or involved in the systematic manipulation of the publication process.

In addition, our investigation has also shown that one or more of the following human-subject reporting requirements has not been met in this article: ethical approval by an Institutional Review Board (IRB) committee or equivalent, patient/participant consent to participate, and/or agreement to publish patient/participant details (where relevant).

Wiley and Hindawi regrets that the usual quality checks did not identify these issues before publication and have since put additional measures in place to safeguard research integrity.

We wish to credit our own Research Integrity and Research Publishing teams and anonymous and named external researchers and research integrity experts for contributing to this investigation.

The corresponding author, as the representative of all authors, has been given the opportunity to register their agreement or disagreement to this retraction. We have kept a record of any response received.

References

[1] T. Tian and D. Deng, "Performance Evaluation of Hospital Economic Management with the Clustering Algorithm Oriented towards Electronic Health Management," *Journal of Healthcare Engineering*, vol. 2022, Article ID 3603353, 15 pages, 2022.

Hindawi
Journal of Healthcare Engineering
Volume 2023, Article ID 9869424, 1 page
https://doi.org/10.1155/2023/9869424

Retraction

Retracted: The Value of Python Programming in General Education and Comprehensive Quality Improvement of Medical Students Based on a Retrospective Cohort Study

Journal of Healthcare Engineering

Received 10 October 2023; Accepted 10 October 2023; Published 11 October 2023

This article has been retracted by Hindawi following an investigation undertaken by the publisher [1]. This investigation has uncovered evidence of one or more of the following indicators of systematic manipulation of the publication process:

(1) Discrepancies in scope
(2) Discrepancies in the description of the research reported
(3) Discrepancies between the availability of data and the research described
(4) Inappropriate citations
(5) Incoherent, meaningless and/or irrelevant content included in the article
(6) Peer-review manipulation

The presence of these indicators undermines our confidence in the integrity of the article's content and we cannot, therefore, vouch for its reliability. Please note that this notice is intended solely to alert readers that the content of this article is unreliable. We have not investigated whether authors were aware of or involved in the systematic manipulation of the publication process.

In addition, our investigation has also shown that one or more of the following human-subject reporting requirements has not been met in this article: ethical approval by an Institutional Review Board (IRB) committee or equivalent, patient/participant consent to participate, and/or agreement to publish patient/participant details (where relevant).

Wiley and Hindawi regrets that the usual quality checks did not identify these issues before publication and have since put additional measures in place to safeguard research integrity.

We wish to credit our own Research Integrity and Research Publishing teams and anonymous and named external researchers and research integrity experts for contributing to this investigation.

The corresponding author, as the representative of all authors, has been given the opportunity to register their agreement or disagreement to this retraction. We have kept a record of any response received.

References

[1] X. Chen and W. Liu, "The Value of Python Programming in General Education and Comprehensive Quality Improvement of Medical Students Based on a Retrospective Cohort Study," *Journal of Healthcare Engineering*, vol. 2022, Article ID 4043992, 8 pages, 2022.

Hindawi
Journal of Healthcare Engineering
Volume 2023, Article ID 9865031, 1 page
https://doi.org/10.1155/2023/9865031

Retraction

Retracted: Clinical Efficacy and Safety of Anterior Cervical Decompression versus Segmental Fusion and Posterior Expansive Canal Plasty in the Treatment of Multilevel Cervical Spondylotic Myelopathy

Journal of Healthcare Engineering

Received 10 October 2023; Accepted 10 October 2023; Published 11 October 2023

This article has been retracted by Hindawi following an investigation undertaken by the publisher [1]. This investigation has uncovered evidence of one or more of the following indicators of systematic manipulation of the publication process:

(1) Discrepancies in scope
(2) Discrepancies in the description of the research reported
(3) Discrepancies between the availability of data and the research described
(4) Inappropriate citations
(5) Incoherent, meaningless and/or irrelevant content included in the article
(6) Peer-review manipulation

The presence of these indicators undermines our confidence in the integrity of the article's content and we cannot, therefore, vouch for its reliability. Please note that this notice is intended solely to alert readers that the content of this article is unreliable. We have not investigated whether authors were aware of or involved in the systematic manipulation of the publication process.

In addition, our investigation has also shown that one or more of the following human-subject reporting requirements has not been met in this article: ethical approval by an Institutional Review Board (IRB) committee or equivalent, patient/participant consent to participate, and/or agreement to publish patient/participant details (where relevant).

Wiley and Hindawi regrets that the usual quality checks did not identify these issues before publication and have since put additional measures in place to safeguard research integrity.

We wish to credit our own Research Integrity and Research Publishing teams and anonymous and named external researchers and research integrity experts for contributing to this investigation.

The corresponding author, as the representative of all authors, has been given the opportunity to register their agreement or disagreement to this retraction. We have kept a record of any response received.

References

[1] C. Xia, F. Shi, C. Chen, J. Lv, and Q. Chen, "Clinical Efficacy and Safety of Anterior Cervical Decompression versus Segmental Fusion and Posterior Expansive Canal Plasty in the Treatment of Multilevel Cervical Spondylotic Myelopathy," *Journal of Healthcare Engineering*, vol. 2022, Article ID 7696209, 9 pages, 2022.

Hindawi
Journal of Healthcare Engineering
Volume 2023, Article ID 9850297, 1 page
https://doi.org/10.1155/2023/9850297

Retraction

Retracted: Data on the Impact of Epidemic on Nursing Staff's Mental Health in the Context of Wireless Network

Journal of Healthcare Engineering

Received 10 October 2023; Accepted 10 October 2023; Published 11 October 2023

This article has been retracted by Hindawi following an investigation undertaken by the publisher [1]. This investigation has uncovered evidence of one or more of the following indicators of systematic manipulation of the publication process:

(1) Discrepancies in scope
(2) Discrepancies in the description of the research reported
(3) Discrepancies between the availability of data and the research described
(4) Inappropriate citations
(5) Incoherent, meaningless and/or irrelevant content included in the article
(6) Peer-review manipulation

The presence of these indicators undermines our confidence in the integrity of the article's content and we cannot, therefore, vouch for its reliability. Please note that this notice is intended solely to alert readers that the content of this article is unreliable. We have not investigated whether authors were aware of or involved in the systematic manipulation of the publication process.

Wiley and Hindawi regrets that the usual quality checks did not identify these issues before publication and have since put additional measures in place to safeguard research integrity.

We wish to credit our own Research Integrity and Research Publishing teams and anonymous and named external researchers and research integrity experts for contributing to this investigation.

The corresponding author, as the representative of all authors, has been given the opportunity to register their agreement or disagreement to this retraction. We have kept a record of any response received.

References

[1] D. Guo, Y. Guo, and Y. Xing, "Data on the Impact of Epidemic on Nursing Staff's Mental Health in the Context of Wireless Network," *Journal of Healthcare Engineering*, vol. 2022, Article ID 3413815, 11 pages, 2022.

Hindawi
Journal of Healthcare Engineering
Volume 2023, Article ID 9840958, 1 page
https://doi.org/10.1155/2023/9840958

Retraction

Retracted: A Research Study to Measure the Efficacy of Terminating Cervical Cancer via Customized Optimum Pathway

Journal of Healthcare Engineering

Received 10 October 2023; Accepted 10 October 2023; Published 11 October 2023

This article has been retracted by Hindawi following an investigation undertaken by the publisher [1]. This investigation has uncovered evidence of one or more of the following indicators of systematic manipulation of the publication process:

(1) Discrepancies in scope
(2) Discrepancies in the description of the research reported
(3) Discrepancies between the availability of data and the research described
(4) Inappropriate citations
(5) Incoherent, meaningless and/or irrelevant content included in the article
(6) Peer-review manipulation

The presence of these indicators undermines our confidence in the integrity of the article's content and we cannot, therefore, vouch for its reliability. Please note that this notice is intended solely to alert readers that the content of this article is unreliable. We have not investigated whether authors were aware of or involved in the systematic manipulation of the publication process.

Wiley and Hindawi regrets that the usual quality checks did not identify these issues before publication and have since put additional measures in place to safeguard research integrity.

We wish to credit our own Research Integrity and Research Publishing teams and anonymous and named external researchers and research integrity experts for contributing to this investigation.

The corresponding author, as the representative of all authors, has been given the opportunity to register their agreement or disagreement to this retraction. We have kept a record of any response received.

References

[1] X. Zhang, H. Ma, X. Lu, and Z. Zhang, "A Research Study to Measure the Efficacy of Terminating Cervical Cancer via Customized Optimum Pathway," *Journal of Healthcare Engineering*, vol. 2022, Article ID 7872915, 6 pages, 2022.

Hindawi
Journal of Healthcare Engineering
Volume 2023, Article ID 9816857, 1 page
https://doi.org/10.1155/2023/9816857

Retraction

Retracted: Clinical Application of Artificial Intelligence: Auto-Discerning the Effectiveness of Lidocaine Concentration Levels in Osteosarcoma Femoral Tumor Segment Resection

Journal of Healthcare Engineering

Received 10 October 2023; Accepted 10 October 2023; Published 11 October 2023

This article has been retracted by Hindawi following an investigation undertaken by the publisher [1]. This investigation has uncovered evidence of one or more of the following indicators of systematic manipulation of the publication process:

(1) Discrepancies in scope
(2) Discrepancies in the description of the research reported
(3) Discrepancies between the availability of data and the research described
(4) Inappropriate citations
(5) Incoherent, meaningless and/or irrelevant content included in the article
(6) Peer-review manipulation

The presence of these indicators undermines our confidence in the integrity of the article's content and we cannot, therefore, vouch for its reliability. Please note that this notice is intended solely to alert readers that the content of this article is unreliable. We have not investigated whether authors were aware of or involved in the systematic manipulation of the publication process.

In addition, our investigation has also shown that one or more of the following human-subject reporting requirements has not been met in this article: ethical approval by an Institutional Review Board (IRB) committee or equivalent, patient/participant consent to participate, and/or agreement to publish patient/participant details (where relevant).

Wiley and Hindawi regrets that the usual quality checks did not identify these issues before publication and have since put additional measures in place to safeguard research integrity.

We wish to credit our own Research Integrity and Research Publishing teams and anonymous and named external researchers and research integrity experts for contributing to this investigation.

The corresponding author, as the representative of all authors, has been given the opportunity to register their agreement or disagreement to this retraction. We have kept a record of any response received.

References

[1] S. Ni, X. Li, and X. Yi, "Clinical Application of Artificial Intelligence: Auto-Discerning the Effectiveness of Lidocaine Concentration Levels in Osteosarcoma Femoral Tumor Segment Resection," *Journal of Healthcare Engineering*, vol. 2022, Article ID 7069348, 12 pages, 2022.

Hindawi
Journal of Healthcare Engineering
Volume 2023, Article ID 9816836, 1 page
https://doi.org/10.1155/2023/9816836

Retraction

Retracted: Clinical Observation of Laser Peripheral Iridoplasty with Number of Laser Shots in the Treatment of Acute Angle-Closure Glaucoma

Journal of Healthcare Engineering

Received 10 October 2023; Accepted 10 October 2023; Published 11 October 2023

This article has been retracted by Hindawi following an investigation undertaken by the publisher [1]. This investigation has uncovered evidence of one or more of the following indicators of systematic manipulation of the publication process:

(1) Discrepancies in scope
(2) Discrepancies in the description of the research reported
(3) Discrepancies between the availability of data and the research described
(4) Inappropriate citations
(5) Incoherent, meaningless and/or irrelevant content included in the article
(6) Peer-review manipulation

The presence of these indicators undermines our confidence in the integrity of the article's content and we cannot, therefore, vouch for its reliability. Please note that this notice is intended solely to alert readers that the content of this article is unreliable. We have not investigated whether authors were aware of or involved in the systematic manipulation of the publication process.

In addition, our investigation has also shown that one or more of the following human-subject reporting requirements has not been met in this article: ethical approval by an Institutional Review Board (IRB) committee or equivalent, patient/participant consent to participate, and/or agreement to publish patient/participant details (where relevant).

Wiley and Hindawi regrets that the usual quality checks did not identify these issues before publication and have since put additional measures in place to safeguard research integrity.

We wish to credit our own Research Integrity and Research Publishing teams and anonymous and named external researchers and research integrity experts for contributing to this investigation.

The corresponding author, as the representative of all authors, has been given the opportunity to register their agreement or disagreement to this retraction. We have kept a record of any response received.

References

[1] C. Ma, Z. Liu, W. Zhao, L. Hei, and S. Yao, "Clinical Observation of Laser Peripheral Iridoplasty with Number of Laser Shots in the Treatment of Acute Angle-Closure Glaucoma," *Journal of Healthcare Engineering*, vol. 2022, Article ID 7968999, 6 pages, 2022.

Hindawi
Journal of Healthcare Engineering
Volume 2023, Article ID 9812937, 1 page
https://doi.org/10.1155/2023/9812937

Retraction

Retracted: Machine Learning Techniques for Human Age and Gender Identification Based on Teeth X-Ray Images

Journal of Healthcare Engineering

Received 10 October 2023; Accepted 10 October 2023; Published 11 October 2023

This article has been retracted by Hindawi following an investigation undertaken by the publisher [1]. This investigation has uncovered evidence of one or more of the following indicators of systematic manipulation of the publication process:

(1) Discrepancies in scope
(2) Discrepancies in the description of the research reported
(3) Discrepancies between the availability of data and the research described
(4) Inappropriate citations
(5) Incoherent, meaningless and/or irrelevant content included in the article
(6) Peer-review manipulation

The presence of these indicators undermines our confidence in the integrity of the article's content and we cannot, therefore, vouch for its reliability. Please note that this notice is intended solely to alert readers that the content of this article is unreliable. We have not investigated whether authors were aware of or involved in the systematic manipulation of the publication process.

In addition, our investigation has also shown that one or more of the following human-subject reporting requirements has not been met in this article: ethical approval by an Institutional Review Board (IRB) committee or equivalent, patient/participant consent to participate, and/or agreement to publish patient/participant details (where relevant).

Wiley and Hindawi regrets that the usual quality checks did not identify these issues before publication and have since put additional measures in place to safeguard research integrity.

We wish to credit our own Research Integrity and Research Publishing teams and anonymous and named external researchers and research integrity experts for contributing to this investigation.

The corresponding author, as the representative of all authors, has been given the opportunity to register their agreement or disagreement to this retraction. We have kept a record of any response received.

References

[1] K. C. Santosh, N. Pradeep, V. Goel et al., "Machine Learning Techniques for Human Age and Gender Identification Based on Teeth X-Ray Images," *Journal of Healthcare Engineering*, vol. 2022, Article ID 8302674, 14 pages, 2022.

Hindawi
Journal of Healthcare Engineering
Volume 2023, Article ID 9807182, 1 page
https://doi.org/10.1155/2023/9807182

Retraction

Retracted: Effect of Carbon Dioxide on Bispectral Index of EEG under Intravenous Target-Controlled Anesthesia Based on Intelligent Medical Treatment

Journal of Healthcare Engineering

Received 10 October 2023; Accepted 10 October 2023; Published 11 October 2023

This article has been retracted by Hindawi following an investigation undertaken by the publisher [1]. This investigation has uncovered evidence of one or more of the following indicators of systematic manipulation of the publication process:

(1) Discrepancies in scope
(2) Discrepancies in the description of the research reported
(3) Discrepancies between the availability of data and the research described
(4) Inappropriate citations
(5) Incoherent, meaningless and/or irrelevant content included in the article
(6) Peer-review manipulation

The presence of these indicators undermines our confidence in the integrity of the article's content and we cannot, therefore, vouch for its reliability. Please note that this notice is intended solely to alert readers that the content of this article is unreliable. We have not investigated whether authors were aware of or involved in the systematic manipulation of the publication process.

In addition, our investigation has also shown that one or more of the following human-subject reporting requirements has not been met in this article: ethical approval by an Institutional Review Board (IRB) committee or equivalent, patient/participant consent to participate, and/or agreement to publish patient/participant details (where relevant).

Wiley and Hindawi regrets that the usual quality checks did not identify these issues before publication and have since put additional measures in place to safeguard research integrity.

We wish to credit our own Research Integrity and Research Publishing teams and anonymous and named external researchers and research integrity experts for contributing to this investigation.

The corresponding author, as the representative of all authors, has been given the opportunity to register their agreement or disagreement to this retraction. We have kept a record of any response received.

References

[1] A. Li, Q. He, R. Li, Y. Chen, and W. Xu, "Effect of Carbon Dioxide on Bispectral Index of EEG under Intravenous Target-Controlled Anesthesia Based on Intelligent Medical Treatment," *Journal of Healthcare Engineering*, vol. 2022, Article ID 4696128, 10 pages, 2022.

Hindawi
Journal of Healthcare Engineering
Volume 2023, Article ID 9754869, 1 page
https://doi.org/10.1155/2023/9754869

Retraction

Retracted: Application of Wearable Sensors in the Treatment of Cervical Spondylosis Radiculopathy with Acupuncture

Journal of Healthcare Engineering

Received 10 October 2023; Accepted 10 October 2023; Published 11 October 2023

This article has been retracted by Hindawi following an investigation undertaken by the publisher [1]. This investigation has uncovered evidence of one or more of the following indicators of systematic manipulation of the publication process:

(1) Discrepancies in scope
(2) Discrepancies in the description of the research reported
(3) Discrepancies between the availability of data and the research described
(4) Inappropriate citations
(5) Incoherent, meaningless and/or irrelevant content included in the article
(6) Peer-review manipulation

The presence of these indicators undermines our confidence in the integrity of the article's content and we cannot, therefore, vouch for its reliability. Please note that this notice is intended solely to alert readers that the content of this article is unreliable. We have not investigated whether authors were aware of or involved in the systematic manipulation of the publication process.

In addition, our investigation has also shown that one or more of the following human-subject reporting requirements has not been met in this article: ethical approval by an Institutional Review Board (IRB) committee or equivalent, patient/participant consent to participate, and/or agreement to publish patient/participant details (where relevant).

Wiley and Hindawi regrets that the usual quality checks did not identify these issues before publication and have since put additional measures in place to safeguard research integrity.

We wish to credit our own Research Integrity and Research Publishing teams and anonymous and named external researchers and research integrity experts for contributing to this investigation.

The corresponding author, as the representative of all authors, has been given the opportunity to register their agreement or disagreement to this retraction. We have kept a record of any response received.

References

[1] L. Chi and Q. Zhang, "Application of Wearable Sensors in the Treatment of Cervical Spondylosis Radiculopathy with Acupuncture," *Journal of Healthcare Engineering*, vol. 2022, Article ID 8428518, 8 pages, 2022.

Hindawi
Journal of Healthcare Engineering
Volume 2023, Article ID 9892756, 1 page
https://doi.org/10.1155/2023/9892756

Retraction

Retracted: Curative Effect of Foraminal Endoscopic Surgery and Efficacy of the Wearable Lumbar Spine Protection Equipment in the Treatment of Lumbar Disc Herniation

Journal of Healthcare Engineering

Received 3 October 2023; Accepted 3 October 2023; Published 4 October 2023

This article has been retracted by Hindawi following an investigation undertaken by the publisher [1]. This investigation has uncovered evidence of one or more of the following indicators of systematic manipulation of the publication process:

(1) Discrepancies in scope
(2) Discrepancies in the description of the research reported
(3) Discrepancies between the availability of data and the research described
(4) Inappropriate citations
(5) Incoherent, meaningless and/or irrelevant content included in the article
(6) Peer-review manipulation

The presence of these indicators undermines our confidence in the integrity of the article's content and we cannot, therefore, vouch for its reliability. Please note that this notice is intended solely to alert readers that the content of this article is unreliable. We have not investigated whether authors were aware of or involved in the systematic manipulation of the publication process.

In addition, our investigation has also shown that one or more of the following human-subject reporting requirements has not been met in this article: ethical approval by an Institutional Review Board (IRB) committee or equivalent, patient/participant consent to participate, and/or agreement to publish patient/participant details (where relevant).

Wiley and Hindawi regrets that the usual quality checks did not identify these issues before publication and have since put additional measures in place to safeguard research integrity.

We wish to credit our own Research Integrity and Research Publishing teams and anonymous and named external researchers and research integrity experts for contributing to this investigation.

The corresponding author, as the representative of all authors, has been given the opportunity to register their agreement or disagreement to this retraction. We have kept a record of any response received.

References

[1] Z. Meng, J. Zheng, K. Fu, Y. Kang, and L. Wang, "Curative Effect of Foraminal Endoscopic Surgery and Efficacy of the Wearable Lumbar Spine Protection Equipment in the Treatment of Lumbar Disc Herniation," *Journal of Healthcare Engineering*, vol. 2022, Article ID 6463863, 12 pages, 2022.

Hindawi
Journal of Healthcare Engineering
Volume 2023, Article ID 9821891, 1 page
https://doi.org/10.1155/2023/9821891

Retraction

Retracted: Analysis of the Effect of Applying Ultrasound-Guided Nerve Block Anesthesia to Fracture Patients in the Context of Internet-Based Blockchain

Journal of Healthcare Engineering

Received 3 October 2023; Accepted 3 October 2023; Published 4 October 2023

This article has been retracted by Hindawi following an investigation undertaken by the publisher [1]. This investigation has uncovered evidence of one or more of the following indicators of systematic manipulation of the publication process:

(1) Discrepancies in scope
(2) Discrepancies in the description of the research reported
(3) Discrepancies between the availability of data and the research described
(4) Inappropriate citations
(5) Incoherent, meaningless and/or irrelevant content included in the article
(6) Peer-review manipulation

The presence of these indicators undermines our confidence in the integrity of the article's content and we cannot, therefore, vouch for its reliability. Please note that this notice is intended solely to alert readers that the content of this article is unreliable. We have not investigated whether authors were aware of or involved in the systematic manipulation of the publication process.

Wiley and Hindawi regrets that the usual quality checks did not identify these issues before publication and have since put additional measures in place to safeguard research integrity.

We wish to credit our own Research Integrity and Research Publishing teams and anonymous and named external researchers and research integrity experts for contributing to this investigation.

The corresponding author, as the representative of all authors, has been given the opportunity to register their agreement or disagreement to this retraction. We have kept a record of any response received.

References

[1] Q. Cai, Y. Han, M. Gao, and S. Ni, "Analysis of the Effect of Applying Ultrasound-Guided Nerve Block Anesthesia to Fracture Patients in the Context of Internet-Based Blockchain," *Journal of Healthcare Engineering*, vol. 2022, Article ID 6324009, 11 pages, 2022.

Hindawi
Journal of Healthcare Engineering
Volume 2023, Article ID 9785132, 1 page
https://doi.org/10.1155/2023/9785132

Retraction

Retracted: Differential Prognostic Analysis of Higher and Lower PEEP in ARDS Patients: Systematic Review and Meta-Analysis

Journal of Healthcare Engineering

Received 3 October 2023; Accepted 3 October 2023; Published 4 October 2023

This article has been retracted by Hindawi following an investigation undertaken by the publisher [1]. This investigation has uncovered evidence of one or more of the following indicators of systematic manipulation of the publication process:

(1) Discrepancies in scope
(2) Discrepancies in the description of the research reported
(3) Discrepancies between the availability of data and the research described
(4) Inappropriate citations
(5) Incoherent, meaningless and/or irrelevant content included in the article
(6) Peer-review manipulation

The presence of these indicators undermines our confidence in the integrity of the article's content and we cannot, therefore, vouch for its reliability. Please note that this notice is intended solely to alert readers that the content of this article is unreliable. We have not investigated whether authors were aware of or involved in the systematic manipulation of the publication process.

Wiley and Hindawi regrets that the usual quality checks did not identify these issues before publication and have since put additional measures in place to safeguard research integrity.

We wish to credit our own Research Integrity and Research Publishing teams and anonymous and named external researchers and research integrity experts for contributing to this investigation.

The corresponding author, as the representative of all authors, has been given the opportunity to register their agreement or disagreement to this retraction. We have kept a record of any response received.

References

[1] M. Liang and X. Chen, "Differential Prognostic Analysis of Higher and Lower PEEP in ARDS Patients: Systematic Review and Meta-Analysis," *Journal of Healthcare Engineering*, vol. 2022, Article ID 5399416, 8 pages, 2022.

Hindawi
Journal of Healthcare Engineering
Volume 2023, Article ID 9767585, 1 page
https://doi.org/10.1155/2023/9767585

Retraction

Retracted: Evaluation of the Effect of Comprehensive Nursing Interventions on Plaque Control in Patients with Periodontal Disease in the Context of Artificial Intelligence

Journal of Healthcare Engineering

Received 3 October 2023; Accepted 3 October 2023; Published 4 October 2023

This article has been retracted by Hindawi following an investigation undertaken by the publisher [1]. This investigation has uncovered evidence of one or more of the following indicators of systematic manipulation of the publication process:

(1) Discrepancies in scope
(2) Discrepancies in the description of the research reported
(3) Discrepancies between the availability of data and the research described
(4) Inappropriate citations
(5) Incoherent, meaningless and/or irrelevant content included in the article
(6) Peer-review manipulation

The presence of these indicators undermines our confidence in the integrity of the article's content and we cannot, therefore, vouch for its reliability. Please note that this notice is intended solely to alert readers that the content of this article is unreliable. We have not investigated whether authors were aware of or involved in the systematic manipulation of the publication process.

In addition, our investigation has also shown that one or more of the following human-subject reporting requirements has not been met in this article: ethical approval by an Institutional Review Board (IRB) committee or equivalent, patient/participant consent to participate, and/or agreement to publish patient/participant details (where relevant).

Wiley and Hindawi regrets that the usual quality checks did not identify these issues before publication and have since put additional measures in place to safeguard research integrity.

We wish to credit our own Research Integrity and Research Publishing teams and anonymous and named external researchers and research integrity experts for contributing to this investigation.

The corresponding author, as the representative of all authors, has been given the opportunity to register their agreement or disagreement to this retraction. We have kept a record of any response received.

References

[1] J. Xu, L. Wang, H. Sun, and S. Liu, "Evaluation of the Effect of Comprehensive Nursing Interventions on Plaque Control in Patients with Periodontal Disease in the Context of Artificial Intelligence," *Journal of Healthcare Engineering*, vol. 2022, Article ID 6505672, 11 pages, 2022.

Hindawi
Journal of Healthcare Engineering
Volume 2023, Article ID 9894304, 1 page
https://doi.org/10.1155/2023/9894304

Retraction

Retracted: Regulatory Mechanism of circEIF4G2 Targeting miR-26a in Acute Myocardial Infarction

Journal of Healthcare Engineering

Received 26 September 2023; Accepted 26 September 2023; Published 27 September 2023

This article has been retracted by Hindawi following an investigation undertaken by the publisher [1]. This investigation has uncovered evidence of one or more of the following indicators of systematic manipulation of the publication process:

(1) Discrepancies in scope
(2) Discrepancies in the description of the research reported
(3) Discrepancies between the availability of data and the research described
(4) Inappropriate citations
(5) Incoherent, meaningless and/or irrelevant content included in the article
(6) Peer-review manipulation

The presence of these indicators undermines our confidence in the integrity of the article's content and we cannot, therefore, vouch for its reliability. Please note that this notice is intended solely to alert readers that the content of this article is unreliable. We have not investigated whether authors were aware of or involved in the systematic manipulation of the publication process.

Wiley and Hindawi regrets that the usual quality checks did not identify these issues before publication and have since put additional measures in place to safeguard research integrity.

We wish to credit our own Research Integrity and Research Publishing teams and anonymous and named external researchers and research integrity experts for contributing to this investigation.

The corresponding author, as the representative of all authors, has been given the opportunity to register their agreement or disagreement to this retraction. We have kept a record of any response received.

References

[1] Z. Zhang, J. Li, C. Long et al., "Regulatory Mechanism of circEIF4G2 Targeting miR-26a in Acute Myocardial Infarction," *Journal of Healthcare Engineering*, vol. 2022, Article ID 5308372, 10 pages, 2022.

Hindawi
Journal of Healthcare Engineering
Volume 2023, Article ID 9891253, 1 page
https://doi.org/10.1155/2023/9891253

Retraction

Retracted: Direct Detection of Antibiotic Resistance in Chinese *Helicobacter pylori* Clinical Isolates by Sequencing-Based Approach

Journal of Healthcare Engineering

Received 26 September 2023; Accepted 26 September 2023; Published 27 September 2023

This article has been retracted by Hindawi following an investigation undertaken by the publisher [1]. This investigation has uncovered evidence of one or more of the following indicators of systematic manipulation of the publication process:

(1) Discrepancies in scope
(2) Discrepancies in the description of the research reported
(3) Discrepancies between the availability of data and the research described
(4) Inappropriate citations
(5) Incoherent, meaningless and/or irrelevant content included in the article
(6) Peer-review manipulation

The presence of these indicators undermines our confidence in the integrity of the article's content and we cannot, therefore, vouch for its reliability. Please note that this notice is intended solely to alert readers that the content of this article is unreliable. We have not investigated whether authors were aware of or involved in the systematic manipulation of the publication process.

In addition, our investigation has also shown that one or more of the following human-subject reporting requirements has not been met in this article: ethical approval by an Institutional Review Board (IRB) committee or equivalent, patient/participant consent to participate, and/or agreement to publish patient/participant details (where relevant).

Wiley and Hindawi regrets that the usual quality checks did not identify these issues before publication and have since put additional measures in place to safeguard research integrity.

We wish to credit our own Research Integrity and Research Publishing teams and anonymous and named external researchers and research integrity experts for contributing to this investigation.

The corresponding author, as the representative of all authors, has been given the opportunity to register their agreement or disagreement to this retraction. We have kept a record of any response received.

References

[1] L. Tian, Y. Yao, L. Yin et al., "Direct Detection of Antibiotic Resistance in Chinese *Helicobacter pylori* Clinical Isolates by Sequencing-Based Approach," *Journal of Healthcare Engineering*, vol. 2022, Article ID 6436256, 6 pages, 2022.

Hindawi
Journal of Healthcare Engineering
Volume 2023, Article ID 9878174, 1 page
https://doi.org/10.1155/2023/9878174

Retraction

Retracted: Analysis of the Mechanism of Ureproofing Technology and Postlaparoscopy on Patients with Urology and Infection

Journal of Healthcare Engineering

Received 26 September 2023; Accepted 26 September 2023; Published 27 September 2023

This article has been retracted by Hindawi following an investigation undertaken by the publisher [1]. This investigation has uncovered evidence of one or more of the following indicators of systematic manipulation of the publication process:

(1) Discrepancies in scope
(2) Discrepancies in the description of the research reported
(3) Discrepancies between the availability of data and the research described
(4) Inappropriate citations
(5) Incoherent, meaningless and/or irrelevant content included in the article
(6) Peer-review manipulation

The presence of these indicators undermines our confidence in the integrity of the article's content and we cannot, therefore, vouch for its reliability. Please note that this notice is intended solely to alert readers that the content of this article is unreliable. We have not investigated whether authors were aware of or involved in the systematic manipulation of the publication process.

Wiley and Hindawi regrets that the usual quality checks did not identify these issues before publication and have since put additional measures in place to safeguard research integrity.

We wish to credit our own Research Integrity and Research Publishing teams and anonymous and named external researchers and research integrity experts for contributing to this investigation.

The corresponding author, as the representative of all authors, has been given the opportunity to register their agreement or disagreement to this retraction. We have kept a record of any response received.

References

[1] S. Chen, Y. Zhang, P. Shen, Z. Huang, M. Lin, and J. Huang, "Analysis of the Mechanism of Ureproofing Technology and Postlaparoscopy on Patients with Urology and Infection," *Journal of Healthcare Engineering*, vol. 2022, Article ID 4373416, 6 pages, 2022.

Hindawi
Journal of Healthcare Engineering
Volume 2023, Article ID 9871960, 1 page
https://doi.org/10.1155/2023/9871960

Retraction

Retracted: Consistency Analysis of CTLM Imaging and Mammography in the Diagnosis of Breast Tumor Lesions

Journal of Healthcare Engineering

Received 26 September 2023; Accepted 26 September 2023; Published 27 September 2023

This article has been retracted by Hindawi following an investigation undertaken by the publisher [1]. This investigation has uncovered evidence of one or more of the following indicators of systematic manipulation of the publication process:

(1) Discrepancies in scope
(2) Discrepancies in the description of the research reported
(3) Discrepancies between the availability of data and the research described
(4) Inappropriate citations
(5) Incoherent, meaningless and/or irrelevant content included in the article
(6) Peer-review manipulation

The presence of these indicators undermines our confidence in the integrity of the article's content and we cannot, therefore, vouch for its reliability. Please note that this notice is intended solely to alert readers that the content of this article is unreliable. We have not investigated whether authors were aware of or involved in the systematic manipulation of the publication process.

In addition, our investigation has also shown that one or more of the following human-subject reporting requirements has not been met in this article: ethical approval by an Institutional Review Board (IRB) committee or equivalent, patient/participant consent to participate, and/or agreement to publish patient/participant details (where relevant).

Wiley and Hindawi regrets that the usual quality checks did not identify these issues before publication and have since put additional measures in place to safeguard research integrity.

We wish to credit our own Research Integrity and Research Publishing teams and anonymous and named external researchers and research integrity experts for contributing to this investigation.

The corresponding author, as the representative of all authors, has been given the opportunity to register their agreement or disagreement to this retraction. We have kept a record of any response received.

References

[1] Z. Song, H. Wang, X. Feng, X. Yang, P. Han, and J. Zhao, "Consistency Analysis of CTLM Imaging and Mammography in the Diagnosis of Breast Tumor Lesions," *Journal of Healthcare Engineering*, vol. 2022, Article ID 5391636, 8 pages, 2022.

Hindawi
Journal of Healthcare Engineering
Volume 2023, Article ID 9862546, 1 page
https://doi.org/10.1155/2023/9862546

Retraction

Retracted: Two Different Transplant Preconditioning Regimens Combined with Irradiation and Chemotherapy in the Treatment of Childhood Leukemia: Systematic Review and Meta-Analysis

Journal of Healthcare Engineering

Received 26 September 2023; Accepted 26 September 2023; Published 27 September 2023

This article has been retracted by Hindawi following an investigation undertaken by the publisher [1]. This investigation has uncovered evidence of one or more of the following indicators of systematic manipulation of the publication process:

(1) Discrepancies in scope
(2) Discrepancies in the description of the research reported
(3) Discrepancies between the availability of data and the research described
(4) Inappropriate citations
(5) Incoherent, meaningless and/or irrelevant content included in the article
(6) Peer-review manipulation

The presence of these indicators undermines our confidence in the integrity of the article's content and we cannot, therefore, vouch for its reliability. Please note that this notice is intended solely to alert readers that the content of this article is unreliable. We have not investigated whether authors were aware of or involved in the systematic manipulation of the publication process.

Wiley and Hindawi regrets that the usual quality checks did not identify these issues before publication and have since put additional measures in place to safeguard research integrity.

We wish to credit our own Research Integrity and Research Publishing teams and anonymous and named external researchers and research integrity experts for contributing to this investigation.

The corresponding author, as the representative of all authors, has been given the opportunity to register their agreement or disagreement to this retraction. We have kept a record of any response received.

References

[1] X. Wang, D. Mu, A. Geng, A. Zhao, and Y. Song, "Two Different Transplant Preconditioning Regimens Combined with Irradiation and Chemotherapy in the Treatment of Childhood Leukemia: Systematic Review and Meta-Analysis," *Journal of Healthcare Engineering*, vol. 2022, Article ID 2825712, 9 pages, 2022.

Hindawi
Journal of Healthcare Engineering
Volume 2023, Article ID 9860989, 1 page
https://doi.org/10.1155/2023/9860989

Retraction

Retracted: Effect of Transumbilical Single-Port Laparoscopic-Assisted Duhamel Operation on Serum CRP and IL-6 Levels in Children with Hirschsprung's Disease

Journal of Healthcare Engineering

Received 26 September 2023; Accepted 26 September 2023; Published 27 September 2023

This article has been retracted by Hindawi following an investigation undertaken by the publisher [1]. This investigation has uncovered evidence of one or more of the following indicators of systematic manipulation of the publication process:

(1) Discrepancies in scope
(2) Discrepancies in the description of the research reported
(3) Discrepancies between the availability of data and the research described
(4) Inappropriate citations
(5) Incoherent, meaningless and/or irrelevant content included in the article
(6) Peer-review manipulation

The presence of these indicators undermines our confidence in the integrity of the article's content and we cannot, therefore, vouch for its reliability. Please note that this notice is intended solely to alert readers that the content of this article is unreliable. We have not investigated whether authors were aware of or involved in the systematic manipulation of the publication process.

In addition, our investigation has also shown that one or more of the following human-subject reporting requirements has not been met in this article: ethical approval by an Institutional Review Board (IRB) committee or equivalent, patient/participant consent to participate, and/or agreement to publish patient/participant details (where relevant).

Wiley and Hindawi regrets that the usual quality checks did not identify these issues before publication and have since put additional measures in place to safeguard research integrity.

We wish to credit our own Research Integrity and Research Publishing teams and anonymous and named external researchers and research integrity experts for contributing to this investigation.

The corresponding author, as the representative of all authors, has been given the opportunity to register their agreement or disagreement to this retraction. We have kept a record of any response received.

References

[1] M. Wang, W. Pang, L. Zhou, J. Ma, and S. Xie, "Effect of Transumbilical Single-Port Laparoscopic-Assisted Duhamel Operation on Serum CRP and IL-6 Levels in Children with Hirschsprung's Disease," *Journal of Healthcare Engineering*, vol. 2022, Article ID 8349851, 8 pages, 2022.

Hindawi
Journal of Healthcare Engineering
Volume 2023, Article ID 9858470, 1 page
https://doi.org/10.1155/2023/9858470

Retraction

Retracted: Opioid-Free Labor Analgesia: Dexmedetomidine as an Adjuvant Combined with Ropivacaine

Journal of Healthcare Engineering

Received 26 September 2023; Accepted 26 September 2023; Published 27 September 2023

This article has been retracted by Hindawi following an investigation undertaken by the publisher [1]. This investigation has uncovered evidence of one or more of the following indicators of systematic manipulation of the publication process:

(1) Discrepancies in scope
(2) Discrepancies in the description of the research reported
(3) Discrepancies between the availability of data and the research described
(4) Inappropriate citations
(5) Incoherent, meaningless and/or irrelevant content included in the article
(6) Peer-review manipulation

The presence of these indicators undermines our confidence in the integrity of the article's content and we cannot, therefore, vouch for its reliability. Please note that this notice is intended solely to alert readers that the content of this article is unreliable. We have not investigated whether authors were aware of or involved in the systematic manipulation of the publication process.

Wiley and Hindawi regrets that the usual quality checks did not identify these issues before publication and have since put additional measures in place to safeguard research integrity.

We wish to credit our own Research Integrity and Research Publishing teams and anonymous and named external researchers and research integrity experts for contributing to this investigation.

The corresponding author, as the representative of all authors, has been given the opportunity to register their agreement or disagreement to this retraction. We have kept a record of any response received.

References

[1] W. Gao, J. Wang, Z. Zhang et al., "Opioid-Free Labor Analgesia: Dexmedetomidine as an Adjuvant Combined with Ropivacaine," *Journal of Healthcare Engineering*, vol. 2022, Article ID 2235025, 7 pages, 2022.

Hindawi
Journal of Healthcare Engineering
Volume 2023, Article ID 9851285, 1 page
https://doi.org/10.1155/2023/9851285

Retraction

Retracted: Effects of Different Intervention Methods on Intestinal Cleanliness in Children Undergoing Colonoscopy

Journal of Healthcare Engineering

Received 26 September 2023; Accepted 26 September 2023; Published 27 September 2023

This article has been retracted by Hindawi following an investigation undertaken by the publisher [1]. This investigation has uncovered evidence of one or more of the following indicators of systematic manipulation of the publication process:

(1) Discrepancies in scope
(2) Discrepancies in the description of the research reported
(3) Discrepancies between the availability of data and the research described
(4) Inappropriate citations
(5) Incoherent, meaningless and/or irrelevant content included in the article
(6) Peer-review manipulation

The presence of these indicators undermines our confidence in the integrity of the article's content and we cannot, therefore, vouch for its reliability. Please note that this notice is intended solely to alert readers that the content of this article is unreliable. We have not investigated whether authors were aware of or involved in the systematic manipulation of the publication process.

Wiley and Hindawi regrets that the usual quality checks did not identify these issues before publication and have since put additional measures in place to safeguard research integrity.

We wish to credit our own Research Integrity and Research Publishing teams and anonymous and named external researchers and research integrity experts for contributing to this investigation.

The corresponding author, as the representative of all authors, has been given the opportunity to register their agreement or disagreement to this retraction. We have kept a record of any response received.

References

[1] Y. Yang, Y. Xiao, L. Zhang, J. Lv, and Q. Huang, "Effects of Different Intervention Methods on Intestinal Cleanliness in Children Undergoing Colonoscopy," *Journal of Healthcare Engineering*, vol. 2022, Article ID 1898610, 7 pages, 2022.

Hindawi
Journal of Healthcare Engineering
Volume 2023, Article ID 9849480, 1 page
https://doi.org/10.1155/2023/9849480

Retraction

Retracted: Prophylactic Use of Antibiotics for Postsurgical Infection in c-TACE and DEB-TACE High-Risk Patients: A Case-Control Study

Journal of Healthcare Engineering

Received 26 September 2023; Accepted 26 September 2023; Published 27 September 2023

This article has been retracted by Hindawi following an investigation undertaken by the publisher [1]. This investigation has uncovered evidence of one or more of the following indicators of systematic manipulation of the publication process:

(1) Discrepancies in scope
(2) Discrepancies in the description of the research reported
(3) Discrepancies between the availability of data and the research described
(4) Inappropriate citations
(5) Incoherent, meaningless and/or irrelevant content included in the article
(6) Peer-review manipulation

The presence of these indicators undermines our confidence in the integrity of the article's content and we cannot, therefore, vouch for its reliability. Please note that this notice is intended solely to alert readers that the content of this article is unreliable. We have not investigated whether authors were aware of or involved in the systematic manipulation of the publication process.

In addition, our investigation has also shown that one or more of the following human-subject reporting requirements has not been met in this article: ethical approval by an Institutional Review Board (IRB) committee or equivalent, patient/participant consent to participate, and/or agreement to publish patient/participant details (where relevant).

Wiley and Hindawi regrets that the usual quality checks did not identify these issues before publication and have since put additional measures in place to safeguard research integrity.

We wish to credit our own Research Integrity and Research Publishing teams and anonymous and named external researchers and research integrity experts for contributing to this investigation.

The corresponding author, as the representative of all authors, has been given the opportunity to register their agreement or disagreement to this retraction. We have kept a record of any response received.

References

[1] B. Li, "Prophylactic Use of Antibiotics for Postsurgical Infection in c-TACE and DEB-TACE High-Risk Patients: A Case-Control Study," *Journal of Healthcare Engineering*, vol. 2022, Article ID 6203817, 8 pages, 2022.

Hindawi
Journal of Healthcare Engineering
Volume 2023, Article ID 9848967, 1 page
https://doi.org/10.1155/2023/9848967

Retraction

Retracted: Effect of Uterine Artery Ligation and Uterine Artery Embolization on Postpartum Hemorrhage Due to Uterine Asthenia after Cesarean Section and Its Effect on Blood Flow and Function of Uterine and Ovarian Arteries

Journal of Healthcare Engineering

Received 26 September 2023; Accepted 26 September 2023; Published 27 September 2023

This article has been retracted by Hindawi following an investigation undertaken by the publisher [1]. This investigation has uncovered evidence of one or more of the following indicators of systematic manipulation of the publication process:

(1) Discrepancies in scope
(2) Discrepancies in the description of the research reported
(3) Discrepancies between the availability of data and the research described
(4) Inappropriate citations
(5) Incoherent, meaningless and/or irrelevant content included in the article
(6) Peer-review manipulation

The presence of these indicators undermines our confidence in the integrity of the article's content and we cannot, therefore, vouch for its reliability. Please note that this notice is intended solely to alert readers that the content of this article is unreliable. We have not investigated whether authors were aware of or involved in the systematic manipulation of the publication process.

Wiley and Hindawi regrets that the usual quality checks did not identify these issues before publication and have since put additional measures in place to safeguard research integrity.

We wish to credit our own Research Integrity and Research Publishing teams and anonymous and named external researchers and research integrity experts for contributing to this investigation.

The corresponding author, as the representative of all authors, has been given the opportunity to register their agreement or disagreement to this retraction. We have kept a record of any response received.

References

[1] W. Liu and W. Yin, "Effect of Uterine Artery Ligation and Uterine Artery Embolization on Postpartum Hemorrhage Due to Uterine Asthenia after Cesarean Section and Its Effect on Blood Flow and Function of Uterine and Ovarian Arteries," *Journal of Healthcare Engineering*, vol. 2022, Article ID 1337234, 6 pages, 2022.

Hindawi
Journal of Healthcare Engineering
Volume 2023, Article ID 9836851, 1 page
https://doi.org/10.1155/2023/9836851

Retraction

Retracted: The Application and Efficacy Evaluation of Autologous Fat Transplantation in Antiaging of the Face: Systematic Review and Meta-Analysis

Journal of Healthcare Engineering

Received 26 September 2023; Accepted 26 September 2023; Published 27 September 2023

This article has been retracted by Hindawi following an investigation undertaken by the publisher [1]. This investigation has uncovered evidence of one or more of the following indicators of systematic manipulation of the publication process:

(1) Discrepancies in scope
(2) Discrepancies in the description of the research reported
(3) Discrepancies between the availability of data and the research described
(4) Inappropriate citations
(5) Incoherent, meaningless and/or irrelevant content included in the article
(6) Peer-review manipulation

The presence of these indicators undermines our confidence in the integrity of the article's content and we cannot, therefore, vouch for its reliability. Please note that this notice is intended solely to alert readers that the content of this article is unreliable. We have not investigated whether authors were aware of or involved in the systematic manipulation of the publication process.

Wiley and Hindawi regrets that the usual quality checks did not identify these issues before publication and have since put additional measures in place to safeguard research integrity.

We wish to credit our own Research Integrity and Research Publishing teams and anonymous and named external researchers and research integrity experts for contributing to this investigation.

The corresponding author, as the representative of all authors, has been given the opportunity to register their agreement or disagreement to this retraction. We have kept a record of any response received.

References

[1] J. Li, K. Zhang, and H. Zhang, "The Application and Efficacy Evaluation of Autologous Fat Transplantation in Antiaging of the Face: Systematic Review and Meta-Analysis," *Journal of Healthcare Engineering*, vol. 2022, Article ID 5744123, 9 pages, 2022.

Hindawi
Journal of Healthcare Engineering
Volume 2023, Article ID 9835702, 1 page
https://doi.org/10.1155/2023/9835702

Retraction

Retracted: Role of miR-181b/Notch1 Axis in circ_TNPO1 Promotion of Proliferation and Migration of Atherosclerotic Vascular Smooth Muscle Cells

Journal of Healthcare Engineering

Received 26 September 2023; Accepted 26 September 2023; Published 27 September 2023

This article has been retracted by Hindawi following an investigation undertaken by the publisher [1]. This investigation has uncovered evidence of one or more of the following indicators of systematic manipulation of the publication process:

(1) Discrepancies in scope
(2) Discrepancies in the description of the research reported
(3) Discrepancies between the availability of data and the research described
(4) Inappropriate citations
(5) Incoherent, meaningless and/or irrelevant content included in the article
(6) Peer-review manipulation

The presence of these indicators undermines our confidence in the integrity of the article's content and we cannot, therefore, vouch for its reliability. Please note that this notice is intended solely to alert readers that the content of this article is unreliable. We have not investigated whether authors were aware of or involved in the systematic manipulation of the publication process.

In addition, our investigation has also shown that one or more of the following human-subject reporting requirements has not been met in this article: ethical approval by an Institutional Review Board (IRB) committee or equivalent, patient/participant consent to participate, and/or agreement to publish patient/participant details (where relevant).

Wiley and Hindawi regrets that the usual quality checks did not identify these issues before publication and have since put additional measures in place to safeguard research integrity.

We wish to credit our own Research Integrity and Research Publishing teams and anonymous and named external researchers and research integrity experts for contributing to this investigation.

The corresponding author, as the representative of all authors, has been given the opportunity to register their agreement or disagreement to this retraction. We have kept a record of any response received.

References

[1] M. Chen, F. Li, Q. Jiang, W. Zhang, Z. Li, and W. Tang, "Role of miR-181b/Notch1 Axis in circ_TNPO1 Promotion of Proliferation and Migration of Atherosclerotic Vascular Smooth Muscle Cells," *Journal of Healthcare Engineering*, vol. 2022, Article ID 4086935, 12 pages, 2022.

Hindawi
Journal of Healthcare Engineering
Volume 2023, Article ID 9824018, 1 page
https://doi.org/10.1155/2023/9824018

Retraction

Retracted: Efficacy of Glucocorticoid plus Intravenous Immunoglobulin in Children with Immunoglobulin-Insensitive Kawasaki Disease

Journal of Healthcare Engineering

Received 26 September 2023; Accepted 26 September 2023; Published 27 September 2023

This article has been retracted by Hindawi following an investigation undertaken by the publisher [1]. This investigation has uncovered evidence of one or more of the following indicators of systematic manipulation of the publication process:

(1) Discrepancies in scope
(2) Discrepancies in the description of the research reported
(3) Discrepancies between the availability of data and the research described
(4) Inappropriate citations
(5) Incoherent, meaningless and/or irrelevant content included in the article
(6) Peer-review manipulation

The presence of these indicators undermines our confidence in the integrity of the article's content and we cannot, therefore, vouch for its reliability. Please note that this notice is intended solely to alert readers that the content of this article is unreliable. We have not investigated whether authors were aware of or involved in the systematic manipulation of the publication process.

Wiley and Hindawi regrets that the usual quality checks did not identify these issues before publication and have since put additional measures in place to safeguard research integrity.

We wish to credit our own Research Integrity and Research Publishing teams and anonymous and named external researchers and research integrity experts for contributing to this investigation.

The corresponding author, as the representative of all authors, has been given the opportunity to register their agreement or disagreement to this retraction. We have kept a record of any response received.

References

[1] Y. Ma, J. Zhang, and R. Fan, "Efficacy of Glucocorticoid plus Intravenous Immunoglobulin in Children with Immunoglobulin-Insensitive Kawasaki Disease," *Journal of Healthcare Engineering*, vol. 2022, Article ID 9011259, 6 pages, 2022.

Hindawi
Journal of Healthcare Engineering
Volume 2023, Article ID 9818379, 1 page
https://doi.org/10.1155/2023/9818379

Retraction

Retracted: Serum Expression Level of MicroRNA-122 and Its Significance in Patients with Hepatitis B Virus Infection

Journal of Healthcare Engineering

Received 26 September 2023; Accepted 26 September 2023; Published 27 September 2023

This article has been retracted by Hindawi following an investigation undertaken by the publisher [1]. This investigation has uncovered evidence of one or more of the following indicators of systematic manipulation of the publication process:

(1) Discrepancies in scope
(2) Discrepancies in the description of the research reported
(3) Discrepancies between the availability of data and the research described
(4) Inappropriate citations
(5) Incoherent, meaningless and/or irrelevant content included in the article
(6) Peer-review manipulation

The presence of these indicators undermines our confidence in the integrity of the article's content and we cannot, therefore, vouch for its reliability. Please note that this notice is intended solely to alert readers that the content of this article is unreliable. We have not investigated whether authors were aware of or involved in the systematic manipulation of the publication process.

Wiley and Hindawi regrets that the usual quality checks did not identify these issues before publication and have since put additional measures in place to safeguard research integrity.

We wish to credit our own Research Integrity and Research Publishing teams and anonymous and named external researchers and research integrity experts for contributing to this investigation.

The corresponding author, as the representative of all authors, has been given the opportunity to register their agreement or disagreement to this retraction. We have kept a record of any response received.

References

[1] Q. Fang, W. Chen, Y. Jian et al., "Serum Expression Level of MicroRNA-122 and Its Significance in Patients with Hepatitis B Virus Infection," *Journal of Healthcare Engineering*, vol. 2022, Article ID 8430276, 7 pages, 2022.

Hindawi
Journal of Healthcare Engineering
Volume 2023, Article ID 9813403, 1 page
https://doi.org/10.1155/2023/9813403

Retraction

Retracted: The Progress of Functional Magnetic Resonance Imaging in Patients with Poststroke Aphasia

Journal of Healthcare Engineering

Received 26 September 2023; Accepted 26 September 2023; Published 27 September 2023

This article has been retracted by Hindawi following an investigation undertaken by the publisher [1]. This investigation has uncovered evidence of one or more of the following indicators of systematic manipulation of the publication process:

(1) Discrepancies in scope
(2) Discrepancies in the description of the research reported
(3) Discrepancies between the availability of data and the research described
(4) Inappropriate citations
(5) Incoherent, meaningless and/or irrelevant content included in the article
(6) Peer-review manipulation

The presence of these indicators undermines our confidence in the integrity of the article's content and we cannot, therefore, vouch for its reliability. Please note that this notice is intended solely to alert readers that the content of this article is unreliable. We have not investigated whether authors were aware of or involved in the systematic manipulation of the publication process.

In addition, our investigation has also shown that one or more of the following human-subject reporting requirements has not been met in this article: ethical approval by an Institutional Review Board (IRB) committee or equivalent, patient/participant consent to participate, and/or agreement to publish patient/participant details (where relevant).

Wiley and Hindawi regrets that the usual quality checks did not identify these issues before publication and have since put additional measures in place to safeguard research integrity.

We wish to credit our own Research Integrity and Research Publishing teams and anonymous and named external researchers and research integrity experts for contributing to this investigation.

The corresponding author, as the representative of all authors, has been given the opportunity to register their agreement or disagreement to this retraction. We have kept a record of any response received.

References

[1] J. Tang, X. Xiang, and X. Cheng, "The Progress of Functional Magnetic Resonance Imaging in Patients with Poststroke Aphasia," *Journal of Healthcare Engineering*, vol. 2022, Article ID 3270534, 7 pages, 2022.

Hindawi
Journal of Healthcare Engineering
Volume 2023, Article ID 9806864, 1 page
https://doi.org/10.1155/2023/9806864

Retraction

Retracted: Clinical Observation and Pharmacoeconomic Evaluations of Original Research Drug and Generic Drug Bortezomib in the Treatment of Multiple Myeloma

Journal of Healthcare Engineering

Received 26 September 2023; Accepted 26 September 2023; Published 27 September 2023

This article has been retracted by Hindawi following an investigation undertaken by the publisher [1]. This investigation has uncovered evidence of one or more of the following indicators of systematic manipulation of the publication process:

(1) Discrepancies in scope
(2) Discrepancies in the description of the research reported
(3) Discrepancies between the availability of data and the research described
(4) Inappropriate citations
(5) Incoherent, meaningless and/or irrelevant content included in the article
(6) Peer-review manipulation

The presence of these indicators undermines our confidence in the integrity of the article's content and we cannot, therefore, vouch for its reliability. Please note that this notice is intended solely to alert readers that the content of this article is unreliable. We have not investigated whether authors were aware of or involved in the systematic manipulation of the publication process.

In addition, our investigation has also shown that one or more of the following human-subject reporting requirements has not been met in this article: ethical approval by an Institutional Review Board (IRB) committee or equivalent, patient/participant consent to participate, and/or agreement to publish patient/participant details (where relevant).

Wiley and Hindawi regrets that the usual quality checks did not identify these issues before publication and have since put additional measures in place to safeguard research integrity.

We wish to credit our own Research Integrity and Research Publishing teams and anonymous and named external researchers and research integrity experts for contributing to this investigation.

The corresponding author, as the representative of all authors, has been given the opportunity to register their agreement or disagreement to this retraction. We have kept a record of any response received.

References

[1] Y. Liang, Y. Zhu, Y. Zhang et al., "Clinical Observation and Pharmacoeconomic Evaluations of Original Research Drug and Generic Drug Bortezomib in the Treatment of Multiple Myeloma," *Journal of Healthcare Engineering*, vol. 2022, Article ID 5201354, 7 pages, 2022.

Hindawi
Journal of Healthcare Engineering
Volume 2023, Article ID 9789750, 1 page
https://doi.org/10.1155/2023/9789750

Retraction

Retracted: Estimation of Soft and Hard Tissue Revolutionization Surrounding Dental Implant: A 2-Year Retrospective Study

Journal of Healthcare Engineering

Received 26 September 2023; Accepted 26 September 2023; Published 27 September 2023

This article has been retracted by Hindawi following an investigation undertaken by the publisher [1]. This investigation has uncovered evidence of one or more of the following indicators of systematic manipulation of the publication process:

(1) Discrepancies in scope
(2) Discrepancies in the description of the research reported
(3) Discrepancies between the availability of data and the research described
(4) Inappropriate citations
(5) Incoherent, meaningless and/or irrelevant content included in the article
(6) Peer-review manipulation

The presence of these indicators undermines our confidence in the integrity of the article's content and we cannot, therefore, vouch for its reliability. Please note that this notice is intended solely to alert readers that the content of this article is unreliable. We have not investigated whether authors were aware of or involved in the systematic manipulation of the publication process.

Wiley and Hindawi regrets that the usual quality checks did not identify these issues before publication and have since put additional measures in place to safeguard research integrity.

We wish to credit our own Research Integrity and Research Publishing teams and anonymous and named external researchers and research integrity experts for contributing to this investigation.

The corresponding author, as the representative of all authors, has been given the opportunity to register their agreement or disagreement to this retraction. We have kept a record of any response received.

References

[1] M. M. Al-Ahmari, "Estimation of Soft and Hard Tissue Revolutionization Surrounding Dental Implant: A 2-Year Retrospective Study," *Journal of Healthcare Engineering*, vol. 2022, Article ID 1540668, 6 pages, 2022.

Hindawi
Journal of Healthcare Engineering
Volume 2023, Article ID 9758310, 1 page
https://doi.org/10.1155/2023/9758310

Retraction

Retracted: Efficacy of Human Adipose Derived Mesenchymal Stem Cells in Promoting Skin Wound Healing

Journal of Healthcare Engineering

Received 26 September 2023; Accepted 26 September 2023; Published 27 September 2023

This article has been retracted by Hindawi following an investigation undertaken by the publisher [1]. This investigation has uncovered evidence of one or more of the following indicators of systematic manipulation of the publication process:

(1) Discrepancies in scope
(2) Discrepancies in the description of the research reported
(3) Discrepancies between the availability of data and the research described
(4) Inappropriate citations
(5) Incoherent, meaningless and/or irrelevant content included in the article
(6) Peer-review manipulation

The presence of these indicators undermines our confidence in the integrity of the article's content and we cannot, therefore, vouch for its reliability. Please note that this notice is intended solely to alert readers that the content of this article is unreliable. We have not investigated whether authors were aware of or involved in the systematic manipulation of the publication process.

Wiley and Hindawi regrets that the usual quality checks did not identify these issues before publication and have since put additional measures in place to safeguard research integrity.

We wish to credit our own Research Integrity and Research Publishing teams and anonymous and named external researchers and research integrity experts for contributing to this investigation.

The corresponding author, as the representative of all authors, has been given the opportunity to register their agreement or disagreement to this retraction. We have kept a record of any response received.

References

[1] L. Zhou, H. Wang, S. Yao, L. Li, and X. Kuang, "Efficacy of Human Adipose Derived Mesenchymal Stem Cells in Promoting Skin Wound Healing," *Journal of Healthcare Engineering*, vol. 2022, Article ID 6590025, 5 pages, 2022.

Hindawi
Journal of Healthcare Engineering
Volume 2023, Article ID 9849835, 1 page
https://doi.org/10.1155/2023/9849835

Retraction

Retracted: Exploring the Effect of Enbrel Softgels on PWI Indicators in VCIND Patients

Journal of Healthcare Engineering

Received 19 September 2023; Accepted 19 September 2023; Published 20 September 2023

This article has been retracted by Hindawi following an investigation undertaken by the publisher [1]. This investigation has uncovered evidence of one or more of the following indicators of systematic manipulation of the publication process:

(1) Discrepancies in scope
(2) Discrepancies in the description of the research reported
(3) Discrepancies between the availability of data and the research described
(4) Inappropriate citations
(5) Incoherent, meaningless and/or irrelevant content included in the article
(6) Peer-review manipulation

The presence of these indicators undermines our confidence in the integrity of the article's content and we cannot, therefore, vouch for its reliability. Please note that this notice is intended solely to alert readers that the content of this article is unreliable. We have not investigated whether authors were aware of or involved in the systematic manipulation of the publication process.

In addition, our investigation has also shown that one or more of the following human-subject reporting requirements has not been met in this article: ethical approval by an Institutional Review Board (IRB) committee or equivalent, patient/participant consent to participate, and/or agreement to publish patient/participant details (where relevant).

Wiley and Hindawi regrets that the usual quality checks did not identify these issues before publication and have since put additional measures in place to safeguard research integrity.

We wish to credit our own Research Integrity and Research Publishing teams and anonymous and named external researchers and research integrity experts for contributing to this investigation.

The corresponding author, as the representative of all authors, has been given the opportunity to register their agreement or disagreement to this retraction. We have kept a record of any response received.

References

[1] L. Cui, P. Li, J. Zhang, and X. Li, "Exploring the Effect of Enbrel Softgels on PWI Indicators in VCIND Patients," *Journal of Healthcare Engineering*, vol. 2022, Article ID 9681235, 7 pages, 2022.

Hindawi
Journal of Healthcare Engineering
Volume 2023, Article ID 3571769, 7 pages
https://doi.org/10.1155/2023/3571769

Research Article

Model Selection and Identification of Osteoporosis Risk Factors in Women to Improve Their Healthcare

Faisal Maqbool Zahid ,[1,2] Shahla Faisal ,[1,2] Shahid Kamal,[3] Khawar Shahzad,[4] Seemi Iram,[1] Bright Opoku Ahinkorah,[5] Abdul-Aziz Seidu,[6,7,8] Abid Rasheed,[9] and John Elvis Hagan [10,11]

[1]*Department of Statistics, Government College University, Faisalabad, Pakistan*
[2]*Center of Data Science, Government College University, Faisalabad, Pakistan*
[3]*College of Statistical and Actuarial Sciences, University of the Punjab, Lahore, Pakistan*
[4]*Consultant Orthopedic Surgeon, District Headquarters (DHQ) Hospital, Faisalabad, Pakistan*
[5]*School of Public Health, University of Technology Sydney, Sydney, New South Wales 2007, Australia*
[6]*Department of Estate Management, Takoradi Technical University, Takoradi, Ghana*
[7]*Centre for Gender and Advocacy, Takoradi Technical University, Takoradi, Ghana*
[8]*College of Public Health, Medical and Veterinary Sciences, James Cook University, Townsville, Queensland 4811, Australia*
[9]*Faculty of Medical Sciences, Government College University, Faisalabad, Pakistan*
[10]*Department of Health, Physical Education,and Recreation, University of Cape Coast, Cape Coast, PMB, Ghana*
[11]*Neurocognition and Action-Biomechanics-Research Group, Faculty of Psychology and Sports Science, Bielefeld University, Postfach 10 01 31, 33501 Bielefeld, Germany*

Correspondence should be addressed to Shahla Faisal; drshahlafaisal@gcuf.edu.pk and John Elvis Hagan; elvis.hagan@ucc.edu.gh

Received 5 February 2022; Accepted 11 April 2022; Published 10 July 2023

Academic Editor: Sahfqat Ullah Khan

Osteoporosis is characterized by low bone mineral density leading to enhanced bone fragility and a consequent increase in fracture risk. The focus of this case-control study was to identify significant socioeconomic risk factors of osteoporosis in Pakistani women and examine how the risk increases for different levels of risk factors. A case-control study was conducted from November 2018 to August 2019 in two main hospitals in Faisalabad, Pakistan. Multiple logistic regression was used to explore the significant risk factors of osteoporosis and how the risk increases in cases (cases = 120) as compared to the control group (controls = 120) in the presence of these risk factors. The mean age ± standard deviation for cases and controls was 59.62 ± 10.75 and 54.27 ± 10.09, respectively. The minimum and maximum ages were 36 and 80 years, respectively. In addition to age, bone fracture, family history, regular physical activity, family size, use of meat, type of birth, breastfeeding, premature menopause, loss of appetite, and use of anticoagulants were significant risk factors with p-values less than 0.05. The risk prediction model with significant risk factors was a good fit with a p-value of 0.28, corresponding to the Hosmer–Lemeshow test value ($\chi 2 = 9.78$). This parsimonious model with Cox–Snell $R2 = 0.50$ (with a maximum value = 0.75) and Nagelkerke $R2 = 0.66$ showed an AUC of 0.924 as compared to the full model with all risk factors under study that exhibited an AUC of 0.949.

1. Introduction

Osteoporosis is not only the prime root of fractures, but it also files a high rank among abnormalities that cause people dependent and bedridden with serious issues [1]. According to an estimate of the WHO [1], osteoporosis causes more than 8.9 million fractures annually worldwide. The estimated number of fractures in Pakistan due to osteoporosis is 9.91 million (7.19 million in women and 2.71 million in men), which is expected to rise to 11.3 million in 2020 and 12.91

million in 2050 [2]. In the last twenty years, the life expectancy at birth in Pakistan has increased by 5.5 years, which is also the reason for the increase in the population suffering from osteoporosis [3, 4]. Osteoporosis is a silent disease, and there are often no symptoms until the first fracture occurs [5]. Fracture is the most significant health issue of osteoporosis. Bones with normal bone mass have a dense matrix of bone cells, whereas osteoporotic bone dissolves and is left with thin strands, resulting in an increase in bone fragility and leading to fracture [6].

Osteoporotic fractures are the leading cause of morbidity and mortality after being discharged from a hospital [1]. The main osteoporosis fractures are hip, forearm, wrist, spine, and proximal humerus fractures [1]. The osteoporotic fractures are expected to touch a figure of 11.3 million in 2020 and 12.91 million in 2050 [7]. According to Sözen et al. [8], osteoporotic fractures not only cause 15–20% increase death rates per year but also cause social segregation, recession, and require long-term care. The age-specific hip fractures in men are half than those in women in most communities [5].

Most of the studies uncover that the process of osteoporosis hastes after menopause in women due to low estrogen levels [9–11]. According to Thulkar and Singh [9], the rate of bone loss due to menopause is 2–5% per year. Different studies revealed that older age is a prime factor of fragile bone [11, 12]. Females are more prone to osteoporotic fractures than are males worldwide [13]. Females with a positive family history of osteoporosis and those who are using steroids or medications for chronic diseases are more exposed to the disease. However, the use of calcium supplements and hormone replacement therapy can be taken as preventive and protective measures [14]. Barret-Connor et al. [15] reported low bone mineral density (BMD) among Asian women compared to other ethnic groups around the globe. Mithal and Kaur [7] predicted that, by 2050, half of the global osteoporotic fractures will be in the Asian population. In consonance with various epidemiological predictions, until 2050, over 70% of all osteoporotic fractures will occur in specific regions of the world including Asia, the Middle East, and Latin America [16]. According to [17, 18], for every osteoporotic man, four women are suffering from osteoporosis. According to Hafeez et al. [13], women from the Indian subcontinent are at a high risk of facing osteoporosis compared to the Caucasian race.

Osteoporosis has not been taken seriously in developing countries, especially in Pakistan. In Asia generally, and in Pakistan specifically, there is a lack of medical facilities and equipment to diagnose osteoporosis and its treatment. The rural population of Pakistan has very little knowledge about dietetics and bone density [10]. In a study in the most populated city, i.e., Karachi of Pakistan, Habib et al. [19] reported a 16.4% prevalence of the disease. It is a dilemma that statistics about the prevalence of osteoporosis and osteoporotic fractures are scarce in Pakistan [13, 19, 20]. Even this disease has not been taken seriously by a common person due to many reasons, e.g., poor literacy rates, lack of awareness about the disease and nutritional imbalance, and considering osteoporosis as the disease of old age and developed states [7, 19, 21]. There is no database or statistics available at the government level about this disease. For research, we are still relying on the western literature about osteoporosis and its diagnosis, cutoff values, and associated risk factors. In addition, rare Pakistani studies are available in the literature that are based on primary data collected from some small-scale studies. Faisalabad is the third largest and the most populated and major industrial city of Pakistan. To the best of our knowledge, no study is available in this region to investigate the prevalence of osteoporosis and the risk factors associated with it. This study is an effort to fill this gap. The main intent of this paper is to identify significant socioeconomic risk factors of osteoporosis in Pakistani women and examine how the risk increases for different levels of risk factors in females of age groups of 30 years or more.

2. Materials and Methods

2.1. Study Area. Faisalabad is a major industrial city of Pakistan located in the center of the most populous province of Pakistan, i.e., Punjab. It is the third biggest city in Pakistan with respect to size and population. The study was conducted in the two main teaching hospitals of Faisalabad, i.e., District Head Quarter (DHQ) Hospital and Allied Hospital.

2.2. Study Design. The study was a case-control study with a 1 : 1 case-control ratio, and convenient sampling was considered to collect the information from cases and controls.

2.3. Duration of the Study and Data. The case-control study was completed in the two teaching hospitals; District Head Quarter (DHQ) Hospital and Allied Hospital, Faisalabad. These two hospitals not only cover the population of Faisalabad city but also manage the patients of the whole Faisalabad division due to the available medical facilities. The study was completed from October 2018–August 2019.

2.4. Inclusion Criteria. Females of age ≥30 years were considered for the study. We considered this age because peak bone mass occurs around the age of 30 years and reduction starts from 40 years of age [22]. Osteoporotic patients were decided based on digital X-ray radiogrammetry. Females having a Metacarpal Index (MCI) value less than 0.4 were considered osteoporotic, whereas an index value higher than 0.6 was considered for the control group [23].

2.5. Sampling Technique and Sample Size. Nagi et al. [24] reported that there are 9.9 million people in Pakistan who are osteoporosis sufferers, among which 7.2 million are women. We used the WHO calculator [25] to obtain the sample size. The estimated sample size with a 95% confidence interval and a 6% margin of error was 240 with a 1 : 1 case-control ratio. We used the convenience sampling technique to select 120 cases, i.e., premenopausal and postmenopausal females with age ≥30 years who were suffering from osteoporosis and 120 controls, i.e., females who were not osteoporosis sufferers.

2.6. Risk Factors. In the literature, different researchers have used different risk factors in their studies [2, 6, 10–16, 19–21]. We tried to consider all of them to investigate how each risk factor increases the risk in osteoporotic females compared to nonsufferers in the presence of other factors. The information about different demographic and socioeconomic risk factors was collected through structured questionnaires with the prior consent of the subjects. Information about the following possible risk factors was collected: age, BMI, locality, education, awareness about the disease, regular physical activity, exposure to sunlight, reproductive history, gynaecological status, and loss of weight. Others were intake of calcium through natural sources and supplements, use of proteins, history of fracture, family history of osteoporosis, number and kind of births, monthly household income, ownership of the house, and use of anticoagulants.

2.7. Ethical Issues. The study was conducted after the approval of the Ethical Review Committee of Govt. College University Faisalabad. The same approval was taken from both hospitals where the study was conducted. The respondents were informed about the study and its objectives before their interview. After knowing about the study, the respondents who agreed to be a part of the study were included in the research.

2.8. Statistical Techniques. Both descriptive and inferential analyses were employed in this study. The inferential analyses were used in drawing the significance of risk factors and the selection of a risk prediction model. Descriptive statistics were considered for continuous demographic and socioeconomic risk factors in terms of mean and standard deviation, whereas frequencies and percentages were considered for qualitative factors. To explore significant risk factors, a logistic regression model was fitted for a dichotomous response mentioning whether a subject is osteoporotic or not. The odds ratios and their confidence intervals were computed for comparing the relative odds of osteoporosis in the presence of a given risk factor. The multiple logistic regression model with p risk factors (predictors) X_1, X_2, . . ., X_p, without interaction terms, is defined as

$$logit\,[\pi(x)] = \log\left[\frac{\pi(x)}{1-\pi(x)}\right] = \beta_0 + \beta_1 X_1 + \ldots + \beta_p X_p, \tag{1}$$

where β's are the regression coefficients of predictors. The statistical programming language R was used to fit the logistic regression model, test the significance of parameter estimates, and compute the odds ratios and their corresponding confidence intervals. The significance of parameter estimates associated with different risk factors was tested using the Wald test. The goodness of fit for the risk prediction model was confirmed using the Hosmer–Lemeshow test [26]. Additionally, Cox–Snell R^2 [27] and its adjusted version, that is, Nagelkerke R^2 [28], were computed to study the variation in the response variable explained by the model. The usual R^2 in case of linear regression is also a special case of Cox–Snell R^2. Usual R^2 has a maximum value of 1, but for Cox–Snell R^2, it is less than one. However, Nagelkerke R^2 has an upper bound of 1 just like the case with linear models.

3. Results

Our focus was on females with age ≥30 because they are more exposed to this disease than males [13, 17, 18]. The average age of the whole sample was 56.95 years (54.27 years for cases and 59.62 years for the control group) with a standard deviation of 10.74 years (6.64 and 5.78 years for cases and controls, respectively). The mean ± SD of the family size was 6.68 ± 2.62 and 6.87 ± 3.45 for the control and patient groups, respectively. The average BMI (body mass index) was little higher in cases (30.95) than in controls (28.10), whereas the average age at menarche was almost the same in both groups, with an average of 14.25 years in the whole sample (Table 1).

The percentage of literate patients and those who have awareness about the disease was low, i.e., 25% and 5%, respectively. The incidence of bone fracture is 35% higher in cases than that in the control group. Among the osteoporotic females considered in our study, 43 were admitted to the hospital for hip fracture surgery, 16 for tibial fracture, and four for some other fracture surgery. Fifty-seven cases had no fracture. In the control group, one woman was admitted to the hospital for hip fracture surgery, six for tibial fracture, fourteen for some other fracture surgery, and 99 had no fracture. Only 13% of cases had a family history of the disease. Fewer patients (14%) were observed to be involved in regular physical activity compared to nonsufferers (64%). The percentage of patients who do not drink milk at least once a week is 19% more than that in the control group. The frequency of eating meat at least once a week was 21% higher in the control group than that in the patient group. In our sample, more than 80% of women had natural delivery in cases and controls as well. There are 90% of women in both groups who fed their children before suffering from the disease. Normal menopause, normal menstrual flow, and 4–7 days of a menstrual cycle were observed in most women in both groups. Most women were not using any calcium supplements. Compared to healthy women (26%), a high percentage (80%) of females suffering from osteoporosis complained of the loss of weight. Half of the patients reported poor appetite (Table 1).

The significant risk factors were age, bone fracture, family history of the disease, daily physical activity, number of family members living in a house, frequency of eating meat, kind of delivery, breastfeeding, menopausal status, appetite, and use of anticoagulants. The results showed that a one-year increase in age may cause a 10% increase in the odds of being osteoporotic. In the case of bone fractures, the odds of disease are 3.5 times higher than those who have not got a fracture. Chances increase 36 times to be a patient of

Table 1: Frequencies and percentages of categorical risk factors.

Variable	Categories	Control	% age	Case	% age	Variable	Categories	Control	% age	Case	% age
Locality	Urban	59	49.17	65	54.17	Delivery kind	None	5	4.17	10	8.33
	Rural	61	50.83	55	45.83		Normal	104	86.67	100	83.33
Literacy	Illiterate	73	60.83	90	75		Major	11	9.17	10	8.33
	Literate	47	39.17	30	25	Feeding as a mother	No	13	10.83	12	10
Awareness	No	108	90	114	95		Yes	107	89.17	108	90
	Yes	12	10	6	5	Feeding as a patient	No	9	7.5	2	1.67
Symptoms	Tiredness	29	24.17	41	34.17		Yes	111	92.5	118	98.33
	Body pain	91	75.83	79	65.83	Menopause status	Normal	106	88.33	94	78.33
Fracture	No	99	82.5	57	47.5		Abnormal	14	11.67	26	21.67
	Yes	21	17.5	63	52.5	Menstruation frequency	High	20	16.67	28	23.33
Fracture history	No	110	91.67	92	76.67		Normal	100	83.33	92	76.67
	Yes	10	8.33	28	23.33	Menstruation duration	4–7 days	117	97.5	110	91.67
Family history	No	117	97.5	104	86.67		≥8 days	3	2.5	10	8.33
	Yes	3	2.5	16	13.33	Menstruation regularity	Irregular	2	1.67	6	5
Physical activity	No	43	35.83	103	85.83		Regular	118	98.33	114	95
	Yes	77	64.17	17	14.17	Regular calcium intake	No	100	83.33	106	88.33
Sun exposure	No	22	18.33	38	31.67		Yes	20	16.67	14	11.67
	Yes	98	81.67	82	68.33	Appetite	Poor	17	14.17	58	48.33
Calcium in preg	No	100	83.33	111	92.5		Normal	103	85.83	62	51.67
	Yes	20	16.67	9	7.5	Abdomen system	Abnormal	23	19.17	56	46.67
House owned	Rented	14	11.67	16	13.33		Normal	97	80.83	64	53.33
	Owned	106	88.33	104	86.67	Sleep disturbance	No	91	75.83	42	35
Milk	0	56	46.67	78	65		Yes	29	24.17	78	65
	>=1	64	53.33	42	35	Mental stress	No	101	84.17	55	45.83
Meat	None	8	6.67	20	16.67		Yes	19	15.83	65	54.17
	Red	30	25	21	17.5	Comorbidity	No	93	77.5	26	21.67
	White + red	82	68.33	79	65.83		Yes	27	22.5	94	78.33
Meat frequency	0	47	39.17	73	60.83	Anticoagulants	No	118	98.33	102	85
	>=1	73	60.83	47	39.17		Yes	2	1.67	18	15
Eggs/week	0	66	55	90	75	Marital status	Married	100	83.33	67	55.83
	>=1	54	45	30	25		Widow	20	16.67	53	44.17

osteoporosis in the case of having a history in the family. The number of persons living in a house is also identified as a significant risk factor, with 24% higher odds for an increase of one member in the same size of the house. The occasional use of meat was not found to be a significant risk factor, but the frequent use of meat (at least once a week) decreases the chances of osteoporosis. The person who eats meat at least once a week is 76% safer than that person who is the occasional consumer of meat. Since the duration of breastfeeding is correlated with the number of births, the results showed that an increased number of births and consequently breastfeeding increase the risk a lot. According to our study, a woman who has fed in the past is seven times more exposed to the disease. The risk in the mothers who were feeding during our study, i.e., feeding as a patient, possessed 120 times more risk than those females who did not feed as a patient. Abnormal menopause in females may also increase the risk of osteoporosis eight times. The results of the study reflected that the chances of suffering from the disease are 91% higher in females who have an issue of loss of appetite. Anticoagulants users are also observed twenty times more exposed to the disease than nonusers. The parameter estimates, their standard errors, Wald-test statistic value, odds ratio, and its 95% confidence interval are given in Table 2. A risk prediction model with significant risk factors was fitted, and the goodness of fit of that model was tested with the Hosmer–Lemeshow test [26]. The test showed that the fitted model is a good fit with a p value of 0.28 for the test-statistic value of $\chi 2 = 9.78$. The values of different pseudo-R^2 were computed for different possible models with available risk factors. The model with significant risk factors showed Cox–Snell's R^2 [27] value of 0.50 corresponding to a maximum value of 0.75. Another pseudo measure of R^2 is Nagelkerke/Crag and Uhler's R^2 [28], which is an adjusted version of Cox–Snell R^2 with a maximum value of 1. This pseudo measure resulted in a value of 0.66.

These measures were better than all possible models fitted with the risk factors under study except the model with all risk factors. These measures were better than all possible models fitted with the risk factors under study except the model with all risk factors. Although the model with all risk factors showed little improvement in the pseudo-R^2 values (Cox–Snell $R2 = 0.55$ and Nagelkerke $R2 = 0.73$), but at the same time, most of the factors in this model were insignificant.

The ROC curve (receiver operating characteristic curve) describing the trade-off between sensitivity (true positive rate) and 1-specificity (false positive rate) for the models with all risk factors and significant risk factors is shown in Figure 1. Both curves show that the performance of a parsimonious model with significant risk factors is as good as for the overall model. The area under the curve (AUC) is

Table 2: Parameter estimates and the Wald statistic value along with their p values. Odds ratios (ORs) and their corresponding 95% confidence intervals (CIs) are in the last two columns.

	Estimate	Wald Z	p value	OR	95% CI of OR
Age	0.09	2.54	0.01*	1.10	(1.02, 1.18)
Locality (rural)	−1.10	−1.90	0.06	0.33	(0.11, 1.04)
BMI	−0.07	−1.59	0.11	0.93	(0.86, 1.02)
Literacy (literate)	−1.02	−1.52	0.13	0.36	(0.10, 1.34)
Awareness (yes)	−0.08	−0.08	0.94	0.92	(0.12, 7.22)
Symptoms (body pain)	−0.19	−0.30	0.77	0.83	(0.24, 2.84)
Fracture (yes)	1.27	1.98	0.047*	3.55	(1.02, 12.38)
Fracture history (yes)	0.09	0.13	0.90	1.10	(0.28, 4.27)
Family history (yes)	3.59	2.91	< 0.01*	36.3	(3.23, 408.55)
Physical activities (yes)	−2.67	−4.45	< 0.01*	0.07	(0.02, 0.22)
Sun exposure (yes)	−0.32	−0.50	0.62	0.73	(0.21, 2.54)
Family size	0.21	2.19	0.03*	1.24	(1.02, 1.49)
House (owned)	0.03	0.04	0.97	1.03	(0.19, 5.53)
Milk frequency per week (>=1)	0.19	0.35	0.73	1.21	(0.41, 3.54)
Meat (red)	−0.22	−0.26	0.80	0.80	(0.15, 4.41)
(Red + white)	0.73	0.88	0.38	2.07	(0.41, 10.49)
Eating meat per week (>=1)	−1.43	−2.48	0.01*	0.24	(0.08, 0.74)
Eating eggs per week (>=1)	−0.64	−1.29	0.20	0.53	(0.20, 1.40)
Marital status (widow)	−0.38	−0.59	0.55	0.69	(0.20, 2.38)
No. of children	−0.21	−1.58	0.11	0.81	(0.63, 1.05)
Calcium supp. during pregnancy (yes)	0.72	0.89	0.37	2.04	(0.42, 9.92)
Delivery kind (normal)	−4.35	−2.27	0.02*	0.01	(0.00, 0.55)
(Operate)	−2.85	−1.50	0.13	0.06	(0.00, 2.42)
Breastfeeding in past	1.96	1.61	0.11	7.12	(0.65, 77.73)
Currently breastfeeding	4.79	2.16	0.03*	120.16	(1.56, 9277.49)
Menopausal status (abnormal)	2.11	2.87	< 0.01*	8.28	(1.95, 35.14)
Age at menarche	0.38	1.60	0.11	1.47	(0.92, 2.35)
Menstrual flow (normal)	−0.49	−0.64	0.52	0.61	(0.14, 2.74)
Menstrual cycle (>=28 days)	−0.15	−0.11	0.91	0.86	(0.05, 13.85)
Menstrual cycle repeat (regular)	−0.93	−0.59	0.55	0.40	(0.02, 8.39)
Cal. supplement >=1 time/week (yes)	0.30	0.41	0.68	1.35	(0.32, 5.75)
Appetite (normal)	−2.42	−4.02	< 0.01*	0.09	(0.03, 0.29)
Anticoagulants use (yes)	3.01	2.54	0.01*	20.31	(1.98, 208.17)

*Significant at the 5% level of significance.

approximately the same for both models. The calibration curve in Figure 1 also reflects that a parsimonious model with significant risk factors can be a good choice as an alternative to a rich model with a large number of possible risk factors.

4. Discussion

In our study, prevalence of osteoporosis was observed to increase with growing age, especially starting from the age of 40 years, which is in accordance with different other studies [29–31]. Age was found to be a significant factor causing osteoporosis similar to the findings in [12, 14, 16, 19, 24, 32–34]. However, according to [35], age was not a significant factor causing osteoporosis. The BMI did not show a significant effect in predicting osteoporosis in our study. The BMI was also not significant in other studies, where height and weight were significant at the same time [12, 13, 32, 36, 37]. In a systematic evaluation, the authors of [38] explored that birth weight has a negative association with BMD and a positive association with fracture risk. A family history of osteoporosis and malnourishment has also been found to be the cause of low BMD [39]. The history of fractures can be helpful to identify the presence of osteoporosis, as identified by [2, 40]. The results of [41, 42] about the significance of exercise/involvement in physical activities match our findings. The number of parity that we considered in this study as the family size also appeared as a significant risk factor [16, 32, 34, 40]. We found that, with an increasing number in parity, the risk of osteoporosis also increases. Also, the kind of delivery that is normal or operated, as compared to those females who had zero parity or gravidity, has an impact on the risk of osteoporosis. Different studies [16, 32, 41] are available in the support of our finding that breastfeeding also significantly increases the risk of osteoporosis. According to our investigation, low appetite can also be a significant factor for identifying the osteoporosis patient. The use of anticoagulants may also significantly increase the risk of osteoporosis. Naz et al. [32] found that diabetes can increase the risk of being osteoporotic, but in our study, comorbidity was not a significant risk factor. Our finding about the significance of abnormal menopause was also consistent with other studies [2, 16, 40]. Fatima et al. [40] in their research found the ownership of the house as a significant risk factor, but in our study, neither this factor nor the income level was found to be a significant risk factor.

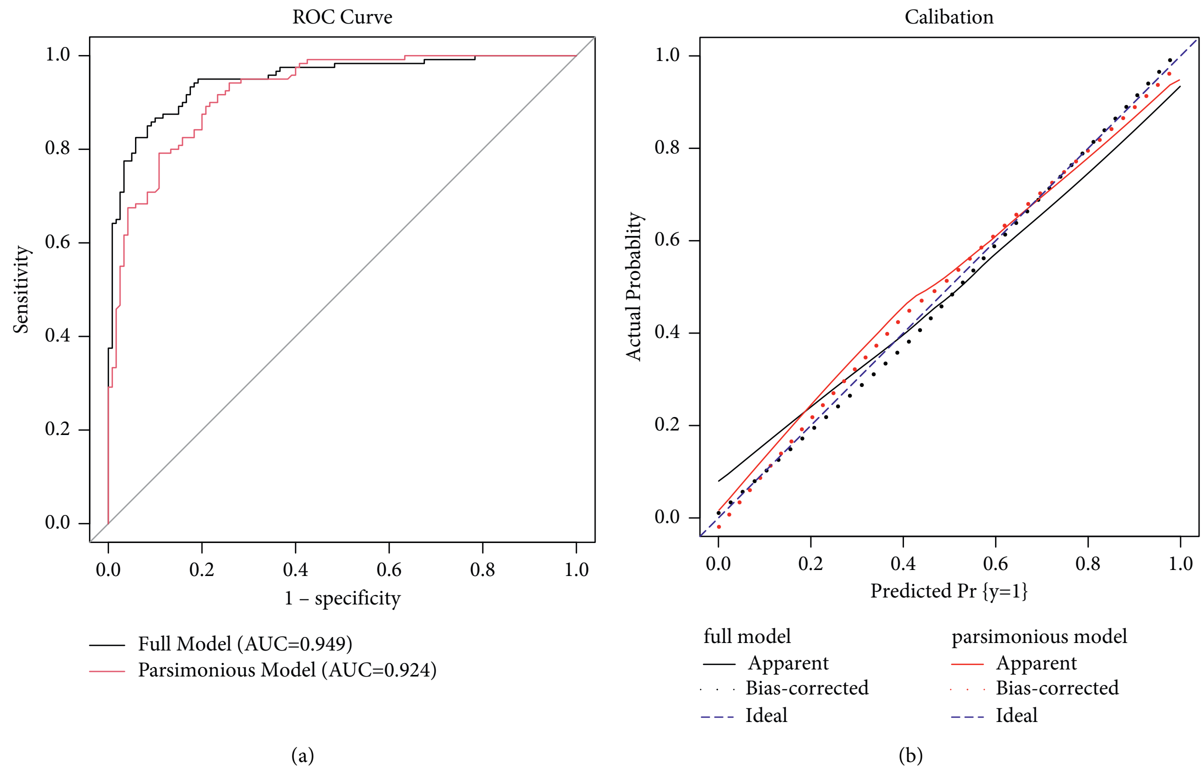

FIGURE 1: ROC curve (a) and calibration curves (b) for the overall model and parsimonious model with significant risk factors.

In some studies [33, 41], the use of calcium supplements has been found to be a significant factor, but in our study, this was not the case.

5. Conclusion

This study was an attempt to address the neglected medical problem of osteoporosis in females and the risk factors associated with it in Pakistan. To cope with this growing issue, we need (i) diagnostic facilities, e.g., DEXA scan or QUS, i.e., quantitative ultrasound, (ii) population-based studies at the government level and some health programs at the national level focusing on this disease, and (iii) awareness and education among people about osteoporosis, its diagnosis, treatment, and adoption of possible changed lifestyles for this disease.

Data Availability

The dataset is available upon reasonable request from the corresponding author.

Conflicts of Interest

The authors declare no conflicts of interest.

Acknowledgments

The authors sincerely thank Bielefeld University, Germany, for providing financial support through the Open Access Publication Fund for the article processing charge.

References

[1] World Health Organization, "WHO scientific group on the assessment of osteoporosis at primary health care level," *Summary meeting report*, vol. 5, pp. 5–7, 2004.

[2] S. Haris, F. Jahan, A. Afreen, H. Ahmed, and Z. Ahmed, "To determine the risk factors and prevalence of osteoporosis among adult Pakistani population residing in Karachi using quantitative ultrasound technique," *Journal of Community Medicine & Health Education*, vol. 04, no. 04, pp. 2–5, 2014.

[3] World Health Organization, "Life expectancy and healthy life expectancy. Data by country," p. 688, 2018, http://apps.who.int/gho/data/node.main.

[4] World Health Organization, *Life Expectancy and Healthy Life Expectancy, Data by WHO Region*, WHO, Geneva, 2018, http://apps.who.int/gho/data/view.main.SDG2016LEXREGv.

[5] J. A. Kanis, L. J. Melton III, C. Christiansen, C. C. Johnston, and N. Khaltaev, "The diagnosis of osteoporosis," *Journal of Bone and mineral Research*, vol. 9, no. 8, pp. 1137–1141, 1994.

[6] S. Miura, O. L. Saavedra, and S. Yamamoto, "Osteoporosis in urban post-menopausal women of the Philippines: prevalence and risk factors," *Archives of Osteoporosis*, vol. 3, no. 1-2, pp. 17–24, 2008.

[7] A. Mithal and P. Kaur, "Osteoporosis in Asia: a call to action," *Current Osteoporosis Reports*, vol. 10, no. 4, pp. 245–247, 2012.

[8] T. Sozen and L. Ozisik, "An overview and management of osteoporosis," *European journal of rheumatology*, vol. 4, no. 1, pp. 46–56, 2017.

[9] J. Thulkar and S. Singh, "Overview of research studies on osteoporosis in menopausal women since the last decade," *Journal of Mid-life Health*, vol. 6, no. 3, p. 104, 2015.

[10] N. M. Lowe, B. Ellahi, Q. Bano, S. A. Bangash, S. R. Mitra, and M. Zaman, "Dietary calcium intake, vitamin D status, and bone health in postmenopausal women in rural Pakistan,"

Journal of Health, Population and Nutrition, vol. 29, no. 5, p. 465, 2011.

[11] A. Shakil, N. E. Gimpel, H. Rizvi et al., "Awareness and prevention of osteoporosis among South Asian women," *Journal of Community Health*, vol. 35, no. 4, pp. 392–397, 2010.

[12] M. M. Pinheiro, E. T. d. Reis Neto, F. S. Machado et al., "Risk factors for osteoporotic fractures and low bone density in pre and postmenopausal women," *Revista de Saúde Pública*, vol. 44, no. 3, pp. 479–485, 2010.

[13] F. Hafeez, S. Zulfiqar, S. Hasan, and R. Khurshid, "An assessment of osteoporosis and low bone density in postmenopausal women," *Pakistan Journal of Physiology*, vol. 30, no. 1, p. 5, 2009.

[14] A. Keramat, B. Patwardhan, B. Larijani et al., "The assessment of osteoporosis risk factors in Iranian women compared with Indian women," *BMC Musculoskeletal Disorders*, vol. 9, no. 1, pp. 28–30, 2008.

[15] E. Barrett-Connor, E. S. Siris, L. E. Wehren et al., "Osteoporosis and fracture risk in women of different ethnic groups," *Journal of Bone and mineral Research*, vol. 20, no. 2, pp. 185–194, 2004.

[16] S. Shilbayeh, "Prevalence of osteoporosis and its reproductive risk factors among Jordanian women: a cross-sectional study," *Osteoporosis International*, vol. 14, no. 11, pp. 929–940, 2003.

[17] J. R. Center, T. V. Nguyen, D. Schneider, P. N. Sambrook, and J. A. Eisman, "Mortality after all major types of osteoporotic fracture in men and women: an observational study," *The Lancet*, vol. 353, no. 9156, pp. 878–882, 1999.

[18] A. Feldstein, P. J. Elmer, E. Orwoll, M. Herson, and T. Hillier, "Bone mineral density measurement and treatment for osteoporosis in older individuals with fractures," *Archives of Internal Medicine*, vol. 163, no. 18, pp. 2165–2172, 2003.

[19] S. Habib, R. Iqbal, M. Shahid, and A. Habib, "Growing prevalence of osteoporosis in Pakistan: call for action," *JPMA. The Journal of the Pakistan Medical Association*, vol. 65, no. 2, pp. 230-231, 2015.

[20] N. Haq, M. Tahir, Q. Iqbal, and Q. Naseem, "Exploration of osteoporosis knowledge and perception among young women in Quetta. Pakistan," *J Osteopor Phys Act*, vol. 3, no. 3, pp. 1–6, 2015.

[21] M. Bilal, A. Haseeb, A. Z. Merchant et al., "Knowledge, beliefs and practices regarding osteoporosis among female medical school entrants in Pakistan," *Asia Pacific Family Medicine*, vol. 16, no. 1, pp. 6-7, 2017.

[22] B. Larijani, A. Hossein-Nezhad, A. Mojtahedi et al., "Normative data of bone mineral density in healthy population of Tehran, Iran: a cross sectional study," *BMC Musculoskeletal Disorders*, vol. 6, no. 1, pp. 38–46, 2005.

[23] S. Vasireddy, "Metacarpal radiographic indices in the assessment of bone strength and fracture risk," Doctoral dissertation, University of Sheffield, Sheffield, UK, 2010.

[24] D. Nagi, Z. Butt, F. Farooq, and A. Aamar, "Frequency of osteoporosis in an ambulatory setting in Lahore using quantitative calcaneal ultrasound," *Journal of Pakistan Medical Association*, vol. 1, no. 63, pp. 965–968, 2013.

[25] World Health Organization, *Sample Size Determination: A User's Manual*, World Health Organization, Geneva, Switzerland, 1986.

[26] D. W. Hosmer Jr, S. Lemeshow, and R. X. Sturdivant, *Applied Logistic Regression*, John Wiley & Sons, Hoboken, NJ, USA, 2013.

[27] D. R. Cox and E. J. Snell, *Analysis of Binary Data*, Routledge, England, UK, 2018.

[28] N. J. D. Nagelkerke, "A note on a general definition of the coefficient of determination," *Biometrika*, vol. 78, no. 3, pp. 691-692, 1991.

[29] S. R. Cummings, J. L. Kelsey, M. C. Nevitt, and K. J. O'Dowd, "Epidemiology of osteoporosis and osteoporotic fractures," *Epidemiologic Reviews*, vol. 7, no. 1, pp. 178–208, 1985.

[30] J. A. Kanis, A. Oden, O. Johnell, B. Jonsson, C. de Laet, and A. Dawson, "The burden of osteoporotic fractures: a method for setting intervention thresholds," *Osteoporosis International*, vol. 12, no. 5, pp. 417–427, 2001.

[31] E. S. Siris, S. K. Brenneman, E. Barrett-Connor et al., "The effect of age and bone mineral density on the absolute, excess, and relative risk of fracture in postmenopausal women aged 50-99: results from the National Osteoporosis Risk Assessment (NORA)," *Osteoporosis International*, vol. 17, no. 4, pp. 565–574, 2006.

[32] M. S. G. Naz, G. Ozgoli, M. A. Aghdashi, and F. Salmani, "Prevalence and risk factors of osteoporosis in women referring to the bone densitometry academic center in Urmia, Iran," *Global Journal of Health Science*, vol. 8, no. 7, pp. 135–145, 2016.

[33] S. H. Danish, F. Ahmad, F. Hassan et al., "Osteoporosis and its associated factors revisited: case control study," *Pakistan Journal of Medicine and Dentistry*, vol. 3, no. 02, pp. 13–20, 2014.

[34] Z. Masood, S. Shahzad, A. Saqib, and K. Ashraf, "Osteopenia and osteoporosis," *The Professional Medical Journal*, vol. 21, no. 03, pp. 477–483, 2014.

[35] R. A. Begum, L. Ali, J. Akter, O. Takahashi, T. Fukui, and M. Rahman, "Osteopenia and osteoporosis among 16-65 Year old women attending outpatient clinics," *Journal of Community Health*, vol. 39, no. 6, pp. 1071–1076, 2014.

[36] R. R. Soomro, S. I. Ahmed, M. Khan, and S. S. Ali, "Comparing the effects of osteoporosis prevention exercise protocol (OPEP) versus walking in the prevention of osteoporosis in younger females," *Pakistan Journal of Medical Sciences*, vol. 31, no. 2, pp. 336–340, 2015.

[37] H. Kaz, D. Johnson, S. Kerry, U. Chinappen, K. Tweed, and S. Patel, "Fall-related risk factors and osteoporosis in women with rheumatoid arthritis," *Rheumatology*, vol. 43, no. 10, pp. 1267–1271, 2004.

[38] X. H. Yu, Y. Y. Wei, P. Zeng, and S. F. Lei, "Birth weight is positively associated with adult osteoporosis risk: observational and Mendelian randomization studies," *Journal of Bone and Mineral Research*, vol. 36, no. 8, pp. 1469–1480, 2021.

[39] A. Mithal, B. Bansal, C. Kyer, and P. Ebeling, "The Asia-pacific regional audit-epidemiology, costs, and burden of osteoporosis in India 2013: a report of international osteoporosis foundation," *Indian journal of endocrinology and metabolism*, vol. 18, no. 4, pp. 449–454, 2014.

[40] M. Fatima, H. Nawaz, M. Kassi et al., "Determining the risk factors and prevalence of osteoporosis using quantitative ultrasonography in Pakistani adult women," *Singapore Medical Journal*, vol. 50, no. 1, pp. 20–28, 2009.

[41] F. M. Mamji, J. A. Hasan, and M. S. Sabri, "Risk factors for osteoporosis in post-menopausal women with hip fractures," *Journal of Surgery Pakistan (International)*, vol. 15, no. 2, pp. 82–86, 2010.

[42] S. A. Sayed, A. Khaliq, and A. Mahmood, "Evaluating the risk of osteoporosis through bone mass density," *Journal of Ayub Medical College, Abbottabad*, vol. 28, no. 4, pp. 730–733, 2016.

Hindawi
Journal of Healthcare Engineering
Volume 2023, Article ID 9837045, 1 page
https://doi.org/10.1155/2023/9837045

Retraction

Retracted: Alteration of Intestinal Microbiota and Hydrogen Sulfide Metabolism in Patients with Hashimoto's Thyroiditis

Journal of Healthcare Engineering

Received 28 November 2023; Accepted 28 November 2023; Published 29 November 2023

This article has been retracted by Hindawi, as publisher, following an investigation undertaken by the publisher [1]. This investigation has uncovered evidence of systematic manipulation of the publication and peer-review process. We cannot, therefore, vouch for the reliability or integrity of this article.

Please note that this notice is intended solely to alert readers that the peer-review process of this article has been compromised.

Wiley and Hindawi regret that the usual quality checks did not identify these issues before publication and have since put additional measures in place to safeguard research integrity.

We wish to credit our Research Integrity and Research Publishing teams and anonymous and named external researchers and research integrity experts for contributing to this investigation.

The corresponding author, as the representative of all authors, has been given the opportunity to register their agreement or disagreement to this retraction. We have kept a record of any response received.

References

[1] S. Zhang, Y. Chi, H. Jin et al., "Alteration of Intestinal Microbiota and Hydrogen Sulfide Metabolism in Patients with Hashimoto's Thyroiditis," *Journal of Healthcare Engineering*, vol. 2023, Article ID 9302189, 7 pages, 2023.

Hindawi
Journal of Healthcare Engineering
Volume 2023, Article ID 9302189, 7 pages
https://doi.org/10.1155/2023/9302189

Research Article

Alteration of Intestinal Microbiota and Hydrogen Sulfide Metabolism in Patients with Hashimoto's Thyroiditis

Shangqing Zhang [1] **Yan Chi,** [2] **Hongfang Jin** [3] **Xiuli Wang,** [3] **Xue Zhao,** [1] **Ying Gao** [1] **and Junqing Zhang** [1]

[1]*Department of Endocrinology, Peking University First Hospital, Beijing 100034, China*
[2]*Department of Gastroenterology, Peking University First Hospital, Beijing 100034, China*
[3]*Department of Pediatric, Peking University First Hospital, Beijing 100034, China*

Correspondence should be addressed to Ying Gao; bjgaoying@yahoo.com

Received 16 March 2022; Revised 1 April 2022; Accepted 6 April 2022; Published 10 July 2023

Academic Editor: Liaqat Ali

Objective. To analyze the intestinal microbiota and H2S levels in patients with HT. *Methods*. Twenty euthyroid HT patients and twenty healthy control individuals were recruited. Fecal samples were collected, and the microbiota was examined using 16S RNA gene sequencing. We also collected serum samples to examine the H2S levels. *Results*. Compared with patients with HT, the ACE and Chao indices were significantly lower in healthy controls ($P = 0.04$, 0.03, respectively). The microbial composition of the HT group differed significantly from that of the healthy group. We observed a significant increase in the proportions of *Bacteroides*, *Fusobacterium*, *Sutterella*, and *Veillonella* in patients with HT ($P < 0.05$). Linear discriminant analysis and effect size analysis also revealed that *Bacteroides* and *Ralstonia* were enriched in patients with HT. Additionally, patients with HT had significantly lower H2S levels than healthy controls ($P < 0.005$). The enrichment of H2S anabolism was linked to the alteration of intestinal microbiota in patients with HT. *Conclusion*. We demonstrated that patients with HT have aberrant intestinal microbiome and that H2S anabolism may contribute to HT pathogenesis.

1. Introduction

Hashimoto's thyroiditis (HT) is the chronic inflammation of the thyroid gland and is considered the most common autoimmune disease worldwide [1]. Clinically, HT is frequently asymptomatic. With the destruction of thyroid cells, patients with HT may develop subclinical or even overt hypothyroidism.

HT is related to an interaction of genetic elements, environmental factors, and epigenetic influences [2]. Dysbiosis of intestinal microbiota can trigger several immune disorders that are adjacent to or distant from the site of their induction [3]. Intestinal microbiota has also been considered to be involved in the pathogenesis of HT. In recent years, several studies have described the alteration of intestinal microbiota in patients with HT [4–8]. Emerging evidence has revealed that the dysbiosis of the intestinal microbiota is associated with the pathogenesis of Hashimoto's thyroiditis (HT). Hydrogen sulfide (H2S) is a metabolite of the intestinal microbiota that can regulate the viability and function of immune cells. However, the link between H2S and HT remains unclear. Changes in microbiota-derived metabolites, such as bile acids and short-chain fatty acids, also have regulatory effects on immune function. These changes in the corresponding metabolites can induce local or systemic inflammation [9]. Therefore, we further speculated that the levels of metabolites of the intestinal microbiota were different between patients with HT and healthy controls and that they may participate in the pathogenesis of HT.

Hydrogen sulfide (H2S), an endogenous product of bacteria and mammals, is the third gasotransmitter (along with nitric oxide and carbon monoxide) [10]. H2S can regulate the viability and function of immune cells. Downregulation of H2S leads to the development or worsens the severity of various immune-mediated diseases, including autoimmune rheumatoid arthritis and asthma [11, 12].

However, the relationship between H2S and HT remains unclear. H2S can also be produced by bacteria in the intestine. Depending on the microorganism, the production of H2S occurs in two ways: assimilatory sulfate reduction (ASR) and dissimilatory sulfate reduction (DSR). The only the terminal product of DSR is H2S [13]. Various gastrointestinal bacteria, especially sulfate-reducing bacteria (SRB), can produce exogenous H2S and regulate host H2S bioavailability and metabolism, consequently regulating physiological responses, such as epithelial cell health and inflammation [14]. Therefore, we speculated that the aberrant intestinal microbiota may downregulate the metabolism of H2S, which impairs immunoregulation and promotes the pathogenesis of HT.

In this study, we explored the differences in intestinal microbiome composition and serum H2S levels between patients with HT and healthy controls. We also analyzed H2S metabolism in the intestinal microbiota of patients with HT and healthy controls.

2. Materials and Methods

2.1. Patients and Samples. Twenty untreated euthyroid HT patients (19 females and one male), with an average age of 35.4 ± 9.4 years, were recruited from the Department of Endocrinology at the Peking University First Hospital from August 2020 to October 2021. The diagnosis of HT was defined as follows [15]: (1) highly elevated serum thyroid peroxidase antibody (TPOAb) and/or thyroglobulin antibody (TgAb) and (2) diffuse thyroid morphological features on an ultrasound examination. Twenty healthy volunteers (19 females and one male) with an average age of 33.9 ± 8.3 years old were recruited as controls. All controls were free of thyroid diseases based on an ultrasound examination and had no history or family history of thyroid diseases. These controls were euthyroid and negative for thyroid autoantibodies. All subjects with other autoimmune diseases or diseases that affected the intestinal microbiota based on the literature were excluded. Subjects treated with antibiotics, proton pump inhibitors, probiotics, or laxatives in the month before fecal sample collection were also excluded. Venous blood and fecal samples were collected from all subjects in the morning and stored at -80°C until use. This study was approved by the Ethics Committee of Peking University First Hospital (No. 2020-089) and conducted in accordance with the guidelines provided by the World Medical Association and the Helsinki Declaration. Informed consent was obtained from all the study subjects.

2.2. DNA Extraction from Human Fecal Samples. Total genomic DNA was extracted from human fecal samples using the CTAB/SDS method. The DNA concentration and purity were evaluated on a 1% agarose gel.

2.3. Polymerase Chain Reaction (PCR) Amplification. The V3-V4 hypervariable region of the 16S rRNA gene was amplified using the primers 515F (5′-GTG CCA GCM GCC GCG GTA A-3′) and 806R (5′-GGA CTA CHV GGG TWT CTA AT-3′). PCR reactions were conducted using Phusion® High-Fidelity PCR Master Mix (New England Biolabs). The PCR products were mixed in equidensity ratios and were agarose gel purified using the Qiagen Gel Extraction Kit (Qiagen, Germany).

2.4. Library Preparation and Sequencing. Sequencing libraries were generated using the TruSeq® DNA PCR-Free Sample Preparation Kit (Illumina, USA) following the manufacturer's recommendations, and index codes were added. Library quality was assessed using a Qubit® 2.0 Fluorometer (Thermo Scientific) and Agilent Bioanalyzer 2100 system. Finally, the library was sequenced on an Illumina NovaSeq 6000 platform, and 250 bp paired-end reads were generated.

2.5. Microbial Analysis. Paired-end reads were merged using overlapping sequences. Sequences were optimized by filtering and quality control. Operational taxonomic units (OTUs) were clustered using a 97% similarity cutoff with USEARCH (Version 11.0.667, https://www.drive5.com/usearch/), and chimeric sequences were identified and removed. The taxonomy of each sequence was annotated using the RDP Classifier (Release 11.1, https://rdp.cme.msu.edu/) in conjunction with the Silva database with a confidence threshold of 0.8. The α diversity was analyzed based on species richness at the OTU level, including the Chao, Shannon, ACE, and Simpson indices. Principal coordinate analysis (PCoA) based on Bray–Curtis dissimilarity was used to analyze structural differences between the samples using β diversity. Linear discriminant analysis effect size (LEfSe) was conducted using a linear discriminant analysis (LDA) ≥ 4 to detect potential bacterial biomarkers. Statistical significance was set at $P < 0.05$.

PICRUSt software was used to predict the functional genes in the sequencing results, and functional classification was performed according to the Kyoto Encyclopedia of Genes and Genome (KEGG) database. We then analyzed the differences in the abundance of the two main metabolic pathways for H2S synthesis: M00176 (assimilating sulfate reduction pathway) and M00596 (dissimilatory sulfate reduction pathway).

2.6. Measurement of Serum H2S Levels by H2S Selective Sensor. H2S levels in serum samples were measured using the free radical analyzer TBR4100 with an H2S selective sensor (ISO-H2S-100, WPI, China), as previously described [16].

2.7. Statistical Analysis. GraphPad Prism (version 9.3.1) and R language 3.6.1 were used to process data, which are reported as mean ± standard deviation (SD). Student's t-test was used to compare the two groups. The Wilcoxon rank sum test was used to analyze the differences of the diversity index, microbiota abundance, and H2S metabolism pathway abundance between the two groups. Bivariate relationships were performed with a Pearson or Spearman rank correlation model. The Kruskal–Wallis rank sum test was used with LEfSe analysis. A P value < 0.05 was considered significant.

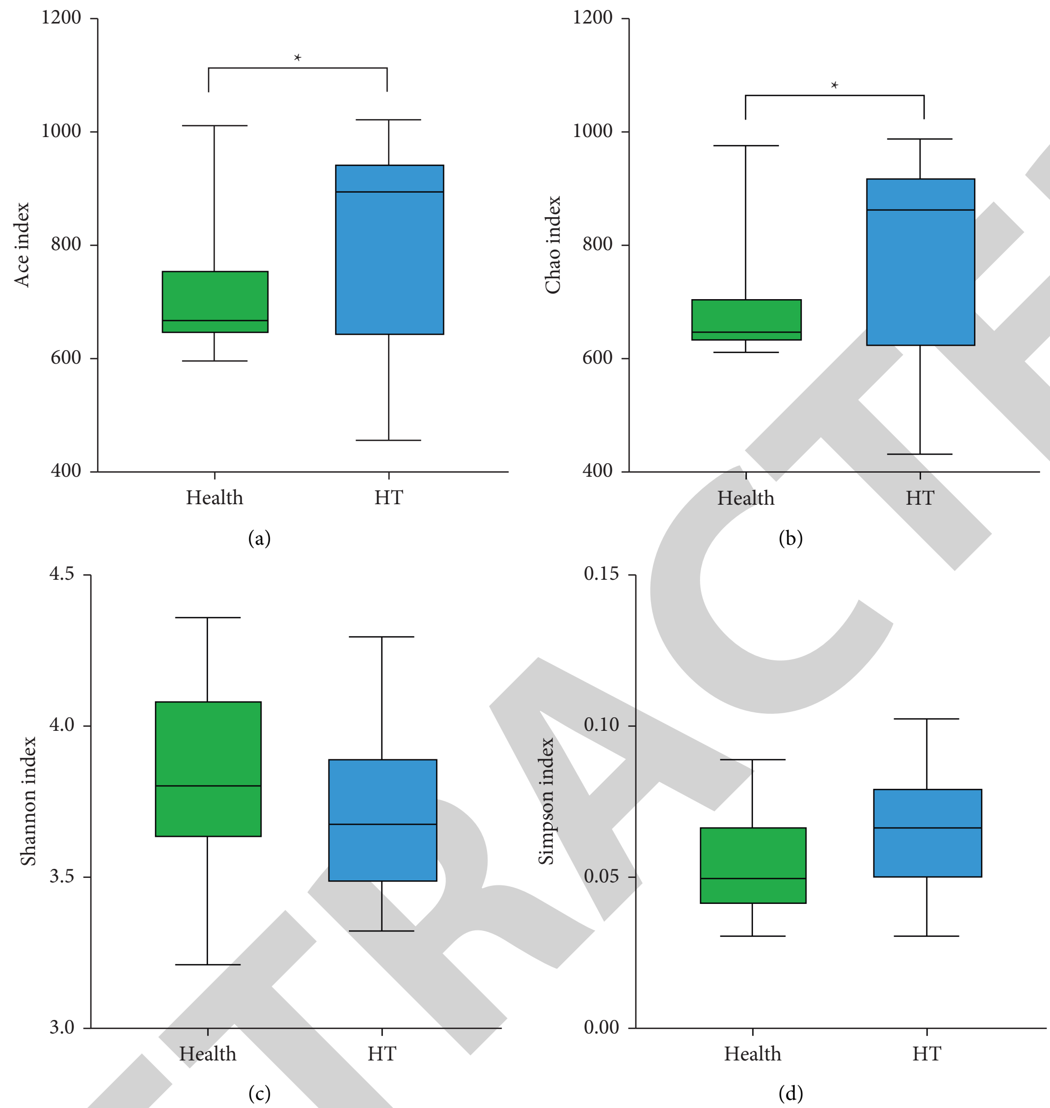

Figure 1: Continued.

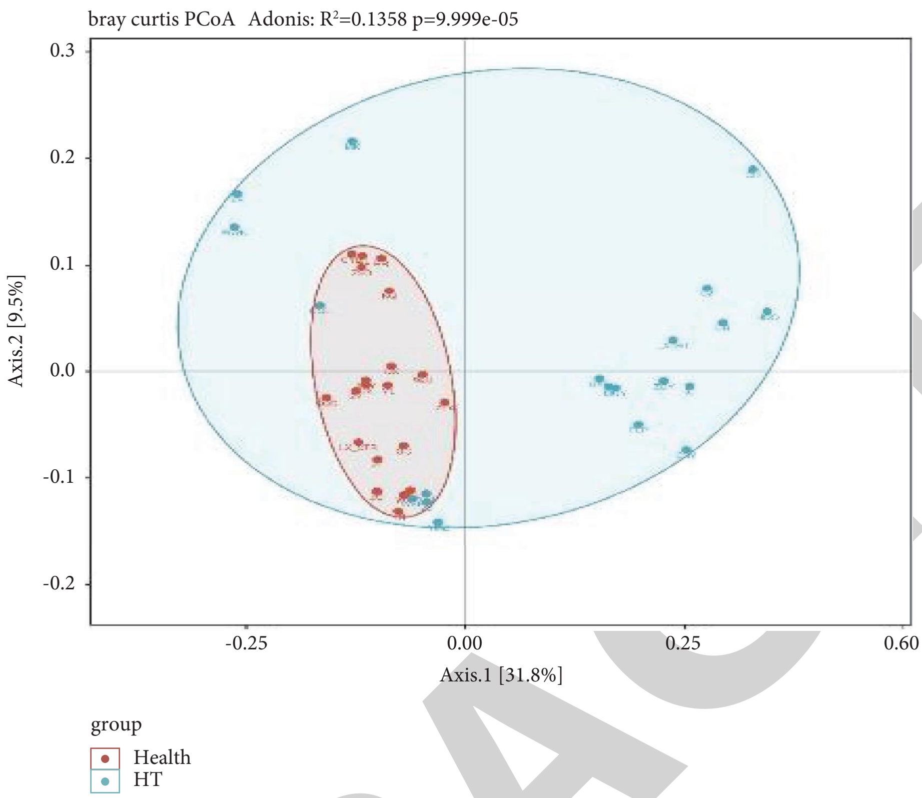

(e)

Figure 1: α and β diversity of the intestinal microbiota in patients with HT and healthy controls. (a–d) Microbial α diversity in patients with HT and healthy controls. The richness was significantly lower in healthy controls according to the ACE and Chao indexes. (e) Microbial β diversity. Bray–Curtis principal coordinate analysis (Bray-Curtis PCoA) revealed that the microbial composition in patients with HT differed from that in healthy controls. $^*P < 0.05$. HT, Hashimoto's thyroiditis.

3. Results

3.1. Intestinal Microbiota Diversity and Composition in Patients with HT and Healthy Controls. Compared with the HT group, the ACE and Chao indices, which reflect abundance, were significantly lower in healthy controls ($P = 0.04$, 0.03, respectively) (Figures 1(a) and 1(b)). We analyzed β diversity using Bray–Curtis principal coordinate analysis (Bray–Curtis PCoA). The results showed that the microbial composition of the HT group was significantly different from the healthy controls (Figure 1(e)). We determined the taxon composition of these two groups and sequenced 32 phyla and 596 genera. At the phylum level, the proportions of Bacteroidetes, Fusobacteria, and Tenericutes in patients with HT were significantly higher than those in healthy controls, and the proportion of Firmicutes in patients with HT was significantly lower ($P < 0.05$). At the genus level, the proportions of *Bacteroides*, *Fusobacterium*, *Sutterella*, and *Veillonella* in patients were significantly higher, and the proportions of *Blautia*, *Lachnoclostridum*, and *Roseburia* in patients were significantly lower ($P < 0.05$). (Figures 2(a) and 2(b)). We also identified specific bacterial taxa associated with the two groups using LEfSe analysis (linear discriminant analysis (LDA) > 4.0, all $P < 0.05$). At the genus level, *Bacteroides* and *Ralstonia* were enriched in patients in the LEfSe analysis. *Escherichia*, *Shigella*, *Blautia*, and *Faecalibacterium* were more enriched in the healthy controls (Figure 2(c)). The above results showed that patients with HT had aberrant intestinal microbiota.

3.2. H2S Levels in Serum Samples Were Lower in Patients with HT Compared to Healthy Controls. We found that H2S levels in serum samples from patients were significantly lower than those in healthy controls ($P < 0.05$) (Figure 3(a)). We also observed that the H2S was negatively correlated with the serum TgAb level ($r = -0.533$, $P = 0.0004$, Figure 3(b)). This indicated that the alteration of the intestinal microbiota and downregulation of H2S were associated with HT.

3.3. H2S DSR Pathway Enrichment in the HT Intestinal Microbiota Was Downregulated. We analyzed the enrichment of the H2S metabolic pathway in the intestinal microbiota. There was no difference in the ASR between the two groups (Figure 3(c)). In DSR, the enrichment of intestinal microbiota from patients with HT decreased when compared to that of healthy controls ($P = 0.06$, Figure 3(d)). This result suggested that the microbiota from patients with HT likely had a reduced ability to synthesize H2S.

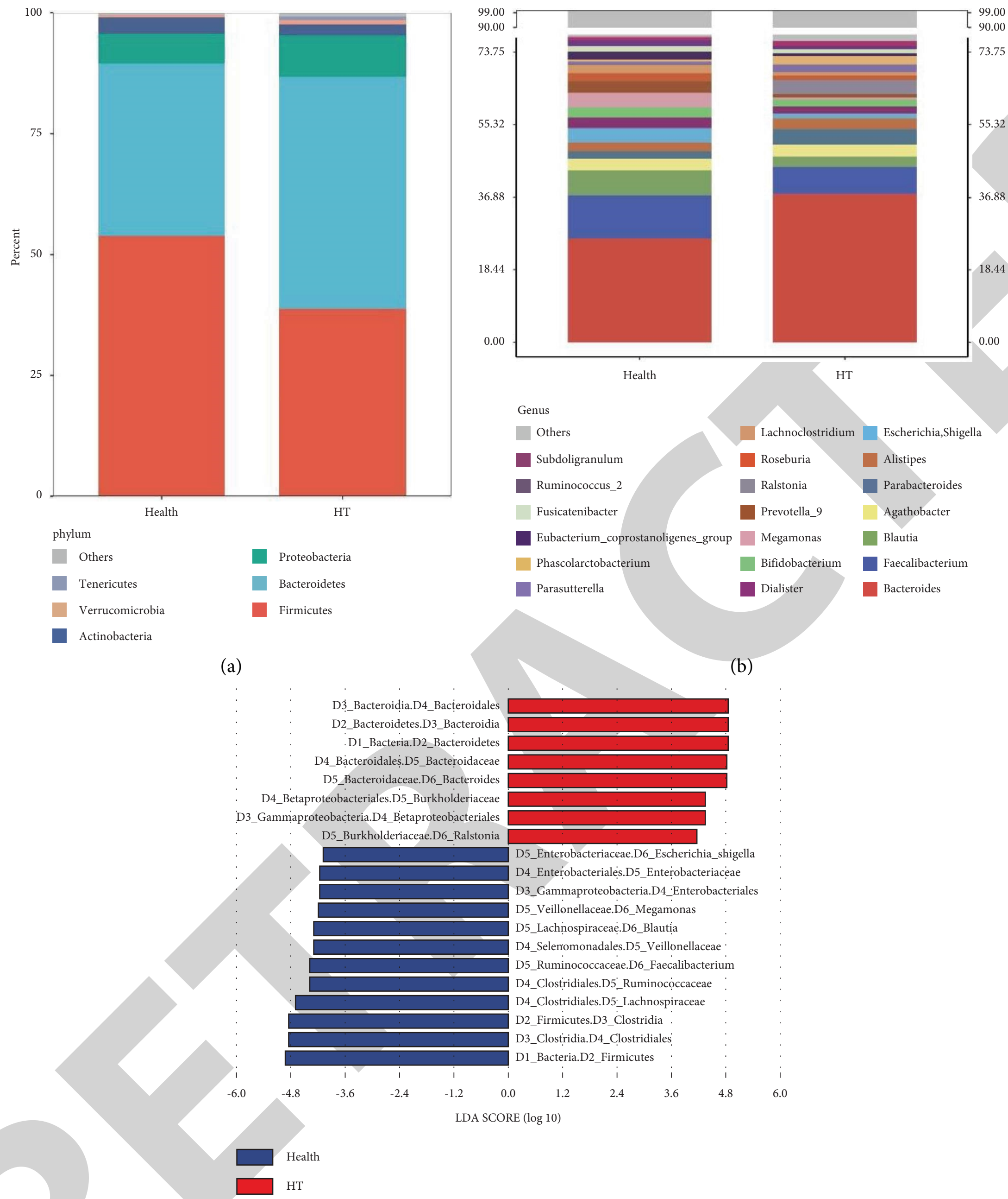

(c)

Figure 2: Altered composition of intestinal microbiota in patients with HT and healthy controls. (a) Composition of the intestinal microbiota at the phylum level. (b) Composition of the intestinal microbiota at the genus level. (c) The LEfSe was used to identify species that significantly differed between patients with HT and healthy controls (LDA score of >4 and a significance of $P < 0.05$). HT, Hashimoto's thyroiditis.

4. Discussion

Several studies have discussed the causes of HT including genetic susceptibility and environmental factors. However, the pathogenesis of HT remains unclear [17]. Here, we verified that the intestinal microbiota in patients with HT differed from that in healthy controls. Patients with HT had lower H2S levels in the serum, and the metabolism of H2S in the microbiota from patients appeared to be downregulated.

Emerging evidence suggests that the intestinal microbiota is associated with the pathogenesis of HT. Several studies have described significantly different ß diversity in patients with HT compared with that in healthy controls [4–8]. A meta-analysis of the association between intestinal microbiota and autoimmune thyroiditis showed that the Chao index was increased in the HT group [18], which was consistent with our findings. The intestinal microbiota of patients was altered.

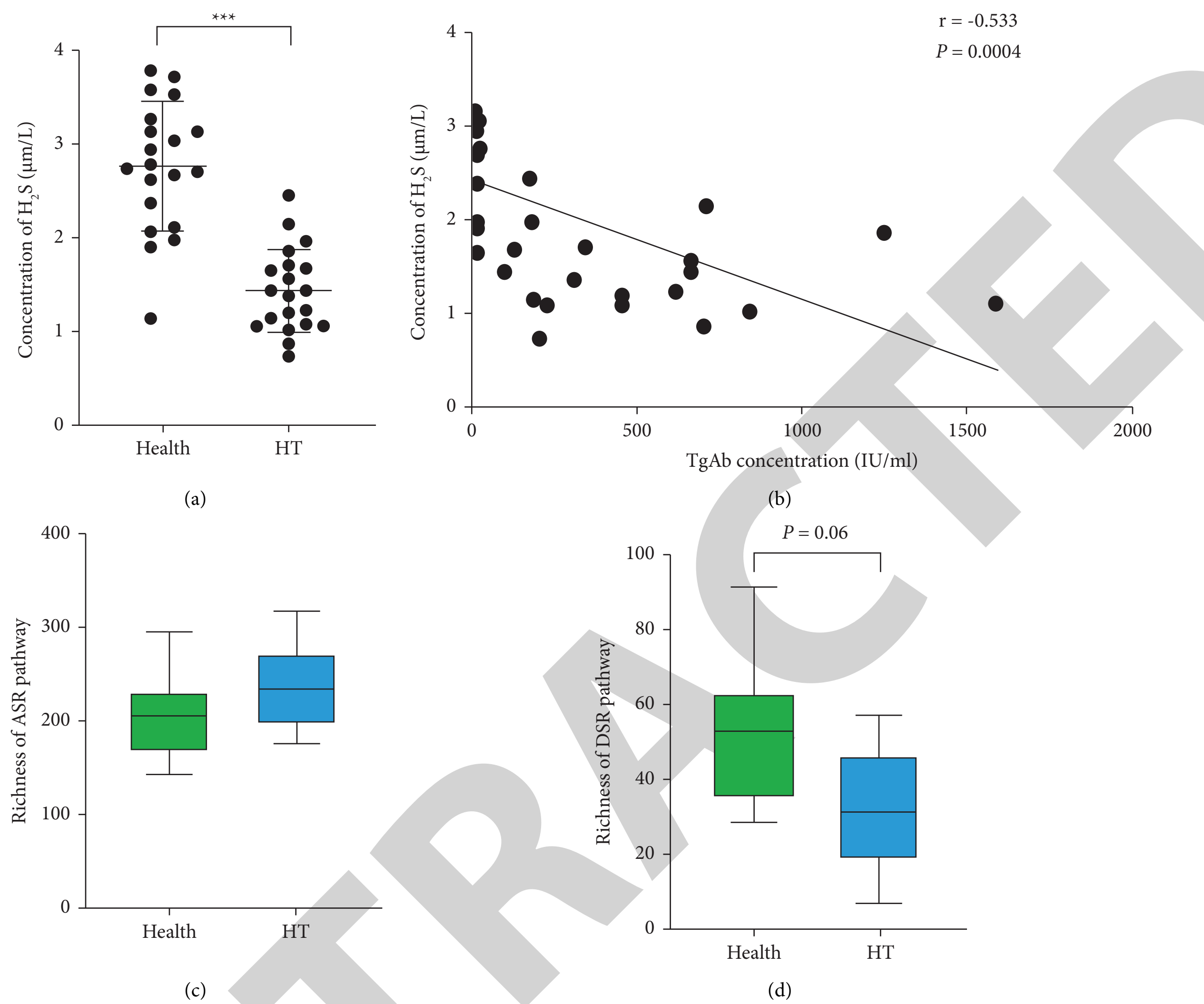

Figure 3: Serum levels of H2S and the metabolism of H2S in intestinal microbiota. (a) The serum levels of H2S in patients with HT and healthy controls. (b) The correlation between H2S and TgAb. (c) The richness of the ASR pathway in intestinal microbiota from two groups. (d) The richness of the DSR pathway in intestinal microbiota from two groups. $^{***}P < 0.05$. ASR, assimilatory sulfate reduction; DSR, dissimilatory sulfate reduction; HT, Hashimoto's thyroiditis; TgAb, thyroglobulin antibody.

Our study showed that the incidence of *Blautia* was significantly lower in patients with HT. *Blautia* plays an important role in maintaining environmental balance in the intestine and preventing inflammation by upregulating intestinal regulatory T cells and producing short-chain fatty acids (SCFAs) [19]. The abundance of *Blautia* is negatively correlated with some inflammatory diseases [20]. Therefore, *Blautia* might be a protective bacterium genus from HT. The data showed that *Bacteroides* were enriched in patients with HT. *Bacteroides* is a pro-inflammatory bacterium that contributes to inflammatory bowel disease [21]. A study by Ishaq et al. also showed augmented *Bacteroides* levels in patients with HT [7]. The altered composition of the beneficial and harmful bacteria might be a possible factor in the pathogenesis of HT.

In addition to discussing the alteration of microbiota, we explored the mechanism by which microbiota affects thyroid autoimmunity. Immune cells are targets of H2S. T cell differentiation and function are significantly regulated by H2S [22]. The dysfunction of T cells, such as Th1, Th17, and regulatory T cells, is associated with the pathogenesis of HT [23–25]. There are no studies about the relationship between H2S and HT, to the best of our knowledge. Our results showed that H2S levels in the serum of patients were lower than those in healthy controls.

The intestinal microbiota can reduce sulfide to produce H2S and subsequently diffuse the H2S through the mucous membranes [26]. The reduction of H2S occurs by two pathways: ASR and DSR. Only the terminal product of DSR is H2S [13]. In our study, the enrichment of DSR in the intestinal microbiota decreased in patients, and this may be attributed to the downregulation of serum H2S levels in patients with HT.

We analyzed the intestinal microbiota in untreated euthyroid HT patients to avoid the influence of different thyroid functions and medications on intestinal microbiota.

Hindawi
Journal of Healthcare Engineering
Volume 2023, Article ID 9815989, 1 page
https://doi.org/10.1155/2023/9815989

Retraction

Retracted: Prediction and Analysis of Autism Spectrum Disorder Using Machine Learning Techniques

Journal of Healthcare Engineering

Received 28 November 2023; Accepted 28 November 2023; Published 29 November 2023

This article has been retracted by Hindawi, as publisher, following an investigation undertaken by the publisher [1]. This investigation has uncovered evidence of systematic manipulation of the publication and peer-review process. We cannot, therefore, vouch for the reliability or integrity of this article.

Please note that this notice is intended solely to alert readers that the peer-review process of this article has been compromised.

Wiley and Hindawi regret that the usual quality checks did not identify these issues before publication and have since put additional measures in place to safeguard research integrity.

We wish to credit our Research Integrity and Research Publishing teams and anonymous and named external researchers and research integrity experts for contributing to this investigation.

The corresponding author, as the representative of all authors, has been given the opportunity to register their agreement or disagreement to this retraction. We have kept a record of any response received.

References

[1] M. S. Qureshi, M. B. Qureshi, J. Asghar, F. Alam, and A. Aljarbouh, "Prediction and Analysis of Autism Spectrum Disorder Using Machine Learning Techniques," *Journal of Healthcare Engineering*, vol. 2023, Article ID 4853800, 10 pages, 2023.

Hindawi
Journal of Healthcare Engineering
Volume 2023, Article ID 4853800, 10 pages
https://doi.org/10.1155/2023/4853800

Research Article

Prediction and Analysis of Autism Spectrum Disorder Using Machine Learning Techniques

Muhammad Shuaib Qureshi,[1] **Muhammad Bilal Qureshi**,[2] **Junaid Asghar**,[3] **Fatima Alam**,[4] **and Ayman Aljarbouh**[1]

[1]*Department of Computer Science, School of Arts and Sciences, University of Central Asia, Naryn, Kyrgyzstan*
[2]*Department of Computer Science & IT, University of Lakki Marwat, KPK 28420, Pakistan*
[3]*Gomal Centre of Pharmaceutical Sciences, Faculty of Pharmacy, Gomal University Dera Ismail Khan, KPK, Pakistan*
[4]*Department of Computer Science, Shaheed Zulfikar Ali Bhutto Institute of Science and Technology, Islamabad 44000, Pakistan*

Correspondence should be addressed to Muhammad Shuaib Qureshi; muhammad.qureshi@ucentralasia.org

Received 14 February 2022; Revised 5 March 2022; Accepted 5 April 2022; Published 10 July 2023

Academic Editor: Liaqat Ali

Autism spectrum disorder is a severe, life-prolonged neurodevelopmental disease typified by disabilities that are chronic or limited in the development of socio-communication skills, thinking abilities, activities, and behavior. In children aged two to three years, the symptoms of autism are more evident and easier to recognize. The major part of the existing literature on autism spectrum disorder is covered by a prediction system based on traditional machine learning algorithms such as support vector machine, random forest, multiple layer perceptron, naive Bayes, convolution neural network, and deep neural network. The proposed models are validated by using performance measurement parameters such as accuracy, precision, and recall. In this research, autism spectrum disorder prediction has been investigated and compared using common parameters such as application type, simulation method, comparison methodology, and input data. The key purpose of this study is to give a centralized framework to use for researchers working on autism spectrum disorder prediction. The best results were obtained by using the random forest algorithm as it performs better than other traditional machine learning algorithms. The achieved accuracy is 89.23%. The workflow representations of the investigated frameworks assist readers in comprehending the fundamental workings and architectures of these frameworks.

1. Introduction

Due to its diverse genetic structure and compound neural connectivity, the human brain is the most structured and complex body organ. A scale-free network is called a neuronal connection between neurons, as it changes with enhancement. The more knowledge the brain receives, the more synaptic associations are formed, and then the analysis becomes more complicated. The connection between cognitive growth and functional brain wiring improves the interpretation of neurological disorder [1]. Owing to the irregular wiring between the various brain areas, autism is one of the heterogeneous and psychological growth disorders [2]. A neurodevelopmental disorder is known as the autism spectrum disorder (ASD) [1] that affects communication and behavior. The rise in the number of people suffering from ASD worldwide demonstrates a significant need for the implementation of ASD prediction models that are efficient and easy to execute. The nature of these models differs greatly with time and skill, and to understand this diversity, the idea of an autism spectrum has been implemented [3]. Around 50% of autistic children suffer from mental impairment. Some have aberrantly enlarged brain size, one-third have had at least two late adolescent epileptic seizures, and around half have a significant speech impairment [4]. Some autistic children have analytical abilities that are highly developed and this originated the word *autism spectrum disorder*. The ASD comprises of an autism disorder, Asperger's syndrome, and pervasive developmental disorder, not otherwise mentioned [5]. Genetic factors play a significant role in ASD. Autism is convincingly attributed to genetic mutations, gene deletions, variations of copy number (CNVs), and other genetic anomalies [6].

Some individuals with ASD are very verbal and communicative, while others do not use any means of communication that are verbal. Additionally, some individuals with ASD are very distracted from all aspects of social contact, while others have relationships and careers [7]. Studies show that the brain development of ASD individuals grows differently from the brain of typical controls. Autism is the most rapid developmental disorder in male and is four times more common than in female [8].

In fact, the ASD identification depends mainly on the medical experience used during direct interviews to determine patient's behavior [9]. The last 25 years are of great importance because it has seen enormous improvements in the detection of autism at an early stage. Before children learned vocabulary and iconic play skills, there was a debate about whether they could recognize autism. Improvements in early activity and structural changes in the brain have been reported in 6–12 month-old babies who continue to develop autism [10]. Machine learning algorithms can be used to evaluate data and obtain the finest biological markers from hundred biological markers if they have sufficient amount of data and also have high computation power [11]. The authors in [12] have used deep neural networks (DNNs) to classify ASD in functional magnetic resonance imaging (fMRI), recognizing the analytical decision-making driven by data and predict ASD.

The motivation behind this study is to present a method for diagnosing the autism spectrum disorder with the help of a better and accurate machine learning model. In order to predict the autism spectrum disorder, the machine learning algorithm provides an exact answer to the medical treatment system.

The major contributions of this research work are as follows:

(i) Balanced and scale data technique is used to test whether it affects the performance?
(ii) Feature selection technique is applied to select optimal features from the whole dataset for prediction,
(iii) Better machine learning-based autism spectrum disorder prediction model is proposed that predicts autism with better accuracy and improves the performance.

2. Previous Studies on Autism Spectrum Disorder Prediction

This section explains previous studies that use machine learning-based approaches to detect and predict the autism spectrum disorder. The main motive is to analyze and find some limitations to propose a new, better, and improved machine-learning based approach for autism spectrum disorder prediction.

Table 1 describes some acronyms that are used in this paper.

Automated algorithms for disease detection are being deeply studied for usage in healthcare. Graph theory and machine learning algorithms were used. For each age range being examined, the pipeline automatically selected 10 biomarkers. In discriminating between ASD and HC, measures of centrality are the most operational [11]. The study [13] used a neural network-based feature selection method from teacher-student which was suggested to have the most discriminating features and applied different classification algorithms. The results are compared with the already presented methods at the overall and site level. The authors in [14] also utilize the neural network to acquire the distributions of PCD for the classification of ASD as it has far more hyper parameters that make the model extra versatile. Payabvash et al. [15] used computer leaning algorithms to classify children with autism based on tissue connectivity metrics, hence, observed decreased connectome edge density in the longitudinal white matter tracts. It illustrated the viability of it in identifying children with ASD, connectome-based machine-learning algorithms. Emerson et al. [16] shows how functional neuroimaging can reliably predict which individuals obtain a clinical diagnosis of ASD at 24 months with 6-month-old infants at high familial risk for ASD.

In ref [17], the authors simulated machine learning techniques on data acquired from rest-state brain imaging to diagnose autism. The drawback of the proposed research is that it does not use any best feature selection method with repeating periods of 2s (sites NYU, SDSU, UM, USM). This led to a dataset of 147 ASD subjects and 146 balanced controls. The authors in [18, 19] conclude that the data may be used to establish diagnostic biomarkers for the progression of autism spectrum disorders and to distinguish those with the condition in the general population. Wang et al. [20] proposed an ASD identification approach which focuses on multi-atlas deep feature representation and ensemble learning technique. In study [21], the multimodal automated disease classification system uses two types of activation maps to predict whether the person is healthy or has autism. It was able to achieve 74% accuracy. Rakić et al. [22] suggested a technique which is based on a system composed of autoencoders and multilayer perceptron. Because of a multimodal approach that included a set of structural and functional data classification classifiers, the highest classification precision was 85.06%. In study [23], advanced deep-learning algorithms are proposed where HPC solutions can increase the accuracy and time of broad fMRI data analysis significantly. The authors in [24] explain what the results of machine learning studies may mean for the ultimate objective of determining an ASD biomarker that is uniquely sensitive and precise. However, the results cannot be applied to the entire ASD functional continuum. The study did not include evidence from other developmental conditions and was thus unable to specifically assess the specificity of typical CRF connections. Thomas et al. [25] introduced a novel analysis technique to identify changes in population dynamics in functional networks

Table 1: Description of acronyms.

Acronym	Description
ASD	Autism spectrum disorder
DNN	Deep neural network
LDA	Linear discriminant analysis
SVM	Support vector machine
ANN	Artificial neural network
CDC	Centers for disease control and prevention
KNN	K-nearest neighbor
LR	Logistic regression
SMOTE	Synthetic minority over sampling technique
RF	Random forest
MLP	Multilayer perceptron
NB	Naïve Bayes
fMRI	Functional magnetic resonance imaging
FC	Functional connectome
RSN	Randomized subspace Newton

under ASD. They have also introduced machine learning algorithms to predict the class of patients with ASD and normal controls by using only population trend quality metrics as functions. The limitation of this approach is that the outcomes of the classification are highly dependent on the threshold parameter T. Another problem is that despite age variations in the experimental samples, the same spatial normalization design was used for all subjects. The authors in ref [26] proposed a collection of new features based on MRI images using machine learning algorithms to diagnose ASD which achieved 77.7% accuracy using the LDA approach.

Yin et al. [27] developed deep learning methods from functional brain networks built with brain functional magnetic resonance imaging (fMRI) data for the diagnosis of ASD. Another study [28] used a graph-based classification approach which yields better results but missing values are not handled and data normalization is not applied. A previous study [29] analyzes and works on brain networks which are inherent. It is deduced that ASD may be caused due to the aberrant mechanisms. The underlying individual variations in ASD symptom severity may be dysfunction in SN and visual systems and associated processes. Smith et al. [30] suggest that a weakened interaction with RSN temporal entitlement (RSN) and a higher degree of symptom severity in ASD people is correlated with the association with symptoms of the autism spectrum disorder. The findings suggest that FC and entropy provide additional details on the temporal spatio-organization of the brain. The authors in [31] proposed a novel element-wise layer incorporating general prior convictions built for connectomes and utilizes Brain-Net CNN and L2 regularization algorithm for classification purposes. The technique was validated using the K-Fold cross-validation method. However, this study does not utilize any pre-processing and feature selection technique as it highly affects the accuracy of the model. A multichannel deep attention neural network called DANN was proposed in [32] in which mechanism-based learning with attention achieved a precision of 0.732. However, this study is limited because the selected cohort is in the population of teenagers and young adults, and hence, restricting the generalizability of the model since the diagnosis of ASD was carried out much earlier. Alvarez-Jimenez et al. [33] presented a multiscale descriptor to classify brain regions and recognize those with discrepancies between groups using a 2D representation and the curvelet transform. With regards to the state-of-the-art methods, including those focused on deep learning, it is shown to be successful. Another study [34] used the scope of the brain network's Laplacian matrix and topology centrality as characteristics. This study utilizes the features that are presented in [26] and acquired 79.2% accuracy. The study [35] suggested a novel architecture using CNN which has to identify autism and monitor patients using RS-fMRI data. This study concludes that through structural MRI images, 3D convolutionary neural networks can also be used to distinguish healthy subjects and patients with autism. Sherkatghanad et al. [36] suggested a CNN architecture. The mean accuracy of the presented model which used 234 test data is 70.2% but no feature selection technique was utilized. The authors in [19] indicate that deep learning techniques can classify broad multi-site datasets accurately which may be useful for the potential application of machine learning to identify psychological conditions. The authors in [37] suggest the ANN algorithm for multisite data and also shares the importance of network connectivity for classification was linked to verbal communication deficits in autism. The study [38] utilizes deep neural network and atlases for classification and acquired the accuracy of 78.07% on real data and 79.13% on augmented data.

3. Proposed Model

The proposed model presented in Figure 1 is a concept of a system made up of the composition of ideas that are used by optimal feature selection to help people learn, understand, or estimate the prediction of autism spectrum disorder. The main purpose of the conceptual model is to communicate the basic principles and characteristics of the system reflected by it. The computational model is built to offer an interpreted understanding of the framework to the consumers of the software.

The proposed model consists of six major steps that are as follows: (1) data collection as data are collected from ABIDE and ABIDE collected data using 17 different sites, (2) data pre-processing which includes following steps such as if missing values present then they are imputed rather than deletion, the whole dataset scaled at same scale to improve results, the number of instances in dataset for two classes has been balanced, outliers first detected than removed from dataset for its biasness in results, and features have been selected using machine learning technique, (3) data splitting technique which splits data into testing, training, and validation datasets, (4) classification model uses four different classifiers such as SVM, MLP, NB, and RF to check which classifier performs the best with selected dataset, (5) model evaluation is performed using parameters like accuracy, precision, and recall, and (6) validation is carried out using the k-fold mechanism.

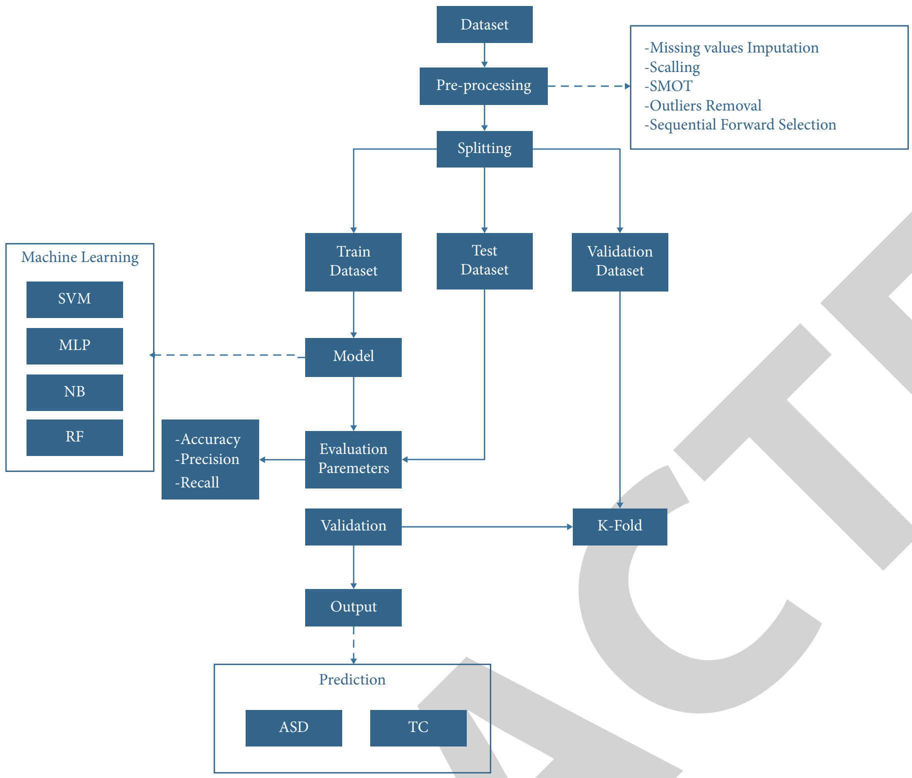

Figure 1: ML-based ASD classification model.

4. Materials and Methods

4.1. Experimental Setup. In Google Co Labs, a free online cloud-based Jupyter Notebook environment is used. Python packages are used for pandas for loading the data set; NumPy for handling the subsets, and pilots for making plots. The pre-processing includes making subsets, selection of best features, removal of missing values, and the application of SMOTE is performed using the programming language Python in the Jupyter Notebook. The machine learning steps are also implemented in Python. To put the features in a better format and split the data in the test and train NumPy was used. To cross-validate the model, sklearn library was used. To smoothly run and validate the proposed model, machine having specification of Windows 10, CPU 2.9 GHz core i7, GPU Intel HD Graphics 620, RAM 12 GB, and free disk space of minimum 5 GB was used for experiments.

4.2. Data. The dataset used in this study is retrieved from the widely recognized ABIDE dataset used by many researchers [11, 13, 14, 16–36]. The dataset aims to diagnose whether or not a patient has autism based on certain diagnostic measures in the dataset. The collection of such instances from a broader database was subject to certain restrictions. In particular, all patients are males aged between 7 and 64 years. The datasets consist of multiple variables of medical predictors and one objective variable, the outcome. Predictor variables include the size of the functional voxel, age, etc. The ABIDE dataset consists of the 1112 subjects' rs-fMRI images, structural MRI images (T1-weighted), and phenotypic information. 539 of these are ASD while 573 are TC subjects as represented in Figure 2. Because of the diversity of the subjects, the ABIDE dataset is a very challenging dataset to work with instances.

4.3. Pre-Processing

4.3.1. Missing Value Imputation. The number of missing values, however, is high. This step involves a data exploratory process to identify and handle the outliers by using the box plot approach. There were various missing values in the dataset, so the missing values were handled by an iterative imputer. In general, the data input method is better because it makes it possible to use as many samples for machine learning as possible. Iterative imputation is a method where every feature is shaped as a function of the other features, e.g., a regression problem where missing values are predicted. After missing value imputation, all of the features have 1112 instances and all missing values are vanished by using the iterative missing value imputation method.

4.3.2. Outliers Detection. Outliers have been detected using box plot and then the interquartile range is defined which uses an upper limit and lower limit of column and removes the values which lie outside the limit. All the outliers are removed using this technique.

4.3.3. SMOTE for Balancing the Dataset. The simplest methodology to cope with the imbalanced datasets is to

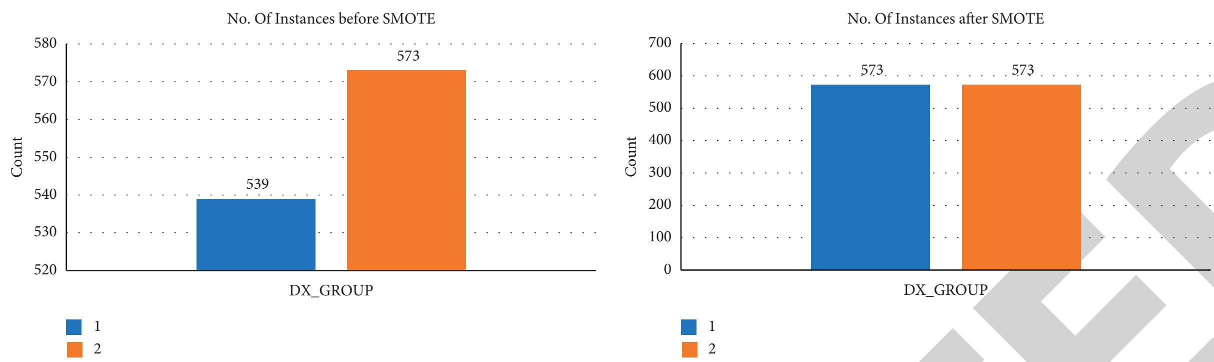

(a) (b)

Figure 2: Dataset before and after SMOTE. (a) Dataset before SMOTE. (b) Dataset after SMOTE.

oversample the minority class with replicating examples in the autism class. The SMOTE is the method that produces artificial instances on a random basis of the minority class from the nearest neighbors of the line joining the minority class sample to increase the number of the already available original instances. Therefore, these artificial instances are created on the basis of the original dataset features so that they become like the original instances of the minority class.

4.3.4. Feature Selection with Sequential Forward Selection. Sequential forward selection (SFS) is used for feature selection due to its immense significance. We have used it because the used dataset is based on 1112 instances and 74 features which mean high dimensional which needs to exclude some features.

4.3.5. Dataset Splitting. In this phase, total number of the autism patient dataset is split into two partitions for training and testing. With respect to the proposed model, training partition contained 70% data while remaining 30% data used for testing purpose. Literature describes 70-30 split strategy of input data. Out of total 1146 instances, 803 training instances were used for building classifying models of machine learning algorithms and remaining 343 training instances for testing partition were used to evaluate the built models.

4.4. Classification. We have used random forest with other machine learning techniques such as naive Bayes, support vector machine, and multiple layer perceptron algorithms.

4.4.1. Random Forest (RF). RF is a machine learning technique for solving classification and regression problems using decision tree algorithms. To train the 'forest' formed by the random forest method, a bagging or bootstrap aggregation method is used. To overcome the drawbacks of a decision tree algorithm, the random forest method is used. It decreases dataset overfitting and enhances accuracy. It makes predictions without requiring extensive package parameters (such as scikit-learn). Let $\hat{c}_b(x)$ be the class prediction of the b-th random-forest tree, then

$$\hat{C}^{B}_{xf}(x) = \left\{\hat{C}_b(x)\right\}_1^B. \tag{1}$$

4.4.2. Naïve Bayes (NB). The naive Bayes technique is a supervised learning procedure for tackling classification issues which is based on the Bayes theorem that makes predictions based on an object's probability. Bayes' theorem is numerically presented as follows:

$$P(A \mid B) = \frac{P(B \mid A)P(A)}{P(B)}, \tag{2}$$

where $P(A|/B)$ is the probability of hypothesis A on the observed event B which is known as posterior probability, $P(B|A)$ is the probability of the evidence given that the probability of a hypothesis is true known as likelihood probability. $P(A)$ is the probability of hypothesis before observing the evidence known as prior probability. $P(B)$ is the probability of evidence known as marginal probability.

4.4.3. Support Vector Machine (SVM). SVM is a supervised classification technique that uses a line to distinguish between two separate groups. In many circumstances, the separation is not that straightforward. The hyperplane dimension must be altered from one to the N^{th} dimension in this scenario called as Kernel. To put it another way, it is the functional link that exists between the two observations.

4.4.4. Multiple Layer Perceptron (MLP). A family of functions is defined by an MLP or multilayer neural network. MLP is a type of feedforward artificial neural network (ANN). MLP, especially those with a single hidden layer, is commonly referred to as "vanilla" neural networks. There are at least three levels of nodes in an MLP: an input layer, a hidden layer, and an output layer. Each node with the exception of the input nodes is a neuron with a nonlinear activation function. Backpropagation is a supervised learning technique used by MLP.

4.5. Model Validation. Cross-validation is a mathematical method for assessing master learning abilities. The K-fold validation method is employed for validation. In the K-fold

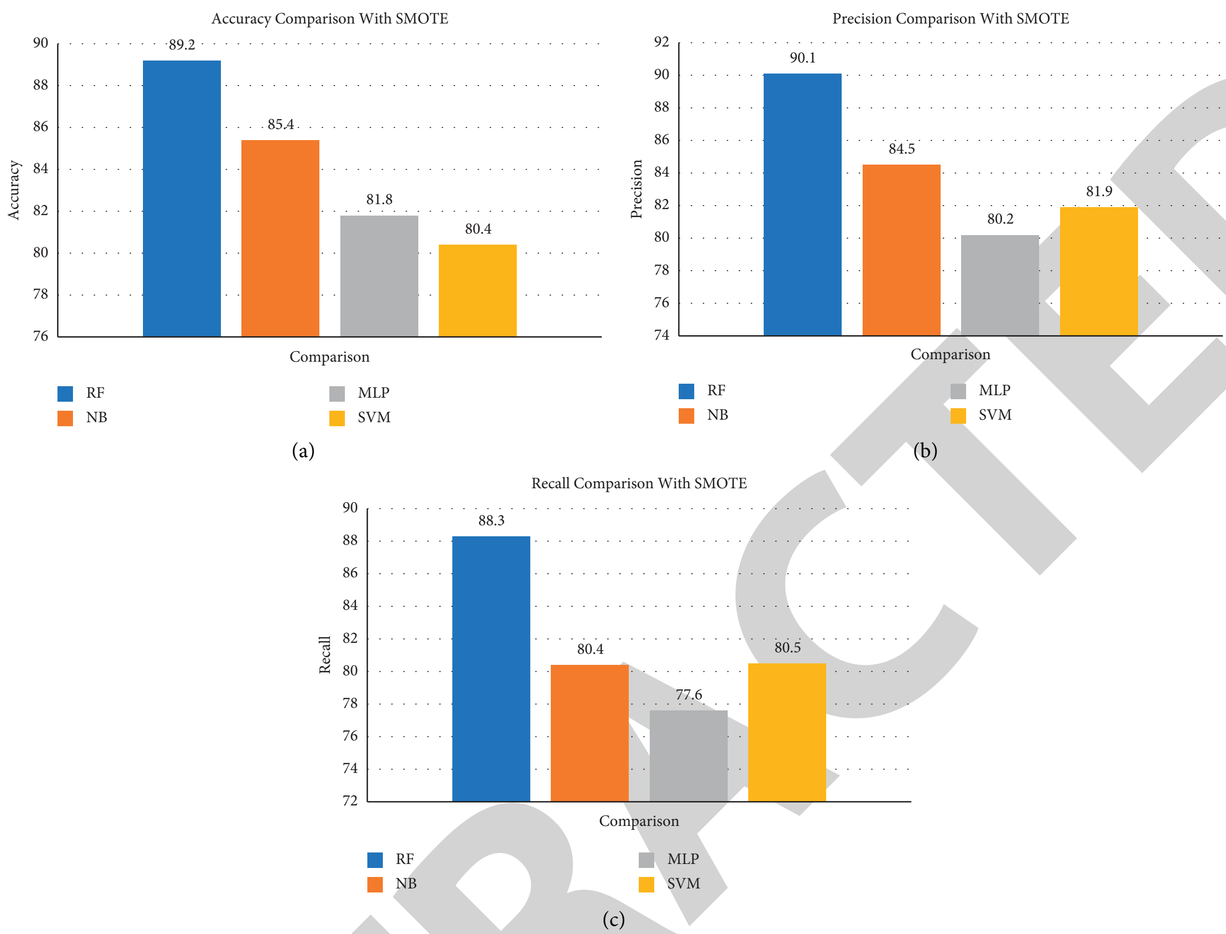

Figure 3: Comparison of RF, NB, MLP, and SVM. (a) Accuracy. (b) Precision. (c) Recall.

approach, the entire dataset serves as both training and testing. In this way, the entire dataset is tested by using 70% data for training and 30% data for testing against the test case and the findings are validated against the dataset.

4.6. Measurement. In this study, we used accuracy, recall, and precision for performance measurement as represented in (3)–(5).

$$\text{Precision} = \frac{\text{True Positive}}{\text{True Positive} + \text{False Positive}}, \tag{3}$$

$$\text{Accuracy} = \frac{\text{True Negative} + \text{True Positive}}{\text{True Negative} + \text{True Positive} + \text{False Negative} + \text{False Positive}}, \tag{4}$$

and

$$\text{Recall} = \frac{\text{True Positive}}{\text{True Positive} + \text{False Negative}}. \tag{5}$$

Here, the term true positive indicates that the model predicts positive class correctly and true negative indicates that model predicts negative class correctly. The four classifiers RF, NB, MLP, and SVM are compared in Figure 3 on the basis of accuracy, precision, and recall.

5. Results and Discussion

The prediction of autism spectrum disorder was carried out on the basis of a traditional machine learning technique consisting SVM, NB, RF, and MLP. The techniques were applied on a dataset balanced by using SMOTE. The technique was applied on the 1146 instances of 16 features on balance dataset. The results were obtained after 50 iterations. The empirical performance of traditional machine learning

Table 2: Accuracy comparison of RF, NB, MLP, and SVM.

Traditional classifier	Accuracy (%)	
	Imbalanced dataset	Balanced dataset (SMOTE)
RF	81.88	89.23
NB	79.12	85.43
MLP	75.11	81.84
SVM	83.33	80.43

Table 3: Precision comparison of RF, NB, MLP, and SVM.

Traditional classifier	Precision (%)	
	Imbalanced dataset	Balanced dataset (SMOTE)
RF	82.56	90.12
NB	77.23	84.52
MLP	75.15	80.21
SVM	79.54	81.89

Table 4: Recall comparison of classifiers.

Traditional classifier	Recall (%)	
	Imbalanced dataset	Balanced dataset (SMOTE)
RF	80.58	88.33
NB	78.32	81.43
MLP	72.23	77.58
SVM	75.65	80.55

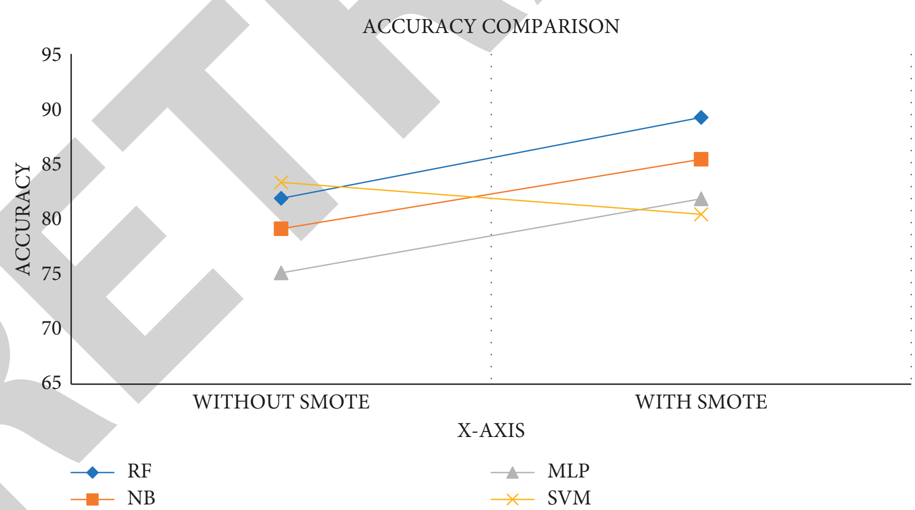

Figure 4: Accuracies comparison in the line chart.

algorithm-based classifiers is demonstrated in Table 2. According to the table, RF shows notable performance with respect to an accuracy of 94.73%. On the other hand, NB and MLP show better performance than SVM with respect to an accuracy of 91.86%, whereas SVM shows the least classification accuracy of 90.43%.

The RF gives a notable empirical result of 81.88% and 89.23% accuracy for imbalanced and balanced dataset, respectively. The NB gives 79.12% accuracy with imbalanced dataset; however, it gives 85.43% accuracy with balanced and scaled dataset. On the other hand, MLP gives 75.11% accuracy with imbalanced dataset and 81.84% with balanced dataset. Likewise, SVM gives 83.33% accuracy with imbalanced dataset but 80.43% with balanced dataset. It clearly shows that all traditional algorithms give improved accuracy with balanced and scaled dataset. The traditional four classifiers RF, NB, MLP, and SVM are compared on the basis of precision in Table 3.

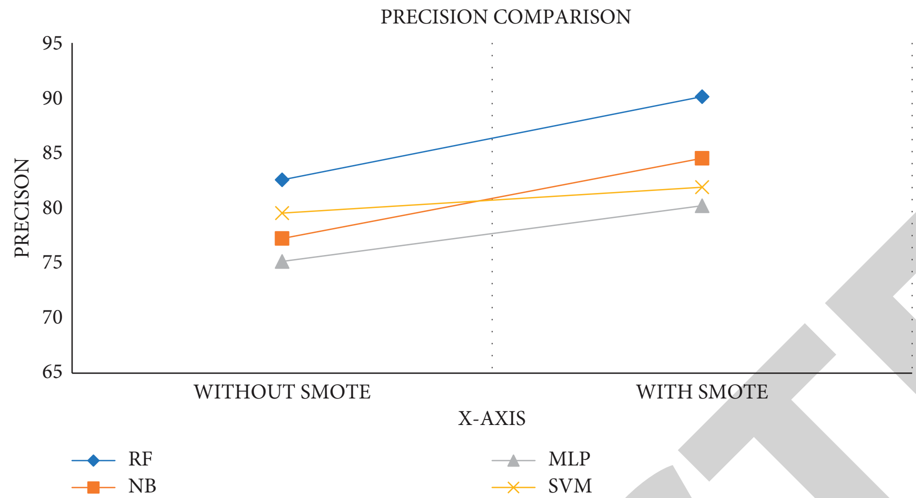

Figure 5: Precision comparison in the line chart.

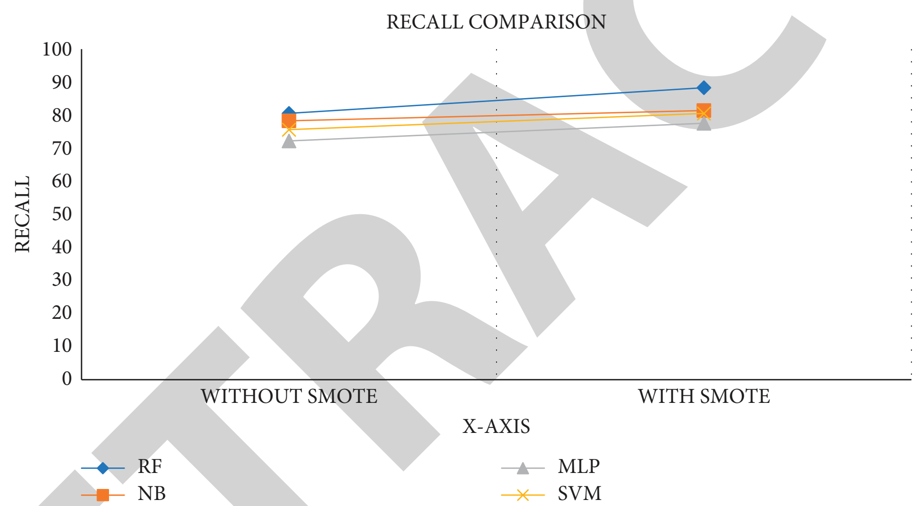

Figure 6: Recall comparison in the line chart.

Table 5: Comparison of existing techniques and the proposed technique.

Ref/Year	Model	Accuracy (%)
[32] 2020	Multichannel DANN model with RF	65.9
[32] 2020	Multichannel DANN model with SVM	69.3
[22] 2020	Classification method using MLP	85.06
[15] 2018	Potential biomarker identification model based on NB	66
	Proposed model	
	RF without balancing the dataset	81.88
	RF with balancing the dataset	89.23

It is clear that precision of RF with balanced dataset is 90.12% which is high as compared to the imbalanced data which is 82.56%. The NB gives precision of 77.23% and 84.52% with imbalance and balanced dataset. The MLP gives precision of 75.15% and 80.21% with imbalanced and balanced dataset. The SVM gives precision of 79.54% and 81.89% with imbalanced and balanced dataset, respectively. The four classifiers are compared in Table 4 on the basis of recall.

It is clear that recall of RF with balanced dataset is 88.33% which is high as compared to the recall with imbalanced data which is 80.58%. The NB gives recall of 78.32% and 81.43% with imbalanced and balanced dataset. The MLP gives recall of 72.23% and 77.58% with the imbalanced and balanced dataset. The SVM gives a recall of 75.65% and 80.55% with the imbalanced and balanced dataset, respectively.

6. Comparisons of Applied Classifier Techniques

We have implemented four classifiers RF, NB, MLP, and SVM algorithms where RF presents notable accuracy and precision performance as compared to the other traditional classifiers portrayed in Figures 4 and 5. Recall comparison is portrayed in Figure 6.

Table 5 shows accuracy comparison of the proposed autism prediction model with and without SMOTE.

7. Conclusion

The prediction model for the autism spectrum disorder plays a vital role in predicting autism and helps in diagnosing in time. In this research, we have surveyed prediction models for the autism spectrum disorder including different machine learning techniques. Theoretically, the working of these techniques have been evaluated and illustrated so that a new researcher can get started on a single board. The detailed comparison based on common parameters allows for the quick identification of architectural and implementation-related similarities and differences among various prediction models. We have given in-depth analysis which sets this study apart from other autism spectrum disorder techniques. Only autism spectrum disorder prediction techniques were consolidated in this study. The state-of-the-art ASD prediction using various machine learning techniques are comprehensively covered in this research but there are still plenty of opportunities for upcoming investigators.

As this model is better than state-of-the-art methods, but in future it can be tested with fuzzy logic algorithms for checking more accuracy for the autism spectrum disorder. In addition, other datasets can be experimented for a comparison purpose.

Data Availability

The dataset used in this study is retrieved from the widely recognized ABIDE (Autism Brain Imaging Data Exchange) dataset.

Conflicts of Interest

The authors declare that they have no conflicts of interest.

References

[1] S. Bhat, U. R. Acharya, H. Adeli, G. M. Bairy, and A. Adeli, "Autism: cause factors, early diagnosis and therapies," *Reviews in the Neurosciences*, vol. 25, no. 6, pp. 841–850, 2014.

[2] J. L. Matson, N. C. Turygin, J. Beighley, R. Rieske, K. Tureck, and M. L. Matson, "Applied behavior analysis in autism spectrum disorders: recent developments, strengths, and pitfalls," *Research in Autism Spectrum Disorders*, vol. 6, no. 1, pp. 144–150, 2012.

[3] U. Frith and F. Happé, "Autism spectrum disorder," *Current Biology*, vol. 15, no. 19, pp. R786–R790, 2005.

[4] I. Rapin, "The autistic-spectrum disorders," *New England Journal of Medicine*, vol. 347, no. 5, pp. 302-303, 2002.

[5] P. J. Landrigan, "What causes autism? Exploring the environmental contribution," *Current Opinion in Pediatrics*, vol. 22, no. 2, pp. 219–225, 2010.

[6] J. S. Sutcliffe, "Insights into the pathogenesis of autism," *Science*, vol. 321, no. 5886, pp. 208-209, 2008.

[7] AUTISM TREATMENT CENTER OF AMERICA: What is autism? 2021, https://autismtreatmentcenter.org/knowledge-base/what-is-autism-overview/?gclid=EAIaIQobChMIu7u77Nq46gIVgtKyCh3OAQQhEAAYASAAEgJk9fD_BwE.

[8] AUTISM SOCIETY: What are the facts and statistics of autism? 2021, https://www.autism-society.org/what-is/facts-and-statistics/.

[9] A. Zunino, P. Morerio, and A. Cavallo, "Video gesture analysis for autism spectrum disorder detection," in *Proceedings of the 2018 24th International Conference on Pattern Recognition (ICPR)*, pp. 3421–3426, IEEE, Beijing, China, November 2018.

[10] G. Dawson and R. Bernier, "A quarter century of progress on the early detection and treatment of autism spectrum disorder," *Development and Psychopathology*, vol. 25, no. 4pt2, pp. 1455–1472, 2013.

[11] A. Kazeminejad and R. C. Sotero, "Topological properties of resting-state fMRI functional networks improve machine learning-based autism classification," *Frontiers in Neuroscience*, vol. 12, p. 1018, 2019.

[12] X. Li, N. C. Dvornek, J. Zhuang, P. Ventola, and J. S. Duncan, "Brain biomarker interpretation in asd using deep learning and fmri," in *Proceedings of the Medical Image Computing and Computer Assisted Intervention - MICCAI 2018*, pp. 206–214, Springer, Granada, Spain, September 2018.

[13] N. A. Khan, S. A. Waheeb, A. Riaz, and X. Shang, "A three-stage teacher, student neural networks and sequential feed forward selection-based feature selection approach for the classification of autism spectrum disorder," *Brain Sciences*, vol. 10, no. 10, p. 754, 2020.

[14] M. N. Parikh, H. Li, and L. He, "Enhancing diagnosis of autism with optimized machine learning models and personal characteristic data," *Frontiers in Computational Neuroscience*, vol. 13, no. 9, p. 9, 2019.

[15] S. Payabvash, E. M. Palacios, J. P. Owen et al., "White matter connectome edge density in children with autism spectrum disorders: potential imaging biomarkers using machine-learning models," *Brain Connectivity*, vol. 9, no. 2, pp. 209–220, 2019.

[16] R. W. Emerson, C Adams, T Nishino et al., "Functional neuroimaging of high-risk 6-month-old infants predicts a diagnosis of autism at 24 months of age," *Science Translational Medicine*, vol. 9, no. 393, Article ID eaag2882, 2017.

[17] R. Tejwani, A. Liska, H. You, J. Reinen, and P. Das, "Autism Classification Using Brain Functional Connectivity Dynamics and Machine Learning," 2017, https://arxiv.org/abs/1712.08041.

[18] R. M. Thomas, S. Gallo, L. Cerliani, P. Zhutovsky, A. El-Gazzar, and G. van Wingen, "Classifying autism spectrum disorder using the temporal statistics of resting-state functional MRI data with 3D convolutional neural networks," *Frontiers in Psychiatry*, vol. 11, p. 440, 2020.

[19] A. S. Heinsfeld, A. R. Franco, R. C. Craddock, A. Buchweitz, and F. Meneguzzi, "Identification of autism spectrum disorder using deep learning and the ABIDE dataset," *NeuroImage: Clinic*, vol. 17, pp. 16–23, 2018.

Hindawi
Journal of Healthcare Engineering
Volume 2023, Article ID 9798461, 1 page
https://doi.org/10.1155/2023/9798461

Retraction

Retracted: Effect of the Holistic Nursing Model of Responsibility System on the Mental State of Elderly Patients with Limb Fractures Fixed by Splints in the Emergency Department

Journal of Healthcare Engineering

Received 28 November 2023; Accepted 28 November 2023; Published 29 November 2023

This article has been retracted by Hindawi, as publisher, following an investigation undertaken by the publisher [1]. This investigation has uncovered evidence of systematic manipulation of the publication and peer-review process. We cannot, therefore, vouch for the reliability or integrity of this article.

Please note that this notice is intended solely to alert readers that the peer-review process of this article has been compromised.

Wiley and Hindawi regret that the usual quality checks did not identify these issues before publication and have since put additional measures in place to safeguard research integrity.

We wish to credit our Research Integrity and Research Publishing teams and anonymous and named external researchers and research integrity experts for contributing to this investigation.

The corresponding author, as the representative of all authors, has been given the opportunity to register their agreement or disagreement to this retraction. We have kept a record of any response received.

References

[1] S. Du, Y. Hao, and Y. Jiao, "Effect of the Holistic Nursing Model of Responsibility System on the Mental State of Elderly Patients with Limb Fractures Fixed by Splints in the Emergency Department," *Journal of Healthcare Engineering*, vol. 2023, Article ID 1271606, 9 pages, 2023.

Hindawi
Journal of Healthcare Engineering
Volume 2023, Article ID 1271606, 9 pages
https://doi.org/10.1155/2023/1271606

Research Article

Effect of the Holistic Nursing Model of Responsibility System on the Mental State of Elderly Patients with Limb Fractures Fixed by Splints in the Emergency Department

Shaolan Du,[1] Yanli Hao,[2] and Yajuan Jiao [3]

[1] *Emergency Department, Baoji Central Hospital, Baoji, Shaanxi 721008, China*
[2] *Department of Ophthalmology, Affiliated Hospital of Yan'an University, Yan'an, Shaanxi 716000, China*
[3] *Department of Orthopedics, Baoji Central Hospital, Baoji, Shaanxi 721008, China*

Correspondence should be addressed to Yajuan Jiao; jiaoyajuan@stu.ahu.edu.cn

Received 16 March 2022; Revised 20 April 2022; Accepted 23 April 2022; Published 7 July 2023

Academic Editor: Liaqat Ali

Objective. To explore the effect of the overall nursing mode of responsibility system on the psychological state of elderly patients with limb fractures fixed by splints. *Methods*. This study selected 150 elderly patients who received emergency treatment of a limb fracture fixed by a traditional Chinese medicine splint in our hospital from May 2018 to June 2021 as the research subjects. They were divided into a control group and an observation group, with 75 cases in each group. The control group was intervened by traditional nursing mode, and the research group was intervened by responsible overall nursing mode. The quality of nursing work was observed and compared with the nursing staff's work quality and satisfaction, patients' psychological states and satisfaction, and the risk of clinical adverse events. *Results*. After management, the quality of nursing work in the two groups was significantly improved. Compared with before management, the scores of basic nursing measures, nursing of critical patients, ward environment management, disinfection and isolation, rescue drugs and instruments, and nursing document management in the observation group were significantly higher than those in the control group ($P < 0.05$). After management, the work quality and satisfaction of nurses in the two groups were significantly higher than those before management. The SERVQUAL scale score and satisfaction score in the observation group were significantly higher than those in the control group ($P < 0.05$). The scores of HAMA and HAMD in the observation group were significantly lower than those in the control group ($P < 0.05$). The overall satisfaction of nursing in the observation group was 96.00%, which was significantly higher than the 80.00% in the control group ($P < 0.05$). The incidence of adverse events in the observation group was 8.00%, which was significantly lower than 17.33% in the control group ($P < 0.05$). *Conclusion*. Giving elderly patients with limb fracture emergencies treated with splint fixation using traditional Chinese medicine the overall nursing mode management and responsibility system can give the elderly patients comprehensive and systematic clinical nursing, increase their trust and compliance with nursing work, improve the patient's psychological state, improve clinical satisfaction, and achieve the ideal doctor-patient relationship, which is worthy of clinical application.

1. Introduction

Limb fracture is one of the common types of orthopedics [1]. With the aging of the population and changes in bone loss, the incidence of fractures in the elderly is increasing year by year, which seriously affects the quality of life and limb function [2]. In order to promote the rapid physical rehabilitation of elderly patients with limb fractures, clinicians often provide targeted treatment and postoperative rehabilitation nursing services according to the type, degree, and course of the fracture. Among them, traditional Chinese splint fixation has the advantages of simple operation, convenient economy, and a remarkable therapeutic effect and has been widely used in clinical practice [3, 4]. However, elderly patients need long-term bed rest after fracture, and the gastrointestinal and metabolic systems are disordered, increasing the psychological pressure and physiological needs of patients. In addition, acute and chronic diseases are often associated with the slow healing of the fracture site after clinical fixation, and the recovery of joint and limb functions is not ideal, which also delays the recovery time of the disease and aggravates the degree of physical and mental trauma [5]. Traditional postoperative rehabilitation nursing modes make it difficult to meet the nursing needs of elderly patients and their families due to their general adaptability. In addition, due to the limited number of nursing staff and trivial nursing affairs, problems such as incomplete nursing work occasionally occur, which will cause secondary harm to patients and is not conducive to compliance during nursing [6, 7]. In order to carry out the humanistic care and quality nursing service project of the Ministry of Health, pay attention to the responsibility system and reform the nursing mode in terms of the breadth and depth of quality nursing service. With the overall nursing mode of responsibility system as the core and patients as the first subject, the responsibilities of nursing staff are refined, and special specialized projects are added to carry out all-round, multilevel, and whole-process scientific nursing. In addition, the implementation of flat management will promote the comfort of nursing staff, relieve the sense of fatigue, and increase the care and nursing treatment for patients. It is applied to the training and management of the whole nursing staff in the hospital, and good nursing effects are achieved. However, no literature has been found on the application of limb fractures to emergency elderly patients [8–10]. In this study, 150 emergency elderly patients with limb fractures treated by TCM splint fixation in our hospital were respectively managed by traditional rehabilitation nursing and the overall nursing mode of responsibility system, and the intervention effects of the two groups of patients were observed. The report is as follows.

2. Materials and Methods

2.1. General Information. In this study, 150 elderly patients who received TCM splint fixation for limb fractures in our hospital from May 2017 to June 2021 were selected as the research subjects and were divided into a control group and an observation group by the numerical random table method. There were 46 males and 29 females in the control group, ranging in age from 38 to 65 years old, with an average age of 57.01 ± 9.42 years old, and the course of the disease was 1.18 to 13.92 days. In the observation group, there were 48 males and 27 females, aged from 39 to 67 years, with an average age of 56.41 ± 9.52 years, and the course of the disease ranged from 1.36 to 14.03 days. There were no statistically significant differences in age, gender, disease course, and other general information between the two groups ($P > 0.05$), indicating comparability. The control group adopted routine nursing mode intervention, and the observation group adopted responsibility holistic nursing mode intervention.

2.2. Inclusion and Exclusion Criteria. The inclusion criteria were as follows: ① in line with the diagnostic and therapeutic criteria of TCM diseases and syndromes [11] and the diagnostic criteria of limb fracture in the scientific basis of TCM bone injury [12]; ② the patient was diagnosed with limb fracture by CT, X-ray, and other imaging examinations; ③ there were obvious traumatic sites, and all fracture types were all closed; ④ the age ranges from 18 to 75 years; ⑤ no cognitive and mental disorders; ⑥ barrier-free communication, capable of completing the questionnaire independently; and ⑦ all subjects were informed of the research content and signed informed consent.

The exclusion criteria were as follows: ① complicated with functional disorders of the heart, liver, lung, and other important organs; ② no previous surgical history, malignant tumor, or infection at the fracture site; ③ with coagulation dysfunction or severe inflammation; ④ have joined or participated in other rehabilitation research work; and ⑤ finding it difficult to comply with medical advice and having poor compliance.

2.3. Research Methods. The control group adopted the traditional rehabilitation nursing management mode, that is, after admission, patients were instructed to fill out basic information (questionnaire, etc.), deal with admission matters, and inform themselves about the precautions of traditional Chinese medicine splint fixation. After fixation, the electrocardiogram, respiratory rate, temperature, and skin status of the patients were recorded regularly. In case of emergency, timely treatment was conducted, and feedback was reported to the attending doctor. The observation group adopted the responsibility system holistic nursing mode intervention, and some orthopedic nursing staff were selected to form a special responsibility group, including 1 orthopedics deputy director nurse, 6 nurses in charge, and 9 nurses and 9 clinical nurses. Organize members of the special responsibility group to learn the professional requirements, team spirit, and significance of the holistic nursing responsibility system and establish good nursing cognition and work attitude. Specific implementation measures were as follows: ① fixed responsibility area and personnel responsibilities: according to the ward distribution and disease situation. The chief nurse, as the head of the team, is responsible for developing nursing plans, supervising the implementation of nursing staff and the quality of work, testing the depth and breadth of nursing work implementation, dealing with critical events, and arranging a new stage of nursing plan. At the same time, I also paid attention to the transfer and arrangement of team members, the examination of first-aid drugs and instruments, and the assistance of nurses and nurses. The personnel should be reasonably arranged according to the working experience, ability, and attitude of team members; one nurse and one nurse were selected as office staff, responsible for sorting out emergency documents and patient information, answering patients' or family members' questions about disease and medication, communicating with other departments in critical situations, and applying for and reporting medication and instruments of the department. In addition, comprehensive and real-time records help grasp the progress of patients' conditions, which makes it convenient to call out emergencies. Two nurses were selected as emergency personnel to pay attention to the environment, temperature, humidity, and other controls in the operating room to increase patients' compliance during treatment. Regularly disinfect and sterilize the operating room, check and replace emergency drugs and instruments, etc., to ensure the smooth operation of fixation. Two nurses were selected as bed nurses, and each nurse guaranteed 6 to 8 patients, providing basic nursing, emergency nursing, special nursing, and psychological comfort actively communicate with patients and their families, increase nurse-patient relationships, improve patient satisfaction, etc. At the same time, pay attention to the patient's physical state and record regularly to ensure the smooth development of nursing work. The nursing nurse should regularly observe the patient's consciousness, body position, skin, pupil, and temperature and make detailed electronic records. In case of an emergency, the office nurse or nurse will sort out the patient's information, past history, and matters needing attention in time. The responsible nurse should timely understand and satisfy the needs of patients, pay attention to effective communication, and provide scientific and detailed, seamless nursing services. The responsible nurse should guide the patient's rehabilitation training regularly and assist the family members with complete body massage, skin warmth, etc. Pay attention to the patient's psychological state and comfort level, guide him/her to eat food with less oil, less salt, and easy digestion, pay attention to the changes in the patient's gastrointestinal function, and alleviate the degree of gastrointestinal function injury. ② Flexible scheduling system: the deputy director of orthopedics nurse on white spot take turns on the day shift, night shift, nurse and nurses according to the actual number of patients and data statistics. Set the morning shift, middle shift, and evening shift. The morning shift is from 8:00 to 16:00, the middle shift is from 16:00 to 24:00, and the evening shift is from 24:00 to 8:00. During the shift, the two groups of nursing staff should carefully check the ward situation, explain the situation of some patients, and address any matters needing attention. During the 2~3 weeks' shift, pay attention to the shift between the primary and secondary situations of the nursing staff's dynamic adjustment. Among them, there are responsible nurses for patients every day, and each patient is taken care of by two responsible nurses in turn. Each nurse is responsible for 6–8 patients in a given area. (3) Perfect supervision and reward and punishment system: check content 2~3 times a week, including ward environment, patient satisfaction, recognition of nursing work, data sorting, summary, drugs, equipment, disinfection work, etc. The inspection results are reviewed by supervisors and dealt with according to the reward and punishment system. Regularly check the professional knowledge, operational skills, and psychological state of nursing staff and constantly improve the professional quality and work quality of the nursing team.

2.4. Observation Indicators. ① Comparison of orthopedic nursing work quality: according to the quality scoring standard of orthopedic nursing work of our hospital, the work quality of the two modes before and after management for 3 months was compared. There are 6 aspects in total, including basic nursing measures, critical patient nursing, ward environmental management, disinfection and isolation, rescue medicine and instruments, nursing document management, etc. ② Work quality and satisfaction of nursing staff: the modified SERVQUAL Service Quality Scale [13] was used to evaluate the service quality of nurses before and after management for 3 months. The scale has 5 dimensions, including reliability, reactivity, assurance, empathy, and tangibility, with a total of 19 items. The 5-level scoring system is adopted. The overall score is positively correlated with patient satisfaction. The Karowski (NSNS)/Miller (MMSS) satisfaction scale [14] was used to measure the job satisfaction of nurses before and after management for 3 months. The scale has eight dimensions, including benefits, scheduling, work-family balance, relationships with colleagues, networking opportunities, professional development opportunities, work recognition and recognition, control over work, and responsibility. There are 31 entries in total. Using a 5-level scoring system, from "very dissatisfied" to "very satisfied," with high authority. ③ Comparison of psychological status: the Hamilton Anxiety Scale [15] was used to measure the anxiety degree of patients in the two groups before and after management for 3 months. There were 14 items in total. The overall score was less than 7 as no anxiety, and 7~13 as low anxiety. 14–20 were marked as significant anxiety; ≥21 is considered extreme anxiety. The Hamilton Depression Scale [16] (HAMD) was used to measure the depression degree of 2 groups before and 3 months after management, including anxiety/somatization, body weight, cognitive impairment, day-night change, block, sleep disturbance, and despair. No depression with an overall score ≤7; 8 to 19 were classified as mild depression; 20 to 34 are classified as moderately depressed; ≥35 was classified as major depression. ④ Comparison of nursing satisfaction: patients were interviewed by using a questionnaire of satisfaction. The questionnaire included 25 items, including nursing environment, nursing staff professional work, nursing service attitude, inpatient environment, and disease awareness. The total score is 25~100 points, with the total score <60 being dissatisfied, 60~74 being generally satisfied, 75~90 being relatively satisfied, and >90 being particularly satisfied. Overall nursing satisfaction = (general satisfaction + relatively satisfaction + special satisfaction) number of cases/total number of cases × 100%. ⑤ Comparison of incidence of adverse events: the incidence of adverse events in the two groups was recorded and observed during the follow-up of 3 months, including falls, bed falls, compression injuries, lost infusion tubes, wound infections, thrombosis, etc.

2.5. Statistical Treatment. The data were processed by SPSS 24.00 statistical software. Measurement data were expressed as $X \pm S$, and comparison between groups was performed by t-test. The statistical data were expressed as the number of cases (n) and percentage (%), and the comparison between groups was performed by χ^2 test. $P < 0.05$ indicated that the difference was statistically significant.

3. Results

3.1. Comparison of General Data between the Two Groups. The results showed that there were no significant differences in gender, age, education level, disease type, and surgical experience between the observation group and the control group ($P > 0.05$), as shown in Table 1.

3.2. Comparison of the Quality of Orthopedic Nursing Work. The results showed that there was no significant difference between the two groups in nursing work quality before mode management ($P > 0.05$). The nursing quality of the two groups after management was significantly improved compared with that before management. The scores of basic nursing measures, critical patient nursing, ward environmental management, disinfection and isolation, rescue medicine and instruments, and nursing document management in the observation group were significantly higher than those in the control group (Figure 1). The difference was statistically significant ($P < 0.05$), as shown in Table 2.

3.3. Comparison of Work Quality and Satisfaction of Nursing Staff. The results showed that there was no significant difference in the quality and satisfaction of nursing staff before management between the two groups ($P > 0.05$). The work quality and satisfaction of nursing staff in the two groups after management were significantly improved compared with that before management (Figure 2). The SERVQUAL scale score and satisfaction score of the observation group were significantly higher than those of the control group, and the differences were statistically significant ($P < 0.05$) (Figure 2), as shown in Table 3.

3.4. Comparison of Psychological Status between the Two Groups. The results showed that there was no significant difference in psychological status score between the two groups before management ($P > 0.05$). HAMA and HAMD scores of 2 groups after management were significantly lower than those before management. HAMA and HAMD scores in the observation group were significantly lower than those in the control group (Figure 3), and the differences were statistically significant ($P < 0.05$), as shown in Table 4.

3.5. Comparison of Clinical Nursing Satisfaction. The results showed that the overall nursing satisfaction of the observation group was 96.00%, which was significantly higher than that of the control group at 80.00% (Figure 4). The difference was statistically significant ($P < 0.05$), as shown in Table 5.

3.6. Comparison of Incidence of Adverse Events. The results showed that the incidence of adverse events in the observation group (8.00%) was significantly lower than that in the control group (17.33%) (Figure 5). The difference was statistically significant ($P < 0.05$), as shown in Table 6.

4. Discussion

In elderly patients, limb fractures can be accompanied by severe pain and other complications due to bone loss and body decline. It causes serious negative effects on patients' physiology and psychology, delays fracture healing time, increases psychological burden, and increases clinical treatment difficulty. Traditional Chinese medicine splint is often used in emergency elderly patients with limb fracture to maintain the original structure such as body diaphysis and joints. In terms of operation, the fracture healing effect is good, and the clinical treatment effect is good. Relevant studies have shown that after splint treatment for elderly fracture patients, high-quality nursing can promote patients' development of a good psychological state, improve nursing satisfaction, and reduce the risk of adverse events [17]. The traditional nursing management mode is mostly assigned according to the work content of medical staff, and there is no unified standard for nursing items and quality, which may cause psychological trauma to patients [18]. The holistic nursing mode of responsibility takes the patient as the core of nursing, rationalizes the arrangement, and refines the work flow and responsibility through the nursing staff. Establish a one-to-one or two-to-one nurse-patient relationship between patients from admission to discharge and take comprehensive and systematic nursing measures for patients. In order to promote their rapid recovery, adjust their psychological state and nursing satisfaction, and achieve high efficiency and excellent nursing quality [19]. At present, the overall nursing mode of responsibility system at home and abroad mostly emphasizes the assistance of nursing staff in multiple departments, with limited effectiveness in personnel management and limited attention to specific groups [20]. In this study, the nursing staff's professional quality and professional ability were significantly improved by adopting responsibility system holistic nursing mode management for elderly patients with limb fracture treated by TCM splint fixation. It can improve the bad mood of elderly patients, improve nursing satisfaction, reduce the risk of adverse events, and provide a basis for rehabilitation nursing of limb fractures.

Quality nursing service can increase patients' trust and tolerance for disease treatment and improve their compliance with clinical work through the assistance ability, professional nursing knowledge, and level of cooperation between nursing teams. Service quality, professional level, and service attitude of nursing staff can be reflected by the SERVQUAL scale and satisfaction scale. The SERVQUAL scale comprehensively evaluates the service quality of service-oriented organizations through the appearance and feeling of service objects to service personnel, the performance of commitment, handling attitude and efficiency, professional knowledge level, and personalized service [21]. Patestos et al. [22] applied holistic nursing education to

Table 1: Comparison of general data between the two groups.

Group	Control group ($n = 75$)	Observation group ($n = 75$)	Statistics	P value
Gender (example)				
Male	46 (61.33)	48 (64.00)	4.613	0.231
Female	29 (38.67)	27 (36.00)		
Average age (years)	57.01 ± 9.42	56.41 ± 9.52	3.921	0.130
Course of disease (day)	1.18~13.92	1.36~14.03	5.032	0.057
Fracture site (case)				
Humerus	18 (24.00)	19 (25.33)		
Foot radius	24 (32.00)	25 (33.33)	0.195	0.104
Femoral	16 (21.33)	14 (18.67)		
Tibiofibula	17 (22.67)	17 (22.67)		
Cause				
Weight crushed	21 (28.00)	26 (34.67)		
Traffic accident	38 (50.67)	35 (46.67)	6.120	0.212
High fall injury	16 (21.33)	14 (18.67)		
Education level				
Technical secondary school and below	21 (28.00)	19 (25.33)		
College or bachelor degree	30 (40.00)	33 (44.00)	6.234	0.068
Master degree or above	24 (32.00)	23 (30.67)		

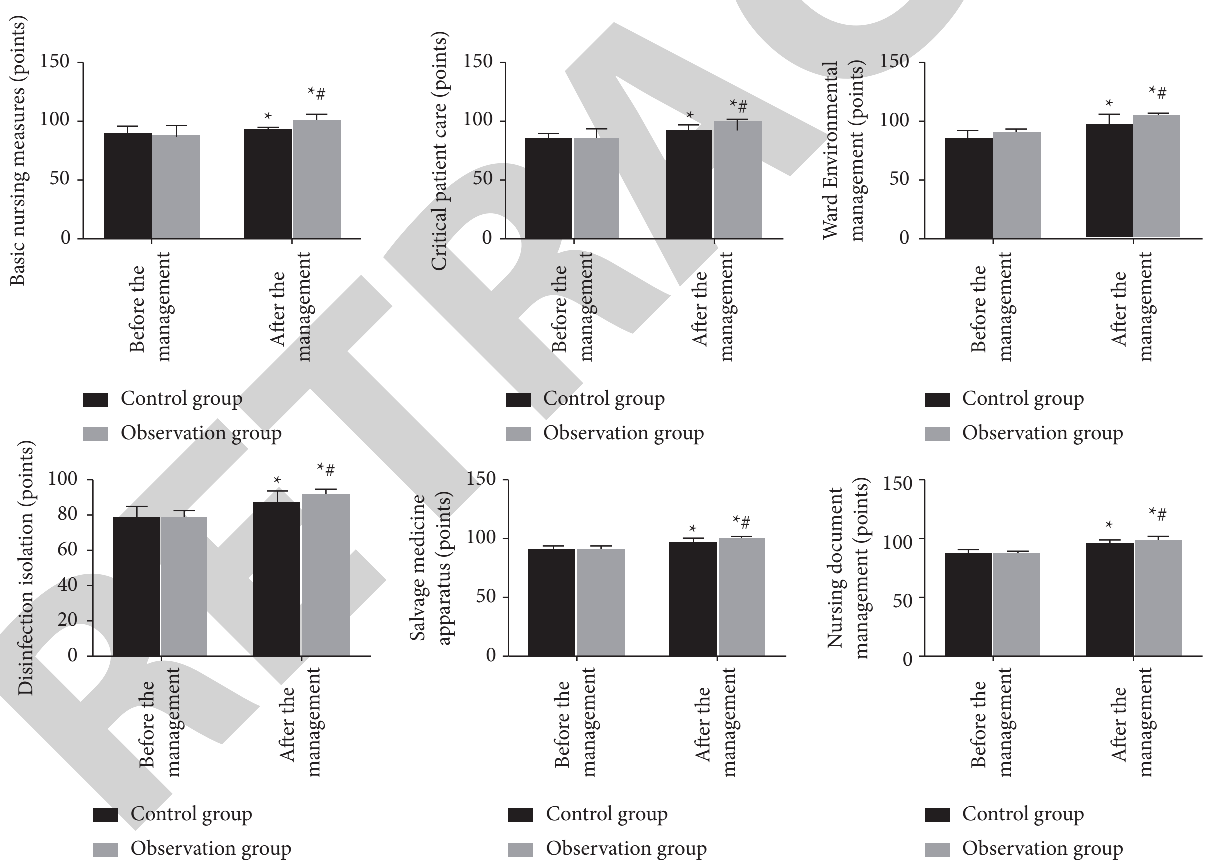

Figure 1: Comparison of orthopedic nursing quality. The scores of basic nursing measures, critical patient nursing, ward environmental management, disinfection and isolation, rescue medicine and instruments, and nursing document management were compared with the two groups in nursing work quality before and after mode management.

comprehensive student growth management, providing holistic and excellent holistic nursing concept for nursing staff, alleviating work fatigue and lack of empathy, devoting themselves to nursing work, and achieving significant self-growth ability. According to Wang et al. [23], in the application of TCM and acupuncture, the holistic nursing model of responsibility can promote the cooperative and positive abilities of nursing staff, provide a good healing space for patients, promote and stimulate the maximum healing ability of patients, and provide a good rehabilitation

Table 2: Comparison of orthopedic nursing quality ($\overline{x} \pm s$, points).

Group	Time	Control group ($n = 75$)	Observation group ($n = 75$)
Basic nursing measures	Before the management	87.02 ± 9.23	87.21 ± 9.31
	After the management	$91.10 \pm 7.75^{*}$	$99.82 \pm 5.36^{*\#}$
Critical patient care	Before the management	84.57 ± 9.08	84.28 ± 9.12
	After the management	$90.35 \pm 7.92^{*}$	$98.30 \pm 6.40^{*\#}$
Ward environmental management	Before the management	86.02 ± 8.61	89.46 ± 8.56
	After the management	$92.37 \pm 7.09^{*}$	$96.92 \pm 6.10^{*\#}$
Disinfection isolation	Before the management	77.01 ± 8.13	77.42 ± 8.35
	After the management	$86.32 \pm 7.25^{*}$	$91.20 \pm 6.84^{*\#}$
Salvage medicine apparatus	Before the management	90.03 ± 8.79	90.04 ± 8.73
	After the management	$95.72 \pm 7.04^{*}$	$98.31 \pm 6.63^{*\#}$
Nursing document management	Before the management	86.90 ± 9.29	86.84 ± 9.32
	After the management	$94.23 \pm 7.48^{*}$	$97.93 \pm 7.05^{*\#}$

Note. Compared with the control group before management, $^{*\#}P < 0.05$.

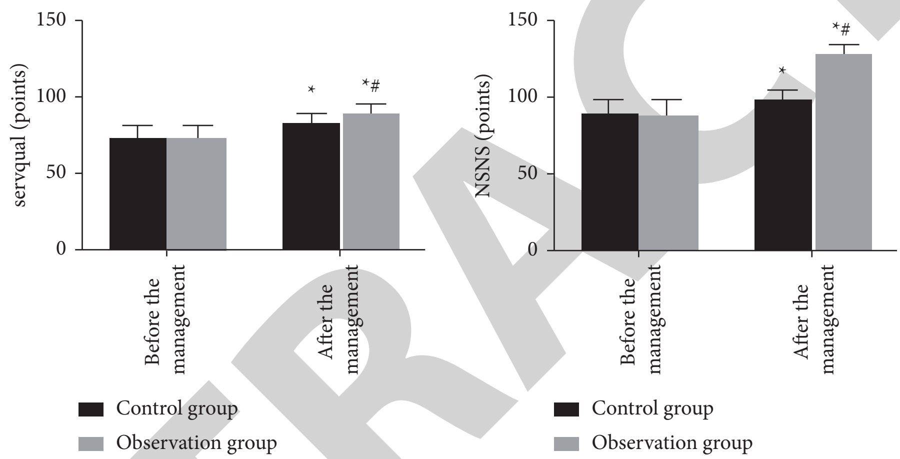

Figure 2: Comparison of work quality and satisfaction of nursing staff. The SERVQUAL score and NSNS score were compared with the two groups in nursing work quality before and after mode management.

Table 3: Comparison of work quality and satisfaction of nursing staff ($\overline{x} \pm s$, points).

Group	Time	Control group ($n = 75$)	Observation group ($n = 75$)
SERVQUAL score	Before the management	73.02 ± 9.68	73.14 ± 9.65
	After the management	$83.27 \pm 8.35^{*}$	$87.92 \pm 8.60^{*\#}$
NSNS score	Before the management	89.54 ± 10.67	89.39 ± 10.71
	After the management	$97.92 \pm 9.41^{*}$	$128.60 \pm 8.25^{*\#}$

Note. Compared with the control group before management, $^{*\#}P < 0.05$.

platform for their functional recovery. The results showed that the quality of nursing work in the two groups was significantly improved after management compared with before management. And the scores of basic nursing measures, critical patient care, ward environmental management, disinfection and isolation, rescue medicine and instruments, and nursing document management in the observation group were significantly increased compared with the control group. After management, the work quality and satisfaction of nursing staff in the two groups were significantly improved compared with those before management, and the SERVQUAL scale score and satisfaction score in the observation group were significantly increased compared with those in the control group. It is consistent with the research results of Patestos and Wang, indicating that the holistic nursing model of responsibility system can significantly improve the quality of department management and improve the work quality and satisfaction of nursing staff. The overall nursing mode of responsibility system can accurately implement the responsibilities and job processes of nursing staff, master professional-related skills, give full play to the work efficiency of nursing staff, increase the enthusiasm of nursing staff, increase the nurse-patient relationship and intimacy, and meet the needs of patients and their families as far as possible. In addition, a clear division of responsibilities and supervision system can

Table 4: Comparison of the psychological status between the two groups ($\overline{x} \pm s$, points).

Group	Time	Control group ($n = 75$)	Observation group ($n = 75$)
HAMA score	Before the management	18.16 ± 3.42	18.19 ± 3.39
	After the management	$15.65 \pm 2.17^{*}$	$12.11 \pm 1.31^{*\#}$
HAMD score	Before the management	22.48 ± 3.24	22.43 ± 3.27
	After the management	$17.93 \pm 2.06^{*}$	$15.28 \pm 1.14^{*\#}$

Note. Compared with the control group before management, $^{*\#}P < 0.05$.

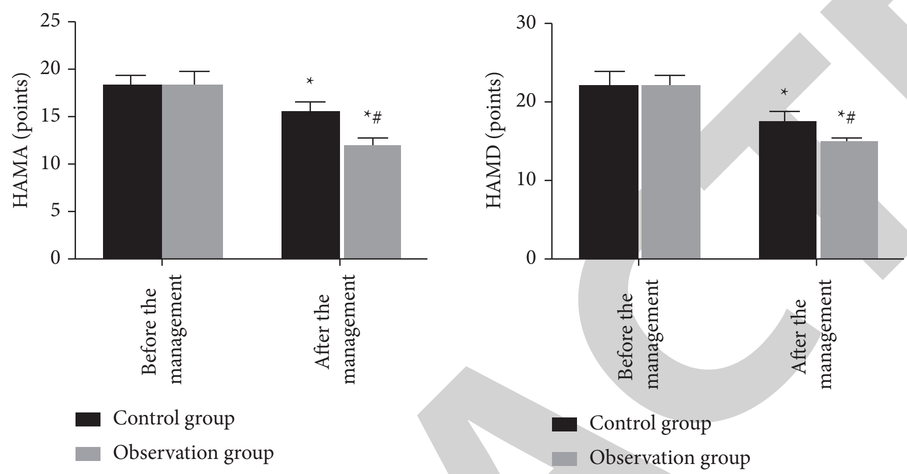

Figure 3: Comparison of the psychological status between the two groups. The HAMA score and HAMD score were compared with the two groups in nursing work quality before and after mode management.

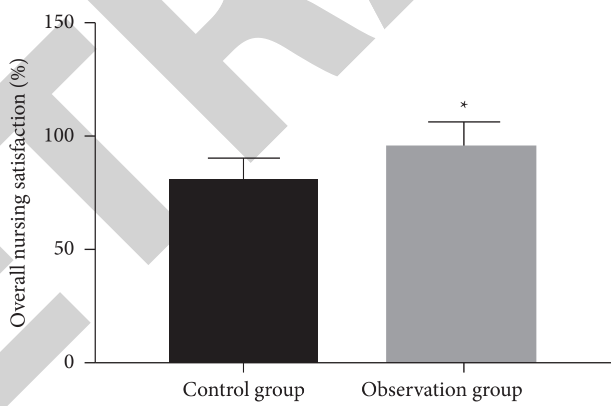

Figure 4: Comparison of overall nursing satisfaction. The overall nursing satisfaction was compared with the two groups after mode management.

Table 5: Comparison of overall nursing satisfaction (cases, %).

Group	Control group ($n = 75$)	Observation group ($n = 75$)	χ^2	P value
Especially satisfied	29 (38.67)	46 (61.33)	—	—
Quite satisfied	18 (24.00)	19 (25.33)	—	—
Generally satisfied	13 (17.33)	7 (9.33)	—	—
Not satisfied	15 (20.00)	3 (4.00)	—	—
Overall nursing satisfaction	80.00%	96.00%	4.319	0.032

accurately track patient conditions, reduce unnecessary waste of time and resources, significantly improve the sense of responsibility and job satisfaction of nursing staff, and lay the foundation for rationalizing the allocation of nursing workers. At the same time, a reasonable and flexible scheduling system can promote the nursing staff to

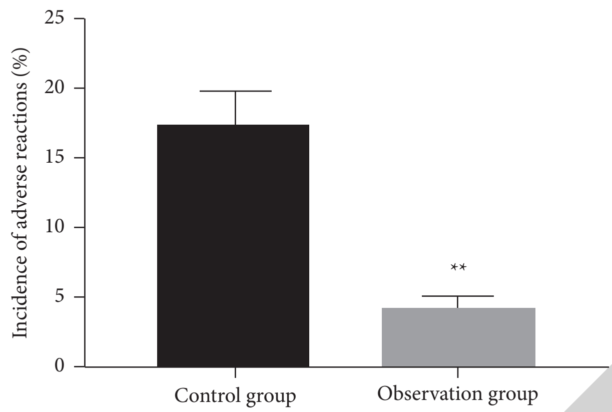

Figure 5: Comparison of adverse events. The adverse events were compared with the two groups after mode management.

Table 6: Comparison of adverse events (cases, %).

Group	Control group ($n = 75$)	Observation group ($n = 75$)	χ^2	P value
Fall	6 (8.00)	3 (4.00)	—	—
Drop from bed	2 (2.67)	1 (1.33)	—	—
Compression injury	1 (1.33)	0 (0.00)	—	—
Infusion tube fell off	0 (0.00)	1 (1.33)	—	—
Wound infection	3 (4.00)	1 (1.33)	—	—
Blood clots	1 (1.33)	0 (0.00)	—	—
Incidence of adverse reactions	17.33%	8.00%	4.160	0.000

coordinate the relationship between life, work, and family, which is beneficial to reducing the sense of empathy fatigue among nursing staff and increasing job satisfaction and self-confidence.

Elderly patients need long-term bed rest after splint fixation after a fracture because limb function is limited and it is easy to produce depression, anxiety, and other bad emotions. In addition, due to the long postoperative recovery time, there will be pain and adverse events during the recovery, further increasing the psychological burden of patients and affecting the prognosis and quality of life. HAMA, HAMD scale, as one of the authoritative mental health test scales in the world, uses multiple aspects to reflect the degree of depression and anxiety, allowing people to quickly determine their own mental health state. Ding and Wang et al. [24] adopted a holistic nursing mode of intervention for patients with chronic pulmonary heart disease combined with heart failure, which can significantly improve the clinical symptoms of patients, relieve their negative emotions, increase the compliance of treatment and prognostic care, and improve their living standards. The results showed that HAMA and HAMD scores in the two groups after management were significantly lower than those before management, and HAMA and HAMD scores in the observation group were significantly lower than those in the control group. The overall nursing satisfaction of the observation group was significantly higher than that of the control group. The incidence of adverse events in the observation group was significantly lower than that in the control group. Consistent with the research results of Ding and Wang et al., it indicates that the application of holistic nursing mode of responsibility system in elderly patients with limb fracture emergencies can relieve their depression, anxiety, and other emotions; reduce the incidence of adverse events; and improve their satisfaction with nursing services. The holistic nursing model of responsibility system can pay comprehensive and systematic attention to patients' physiological and psychological changes through a clear division of responsibilities. The whole process of tracking and taking special nursing services with patients and their families is intended to establish a harmonious, kind doctor-patient relationship, increase patients' awareness of the disease and confidence, and relieve the psychological pressure on patients. Timely adjustment of rehabilitation nursing training programs and indicators reduces the risk of adverse events and improves patients' recognition of and satisfaction with nursing work.

To sum up, the elderly patients with limb fractures treated with traditional Chinese medicine splint fixation emergency management system holistic nursing model. On the one hand, it can standardize the working process and operation of nursing staff, optimize their own professional skills, improve their job satisfaction, and improve their work enthusiasm. On the other hand, it can provide comprehensive, systematic, and scientific high-quality nursing services for fracture patients, improve their psychological state, reduce the incidence of adverse events, and meet their clinical nursing needs. However, the sample size of this study is limited, so it is necessary to expand the sample size to explore its universality. In addition, no systematic

Hindawi
Journal of Healthcare Engineering
Volume 2023, Article ID 9815494, 1 page
https://doi.org/10.1155/2023/9815494

Retraction

Retracted: Research on the Mechanism of HMGB1 Regulating Autoimmune Encephalomyelitis by Regulating NF-κB

Journal of Healthcare Engineering

Received 23 May 2023; Accepted 23 May 2023; Published 24 May 2023

This article has been retracted by Hindawi following an investigation undertaken by the publisher [1]. This investigation has uncovered evidence of one or more of the following indicators of systematic manipulation of the publication process:

(1) Discrepancies in scope
(2) Discrepancies in the description of the research reported
(3) Discrepancies between the availability of data and the research described
(4) Inappropriate citations
(5) Incoherent, meaningless and/or irrelevant content included in the article
(6) Peer-review manipulation

The presence of these indicators undermines our confidence in the integrity of the article's content and we cannot, therefore, vouch for its reliability. Please note that this notice is intended solely to alert readers that the content of this article is unreliable. We have not investigated whether authors were aware of or involved in the systematic manipulation of the publication process. Wiley and Hindawi regrets that the usual quality checks did not identify these issues before publication and have since put additional measures in place to safeguard research integrity.

We wish to credit our own Research Integrity and Research Publishing teams and anonymous and named external researchers and research integrity experts for contributing to this investigation.

The corresponding author, as the representative of all authors, has been given the opportunity to register their agreement or disagreement to this retraction. We have kept a record of any response received.

References

[1] L. Liu, J. Pang, H. Yuan et al., "Research on the Mechanism of HMGB1 Regulating Autoimmune Encephalomyelitis by Regulating NF-κB," *Journal of Healthcare Engineering*, vol. 2022, Article ID 9900916, 11 pages, 2022.

Hindawi
Journal of Healthcare Engineering
Volume 2023, Article ID 9812052, 1 page
https://doi.org/10.1155/2023/9812052

Retraction

Retracted: Automatic COVID-19 Lung Infection Segmentation through Modified Unet Model

Journal of Healthcare Engineering

Received 23 May 2023; Accepted 23 May 2023; Published 24 May 2023

This article has been retracted by Hindawi following an investigation undertaken by the publisher [1]. This investigation has uncovered evidence of one or more of the following indicators of systematic manipulation of the publication process:

(1) Discrepancies in scope
(2) Discrepancies in the description of the research reported
(3) Discrepancies between the availability of data and the research described
(4) Inappropriate citations
(5) Incoherent, meaningless and/or irrelevant content included in the article
(6) Peer-review manipulation

The presence of these indicators undermines our confidence in the integrity of the article's content and we cannot, therefore, vouch for its reliability. Please note that this notice is intended solely to alert readers that the content of this article is unreliable. We have not investigated whether authors were aware of or involved in the systematic manipulation of the publication process. Wiley and Hindawi regrets that the usual quality checks did not identify these issues before publication and have since put additional measures in place to safeguard research integrity.

We wish to credit our own Research Integrity and Research Publishing teams and anonymous and named external researchers and research integrity experts for contributing to this investigation.

The corresponding author, as the representative of all authors, has been given the opportunity to register their agreement or disagreement to this retraction. We have kept a record of any response received.

References

[1] S. Shamim, M. J. Awan, A. Mohd Zain, U. Naseem, M. A. Mohammed, and B. Garcia-Zapirain, "Automatic COVID-19 Lung Infection Segmentation through Modified Unet Model," *Journal of Healthcare Engineering*, vol. 2022, Article ID 6566982, 13 pages, 2022.

Hindawi
Journal of Healthcare Engineering
Volume 2023, Article ID 9795025, 1 page
https://doi.org/10.1155/2023/9795025

Retraction

Retracted: Ten Hotspot MicroRNAs and Their Potential Targets of Chondrocytes Were Revealed in Osteoarthritis Based on Bibliometric Analysis

Journal of Healthcare Engineering

Received 23 May 2023; Accepted 23 May 2023; Published 24 May 2023

This article has been retracted by Hindawi following an investigation undertaken by the publisher [1]. This investigation has uncovered evidence of one or more of the following indicators of systematic manipulation of the publication process:

(1) Discrepancies in scope
(2) Discrepancies in the description of the research reported
(3) Discrepancies between the availability of data and the research described
(4) Inappropriate citations
(5) Incoherent, meaningless and/or irrelevant content included in the article
(6) Peer-review manipulation

The presence of these indicators undermines our confidence in the integrity of the article's content and we cannot, therefore, vouch for its reliability. Please note that this notice is intended solely to alert readers that the content of this article is unreliable. We have not investigated whether authors were aware of or involved in the systematic manipulation of the publication process. Wiley and Hindawi regrets that the usual quality checks did not identify these issues before publication and have since put additional measures in place to safeguard research integrity.

We wish to credit our own Research Integrity and Research Publishing teams and anonymous and named external researchers and research integrity experts for contributing to this investigation.

The corresponding author, as the representative of all authors, has been given the opportunity to register their agreement or disagreement to this retraction. We have kept a record of any response received.

References

[1] W. Hu, Q. Zhang, S. Li, S. Ai, and Q. Wu, "Ten Hotspot MicroRNAs and Their Potential Targets of Chondrocytes Were Revealed in Osteoarthritis Based on Bibliometric Analysis," *Journal of Healthcare Engineering*, vol. 2022, Article ID 8229148, 11 pages, 2022.

Hindawi
Journal of Healthcare Engineering
Volume 2023, Article ID 9789870, 1 page
https://doi.org/10.1155/2023/9789870

Retraction

Retracted: Impact of Yiqi Huoxue Decoction on the Relationship between Remodeling of Cardiac Nerves and Macrophages after Myocardial Infarction in Rats

Journal of Healthcare Engineering

Received 23 May 2023; Accepted 23 May 2023; Published 24 May 2023

This article has been retracted by Hindawi following an investigation undertaken by the publisher [1]. This investigation has uncovered evidence of one or more of the following indicators of systematic manipulation of the publication process:

(1) Discrepancies in scope
(2) Discrepancies in the description of the research reported
(3) Discrepancies between the availability of data and the research described
(4) Inappropriate citations
(5) Incoherent, meaningless and/or irrelevant content included in the article
(6) Peer-review manipulation

The presence of these indicators undermines our confidence in the integrity of the article's content and we cannot, therefore, vouch for its reliability. Please note that this notice is intended solely to alert readers that the content of this article is unreliable. We have not investigated whether authors were aware of or involved in the systematic manipulation of the publication process. Wiley and Hindawi regrets that the usual quality checks did not identify these issues before publication and have since put additional measures in place to safeguard research integrity.

We wish to credit our own Research Integrity and Research Publishing teams and anonymous and named external researchers and research integrity experts for contributing to this investigation.

The corresponding author, as the representative of all authors, has been given the opportunity to register their agreement or disagreement to this retraction. We have kept a record of any response received.

References

[1] Y. Liu, S. Guo, Y. Zhang et al., "Impact of Yiqi Huoxue Decoction on the Relationship between Remodeling of Cardiac Nerves and Macrophages after Myocardial Infarction in Rats," *Journal of Healthcare Engineering*, vol. 2022, Article ID 4441603, 13 pages, 2022.

Hindawi
Journal of Healthcare Engineering
Volume 2023, Article ID 9756286, 1 page
https://doi.org/10.1155/2023/9756286

Retraction

Retracted: Signal-to-Noise Ratio Comparison of Several Filters against Phantom Image

Journal of Healthcare Engineering

Received 23 May 2023; Accepted 23 May 2023; Published 24 May 2023

This article has been retracted by Hindawi following an investigation undertaken by the publisher [1]. This investigation has uncovered evidence of one or more of the following indicators of systematic manipulation of the publication process:

(1) Discrepancies in scope
(2) Discrepancies in the description of the research reported
(3) Discrepancies between the availability of data and the research described
(4) Inappropriate citations
(5) Incoherent, meaningless and/or irrelevant content included in the article
(6) Peer-review manipulation

The presence of these indicators undermines our confidence in the integrity of the article's content and we cannot, therefore, vouch for its reliability. Please note that this notice is intended solely to alert readers that the content of this article is unreliable. We have not investigated whether authors were aware of or involved in the systematic manipulation of the publication process. Wiley and Hindawi regrets that the usual quality checks did not identify these issues before publication and have since put additional measures in place to safeguard research integrity.

We wish to credit our own Research Integrity and Research Publishing teams and anonymous and named external researchers and research integrity experts for contributing to this investigation.

The corresponding author, as the representative of all authors, has been given the opportunity to register their agreement or disagreement to this retraction. We have kept a record of any response received.

References

[1] M. H. Siddiqi and Y. Alhwaiti, "Signal-to-Noise Ratio Comparison of Several Filters against Phantom Image," *Journal of Healthcare Engineering*, vol. 2022, Article ID 4724342, 11 pages, 2022.

Hindawi
Journal of Healthcare Engineering
Volume 2023, Article ID 9896325, 1 page
https://doi.org/10.1155/2023/9896325

Retraction

Retracted: Effects of Four Types of Watermelon Frost Combination Medications for the Treatment of Oral Ulcers: A Network Meta-Analysis

Journal of Healthcare Engineering

Received 23 May 2023; Accepted 23 May 2023; Published 24 May 2023

This article has been retracted by Hindawi following an investigation undertaken by the publisher [1]. This investigation has uncovered evidence of one or more of the following indicators of systematic manipulation of the publication process.

(1) Discrepancies in scope
(2) Discrepancies in the description of the research reported
(3) Discrepancies between the availability of data and the research described
(4) Inappropriate citations
(5) Incoherent, meaningless and/or irrelevant content included in the article
(6) Peer-review manipulation

The presence of these indicators undermines our confidence in the integrity of the article's content and we cannot, therefore, vouch for its reliability. Please note that this notice is intended solely to alert readers that the content of this article is unreliable. We have not investigated whether authors were aware of or involved in the systematic manipulation of the publication process. Wiley and Hindawi regrets that the usual quality checks did not identify these issues before publication and have since put additional measures in place to safeguard research integrity.

We wish to credit our own Research Integrity and Research Publishing teams and anonymous and named external researchers and research integrity experts for contributing to this investigation.

The corresponding author, as the representative of all authors, has been given the opportunity to register their agreement or disagreement to this retraction. We have kept a record of any response received.

References

[1] Z. Liu and H. Dou, "Effects of Four Types of Watermelon Frost Combination Medications for the Treatment of Oral Ulcers: A Network Meta-Analysis," *Journal of Healthcare Engineering*, vol. 2022, Article ID 2712403, 7 pages, 2022.

Hindawi
Journal of Healthcare Engineering
Volume 2023, Article ID 9892301, 1 page
https://doi.org/10.1155/2023/9892301

Retraction

Retracted: Anti-DDI Resource: A Dataset for Potential Negative Reported Interaction Combinations to Improve Medical Research and Decision-Making

Journal of Healthcare Engineering

Received 23 May 2023; Accepted 23 May 2023; Published 24 May 2023

This article has been retracted by Hindawi following an investigation undertaken by the publisher [1]. This investigation has uncovered evidence of one or more of the following indicators of systematic manipulation of the publication process:

(1) Discrepancies in scope
(2) Discrepancies in the description of the research reported
(3) Discrepancies between the availability of data and the research described
(4) Inappropriate citations
(5) Incoherent, meaningless and/or irrelevant content included in the article
(6) Peer-review manipulation

The presence of these indicators undermines our confidence in the integrity of the article's content and we cannot, therefore, vouch for its reliability. Please note that this notice is intended solely to alert readers that the content of this article is unreliable. We have not investigated whether authors were aware of or involved in the systematic manipulation of the publication process. Wiley and Hindawi regrets that the usual quality checks did not identify these issues before publication and have since put additional measures in place to safeguard research integrity.

We wish to credit our own Research Integrity and Research Publishing teams and anonymous and named external researchers and research integrity experts for contributing to this investigation.

The corresponding author, as the representative of all authors, has been given the opportunity to register their agreement or disagreement to this retraction. We have kept a record of any response received.

References

[1] A. Assiri and A. Noor, "Anti-DDI Resource: A Dataset for Potential Negative Reported Interaction Combinations to Improve Medical Research and Decision-Making," *Journal of Healthcare Engineering*, vol. 2022, Article ID 8904342, 6 pages, 2022.

Hindawi
Journal of Healthcare Engineering
Volume 2023, Article ID 9876909, 1 page
https://doi.org/10.1155/2023/9876909

Retraction

Retracted: An Ensembled Spatial Enhancement Method for Image Enhancement in Healthcare

Journal of Healthcare Engineering

Received 23 May 2023; Accepted 23 May 2023; Published 24 May 2023

This article has been retracted by Hindawi following an investigation undertaken by the publisher [1]. This investigation has uncovered evidence of one or more of the following indicators of systematic manipulation of the publication process:

(1) Discrepancies in scope
(2) Discrepancies in the description of the research reported
(3) Discrepancies between the availability of data and the research described
(4) Inappropriate citations
(5) Incoherent, meaningless and/or irrelevant content included in the article
(6) Peer-review manipulation

The presence of these indicators undermines our confidence in the integrity of the article's content and we cannot, therefore, vouch for its reliability. Please note that this notice is intended solely to alert readers that the content of this article is unreliable. We have not investigated whether authors were aware of or involved in the systematic manipulation of the publication process. Wiley and Hindawi regrets that the usual quality checks did not identify these issues before publication and have since put additional measures in place to safeguard research integrity.

We wish to credit our own Research Integrity and Research Publishing teams and anonymous and named external researchers and research integrity experts for contributing to this investigation.

The corresponding author, as the representative of all authors, has been given the opportunity to register their agreement or disagreement to this retraction. We have kept a record of any response received.

References

[1] M. H. Siddiqi and A. Alsirhani, "An Ensembled Spatial Enhancement Method for Image Enhancement in Healthcare," *Journal of Healthcare Engineering*, vol. 2022, Article ID 9660820, 12 pages, 2022.

Hindawi
Journal of Healthcare Engineering
Volume 2023, Article ID 9875271, 1 page
https://doi.org/10.1155/2023/9875271

Retraction

Retracted: The Current Status of SSRP1 in Cancer: Tribulation and Road Ahead

Journal of Healthcare Engineering

Received 23 May 2023; Accepted 23 May 2023; Published 24 May 2023

This article has been retracted by Hindawi following an investigation undertaken by the publisher [1]. This investigation has uncovered evidence of one or more of the following indicators of systematic manipulation of the publication process:

(1) Discrepancies in scope
(2) Discrepancies in the description of the research reported
(3) Discrepancies between the availability of data and the research described
(4) Inappropriate citations
(5) Incoherent, meaningless and/or irrelevant content included in the article
(6) Peer-review manipulation

The presence of these indicators undermines our confidence in the integrity of the article's content and we cannot, therefore, vouch for its reliability. Please note that this notice is intended solely to alert readers that the content of this article is unreliable. We have not investigated whether authors were aware of or involved in the systematic manipulation of the publication process. Wiley and Hindawi regrets that the usual quality checks did not identify these issues before publication and have since put additional measures in place to safeguard research integrity.

We wish to credit our own Research Integrity and Research Publishing teams and anonymous and named external researchers and research integrity experts for contributing to this investigation.

The corresponding author, as the representative of all authors, has been given the opportunity to register their agreement or disagreement to this retraction. We have kept a record of any response received.

References

[1] S. Jia, B. Guo, L. Wang, L. Peng, and L. Zhang, "The Current Status of SSRP1 in Cancer: Tribulation and Road Ahead," *Journal of Healthcare Engineering*, vol. 2022, Article ID 3528786, 9 pages, 2022.

Hindawi
Journal of Healthcare Engineering
Volume 2023, Article ID 9869570, 1 page
https://doi.org/10.1155/2023/9869570

Retraction

Retracted: Recent Progress in Traditional Chinese Medicines and Their Mechanism in the Treatment of Allergic Rhinitis

Journal of Healthcare Engineering

Received 23 May 2023; Accepted 23 May 2023; Published 24 May 2023

This article has been retracted by Hindawi following an investigation undertaken by the publisher [1]. This investigation has uncovered evidence of one or more of the following indicators of systematic manipulation of the publication process:

(1) Discrepancies in scope
(2) Discrepancies in the description of the research reported
(3) Discrepancies between the availability of data and the research described
(4) Inappropriate citations
(5) Incoherent, meaningless and/or irrelevant content included in the article
(6) Peer-review manipulation

The presence of these indicators undermines our confidence in the integrity of the article's content and we cannot, therefore, vouch for its reliability. Please note that this notice is intended solely to alert readers that the content of this article is unreliable. We have not investigated whether authors were aware of or involved in the systematic manipulation of the publication process. Wiley and Hindawi regrets that the usual quality checks did not identify these issues before publication and have since put additional measures in place to safeguard research integrity.

We wish to credit our own Research Integrity and Research Publishing teams and anonymous and named external researchers and research integrity experts for contributing to this investigation.

The corresponding author, as the representative of all authors, has been given the opportunity to register their agreement or disagreement to this retraction. We have kept a record of any response received.

References

[1] D. Mao, Z. He, L. Li et al., "Recent Progress in Traditional Chinese Medicines and Their Mechanism in the Treatment of Allergic Rhinitis," *Journal of Healthcare Engineering*, vol. 2022, Article ID 3594210, 18 pages, 2022.

Hindawi
Journal of Healthcare Engineering
Volume 2023, Article ID 9867516, 1 page
https://doi.org/10.1155/2023/9867516

Retraction

Retracted: Enamel Matrix Derivatives for Periodontal Regeneration: Recent Developments and Future Perspectives

Journal of Healthcare Engineering

Received 23 May 2023; Accepted 23 May 2023; Published 24 May 2023

This article has been retracted by Hindawi following an investigation undertaken by the publisher [1]. This investigation has uncovered evidence of one or more of the following indicators of systematic manipulation of the publication process:

(1) Discrepancies in scope
(2) Discrepancies in the description of the research reported
(3) Discrepancies between the availability of data and the research described
(4) Inappropriate citations
(5) Incoherent, meaningless and/or irrelevant content included in the article
(6) Peer-review manipulation

The presence of these indicators undermines our confidence in the integrity of the article's content and we cannot, therefore, vouch for its reliability. Please note that this notice is intended solely to alert readers that the content of this article is unreliable. We have not investigated whether authors were aware of or involved in the systematic manipulation of the publication process. Wiley and Hindawi regrets that the usual quality checks did not identify these issues before publication and have since put additional measures in place to safeguard research integrity.

We wish to credit our own Research Integrity and Research Publishing teams and anonymous and named external researchers and research integrity experts for contributing to this investigation.

The corresponding author, as the representative of all authors, has been given the opportunity to register their agreement or disagreement to this retraction. We have kept a record of any response received.

References

[1] L. Fan and D. Wu, "Enamel Matrix Derivatives for Periodontal Regeneration: Recent Developments and Future Perspectives," *Journal of Healthcare Engineering*, vol. 2022, Article ID 8661690, 10 pages, 2022.

Hindawi
Journal of Healthcare Engineering
Volume 2023, Article ID 9862375, 1 page
https://doi.org/10.1155/2023/9862375

Retraction

Retracted: An Effective and Lightweight Deep Electrocardiography Arrhythmia Recognition Model Using Novel Special and Native Structural Regularization Techniques on Cardiac Signal

Journal of Healthcare Engineering

Received 23 May 2023; Accepted 23 May 2023; Published 24 May 2023

This article has been retracted by Hindawi following an investigation undertaken by the publisher [1]. This investigation has uncovered evidence of one or more of the following indicators of systematic manipulation of the publication process:

(1) Discrepancies in scope
(2) Discrepancies in the description of the research reported
(3) Discrepancies between the availability of data and the research described
(4) Inappropriate citations
(5) Incoherent, meaningless and/or irrelevant content included in the article
(6) Peer-review manipulation

The presence of these indicators undermines our confidence in the integrity of the article's content and we cannot, therefore, vouch for its reliability. Please note that this notice is intended solely to alert readers that the content of this article is unreliable. We have not investigated whether authors were aware of or involved in the systematic manipulation of the publication process. Wiley and Hindawi regrets that the usual quality checks did not identify these issues before publication and have since put additional measures in place to safeguard research integrity.

We wish to credit our own Research Integrity and Research Publishing teams and anonymous and named external researchers and research integrity experts for contributing to this investigation.

The corresponding author, as the representative of all authors, has been given the opportunity to register their agreement or disagreement to this retraction. We have kept a record of any response received.

References

[1] H. Ullah, M. B. Bin Heyat, H. AlSalman et al., "An Effective and Lightweight Deep Electrocardiography Arrhythmia Recognition Model Using Novel Special and Native Structural Regularization Techniques on Cardiac Signal," *Journal of Healthcare Engineering*, vol. 2022, Article ID 3408501, 18 pages, 2022.

Hindawi
Journal of Healthcare Engineering
Volume 2023, Article ID 9860360, 1 page
https://doi.org/10.1155/2023/9860360

Retraction

Retracted: Automated Detection of Rehabilitation Exercise by Stroke Patients Using 3-Layer CNN-LSTM Model

Journal of Healthcare Engineering

Received 23 May 2023; Accepted 23 May 2023; Published 24 May 2023

This article has been retracted by Hindawi following an investigation undertaken by the publisher [1]. This investigation has uncovered evidence of one or more of the following indicators of systematic manipulation of the publication process:

(1) Discrepancies in scope
(2) Discrepancies in the description of the research reported
(3) Discrepancies between the availability of data and the research described
(4) Inappropriate citations
(5) Incoherent, meaningless and/or irrelevant content included in the article
(6) Peer-review manipulation

The presence of these indicators undermines our confidence in the integrity of the article's content and we cannot, therefore, vouch for its reliability. Please note that this notice is intended solely to alert readers that the content of this article is unreliable. We have not investigated whether authors were aware of or involved in the systematic manipulation of the publication process. Wiley and Hindawi regrets that the usual quality checks did not identify these issues before publication and have since put additional measures in place to safeguard research integrity.

We wish to credit our own Research Integrity and Research Publishing teams and anonymous and named external researchers and research integrity experts for contributing to this investigation.

The corresponding author, as the representative of all authors, has been given the opportunity to register their agreement or disagreement to this retraction. We have kept a record of any response received.

References

[1] Z. U. Rahman, S. I. Ullah, A. Salam, T. Rahman, I. Khan, and B. Niazi, "Automated Detection of Rehabilitation Exercise by Stroke Patients Using 3-Layer CNN-LSTM Model," *Journal of Healthcare Engineering*, vol. 2022, Article ID 1563707, 12 pages, 2022.

Hindawi
Journal of Healthcare Engineering
Volume 2023, Article ID 9853278, 1 page
https://doi.org/10.1155/2023/9853278

Retraction

Retracted: Overexpressed RING Finger 44 Correlates with Poor Prognosis in Hepatocellular Carcinoma

Journal of Healthcare Engineering

Received 23 May 2023; Accepted 23 May 2023; Published 24 May 2023

This article has been retracted by Hindawi following an investigation undertaken by the publisher [1]. This investigation has uncovered evidence of one or more of the following indicators of systematic manipulation of the publication process:

(1) Discrepancies in scope
(2) Discrepancies in the description of the research reported
(3) Discrepancies between the availability of data and the research described
(4) Inappropriate citations
(5) Incoherent, meaningless and/or irrelevant content included in the article
(6) Peer-review manipulation

The presence of these indicators undermines our confidence in the integrity of the article's content and we cannot, therefore, vouch for its reliability. Please note that this notice is intended solely to alert readers that the content of this article is unreliable. We have not investigated whether authors were aware of or involved in the systematic manipulation of the publication process. Wiley and Hindawi regrets that the usual quality checks did not identify these issues before publication and have since put additional measures in place to safeguard research integrity.

We wish to credit our own Research Integrity and Research Publishing teams and anonymous and named external researchers and research integrity experts for contributing to this investigation.

The corresponding author, as the representative of all authors, has been given the opportunity to register their agreement or disagreement to this retraction. We have kept a record of any response received.

References

[1] Y. Liu, H. Xia, M. Li et al., "Overexpressed RING Finger 44 Correlates with Poor Prognosis in Hepatocellular Carcinoma," *Journal of Healthcare Engineering*, vol. 2022, Article ID 3522866, 18 pages, 2022.

Hindawi
Journal of Healthcare Engineering
Volume 2023, Article ID 9852613, 1 page
https://doi.org/10.1155/2023/9852613

Retraction

Retracted: Evolution of Oncology and Palliative Nursing in Meeting the Changing Landscape of Cancer Care

Journal of Healthcare Engineering

Received 23 May 2023; Accepted 23 May 2023; Published 24 May 2023

This article has been retracted by Hindawi following an investigation undertaken by the publisher [1]. This investigation has uncovered evidence of one or more of the following indicators of systematic manipulation of the publication process.

(1) Discrepancies in scope
(2) Discrepancies in the description of the research reported
(3) Discrepancies between the availability of data and the research described
(4) Inappropriate citations
(5) Incoherent, meaningless and/or irrelevant content included in the article
(6) Peer-review manipulation

The presence of these indicators undermines our confidence in the integrity of the article's content and we cannot, therefore, vouch for its reliability. Please note that this notice is intended solely to alert readers that the content of this article is unreliable. We have not investigated whether authors were aware of or involved in the systematic manipulation of the publication process. Wiley and Hindawi regrets that the usual quality checks did not identify these issues before publication and have since put additional measures in place to safeguard research integrity.

We wish to credit our own Research Integrity and Research Publishing teams and anonymous and named external researchers and research integrity experts for contributing to this investigation.

The corresponding author, as the representative of all authors, has been given the opportunity to register their agreement or disagreement to this retraction. We have kept a record of any response received.

References

[1] K. Zhou and J. Fu, "Evolution of Oncology and Palliative Nursing in Meeting the Changing Landscape of Cancer Care," *Journal of Healthcare Engineering*, vol. 2022, Article ID 3831705, 8 pages, 2022.

Hindawi
Journal of Healthcare Engineering
Volume 2023, Article ID 9850271, 1 page
https://doi.org/10.1155/2023/9850271

Retraction

Retracted: A Data-Driven Medical Decision Framework for Associating Adverse Drug Events with Drug-Drug Interaction Mechanisms

Journal of Healthcare Engineering

Received 23 May 2023; Accepted 23 May 2023; Published 24 May 2023

This article has been retracted by Hindawi following an investigation undertaken by the publisher [1]. This investigation has uncovered evidence of one or more of the following indicators of systematic manipulation of the publication process:

(1) Discrepancies in scope
(2) Discrepancies in the description of the research reported
(3) Discrepancies between the availability of data and the research described
(4) Inappropriate citations
(5) Incoherent, meaningless and/or irrelevant content included in the article
(6) Peer-review manipulation

The presence of these indicators undermines our confidence in the integrity of the article's content and we cannot, therefore, vouch for its reliability. Please note that this notice is intended solely to alert readers that the content of this article is unreliable. We have not investigated whether authors were aware of or involved in the systematic manipulation of the publication process. Wiley and Hindawi regrets that the usual quality checks did not identify these issues before publication and have since put additional measures in place to safeguard research integrity.

We wish to credit our own Research Integrity and Research Publishing teams and anonymous and named external researchers and research integrity experts for contributing to this investigation.

The corresponding author, as the representative of all authors, has been given the opportunity to register their agreement or disagreement to this retraction. We have kept a record of any response received.

References

[1] A. Noor, "A Data-Driven Medical Decision Framework for Associating Adverse Drug Events with Drug-Drug Interaction Mechanisms," *Journal of Healthcare Engineering*, vol. 2022, Article ID 9132477, 7 pages, 2022.

Hindawi
Journal of Healthcare Engineering
Volume 2023, Article ID 9845732, 1 page
https://doi.org/10.1155/2023/9845732

Retraction

Retracted: Brain Tumor Detection and Classification by MRI Using Biologically Inspired Orthogonal Wavelet Transform and Deep Learning Techniques

Journal of Healthcare Engineering

Received 23 May 2023; Accepted 23 May 2023; Published 24 May 2023

This article has been retracted by Hindawi following an investigation undertaken by the publisher [1]. This investigation has uncovered evidence of one or more of the following indicators of systematic manipulation of the publication process:

(1) Discrepancies in scope
(2) Discrepancies in the description of the research reported
(3) Discrepancies between the availability of data and the research described
(4) Inappropriate citations
(5) Incoherent, meaningless and/or irrelevant content included in the article
(6) Peer-review manipulation

The presence of these indicators undermines our confidence in the integrity of the article's content and we cannot, therefore, vouch for its reliability. Please note that this notice is intended solely to alert readers that the content of this article is unreliable. We have not investigated whether authors were aware of or involved in the systematic manipulation of the publication process. Wiley and Hindawi regrets that the usual quality checks did not identify these issues before publication and have since put additional measures in place to safeguard research integrity.

We wish to credit our own Research Integrity and Research Publishing teams and anonymous and named external researchers and research integrity experts for contributing to this investigation.

The corresponding author, as the representative of all authors, has been given the opportunity to register their agreement or disagreement to this retraction. We have kept a record of any response received.

References

[1] M. Arif, F. Ajesh, S. Shamsudheen, O. Geman, D. Izdrui, and D. Vicoveanu, "Brain Tumor Detection and Classification by MRI Using Biologically Inspired Orthogonal Wavelet Transform and Deep Learning Techniques," *Journal of Healthcare Engineering*, vol. 2022, Article ID 2693621, 18 pages, 2022.

Hindawi
Journal of Healthcare Engineering
Volume 2023, Article ID 9841704, 1 page
https://doi.org/10.1155/2023/9841704

Retraction

Retracted: Unilateral Sciatic Nerve Crush Induces White Blood Cell Infiltration of the Contralateral Nerve

Journal of Healthcare Engineering

Received 23 May 2023; Accepted 23 May 2023; Published 24 May 2023

This article has been retracted by Hindawi following an investigation undertaken by the publisher [1]. This investigation has uncovered evidence of one or more of the following indicators of systematic manipulation of the publication process:

(1) Discrepancies in scope
(2) Discrepancies in the description of the research reported
(3) Discrepancies between the availability of data and the research described
(4) Inappropriate citations
(5) Incoherent, meaningless and/or irrelevant content included in the article
(6) Peer-review manipulation

The presence of these indicators undermines our confidence in the integrity of the article's content and we cannot, therefore, vouch for its reliability. Please note that this notice is intended solely to alert readers that the content of this article is unreliable. We have not investigated whether authors were aware of or involved in the systematic manipulation of the publication process. Wiley and Hindawi regrets that the usual quality checks did not identify these issues before publication and have since put additional measures in place to safeguard research integrity.

We wish to credit our own Research Integrity and Research Publishing teams and anonymous and named external researchers and research integrity experts for contributing to this investigation.

The corresponding author, as the representative of all authors, has been given the opportunity to register their agreement or disagreement to this retraction. We have kept a record of any response received.

References

[1] J. Cheng, L. Ding, M. Yang, Y. Zhu, Z. Gu, and G. Lv, "Unilateral Sciatic Nerve Crush Induces White Blood Cell Infiltration of the Contralateral Nerve," *Journal of Healthcare Engineering*, vol. 2022, Article ID 1101383, 6 pages, 2022.

Hindawi
Journal of Healthcare Engineering
Volume 2023, Article ID 9838676, 1 page
https://doi.org/10.1155/2023/9838676

Retraction

Retracted: Critical Retrospection of Performance of Emerging Mobile Technologies in Health Data Management

Journal of Healthcare Engineering

Received 23 May 2023; Accepted 23 May 2023; Published 24 May 2023

This article has been retracted by Hindawi following an investigation undertaken by the publisher [1]. This investigation has uncovered evidence of one or more of the following indicators of systematic manipulation of the publication process:

(1) Discrepancies in scope
(2) Discrepancies in the description of the research reported
(3) Discrepancies between the availability of data and the research described
(4) Inappropriate citations
(5) Incoherent, meaningless and/or irrelevant content included in the article
(6) Peer-review manipulation

The presence of these indicators undermines our confidence in the integrity of the article's content and we cannot, therefore, vouch for its reliability. Please note that this notice is intended solely to alert readers that the content of this article is unreliable. We have not investigated whether authors were aware of or involved in the systematic manipulation of the publication process. Wiley and Hindawi regrets that the usual quality checks did not identify these issues before publication and have since put additional measures in place to safeguard research integrity.

We wish to credit our own Research Integrity and Research Publishing teams and anonymous and named external researchers and research integrity experts for contributing to this investigation.

The corresponding author, as the representative of all authors, has been given the opportunity to register their agreement or disagreement to this retraction. We have kept a record of any response received.

References

[1] S. Vyas, D. Bhargava, J. Bhola, J. A. Ujjan, S. Eswaran, and A. W. Rahmani, "Critical Retrospection of Performance of Emerging Mobile Technologies in Health Data Management," *Journal of Healthcare Engineering*, vol. 2022, Article ID 8903604, 12 pages, 2022.

Hindawi
Journal of Healthcare Engineering
Volume 2023, Article ID 9836767, 1 page
https://doi.org/10.1155/2023/9836767

Retraction

Retracted: Facile Synthesis of NaYF4:Yb Up-Conversion Nanoparticles Modified with Photosensitizer and Targeting Antibody for In Vitro Photodynamic Therapy of Hepatocellular Carcinoma

Journal of Healthcare Engineering

Received 23 May 2023; Accepted 23 May 2023; Published 24 May 2023

This article has been retracted by Hindawi following an investigation undertaken by the publisher [1]. This investigation has uncovered evidence of one or more of the following indicators of systematic manipulation of the publication process:

(1) Discrepancies in scope
(2) Discrepancies in the description of the research reported
(3) Discrepancies between the availability of data and the research described
(4) Inappropriate citations
(5) Incoherent, meaningless and/or irrelevant content included in the article
(6) Peer-review manipulation

The presence of these indicators undermines our confidence in the integrity of the article's content and we cannot, therefore, vouch for its reliability. Please note that this notice is intended solely to alert readers that the content of this article is unreliable. We have not investigated whether authors were aware of or involved in the systematic manipulation of the publication process. Wiley and Hindawi regrets that the usual quality checks did not identify these issues before publication and have since put additional measures in place to safeguard research integrity.

We wish to credit our own Research Integrity and Research Publishing teams and anonymous and named external researchers and research integrity experts for contributing to this investigation.

The corresponding author, as the representative of all authors, has been given the opportunity to register their agreement or disagreement to this retraction. We have kept a record of any response received.

References

[1] J. Ding, Y. Jin, F. Zhu et al., "Facile Synthesis of NaYF4:Yb Up-Conversion Nanoparticles Modified with Photosensitizer and Targeting Antibody for In Vitro Photodynamic Therapy of Hepatocellular Carcinoma," *Journal of Healthcare Engineering*, vol. 2022, Article ID 4470510, 12 pages, 2022.

Hindawi
Journal of Healthcare Engineering
Volume 2023, Article ID 9832729, 1 page
https://doi.org/10.1155/2023/9832729

Retraction

Retracted: Optimization and Evaluation of an Intelligent Short-Term Blood Glucose Prediction Model Based on Noninvasive Monitoring and Deep Learning Techniques

Journal of Healthcare Engineering

Received 23 May 2023; Accepted 23 May 2023; Published 24 May 2023

This article has been retracted by Hindawi following an investigation undertaken by the publisher [1]. This investigation has uncovered evidence of one or more of the following indicators of systematic manipulation of the publication process:

(1) Discrepancies in scope
(2) Discrepancies in the description of the research reported
(3) Discrepancies between the availability of data and the research described
(4) Inappropriate citations
(5) Incoherent, meaningless and/or irrelevant content included in the article
(6) Peer-review manipulation

The presence of these indicators undermines our confidence in the integrity of the article's content and we cannot, therefore, vouch for its reliability. Please note that this notice is intended solely to alert readers that the content of this article is unreliable. We have not investigated whether authors were aware of or involved in the systematic manipulation of the publication process. Wiley and Hindawi regrets that the usual quality checks did not identify these issues before publication and have since put additional measures in place to safeguard research integrity.

We wish to credit our own Research Integrity and Research Publishing teams and anonymous and named external researchers and research integrity experts for contributing to this investigation.

The corresponding author, as the representative of all authors, has been given the opportunity to register their agreement or disagreement to this retraction. We have kept a record of any response received.

References

[1] Y. Zhang and G. Gao, "Optimization and Evaluation of an Intelligent Short-Term Blood Glucose Prediction Model Based on Noninvasive Monitoring and Deep Learning Techniques," *Journal of Healthcare Engineering*, vol. 2022, Article ID 8956850, 16 pages, 2022.

Hindawi
Journal of Healthcare Engineering
Volume 2023, Article ID 9821301, 1 page
https://doi.org/10.1155/2023/9821301

Retraction

Retracted: Biometric Authentication for Intelligent and Privacy-Preserving Healthcare Systems

Journal of Healthcare Engineering

Received 23 May 2023; Accepted 23 May 2023; Published 24 May 2023

This article has been retracted by Hindawi following an investigation undertaken by the publisher [1]. This is investigation has uncovered evidence of one or more of the following indicators of systematic manipulation of the publication process:

(1) Discrepancies in scope
(2) Discrepancies in the description of the research reported
(3) Discrepancies between the availability of data and the research described
(4) Inappropriate citations
(5) Incoherent, meaningless and/or irrelevant content included in the article
(6) Peer-review manipulation

The presence of these indicators undermines our confidence in the integrity of the article's content and we cannot, therefore, vouch for its reliability. Please note that this notice is intended solely to alert readers that the content of this article is unreliable. We have not investigated whether authors were aware of or involved in the systematic manipulation of the publication process. Wiley and Hindawi regrets that the usual quality checks did not identify these issues before publication and have since put additional measures in place to safeguard research integrity.

We wish to credit our own Research Integrity and Research Publishing teams and anonymous and named external researchers and research integrity experts for contributing to this investigation.

The corresponding author, as the representative of all authors, has been given the opportunity to register their agreement or disagreement to this retraction. We have kept a record of any response received.

References

[1] D. Nigam, S. N. Patel, P. M. D. Raj Vincent, K. Srinivasan, and S. Arunmozhi, "Biometric Authentication for Intelligent and Privacy-Preserving Healthcare Systems," *Journal of Healthcare Engineering*, vol. 2022, Article ID 1789996, 15 pages, 2022.

Hindawi
Journal of Healthcare Engineering
Volume 2023, Article ID 9816424, 1 page
https://doi.org/10.1155/2023/9816424

Retraction

Retracted: Fuzzy Logic System Implementation on the Performance Parameters of Health Data Management Frameworks

Journal of Healthcare Engineering

Received 23 May 2023; Accepted 23 May 2023; Published 24 May 2023

This article has been retracted by Hindawi following an investigation undertaken by the publisher [1]. This investigation has uncovered evidence of one or more of the following indicators of systematic manipulation of the publication process:

(1) Discrepancies in scope
(2) Discrepancies in the description of the research reported
(3) Discrepancies between the availability of data and the research described
(4) Inappropriate citations
(5) Incoherent, meaningless and/or irrelevant content included in the article
(6) Peer-review manipulation

The presence of these indicators undermines our confidence in the integrity of the article's content and we cannot, therefore, vouch for its reliability. Please note that this notice is intended solely to alert readers that the content of this article is unreliable. We have not investigated whether authors were aware of or involved in the systematic manipulation of the publication process. Wiley and Hindawi regrets that the usual quality checks did not identify these issues before publication and have since put additional measures in place to safeguard research integrity.

We wish to credit our own Research Integrity and Research Publishing teams and anonymous and named external researchers and research integrity experts for contributing to this investigation.

The corresponding author, as the representative of all authors, has been given the opportunity to register their agreement or disagreement to this retraction. We have kept a record of any response received.

References

[1] S. Vyas, S. Gupta, D. Bhargava, and R. Boddu, "Fuzzy Logic System Implementation on the Performance Parameters of Health Data Management Frameworks," *Journal of Healthcare Engineering*, vol. 2022, Article ID 9382322, 11 pages, 2022.

Hindawi
Journal of Healthcare Engineering
Volume 2023, Article ID 9857931, 1 page
https://doi.org/10.1155/2023/9857931

Retraction

Retracted: A Method for Expanding the Training Set of White Blood Cell Images

Journal of Healthcare Engineering

Received 28 November 2023; Accepted 28 November 2023; Published 29 November 2023

This article has been retracted by Hindawi, as publisher, following an investigation undertaken by the publisher [1]. This investigation has uncovered evidence of systematic manipulation of the publication and peer-review process. We cannot, therefore, vouch for the reliability or integrity of this article.

Please note that this notice is intended solely to alert readers that the peer-review process of this article has been compromised.

Wiley and Hindawi regret that the usual quality checks did not identify these issues before publication and have since put additional measures in place to safeguard research integrity.

We wish to credit our Research Integrity and Research Publishing teams and anonymous and named external researchers and research integrity experts for contributing to this investigation.

The corresponding author, as the representative of all authors, has been given the opportunity to register their agreement or disagreement to this retraction. We have kept a record of any response received.

References

[1] Y. Su, Y. Zang, Q. Su, and L. Peng, "A Method for Expanding the Training Set of White Blood Cell Images," *Journal of Healthcare Engineering*, vol. 2022, Article ID 1267080, 11 pages, 2022.

Hindawi
Journal of Healthcare Engineering
Volume 2022, Article ID 1267080, 11 pages
https://doi.org/10.1155/2022/1267080

Research Article

A Method for Expanding the Training Set of White Blood Cell Images

Yang Su [1], **Yu Zang** [2], **Qichen Su** [3] **and Ling Peng** [1]

[1] *School of Computer and Information, Dongguan City College, Dongguan 523419, China*
[2] *Department of Hematology, Huizhou First Hospital, Huizhou 516000, China*
[3] *School of Mathematics and Statistics, Huizhou University, Huizhou 516000, China*

Correspondence should be addressed to Qichen Su; sqc20202001@hzu.edu.cn

Received 17 February 2022; Revised 8 April 2022; Accepted 15 April 2022; Published 9 November 2022

Academic Editor: Liaqat Ali

In medicine, the count of different types of white blood cells can be used as the basis for diagnosing certain diseases or evaluating the treatment effects of diseases. The recognition and counting of white blood cells have important clinical significance. But the effect of recognition based on machine learning is affected by the size of the training set. At present, researchers mainly rely on image rotation and cropping to expand the dataset. These methods either add features to the white blood cell image or require manual intervention and are inefficient. In this paper, a method for expanding the training set of white blood cell images is proposed. After rotating the image at any angle, Canny is used to extract the edge of the black area caused by the rotation and then fill the black area to achieve the purpose of expanding the training set. The experimental results show that after using the method proposed in this paper to expand the training set to train the three models of ResNet, MobileNet, and ShuffleNet, and comparing the original dataset and the method trained by the simple rotated image expanded dataset, the recognition accuracy of the three models is obviously improved without manual intervention.

1. Introduction

Human blood contains components such as plasma, red blood cells, white blood cells, and platelets. Although white blood cells only account for 0.2% of whole blood, they play an important role in protecting human health [1]. White blood cells are generally divided into neutrophils, eosinophils, basophils, monocytes, and lymphocytes [2], and changes in these cell counts can be used as the basis for diagnosing certain diseases or evaluating the therapeutic effect of certain diseases [3–9]. Therefore, the accuracy and efficiency of white blood cell detection and classification are very important for the auxiliary diagnosis of diseases [10].

The traditional method of white blood cell classification is mainly the staining method, which stains blood cells and then identifies and counts them under a light microscope [11]. This method has a large workload, low efficiency, and high requirements for practitioners, and the effect of classification and counting is easily affected by human factors [12]. At present, there are many computer-aided methods for the classification and counting of white blood cells. Early computer-aided methods were mainly based on morphology, in which the shape, color, and other characteristics of white blood cells are artificially analyzed, and morphological processing is used to separate white blood cells from the background to achieve the purpose of classification, such as the method proposed in the literature [13–16]. With the development of machine learning technology, some machine learning-based white blood cell classification methods have emerged.

The main work of these methods is to design a model, use the training set to train it, get a model that performs better on the training set, and then use the test set to test the classification effect of the model. For example, Patil et al. used the CCA (canonical correlation analysis) method based on the CNN-LSTM network structure to address the issues of multiple cells overlap to improve the recognition accuracy [17]; Su et al. used morphological correlation operations to extract the characteristics of white blood cells and then brought them into three kinds of neural networks to achieve the purpose of classification [18]; Jiang et al. proposed a new CNN model combining a batch normalization algorithm and residual convolution structure [19]; Liang et al. proposed a CNN-RNN framework to fully extract image features recursively to achieve better classification accuracy [20]. When there is enough computation and dataset, machine learning can replace the manual extraction of image features and can have higher efficiency than complex programming to extract image features manually [21].

The classification effect of machine learning is affected by the number of samples in the training set. When the number of samples in the training set is small, the problem of underfitting will occur [22], resulting in low learning accuracy and a poor classification effect. Currently, there are three main sources of white blood cell image data: (1) own dataset [19]; (2) BCCD original dataset [23–25]; (3) the white blood cell image is generated by the DC-GAN (deep convolutional generative adversarial network) algorithm, the BCCD original data are rotated and cropped, and the two are mixed into a dataset [25]. The own dataset is relatively small, and it is not easy for nonmedical personnel to obtain real white blood cell images; the BCCD original dataset is also relatively small, with only 346 images; since the dataset generated by the DC-GAN algorithm is not real white blood cell imaging, it is still necessary to manually check whether the generated image is close to the real white blood cell. In order to solve the problem of the small white blood cell dataset, the commonly used method is to rotate the image on the basis of the BCCD original dataset to achieve the purpose of expanding the dataset: the first method is to rotate the image horizontally and vertically [25]. Due to the limited rotation angle, the expansion of the dataset is also limited. The second method is to randomly select an angle to rotate the image in the range of 0–360°. This method will greatly expand the dataset, but the rotated image will have a black area, as shown in Figure 1. These black areas have obvious boundaries, which may be used as image features for classification, thereby affecting the classification effect. In order to eliminate the influence of the black area, some researchers have adopted a clipping method to completely remove the black area and retain only the white blood cell image, as shown in Figure 2. This method requires manual intervention and is inefficient. The third method is to multiply the image by the rotation matrix [20]. This method will cause obvious image deformation, resulting in a large change in the morphological characteristics of white blood cells, which in turn affects the classification accuracy, as shown in Figure 3.

In the experimental phase, the impact of a small dataset also exists. Now scholars generally divide the expanded dataset into a training set and a test set in proportion, that is, the test set to verify the effect of the model is the white blood cell images processed by a certain method, not the original image. For example, using the method of randomly rotating the image to expand the dataset, the images in the test set were also rotated and also contain the black area left after the rotation. The real situation is that the images first obtained by medical institutions are all original images that are not rotated. If you want to achieve the effect in the experiment, you need to randomly rotate the original image, which reduces its efficiency.

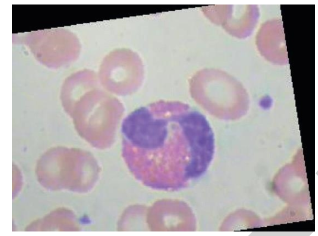

Figure 1: Rotated image.

Figure 2: Cropped image.

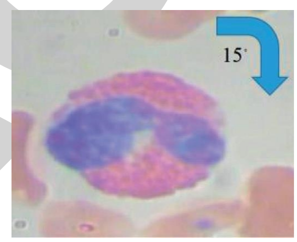

Figure 3: Image rotated by rotation matrix.

This paper proposes a new method for expanding the training set of white blood cell images that can achieve the purpose of expanding the training set without manual intervention while retaining the morphological characteristics of white blood cells. First, rotate the white blood cell image randomly, and then use the Canny edge detection algorithm [26] to extract the edge of the black area in the image. Then, count the pixel values that appear most frequently in the unrotated image. Along the edge of the extracted black area, fill the black area in the rotated image with a random value near the pixel value obtained by the above statistics. Finally, obtain an image with the characteristics of the black area eliminated so as to achieve the purpose of expanding the white blood cell image dataset. Use this dataset to train a machine learning model. This paper is organized as follows: Section 2 presents the techniques and methods followed to achieve the research goals; in Section 3, we present experimental results and discussions; the paper concludes in Section 4 at the end.

2. Method

This section describes the method of expanding the white blood cell image dataset. In order to ensure the initial characteristics of white blood cells to the greatest extent, this paper rotates the image around the center point as a whole. In order to eliminate the possible influence of the black area caused by rotation on the classification effect, this paper counts the pixels with the most occurrences in the unrotated image and uses a random value near the pixel to fill the black area. The working flow chart of this method is shown in Figure 4.

2.1. Image Rotation. The rotation method in this paper takes the image center point as the axis and rotates by a specific angle. The formula is shown in equation (1), where x0, y0, and 1 represent the abscissa, ordinate, and dimension of the pixel after rotation. x, y, and 1 represent the abscissa, ordinate, and dimension before rotation. W and H represent the width and height of the image. θ represents the rotation angle. After image rotation, use bilinear interpolation [27] to enhance image quality. The rotated image is shown in Figure 5, and the image is hereinafter referred to as IMG_Rotated.

$$\begin{bmatrix} X_0 & Y_0 & 1 \end{bmatrix} = \begin{bmatrix} X & Y & 1 \end{bmatrix} \begin{bmatrix} \cos\theta & -\sin\theta & 0 \\ \sin\theta & \cos\theta & 0 \\ -0.5W\cos\theta - 0.5H\sin\theta + 0.5W & 0.5W\sin\theta - 0.5H\cos\theta + 0.5H & 1 \end{bmatrix}. \tag{1}$$

2.2. Edge Extraction. After the image is rotated, an obvious black area will appear. Intuitively, the RGB pixel value of this area is #000000. However, when the RGB pixel value of #000000 is used as the judgment condition to fill the black area, it is difficult to fill the edges of the black area, as shown in Figure 6. This paper uses the Canny algorithm to extract the edge of IMG_Rotated, then fill the black area with the edge as the starting point. The Canny algorithm is divided into the following steps:

(1) *Gaussian filter*: For a pixel located at (x,y), its gray value is f(x,y) and the gray value after Gaussian filtering becomes

$$g_\sigma(x, y) = \frac{1}{\sqrt{2\pi\sigma^2}} e^{\left(-x^2+y^2/2\sigma^2\right)} \cdot f(x, y). \tag{2}$$

(2) Calculate gradient value and gradient direction: Calculate the gradients in the horizontal and vertical directions, respectively, and comprehensively obtain the final gradient value and gradient direction, see (3) and (4), where gx(x,y) and gy(x,y) are the gradients in the horizontal and vertical directions, respectively. The result of (4) is the gradient direction.

$$G(x, y) = \sqrt{g_x(x, y)^2 + g_y(x, y)^2}, \tag{3}$$

$$\theta = \arctan\frac{g_y(x, y)}{g_x(x, y)}. \tag{4}$$

(3) Filter nonmaximum values.

(4) Use upper and lower thresholds to detect edges.

It sets two thresholds: maxVal and minVal. The pixels above maxVal are detected as edges, and the pixels below minVal are detected as nonedges. For a pixel in the middle, if it is adjacent to a pixel determined to be an edge, it is determined to be an edge; otherwise, it is a nonedge. The edge extracted using the Canny algorithm is shown in Figure 7.

2.3. Pixel Filled. There are a lot of monotonous backgrounds in the white blood cell image; see Figure 8. The box is the background, and the pixel value with the most occurrences in the original image is obtained by statistics. We use this pixel value as the pixel value of the image background and use a random value N near the pixel value as the filled pixel value. After obtaining the edge pixels of the black area, count the values of the pixels around the edge pixels and fill in the horizontal or vertical direction with small pixel values until the edge of the image, as shown in Figure 9. The effect of pixel filling is shown in Figure 10. It can be seen from Figure 10(b) that, using the method in this paper, the edges of the black area are well filled.

3. Experiment

3.1. Experiment Environment. The experimental environment of this paper is as follows:

(i) CPU: Inter Core i5-11600 KF

(ii) RAM: 16G

(iii) GPU: NVIDIA GEFORCE 1050Ti

(iv) Operating system: Windows 10 64 bit

(v) *Python*: 3.9
TensorFlow: 2.6.0

3.2. Dataset. This paper uses three sets of datasets, namely, the BCCD original image dataset, the randomly rotated image dataset, and the image dataset processed by the method in this paper. In order to restore the real application scenario, the BCCD original image dataset is divided into a training set and a test set using 10-fold cross-validation. The randomly rotated image and the image dataset processed by the method in this paper are used as the training set, and the BCCD original image dataset is used as the test set, so as to ensure that the test images used are the original, unprocessed white blood cell images when verifying the effect. The datasets are shown in Table 1, the four different types of

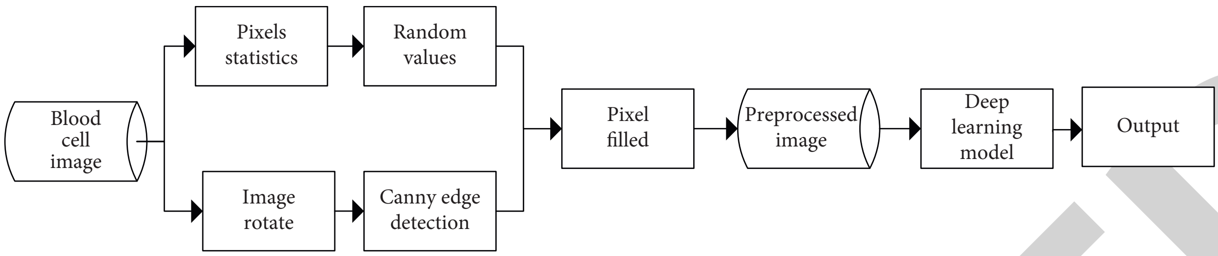

Figure 4: Working flow chart.

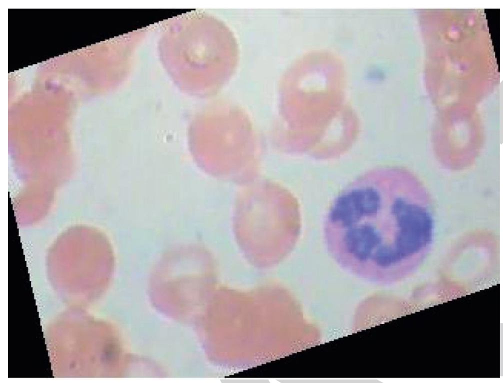

Figure 5: Rotated image.

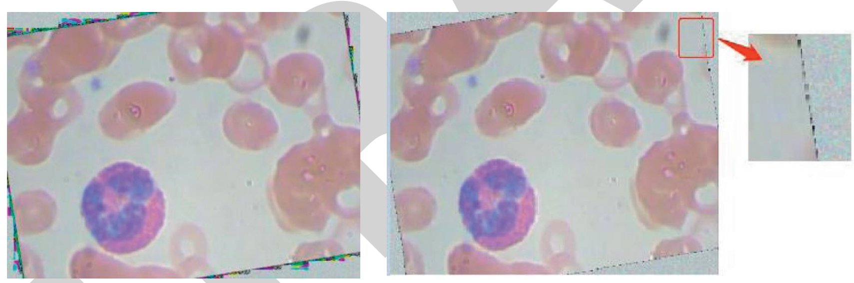

(a) (b)

Figure 6: Fill black area directly. (a) The image obtained by directly filling the area with the RGB pixel value of #000000. (b) The image obtained by directly filling areas with pixel values below 30.

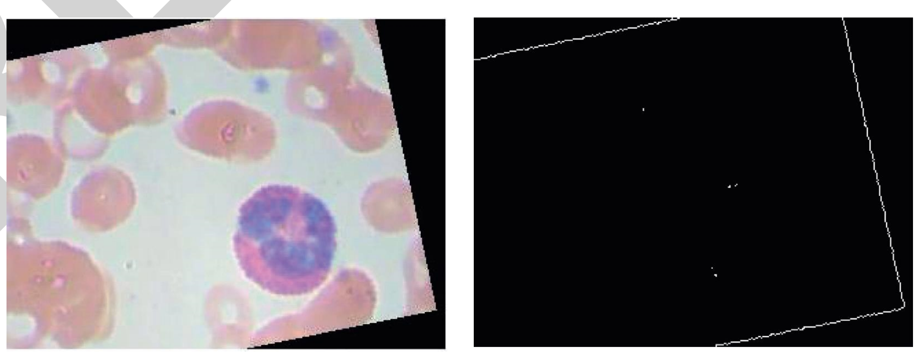

(a) (b)

Figure 7: (a) The image of rotated white blood cells. (b) The image after extracting black area edges using Canny.

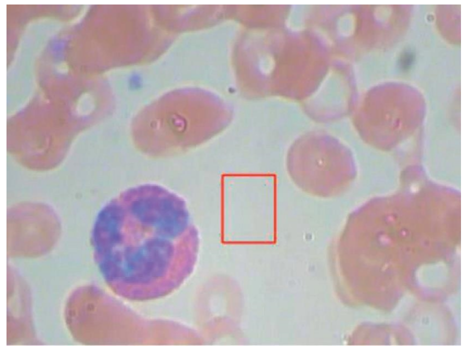

Figure 8: Original image of white blood cells.

$$\begin{bmatrix} 177 & 0 & 0 \\ 178 & 167 & 0 \\ 183 & 174 & 187 \end{bmatrix}$$

Figure 9: Fill black area (the arrow is the fill direction, it is also possible to fill in the vertical direction).

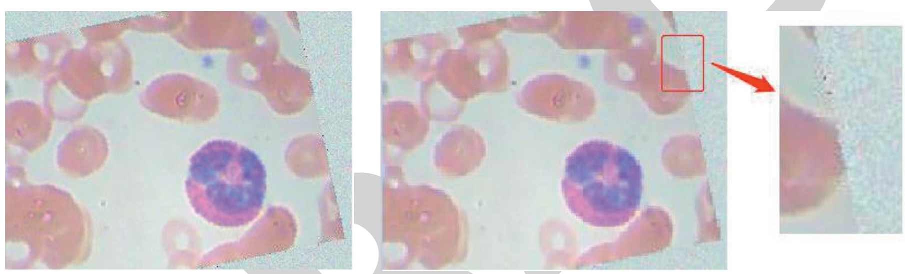

(a) (b)

Figure 10: Filled white blood cell image.

Table 1: Datasets.

		BCCD original image dataset	Randomly rotated image dataset	Image dataset processed by the algorithm in this paper
Training set	Eosinophil	79	2497	2497
	Lymphocyte	30	2483	2483
	Monocyte	18	2478	2478
	Neutrophil	185	2499	2499
	Total	312	346	346
Test set	Eosinophil	8	87	87
	Lymphocyte	3	33	33
	Monocyte	2	20	20
	Neutrophil	21	206	206
	Total	34	346 (all from the BCCD original dataset)	346 (all from the BCCD original dataset)

white blood cells included in the datasets are shown in Figure 11, and the images included in the three datasets are shown in Figure 12.

3.3. Evaluation Indicators. In this paper, four parameters: loss, validation accuracy (VA), precision (P), and recall (R), are used as evaluation indicators. This paper uses the cross-entropy loss function, and the calculation formulas for VA, P, and R are shown in equations (5)–(7).

$$VA = \frac{\text{TruePositive} + \text{TrueNegative}}{\text{TotalSamples}}, \tag{5}$$

$$P = \frac{\text{TruePositive}}{\text{TruePositive} + \text{FalsePositive}}, \tag{6}$$

$$R = \frac{\text{TruePositive}}{\text{TruePositive} + \text{FalseNegative}}. \tag{7}$$

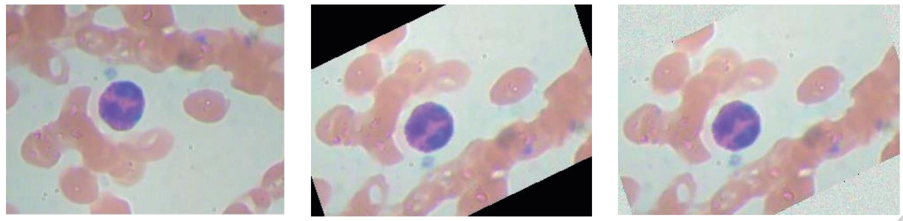

Figure 11: Images from three datasets. (a) The BCCD original image. (b) The randomly rotated image. (c) The image processed by the method in this paper.

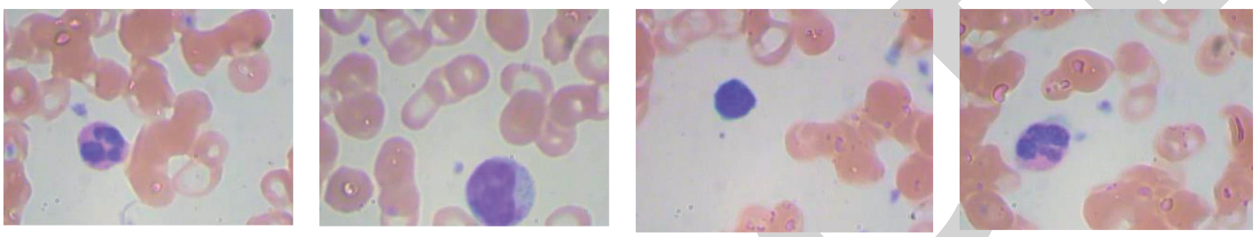

Figure 12: Four different types of white blood cells. (a) Eosinophil. (b) Monocyte. (c) Lymphocyte. (d) Neutrophil.

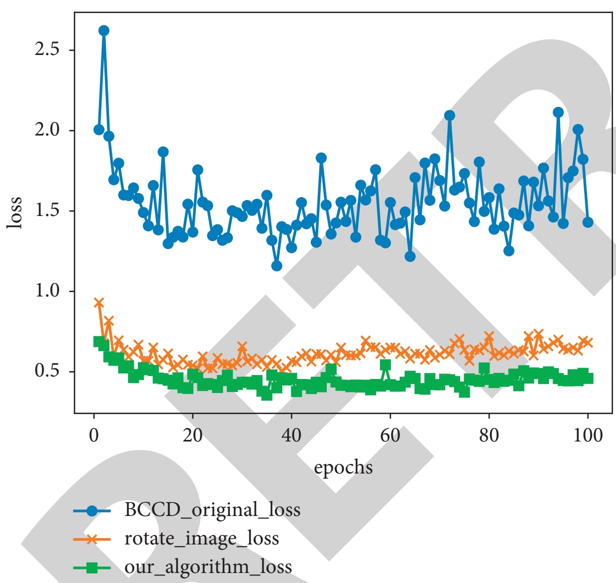

Figure 13: ResNet50 model loss value curve.

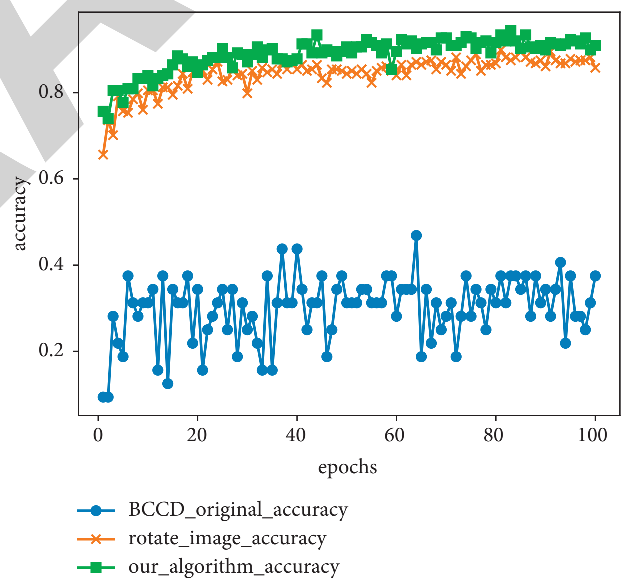

Figure 14: ResNet50 model VA value curve.

3.4. Experimental Results and Discussion. This paper uses three models of ResNet50 [28], MobileNet [29], and ShuffleNet [30] to verify the method. Each model is trained for 100 epochs, the learning rate is 0.005, and (n) is 30. The loss value, VA, P, and (r) verification results of each model are shown in Figures 13–24. All the ordinates in the picture are the values obtained during testing.

It can be seen from Figure 13 and 17 that, after training ResNet50 and MobileNet using the dataset generated by the method proposed in this paper, the loss curve of the test is stable, good convergence can be obtained, and the loss value is the smallest. As can be seen from Figure 21, after the ShuffleNet model is trained on the dataset generated by the method proposed in this paper, although the loss value curve fluctuates more than the loss value curve after training with the BCCD original image dataset, the loss value is the smallest in most cases. As can be seen from Figures 13–16, when ResNet50 is trained using the BCCD original image dataset, the loss value of the test cannot achieve good convergence, and the VA, P, and R values have large fluctuations, so a stable prediction effect cannot be obtained. As can be seen from Figure 17, when the BCCD original image dataset trains the MobileNet, the gradient explosion occurs in the 13th epoch loss function, the loss value rises sharply,

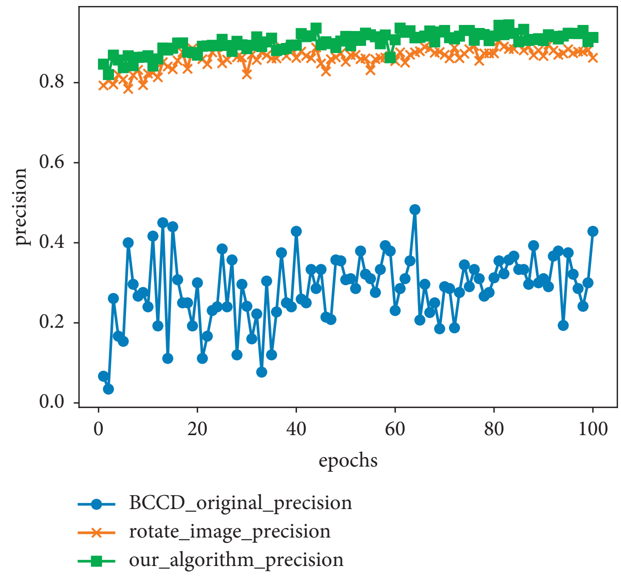

Figure 15: ResNet50 model P value curve.

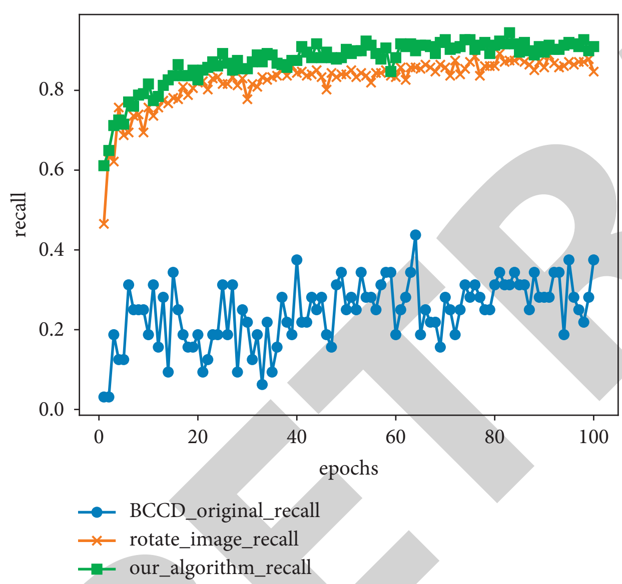

Figure 16: ResNet50 model R value curve.

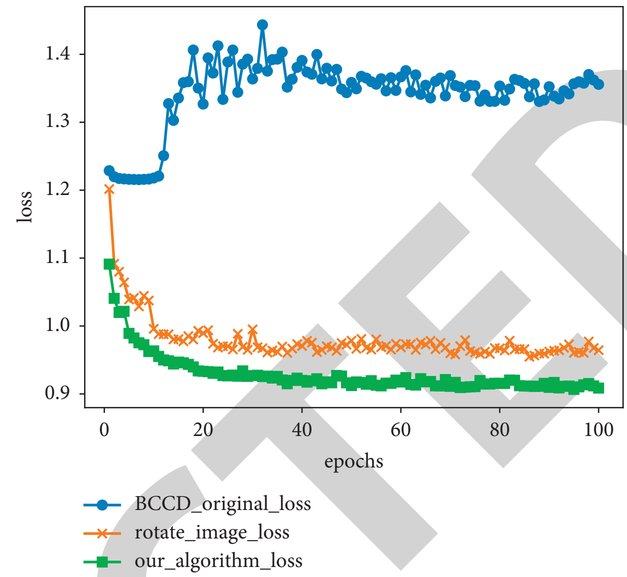

Figure 17: MobileNet model loss value curve.

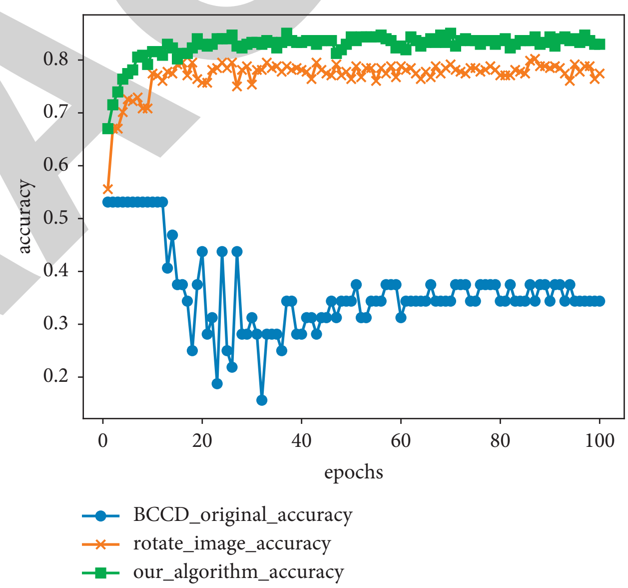

Figure 18: MobileNet model VA value curve.

and its VA, P, and R values all drop significantly. As can be seen from Figure 21, when the ShuffleNet is trained using the rotated image dataset, at the 73th epoch, the loss function has a gradient explosion, the loss value rises sharply, and its VA, P, and R values all drop significantly. Looking at Figures 13–24, using the dataset generated by the method in this paper to train the three models did not experience a gradient explosion. After training with multiple epochs, the loss value, VA, P, and R values can all reach a relatively stable state and have good robustness. When training the ResNet50 and MobileNet, the loss value is the smallest, and the VA, P, and R values are the largest. When training the ShuffleNet, the loss value is also the smallest most of the time, and the VA, P, and R values are the largest.

We use (8) to make a quantitative evaluation of the improvement in loss, VA, P, and R values. Based on the loss value, VA, P, and R values obtained by training the three models on the BCCD original image dataset, calculate the value of each parameter improvement of the 20 epochs after stabilization; this paper uses the 80th epoch to the 100th epoch. *Pan* is the loss value, VA, P, or R at the nth epoch using the rotated image dataset or the dataset generated by the method in this paper; Bn is the loss value, VA, P, or R at the nth epoch using the BCCD original dataset; the total training times of epochs and the results are shown in Table 2–4.

$$I = \frac{\sum_{n=i}^{i+19}\left(\left(Pa_n - B_n\right)/B_n\right)}{20}. \quad (8)$$

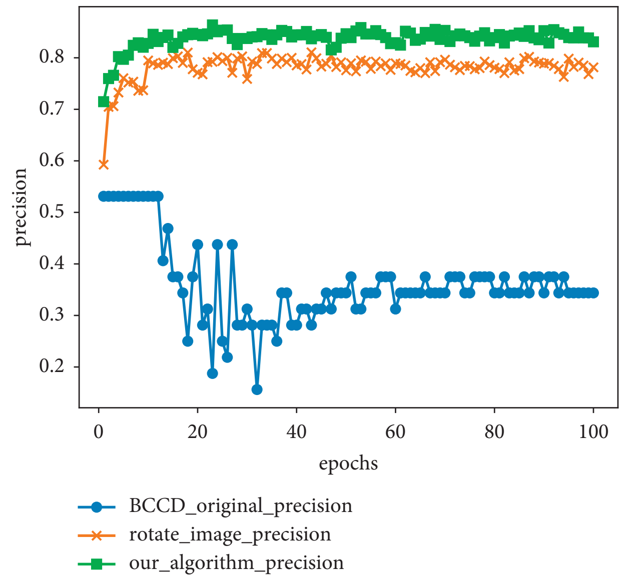

Figure 19: MobileNet model P value curve.

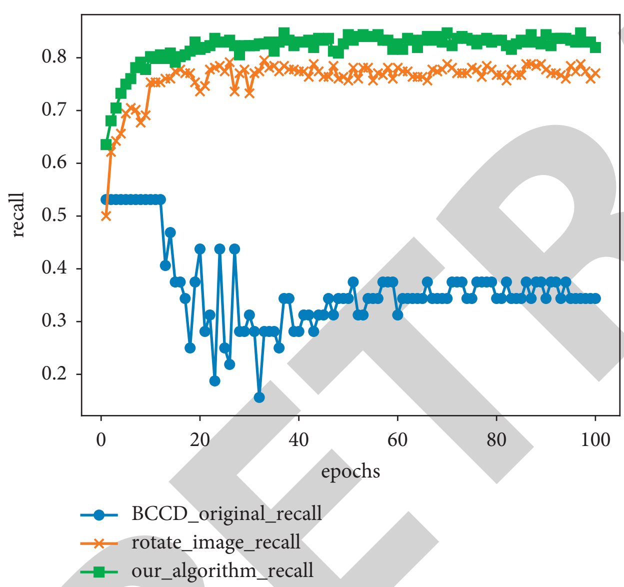

Figure 20: MobileNet model R value curve.

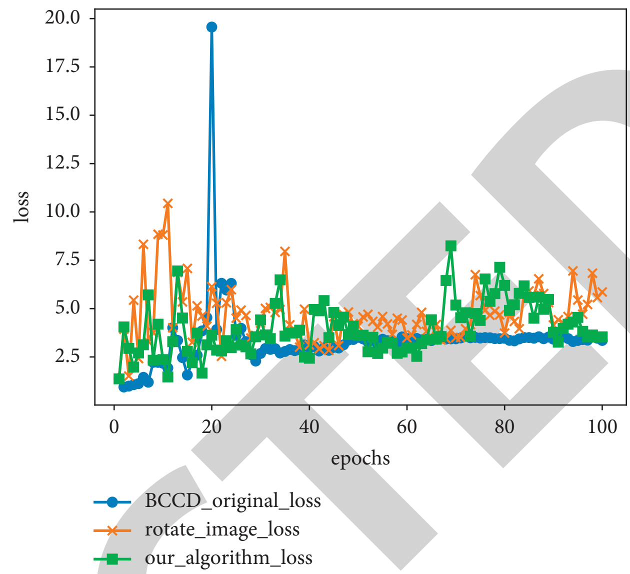

Figure 21: ShuffleNet model loss value curve.

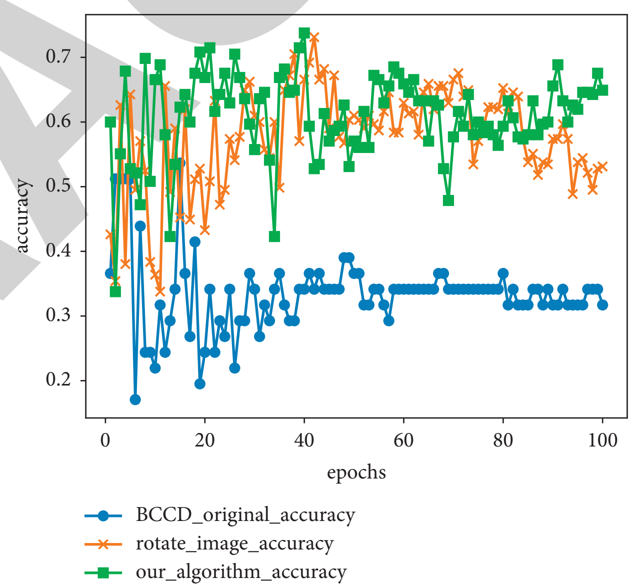

Figure 22: ShuffleNet model VA value curve.

It can be seen from Table 2–4 that when the rotated image dataset is compared with the original BCCD dataset, the VA, P, and R values are significantly improved, except that the loss value in the ShuffleNet is not improved. Using the dataset generated by the method in this paper to train the three models, the loss value, VA, P, and R values are further improved compared with the rotated image dataset.

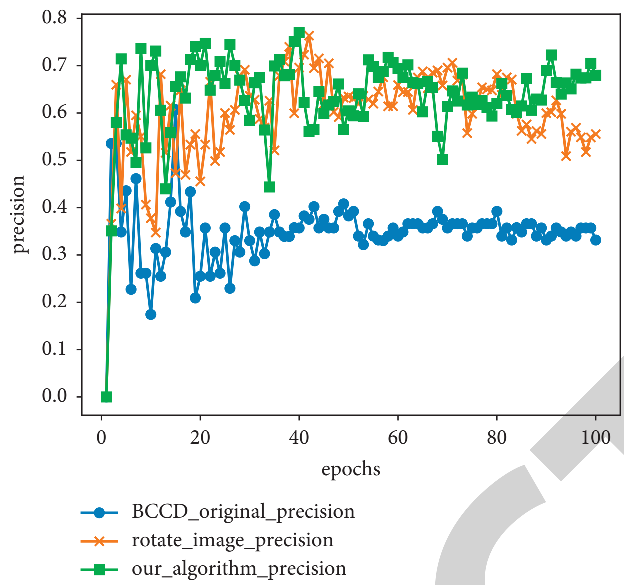

FIGURE 23: ShuffleNet model P value curve.

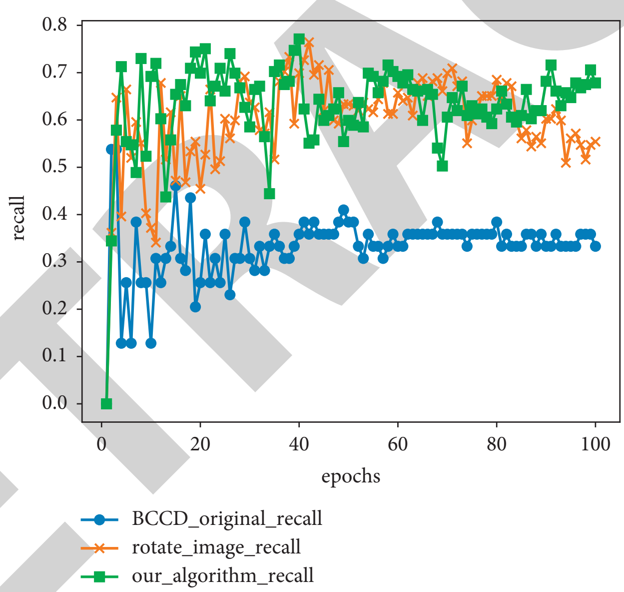

FIGURE 24: ShuffleNet model R value curve.

TABLE 2: The effect of ResNet improvement.

	Using rotated image dataset	Using the dataset generated by the method in this paper
Loss	−61.4%	−74.07%
VA	181.84%	194.69%
P	186.49%	198.89%
R	206.01%	221.14%

TABLE 3: The effect of MobileNet improvement.

	Using rotated image dataset	Using the dataset generated by the method in this paper
Loss	−29.96%	−34%
VA	126.89%	143.29%
P	127.93%	145.06%
R	124.84%	141.95%

Table 4: The effect of ShuffleNet improvement.

	Using rotated image dataset (%)	Using the dataset generated by the method in this paper (%)
Loss	54.77	35.31
VA	74.24	93.98
P	70.64	91.15
R	73.49	92.88

4. Conclusion

White blood cell image classification based on machine learning has important clinical significance, but for non-medical practitioners, it is difficult to obtain white blood cell image datasets for training and learning, and the size of the dataset affects the training and validation of the model. This paper proposes a white blood cell dataset expansion method, which uses the black area edges that appear after image rotation and the original image pixels to count and fill the black area, so as to reduce the possibility of the black area generated by rotation as a feature affecting the classification effect. Experiments show that the dataset obtained by using the method in this paper is used for ResNet, MobileNet, and ShuffleNet training, and the model obtained by training has better robustness and the prediction accuracy is significantly improved.

The main idea of the method in this paper is to use white blood cell images with a large number of monotonous backgrounds; image rotation will produce black areas, and the obvious edges between this area and the original image; fill the black area with pixels from the edge as the starting point, and then study images with the same characteristics in other fields to study the possibility of applying this algorithm in other fields.

Data Availability

The data used to support the findings of this study are included within the article.

Conflicts of Interest

The authors declare that they have no conflicts of interests.

Acknowledgments

This work was supported and funded by the Guangdong Provincial Department of Education's undergraduate college teaching quality and teaching reform project: Traditional Chinese Medicine Digital Science, Industry and Education Integration Practice Teaching Base, under grant Yuejiao Gaohan (2021) No. 29.

References

[1] H. F. Jia, *The Research of Leukocytes Classification Based on Deep Learning*, ShenZhen University, ShenZhen, China, 2017.

[2] S. F. Bikhet, "Segmentation and classification of white blood cells," in *Proceedings of the IEEE International Conference on Acoustics, Speech, and Signal Processing Proceedings (Cat. No. 00CH37100)*, vol. 4, IEEE, Istanbul, Turkey, May 2000.

[3] A. Picca, A. E. Wahlquist, and M. Hudspeth, "Incorporating absolute phagocyte count with absolute neutrophil count as a measure for safe discharge for pediatric oncology febrile neutropenia: a pilot study," *Journal of Pediatric Hematology*, vol. 43, no. 7, pp. e1000–e1002, 2021.

[4] J. A. Cuoco, E. L. Guilliams, B. J. Klein et al., "Neutrophil count on admission predicts acute symptomatic hydrocephalus after aneurysmal subarachnoid hemorrhage," *World Neurosurgery*, vol. 156, pp. e338–e344, 2021.

[5] W.-C. Chao, C.-L. Wu, J.-A. Huang et al., "Association between early absolute neutrophil count and level of D-dimer among patients with COVID-19 infection in central taiwan," *Journal of Clinical Medicine*, vol. 10, no. 17, Article ID 3891, 2021.

[6] W. Xuan, X. Jiang, L. Huang et al., "Predictive value of eosinophil count on COVID-19 disease progression and outcomes, a retrospective study of Leishenshan Hospital in Wuhan, China," *Journal of Intensive Care Medicine*, vol. 37, no. 3, pp. 359–365, 2022.

[7] C. C. Reed, R. M. Genta, B. A. Youngblood, J. B. Wechsler, and E. S. Dellon, "Mast cell and eosinophil counts in gastric and duodenal biopsy specimens from patients with and without eosinophilic gastroenteritis," *Clinical Gastroenterology and Hepatology*, vol. 19, no. 10, pp. 2102–2111, 2021.

[8] X. Huang, B. Zha, M. Zhang et al., "Decreased monocyte count is associated with gestational diabetes mellitus development, macrosomia, and inflammation," *Journal of Clinical Endocrinology & Metabolism*, vol. 107, no. 1, pp. 192–204, 2022.

[9] K. Ueda, S. Suekane, H. Kurose et al., "Absolute lymphocyte count is an independent predictor of survival in patients with metastatic renal cell carcinoma treated with nivolumab," *Japanese Journal of Clinical Oncology*, vol. 52, no. 2, pp. 179–186, 2022.

[10] J. Wang, Z. Y. Sun, P. Guo, and L. M. Zhang, "Improved leukocyte detection algorithm of YOLOV5," *Computer Engineering and Application*, vol. 52, no. 4, pp. 1–12, 2022, http://kns.cnki.net/kcms/detail/11.2127.TP.20211117.0922.002.html.

[11] J. W. Zhao, M. S. Zhang, and Z. H. Zhou, "A classification algorithm for five types of white blood cells based on hierarchical method," *Journal of Shanxi University (Natural Science Edition)*, vol. 38, no. 3, pp. 420–425, 2015.

[12] Y. Duan, J. Wang, M. Hu et al., "Leukocyte classification based on spatial and spectral features of microscopic hyperspectral images," *Optics & Laser Technology*, vol. 112, pp. 530–538, 2019.

[13] B. Azam, R. Qureshi, and T. K. Khattak, "Color based segmentation of white blood cells in blood photomicrographs using image quantization," *Research Journal of Recent Sciences*, vol. 2277, pp. 2502–2509, 2014.

[14] Z. Alreza, K. Khadem, and A. Karimian, "Design a new algorithm to count white blood cells for classification leukemic blood image using machine vision system," in *Proceedings of the 2016 6th International Conference on Computer and Knowledge Engineering (ICCKE)*, October 20-21, 2016.

Hindawi
Journal of Healthcare Engineering
Volume 2023, Article ID 9869424, 1 page
https://doi.org/10.1155/2023/9869424

Retraction

Retracted: The Value of Python Programming in General Education and Comprehensive Quality Improvement of Medical Students Based on a Retrospective Cohort Study

Journal of Healthcare Engineering

Received 10 October 2023; Accepted 10 October 2023; Published 11 October 2023

This article has been retracted by Hindawi following an investigation undertaken by the publisher [1]. This investigation has uncovered evidence of one or more of the following indicators of systematic manipulation of the publication process:

(1) Discrepancies in scope
(2) Discrepancies in the description of the research reported
(3) Discrepancies between the availability of data and the research described
(4) Inappropriate citations
(5) Incoherent, meaningless and/or irrelevant content included in the article
(6) Peer-review manipulation

The presence of these indicators undermines our confidence in the integrity of the article's content and we cannot, therefore, vouch for its reliability. Please note that this notice is intended solely to alert readers that the content of this article is unreliable. We have not investigated whether authors were aware of or involved in the systematic manipulation of the publication process.

In addition, our investigation has also shown that one or more of the following human-subject reporting requirements has not been met in this article: ethical approval by an Institutional Review Board (IRB) committee or equivalent, patient/participant consent to participate, and/or agreement to publish patient/participant details (where relevant).

Wiley and Hindawi regrets that the usual quality checks did not identify these issues before publication and have since put additional measures in place to safeguard research integrity.

We wish to credit our own Research Integrity and Research Publishing teams and anonymous and named external researchers and research integrity experts for contributing to this investigation.

The corresponding author, as the representative of all authors, has been given the opportunity to register their agreement or disagreement to this retraction. We have kept a record of any response received.

References

[1] X. Chen and W. Liu, "The Value of Python Programming in General Education and Comprehensive Quality Improvement of Medical Students Based on a Retrospective Cohort Study," *Journal of Healthcare Engineering*, vol. 2022, Article ID 4043992, 8 pages, 2022.

Hindawi
Journal of Healthcare Engineering
Volume 2022, Article ID 4043992, 8 pages
https://doi.org/10.1155/2022/4043992

Research Article

The Value of Python Programming in General Education and Comprehensive Quality Improvement of Medical Students Based on a Retrospective Cohort Study

Xiuqing Chen and Wei Liu

School of Medical Information & Engineering of Xuzhou Medical College, Xuzhou 221004, Jiangsu, China

Correspondence should be addressed to Wei Liu; lw_xzmc@xzhmu.edu.cn

Received 13 March 2022; Accepted 11 April 2022; Published 21 April 2022

Academic Editor: Liaqat Ali

Objective. A retrospective cohort study was conducted to analyze the application value of Python programming in general education and comprehensive quality improvement of medical students. *Methods.* A retrospective analysis was made on the application value of Python programming in the general education classroom of medical students from September 2020 to July 2021 by undergraduate students majoring in anesthesia in grade 2020, imaging in grade 2019, clinical in grade 2020, and laboratory sciences in grade 2020 in our university. A hundred students who used Python programming in general education class were divided into study group and control group. The teaching satisfaction, medical knowledge and lifelong learning ability, clinical skills, medical service ability, disease prevention, health promotion ability, interpersonal communication ability, and information management and research ability were compared between the two groups. *Results.* In a comparison of teaching satisfaction between the two groups, the study group was very satisfied in 89 cases, satisfactory in 10 cases, and general in 1 case, and the satisfaction rate was 100.00%; the control group was very satisfied in 54 cases, satisfactory in 23 cases, general in 13 cases, and dissatisfied in 10 cases, and the satisfaction rate was 90.00%. The teaching satisfaction in the study group was higher than that in the control group, and the difference was statistically significant ($P < 0.05$). Compared with the control group, medical knowledge ability (basic knowledge, general education, and professional knowledge) and lifelong learning ability (learning concept and professional learning attitude) in the research group were significantly higher than those in the research group ($P < 0.05$). The scores of clinical skills (medical history analysis, basic diagnosis, treatment techniques, and disease analysis) and medical service ability (first aid ability, comprehensive analysis ability, and disease analysis ability) in the study group were significantly higher than those in the control group ($P < 0.05$). In terms of the ability of disease prevention and health promotion, the scores of disease prevention (health guidance, health education, and self-care) and health promotion ability (cooperative participation in diagnosis and treatment, guidance of medical and health work, and rational use of health resources) in the study group were higher than those in the control group, and the difference was statistically significant ($P < 0.05$). In the comparison of interpersonal communication ability, the scores of listening, expression, understanding, trust, medical terminology, and communication ability in the study group were higher than those in the control group, and the difference was statistically significant ($P < 0.05$). Comparing information management with research ability, the scores of information management ability (searching information, screening information, and sorting information) and research ability (arrangement ability, planning ability, and execution ability) in the research group were higher than those in the control group, and the data difference was statistically significant ($P < 0.05$). *Conclusion.* The application of the Python programming method in general education and comprehensive quality improvement of medical students can effectively improve medical students' teaching satisfaction and medical knowledge such as lifelong learning ability, clinical skills, medical service ability, disease prevention, health promotion ability, interpersonal communication ability, and information management and research ability, which has a positive impact on the improvement of comprehensive quality.

1. Introduction

Talent training has always been the basic and primary function of universities. Scientific and technological progress and economic development not only provide opportunities and space for the development of higher education but also put forward higher requirements for it. The existing higher education model attaches importance to professional education, which leads to defects such as weak foundation, low quality, and narrow vision, which cannot meet the needs of society [1]. In order to change the situation that the training of talents is too narrow and too specialized, China has carried out the pilot work of strengthening the cultural quality education of college students in 52 colleges and universities since 1995. Since then, cultural quality education has become the focus of higher education reform and research. Cultural quality education is mainly put forward in view of the fact that higher education puts too much emphasis on professional education while neglecting to cultivate students' comprehensive literacy, which aims to improve the quality of students' all-round development [2]. Although some scholars deliberately distinguish "general education" from "cultural quality education," they are essentially the same. In other words, cultural quality education is the "Chinese version" of general education. The local comprehensive university, which plays an important role in China's higher education, aims to cultivate compound applied talents. This kind of talent needs "both knowledge application and theoretical innovation" and "the combination of learning and application, the combination of learning and creation." They pay attention not only to the ability of practical application but also to the comprehensiveness of humanities and literature. The development of general education provides the most scientific and suitable training environment for this kind of talents [3, 4].

General required courses mainly include English, ideological and political courses, physical education, Chinese, and computer basics. General elective courses are composed of five modules: innovation and leadership, humanities, social sciences, natural sciences, and art appreciation [5]. The general courses of other comprehensive universities in China also basically adopt the mode of combining general compulsory courses with general elective courses, but there are some differences in the offering of specific general courses and, especially, the differences in the module design of general elective courses are slightly obvious; however, they are basically the same [6]. The traditional teaching mode ignores the cultivation of students' computational thinking, which is an extension of a person's ability to solve problems. People refocus to develop their creativity and critical thinking ability. Students use computational thinking, algorithms to solve problems, and computing to solve problems. Python is an object-oriented, interpretive, high-level computer programming language, which was invented by Guido van Rossum in 1989 and published its first public release in 1991. Python programming has been used in the classroom of higher education in our country in the past, but there are few reports on the application of general education and comprehensive quality improvement of medical students. Some studies have pointed out that [7, 8] Python programming focuses on improving students' English application ability, logical thinking and language expression ability, scientific research ability, and traditional cultural literacy, which can effectively expand their comprehensive quality. Based on this, this study analyzes the application value of Python programming in general education and the comprehensive quality improvement of medical students through a retrospective cohort study.

2. Patients and Methods

2.1. General Information. A retrospective analysis was made on the application value of Python programming in the general education classroom of medical students from September 2020 to July 2021 by undergraduate students majoring in anesthesia in grade 2020, imaging in grade 2019, clinical in grade 2020, and laboratory sciences in grade 2020 in our university. One hundred students who adopted Python programming in the general education classroom were divided into the study group and the control group. In the control group, the age was 19–21 years old, with an average of 20.34 ± 0.63 years, including 43 males and 57 females, while in the study group, the age was 19–21 years old, with an average of 20.15 ± 0.56 years, including 45 males and 55 females. There was no statistical significance in the general data of the two groups of students.

2.2. Treatment Methods. Routine teaching methods were used in the control group. The research group adopts the Python programming method in the general education classroom as follows. (1) Literature research method: at the beginning of the research, this article uses the literature research method, collects and selects a large number of related data and other databases in the knowledge network, carefully studies and understands the literature published by the predecessors, deeply studies and extends, and obtains its own views based on a large number of readings and accumulating strength and with the support of relevant theories. The literature research method is used to analyze the articles and viewpoints of different scholars in the early stage and carefully study the current research situation, concept definition, theoretical basis, typical teaching mode analysis, and other aspects, taking the learned experience and theory as the basis of constructing the teaching model of Python course, as a valuable reference and reference for this research. (2) Questionnaire method: in the study, according to the needs, the method of questionnaire survey was used to investigate the teachers and students. Before designing the Python course teaching model, a questionnaire survey was conducted to understand the students' comprehensive ability, analyze the learners, and provide relevant data for the follow-up experiments. In addition, according to the current teaching situation and demand for general education course Python and the effect after implementing the teaching model, we send out a questionnaire to understand the changes of students' comprehensive ability. After the questionnaire is collected, we use SPSS to do statistical analysis of the survey data and obtain quantitative survey results, such as students' learning performance and computational thinking ability, in order to better modify and improve the teaching model. (3) Interview method: after the educational experiment, the students were interviewed to understand the students' feelings about the Python course and listen to the students' suggestions. A comprehensive evaluation of the teaching model in the process of the interview will facilitate a better understanding of the factors that affect computational thinking and find out the problems and deficiencies in the teaching model. (4) Educational experiment method: the Python curriculum teaching mode of cultivating computational thinking is applied to the general education teaching, the control class and the experimental class are set up in the practice school, the traditional teaching mode of the practice school is followed in the control class, and the Python curriculum teaching model of junior middle school is implemented in the experimental class. Before the beginning of the experiment and after the end of the experiment, the questionnaires of the two groups were collected to evaluate the teaching effect.

2.3. Observation Index

2.3.1. Teaching Satisfaction [9]. Teaching satisfaction can be divided into four levels: very satisfied, satisfied, general, and dissatisfied. Students are asked to score teaching methods, teaching effects, and teaching results, with 0–70 as dissatisfied, 71–80 as general, 81–90 as satisfactory, and more than 90 as very satisfied. Satisfaction rate = very satisfaction rate + satisfaction rate + general rate.

2.3.2. Medical Knowledge and Lifelong Learning Ability [10]. Medical knowledge includes basic knowledge, general education, and professional knowledge; lifelong learning ability includes learning concept, professional skills learning, and learning attitude. Each dimension was scored by Likert score: very good, good, neutral, poor, and very poor, corresponding to 5, 4, 3, 2, and 1 points, respectively.

2.3.3. Clinical Skills and Medical Service Capacity [11]. Clinical skills include medical history analysis, basic diagnosis and treatment techniques, and disease analysis; medical service ability includes first aid ability, comprehensive analysis ability, and disease analysis ability. The 5-point Likert score method was used to score each dimension: very good, good, neutral, bad, and very bad, corresponding to 5, 4, 3, 2, and 1 points, respectively.

2.3.4. Health Education and Cooperation Ability [12]. The scope of health education includes the ability to provide health guidance, health education, and self-care to the public, and health promotion capacity includes the ability to cooperate with frontline physicians to participate in diagnosis and treatment and to assist medical staff and the health system and the ability to make rational use of health resources in the current environment.The 5-point Likert score method was used to score each dimension: excellent, very good, good, not bad, and bad, corresponding to 5, 4, 3, 2 and 1 points, respectively.

2.3.5. Interpersonal Communication Skills [13]. Interpersonal communication ability is divided into six dimensions: listening, expression, understanding, trust, medical terminology, transmission of information, 20 points in each dimension; the higher the score, the stronger the academic interpersonal communication ability.

2.3.6. Information Management and Research Capabilities [14]. Information management ability includes searching information, screening information, and collating information; research ability includes arrangement ability, planning ability, and execution ability. The 5-point Likert score method was used to score each dimension: excellent, very good, good, not bad, and bad, corresponding to 5, 4, 3, 2, and 1 points, respectively.

2.4. Statistical Analysis. After sending and collecting the questionnaire, input it with EpiData3.1 software, set up the database, and correct the logic error. Statistical analysis was carried out with SPSS22.0 statistical software. A t-test was used to compare the counting data between the two groups. In terms of counting data, it is expressed by n (%), and χ 2 test is used to test the counting data. The difference was statistically significant ($P < 0.05$).

3. Results

3.1. Comparison of Teaching Satisfaction. We compared the teaching satisfaction of the students in the two groups. The study group was very satisfied with 89 cases, satisfactory 10 cases, and general 1 case, and the satisfaction rate was 100.00%; the control group was very satisfied with 54 cases, satisfactory 23 cases, general 13 cases, and dissatisfied 10 cases, and the satisfaction rate was 90.00%. The teaching satisfaction of the study group was higher than that of the control group, and the difference was statistically significant ($P < 0.05$). All the data are shown in Table 1.

3.2. Comparison of Medical Knowledge and Lifelong Learning Ability. We compared the medical knowledge and lifelong learning ability of the two groups of students. The scores of medical knowledge (basic knowledge, general education, and professional knowledge) and lifelong learning ability (learning view, professional skills learning, and learning attitude) in the study group were significantly higher than those in the control group ($P < 0.05$). All the data are shown in Table 2.

3.3. Comparison of Clinical Skills and Medical Service Ability. We compared the clinical skills and medical service ability of the two groups of students. The scores of clinical skills (history analysis basic diagnosis, treatment techniques, and

Table 1: Comparison of teaching satisfaction between two groups of patients [n/%].

Group	N	Very satisfied	Satisfied	General	Not satisfied	Satisfaction rate
Control group	100	54 (54.00)	23 (23.00)	13 (13.00)	10 (10.00)	90 (90.00)
Research group	100	89 (89.00)	10 (10.00)	1 (1.00)	0	100 (100.00)
$\chi 2$						10.526
P						0.000

Table 2: Comparison of medical knowledge and lifelong learning ability between the two groups of students [$\overline{x} \pm s$, points].

Group	Cases	Medical knowledge			Lifelong learning ability		
		Basic knowledge	General education	Professional knowledge	Learning view	Professional skills learning	Learning attitude
Control group	100	3.21 ± 1.22	3.59 ± 0.35	3.16 ± 0.34	2.96 ± 1.22	3.68 ± 0.65	3.55 ± 0.42
Research group	100	4.31 ± 0.12	4.66 ± 0.11	4.51 ± 0.12	4.07 ± 0.21	4.23 ± 0.21	4.52 ± 0.12
t		8.973	29.164	37.442	8.966	8.051	22.206
P		0.900	<0.01	<0.01	<0.01	<0.01	<0.01

disease analysis) and medical service ability (first aid ability, comprehensive analysis ability, and disease analysis ability) in the study group were significantly higher than those in the control group ($P < 0.05$). All the data are shown in Table 3.

3.4. Comparison of the Ability of Disease Prevention and Health Promotion. We compared the abilities of disease prevention and health promotion between the two groups. The scores of disease prevention (health guidance, health education, and self-care) and health promotion ability (cooperate to participate in diagnosis and treatment, guide medical and health work, and make rational use of health resources in the study group) were significantly higher than those in the control group ($P < 0.05$). All the data are shown in Table 4.

3.5. Comparison of Interpersonal Communication Skills. We compared the interpersonal communication ability of the two groups. The scores of listening, expression, comprehension, trust, medical terminology, and communication ability in the study group were significantly higher than those in the control group ($P < 0.05$). The results of all the data are shown in Table 5.

3.6. Comparison of Information Management and Research Ability. We compared the information management and research ability of the two groups of students. The scores of information management ability (searching information, screening information, and sorting information) and research ability (arrangement ability, planning ability, and execution ability) in the study group were higher than those in the control group, and the data difference was statistically significant ($P < 0.05$). All the data are shown in Table 6.

4. Discussion

General education is a kind of comprehensive education, a kind of basic education for students to study professionally, a kind of education to cultivate complete and responsible citizens, and an education to teach students how to think systematically about the overall situation, how to judge carefully, how to communicate effectively, and how to solve problems creatively [15]. In terms of nature, general education has two meanings: one is that Packard's general education is a kind of comprehensive basic education, and the other is that Li Manli and Chen Xiuping's general education is a kind of nonprofessional education relative to professional education. In terms of purpose, most domestic and foreign researchers agree that general education is to cultivate complete, socially responsible, and free citizens [16, 17]. In content, general education pays attention to the education of broad and comprehensive knowledge and ability, that is, broad access to knowledge in different fields. In addition to rational knowledge, it also includes the ability of emotion and will. Although general education has been implemented in China for more than 20 years, the general curriculum has also become an indispensable part of universities; however, so far, principals, administrators, and teachers have not reached a consensus on general education, the understanding of general education is still far from in place; this situation makes our attention to general education still stay at the "slogan" level [16]. It is not difficult to see that the lack of understanding of general education by school administrators and teachers is the key to restraining students' awareness of general education [18]. School administrators and teachers' limited cognition of general education comes from two factors: one is practical utilitarianism, they think that practical and "immediate" knowledge is useful, and the other is professionalism. Deeply influenced by the education model of the former Soviet Union, it is considered that it is particularly important for students to specialize in special skills, and it is a waste of time to take courses other

Table 3: Comparison of clinical skills and medical service ability between the two groups of students [$\overline{x} \pm s$, points].

Group	N	Clinical skills			Medical service capacity		
		History analysis	Basic diagnosis and treatment techniques	Disease analysis	First aid ability	Comprehensive analysis ability	Disease analysis ability
Control group	100	3.67 ± 1.34	3.47 ± 0.23	3.66 ± 0.45	3.44 ± 1.54	3.44 ± 0.65	3.77 ± 0.12
Research group	100	4.33 ± 0.17	4.43 ± 0.25	4.36 ± 0.32	4.22 ± 0.13	4.89 ± 0.21	4.78 ± 0.07
t		4.886	28.259	12.677	5.046	21.227	72.701
P		0.900	<0.01	<0.01	<0.01	<0.01	<0.01

Table 4: Comparison of disease prevention and health promotion ability [$\overline{x} \pm s$, points].

Group	N	Disease prevention			Health promotion ability		
		Health guidance	Health education	Self-care	Participate in	Guide medical	Rational use of health resources
C group	100	3.44 ± 1.56	3.34 ± 0.42	3.34 ± 0.33	3.16 ± 1.67	3.77 ± 0.33	3.12 ± 0.18
R group	100	4.35 ± 0.22	4.56 ± 0.17	4.77 ± 0.06	4.07 ± 0.31	4.66 ± 0.21	4.45 ± 0.44
t		5.776	26.925	42.634	5.357	22.753	27.976
P		0.900	<0.01	<0.01	<0.01	<0.01	<0.01

Table 5: Comparison of interpersonal communication skills between the two groups of students [$\overline{x} \pm s$, points].

Group	N	Listen	Express	Understand	Trust	Medical terminology	Transmit information
C group	100	13.6 ± 3.56	13.46 ± 2.67	15.4 ± 2.34	14.78 ± 2.41	14.67 ± 2.35	14.66 ± 2.56
R group	100	17.4 ± 1.22	16.88 ± 2.45	18.34 ± 2.11	17.31 ± 1.25	18.31 ± 2.21	17.66 ± 2.45
t		10.044	9.437	9.235	9.318	11.283	8.466
P		0.900	<0.01	<0.01	<0.01	<0.01	<0.01

Table 6: Comparison of information management and research ability between two groups of students [$\overline{x} \pm s$, points].

Group	N	Information management			Research ability		
		Retrieve information	Filter information	Organize information	Arranging ability	Planning capacity	Executive ability
C group	100	3.56 ± 1.21	3.39 ± 0.31	3.42 ± 0.31	3.10 ± 1.56	3.31 ± 0.21	3.56 ± 0.65
R group	100	4.35 ± 0.17	4.56 ± 0.31	4.33 ± 0.17	4.53 ± 0.34	4.45 ± 0.31	4.56 ± 0.21
t		6.465	26.687	25.738	8.956	30.446	144.639
P		0.900	<0.01	<0.01	<0.01	<0.01	<0.01

than professional courses. In order to remove the cognitive barriers, managers, and teachers need to recognize the sustainable development and variability of students, the social environment is constantly changing, students are also constantly changing, and students may not be able to become professionals in a certain field but become a new generation of young people who can adapt to and lead social changes. Teachers should also be aware that students' ability to adapt and lead social change requires a sense of social responsibility, broad knowledge, and mindset [19]. In addition, professional education and general education are not opposed to each other. Professional education also contains rich connotations of general education. While imparting professional skills to students, teachers should explore the humanistic feelings contained in this course. School general education administrators and teachers should set up general awareness and emphasize the development of general education and professional education, and it is particularly important to have a deep understanding of students' general education. The establishment of this awareness requires schools to strengthen the promotion and promotion of the general concept of "top-down" and also requires all teachers and students to participate in general education from the bottom-up [20].

Cramming teaching is a teaching mode under examination-oriented education, which is suitable for students who lack active thinking and enthusiasm in learning, that is, as long as the students understand what the teacher says, as long as the students understand what the teacher is saying, the academic performance will not be too bad, but these students trained under the cramming teaching mode will lack the ability to think independently and deal with problems and things on their own [21]. The understanding and learning of knowledge only stay on the surface, and will not dig deeply to ask why, which is extremely disadvantageous to the cultivation of students' critical thinking and comprehensive quality [21]. In the 21st century with the rapid development of information, computational thinking has become a necessary basic quality for learners. Computing power affects not only all aspects of our lives, but also all aspects of our future lives. The cultivation of computational thinking needs a long process, and the teaching model needs to be constantly modified and improved to meet the needs of teachers' teaching and students' continuous development [22].

In previous studies, some scholars pointed out that the relationship between computer professional research and development and learning computer science and technology knowledge is not very close, so they put forward the concept of computational thinking and think that computational thinking is helpful to every ordinary people, which is universal and suitable for professionals and nonprofessionals. Professor Simon Pipert of the Massachusetts Institute of Technology was the first researcher to put forward this concept [23]. After Professor Zhou Yizhen systematically defined computational thinking, in 2006, Zhou Yizhen, a Chinese computer scientist at Carnegie Mellon University, first proposed in Communications of the ACM magazine that Professor Zhou Yizhen put forward constructive suggestions on the concept of computational thinking. Professor Zhou believed that computational thinking has six characteristics: first, computational thinking is a conceptual theory. Second, computational thinking is fundamental, not the ability in people's stereotype; third, the subject of computational thinking is human thinking, not computer thinking; fourth, whether computational thinking is concrete and abstract; fifth, the combination of engineering and mathematical thinking is the source of computer science, which is the essence of computer science; sixth, computational thinking is for everyone and can be seen everywhere. Some scholars have pointed out that computational thinking is a process of solving problems, including the following properties: analyzing problems in a way that computers or other tools can help solve problems; arranging and analyzing data in a logical way; representing, modeling, and simulating data in an abstract way; migrating solutions with the help of algorithmic thinking [24]. In 2015, the American Association for International Educational Technology defined computational thinking from a new perspective, including problem-solving ability, algorithmic thinking, critical thinking, cooperative ability, and creativity. Computational thinking has been redefined. It is emphasized that the purpose of computational thinking in education is not to bring students to the leading position in computer science but to apply their computational thinking skills to other courses as a habit [25].

Python can be used in Web and Internet development; desktop interface development; back-end development; statistics and education. The Python language abandons complex syntax and chooses one that is clear and rarely ambiguous. Simple syntax rules are conducive to the readability of the Python language, and this advantage can be taken advantage of in large-scale software development [26]. Python is a completely object-oriented language. In Python, modules, numbers, and strings are all objects. Python has a powerful standard library, and common types and functions such as numbers, strings, lists, dictionaries, and files are the core of the Python language. In addition, Python has good interpretation, good compilation, and excellent interaction; these features give Python more advantages; Python can run on many platforms, such as Windows, MacOs, and Linux. With the continuous development and update of Python, some new features have been added, which are more favored by independent projects, such as domestic Douban, Zhihu, fruit shell, and other large websites built in Python language. Python language is a good interpretation of the idea of simplicity, and its simplicity allows users to better focus on the solution of the problem rather than the language itself [26]. For learners, the Python language is easier to teach. Python language strengthens the algorithm implementation of problem-solving and weakens grammar rules. With the development of technology, open-source software has more vitality, and users can adopt Python to write and read programs for free. The features of the Python high-level language make it possible to employ it without considering the underlying details, such as the memory used by the hypervisor [27].

Combined with the results of this study, the teaching satisfaction of the research group is higher than that of the control group. Specifically, medical knowledge is superior to the control group in terms of lifelong learning ability, clinical skills, medical service ability, disease prevention, health promotion ability, interpersonal communication ability, and information management research ability. The analysis shows that the design of "activities" in the teaching practice of the Python course can encourage students to decompose knowledge and problems and solve them step by step. Similarly, teachers' activity design is conducive to the overall grasp of the teaching model and activity theory as the theoretical basis is conducive to the construction of the teaching model and ultimately promotes the achievement of teaching goals and the cultivation of students' computational thinking ability. On the other hand, from the perspective of "activity" design, we can carry out teaching design according to the proposed teaching model, give full play to the effectiveness of the teaching model, and achieve the cultivation and promotion of computing thinking in the Python course of medical students. Therefore, the construction of the Python course teaching model of computational thinking should be closely linked with the activity learning theory, and the teaching activities should be designed from the perspective of computational thinking so as to achieve the purpose of improving the comprehensive quality of students [28]. The same idea can be found in the diagnostic model proposed by Ashir Javeed et al. [29], who have applied new methods to help doctors make accurate decisions in the diagnosis of heart disease.

In conclusion, the application of the Python programming method in medical students' general education and comprehensive quality improvement can effectively improve medical students' teaching satisfaction and medical knowledge such as lifelong learning ability, clinical skills, medical service ability, disease prevention, health promotion ability, interpersonal communication ability, and information management and research ability, which has a positive impact on the improvement of comprehensive quality. This teaching model is worth popularizing. As this study is a retrospective analysis, the sample size is small and there is a certain bias; in addition, it is necessary for a large number of scholars to continue to expand educational experiments and expand research objects to carry out educational experiments in different grades and different areas, in order to further verify the effectiveness and universality of the model. In addition, it is necessary to further explore the measurement tools of computational thinking and evaluate the computational thinking of different students in many aspects and dimensions so as to make the evaluation system of computational thinking more and more perfect. In the future, the teaching mode of cultivating computational thinking ability will be continuously optimized and improved. We hope to make efforts for the promotion of the Python curriculum and arouse educators' attention to computational thinking.

Data Availability

The datasets used and analyzed during the current study are available from the corresponding author upon reasonable request.

Conflicts of Interest

The authors declare that they have no conflicts of interest.

Acknowledgments

The study was suppored by the research project of Higher Education Reform in Jiangsu Province, 2021JSJG628; the project of "quality education and digital curriculum construction of college students" in Jiangsu Universities, 2020JDKT040; and the project of National computer basic Education Research Association of Colleges and Universities, 2021-AFCEC-102.

References

[1] J. R. Wies and H. J. Haldane, *Applying anthropology to general education:reshaping colleges and universities for the 21st century*, Taylor and Francis, vol. 10, no. 9, Oxfordshire, UK, 2021.

[2] S. Gupta, M. Kumar, R. Rozatkar Abhijit et al., "Feasibility and effectiveness of telecounseling on the psychological problems of frontline healthcare workers amidst COVID-19: a randomized controlled trial from Central India," *Indian Journal of Psychological Medicine*, vol. 43, no. 4, pp. 183–186, 2021.

[3] Y. Yang, "Does greater engagement in online general education courses lead to better academic performance? Evidence from Chinese university students," *Open Journal of Social Sciences*, vol. 9, no. 6, pp. 83–89, 2021.

[4] M. McCabe and K. Nye-Lengerman, "Putting policy into practice: impact of the every student succeeds act on speech-language pathologists and students with disabilities," *Language, Speech, and Hearing Services in Schools*, vol. 52, no. 3, pp. 949–954, 2021.

[5] M. E. Sheppard and K. Moran, "The role of early care providers in early intervention and early childhood special education systems," *Early Childhood Education Journal*, vol. 46, no. 96, pp. 19–23, 2021.

[6] Y. Lai, L. Ye, and P. Xie, "Teaching reform of entrepreneurial project management based on curriculum ideological and political education," *Education Research Frontier*, vol. 11, no. 2, pp. 186–189, 2021.

[7] J. E. Brodsky, P. J. Brooks, D. Scimeca et al., "Improving college students' fact-checking strategies through lateral reading instruction in a general education civics course," *Cognitive Research: Principles and Implications*, vol. 6, no. 1, pp. 23–189, 2021.

[8] G. Hongbin, W. Zhengyang, W. Yingfeng, L. Xinwei, and W. Yirong, "Application of formative evaluation based on Python programming in cultivating clinical thinking ability of neurosurgical residents," *Chinese Journal of Medical Education*, vol. 41, no. 2, pp. 175–178, 2021.

[9] S. Jane and K. Storey, "Case Studies for Inclusion in Education. Strategies and guidelines for educating students with disabilities in the general education environment. Springfield, IL, USA: Charles C Thomas," *British Journal of Special Education*, vol. 48, no. 1, pp. 583–589, 2020.

[10] V. M. McClurg, J. Wu, and R. Steve McCallum, "Academic success of general education college students compared to those screened as twice-exceptional and gifted," *Innovative Higher Education*, vol. 46, no. 6, pp. 193–198, 2021.

[11] S. Irene, N. P. Mei Lan, W. W. Sum Phoebe, and L. Yip, "Perceived benefits of studying general education for undergraduate students in the self-financing institutions in Hong Kong," *Asia Pacific Journal of Education*, vol. 41, no. 1, pp. 95–98, 2021.

[12] Z. Wang and T. Tao, "The cultivation of humanistic care spirit of medical students from the perspective of general education," *Chinese adult education*, vol. 78, no. 7, pp. 89–91, 2017.

[13] B. Mu, Yi Yang, and W. Liu, "Developing the extension of general education in physics under the background of double first-class construction—the construction of the course of physical thinking and scientific research literacy," *Advances in Education*, vol. 11, no. 1, pp. 456–459, 2020.

[14] B. Mu, Yi Yang, and W. Liu, "Ideological and political discussion of hidden curriculum in universities under the background of "double first-class" discipline construction—a case study of undergraduate physics teaching in chengdu university of traditional Chinese medicine," *Advances in Education*, vol. 11, no. 1, pp. 574–576, 2020.

[15] H. Shi, "Research on folk art entering general education in Higher Vocational Colleges——taking the course construction of Northeast Folk Painting as an example," *Lifelong Education*, vol. 9, no. 8, pp. 175–178, 2020.

[16] J. Yang and H. Yu, "Exploration and reflection on immunology teaching of general education for undergraduates from the perspective of "great health" and "new medicine"," *Chinese Journal of Preventive Medicine*, vol. 54, no. 10, pp. 1165–1168, 2020.

[17] J. Yang and H. J. Yu, "Practices and reflections on lecturing of vaccinology in general education towards undergraduate students: from the perspective of Comprehensive Health and New Medicine," *Zhonghua yu fang yi xue za zhi [Chinese journal of preventive medicine]*, vol. 54, no. 10, pp. 1165–1168, 2020.

[18] E. Astapova, O. Zamyatina, and E. Panova, "Implementing the model of specialized education based on the principle of distributed responsibilities of educational cluster participants [C]//International science and culture center for academic contacts(moscow, Russia)、Tomsk regional Institute for

Hindawi
Journal of Healthcare Engineering
Volume 2023, Article ID 9878174, 1 page
https://doi.org/10.1155/2023/9878174

Retraction

Retracted: Analysis of the Mechanism of Ureproofing Technology and Postlaparoscopy on Patients with Urology and Infection

Journal of Healthcare Engineering

Received 26 September 2023; Accepted 26 September 2023; Published 27 September 2023

This article has been retracted by Hindawi following an investigation undertaken by the publisher [1]. This investigation has uncovered evidence of one or more of the following indicators of systematic manipulation of the publication process:

(1) Discrepancies in scope
(2) Discrepancies in the description of the research reported
(3) Discrepancies between the availability of data and the research described
(4) Inappropriate citations
(5) Incoherent, meaningless and/or irrelevant content included in the article
(6) Peer-review manipulation

The presence of these indicators undermines our confidence in the integrity of the article's content and we cannot, therefore, vouch for its reliability. Please note that this notice is intended solely to alert readers that the content of this article is unreliable. We have not investigated whether authors were aware of or involved in the systematic manipulation of the publication process.

Wiley and Hindawi regrets that the usual quality checks did not identify these issues before publication and have since put additional measures in place to safeguard research integrity.

We wish to credit our own Research Integrity and Research Publishing teams and anonymous and named external researchers and research integrity experts for contributing to this investigation.

The corresponding author, as the representative of all authors, has been given the opportunity to register their agreement or disagreement to this retraction. We have kept a record of any response received.

References

[1] S. Chen, Y. Zhang, P. Shen, Z. Huang, M. Lin, and J. Huang, "Analysis of the Mechanism of Ureproofing Technology and Postlaparoscopy on Patients with Urology and Infection," *Journal of Healthcare Engineering*, vol. 2022, Article ID 4373416, 6 pages, 2022.

Hindawi
Journal of Healthcare Engineering
Volume 2022, Article ID 4373416, 6 pages
https://doi.org/10.1155/2022/4373416

Research Article

Analysis of the Mechanism of Ureproofing Technology and Postlaparoscopy on Patients with Urology and Infection

Si Chen,[1] Yuanfeng Zhang,[2] Peilin Shen,[1] Zhuangcheng Huang,[1] Mingen Lin,[1] and Jiansheng Huang[1]

[1]*Department of Urology, The First Affiliated Hospital of Shantou University Medical College, Shantou, Guangdong 515041, China*
[2]*Department of Urology, Shantou Central Hospital, Shantou, Guangdong, China*

Correspondence should be addressed to Jiansheng Huang; 10zchuang1@stu.edu.cn

Received 4 January 2022; Revised 27 February 2022; Accepted 7 April 2022; Published 21 April 2022

Academic Editor: Liaqat Ali

Objective. To analyze the effect of ureteroscopy and retrolaparoscopy on urinary calculi and infection. *Method*. A total of 64 patients with urinary calculi and infection who received treatment in our hospital from June 2018 to January 2018 were selected. According to the different treatment methods, they were divided into two groups: a control group and a study group. The study group was treated with laparoscopic ureteroscopy, and the control group was treated with ureteroscopy. The surgical results, complications, renal function, stress response, and inflammatory reaction were compared between the two groups. *Results*. Compared with the control group, the study group stone clearance rate was higher, the surgical time was shorter ($P < 0.05$); the incidence of complications in the study group (23.3%) was lower than that in the control group (5.9%) ($P < 0.05$); there was no significant difference in kidney function indicators before treatment ($P > 0.05$); after treatment, the SCR, BUN, NGAL, and Cys-C indicators of the two groups were significantly increased. Compared with the control group, the study group change was more obvious, and the difference was statistically significant ($P < 0.05$); after treatment, the two sets of stress response indicators were significantly increased, but relative to the control group, the study group stress response indicator was lower ($P < 0.05$); before treatment, there was no significant difference in inflammatory factors ($P > 0.05$); after treatment, the two sets of inflammatory factor levels were significantly increased, but relative to the control group, the study group was lower ($P < 0.05$). *Conclusion*. In the clinical treatment of urinary stones, ureteroscopy technology and the laparoscopic technique have played an important role. But the laparoscopic technique is shorter, the stone clearance is higher, and the patient's renal function can be improved, and the patient is postoperative. The stress reaction should be small. Therefore, in the clinical treatment of urinary stones and infection, laparoscopic technical treatment is worth promoting.

1. Introduction

The ureter, urethra, and bladder are prone to highly pathogenic disease, and the clinical treatment of ureteral calculi is focused on [1]. Data show that about 70% of ureteral stones can be passed naturally. If the past medical history is large, it is difficult to discharge naturally [2]. At present, urological equipment is becoming more and more advanced, surgical technology is improving, and ureteroscopy and laparoscopy have been widely used [3].

Due to the ureteral mirror crimping stone, the stone residue is prone to stones, but the laparoscopic urinary tube is cut into the ureteral tour at the stone, and the ureteral expansion is blocked above the stone, and there will be little stone residual phenomenon [4, 5]. However, the current research on the safety and mechanism of the abovementioned two treatment methods is limited. The study selection included 64 cases of urinary stones admitted to our hospital from June 2018 to January 2021, and the abovementioned two methods were selected. The report of the analysis of the treatment effects of urinary stones in infected patients is further discussed in this study.

2. Data and Methods

2.1. General Information. A total of 64 patients with urinary tract stones complicated by infection who were treated in our hospital from June 2018 to January 2018 were selected and divided into the control group and the study group according to different treatment methods. The study group ($n = 34$) had 18 males and 16 females with an average age of 48.5 ± 5.5; the control group ($n = 30$) had 16 males and 14 with an average age of 48.3 ± 5.6. This study was approved by the patients' consent and the hospital ethics committee, and the data were comparable ($P > 0.05$).

Inclusion Criteria: (1) age of 20–72; (2) imaging and clinical diagnosis of CT and ultrasound, diagnosed as urinary stones and infected; (3) acceptable forecast follow-up; and (4) high quality, which can be combined with the researcher

Exclusion Criteria: (1) congenital ureteral narrow malformation; (2) urinary tuberculosis and ureterodialysis; (3) combined with hemorrhagic diseases; (4) hepato cutter is abnormal; (5) kidney damaged features due to consolidation of severe renal water; and (6) surgical contraindications

2.2. Method

(1) Laparoscopic ureterotomy: the patient is placed in a supine position, tracheal intubation is anesthetized, and the dilated ureter bursts at the extraction site of the lower part of the kidney, which can be freely descended. The ureter is clamped by the separation clip, the electric hook is removed longitudinally, the ureter is cut off, and the stone is taken out. The 5f double-J tube was inserted through the proximal and distal ends of the ureteral incision, and absorbable sutures were selected to suture the ureteral incision, leaving the abdominal drainage tube.
(2) Ureteroscopic lithotripsy: the patient was placed in a supine position, and the back was anesthetized with hard lumbar anesthesia, and an 8/9.8F ureteroscope was placed in the urethra. Under the guidance of a zebra wire, it is placed into the patient's ureter to control the appropriate perfusion pressure. After the stone was detected, the holmium laser 400 μm fiber had reached the catheter, and the edge of the stone was gradually crushed. Finally, the retrograde 5F double J tube.

2.3. Observation Indicator

Surgical Results: it includes the operation time, hospitalization time, postoperative analgesic pump, calculi clearance rate, and polyps discovery rate

Complications: statistical ureteral vacation, fever, incision infection patients, and calculation incidence

Renal Function [6]: 3 ml of venous blood is taken, centrifuged at 3000 rpm for 10 minutes, and an automatic biochemical analysis of serum, serum creatinine (SCR), blood urea nitrogen (BUN), and apolipoprotein (NGAL) indicators instrument (Ponzi Medical, model: PUZS-300X) is used and operated according to the instruction manual

Stress Reaction [7]: serum tyrosinase (NE), adrenal hormone (ACTH), cortical hormone (COR) index, application of enzyme-linked immunosorbent assay (ELISA), and fat were provided by American Beckman Box, and the operation was carried out according to the instruction manual

Inflammatory Reaction [8]: application of immunimosis for the detection of C-reactive protein (CRP), automatic biochemical analyzer is applied to detect white blood cells (WBCs), application of the enzyme immunization adsorption method to detect interleukin-10 (IL-10)

2.4. Statistical Method. The data were analyzed and processed by SPSS22.0 statistical software. The quantitative data were represented by the mean ± standard deviation, the T test was performed, group data were analyzed by variance, the X^2 test was used for qualitative data, two-sided test statistics were used, and $P < 0.05$ was different; graphs were used. Rates were made by GraphPad Prism 8, $P < 0.05$ was significantly different.

3. Results

3.1. General Data Analysis of Two Groups. In the control group and research group, gender, age, preoperative culture positive, and preoperative indwelling double J tube rate, there is a statistical significance ($P > 0.05$) (Table 1).

3.2. Surgical Results of Two Groups Were Analyzed in Two Groups of Hospitalization Time. The time of use of postoperative analgesia did not show a significant difference ($P > 0.05$). In the control group and the study group, the stone clearance was 81.7% and 100%, respectively. In comparison, the stones of the study group were higher, the surgical time was shorter, and there was statistical significance ($P < 0.05$) (Table 2).

3.3. Comparison of Complications between the Two Groups. The incidence of complications in the study group was lower than that in the control group (Figure 1).

3.4. Two-Group Kidney Function Index Contrast. Before the analysis of kidney function indicators, the two groups of renal function indicators have no significant difference ($P > 0.05$). After treatment, SCR, BUN, NGAL, and Cys-C indicators of two groups were significantly increased. Compared with the control group, the study group change is more obvious, and there is a statistical significance of the difference ($P < 0.05$) (Figure 2).

3.5. Comparison of Two Groups of Oxidative Stress Indicators. There was no significant difference in oxidative stress indicators between the two groups ($P > 0.05$), and the stress response indicators in the two groups were significantly

Table 1: Analysis of the general data of two groups.

Project	Control group ($n = 30$)	Research group ($n = 34$)	X^2/t	P
Gender (male/female)	16/14	18/16	0.682	> 0.05
Age	48.3 ± 5.6	48.5 ± 5.5	1.524	> 0.05
Preoperative urine culture positive (example, %)	5 (16.7)	5 (14.7)	0.638	> 0.05
Introduction double J tube (example, %) before surgery	20 (66.7)	23 (67.6)	1.724	> 0.05

Table 2: Analysis of the surgical results of the two groups.

Group	Count	Surgery time (min)	Hospital stay (day)	Postoperative analgesia pump usage time (D)	Stone clearance (%)	Polyps discovery rate (%)
Control group	30	49.3 ± 7.8	5.2 ± 1.4	2.2 ± 0.6	49 (81.7)	33 (55.0)
Research group	34	41.4 ± 5.4	5.1 ± 1.3	2.3 ± 0.5	68 (100.0)	37 (54.4)
X^2	—	17.625	1.082	1.824	5.638	0.724
P	—	< 0.05	> 0.05	> 0.05	< 0.05	> 0.05

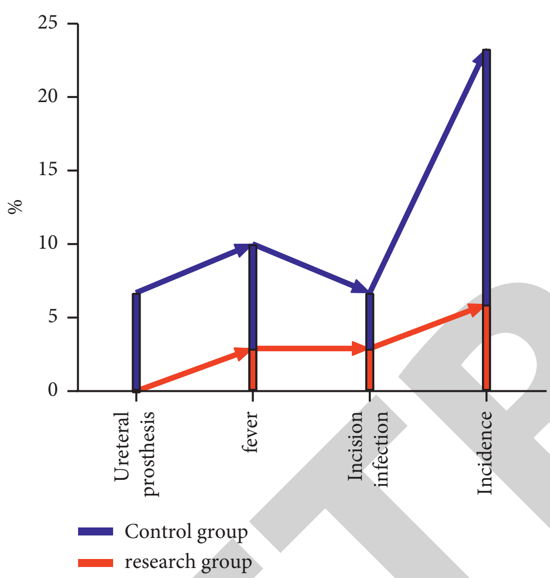

Figure 1: Comparison of complications between the two groups.

increased after treatment, which should be higher in the study group than in the control group ($P < 0.05$) (Figure 3).

3.6. Comparison of Inflammatory Response Indexes between the Two Groups. There was no significant difference in inflammatory factors between the two groups before treatment ($P > 0.05$), and after treatment, the inflammatory factors in the two groups were significantly increased, but compared with the control group, the study group was lower ($P < 0.05$) (Figure 4).

4. Discussion

The treatment of ureteral calculi is particularly special, and open surgery, ureteroscopy, laparoscopy, and transdermal nephroscopy are often used [9–11]. Minimally invasive surgery is used if the patient has contraindications to traditional surgery [12, 13]. At present, laparoscopy and ureteroscopy have been widely used in the treatment of urology, and ureteroscopic lithotripsy can be operated according to the characteristics of the human body's natural cavity and low wound surface. Combined with laser treatment, it can effectively crush stones. Stenosis can be treated concurrently, but ureteral stones are less effective [14, 15]. The main reasons are that the ureteral walker is long, stones are often used by ureteral budding polyps, and factors such as ureteral transformation will also affect the treatment effect. The high rate of ureteral perforation and tearing enables the clinical treatment of ureteral mirror crimping stones [16, 17]. Therefore, when choosing the treatment method for ureteral calculi, the situation of the distal ureter should be comprehensively analyzed. Ureteroscopy is widely used in the treatment of larger ureteral calculi, and the treatment effect is good and the safety is relatively high [18]. After the end of the study, the patients were treated with ureteroscopy. No obvious complications were found, and the prognosis of the patients was good [19]. During ureteroscopy treatment, stone movement is common, and the following measures can be taken to reduce the incidence of stones on stones. The patient's position is lower than their head [20]. Second, perform low-pressure perfusion during operation, maintaining low-speed flushing. Third, when placing the ureteral stent, the edge should be placed on the edge of the stone and should be pressed to the ureteral side [21]. Fourth, when selecting cases, the specific characteristics of the patients should be considered, and patients with a combined case with a stone diameter greater than or equal to 1.0 cm, a fixed stone, and a longer course of disease should be selected [22].

In urology, laparoscopy has been widely used, which has accelerated the progress of ureteral diameter technology. It has the characteristics of fast postoperative recovery and small damage, which can make up for the defects of traditional open surgery and be used for the treatment of ureteral stones [23]. Laparoscopic urinalysis can complete one-time stones, but laparoscopy is skilled. In this study, laparoscopy was used to treat patients with ureteral calculi, and the effect was satisfactory, with a stone clearance rate of 100% and a shorter operation time [24]. This study analyzed the effects of ureteroscopy and laparoscopy on the prognosis of patients with urinary calculi and infections. The incidence of complications was consistent with the findings of other scholars. The results confirmed that laparoscopic urinary tandem resection had lower complication rates and

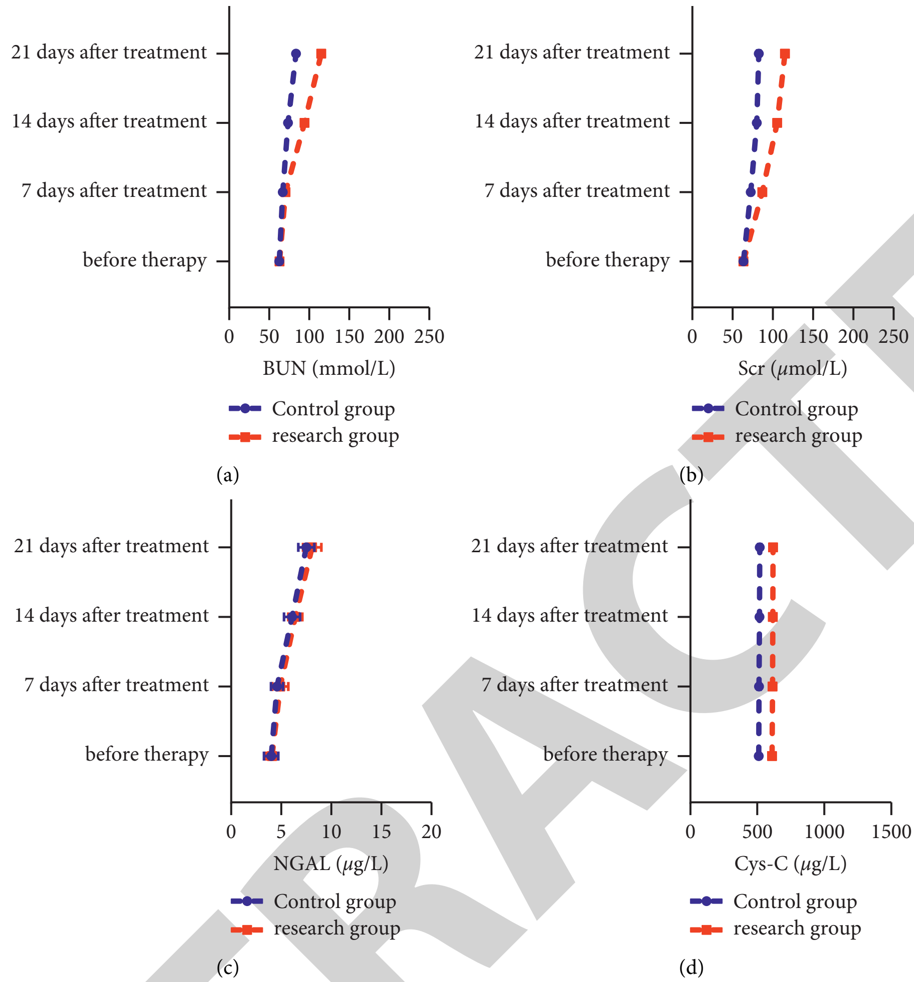

Figure 2: Two-group kidney function index contrast.

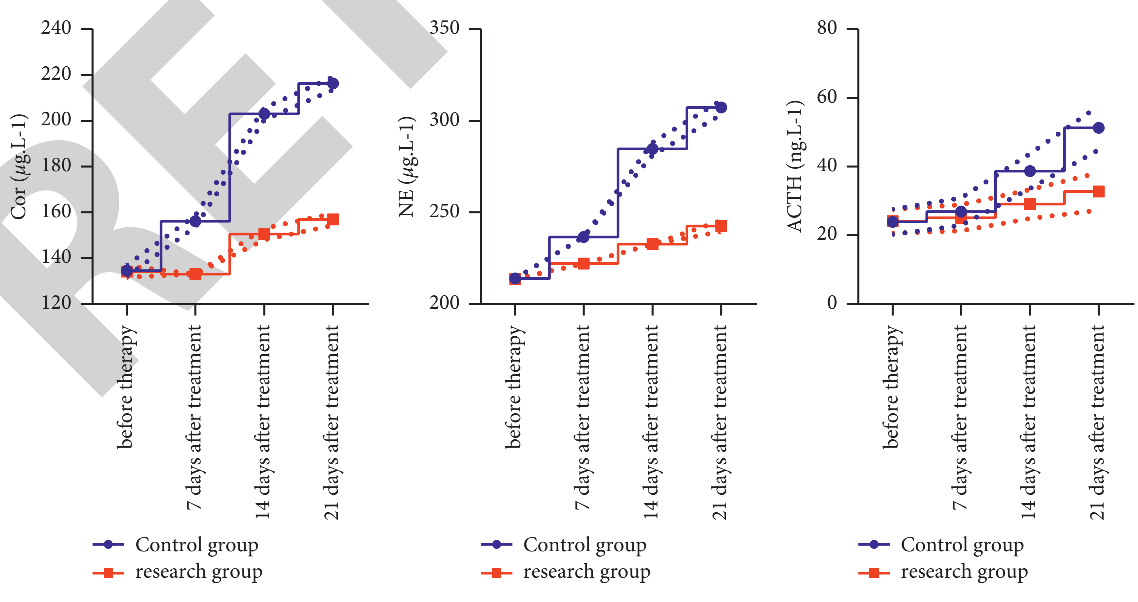

Figure 3: Comparison of two groups of oxidative stress indicators.

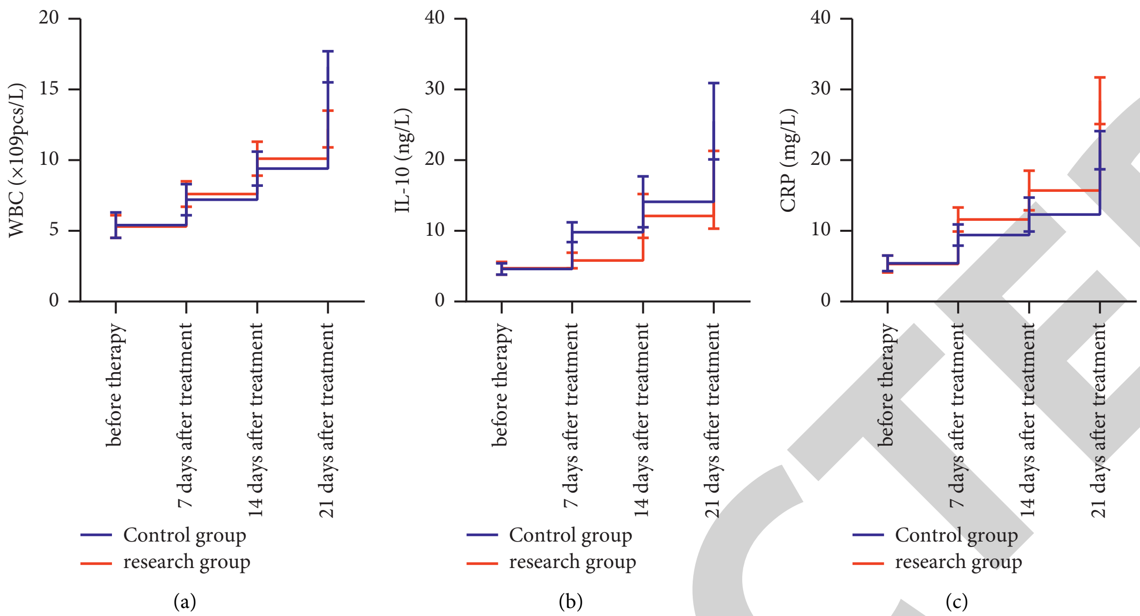

FIGURE 4: Comparison of inflammatory response indexes between the two groups.

higher surgical success rates compared with ureteroscopic culprits. Surgery is an invasive treatment, which will stimulate the body to a certain extent. The patient will be accompanied by stress, and the immune function of the patient will be reduced, which will affect the postoperative recovery. Among them, the activation of the hypothalamus-pituitary-adrenal axis is mainly due to the stress response, and the amount of Ne, ACTH, COR, and other hormones increases significantly, which can reflect the stress state of the body [25]. This study analyzed the effects of ureteroscopy and postlaparoscopic techniques on stress response indicators in patients with urinary calculi and infection. The results showed that the stress response indexes of the two groups were significantly increased after treatment, but compared with the control group, the stress response indexes of the study group were lower ($P < 0.05$). The results confirmed that after reducing the stress response, the advantages of laparoscopic technology were more obvious, causing less damage to the patient and speeding up the recovery of the disease.

However, after the laparoscopic urine test, pay attention to the following aspects: (1) accurately locate by X-ray mode before operation, determine the anatomical signs such as calculus, kidney compression, lumbar bust, and peritoneum, and explore the ureter. (2) The cutter is held over the stone with breakaway pliers to prevent mobilization of the stone [26]. (3) Shorten the time of the double J tube. After the double J tube is placed, the ureteral catheter needs to be removed. The development of medical technology after the laparoscopic urine test has the possibility of shortening [27].

5. Conclusion

In the clinical treatment of urinary stones, ureteroscopy technology and the laparoscopic technique have played an important role, but the laparoscopic surgery time is shorter, and the stone clearance rate is higher, and the patient's renal function can be improved to a greater degree of kidney function. The patient's stress reaction should be small after surgery. Therefore, in the clinical treatment of urinary stones and infection, laparoscopic technical treatment is worth promoting.

Data Availability

The data used to support the findings of this study are available from the corresponding author upon request.

Conflicts of Interest

The authors declare that there are no conflicts of interest.

Acknowledgments

This work in this paper was supported by the Department of Urology, the First Affiliated Hospital of Shantou University Medical College.

References

[1] H. Chen, G. Chen, H. Chen et al., "Comparison of the safety and efficacy between transperitoneal and retroperitoneal approach of laparoscopic ureterolithotomy for the treatment of large (>10 mm) and ProximalUreteral stones: a systematic review and meta-analysis," *Urology Journal*, vol. 18, 2020.

[2] H. Chen, G. Chen, H. Chen et al., "Comparison of the SafetyAnd efficacy between transperitoneal and retroperitoneal approach of laparoscopic UReterolithOTomy for the treatment of large (>10 mm) and proximal ureteral stones: a systematic review and meta-analyysis," *Urology Journal*, vol. 18, no. 1, pp. 11–18, 2020.

Hindawi
Journal of Healthcare Engineering
Volume 2023, Article ID 9813403, 1 page
https://doi.org/10.1155/2023/9813403

Retraction

Retracted: The Progress of Functional Magnetic Resonance Imaging in Patients with Poststroke Aphasia

Journal of Healthcare Engineering

Received 26 September 2023; Accepted 26 September 2023; Published 27 September 2023

This article has been retracted by Hindawi following an investigation undertaken by the publisher [1]. This investigation has uncovered evidence of one or more of the following indicators of systematic manipulation of the publication process:

(1) Discrepancies in scope
(2) Discrepancies in the description of the research reported
(3) Discrepancies between the availability of data and the research described
(4) Inappropriate citations
(5) Incoherent, meaningless and/or irrelevant content included in the article
(6) Peer-review manipulation

The presence of these indicators undermines our confidence in the integrity of the article's content and we cannot, therefore, vouch for its reliability. Please note that this notice is intended solely to alert readers that the content of this article is unreliable. We have not investigated whether authors were aware of or involved in the systematic manipulation of the publication process.

In addition, our investigation has also shown that one or more of the following human-subject reporting requirements has not been met in this article: ethical approval by an Institutional Review Board (IRB) committee or equivalent, patient/participant consent to participate, and/or agreement to publish patient/participant details (where relevant).

Wiley and Hindawi regrets that the usual quality checks did not identify these issues before publication and have since put additional measures in place to safeguard research integrity.

We wish to credit our own Research Integrity and Research Publishing teams and anonymous and named external researchers and research integrity experts for contributing to this investigation.

The corresponding author, as the representative of all authors, has been given the opportunity to register their agreement or disagreement to this retraction. We have kept a record of any response received.

References

[1] J. Tang, X. Xiang, and X. Cheng, "The Progress of Functional Magnetic Resonance Imaging in Patients with Poststroke Aphasia," *Journal of Healthcare Engineering*, vol. 2022, Article ID 3270534, 7 pages, 2022.

Hindawi
Journal of Healthcare Engineering
Volume 2022, Article ID 3270534, 7 pages
https://doi.org/10.1155/2022/3270534

Review Article

The Progress of Functional Magnetic Resonance Imaging in Patients with Poststroke Aphasia

Jinping Tang,[1] Xuli Xiang,[2] and Xianglin Cheng [1]

[1]*The First Affiliated Hospital of Yangtze University, Jingzhou 434000, Hubei, China*
[2]*The Second People's Hospital of Gongan County, Jingzhou 434000, Hubei, China*

Correspondence should be addressed to Xianglin Cheng; 45423626@qq.com

Received 12 March 2022; Accepted 7 April 2022; Published 21 April 2022

Academic Editor: Liaqat Ali

Aphasia after stroke is one of the common complications of cerebral infarction. Early diagnosis and treatment of aphasia after stroke is of great significance for the recovery of language function. At present, there are different views on the pathogenesis of aphasia after stroke. Functional magnetic resonance imaging (fMRI) can reflect the brain function, brain tissue metabolism, and the level of brain local blood flow. It has the advantages of noninvasive, high resolution and sensitivity, low price, and so on. It has been widely used in the study of sensory aphasia after stroke. This study focuses on the development of functional magnetic resonance imaging in patients with poststroke aphasia and summarizes the published studies on functional magnetic resonance imaging in patients with poststroke aphasia. *Evidence acquisition*: A literature search was conducted in PubMed, Hindawi, PLoS, IEEE, Wiley, ScienceDirect, Springer, EMBASE, and web of science, with the keywords of "stroke" and "Aphasia" and "functional magnetic resonance imaging", "RS fMRI", or "DTI", to review the research of functional magnetic resonance imaging in patients with aphasia after stroke. The results included clinical evaluation, diagnostic scale, and imaging analysis; the study design was a randomized controlled trial, case series and case report, and observational study. A total of 67 articles were identified in the first search and 43 after the second search. Based on the analysis of 43 selected articles, 19 articles were included, and 24 articles were excluded. The selected information is shown in Table 1. Eleven of them did not contain imaging-related data. Six articles are related review articles. Four studies were conducted on patients without poststroke aphasia. Three studies studied the effect of poststroke aphasia on patients' social participation.

1. Introduction

Stroke is caused by cerebral circulation and blood circulation disorder, which causes cerebral tissue ischemia and hypoxia to cause softening and necrosis. Incidence rate, disability rate, and mortality rate are all higher than the study of [1]. With the gradual increase of the aging trend of the population in China, the incidence rate of stroke increases gradually. Cerebral infarction is the most common stroke type, accounting for 69.6% to 70.8% [2] of stroke in China. Aphasia is a common symptom of cerebral infarction, accounting for 21% ~ 38% of patients with acute cerebral infarction. Language disorders seriously endanger the physical and mental health of patients, bring mental and economic pressure to patients and families, and increase social burden [3, 4]. Many patients have aphasia. Aphasia refers to acquired language dysfunction, that is, the acquired language ability. Due to the language processing disorder caused by the brain damage of language function, the ability to understand and form language is impaired [5]. Aphasia patients can have various language or speech disorders, most of which are limited or even lost in spontaneous language, naming, retelling, reading, writing, and understanding. Aphasia seriously affects the daily communication ability of patients. Language is an indispensable part of cognitive function. At the same time, it also affects the memory, understanding, and other functions of patients [6, 7]. Moreover, the occurrence of aphasia seriously affects the quality of life of stroke patients and their ability to return to family and society and causes a heavy burden on patients, family, and society. Aphasia after stroke is caused by direct damage to the cerebral cortex or the brain-related network dysfunction after stroke, and the incidence rate is about 30% [8,9] of stroke patients. Early diagnosis and treatment of aphasia after stroke is of great significance for the recovery of language function, Table 1.

In recent years, functional magnetic resonance has made some achievements in the diagnosis and treatment of poststroke aphasia. Functional brain imaging, such as functional magnetic resonance imaging (fMRI), is a popular method to study aphasia. FMRI mainly includes diffusion tensor imaging (DTI) and blood-oxygen-level-dependent (BOLD) imaging. DTI is the only new magnetic resonance imaging technology developed rapidly in recent years, which can image the structure of brain white matter in vivo. It provides the possibility to study brain white matter fibers and makes up for the shortcomings of other neuroimaging technologies in this regard. It uses the diffusion anisotropy of water molecules in biological tissue to image the biological tissue structure, which can provide white matter fiber information that other neuroimaging technologies cannot provide and can visualize the white matter fiber neural pathway in 3D. Therefore, DTI has become one of the most popular fMRI techniques in brain function research and clinical application. Resting-state functional MRI (rs-fMRI) belongs to BOLD fMRI. Because the detection of rs-fMRI does not require the patient to perform specific language tasks, it is simple and easy, and the patient's compliance is good. It has developed rapidly in recent years. It has become the most commonly used tool for the study of language function recovery after stroke and is widely used in the study of neurological diseases and mental disorders.

However, there is no research on the application of RS fMRI and DTI in poststroke aphasia. Therefore, this paper reviews the research progress of functional magnetic resonance imaging in patients with poststroke aphasia to provide an overall outline of the impact of fMRI in poststroke aphasia.

2. Poststroke Aphasia

Modern studies generally believe that poststroke aphasia is a clinical syndrome of patients with abstract signal thinking disorder caused by central neuropathy and then loss of the ability of oral and written expression and comprehension. It is an acquired language disorder caused by the damage of language distribution network with extensive language distribution in the cortex and subcortical structure of language dominant hemisphere [10]. Aphasia can be caused by many diseases, especially stroke. The pathogenesis of aphasia caused by stroke is mostly caused by the damage of brain language functional areas and related nerve fibers. Due to the obstacles in language expression, understanding and related reading and writing skills, the social ability of stroke patients with aphasia is affected, which prevents them from returning to society [11, 12].

Aphasia is the loss or damage of language function caused by brain damage. It is common in cerebrovascular diseases, brain trauma, brain tumors, brain inflammation, and so on. Most of the patients are caused by acute cerebrovascular disease in the left (dominant hemisphere). Aphasia patients often show different degrees of defects in oral expression, listening comprehension, retelling, naming, reading, and writing [13]. Clinically, aphasia is divided into Broca aphasia, Wernicke aphasia, conductive aphasia, transcortical motor aphasia, transcortical sensory aphasia, mixed transcortical aphasia, naming aphasia, and complete aphasia according to the characteristics of patients' language disorders [14, 15].

The pathogenesis of traditional aphasia includes localization theory and antilocalization theory. Aphasia localization theory refers to the theory that language activities are related to specific parts of cerebral cortex, such as Broca and Wernicke cortical language areas (Geschwind-Wernicke language model theory). Language information is introduced into Wernicke area and processed and transmitted to Broca area by arcuate fiber bundle. Finally, Broca area processes the information and transforms it into language activities [16]. Most scholars believe that speech disorders caused by lesions in different parts of the left cerebral hemisphere have their own characteristics, including Broca aphasia caused by damage to the Broca area in the posterior part of the left inferior frontal gyrus, Wernicke aphasia caused by damage to the Wernicke area in the posterior part of the temporal transverse gyrus of the auditory cortex, conductive aphasia caused by damage to the projection fibers or arcuate bundles between the temporal-parietal and frontal lobes, and complete aphasia caused by Broca area, Wernicke area, basal ganglia area, and insula damage [17–19]. However, localization theory cannot well explain aphasia caused by subcortical structures, such as white matter or nuclear lesions. The other is the antipositioning theory, which holds that language activities are formed by the participation of the whole brain; that is, the occurrence of language dysfunction is not caused by the damage or loss of function of specific brain regions but involves the dysfunction of the whole brain neural network [20]. In addition, the more typical language neurobiology model is the dual flow structure model similar to the visual system proposed by Ungerleider and Haxby in 1994. This model proposes a method to map auditory speech to the dorsal flow of pronunciation (movement) and auditory speech to the ventral flow of semantics; that is, backflow mainly supports speech generation and speech perception, while the abdominal flow is responsible for semantic understanding/processing, which may be more in line with the mechanism of language network generation and understanding. At present, the classification of aphasia is mainly divided into Broca, Wernicke, conductive, transcortical (motor and sensory), complete, nominal aphasia, and some rare types of aphasia [21]. Understanding the mechanism and classification of aphasia is helpful to further explore the changes in brain function in patients with poststroke aphasia after treatment. At present, functional magnetic resonance imaging is gradually more and more widely used in the field of poststroke aphasia.

Table 1: Literature inclusion.

Authors	Study design	Authors	Study design
Gray M.	Case report	François C.	Retrospective study
Lee J. K.	RCT	Zhang J.	Retrospective study
Inatomi Y.	Case report	Fridrikson J.	RCT
Stampacchia S.	RCT	Yin J.	Case report
Allendorfer J. B.	Case report	Yi K.	Case report
Wang Y.	Retrospective study	Kawano T.	Retrospective study
Dickens J. V.	Retrospective study	Iorga M.	Retrospective study
Kristinsson S.	RCT	Ellis C.	Retrospective study
Kim G.	Retrospective study	Krishnamurthy S.	Case report
Hybinette H.	Retrospective study	Brady MC	RCT

RCT: randomized controlled trial.

3. Principle and Background of Functional Magnetic Resonance Imaging

Functional magnetic resonance imaging (fMRI) mainly includes diffusion tensor imaging (DTI) and blood-oxygen-level-dependent (BOLD) imaging. BOLD fMRI is an MR imaging technology that uses the change of T2-weighted image of local tissue caused by the change of the ratio of oxygenated hemoglobin to deoxyhemoglobin in the local blood of brain activity area, so that the local activity function of brain tissue can be reflected on T2-weighted image, which can not only reflect the patient's brain function, brain tissue metabolism, and the level of brain local blood flow (Figure 1). Moreover, it has been widely used in the study of sensory aphasia after stroke because of its noninvasive, high resolution, sensitivity, and low price [22]. BOLD fMRI is mainly divided into task fMRI and resting fMRI. During the implementation of task fMRI, patients need to perform specific tasks or receive preset external stimuli to induce neuronal activities in different states of the brain, so as to obtain the activation map of the difference in brain neuronal activity signals and to reveal the law of brain activity in specific task states [23]. Resting state functional MRI (RS fMRI) and diffusion tensor imaging (DTI) overcome some defects of task fMRI. The detection of RS fMRI or DTI does not require the patient to perform specific language tasks. It is simple and easy, and the patient's compliance is good. It has developed rapidly in recent years. It has become the most commonly used tool for the study of language function recovery after stroke and is widely used in the study of neurological diseases and mental disorders [24].

4. Research Progress of rs-fMRI

Rs-fMRI reflects a long-range coherent functional model and is the spontaneous activity of the central nervous system in the basic state. At present, the research on resting brain network has two directions: one is seed-based correlation analysis (seed-based correlation analysis) and independent component analysis (ICA), which studies the synchronization of time series in distant brain regions and the functional connection between brain regions [17, 25]. The second is the analysis method of regional consistency (ReHo) and amplitude of low-frequency oscillation (ALFF) to study the synchronization of local brain regions in time series and the degree of spontaneous neural activity in local brain regions [8, 26]. Brain functional connectivity analysis is a common processing method of rs-fMRI.

According to traditional linguistics, Broca area is mainly responsible for language generation, Wernicke area (posterior part of left superior temporal gyrus) is responsible for language acceptance and understanding, and the arcuate bundle between Wernicke area and Broca area is responsible for the traffic connection between them [27]. Krishnamurthy S. [28] found that there is a language understanding network centered on the posterior temporal gyrus of the dominant hemisphere in the resting state, which may be the neural basis of the brain's language understanding function. Yi K. [29] found that the recovery of language function is accompanied by the dynamic change of functional connection: the functional connection coefficient of language neural network in stroke patients in the acute stage is significantly reduced, and the functional connection coefficient of language neural network in chronic stage is enhanced. It was also found that high-risk patients had reduced resting functional connectivity. Naeser M. A. [30] studied 13 patients with poststroke motor aphasia with left hemisphere injury. It was found that the average functional connectivity index of the left frontal-parietal lobe decreased, accompanied by an obvious loss of language understanding. With the improvement of language comprehension, the average connectivity index of the left frontoparietal lobe also increased. Therefore, Naeser Ma [30] believes that brain tissue injury may affect language understanding ability by changing the functional connection of brain interval, and the recovery of language function is also related to the change of functional connection.

Brain functional connectivity analysis was used to observe the effect of intervention measures on brain functional connectivity. Patients with motor aphasia after stroke can recover spontaneously without intervention. The recovery is obvious in the acute phase and slows in the chronic phase [31]. However, studies have shown that the recovery effect of language rehabilitation treatment in the acute stage of motor aphasia after stroke is almost twice that of natural recovery [32]. Lee J. K. [33] used resting-state functional connectivity to evaluate the effect of naming in the treatment of post-stroke motor aphasia. Eight patients with poststroke motor

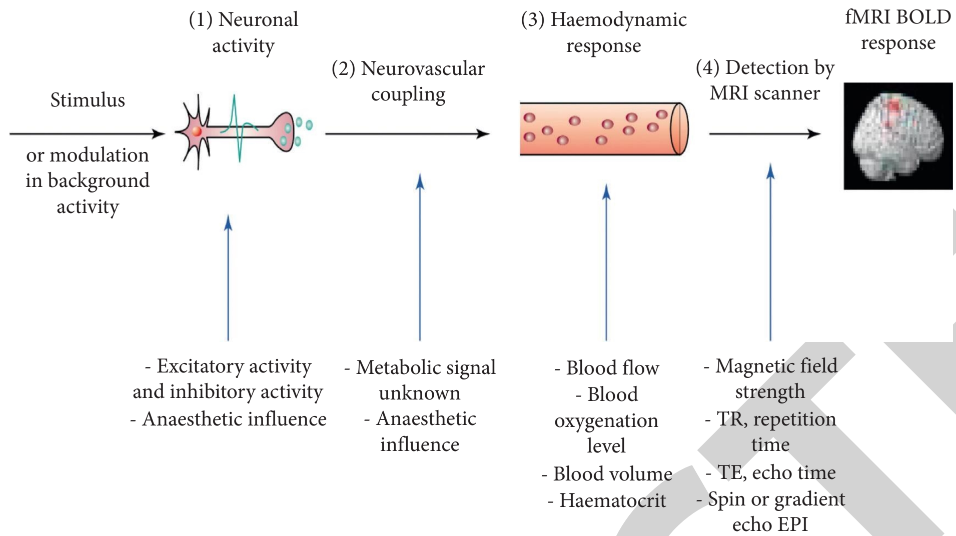

Figure 1: FMRI working principle.

aphasia received 12 treatment courses of improved naming. Before treatment, the activation of the right middle temporal gyrus gradually shifted to the left with the improvement of language function.

5. Research Progress of DTI

DTI is a new image expression method based on conventional magnetic resonance imaging technology. DTI is a special form of MRI, which can not only display the signal intensity of each voxel but also calculate the specific data of tensor direction in three-dimensional space [34]. Then, the single arrow displayed by each voxel is sorted according to the difference in nerve bundle direction to generate a group of direction arrows. Then, the direction arrows of each group are processed through the processing of image data to form a linear image of the nerve bundle. DTI allows us to objectively study poststroke aphasia from the perspective of the structural connection of white matter fibers. Zavanone C. [35] believes that DTI can be used as a good indicator of peripheral nerve regeneration and a noninvasive diagnostic tool for a variety of nervous system diseases. Carragher M. [36] and other researchers collected aphasia patients with different severity and examined the damage of white matter fiber bundle with DTI. They found that DTI examination was helpful to predict the severity of language disorder in aphasia patients after stroke. At present, the research related to DTI mainly involves the occurrence mechanism, recovery mechanism, and prognosis of aphasia.

The formation mechanism of poststroke aphasia has been unclear. At present, it is recognized that the occurrence of aphasia is related to the damage of language functional areas of the cerebral cortex. The lesion location of poststroke aphasia is closely related to the specific functional language area and arcuate fiber bundle of the brain. The injury of arcuate fiber bundles in specific functional language areas of the brain is the main factor leading to aphasia after stroke, which can also be used as an imaging auxiliary tool to evaluate the patient's condition [37]. François C. [38] found that patients with Broca aphasia, Wernicke aphasia, and conductive aphasia had different degrees of damage to the arcuate fiber bundle, and the damage location was related to the type of aphasia: Patients with Broca aphasia mainly had damage and displacement of the integrity of the front end of the arcuate fiber bundle, and patients with Wernicke aphasia mainly had middle and rear damage. In patients with conductive aphasia, the central part of the arcuate fiber bundle on the functional side was mainly damaged. Zhang J performed DTI and fiber bundle imaging on patients with language disorders to check the integrity of the arcuate bundle. DTI and fiber bundle imaging showed that the arcuate bundle was seriously damaged [39]. Patients with sports aphasia have left arcuate fasciculus injury with anterior changes in varying degrees, and the degree of injury is positively correlated with the severity of aphasia, indicating that arcuate fasciculus is an important channel for the communication between anterior and posterior language function zoning. Yao J and others believe that arcuate fiber bundle damage and lesions in cortical language functional areas such as Broca area and Wernicke area can cause conductive aphasia. If the lesion is close to the Broca area, the patient's language disorder is similar to Broca aphasia; if the lesion is close to the Wernicke area, it is similar to Wernicke aphasia [40]. It can be seen that the research on the mechanism of aphasia using DTI breaks the previous understanding of the mechanism of aphasia. For example, the Broca area of Broca aphasia patients is not necessarily damaged, and conductive aphasia can also be caused by lesions in cortical language functional areas such as the Broca area and Wernicke area. These findings make the mechanism of aphasia more complex and need more in-depth research.

The application of DTI makes us to have a deeper understanding of the rehabilitation mechanism of aphasia after stroke. Brain plasticity and language function reorganization are generally accepted at present. Some scholars believe that the study of arcuate fiber bundle by DTI shows that the study of brain white matter fibers can explore the recovery mechanism of aphasia from the level of brain structural changes to a certain extent [41]. Gleichgerrcht E. [42] included 6 patients with left hemisphere stroke with moderate and severe nonfluent aphasia. DTI was tested before and after 75 times of intensive speech therapy. It was found that the number of arcuate fiber bundle fibers and the volume of arcuate fiber bundle were significantly increased after treatment compared with that before treatment, suggesting that the recovery of speech function was related to arcuate fiber bundle remodeling. After one month of intensive rehabilitation treatment, Forkel S. J. found that the number and integrity of left arcuate fiber bundles in a patient with poststroke aphasia also increased [43]. These studies show that the arcuate fiber bundle of patients with poststroke aphasia will change structurally after speech intervention. Detecting this change by DTI will help to explore the recovery mechanism of aphasia.

The prognosis of aphasia after stroke is of great concern to clinical workers and patients. The prognosis prediction of aphasia patients after stroke has very important guiding significance for the formulation of the rehabilitation treatment plan and rehabilitation duration. The lesion location of the arcuate fiber bundle can predict speech rate, information content, overall efficiency, and naming ability [44]. Keser Z. believes that arcuate fiber bundle lesion load (lesion size and location) can predict speech fluency and naming ability in patients with poststroke aphasia [45]. Sanches C. [46] used DTI to study the recovery and prognosis of aphasia. It shows that the arcuate fiber bundle has clinical value in predicting the prognosis of aphasia after stroke.

In conclusion, DTI has irreplaceable advantages over other neuroimaging methods in the study of the white matter fiber pathway. At present, the research on poststroke aphasia using DTI has been preliminarily carried out, involving the discussion of the occurrence and recovery mechanism of aphasia and the prediction of prognosis, and also reflects its certain clinical application value. However, there is still a lack of research on the characteristics and differences of lesion location and mechanism between different types of aphasia, which needs more in-depth or detailed research. As an important pathway of brain nerve signal transmission, the cerebral white matter fiber bundle plays an important role in the occurrence of poststroke aphasia, but its mechanism has not been clarified. DTI technology can be used for in-depth research to objectively and effectively evaluate poststroke aphasia, explore the rehabilitation mechanism of poststroke aphasia, and predict the prognosis of poststroke aphasia patients.

6. Conclusion

The mechanism of language disorder in patients with poststroke aphasia has not been fully explained. At the time of acute cerebral infarction, there is low perfusion and low metabolism in the infarct area, and the place where the metabolic rate decreases the lowest is in the ischemic infarct area. At the same time, it is also found that the metabolic rate decreases in the ipsilateral language functional area; that is, the low metabolism in the language functional area may be the pathogenesis of aphasia [47]. This suggests that we can properly restore the perfusion and metabolism of the language center in the rehabilitation treatment of aphasia, so as to improve the language function. Functional magnetic resonance imaging technology provides a favorable clue to explore the pathogenesis and recovery mechanism of aphasia after stroke and provides a theoretical basis for the rehabilitation treatment of the brain. Rs-fMRI to evaluate the changes of language network functional connectivity in patients with poststroke motor aphasia is not only of great value for the discussion of aphasia occurrence and rehabilitation mechanism but also has a good application prospect for the early diagnosis, rehabilitation prognosis, and curative effect evaluation of poststroke motor aphasia. However, the current research results are quite different, and the potential recovery mechanism of motor aphasia after stroke has not been fully clarified. Rs-fMRI processing method still faces many major challenges. As an important pathway of brain nerve signal transmission, the cerebral white matter fiber bundle plays an important role in the occurrence of poststroke aphasia, but its mechanism has not been clarified. DTI technology can be used for in-depth research to objectively and effectively evaluate poststroke aphasia and explore the rehabilitation mechanism of poststroke aphasia. However, there is still much room for improvement in the study of functional magnetic resonance imaging in poststroke aphasia. With the development of imaging technology, functional magnetic resonance imaging may play a more important role in the individualized treatment evaluation of patients with poststroke aphasia in the future.

Data Availability

The datasets used and analyzed during the current study are available from the corresponding author upon reasonable request.

Conflicts of Interest

The authors declare that they have no conflicts of interest.

References

[1] I. R. Montenegro, J. A. Álvarez Montesinos, A. J. Estudillo, and J. García Orza, "Estimulación eléctrica por corriente continua en el tratamiento de la afasia," *Revista de Neurologia*, vol. 65, no. 12, pp. 553–562, 2017.

[2] C. Ellis and S. Urban, "Age and aphasia: a review of presence, type, recovery and clinical outcomes," *Topics in Stroke Rehabilitation*, vol. 23, no. 6, pp. 430–439, 2016.

[3] M. L. Berthier, "Poststroke aphasia," *Drugs & Aging*, vol. 22, no. 2, pp. 163–182, 2005.

[4] C. R. Marshall, C. J. D. Hardy, A. Volkmer et al., "Primary progressive aphasia: a clinical approach," *Journal of Neurology*, vol. 265, no. 6, pp. 1474–1490, 2018.

[5] M. Radanovic and V. N. Almeida, "Subcortical aphasia," *Current Neurology and Neuroscience Reports*, vol. 21, no. 12, p. 73, 2021.

[6] M. M. Jiménez de la Peña, L. Gómez Vicente, R. García Cobos, and V. Martínez de Vega, "Neuroradiologic correlation with aphasias. Cortico-subcortical map of language," *Radiologia (English Edition)*, vol. 60, no. 3, pp. 250–261, 2018.

[7] I. Minkina, S. Rosenberg, M. Kalinyak-Fliszar, and N. Martin, "Short-Term memory and aphasia: from theory to treatment," *Seminars in Speech and Language*, vol. 38, no. 1, pp. 17–28, 2017.

[8] S. M. Sheppard and R. Sebastian, "Diagnosing and managing post-stroke aphasia," *Expert Review of Neurotherapeutics*, vol. 21, no. 2, pp. 221–234, 2021.

[9] A. Dietz, S. E. Wallace, and K. Weissling, "Revisiting the role of augmentative and alternative communication in aphasia rehabilitation," *American Journal of Speech-Language Pathology*, vol. 29, no. 2, pp. 909–913, 2020.

[10] F. Ehsaan, N. Mumtaz, and G. Saqulain, "Novel therapeutic techniques for post stroke aphasia: a narrative review," *The Journal of the Pakistan Medical Association*, vol. 72, no. 1, pp. 121–125, 2022.

[11] M. C. Brady, H. Kelly, J. Godwin, P. Enderby, and P. Campbell, "Speech and language therapy for aphasia following stroke," *Cochrane Database of Systematic Reviews*, vol. 2016, no. 6, Article ID CD000425, 2016.

[12] A. Beuter, A. Balossier, F. Vassal, S. Hemm, and V. Volpert, "Cortical stimulation in aphasia following ischemic stroke: toward model-guided electrical neuromodulation," *Biological Cybernetics*, vol. 114, no. 1, pp. 5–21, 2020.

[13] B. Elsner, J. Kugler, M. Pohl, and J. Mehrholz, "Transcranial direct current stimulation (tDCS) for improving aphasia in adults with aphasia after stroke," *Cochrane Database of Systematic Reviews*, vol. 5, no. 5, Article ID CD009760, 2019.

[14] J. Fridriksson, C. Rorden, J. Elm, S. Sen, M. S. George, and L. Bonilha, "Transcranial direct current stimulation vs sham stimulation to treat aphasia after stroke," *JAMA Neurology*, vol. 75, no. 12, pp. 1470–1476, 2018.

[15] J. Akabogu, A. Nnamani, M. S. Otu et al., "Efficacy of cognitive behavior language therapy for aphasia following stroke: implications for language education research," *Medicine*, vol. 98, no. 18, Article ID e15305, 2019.

[16] Y. Inatomi, M. Nakajima, and T. Yonehara, "Aphasia induced by infratentorial ischemic stroke: two case reports," *Cognitive and Behavioral Neurology*, vol. 34, no. 2, pp. 129–139, 2021.

[17] P. D. Barrows, S. A. Thomas, and W. Van Gordon, "Assessing self-reported mood in aphasia following stroke: challenges, innovations and future directions," *Journal of Stroke and Cerebrovascular Diseases*, vol. 30, no. 1, Article ID 105425, 2021.

[18] J. D. Stefaniak, A. D. Halai, and M. A. Lambon Ralph, "The neural and neurocomputational bases of recovery from post-stroke aphasia," *Nature Reviews Neurology*, vol. 16, no. 1, pp. 43–55, 2020.

[19] F. Mattioli, "The clinical management and rehabilitation of post stroke aphasia in Italy: evidences from the literature and clinical experience," *Neurological Sciences*, vol. 40, no. 7, pp. 1329–1334, 2019.

[20] J.-F. Landrigan, F. Zhang, and D. Mirman, "A data-driven approach to post-stroke aphasia classification and lesion-based prediction," *Brain*, vol. 144, no. 5, pp. 1372–1383, 2021.

[21] A. Thiel and A. Zumbansen, "The pathophysiology of post-stroke aphasia: a network approach," *Restorative Neurology and Neuroscience*, vol. 34, no. 4, pp. 507–518, 2016.

[22] J. B. Allendorfer, R. Nenert, S. Nair, J. Vannest, and J. P. Szaflarski, "Functional magnetic resonance imaging of language following constraint-induced aphasia therapy primed with intermittent theta burst stimulation in 13 patients with post-stroke aphasia," *Medical Science Monitor*, vol. 27, Article ID e930100, 2021.

[23] J. Yin, J. Zhu, D. Huang et al., "Unilateral symptomatic intracranial arterial stenosis and myopathy in an adolescent with Graves disease: a case report of an high-resolution magnetic resonance imaging study," *Journal of Stroke and Cerebrovascular Diseases*, vol. 24, no. 1, pp. e49–e52, 2015.

[24] S. Sreedharan, K. Arun, P. Sylaja, C. Kesavadas, and R. Sitaram, "Functional connectivity of language regions of stroke patients with expressive aphasia during real-time functional magnetic resonance imaging based neurofeedback," *Brain Connectivity*, vol. 9, no. 8, pp. 613–626, 2019.

[25] A. Imamura, N. Matsuo, M. Ariki, H. Horikoshi, and T. Hattori, "MR imaging and 1H-MR spectroscopy in a case of cerebral infarction with transient cerebral arteriopathy," *Brain & Development*, vol. 26, no. 8, pp. 535–538, 2004.

[26] T. Hara and M. Abo, "New treatment strategy using repetitive transcranial magnetic stimulation for post-stroke aphasia," *Diagnostics*, vol. 11, no. 10, p. 1853, 2021.

[27] S. Payabvash, S. Kamalian, S. Fung et al., "Predicting language improvement in acute stroke patients presenting with aphasia: a multivariate logistic model using location-weighted atlas-based analysis of admission CT perfusion scans," *American Journal of Neuroradiology*, vol. 31, no. 9, pp. 1661–1668, 2010.

[28] S. Krishnamurthy, D. Tong, K. P. McNamara, G. K. Steinberg, and K. M. Cockroft, "Early carotid endarterectomy after ischemic stroke improves diffusion/perfusion mismatch on magnetic resonance imaging: report of two cases," *Neurosurgery*, vol. 52, no. 1, pp. 238–242, 2003.

[29] K. Yi, M. Inoue, K. Irie et al., "Tissue plasminogen activator for cortical Embolism stroke with magnetic resonance perfusion imaging: a report of two cases," *Case Reports in Neurology*, vol. 11, no. 2, pp. 222–229, 2019.

[30] M. A. Naeser, P. I. Martin, E. Treglia et al., "Research with rTMS in the treatment of aphasia," *Restorative Neurology and Neuroscience*, vol. 28, no. 4, pp. 511–529, 2010.

[31] F. M. Filippopulos, C. Brem, K. Seelos et al., "Uncrossed corticospinal tract in health and genetic disorders: review, case report, and clinical implications," *European Journal of Neurology*, vol. 28, no. 8, pp. 2804–2811, 2021.

[32] H. Wang, S. Li, Y. Dai, and Q. Yu, "Correlation between speech repetition function and the arcuate fasciculus in the dominant hemisphere detected by diffusion tensor imaging tractography in stroke patients with aphasia," *Medical Science Monitor: International Medical Journal of Experimental and Clinical Research*, vol. 26, Article ID e928702, 2020.

[33] J.-K. Lee, M.-H. Ko, S.-H. Park, and G.-W. Kim, "Prediction of aphasia severity in patients with stroke using diffusion tensor imaging," *Brain Sciences*, vol. 11, no. 3, p. 304, 2021.

[34] J. D. Stefaniak, F. Geranmayeh, and M. A. Lambon Ralph, "The multidimensional nature of aphasia recovery post-stroke," *Brain*, vol. 10, Article ID awab377, 2022.

[35] C. Zavanone, Y. Samson, C. Arbizu, S. Dupont, D. Dormont, and C. Rosso, "Critical brain regions related to post-stroke aphasia severity identified by early diffusion imaging are not the same when predicting short- and long-term outcome," *Brain and Language*, vol. 186, pp. 1–7, 2018.

[36] S. M. Wilson and S. M. Schneck, "Neuroplasticity in post-stroke aphasia: a systematic review and meta-analysis of functional imaging studies of reorganization of language processing," *Neurobiology of Language (Cambridge, MA, USA)*, vol. 2, no. 1, pp. 22–82, 2021.

Hindawi
Journal of Healthcare Engineering
Volume 2023, Article ID 9853278, 1 page
https://doi.org/10.1155/2023/9853278

Retraction

Retracted: Overexpressed RING Finger 44 Correlates with Poor Prognosis in Hepatocellular Carcinoma

Journal of Healthcare Engineering

Received 23 May 2023; Accepted 23 May 2023; Published 24 May 2023

This article has been retracted by Hindawi following an investigation undertaken by the publisher [1]. This investigation has uncovered evidence of one or more of the following indicators of systematic manipulation of the publication process:

(1) Discrepancies in scope
(2) Discrepancies in the description of the research reported
(3) Discrepancies between the availability of data and the research described
(4) Inappropriate citations
(5) Incoherent, meaningless and/or irrelevant content included in the article
(6) Peer-review manipulation

The presence of these indicators undermines our confidence in the integrity of the article's content and we cannot, therefore, vouch for its reliability. Please note that this notice is intended solely to alert readers that the content of this article is unreliable. We have not investigated whether authors were aware of or involved in the systematic manipulation of the publication process. Wiley and Hindawi regrets that the usual quality checks did not identify these issues before publication and have since put additional measures in place to safeguard research integrity.

We wish to credit our own Research Integrity and Research Publishing teams and anonymous and named external researchers and research integrity experts for contributing to this investigation.

The corresponding author, as the representative of all authors, has been given the opportunity to register their agreement or disagreement to this retraction. We have kept a record of any response received.

References

[1] Y. Liu, H. Xia, M. Li et al., "Overexpressed RING Finger 44 Correlates with Poor Prognosis in Hepatocellular Carcinoma," *Journal of Healthcare Engineering*, vol. 2022, Article ID 3522866, 18 pages, 2022.

Hindawi
Journal of Healthcare Engineering
Volume 2022, Article ID 3522866, 18 pages
https://doi.org/10.1155/2022/3522866

Research Article

Overexpressed RING Finger 44 Correlates with Poor Prognosis in Hepatocellular Carcinoma

Yue Liu, Huasong Xia, Meng Li, Yuxin Chen, Wei Zhou, Yi Chen, and Yanqing Wu

The Second Affiliated Hospital of Nanchang University, Nanchang, China

Correspondence should be addressed to Yanqing Wu; wuyanqing01@sina.com

Received 7 March 2022; Revised 18 March 2022; Accepted 21 March 2022; Published 19 April 2022

Academic Editor: Liaqat Ali

Introduction. Liver carcinoma is one of the most common cancers in the world and remains one of the most difficult cancers to treat. Hepatocellular cancer is the most important type of liver cancer (90%). RING Finger 44 (RNF44) is one of the E3 ligases, which play an important role in substrate recognition. It was also reported that RING Finger 44 was connected with resistant melanoma. But the relationship between RNF44 and HCC remained unknown. *Materials and Methods*. To analyze the role of RING Finger 44 gene in hepatocellular carcinoma, we used bioinformatics to analyze the expression level, genetic changes, immunohistochemistry, immune infiltration, diagnostic value, survival, and functional enrichment of RING Finger 44. *Results*. Through analyzing The Genotype-Tissue Expression and The Cancer Genome Atlas databases, we found that the expression level of RING Finger 44 was significantly increased in hepatocellular carcinoma tissues. Meanwhile, the expression of RING Finger 44 was connected with immune cell infiltration and survival time, and the expression level of RING Finger 44 could perform as a useful diagnostic and prognostic index. The functional enrichment analysis of RING Finger 44 provided some possible pathways of RING Finger 44 in hepatocellular carcinoma, which provided an important direction for the further experiments in vitro or in vivo. *Conclusions*. RING Finger 44, the high expression level of which predicts poor prognosis, is a potential oncogene in hepatocellular carcinoma.

1. Introduction

Liver cancer is a highly malignant tumor and a common carcinoma [1, 2]. The mortality and incidence of liver cancer have been sustainable growth, posing a huge threat to people's lives and health [3–5]. Most hepatocellular carcinoma (HCC) cases occur in developing countries, mainly in Southeast Asia and East Asia [6, 7]. China accounts for more than half of all global cases [8]. Hepatocellular carcinoma is the main type of liver malignant tumor, accounting for about 90% [9]. Hepatitis B virus (HBV) or hepatitis C virus (HCV) infection is related to the occurrence of HCC [7, 10]. The incidence of HCV-related HCC has been gradually increasing and will continue to increase in the coming decades in the United States [7]. Multiple options of HCC treatment could be chosen, while hepatectomy is still the most effective choice [11, 12]. Despite enormous progresses in the treatment and diagnosis of liver tumors over the past few decades, liver cancer remains one of the most difficult cancers to treat, and the prognosis for liver tumors remains poor [13, 14].

E3 ubiquitin ligases (E3s) are a class of proteins that play an important role in substrate recognition and catalyze the transfer of ubiquitin to specific substrate proteins [15]. E3s are enzymes that determine the specificity of protein substrates [16]. E3 can bind to oncogenes or pathway proteins to play a role in tumor resistance [15]. Studies have found that RING Finger 44 (RNF44) is one of the E3 ligases. RNF44 is responsible for promoting AMPK-$\alpha1$ degradation in BRAF inhibitor resistant melanoma cells [17]. RNF44 can also play a key role in the development of osteoarthritis [18]. However, no studies have found the relationship between RNF44 and HCC.

In our study, RNF44 was found to be overexpressed in hepatocellular carcinoma in The Genotype-Tissue Expression (GTEx) and The Cancer Genome Atlas (TCGA) databases. Immune infiltration analysis showed that RNF44 was associated with a variety of immune cells, suggesting that RNF44 may affect cellular immunity. COX survival analysis showed that RNF44 overexpression might lead to poor prognosis of HCC. In a word, our study suggested that RNF44 may be a potential oncogene for HCC.

2. Methods and Methods

2.1. Characteristics Analysis. Standardized RNA-Seq data and the corresponding clinical information were downloaded from Genotype-Tissue Expression (GTEx, https://gtexportal.org/home/index.html) and the Cancer Genome Atlas (TCGA, https://cancergenome.nih.gov/) database. The format of RNA-Seq was converted from fragments per kilobase per million (FPKM) to transcripts per million reads (TPM) with log2 conversion. The dividing line between the high expression set and low expression of RNF44 was the median of RNF44 expression in the HCC samples of TCGA cohort. The basic package of *R* software (version 3.6.3) was used to analyze the association between clinical factors and RNF44.

2.2. Gene Expression Analysis. In addition to using data from TCGA database, the normal tissue data was supplemented from GTEx database. The visualization of RNF44 expression in was achieved by ggplot2 package (version 3.3.3) of *R* software (version 3.6.3).

2.3. Analysis of Genetic Variation. UCSC Xena (https://xenabrowser.net/) and cBioPortal (https://www.cbioportal.org) were used to analyze the variation characteristics of RNF44, including variation types, variation frequency, and copy number variation. The data of cBioPortal and UCSC Xena was obtained from TCGA database.

2.4. Immune Infiltration Analysis. We used GSVA package (version 1.34.0) of *R* software (version 3.6.3) and single-sample gene set enrichment analysis (ssGSEA) algorithm to analyze the correlation between RNF44 and infiltration level of multiple immune cells. We used Spearman's correlation coefficient to evaluate the association between RNF44 and immune infiltration.

2.5. ROC Curve and Survival Analysis. ROC curves were drawn using PROC packages (version 1.17.0.1) and ggplot2 packages (version 3.3.3) of *R* software (version 3.6.3). In addition, the survival package (3.2-10 version) of *R* software (version 3.6.3) was applied to analyze the association between RNF44 expression and the survival time of HCC by COX regression model.

2.6. Nomogram Prediction Model. To predict the probability of survival at 1, 3, and 5 years after diagnosis for patients with HCC, we constructed a nomogram prediction model based on the multivariate Cox regression model. The Rms package (version 6.2-0) and survival package (version 3.2–10) of *R* software (version 3.6.3) were used as tools for plotting the nomogram. Concordance index (C-index) was the evaluation criterion to judge the consistency of this model.

2.7. RNF44-Binding Proteins and RNF44-Correlated Genes Analysis. The top 19 RNF44-binding proteins were downloaded using the STRING (https://string-db.org/) tool. And we downloaded the top 100 RNF44-related genes from Gene Expression Profiling Interactive Analysis 2 (GEPIA2, http://gepia2.cancer-pku.cn/#index). The intersection of the top 19 RNF44-binding proteins and the top 100 RNF44-related genes was obtained using a Venn diagram, which was drawn by ggplot2 package (version 3.3.3) of *R* software (version 3.6.3). The scatter plot and heat maps of the top 5 RNF44-related genes and the integrated gene were also created by ggplot2 package (version 3.3.3) of *R* software (version 3.6.3).

2.8. Functional Enrichment Analysis. We did Kyoto Encyclopedia of Genes and Genomes (KEGG) and Gene ontology (GO) enrichment analysis by clusterProfiler package (version 3.14.3) and org.hs.eg.db package (version 3.10.0) of *R* software (version 3.6.3). The data of gene set enrichment analysis (GSEA) were from MSigDB Collections (https://www.gsea-msigdb.org/gsea/msigdb/index.jsp). GSEA enrichment analysis was done by ggplot2 package (version 3.3.3) of *R* software (version 3.6.3). STRING tools were used to draw protein-protein interaction (PPI) network.

2.9. Statistical Analysis. Shapiro–Wilk tests are used to verify the distribution of data. If the variables followed a normal distribution, they would be analyzed by the Student *t*-test. If the variable did not follow a normal distribution, it would be analyzed by Wilcoxon's test or Mann–Whitney test. And the comparison of multiple groups was analyzed using one-way ANOVA. Comparison of two groups was evaluated by Student's *t*-test. Spearman correlation analysis was used to evaluate the monotonic relationship between two continuous or sequential variables. The differences between two Kaplan–Meier survival curves groups were analyzed by Log-rank test. Logistic regression was used to analyze the association between RNF44 expression and clinicopathological features. Cox regression was used to analyze the survival prognosis of HCC patients. The statistically significant index was $P < 0.05$. SPSS 25.0 software and *R* 3.6.3 software were used for statistical analysis. Data visualization was done by *R* 3.6.3 software.

3. Results

3.1. RNF44 Was Overexpressed in HCC. To validate our hypothesis, we assessed the levels of RNF44 expression, exon expression, and methylation in the TCGA cohort. As shown in Figure 1(a), we found that RNF44 expression and exon expression were higher in tumors, but there was no significant difference of RNF44 methylation level between tumor tissue and normal tissue. Besides the unpaired

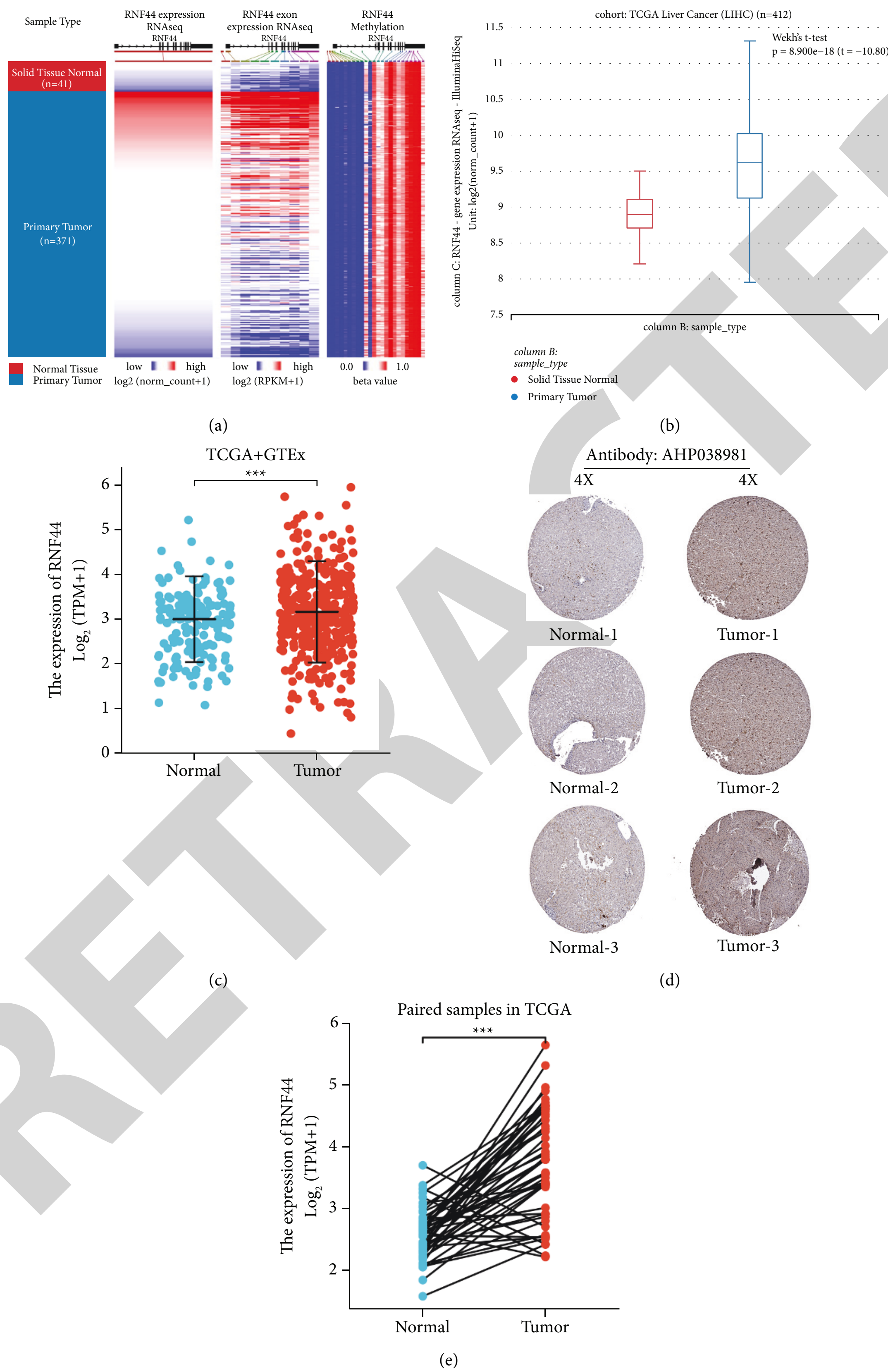

Figure 1: The expression level of RNF44 in HCC. (a) The heat maps of RNF44 mRNA expression, exon expression, and methylation in HCC and corresponding normal tissues from UCSC Xena. (b) The RNF44 expression level of no paired HCC samples in TCGA dataset. (c) RNF44 expression of no HCC samples in TCGA + GTEx dataset. (d) IHC slices of RNF44 in liver samples from HPA. (e) RNF44 expression level of paired HCC samples in TCGA dataset. $^{*}P < 0.05$, $^{**}P < 0.01$, $^{***}P < 0.001$, and $^{****}P < 0.0001$.

samples statistical analysis of TCGA cohort and TCGA + GTEx cohort, the paired samples statistical analysis of TCGA cohort also showed that RNF44 was highly expressed in HCC (Figures 1(b), 1(c), and 1(e)). Baseline characteristics of HCC patients from TCGA are listed in Table 1. Immunohistochemical sections (IHC) from the Human Protein Atlas Database (HPA, https://www.proteinatlas.org/) also showed that RNF44 was overexpressed in tumor tissues of patients with hepatocellular carcinoma (Figure 1(d)). The basic information of the 6 IHC sections is listed in Table 2. These results suggested that RNF44 was overexpressed in HCC and might perform as an oncogene in HCC.

3.2. The Location Site and Variation of RNF44 in HCC. We found that RNF44 was mainly expressed in cell nucleus, as shown in Figure 2(b), from HPA. The 3D morphology, common mutation sites, and basic gene information of RNFF44 were described in Figures 2(c) and 2(d). Furthermore, we found that 2.7% of RNF44 mutations were present in HCC samples, of which proliferation was the most frequent, by analyzing the molecular characteristics of RNF44 (Figure 2(a)). And after analyzing the correlation between the mRNA expression level, genetic changes, and copy number of RNF44, we found that the mutations of proliferation increased the mRNA expression level of RNF44 (Figures 2(e)–2). These results further confirmed that RNF44 was overexpressed in HCC and might play a carcinogenic role in hepatocytes.

3.3. Correlation between Immune Infiltration Level of Different Immune Cells and RNF44 Expression Level. As shown in Table 3 and Figure 3, among different immune cell types, the expression level of RNF44 was correlated with aDC, cytotoxic cells, DC, eosinophils, neutrophils, NK D56 bright cells, pDC, T helper cells, Tcm, TFH, Tgd and Th2 cells, and Treg infiltration level. The expression levels of T helper cells, Th2 cells, TFH, Tcm, eosinophils, NK CD56 bright cells, aDC, and macrophages were positively correlated with RNF44 expression. The expression levels of Tgd, Treg, neutrophils, cytotoxic cells, DC, and pDC were significantly negatively correlated with RNF44 expression. These results suggested that the expression level of RNF44 might be related to tumor immunity and influence tumor immunity, which might help to guide the immunotherapy of HCC. RNF44 might be a new immunotherapy target of HCC patients in the future.

3.4. The Relationship between RNF44 Expression Level and Some Clinical Features. To further understand the relationship between RNF44 and HCC, we analyzed the expression level of RNF44 and clinicopathological characteristics data from TCGA database. The patients were divided into the low expression group and the high expression group based on the median value. The results showed that age ($P = 0.026$), weight ($P = 0.039$), histologic grade ($P = 0.002$), pathologic stage ($P = 0.021$), and AFP ($P = 0.002$) were significantly correlated with RNF44 expression. There was a part correlation with T stage ($P = 0.053$) (Table 4). Figure 4 showed the visualization of the correlation between the above clinical features and the expression level of RNF44. These results showed that patients with younger age, lower body weight, higher histologic grade, higher tumor stage, higher pathologic stage, and higher blood AFP value were more prone to express higher RNF44. In other words, higher RNF44 expression predicted early-onset HCC, increased probability of tumor cachexia, poorer histologic grade, larger tumor size, higher pathologic stage, and higher blood AFP value. All these indicated a poor prognosis of HCC.

3.5. The Diagnostic Value of RNF44 Expression in HCC. In this study, ROC analysis was performed to explore the diagnostic value of RNF44 expression level in HCC. As shown in Figure 5(a), the area under the curve (AUC) of RNF44 is 0.897, indicating a high diagnostic value in distinguishing HCC tumors from normal liver tissues.

3.6. Relationship between RNF44 Expression and Survival Time in Patients with Hepatocellular Carcinoma. To analyze the association between RNF44 and survival, Kaplan–Meier analysis was performed. Univariate Cox regression analysis revealed that RNF44 expression was connected with overall survival time ($P = 0.027$, hazard ratio [HR] = 1.48, 95% CI = 1.05–2.10, Figure 5(b)) and progression-free interval time ($P = 0.007$, risk ratio [HR] = 1.49, 95% CI = 1.11–2.00, Figure 5(c)). Similarly, Kaplan–Meier analysis was performed in different subgroups of patients with HCC, and the results were shown in Figures 5(d)–5(l). Kaplan–Meier analysis results of different clinical subgroups of HCC also suggested that the expression of RNF44 was related to progression-free interval, disease-specific survival, and overall survival. In further Cox univariate and multivariate analyses, we found that higher expression of RNF44, higher tumor stage, higher pathologic stage, distant metastasis, and vascular invasion were correlated with poor progression-free interval (Table 5). The expression level of RNF44 was an independent risk factor for progression-free interval. This reminded us that higher expression of RNF44 predicted poor overall survival, poor disease-specific survival, and poor progression-free interval in HCC patients. Therefore, we drawn a nomogram for predicting the 1-year, 3-year, and 5-year progression-free interval possibility of patients with HCC (C-index = 0.632, 95% CI = 0.575–0.688) (Figure 6(a)). We used ROC analysis to test the diagnostic specificity of the nomogram. As shown in Figure 6(h), the area under the curve (AUC) of 1 year, 3 years, and 5 years was 0.783, 0.703, and 0.617, indicating the effective predictive value of the model.

3.7. Functional Enrichment Analysis of RNF44. To further explore the carcinogenic mechanism of RNF44, we used the STRING tools to download the top 19 RNF44-binding proteins and the top 100 RNF44-related genes from

Table 1: Baseline characteristics of the RNF44 high-expression set and the low-expression set in the TCGA cohort.

Characteristic	Low expression of RNF44	High expression of RNF44
Total	187	187
T Stage		
T1	100 (27%)	83 (22.4%)
T2	46 (12.4%)	49 (13.2%)
T3	33 (8.9%)	47 (12.7%)
T4	5 (1.3%)	8 (2.2%)
N stage		
N0	126 (48.8%)	128 (49.6%)
N1	1 (0.4%)	3 (1.2%)
M stage		
M0	135 (49.6%)	133 (48.9%)
M1	2 (0.7%)	2 (0.7%)
Pathologic stage		
Stage I	96 (27.4%)	77 (22%)
Stage II	45 (12.9%)	42 (12%)
Stage III	33 (9.4%)	52 (14.9%)
Stage IV	3 (0.9%)	2 (0.6%)
Tumor status		
Tumor free	108 (30.4%)	94 (26.5%)
With tumor	71 (20%)	82 (23.1%)
Gender		
Female	55 (14.7%)	66 (17.6%)
Male	132 (35.3%)	121 (32.4%)
Race		
Asian	74 (20.4%)	86 (23.8%)
Black or African American	7 (1.9%)	10 (2.8%)
White	98 (27.1%)	87 (24%)
Age		
≤60	78 (20.9%)	99 (26.5%)
>60	109 (29.2%)	87 (23.3%)
Weight (kg)		
≤70	84 (24.3%)	100 (28.9%)
>70	92 (26.6%)	70 (20.2%)
Height (cm)		
<170	96 (28.2%)	105 (30.8%)
≥170	76 (22.3%)	64 (18.8%)
BMI		
≤25	83 (24.6%)	94 (27.9%)
>25	88 (26.1%)	72 (21.4%)
Residual tumor		
R0	165 (47.8%)	162 (47%)
R1	6 (1.7%)	11 (3.2%)
R2	1 (0.3%)	0 (0%)
Histologic grade		
G1	37 (10%)	18 (4.9%)
G2	94 (25.5%)	84 (22.8%)
G3	49 (13.3%)	75 (20.3%)
G4	5 (1.4%)	7 (1.9%)
Adjacent hepatic tissue inflammation		
None	66 (27.8%)	52 (21.9%)
Mild	51 (21.5%)	50 (21.1%)
Severe	8 (3.4%)	10 (4.2%)
AFP (ng/ml)		
≤400	123 (43.9%)	92 (32.9%)
>400	23 (8.2%)	42 (15%)
Albumin (g/dl)		
<3.5	37 (12.3%)	32 (10.7%)
≥3.5	119 (39.7%)	112 (37.3%)
Prothrombin time (s)		
≤4	105 (35.4%)	103 (34.7%)

Table 1: Continued.

Characteristic	Low expression of RNF44	High expression of RNF44
>4	48 (16.2%)	41 (13.8%)
Child–Pugh grade		
A	120 (49.8%)	99 (41.1%)
B	12 (5%)	9 (3.7%)
C	0 (0%)	1 (0.4%)
Vascular invasion		
No	108 (34%)	100 (31.4%)
Yes	56 (17.6%)	54 (17%)
OS event		
Alive	129 (34.5%)	115 (30.7%)
Dead	58 (15.5%)	72 (19.3%)
DSS event		
Alive	145 (39.6%)	142 (38.8%)
Dead	38 (10.4%)	41 (11.2%)
PFI event		
Alive	102 (27.3%)	89 (23.8%)
Dead	85 (22.7%)	98 (26.2%)

RNF44: ring finger protein 44; AJCC7: American Joint Committee on Cancer 7th edition.

Table 2: The basic information of IHC slices.

Tissue type	ID	Age	Gender
Normal-1	2429	55	Male
Normal-2	3222	63	Female
Normal-3	3402	54	Female
Tumor-1	2766	73	Female
Tumor-2	2399	52	Female
Tumor-3	3346	73	Female

GEPIA2. Then, we made enrichment analysis. The protein-protein interaction (PPI) network between the top 19 RNF44 binding proteins is shown in Figure 7(a). Among the top 100 RNF44-related genes, MAML1 ($P < 0.01$, $R = 0.859$), KDM3B1 ($P < 0.01$, $R = 0.832$), TCERG1 ($P < 0.01$, $R = 0.832$), UIMC1 ($P < 0.01$, $R = 0.794$), and CPSF6 ($P < 0.01$, $R = 0.817$) had the strongest correlation with RNF44 (Figures 7(b)–7(d)) and showed a significant positive correlation with the expression level of RNF44. FAF2 ($P < 0.01$, $R = 0.775$, Figures 7(b)– 7(d)) was the common gene of the top 19 proteins and the top 100 genes (Figure 7(c)). Then, we combined these genes and proteins for the following GO and KEGG analyses. GO enrichment analysis includes three functional groups, that is, molecular functions, cellular components, and biological processes (Figures 8(a)–8(c)). Figure 8(d) shows the results of KEGG analysis. Figure 7(e) shows the GO and KEGG enrichment interaction network. These results showed that RNF44 and other related genes were mainly related to regulation of mRNA splicing and protein complex.

To further explore the signaling pathway activated by RNF44 in HCC, we performed GSEA analysis about those 118 related genes. We identified several important RNF44-related signaling pathways. In this study, we mapped the first four pathways including REACTOME_CD22_MEDIATED_BCR_REGULATION, REACTOME_FCGR_ACTIVATION, REACTOME_ANTIGEN_ACTIVATES_B_CELL_RECEPTOR_BCR_LEADING_TO_GENERATION_OF_SECOND_MESSENGERS, and REACTOME_ROLE_OF_PHOSPHOLIPIDS_IN_PHAGOCYTOSIS (Figure 9). GSEA functional enrichment analysis suggested that RNF44 might be correlated with FCGR and CD22, as well as with immune function.

4. Discussion

Liver cancer is a common cancer, showing a high degree of malignancy and posing a serious threat to people's health and life. Liver patients in China account for more than half of the total number of global cases [1–5]. Among liver cancer subtypes, HCC is the most important subtype, accounting for about 90% [9]. Although there was a great progress in the diagnosis and treatment of liver tumors. The treatment of liver cancer includes surgery, chemotherapy, radiotherapy, TACE, immunotherapy, targeted therapy liver, and liver transplantation. Liver cancer is still one of the most difficult cancers to treat, and the prognosis of liver tumors is still poor [11–14].

E3s are a class of specific enzymes that play an important role in substrate recognition and catalyzing ubiquitin transfer to specific substrate proteins [15, 16] and also play a certain role in tumor drug resistance [15]. RING Finger 44 is one of the E3 ligases. Therefore, there might be a certain correlation with the occurrence and development of HCC. In this study, we evaluated RNF44 expression in the TCGA cohort and found that RNF44 expression and exon expression were higher in tumors. Amplification, among many variants, was the main change in HCC, further confirming high expression of RNF44 in HCC. Immune infiltration analysis showed that RNF44 was associated with a variety of immune cells, suggesting that RNF44 might affect cellular immunity, which was consistent with our initial conjecture that RNF44 might affect tumor drug resistance by affecting E3 ubiquitin ligase. This can guide the immunotherapy of HCC. To further understand the relationship between RNF44 and HCC, we also analyzed the association between

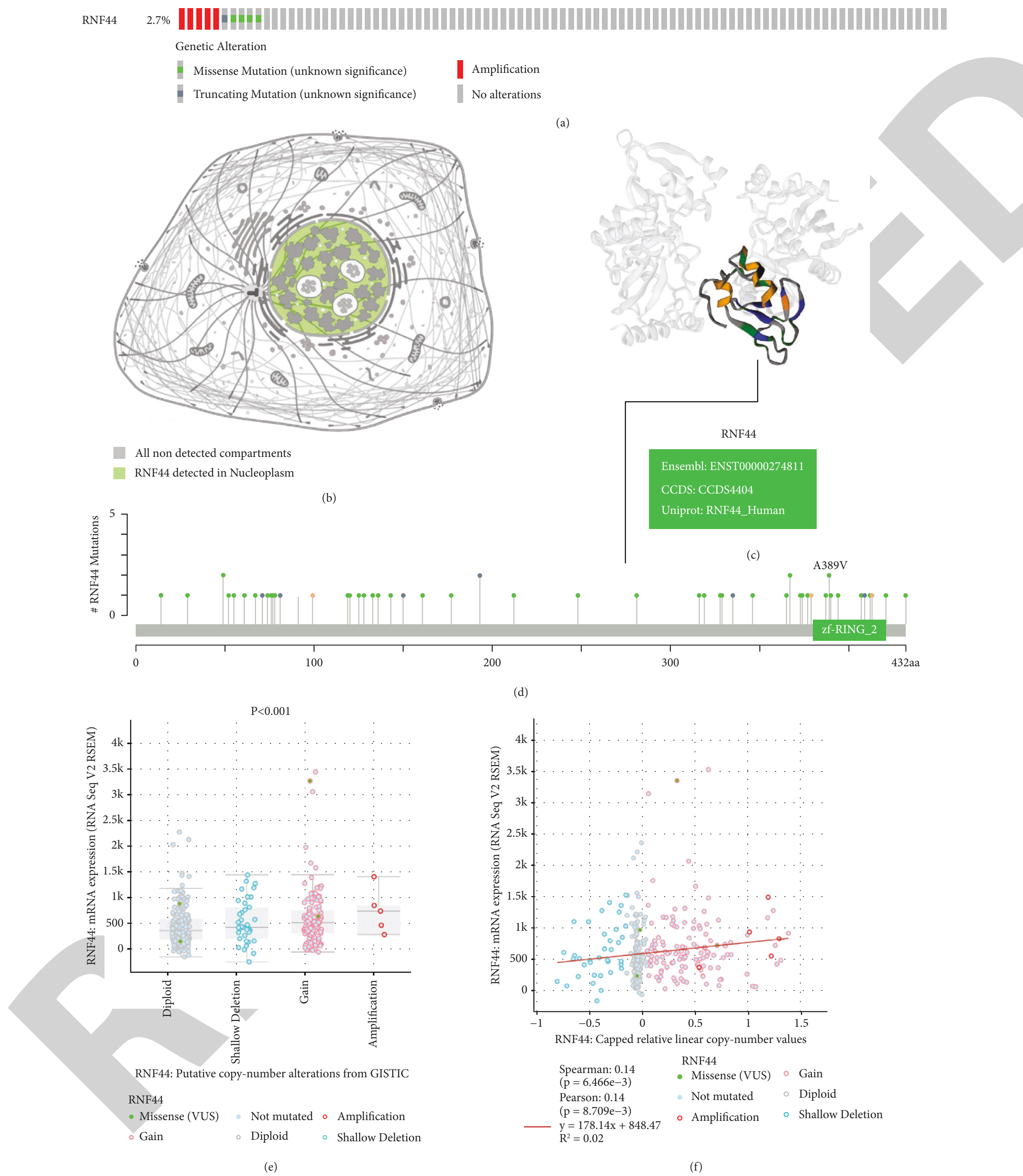

FIGURE 2: The location site and variation of RNF44 in HCC. (a) The genetic alteration frequency of RNF44 in HCC using the cBioPortal tool. (b) The location site of RNF44 in HCC. (c) The 3D structure of RNF44 in HCC from cBioPortal. (d) The mutation sites of RNF44 in HCC from cBioPortal. (e) The difference between the mRNA expression level and copy number of RNF44 from cBioPortal. (f) The correlations between the mRNA expression level and copy number of RNF44 from cBioPortal. $^{*}P < 0.05$, $^{**}P < 0.01$, $^{***}P < 0.001$, and $^{****}P < 0.0001$.

clinical features and RNF44. In the TCGA cohort, higher expression of RNF44 might predict earlier hepatocellular carcinoma, increased probability of tumor cachexia, poorer histologic grade, larger tumor size, higher pathologic stage, and higher blood AFP values. These clinicopathological features were suggestive of poorer disease survival outcomes.

Table 3: Connection between the expression level of RNF44 and the immune infiltration in the tumor microenvironment.

Immune cell	Spearman's correlation	P value
T helper cells	0.413	<0.001
B cells	0.023	0.657
CD8 T cells	−0.025	0.635
Th2 cells	0.331	<0.001
iDC	0.045	0.386
Mast cells	−0.041	0.427
TFH	0.241	<0.001
Tcm	0.223	<0.001
NK CD56dim cells	−0.055	0.286
NK cells	−0.014	0.782
Eosinophils	0.211	<0.001
T cells	−0.014	0.791
NK CD56bright cells	0.197	<0.001
aDC	0.128	0.013
Th1 cells	0.076	0.143
Th17 cells	−0.061	0.239
Macrophages	0.103	0.047
Tem	0.102	0.050
Tgd	−0.131	0.011
Treg	−0.157	0.002
Neutrophils	−0.200	<0.001
Cytotoxic cells	−0.304	<0.001
DC	−0.312	<0.001
pDC	−0.345	<0.001

aDC: activated dendritic cell; DC: dendritic cell; iDC: immature dendritic cell; Macrophages: Mast cells; pDC : plasmacytoid dendritic cell; Tcm : T central memory; Tem : T effector memory; Tfh : T follicular helper; Tgd : T gamma delta; and Treg: T regulatory cell.

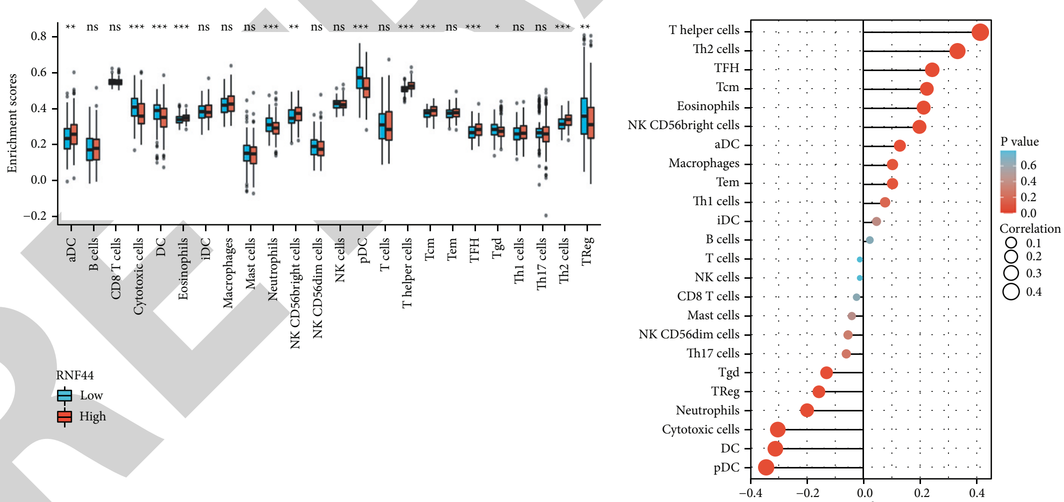

(a) (b)

Figure 3: Continued.

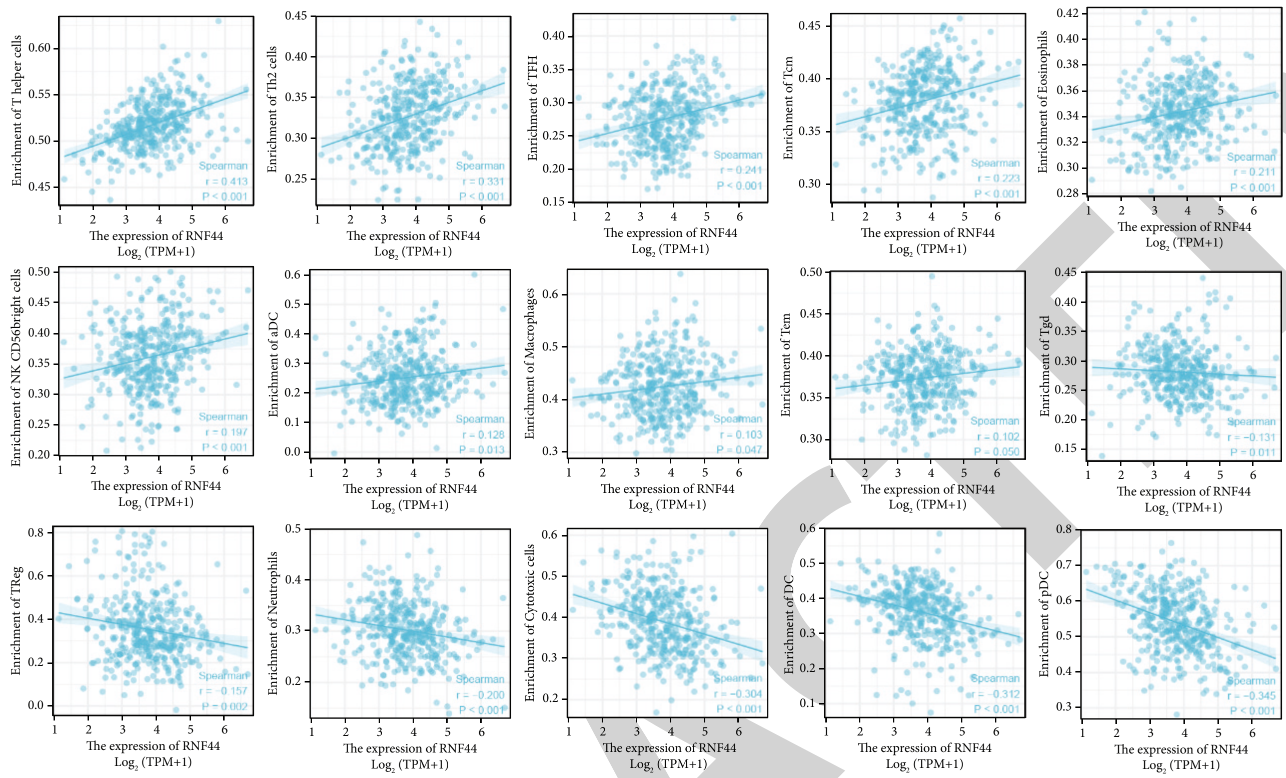

(c)

Figure 3: Correlations between the expression level of RNF44 and immune infiltration. (a) The bar graph about the immune infiltration level of different immune infiltration cells in RNF44 high set and low set. (b) The lollipop figure about the correlations between the expression level of RNF44 and immune infiltration of different immune infiltration cells. (c) The scatter diagrams about the correlations between the expression level of RNF44 and immune infiltration level of different immune infiltration cells. $^{*}P < 0.05$, $^{**}P < 0.01$, $^{***}P < 0.001$, and $^{****}P < 0.0001$.

Table 4: The correlation between RNF44 expression and clinicopathologic factors in the TCGA cohort.

Characteristics	Total (*N*)	Odds ratio (OR)	*P* value
Age (>60 vs. ≤60)	373	0.629 (0.417–0.946)	0.026
Weight (kg) (>70 vs. ≤70)	346	0.639 (0.417–0.976)	0.039
Histologic grade (G3 and 4 vs. G1 and 2)	369	1.950 (1.272–3.009)	0.002
T stage (T3 and 4 vs. T1 and 2)	371	1.601 (0.998–2.589)	0.053
Pathologic stage (stage III & IV vs. stage I & II)	350	1.777 (1.096–2.910)	0.021
N stage (N1 vs. N0)	258	2.953 (0.373–60.136)	0.351
M Stage (M1 vs. M0)	272	1.015 (0.120–8.560)	0.988
AFP (ng/ml) (>400 vs. ≤400)	280	2.441 (1.384–4.396)	0.002

Note. The stages were graded according to AJCC7. RNF44: RING Finger protein 44; AJCC7: American Joint Committee on Cancer 7th edition.

Further COX survival analysis also showed that RNF44 overexpression was an independent risk factor for progression-free interval of HCC.

Taken together, our results suggested that RNF44 might be a potential oncogene for HCC. Based on COX regression analysis, we constructed an exploratory nomogram to predict the 1-year, 3-year, and 5-year progression-free interval survival probability of HCC patients. ROC curve analysis indicated that the nomogram had a good predictive value, which might provide some help for the clinical diagnosis and treatment of HCC patients in the future. Subsequent GO, KEGG, and GSEA functional enrichment analysis suggested that RNF44 might be involved in RNA binding and protein complex processes; RNF44 might be correlated with FCGR and CD22 genes; and RNF44 might be associated with immune phagocytosis [19]. High RNF44 expression also relates to high infiltration level of NK and macrophages in hepatocellular carcinoma; NK markers such as CD56 also show significant correlations with RNF44 expression. These results further reveal that there is a strong relationship between RNF44 and NK cells infiltration. These had certain guiding significance for further basic

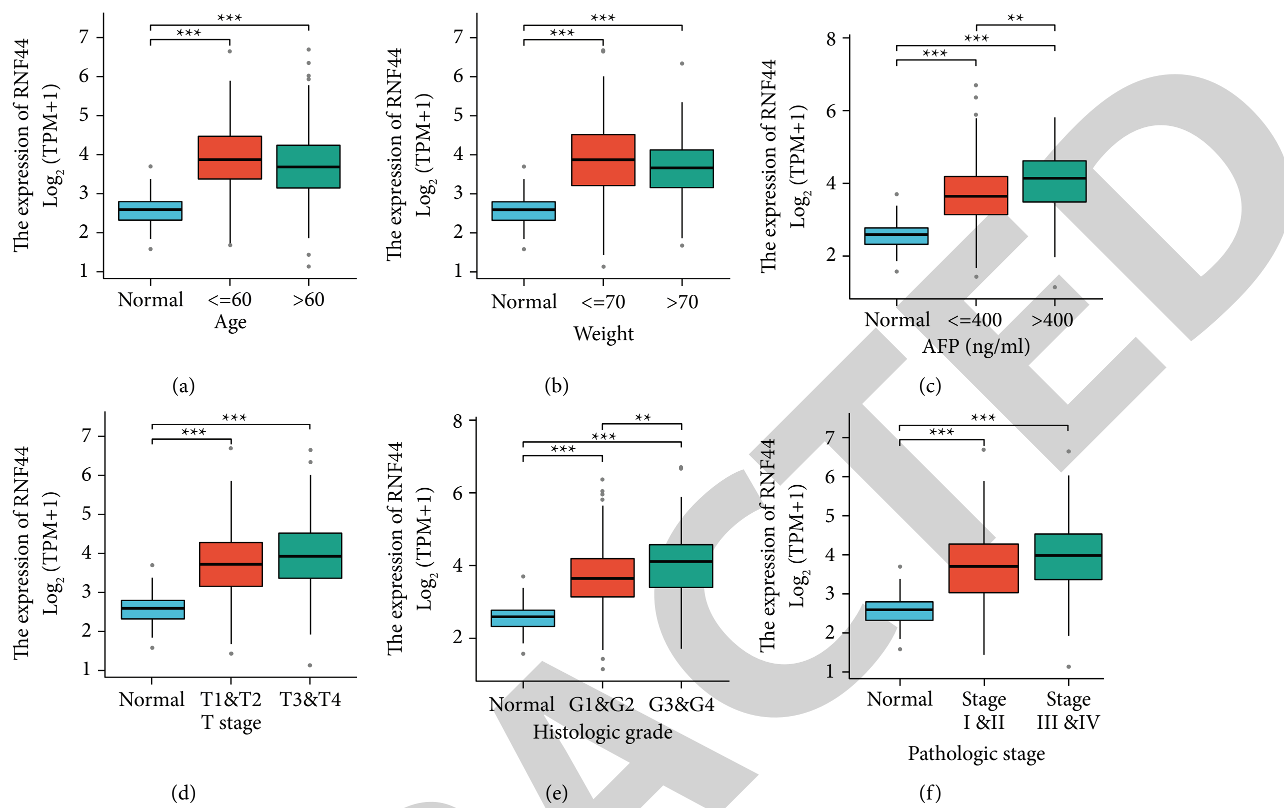

FIGURE 4: The correlation between RNF44 expression and clinical factors in TCGA. The correlation between RNF44 expression and (a) age, (b) weight, (c) AFP, (d) T stage, (e) histological grade, and (f) pathological stage. $^{*}P < 0.05$, $^{**}P < 0.01$, $^{***}P < 0.001$, and $^{****}P < 0.0001$.

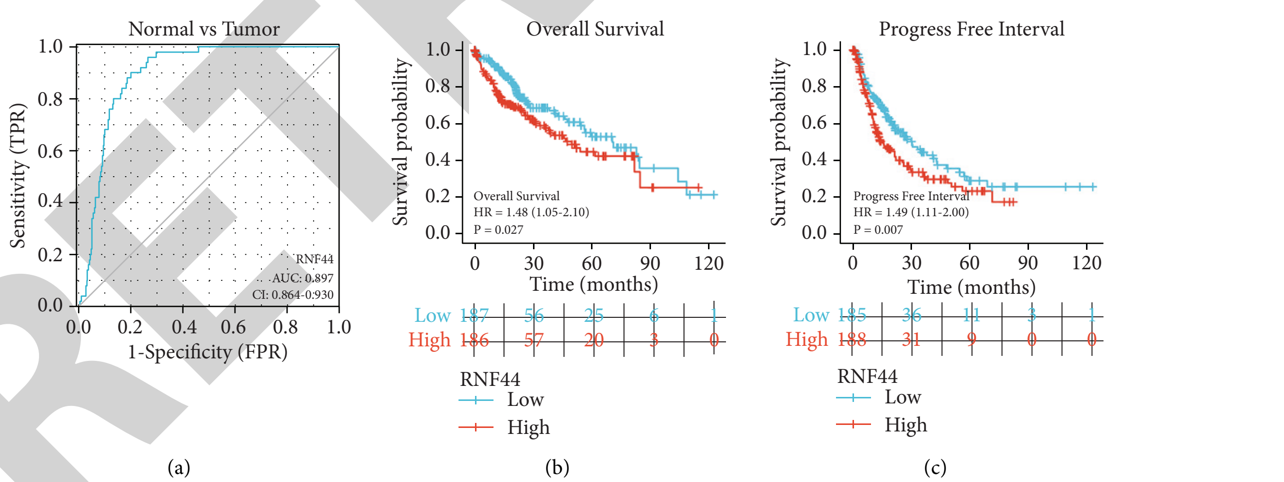

FIGURE 5: Continued.

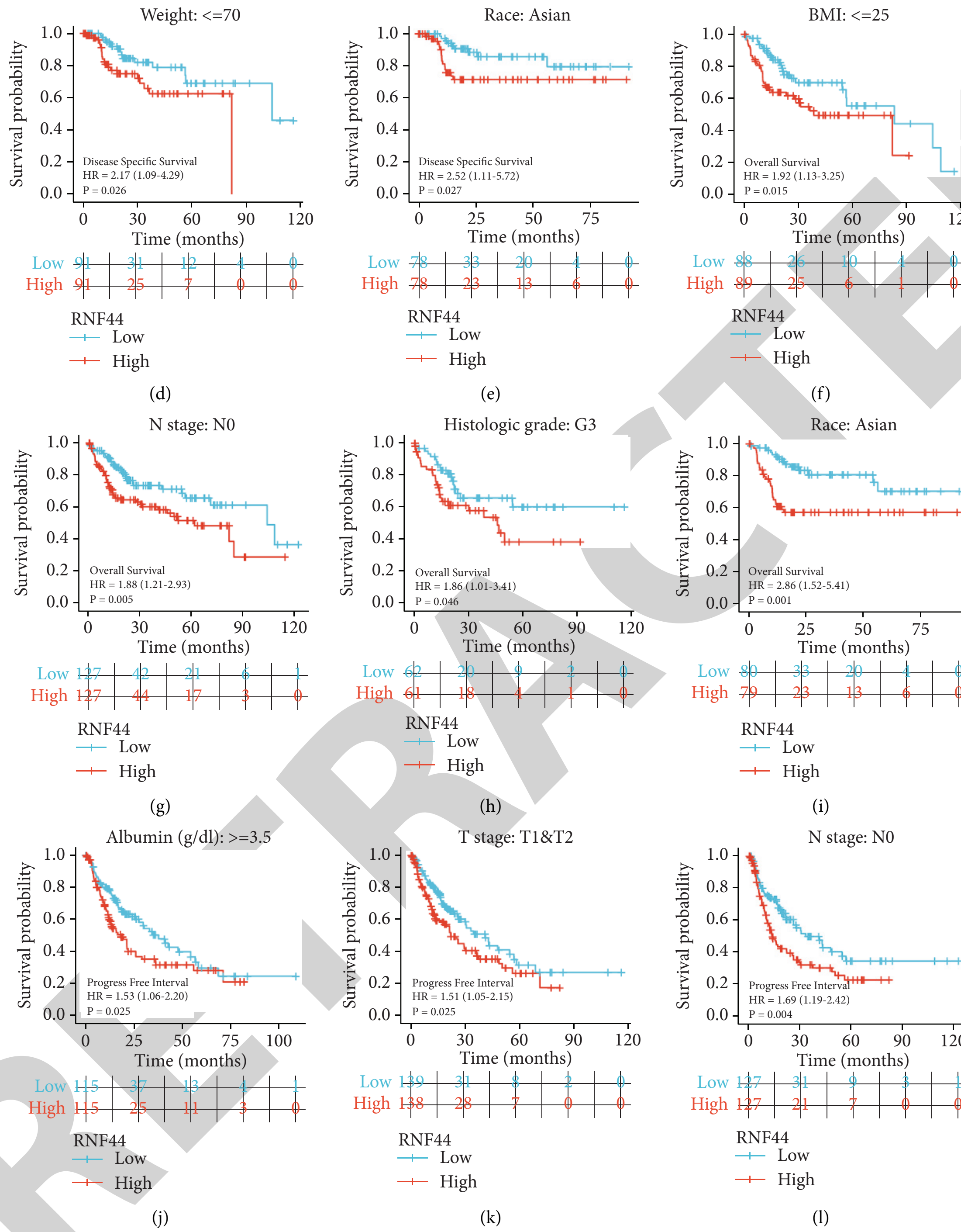

Figure 5: Diagnostic value of the expression and the survival analysis of RNF44 in HCC. (a) ROC curve for differentiating normal people and HCC patients. (b) Overall survival plot of HCC patients that are grouped by RNF44 expression level. (c) Progression-free interval plot of HCC patients that are grouped by RNF44 expression level. ((d)–(e)) Disease-free survival plot of (d) weight <70 kg and (e) Asian subtypes. ((f)–(i)) Overall survival plots of (f) BMI <25, (g) N stage = $N0$, (h) histologic grade = $G3$, and (f) Asian subtypes HCC subgroup patients. ((j)–(l)) Progression-free interval survival plots of (j) albumin (g/dl) ≥3.5, (k) T stage = $T1$-2, and (l) N stage = $N0$ and subtypes HCC subgroup patients. $^{*}P < 0.05$, $^{**}P < 0.01$, $^{***}P < 0.001$, and $^{****}P < 0.0001$.

experiments. Despite our meaningful findings, this study also showed some limitations. On the one hand, a sufficient number of local validation groups should be used to validate the analysis results of the common database. On the other hand, there was a lack of in vivo and in vitro experiments to probe the mechanism of RNF44 in the development of HCC.

In conclusion, this study demonstrated that the expression of RNF44 was significantly elevated in HCC and

Table 5: Univariate and multivariate COX regression analysis for disease-specific survival in the TCGA cohort.

Characteristics	Total (*N*)	Univariate analysis		Multivariate analysis	
		Hazard ratio (95% CI)	*P* value	Hazard ratio (95% CI)	*P* value
T stage	370				
T1 & T2	277	Reference			
T3 & T4	93	2.177 (1.590–2.980)	**<0.001**	0.372 (0.080–1.732)	0.207
Pathologic stage	349				
Stage I & stage II	259	Reference			
Stage III & stage IV	90	2.201 (1.591–3.046)	**<0.001**	4.112 (0.871–19.421)	0.074
Gender	373				
Female	121	Reference			
Male	252	0.982 (0.721–1.338)	0.909		
Age	373				
≤60	177	Reference			
>60	196	0.960 (0.718–1.284)	0.783		
BMI	336				
≤25	177	Reference			
>25	159	0.936 (0.689–1.272)	0.673		
Histologic grade	368				
G1 & G2	233	Reference			
G3 & G4	135	1.152 (0.853–1.557)	0.355		
AFP (ng/ml)	279				
≤400	215	Reference			
>400	64	1.045 (0.698–1.563)	0.832		
Fibrosis Ishak score	214				
0	75	Reference			
1/2 and 3/4 and 5/6	139	1.363 (0.911–2.039)	0.132		
N stage	258				
N0	254	Reference			
N1	4	1.370 (0.338–5.552)	0.659		
M stage	272				
M0	268	Reference			
M1	4	3.476 (1.091–11.076)	**0.035**	2.266 (0.632–8.123)	0.209
Weight	345				
≤70	184	Reference			
>70	161	1.016 (0.750–1.375)	0.920		
Height	340				
<170	201	Reference			
≥170	139	1.252 (0.919–1.706)	0.154		
Albumin (g/dl)	299				
<3 5	69	Reference			
≥3 5	230	0.911 (0.618–1.341)	0.636		
Adjacent hepatic tissue inflammation	236				
None	118	Reference			
Mild & severe	118	1.238 (0.867–1.768)	0.241		
Prothrombin time	296				
≤4	207	Reference			
>4	89	1.100 (0.785–1.541)	0.581		
Child–Pugh grade	240				
A	218	Reference			
B & C	22	1.395 (0.765–2.545)	0.277		
Vascular invasion	317				
No	208	Reference			
Yes	109	1.676 (1.196–2.348)	**0.003**	1.332 (0.885–2.006)	0.169
RNF44	373				
Low	187	Reference			
High	186	1.511 (1.129–2.022)	**0.006**	1.483 (1.003–2.195)	**0.049**

Note. The stages were graded according to AJCC7. RNF44: RING Finger protein 44; AJCC7: American Joint Committee on Cancer 7th edition. Bold means statistically significant.

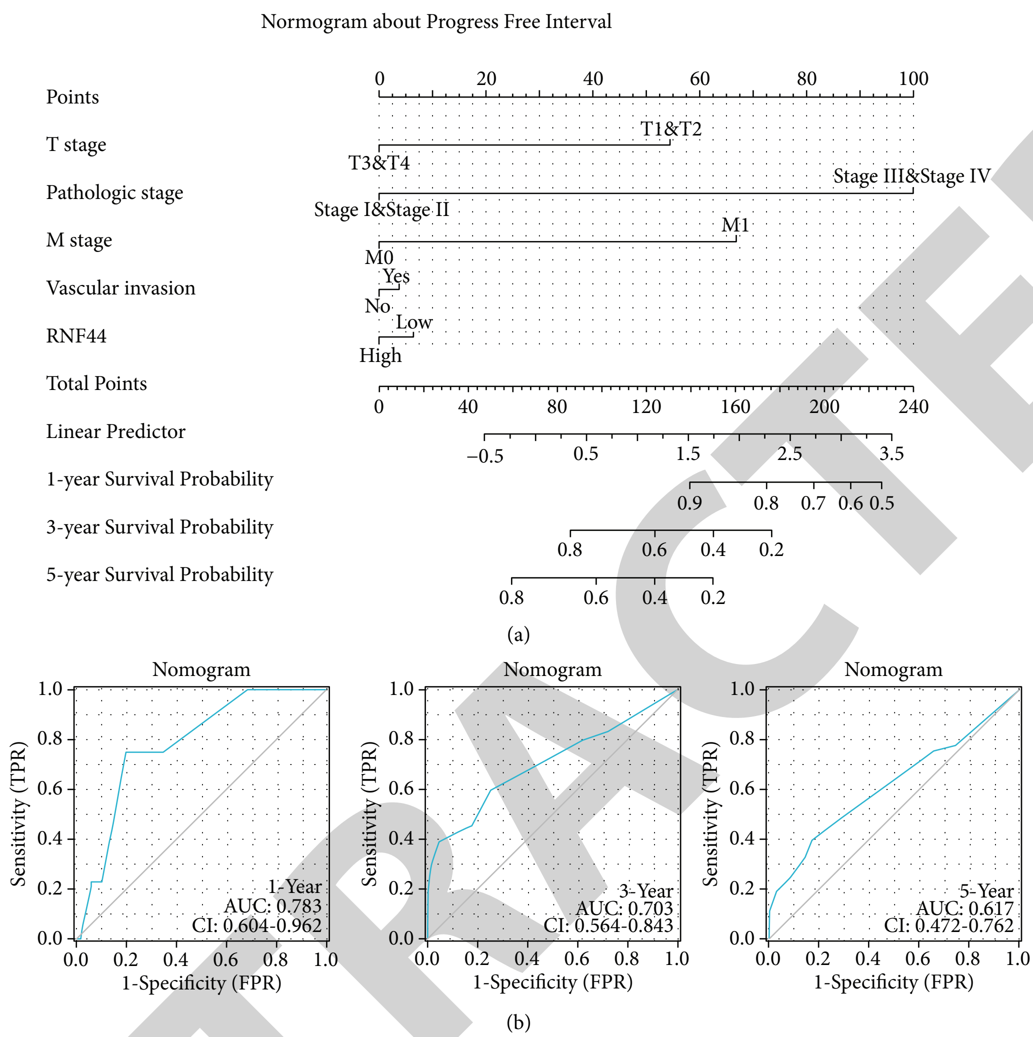

Figure 6: A nomogram about progression-free interval. (a) A nomogram for predicting the 1-year, 3-year, and 5-year progression-free interval survival probability of HCC patients. (b) ROC curves of the nomogram. $^{*}P < 0.05$, $^{**}P < 0.01$, $^{***}P < 0.001$, and $^{****}P < 0.0001$.

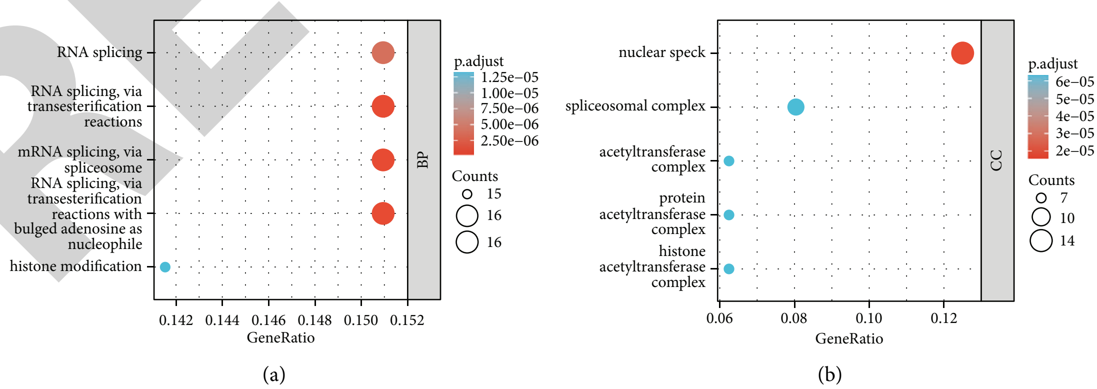

Figure 7: Continued.

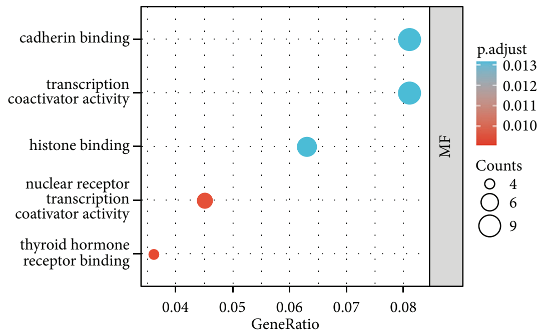

(c)

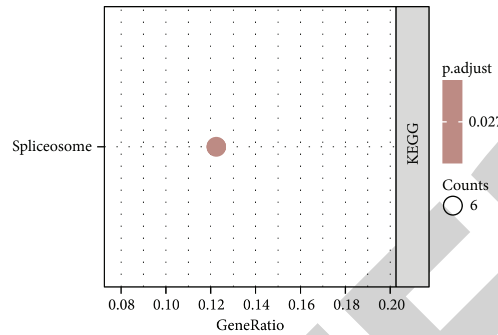

(d)

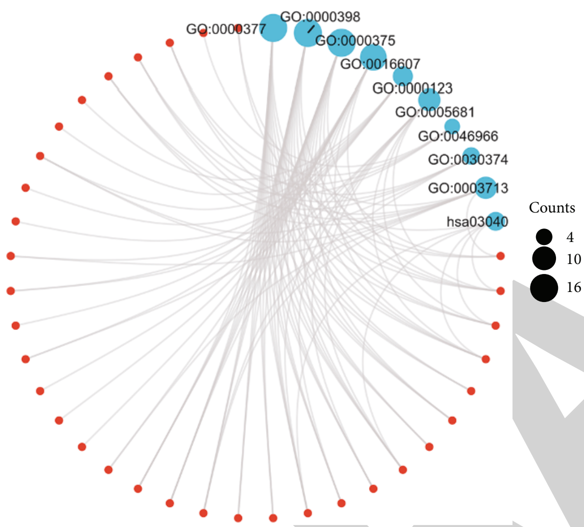

Ontology	ID	Description
BP	GO:0000377	RNA splicing, via transesterification reactions with bulged adenosine as nucleophile
BP	GO:0000398	mRNA splicing, via spliceosome
BP	GO:0000375	RNA splicing, via transesterification reactions
CC	GO:0016607	nuclear speck
CC	GO:0000123	histone acetyltransferase complex
CC	GO:0005681	spliceosomal complex
MF	GO:0046966	thyroid hormone receptor binding
MF	GO:0030374	nuclear receptor transcription coactivator activity
MF	GO:0003713	transcription coactivator activity
KEGG	hsa03040	Spliceosome

(e)

FIGURE 7: RNF44-related gene and RNF44-binding proteins enrichment analysis. (a) Protein–protein interaction network of RNF44. (b) Heat map about the top 5 RNF44-related gene enrichment. (c) A Venn diagram about intersection analysis of the top 50 proteins and the top 100 genes. (d) The scatter diagrams about the top 5 RNF44-related gene and the intersection gene of Venn. $^{*}P < 0.05$, $^{**}P < 0.01$, $^{***}P < 0.001$, and $^{****}P < 0.0001$.

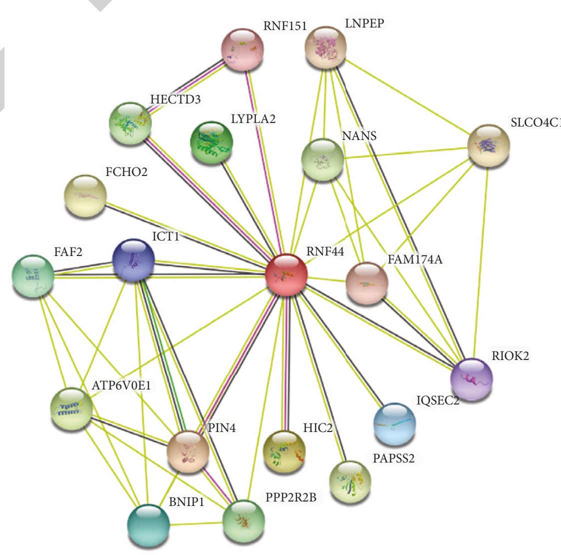

(a)

FIGURE 8: Continued.

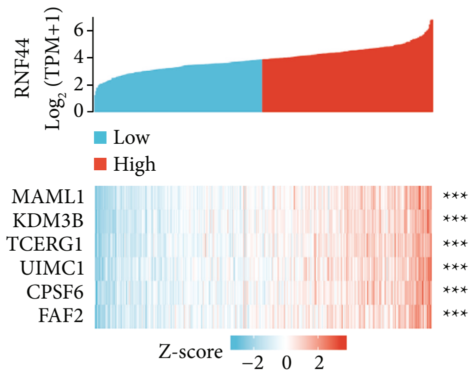

(b)

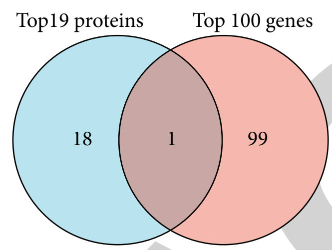

(c)

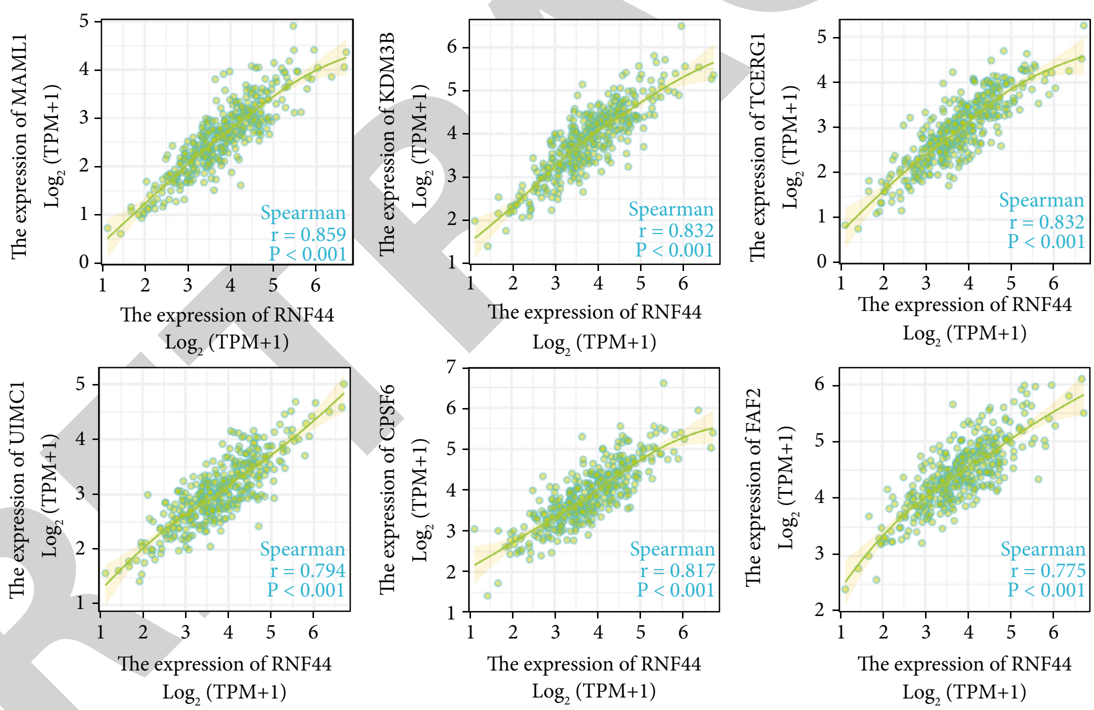

(d)

Figure 8: GO and KEGG enrichment analyses of RNF44. ((a)–(c)) GO enrichment analyses of RNF44. (d) KEGG enrichment analyses of RNF44. (e) GO and KEGG enrichment interactive network. $^{*}P < 0.05$, $^{**}P < 0.01$, $^{***}P < 0.001$, and $^{****}P < 0.0001$.

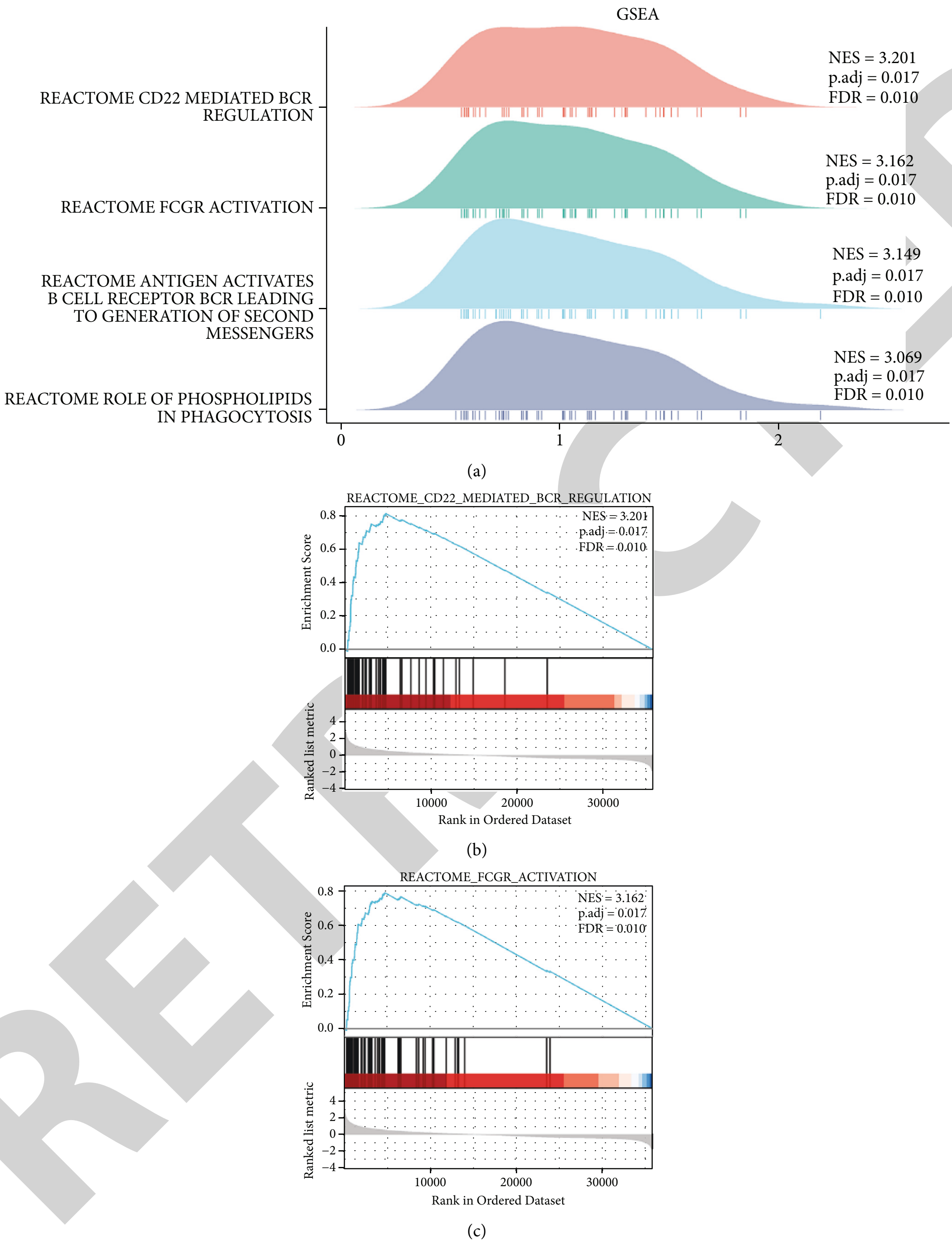

Figure 9: Continued.

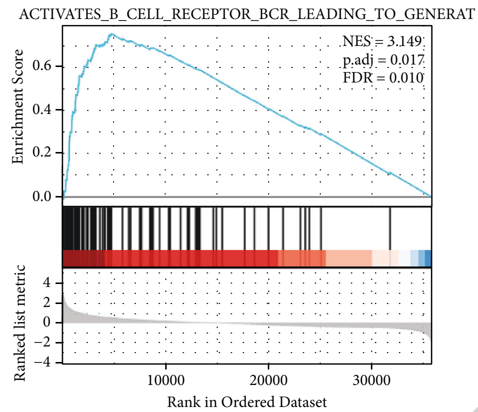

(d)

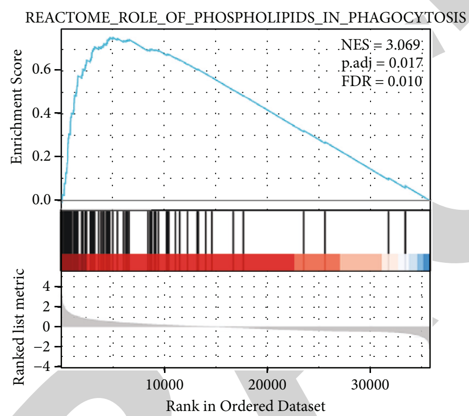

(e)

Figure 9: GSEA enrichment analysis of RNF44.

was correlated with the degree of immune invasion of some immune cells, as well as the prognosis of hepatocellular carcinoma. The results of this study provided a new potential marker and target for HCC therapy.

Data Availability

The data used to support this study are available from the corresponding author upon request.

Conflicts of Interest

The authors declare that they have no conflicts of interest regarding the publication of this paper.

Authors' Contributions

Yue Liu and Huasong Xia contributed equally to this research.

References

[1] K. McGlynn, J. Petrick, and H. J. H. El-Serag, "Epidemiology of hepatocellular carcinoma," *Hepatology*, vol. 73, pp. 4–13, 2021.
[2] F. Bray, J. Ferlay, I. Soerjomataram, R. L. Siegel, L. A. Torre, and A. Jemal, "Global cancer statistics 2018: GLOBOCAN estimates of incidence and mortality worldwide for 36 cancers in 185 countries," *CA: A Cancer Journal for Clinicians*, vol. 68, no. 6, pp. 394–424, 2018.
[3] H. Chen and W. Jia, "Progress in hepatectomy for hepatocellular carcinoma and peri-operation management," *Genes & Diseases*, vol. 7, no. 3, pp. 320–327, 2020.
[4] D. Dimitroulis, C. Damaskos, S. Valsami et al., "From diagnosis to treatment of hepatocellular carcinoma: an epidemic problem for both developed and developing world," *World Journal of Gastroenterology*, vol. 23, no. 29, pp. 5282–5294, 2017.
[5] A. Forner, M. Reig, and J. Bruix, "Hepatocellular carcinoma," *The Lancet*, vol. 391, no. 10127, pp. 1301–1314, 2018.
[6] Y.-F. Han, J. Zhao, L. Y. Ma et al., "Factors predicting occurrence and prognosis of hepatitis-B-virus-related hepatocellular carcinoma," *World Journal of Gastroenterology*, vol. 17, no. 38, pp. 4258–4270, 2011.
[7] H. B. El-Serag, "Epidemiology of viral hepatitis and hepatocellular carcinoma," *Gastroenterology*, vol. 142, no. 6, pp. 1264–1273, 2012.
[8] K. A. McGlynn, J. L. Petrick, and W. T. London, "Global epidemiology of hepatocellular carcinoma," *Clinics in Liver Disease*, vol. 19, no. 2, pp. 223–238, 2015.
[9] J. M. Llovet, J. Zucman-Rossi, E. Pikarsky et al., "Hepatocellular carcinoma," *Nature Reviews Disease Primers*, vol. 2, no. 1, Article ID 16018, 2016.
[10] W.-L. Tsai and R. T. Chung, "Viral hepatocarcinogenesis," *Oncogene*, vol. 29, no. 16, pp. 2309–2324, 2010.

Hindawi
Journal of Healthcare Engineering
Volume 2023, Article ID 9836851, 1 page
https://doi.org/10.1155/2023/9836851

Retraction

Retracted: The Application and Efficacy Evaluation of Autologous Fat Transplantation in Antiaging of the Face: Systematic Review and Meta-Analysis

Journal of Healthcare Engineering

Received 26 September 2023; Accepted 26 September 2023; Published 27 September 2023

This article has been retracted by Hindawi following an investigation undertaken by the publisher [1]. This investigation has uncovered evidence of one or more of the following indicators of systematic manipulation of the publication process:

(1) Discrepancies in scope
(2) Discrepancies in the description of the research reported
(3) Discrepancies between the availability of data and the research described
(4) Inappropriate citations
(5) Incoherent, meaningless and/or irrelevant content included in the article
(6) Peer-review manipulation

The presence of these indicators undermines our confidence in the integrity of the article's content and we cannot, therefore, vouch for its reliability. Please note that this notice is intended solely to alert readers that the content of this article is unreliable. We have not investigated whether authors were aware of or involved in the systematic manipulation of the publication process.

Wiley and Hindawi regrets that the usual quality checks did not identify these issues before publication and have since put additional measures in place to safeguard research integrity.

We wish to credit our own Research Integrity and Research Publishing teams and anonymous and named external researchers and research integrity experts for contributing to this investigation.

The corresponding author, as the representative of all authors, has been given the opportunity to register their agreement or disagreement to this retraction. We have kept a record of any response received.

References

[1] J. Li, K. Zhang, and H. Zhang, "The Application and Efficacy Evaluation of Autologous Fat Transplantation in Antiaging of the Face: Systematic Review and Meta-Analysis," *Journal of Healthcare Engineering*, vol. 2022, Article ID 5744123, 9 pages, 2022.

Hindawi
Journal of Healthcare Engineering
Volume 2022, Article ID 5744123, 9 pages
https://doi.org/10.1155/2022/5744123

Review Article

The Application and Efficacy Evaluation of Autologous Fat Transplantation in Antiaging of the Face: Systematic Review and Meta-Analysis

Jin Li,[1] Kairui Zhang,[2] and Hongwei Zhang[1]

[1]*The Affiliated Friendship Plastic Surgery Hospital With Nanjing Medical University, Nanjing, China*
[2]*Hangzhou Raily Aesthetic and Plastic Hospital, Hangzhou, Zhejiang, China*

Correspondence should be addressed to Hongwei Zhang; hongweizhang2022@163.com

Received 8 February 2022; Revised 27 February 2022; Accepted 3 March 2022; Published 18 April 2022

Academic Editor: Liaqat Ali

Objective. To evaluate the therapy of autologous fat fine-grain transplantation in the application of antiaging facial by metaelaboration method. *Methods*. In Chinese and English databases, such as Wanfang, Weipu, CNKI, PubMed, Cochrane Library, and EMBASE, the literature on the use of autologous fat fines graft in antiaging facial was collected, covering randomized comparative trials, nonrandomized comparative studies, comparative case studies, cohort studies, case reports, and so forth. Meta-analyses were also conducted on complication rates, beauty seeker satisfaction, and one-shot success rates. *Results*. This study included 23 studies that held metaelaborations, including a total of 2852 beauty seekers. According to metaelaboration, the complication rate was 0.02 (95% CI: 0.01, 0.04), the satisfaction rate of beauty seekers was 0.95 (95% CI: 0.91, 0.97), and the success rate of one injection is 0.79 (95% CI: 0.73, 0.84). *Conclusion*. Autologous fat fine-grain transplantation is obvious and stable in the use of antiaging facial, and it is necessary to popularize the use in clinical practice.

1. Introduction

Studies have found that the important reasons for facial aging are sagging skin, subcutaneous soft tissue reduction, volume reduction, and deep tissue relaxation leading to wrinkles and depressions in the face. For the above reasons, plastic surgeons often use the method of facial supplementation to enable beauty seekers to achieve antiaging results in the face [1]. The facial supplements that are often used in plastic surgery now mainly need sodium hyaluronate, collagen egg whites, and autologous fat fines. This autologous fat fine grain has reached the application of all-round application in the face antiaging because of its roots, material selection bento, nonimmune exclusion response, and so on.

In order to illustrate the clinical effect and stability of this method, we searched the literature published at home and abroad on the use of autologous fat fine particle transplantation in antiaging facial, and this skill is elaborated on the physical meta-analysis, with a view to using the technique in the antiaging of the face in plastic surgery.

2. Materials and Methods

2.1. Search Strategy. We comply with the requirements of the PRISMA statement and write meta-anaylsis. Wanfang, Wipu, CNKI, PubMed, Cochrane Library, EMBASE and other Chinese and English databases are searched. The time is indeed from the construction of the library to October 2021. The important Chinese words used are "fat grafting" and "face anti-aging." This study seeks to have no language restrictions, only the values available in the literature.

2.2. Criteria for Inclusion and Exclusion of Literature

2.2.1. Inclusion Criteria. The literature review was conducted by 2 researchers, and the literature was screened according to the specially formulated inclusion criteria: (1)

The research strategy was randomized comparison experiments and nonrandomized comparison experiments for autologous fat fine-grain transplantation in the use of antiaging facial, as well as comparative case studies, cohort studies, and case complaints. (2) The evaluation goals of the study covered the postoperative complication rate, the satisfaction of the beauty seekers (the satisfaction of the beauty seekers after they treated the injection of autologous fat particles), and the success rate of one injection (i.e., only one injection of autologous lipids) [2].

2.2.2. Exclusion Criteria. Exclusion criteria were repeated publications of the literature and acceptance of non-autologous fat fine-grain transplantation methods for antiaging facial.

2.2.3. Numerical Collection and Literature Evaluation. The first browsing of literature should be selected to hold literature selection, clear the contradictory literature that does not conform to the norms, and select again after the selection of literature browsing the full text. If there is a disagreement on the literature choice, the decision is made by the participation of the third reviewer or after discussion between the two researchers. In order to facilitate the extraction of data, meta-analysis elaborated a special data extraction table, the author's name, publication time, research area, sample volume, number of events generated, and evaluation objectives of important extracted documents. Literature quality evaluation is achieved using the Newcastle-Ottawa Scale (NOS), from the selection of the number of diseases to the comparison and follow-up of results. 3 literature quality evaluation is oriented in different ways. The highest quality of literature is 9 stars and the lowest is 0 stars [3].

2.3. Statistical Analysis Methods for Data. STATA version 12.0 was used for this metaelaboration. Q inspection and I^2 inspection are used to check the heterogeneity of the literature classified, and it is stipulated that $P < 0.1$ in Q inspection indicates heterogeneity. In accordance with the Cochrane text, 50% of the $P >$ in the I^2 test denotes heterogeneity. Following the check effect, if the heterogeneity of the literature is classified, the random-effects model is used for elaboration; conversely, the solid-effects model is used for explanation. In the original values of the literature, if P is between [0.3, 0.7], the metaexposition is held directly, and, conversely, the double sine cosine (the double arcsine method) transforms the values so that they fit into a normal distribution before holding metaelaboration. The final results obtained from the application are illustrated by applying the recovery of the numerical conversion hysteresis line meta-analysis. The Begger check was used to assess the distribution bias of the entrenched literature, and $P < 0.05$ was specified as the residual distribution bias [4].

$$p = \left[\sin\left(\frac{tp}{2}\right)\right]^2. \quad (1)$$

2.4. Search Policy. Comply with the code of the Cochrane Interventions System Assessment Manuscript and accept the system evaluation and metaelaboration of the preferred application for the business (PRISMA) to declare the supply of styles, as "fatgrafting, fatgraft," fattransplantation, fattransfer, fatinjection, fatImplantation, fatfiller, lipofilling, lipotransfer, lipomodeling, lipostructuring, lipofiller, lipoinjection, lipograft, and adipocytegraft. For search terms, overall, repeatable electronic searches were made in PubMed, EMBASE, and Cochrane Library, ranging from library construction to 2021. In November, it was determined that all published studies included subjects who received autologous fat grafting to the face as a dry premeasure, with no limits on literature or language.

3. Research Design

3.1. Exclusion Specification

(1) Exclusion of those who receive autologous fat grafting due to facial defects caused by external sores, removal of masses or iatrogenic causes, and exclusion of those who have a personal or clan history of facial cancer.

3.2. Literature Selection. Following the above rules, two researchers independently read all the retrieved literature titles and abstracts and, after clearing the studies that were obviously self-contradictory and classified into the norm, held a full-text view of the studies that were roughly suitable for inclusion. The two researchers interspersed the effect of the classification of the study; if there is a different discussion treatment, the discussion is not handled, and the third researcher is asked to determine whether to be classified.

3.3. Literature Value Collection. The two researchers collected the entire selected literature in detail. When the original data is not neat or missing, the supplementary value published by the author will be applied. When key values are reported only in pattern form, the Digitizer soft device is used to collect the values. Using the canonical estimation equation applied in meta-analysis, the continuous values of the pattern from the digital maximum to the small value domain are converted to the equivalent gauge difference. The presentation is held on the basis of the value of the material presentation (e.g., satisfaction) transferred to a ratio.

The collection of usual materials is held in accordance with the predrawn table, such as the author, the time of publication, the place of jurisdiction of the author, the type of research, the total number, the grade, and the average age of the research subjects. Then, more detailed data collection was held on the classified studies in three departments, which were the fundamental and quota numerical groups, covering detailed treatment methods, and body mass index (BMI). Uniform surgical frequency, follow-up length, number of cases of patient number, number of patient heart cases, number of complication cases, number of biopsy cases, uniform fat injection volume and fat survival rate; the second type of information is the corresponding information of the perioperative period. It covers the anesthesia variety, supply area location, liposuction status, fat resolution status, fat injection condition, injection organization, uniform surgery, and postoperative care; the third type of information is postoperative follow-up content, covering the variety, time, and unusual conditions of the imaging examination, the accuracy of the measurement method of facial material change, the variety of complications, and detailed cases number [5].

4. Result Objectives

The merger effect objectives of the study covered patient number satisfaction, operator satisfaction, uniform number of surgeries, postoperative complication rate, and postoperative biopsy rate.

4.1. Data Solutions. STATA/SE15.1 (TX 77845, USA, package meta-analysis) was applied for metaelaboration. The heterogeneity test method is I^2 statistics, and the merger effect refers to the target method as inverted variance (IV) method. Goals such as patient number satisfaction, operator satisfaction, postoperative complication rate, and postoperative biopsy rate are all in areas that are relatively large or may not be large, and about 95% believe in interval CI. In the case outside of (0,1), perhaps the P value is too close to 0 to show a variance of 0, and it is not possible to hold an inverted variance merger, so the value of this rate needs to pass the sine and cosine. The technique holds a numerical conversion, and the amount of the merger effect is then returned to the conversion rate for indication. All effect targets are random-effects models and are expressed in the pattern of forest diagrams. All of the merger effects described above are expressed in the rate and 95% confidence interval. Uniform surgical frequency is a metaelaboration of the incidence density of the one-handed study, using a random-effects model, and therefore the forest schema is revealed, with a uniform surgical frequency and a 95% confidence interval.

5. Results

5.1. Classified into Literature. A total of 629 articles were searched, of which 166 were cleared due to repeated searches and 404 were requested to be cleared due to the paradoxical acceptance of surgical methods other than autologous fat fine-grain transplantation and evaluation specifications due to brief descriptions of styles, interference methods, and so forth. After browsing the full text, the literature was removed due to self-contradictory inclusion in the norm or the inability to collect useful values. In the end, 23 articles were selected, including 2852 cases of beauty seekers. The detailed operation process is shown in Figure 1.

5.2. List of Values Classified into Documents. Metaelaboration effect of the complication rate of the effect is as follows: Because the original value P is not all in the field of [0.3, 0.7], the double sine cosine method is used to transform the value to fit the normal distribution and then held metaelaboration. The effect obtained after applying the random effects model was $P = 0.28$ (95% CI: 0.18, 0.38) for the heterogeneity ($P = 0$, I2 = 84.1%) retained in the literature [6]. Application 1 restored the effect and obtained the full postoperative complication rate $P = 0.02$ (95% CI: 0.01, 0.04), as shown in Figure 2.

For meta-analysis of the satisfaction of the seeker, because the original data P is not all in the [0.3, 0.7] field, the values are transformed to fit a normal distribution using the double sine cosine method, and then the meta-analysis is elaborated. Heterogeneity ($P = 0$, $I^2 = 89.2\%$) was included, and the effect obtained was $P = 2.67$ (95% CI: 2.53, 2.80) using random-effects model. Then application 1 was applied to restore the effect, obtaining a total satisfaction $P = 0.95$ (95% CI: 0.91, 0.97).

As regards the results of the meta-analysis of the success rate of one injection, because the original value P is not all in the field of [0.3, 0.7], the double sine cosine method is first accepted to convert the value to make it fit the normal spread, and then the metaelaboration is held. For the heterogeneity of literature retention ($P = 0$, $I^2 = 89.5\%$) and the application of random-effects model to hold merger elaboration, the effect obtained was $P = 2.18$ (95% CI: 2.05, 2.31). Application 1 restores the effect and obtains a total one-shot success rate $P = 0.79$ (95% CI: 0.73, 0.84).

5.3. Publication Bias. Apply Begger check to check publication bias, stipulating that $P < 0.05$ is the persistence of publication bias. The effects of postoperative complication rate, disease number satisfaction, and success rate of a single injection were $P = 0.218$, 0.367, and 0.270, respectively, suggesting no significant publication bias.

The metaelaboration analysis showed that the postoperative complication rate of autologous fat fine-grain transplantation in the application of antiaging facial was $P = 0.02$ (95% CI: 0.01, 0.04), and the satisfaction of beauty seekers was $P = 0.95$ (95% CI: 0.91, 0.97). The success rate of a single injection was $P = 0.79$ (95% CI: 0.73, 0.84). The postoperative complication rate of autologous fat fine-grain transplantation in the use of antiaging facial disease is 2%, and, according to the literature, the important complications are inflammation, fat nodules at the injection site, and excessive fat filling. 95% of the beauty seekers were satisfied with the method used in antiaging facial, and the success rate of a single injection was 79%. It can be seen that this method is safer and has a good effect [7].

This study is metaelaborated and, after Q inspection and I^2 inspection, it was found that the literature was classified as heterogeneous. The reasons may be as follows: (1) The types of studies classified in the literature are different, including

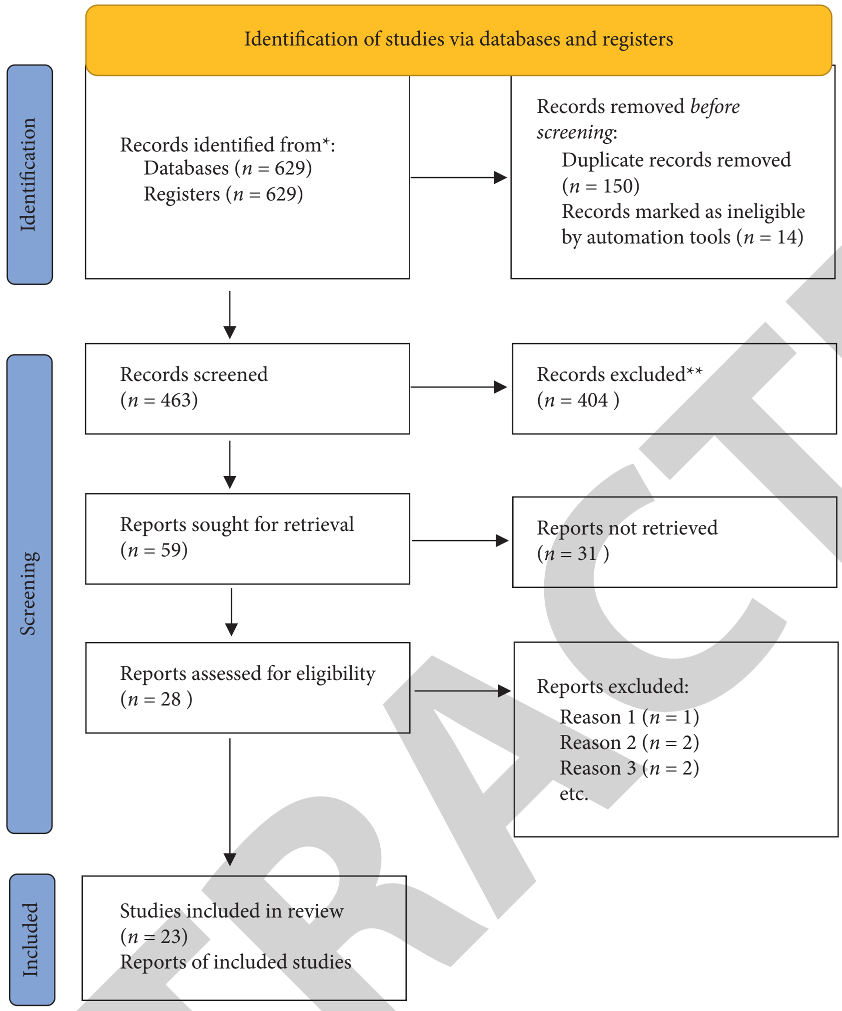

Figure 1: Flow chart of meta-analysis literature screening.

randomized comparative studies, nonrandom comparative studies, case comparisons research, and formation studies. (2) The beauty seekers who study needle pairs are from North America, Europe, and Asia, and the aesthetics are different. (3) There are differences in the way autologous fat fines are used in the study. (4) At the time of follow-up of researchers, the evaluation norms accepted by each study were different. (5) After the test of the NOS scale, the quality of the literature classified is different, and the high-quality literature is less [8].

Due to the limitations of this study, clinical studies on the use of autologous fat particle grafting in antiaging facial applications, especially large-scale clinical randomized controlled studies, still need to be further studied in depth.

5.4. Literature Search Effect. According to the search strategy that has been formulated, a total of 1389 articles were searched; 1 document was obtained by reference to literature, and 867 documents were obtained after excluding repeated literature. After browsing the title and abstract, 763 articles were cleared, and 104 articles were obtained in the initial screening. After browsing the full text, a total of 30 articles without full text and corresponding author were cleared, and 74 articles classified as definitive evaluations were obtained. The meta-analysis was followed to classify the number of canonical clearance cases in 5 and below, and 59 cases were obtained after the respondents said that the heart rate was at least one. There were still two studies suspected of stacking finished products with the same author, and the most appropriate research was accepted, and 26 literature were obtained for inclusion in the study [9].

5.5. Basic Data Characteristics of the Included Studies. A total of 2852 beauty seekers were included in 23 studies, aged 11 to 63 years. The publication period was from January 1987 to October 2021, and most of the studies were after 2008. Those studies have their roots in 20 countries around the world, mostly in Europe, North America, and Asia, and the current three countries in the number of studies are France, the United States, and Italy. Most of the studies were based on a low grade; only one study was a randomized comparative study, but the comparison group was not actually included in the evaluation content of this system, so the literature was based on grade 2b to 5 (grading follows

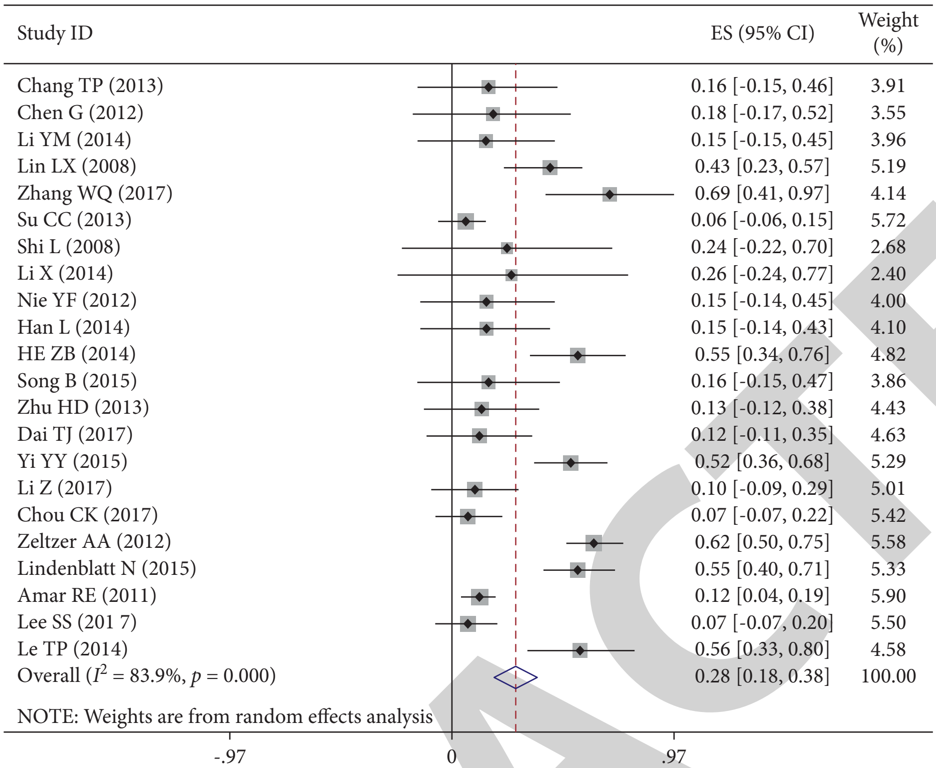

Figure 2: The incidence of postoperative complications in a meta-analysis forest map.

Oxford College's Five-Level Norms for Documentation Categories by the Central Centre for Evidence-Based Medicine).

Twenty studies in 1885 cases were classified as meta-elaborations, published from 2007 to 2021. There were 21 cohort studies, 17 prospective cohort studies, and 4 retrospective cohort studies. There were 4 comparative case studies and 32 case combination studies. The follow-up period ranged from 3 months to 25 years, with an average of 23 months. BMI was 17~30 kg/m^2. Patient numbers can be divided into two categories: facial aging (93.1%, 2655 cases) and facial profile moulding (6.9%, 197 cases). To achieve a larger result, the number of surgeries is usually 1 to 5 times. Five studies had a comparison group, three of which were not related to fat grafting and only the fat grafting group was included in the study. Because most studies did not have a comparison group, it was not possible to compare AFT with a comparison group in a meta-analysis. Complication rates were the most common reported effect in the studies (19 studies, 2031 case numbers). This was followed by 11 studies (1086 case numbers) that reported uniform surgical frequency, as well as patient number satisfaction (17 studies, 1137 patient numbers) and operator satisfaction (11 studies, 742 case numbers). Twenty-one studies (1483 case numbers) reported at least one-time point face measurement 3, 6, 12, and 18 months postoperatively to affirm the survival rate of grafted fat regardless of when it is changed. Twelve studies (670 cases) complained of biopsy rates due to unusual clinical indications (e.g., mass involvement) or radiological indications, including 2852 patient numbers; 2 cases of facial cancer were consulted (0.04%). Another common satisfaction assessment method is the VAS method (1 study, 31 case numbers) and its scale (4 studies, 116 case numbers). The scale assesses the patient number's satisfaction with the various margins of antiaging facial and the quality corresponding to the face. Finally, one study evaluated the fat-based vascular component SVF, but the numerical values are lacking and cannot be classified into metaelaboration [10].

According to the different application methods of autologous fat transplantation, it can be divided into four types according to (AFT), autologous fat transplantation plus (SUPP) (AFT + SUPP), autologous fat transplantation plus BRAVA extension skills (AFT + BRAVA), autologous fat transplantation combined with implantation (AFT + IMP). Four groups conduct effect orientation surveys to reduce heterogeneity between studies. They included fatty vascular builder (SVF), platelet-rich plasma (PRP), adipose-derived stem cells (ASC), and autologous adipose-derived regenerative cells (ADRCS) of 17 groups (1,164 cases) in simple AFT group, 3 groups (92 cases) in AFT + SUPP group, 4 groups (750 cases) in AFT + BRAVA group, and 6 groups (846 cases) in AFT + IMP group.

6. Perioperative Condition

6.1. Preoperative Preparation. Most of the studies were conducted under general anesthesia combined with partial anesthesia, which covered both general anesthesia intubation and intravenous general anesthesia. Some patients used local infiltrative anesthesia alone; most of them were typical of Klein solution, that is, swelling anesthesia technique, which contains 30 to 50 ml of 1% lidocaine per liter of normal saline or sodium lactate forest format solution, 1 ml of 1 : 100,000 epinephrine, with infiltration for 10 to 15 minutes. However, in five studies (748 patients), there was no lidocaine in the swelling fluid. Four studies (331 patients) used antibiotics, and only one study detailed how to use them [11].

BRAVA was used in six studies to hold preenlargement, and the important goal was to preexpand the receiving area space, making it easier to obtain sufficient blood transport of grafted fat to survive. Detailed application method: wearing 3 to 4 weeks before surgery, 10 to 12 hours a day, will have a good effect.

6.2. Fat Supply Area Location. The belly, thighs, and lateral belly are the most used parts in various studies, and the rest of the back, waist, hips, arms, knees, buttocks, legs, and stomach are less used, but the preferred parts are not recommended, mainly according to the specific situation of the patient.

6.3. Liposuction Status. Liposuction skills are all about accepting Coleman's large-aperture sleeve and low-pressure liposuction.

The pore size is usually 2 to 4 mm, led by a porous blunt head, and the negative pressure is usually 0.4 to 0.6 standard air pressure. However, there were some minor differences between each of the studies, such as the negative root source covering manual needle dispenser manipulation and machine liposuction machine manipulation. There were 21 studies on liposuction with manual syringes, 10 ml, 20 ml, and 60 ml size needle syringes, 32 studies on liposuction with machine liposuction machines, and 7 studies on the application of hydrodynamic liposuction machines.

6.4. Fat Treatment Situation. The adipose tissue in 33 studies was resolved by centrifugation, taking the pure adipose tissue in the middle at a speed of 3000 rpm for 2 to 4 minutes. 110 studies used precipitation techniques, 3 studies used filtration techniques, and 4 studies used cleaning methods. Kang reported on the effects of slow centrifugation and accumulation on postoperative fat dysphoria, suggesting that slow centrifugation was simpler to cause postoperative refractory nodules [12]. In particular, the history of facial surgery or the number of patients who need repeated fat transplantation is a significant risk factor. Twelve studies used SVF, ASCs and ADRCs, and one used monocytes derived from iliac bone marrow to enrich the body. Compared with AFT group and AFT + SVF group, there was no significant difference in fat survival rate at 6 and 12 months after operation. SVF is divided into low-solubility and high-solubility groups. There was still a great difference in fat survival rate within 18 months (50% : 75%) [13].

6.5. Fat Injection Process. Multistroke, multilayer, multipoint, fan-shaped, and small oiler is commonly used in grease injection. Syringes ranged from 1 ml to 60 ml and screw push syringes were equipped, each pumping 0.28 ml of fat. Most of the injection needle research is in the lower layer of the skin and the lower part of the gland, which may be the gap of facial height, but the controversy lies in the fact that injecting a needle into the facial muscularis will lead to the formation of nodules in the muscularis and pain during exercise. The injection volume is large, but scientists are different. Only the AFT group is injected with 50–420 ml at a time, while the AFT + SUPP group is injected with 195–380 ml, with 245–430 ml in AFT + BRAVA group and 27–134 ml in AFT + IMP group. Five studies confirmed that, due to the direct absorption of adipose tissue after operation, the amount of transplantable fat should be increased by 30–50% compared with the design index. Therefore, after astrological stability, the survival of all fat takes 6–12 months. In addition, both studies indicated that the interval between two operations was 3 or 6 months, which was similar to the method, during the postoperative visit, and fat survival and survival variables, i.e., E. Education. [14].

6.6. Duration of Surgery. 14 studies on the duration of surgery ranged from 60 hours to 240 hours, mainly about 120 hours. Long-term studies were conducted during the operation. It may be related to the preparation of SVF, sometimes requiring a large amount of fat injection and longer liposuction time [15].

Almost all studies conducted one year after surgery and within one year after surgery were accompanied by facial audio and myocardial angiography; most of them were reclassified within 6 months, compared with BI-RADS3 and BI-RADS1 or BI-RADS2. Spear company reported a case of BI-RADS type 4 disease, which was negative in field test [16].

6.7. Concurrent Condition. 19 studies (2031 cases) reported complications mainly caused by lime kilns of different sizes, lipodystrophy and lymph nodes, infection, dislocation, transplant defects, and dents in supply areas in affected areas. In 30 cases, postoperative complications required further operation [17].

After 23 months of unified visit, the data of 2852 patients in 23 studies were transformed into two-level vertical lines, which were taken on the basis of random-effects model *l*. The cumulative case satisfaction was 93%, the confidence interval was 95%, and the intergroup heterogeneity analysis was $P > 0.01$. There were no significant group differences. In addition, in 11 studies of 742 patients, 87% of respondents were satisfied with the treatment effect and 95% believed that treatment and time intervals are long [18].

According to our analysis of Aloe vera, 4,031 patients in 49 studies had an 8% reduction in clinical complications and 95% of patients had intervals [19].

In 21 studies, 2093 cases were diagnosed, and the metadata was crushed. The investigation of intergroup heterogeneity was $I^2 = 98.8\%$ and $P < 0.01$. Other surgeons may consider surgery, and the difference between the number of diseases and perinatal conditions is more

Table 1: Research basic data sheet.

Author (year)	Author territory	Type of study	Total number of people	Level of evidence	Average age
Meyer-Marcotty (2021)	America	Prospective cohort studies	78	2b	39
Zhu L (2022)	China	Case series studies	8	6	37
Zhang HY (2021)	China	Case series studies	46	4	34
Manuneedhi Cholan P (2021)	UK	Case series studies	20	5	32
Burian M (2021)	Australia	Case series studies	30	4	36.9
Wang Y (2021)	China	Case series studies	32	4	45

relevant. The total uniform operation frequency of random-effects model is 1.59 times of 95% confidence interval (1.27, 1.91).

The meta-analysis showed that 5% of the 12 studies (670) were to treat autoimmune fat at the waiting interval (−2.12). Because the bed may be associated with unusual images or tumors, histopathological examination is required [20].

6.8. Metaregression Model. In 21 studies (1483), the results of 4 groups varied according to the method of artificial or mechanical transplantation of lipids and fats. The survival rate of fat was different. A regression model with $P < 0.01$ was established, and the relationship between the studies immediately after operation was pointed out; differences remained. Especially 6 months and 12 months after operation, there was no difference in covariance between liposuction and fat transplantation ($P > 0.01$); see Table 1 [21].

Within 12 months after operation, the fat survival rate and time ratio gradually decreased by 50% to 70%. Over an 18-month period, only one study (57 patients) had a significant but unrepresentative impact on the trend chart. Longer access times require wider coverage.

7. Discussion

Many factors affect the survival rate of adipose tissue, such as fat survival rate during transplantation, liposuction position, lipid extraction method, and fat purification solution, as well as injection methods, space and pressure in the transplant environment, use of supplements, blood circulation, and general nutrition. There are two methods of liposuction: traditional manual liposuction and mechanical liposuction. Liquid liposuction is a new method of mechanical liposuction. Current cleaning methods include stacking, screening, cleaning, and centrifuging. One of the ways to improve blood supply after autologous fat transplantation is cellular fat transfer (CFL). Increase the local solubility of adipose stem cells (ASC) to improve survival, as well as related cytokines, such as hypertrophic plasma (HP). It is used to improve vascular fat transplantation and reduce fibrosis and calcification [22].

Autologous facial reconstruction has been widely used in plastic surgery, but there is no unified method to evaluate the postoperative efficacy. At present, the satisfaction assessment of patients or operators mainly includes Likert form and VAS form. The postoperative survival rate of fat includes examination method, volume acquisition rate, survival rate, and growth rate. Among these evaluation methods, most researchers use the survival index as a method to evaluate the effect of autoimmune fat on facial aging. Face volume measurement methods include molding, drainage, and image forming methods, such as BSM, CT, MRI, and 3D scanning, However, the most common imaging methods are still CT and MRI. Another objective indicator of efficacy is the number of operations. The biopsy rate reflects the safety of surgical tumors [23].

In this study, we systematically evaluated various methods of facial fat transplantation. The research topic, perinatal status, and surgical methods of autologous fat transplantation were described in detail. Postoperative video surveillance and complications were described from the aspects of satisfaction of potential patients and surgeons and operation frequency. The incidence of complications, the survival rate of the fat at the time of grafting, and the stability of the tumour margins after surgery are strong evidence for clinical application.

Autologous fat transplantation (AFT) refers to the extraction and dispersion of subcutaneous fat in the abdomen, thighs, and other parts of the body. Then inject it into other necessary parts of the body, such as face and scar. The facial fat transplant changed. In recent years, no negative side effects have been reported, so this technology is more and more widely used in the field of plastic surgery.

According to the electronic evaluation method of COCHRANE system, the Preferred Reporting Items for Systematic Reviews and Meta-analyses (PRISMA) is systematically analyzed and optimized. The search dates were PubMed (1950-2021.11), EMBASE (1946-2018.11), and Corcoran Library (Architecture-2021.11), respectively. In the digital library, there are no restrictions on the language and category of literature. According to the classification law of literature selection, autologous fat is selected for face transplantation. For antiaging of relevant documents, collection of adjustment values, and convergence of relevant values into system evaluation, according to the quantitative meta-analysis method, STATA/se15 statistics are used to summarize the performance indicators. Efficacy indicators include patient satisfaction, operator satisfaction, average number of operations, incidence of complications, fat survival rate, and biopsy index [24].

A total of 23 studies were conducted under the regulation, involving 2852 cases, of which 10 were individual cases, seven case studies were excluded because their significance could not be confirmed, and 16 studies included 2800 cases. Fourteen studies were conducted according to the five-step normative transformation of the document classification center of Oxford Medical School, fact-based studies, mostly based on lower indicators, and only one study was conducted randomly, However, it is not included in the system overview. Therefore, literature ranks from 2b to 5. These studies have been carried out in 20 countries around the world, mainly in Europe, North America, and Asia, and three countries ranked first, second, and third in the number of studies, that is, France, the United States, and Italy. Among them, 57 were divided into 21 cohort studies, 17 advanced cohort studies, and 4 cohort studies. A total of 4 comparative studies and 32 studies were conducted. For a long time, the stability of cancer tumors in these patients has not been established. According to the results of Omega optimization, the overall satisfaction of patients was 93% and that of surgeons was 87%, and these percentages were generally high.

8. Conclusion

Autologous fat transplantation is an important method of facial plastic surgery, with high patient satisfaction and less surgery; the rate of clinical and radiological complications is low, the survival rate of fat is poor, and there is no clear conclusion. The safety of tumor needs continuous observation.

Automobile fat transplantation has been used for more than 100 years. In 1893, the operation of filling soft tissue defects with small pieces of free fat was first reported. In 1987, a patient's own fat was injected into his face for the first time. Since then, autologous fat transplantation has opened a new chapter in facial plastic surgery.

Data Availability

The data used to support this study are available from the corresponding author upon request.

Conflicts of Interest

The authors declare that they have no conflicts of interest.

References

[1] Y. Chai, Y. Chen, B. Yin et al., "Dedifferentiation of human adipocytes after fat transplantation," *Aesthetic Surgery Journal*, p. sjab402, 2021.

[2] B. Hohendorff, F. Neubrech, C. K. Spies, F. Unglaub, L. P. Müller, and C. Ries, "Minimal-invasive Verfahren im Frühstadium der Daumensattelgelenksarthrose," *Orthopäde, Der*, vol. 51, no. 1, pp. 13–22, 2022.

[3] S. A. Wolfe, "Invited discussion on: oral and maxillofacial autologous fat transplantation: history, clinical application status and research progress," *Aesthetic Plastic Surgery*, vol. 46, no. 1, pp. 308-309, 2021.

[4] M. V. Meyer-Marcotty, I. Batsilas, H. Fischer, S. Dahmann, C. Happe, and C. Herold, "Prospektive Untersuchung der mittelfristigen Ergebnisse nach autologer Fetttransplantation in arthrotische Sattelgelenke," *Handchirurgie, Mikrochirurgie, Plastische Chirurgie*, vol. 54, no. 01, p. 43, 2021.

[5] H. Y. Zhang, Y. Ren, and W. Xu, "[Combined autologous fascia transplantation with autologous fascia and fat injection into the vocal fold for sulcus vocalis]," *Zhonghua er bi yan hou tou jing wai ke za zhi*, vol. 56, pp. 1080–1086, 2021.

[6] P. Manuneedhi Cholan, S. Morris, and K. Luo, "Transplantation of high fat fed mouse microbiota into zebrafish larvae identifies MyD88-dependent acceleration of hyperlipidaemia by Gram-positive cell wall components," *BioFactors*, 2021.

[7] M. Burian, M. Hajek, P. Sedivy, I. Mikova, P. Trunecka, and M. Dezortova, "Lipid profile and hepatic fat content measured by (1)H MR spectroscopy in patients before and after liver transplantation," *Metabolites*, vol. 11, no. 9, p. 625, 2021.

[8] Y. Wang, X. Wang, and J. Zhao, "Transposition mucosal flap combined with autologous fat transplantation to repair lip defects caused by sclerotherapy of hemangioma," *Journal of Craniofacial Surgery*, 2021.

[9] G. Liu, K. Zhang, Y. Shi, and Y. Lai, "Glabellar wrinkle correction by autologous fat transplantation and evidence of human adipose tissue regeneration in a nude mouse model," *Journal of Cosmetic Dermatology*, vol. 20, pp. 3213–3219, 2021.

[10] T. Dienemann, S. L. Ziolkowski, and S. Bender, "Changes in body composition, muscle strength, and fat distribution following kidney transplantation," *American Journal of Kidney Diseases*, vol. 78, pp. 816–825, 2021.

[11] M. Dong and F. Li, "Diagnosis and management of fat necrosis after autologous fat transplantation of breast," *Zhongguo Xiu Fu Chong Jian Wai Ke Za Zhi*, vol. 35, pp. 918–922, 2021.

[12] M. A. Nilforoushzadeh, M. Heidari-Kharaji, S. Alavi et al., "Transplantation of autologous fat, stromal vascular fraction (SVF) cell, and platelet-rich plasma (PRP) for cell therapy of atrophic acne scars: clinical evaluation and biometric assessment," *Journal of Cosmetic Dermatology*, 2021.

[13] I. Olaru, A. Sava, and C. Tamas, "The significance of erythropoietin and insulin administration on survival of fat tissue after autologous fat transplantation in Wistar rats. An experimental study," *Romanian Journal of Morphology and Embryology*, vol. 61, pp. 1143–1151, 2020.

[14] N. Sakata, G. Yoshimatsu, and R. Kawakami, "Fat-covered islet transplantation using epididymal white adipose tissue," *Journal of Visualized Experiments*, vol. 171, 2021.

[15] D. Yan, S. H. Li, and A. L. Zhang, "A clinical study of platelet-rich fibrin combined with autologous high-density fat transplantation in augmentation rhinoplasty," *Ear, Nose, & Throat Journal*, vol. 1-7, p. 1455613211016902, 2021.

[16] Q. Niu, J. Zhang, and B. Lu, "Invited response on: comment on: oral and maxillofacial autologous fat transplantation: history, clinical application status and research progress," *Aesthetic Plastic Surgery*, vol. 45, pp. 3073-3074, 2021.

[17] S. Y. Hoon, J. Gao, L. Xu et al., "Effect of additive-assisted fat transplantation on fat graft survival rate: a preliminary experimental study based on a rabbit animal model," *In Annales de Chirurgie Plastique Esthétique*, Masson, vol. 66, no. 6, pp. 440–446, Paris, France, 2021.

[18] Q. Qi, A. K. Weinstock, K. Chupetlovska et al., "Magnetic resonance imaging-derived proton density fat fraction (MRI-PDFF) is a viable alternative to liver biopsy for steatosis quantification in living liver donor transplantation," *Clinical Transplantation*, vol. 35, p. e14339, 2021.

[19] A. Battistini, M. A. Romeo, V. Bandi, V. Vinci, and F. Caviggioli, "Comment on: oral and maxillofacial autologous fat transplantation: history, clinical application status and research progress," *Aesthetic Plastic Surgery*, vol. 45, pp. 3071-3072, 2021.

[20] Z. Zheng, Y. Hao, J. Yin, W. Huang, B. Cheng, and X. Lei, "Autogenous fat transplantation and botulinum toxin

Hindawi
Journal of Healthcare Engineering
Volume 2023, Article ID 9851285, 1 page
https://doi.org/10.1155/2023/9851285

Retraction

Retracted: Effects of Different Intervention Methods on Intestinal Cleanliness in Children Undergoing Colonoscopy

Journal of Healthcare Engineering

Received 26 September 2023; Accepted 26 September 2023; Published 27 September 2023

This article has been retracted by Hindawi following an investigation undertaken by the publisher [1]. This investigation has uncovered evidence of one or more of the following indicators of systematic manipulation of the publication process:

(1) Discrepancies in scope
(2) Discrepancies in the description of the research reported
(3) Discrepancies between the availability of data and the research described
(4) Inappropriate citations
(5) Incoherent, meaningless and/or irrelevant content included in the article
(6) Peer-review manipulation

The presence of these indicators undermines our confidence in the integrity of the article's content and we cannot, therefore, vouch for its reliability. Please note that this notice is intended solely to alert readers that the content of this article is unreliable. We have not investigated whether authors were aware of or involved in the systematic manipulation of the publication process.

Wiley and Hindawi regrets that the usual quality checks did not identify these issues before publication and have since put additional measures in place to safeguard research integrity.

We wish to credit our own Research Integrity and Research Publishing teams and anonymous and named external researchers and research integrity experts for contributing to this investigation.

The corresponding author, as the representative of all authors, has been given the opportunity to register their agreement or disagreement to this retraction. We have kept a record of any response received.

References

[1] Y. Yang, Y. Xiao, L. Zhang, J. Lv, and Q. Huang, "Effects of Different Intervention Methods on Intestinal Cleanliness in Children Undergoing Colonoscopy," *Journal of Healthcare Engineering*, vol. 2023, Article ID 1898610, 7 pages, 2022.

Hindawi
Journal of Healthcare Engineering
Volume 2022, Article ID 1898610, 7 pages
https://doi.org/10.1155/2022/1898610

Research Article

Effects of Different Intervention Methods on Intestinal Cleanliness in Children Undergoing Colonoscopy

Yirong Yang,[1,2] Yuan Xiao,[2] Li Zhang,[2] Jiajia Lv,[2] and Qiyun Huang [1,3]

[1] *Department of Nursing, Ruijin Hospital Affiliated to Shanghai Jiaotong University School of Medicine, Shanghai 200025, China*
[2] *Department of Pediatrics, Ruijin Hospital Affiliated to Shanghai Jiaotong University School of Medicine, Shanghai 200025, China*
[3] *Department of Radiotherapy, Ruijin Hospital Affiliated to Shanghai Jiaotong University School of Medicine, Shanghai 200025, China*

Correspondence should be addressed to Qiyun Huang; huangqiyun@stu.ahu.edu.cn

Received 10 February 2022; Revised 2 March 2022; Accepted 16 March 2022; Published 16 April 2022

Academic Editor: Liaqat Ali

Objective. To explore the effects of different intervention methods on intestinal cleanliness in children undergoing colonoscopy. *Methods*. 61 children who underwent colonoscopy in our hospital from May 2020 to May 2021 were randomly divided into group A ($n = 21$), group B ($n = 30$), and group C ($n = 10$). The children in the three groups were intervened in different ways before the colonoscopy. Group A received a long-handled Kaiselu +1 cathartic intervention, while group B received a long-handled Kaiselu +2 cathartic intervention, and group C received an enema plus one cathartic intervention. The patients in the three groups were given the same diet before the examination until the examination was completed. The time-related indexes, cleanliness, adverse reactions, tolerance, and adaptability of the three groups under different dietary interventions and cleaning methods were evaluated. *Results*. The first defecation time in group C was lower than that in group A and group B, the hospital stay was longer than that in group A and group B ($p > 0.05$), and the colonoscopy time in group C was shorter than that in group A and group B ($p < 0.05$). The BBPS score of group C was (2.10 ± 0.32), which was significantly higher than that of group A (1.16 ± 0.19) and group B (1.77 ± 0.18) ($p < 0.05$). The BBPS scores of children with liquid food in the three groups were significantly higher than those of common food, and the BBPS scores of liquid food and common food in group C were significantly higher than those in group A and group B ($p < 0.05$). The incidence of adverse reactions in group C was 20.00%, which was significantly lower than 33.33% in group A and 23.33% in group B ($p < 0.05$). The proportion of grade I in group C was 50.00%, which was significantly higher than 38.10% in group A and 43.33% in group B ($p < 0.05$). *Conclusion*. Children undergoing colonoscopy take preintestinal preparation under different diets and intervention methods. The cleanliness of liquid food and enema + one-time laxative one day before colonoscopy is the best, which can significantly reduce adverse reactions and increase the acceptability and adaptability of children. It is worthy of clinical application.

1. Introduction

As one of the clinical fiber endoscopes, colonoscopy can observe the internal conditions of the rectum, colon, cecum, and part of the small intestine through anal reverse insertion. The lesions and degree of the digestive system can be clearly understood by using an objective lens and a light image conversion system to assist in clinical surgical examination and operation [1, 2]. Colonoscopy has been used for pediatric digestive tests since the 1980s. As the main examination method for the diagnosis of colorectal diseases in children, its disease detection rate and safety are high, and it is widely used in pediatrics [3]. Whether colonoscopy can be carried out smoothly depends mainly on intestinal preparation. High-quality intestinal preparation can not only clear the observed lesion location and degree, improve the disease detection rate and the success rate of endoscopic treatment, but also shorten the examination time. At the same time, it is convenient for medical staff to check the operation and relieve patients' discomfort [4, 5]. During clinical colonoscopy for children, the examination is often performed under general anesthesia, considering the acceptance degree, physical dosage, and tolerance of children. Intestinal examination preparation should be arranged according to child's age, physical condition, clinical symptoms, digestive status, and examination willingness [6]. At present, there are many preparation programs, among which physiological saline enema, oral magnesium sulfate, or mannitol are important drugs for adults to clean the intestine before examination. However, it may cause adverse reactions such as hypoglycemia, and the cleaning effect is not good. Therefore, it is necessary to further find a safer, feasible, and cleaner plan for the intestinal preparation of children [7, 8]. Casserole long stem uses hypertonic reactions caused by glycerin or sorbitol to soften metabolites and stimulate intestinal wall reflexes to cause defecation behavior, which has limited stimulation to the body and is often applied in constipation and intestinal preparation with minor adverse reactions [9, 10]. In this study, children undergoing colonoscopy were treated with different intestinal prepreparation interventions since May 2020, aiming to explore the effects of different interventions on intestinal cleanliness and comfort of general diet and liquid food. The report is as further discussed in this study.

2. Data and Methods

2.1. General Information. In this study, 61 children who underwent colonoscopy in our hospital from May 2020 to May 2021 were selected as the subjects and randomly divided into group A ($n = 21$), group B ($n = 30$), and group C ($n = 10$) according to the time of admission. There were 9 males and 12 females in group A with an average age of 11 ± 1.2 months, including 2 abdominal distension, 2 diarrhea, 2 constipation, 1 mucus, and no fistula. In group B, there were 14 males and 16 females, with an average age of 9.2 ± 0.8 months, including 1 case of abdominal distension, 12 cases of diarrhea, 2 cases of constipation, 1 case of mucus, and no fistula. In group C, there were 7 males and 3 females, with an average age of 8.4 ± 0.6 months, including 2 abdominal distension, 3 diarrhea, 1 mucus, no fistula, or constipation. There was no significant difference in baseline data between the three groups ($p > 0.05$), indicating comparability. Before colonoscopy, three groups of children were given different interventions: group A was given carcerol long-stalk +1 time of laxative intervention, group B was given carcerol long-stalk +2 times of laxative intervention, and group C was given enema +1 time of laxative intervention. All patients in the three groups were given the same diet before the examination until the examination was completed. This study was approved by the hospital medical committee.

2.2. Inclusion and Exclusion Criteria. The inclusion criteria were as follows: (1) in line with the diagnostic indication criteria in Expert Consensus on Standardized Operation of Gastroscopy and Colonoscopy for Children in China [11]; (2) the colonoscopy was performed for the first time, and the colonoscopy criteria were met; (3) aged from 3 to 18; (4) clinical manifestations include lower gastrointestinal bleeding, abdominal pain, diarrhea, anemia, perianal lesions, and lower gastrointestinal diseases; (5) no cognitive impairment, mental system diseases, and so on; and (6) complete clinical data; study subjects, family members or legal guardians, were informed of the contents of the project and signed informed consent.

The exclusion criteria were as follows: (1) patients with serious dysfunction of heart, liver, kidney and blood vessels; (2) with intestinal obstruction, gastrointestinal bleeding or perforation, intestinal infection, toxic enteritis, and intestinal volvulus; (3) complicated with peritonitis, abdominal mucosa, megacolon crisis, and abdominal malignant tumor; (4) patients with hypertension, hyperglycemia, and other chronic diseases; (5) With moderate or severe diarrhea and constipation; (6) with coagulation disorder, allergic to the study drugs or have a history of severe allergy; and (7) poor compliance, do not cooperate with visitors.

2.3. Research Methods. Preenteral preparation: after admission, all children were given psychological education, explaining the examination items and telling their relatives to soothe their anxiety. The history of allergy, surgery, disease, and medication was filled in, and the specific physical symptoms and basic information were explained. A blood routine, a urine routine, and a cardiohepatic examination were performed. The diet, medication, time arrangement, and matters needing attention during the preparation period were informed. The number of defecations, character, and physiological reactions were observed during the preparation period. According to the physical condition and tolerance of children, all patients in the three groups ate as recommended the day before the examination. In group A, there was 1 case of liquid food, 10 cases of semiliquid food, and 10 cases of general food. In group B, there were 3 cases of liquid diet, 8 cases of semiliquid diet, and 19 cases of general diet. In group C, there were 2 cases of liquid diet, 3 cases of semiliquid diet, and 5 cases of general diet. In order to prevent hypoglycemia, a supplement glucose electrolyte solution was given before the examination. At the same time, fasting was recommended for 4h to 6h before liquid food examinations and 8h before general food examinations according to different types of diet.

According to the Intestinal Preparation Guidelines related to the Diagnosis and Treatment of Digestive Endoscopy in China [12], the dosage requirements of Kaiselu, compound polyethylene glycol electrolyte powder (Shutaiqing (Beijing) Biopharmaceutical Co., Ltd.; State Drug Approval H20040034), and enema for all children were based on their physique, weight, and degree of disease. One day before the examination, after dietary management, all patients were given compound polyethylene glycol electrolyte powder orally, 300g in 3000 mL, and it was taken completely internally for 1h. Among them, patients in group B received 80 mL/kg polyglycol electrolyte again at 8 : 00 a.m. on the day of examination. Patients in group A and group B were treated with long-handled Kaiselu intervention. All the glycerin in Kaiselu (20 ml) was inhaled into a syringe (without a needle), a part of the scalp needle was inserted and paraffin oil was applied, and the needle was slowly inserted into the child's anus to the scalp, and the drug solution was slowly injected into the rectum for 10 to 20 minutes before defecation. Group C was given a normal saline enema and a glycerin enema after admission. Children under 3 years old were given 250 ml of warn water. At the age of 4–6 years old, 550 ml of warn water given. From 6 to 9 years old, 800 ml of warn water was given. Aged 10 years and above, 1100 ml of warn water was given. During the guidance of the prone position, it was kept longer.

2.4. Observation Indicators. Time-related indicators were evaluated, including time of initial defecation, colonoscopy time, and length of hospital stay, wherein colonoscopy time was the time from colonoscopy insertion to complete withdrawal. (2) Evaluation of intestinal cleanliness after different intervention methods: the Boston Bowel Preparation Scale [13] (BBPS) was used to measure the quality of bowel preparation in the three groups, which divides the colon into three parts. They were the right colon (ileocecal colon, ascending colon), the middle colon (transverse colon, descending colon), and the left colon (sigmoid colon, rectum), with a total of 3 points for each colon and a total of 9 points. The higher the score, the better the cleaning effect. (3) To evaluate the intestinal cleanliness of different diets; (4) the incidence of adverse reactions in the three groups was evaluated, including nausea, vomiting, abdominal distention, abdominal pain, cold sweat, palpitation, and dizziness; (5) the tolerance and comfort level of the children in the three groups were evaluated. After colonoscopy, questionnaire survey was conducted to evaluate their comfort level and tolerance. And ask if you would like to have another colon examination or preparation.

2.5. Clinical Evaluation Criteria. Performed and recorded by the same experienced endoscopic surgeon, intestinal cleanliness was assessed by the double-blind method.

The scoring standard for the segmented cleanliness of the intestinal tract was as follows [14]: the intestinal tract was poorly cleaned, the intestinal lumen was filled with a large amount of feces and feces residue, and no mucous membrane was found, so the endoscopic observation was not possible, and it was judged as 0. Intestinal cleanliness is poor, a large number of feces and feces residue can be seen in the intestinal lumen, and some mucous membranes can be seen. Experienced patients can be forced into the microscope and observation, and it is judged as 1 point. Intestinal cleanliness was fair, a small amount of feces and fecal residue remained in the intestinal lumen, and mucous membrane could be seen. There was no obstruction in endoscopic and observation, and the field of vision was still clear, which was judged as 2 points. The intestinal tract was well cleaned, no feces or feces residue was found in the intestinal lumen, the mucous membrane was clearly visible, and the field of vision was good, which had no influence on the endoscopy and observation. It was judged as 3 points.

Overall intestinal cleanliness scoring standard [15]: the total score is less than 5 points or the score in any section is less than 2 points, which indicates that the intestinal fecal and fecal residue accumulation during colonoscopy is serious and the examination cannot be carried out smoothly. The total score of 6–7 was judged as good intestinal cleanliness, indicating that the residual feces and fecal residue in the intestinal tract during colonoscopy would not affect the observation and treatment under colonoscopy. Those with a total score of 8–9 were judged to have excellent intestinal cleanliness, indicating that there was no feces and fecal residue in the intestine during colonoscopy, and the intestine was fully prepared.

Tolerance evaluation criteria [16]: i degree no obvious discomfort, complete tolerance, complete acceptance of second colonoscopy, and preparation. Degree ii mild discomfort, tolerable, but acceptable for a second colonoscopy and preparation. Grade iii was moderate/severe discomfort, totally intolerable, and the second colonoscopy was refused and prepared.

2.6. Statistical Treatment. The data were processed by SPSS 24.00 statistical software. The measurement data were expressed as $X \pm S$, and comparison between groups was performed by the T test. The counting data were expressed as case number (n) and percentage (%). The $\chi 2$ test was used for comparison between groups, and $p < 0.05$ indicated statistically significant differences.

3. Results

3.1. Comparison of Time-Related Indicators. The results showed that the time of initial defecation in group C was shorter than that in groups A and B, and the length of hospital stay was longer than that in groups A and B, with no statistical significance ($p > 0.05$). The colonoscopy time of group C was shorter than that of group A and group B. The difference was statistically significant ($p < 0.05$), as shown in Table 1.

3.2. Comparison of Intestinal Cleanliness with Different Intervention Methods. The results showed that the BBPS score of group C (2.10 ± 0.32) was significantly higher than that of group A (1.16 ± 0.19) and group B (1.77 ± 0.18). The difference was statistically significant ($p < 0.05$), as shown in Figure 1.

3.3. Comparison of Intestinal Cleanliness between Different Diets. The results showed that the BBPS score of liquid food in three groups was significantly higher than that of general food, and the difference was statistically significant ($p < 0.05$). The BBPS scores of liquid diet and general diet in group C were significantly higher than those in group A and group B. The difference was statistically significant ($p < 0.05$), as shown in Table 2.

Table 1: Comparison of time related indicators ($\overline{x} \pm s$).

Group	Group A ($n = 21$)	Group B ($n = 30$)	Group C ($n = 10$)	F	p
Time of first defecation (min)	8.32 ± 1.92	8.25 ± 1.89	8.03 ± 1.97	0.253	0.316
Colonoscopy time (min)	21.79 ± 8.46	18.65 ± 7.24	14.09 ± 6.03	2.420	0.025
Length of hospital stay (D)	3.54 ± 0.68	3.94 ± 0.72	4.23 ± 0.79	4.071	0.102

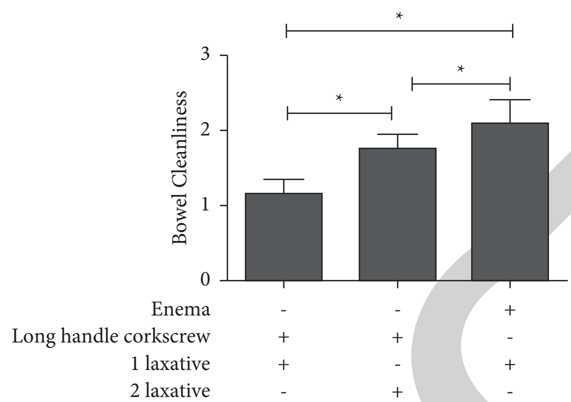

Figure 1: Comparison of BBPS scores by different intervention methods (note, compared with group (C) $^{*}p < 0.05$).

Table 2: Comparison of BBPS scores by different dietary patterns ($\chi \pm s$).

Group	Group A ($n = 21$)	Group B ($n = 30$)	Group C ($n = 10$)
Liquid diets	$1.22 \pm 0.32^{\#}$	$1.91 \pm 0.34^{\#}$	2.20 ± 0.37
Ordinary food	$1.08 \pm 0.19^{*\#}$	$1.67 \pm 0.23^{*\#}$	$2.00 \pm 0.55^{*}$

Note: compared with liquid diet, $^{*}p < 0.05$. Compared with group C, $\# p < 0.05$, as shown as Figure 2.

3.4. Comparison of Incidence of Adverse Reactions. The results showed that the incidence of adverse reaction in group C (20.00%) was significantly lower than that in group A (33.33%) and group B (23.33%). The difference was statistically significant ($p < 0.05$), as shown in Table 3.

3.5. Comparison of Tolerance and Comfort. The results showed that the proportion of i degree in group C (50.00%) was significantly higher than that in group A (38.10%) and group B (43.33%). The difference was statistically significant ($p < 0.05$), as shown in Table 4.

4. Discussion

With the change of people's health consciousness and eating habits, the examination of the upper and lower digestive tract has been paid more and more attention. As a major examination device, colonoscopy can accurately detect the location, type, and degree of lesions in the colon with significant safety and feasibility [17]. The accuracy and quality of colonoscopy largely depend on the cleanliness of intestinal pre-preparation. Excellent cleanliness can smoothly insert the colonoscopy, observe the mucosa and pathological tissues, and improve the detection rate and treatment success rate of intestinal diseases [18]. Intestinal cleanliness quality is closely related to many factors, including diet before examination, dosage and frequency of laxative, patient psychology, and disease status. At present, most studies at home and abroad focus on adult disease types, laxative selection and dosage, diet, and other aspects. Most scholars believe that liquid or semiliquid food should be eaten one day before the examination, and fasting should be required for 4 to 6 hours before the examination. Biopsy or treatment is not suitable for such patients, and a large number of samples are required for verification. However, domestic studies on the intestinal preparation of children are limited, especially in dietary control [19, 20]. Due to the gastrointestinal function development and dietary habits of children, the probability of colonoscopy is increasing year by year, and the demand for pediatric gastrointestinal preparation is increasing [21]. In this study, children who underwent colonoscopy were treated with different dietary controls and cathartic interventions, respectively, to observe the cleanliness, tolerance, and adaptability of intestinal preparation in each group.

There are many kinds of drugs for intestinal preparation before colonoscopy, and their combinations and uses are different. Due to the weak gastrointestinal function of children, medication and dose need to be improved. Shan *J* et al. [22] separately administered polyethylene glycol electrolytes to patients undergoing morning colonoscopy for intestinal prepreparation with a separate dose and a single dose, and BBPS scores in the separate dose group were significantly higher than those in the single dose group,

Table 3: Comparison of adverse reaction rate (cases, %).

Group	Group A ($n = 21$)	Group B ($n = 30$)	Group C ($n = 10$)	F	p
Nausea	1 (4.76)	2 (6.67)	0 (0.00)	—	—
Vomiting	0 (0.00)	1 (3.33)	1 (10.00)	—	—
Abdominal distension	2 (9.52)	2 (6.67)	0 (0.00)	—	—
Abdominal pain	2 (9.52)	1 (3.33)	1 (10.00)	—	—
Cold sweat	1 (4.76)	0 (0.00)	0 (0.00)	—	—
Heart palpitations	0 (0.00)	1 (3.33)	0 (0.00)	—	—
Dizzy	1 (4.76)	0 (0.00)	0 (0.00)	—	—
Incidence of adverse reactions	33.33%	23.33%	20.00%	1.214	0.001

Table 4: Comparison of tolerance and comfort (cases, %).

Group	Group A ($n = 21$)	Group B ($n = 30$)	Group C ($n = 10$)
I	8 (38.10)	13 (43.33)	5 (50.00)
II	7 (33.33)	10 (33.33)	3 (30.00)
III	6 (28.57)	7 (23.33)	2 (20.00)

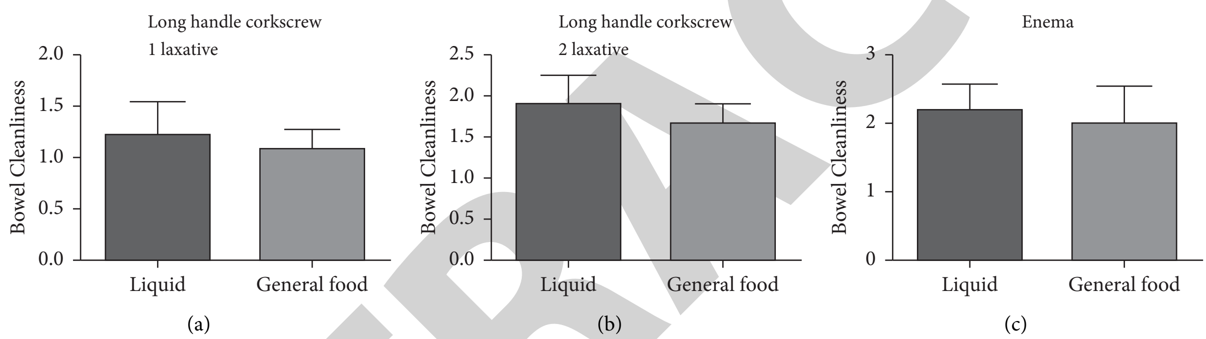

Figure 2: Comparison of BBPS scores of different dietary patterns (left: group A; middle: group B; right: group C; note: compared with liquid diet, $^{*}p < 0.05$; compared with group (C) ($^{*}p < 0.05$).

showing more significant tolerance and satisfaction. Gimeno-Garcia AZ et al. [23] believed that a low-residue diet was more conducive to improving intestinal cleanliness in patients undergoing colonoscopy during intestinal pre-preparation, especially the effect of liquid or semiliquid food intake one day before the examination was more significant. The results of this study showed that the colonoscopy time of group C was shorter than that of group A and group B; the BBPS score of group C (2.10 ± 0.32) was significantly higher than that of group A (1.16 ± 0.19) and group B (1.77 ± 0.18). The BBPS score of liquid diet was significantly higher than that of general diet in the three groups, and the BBPS score of liquid diet and general diet in group C was significantly higher than that in group A and group B. Similar to the study of Shan *J* and Gimeno-Garcia AZ, it indicated that taking liquid food, enema, and one laxative one day before colonoscopy had the most significant cleaning effect. Semifluid diet in intestinal preparation can drain the colon in a short time and does not cause changes in colonic protein, water electrolyte, and mucosa. In addition, it is necessary to meet the physiological needs of children, improve the cleanliness of the colon, and reduce the impact on colonoscopy. Enema combined with polyethylene glycol electrolyte can increase the osmotic pressure in the colon, have the advantages of being rapid and thorough, and reduce the colon empty time. At the same time, it will not cause electrolyte disorder in the field, reduce the intestinal examination time and discomfort of children, making it more suitable for children with intestinal fragility.

During intestinal preparation, different patients may experience adverse reactions such as nausea, abdominal distension, and cold sweat due to different physical signs, gastrointestinal function, and tolerance degree. In addition, due to the metabolic imbalance of the body itself, it will aggravate gastrointestinal dysfunction and affect the detection rate and treatment rate of microscopic lesions by colonoscopy. Chen *E* et al. [24] used low-residue food and no-residue food, respectively, for adenocarcinoma patients undergoing colon cancer examinations. The results showed that there was no significant difference in cleanliness between the two diets. The tolerance degree and fitness degree of patients with a low-residue diet were higher than those with a clear liquid diet, and the hunger of patients was reduced. Yokoi A et al. [25] applied olive oil enema for children with severe chronic constipation, and the results showed that olive oil had a significant lubrication effect and could treat most children with good results, with ideal tolerance effect and adaptability. The results showed that the incidence of adverse reactions in group C was significantly lower than that in group A and group B. The proportion of degree i in group C was significantly higher than that in group A and group B. Similar to the study of Chen *E* and Yokoi A, it indicated that children undergoing colonoscopy had a lower risk of adverse reactions and a higher tolerance and adaptability by eating dreg-free food, enema, and one laxative for intestinal preparation one day before the colonoscopy. As a commonly used laxative, Kaiselu is passed into the rectum through glycerin or sorbitol to soften the stool and stimulate the intestinal physiology to cause a defecation reaction. Glycerin will accompany lubrication, making it more conducive to defecation. However, carcerol can cause swelling and pain in the perianal mucosa in children and even stimulate the rectal mucosa, causing discomfort in children. Through warm water or physiological saline enema to promote physical absorption of water in the large intestine and maintain the body water and electrolyte balance. At the same time, can use pressure or chemical stimulation to promote spontaneous defecation and improve the coordination and tolerance of children.

5. Conclusion

In conclusion, children undergoing colonoscopy can eat liquid or semiliquid food 1d before the examination and take one enema and laxative bowel preparation to achieve ideal intestinal cleanliness, reduce the incidence of adverse reactions, improve the tolerance and adaptability of children, and provide a good intestinal environment for clinical examination and treatment. However, the following problems still exist in this study: the sample size is limited, so it is necessary to expand the sample size to explore its universality. The follow-up time is short, so it is necessary to observe the gastrointestinal injuries of children for a long time and adopt appropriate laxatives. The scope of the study is one-sided, and the influence of other factors of intestinal cleanliness on the experimental results should be discussed.

Data Availability

The data used to support the findings of this study are available from the corresponding author upon request.

Conflicts of Interest

The authors declare that they have no conflicts of interest.

Acknowledgments

This work was supported by Shanghai Jiaotong University.

References

[1] S. Cadoni, C. Hassan, L. Frazzoni, S. Ishaq, and F. W. Leung, “Impact of water exchange colonoscopy on endoscopy room efficiency: a systematic review and meta-analysis,” *Gastrointestinal Endoscopy*, vol. 89, no. 1, pp. 159–167, 2019.

[2] T. Thulin, U. Strömberg, A. Holmén, R. Hultcrantz, and A. Forsberg, “Sociodemographic changes in the population frequency of colonoscopy following the implementation of organised bowel cancer screening: an analysis of data from Swedish registers, 2006-2015,” *Journal of Medical Screening*, vol. 28, no. 3, pp. 244–251, 2021.

[3] H.-S. Chen, J.-F. Wu, H.-L. Chen, and Y.-H. Ni, “Does one-man method better than two-man method for colonoscopy insertion in children,” *Journal of the Formosan Medical Association*, vol. 118, no. 11, pp. 1546–1550, 2019.

[4] M.-K. A. Piegu, F. J. Yakubu, T. Kudese, and P. A. Fokuoh, “Effects of nordox 75 WG on the health quality of tomatoes,” *Science Progress and Research*, vol. 1, no. 3, pp. 113–120, 2021.

[5] W. J. Adams, A. P. M Ea Gher, D. Z. Lubowski, and D. W. King, “Bisacodyl reduces the volume of polyethylene glycol solution required for bowel preparation,” *Diseases of the Colon & Rectum*, vol. 37, no. 3, pp. 229–233, 2019.

[6] M. E. Bizri, M. E. Sheikh, G. E. Lee, and M. J. Sewitch, “Mobile health technologies supporting colonoscopy preparation: a systematic review and meta-analysis of randomized controlled trials,” *PLOS ONE*, vol. 16, no. 3, pp. 248679–248685, 2021.

[7] R. Hayashida, K. Tsuchiya, S. Nakamura et al., “Acute kidney injury with hemolysis after glycerin enema-induced rectal injury in a patient with type 2 diabetes,” *Internal Medicine*, vol. 59, no. 13, pp. 1659–1663, 2020.

[8] A. Peña, L. De La Torre, J. Belkind-Gerson, M. Lovell, J. Ketzer, and J. Bealer, “A Bischoff Enema-Induced spastic left colon syndrome: an unintended consequence of chronic enema use,” *Journal of Pediatric Surgery*, vol. 56, no. 2, pp. 424–428, 2021.

[9] F. Mocciaro, B. Magro, E. Conte, A. Bonaccorso, D. Scimeca, and R. Di Mitri, “P129 Endoscopy and inflammatory bowel disease: data from a pilot experience to investigate the gap between the current guidelines and the real clinical practice,” *J Crohn’s Colitis*, vol. 26, no. 1, pp. 2192–2198, 2019.

[10] S. P. Nordt, K. J. Won, C. Tomaszweski, and R. F. Clark, “Polyethylene glycol electrolyte lavage solution increases tablet dissolution of acetaminophen in an in vitro model mimicking acute poisoning,” *The American Journal of Emergency Medicine*, vol. 38, no. 2, pp. 325–328, 2020 Feb.

[11] Y. H. Tam, K. H. Lee, and K. W. Chan, “Colonoscopy in Hong Kong Chinese children,” *World Journal of Gastroenterology*, vol. 16, no. 9, pp. 1119–1122, 2010.

[12] Digestive, Endoscopy, and Special, “Chinese guideline for bowel preparation for colonoscopy (2019, Shanghai),” *Zhonghua Nei Ke Za Zhi*, vol. 58, no. 7, pp. 485–495, 2019.

[13] E. J. Lai, A. H. Calderwood, and G. Doros, “The Boston bowel preparation scale: a valid and reliable instrument for colonoscopy-oriented research,” *Gastrointestinal Endoscopy*, vol. 69, no. 32, pp. 620–625, 2009.

[14] H. Zhou, X. Zhang, and J. Yang, “Correlation of cleanliness among different bowel segments during colonoscopy: a retrospective study,” *Gastroenterol Res Pract*, vol. 26, no. 3, pp. 1–8, 2020.

[15] R. Fushimi, M. Takashina, H. Yoshikawa et al., “Comparison of adenosine triphosphate, microbiological load, and residual protein as indicators for assessing the cleanliness of flexible gastrointestinal endoscopes,” *American Journal of Infection Control*, vol. 41, no. 2, pp. 161–164, 2013.

[16] S. L. Eswaran, D. A. Howell, M. K. Sanders et al., “Factors predicting uncomfortable colonoscopy: pre-procedure selection criteria for sedation,” *Gastrointestinal Endoscopy*, vol. 63, no. 5, pp. 2304–2311, 2006.

[17] G. Kaur, Garima, and S. Sharma, “Functional matrix hypothesis: a review of literature,” *SPR*, vol. 1, no. 2, pp. 33–42, 2021.

Hindawi
Journal of Healthcare Engineering
Volume 2023, Article ID 9852613, 1 page
https://doi.org/10.1155/2023/9852613

Retraction

Retracted: Evolution of Oncology and Palliative Nursing in Meeting the Changing Landscape of Cancer Care

Journal of Healthcare Engineering

Received 23 May 2023; Accepted 23 May 2023; Published 24 May 2023

This article has been retracted by Hindawi following an investigation undertaken by the publisher [1]. This investigation has uncovered evidence of one or more of the following indicators of systematic manipulation of the publication process.

(1) Discrepancies in scope
(2) Discrepancies in the description of the research reported
(3) Discrepancies between the availability of data and the research described
(4) Inappropriate citations
(5) Incoherent, meaningless and/or irrelevant content included in the article
(6) Peer-review manipulation

The presence of these indicators undermines our confidence in the integrity of the article's content and we cannot, therefore, vouch for its reliability. Please note that this notice is intended solely to alert readers that the content of this article is unreliable. We have not investigated whether authors were aware of or involved in the systematic manipulation of the publication process. Wiley and Hindawi regrets that the usual quality checks did not identify these issues before publication and have since put additional measures in place to safeguard research integrity.

We wish to credit our own Research Integrity and Research Publishing teams and anonymous and named external researchers and research integrity experts for contributing to this investigation.

The corresponding author, as the representative of all authors, has been given the opportunity to register their agreement or disagreement to this retraction. We have kept a record of any response received.

References

[1] K. Zhou and J. Fu, "Evolution of Oncology and Palliative Nursing in Meeting the Changing Landscape of Cancer Care," *Journal of Healthcare Engineering*, vol. 2022, Article ID 3831705, 8 pages, 2022.

Hindawi
Journal of Healthcare Engineering
Volume 2022, Article ID 3831705, 8 pages
https://doi.org/10.1155/2022/3831705

Review Article

Evolution of Oncology and Palliative Nursing in Meeting the Changing Landscape of Cancer Care

Kaiping Zhou and Jing Fu

School of Nursing, Southwest Medical University, Luzhou 646000, China

Correspondence should be addressed to Jing Fu; jingfu_edu@126.com

Received 18 February 2022; Accepted 24 March 2022; Published 16 April 2022

Academic Editor: Liaqat Ali

Nursing is a vital health profession. In almost all clinical and hospital settings, nurses offer primary palliative care. Nurses are recognized for their strong philosophy of care for a wide spectrum of disorders. No matter the sickness, condition, or clinical situation, palliative care is considered essential in nursing practice. Palliative care nursing is the provision of palliative care services to cancer patients and their families, regardless of whether cancer can be cured or not. A large body of evidence shows that early palliative care nursing integration improves the quality of life and survival of cancer patients. Due to the intricacy of cancer, the landscape of cancer care is shifting. Cancer is a life-threatening disease with a high mortality rate. Oncology nurses' skills and experience are vital in providing specialized patient care and fulfilling the needs of patients and their families. The current study examines the shifting environment of palliative care nursing in oncology. However, new palliative care nursing approaches are required to adapt to the evolving cancer scenario.

1. Introduction

An illness always needs proper caring along with the treatment course to improve patient's life quality throughout the period of illness [1]. The centred care provided by the family members and caregivers of the patient to relieve stress, anxiety, and ease the signs and symptoms, while suffering from a life-threatening illness is called palliative care [2, 3]. Palliative care is a measurable and most important factor to bring ease in life and pleasure before the end of life in patient's life suffering from severe illness. The major modules of palliative care are physical, spiritual, social, psychological, and proper guidance to family members for making the right decisions about patient's illness [4].

The provision of palliative care together with therapy of the disease is crucial from the diagnosis to the life-threatening conditions. Nurse is an ideal role model, who provides palliative care to the patient, reducing emotional and psychological burden of the patient and the family members of the patient. Comprehensive palliative care recognizes the end of life as natural death and delivers sociological care to reduce the patient and family discomfort. Cancer is one of the most lethal types of diseases, causing a majority of deaths worldwide and putting severe discomfort inpatients' lives and family members. It is characterized by the irregular and rapid growth of immature cells that occur in different types of cells and tissues, and such cells are circulated in the blood and spread to other distant sites and organs, thereby causing metastases. Cancer is a chronic disease that has the highest mortality rate, and its treatment is long and troublesome for patients, family, caregivers, doctors, and other healthcare professionals. However, current treatment technology is providing the best therapeutic resources, but still palliative care benefits are crucial and significant for patients and their family members [4]. Among the cancer population, profound demographic shifts are contributing to an increasingly elderly and diverse cancer population. The number of people suffering from cancer at age of 65 and older is expected to be double from 48 million to 85 million in 2050 [5, 6].

The increasing cancer population will face multiple changes regarding the treatment course and high-paid cost for the treatment, as well as exceedingly high-level discomfort, anxiety, and psychosocial issues [7]. All these issues are concerned with proper cancer care, which has also high-cost share along with this course [8]. Such a high expense may increase the burden of cancer care and treatment that may be beyond the affordable range for patients and family members. The patients may feel a severe economic burden, which may lead to emotional and spiritual discomfort [9, 10]. The cancer patients often acquire multiple chronic conditions, requiring extensive and expensive palliative care services [11, 12]. So, this poses challenges because cancer acquires multiple chronic conditions that need long and intensive care to increase the average survival and improve patient's life quality [13].

In high-quality caring of cancer patients, family caregivers have also a crucial role [14]. In general, for cancer patients' longer survival, their family caregivers like relatives, friends, and neighbours provide quality care without being paid for these services. These caregivers are responsible managers during cancer treatment, as they manage side effects from both cancer and treatment, even having no professional experiences. At the same time, they offer extraordinary emotional spirit to the cancer patient [15, 16]. Research studies declared that caregivers often experience a huge burden while caring for the cancer patients [17]. Nurses are the prime heathcare professionals, who offer bedside care to cancer patients and can effectively engage the family caregivers in caring for the cancer patients. Nursing practice is very significant in the establishment of the relationship between patients, family, and caregivers. The palliative care nursing is the philosophical and comprehensive care, which is deeply expressed in palliative care policy, research, and practice [18]. Palliative care offered by nurses to the cancer patients is considered a hope of change in lives of cancer patients since last decade [19]. Palliative care nursing is the mainstream healthcare service for cancer patients, which assures that how, when, where, and to whom the palliative care should be provided [20, 21].

The main therapeutic model proposed by healthcare professional is the treatment or surgical removal of pathology, which resulted in manifestation, and dominating strategy for individual's health recovery [22]. The emergence of the palliative care nursing in this strategy may lead to help the faster recovery of individual's health by approaching patient's care in the sense of health, psychological issues, emotional, and spiritual aspects of patient and family. So, the cancer patients not only need treatment and management but also need palliative care nursing, and the need of palliative care nursing is also crucial and can be an emerging factor to improve life quality of the individuals with a life-limiting illness like terminal cancer [23, 24]. Furthermore, the increase in deaths of aged population due to cancer even with the availability of improved treatment options is another challenging issue for palliative care nursing for the provision of care [25, 26]. However, malignant illness always has a lot of expenditure and the provision of palliative care nursing can expand the cost [27], but still the palliative care nursing has crucial role in the improvement of life quality of cancer patients and has the emerging landscape in oncology. Additionally, the investigation revealed that the introduction of palliative care has valuable improvement in the early phase of illness when disease diagnosis is confirmed, rather than in those patients who receive standard treatment and care at the late phase of the disease or illness [28]. The practice of palliative care becomes more broadened with the advancement in all aspects and leads to a disconnection between policy and practice [29] and confusion about the provision of palliative care.

We searched PubMed and Web of sciences using the terms "Palliative care," "Nursing," "oncology," and "Cancer care." We included only English literature and excluded abstract and conferences papers. The current work describes the changing landscape and concept of palliative care nursing for cancer patients with increased mortality and morbidity. This work can be useful for the reader to understand the role of palliative care nursing while treating and caring for the cancer patients, where palliative care nursing can play a surprising role to improve the patient's life quality and provide an ease to the family members and caregivers.

2. Palliative Care and Cancer

Conferring to World Health Organization (WHO), palliative care can be described as "the overall needs for care services to the patients where patient's treatment is of prime importance together with emotional, mental, and physical care," where the primary goal is to achieve ease of life for patients and family members resulting in improved quality of life for the individuals suffering from life-terminating diseases like cancer [30]. However, the actual purpose and sense of the palliative care is still debatable and known with little evidences. Palliative care is thought to be an indicator of the patient quality of care and improvements in life quality [31]. Previously, without the provision of palliative care the death or disease complications were thought to be the biological indicators. Currently, due to the discovery of health monitoring apparatuses, the significance of palliative care can be reflected as the quality of care can be monitored with such instruments. In this way, the importance and outcomes of palliative care can be explored. Palliative care nursing in oncology is the integration of cancer-directed care along with the whole course of the disease condition, regardless of cancer stages, therapeutic options (chemotherapy, radiotherapy, or surgery), and other clinical complications [31, 32].

Palliative care nursing plays a unique and very important role in the provision of palliative care to cancer patients, which realize complete potential of treatment to patients and their families whether it can be treated or not. Palliative care nursing provided to cancer patients can specifically address the issues like symptomatic control, psychological and social care, ease of communication for patient, ease in making serious decisions, and care at the terminal stage of cancer. The United Kingdom had been declared palliative care, a significant component of cancer care and treatment [32–34]. A huge content of records justifies that the integration of early palliative care nursing results in the improvement of life quality and improved survival of cancer patients [35–37].

The palliative care improves the outcomes of caregivers and helps in reducing the adverse sides of chemotherapeutics at the terminal stage of cancer [36, 38–41]. In the light of these outcomes, palliative care nursing models have been developed and applied in a large number of cancer hospitals and oncology care centres around the globe [42, 43], but even though with huge benefits and paramount understanding only a small number of cancer patients are integrated for palliative care and those are often suffering from the late stage of cancer [44]. The lack of feasible palliative care services and care models is a great challenge for both inpatients and outpatients [44]. Deep and comprehensive institutional efforts are required for the multidimensional cancer care and specialized palliative care services.

Previously, an investigational survey made in the United States had been revealed that twelve percent of the total cancer care centres had no palliative care programs, twenty-seven percent of the centres had no physician specialist for the palliative care services, twenty-six percent of the total did not have palliative care taskforce (nurses and physicians) for the inpatients, and seventy-seven percent among them did not have specified beds and units for palliative care [44]. And thirty percent of the centres in this survey possessed combined clinics for oncology and palliative care, where the nature and direction of the setting were unknown [44]. There was unpredictable palliative cancer care in most of the settings, where the implementation of beneficial interventions was in-applicable and standards were not meeting the minimum criterion to recognize the benefits. The limited resources and high-cost burden in almost all institutions were the main reasons that could not display palliative care services in oncology units, where proper management of the palliative care and oncology was surprisingly needed [44].

These investigations prove that in the United States, there are huge deficiencies in specialized palliative care nursing staff for oncology clinics, and there are deficiencies of regulatory authorities to promote palliative care services for cancer patients, and workforce for palliative care services is required to meet the needs of patient's care. Proper legislation is strongly demanded around the globe for the promotion of palliative care nursing in oncology hospitals and institutes. However, several countries have been incorporated palliative care into the common cancer treatment regimen, while the United States has been also taken serious decisions about integrating the palliative care services as a compulsory part of comprehensive cancer treatments [45, 46]. The American Society of Clinical Oncology (ASCO) has detailed that eminence cancer care "requires access to and the availability of state-of-the-art palliative cancer care rendered by skilled clinicians, buttressed when necessary by palliative care experts" [47]. Realizing this prophecy will need the expansion of a service model that is cost-effective and freely reachable to patients in a range of care settings.

The needs of palliative care nursing are increased day by day worldwide, with the increasing population diagnosed with cancer and its complexity [48, 49]. The demanding palliative care needs suggest comprehensive models for palliative care nursing especially for cancer patients [50]. Nurses are the one who can resolve the palliative care issue for cancer patients in more smooth and reliable way. At present, there are no cancer palliative care-related courses in nursing education (both undergraduate and graduate). In the light of this context, special contents about palliative care should be integrated into the oncology centres and nursing education programmes, which can play mighty role in cancer treatment [51]. However, the nurses practising in other departments rather than oncology may lack expertise of caring cancer patients [52].

Therefore, nurses practising in other departments may need special education and training for palliative care nursing to work in oncology wards and departments. It is an unmet and empirical need to develop strategies and agendas for palliative care nursing to cover the demanding and complex needs of cancer patients, where the nurses should be educated (college, undergraduate, and graduate levels) regarding the intake of oral targeted oncodrugs, caring and advocating of patients, and their family members [53, 54]. As the national organization for oncology nurses, in 2001 CANO/ACIO developed Standards of Care focused on patients. Subsequently, in 2006, CANO/ACIO developed Practice Standards and Competencies for the Specialized Oncology Nurse. The emphasis of these standards and competencies was primarily on specialized oncology nursing practice [54]. Professional nurses have been recognized the gaps while educating nurses for palliative care nursing in oncology departments, so smooth and clear framework for palliative care nursing can be implemented in hospitals. The developed framework provides guidance to nurses working in all practice settings assuring the provision of high-quality services and care to patients living with cancer and those at the stage of end of life. The well-trained nursing community can indeed reduce the burden of cancer globally [53, 54].

There is an empirical need of cancer knowledge for the nurses who are caring for the cancer patients and dealing with their families. Due to huge increase in the number of patients suffering from cancer, a number of patients are considered as outpatients; therefore, nurses may the patients and families regardless of the setting in inpatients or outpatients.

3. Palliative Nursing in Changing Landscape of Cancer Care

The landscape of cancer care is changing and becoming more complex due to the complexity of cancer. In fact, cancer is a life-threatening disease and has a high rate of end-of-life conditions. Nevertheless, inpatients have increased emergence in the cancer hospitals for surgery, diagnosis, chemotherapy, symptomatic treatment, and palliative care, so the landscape of cancer care changed with the changing dimensions of cancer treatment and care towards outpatients [54]. The knowledge and experience of the oncology nurses play important roles in specialized patient care and meeting the care services of patient's care and their families. The Canadian Cancer Society's Advisory Committee on Cancer Statistics (2015) approximations demonstrated that nearly half of whole Canadian populations will develop cancer in their lifetime and approximately 25% of that will die of the disease.

The rapid increase in the cancer patients over last few decades is because of the increasing population, aging, and advancement in the diagnostic procedures. This rapid increase is expected to be continued and may become double in the future decade [53, 54]. With the increasing cancer ratio, palliative care nursing in oncology will also face challenges and need special attentions of the concern departments and policymakers. Nurses in oncology unit secure both physical and mental care of inpatients [55]. Care attitudes necessitate addressing the physical, psychological, social, and spiritual healthcare essentials of cancer patients and their families.

Moreover, the direction of palliative care nursing can be demonstrated as "reducing the pain of cancer and care provision to improve the life quality of the patients, and support for the best possible ways to increase the patient's survival..." [56]. The nurses working in oncology departments can recognize various factors such as systematic therapeutics plans, care services plan, patient's needs, complexity of the illness, contact with patients and family members, emotional attachment with patients who are in the terminal phase of cancer, and facing end-of-life stress [57, 58]. However, there is an inadequate investigation of the experiences of oncology nurses. One example, a hermeneutic study was carried out to describe the experience of oncology nurses caring for dying patients [59]. In-depth interviews were conducted with six oncology nurses who had at least five years of oncology nursing experience and had cared for dying patients. Four themes were described as follows: (1) "knowing the patient," (2) "preserving hope," (3) "easing the struggle," and (4) "providing for privacy." The investigators determined that nurses accomplished the emotional demands of their work by establishing varying degrees of closeness with patients as they were dying. The nurses described developing close bonds with some patients and, despite not developing these relationships with all patients, they felt they provided good care for those who were dying.

4. Palliative Care Nursing Models in Oncology

There are various palliative care nursing models developed for the care provision to cancer patients and still continued to be developed for the large cancer population including paediatrics, geriatrics, and adult cancer patients. These various models differ in planning, organizing, and focus. However, all of them rely on oncology nurse, and in all models, oncology nurse is the key provider of palliative care to the patients and their families [60–62]. All the models are explained in Figure 1 concisely with their imperative focus.

Although having direct contact with cancer patients and with the presence of a number of palliative care programs, there is an urgent and unmet need of educational and training programs for oncology nurses to provide quality palliative care to the patients suffering with life-threatening cancer diseases. Different types of palliative care nursing are listed and explained below.

4.1. Paediatric Long-Term Follow-Up Models. These programmes comprise "late effects clinics" inside children's clinics or hospitals. It was developed for the paediatric cancer patients and was an initiation towards adult's oncology models [64, 65]. The continuous follow-up is recommended in this model to expand the understanding of cancer effects; otherwise, it may develop second cancers. These clinical programmes are not disease-specific and often need multidisciplinary oncology nurse for palliative care servicer.

4.2. Adult Follow-Up Clinic Models. In various adult clinical models, oncology nurse is a key provider of the care services. They may work together with other healthcare teams and may work independently. In this context, the care services need of patients and family members or fulfilled in either national hearth institutes or private clinical settings.

4.3. Disease-Specific Model. Initially, when clinical models were started to develop, clinical programmes were established for the early diagnosis and the provision of care services before treatment of the breast cancer. The oncology nurse not only has the responsibility of palliative care provision but also needs to identify early problems and symptoms. This model is costly enough and may increase the total burden on the family members [66].

4.4. General Survivorship Clinic Model. It is noteworthy that the palliative care nursing cannot be implied in disease-specific clinical settings in most of the cases. Instead, palliative care can be provided in generalized clinical or institutional settings. Such programmes may be staffed by oncology nurse in collaboration with oncologist. In such settings, particular treatment plan is designed by oncologist, oncology nurse, and other healthcare team members. Further care services are provided upon investigation and family member recommendations [67, 68].

4.5. Consultative Clinic Model. In these types of models, patients together with the family members only visit the clinic or hospital once. Comprehensive check-up is proceeded with the continuation of the ongoing palliative care. In such programmes, oncology nurse prepared detailed treatment plan and care summary for the patient and family members. The oncology nurse discusses the improvements in health with the patients and also aware them about the prevention of cancer by quitting bad habits such as smoking, diet, and use of alcohol. Oncology nurses also compel them to exercise and healthy habits. This type of programmes is very simple and cost-effective and can be widely applied [67, 69].

4.6. The Multidisciplinary Clinic Model. It was the earliest applied models and was used in paediatric clinics and oncology units. Although this is a significant model from theoretical point of view, it is not practical in the cancer

FIGURE 1: Various palliative care nursing models for cancer patients [63].

institutes and hospitals because it extremely challenging to provide multidisciplinary care service to the patients at the same place in the same clinics. With changing landscape of oncology, it becomes more difficult to provide care services to patients and apply these models.

4.7. The Integrated Care Model. The increasing complexity of cancer and its changing landscape are noteworthy to identify the type of best palliative care model for cancer patients to improve care services and save the workload. In this model, the formal visits of oncology nurse and oncology team are made. The patients in this model are in the supervision of oncology nurse receiving care and treatment at the same place. In this model, oncology nurse provides palliative care services even when the treatment ends and patient is on maintenance therapy. In this model, routine follow-up is made by oncology nurses and family members are given with proper information and understanding about the disease condition and care service [67, 69].

5. Transition to Primary Care

The care needs of cancer patients are challenging for family members, where oncology nurse plays a key role in care provision, as well as making positive contact with the family members of the patients. The patients not only need care services in the cancer institutes but also need care services after the termination of treatment. So, the primary care providers in homes (family members and caregivers) must be educated with proper information about care and symptoms. In such situation, oncology nurse together with oncology team or in collaboration with oncology team can give guidelines about the primary care and disease symptoms. Hence, strong communication between oncology nurse, patients, family member, and primary care provider is always demanded [70, 71].

6. Conclusion and Future Perspective

The current study emphasizes the wide role of oncology nurses in palliative care, which encircles the key and major contribution of nurses. In oncology hospitals and clinics, the philosophy of palliative care has a major conflict with nursing practice. The palliative care nursing can be understandable when experienced it in specific illness and nursing theory comprehensively supports it. Nurses are well trained and aware of the pathophysiology and required skills to evaluate the patients' needs of care in all domains of life, giving hope of life to the patients suffering from life-threatening illness like cancer. However, it should be comprehended that with the changing landscape of cancer, palliative care nursing is facing many challenges and needs special attention to fulfil the care needs of the patients in oncology units and clinics. Nurses secure central position in providing palliative care to the patients and their family members. The direct contact with patients, family members, and caregivers makes them able to provide mental, social, emotional and physical care, and support. As with changing landscape of oncology, the needs of cancer patients are changing; therefore, nurses need to adopt with the changing healthcare needs of the patients and their families. The development of more unique palliative care nursing models is needed to cope with the changing landscape of cancer.

Data Availability

All the data are included in the paper.

Conflicts of Interest

The authors declare no conflicts of interest.

References

[1] A. H. Kamal, C. Bausewein, D. J. Casarett, D. C. Currow, D. J. Dudgeon, and I. J. Higginson, "Standards, guidelines, and quality measures for successful specialty palliative care integration into oncology: current approaches and future directions," *Journal of Clinical Oncology*, vol. 38, no. 9, pp. 987–994, 2020.

[2] W. E. Rosa, A. Parekh de Campos, N. C. Abedini et al., "Optimizing the global nursing workforce to ensure universal palliative care access and alleviate serious health-related suffering worldwide," *Journal of Pain and Symptom Management*, vol. 63, no. 2, pp. e224–e236, 2022.

[3] National Hospice and Palliative Care Organization (NHPCO), "NHPCO's Facts and Figures: Pediatric Palliative & Hospice Care in America," 2015, https://www.nhpco.org/sites/default/fles/public/quality/Pediatric_FactsFigures.pdf.

[4] A. D. R. S. E. Sousa, L. F. D. Silva, and E. D. Paiva, "Nursing interventions in palliative care in Pediatric Oncology: an integrative review," *Rev Bras Enferm [Internet]*, vol. 72, no. 2, pp. 531–540, 2019.

[5] United States Census Bureau, "Population Projections," 2015, http://www.census.gov/population/projections/data/national/2012/summarytables.html.

[6] H. K. Weir, T. D. Thompson, S. L. Stewart, and M. C. White, "Cancer incidence projections in the United States between 2015 and 2050," *Preventing Chronic Disease*, vol. 18, p. E59, 2021.

[7] The Henry J. Kaiser Family Foundation, "Health Care Costs: A Primer," 2016, http://kff.org/health-costs/issue-brief/health-care-costs-a-primer/.

[8] A. B. Mariotto, K. Robin Yabroff, Y. Shao, E. J. Feuer, and M. L. Brown, "Projections of the cost of cancer care in the United States: 2010-2020," *JNCI Journal of the National Cancer Institute*, vol. 103, no. 2, pp. 117–128, 2011.

[9] R. C. Young, "Value-based cancer care," *New England Journal of Medicine*, vol. 373, no. 27, pp. 2593–2595, 2015.

[10] M. O. Owolabi, A. G. Thrift, A. Mahal et al., "Primary stroke prevention worldwide: translating evidence into action," *The Lancet Public Health*, vol. 7, no. 1, pp. e74–e85, 2022.

[11] G. Anderson, *Chronic Care: Making the Case for Ongoing Care*, Robert Wood Johnson Foundation, Princeton, NJ, 2010.

[12] S.-K. H. Bøhn, H. C. Lie, K. V. Reinertsen et al., "Lifestyle among long-term survivors of cancers in young adulthood," *Supportive Care in Cancer*, vol. 29, no. 1, pp. 289–300, 2021.

[13] C. B. Warinner, R. W. Bergmark, R. Sethi, and E. M. Rettig, "Cancer-related activity limitations among head and neck cancer survivors," *The Laryngoscope*, vol. 132, no. 3, pp. 593–599, 2022.

[14] Institute of Medicine, *Delivering High-Quality Cancer Care: Charting a New Course for a System in Crisis*, The National Academies Press, Washington DC, USA, 2013.

[15] S. C. Reinhard, C. Levine, and S. Samis, *Home Alone: Family Caregivers Providing Complex Chronic Care*, AARP Public Policy Institute, Washington DC, USA, 2012.

[16] B. A. Given and C. W. Given, "Caregiving for patients with cancer," in *The Spectrum of Family Caregiving for Adults and Elders with Chronic Illness*, L. D. Burgio, J. E. Gaugler, and M. M. Hilgeman, Eds., Oxford University Press, New York, USA, pp. 86–117, 2016.

[17] S. Priya, G. Shavi, R. Sanga et al., "Assessment of the perceived stress and burden of family caregivers of the head-and-neck cancer patients at a tertiary care cancer center: a cross-sectional study," *Journal of Cancer Research and Therapeutics*, vol. 17, no. 4, pp. 1039–1046, 2021.

[18] M. Matzo, D. W. Sherman, and T. Metheny, "The inter professional practice of palliative care nursing," in *Palliative Care Nursing: Quality Care to the End of Life*, M. Matzo and D. W. Sherman, Eds., Springer Publishing Company, London, United Kingdom, 4 edition, 2015.

[19] D. Clark, F. Graham, and C. Centeno, "Changes in the world of palliative care," *Medicine*, vol. 43, no. 12, pp. 696–698, 2015.

[20] K. J. Llamas, A. M. Pickhaver, and N. B. Piller, "Mainstreaming palliative care for cancer patients in the acute hospital setting," *Palliative Medicine*, vol. 15, no. 3, pp. 207–212, 2001.

[21] H. G. Buck and C. H. Zambroski, "Upstreaming palliative care for patients with heart failure," *Journal of Cardiovascular Nursing*, vol. 27, no. 2, pp. 147–153, 2012.

[22] D. T. Wade and P. W. Halligan, "Do biomedical models of illness make for good healthcare systems?" *BMJ*, vol. 329, no. 7479, pp. 1398–1401, 2004.

[23] T. Pastrana, S. Jünger, C. Ostgathe, F. Elsner, and L. Radbruch, "A matter of definition - key elements identified in a discourse analysis of definitions of palliative care," *Palliative Medicine*, vol. 22, no. 3, pp. 222–232, 2008.

[24] J. Seymour, D. Clark, P. Bath et al., "Clinical nurse specialists in palliative care. Part 3. Issues for the Macmillan Nurse role," *Palliative Medicine*, vol. 16, no. 5, pp. 386–394, 2002.

[25] M. Gott, C. Ingleton, M. I. Bennett, and C. Gardiner, "Transitions to palliative care in acute hospitals in England: qualitative study," *BMJ*, vol. 342, p. d1773, 2011.

[26] J. T. V. D. Steen, N. L. Dekker, M.-J. H. E. Gijsberts, L. H. Vermeulen, M. M. Mahler, and B. A.-M. The, "Palliative care for people with dementia in the terminal phase: a mixed-methods qualitative study to inform service development," *BMC Palliative Care*, vol. 16, no. 1, p. 28, 2017.

[27] W. H. Lewin and K. G. Schaefer, "Integrating palliative care into routine care of patients with heart failure: models for clinical collaboration," *Heart Failure Reviews*, vol. 22, no. 5, pp. 517–524, 2017.

[28] J. S. Temel, J. A. Greer, A. Muzikansky et al., "Early palliative care for patients with metastatic non-small-cell lung cancer," *New England Journal of Medicine*, vol. 363, no. 8, pp. 733–742, 2010.

[29] M. Gott, J. Seymour, C. Ingleton, C. Gardiner, and G. Bellamy, "'That's part of everybody's job': the perspectives of health care staff in England and New Zealand on the meaning and remit of palliative care," *Palliative Medicine*, vol. 26, no. 3, pp. 232–241, 2012.

[30] D. Doyle, "Editorial," *Palliative Medicine*, vol. 17, no. 1, pp. 9-10, 2003.

[31] H. F. Treurniet, M.-L. Essink-Bot, J. P. Mackenbach, and P. J. V. D. Maas, "Health-related quality of life: an indicator of quality of care?" *Quality of Life Research*, vol. 6, no. 4, pp. 363–369, 1997.

[32] G. Miccinesi, A. Caraceni, F. Garetto et al., "The path of cicely saunders: the "peculiar beauty" of palliative care," *Journal of Palliative Care*, vol. 35, no. 1, pp. 3–7, 2020.

[33] T. J. Smith, S. Temin, E. R. Alesi et al., "American Society of Clinical Oncology provisional clinical opinion: the integration of palliative care into standard oncology care," *Journal of Clinical Oncology*, vol. 30, no. 8, pp. 880–887, 2012.

[34] A. El-Jawahri, J. A. Greer, and J. S. Temel, "Does palliative care improve outcomes for patients with incurable illness? A review of the evidence," *Journal of Supportive Oncology*, vol. 9, no. 3, pp. 87–94, 2011.

[35] M. Bakitas, K. D. Lyons, M. T. Hegel et al., "Effects of a palliative care intervention on clinical outcomes in patients with advanced cancer," *JAMA*, vol. 302, no. 7, pp. 741–749, 2009.

[36] J. S. Temel, J. A. Greer, A. Muzikansky et al., "Early palliative care for patients with metastatic non-small-cell lung cancer," *New England Journal of Medicine*, vol. 363, no. 8, pp. 733–742, 2010.

[37] A. A. Wright, B. Zhang, A. Ray et al., "Associations between end-of-life discussions, patient mental health, medical care near death, and caregiver bereavement adjustment," *JAMA*, vol. 300, no. 14, pp. 1665–1673, 2008.

[38] R. Kane, L. Bernstein, J. Wales, A. Leibowitz, and S. Kaplan, "A randomised controlled trial of hospice care," *The Lancet*, vol. 323, no. 8382, pp. 890–894, 1984.

[39] M. S. Jordhoy, P. Fayers, J. H. Loge, M. Ahlner-Elmqvist, and S. Kaasa, "Quality of life in palliative cancer care: results from a cluster randomized trial," *Journal of Clinical Oncology*, vol. 19, no. 18, pp. 3884–3894, 2001.

[40] E. Bruera and C. Sweeney, "Palliative care models: international perspective," *Journal of Palliative Medicine*, vol. 5, no. 2, pp. 319–327, 2002.

[41] K. Muszbek, "Enhancing Hungarian palliative care delivery," *Journal of Pain and Symptom Management*, vol. 33, no. 5, pp. 605–609, 2007.

[42] E. McDermott, L. Selman, M. Wright, and D. Clark, "Hospice and palliative care development in India: a multimethod review of services and experiences," *Journal of Pain and Symptom Management*, vol. 35, no. 6, pp. 583–593, 2008.

[43] D. Hui, A. De La Rosa, J. Chen et al., "Palliative care education and research at US cancer centers: a national survey," *Cancer*, vol. 127, no. 12, pp. 2139–2147, 2021.

[44] UICC, "The Refreshed World Cancer Declaration," http://www.uicc.org/refreshed-world-cancerdeclaration.

[45] F. D. Ferris, E. Bruera, N. Cherny et al., "Palliative cancer care a decade later: accomplishments, the need, next steps-from the American society of clinical oncology," *Journal of Clinical Oncology*, vol. 27, no. 18, pp. 3052–3058, 2009.

[46] E. Bruera and D. Hui, "Integrating supportive and palliative care in the trajectory of cancer: establishing goals and models of care," *Journal of Clinical Oncology*, vol. 28, no. 25, pp. 4013–4017, 2010.

[47] D. L. Berry, F. Hong, B. Halpenny et al., "Electronic self-report assessment for cancer and self-care support: results of a multicenter randomized trial," *Journal of Clinical Oncology*, vol. 32, no. 3, pp. 199–205, 2014.

[48] K. Bilodeau, D. Tremblay, and M. J. Durand, "Gaps and delays in survivorship care in the return-to-work pathway for survivors of breast cancer—a qualitative study," *Current Oncology*, vol. 26, no. 3, 2019.

[49] M. G. Saria, A. Nyamathi, L. R. Phillips et al., "The hidden morbidity of cancer," *Nursing Clinics of North America*, vol. 52, no. 1, pp. 159–178, 2017.

[50] S. Shakeel, J. Tung, R. Rahal, and C. Finley, "Evaluation of factors associated with unmet needs in adult cancer survivors in Canada," *JAMA Network Open*, vol. 3, no. 3, Article ID e200506, 2020.

[51] A. Charalambous and C. Kaite, "Undergraduate nursing students caring for cancer patients: hermeneutic phenomenological insights of their experiences," *BMC Health Services Research*, vol. 13, no. 63, 2013.

[52] Canadian Nurses Association, "Advanced Practice Nursing, A Pan-Canadian Framework. Canadian Nurses Association," 2019, https://cna-aiic.ca/-/media/cna/page-content/pdf-en/apn-a-pan-canadian-framework.pdf?la=en&hash=E1387634D492FD2B003964E3CD4188971305469E.

[53] J. B. Reese, L. S. Porter, K. R. Regan et al., "A randomized pilot trial of a telephone-based couples intervention for physical intimacy and sexual concerns in colorectal cancer," *Psycho-Oncology*, vol. 23, no. 9, pp. 1005–1013, 2014.

[54] A. Bonacchi, G. Miccinesi, S. Galli et al., "Use of the needs evaluation questionnaire with cancer outpatients," *Supportive Care in Cancer*, vol. 24, no. 8, pp. 3507–3515, 2016.

[55] C. E. Sullivan, A. R. King, J. Holdiness et al., "Reducing compassion fatigue in inpatient pediatric oncology nurses," *Oncology Nursing Forum*, vol. 46, no. 3, pp. 338–347, 2019.

[56] D. Heidrich, "Palliative care," in *Oncology Nursing*, M. E. Langhorne, J. S. Fulton, and S. E. Otto, Eds., pp. 602–619, Elsevier, Amsterdam, Netherland, 5th edition, 2007.

[57] E. C. de Carvalho, M. Muller, P. B. de Carvalho, and A. de Souza Melo, "Stress in the professional practice of oncology nurses," *Cancer Nursing*, vol. 28, no. 3, pp. 187–192, 2005.

[58] E. Grunfeld, T. J. Whelan, L. Zitzelsberger, A. R. Willan, B. Montesanto, and W. K. Evans, "Cancer care workers in Ontario: prevalence of burnout, job stress and job satisfaction," *CMAJ: Canadian Medical Association journal = journal de l'Association medicale canadienne*, vol. 163, pp. 166–169, 2000.

[59] K. Enskär, L. Darcy, M. Björk, S. Knutsson, and K. Huus, "Experiences of young children with cancer and their parents with nurses' caring practices during the cancer trajectory," *Journal of Pediatric Oncology Nursing: Official Journal of the Association of Pediatric Oncology Nurses*, vol. 37, no. 1, pp. 21–34, 2020.

[60] P. A. Ganz, "Monitoring the physical health of cancer survivors: a survivorship-focused medical history," *Journal of Clinical Oncology*, vol. 24, no. 32, pp. 5105–5111, 2006.

[61] C. T. Stricker, L. A. Jacobs, B. Risendal et al., "Survivorship care planning after the institute of medicine recommendations: how are we faring?" *Journal of Cancer Survivorship*, vol. 5, no. 4, pp. 358–370, 2011.

[62] C. L. Shapiro, M. S. McCabe, K. L. Syrjala et al., "The LIVESTRONG survivorship center of excellence network," *Journal of Cancer Survivorship*, vol. 3, no. 1, pp. 4–11, 2009.

[63] M. S. Mccabe and L. A. Jacobs, "Clinical update: survivorship care – models and programs," *Seminars in Oncology Nursing*, vol. 28, no. 3, pp. e1–e8, 2012.

[64] K. C. Oeffinger, D. A. Eshelman, G. E. Tomlinson, and G. R. Buchanan, "Programs for adult survivors of childhood cancer," *Journal of Clinical Oncology*, vol. 16, no. 8, pp. 2864–2867, 1998.

Hindawi
Journal of Healthcare Engineering
Volume 2023, Article ID 9891253, 1 page
https://doi.org/10.1155/2023/9891253

Retraction

Retracted: Direct Detection of Antibiotic Resistance in Chinese *Helicobacter pylori* Clinical Isolates by Sequencing-Based Approach

Journal of Healthcare Engineering

Received 26 September 2023; Accepted 26 September 2023; Published 27 September 2023

This article has been retracted by Hindawi following an investigation undertaken by the publisher [1]. This investigation has uncovered evidence of one or more of the following indicators of systematic manipulation of the publication process:

(1) Discrepancies in scope
(2) Discrepancies in the description of the research reported
(3) Discrepancies between the availability of data and the research described
(4) Inappropriate citations
(5) Incoherent, meaningless and/or irrelevant content included in the article
(6) Peer-review manipulation

The presence of these indicators undermines our confidence in the integrity of the article's content and we cannot, therefore, vouch for its reliability. Please note that this notice is intended solely to alert readers that the content of this article is unreliable. We have not investigated whether authors were aware of or involved in the systematic manipulation of the publication process.

In addition, our investigation has also shown that one or more of the following human-subject reporting requirements has not been met in this article: ethical approval by an Institutional Review Board (IRB) committee or equivalent, patient/participant consent to participate, and/or agreement to publish patient/participant details (where relevant).

Wiley and Hindawi regrets that the usual quality checks did not identify these issues before publication and have since put additional measures in place to safeguard research integrity.

We wish to credit our own Research Integrity and Research Publishing teams and anonymous and named external researchers and research integrity experts for contributing to this investigation.

The corresponding author, as the representative of all authors, has been given the opportunity to register their agreement or disagreement to this retraction. We have kept a record of any response received.

References

[1] L. Tian, Y. Yao, L. Yin et al., "Direct Detection of Antibiotic Resistance in Chinese *Helicobacter pylori* Clinical Isolates by Sequencing-Based Approach," *Journal of Healthcare Engineering*, vol. 2022, Article ID 6436256, 6 pages, 2022.

Hindawi
Journal of Healthcare Engineering
Volume 2022, Article ID 6436256, 6 pages
https://doi.org/10.1155/2022/6436256

Research Article

Direct Detection of Antibiotic Resistance in Chinese *Helicobacter pylori* Clinical Isolates by Sequencing-Based Approach

Lixia Tian,[1] Yi Yao,[2] Li Yin,[3] Lanxiang Wang,[4] Ze An,[4] Lin Kang,[5] Chenglin Ru,[6] and Jinping Li[4,7]

[1]*Department of Emergency Medicine, The Eighth Medical Center, Chinese PLA General Hospital, Beijing, China*
[2]*Department of Gastroenterology, The Eighth Medical Center, Chinese PLA General Hospital, Beijing, China*
[3]*Western Medical District of Chinese PLA General Hospital, Beijing, China*
[4]*Department of Xiangshan Road Clinic, The Eighth Medical Center, Chinese PLA General Hospital, Beijing, China*
[5]*State Key Laboratory of Pathogen and Biosecurity, Beijing Institute of Microbiology and Epidemiology, Beijing, China*
[6]*Department of Ultrasound, The Eighth Medical Center, Chinese PLA General Hospital, Beijing, China*
[7]*Department of Gastroenterology, The First Medical Center, Chinese PLA General Hospital, Beijing, China*

Correspondence should be addressed to Lin Kang; kang_lin@hotmail.com, Chenglin Ru; tougao_career@sina.com, and Jinping Li; lijinpingsubmit@163.com

Received 30 January 2022; Revised 20 March 2022; Accepted 23 March 2022; Published 15 April 2022

Academic Editor: Liaqat Ali

Objective. The detection of *Helicobacter pylori* mutations that result in antimicrobial resistance can serve as a guideline of antimicrobial therapeutics and probably prevent the failure of clinical treatments. Evaluating the potential of Sanger sequencing to identify genetically resistant determinants in *Helicobacter pylori* clinical isolates will be important. *Methods*. 180 cultured strains have been tested using agar dilution for antibiotic susceptibility. NCBI BLAST was used to perform genotypic analysis on the sequencing data. Sanger sequencing was evaluated as an alternative method to detect resistant genotypes and susceptibility. *Results*. By the conventional E-test, resistance to levofloxacin, amoxicillin, metronidazole, and clarithromycin was 67.3%, 15.1%, 96.4%, and 25.5%, respectively. In contrast, tetracycline had no resistance. Resistance to multiple drugs was observed in 8.12% of the strains. The genetic determinants of resistance to CLA was 23s rRNA, the determinants of resistance to amoxicillin was Pbp1, the determinants of resistance to metronidazole was rdxA, and the determinants of resistance to levofloxacin were GyrA and GyrB. However, there was no association of resistance in tetracycline. *Conclusion*. We found increased rates of metronidazole antibiotic resistance, highlighting the necessity for alternative therapies and periodic evaluation. Sanger sequencing has proved to be highly effective and holds the potential to be implemented in policies catering to local treatments.

1. Introduction

Widespread use of antibiotics has had a profound impact on the whole life of bacteria [1]. Many pathogen strains have become resistant to antibiotics and even multidrug resistance [2]. It has been proven that drug resistance can make the efficacy of many existing drugs and decrease and disappear, leading to more than 700,000 deaths in one year [3, 4], which is one of the greatest public health issues [5, 6].

According to the WHO, *Helicobacter pylori* can cause many gastrointestinal disorders such as gastritis, peptic ulcers, and gastric cancer [7], which is the main threat to human health [8]. However, the efficacy of current therapies for *Helicobacter pylori* was dramatically decreasing because of the increased antibiotic resistance [9]. Therefore, many conferences for *Helicobacter pylori* treatments have been held to deal with antibiotic resistance [10, 11]. In developed countries, the infection rate of *Helicobacter pylori* ranges from 25% to 50%, whereas in developing countries, the rate is up to 80%. The infection rate in China is also numbered as high as 56.2% [12]. The widespread use of eradication therapeutic regimens, consisting of at least two antimicrobial agents, has recently shown that the resistance of *Helicobacter pylori* to antimicrobial agents such as clarithromycin, fluoroquinolones like levofloxacin, and metronidazole shows an increasing trend year by year.

Routine *Helicobacter pylori* sensitivity tests are very difficult under current conditions because *Helicobacter pylori* needs a nutrient-rich, selective medium [13]. Therefore, it is particularly important to find a timely and accurate method to diagnose drug resistance in the clinical treatment of *Helicobacter pylori*. Molecular biology techniques can identify the molecular mechanisms of various antimicrobial agents [14–16]. And a molecular testing strategy also can comprehensively assess the multifaceted information associated with *Helicobacter pylori* therapy in one test [17]. It can not only assist clinicians in issuing individualized solutions for *Helicobacter pylori* treatment for different patients, but also help to promote the progress of research on the mechanism of molecular treatment for *Helicobacter pylori* [18, 19].

Based on the abovementioned, we characterized the resistance rate of amoxicillin, clarithromycin, metronidazole, levofloxacin, and tetracycline from *Helicobacter pylori*, which are the five antibiotics commonly used in *Helicobacter pylori* treatments. We also use Sanger sequencing, which is the most common approach to determine the mutations conferring resistance, to detect resistant genotypes, determine susceptibility, and evaluate the correlation between their phenotypes and genotypes.

2. Materials and Methods

2.1. Sample Collection. The study included 160 *Helicobacter pylori* treatment naive outpatients (80 in 2014-2015 and 80 in 2018-2019). They had an esophagogastroduodenoscopy examination at Chinese PLA General Hospital in 2014-2015 and 2018-2019. During the endoscopic procedure, gastric biopsy specimens were taken, then we inoculated them on a *Helicobacter pylori*-selective plate [20]. After performing a series of biochemical reactions using catalase, oxidase, urease, and stained gram, *Helicobacter pylori* colonies, which were circular, clear, convex, and purple, were identified under light microscopy observation [21]. All procedures were incubated at 37°C and performed in microaerophilic conditions (10% O_2, 5% CO_2, and 85% N_2).

2.2. Phenotypic Characterization of Antimicrobial Susceptibility. The agar dilution assay was used to define the antibiotic susceptibility phenotype. Five antibiotics such as amoxicillin, metronidazole, clarithromycin, tetracycline, and levofloxacin were used in this experiment. *Helicobacter pylori* were cultured for 72 h, then the antibiotic MIC was inferred using *Helicobacter pylori* strain 26695 as the control. Antibiotic MIC is the minimum inhibitory concentration of antibiotics, which is always used to define the antibiotic susceptibility phenotype. When the MIC of metronidazole exceeded 8 mg/L, tetracycline and levofloxacin exceeded 1 mg/L, clarithromycin exceeded 0.25 mg/L, and amoxicillin exceeded 0.125 mg/L, it was defined as antibiotic resistance [22, 23].

Table 1: Resistance pattern of *Helicobacter pylori* strains.

Resistance pattern	Number of strains
All susceptible	14
All resistance	0
Levofloxacin	108
Amoxicillin	24
Metronidazole	154
Clarithromycin	41
Tetracycline	0
Mono resistance	
Levofloxacin only	13
Amoxicillin only	5
Metronidazole only	0
Clarithromycin only	5
Tetracycline only	12
Multiple resistance	
Levofloxacin + metronidazole	64
Clarithromycin + metronidazole	12
Amoxicillin + levofloxacin + metronidazole	15
Clarithromycin + levofloxacin + metronidazole	29

2.3. Genotype Analysis of Antibiotic Susceptibility. Snippy v.3.2 and Gubbinsv2.3.4 were used to core SNP alignment and predict recombinant regions aimed to assess the relatedness between *Helicobacter pylori* strains. The antibiotic susceptibility genotypes, such as GyrA and GyrB for levofloxacin, 23S rRNA for clarithromycin, Pbp1 for amoxicillin, RdxA for metronidazole, and 16S rRNA for tetracycline were assessed. Variant identification, summarization, and assessment were performed for the association with the resistance phenotype. Besides, Phandango was used to perform the phenotypic resistance patterns to heat maps and antibiotic resistance.

2.4. Statistical Analysis. SPSS 17.0 statistical software was used for statistical analysis. The quantitative data were expressed as the mean ± standard deviation (mean ± SD). The *t*-test was used for comparison between two groups, and $P < 0.05$ was considered a statistically significant difference.

3. Results

As the antibiograms of 160 isolates from Beijing in Table 1, we noted the resistance rates of metronidazole, levofloxacin, clarithromycin, amoxicillin, and tetracycline decreased in the order of 96%, 67%, 25%, 15%, and 0, respectively, and 14 strains were susceptible to all (Figure 1).

3.1. Helicobacter pylori Antibiotic Susceptibility in Beijing. The proportion of single-drug resistance was 21.8% among all drug-resistant isolates, and all were metronidazole resistant. The proportion of multi-drug resistance was 76.4%. Among all clinical isolates, the dual resistance rate to levofloxacin + metronidazole was 40%, and the dual resistance rate to metronidazole + clarithromycin was 7.3%. Triple resistance to amoxicillin + levofloxacin + metronidazole was 9.1% and to clarithromycin + levofloxacin + metronidazole was 18.2% (Figure 2).

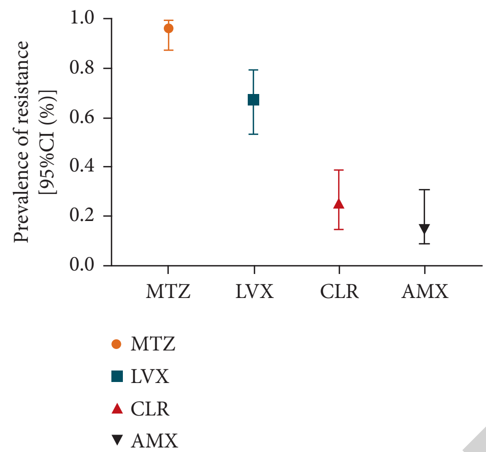

Figure 1: The range and distribution of MIC values for each antibiotic. A resistance profile with the highest prevalence of resistance to metronidazole 96.4% (95% CI, 87.5–99.6), followed by levofloxacin 67.3% (95% CI, 53.3–79.3), clarithromycin 25.5% (95% CI, 14.7–39), and amoxicillin 15.1% (95% CI, 10.1–31.9).

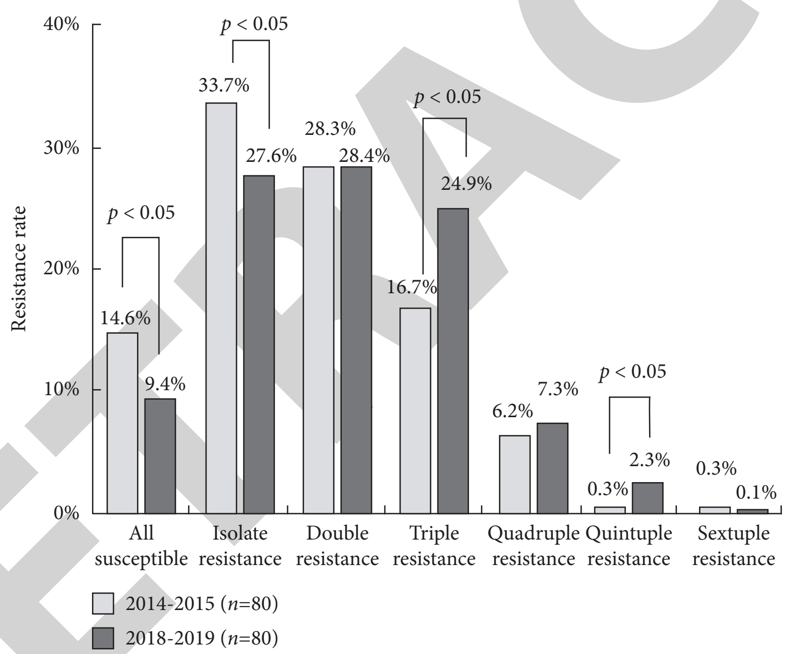

Figure 2: Comparisons of multiple antibiotic resistance rates. In 2014-2015, 14.6% of *Helicobacter pylori* isolates were susceptible to all antibiotics, with 33.7%, 28.3%, 16.7%, 6.2%, 0.3%, and 0.3% being isolate resistance, double resistance, triple resistance, quadruple resistance, quintuple resistance, and sextuple resistance, respectively. In 2018-2019, 9.4% of *Helicobacter pylori* isolates were susceptible to all antibiotics, with 27.6%, 28.4%, 24.9%, 7.3%, 2.3%, and 0.1% being isolate resistance, double resistance, triple resistance, quadruple resistance, quintuple resistance, and sextuple resistance, respectively.

3.2. Comparison between Genotypes and Phenotypes. After the comparison of the phenotypes and the corresponding genotypes, we found that the determinants of resistance to levofloxacin were GyrA and GyrB, the determinant of resistance to amoxicillin was Pbp1, the determinant of resistance to metronidazole was rdxA, and the determinant of resistance to CLA was 23s rRNA (Figure 3). There was complete concordance between genotype and phenotype for clarithromycin and concordance for levofloxacin and amoxicillin (Table 2).

4. Discussion

Our study suggests that the resistance of *Helicobacter pylori* isolates may be due to the extensive use of antibiotics, especially metronidazole, clarithromycin, and amoxicillin. For example, the resistance to metronidazole in *Helicobacter pylori* clinical isolates may be because of prescriptions for parasitic infections, pelvic inflammation, or dental infections [24–26]. Furthermore, resistance of drug-resistant *Helicobacter pylori* to levofloxacin is similarly high, which

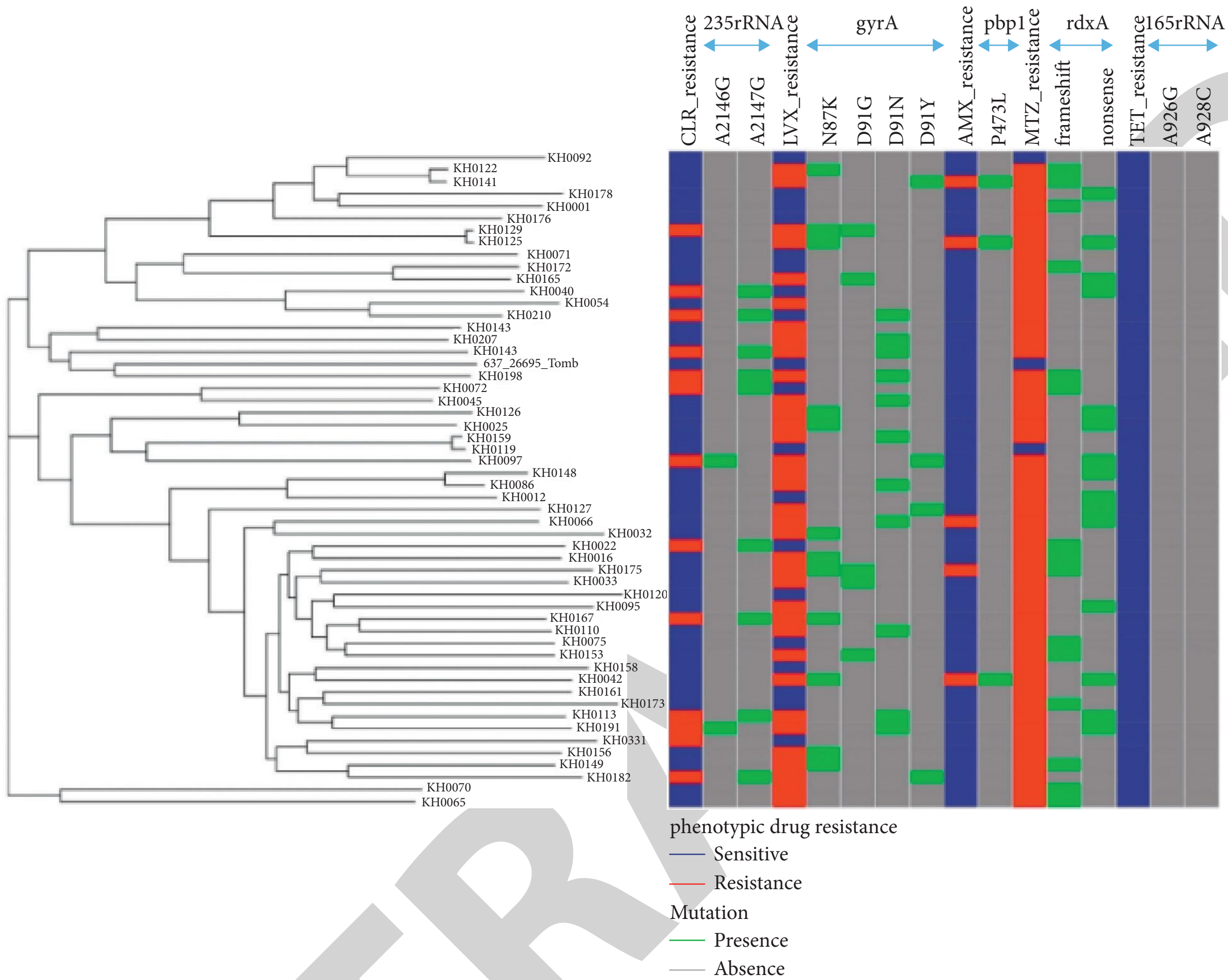

Figure 3: Comparison between antibiotic susceptibility genotypes and phenotypes. Maximum likelihood phylogenetic trees were built for the resistance patterns of each antibiotic and their corresponding genetic determinants. Dark blue and red rectangles represented sensitive and resistant patterns. Green and grey rectangles denote mutations and no mutation, respectively.

Table 2: Comparison between genotypes and phenotypes.

Antibiotics	Phenotypic	Genotypic Yes	Genotypic No	Kappa values
Metronidazole	Yes	139	15	0.279
	No	2	4	
Levofloxacin	Yes	91	17	0.705
	No	5	47	
Clarithromycin	Yes	35	5	0.848
	No	4	116	
Amoxicillin	Yes	17	8	0.727
	No	2	134	

may be caused by using levofloxacin to treat urinary and respiratory tract infections [27–29].

As high MIC values in metronidazole and clarithromycin resistant strains are associated with resistance patterns in vivo, they are perhaps potential markers for predicting curable rates. As no plasmids were found in all strains, indicating that *Helicobacter pylori* resistance is based on mutations, it also inspired us to think that detection of point mutations in the genome can be used to identify *Helicobacter pylori* resistance.

Molecular susceptibility testing is becoming the ideal for detecting drug resistance in *Helicobacter pylori* clinical isolates due to greater speed as well as greater accuracy [30]. Sanger sequencing may not have an impact on strain resistance [31–33]. We thus need to explore new approaches like phenotypic characterization of antimicrobial susceptibility and genotype analysis of antibiotic susceptibility [34, 35]. Furthermore, regular assessment and alternative therapies are also important to control the resistance status. This study's novelty lies in the reporting of resistance patterns of *Helicobacter pylori* clinical isolates, providing an overview of the current state of antibiotic resistance, which can guide the elimination of *Helicobacter pylori*.

However, this study also has partial limitations. First of all, the samples in this study were all patients from a hospital, which cannot reflect *Helicobacter pylori* patterns in the general population. Second, the sample size of partial resistance to antibiotics in this study was small, and the strength of the association was only associated with few or no resistant strains, such as amoxicillin and TET. Third, the present study was conducted at the *in vitro* level, and the commonly used antibiotic resistance rates revealed by the study data were not completely accurate, and clinical trials are needed for further validation.

5. Conclusion

This findings show that *Helicobacter pylori* had resistance to antibiotics and was also likely to be pathogenic and virulent. In addition, molecular susceptibility testing that detects genetic determinants associated with drug resistance can be used in detection tests for *Helicobacter pylori* drug resistance. However, due to various limitations, it is necessary to continue to expand the sample size and continue clinical trials in the future.

Data Availability

The data used to support this study are available from the corresponding author upon request.

Consent

All the informed consent forms shall be recorded in the form of written, signed, and dated.

Conflicts of Interest

The authors declare that they have no conflicts of interest.

Authors' Contributions

Lixia Tian, Yi Yao, and Li Yin contributed equally.

Acknowledgments

This paper was funded by the Special Scientific Research Projects of Military Health 16BJZ05.

References

[1] A. D. McEachran, B. R. Blackwell, J. D. Hanson et al., "Antibiotics, bacteria, and antibiotic resistance genes: aerial transport from cattle feed yards via particulate matter," *Environmental Health Perspectives*, vol. 123, no. 4, pp. 337–343, 2015.

[2] T. J. Kawecki, "Sexual selection reveals a cost of pathogen resistance undetected in life-history assays," *Evolution*, vol. 74, no. 2, pp. 338–348, 2020.

[3] M. A. A. Majumder, S. Rahman, D. Cohall et al., "Antimicrobial stewardship: fighting antimicrobial resistance and protecting global public health," *Infection and Drug Resistance*, vol. 13, pp. 4713–4738, 2020.

[4] C. Y. Effah, T. Sun, S. Liu, and Y. Wu, "*Klebsiella pneumoniae*: an increasing threat to public health," *Annals of Clinical Microbiology and Antimicrobials*, vol. 19, no. 1, p. 1, 2020.

[5] N. Loo, B. Hanysak, J. Mann et al., "Real-world observational experience with direct-acting antivirals for hepatitis C: baseline resistance, efficacy, and need for long-term surveillance," *Medicine*, vol. 98, no. 26, p. e16254, Article ID e16254, 2019.

[6] J. Y. Chung, J. Hong, H. J. Kim et al., "White adipocyte-targeted dual gene silencing of FABP4/5 for anti-obesity, anti-inflammation and reversal of insulin resistance: efficacy and comparison of administration routes," *Biomaterials*, vol. 279, Article ID 121209, 2021.

[7] L. H. Eusebi, R. M. Zagari, and F. Bazzoli, "Epidemiology of Helicobacter pylori infection," *Helicobacter*, vol. 19, no. Suppl 1, pp. 1–5, 2014.

[8] E. Tacconelli, E. Carrara, A. Savoldi et al., "Discovery, research, and development of new antibiotics: the WHO priority list of antibiotic-resistant bacteria and tuberculosis," *The Lancet. Infectious diseases*, vol. 18, no. 3, pp. 318–327, 2018.

[9] S. M. Smith, C. O'Morain, and D. McNamara, "*Helicobacter pylori* resistance to current therapies," *Current Opinion in Gastroenterology*, vol. 35, no. 1, pp. 6–13, 2019.

[10] H. B. El-Serag, J. Y. Kao, F. Kanwal et al., "Houston consensus conference on testing for *Helicobacter pylori* infection in the United States," *Clinical Gastroenterology and Hepatology*, vol. 16, no. 7, pp. 992–1002, 2018.

[11] "Abstracts from the 3rd international genomic medicine conference (3rd IGMC 2015): jeddah, kingdom of Saudi arabia," *BMC Genomics*, vol. 17, no. Suppl 6, p. 487, 2015.

[12] B. Dolan, L. Burkitt-Gray, S. Shovelin et al., "The use of stool specimens reveals *Helicobacter pylori* strain diversity in a cohort of adolescents and their family members in a developed country," *International Journal of Medical Microbiology*, vol. 308, no. 2, pp. 247–255, 2018.

[13] K. Imase, H. Sugano, and S. Takahashi, "[Drug sensitivity test for *Helicobacter pylori*]," *Nihon Rinsho*, vol. 63, no. Suppl 11, pp. 245–248, 2005.

[14] P. Fortugno, F. Angelucci, G. Cestra et al., "Recessive mutations in the neuronal isoforms of DST , encoding dystonin, lead to abnormal actin cytoskeleton organization and HSAN type VI," *Human Mutation*, vol. 40, no. 1, pp. 106–114, 2019.

[15] LG. Cui, JX. Shan, M. Shi, JP. Gao, and HX. Lin, "DCA1 acts as a transcriptional Co-activator of DST and contributes to drought and salt tolerance in rice," *PLoS Genetics*, vol. 11, no. 10, Article ID e1005617, 2015.

[16] M.-L. Han, Q.-Y. Lv, J. Zhang et al., "Decreasing nitrogen assimilation under drought stress by suppressing DST-mediated activation of Nitrate Reductase 1.2 in rice," *Molecular Plant*, vol. 15, no. 1, pp. 167–178, 2022.

[17] P. Sabbagh, M. Javanian, V. Koppolu, V. R. Vasigala, and S. Ebrahimpour, "*Helicobacter pylori* infection in children: an overview of diagnostic methods," *European Journal of Clinical Microbiology & Infectious Diseases*, vol. 38, no. 6, pp. 1035–1045, 2019.

[18] D. Pohl, P. M. Keller, V. Bordier, and K. Wagner, "Review of current diagnostic methods and advances inHelicobacter pyloridiagnostics in the era of next generation sequencing," *World Journal of Gastroenterology*, vol. 25, no. 32, pp. 4629–4660, 2019.

[19] E. A. Argueta and S. F. Moss, "Treatment of *Helicobacter pylori*," *Current Opinion in Gastroenterology*, vol. 35, no. 6, pp. 544–550, 2019.

[20] S. Krakowka, D. M. Rings, and J. A. Ellis, "Experimental induction of bacterial gastritis and gastric ulcer disease in gnotobiotic swine inoculated with porcine Helicobacter-like species," *American Journal of Veterinary Research*, vol. 66, no. 6, pp. 945–952, 2005.

[21] Y. Xiong, Z. Yang, J. Zhang, J. Li, P. Chen, and Y. Xiang, "Panning using a phage-displayed random peptide library to identify peptides that antagonize the *Helicobacter pylori* ArsS

Hindawi
Journal of Healthcare Engineering
Volume 2023, Article ID 9821891, 1 page
https://doi.org/10.1155/2023/9821891

Retraction

Retracted: Analysis of the Effect of Applying Ultrasound-Guided Nerve Block Anesthesia to Fracture Patients in the Context of Internet-Based Blockchain

Journal of Healthcare Engineering

Received 3 October 2023; Accepted 3 October 2023; Published 4 October 2023

This article has been retracted by Hindawi following an investigation undertaken by the publisher [1]. This investigation has uncovered evidence of one or more of the following indicators of systematic manipulation of the publication process:

(1) Discrepancies in scope
(2) Discrepancies in the description of the research reported
(3) Discrepancies between the availability of data and the research described
(4) Inappropriate citations
(5) Incoherent, meaningless and/or irrelevant content included in the article
(6) Peer-review manipulation

The presence of these indicators undermines our confidence in the integrity of the article's content and we cannot, therefore, vouch for its reliability. Please note that this notice is intended solely to alert readers that the content of this article is unreliable. We have not investigated whether authors were aware of or involved in the systematic manipulation of the publication process.

Wiley and Hindawi regrets that the usual quality checks did not identify these issues before publication and have since put additional measures in place to safeguard research integrity.

We wish to credit our own Research Integrity and Research Publishing teams and anonymous and named external researchers and research integrity experts for contributing to this investigation.

The corresponding author, as the representative of all authors, has been given the opportunity to register their agreement or disagreement to this retraction. We have kept a record of any response received.

References

[1] Q. Cai, Y. Han, M. Gao, and S. Ni, "Analysis of the Effect of Applying Ultrasound-Guided Nerve Block Anesthesia to Fracture Patients in the Context of Internet-Based Blockchain," *Journal of Healthcare Engineering*, vol. 2022, Article ID 6324009, 11 pages, 2022.

Hindawi
Journal of Healthcare Engineering
Volume 2022, Article ID 6324009, 11 pages
https://doi.org/10.1155/2022/6324009

Research Article

Analysis of the Effect of Applying Ultrasound-Guided Nerve Block Anesthesia to Fracture Patients in the Context of Internet-Based Blockchain

Qiang Cai,[1] Yi Han,[2] Meiling Gao ,[3] and Shuqin Ni [4]

[1] *Department of Orthopedics, Xiangyang Central Hospital, Affiliated Hospital of Hubei University of Arts and Science, Xiangyang 441000, Hubei, China*
[2] *Department of Anesthesiology, The Central Hospital of Wuhan, Tongji Medical College, Huazhong University of Science and Technology, Wuhan, Hubei, China*
[3] *Department of Anesthesiology, Taihe Hospital, Hubei University of Medicine, Shiyan 442000, Hubei, China*
[4] *Department of Anesthesiology, Yantaishan Hospital, Yantai 264003, Shandong, China*

Correspondence should be addressed to Meiling Gao; 20201110325@nxmu.edu.cn and Shuqin Ni; ni518866@163.com

Received 14 February 2022; Revised 27 February 2022; Accepted 28 February 2022; Published 14 April 2022

Academic Editor: Liaqat Ali

In the process of surgical treatment, the introduction of ultrasound technology to implement nerve block anesthesia can make the operations of patients with fractures under visualization and it can also significantly improve the anesthesia effect. With this technology, it is possible to minimize the anesthesia operation causing accidental injury and lay a good foundation for the smooth operation of surgical treatment. Blockchain technology is a new decentralized infrastructure and distributed computing paradigm. This technology has great development opportunities in the medical field and is expected to play an important role in the construction of Internet medical ecology. This study aims to investigate the effect of ultrasound-guided nerve block anesthesia on fracture treatment in the context of blockchain. This method has high application value and potential in medical data sharing, reducing treatment costs, improving the medical claims system, strengthening medical management, and optimizing medical decision-making using blockchain technology. This study also addresses the uniqueness and complexity of ultrasound-guided nerve block anesthesia itself and analyzes the effect of the proposed method. The analysis shows that using the internet-based blockchain ultrasound-guided subacromial nerve block anesthesia for fracture patients is effective, and the patient's vital signs are stable, and the block is effective.

1. Introduction

Anesthesiologists play an important role in the treatment of fractures by providing preoperative nerve block analgesia to help reduce pain, relieve fear, and help improve prognosis. An effective preoperative analgesic regimen is essential because of the tremendous pain caused by fractures. Opioid analgesics may produce adverse effects such as perioperative delirium, which increases the risk of surgery and increases perioperative mortality, while nonsteroidal anti-inflammatory drugs (NSAIDs) may produce adverse effects on the cardiovascular system. The Association of Anesthesiologists of Great Britain and Ireland (AAGBI) recommends that opioids and NSAIDs should be used with caution in high-risk groups and that regional nerve block anesthesia may be used to minimize drug-related complications. Once a patient is diagnosed with a hip fracture [1–3], preoperative analgesia should be administered by an experienced anesthesiologist, usually with an iliac fascia gap block or a femoral nerve block. Iliofascial gap blocks and femoral nerve blocks can be administered by injection alone or in combination with an infusion pump for continuous analgesia, but the risk of infection is higher with the combination, with a local infection rate of 0.3% to 2%. Anesthesia for fracture surgery includes general anesthesia and intralesional anesthesia, which is more beneficial to reduce postoperative complications and reduce perioperative mortality, so the appropriate anesthesia should be selected according to the patient's own situation. For elderly patients with poor cardiopulmonary function, intralesional anesthesia is preferred, which can help reduce the occurrence of postoperative delirium and the risk of deep vein thrombosis, with relative contraindications for aortic stenosis and coagulation abnormalities [2–5]. Among them, epidural anesthesia has a slower onset than subarachnoid anesthesia and is more suitable for patients with cardiovascular disease. Regardless of the type of anesthesia chosen, intraoperative hypotension should be avoided. It has been found that intraoperative hypotension increases mortality within 30 days after surgery, and the incidence of intraoperative hypotension is significantly higher with general anesthesia than with intralesional anesthesia, and the risk of hypotension is higher when general anesthesia is combined with intralesional anesthesia. The localization technique of peripheral nerve block anesthesia is important for accurate anesthetic injection. At present, the clinical application of localization techniques includes blind exploration of peripheral nerve anatomy, nerve stimulator, and ultrasound-guided localization. Because ultrasound guidance has the characteristics of simplicity, ease of use, and excellent image quality, it has been increasingly used in peripheral nerve block anesthesia. Figure 1 illustrates the physical characteristics and visualization of the ultrasound guidance technique.

Ultrasound mainly uses acoustic wave penetration and resolution for imaging. Wavelength and frequency specific waves have unique penetration and resolution, and the longer the acoustic wave of the wave, the better the penetration and the better the penetration ability. At present, the frequency of ultrasound commonly used in clinical practice is mostly 2.0~50.0 MHz; with the increase in frequency, the acoustic resolution rises, image clarity increases [6, 7], and penetration decreases; that is, its penetration and resolution are inversely proportional. Because ultrasound will be attenuated when encountering obstacles, for the application of ultrasound for peripheral nerve examination, ultrasound frequency needs to be selected according to the anatomical structure of the nerve, as well as more superficial nerves with higher frequency ultrasound; deep nerves are selected with lower frequency ultrasound. Ultrasound images are divided into transverse and longitudinal sections according to the specific shape of the nerve. Transverse ultrasound images show a hypoechoic pattern with a circular shape surrounded by high echogenicity, while longitudinal sections show a distribution of high echogenicity and low echogenicity, mostly in the form of parallel strips. In clinical practice, the use of ultrasound for peripheral nerve examination can obtain clear ultrasound images of peripheral nerves at frequencies higher than 5 MHz. When using 6–15 MHz ultrasound to investigate peripheral nerve injury, it was found that normal peripheral nerve longitudinal sections were mostly hypoechoic parallel to each other, and these hypoechoic bands were interspersed with linear hyper echoes, while transverse sections were mostly moderate echogenic with dotted hypoechogenicity inside, mostly showing a "sieve hole" shape. The study also found that the peripheral nerve in the direction perpendicular to the direction of ultrasound emission was not easily visualized, while the nerve in the same direction as the emission could be clearly visualized with "low internal and high external." The nerves in the same direction as the emission direction can be clearly shown as "low inside and high outside" with a halo-like shape [8]. Peripheral nerves are associated with other soft tissue organs, such as blood vessels or ligaments, and understanding these soft tissue ultrasound images can help detect peripheral nerves quickly and correctly. In clinical practice, different tissues are identified based on their echogenic characteristics, in which substantial tissues tend to show homogeneous echogenicity, the presence of gas tissues tends to be bright and strongly echogenic, and the presence of fluid tissues tends to be hypoechoic or nonechogenic. Ultrasound-guided technique in clinical practice is mainly performed in two ways: The first one is body marker technique, which is simple and easy to perform. In this method, nerves located in the superficial plexus with clear tissue are identified first and then marked and blocked by puncture in the usual way. Another method is ultrasound-guided real-time localization, which is performed by a skilled physician who holds an ultrasound probe in his left hand and accurately locates the target nerve using in-plane techniques. When the block needle is close to the nerve, the local anesthetic drug can be slowly injected. If there is a wrong injection site, it is necessary to adjust the position of the block needle in time, and when the nerve can be observed to form a typical "donut sign" with the anesthetic drug, the block is successful and the block is effective. When performing a block, multiple blocks can be performed around the peripheral nerve to avoid poor diffusion of anesthetic drugs in a single block [9–12]. Figure 2 illustrates the healthcare blockchain architecture.

Blockchain, also known as distributed ledger technology, is a technical solution that collectively maintains a reliable database through decentralization and detrust. This technical solution mainly allows any number of nodes participating in the system to pass a string of data blocks (blocks) associated with each other using cryptographic methods. Each data block contains all the information exchange data of the system within a certain period of time and generates a data fingerprint for verifying the validity of its information and linking (Chain) to the next database block [13–16]. At present, the concept of blockchain technology is recognized as explained in the White Paper on the Development of Blockchain Technology and Applications in China, which defines it as a new Internet application model with distributed data storage, peer-to-peer transmission, consensus mechanism, cryptographic algorithms, and other computer technologies. The unique features of blockchain include decentralization, being autonomous, security and trustworthiness, and openness and transparency [14].

Clinical experimental research requires demanding records of experimental results, and blockchain technology can provide researchers with traceable records of experimental results and clinical reports, which plays an important role in preserving experimental results and reducing falsification of clinical experimental records. According to statistics, half of the current experimental studies have unreported experimental results, and blockchain technology

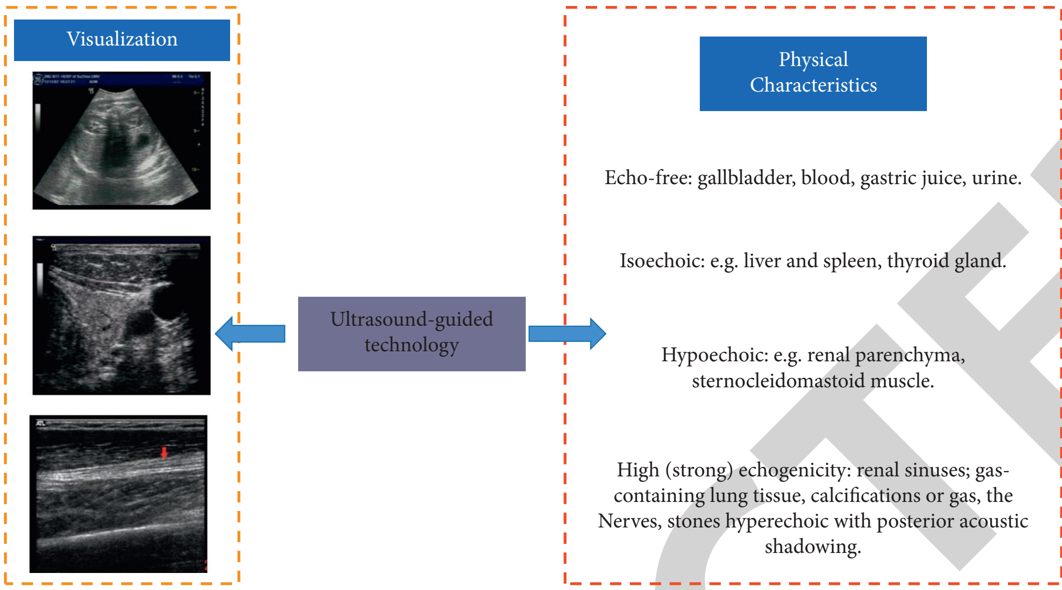

Figure 1: Ultrasound guidance technology features and visualization.

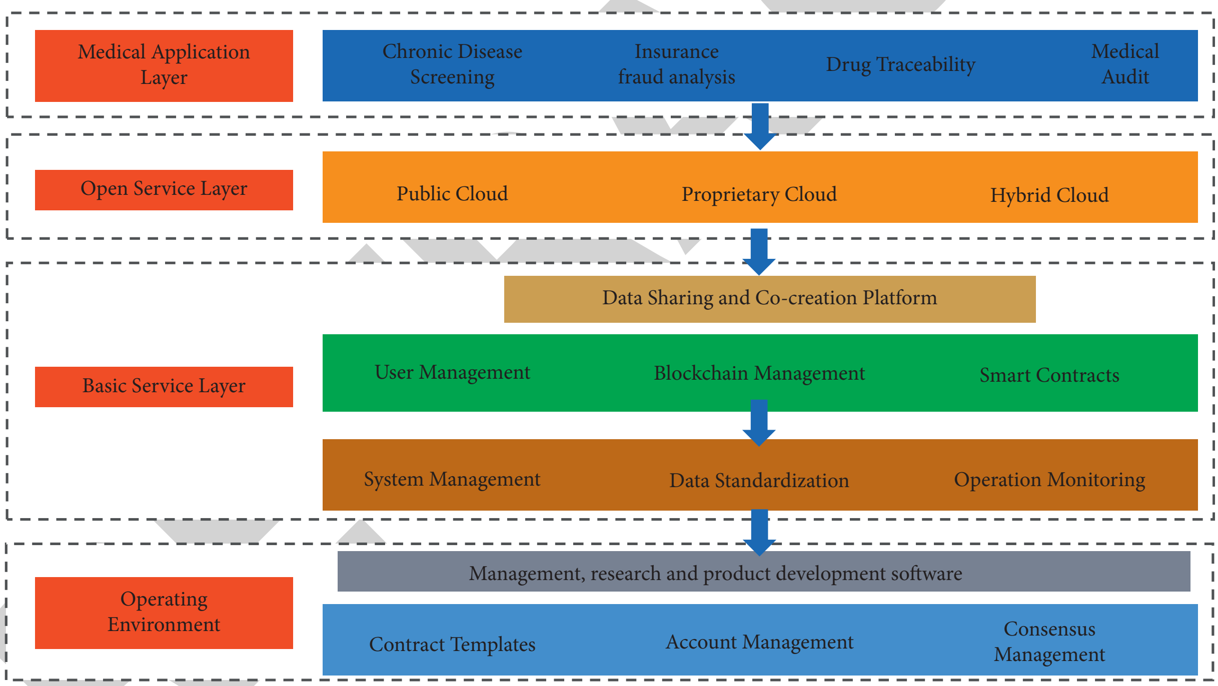

Figure 2: Medical blockchain architecture.

can address the selective reporting and untrue results in clinical experiments, thus reducing the occurrence of academic misconduct. Blockchain-based research data would be time-stamped and publicly transparent, and all plans, consents, protocols, and possible outcomes could be stored on the blockchain even before clinical trials begin [14]. The blockchain could also link the several phases of a clinical trial together, and the trial would only move to the next phase if all steps were followed and the methods used were properly validated, thus ensuring transparency and credibility of the clinical trial. This idea is extended by using smart contracts that reside at a specific address in the blockchain and whose execution rights are cryptographically verified by a network key to demonstrate how trust in clinical experiments can be better enforced and how data tampering can be eliminated. It is demonstrated that the cryptographic guarantees provided by modern protocols can go beyond "proof of existence" and be used in complex clinical settings. Blockchain technology could significantly improve surgical outcomes research and experimental design, change the way we think about experimental design, and potentially produce truly verifiable and immutable data. Of course, it is still too early for blockchain technology to enter surgical outcomes research, but its fundamental property as a public cryptographically controlled data store cannot be denied and could improve the authenticity of experimental data [17]. With the widespread use of ultrasound devices and the great development of ultrasound guidance technology, ultrasound-guided peripheral nerve blocks have been gradually applied to various clinical procedures. Relevant studies have confirmed that the application of ultrasound guidance technology can effectively improve the success rate of anesthesia, reduce complications, and decrease the amount of anesthesia [14].

This paper proposes an internet-based blockchain technology for the application of ultrasound-guided nerve block anesthesia for fracture patients. This can better solve the problems of Information Island, information exchange, and information security caused by different manufacturers, different technologies, different standards, and different software system integration when applying ultrasound-guided nerve block anesthesia for fracture patients by using blockchain technology. The effectiveness of the proposed method is demonstrated by analyzing some relevant dataset.

2. Related Work

2.1. Application of Ultrasound-Guided Nerve Block Anesthesia in Patients with Fractures. Surgical treatment is an important source of psychological and physiological stress, which can cause patients to experience anxiety, fear, depression, and other adverse psychological states, which severely restrict the outcome of surgical treatment and postoperative patient recovery. The presence of extremely pronounced anxiety and depression in patients during anesthesia seriously interferes with the operation. In order to improve the surgical treatment effect of nerve block patients and promote the rehabilitation process of patients, nerve block anesthesia patients are given routine care and psychological care based on routine care, respectively. Ultrasound-guided peripheral nerve block anesthesia types of subclavian brachial plexus block should be performed using a frequency of 4–7 MHz arc probe [18], and the probe is placed in the downward depressed position of the clavicle 1 cm away from the rostral prominence position of the patient. The patient's brachial plexus nerve is clearly observed to show a grape-like shape of low-density ring-shaped hyperechoic, and the phenomenon of anesthetic drug wrapping the nerve is visible after performing the block. The application of ultrasound-guided continuous subclavian brachial plexus block in patients with multiple upper extremity fractures not only effectively improved analgesia but also effectively reduced the inflammatory response and decreased the incidence of postoperative related complications. Another researcher found that, by comparing the effect of different concentrations of ropivacaine in ultrasound-guided brachial plexus block, the blocking effect was the same when the concentration of anesthetic drug was the same, independent of the drug dose. The lumbar plexus nerve, because it is in the deep interstitial space of the psoas major muscle next to the lumbar spine, consists of multiple tiny nerves, and improper block is prone to phenomena such as renal hematoma. BORE has found in ultrasound-guided lumbar plexus blocks in children and adolescents that ultrasound-guided lateral imaging of the transverse process, vertebral body, and psoas muscle allows the surgeon to quickly locate the lumbar plexus nerve and perform a successful nerve block. Ultrasound imaging of the sciatic nerve at the popliteal fossa is more obvious, so its ultrasound-guided nerve block is easier to perform with accurate localization. A 4–7 MHz probe is applied to identify the sciatic nerve location in the transverse direction, and the needle is inserted from the lateral side perpendicular to the ultrasound direction at 1 to 2 cm from the sciatic nerve location, so that the anesthetic drug completely wraps the nerve sheath [19, 20]. Ultrasound-guided distal approach to the knee sciatic nerve block anesthesia in severely obese patients is more effective and can effectively reduce the pain perception of patients. It is more difficult to apply ultrasound imaging to the femoral nerve. Clinically, it is often used in combination with a nerve stimulator to locate the femoral nerve, applying a probe with a straight shape and a frequency of 4–9 MHz to clearly observe the femoral nerve and its nearby tissues in the transverse plane and then injecting anesthetic drugs at several points near the femoral nerve by entering the needle in the perpendicular direction of the acoustic waves on the outside of the probe. In pediatric femoral nerve fracture surgery, ultrasound-guided femoral nerve block combined with general anesthesia is used to stabilize the hemodynamics and reduce the pain perception of the child. Other types of peripheral nerve blocks include oblique angle interval brachial plexus block, axillary brachial plexus block, and transgluteal sciatic nerve block, all of which require the selection of a suitable shape and frequency probe according to the relevant nerve anatomy. Compared with the blind positioning method and nerve stimulator positioning method, ultrasound-guided peripheral nerve block has the advantages of simplicity, economy, convenience and safety, and good blocking effect. The use of ultrasound-guided peripheral nerve block for lower extremity nerve block can effectively improve the blocking effect and fast onset of anesthesia and effectively reduce anesthesia-related complications. Ultrasound-guided peripheral nerve block can clearly observe the diffusion of anesthetic drugs, and the number of anesthetic drugs used for block is 30% to 40% less than that of conventional block, which can effectively reduce the complications caused by the use of anesthetic drugs in patients. Although the advantages of ultrasound-guided peripheral nerve block anesthesia are obvious, it also has some limitations, such as the adverse effects on the tissues near the nerve, the difficulty of blocking nerves with complex anatomical structures and deeper locations, which may lead to poor blocking effects, and whether the frequency and examination time of different peripheral nerve block application probes will increase peripheral nerve injury, vascular injury and hematoma, and nerve ischemia. Whether different peripheral nerve block application probe frequencies and examination times may increase peripheral nerve injury, vascular injury, and peripheral nerve complications such as hematoma and nerve ischemia still needs to be further determined. These issues will be the focus of subsequent research on ultrasound-guided peripheral nerve blocks, and as these issues are gradually resolved, ultrasound-guided peripheral nerve blocks are expected to become a common mode of clinical nerve blocks. As regards anesthesia methods, the blind exploration group of brachial plexus nerve block methods includes three methods: interosseous groove approach alone, axillary approach alone, and interosseous groove combined with axillary approach. In the ultrasound group, the brachial plexus nerve block methods included interosseous groove approach alone, supraclavicular approach alone, axillary approach alone, and combined interosseous groove axillary approach, combined supraclavicular axillary approach, and combined interosseous groove ulnar nerve block. In the blinded group, the interosseous sulcus approach was performed with the patient lying flat on the pillow, head turned to the opposite side, and arm to the side of the body, with the operator standing in front of the patient's head, first having the patient raise his head, revealing the sternal and clavicular heads of the sternocleidomastoid muscle, identifying the anterior and middle oblique muscle gaps [21], and entering the needle vertically through the lateral edge of the interosseous sulcus to find the hypophysis. The local anesthetic drug was pushed in after the sensation was detected. In blind exploration group axillary block method, the patient was placed in a supine position with the head slightly tilted to the opposite side, the affected upper limb was abducted by 90°, the elbow was flexed by 90°, the forearm was externally rotated, the most obvious place of axillary artery pulsation was touched as the puncture point, and the needle was injected with the local anesthetic drug after encountering the sense of breakthrough and the pulsation of the axillary artery, and there was no return blood in the retraction.

2.2. Internet Blockchain Medicine. As a decentralized, detrusted database technology solution with complete and transparent information and privacy protection, blockchain can build an efficient and reliable value transmission system and promote the Internet as a network infrastructure for building social trust [14]. Blockchain has significant advantages in optimizing business processes, reducing operating costs, and improving collaboration efficiency in the financial industry, and its application in other industries is also rapidly developing. Focusing on the health sector, the construction of healthcare big data faces the dual challenge of information security and privacy protection. Blockchain is highly fault-tolerant, tamper-proof, and privacy-protective and has important applications in medical, pharmaceutical, health insurance, and genomics fields. In the field of health services, patients' medical data has been an asset. Due to the uneven progress of hospital informatization construction, some hospitals cannot integrate their internal information systems, poor interaction of information systems between hospitals, nonuniform data structure of medical records, and nonstandardized data standards of electronic medical records, which makes medical data sharing very difficult. There are many problems with the storage, transmission, and utilization of medical data, among which the problem of sensitive data leakage is very prominent [14]. In 2017, a medical enterprise in the United States caused about 47.5 GB of data leakage due to system mismanagement, involving sensitive private information such as names, addresses, and case records of about 150,000 patients. An individual's medical records involve personal privacy and are personal data that can only be accessed by authorized users. Traditional medical data adopts a centralized storage strategy, and a large amount of medical data accumulates in hospital information centers or regional health data centers. With the proliferation of medical data, the load carried by the centers continues to strengthen, and security risks continue to increase. In response to the problems of medical data, blockchain technology provides a good solution for data storage and transmission with its special technical architecture. Based on the current demand of medical data utilization and the technical characteristics of blockchain, a new medical data storage architecture based on blockchain is proposed, as shown in Figure 3. The architecture is mainly divided into four layers: data layer, communication layer, consensus layer, and application layer. In the data layer, patients' medical records are stored permanently in blocks, and the blocks are connected into chains by timestamps through the creation of mapping pointers by hash functions to ensure the tamper-evident nature of medical records. The transmission of medical data chain adopts asymmetric encryption algorithm [14]. After generating the data, the medical data generator (e.g., hospital) encrypts the data using public key, and the patient parses the data using private key to ensure the security of data transmission. In addition, medical data blockchain can also stipulate different permissions for different people by setting multiple private keys, single authorization, or multiple authorizations in complex time and space and restrict them in time; for example, only the corresponding doctors can access the data during a specific consultation time interval. At the same time, each medical record must have the digital signature of the corresponding medical personnel, which is also an important guarantee of the transparency of blockchain technology. In case of medical disputes, it is easy to trace the medical records. The ability of medical data to be created, appended, and shared by multiple authorized parties will reshape the efficiency and transparency of the entire medical industry. In the communication layer, medical data chain usually adopts P2P technology to organize each node, which is different from the traditional centralized network model. The nodes in the P2P network are equal and there is no centralized server, which is a good preventive effect for the large-scale leakage of medical data. The distributed data storage also improves the redundancy and stability of the whole system. The consensus layer is a strategy and method for the nodes in the medical data chain to reach agreement, which solves the problem of transmitting trusted information and transferring value over untrustworthy channels and achieves a state of mutual trust among nodes in a decentralized context. Traditional proof-of-work requires mathematical operations to obtain bookkeeping rights, which consumes higher resources and is less supervisee, and reaching consensus relies on the joint participation of the whole network [14]. The main idea of

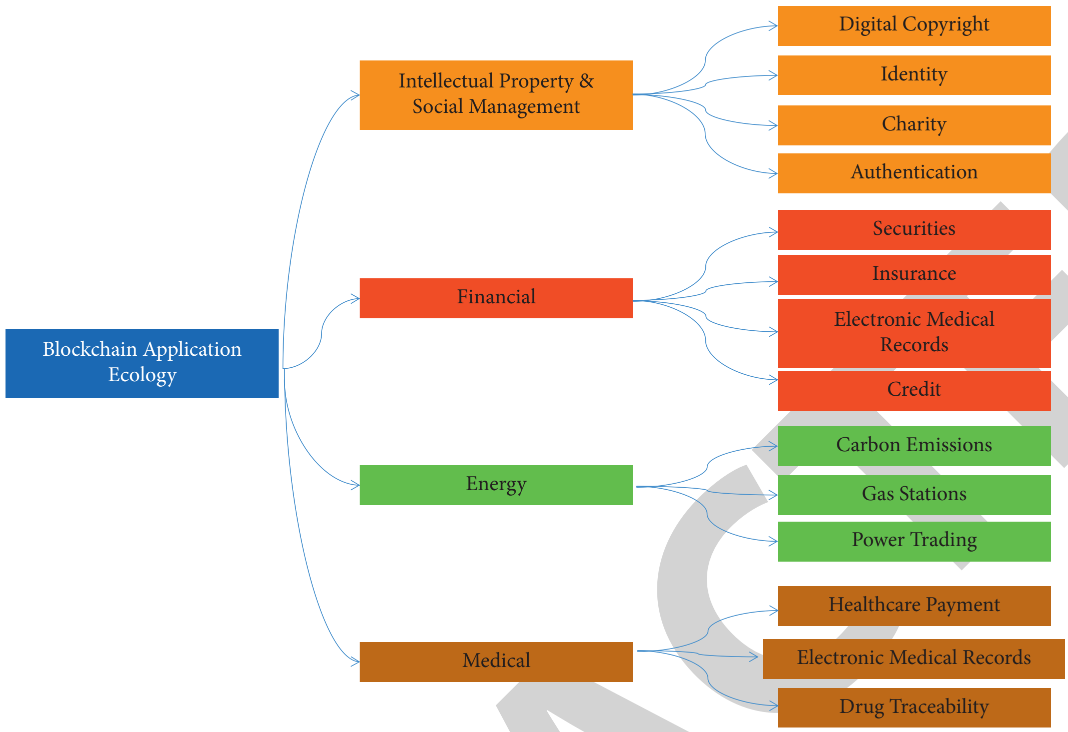

Figure 3: Blockchain application scenarios.

proof-of-stake is that the ease of access to node bookkeeping rights is positively correlated with the benefits held by nodes, which reduces resource consumption and improves performance compared to proof-of-work. Smart contracts in the application layer can meet the needs of healthcare providers for healthcare data collection and exchange solutions [22]. It is a multiuser participatory formulation, proliferation through P2P networks, and automatic execution on the blockchain, which enables patients to deliver medical data to data researchers with confidence and promotes the analysis and deeper utilization of healthcare big data [14].

Apart from the blockchain-based solutions, a large number of artificial intelligence- and machine learning-based clinical and healthcare systems have been developed in clinical and wellbeing setups for cancer [23], diabetes mellitus [24], and wellness recommendations [25, 26].

3. Method

3.1. Model Architecture. There is currently no uniform definition of blockchain in the industry. Blockchain is a decentralized shared ledger that stores blocks of data in a cryptographic chain structure in chronological order and is maintained collectively and tamper-proof by consensus algorithms. Blockchain technology provides a decentralized, open, Byzantine fault-tolerant transaction mechanism that is expected to be the foundational framework for the next generation of Internet transactions. The basic framework of blockchain mainly consists of a data layer, a network layer, a consensus layer, and an application layer, as shown in Figure 4.

3.2. Analysis of Sequencing Mutual Information in Anesthesia. The determination of the patient's state of consciousness during anesthesia has been an important issue for scientific research. There is still no monitor that can demonstrate its ability to analyze the patient's state of consciousness. Most monitors assess the state of sedation in anesthesia only by analyzing changes in the Electroencephalography (EEG) signal of a single channel [27]. The state of consciousness of the brain is importantly related to the coupling of information in the brain domain as well as to synchronous oscillations, and, especially in recent years, many theories have supported the important hypothesis that information coupling is an important condition for the existence of consciousness. For example, changes in cortical neural activity shifting from high to low frequencies with deepening anesthesia, enhancement of gamma waves during learning, and 40 Hz oscillations were related to higher cognitive functions and consciousness. It is generally believed that the "information coupling" between the allocortex and the cortical cortex is one of the conditions for the emergence of consciousness. In anesthesia or sleep, the loss of consciousness is manifested by the decoupling and loss of connections between the functional areas of thalamocortical and cortical cortices. The algorithm of mutual information analysis based on sorting entropy is called sorting mutual information. Since the kinetic properties of EEG signals can be viewed as changes in various modes on the time scale, the sorting entropy theory can be a good way to calculate the degree of mode changes in complex system motions. As a time-varying signal, the amplitude and frequency of the EEG change over time include both rising and falling modes. Statistics of such pattern changes can be used to analyze

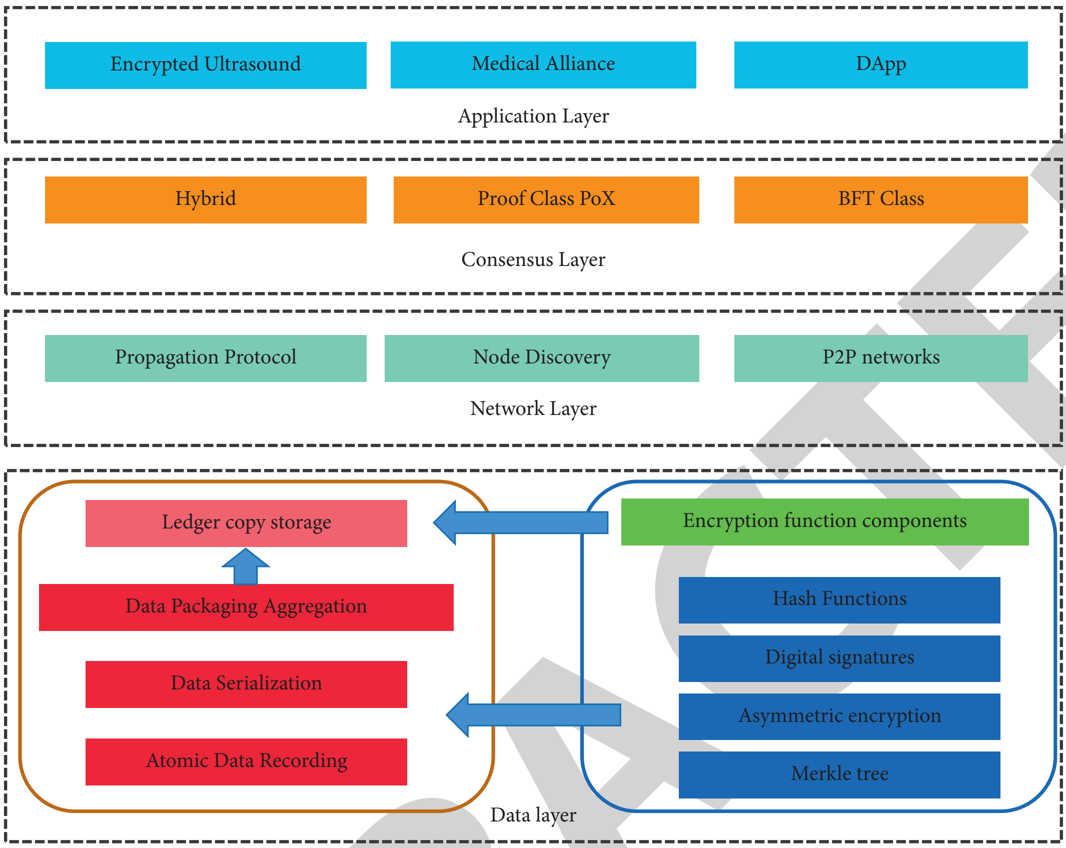

Figure 4: Model structure.

brain activity. Mutual information is used to measure the dynamical coupling and information transfer of systems X and Y.

The details of the PMI algorithm are described as follows:

(1) Given a time series $x_t\,(t = 1, 2, \ldots)$, map the time series to the vector $X_t[x_t, x_{t+\tau}, \ldots, x_{t+m\tau}]$ with embedding dimension of m and time delay of τ.

(2) Arrange X_t in ascending order.

$$[x(t+(j_1-1)\tau) \le x(t+(j_2-1)\tau) \le \ldots \le x(t+(j_m-1)\tau)]. \quad (1)$$

(3) Compute the probability distribution $p_1, p_2, \ldots, p_k$ of the sequence of symbols, where $k \le m!$ For m-dimensional numbers, there are $m!$ kinds of ordering, and each vector X_t can be mapped to one of $m!$

(4) Calculate the entropy of the ordering of the time series $\{x(t),\ t = 1, 2, \ldots\}$.

$$H(X) = -\sum_{j=1}^{J} p_j \log p_j. \quad (2)$$

(5) Meanwhile, compute the sorting entropy of another time series $y_t\,(t = 1, 2, \ldots)$, which is recorded synchronously with t_x.

$$H(Y) = -\sum_{j=1}^{J} p_j \log p_j. \quad (3)$$

(6) Calculate the entropy of the joint probability distribution.

$$H(X,Y) = -\sum_{x\in X}\sum_{y\in Y} p(x,y)\log p(x|y). \quad (4)$$

(7) Obtain sorting mutual information based on sorting entropy.

$$I(X;Y) = H(X) + H(Y) - H(X,Y). \quad (5)$$

3.3. Analysis of Sequencing Mutual Information in Anesthesia. Not only does the emergence of Bitcoin solve the problem of value transfer in a detrusted peer-to-peer network, but also its proof-of-work (PoW) consensus algorithm combined with economic incentives and cryptography makes blockchain cross the Byzantine fault-tolerance gap in distributed systems, bringing great innovations and breakthroughs in how to reach consensus in distributed scenarios. Since then, many new Byzantine fault-tolerant consensus algorithms inspired by Bitcoin have emerged [14]. In its seminal paper on Bitcoin, the PoW consensus algorithm was adopted, where one party submits a computational result that is known to be difficult to compute but easy to verify, and everyone else can verify this result by being confident that the submitting party has completed a significant amount of computation to obtain the result. The larger the number of possible hashes is, the smaller the chance that two values will create the same hash. This made it uneconomical for spammers to send large amounts of spam while still allowing users to send normal e-mail to other users when needed [14]. Bitcoin uses a similar system for the same purpose, where nodes compete against each other based on their computer's computing power to solve a complex but easy-to-verify SHA256 mathematical puzzle (a process known as mining), and the node that solves the puzzle the fastest receives the right to keep track of the blocks and the system automatically generates Bitcoin rewards and transaction fees within the blocks. The Bitcoin system controls the average block generation time of about ten minutes by flexibly adjusting the difficulty of the random number search. In general, the PoW consensus algorithm's random number search process is shown in Figure 5.

Suppose that an attacker opens another chain on the main chain, called the attack chain. The probability that the attacker succeeds in filling a given gap can be approximated as Gambler's Ruin Problem [14]. According to the longest chain mechanism, the attacking chain has to catch up with the main chain to succeed; then its probability that the attacker opens another chain, called the attacking chain, on the main chain is assumed. The probability that the attacker succeeds in filling a given gap can be approximated as Gambler's Ruin Problem.

According to the longest chain mechanism, the attacking chain must catch up with the main chain in order to succeed, and then its probability is

$$P_z = \begin{cases} 1 & q \geqslant p \\ \left(\dfrac{q}{p}\right)^z & q < p \end{cases}, \tag{6}$$

where p is the probability that the honest node makes the next block, q is the probability that the attacking node makes the next block, and P_z is the probability that the attacker finally closes the gap of z blocks and overtakes the attacking chain. If honest blocks will take the average expected time to produce a block, the potential progress of the attacker is a Poisson distribution with the expected value of the distribution.

$$\lambda = z\frac{q}{p}. \tag{7}$$

Therefore, to calculate the probability of the attacker catching up, the probability density of the Poisson distribution of the number of progress blocks made by the attacker needs to be multiplied by the probability of the attacker still being able to catch up given that number to obtain the following equation:

$$\sum_{k=0}^{\infty}\frac{\lambda^k e^{-\lambda}}{k!}\begin{cases} \left(\dfrac{q}{p}\right)^{(z-k)}, & k \leqslant z \\ 1, & k > z. \end{cases} \tag{8}$$

To avoid summing over an infinite series, Equation (8) is simplified to the following form:

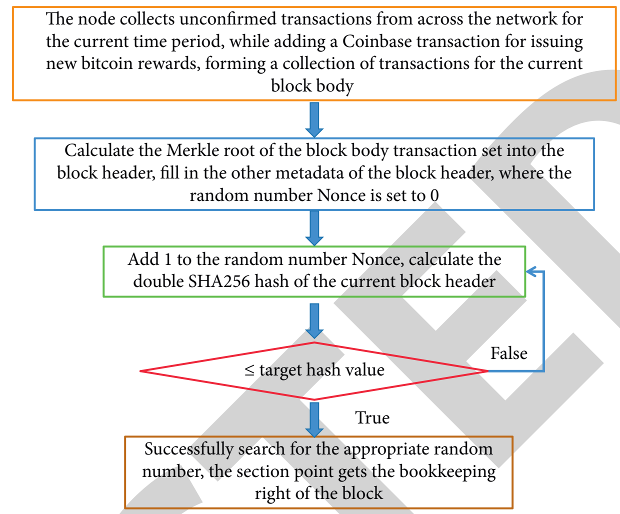

Figure 5: Consensus algorithm search process.

$$P = 1 - \sum_{k=0}^{z}\frac{\lambda^k e^{-\lambda}}{k!}\left[1 - \left(\frac{q}{p}\right)^{n-k}\right]. \tag{9}$$

It is calculated that in the case where the malicious attacking node has less than 50% of the computing power, its probability of successfully achieving an attack decreases exponentially as z increases [14]. In general, Bitcoin takes z to be 6, that is, a new block is created and followed by 6 blocks before the transactions in that block are considered secure. To reduce the risk of forking and waiting for enough blocks to be confirmed, blockchains with the PoW consensus algorithm are limited in throughput but are very scalable and nodes are free to join or exit.

4. Experimentation and Evaluation

4.1. Dataset. Eighty-six patients with femoral neck fractures who underwent surgical treatment in a hospital from July 2016 to July 2018 were selected for the study, and they were randomly divided into an observation group and a control group, with 43 cases in each group. The patients in the observation group were aged 60 to 85 years, with an average age of 63.52 ± 1.29 years; 28 cases were males, and 15 cases were females. The patients in the control group were aged 61 to 84 years, with a mean age of 63.19 ± 1.18 years; 26 cases were males, and 17 cases were females. There was no statistically significant difference between the general data of the two groups of patients ($P > 0.05$). The study was approved by the hospital ethics committee, and the patients and their families gave informed consent. Inclusion criteria were as follows: meeting the indication for surgery; being confirmed as femoral neck fracture by MRI, CT, and X-ray; normal mental status; performing internal fixation treatment; and fracture time within 1 week. Exclusion criteria were as follows: combination of other injuries; combination of lower limb deformities; bilateral femoral neck fractures; old fractures; pathological fractures; low cooperation; presence of cognitive and mental disorders; and

Table 1: Comparison of analgesic effects between the two groups of patients at different time points ($n = 43$, $x \pm s$).

Group	Preoperative	6 h postoperatively	12 h postoperatively	24 h postoperatively	48 h postoperatively
Control group	6.52 ± 1.23	7.42 ± 1.85	10.85 ± 1.43	12.52 ± 1.32	14.89 ± 2.62
Observation group	6.61 ± 1.18	9.48 ± 1.89	14.98 ± 2.85	16.85 ± 2.96	18.79 ± 2.63
T	0.3462	5.1076	9.2558	6.1192	4.5268
P	0.7300	0.0000	0.0000	0.0000	0.0000

Table 2: Comparison of HR, SBP, and DBP at different time points between the two groups of patients ($n = 43$, $x \pm s$).

Group	Indicator	Before anesthesia	5 min after anesthesia	10 min after anesthesia	20 min after anesthesia	30 min after anesthesia	60 min after anesthesia
Control group	HR (beats/min)	80.02 ± 15.02	90.02 ± 14.52	80.36 ± 1.52	90.29 ± 2.15	85.03 ± 0.96	78.96 ± 1.26
	SBP (mmHg)	139.02 ± 17.05	152.96 ± 2.16	157.02 ± 2.35	137.05 ± 1.39	149.63 ± 18.06	139.63 ± 1.38
	DBP (mmHg)	90.95 ± 12.35	99.89 ± 11.27	94.02 ± 1.15	91.96 ± 1.52	90.02 ± 1.52	92.96 ± 3.28
Observation group	HR (beats/min)	80.12 ± 14.93	82.96 ± 15.16	83.56 ± 12.16	84.15 ± 13.13	84.02 ± 14.15	80.12 ± 1.01
	SBP (mmHg)	138.37 ± 17.15	140.15 ± 16.39	142.34 ± 15.05	139.86 ± 17.85	139.98 ± 18.69	137.96 ± 15.39
	DBP (mmHg)	89.63 ± 13.02	92.96 ± 0.32	93.93 ± 12.15	92.25 ± 10.26	93.36 ± 15.02	92.25 ± 14.26

combination of coronary heart disease, diabetes mellitus, and hypertension.

4.2. Data Preprocessing. After the patients in both groups were admitted to the room, cardiac monitoring was connected, intravenous access was quickly established, and all vital signs such as pulse rate, oxygen saturation, heart rate (HR), and blood pressure were closely monitored. The control group analyzed the decentralized information of users using the algorithm based on Internet blockchain proposed in this paper, as well as parallel intravenous inhalation compound anesthesia, and, at the induction of anesthesia, patients were given intravenous injection of 0.05 mg/kg midazolam, 3 μg/kg fentanyl citrate injection (0.8 mg/kg *cis*-atracurium with 1.5 mg/kg propofol), and inhalation of sevoflurane, and, after completing tracheal intubation, the patients were given 4~6 mg/(kg-h) propofol by micropump, and the EEG dual frequency index was maintained at 40~60, with additional fentanyl and *cis*-atracurium if necessary. In the observation group, ultrasound-guided nerve block anesthesia was performed, and the patients were given 0.5 mg of atropine sulfate injection intramuscularly before surgery. After admission, the peripheral veins were opened, HR and blood pressure were routinely monitored, and the patients were given 0.03 mg/kg midazolam intravenously for proper sedation. The posterior unilateral sciatic and lumbar plexus nerve block was performed under ultrasound (GELOGIQE9 color Doppler ultrasound) guidance, and, after the small articular prominence was detected, the ultrasound probe was continued to move upward until the images of L4~5 and L3~4 lumbar transverse process were clearly displayed; the needle tip was placed close to the probe, and the out-of-plane method was used to enter the needle, which could be observed under ultrasound. The puncture needle was observed to pass through the L3~4 transverse process gap until it reached the posterior 2/3, and local anesthetic drugs were injected immediately after the nerve plexus was found; the patient's nerve bundle was infiltrated with the drug solution as observed on the ultrasound image, and, for the nerve bundle that was not successfully infiltrated, the needle tip orientation was changed to be close to the nerve before the drug was injected until it was completely infiltrated with the drug solution.

4.3. Evaluation Metrics. The analgesic effects of the two groups were compared. The mechanical pain threshold of the skin around 2 cm of the patient's surgical incision was measured at 6, 12, 24, and 48 h postoperatively using the tactile measurement kit Nonfruit, respectively, and the intensity of the measurement tool was increased from 0.4 g with the fiber tip in vertical contact with the skin, ensuring that the fiber tip was in a bent state for at least 2 s. The corresponding intensity value of the fiber at the time of the patient's tingling sensation (Xf) was recorded as the final measured intensity value. The HR, systolic blood pressure (SBP), and diastolic blood pressure (DBP) before and 5, 10, 20, 30, and 60 min after anesthesia were compared between the two groups. The onset and maintenance time of sensory block and the duration and maintenance time of motor block were compared between the two groups. SPSS 19.0 statistical software was used to process the data, and the count data were expressed as n/% by $x2$ test, and the measurement data were expressed as $x \pm s$ by t-test, and the difference was considered statistically significant at $P < 0.05$.

4.4. Results. From the comparison of the analgesic effects of the two groups of patients at different time points, there was no statistically significant difference between the preoperative mechanical pain thresholds of the two groups ($P > 0.05$); the mechanical pain thresholds of the patients in the observation group were higher than those in the control group at 6, 12, 24, and 48 h after surgery, and the difference was statistically significant ($P < 0.05$). See Table 1.

Table 3: Comparison of blockage between the two groups ($n = 43$, $x \pm s$, min).

Group	Sensory blockade takes effect	Sensory blockade maintenance	Motor block onset	Motor block maintenance
Control group	Time	Time	Time	Time
Observation group	7.12 ± 1.85	325.63 ± 40.02	8.15 ± 1.28	152.02 ± 32.85
T	5.36 ± 1.62	426.96 ± 45.63	9.86 ± 1.56	189.63 ± 43.02
P	25.6326	12.2285	9.6325	20.6324

The HR, SBP, and DBP of the two groups at different times were not statistically significant when comparing the HR, SBP, and DBP of the observation group at 5, 10, 20, 30, and 60 min after anesthesia with those before anesthesia ($P > 0.05$); the amplitude of HR, SBP, and DBP fluctuations of the observation group at each time point was smaller than that of the control group. See Table 2.

The onset of sensory block was shorter in the observation group than in the control group, and the maintenance time of sensory block, the onset of motor block, and the maintenance time of motor block were longer in the observation group than in the control group, and the differences were statistically significant ($P < 0.05$, Table 3).

5. Conclusion

In this paper, we proposed a method of applying ultrasound-guided nerve block anesthesia to fracture patients in the context of Internet blockchain, and two groups of patients were given intravenous inhalation complex anesthesia and ultrasound-guided nerve block anesthesia, and the control group used the method proposed in this paper and the observation group did not ($P < 0.05$), suggesting that ultrasound-guided nerve block anesthesia can more effectively reduce the pain level of patients compared with intravenous inhalation compound anesthesia. Secondly, the differences in HR, SBP, and DBP at 5, 10, 20, 30, and 60 min after anesthesia in the observation group were not statistically significant compared with those before anesthesia ($P > 0.05$), and the fluctuations of HR, SBP, and DBP at all time points in the observation group were smaller than those in the control group; the onset time of sensory block in the observation group was shorter than that in the control group, and the onset time of sensory block, the onset time of motor block, and the maintenance time of motor block were longer than those in the control group. The difference was statistically significant ($P < 0.05$), indicating that the patient's vital signs were more stable, and the onset time of anesthesia was shorter, and the maintenance time was longer during ultrasound-guided nerve block anesthesia based on the Internet block chain. The reason for this is that Internet blockchain-based ultrasound-guided nerve block anesthesia can be operated intuitively through decentralization and under ultrasound guidance, which facilitates effective identification of the branch nerves of each trunk, femur, and bundle of the lumbar plexus and sciatic nerve and effectively improves the success rate of the block. In conclusion, the application of Internet-based blockchain ultrasound-guided subacromial nerve block anesthesia for fracture patients was effective, and the patient's vital signs were stable, and the block was effective, which is worth promoting.

Data Availability

The datasets used during the current study are available from the corresponding author upon reasonable request.

Conflicts of Interest

The authors declare that they have no conflicts of interest.

Authors' Contributions

Qiang Cai and Yi Han contributed equally to this work.

References

[1] T. Mori, O. Nomura, and T. Ihara, "Ultrasound-guided peripheral forearm nerve block for digit fractures in a pediatric emergency department," *The American Journal of Emergency Medicine*, vol. 37, no. 3, pp. 489–493, 2019.

[2] M. D. Baker and J. P. Gullett, "Ultrasound-guided femoral nerve blocks," *Pediatric Emergency Care*, vol. 31, no. 12, pp. 864–868, 2015.

[3] S. Ranjit and B. B. Pradhan, "Ultrasound guided femoral nerve block to provide analgesia for positioning patients with femur fracture before subarachnoid block: comparison with intravenous fentanyl," *Kathmandu University Medical Journal*, vol. 14, no. 54, pp. 125–129, 2016.

[4] E. Clattenburg, A. Herring, C. Hahn, B. Johnson, and A. Nagdev, "ED ultrasound-guided posterior tibial nerve blocks for calcaneal fracture analagesia," *The American Journal of Emergency Medicine*, vol. 34, no. 6, pp. 1183–3, 2016.

[5] M. Siebelt, K. A. Hartholt, D. F. M. van Winden et al., "Ultrasound-guided nerve blocks as analgesia for n management of distal radius fractures-two consecutive randomized controlled trials," *Journal of Orthopaedic Trauma*, vol. 33, no. 4, pp. e124–e130, 2019.

[6] C. Kang, S.-B. Kim, Y.-M. Heo et al., "Comparison of time to operation and efficacies of ultrasound-guided nerve block and general anesthesia in emergency external fixation of lower leg fractures (AO 42, 43, 44)," *The Journal of Foot & Ankle Surgery*, vol. 56, no. 5, pp. 1019–1024, 2017.

[7] L. Cheng and S. Luo, "Observation on the anesthesia effect of ultrasound-guided nerve block for elderly patients with lower limb fractures," *Proceedings of Anticancer Research*, vol. 5, no. 3, 2021.

[8] N. Jain, P. R. Mathur, V. Patodi, and S. Singh, "A comparative study of ultrasound-guided femoral nerve block versus fascia iliaca compartment block in patients with fracture femur for reducing pain associated with positioning for subarachnoid block," *Indian Journal of Pain*, vol. 32, no. 3, p. 150, 2018.

[9] T. A. Jaffe, H. Shokoohi, A. Liteplo, and A. Goldsmith, "A novel application of ultrasound-guided interscalene anesthesia for proximal humeral fractures," *Journal of Emergency Medicine*, vol. 59, no. 2, pp. 265–269, 2020.

Hindawi
Journal of Healthcare Engineering
Volume 2023, Article ID 9754869, 1 page
https://doi.org/10.1155/2023/9754869

Retraction

Retracted: Application of Wearable Sensors in the Treatment of Cervical Spondylosis Radiculopathy with Acupuncture

Journal of Healthcare Engineering

Received 10 October 2023; Accepted 10 October 2023; Published 11 October 2023

This article has been retracted by Hindawi following an investigation undertaken by the publisher [1]. This investigation has uncovered evidence of one or more of the following indicators of systematic manipulation of the publication process:

(1) Discrepancies in scope
(2) Discrepancies in the description of the research reported
(3) Discrepancies between the availability of data and the research described
(4) Inappropriate citations
(5) Incoherent, meaningless and/or irrelevant content included in the article
(6) Peer-review manipulation

The presence of these indicators undermines our confidence in the integrity of the article's content and we cannot, therefore, vouch for its reliability. Please note that this notice is intended solely to alert readers that the content of this article is unreliable. We have not investigated whether authors were aware of or involved in the systematic manipulation of the publication process.

In addition, our investigation has also shown that one or more of the following human-subject reporting requirements has not been met in this article: ethical approval by an Institutional Review Board (IRB) committee or equivalent, patient/participant consent to participate, and/or agreement to publish patient/participant details (where relevant).

Wiley and Hindawi regrets that the usual quality checks did not identify these issues before publication and have since put additional measures in place to safeguard research integrity.

We wish to credit our own Research Integrity and Research Publishing teams and anonymous and named external researchers and research integrity experts for contributing to this investigation.

The corresponding author, as the representative of all authors, has been given the opportunity to register their agreement or disagreement to this retraction. We have kept a record of any response received.

References

[1] L. Chi and Q. Zhang, "Application of Wearable Sensors in the Treatment of Cervical Spondylosis Radiculopathy with Acupuncture," *Journal of Healthcare Engineering*, vol. 2022, Article ID 8428518, 8 pages, 2022.

Hindawi
Journal of Healthcare Engineering
Volume 2022, Article ID 8428518, 8 pages
https://doi.org/10.1155/2022/8428518

Research Article

Application of Wearable Sensors in the Treatment of Cervical Spondylosis Radiculopathy with Acupuncture

Lei Chi and Qian Zhang

Department of Acupuncture and Moxibustion, Heilongjiang University of Chinese Medicine Second Affiliated Hospital, Harbin 150000, Heilongjiang, China

Correspondence should be addressed to Lei Chi; 3321020566@stu.cpu.edu.cn

Received 14 February 2022; Accepted 5 March 2022; Published 13 April 2022

Academic Editor: Liaqat Ali

Research shows that cervical spondylosis radiculopathy (CSR) is the most common type of cervical spondylosis in clinic, and Chinese medicine treatment has obvious advantages, among which acupuncture therapy has received increasing attention. CSR has the characteristics of high incidence, long treatment time, and easy recurrence after treatment. In order to meet the different needs of different patients, this paper uses wearable sensors to collect patient dynamic data, extracts the action features of cervical spondylosis to design a scoring system, analyzes the input feature scores through a convolutional neural network (CNN) model, and then outputs personalized acupuncture treatment plan. The development status of wearable sensors at home and abroad is introduced, and the modules and functions of the wearable sensors are designed. The CNN network is used as the network model for classification and recognition. The experimental results show that the CNN model used in this paper has a high classification accuracy, achieving an accuracy of up to 97%, and can help produce an effective treatment plan. In order to determine whether the treatment plan output by the model is effective, each group of data is handed over to two cervical spondylosis experts for scoring, and then the final treatment plan is determined from 10 acupuncture plans. In our experiments, 9 out of 10 plans generated by the CNN model were the same as generated by the experts, which shows the effectiveness of the model.

1. Introduction

Because of the cervical degenerative process, spondylosis occurs when the cervical spinal canal or intervertebral foramen are deformed, restricted, or stimulated. This results in structural or functional damage to the cervical spinal cord, nerve roots, and sympathetic nerves; this is known as cervical spondylosis in the medical community [1, 2]. This disease often occurs in people over the age of 40. Since the world entered the internet era, people's work, life, and study methods have undergone great changes. The frequency of desk work and cervical flexion has increased significantly, and the incidence of cervical spondylosis has also increased year by year. There is an obvious trend of younger age, and it has become a modern disease that commonly exists in the working group, which has a great impact on people's quality of life and health [3]. According to the pathological changes, cervical spondylosis can be divided into 6 types: cervical type, nerve root type, vertebral artery type, sympathetic nerve type, spinal type, and mixed type. The incidence of CSR is the highest (about 60% to 70%), and most of the onset is over the age of 30 [4]. The pathogenesis of CSR is mainly due to the degeneration of the cervical intervertebral disc, which reduces the nutritional supply of the degenerated intervertebral disc, the aging and apoptosis of the cells in the disc, and the degradation of the matrix, resulting in the bulge, herniation, and rupture of the annulus fibrosus of the intervertebral disc, which leads to the occurrence of cervical spondylosis. Radicular discomfort is one of the most common clinical complaints [5, 6]. It is now thought that radicular pain is created by a combination of mechanical compression and biochemical variables acting on the nerve root to induce pain, and the two work in tandem to produce the sensation of pain. The onset of CSR is slow; the course of the disease is long; and it is prone to recurring attacks. Conservative therapy is often used to treat it. Among them, traditional Chinese medicine therapy has the advantages of effectiveness, diversity, and safety; especially, traditional acupuncture and massage therapy have played a very important role [7]. Acupuncture can activate blood and remove blood stasis, relax tendons and collaterals, and relieve pain. Acupuncture treatment can interfere with the release of inflammatory substances, stimulate brain fibrin neurons and excite crude fibers, and can relieve chemical pain caused by biochemical factors. However, the improvement of neck and back muscle strength and the correction of the disorder of the internal structure are not very obvious [8]. Therefore, the wearable sensor collects the dynamic data of the patient's cervical spine and provides a tailored treatment plan for the patient, which can achieve a more obvious treatment effect. This system is based on the classic monitoring system but adds a wireless transmission module, a remote transmission module, and employs the wearable sensor node to allow the monitoring of the human body when it is on the move. Using the wireless sensor self-organizing network, sensor nodes are found, and the minimization protocol stack is used to manage the energy and hardware resources of the wireless sensor network. Therefore, the design requirements of convenience, speed, comfort, and humanization of the human body multiparameter monitoring system are realized as a whole [9].

This paper summarizes the current progress of cervical spondylosis treatment, according to the current situation of clinical treatment, synthesizes the treatment situation of each treatment method, and discusses the collection of relevant data of patients through wearable sensors. Using trocar acupuncture as a treatment tool, through artificial intelligence, a personalized treatment plan for cervical spondylosis is formulated. When a wearable sensor is combined with a sensor network and wearable technology to monitor a patient's condition wirelessly, it is called a "wearable sensor." Remote patient data monitoring is now feasible because of a combination of wearable medical monitoring devices, wireless sensor network technology, and long-distance wireless communication technology [10]. Today, as society and technology advance, wearable sensors are able to address the health monitoring needs of families or communities and patients due to their small size, high wireless connection speeds, and precise physiological information gathering. [11].

The main contributions of this paper are as follows:

(i) We first analyze the cervical spondylosis disease, its reasons, and characteristics and introduce the development status of wearable sensors and the design of the modules and functions of the sensors

(ii) Then we use wearable devices to collect dynamic data of the patients with cervical spondylosis, extract its features, and design a scoring system

(iii) Next, we use the convolutional neural network-based model to analyze the feature scores and generate an acupuncture treatment plan

(iv) Finally, each group of data is provided to two cervical spondylosis experts for scoring in order to determine and generate a final acupuncture treatment plan from the 10 plans

The rest of the paper is organized as follows. Section 2 discusses related work in the area. In Section 3, we discuss the method used in this paper in detail. Section 4 presents experiments and discusses the results, and Section 5 is the conclusion of the research work.

2. Related Work

Nations across the globe place a high priority on wearable technology research and development, notably in some of the world's most industrialized countries, which have substantial financial resources [12, 13]. In both the United States and Europe, wireless wearable sensor technology has grown in popularity. Research on wearable sensor technology is now taking place across the globe. Wireless wearable sensors, a major focus of today's scientific and technical study, have been achieved by all nations across the globe [14]. Currently, wireless wearable technology is maturing rapidly, making it an increasingly important component in the design and development of human body multiparameter monitoring systems. Research on wearable sensing devices is being carried out by a number of universities and research institutes in the United States and Europe [15]. Wireless wearable sensors have flourished in China as a result of the expansion of modern technology throughout the country. Context-aware wearable computing is the name of the platform being developed by the MIT Media Lab for context-aware wearable computers. The technology of human-machine exchange will be applied to wearable sensors, and the system using the tunic as a platform will integrate physiological sensors, wearable computing, and wireless communication technology and provide patients with situational awareness "memory glasses" [16]. The T-shirt researcher with sensing function developed by Fraunhofer IZM in Germany mainly selects miniaturized flexible electrodes and conductive yarns and uses ordinary T-shirts to complete the basic measurement of various physiological parameters. Conductive circuits are built into the fabric pattern for electrical connections. This T-shirt with an electrical connection can basically measure ECG signals, and a higher level will realize the monitoring of EMG signals, blood oxygen saturation, and free physical activity [17]. The simple and low-cost wireless medical monitoring system of the Universities of Malaga and Almería in Spain is mainly based on the blood oxygen saturation sensor. The system has a piece of software, installed on a PDA or PC, that can monitor pulse rate and oxygen saturation for many patients simultaneously. An additional hybrid interface is added to this system, which is connected to the GPRS or WLAN module [18]. At present, domestic wireless wearable sensor research institutions and some institutions are also rapidly emerging. Under the leadership of the Chinese Academy of Sciences, wireless wearable sensors have developed rapidly. Among the units that entered the field of wearable biomedical equipment research earlier, the achievements of the Biomedical Engineering Joint Research Center of the Chinese University of Hong Kong are also more prominent. Their core lies in noninvasive measurement, which has been applied to the monitoring of physiological parameters such as blood oxygen saturation, heart rate, and blood pressure and has achieved obvious results. The reason why the sphygmomanometer can accurately measure physiological parameters is mainly because the electronic fabric has conductivity, and the electrical signals and photoplethysmography signals can be accurately transmitted. The user interface implements the display function, and the audible alarm function is also integrated into the sphygmomanometer [19]. The wireless physiological signal monitoring system researched by the National Chinese University of Taiwan has great flexibility and mobility and can also improve the quality of healthcare. The reason why this effect can be achieved is that the system combines Wi-Fi and Bluetooth technologies, and the four monitoring modules that constitute the system mainly rely on Wi-Fi for data communication [20]. The research content and thesis structure of wireless wearable sensors combine wireless sensor network technology, wearable technology, and computer technology organically through the research and analysis of the structure principle of the traditional monitoring system. Conduct research on wireless sensor nodes, wireless sensor networks, and physiological signal processing and realize a wireless wearable human body multiparameter monitoring system that can meet the needs of real-time monitoring of family patients [21].

In recent years, many researchers have focused on the area of treatment planning and dose calculation using deep learning-based models. Bai et al. [22] developed a real-time DL-based dose calculator that could be plugged into a Monte Carlo (MC) dose engine. Their system can effectively output a dose plan in real time. Nguyen et al. [23] proposed a deep learning dosage prediction model, based on two different network architectures, U-net and DenseNet. They claimed that their proposed architecture can accurately predict the dose distribution as compared to other existing models. Tanikawa et al. [24] state that an automated treatment plan may reduce interplanner variability and can be more time-effective. They discuss the use of artificial intelligence in suggesting a treatment plan and analyze various such systems. They present a new AI-based system that evaluates the clinical text and develops treatment protocols by making use of natural language processing. Liu et al. [25] developed a DL-based system for the prediction of three-dimensional dose distributions of helical tomotherapy. They converted dose volumes of a data set into a 3D matrix that was input into the deep learning-based model. The model correlated the anatomical features and predicted dose distribution. Fan et al. [26] proposed a DL-based system to check and verify the treatment plan of high-dose rate brachytherapy by verifying the dwell positions and times for a given treatment plan. They used data from 110 brachytherapy cervical patients to train the model, and the results were verified by a number of other patients.

There are a number of clinical decision support systems in clinical and healthcare setups for cancer [27], diabetes mellitus [28, 29], and wellness recommendations [30, 31] that exploit machine learning, data mining, and roughest methods for decision-making.

Cervical spondylosis refers to the degenerative changes, degeneration, or secondary changes of the cervical intervertebral disc that stimulate or compress the corresponding spinal cord, cause the nerve root to be compressed, affect the vertebral artery, stimulate the sympathetic nerves and other adjacent tissues, and cause corresponding symptoms. Most of the disease occurs in people aged 31 to 60. With the popularization of modern artificial intelligence devices, NRTCSR has gradually become a common clinical disease, and the incidence rate has increased. According to data not directly reported, statistics show that about 8.0% to 9.8% of people in the country have neck discomfort symptoms of varying degrees, and epidemiological surveys show that the incidence is gradually increasing, among which the occurrence of CSR ranks first. With the degeneration of the spine year by year, the incidence rate also has an increasing trend. The changes in the learning and living environment of the new generation are also closely related to the degenerative changes in the spine. Therefore, the real-time collection of dynamic data of the patient's relevant parts through wearable sensors and then formulation of an appropriate personalized acupuncture treatment plan through artificial intelligence technology are the focus of this paper.

3. Method

In this section, we will discuss wearable sensors and the design and function of each of their modules. We will discuss the convolutional neural network and how they will be used for the construction of an input indicator system.

3.1. Construction Targets of Wearable Sensors. The wearable sensor adopts the mode of module independence and central control, with the central monitoring and control unit as the control core. The wireless sensor monitoring nodes of each physiological parameter are independent of each other to construct the system. Wearable sensors not only can meet the needs of different patients for wireless sensor nodes with different physiological parameters but also can meet the needs of patients without economic conditions for wireless physiological sensor nodes. Therefore, the system can be well adapted to the patient and provides cheap and safe monitoring services for the patient. Figure 1 shows the framework of the wireless wearable sensor system. According to the design and analysis of the system functions, the entire human body multiparameter monitoring system is divided into three parts in structure: the user terminal, the user's family mobile phone, the hospital or community monitoring center, and the public network service. The dotted line part is the user end, which is composed of two parts: a physiological data acquisition unit and a central monitoring and control unit.

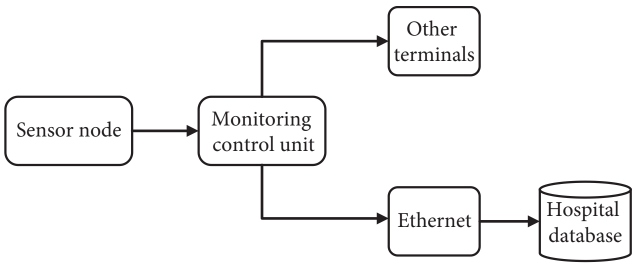

Figure 1: Wireless wearable sensor system architecture.

The design goal of the wireless wearable sensor is to realize the convenient, fast, accurate, and mobile remote real-time tracking and monitoring of the patient and provide a reliable data analysis basis for the accurate diagnosis and early prevention of diseases. The wireless wearable sensor initializes the wireless sensor node and the monitoring control unit by issuing commands from the central monitoring and control unit and at the same time detects the connectable wireless sensor nodes for network discovery and linking. The wireless sensor node receives the request of the monitoring control unit to collect the physiological signal data and send it to the monitoring control unit through the wireless module of the wireless sensor node. The monitoring and control unit processes and integrates the physiological signal data and analyzes the algorithm and then packs the data and transmits it to the user's family mobile phone through the wireless wide area network or connects the Internet with the hospital database through routing for data exchange and file management, so as to diagnose and prevent diseases in a timely manner. The construction of wireless wearable sensors should not only realize the functions of real-time acquisition of human physiological parameters of patients, wireless network transmission, and storage of analysis and diagnosis data but also realize the long-term, continuous, and mobile monitoring process. This is a relatively big challenge; therefore, the system has new requirements for the monitoring method. The amount of data obtained by long-term continuous monitoring is huge, and valuable and regular content must be screened out from this massive amount of data, which is difficult or even impossible to accomplish manually. Therefore, intelligent data analysis is also a functional requirement of the system. The aim of this paper is to collect real-time and effective dynamic data of cervical vertebrae patients and use acupuncture tools to formulate reasonable treatment plans by analyzing the collected features through artificial intelligence to obtain diagnostic results.

3.2. Design and Function of Each Module. The wearable sensors consist of basically two modules: the head and neck motion acquisition module and the head and neck motion recognition module. This section discusses the design and function of these modules.

(1) Head and neck motion acquisition module: The acceleration sensor is the core part of the head and neck motion acquisition module, which records the acceleration signal generated by the head and neck motion. The MMA7361 three-axis acceleration sensor is used in the design. Because the sensor has its own sleep mode, it can reduce power consumption to improve the battery life of the system and is suitable for wearable cervical spondylosis prevention systems. Considering the head and neck motion characteristics, the working mode of MMA7361 is set to 1.5 g mode, and the sampling rate is set to 200 Hz. For the signal control and processing functions of the system, the endurance of the head and neck motion acquisition module and the algorithm complexity of head and neck motion recognition are considered. We adopted the scheme of realizing the functions of head and neck motion acquisition and recognition in the lower computer and the upper computer, respectively. As the lower computer of the system, the head and neck motion acquisition module are responsible for the control function of the head and neck motion acquisition module. On the other hand, the signal collected by the acceleration sensor is directly forwarded to the host computer according to the protocol code, without processing the remaining digital signals.

(2) Head and neck motion recognition module: For the application scenario of cervical spondylosis prevention, we choose a smartphone as the host computer, that is, the implementation carrier of the head and neck motion recognition module. Considering the data processing capability and algorithm power consumption of the smartphone, the implementation algorithms of each function in the module have been specially designed. Considering the characteristics of head and neck motion, a time window with a width of 2 s is set to intercept the signal with a sliding window, and a window overlap of 50% is set. The head and neck motion recognition module processes the data of each 2 s segment and mainly realizes three functions: data preprocessing, specific head and neck gesture recognition, and effective head and neck motion recognition. Data preprocessing mainly removes the gravitational acceleration in the signal and collects the acceleration signal in a continuous static state. Use this as the reference value of the system's gravitational acceleration and remove 0 from it in subsequent signals. The reference value of the gravitational acceleration is corrected in real time during the system operation in an adaptive manner. Since most of the usage scenarios of cervical spondylosis are that the user maintains a fixed posture of the head and neck for a long time, the signal-to-noise ratio of the data obtained by the motion acquisition module is relatively high. Therefore, the data preprocessing in this study does not include filtering of the signal. Considering the performance and the complexity of the algorithm, the head and neck fixed pose recognition function is realized by the threshold method. In this

study, the total energy of the acceleration signal in the static state of 2 s is used as the basic threshold value, and the basic value of the threshold value is corrected in real time. Experiments have verified that in this study, the basic value of 2 times the threshold value is used as the threshold for determining the fixed posture of the head and neck, and the basic value of 5 times the threshold value is used as the threshold value for determining the effective movement of the head and neck. Based on the physiological basis of neck muscles and the research results of cervical spondylosis prevention exercise therapy, the effective motion recognition function of the head and neck divides the effective motion into 8 categories: bowing, tilting, turning left, turning right, flexing left, flexing right, left loop, and right loop, in addition to invalid motion. Finally, the valid motion and invalid motion segments are input into the convolutional neural network for classification and recognition, and the fully connected feedforward neural network is selected as the basic structure. The whole network is divided into 3 layers: input layer, hidden layer, and output layer. At the same time, in order to simplify the connection structure between neurons in each layer and improve the training efficiency of the neural network, the dropout layer is used in the training of the first two layers of the network to suppress the overfitting tendency of the network.

3.3. 1D Convolutional Neural Networks. Convolutional neural network (CNN) is a supervised training method that was first used for handwritten digit recognition and occupies a dominant position in solving this type of problem. Compared with the fully connected neural network, the convolutional neural network has the advantages of low model complexity and short training time. One-dimensional convolutional neural network (1D CNN) structure includes an input layer, convolution layer, pooling layer, fully connected layer, and output layer. The neural network automatically extracts features from the input signal layer by layer by alternately using convolutional layers and pooling layers and finally sends the extracted features to the fully connected layer and the output layer.

3.3.1. Convolutional Layer. The convolutional layer is mainly composed of several convolution kernels with local perception and parameter sharing characteristics. By performing the convolution operation to extract the features of the input data, the calculation parameters and the amount of calculation can be reduced while learning a variety of features. The input of 1DCNN is a one-dimensional vector, so the convolution kernel is one-dimensional, and the one-dimensional convolution operation is as follows:

$$x_q^p = \sum_{n=1}^{N_{p-1}} \mathrm{con}\left(K_{nq}^{p-1}, O_n^{p-1}\right) + B_q^p, \tag{1}$$

where x_q^p and B_q^p are the input and bias of the q-th neuron in the p-th layer, respectively; K_{nq}^{p-1} is the convolution kernel between the n-th neuron in the $p-1$-th layer and the q-th neuron in the p-th layer; O_n^{p-1} is the output of the n-th neuron in the $p-1$ layer; N_{p-1} is the number of neurons in the $p-1$ layer; and con is a one-dimensional convolution operation.

After the convolution calculation is completed, in order to increase the nonlinearity of the neural network model, an activation function needs to be introduced. Because the modified linear unit ReLU function can accelerate the convergence of the network, this function is generally selected as the activation function, and its expression is as follows:

$$f(x) = \max(0, x). \tag{2}$$

Therefore, the following formula is the final output of each neuron in the convolutional layer:

$$O_q^p = f\left(x_q^p\right). \tag{3}$$

3.3.2. Pooling Layer. After the convolutional layer, the pooling layer is usually used to speed up the calculation, reduce the computational cost, and prevent the overfitting problem and can maintain the translation invariance of the features.

3.3.3. Fully Connected Layer. The output of each layer of the fully connected layer is calculated by the following formula, and its input is a one-dimensional vector flattened by multidimensional feature vectors after multiple convolutional layers and pooling layers:

$$A_m^{p+1} = \sum_{n=1}^{r} W_{nm}^p a_n^p + B_m^p, \tag{4}$$

where A_m^{p+1} is the activation value of the j-th neuron in the $p+1$-th layer, a_n^p is the activation value of the n-th neuron in the p-th layer, W_{nm}^p is the weight between the m-th neuron in the $p+1$ layer and the n-th neuron in the p-th layer, and B_m^p is the bias of all the neurons in the p layer to the m-th neuron in the $p+1$ layer.

3.4. Construction of Input Indicator System Based on CNN Network. In order to accurately output a personalized treatment plan according to the specific pathological condition of the patient, this paper sets the input indicators in Table 1 according to the pathological characteristics of cervical spondylosis. The constructed CNN network model outputs 10 sets of acupuncture treatment CSR plans through different input indicators.

The index system is based on the physiological basis of neck muscles and the research results of cervical spondylosis prevention exercise therapy. The effective motion recognition function of the head and neck is divided into the above 8 categories and is scored according to the fluency of the motion and the degree of stretching, and the scoring range is

Table 1: Action index system for nerve root type cervical spondylosis.

Num.	Action	Label	Score
1	Turn left	A1	1–5
2	Turn right	A2	1–5
3	Left flexion	A3	1–5
4	Right flexion	A4	1–5
5	Head down	A5	1–5
6	Head up	A6	1–5
7	Left loop	A7	1–5
8	Right loop	A8	1–5

1–5 points. The higher the score, the better the exercise effect. It is best to input the index score into the CNN model to get an accurate acupuncture treatment plan.

4. Experiment and Analysis

A number of experiments were performed using a data set of 12,000 samples and a CNN network with 6 hidden layers. The results obtained with the CNN models were compared with the data from the human experts to measure the effectiveness of the model. This section presents the experiments and analyzes the results.

4.1. Data Set. In order to train the convolutional neural network of this system, the head and neck motion acquisition module uploads the data to the PC for saving. In daily use, it communicates with the smartphone via Bluetooth, and the integrated training on the smartphone side completes the head and neck motion recognition module. This study collected 15 volunteers, 10 men and 5 women, and a total of 12,000 acceleration data of head and neck movements. The specific data are shown in Table 2.

The training of the network randomly scrambled the data set and extracted 2,400 pieces of data to form the test set, and the remaining 9,600 pieces of data were used as the training set for CNN training. In order to achieve a better training effect and improve training efficiency, the iterative method is used for training, and the batch size is set to 200 and the epoch to 20. In addition, the learning rate is set to an adaptive adjustment mode, that is, when the loss tends to be stable and cannot be reduced further, the neural network further approaches the optimal result by reducing the learning rate.

4.2. Determination of the Number of Hidden Layer Nodes. In order to obtain the optimal number of nodes in the hidden layer, the range of the number of nodes in the hidden layer is first determined as [5–15]. In order to determine the specific number of hidden layer nodes, the number of nodes is selected as 6, 9, 12, and 15, and the following experiments are carried out, and the experimental results obtained are shown in Figures 2–5.

Finally, according to the experimental results, the best simulation results can be obtained when the number of nodes is 6, so the number of hidden layer nodes of the CNN model is determined to be 6.

Table 2: Head and neck motion acceleration data used in this article.

Num.	Action	Quantity
1	Turn left	1500
2	Turn right	1500
3	Left flexion	1500
4	Right flexion	1500
5	Head down	1500
6	Head up	1500
7	Left loop	1500
8	Right loop	1500

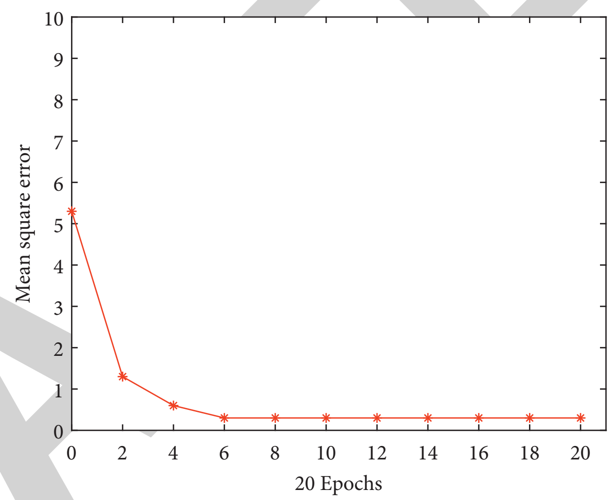

Figure 2: Training effect when $N = 6$.

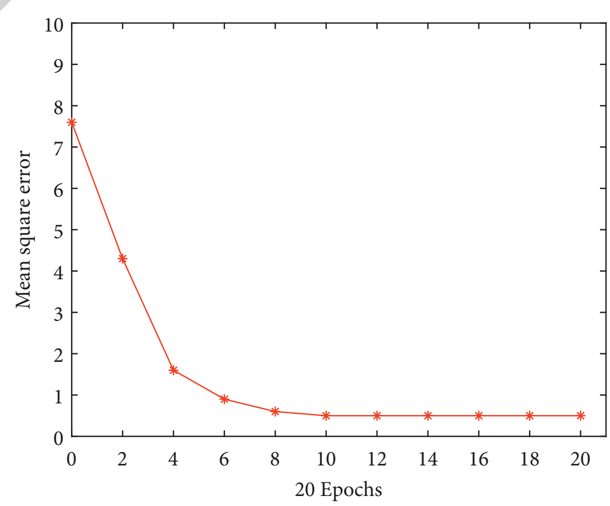

Figure 3: Training effect when $N = 9$.

4.3. Classification Accuracy Experiment of CNN Model. In order to highlight the classification accuracy of the CNN model used in this paper, a traditional BP neural network is used for comparison. The final experimental results are shown in Figure 6.

The experimental results show that the CNN model used in this paper has a high classification accuracy, and it is helpful to produce an effective acupuncture treatment plan.

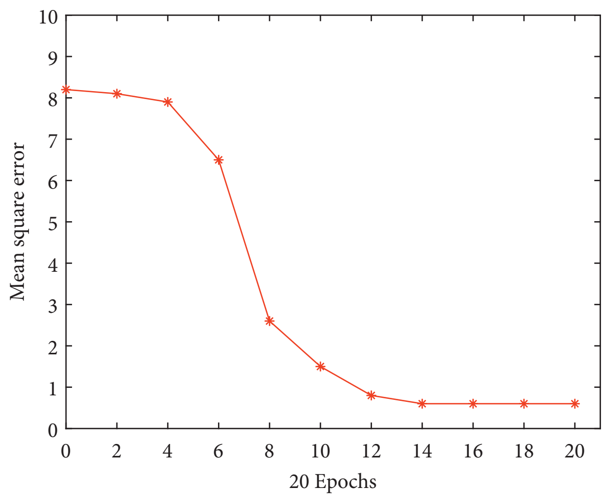

Figure 4: Training effect when $N = 12$.

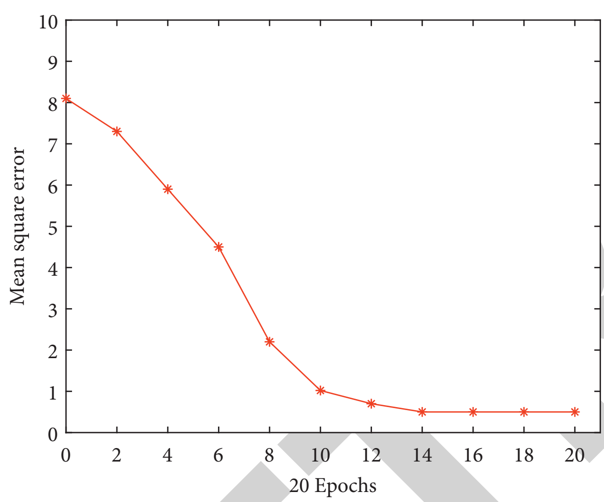

Figure 5: Training effect when $N = 15$.

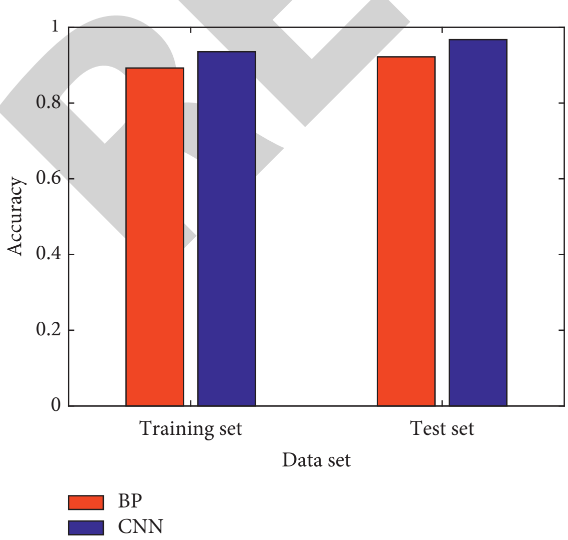

Figure 6: The accuracy comparison between the CNN model and the BP model.

Table 3: Output solution comparison between this paper and the experts.

Number	1	2	3	4	5	6	7	8	9	10
Expert solution	A	J	B	E	B	C	I	F	J	D
CNN solution	A	J	B	E	B	C	I	F	J	G

4.4. The Scheme Output in This Article Is Compared with the Expert Scheme. To determine whether the treatment regimen output by the model used in this paper is effective. In this paper, each set of data was handed over to two cervical spondylosis experts for scoring, and then the final treatment plan was determined from 10 acupuncture protocols. These 10 schemes are represented by A, B, C, D, E, F, G, H, I, and J, respectively. The final experimental results are shown in Table 3.

The final experimental results show that the accuracy rate of the output scheme of the CNN model exceeds 90%, thus proving that the model used in this paper can be used for the output of the acupuncture treatment scheme for cervical spondylosis.

5. Conclusion

In the process of treating CSR, the symptoms quickly relieve, but with the passage of time, they are noticed to appear again. In this paper, the wearable sensor is used for the output of acupuncture treatment CSR personalized plan, which collects the patient-related action data. The extracted feature index score is input to a CNN-based model, and through artificial intelligence analysis, a personalized treatment plan is an output to achieve the optimal treatment effect. This study introduces an innovative wearable sensor, hardware that can capture different features of the user's various possible neck movement postures; the software is partly based on deep learning for action classification and recognition, and the comprehensive recognition accuracy rate is 96.75%. In general, the system has a simple structure, high algorithm efficiency, and high precision; can monitor neck movements in real time, continuously, and accurately; and is expected to be used for the output of individualized treatment plans for acupuncture treatment of cervical spondylosis. The CNN-based model achieves a high classification accuracy and can effectively produce a personalized treatment. In order to determine whether the treatment plan output by the model is effective, two cervical spondylosis experts analyze and score each group of data, and then the final treatment plan is determined from 10 acupuncture plans.

In the future, we plan to improve the system to achieve higher accuracy and be able to output a personalized treatment plan with a lesser human intervention needed so that an effective plan is produced in lesser time with less effort. Moreover, we plan to extend our work and be able to generate treatment plans for other diseases where the wearable sensors can assist the process of collecting required data.

Data Availability

The data sets used during the current study are available from the corresponding author on reasonable request.

Hindawi
Journal of Healthcare Engineering
Volume 2023, Article ID 9875271, 1 page
https://doi.org/10.1155/2023/9875271

Retraction

Retracted: The Current Status of SSRP1 in Cancer: Tribulation and Road Ahead

Journal of Healthcare Engineering

Received 23 May 2023; Accepted 23 May 2023; Published 24 May 2023

This article has been retracted by Hindawi following an investigation undertaken by the publisher [1]. This investigation has uncovered evidence of one or more of the following indicators of systematic manipulation of the publication process:

(1) Discrepancies in scope
(2) Discrepancies in the description of the research reported
(3) Discrepancies between the availability of data and the research described
(4) Inappropriate citations
(5) Incoherent, meaningless and/or irrelevant content included in the article
(6) Peer-review manipulation

The presence of these indicators undermines our confidence in the integrity of the article's content and we cannot, therefore, vouch for its reliability. Please note that this notice is intended solely to alert readers that the content of this article is unreliable. We have not investigated whether authors were aware of or involved in the systematic manipulation of the publication process. Wiley and Hindawi regrets that the usual quality checks did not identify these issues before publication and have since put additional measures in place to safeguard research integrity.

We wish to credit our own Research Integrity and Research Publishing teams and anonymous and named external researchers and research integrity experts for contributing to this investigation.

The corresponding author, as the representative of all authors, has been given the opportunity to register their agreement or disagreement to this retraction. We have kept a record of any response received.

References

[1] S. Jia, B. Guo, L. Wang, L. Peng, and L. Zhang, "The Current Status of SSRP1 in Cancer: Tribulation and Road Ahead," *Journal of Healthcare Engineering*, vol. 2022, Article ID 3528786, 9 pages, 2022.

Hindawi
Journal of Healthcare Engineering
Volume 2022, Article ID 3528786, 9 pages
https://doi.org/10.1155/2022/3528786

Review Article

The Current Status of SSRP1 in Cancer: Tribulation and Road Ahead

Shengnan Jia,[1,2] Baofeng Guo,[3] Lihui Wang,[1] Liping Peng,[1] and Ling Zhang[4]

[1]*Department of Respiratory Medicine, The First Hospital of Jilin University, 71 Xinmin Street, Changchun, Jilin 130021, China*
[2]*Department of Hepatopancreatobiliary Medicine, The Second Hospital of Jilin University, Changchun, China*
[3]*Department of Plastic Surgery, China-Japan Union Hospital of Jilin University, Changchun, China*
[4]*Key Laboratory of Pathobiology, Ministry of Education and Department of Pathophysiology, College of Basic Medical Sciences, Jilin University, 126 Xinmin Street, Changchun, Jilin 130021, China*

Correspondence should be addressed to Liping Peng; penglp@jlu.edu.cn and Ling Zhang; zhangling3@jlu.edu.cn

Received 14 February 2022; Accepted 21 March 2022; Published 13 April 2022

Academic Editor: Liaqat Ali

Background and Objectives. Owing to the complexity and heterogeneity of tumors, cancer's early diagnoses and treatment have become a provocation. Structure-specific recognition protein-1 (SSRP1) is a histone (H3-H4 or H2A-H2B) chaperone in chromatin-related processes such as transcription, cell cycle control, and DNA replication, reported in various tumor tissues. It may also be used as a biomarker. This study aimed to highlight the role of SSRP1 in cancer with a focus on the current progress and future perspective. *Methods*. We search PubMed and Web of Sciences with keywords "SSRP1" and "Cancer." Only English literature was included, and conference papers and abstract were all excluded. *Results*. Transcription factors are classified into three groups based on their DNA binding motifs: simple helix-loop-helix (bHLH), classical zinc fingers (ZF-TFs), and homeodomains. The tumor-suppressive miR-497 (microRNA-497) acted as an undesirable regulator of SSRP1 upregulation, which led to tumor growth. The siRNA (small interfering RNA) knockdown of SSRP1 hindered cell proliferation along with incursion and glioma cell migration. Through the AKT (also known as protein kinase B) signaling pathway, SSRP1 silencing affected cancer apoptosis and cell proliferation. *Conclusion*. The MAPK (mitogen-activated protein kinase) signaling pathway's phosphorylation was suppressed when SSRP1 was depleted. The effect of curaxins on p53 and NF-B (nuclear factor-κB), and their toxicity to cancer cells, is attributable to the FACT (facilitates chromatin transcription) complex's chromatin trapping.

1. Introduction

Cancer has been considered the world's second largest reason for death worldwide [1]. The complexity and heterogeneity of tumors have provocation for comprehensive initiatives in cancer diagnosis and treatment [2, 3]. Tumor cell genomic heterogeneity and an environment of proinflammation are important influences in the development of tumors [4, 5]. TNAs, including genes, siRNAs/miRNAs, and oligonucleotides, were delivered to cancer cells, which enabled cancer to be tackled by restored tumor-suppressor expression and silencing oncogenes [6–10].

The key techniques in cancer treatment using nonviral gene therapies are shown in Figure 1. Angiogenesis-targeting therapy, immunization gene therapy, cancer-related fibroblast targeting, and tumor cells-derived exosome targeting are all forms of tumor microenvironment therapies (in green). Genetic strategies include genome editing, miRNA preferential treatment, transcription factor decoys, oncogene silencing, tumor-suppressor gene deletion, and suicide gene therapy (in purple).

The downregulation of specific genes happens as nucleic acids are introduced into tumor cells, a mechanism known as gene silencing [11, 12]. Typically, gene silencing therapy is carried out by vaccinating siRNA or shRNA into tumor cells to mark a particular corresponding classification to RNA (mRNA) of a specific genetic factor, enabling it to degrade or suppress protein synthesis [13, 14].

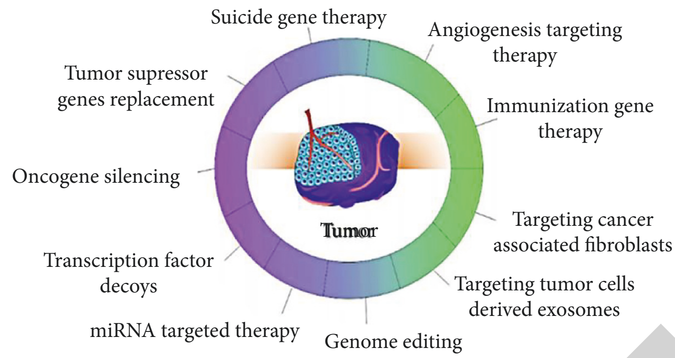

Figure 1: Major strategies in cancer therapy.

Ribosomes are protein synthesis catalysts with diverse arrangements that include protein and RNA elements. They are overexpressed proteins in cancer. Eukaryotic ribosomes are classified into two subunits, the 40S and 60S, which are named for their sedimentation coefficients. The small subunit comprises an 18S ribosomal RNA (rRNA) particle and about 33 proteins. The large subunit contains about 49 proteins [15–17]. mRNA and TRNA are connected to the minor subunit throughout protein synthesis, and a large subunit catalyzes the peptide bond. Ribosome catalytic processes are thought to be regulated primarily by rRNA molecules. Many ribosomal proteins may not seem necessary for the operation of ribosomes, and the likely task is to increase the rRNA's function. The ribosomal protein S6's phosphorylation in response to numerous growth factors has been discovered as a growth regulator, whereas some roles of other ribosomal proteins are not recognized [17, 18]. Ribosomal proteins are overexpressed in breast cancer, liver, and colon [19]. Increased cell proliferation or development does not immediately increase ribosomal protein mRNA [20] immediately. In other words, there is valid proof that ribosomal proteins are likely to lead to cell's malignant transformation [21].

Invasive colorectal cancer was first identified to amplify and overexpress ZKSCAN3 (ZNF306 or ZNF309). The investigators found that ZKSCAN3 knockdown in colorectal cancer cells dislocated self-governing development and orthotopic tumor production, while ZKSCAN3 overexpression had the reverse effect [22].

Specific protein-1 (Sp1) was called proponent-specific binding factor needed for SV40 immediate early (IE) gene transcription [23]. Sp1 was once thought to be the general transcript factor used to transcribe many "housekeeping genes," also known as maintenance genes [24]. Many of the housekeeping genes that are indispensable in cancer instigation and growth have become even more apparent. Sp1 sustains basal levels and a large range of cellular genes, activating and inhibiting them [25, 26].

2. Structure-Specific Recognition Protein-1 (SSRP1)

SSRP1 is based on a chromatin transcription facilitated complex (also known as FACTp80) that replicates, transcribes, and repairs DNA. The cell differentiation stage is associated with SSRP1. In proliferation and undifferentiated cells, SSRP1 is highly articulated [27]. Figure 2 shows the STRING interaction network highlighting SSRP1. Transcriptional control, damage repair of DNA, and cell regulation cycle are functions of structural-specific recognition protein-1 (SSRP1) [28]. SSRP1 is overexpressed in several tumor tissues, but is underexpressed in mature tissues [29]. SSRP1 is expressed at significantly elevated levels in multiple human tumor cells [30, 31]. In many cancer-related cases, elevated SSRP1 expression has been linked to metastasized tumors, making SSRP1 a potential prognostic marker and an anticancer target for tumor inhibition [32, 33]. SSRP1 knockdown in colorectal tumors inhibits relocation, propagation, and invasion and encourages apoptosis [34]. FACT aids as a marker and a target for active breast cancer cells [35]. SSRP1 expression is higher in stem cells and cells that are less differentiated, but it is lower in more differentiated cells [36]. The biological activities of SSRP1 are regulated by the HMG domain [37].

3. Possible Mechanisms of SSRP1

MicroRNAs (miRNAs) are 18–25 nt noncoding RNAs that bind to the three untranslated regions (UTRs) of target mRNAs to impede translation [38]. MicroRNAs play several roles in the growth of the disease. Tissue morphogenesis, proliferation, and apoptosis are cellular processes that miRNAs play a role in [39, 40]. MicroRNA-28-5p (miR-28-5p) [41] has been shown to suppress tumor growth in several cancers [42], including natural killer lymphoma, hepatocellular carcinoma, and prostate cancer [43–45]. Cheng Wang et al. discovered that miR-28-5p prevents the migration and proliferation of human renal carcinoma cell lines. miR-28-5p blocks the migration of breast cancer cells, according to Liang Ma et al. The miR-28-5p/CAMTAN2 axis controls colorectal cancer development, and miR-28-5p undesirably controls SSRP1 [46]. If the transcription of the mRNAs is decreased, the stability of the protein complex is significantly reduced and its levels rapidly decrease (Figure 3) [47].

According to immunohistochemistry results, downregulation of SSRP1 in xenograft tumors weakens migration and invasion potential in vivo. Organs such as the kidney, heart, lung, liver, and spleen were not affected by SSRP1

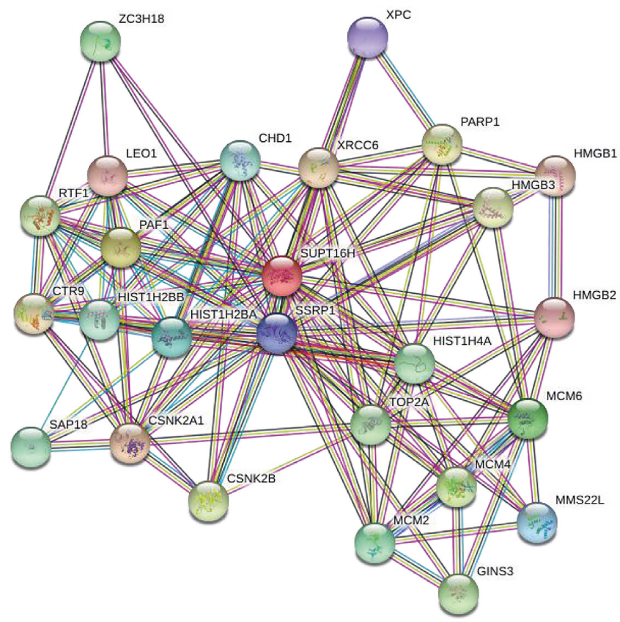

Figure 2: STRING network analysis showing SSRP1 (https://www.genecards.org/cgi-bin/carddisp.pl?gene=SSRP1).

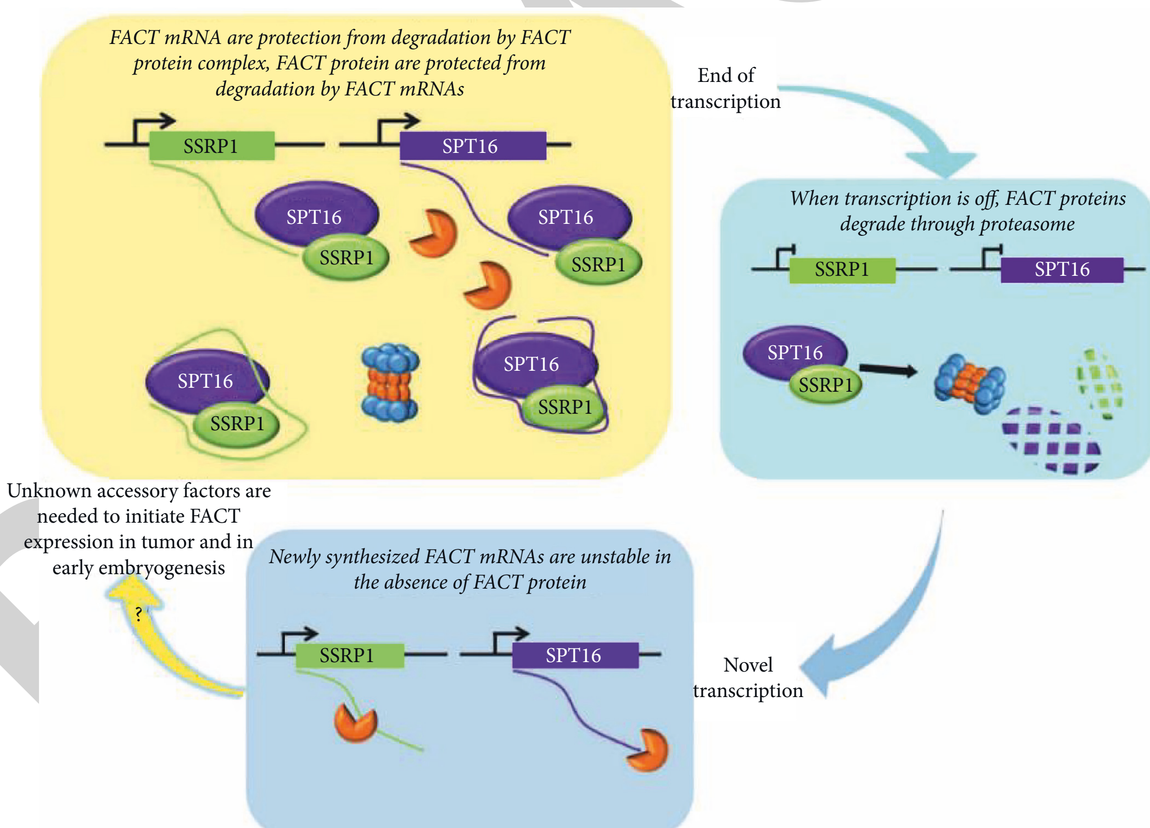

Figure 3: Proposed scheme of regulating FACT complex subunits in mammalian cells. Reproduced with permission from [47].

knockdown [48]. Diagnosing some diseases, such as heart failure, is a difficult undertaking, much more, so in underdeveloped and emerging nations, human expertise and technology are few [49, 50]. Curaxins, anti-SSRP1 molecules, cause apoptosis in tumor cells [51]. In vivo, silencing SSRP1 activated the AKT signaling pathway, causing downstream apoptosis and cell cycle proteins to alter their expression. In vivo and in vitro, SSRP1 inhibition substantially decreased colorectal cancer proliferation and metastasis and promoted apoptosis [40, 52].

Data show that miR-497 inhibits CCND1 and several other well-studied oncogenic proteins [53]. In most adult tissues, SSRP1 protein levels are modest, but the pathways behind the upregulation of SSRP1 in cancer are still unknown. SSRP1 was miR-497's first direct goal. The miR-497 expression is undesirably associated with SSRP1 expression. SSRP1 is also implicated in cancer cell chemosensitivity. It indicates that miR-497 downregulation can play a role in cancer cells developing a chemoresistance phenotype [54, 55]. Phosphor-Ets-1 translocation from the cytoplasm to the cell nucleus is assisted by SSRP1. The expression and phosphorylation of Ets-1 were only slightly influenced. Ets-1 is a positive regulator of Pim-3 [45]. Docetaxel treatment after SSRP1, Ets-1, or Pim-3 knockdown on apoptosis, inhibition of incursion, and clonogenicity in HNE-1 cells were not effective as NPC cell proliferation, apoptosis, autophagy, incursion, and clonogenicity have all been linked to SSRP1/Ets-1/Pim-3 signaling in the past. Docetaxel chemosensitivity in cells is increased when this signaling is blocked [56, 57]. A previous study reported that active DNA demethylation by DME needs SSRP1 function through a distinct process from direct DNA methylation control (Figure 4) [58].

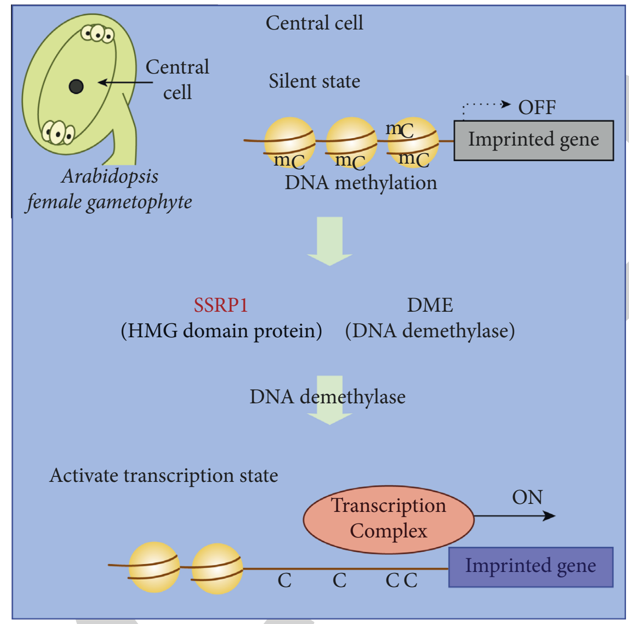

Figure 4: DNA demethylation by DME requires SSRP1 function. Reproduced with permission from [58].

4. Role of SSRP1 in Various Tumors

In the following, we discussed the role of SSRP1 in some well-developed tumors. We highlight the recent progress with recent challenges in each cancer and future perspectives.

4.1. Hepatocellular Carcinoma (HCC) and SSRP1. Protein expression and its levels in HPA, SSRP1, and mRNA were significantly higher in HCC than in normal liver tissue [59]. Furthermore, in HCC patients, higher SSRP1 expression was linked to shorter survival and progression-free survival period. As a possible prognostic marker, SSRP1 needs further clinical research. SSRP1 prevents acute lipid catabolism cycles, inflammatory reactions, and peroxisome structure [34, 60]. The molecular mechanism of HCC carcinogenesis is dependable with these results. SSRP1 affects immune cell infiltration, which facilitates the production of HCC and can influence the impact of immunotherapy [59, 61]. In transgenic mice expressing the Her2/neu protooncogene, FACT expression upregulated during tumorigenesis of mammary carcinoma in vivo. The mRNA and protein levels are upregulated in HCC [62]. The upregulation of SSRP1 may help the accumulation of DNA and gene mutations in HCC cells. In HCC, SSRP1 was discovered to be an oncogene. After curative hepatectomy, it could be a new prognostic factor for HCC [43]. The dominator in the process of reality engaging in HCC progression is SSRP1.

In HCC cells, SSRP1 controls both cell cycle and apoptosis [63]. When SSRP1 was overexpressed, cell migration and incursion increased. SSRP1 was inhibited, and cell migration and incursion decreased [64]. These findings suggested that SSRP1 played a role in reducing HCC cells' chemotherapeutic drug sensitivity. Though several theories have been suggested to explain it, the fundamental mechanism is still unknown. In the normal process of DNA replication, SSRP1 is an essential regulator. FACT interrelates with MCM helicase to conduct DNA unwinding on the nucleosome template. DNA replication is delayed when the FACT-MCM complex is interrupted [62, 65]. FACT has also been shown to influence the NF-B and p53 pathways in nearly all tumors, and its absence can lead to abnormal homologous recombination [66]. As a result, SSRP1 dysregulation triggers cancer genome instability, facilitating HCC progression in cells. SSRP1 has been identified as a key target in HCC for preventing metastasis and reversing opioid tolerance [65]. In a liver biopsy, SSRP1 can be assessed to predict the genetic activities of HCC. Multiple cancers have been identified to downregulate miR-497 and its tumor-suppressive activity, including head and neck, cervical, breast, lung, and prostate/ovarian cancer [67]. MYC activated DLG1-AS1 and the proliferation and migration of HCC through the SSRP1 axis (Figure 5). SSRP1 functions as an oncogene in HCC [68].

4.2. Colorectal Cancer and SSRP1. The lncRNA LOC101927746 inhibits colorectal cancer growth by overturning miR-584-3p and stimulating its target gene SSRP1 [69]. SSRP1 silencing inhibits colorectal cancer replication, migration, and incursion. It prevents the MAPK signaling pathway from being phosphorylated, which causes glioma cell production and metastasis. SSRP1 slows cancer cell growth and prevents erlotinib resistance by modulating the nuclear factor-kappa B signaling pathway. Disrupting the WNT signaling pathway, silencing SSRP1 with siRNA inhibits lung cancer progression, migration, and incursion. By inhibiting proliferation and encouraging apoptosis, SSRP1

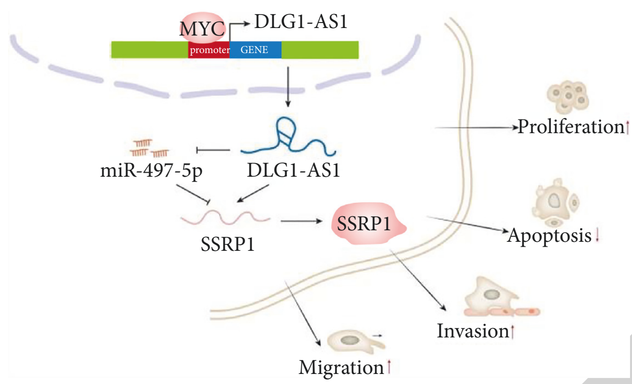

Figure 5: SSRP1 functions as an oncogene in HCC and activates the proliferation and migration of HCC. Reproduced with permission from [68].

silencing can activate the AKT signaling cascade. SSRP1 downregulation mediated by siRNA suppressed migration [28, 70]. In vivo, silencing SSRP1 inhibits the AKT signaling pathway, allowing downstream proteins to alter their expression. According to the researchers, SSRP1 inhibition prevents colorectal cancer proliferation and metastasis while also promoting apoptosis in vivo and vitro. The PI3K-AKT signaling pathway connects the survival and apoptosis of cells. In mammals, the serine/threonine kinase AKT (also known as protein kinase B), which has three isoforms (AKT1, 2, and 3), is a critical propagator of PI3K signaling [71, 72]. Metabolism, cell survival and its development, metastasis, and tumorigenesis are regulated by activated AKT, which phosphorylates a broad range of substrates. Silencing SSRP1 activated the AKT signaling pathway, which controls colorectal cancer [39]. SSRP1 silencing can trigger the AKT signaling pathway by preventing proliferation and encouraging apoptosis. Including siRNA, the migration was slowed by SSRP1 downregulation [73–75].

4.3. Ovarian Cancer and SSRP1. SSRP1 expression was more complex in ovarian cancer cells [73]. FACT provides a selective benefit to tumor cells under normal conditions and renders them more susceptible to curaxins cytotoxicity (Figure 6) [76]. Curaxins' tumor selectivity may be attributed to chromatin variations that allow tumor cells to have a higher demand for proof action than normal cells. FACT may have the same effect in normal tumor tissues. But NF-B-directed transcription can be more significant for tumor cells than normal cells. FACT's roles include histone dimer and tetramer attachment, including nucleosome remodeling in the vicinity of RNAPs.

The transcription of nucleosome-structured genes includes [48, 77] the presence of free soluble FACT. Owing to their near interaction with chromatin, curaxins promote FACT localization, resulting in the removal of soluble FACT. The affinity of truth for altered chromatin construction triggered by DNA intercalation of curaxins [78] is possible at the center of its "trapping" in chromatin. Curaxins-treated cells cause NF-B-dependent transcription to be suppressed by decreasing free FACT. It can also affect other transcriptional programs. The activation of p53 is also triggered by FACT binding to curaxins-impregnated chromatin. The SSRP1 HMG domain of FACT binds to twisted DNA [79]. This tends to prohibit CK2 from phosphorylating SSRP1's intrinsically disordered neighboring domain. CK2 does not have SSRP1 as a substrate and shifts its focus and phosphorylates p53 to Ser392. However, the existence of curaxins-induced changes in chromatin structure is uncertain. There was no significant curaxins-induced binding of FACT to nucleosomes in vitro assays [80]. Curaxins impregnation is insufficient because DNA cross-links caused by cisplatin recruit FACT to twist DNA. In the context of chromatin, stronger/different DNA structure modifications are created [81, 82].

4.4. Gliomas and SSRP1. The MAPK signaling pathway is activated in over 88% of gliomas [83]. While the role of SSRP1 as a histone chaperone has been studied, little is known about its expression and possible molecular mechanism in glioma [59]. There was no discernible connection between SSRP1 expression and the patients' age or gender [54]. Based on cues, the MAPK pathway regulated many cellular programs, including differentiation, apoptosis, embryogenesis, and proliferation. The downregulation of SSRP1 led to a major reduction in phosphorylation of p38, ERK, and JNK, as well as overall p38 and ERK protein expression. The MAPK pathway could play a role in SSRP1's role in tumor progression [61]. The mesenchymal cells are at crossroads for SSRP1. It prevents adipocyte differentiation while fostering osteoblast differentiation. This phenomenon is greatly mediated by the modulation of the canonical Wnt/catenin signaling pathway having opposite effects on adipocyte and osteoblast differentiation being activated [53, 79]. siRNA inhibits U87 and U251 glioma cell proliferation by downregulation of SSRP1 [84]. p53 and NF-B are defined by their ability to change functions. Since it arbitrates the antitumor benefits of curaxins, FACT may be a future anticancer therapeutic goal. FACT expression is not apparent in Wi38 normal diploid fibroblasts and tumor cells [74, 75].

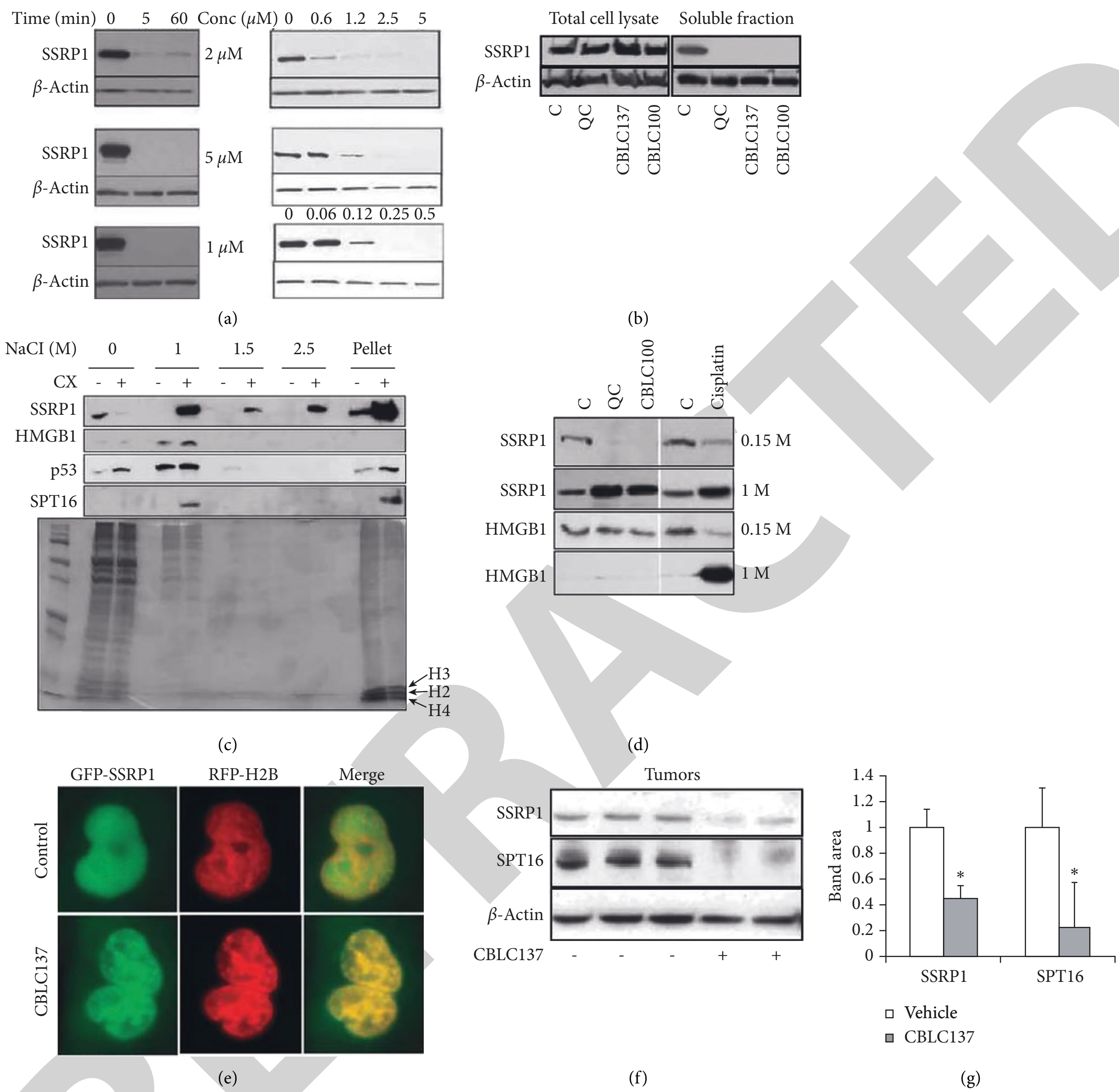

Figure 6: (a) SSRP1 from the protein following curaxin treatment. (b) SSRP1 in cell lysates through Western blot analysis. (c) SPT16 and SSRP1 redistribution from the nucleoplasm to chromatin following curaxin treatment. (d) Anti-HMGB1 and anti-SSRP1 Western analysis. (e) Images of HT1080 cells infected with GFP-tagged SSRP1 and RFP-tagged histone H2B expression constructs. (f) Curaxin-induced depletion of soluble SSRP1 and SPT16 in vivo. (g) Western blot quantification of the data in (f). Reproduced with permission from [76].

5. Concluding Remarks

SSRP1 is based on a chromatin transcription facilitated complex (also known as FACTp80) that replicates, transcribes, and repairs DNA. The cell differentiation stage is associated with SSRP1. In proliferation and undifferentiated cells, SSRP1 is highly articulated. SSRP1 is overexpressed in several tumor tissues but is underexpressed in mature tissues. In many cancer-related cases, elevated SSRP1 expression has been linked to metastasized tumors, making SSRP1 a potential prognostic marker and an anticancer target for tumor inhibition. Previous studies reported the emerging role of SSRP1 in various cancers, including HCC, colon, and ovarian cancer. However, there is still a long way ahead and tribulation in elucidating the complete role of SSRP1 in various human cancers. Furthermore, preclinical and clinical studies on the mechanism of SSRP1 will help explore the open new avenue for treating different human cancers.

Data Availability

The data used to support the findings of this study are available from the corresponding author upon request.

Conflicts of Interest

The authors declare that they have no conflicts of interest.

Authors' Contributions

Liping Peng and Ling Zhang contributed equally to this work.

Acknowledgments

This study was funded by the Fundamental Research Funds for the Central Universities, JLU, the National Natural Science Foundation of China (81773217 to L.Z.), the Research Fund for International Cooperation Project of the Jilin Provincial Science and Technology Department (20190701065GH to L.Z.), the Jilin Province Health Technology Innovation Project (230 to L.Z.), the National Science and Technology Major Project (2017ZX10103004 to LP.P.), Jilin provincial Department of Finance (2018SCZWSZX-021 to LP.P.), and Jilin Province Health Project (2020SCZT057 to SN.J.).

References

[1] H. Sung, J. Ferlay, R. L. Siegel et al., "Global cancer statistics 2020: GLOBOCAN estimates of incidence and mortality worldwide for 36 cancers in 185 countries," *CA: A Cancer Journal for Clinicians*, vol. 71, pp. 209–249, 2021.

[2] S. Loponte, S. Lovisa, A. K. Deem, A. Carugo, and A. Viale, "The many facets of tumor heterogeneity: is metabolism lagging behind?" *Cancers*, vol. 11, p. 1574, 2019.

[3] R. Vinhas, R. Mendes, A. R. Fernandes, and P. V. Baptista, "Nanoparticles—emerging potential for managing leukemia and lymphoma," *Frontiers in Bioengineering and Biotechnology*, vol. 5, p. 79, 2017.

[4] D. Hanahan and R. A. Weinberg, "Hallmarks of cancer: the next generation," *Cell*, vol. 144, pp. 646–674, 2011.

[5] C. Roma-Rodrigues, F. Pereira, A. P. A. de Matos, M. Fernandes, P. V. Baptista, and A. R. Fernandes, "Smuggling gold nanoparticles across cell types–a new role for exosomes in gene silencing," *Nanomedicine: Nanotechnology, Biology and Medicine*, vol. 13, pp. 1389–1398, 2017.

[6] K. Kamimura, T. Yokoo, H. Abe, and S. Terai, "Gene therapy for liver cancers: current status from basic to clinics," *Cancers*, vol. 11, p. 1865, 2019.

[7] J. Li, J. Chen, S. Wang et al., "Blockage of transferred exosome-shuttled miR-494 inhibits melanoma growth and metastasis," *Journal of Cellular Physiology*, vol. 234, pp. 15763–15774, 2019.

[8] D. Senapati, B. C. Patra, A. Kar et al., "Promising approaches of small interfering RNAs (siRNAs) mediated cancer gene therapy," *Gene*, vol. 719, Article ID 144071, 2019.

[9] Y.-T. Shao, L. Ma, T.-H. Zhang, T.-R. Xu, Y.-C. Ye, and Y. Liu, "The application of the RNA interference technologies for KRAS: current status, future perspective and associated challenges," *Current Topics in Medicinal Chemistry*, vol. 19, pp. 2143–2157, 2019.

[10] W. Xiao, W. Zhang, H. Huang et al., "Cancer targeted gene therapy for inhibition of melanoma lung metastasis with eiF3i shRNA loaded liposomes," *Molecular Pharmaceutics*, vol. 17, pp. 229–238, 2019.

[11] S. Jain, K. Pathak, and A. Vaidya, "Molecular therapy using siRNA: recent trends and advances of multi target inhibition of cancer growth," *International Journal of Biological Macromolecules*, vol. 116, pp. 880–892, 2018.

[12] Y. Xin, M. Huang, W. W. Guo, Q. Huang, L. zhen Zhang, and G. Jiang, "Nano-based delivery of RNAi in cancer therapy," *Molecular Cancer*, vol. 16, pp. 1–9, 2017.

[13] M. Larsson, W.-T. Huang, D.-M. Liu, and D. Losic, "Local co-administration of gene-silencing RNA and drugs in cancer therapy: state-of-the art and therapeutic potential," *Cancer Treatment Reviews*, vol. 55, pp. 128–135, 2017.

[14] A. Singh, P. Trivedi, and N. K. Jain, "Advances in siRNA delivery in cancer therapy," *Artificial cells, nanomedicine, and biotechnology*, vol. 46, pp. 274–283, 2018.

[15] J. K. Lam, M. Y. Chow, Y. Zhang, and S. W. Leung, "SiRNA versus miRNA as therapeutics for gene silencing," *Molecular Therapy - Nucleic Acids*, vol. 4, p. e252, 2015.

[16] A. Pecoraro, M. Pagano, G. Russo, and A. Russo, "Ribosome biogenesis and cancer: overview on ribosomal proteins," *International Journal of Molecular Sciences*, vol. 22, p. 5496, 2021.

[17] R. Vinhas, A. R. Fernandes, and P. V. Baptista, "Gold Nanoparticles for BCR-ABL1 gene silencing: improving tyrosine kinase inhibitor efficacy in chronic myeloid leukemia," *Molecular Therapy - Nucleic Acids*, vol. 7, pp. 408–416, 2017a.

[18] G. Thomas, J. Martin-Perez, M. Siegmann, and A. M. Otto, "The effect of serum, EGF, PGF2α and insulin on S6 phosphorylation and the initiation of protein and DNA synthesis," *Cell*, vol. 30, pp. 235–242, 1982.

[19] W. El Khoury and Z. Nasr, "Deregulation of ribosomal proteins in human cancers," *Bioscience Reports*, vol. 41, Article ID BSR20211577, 2021.

[20] M. Mercer, S. Jang, C. Ni, and M. Buszczak, "The dynamic regulation of mRNA translation and ribosome biogenesis during germ cell development and reproductive aging," *Frontiers in Cell and Developmental Biology*, vol. 9, Article ID 710186, 2021.

[21] J. Kang, N. Brajanovski, K. T. Chan, J. Xuan, R. B. Pearson, and E. Sanij, "Ribosomal proteins and human diseases: molecular mechanisms and targeted therapy," *Signal Transduct Target Ther*, vol. 6, p. 323, 2021.

[22] L. Yang, S. R. Hamilton, A. Sood et al., "The previously undescribed ZKSCAN3 (ZNF306) is a novel "driver" of colorectal cancer progression," *Cancer Research*, vol. 68, pp. 4321–4330, 2008.

[23] D. Fan, M. Wang, A. Cheng et al., "The role of VP16 in the life cycle of alphaherpesviruses," *Frontiers in Microbiology*, vol. 11, 2020.

[24] A. R. Black, J. D. Black, and J. Azizkhan-Clifford, "Sp1 and krüppel-like factor family of transcription factors in cell growth regulation and cancer," *Journal of Cellular Physiology*, vol. 188, pp. 143–160, 2001.

[25] J. Gilmour, S. A. Assi, U. Jaegle et al., "A crucial role for the ubiquitously expressed transcription factor Sp1 at early stages of hematopoietic specification," *Development*, vol. 141, pp. 2391–2401, 2014.

[26] C. Oleaga, S. Welten, A. Belloc et al., "Identification of novel Sp1 targets involved in proliferation and cancer by functional genomics," *Biochemical Pharmacology*, vol. 84, pp. 1581–1591, 2012.

[27] K. D. Miller, A. Goding Sauer, A. P. Ortiz et al., "Cancer statistics for hispanics/latinos, 2018. CA," *A Cancer Journal for Clinicians*, vol. 68, pp. 425–445, 2018.

[28] Q. Ding, K. He, T. Luo et al., "SSRP1 contributes to the malignancy of hepatocellular carcinoma and is negatively

regulated by miR-497," *Molecular Therapy*, vol. 24, pp. 903–914, 2016.

[29] H. Huang, N. Santoso, D. Power et al., "FACT proteins, SUPT16H and SSRP1, are transcriptional suppressors of HIV-1 and HTLV-1 that facilitate viral latency," *Journal of Biological Chemistry*, vol. 290, pp. 27297–27310, 2015.

[30] P. Brennan, P. Hainaut, and P. Boffetta, "Genetics of lung-cancer susceptibility," *The Lancet Oncology*, vol. 12, pp. 399–408, 2011.

[31] D. S. Siegel, T. Martin, M. Wang et al., "A phase 2 study of single-agent carfilzomib (PX-171-003-A1) in patients with relapsed and refractory multiple myeloma," *Blood*, vol. 120, pp. 2817–2825, 2012.

[32] H. Garcia, J. C. Miecznikowski, A. Safina et al., "Facilitates chromatin transcription complex is an "accelerator" of tumor transformation and potential marker and target of aggressive cancers," *Cell Reports*, vol. 4, pp. 159–173, 2013.

[33] K. V. Gurova, H. Garcia, J. Miecznikowski, A. R. Omilian, and C. Morrison, "Level of SSRP1 in cancer as a prognostic marker of aggressive disease," *American Journal of Clinical Pathology*, vol. 140, p. A152, 2013.

[34] Q. Wang, S. Jia, Y. Jiao et al., "SSRP1 influences colorectal cancer cell growth and apoptosis via the AKT pathway," *International Journal of Medical Sciences*, vol. 16, p. 1573, 2019.

[35] D. Fleyshman, L. Prendergast, A. Safina et al., "Level of FACT defines the transcriptional landscape and aggressive phenotype of breast cancer cells," *Oncotarget*, vol. 8, p. 20525, 2017.

[36] H. Garcia, D. Fleyshman, K. Kolesnikova et al., "Expression of FACT in mammalian tissues suggests its role in maintaining of undifferentiated state of cells," *Oncotarget*, vol. 2, p. 783, 2011.

[37] K. Röttgers, N. M. Krohn, J. Lichota, C. Stemmer, T. Merkle, and K. D. Grasser, "DNA-interactions and nuclear localisation of the chromosomal HMG domain protein SSRP1 from maize," *The Plant Journal*, vol. 23, pp. 395–405, 2000.

[38] A. Pedroza-Torres, S. L. Romero-Córdoba, M. Justo-Garrido et al., "MicroRNAs in tumor cell metabolism: roles and therapeutic opportunities," *Frontiers in Oncology*, vol. 9, p. 1404, 2019.

[39] X. F. Luan, L. Wang, and X. F. Gai, "The miR-28-5p-CAMTA2 axis regulates colon cancer progression via Wnt/β-catenin signaling," *Journal of Cellular Biochemistry*, 2019.

[40] G. Luo, J. Xu, Z. Xia et al., "SSRP1 is a prognostic biomarker correlated with CD8+ T cell infiltration in hepatocellular carcinoma (HCC)," *BioMed Research International*, vol. 2021, Article ID 9409836, 10 pages, 2021.

[41] J. T. Mendell, "MicroRNAs: critical regulators of development, cellular physiology and malignancy," *Cell Cycle*, vol. 4, pp. 1179–1184, 2005.

[42] W. P. Kloosterman and R. H. Plasterk, "The diverse functions of microRNAs in animal development and disease," *Developmental Cell*, vol. 11, pp. 441–450, 2006.

[43] S. Fazio, G. Berti, F. Russo et al., "The miR-28-5p Targetome discovery identified SREBF2 as one of the mediators of the miR-28-5p tumor suppressor activity in prostate cancer cells," *Cells*, vol. 9, p. 354, 2020.

[44] S.-B. Ng, J. Yan, G. Huang et al., "Dysregulated microRNAs affect pathways and targets of biologic relevance in nasal-type natural killer/T-cell lymphoma," *Blood*, vol. 118, pp. 4919–4929, 2011.

[45] S. L. Zhou, Z. Q. Hu, Z. J. Zhou et al., "miR-28-5p-IL-34-macrophage feedback loop modulates hepatocellular carcinoma metastasis," *Hepatology*, vol. 63, pp. 1560–1575, 2016.

[46] T. Shingu, L. Holmes, V. Henry et al., "Suppression of RAF/MEK or PI3K synergizes cytotoxicity of receptor tyrosine kinase inhibitors in glioma tumor-initiating cells," *Journal of Translational Medicine*, vol. 14, pp. 1–16, 2016.

[47] A. Safina, H. Garcia, M. Commane et al., "Complex mutual regulation of facilitates chromatin transcription (FACT) subunits on both mRNA and protein levels in human cells," *Cell Cycle*, vol. 12, pp. 2423–2434, 2013.

[48] Z. Han, Y. Zhang, Q. Yang et al., "miR-497 and miR-34a retard lung cancer growth by co-inhibiting cyclin E1 (CCNE1)," *Oncotarget*, vol. 6, p. 13149, 2015.

[49] A. Javeed, S. S. Rizvi, S. Zhou, R. Riaz, S. U. Khan, and S. J. Kwon, "Heart risk failure prediction using a novel feature selection method for feature refinement and neural network for classification," *Mobile Information Systems*, vol. 2020, Article ID 8843115, 2020.

[50] A. Javeed, S. Zhou, L. Yongjian, I. Qasim, A. Noor, and R. Nour, "An intelligent learning system based on random search algorithm and optimized random forest model for improved heart disease detection," *IEEE Access*, vol. 7, pp. 180235–180243, 2019.

[51] S. Yadav, A. Pandey, A. Shukla et al., "miR-497 and miR-302b regulate ethanol-induced neuronal cell death through BCL2 protein and cyclin D2," *Journal of Biological Chemistry*, vol. 286, pp. 37347–37357, 2011.

[52] I. E. Koman, M. Commane, G. Paszkiewicz et al., "Targeting FACT complex suppresses mammary tumorigenesis in Her2/neu transgenic mice," *Cancer Prevention Research*, vol. 5, pp. 1025–1035, 2012.

[53] J. Liao, X. Tao, Q. Ding et al., "SSRP1 silencing inhibits the proliferation and malignancy of human glioma cells via the MAPK signaling pathway," *Oncology Reports*, vol. 38, pp. 2667–2676, 2017.

[54] S. Jia, Q. Wang, Y. Jiao et al., "Ssrp1 promotes lung cancer progression by blocking the wnt pathway and is negatively regulated," *Mirna*, 2021.

[55] J. Koessler, V.-N. Trulley, A. Bosch et al., "The role of agonist-induced activation and inhibition for the regulation of purinergic receptor expression in human platelets," *Thrombosis Research*, vol. 168, pp. 40–46, 2018.

[56] C. Dai, Y. Xie, X. Zhuang, and Z. Yuan, "MiR-206 inhibits epithelial ovarian cancer cells growth and invasion via blocking c-Met/AKT/mTOR signaling pathway," *Biomedicine & Pharmacotherapy*, vol. 104, pp. 763–770, 2018.

[57] H. Guo, P. German, S. Bai et al., "The PI3K/AKT pathway and renal cell carcinoma," *Journal of genetics and genomics*, vol. 42, pp. 343–353, 2015.

[58] Y. Ikeda, Y. Kinoshita, D. Susaki et al., "HMG domain containing SSRP1 is required for DNA demethylation and genomic imprinting in arabidopsis," *Developmental Cell*, vol. 21, pp. 589–596, 2011.

[59] M. Laplante and D. M. Sabatini, "mTOR signaling in growth control and disease," *Cell*, vol. 149, pp. 274–293, 2012.

[60] W. Wu, K. He, Q. Guo et al., "SSRP1 promotes colorectal cancer progression and is negatively regulated by miR-28-5p," *Journal of Cellular and Molecular Medicine*, vol. 23, pp. 3118–3129, 2019.

[61] S. Mabuchi, H. Kuroda, R. Takahashi, and T. Sasano, "The PI3K/AKT/mTOR pathway as a therapeutic target in ovarian cancer," *Gynecologic Oncology*, vol. 137, pp. 173–179, 2015.

[62] R. A. Singer and G. C. Johnston, "The FACT chromatin modulator: genetic and structure/function relationships," *Biochemistry and Cell Biology*, vol. 82, pp. 419–427, 2004.

[63] Y. Tsunaka, J. Toga, H. Yamaguchi, S.-i. Tate, S. Hirose, and K. Morikawa, "Phosphorylated intrinsically disordered region of FACT masks its nucleosomal DNA binding elements,"

Hindawi
Journal of Healthcare Engineering
Volume 2023, Article ID 9824018, 1 page
https://doi.org/10.1155/2023/9824018

Retraction

Retracted: Efficacy of Glucocorticoid plus Intravenous Immunoglobulin in Children with Immunoglobulin-Insensitive Kawasaki Disease

Journal of Healthcare Engineering

Received 26 September 2023; Accepted 26 September 2023; Published 27 September 2023

This article has been retracted by Hindawi following an investigation undertaken by the publisher [1]. This investigation has uncovered evidence of one or more of the following indicators of systematic manipulation of the publication process:

(1) Discrepancies in scope
(2) Discrepancies in the description of the research reported
(3) Discrepancies between the availability of data and the research described
(4) Inappropriate citations
(5) Incoherent, meaningless and/or irrelevant content included in the article
(6) Peer-review manipulation

The presence of these indicators undermines our confidence in the integrity of the article's content and we cannot, therefore, vouch for its reliability. Please note that this notice is intended solely to alert readers that the content of this article is unreliable. We have not investigated whether authors were aware of or involved in the systematic manipulation of the publication process.

Wiley and Hindawi regrets that the usual quality checks did not identify these issues before publication and have since put additional measures in place to safeguard research integrity.

We wish to credit our own Research Integrity and Research Publishing teams and anonymous and named external researchers and research integrity experts for contributing to this investigation.

The corresponding author, as the representative of all authors, has been given the opportunity to register their agreement or disagreement to this retraction. We have kept a record of any response received.

References

[1] Y. Ma, J. Zhang, and R. Fan, "Efficacy of Glucocorticoid plus Intravenous Immunoglobulin in Children with Immunoglobulin-Insensitive Kawasaki Disease," *Journal of Healthcare Engineering*, vol. 2022, Article ID 9011259, 6 pages, 2022.

Hindawi
Journal of Healthcare Engineering
Volume 2022, Article ID 9011259, 6 pages
https://doi.org/10.1155/2022/9011259

Research Article

Efficacy of Glucocorticoid plus Intravenous Immunoglobulin in Children with Immunoglobulin-Insensitive Kawasaki Disease

Yongmei Ma,[1] Jingjing Zhang,[2] and Rong Fan[1]

[1]*Department of Child Immunology and Endocrinology, Baoji Maternal and Child Health Hospital, Baoji 721000, Shaanxi, China*
[2]*Department of Pediatrics, Xijing Hospital, The First Affiliated Hospital of Air Force Military Medical University, Xi'an 710032, Shaanxi, China*

Correspondence should be addressed to Rong Fan; fanrong3112022@163.com

Received 4 March 2022; Accepted 24 March 2022; Published 13 April 2022

Academic Editor: Liaqat Ali

This study mainly analyzes the clinical effect of glucocorticoid (GC) plus intravenous immunoglobulin (IVIG) in treating children with immunoglobulin (Ig)-insensitive Kawasaki disease (KD). From September 2013 to November 2021, 86 Ig-insensitive KD children were selected, including 46 children (observation group, Obs) treated with GC plus IVIG, and 40 children (control group, Con) treated with IVIG. The symptom (fever and fever) resolution time, inflammatory factors (C-reactive protein, CRP; procalcitonin, PCT; interleukin-6, IL-6), immune indicators ($CD3^+$, $CD4^+$, $CD8^+$ T lymphocytes $CD3^+$, $CD4^+$, and $CD4^+/CD8^+$), and incidence of adverse reactions were compared between the groups. The results identified shorter fever and rash resolution time in Obs compared with Con. The posttreatment CRP, PCT, IL-6, and $CD8^+$ and the incidence of adverse events reduced notably in Obs and were lower than Con, while $CD3^+$, $CD4^+$, and $CD4^+/CD8^+$ elevated statistically and were higher than that of Con. Our results indicate that GC plus IVIG can significantly promote symptom resolution, alleviate inflammatory response, and improve immune function in children with Ig-insensitivity KD, with favorable safety and clinical promotion value.

1. Introduction

Kawasaki disease (KD), a mucocutaneous lymph node syndrome named after its discoverer (Kawasaki), is an acute febrile inflammatory disease that tends to occur among infants and children [1, 2]. KD is the most common cause of acquired heart disease in children in developed countries and even leads to coronary artery aneurysms (CAA), elevating the risk of coronary artery thrombosis in the later stage [3]. In addition, the main clinical presentations of KD include persistent fever, pleural rash, conjunctival congestion, oral mucosal lesions, swollen neck lymph nodes, and severe hand swelling, which seriously threaten children's physical and mental health [4]. Although the diagnosis and treatment strategies of KD are constantly optimized, the clinical effects still leave much to be desired [5]. At present, the etiology and pathogenesis of the disease have yet to be clarified. Some studies have confirmed that it is related to the body's inflammatory microenvironment and immune dysfunction, which is mainly manifested as host immune dysregulation under inflammatory stimulation, and even activation of a series of immune-related cell groups including T lymphocyte groups in the acute phase of the disease [6]. Interestingly, in this regard, various intelligent diagnostic systems for improved heart disease diagnosis were also developed as it is most common in KD patients, which can facilitate the researchers towards KD treatment [7, 8]. It would be great if we could start from the pathogenesis of KD to find a more ideal and reliable treatment method, which will help improve the efficacy of KD children, reduce the risk of adverse events, and ease the public health burden related to KD.

Immunoglobulin (Ig), a regulator of the inflammatory process and immune response, is also vital in the effective connection between adaptability and the innate immune system [9]. Intravenous immunoglobulin (IVIG) has also been proved to be one of the standard treatments for KD, which can not only suppress inflammatory reactions through various regulatory mechanisms but also prevent the activation of innate immune cells [10]. However, some children with KD did not respond to IVIG treatment, which brings great challenges to disease treatment [11]. Glucocorticoid (GC) is a final product activated by the hypothalamus-pituitary-adrenal axis used to treat inflammation and autoimmune diseases and can regulate the cardiovascular tone, immune system, metabolism, and other physiological functions [12]. Besides, it can be used as a combination therapy with IVIG for myasthenia gravis in children with proven efficacy [13]. Previous studies have shown that GC plus IVIG is also applicable to treat acute KD, significantly shortening the fever time of children and inhibiting cytokines such as interleukin (IL)-2, IL-6, and IL-8 [14].

Given the current lack of research on the combined use of GC and IVIG in children with Ig-insensitive KD, we conduct related research to provide new clues for the treatment of this type of patient population.

2. Data and Methods

2.1. Baseline Data. From September 2013 to November 2021, 86 children with Ig-insensitivity KD were selected and assigned to an observation group (Obs; $n = 46$) and the control group (Con; $n = 40$) based on different therapies (GC plus IVIG and IVIG alone, respectively). The male-to-female and the mean age in Obs were 32 : 14 and (6.18 ± 1.12) years, respectively, while the data in Con were 28 : 12 and (5.85 ± 1.03) years. The two cohorts of patients exhibited no evident difference in baseline data like gender and age ($p > 0.05$; Table 1). This study is a retrospective study approved by the Ethics Committee of the Baoji Maternal and Child Health Hospital. The informed consent was signed by the patient's parent or guardian.

2.2. Eligibility Criteria. Inclusion criteria: meeting the diagnostic criteria for Ig-insensitive KD [15], ≤10 years old, normal cognitive and communication skills, no history of drug allergy, and no medication that may affect the results of this study within the past six months.

Exclusion criteria: presence of IVIG or GC contraindications, hematological system disorders or congenital diseases, organ dysfunction such as cardiac and hepatorenal dysfunction, and malignant tumors or infectious diseases.

2.3. Drug Treatments. Both groups were given oral aspirin (10–15 mg/kg, 3 times/day), and the dose was reduced to 3–5 mg/kg per day when fever subsided. On this basis, Con was given IVIG therapy, 1 g/kg per day for 15 days. Obs was additionally treated with GC based on the control group. Methylprednisolone sodium succinate (3–5 mg/kg/d) was injected intravenously for 30 min each time, once a day. After three consecutive days of treatment, it was changed to oral administration. The course of treatment was 15 days.

2.4. Measurement Indicators. Symptom resolution time: we mainly recorded the fever and rash resolution time of the two groups of children.

Inflammatory factors: we collected 5 mL of fasting cubital venous blood from both groups the next morning before and after treatment. After serum separation, enzyme-linked immunosorbent assay (ELISA) [16] was used to measure C-reactive protein (CRP), procalcitonin (PCT), and IL-6 in children following the operation steps of ELISA kits.

Immune indices: T lymphocytes ($CD3^+$, $CD4^+$, $CD8^+$, and $CD4^+/CD8^+$) of children were detected by flow cytometry, and the experimental operation strictly followed the instrument instructions.

Incidence of adverse reactions (ARs): we mainly observed, recorded, and statistically analyzed the number of cases of adverse events such as nausea and vomiting, diarrhea, rash, dizziness and headache, renal function injury, and thromboembolic diseases in the two groups.

2.5. Statistical Processing. We used SPSS software (IBM Inc., version 17.0) for statistical analysis and exported the images through the GraphPad Prism software (version 6.0). The chi-square test (χ^2) was utilized for comparisons of categorical data expressed as several cases/percentages (n/%) in the two groups. The intergroup and intragroup (before and after treatment) comparisons of continuous data represented by mean ± SEM were made using the independent samples t-test and paired t-test, respectively. P values less than 0.05 were considered statistically significant.

3. Results

3.1. Baseline Information. We analyzed children's general data and determined that the two arms were comparable ($p > 0.05$). The results were as follows: significant differences were absent between the groups in terms of sex, average age, time from disease onset to hospital admission, duration of fever, coronary artery disease, acute fever, rash, mucosal congestion, cardiovascular system damage, and family history ($p > 0.05$), as given in Table 1.

3.2. Impact of GC plus IVIG on Symptom Resolution Time. Fever and rash resolution time in Obs was observed as (1.22 ± 0.19) d and (2.53 ± 0.51) d, respectively. While, the data in Con was found to be (5.42 ± 1.24) d and (6.93 ± 1.51) d. Fever and rash resolution time was shorter in Obs than that of Con (Figure 1).

3.3. Impact of GC plus IVIG on Inflammatory Factors in Children. We detected and compared inflammatory factors CRP, PCT, and IL-6 between groups to evaluate the influence of the two treatments on children's inflammatory responses. The data showed no significant difference in inflammatory indexes between groups before treatment ($p > 0.05$). While, the posttreatment levels of the above inflammatory factors decreased in both groups ($p < 0.05$), with notably lower parameters in Obs ($p < 0.05$) (Figure 2).

Table 1: General information of children in the two groups (n (%), mean ± SD).

Variables	n	Control group ($n = 40$)	Observation group ($n = 46$)	Statistics (χ^2 or t)	P
Gender				0.002	0.965
Male	60	28 (70.00)	32 (69.57)		
Female	26	12 (30.00)	14 (30.43)		
Average age (years)	86	5.85 ± 1.03	6.18 ± 1.12	1.414	0.161
Time from disease onset to hospital admission (d)	86	6.68 ± 1.49	6.54 ± 1.14	0.493	0.624
Duration of fever (d)	86	3.66 ± 0.71	3.74 ± 0.77	0.498	0.620
Coronary artery disease				0.089	0.765
No	61	29 (72.50)	32 (69.57)		
Yes	25	11 (27.50)	14 (30.43)		
Acute fever				0.024	0.877
No	33	15 (37.50)	18 (39.13)		
Yes	53	25 (62.50)	28 (60.87)		
Rash				0.040	0.841
No	42	20 (50.00)	22 (47.83)		
Yes	44	20 (50.00)	24 (52.17)		
Mucosal hyperemia				0.013	0.911
No	50	23 (57.50)	27 (58.70)		
Yes	36	17 (42.50)	19 (41.30)		
Cardiovascular system damage				0.055	0.815
No	57	26 (65.00)	31 (67.39)		
Yes	29	14 (35.00)	15 (32.61)		
Family medical history				0.050	0.823
No	57	27 (67.50)	30 (65.22)		
Yes	29	13 (32.50)	16 (34.78)		

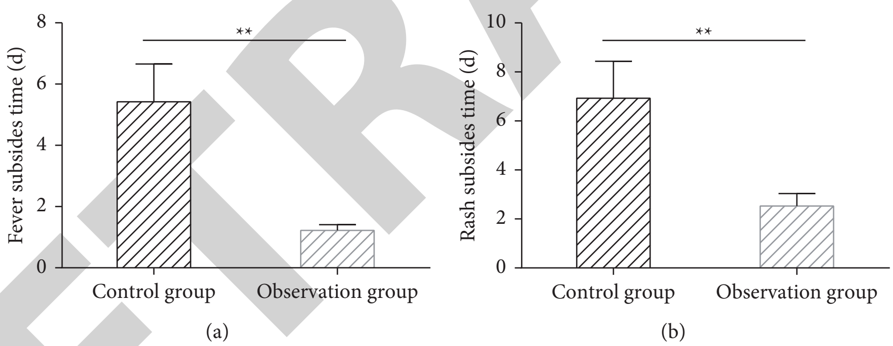

Figure 1: Effect of glucocorticoid combined with IVIG on symptom resolution time in children. (a) Comparison of fever resolution time between two groups. (b) Comparison of rash resolution time between two groups. $**P < 0.01$.

3.4. Impacts of GC plus IVIG on Immune Function of Children. We compared the effects of the two treatment methods on children's immune function by detecting T lymphocytes before and after treatment. The data revealed no evident difference in T lymphocytes between the groups before treatment ($p > 0.05$). After treatment, $CD3^+$, $CD4^+$, and $CD4^+/CD8^+$ increased ($p < 0.05$), while $CD8^+$ decreased ($p < 0.05$), with significant differences in T lymphocytes between the groups ($p < 0.05$) (Figure 3).

3.5. Impacts of GC plus IVIG on ARs in Children. In Obs, nausea, vomiting, rash, dizziness, and headache mainly occurred in 1 case each, and the incidence of ARs was 6.51%. In Con, there were 3 cases of dizziness and headache, followed by nausea, vomiting, diarrhea, and rash with 2 cases each, with an incidence of ARs of 22.50%. The incidence of ARs was lower in Obs than in Con ($p < 0.05$) (Table 2).

4. Discussion

KD is a self-limiting systemic vasculitis that can cause multiorgan arteritis, resulting in impaired multiple organ function [17]. Its incidence rate is still increasing, especially among men and children of Asian races [18]. This study mainly discusses the clinical effects of GC and IVIG in Ig-insensitive KD, aiming at contributing to the treatment of the disease.

In this study, we included 86 Ig-insensitive KD children and intervened with either the combination therapy of GC and IVIG (Obs) or IVIG monotherapy (Con). Our research results showed that the combined treatment had a remarkable effect on resolving the symptoms of fever and rash

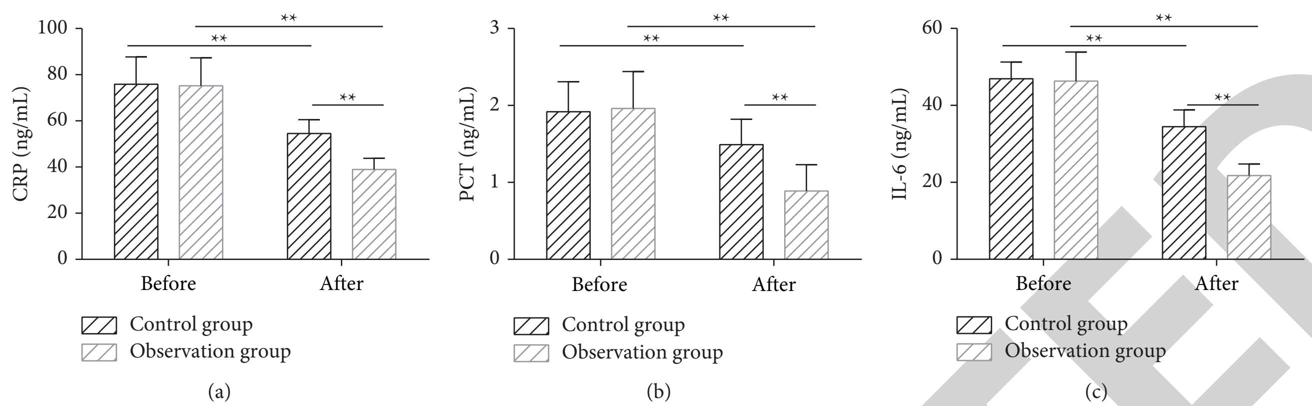

Figure 2: Effect of glucocorticoid combined with IVIG on inflammatory factors in children. (a) Comparison of CRP between two groups of children. (b) Comparison of PCT between two groups of children. (c) Comparison of IL-6 between two groups of children. $^{**}P < 0.01$.

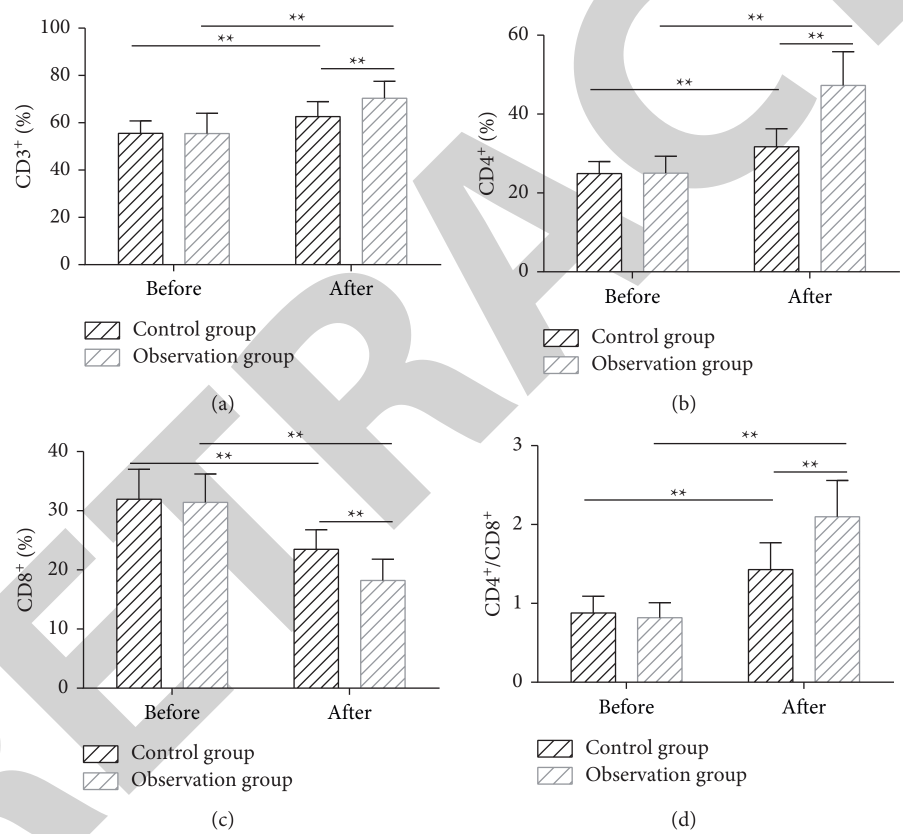

Figure 3: Effect of glucocorticoid combined with IVIG on immune function of children. (a) Comparison of $CD3^+$ between two groups of children. (b) Comparison of $CD4^+$ between two groups of children. (c) Comparison of $CD8^+$ between two groups of children. (d) Comparison of $CD4^+/CD8^+$ between two groups of children. $^{**}P < 0.01$.

Table 2: Effect of glucocorticoid combined with IVIG on adverse events in children (n (%)).

Categories	Control group ($n = 40$)	Observation group ($n = 46$)	χ^2 value	P value
Nausea and vomiting	2 (5.00)	1 (2.17)	—	—
Diarrhea	2 (5.00)	0 (0.00)	—	—
Rash	2 (5.00)	1 (2.17)	—	-
Dizziness and headache	3 (7.50)	1 (2.17)	—	-
Renal function injury	0 (0.00)	0 (0.00)	—	—
Thrombosis disease	0 (0.00)	0 (0.00)	—	—
Total	9 (22.50)	3 (6.51)	4.549	0.033

in children, suggesting that the combined intervention is more conducive to the clinical symptoms of children. IVIG preparations are composed of polyclonal plasma-derived IgG from thousands of donors, which secrete a large number of antibodies that are specific and conducive to play an anti-inflammatory role [19–21]. In KD, IVIG can reverse the abnormally delayed apoptosis of circulating neutrophils via lowering the blood neutrophil count [22]. At present, IVIG has been widely used in childhood diseases such as Guillain–Barre syndrome, Henoch–Schönlein purpura, and multiple-system inflammatory syndrome, exerting positive effects on relieving inflammation and clinical symptoms to varying degrees [23–25]. The antifever effect of GC has also been confirmed in infantile influenza, which can alleviate fever symptoms by inhibiting the secretion of proinflammatory cytokines [26]. It is known that in the acute stage of KD, the immune system will be activated, and excessive secretion of proinflammatory cytokines in circulation will be induced, leading to local and systemic injuries [27]. In the evaluation of inflammation, our data showed that the combination therapy significantly inhibited inflammatory indexes such as CRP, PCT, and IL-6, with more obvious inhibition than the monotherapy. This shows that the combined action of GC and IVIG is more effective in alleviating the inflammatory reaction of children. In terms of immune function, a more obvious improvement of T lymphocytes was observed in Obs, suggesting that the combined treatment can validly improve the immune function of children. Finally, we evaluated the safety of the two treatments and determined a higher safety profile in children treated with GC plus IVIG, which was manifested in a lower incidence of adverse events.

This study has confirmed the efficacy and safety of GC plus IVIG in treating children with Ig-insensitive KD, which can significantly resolve clinical symptoms, alleviate inflammation, and improve the immune function of children. However, this research still has potential limitations, which need to be gradually addressed in future research. First of all, the sample size of the study is small, and increasing the sample size will be more beneficial for the accuracy of the results. Second, if follow-up can be supplemented for prognostic analysis, the impact of the combined treatment on the prognosis of children with Ig-insensitive KD can be further evaluated. Finally, the underlying mechanism of their therapeutic effect can be further elucidated if the relevant basic research of combination therapy can be supplemented and their therapeutic mechanism in Ig-insensitive KD can be explored.

5. Conclusion

Here, we demonstrated the effect of the combined therapy of GC and IVIG in children with Ig-insensitive KD, and the results revealed that the combined therapy of GC and IVIG exhibited a remarkable effect for resolving the clinical symptoms of fever and rash in children. Additionally, in terms of inflammation, combination therapy significantly inhibited inflammatory indexes such as CRP, PCT, and IL-6, with more obvious inhibition than monotherapy. The combined treatment of GC and IVIG validly improve the immune function of children by causing significant improvement in T lymphocytes. Hence, this study suggests that GC plus IVIG has satisfactory clinical effects in treating children with Ig-insensitive KD, which can resolve the clinical symptoms, inflammatory reaction, and immune function of children to varying degrees, with certain safety, providing a new understanding for the treatment of such children.

Data Availability

The data used to support the findings of this study are available from the corresponding author upon request.

Conflicts of Interest

The authors declare that they have no conflicts of interest.

References

[1] Q. Zhou, J. Chen, D. Wu et al., "Differential expression of long non-coding RNAs SRA, HCG22 and MHRT in children with Kawasaki disease," *Experimental and Therapeutic Medicine*, vol. 22, no. 3, p. 1022, 2021.

[2] T. M. Nielsen, N. H. Andersen, C. Torp-Pedersen, P. Søgaard, and K. H. Kragholm, "Kawasaki disease, autoimmune disorders, and cancer: a register-based study," *European Journal of Pediatrics*, vol. 180, no. 3, pp. 717–723, 2021.

[3] K. Guo, L. Qiu, Y. Xu et al., "Single-nucleotide polymorphism LncRNA ac008392.1/rs7248320 in CARD8 is associated with Kawasaki disease susceptibility in the han Chinese population," *Journal of Inflammation Research*, vol. 14, pp. 4809–4816, 2021.

[4] B. Tang, H. H. Lo, C. Lei et al., "Adjuvant herbal therapy for targeting susceptibility genes to Kawasaki disease: an overview of epidemiology, pathogenesis, diagnosis and pharmacological treatment of Kawasaki disease," *Phytomedicine*, vol. 70, Article ID 153208, 2020.

[5] D. Zhang, L. Liu, X. Huang, and J. Tian, "Insights into coronary artery lesions in Kawasaki disease," *Frontiers in Pediatrics*, vol. 8, p. 493, 2020.

[6] T.-M. Ko, J.-S. Chang, S.-P. Chen et al., "Genome-wide transcriptome analysis to further understand neutrophil activation and lncRNA transcript profiles in Kawasaki disease," *Scientific Reports*, vol. 9, no. 1, p. 328, 2019.

[7] A. Javeed, S. Zhou, L. Yongjian, I. Qasim, A. Noor, and R. Nour, "An intelligent learning system based on random search algorithm and optimized random forest model for improved heart disease detection," *IEEE Access*, vol. 7, pp. 180235–180243, 2019.

[8] A. Javeed, S. S. Rizvi, S. Zhou, R. Riaz, S. U. Khan, and S. J. Kwon, "Heart risk failure prediction using a novel feature selection method for feature refinement and neural network for classification," *Mobile Information Systems*, vol. 2020, Article ID 8843115, 11 pages, 2020.

[9] E. A. Ermakov, G. A. Nevinsky, and V. N. Buneva, "Immunoglobulins with non-canonical functions in inflammatory and autoimmune disease states," *International Journal of Molecular Sciences*, vol. 21, no. 15, p. 5392, 2020.

[10] M. L. Rodríguez de la Concepción, E. Ainsua-Enrich, E. Reynaga et al., "High-dose intravenous immunoglobulins

Hindawi
Journal of Healthcare Engineering
Volume 2023, Article ID 9862375, 1 page
https://doi.org/10.1155/2023/9862375

Retraction

Retracted: An Effective and Lightweight Deep Electrocardiography Arrhythmia Recognition Model Using Novel Special and Native Structural Regularization Techniques on Cardiac Signal

Journal of Healthcare Engineering

Received 23 May 2023; Accepted 23 May 2023; Published 24 May 2023

This article has been retracted by Hindawi following an investigation undertaken by the publisher [1]. This investigation has uncovered evidence of one or more of the following indicators of systematic manipulation of the publication process:

(1) Discrepancies in scope
(2) Discrepancies in the description of the research reported
(3) Discrepancies between the availability of data and the research described
(4) Inappropriate citations
(5) Incoherent, meaningless and/or irrelevant content included in the article
(6) Peer-review manipulation

The presence of these indicators undermines our confidence in the integrity of the article's content and we cannot, therefore, vouch for its reliability. Please note that this notice is intended solely to alert readers that the content of this article is unreliable. We have not investigated whether authors were aware of or involved in the systematic manipulation of the publication process. Wiley and Hindawi regrets that the usual quality checks did not identify these issues before publication and have since put additional measures in place to safeguard research integrity.

We wish to credit our own Research Integrity and Research Publishing teams and anonymous and named external researchers and research integrity experts for contributing to this investigation.

The corresponding author, as the representative of all authors, has been given the opportunity to register their agreement or disagreement to this retraction. We have kept a record of any response received.

References

[1] H. Ullah, M. B. Bin Heyat, H. AlSalman et al., "An Effective and Lightweight Deep Electrocardiography Arrhythmia Recognition Model Using Novel Special and Native Structural Regularization Techniques on Cardiac Signal," *Journal of Healthcare Engineering*, vol. 2022, Article ID 3408501, 18 pages, 2022.

Hindawi
Journal of Healthcare Engineering
Volume 2022, Article ID 3408501, 18 pages
https://doi.org/10.1155/2022/3408501

Research Article

An Effective and Lightweight Deep Electrocardiography Arrhythmia Recognition Model Using Novel Special and Native Structural Regularization Techniques on Cardiac Signal

Hadaate Ullah,[1] Md Belal Bin Heyat ,[2,3,4] Hussain AlSalman ,[5] Haider Mohammed Khan,[6] Faijan Akhtar,[7] Abdu Gumaei ,[8] Aaman Mehdi,[9] Abdullah Y. Muaad ,[10,11] Md Sajjatul Islam,[12] Arif Ali,[13] Yuxiang Bu,[14] Dilpazir Khan,[13] Taisong Pan,[1] Min Gao,[1] Yuan Lin ,[1] and Dakun Lai [14]

[1]*School of Materials and Energy, State Key Laboratory of Electronic Thin Films and Integrated Devices, University of Electronic Science and Technology of China, Chengdu 610054, Sichuan, China*
[2]*IoT Research Center, College of Computer Science and Software Engineering, Shenzhen University, Shenzhen 518060, Guangdong, China*
[3]*International Institute of Information Technology, Hyderabad, Telangana 500032, India*
[4]*Department of Science and Engineering, Novel Global Community Educational Foundation, Hebersham, NSW 2770, Australia*
[5]*Department of Computer Science, College of Computer and Information Sciences, King Saud University, Riyadh 11543, Saudi Arabia*
[6]*Department of Orthopedics Surgery, West China Hospital, Sichuan University, Chengdu 610041, Sichuan, China*
[7]*School of Computer Science and Engineering, University of Electronic Science and Technology of China, Chengdu, Sichuan, 610054, China*
[8]*Computer Science Department, Faculty of Applied Sciences, Taiz University, Taiz 6803, Yemen*
[9]*Faculty of Medicine, Perm State Medical University, Perm 614000, Russia*
[10]*Department of Studies in Computer Science, University of Mysore, Mysore, Karnataka, India*
[11]*IT Department, Sana'a Community College, Sana'a 5695, Yemen*
[12]*College of Computer Science, Data Intelligence and Computing Art Lab, Sichuan University, Chengdu 610065, China*
[13]*Department of Computer Science, University of Science and Technology, Bannu, Pakistan*
[14]*Biomedical Imaging and Electrophysiology Laboratory, School of Electronic Science and Engineering, University of Electronic Science and Technology of China, Chengdu 610054, Sichuan, China*

Correspondence should be addressed to Abdu Gumaei; abdugumaei@gmail.com, Yuan Lin; linyuan@uestc.edu.cn, and Dakun Lai; dklai@uestc.edu.cn

Received 7 November 2021; Revised 19 January 2022; Accepted 15 March 2022; Published 12 April 2022

Academic Editor: Sahfqat Ullah Khan

Recently, cardiac arrhythmia recognition from electrocardiography (ECG) with deep learning approaches is becoming popular in clinical diagnosis systems due to its good prognosis findings, where expert data preprocessing and feature engineering are not usually required. But a lightweight and effective deep model is highly demanded to face the challenges of deploying the model in real-life applications and diagnosis accurately. In this work, two effective and lightweight deep learning models named Deep-SR and Deep-NSR are proposed to recognize ECG beats, which are based on two-dimensional convolution neural networks (2D CNNs) while using different structural regularizations. First, 97720 ECG beats extracted from all records of a benchmark MIT-BIH arrhythmia dataset have been transformed into 2D RGB (red, green, and blue) images that act as the inputs to the proposed 2D CNN models. Then, the optimization of the proposed models is performed through the proper initialization of model layers, on-the-fly augmentation, regularization techniques, Adam optimizer, and weighted random sampler. Finally, the performance of the proposed models is evaluated by a stratified 5-fold cross-validation strategy along with callback features. The obtained overall accuracy of recognizing normal beat and three arrhythmias (V-ventricular ectopic, S-supraventricular ectopic, and F-fusion) based on the Association for the Advancement of Medical Instrumentation (AAMI) is 99.93%, and 99.96% for the proposed Deep-SR model and Deep-NSR model, which demonstrate that the effectiveness of the proposed models has surpassed the state-of-the-art models and also expresses the higher model generalization. The received results with model size suggest that the proposed CNN models especially Deep-NSR could be more useful in wearable devices such as medical vests, bracelets for long-term monitoring of cardiac conditions, and in telemedicine to accurate diagnose the arrhythmia from ECG automatically. As a result, medical costs of patients and work pressure on physicians in medicals and clinics would be reduced effectively.

1. Introduction

Cardiovascular disease (CVD) is one of the leading human life-threatening disease; with around 17.7 million people lose their lives due to CVDs annually [1]. The mortality and prevalence of CVDs are still on rise in worldwide, therefore continuous monitoring of heart rhythm is becoming a crucial issue to prevent and control the CVDs. Arrhythmia is common rhythm but a complex CVD that leads other heart diseases. ECG is the primary medical diagnostic tool for CVD in practice and provides a comprehensive picture of patient's cardiac conditions. Currently, physicians perform post hoc analysis through ECG waveforms to diagnose whether a patient is well or sick, which is inefficient, time-consuming, and also not so reliable due to the factors of physicians' experience and expertise level. Computer-aided automatic ECG analysis could effectively enhance the diagnosis efficiency as well as shorten diagnosis time. Nowadays, automatic arrhythmia recognition systems are becoming more essential to diagnose the heart diseases. It is more useful in wearable or portable devices. The basis of a traditional automatic system is to extract features correctly and then classify or diagnose with a shallow machine learning approach. A traditional automatic ECG arrhythmia recognition system usually comprises of four parts: (1) preprocessing [2]; (2) beat segmentation [3]; (3) feature extraction such as QRS width finding [4], R-R intervals [5], and wavelet transform [6]; and (4) classification algorithms such as support vector machine (SVM) [7], genetic algorithm (GA) for SVM optimization [8], artificial neural network (ANN) [9], and random forest (RF) [10]. After extracting the features, sometimes feature selection techniques such as linear discriminant analysis (LDA) [6], independent component analysis (ICA) [5, 6], and principal component analysis (PCA) [6, 9, 11] are needed to alleviate the dimensions and dispel the related features to enhance the accuracy. Recently, Jha and Kolekar [12] proposed an efficient ECG arrhythmia classification approach using the tunable Q-wavelet transform and SVM classifier to detect the normal and seven types of arrhythmias, where ECG beats were decomposed up to the level of sixth. The achieved average accuracy, sensitivity, and specificity are 99.27%, 96.22%, and 99.58%, respectively, for eight different beat classes. Abdalla et al. [13] also presented a complete ensemble nonstationary and nonlinear decomposition method to extract the features of ECG beats with intrinsic mode functions (IMFs), where four parameters (coefficient of dispersion, singular values, average power, and sample entropy) were computed from first six IMFs to construct the features' vector. Their received average accuracy, sensitivity, and specificity are 99.9%, 99.7%, and 99.9%, respectively, to identify the normal and four different arrhythmias. An automatic heartbeat classification method was addressed by Mondéjar-Guerra et al. [14] with the combination of multiple SVMs to classify the normal and three abnormal beats and achieve satisfactory results, where various descriptors (LBP-local binary patterns, HOS-higher order statistics, and several amplitude values) based on wavelets were employed to extract the morphological and temporal characteristics of ECG beats. Sometimes, ensemble or hybrid methods in shallow machine learning algorithms are developed to achieve better predictive performance than the constituent learning algorithms alone [15–17]. Although many shallow machine learning methods, for examples [12–14], have been proposed to classify ECG arrhythmia with good findings and encouraging results, they are still facing challenges in feature extraction using engineering techniques as well as dealing the imbalanced data [18, 19]. Several researchers have tried to solve the issue by optimizing the classifiers with the generalization capabilities [20–29]. In the conventional methods, learning parameters during training the proposed techniques are able to cover multiple features with the confined nonlinear fitting and approximated capabilities in the facing of complex ECG waveforms. So, in the training of big data-driven context, the classification efficiency of conventional classifiers is not satisfactory [30].

In contrast, recent deep learning approaches could offer the solutions to overcome the challenges of shallow machine learning algorithms performing feature learning automatically [31–34] followed the human brain structure. These approaches usually combine feature extraction and classification steps of traditional methods, optimize them with the sufficient amount of data, and provide good interpretability. Besides, deep learning concepts play a vital role at present because acquired ECG data in medical and clinics are enlarged day by day, around more than 300 million ECGs are preserved worldwide annually [34, 35]. More data are helpful in the deep learning models for handling the large number of variables during training. Therefore, nowadays, it is becoming a difficult task to analyze the ECG beat-by-beat with the traditional techniques, especially in the wearable health monitoring circumstances. Hence, engineers and researches are shifting their concentrations on beat classification studies with the deep learning approaches. The reported findings in the literature [36–42] show that with the different layer initialization strategies and some promising techniques such as k-fold cross-validation, stratified k-fold cross-validation, regularization techniques (dropout [36] and batch normalization (BN) [37]), and Adam optimizer [38] in deep learning networks perform such good job. Deep neural networks (DNNs) [39, 43], CNN [40], long short-term memory (LSTM) [41], recurrent neural networks

(RNNs) [40], and also merging of these approaches [42] were employed to classify the ECG arrhythmia. Hannun et al. [39] developed an end-to-end approach in deep learning to identify the 12 classes of ECG rhythms from 53,549 patients with 91,232 single-leads monitoring device in ambulatory condition. Their achieved results validated with a consensus board committee of certified practicing cardiologists and findings demonstrated that the deep learning approach is able to classify 12 distinct rhythms with a good performance approximately same to that of cardiologists. It states that deep learning approaches could reduce the misdiagnosed rate of computerized interpretations and enhance the efficiency of cardiologists in urgent circumstances. RNNs and LSTM are mainly emerged for sequential analysis of data and a great progress of deep learning due to its successful adaptations of various versions in the basic architecture depending on the applications. Yildirim [41] presented a deep bidirectional LSTM (DBLSTM) based on the wavelet sequences of input data to classify five different heartbeats from the MIT-BIH arrhythmia dataset and experimental results provide the recognition accuracy of 99.39%. CNNs are the hierarchical neural networks where convolutional layers are changed with the subsampling of layers and reminiscent of complex and simple cells similar to the human visual cortex [44] following the fully connected layers, which are same as multilayer perceptron (MLP). CNNs are commonly employed in deep learning for object detection from complex images, achieving high accuracy results compared with the state-of-the-arts methods [45]. Recently, it is widely used in anomaly detection and ECG classification. Among the various categories of deep learning models, CNN is a more promising technique due to its good detecting capability of vital features from the raw information at the various levels of networks automatically without any human supervision. The raw ECG signals usually belong to 1D data features. CNN allows its input as the multidimensional (1D, 2D, and 3D) forms that narrate the attributes of raw signal. Kiranyaz et al. [46] proposed a patient-specific arrhythmia classification approach with 1D convolutional neural network in real time, which could be utilized to identify long ECG streams of patients with a wearable device. Some attractive works with 1D CNNs [46–48] are introduced to identify the arrhythmia from the ECG signals but the received performance results are not so satisfactory. The factors behind such performance are as follows: (i) 1D CNN is less versatile, and (ii) it does not attain the intended aim of attainment [49]. In contrast, 2D CNN is a promising approach that could handle such types of oversights in 1D CNN due to the representing of time-series data in 2D format as the input. And hence, we have chosen 2D CNN for our study, where 2D transformations of raw time-series data are performed to make it suitable as the input of 2D CNN. The more vital information can be achieved in 2D CNN compared to 1D CNN that helps to improve the accuracy easily [50], herein the authors first extract PQRST features of a single heartbeat from the raw ECG signals after some preprocessing. In [51, 52], it was reported that image-based 2D CNN arrhythmia classification structures obtain better performance compared to 1D CNN, where time domain ECG signals belonging to the heartbeats were transformed into 2D time frequency spectrograms by STFT (short time Fourier transform) to be compatible with the input of their proposed 2D CNN model. The raw ECG signals from the MIT-BIH arrhythmia dataset were first segmented into the heartbeats and then transformed into 2D gray-scale images, which were used as the input of 2D CNN architecture [53, 54] and achieved satisfactory results for identifying the heartbeats. Recently, Ullah et al. [55] proposed a 2D CNN model to classify the heartbeats from the raw ECG signals of MIT-BIH arrhythmia dataset and the performance is compared to the 1D CNN, where the experimental results demonstrate that the performance of their proposed 2D CNN model is better than 1D CNN. Therefore, 2D CNN is more feasible to diagnose arrhythmia from the ECG signals.

Moreover, although several 2D CNN approaches [49–55] have achieved impressive results to detect the arrhythmia from the ECG signal with good accuracy, a 2D CNN model with superior accuracy, guaranteed data imbalance problem-solving, and a lightweight end-to-end 2D deep learning model is more essential for real-life applications. Meanwhile, an imbalanced dataset would decline the overall accuracy of the model and result in diagnosis errors of the diseases, because a small increase in accuracy has a great impact on the diagnosis [56, 57]. In this study, two deep learning models, namely Deep-SR and Deep-NSR, based on 2D CNN approaches were proposed, which are more effective(superior accuracy), efficient (lightweight), and generalized that alleviate the data imbalance problem than the state-of-the-art models to recognize the arrhythmias in practical life. The major factors behind such satisfactory results are as follows: (i) proper model designing with proper initialization of layers and usage of some diverse regularization techniques such as BN [37] and dropout [36], and (ii) usage of weighted random sampler [58], Adam optimizer [38], and early stopping [59] in the developed model training module. The Deep-NSR is lightweight compared to Deep-SR; it is more applicable than Deep-SR for deploying in real-life applications. In the proposed Deep-NSR, (i) the adaptive pooling layer is directly connected to the softmax layer and has no dropout and fully connected layers, and (ii) the number of kernels or filters in the last convolution layer is equal to the number of target classes following the structural regularization technique [60]. As a result, the total learnable parameters are drastically reduced in the designed model and play an impact to the size of model. So far we are concerned; it is the first attempt to apply the structural regularization concept [60] in a model to diagnose ECG arrhythmia diseases that drastically reduce the learnable parameters in a model which results in a lightweight model as well as a low computational cost.

To the end, the major contributions are as follows:

(i) Two lightweight 2D CNN models are developed compared to the state-of-the-art 2D CNN models to identify the ECG arrhythmia, which could be more useful in real-life applications to diagnose the diseases automatically.

(ii) Any handcrafted feature extraction technique is not required in this study.

(iii) A state-of-the-art improvement in performance is acquired for both proposed models with the 2D transformed images as the input of deep models in ECG arrhythmia classification, which expresses high model generalization.

(iv) The achievement of model performance is due to the usage of several diverse regularization techniques (BN [37] and dropout [36]), Adam optimizer [38], weighted random sampler [58], early stopping [59], on-the-fly data augmentation [61], and proper initialization of layers [62, 63] in the designed models. As such, data imbalance shortcoming on the publicly available datasets, even on clinical or own producing data, could be overcome.

The rest of the article is organized as follows: The proposed methods and materials are demonstrated in Section 2 with details. Results with discussion are illustrated in Section 3. Finally, a conclusion with some future directions is provided in Section 4.

2. Materials and Methods

The whole architecture of our proposed system in ECG arrhythmia classification is depicted in Figure 1. In this study, we have used a benchmark dataset MIT-BIH arrhythmia database [64] to train and test the proposed models. First, ECG signals from this dataset are transformed into two-dimensional 128×128 RGB images in the preprocessing step that are fed as the input of our proposed models. Among the fourteen annotated beat and three nonbeat types in the MIT-BIH arrhythmia database, we have considered the class mappings based on AAMI recommendation, which is expressed as (i) N-normal (N-normal, R-right bundle branch block, L-left bundle branch block, e-atrial escape, and j-nodal (junctional) escape), (ii) V-ventricular ectopic (E-ventricular escape and V-premature ventricular contraction), (iii) S-supraventricular ectopic (a-aberrated atrial premature, S-supraventricular premature, J-nodal (junctional) premature, and A-Atrial premature), (iv) F-fusion (fusion of normal and ventricular), and (v) Q-unknown (/-Paced, Q-unclassified, and f-fusion of normal and paced). Herein, Q class is not taken into account due to the involvement of paced and unclassified beats. So, our proposed models have performed recognition on the total four types of beats identified as N, S, V, and F classes in the classification step. The overall system consists of the following three subsections: (i) data preprocessing, (ii) feature extraction and classification based on the proposed CNN models, and (iii) model evaluation.

2.1. Dataset Description and Acquisition. The MIT-BIH arrhythmia benchmark dataset [64] contains a total of 48 records from 47 patients, where 25 are men of age 32–89 and 22 women of age 23–89, two-channel ECG recordings, the sampling rate is 360 Hz and each record has a duration of half an hour. The resolution of digitization for each recording is 11-bit over a 10 mV range. The dataset is established by the MIT lab and Beth-Israel Hospital in Boston. In most records of the dataset, the upper signal is MLII (a modified limb lead II) while the lower signal is modified lead V1 (seldom V2 or V5 and V4 in one instance), all are placed on the chest [64]. QRS complexes of normal ECG signal are commonly noticeable in the upper signal lead II based on the website located at https://www.physionet.org for the dataset. So, we have chosen the lead II signal in our experiment. Records 102 and 104 are involved with the surgical dressings of patients, and records 102, 104, 107, and 217 have the involvements of paced beats, so we have eliminated these records in our experiment.

2.2. Data Preprocessing. Here, each ECG record is transformed into its equivalent RGB images after segmentation of each ECG beat from all the records of dataset. In the dataset, each record has three files which are annotation, signals, and header files. First, the dataset is downloaded manually from https://physionet.org/content/mitdb/1.0.0/. Then annotation file is accessed and processed with the Glob module of python and WFDB Toolbox. After reading the annotation of all records from the dataset, the data for each beat are sliced with the sampling frequency of 360 Hz. Herein, segmentation is accomplished by detecting the R peaks from all records with the help of Python Biosppy module and forming a CSV file with a sequence of the heartbeats for each beat type. Pan and Tompkins algorithm [65] for R-peak detection is well commenced and comparatively more accurate as well as arrhythmia is mainly labeled at the peak of each R-peak wave. And hence, this R peaks detection technique is chosen in this study. Once the R-peaks are detected to segment a beat, the present and next R peaks are also considered and have taken half of the distance of those, the included signals represent a segmented beat. A similar process is maintained for the segmentation of all beats. For transforming the segmented beats into the beat images, OpenCV and Matplotlib modules of python are employed. Finally, we have got a total of 97720 images of 128×128 scale size from the MIT-BIH arrhythmia dataset for four-beat types. The obtained beat images are fed into our automatic deep-based feature extractor models as the input to extract the local area-specific features by mapping the subtle spatial change of beat images. Then a high-level feature vector is formed from the extracted features. Next, the recognition of beats is performed with the softmax classifier based on this vector, which ensures the summation of the class label scores is 1.

The augmentation of input images of the models for the training set could provide the benefit of less over-fitting dealing with class imbalance problems. Our proposed models receive 2D beat images as the input, so we can easily resize, rotate, and crop the images in the training module that do not degrade the model's performance but increase the training data numbers and may help to alleviate the overfitting of models maintaining equal distribution among the classes. To maintain the equal distribution of classes, it is

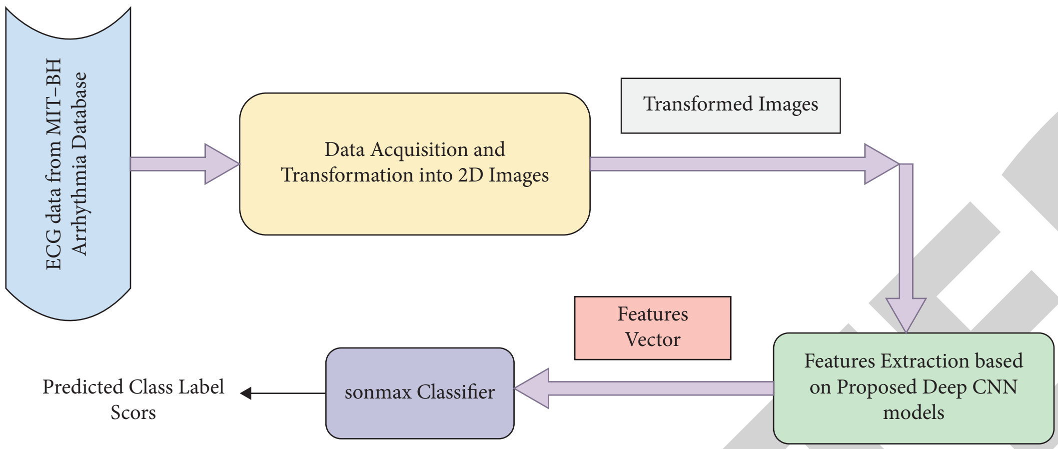

Figure 1: Workflow diagram of our proposed method for ECG arrhythmia classification.

particularly so essential in medicals and clinics to diagnosis the diseases accurately through data analysis. Most data in medicals and clinics are normal and only a few numbers of data are abnormal. Some anterior arrhythmia works performed augmentation manually but herein we have performed online augmentation on-the-fly [61] of images. The major benefits of this concept are hassle-free and time-saving unlike manual augmentation. In this work, beat images are rotated randomly at a maximum of 6 degrees. Then the augmented images are resized into a 64×64 scale size before converting it into tensors inside the model to speed up the learning. The augmentation in a model usually provides better results compared to nonaugmented data [52, 53].

2.3. Feature Extraction Based on the Proposed CNN Models and CNN Classifier. In this study, we have developed two 2D CNN models, where convolutional and pooling layers are more compatible to the spatial locality of a filter for extracting the features from an image. A competition on ImageNet Large Visual Perception Challenge (ILSVRC) [66] has found some successful developed CNN models such as AlexNet [45], GoogleNet [67], and VGGNet [68], which are widely shown in the computer vision field. ResNet [69], and DenseNet [70] are also interesting CNN models as the deeper networks, recently appeared in image classification. In our developed CNN models, we have used some basic structures of AlexNet and VGGNet. So, the performance of our proposed models is compared to AlexNet and VGGNet. Our transformed beat images are relatively simple backgrounds of 128×128 sized RGB images. Therefore, high depth layers are not needed to optimize the proposed models, which may cause over-fitting and subsequently might degrade the model performance. Figures 2 and 3 demonstrate end-to-end internal layer architecture of the proposed Deep-SR model and Deep-NSR model, respectively. Careful consideration has been taken to determine the depth and organization of relevant layers. This is very crucial to recognize the transformed beat images correctly without any over-fitting of the proposed models from a small dataset due to the lack of a sufficient number of samples.

The first proposed model is comprised of five convolution blocks, one maxpooling layer, and one average pooling layer to capture the area-specific features and followed by a fully connected layer or linear layer to classify the arrhythmia. After each convolution layer, a nonlinear activation function rectified linear unit (ReLU) is used to alleviate the vanishing gradient problem usually generated from the output range of activation function during gradient computation loss in the back-propagation step. It helps the optimizer to receive the optimal set of weights quickly and results are a faster convergence of stochastic gradient descent and low computational cost. Let x^i and y^j represent the i^{th} input and j^{th} output feature map of a convolutional layer, respectively, then activation function employed in CNNs could be expressed as under:

$$y^j = \max\left(0, b^j + \sum_i z^{ij} * x^i\right), \quad (1)$$

where z^{ij} indicates the convolutional filters between x^i and y^j, and b^j represents the bias. The symbol $*$ expresses the convolutional operation.

If a layer has M input and N output maps, then it will hold N 3D filters of size $d \times d \times M$, where $d \times d$ signify the size of local receptive fields as well as every filter has its own bias. In the later, it is addressed as max $(x, 0)$ since ReLU allows only values above of zero analogous to its biological counterpart of action potential. This feature of ReLU allows resolving the nonlinear problems of the models. After each ReLU, batch normalization (BN) layer has been employed to accelerate the training. As a result, the learnable parameters are converged at the earliest possible training time providing better accuracy [37]. It also reduces the internal covariate shift and the sensitivity of training toward weight initialization. This is one kind of regularization technique to cut down the over-fitting in the training phase. The relevant features from our preprocessed images are mainly extracted by the convolutional layers in the proposed models. The convolutional layers are the prime components of CNNs, where major functions of CNNs are performed. The operation of a convolutional layer is expressed as under:

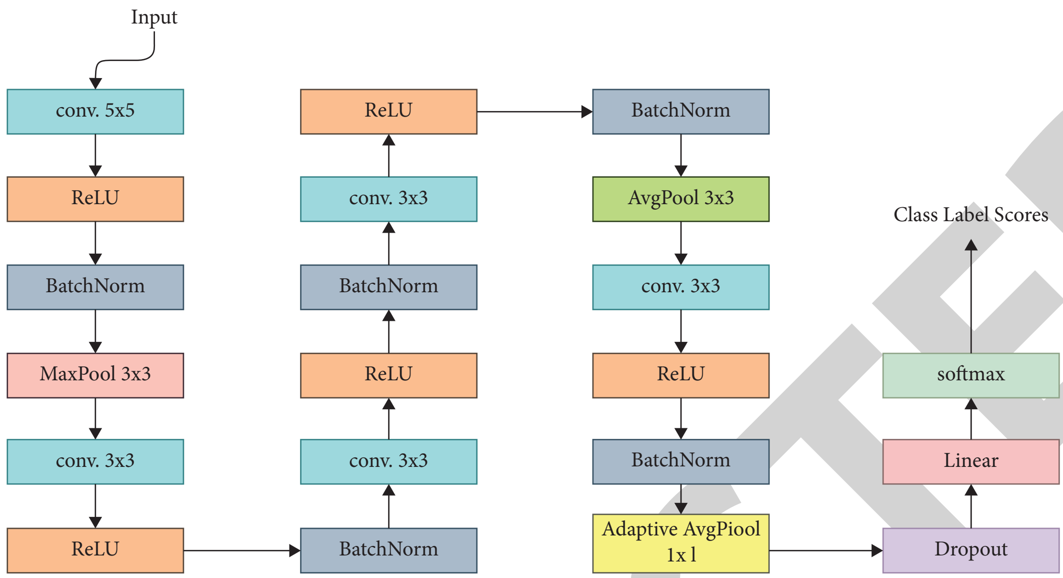

Figure 2: An end-to-end internal layer architecture of the proposed Deep-SR model.

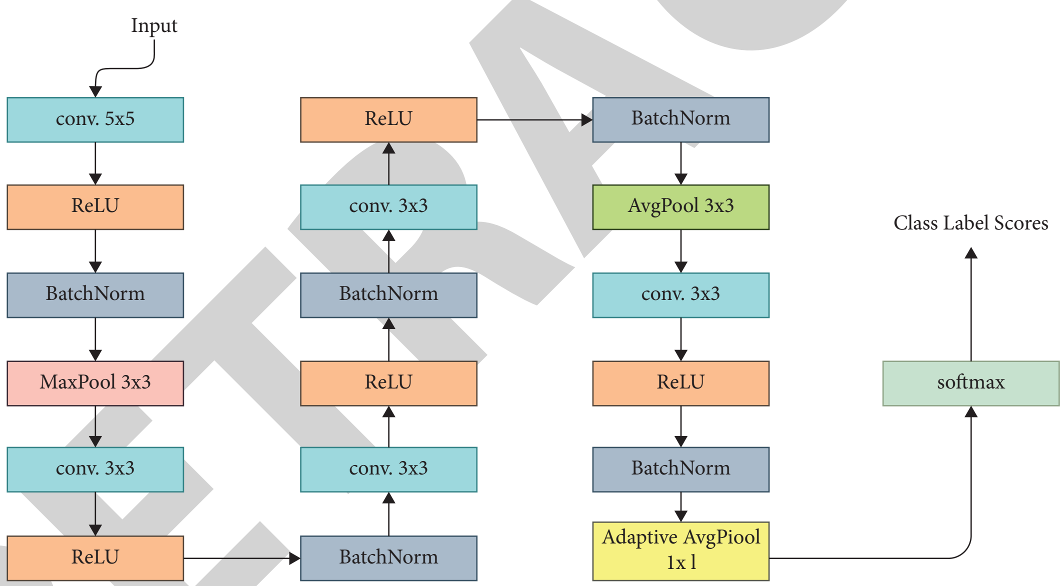

Figure 3: The layered end-to-end internal architecture of the proposed Deep-NSR model.

$$y = f\left(\sum_{i=1}^{n} \theta_i^T x_i + b\right). \quad (2)$$

Here θ and b indicate the weight and bias parameters of the layer, and $f(.)$ represents the activation function.

We have tested the first convolution layer with 5×5 kernel size, 32 kernels, 2 strides, false bias, and other parameters such as dilation and padding as default. The remaining four convolution layers are with 3×3 kernel size, false bias, and other parameters as default, and subsequently 64, 128, 256, and 512 kernels for the second, third, fourth, and fifth convolution layers, respectively. Large filter size at the starting with spatial down-sampling by convolution of striding 2 and a successive maxpooling with stride of 2 are employed to suppress the irrelevant features from the images. In the ECG beat images, the relevant features remain in the small part of the whole image. The subsequent convolution layers with small size and no spatial down-sampling can easily extract locally repeating features and reduce the computational cost. Pooling layers (maxpooling and average pooling) are operated independently on every depth slice of the input and act as the translation-invariant, which compute a fixed function of the input volume with some hyperparameters and have no learnable parameters. So, pooling layers are also called subsampling layers and alleviate the resolution of feature maps on the inputs. Here, after the first convolution layer, only a maxpooling layer with the kernel size of 3×3 and the stride of 2 is added to reduce the spatial dimension of the feature map. It helps to control the

Table 1: The internal architecture of the proposed Deep-SR model with its relevant hyperparameters. Here, ReLU is used after each convolution layer and BN is used after each ReLU and dropout; fully connected and softmax layers are not shown.

Layer name	Output size	Kernel size	# Filters	Stride
Conv2d-1	62 × 62	5 × 5	32	2
MaxPool2d-4	30 × 30	3 × 3	1	2
Conv2d-5	28 × 28	3 × 3	64	1
Conv2d-8	26 × 26	3 × 3	128	1
Conv2d-11	24 × 24	3 × 3	256	1
AvgPool2d-14	11 × 11	3 × 3	1	2
Conv2d-15	9 × 9	3 × 3	512	1
AdaptiveAvgPool2d-18	1 × 1	9 × 9	1	—

Table 2: The internal architecture of the proposed Deep-NSR model with its relevant hyperparameters. Here, ReLU is used after each convolution layer and BN is used after each ReLU and dropout; fully connected and softmax layers are not shown.

Layer name	Output size	Kernel size	# Filters	Stride
Conv2d-1	62 × 62	5 × 5	32	2
MaxPool2d-4	30 × 30	3 × 3	1	2
Conv2d-5	28 × 28	3 × 3	64	1
Conv2d-8	26 × 26	3 × 3	128	1
Conv2d-11	24 × 24	3 × 3	256	1
AvgPool2d-14	11 × 11	3 × 3	1	2
Conv2d-15	9 × 9	3 × 3	8	1
AdaptiveAvgPool2d-18	1 × 1	9 × 9	1	—

over-fitting of the models by decreasing the learnable parameters in the subsequent convolution layers. Extractions of global features related to the pixel of neighborhood are accomplished with the maxpooling and convolution. The maxpooling operation in this study enumerates the maximum value as a set of neighboring inputs. The pooling of feature map in a layer can be expressed as follows:

$$P_i^{1,j} = \max_{r\in R}\left(c_{i\times T+r}^{1,j}\right), \tag{3}$$

where T indicates pooling stride and r represents pooling window size. The average pooling layer with the size of 3×3 and the stride of 2 is added just before the last convolution block to extract the average spatial high-level features and it provides an output shape of 11×11. After bypassing four convolution blocks, maxpooling, and average pooling layers, the output shape of the last convolution block is reduced to 9×9. Finally, the adaptive average pooling reduces the dimension of the tensors so that they might be fitted into the fully connected layer.

The dropout layer [36] is also a regularization method, which reduces over-fitting by alleviating the dependency between the layers introduced by Hinton. It excludes some neurons from learning in the training phase that helps to prevent over-fitting. It randomly sets its input units 0 to 1. In this study, we have used a dropout layer with the probability of 0.3 and its location just before the fully connected layer. Usually, it is not used in the convolutional blocks to maintain the co-adaptation between the nodes. The high-level decision of the model has appeared at the output end of fully connected layer, which can be considered as the classification phase. Each neuron herein is linked to all activations of the previous layers. This layer reads up the feature vector for the softmax layer to classify accurately, whereas the earlier layers carry out the feature learning. Finally, a softmax layer is added at the end of the models to classify the arrhythmia labels with a numerical processing. It is extensively employed in machine learning as well as deep learning. The function can be defined as below:

$$y^{(i)} = \frac{\exp\left(z^{(i)}\right)}{\sum_{j-1}^{C}\exp\left(z^{(j)}\right)}, \tag{4}$$

where $z^{(i)}$ is the last output vector of fully connected layer and fed to the softmax layer to measure the probability, $y^{(i)}$ of each beat class, C is the total number of beat classes, and i indicate the class index.

The complete weights are learned with the gradient-based back-propagation algorithm. A series of convolution layers with batch BN and ReLU layers and pooling layers provides the screening of high-level features from the desired areas of beat images. The architecture with the hyperparameters of the Deep-SR model is illustrated in Table 1. The above explanation for all layers of Deep-SR model is also applicable for Deep-NSR model. The difference is in the last convolution layer. First, the number of the kernel is equal to the number of class label numbers instead of 512. Second, the adaptive average pooling layer is directly connected to the softmax layer through the fully connected layer and has no dropout layer. This technique is called the native structural regularized method in CNN [60] and applied as the first on 2D CNN to detect ECG arrhythmia. As a result, the total number of model learnable parameters is drastically reduced and the model size become too small in comparison with the Deep-SR model. This technique helps to alleviate model over-fitting and accelerate the training as well as enhance the model efficiency. The architecture with the hyperparameters of the Deep-NSR model is given in Table 2.

2.4. Cost Function and Evaluation Metrics. The cross-entropy loss or cost functions in equations (5)–(7) measure how well the model is trained and receives the differentiation between the training sample and predicted output to calculate the training loss. The loss function might be alleviated through the optimizer function, which is more adaptable for high-class imbalanced data compared to other available loss functions.

$$\operatorname{loss}(x, \text{class}) = -\log\left(\frac{(\exp(x[\text{class}]))}{\sum_j \exp(x[j])}\right), \tag{5}$$

$$\operatorname{loss}(x, \text{class}) = -x[\text{class}] + \log\left(\sum_j \exp(x[j])\right). \tag{6}$$

For class weights:

$$\text{loss}(x, \text{class}) = \text{wieght}[\text{class}]\left(-x[\text{class}] + \log\left(\sum_j \exp(x[j])\right)\right). \tag{7}$$

The above cost function is the combination of equations (8)–(10). Here x is the output of the fully connected layer and it is fed to the input function of softmax classifier that acts as the normalized score for each class. If the number of classes is C, then each class represents the index in the range $[0, C-1]$. The model is trained on a mini-batch of the training samples and x is in range (mini-batch, C). In the case of a mini-batch, the losses are averaged across all samples within it. The log softmax function is computed based on the following equation:

$$\log\text{soft}\max(x_i) = \log\left(\frac{\exp(x_i)}{\sum_j \exp(x_j)}\right). \tag{8}$$

Here x_i is the i^{th} dimension of output tensors in which the Log SoftMax function is computed. The negative log-likelihood loss is defined by the following equation:

$$\begin{aligned} \text{nllloss}(x, y) &= L \\ &= \{l_1, l_2, \ldots, l_n\}, \\ \text{ln} &= -\left(w_{y_n} x_{n,y_n}\right). \end{aligned} \tag{9}$$

For unreduced loss:

$$\text{nllloss}(x, y) = \begin{cases} \displaystyle\sum_{n=1}^{N} \frac{1}{\sum_{n=1}^{N} w_{y_n}} \text{ln} & \text{if reduction} = '\text{mean}', \\ \displaystyle\sum_{n=1}^{N} \text{ln} & \text{if reduction} = '\text{sum}'. \end{cases} \tag{10}$$

Here N is the batch size.

In this study, we have considered three performance metrics for the evaluation of our proposed models on the MIT-BIH dataset that is highly imbalanced. The exactness and sensitivity of a model are measured by precision and recall, respectively. The unweighted average $F_{1\text{-score}}$ (UAF_1) captures the accuracy on class imbalance by summing up the UAF_1 calculated on precision and recall for each predicted class sample, then divided by the number of classes to reduce the biasing of large classes samples. The unweighted average recall (UAR) measures the sensitivity of the models based on the recall of each predicted class sample that represents the balanced accuracy to reduce the impact of unbalanced class bias. These two metrics are suitable for the classification of unbalanced classes. The standard accuracy is measured based on the total true positive (TP) and true negative (TN) samples out of the total number of samples. The matrices are measured by the following equations [23, 71–73]:

$$\begin{aligned} \text{Precision} &= \frac{\text{TP}}{\text{TP} + \text{FP}}, \\ \text{Recall} &= \frac{\text{TP}}{\text{TP} + \text{FN}}, \\ \text{UAF}_1 &= 2 \times \frac{\text{precision} \times \text{recall}}{\text{precision} + \text{recall}} \\ &= \frac{2\text{TP}}{2\text{TP} + \text{FP} + \text{FN}}, \\ \text{UAR} &= \frac{\sum \text{per\_class\_accuracy}}{c}, \\ \text{Accuracy} &= \frac{\text{TP} + \text{TN}}{\text{TP} + \text{FP} + \text{TN} + \text{TF}}, \end{aligned} \tag{11}$$

where TP represents true positive, FP represents false positive, TN represents true negative, FN represents false negative, and c is the number of classes.

2.5. Implemetation Details. Proposed CNN models are implemented in Python language (version 3.6) with an open-source software library PyTorch [74] framework for deep learning launched by Facebook. Herein, Anaconda 3-5.3.1 provides the Jupyter Notebook facility. Google Tensorboard is applied to visualize the required graphs of various evaluation matrices with the respective CSV files. A GPU-supported computer is essential to reduce the learning time of models. We have employed Core i5-7400 CPU @ 3.00 GHz, 8 GB RAM processor with NVIDIA GeForce RTX 2070 graphic card with 8 GB memory to perform our experiments. With these NVIDIA GPUs, PyTorch is accelerated by CUDA and CUDNN [75]. Some open-source library packages such as Scikit-Learn, Numpy, Pandas, Matplotlib, Wfdb, and Biosspy are also employed to perform the whole work. Herein, at first, the convolution, batch normalization [37], and fully connected layers of proposed models are needed to initialize. The major problem of gradient descent learning algorithm is that it is needed to diverge a model into a local minimum point. So, an intellectual weight initializer is required to achieve the convergence. In CNN, these weights are described as kernels and a group of kernels that form a single layer. In our proposed models, kaiming normal distribution [62] initializes the weights of all the convolution layers. The weight and bias of all batch normalization layers have been initialized with 1 and 0, respectively. Xavier initializer [63] initializes the weights of fully connected layer and bias is initialized with a constant 0. The main worth of these initializers is the balance of gradient scale roughly equivalent in all kernels. We have

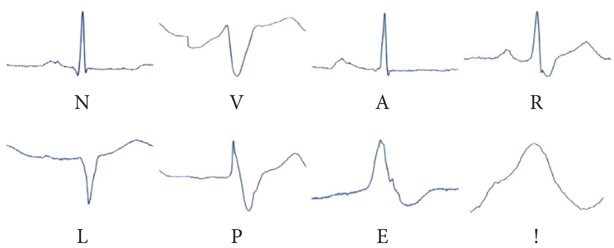

Figure 4: Normal and seven ECG arrhythmia beats. N, normal beat; V, premature ventricular contraction (PVC) beat; A, atrial premature contraction (APC) beat; R, right bundle branch block (RBB) beat; L, left bundle branch block (LBB) beat; P, paced beat; E, ventricular escape beat (VEB); and !-ventricular flutter wave (VFW) beat.

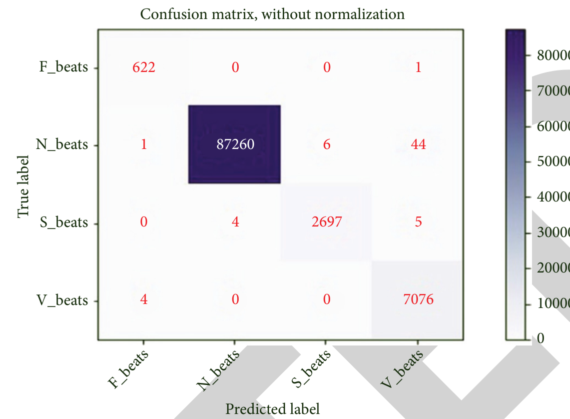

Figure 5: Confusion matrix for the proposed Deep-SR model.

also excluded the padding procedure to sustain the actual size of images through the convolution and pooling layers. The models' performance with the test data is greatly deflected by altering the ratio of training set and test set. In this study, the whole dataset is divided into a validation set by the random split feature with a given ratio. A validation set is needed to determine either the model is reached at adequate accuracy with the given training set or not. The model is usually falling in over-fitting without a validation set. The random selection mechanism is facing various evaluation effects on a relatively small dataset. K-fold cross-validation is a good evaluation technique to solve such a type of problem. In k-fold, the samples are grouped into the total k-fold randomly. If $k = 10$, the samples are grouped into 10-fold randomly and 10 splits have been generated. In each split one fold acts as the testing set and the remaining nine folds act as the training sets. In our work, we have implemented stratified five-fold cross-validation technique. First, we have chosen five-fold to cut down the computational cost and enhance the change of keeping all samples to each fold from each class. Second, we have chosen stratified to ensure the samples from each class to each fold, which alleviates the class imbalance problem of a dataset. Our used MIT-BIH arrhythmia dataset is a class imbalance dataset. The batch size and initial learning rate are set to 64 and 0.0001, respectively. The proposed models are also tested with some other initial learning rates such as 0.001 and 0.00001. But the achieved performance parameters with the initial learning rate 0.001 are better compared to others. This result is due to smooth convergence of the models with this learning rate. The efficient convergence is usually appeared by the internal covariate shift and normalization accelerates and stabilizes the learning process [76]. To optimize the cost function, a gradient descent-based optimizer is utilized with the indicated learning rate. Herein, we have used a stochastic Adam optimizer [38] to receive the better performance compared to some other optimizers such as Adagrad, Adadelta, and stochastic gradient decent (SGD). The learning rate is decreased with the factor of 0.1 if the validation loss is a plateau for five consecutive epochs with the help of learning rate scheduler (REDUCELRONPLATEAU). To ensure the equal representativeness of samples in each class, a weighted random sampler [58] is also chosen in this study. The early stopping [59] regularization is employed to stop the training if the validation loss does not improve for eight consecutive epochs, which helps to receive the optimal training time and reduce the over-fitting. Finally, the acquired overall recognition accuracies are 99.3% and 99.6% for the Deep-SR model and Deep-NSR model, respectively, on four-beat categories.

3. Results and Discussion

3.1. Performance Analysis of the Proposed Deep-SR and Deep-NSR Models. We have considered the beat samples of four categorical classes (N, S, V, and F) from a benchmark dataset, MIT-BIH arrhythmia based on AAMI. Q class is not considered in this study due to the involvement of unclassified and paced beats. The beat categorization based on AAMI is discussed in detail in Section 2. There are 14 annotated beats and three non-beats in the MIT-BIH arrhythmia dataset. Herein, we have depicted eight transformed beat images in Figure 4 among 14 annotated beats.

An ECG signal usually contains five important waves named as P, Q, R, S, and T. Sometimes, U as the sixth wave may be appeared following T. QRS complex come from Q, R, and S waves. The detection of these waves is a crucial issue in ECG signal analysis for extracting the hidden patterns. In this study, the marked peak value of R wave in the MIT-BIH arrhythmia dataset is utilized as reference point to segment the heartbeats. The R peaks detection is performed by Pan and Tompkins algorithm [65]. After the detection of R peaks, a single beat is considered by taking the half distance of present and next R peaks of detected peak. The characteristics of a normal beat including clinical information is represented in [77]. The drift from the characteristics of a regular beat indicates arrhythmias. The number of beats in each class label is highly imbalanced. To tackle the over-fitting problem due to the high-class imbalance, we have followed and employed the aforementioned strategies and techniques in Section 2.5. The confusion matrix of the proposed Deep-SR model is given in Figure 5, which represents the higher accuracy in each class despite the class imbalance problem in the MIT-BIH arrhythmia dataset

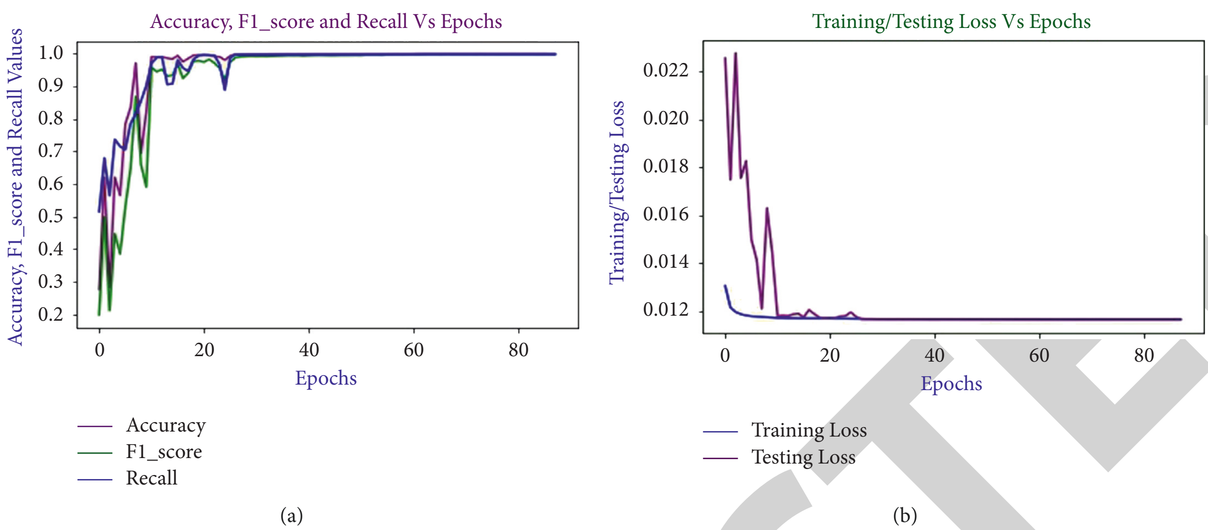

Figure 6: Stratified five-fold cross-validation results for arrhythmia recognition for the proposed Deep-SR model: (a) Average accuracy, UAR, and UAF_1; (b) Training and testing loss curve.

Table 3: A summary of all metrics from the confusion matrix of Deep-SR model.

Accuracy (%)		Precision (%)		Recall (%)		F_{1score} (%)	
N	99.94	N	99.99	N	99.94	N	99.97
S	99.98	S	99.78	S	99.67	S	99.63
V	99.94	V	99.27	V	99.94	V	99.62
F	99.99	F	99.20	F	99.84	F	99.52
Average	99.96	Average	99.56	Average	99.85	Average	99.67

indicating the generalization of Deep-SR model. From the confusion matrix, it is observed that the proposed Deep-SR model classifies properly 622 F beats out of 623, 87260 N beats out of 87311, 2697 S beats out of 2706, and 7076 V beats out of 7080. Only 1 F beats, 51 N beats, 9 S beats, and 4 V beats are not classified correctly. The model is converged with a high accuracy due to few catalytic facts such as online augmentation, weighted random sampling, early stopping regularization technique, adaptive learning rate optimization which adjust the weights and cross-entropy loss. From the confusion matrix, it is also evident that the model is unbiased for the different classes. Due to the use of an early stopping regularization scheme, the training of the model is halted if validation loss is not changed in eight consecutive epochs, and the model is evaluated on the test set. The evaluation is performed with the stratified five-fold cross-validation strategy, where the samples are grouped into five folds using stratified sampling, which tries to pick up the samples from each class for reducing the class imbalance problem. Since each fold act as a test set, it is fair strategy to compute the desired metrics.

The model is evaluated on three metrics, namely standard testing accuracy, UAR, and UAF_1. The results of the respective metrics are depicted in Figure 6(a). The training and testing loss curves are shown in Figure 6(b). From these curves, it is depicted that the training loss curve is declined smoothly and almost stable after nearly 26 epochs, whereas the testing loss curve is abruptly changed initially and becomes stable after around 26 epochs like the training loss curve. This is due to taking time of testing samples to adjust with the trained model at the starting. It is also clear from both curves that the model is halted at 88 epochs due to using early stopping regularization technique. The minimum validation loss, overall accuracy, UAR, and UAF_1 are 0.0117, 0.9993, 0.9985, and 0.9971, respectively, for the proposed Deep-SR model. A summary of all evaluated metrics from the confusion matrix depicted in Figure 5 is shown in Table 3. The average accuracy, precision, recall, and F_{1score} are 99.96, 99.56, 99.85, and 99.67, respectively. From Table 3, it is obvious that the average values of these metrics are almost same to the overall values represented in Table 4; it represents the generalization of our developed training and testing module for the experiment.

The confusion matrix of the proposed Deep-NSR model is depicted in Figure 7, which represents higher learning unbiased accuracy for ECG arrhythmia classification indicating the generalization of Deep-NSR. From the confusion matrix, it is observed that the proposed Deep-NSR model classifies properly all F beats, 87270 N beats out of 87311, all S beats, and 7078 V beats out of 7080. Only 41 N beats and 2 V beats are misclassified. The results of the desired metrics are depicted in Figure 8(a). The training and testing loss curve are shown in Figure 8(b). From these curves, it is depicted the training loss curve is declined smoothly and almost become stable after nearly 59 epochs while the testing loss curve is abruptly changed initially and become stable after around 59 epochs like the training loss curve. This is due to taking time of testing samples to adjust with the trained model at the starting. It is also clear from both curves that the model is halted at 97 epochs due to early stopping regularization technique. The minimum validation loss, overall accuracy, UAR, and UAF_1 are 0.0200, 0.9996, 0.9998, and 0.9987, respectively, for Deep-NSR. A summary of all evaluated metrics from the confusion matrix shown in

Table 4: The comparison of evaluation matrices, validation loss, and size of both models.

Evaluation matrices/validation loss/learnable parameters/model size	Proposed Deep-SR model	Proposed Deep-NSR model
Overall testing accuracy	0.9993	0.9996
Unweighted overall recall	0.9985	0.9998
Unweighted overall F_{1_score}	0.9971	0.9987
Minimum validation loss	0.0117	0.0200
Learnable parameters	1573156	**399656**
Model size	16.92 MB	**11.49 MB**

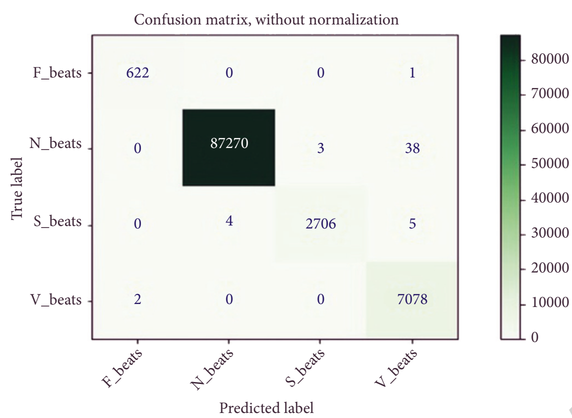

Figure 7: Confusion matrix for the proposed Deep-NSR model.

Figure 7 is presented in Table 5. The average accuracy, precision, recall, and F_{1score} are 99.98, 99.76, 99.97, and 99.87, respectively. From Table 5, it is obvious that the average values of all matrices are better than those for Deep-SR, which indicates Deep-NSR will be better to diagnosis the arrhythmias compared to Deep-SR.

From the above analysis, it is evident the behavior and characteristics of both proposed models are similar. The total learnable parameters with size of Deep-SR model and Deep-NSR model are 1573156(16.92 MB) and 399656(11.49 MB), respectively, illustrated in Table 4. The learnable parameters are drastically reduced for the Deep-NSR model compared to Deep-SR, which indicates better model efficiency. As a result, the native structural regularization technique in a model indicates a prosperous concept in ECG arrhythmia detection for real-life applications. Table 4 represents the comparison of evaluation matrices for both models.

3.2. Comparison with the State-of-the-Art Models. In this study, we have adopted CNN-based models as the feature extraction and classifier. In 1989, CNN was first commenced by LeCun et al. [78] and flourished by a project for recognizing handwritten zip codes, which resolve the oversights of feed-forward neural networks. With the CNN models, it is possible to extract the interrelation of spatially neighboring pixels and different local features of images through the nonlinear multiple filters. We have compared the performance of our proposed CNN models with the anterior ECG arrhythmia classification tasks. Actually, it is not fully reasonable to directly compare our task with the previous works due to the usage of different strategies as well as different arrhythmia categories. However, Table 6 illustrates the performance comparison of our proposed models to the anterior tasks. From this table, it is evident that our proposed models provide the best results in standard testing accuracy, and UAR compared to previous tasks, which indicates the better effectiveness of our proposed models in ECG arrhythmia recognition. The obtained standard testing accuracy of the proposed Deep-SR and Deep-NSR are 99.93% and 99.96%, respectively. The UAF_1 is a good evaluation matric for representing the effectiveness of a method on the class imbalance dataset by summing up the precision and recall expressing the exactness and sensitivity of a model at a time. The received UAF_1 for the Deep-SR model and Deep-NSR model are 99.71% and 99.87%, respectively, as shown in Table 6. The received UAF_1 on both proposed models represents high generalization and stability compared to the state-of-the-art methods. The UARs are achieved as 99.85% and 99.98% for the Deep-SR and Deep-NSR models, respectively, and surpasses the recall of the state-of-the-art methods, as shown in Table 6. From the comparison (Table 6), it is observed that the traditional machine learning methods with feature engineering techniques provide excellent results in some cases, but (i) it easily tends to over-fitting [34] especially for dealing big data, (ii) it is hard to describe some complex characteristics and high chaos of ECG optimally [79], (iii) high skilled person in this field is required for interpretation the diseases [56], and (iv) more challenges have to be faced for dealing the data imbalance problems [57]. The raw cardiac information from the publicly available datasets or medical/clinics or own developed sensors are usually data imbalance, which has inevitable effect in classification rate. This is due to the lack of availability of some classes and the scoring result is biased toward the dominance classes, which enhances the misclassification rate in machine learning algorithms. In contrast, over-fitting and data imbalance problems in traditional methods could be easily handled for dealing the big data with the deep learning approaches following the techniques and strategies discussed in Section 2.5. As a result, good findings could be achieved with minimum skilled persons in medical and clinics, where ECG data are enlarged day by day, around more than 300 million ECGs are preserved worldwide annually [34, 35]. Large amount of data helps the deep learning approaches to optimize during training. From the confusion matrix graphs (Figures 5 and 7), it is observed that that N is more noticeable compared to the remaining beats, also V and S beats are remarkable than F. It exposes that their ratio is misbalancing, but the proposed models classify each category properly without any biasing.

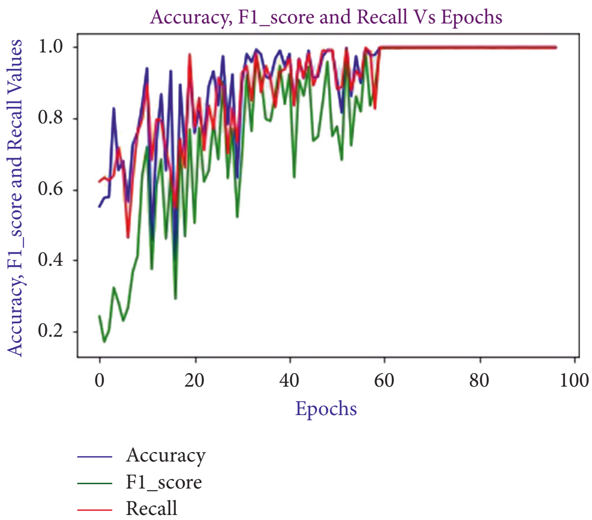

(a)

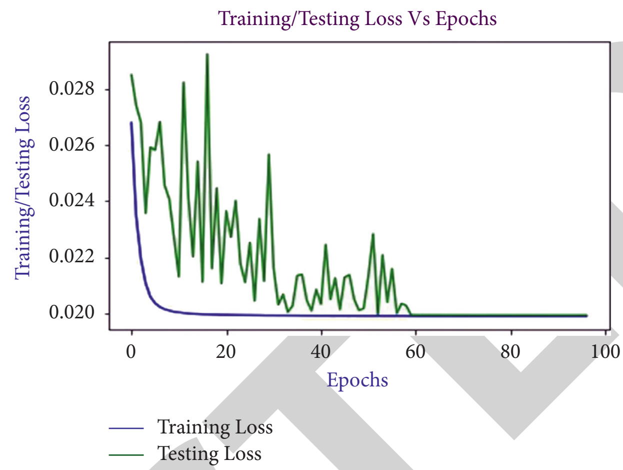

(b)

Figure 8: Stratified five-fold cross-validation results for arrhythmia recognition for the proposed Deep-NSR model: (a) average accuracy, UAR, and UAF1; (b) training and testing loss curve.

Table 5: A summary of all metrics from the confusion matrix of Deep-NSR model.

Accuracy (%)		Precision (%)		Recall (%)		F_{1score} (%)	
N	99.96	N	100	N	99.95	N	99.98
S	99.99	S	99.89	S	100	S	99.94
V	99.96	V	99.47	V	99.94	V	99.72
F	99.99	F	99.68	F	100	F	99.84
Average	99.98	Average	99.76	Average	99.97	Average	99.87

Table 6: Comparison with the state-of-the-art models.

Classifier type	Works	#Class category	Accuracy (%)	Recall (%)	F_{1score}
2D CNN (Prop.)	Deep-SR	4	$\mathbf{99.93}^{**}$	$\mathbf{99.85}^{**}$	$\mathbf{99.71}^{**}$
2D CNN (Prop.)	Deep-NSR	4	$\mathbf{99.96}^{**}$	$\mathbf{99.98}^{**}$	$\mathbf{99.87}^{**}$
2D CNN	Ullah et al. [52]	8	98.92^{*} 99.11^{**}	97.26^{*} 97.91^{**}	98.00^{*} 98.00^{**}
2D CNN	Jun et al. [53]	8	99.05^{*} 98.90^{**}	97.85^{*} 97.20^{**}	—
2D CNN	Alex Net [53]	8	98.85^{*} 98.81^{**}	97.08^{*} 96.81^{**}	—
2D CNN	VGG Net [53]	8	98.63^{*} 98.77^{**}	96.93^{*} 97.26^{**}	—
2D CNN	Izci et al. [54]	5	99.05^{*}	—	—
2D CNN	Huang et al. [51]	5	99.00^{*}	—	—
2D CNN	Lu et al. [50]	5	96.00^{*}	96.80^{*}	96.40^{*}
1D CNN	Zubai et al. [47]	5	92.70^{*}	—	—
1D CNN	Ullah et al. [52]	8	97.80^{*}	—	—
1D CNN	Huang et al. [51]	5	90.93^{*}	—	—
1D CNN	Li et al. [48]	5	97.50^{*}	—	—
1D CNN	Lu et al. [50]	5	94.00^{*}	96.00^{*}	95.19^{*}
TQWT + SVM	Jha et al. [12]	8	99.27^{*}	—	—
CEEMDAN + PCA + ANN	Abdalla et al. [13]	5	99.90^{*}	—	—
LBP, HOS + Ensemble SVM	Mondéjar-Guerra et al. [14]	4	94.50^{*}	—	—

**With augmentation on-the-fly or manual, *without augmentation, TQWT-tunable Q-wavelet transform, and CEEMDAN-complete ensemble empirical mode decomposition with adaptive noise.

This expresses the generalization of the developed models and a solution of data imbalance problem. From the comparison (Table 6), it is also observed that all 2D CNN approaches deliver better results compared to 1D CNN. So, the transformation of sequential beat information into their corresponding beat images is a promising strategy. The R-R intervals or R-peaks, duration, and amplitude of the QRS are highly sensitive to the dynamic and morphology features of complex ECG. The transformation-based method reduces the problem of strict time alignment; it ignores the scoring of fiducial points of heartbeats. The nonlinear and nonstationary characteristics of ECG heartbeats due to the episodic electrical conduction of heart are the major factors behind the facing of such sensitivity. The developed models extract the desirable activation on intensity, edge, and shape of peak of our preprocessed beat images. Background is not a big deal in this study because extracted beat is appeared only at a small portion of the whole image. The peaks are more crucial factor due to the describing of both P-wave shape and R-R intervals at a time. The satisfactory performance of developed models represents the learned features from the images are well correlated and embedded with the desired classes in respect to the high dimensional (mapped in two dimension) feature space, which is more obvious from the confusion matrix graphs and evaluated matrices. Now we will discuss the issues why our proposed models provide the satisfactory findings in arrhythmia recognition. First, CNNs models learn the dominant features from its first convolution layer and finally it is investigated with the resulted classifier. Second, the most crucial stage of the experiments is segmenting and transforming ECG signals into the corresponding beat images, the work is performed with a developed python module following a well-known and effective R-peak detection algorithm [65]. Third, AlexNet and VGGNet architecture have some inspirable benefits compared to other CNN architectures such as easy GoogleNet, ResNet, DenseNet, and especially less parameters are required to train the models and result is lightweight of model. Fourth, because of using some diverse mechanisms such as early stopping [59] that helps to stop over-fitting of the models, weighted random sampler [58] for reducing the class imbalance problem of the samples, Adam optimizer [38] for handling the minimum validation loss and quick training, on-the-fly augmentation [61], stratified evaluation strategy for ensuring the samples from each class to each fold, and reducing the effect of the class imbalance problem [62, 63].

In this study, we experimented and analyzed the performance of our proposed models only on the ECG arrhythmia data as the input of models for arrhythmia recognition. But the models could be employed for other categories of data such as HomePap, sleep-EDF, and sleep heart health study (SHHS) as the input of proposed models for analyzing the sleep disorders. For example, a deep learning approach with 2D CNN is addressed by Erdenebayar et al. for automatic detection of sleep apnea (SA) events from ECG signal recordings by an Embla N70 0 0 amplifier device (Embla System Inc., U.S.A.) at the Samsung Medical Center (Seoul, Korea) and demonstrated good results [80]. Recently, deep learning has also proved its potentiality applications in all physiological signals such as electroencephalogram (EEG), electromyogram (EMG), and 2D medical imaging [81]. Different neurological diseases such as epilepsy, Parkinson's disease (PD) [82], and Alzheimer's disease (AD) could be easily diagnosed with the EEG signals from a patient taking the benefits of 2D CNN models. For example, a novel 2D CNN model is presented by Madhavan et al. [83] for identifying the focal epilepsy from Bern-Barcelona EEG database and received the satisfactory results, where time-series EEG signals are transformed into 2D images with Fourier synchro squeezing transform (FSST) and wavelet SST (WSST) and evaluated on both cases. In addition, with EEG signals, these diseases could also be detected from the speech data [26, 84]. EMG signals are widely used in human activity and hand gesture recognition, nowadays which are more interesting for rehabilitation robots, artificial intelligence robots, active prosthetic hands, and entertainment robots as well. Besides, it is also used to diagnosis several neuromuscular diseases such as ALS (amyotrophic lateral sclerosis) because of containing some brain information [85]. Zhai et al. [86] proposed a 2D CNN model to recognize the patterns from surface electromyography (sEMG) signals of NinaPro publicly available database for controlling the upper limb neuro prosthetic and achieved better findings compared to a traditional method. Beyond the disease identification, with the preprocessing of raw information, 2D CNN could also be employed in others field such as detecting the faulty sensors in array antennas [87, 88]. Therefore, our developed models are a good prospect for the researchers who work in deep learning for identifying signal patterns.

The lightweight of our proposed models compared to the state-of-the-art methods expresses the strength of models to deploy in real-life applications, as shown in Table 7. Small model size indicates better model efficiency. In this study, the efficiency of the proposed Deep-NSR model is too attractive compared to Deep-SR, because the total learnable parameter is drastically reduced in Deep-NSR. So, the Deep-NSR could be easily deployed in practical application to diagnose arrhythmia from the ECG signal. This result is mainly due to its design strategy. Saadatnejad et al. [89] proposed and experimented a novel lightweight deep learning approach on the wearable devices with a confined capacity for the continuous monitoring of cardiac rhythm. The measurements on various hardware platforms demonstrate that their proposed algorithm fulfills the requirements for continuous monitoring of heart rhythm in real time. This is an inspiration for us to deploy our proposed models especially Deep-NSR in real-life applications in future.

When it comes to the limitations of our proposed work, we must first take into account that our arrhythmia recognition method is only tested on publicly available datasets, no real-time data/clinical data are used for testing, but the data in MIT-BIH arrhythmia database are collected under various environmental circumstances, and devices in real time with different degrees consider various interference

Table 7: Comparison with the existing models.

Classifier type	Works	#Class category	Model Size(MB)	#Learnable Parameters
2D CNN (Proposed)	Deep-SR Model	4	**16.92**	1573156
2D CNN (Proposed)	Deep-NSR Model	4	**11.49**	399656
2D CNN	Ullah et al. [52]	8	49.91	1557016
2D CNN	Jun et al. [53]	8	81.67	1149272
2D CNN	Alex Net [53]	8	34.05	947092
2D CNN	VGG Net [53]	8	84.66	7639440

issues. The dataset uses standard data storage format and all data are labeled by the professional physicians. So, the dataset is more reliable data source for testing the model. Second, we have followed intra-patient paradigm in this study, where the same patient heartbeats are likely to arrive both in training and testing sets. This circumstance may lead the biased results. The patient-specific study could be the solution of the challenge. Third, our used dataset is publicly available, which is small in scale. Deep learning models consist of numerous numbers of layers with huge learnable parameters. They process the data repeatedly to acquire the optimal number of parameters during training; as a result, it may face the over-fitting problem with the small volume of datasets. This challenge could be addressed to employ the transfer learning technique [90] in the model that is trained on large volume of data previously. In addition, comprehending a relationship between the feature extraction and fundamental physiology is very important to recognize the specific disease. So, feature-based diagnosing is an interesting field to study in future.

3.3. Open Challenges and Opportunities of Deep Learning Methods in ECG Data. In spite of great successes of deep learning in recognition and detection such as learning the important features, it faces several challenges: first, high computational complexity is required for model training due to the deficiency of powerful hardware [91], so it is more feasible to utilize the deep learning methods in offline processing to diagnose the cardiac arrhythmias. Using the high-level API (application programming interface) data frame provided by structured streaming platform, where fast SQL (Structured Query Language) functions on streaming data are implemented, could be a solution of overcoming this challenge of deep learning methods for online diagnosis with less delay. Generally, the computational complexity of a deep learning method depends on the required floating-point operations for processing that model, where there is a strong correlation among the floating-point operations, energy consumption ($R^2 = 0.9641$, p– value < 0.0001), and inference time ($R^2 = 0.8888$, p–value < 0.0015) of a CNN model. The real inference time of a deep learning method depends on the different parameters including compiler optimization, hardware platform, and used APIs to implement the model [92]. Besides, PyTorch provides optimized performance, memory usage, and energy consumption using CUDA and CUDNN with our used graphics processing unit (GPU, NVIDIA) [75]. In our experiments, the complete total computational time of Deep-SR was 451 minutes 1 second using the hardware configuration indicated in Section 2.5, while the testing computation time for a single image was 0.2769 second. On the other hand, the total computational time of Deep-NSR was 379 minutes 7 seconds, while the testing computation time for a single image was 0.2328 second. The computation time will be varied with the changing of hardware configuration of used PC. We see that the testing computation time in Deep-NSR model is less than Deep-SR, which indicates that Deep-NSR model will be more suitable to deploy in resource-constraint devices such as mobile phone, portable/wearable healthcare devices compared to Deep-SR. The occupied memory space for Deep-SR was 16.92 MB, while it was 11.49 MB for Deep-NSR, which also expresses that Deep-NSR model will be more effective to deploy in resource-constraint devices compared to Deep-SR. However, both models outperform the state-of-the-art models in the sense of performance and model size, depicted in Tables 6 and 7. So, both could be chosen to deploy in real-life applications such as resource-constraint devices and offline diagnosis in medical and clinics. Indeed, deep learning methods demand more computing resource compared to machine learning-based techniques for real-time processing, and hence these are slower [93]. Second, interpretability; it is hard to understand the reasons for human beings why a particular result is received by a deep model compared to traditional machine learning algorithms, because the deep learning models are usually considered as the black box models with huge learnable parameters. This challenge has become more severe in clinical tasks because diagnosis is not perceptible by physicians without any interpretation. To tackle the challenge, two directions are worth noted, (i) replacing a complex model by relatively a simple model, and (ii) one can add attention mechanism on the hidden layers or imitate neuron connection concepts from the tree-based model. Third, efficiency; it is difficult to deploy the big deep models into the portable healthcare devices for real-life applications. In this case, promising direction is lightweight deep model, or model compression technique such as knowledge distillation, weight sharing, and quantization. Fourth, integration with expert features; it is difficult to integrate a trained deep model with the existing expert knowledge/features. To tackle the issue, (i) one can use domain expert knowledge for designing the deep models, and (ii) coining or explicitly extract the latent embedding features from the deep models. Then one easily assembles deep and expert features and makes the traditional machine learning methods from them. Fifth, noise robustness; deep learning methods automatically extract all features from ECG signals including the various categories of real-world noises such as motion artifacts, baseline wander, electrode contact, and power line interference appeared in it, which leads to incorrect results. The issue could be something resolved by using a de-noising/filtering technique before fitting data into the input of deep models, but some valuable information may be omitted in this way [94]. So, we have not performed any de-noising/filtering technique on the raw data in our study. In our experiments, we have used MIT-BIH arrhythmia database, where ECG raw data contain several real-world noises and filtered with band-pass filter at 0.1100 Hz [64]. Recently, de-noising autoencoder (DAE), sparse autoencoder (SAE), contractive autoencoder (CAE), and generative adversarial network (GAN) are some widely used promising techniques to remove such suspected noises appeared in ECG signals. In addition to above, one more challenge of deep learning methods is the lack of availability of training data, because large volume of data are required during training the models to handle the over-fitting problem. Transfer learning techniques could recover this challenge at some extends. Finally, we should tell that the major failure case of our proposed models along with the facing challenges mentioned above is the inability to classify other categories of images properly available in real worlds beyond the ECG beat images as well as identify of all beat images correctly, which is depicted in Figures 5 and 7 (confusion matrixes for both models). However, deep learning, especially CNN-based methods are promising for diagnosing various cardiovascular diseases in offline and online.

4. Conclusion and Future Works

The automatic arrhythmia recognition with machine learning algorithms has gained its importance day by day since it helps the experts to diagnose cardiovascular diseases easily, which are seen in ECG signals. In this work, the received classification performances for four cardiac rhythms on both models surpassed the state-of-the-art models that represent the better effectiveness of the proposed models. Importantly, the UAF_1 for both models indicated that the proposed models were more generalized for imbalance classes. The lightweight of Deep-NSR model narrates its better efficiency compared to the state-of-the-art models. As such, it could be easily deployed in real-life applications in deep learning approaches. Moreover, the proposed models would be more applicable with the different amplitudes and sampling rates in various ECG devices. The present study employed ECG signals from a single lead. Signals from multiple leads will be studied in future to more enrich the experimental cases. Furthermore, we have also planned to work on such interesting, related directions as (i) adapting the models for other diseases like sleep apnea with the corresponding datasets related to ECG signals, (ii) expanding the adaptation scope of our proposed models for EEG and EMG signal-related dataset, and (iii) verifying the performance of proposed models with own developed sensor/real-time data.

Data Availability

The data used to support the findings of the study are available from the corresponding authors upon request.

Conflicts of Interest

No conflicts of interest.

Acknowledgments

This work was supported by the (i) Researchers Supporting Project (RSP-2021/244), King Saud University, Riyadh, Saudi Arabia; (ii) National Natural Science Foundation of China (61771100 and 62001083) and Sichuan Science and Technology Program (2021YFH0093). The authors are thankful to Prof. Wu, Prof. Naseem, Prof. Siddiqui, Prof. Rahman, Prof. Singh, Prof. Chandel, Prof. Umar, Prof. Tumrani, and Dr. Nasir for a useful discussion.

References

[1] K. Mc Namara, H. Alzubaidi, and J. K. Jackson, “Cardiovascular disease as a leading cause of death: how are pharmacists getting involved?” *Integrated Pharmacy Research and Practice*, vol. 8, pp. 1–11, 2019.

[2] O. Sayadi and M. B. Shamsollahi, “ECG denoising and compression using a modified extended Kalman filter structure,” *IEEE Transactions on Biomedical Engineering*, vol. 55, no. 9, pp. 2240–2248, 2008.

[3] Y. Li, X. Tang, and Z. Xu, “An approach of heartbeat segmentation in seismocardiogram by matched-filtering,” *Proc. - 2015 7th Int. Conf. Intell. Human-Machine Syst. Cybern. IHMSC 2015*, vol. 2, pp. 47–51, 2015.

[4] J. M. Hsing, K. A. Selzman, C. Leclercq et al., “Paced left ventricular QRS width and ECG parameters predict outcomes after cardiac resynchronization therapy,” *Circulation: Arrhythmia and Electrophysiology*, vol. 4, no. 6, pp. 851–857, 2011.

[5] S. Yu and K. Chou, “Integration of independent component analysis and neural networks for ECG beat classification,” *Expert Systems with Applications*, vol. 34, no. 4, pp. 2841–2846, 2008.

[6] R. J. Martis, U. R. Acharya, and L. C. Min, “ECG beat classification using PCA, LDA, ICA and Discrete Wavelet Transform,” *Biomedical Signal Processing and Control*, vol. 8, no. 5, pp. 437–448, 2013.

[7] B. M. Asl, S. K. Setarehdan, and M. Mohebbi, “Support vector machine-based arrhythmia classification using reduced features of heart rate variability signal,” *Artificial Intelligence in Medicine*, vol. 44, no. 1, pp. 51–64, 2008.

[8] L. Ali, I. Wajahat, N. A. Golilarz, F. Keshtkar, and S. A. C. Bukhari, “LDA-GA-SVM: improved hepatocellular carcinoma prediction through dimensionality reduction and genetically optimized support vector machine,” *Neural Computing & Applications*, vol. 33, no. 7, pp. 2783–2792, 2021.

[9] R. Ceylan and Y. Özbay, “Comparison of FCM, PCA and WT techniques for classification ECG arrhythmias using artificial neural network,” *Expert Systems with Applications*, vol. 33, no. 2, pp. 286–295, 2007.

[10] T. Li, M. Zhou, C. M. Travieso-González, and J. B. Alonso-Hernández, “ECG classification using wavelet packet entropy and random forests,” *Entropy*, vol. 18, no. 8, p. 285, 2016.

[11] A. Rehman, A. Khan, M. A. Ali, M. U. Khan, S. U. Khan, and L. Ali, "Performance analysis of PCA, sparse PCA, kernel PCA and incremental PCA algorithms for heart failure prediction," in *Proceedings of the 2nd Int. Conf. Electr. Commun. Comput. Eng. ICECCE 2020*, Istanbul, Turkey, June 2020.

[12] C. K. Jha and M. H. Kolekar, "Cardiac arrhythmia classification using tunable Q-wavelet transform based features and support vector machine classifier," *Biomedical Signal Processing and Control*, vol. 59, 2020.

[13] F. Y. O. Abdalla, L. Wu, H. Ullah, G. Ren, A. Noor, and Y. Zhao, "ECG arrhythmia classification using artificial intelligence and nonlinear and nonstationary decomposition," *Signal, Image Video Process.*vol. 13, 2019.

[14] V. Mondéjar-Guerra, J. Novo, J. Rouco, M. G. Penedo, and M. Ortega, "Heartbeat classification fusing temporal and morphological information of ECGs via ensemble of classifiers," *Biomedical Signal Processing and Control*, vol. 47, pp. 41–48, 2019.

[15] M. B. B. Heyat, F. Akhtar, A. Khan et al., "A novel hybrid machine learning classification for the detection of bruxism patients using physiological signals," *Applied Sciences*, vol. 10, no. 21, p. 7410, 2020.

[16] W. Akbar, W. P. Wu, S. Saleem et al., "Development of hepatitis disease detection system by exploiting sparsity in linear support vector machine to improve strength of AdaBoost ensemble model," *Mobile Information Systems*, vol. 2020, Article ID 8870240, 9 pages, 2020.

[17] F. S. Ahmad, H. A. Khattak, T. Hameed, I. Wajahat, S. Kadry, and S. A. C. Bukhari, "A hybrid machine learning framework to predict mortality in paralytic ileus patients using electronic health records (EHRs)," *Journal of Ambient Intelligence and Humanized Computing*, vol. 12, no. 3, pp. 3283–3293, 2021.

[18] A. K. Jain, P. W. Duin, and J. Mao, "Statistical pattern recognition: a review," *IEEE Transactions on Pattern Analysis and Machine Intelligence*, vol. 22, no. 1, pp. 4–37, 2000.

[19] H. He and E. A. Garcia, "Learning from imbalanced data," *IEEE Transactions on Knowledge and Data Engineering*, vol. 21, no. 9, pp. 1263–1284, 2009.

[20] M. B. B. Heyat, F. Akhtar, M. H. Khan et al., "Detection, treatment planning, and genetic predisposition of bruxism: a systematic mapping process and network visualization technique," *CNS & Neurological Disorders - Drug Targets*, vol. 20, no. 8, pp. 755–775, 2021.

[21] H. Mbb, F. Akhtar, A. Mehdi, S. Azad, S. Azad, and S. Azad, "Normalized power are used in the diagnosis of insomnia medical sleep syndrome through EMG1-EMG2 channel," *Austin Journal of Sleep Disorders*, vol. 4, no. 1, pp. 2–4, 2017.

[22] D. Lai, Y. Zhang, X. Zhang, Y. Su, and M. B. B. Heyat, "An automated strategy for early risk identification of sudden cardiac death by using machine learning approach on measurable arrhythmic risk markers," *IEEE Access*, vol. 7, Article ID 94716, 2019.

[23] M. B. Bin Heyat, D. Lai, F. I. Khan, and Y. Zhang, "Sleep bruxism detection using decision tree method by the combination of C4-P4 and C4-A1 channels of scalp EEG," *IEEE Access*, vol. 7, Article ID 102553, 2019.

[24] D. Lai, M. B. B. Heyat, F. I. Khan, and Y. Zhang, "Prognosis of sleep bruxism using power spectral density approach applied on EEG signal of both EMG1-EMG2 and ECG1-ECG2 channels," *IEEE Access*, vol. 7, Article ID 82562, 2019.

[25] B. Bin Heyat, F. Akhtar, S. Azad, and S. Azad, *Dual Tone Multi-Frequency Based Premises Appliance Control Switch*, vol. 1, no. 7, pp. 215–218, 2016.

[26] L. Ali, Z. He, W. Cao, H. T. Rauf, Y. Imrana, and M. B. B. Heyat, "MMDD-ensemble: a multimodal data–driven ensemble approach for Parkinson's disease detection," *Frontiers in Neuroscience*, vol. 15, no. November, pp. 1–11, 2021.

[27] L. Ali, C. Zhu, Z. Zhang, and Y. Liu, "Automated detection of Parkinson's disease based on multiple types of sustained phonations using linear discriminant analysis and genetically optimized neural network," *IEEE J. Transl. Eng. Heal. Med.*vol. 7, 2019.

[28] L. Ali and S. A. C. Bukhari, "An approach based on mutually informed neural networks to optimize the generalization capabilities of decision support systems developed for heart failure prediction," *IRBM*, vol. 42, no. 5, pp. 345–352, 2021.

[29] M. B. Heyat, F. Akhtar, M. A. Ansari et al., "Progress in detection of insomnia sleep disorder: a comprehensive review," *Current Drug Targets*, vol. 22, no. 6, pp. 672–684, 2021.

[30] W. Yan and Z. Zhang, "Online automatic diagnosis system of cardiac arrhythmias based on MIT-BIH ECG database," *Journal of Healthcare Engineering*, vol. 2021, Article ID 1819112, 9 pages, 2021.

[31] B. Guragai, O. AlShorman, M. Masadeh, and M. B. B. Heyat, "A survey on deep learning classification algorithms for motor imagery," in *Proceedings of the 2020 32nd International Conference on Microelectronics (ICM)*, pp. 1–4, Aqaba, Jordan, December 2020.

[32] F. Akhtar, M. B. Bin Heyat, J. P. Li, P. K. Patel, Rishipal, and B. Guragai, "Role of machine learning in human stress: a review," in *Proceedings of the 2020 17th International Computer Conference on Wavelet Active Media Technology and Information Processing (ICCWAMTIP)*, pp. 170–174, Chengdu, China, December 2020.

[33] R. Pal, H. Bin, Z. You et al., "Effect of Maha Mrityunjaya HYMN recitation on human brain for the analysis of single EEG channel C4-A1 using machine learning classifiers on yoga practitioner," in *Proceedings of the 2020 17th International Computer Conference on Wavelet Active Media Technology and Information Processing (ICCWAMTIP)*, pp. 89–92, Chengdu, China, December 2020.

[34] Y. Lecun, Y. Bengio, and G. Hinton, "Deep learning," *Nature*, vol. 521, no. 7553, pp. 436–444, 2015, 2015 5217553.

[35] H. Holst, M. Ohlsson, C. Peterson, and L. Edenbrandt, "A confident decision support system for interpreting electrocardiograms," *Clinical Physiology*, vol. 19, no. 5, pp. 410–418, 1999.

[36] N. Srivastava, G. Hinton, A. Krizhevsky, I. Sutskever, and R. Salakhutdinov, "Dropout: a simple way to prevent neural networks from overfitting," *Journal of Machine Learning Research*, vol. 15, no. 56, 2014.

[37] S. Ioffe and C. Szegedy, "Batch normalization: accelerating deep network training by reducing internal covariate shift," *32nd Int. Conf. Mach. Learn. ICML*, vol. 1, pp. 448–456, 2015.

[38] D. P. Kingma and J. L. Ba, "Adam: a method for stochastic optimization," in *Proceedings of the 3rd Int. Conf. Learn. Represent (ICLR), 2014*, Conf. Track Proc., Banff, AB, Canada, December 2014.

[39] A. Y. Hannun, P. Rajpurkar, M. Haghpanahi et al., "Cardiologist-level arrhythmia detection and classification in ambulatory electrocardiograms using a deep neural network," *Nature Medicine*, vol. 25, no. 1, pp. 65–69, 2019.

[40] M. Zihlmann, D. Perekrestenko, and M. Tschannen, "Convolutional recurrent neural networks for electrocardiogram classification," *Computers in Cardiology*, vol. 44, pp. 1–4, 2017.

[41] Ö. Yildirim, "A novel wavelet sequence based on deep bidirectional LSTM network model for ECG signal classification," *Computers in Biology and Medicine*, vol. 96, pp. 189–202, 2018.
[42] C. Chen, Z. Hua, R. Zhang, G. Liu, and W. Wen, "Automated arrhythmia classification based on a combination network of CNN and LSTM," *Biomedical Signal Processing and Control*, vol. 57, 2020.
[43] F. S. Ahmed, L. Ali, B. A. Joseph, A. Ikram, R. Ul Mustafa, and S. A. C. Bukhari, "A statistically rigorous deep neural network approach to predict mortality in trauma patients admitted to the intensive care unit," *Journal of Trauma and Acute Care Surgery*, vol. 89, no. 4, pp. 736–742, 2020.
[44] D. H. Hubel and T. N. Wiesel, "Receptive fields of single neurones in the cat's striate cortex," *The Journal of Physiology*, vol. 148, no. 3, pp. 574–591, 1959.
[45] A. Krizhevsky, I. Sutskever, and G. E. Hinton, *Imagenet classification with deep convolutional neural networks*, Communications of the ACM, vol. 60, no. 6, pp. 84–90, 2017.
[46] S. Kiranyaz, T. Ince, and M. Gabbouj, "Real-time patient-specific ECG classification by 1-D convolutional neural networks," *IEEE Transactions on Biomedical Engineering*, vol. 63, no. 3, pp. 664–675, 2016.
[47] M. Zubair, J. Kim, and C. Yoon, "An automated ECG beat classification system using convolutional neural networks," in *Proceedings of the 2016 6th Int. Conf. IT Converg. Secur. ICITCS 2016*, Prague, Czech Republic, September 2016.
[48] D. Li, J. Zhang, Q. Zhang, and X. Wei, "Classification of ECG signals based on 1D convolution neural network," in *Proceedings of the 2017 IEEE 19th Int. Conf. e-Health Networking, Appl. Serv. Heal. 2017*, pp. 1–6, Dalian, China, December 2017.
[49] O. Yildirim, M. Talo, B. Ay, U. B. Baloglu, G. Aydin, and U. R. Acharya, "Automated detection of diabetic subject using pre-trained 2D-CNN models with frequency spectrum images extracted from heart rate signals," *Computers in Biology and Medicine*, vol. 113, Article ID 103387, 2019.
[50] W. Lu, H. Hou, and J. Chu, "Feature fusion for imbalanced ECG data analysis," *Biomedical Signal Processing and Control*, vol. 41, pp. 152–160, 2018.
[51] J. Huang, B. Chen, B. Yao, and W. He, "ECG arrhythmia classification using STFT-based spectrogram and convolutional neural network," *IEEE Access*, vol. 7, Article ID 92880, 2019.
[52] A. Ullah, S. M. Anwar, M. Bilal, and R. M. Mehmood, "Classification of arrhythmia by using deep learning with 2-D ECG spectral image representation," *Remote Sensing*, vol. 12, no. 10, 2020.
[53] T. J. Jun, H. M. Nguyen, D. Kang, D. Kim, D. Kim, and Y. H. Kim, "ECG arrhythmia classification using a 2-D convolutional neural network," 2018, https://arxiv.org/abs/1804.06812.
[54] E. Izci, M. A. Ozdemir, M. Degirmenci, and A. Akan, "Cardiac arrhythmia detection from 2d ecg images by using deep learning technique," in *Proceedings of the TIPTEKNO 2019*, Izmir, Turkey, October 2019.
[55] A. Ullah, S. U. Rehman, S. Tu, R. M. Mehmood, M. Fawad, and M. Ehatisham-ul-haq, "A hybrid deep CNN model for abnormal arrhythmia detection based on cardiac ECG signal," *Sensors*, vol. 21, no. 3, p. 951, 2021.
[56] X. Liu, H. Wang, Z. Li, and L. Qin, "Deep learning in ECG diagnosis: a review," *Knowledge-Based Systems*, vol. 227, 2021.
[57] B. Krawczyk, "Learning from imbalanced data: open challenges and future directions," *Progress in Artificial Intelligence*, vol. 5, no. 4, pp. 221–232, 2016.
[58] P. Efraimidis and P. Spirakis, "Weighted random sampling, Encyclopedia of Algorithms," in M. Y. Kao, Springer, New York, NY, USA, pp. 1024–1027, 2008.
[59] A. Lodwich, Y. Rangoni, and T. Breuel, "Evaluation of robustness and performance of early stopping rules with multi layer perceptrons," in *Proceedings of the International Joint Conference on Neural Networks*, pp. 1877–1884, Atlanta, GA, USA, June 2009.
[60] M. Liang and X. Hu, "Recurrent convolutional neural network for object recognition," in *of the IEEE Computer Society Conference on Computer Vision and Pattern Recognition*, pp. 3367–3375, Boston, MA, USA, June 2015.
[61] T. K. Lam, M. Ohta, S. Schamoni, and S. Riezler, "On-the-Fly aligned data augmentation for sequence-to-sequence ASR," 2021, https://arxiv.org/abs/2104.01393.
[62] H. Kaiming, Z. Xiangyu, R. Shaoqing, and S. Jian, "Delving deep into rectifiers: surpassing human-level performance on ImageNet classification kaiming," *Biochemical and Biophysical Research Communications*, vol. 498, no. 1, pp. 254–261, 2018.
[63] X. Glorot and Y. Bengio, "Understanding the difficulty of training deep feedforward neural networks," in *Proceedings of the JMLR Workshop and Conference Proceedings*, pp. 249–256, Sardinia, Italy, May. 2010.
[64] G. B. Moody and R. G. Mark, "The impact of the MIT-BIH arrhythmia database," *IEEE Engineering in Medicine and Biology Magazine*, vol. 20, no. 3, pp. 45–50, 2001.
[65] J. Pan and W. J. Tompkins, "A Real-Time QRS Detection Algorithm," *IEEE Transactions on Biomedical Engineering*, vol. BME-32, no. 3, 1985.
[66] O. F. Russakovsky, "ImageNet large scale visual recognition challenge," *International Journal of Computer Vision*, vol. 115, no. 3, pp. 211–252, Dec. 2015.
[67] C. Szegedy, W. Liu, Y. Jia et al., "Going deeper with convolutions," 2014, https://arxiv.org/abs/1409.4842.
[68] K. Simonyan and A. Zisserman, "Very deep convolutional networks for large-scale image recognition," in *Proceedings of the 3rd Int. Conf. Learn. Represent. ICLR 2015 - Conf. Track Proc.*, CA, USA, September 2014.
[69] K. He, X. Zhang, S. Ren, and J. Sun, "Deep residual learning for image recognition," 2015, https://arxiv.org/abs/1512.03385.
[70] G. Huang, Z. Liu, L. V. M. Maaten, and K. Q. Weinberger, "Densely connected convolutional networks," in *Proceedings of the 2017 IEEE Conf. Comput. Vis. Pattern Recognit.*, pp. 2261–2269, Honolulu, Hawaii, July 2017.
[71] C. Chola, B. H. Bin, A. Faijan et al., "IoT based intelligent computer-aided diagnosis and decision making system for health care," in *Proceedings of the 2021 International Conference on Information Technology (ICIT)*, pp. 184–189, Amman, Jordan, July 2021.
[72] O. AlShorman, M. Masadeh, A. Alzyoud, M. B. B. Heyat, F. Akhtar, and Rishipal, "The effects of emotional stress on learning and memory cognitive functions: an EEG review study in education," in *Proceedings of the 2020 Sixth International Conference on E-Learning (Econf)*, pp. 177–182, Sakheer, Bahrain, December 2020.
[73] M. B. B. Heyat, D. Lai, F. Akhtar, M. A. B. Hayat, and S. Azad, "Short time frequency analysis of theta activity for the diagnosis of bruxism on EEG sleep record," in *Advanced Computational Intelligence Techniques for Virtual Reality in Healthcare, Studies in Computational Intelligence,* vol. 875, pp. 63–83, Springer, 2020.

Hindawi
Journal of Healthcare Engineering
Volume 2023, Article ID 9816424, 1 page
https://doi.org/10.1155/2023/9816424

Retraction

Retracted: Fuzzy Logic System Implementation on the Performance Parameters of Health Data Management Frameworks

Journal of Healthcare Engineering

Received 23 May 2023; Accepted 23 May 2023; Published 24 May 2023

This article has been retracted by Hindawi following an investigation undertaken by the publisher [1]. This investigation has uncovered evidence of one or more of the following indicators of systematic manipulation of the publication process:

(1) Discrepancies in scope
(2) Discrepancies in the description of the research reported
(3) Discrepancies between the availability of data and the research described
(4) Inappropriate citations
(5) Incoherent, meaningless and/or irrelevant content included in the article
(6) Peer-review manipulation

The presence of these indicators undermines our confidence in the integrity of the article's content and we cannot, therefore, vouch for its reliability. Please note that this notice is intended solely to alert readers that the content of this article is unreliable. We have not investigated whether authors were aware of or involved in the systematic manipulation of the publication process. Wiley and Hindawi regrets that the usual quality checks did not identify these issues before publication and have since put additional measures in place to safeguard research integrity.

We wish to credit our own Research Integrity and Research Publishing teams and anonymous and named external researchers and research integrity experts for contributing to this investigation.

The corresponding author, as the representative of all authors, has been given the opportunity to register their agreement or disagreement to this retraction. We have kept a record of any response received.

References

[1] S. Vyas, S. Gupta, D. Bhargava, and R. Boddu, "Fuzzy Logic System Implementation on the Performance Parameters of Health Data Management Frameworks," *Journal of Healthcare Engineering*, vol. 2022, Article ID 9382322, 11 pages, 2022.

Hindawi
Journal of Healthcare Engineering
Volume 2022, Article ID 9382322, 11 pages
https://doi.org/10.1155/2022/9382322

Review Article

Fuzzy Logic System Implementation on the Performance Parameters of Health Data Management Frameworks

Sonali Vyas[1], **Shaurya Gupta**[1], **Deepshikha Bhargava**[2], **and Rajasekhar Boddu**[3]

[1]*University of Petroleum and Energy Studies, Dehradun, India*
[2]*School of Computing, DIT University, Dehradun, India*
[3]*Department of Software Engineering, College of Computing and Informatics, Haramaya University, Dire Dawa, Ethiopia*

Correspondence should be addressed to Deepshikha Bhargava; deepshikhabhargava@gmail.com and Rajasekhar Boddu; rajsekhar.boddu@haramaya.edu.et

Received 26 December 2021; Revised 8 February 2022; Accepted 17 February 2022; Published 12 April 2022

Academic Editor: Liaqat Ali

The development of wireless sensors and wearable devices has led health care services to the new paramount. The extensive use of sensors, nodes, and devices in health care services generate an enormous amount of health data which is generally unstructured and heterogeneous. Many generous methods and frameworks have been developed for efficient data exchange frameworks, security protocols for data security and privacy. However, very less emphasis has been devoted to structuring and interpreting health data by fuzzy logic systems. The wireless sensors and device performances are affected by the remaining battery/energy, which induces uncertainties, noise, and errors. The classification, noise removal, and accurate interoperation of health data are critical for taking accurate diagnosis and decision making. Fuzzy logic system and algorithms were found to be effective and energy efficient in handling the challenges of raw medical data uncertainties and data management. The integration of fuzzy logic is based on artificial intelligence, neural network, and optimization techniques. The present work entails the review of various works which integrate fuzzy logic systems and algorithms for enhancing the performance of healthcare-related apps and framework in terms of accuracy, precision, training, and testing data capabilities. Future research should concentrate on expanding the adaptability of the reasoning component by incorporating other features into the present cloud architecture and experimenting with various machine learning methodologies.

1. Introduction

The development of artificial intelligence (AI) as a tool for improving health care provides tremendous prospects to improve clinical results and patient outcomes, reduce costs, and influence community health. A1 health check monitoring jobs can take care of executing certain basic and recommended rules of cleaning up data repositories that are not used to managing assets that have been referred for a long time deleting and that large corporations' contents and assets struggle to keep the server up and running 24 hours a day, seven days a week [1, 2]. Due to population increase and the emergence of multiple ailments, the number of medical practitioners available to manage the community's health requirements is sometimes insufficient, particularly in less developed countries. Fuzzy logic is the form of logic theory, and the truth value of logic may be considered a real number values between 0 and 1. We can also say that it is a type of artificial intelligence. Whereas, neuro fuzzy is the combination of artificial intelligence and fuzzy logic in the field of artificial neural network (ANN) [3]. The term fuzzy logic is discovered by the scientist Lotfi Zadeh in 1965, and it is first noticed by Lukasiewicz and Tarski in 1920 in the form of infinite valued logic which is based on the observations of decision making by people in the form of nonnumerical information and can be represented as a set of mathematical terms [4]. The fuzzy models are able to recognise, manipulating, representing, interpreting, and utilizing data and information.

Fuzzy models are working based on the following Mamdani rule-based systems.

(1) Fuzzify all the input values into fuzzy membership functions.

(2) Execute all applicable rules in the rule based to compute the fuzzy output functions.

(3) Defuzzify the values of fuzzified values.

The fuzzy model system works in the layer form known as fuzzification.

Fuzzification is the process of conversion of a numerical input system to fuzzy sets with some degree of membership. These fuzzy sets are described in the form of words. It is observed in between 0 and 1. If the values are 0, then it is not belonging to the fuzzy set, and if the values are within 1, then it belongs to the fuzzy sets. Fuzzy sets are represented as triangle and trapezoid curves in the graphical representation. It shows slope where the values are changing. The peak is at the value of 1, and when the value decreases, the slope shows the sigmoid curve. Figure 1 shows the comparison of boolean and fuzzy logic systems.

Various fuzzy logic models and algorithms are implemented in the domain of health data management, security protocols, and decision-making processes [5]. Due to the rapid development in the field of wireless communication and sensor technology by 5/6G and industry 5.0, the emergence of wireless body area network (WBAN) sensors and devices has made the real-time monitoring and health management more simpler [6, 7]. Main drawbacks of the WBAN sensors are the uncertainty and error in data sensing and data exchange when working on low power consumption [8]. The performance analysis of fuzzy logic-based models and systems is essential.

The adaptive neuro fuzzy models are applicable and provide models which are able to detect chronic diseases, neurodegenerative diseases, glaucoma, Parkinson's disease, carcinogenic tumors such as blood cancer, breast cancer, and lung cancer are many more to name a few. These diseases need early detection and treatment by using certain devices such as computer-aided diagnosis (CAD), which is most commonly applied by clinicians and medical professionals as possible by introducing medical equipment with sensors. The CAD is applied before making a critical decision for the treatment of patients with crucial conditions. The CAD system is working in two major parts such as feature extraction and classification. The common classifiers are used in CAD system, decision tree (DT), random forest (RF), support vector machine (SVM), and adaptive neuro fuzzy inference system (ANFIS). This can be improved by using the algorithm modified glow worm swarm optimisation algorithm (M-GSO). For the improvement of M-GSO algorithm, the differential evolution (DE) algorithm is applied. For the proven of better results of DE algorithm, the result of this was compared with the traditional ANFIS model, genetic algorithm, ANFIS, lion optimisation algorithms ANFIS differential evolution algorithms, and many more [9].

Neurological disorders include epilepsy, cognitive impairment, neuromuscular disorders, autism, ADD, brain tumours, and cerebral palsy, to name a few. Some neurological problems are congenital, which means they develop before birth. Other issues might arise as a result of tumours, degeneration, trauma, infections, and structural faults. All neurologic deficits are produced by nervous system damage, regardless of the source. The extent to which communication, vision, hearing, movement, and cognition are harmed is determined on the location of the injury [10, 11]. The neurological diseases are most common in people of every age due to depression, anxiety, and such neurological diseases related to the nervous system are Parkinson's disease, Alzheimer's disease, brain tumour, epilepsy, dementia, memory loss, and brain stroke. According to World Health Organization (WHO), hundreds of millions of people suffer from these diseases and the mortality rate and infirmity rate increases day by day because of neurological diseases. However, we know that neurological diseases cannot be easily diagnosed due to the complexity of diagnosis procedures. All these chronic diseases can be diagnosed in early stages and earlier treatments and accurate management in this modern time by the use of modern censored equipment [9, 12]. For the accurate diagnosis and treatment, many researchers are working on the deep learning of neurological diseases with the help of artificial intelligence [13, 14]. The computing system plays an important role in the diagnosis and treatments; the most common and popular artificial intelligence (AI) technology is the neuro fuzzy system that is applied for the effective classification and detection of diseases [9, 15]. This system decreases the staff workload. In short, the fuzzy neural system is a form of machine learning system which is upgraded using machine learning algorithms [16]. The fuzzy neural system plays an essential role in the medical line for the early detection of chronic diseases such as blood infection, Alzheimer's disease, and heart diseases. [17]. The FNS not only provides the higher proficiency and accuracy but also provides the underexcretion of data or information; the artificial neural network (ANN) given by the scientist (Fojnica) is the type of artificial intelligence that also provides facilities for the understanding of physical problems and helps in the decision making in critical cases due to high accuracy in the detection of diseases [18]. For the accuracy and improved concert, the NF system is executed by the merging of neural network and fuzzy logic. The ANN is working in the form of layers such as input layer, hidden layer, and output layer. ANN is working like an artificial human brain and is also used for making artificial animal brain for pattern recognition. The NFSs are important in the medical field due to their effectiveness in improving diagnosis about 36 NF models are applied. Figure 2 shows the applications of fuzzy logic systems in various fields. NFS plays the most important role in the treatment of diabetic patients and has healing properties on diabetic foot ulcer wounds and provides the equipment which is able to recognise the early symptoms of diabetes.

Various fuzzy logic models and algorithms are implemented in the domain of health data management, security protocols, and decision-making processes [5]. Due to the rapid development in the field of wireless communication

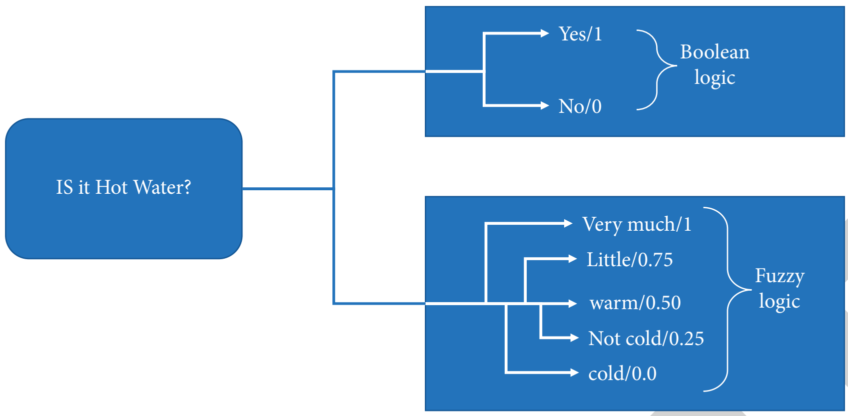

Figure 1: Comparison of Boolean and fuzzy logic systems.

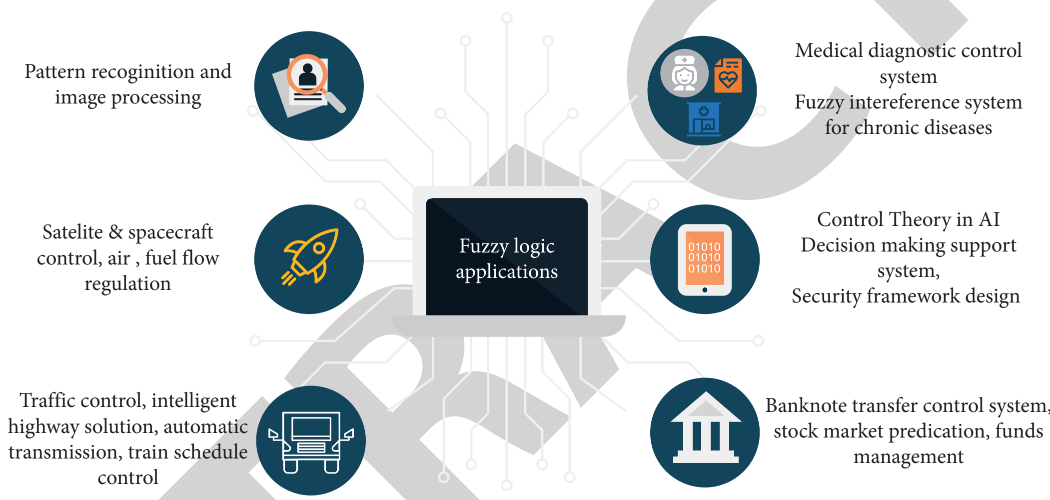

Figure 2: Applications of fuzzy logic systems in various fields.

and sensor technology by 5/6G and industry 5.0, the emergence of wireless body area network (WBAN) sensors and devices has made the real-time monitoring and health management more simpler [6, 7]. Main drawbacks of the WBAN sensors are the uncertainty and error in data sensing and data exchange when working on low power consumption [8]. The performance analysis of fuzzy logic-based models and systems is essential.

As we have seen that with the advancement in wireless communication technology and industry 5.0 revolution, the exponential growth in the WBAN sensors and wearable devices has been observed [19]. The enormous data generated are heterogeneous and unstructured in nature. Various models and algorithms have been proposed for the interpretation, classification, and analysis of data but lacks in consistency and reliability [20]. The implementation of fuzzy logic in health data management, health care apps, and hospital management system has shown a proven record [21, 22]. The practical applicability of the proposed model is for heart diseases and diabetic patients. The offloading of old-aged patients from hospital services and remote monitoring is another application. The FIS-driven model can be used for automation in the health data, management of security critical applications, better prediction and forecast of patients, accurate diagnosis, and effectively helping medical practitioners, scientists, and researchers.

The systematic review of the implementation of fuzzy logic algorithms on the performance parameters of health care apps and WBAN sensor performance is lacking. This motivates the author to present the effect of fuzzy logic on the performance parameters of health data management framework.

2. Fuzzy Logic System Integration

Haque et al. [23] proposed the accurate values of accuracy, specificity, and sensitivity with the help of the deep learning algorithm of DSPN diabetic sensorimotor which collects the data of foot ulceration and complexity in diabetic patients. The distal symmetric polyneuropathy is the common chronic complication of diabetes which affects various parts of the nervous system due to carelessness or poor treatments; it may be responsible for the damaging of the nervous system, and the common symptoms of the impairment of the peripheral nervous system in about 50% of diabetic

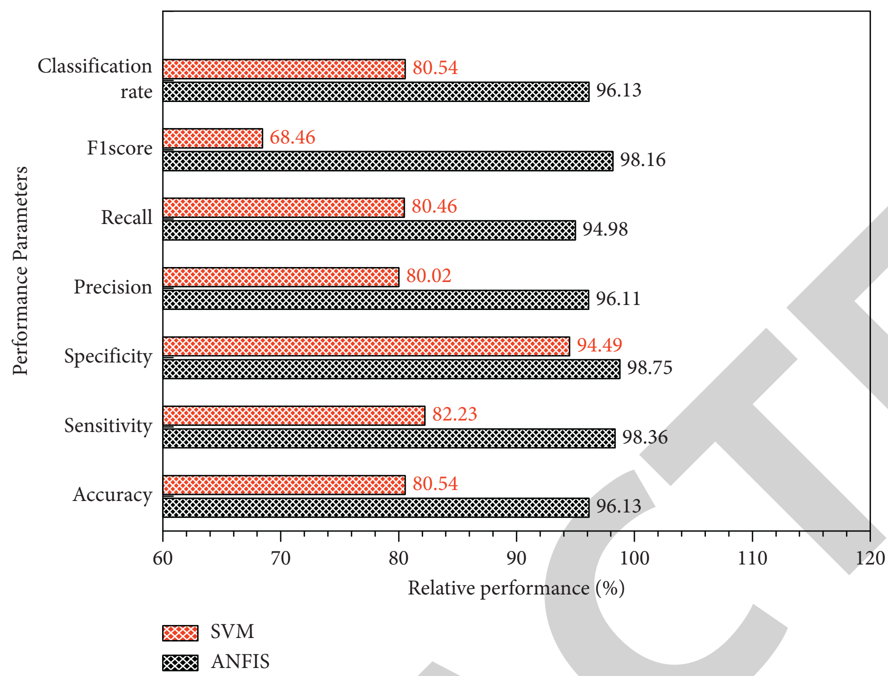

Figure 3: Performance parameters comparative analysis for the ANFIS and SVM models.

patients, and the symptoms of it may be vary from individual to individual. According to the 9th International Diabetic Federation diabetes (IDFD) Atlas, about 463 million population are affected by diabetes. According to some universities, for example, American Diabetic association (ADA), about 50% of diabetic patients does not show any symptoms; hence, it is announced as a chronic disease because it is fatal and may attack silently. The detection of this disease is very difficult; hence, there are many researchers who are working on the advancement of the intelligent system in the medical profession. They tried to identify or discover the devices by which they easily examine the complications of diabetic patients; out of them, the corneal confocal microscopy (CCM) system is emphasised for the accurate detection of DSPN. However, this method is very expensive; hence, it is difficult to find in regular clinics. At the initial stage of DSPN, the screening test by different tests, such as neuropathy disability score (NDS) and Michigan neuropathy screening instrumentation (MNSI), is based on the real-time condition of patients examines the pain, touch, vibrations, loss of sensation, and temperature. These diagnostic methods are working with artificial intelligence. The FIS method is the most common, easy, and very popular in decision-making methods; this is due to having the capability to diagnose the future condition on the basis of the present condition.

As shown in Figure 3, the ANFSI classify the MNSI data collected from the number of people (about 100) shows the performance parameter of the model which records the muscle activity and EMG is used for the diagnosis of the seriousness level [23].

The MIoTs play a vital role in the medical field [24]. It helps in improving the health care system by minimising the time, cost, and unwanted visits of the hospitals. The MIoTs have the ability to recognise the real-time condition of the patients with the help of wearable devices or gadgets (smart phones, iPhone, smart bands, smart cloths, and smart house with smart beds, floor, toilet seats, etc.) which are implemented with a number of sensors that are able to recognise the condition of the patients from the daily life activities such as walking, eating, bathing, running, and sleeping. The whole data collected by these devices are transfer to the medical staff with the help of cloud network by which the doctors and other medical staff recognise the condition and initialise the treatment and medication. The MIoTs are made up off three basic layers such as perception layer, network layer, and application layer. The first layer is able to collect the whole data or information with the help of various types of devices and methods. The second layer, network layer, helps to transfer the collected data from the devices to the clouds system; this is transferred with the help of wireless or wired connection.

Wireless connectivity is beneficial for patients, but it has significant drawbacks, including security concerns. Sometimes this is due to the wireless connection's weak capabilities and absence of encryption features, which allows hackers to easily access the data. The security complexes can overcome by applying various types of algorithms and fuzzy logic systems, a hybrid approach of deep learning. The ANFIS is also used for improving and recognising the security parameters. The fuzzy logic system is more appropriate for secure data due to their suitable capabilities such as adaptability and versability. The proven of the best performance of fuzzy logic system is shown in Figure 4. According to this figure, the first patient`s health data are undergoing the classification process with the help of five types of classifiers (data set classifiers) such as support vector machine (SVM), decision tree (DT), random forest (RF),

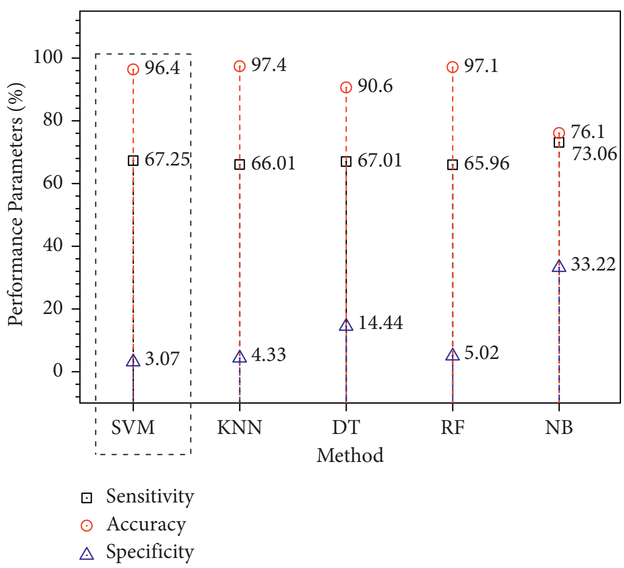

FIGURE 4: Comparison of various models performance parameters in recording daily life activities.

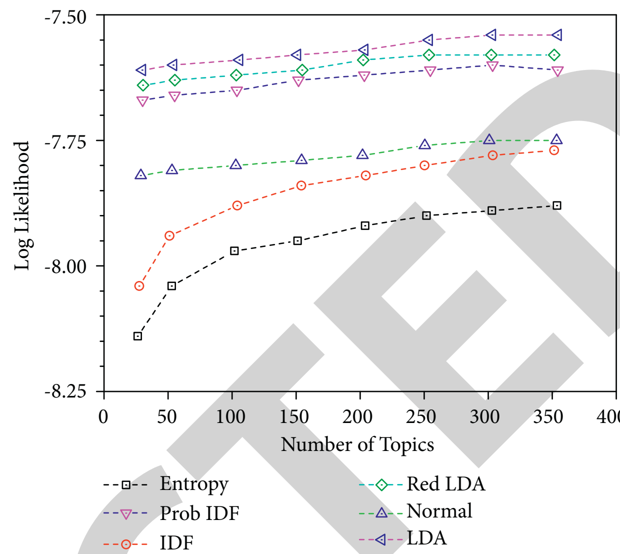

FIGURE 5: Comparative performance analysis of prob IDF with other similar models for varying number of topics.

naive Bayes (NB), and k-nearest neighbor (KNN), each one is further divided into subcategories; the classified data are also divide into two classes 0 as positive and 1 as a negative. In Figure 4 (X axis shows classifiers and Y axis shows the no. of classified instances), the NB achieves a highest sensitivity of 0.730 and a specificity of 0.332 and KNN achieves the highest accuracy with 0.974%. We can say that the SVM is the best classifier out of five. However, it is used to overcome the security issues with the help of ANFIS parameters [25].

3. Fuzzy Latent Semantic Analysis (FLSA)

IoT plays an important role in saving the corpora related to health information. The large amount of documentation, medical records, and electronics health records are in the text form which creates difficulty to find relevant data related to health, and it can have the automatic system for storage. There are a number of methods which are in the market for automation but need to find the best and easy methods. Out of them, the best method for automatic storage is fuzzy latent semantic analysis (FLSA). This method is most popular and qualitative and makes superior performance. According to National Science Foundation (NSF), there is a great challenge for secure data storage and it would have a great need for collection of electronic documentation, digital storage, proper browsing, organisation, indexing, and searching. The second most popular method of digital sortation is bag-of-words (BOW). This method is used for computer vision. It involves the collection of words and grammars which are present in the digital documents. The bag-of-words method is discovered by Zellig Harries in 1954. The next popular method is the topic modelling method that includes the text analysis techniques in which objects are documented and features are in terms of frequency. In topic modelling method, it converts the words × documents into two metrics. As an example, 100 topics in corpus, 5000 documents, 10,000 words, $W \times D$ word with 10,000 rows, 100 columns, and topics × documents matrix 100 rows and 5000 columns. The topic modelling method is a very effective method, but there is still need to improve performance, and the fuzzy latent semantic analysis (FLSA) model shows the better performance in redundant as well as in nonredundant.

In this method, every cluster is a topic and documents as a fuzzy cluster. It works in the form of fuzzy logic spectrum with seven steps. As shown in Figure 5, the fuzzy latent semantic analysis compares with various types of modelling such as LDA-T data set. The most suitable method is warped Gibbs sampling. From the figure, we can say that the FLSAs (Prob IDF) method improves their performance better than the LDA; this is due to the maintained stability with the increased number of topics and avoid negative topics and also works with in cooperation with discreate and nonstop data [8].

When the actual monitoring of the health condition is in place via a smart medical device connected to a mobile application, patient monitoring devices can collect medical and other required health data and use the smartphone's data connection to transfer the collected information to a physician or to a cloud platform. Remote patient monitoring on heart failure patients led in 50 percent. It resulted in a reduction in 30-day readmission rates, according to a study conducted by the Centre for Connected Health Policy. The Internet of Things device collects and sends health data such as heart rate, oxygen levels, blood sugar levels, weight, and ECGS. These data are maintained in the cloud and may be accessed by an authorised user, such as a physician, your insurance company, a cooperating health firm, or an external consultant, regardless of location, time, or device [21, 22]. The IoT-based health monitoring system has facilitated the real-time monitoring of patients even from remote locations [20]. This is all possible due to the industry 5.0 and 4 G/5G communication technology [26]. The recent shift in the paradigm of health monitoring by WBAN sensors and wearable devices is phenomenal. The advantages come with such disguise of data management. The data generated by these sensors and devices are enormous and heterogeneous in nature. Most of the developed health care systems and framework implement type 1 fuzzy logic system which causes inconsistency as well as uncertainty in the sensed data [27]. To overcome such hurdles of data management, Ullah et al. [28] presented the data fusion scheme by incorporating type 2 fuzzy logic and Dempster–Shafer theory for extracting precise information and giving correct results. The data obtained from various sensors attached to the patient, and the contextual data obtained from the sensors attached to the surrounding of the patient produce heterogeneous data which are often imprecise and give false indications. Thus, fusion of data from multisources (nodes/sensors) is required for better quality of service and accurate delivery of results. Various methods of fusing data, namely, probability-based, artificial intelligence-based, and evidence-based fusion type 1 fuzzy logic-based decisions become inaccurate when the data are voluminous. The type 2 fuzzy logic is found to be suitable in decision making for data with high uncertainty. The proposed fusion model works in two phases. The patient data collected from the sensors are processed by T2FL for extracting a precise membership value in phase one. The DST is used to synthesise the inferences gathered from multiple nodes/sensors in phase two. The inferred data were sent to the patient and doctors for consideration and analysis. The sensitivity, specificity, and accuracy of the proposed work has been compared with similar models and presented in terms of precision, accuracy, and recall. The proposed fusion method has been run for two folds of data sets. The comparative analysis of the F_1 score between the proposed model with existing model outperforms. For more precise and repeatability and cross-validation of results, the model runs for 10 folds of data set. The proposed T2FLD outperforms the COS and T1FL-COS by 12% to 19%. Two-fold data sets are shown in Figure 6.

The similar approach has been used by Sengan et al. [14] for developing a medical information retrieval system from electronic health care records by the integration of fuzzy logics and machine learning. This system has been focused and developed to tame the complexities of the health care system, which is overburdened by the ageing population, continuous downfall in the standard of medical services, and increased cost of treatment. The novel technique is implemented to harness and analysis the large amount of data stored in e-healthcare records using machine learning. Such integration will help in developing a smart decision support structure, improving decision making, and providing evidence-based medication service, thereby accurately depicting the patient condition from the electronic healthcare records (e-HCR). e-HCR combines individual or independent evidence-based information required for the proper treatment of the patient. e-HCR is generally classified into structured and unstructured data. The fuzzy interference system (FIS) has been used in the proposed network for rendering real-time decision making with human expert information in mind. The cross-validation of FIS has been done by the k-fold method for understanding the ability of forecasting and decision making. The proposed framework

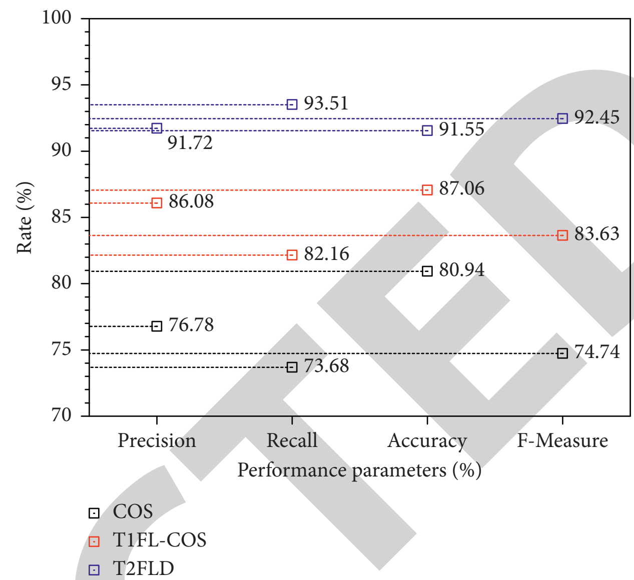

Figure 6: Comparative performance of precision, recall, accuracy, and $F1$ measure of the T2FLD model and similar models.

has been evaluated and compared to the manual and machine models for different number groups of e-HCR for forecasting the 30-day readmission of test patients as shown in Figure 7.

The proposed model outperforms the similar existing models by fair margin for different groups of e-HCR. The precision, recall, and the f1 score for the proposed model for different number of grouped e-HCR are shown in Figure 8.

4. Fuzzy Allocation-Based Model in Health Care Data Management

The fuzzy logic-based dynamic time slot mechanism has been developed by Sharavana et al. [29]. This fuzzy allocation-based model in health care data management for WBAN sensors and wearable devices was found to be effective for reliable communication in case of critical applications, minimum cost energy-based data packet routing, and improved overall performance. WBAN sensors and wearable devices enable the real-time monitoring of patient vital body signals; however, their performance is limited by the small battery size and network connectivity. Since the WBAN sensors are meant for critical applications where poor quality of service and quality of performance can be disastrous for patients and health care professional, thus the data latency, data collision, data scrambling, and increment in hopping are some major challenges in the WBAN network. Many data transmission protocols such as MAC and IEEE protocols are available for the exchange of data in WBAN network and face inefficiency challenges. The integration of heuristic hybrid time slot fuzzy allocation algorithm in WBAN network for the exchange of data among nodes and central coordinator. The proposed algorithm has been implemented for a group of 50 patients equipped with sensors and wearable devices for real-time monitoring of vital body signals. This led to an improvement in latency, energy

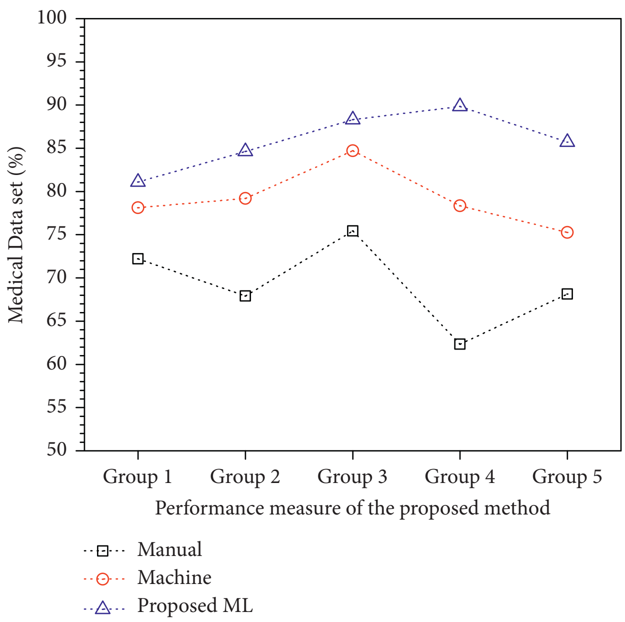

FIGURE 7: Purposed ML relative performance compared to manual and machine models for different groups of data set.

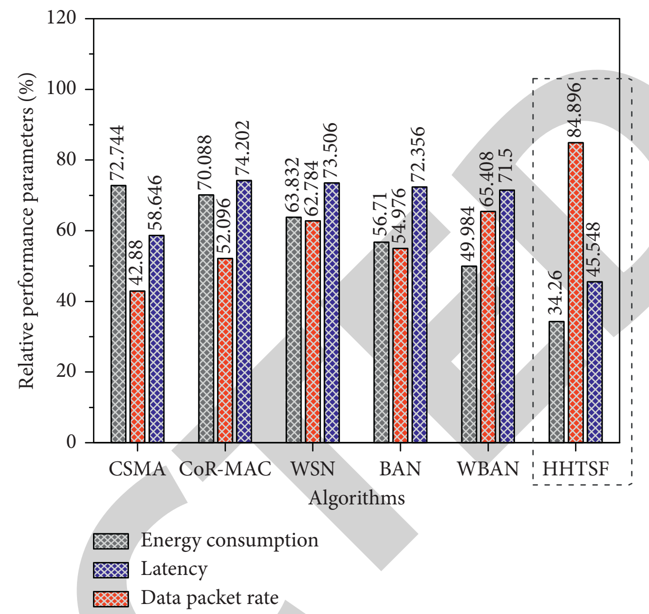

FIGURE 9: Comparative performance of HHTSF model for energy consumption, data packet rate, and latency compared to similar models.

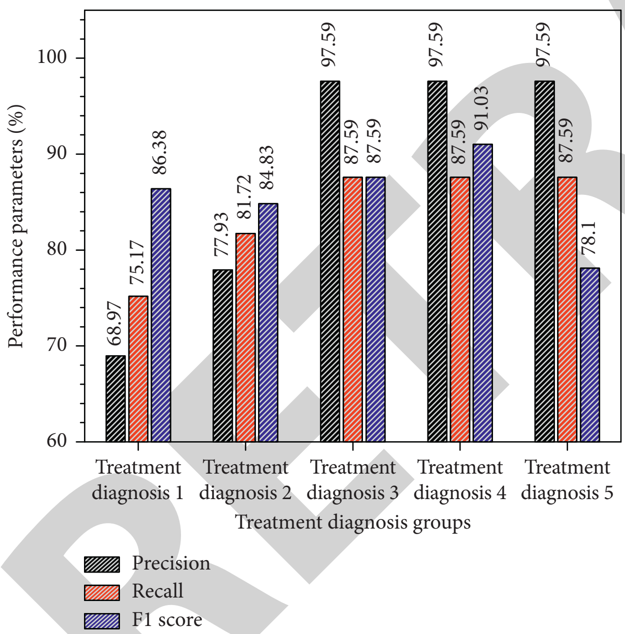

FIGURE 8: Performance of the ML model for treatment diagnosis of varying groups.

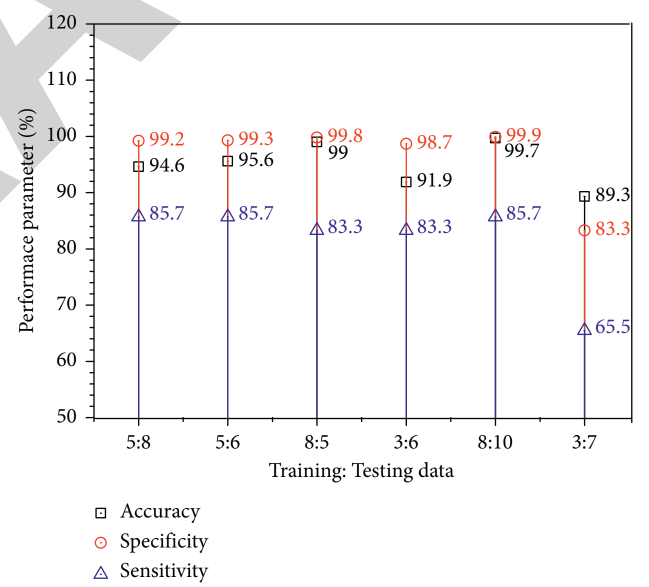

FIGURE 10: Effect of training and testing the data ratio on accuracy, specificity, and sensitivity of the T2FLIS model.

consumption, and packet delivery ratio as shown in Figure 9. The proposed model outperforms the other similar models.

The CNN and fuzzy logic-based framework proposed by Sharma et al. [30] found to be effective in predicting risk and severity by recommendation systems interlinked in health care. The CNN is using all disease classifying mechanism by the analysis of the WBAN sensors data. The integration of the fuzzy interference system helps to compute the risk level and severity conditions in a patient, followed by exchange of medical reports and evidence-based recommendations. The use of health recommender system (HRS) posts to COVID-19 pandemic has become popular across the globe. Several HRS are available for conditional logical data proposal, personal-contextual decision-making purposes. Most of HRS are struggling for reliability, quality, and dependability issues. However, the integration of fuzzy and deep learning can enhance the HRS quality of service. Type 2 fuzzy logic interference system (T2FLIS) is used in the proposed model. To check the model ability, a data set of 1032 patients is considered, which comprises 43 attributes and divided into 3 classes for each patient. The data set of patients with heart,

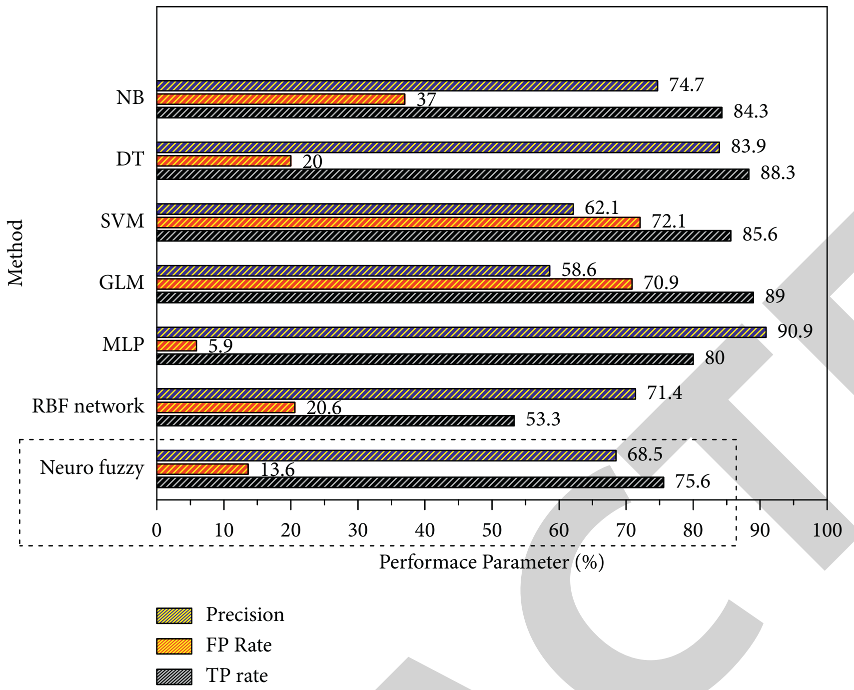

Figure 11: Comparative performance of the neuro fuzzy model with similar models for precision, FP, and TP rate in detection of HELLP syndrome detection.

liver, and kidney diseases was considered. The data set is utilized for training as well as testing purposes. The following Figure 10 shows the accuracy, sensitivity, and specificity for various combinations of training and testing data sets.

In these days, the demands of computational technologies, digital data processing, and data storage increase day by day. This is due to the less price of internet supply, fast and transformation, and the numbers of mobile applications which are helping in daily life activities most important in health department; there are more applications which help in the detection of chronic as well as other general diseases, and these apps consume less power of mobile phones such as the electronic patient's records (EPRs) i.e. the computational records, big analytical devices which are responsible for the records of big data related to individual patients and keeps the serious or normal conditions of them that helps in to recognise the syndrome`s symptoms and make easy for future medication and treatment. With the help of e-working, we can see that the medical staff are also becoming more active than previous time. The numbers of IoTs are existing in clinics, hospitals, and mobiles which are able to monitor the chronic diseases such as eclampsia, haemolysis, elevated liver enzyme, and low platelet count (HELLP) syndrome; telemedicine plays an essential role in the serious condition or in that case when the patients are not coming from the hospitals such as pregnant women. The telemedicine helps in to minimise the unwanted visits and pain, and it can be applied with the help of algorithms. The HELLP syndrome is the complicated syndrome in pregnancy, and it is difficult to diagnose at an initial stage; hence, sometimes it is responsible for the death of pregnant women.

The main diagnostic symptoms of this syndrome are less count of platelet counts, haemolytic anaemia; basically, this is seen in the women who are suffering from preeclampsia (hypertension during pregnancy). According to World Health Organization (WHO), about 8% women with preeclampsia are affected with HELLP syndrome and about 0.2% to 0.6% women suffer from this throughout the world. The reasons of this syndrome are unknown until now. The basic diagnostic method is laboratory tests. The diagnosis of syndrome can be making the easy process by applying the fuzzy logic algorithms and others. There are some algorithms shown in Figure 11. depicts a comparison of algorithms for diagnosis, treatment, and better care of pregnant women. The radial basis function network (RBF) algorithm seems too good compared to others. In the figure, it shows that the true positive rate of RBF and neuro fuzzy methods is high as compared to others; this is due to the randomness behaviour which decreases the reliability [31].

The decision-making capabilities improve their performances with the help of big data analytical algorithms and by five vs issues (variety, volume, velocity, validity, volatility, and veracity); the big data may provide important results if it is combined with artificial intelligence, machine learning, and soft neural network such as fuzzy logic and neural network. The limitation of artificial neural network is that it can handle only the crisps input and is not able to take big data in the form of linguistic expression. The definite term of fuzzy logic system is Sugeno-like fuzzy system (SFZ) which works in linear system, and the working output is discovered by Jang in 1993 which is also known as the adaptive neural fuzzy inference system (ANFIS). It has very good qualities such as strong generalised properties, simply merged in both methods linguistic as well as numeric knowledge. ANFIS plays a very important role in various fields such as engineering, economics, transportation, and especially in

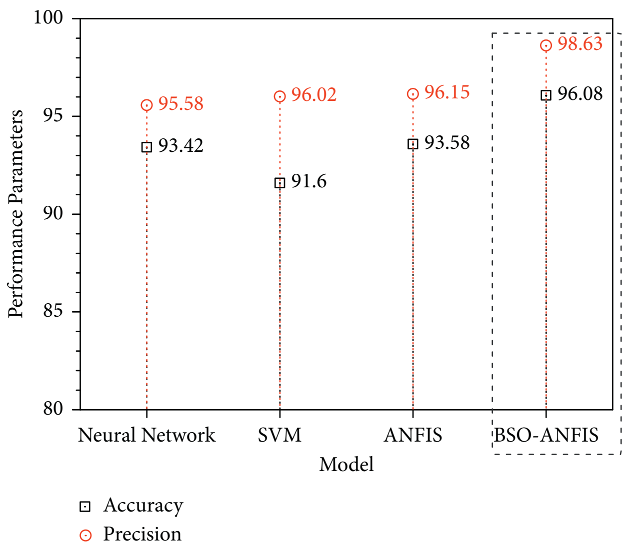

Figure 12: Comparison of performance parameters of SVM, ANFIS, with BSO-ANFIS for detecting multidiseases from given medical data set.

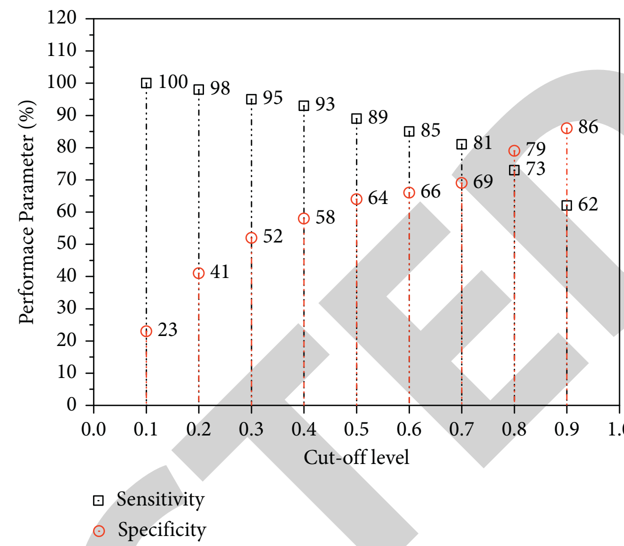

Figure 13: Accuracy and precision vs the cut-off level for the proposed fuzzy logic system.

medical field. There are some challenges of the use of ANFIS which are its complex working system, problems in handling large amount of computational cost, and complication in handling of high dimensional problems. To minimise these problems, other algorithms are applied such as new combination forms in between ANFIS and beetle swarm optimisation (BSO) algorithm which can call as a BSO-ANFIS algorithm. This algorithm is able to diagnose the typical diseases and analyses the big health care data in this system, and the beetle antennae search (BAS) and metaheuristic algorithm (MA) are combined with particle swarm optimization (PSO) methods. The BAS algorithm is less complicated as compares to others. It can be a new combination of algorithm and is formed as BSO the combination of BAS and PSO algorithms. The modified algorithm modified crow search algorithms (MCSA) is also used for the diagnosis the typical diseases.

An ANFIS algorithms the autogram analysis as an input data of diagnosis. There are many proves by the doctors that the better uses of which algorithms simultaneously aided diagnosis model (SADM) which is helpful ineasy diagnosis of diseases. For the prove of this algorithm that it is better performed than others, it is compared with some other such as support vector machine (SVM) and artificial neural network (ANN), for the hyperlipemia disease in which the level of lipids are high in the blood. It can be proved that the SADM method provides the accurate detection of this disease, but sometimes some drawbacks have been seen i.e., the accuracy turned out to be very sensitive. This method is working on the basis of deep and machine learning. Figure 12 shows the comparison of better performance for heart diseases in between various algorithms that are neural network, SVM, ANFIS, and BSO-ANFIS. In Figure 12, we can say that BSO-ANFIS better than others; it shows the accuracy and precision near about 96.08 and 98.63, respectively, which is higher as compared to the others. With the help of these algorithms, the multidiseases can be detected by the advancement in this field [15].

The fuzzy logic technique is used in every field for better performances; one of them is online monitoring of conductivity of goat`s milk in health care system. For the purpose of better health, the healthy milk is beneficial i.e., disease free and unaffected by the microorganisms. The attack of microorganisms affects the quality and quantity of milk. There are various types of bacterial, viral, protozoal, and parasitical diseases which influence the yield of milk and milk products. The common infection of mammary glands is intramammary infection (IMI) which affects the quality and quantity of the milk of dairy goats. In these days, the milk of goat plays a very important role in the health care system; according to some researchers, it is most beneficial for the less count of blood cells; hence, it needs better care. The IMI is caused by the presence of the large number of somatic cell count (SCC). The addition of somatic cell count is a very common method to increase the milk yielding, but the very much large amount of these cells cause infection in the mammary glands in cows and ruminants. The limit of somatic cells in the raw milk is 1,500,000 cells/ml, and the A grade milk of goats contains 1,00,000 cells/ml. Indirectly, the large number of somatic cells in the blood causes the ill effects on the human health. This type of milk contains the large number of pathogens which enter into the human body. These microbes cause the proteolysis of the milk products like [R] curd and cheese, which is responsible for ions balancing in the human body; hence, it is needed for the early detection; the electrolytical conductivity is introduced for the anions and cation balancing. This parameter is wrought in effective manner. The early detection may be preventing food spoilage and improving milk quality and quantity. The electrical conductivity of the milk is determined by the conductimetry which is present in the goat cluster. The identification of better milk is detected by comparison of readings in milk from intrinsic variation of animals and previous milk; the variated forms of animals may be developed by the use of fuzzy logic system, and this method is very easy and effective. This method helps in converting the general knowledge into computational mathematical values, in which the milk comparison between different diary milks with variable numbers of somatic cells. By the fuzzy logic system, we can increase the specificity and accuracy. Figure 13 presents the accuracy specificity cut-off level; when it is increased or decreased by the cut-off level, the accuracy level reached by the fuzzy logic system. According to the recent study, the fuzzy logic models are beneficial to recognise the health status of dairy goats and also helpful in better health of the animal [32].

5. Conclusion and Future Scope

The present work reviews the uncertainty challenges in health data management. For accurate diagnosis and treatment to be prescribed by a doctor, accurate and certain data are required. The present WBAN sensors, wearable devices, data acquisition, and transmission capabilities are constrained by limited power sources. As the power source is depleted, the uncertainty in sensing and exchanging data decreases. This hampers the doctors in taking the right decisions from the diagnosis and prescribing accurate treatment. Decision making is an intuitive and rational process which is difficult to achieve by machine. The use of artificial intelligence and fuzzy logic-based frameworks is implemented for data management in health care where data heterogeneity, uncertainty, and noise are above the permissible level. The implemented fuzzy logic in medical health data management has not reached to its full potential; however, it has been able to assist in decision making. The recent development in fuzzy logic models and algorithms has been attracting the researchers to explore its full potential in the domain of health data management. To precisely understand the loopholes and unexplored areas of health data management, a strong and fundamental review of the recent work is lacking and there is a need to present in the public domain. The comparative study of performance parameters of fuzzy logic-based models in the recent time has been thoroughly reviewed in the present work. This review work lays a foundation for further research in the domain of fuzzy logic models in health data management based on loopholes and unexplored areas to provide better quality of management and quality of service.

Data Availability

All the data pertaining to this article are given in the article itself.

Conflicts of Interest

The authors declare that there are no conflicts of interest.

References

[1] G. Verma, N. Pathak, and N. Sharma, "A secure framework for health record management using blockchain in cloud environment," *Journal of Physics: Conference Series*, vol. 1998, no. 1, p. 012019, 2021.

[2] S. Saxena, S. Vyas, B. S. Kumar, and S. Gupta, "Survey on Online Electronic Paymentss Security. In 2019 Amity International Conference on Artificial Intelligence (AICAI)," in *Proceedings of the 2019 Amity International Conference on Artificial Intelligence (AICAI), IEEE, Dubai*, February 2019.

[3] K. Mittal, A. Jain, K. S. Vaisla, O. Castillo, and J. Kacprzyk, "A comprehensive review on type 2 fuzzy logic applications: past, present and future," *Engineering Applications of Artificial Intelligence*, vol. 95, Article ID 103916, 2020.

[4] L. A. Zadeh, "Outline of a new approach to the analysis of complex systems and decision processes," *IEEE Transactions on Systems, Man, and Cybernetics*, vol. SMC-3, no. 1, pp. 28–44, 1973.

[5] A. Karami, A. Gangopadhyay, B. Zhou, and H. Kharrazi, "Fuzzy approach topic discovery in health and medical corpora," *International Journal of Fuzzy Systems*, vol. 20, no. 4, pp. 1334–1345, 2017.

[6] J. Bhola, S. Soni, and J. Kakarla, "A scalable and energy-efficient MAC protocol for sensor and actor networks," *International Journal of Communication Systems*, vol. 32, pp. 1–16, 2019.

[7] M. Shabaz and A. Kumar, "SA sorting: a novel sorting technique for large-scale data," *J Comput Networks Commun*, vol. 2019, Article ID 3027578, 7 pages, 2019.

[8] J. Bhola, S. Soni, and G. K. Cheema, "Genetic algorithm based optimized leach protocol for energy efficient wireless sensor networks," *Journal of Ambient Intelligence and Humanized Computing*, vol. 11, no. 3, pp. 1281–1288, 2020.

[9] K. Balasubramanian and N. P. Ananthamoorthy, "Improved adaptive neuro-fuzzy inference system based on modified glowworm swarm and differential evolution optimization algorithm for medical diagnosis," *Neural Computing & Applications*, vol. 33, no. 13, pp. 7649–7660, 2021.

[10] A. Sharma and R. Kumar, "Computation of the reliable and quickest data path for healthcare services by using service-level agreements and energy constraints," *Arabian Journal for Science and Engineering*, vol. 44, no. 11, 2019.

[11] G. Rastogi and R. Sushil, "Cloud computing implementation: key issues and solutions," in *Proceedings of the 2015 2nd International Conference on Computing for Sustainable Global Development (INDIACom)*, pp. 320–324, IEEE, New Delhi, India, March 2015.

[12] C. Stamate, G. D. Magoulas, S. Küppers et al., "Deep learning Parkinson's from smartphone data," in *Proceedings of the 2017 IEEE International Conference on Pervasive Computing and Communications (PerCom)*, pp. 31–40, Kona. USA, March 2017.

[13] M. A. Qureshi, K. N. Qureshi, G. Jeon, and F. Piccialli, "Deep learning-based ambient assisted living for self-management of cardiovascular conditions," *Neural Computing & Applications*, Article ID 0123456789, 2021.

[14] L. Ajp, S. Sengan, G. K. Kamalam et al., "Medical information retrieval systems for e-Health care records using fuzzy based machine learning model," *Microprocessors and Microsystems*, Article ID 103344, 2020.

[15] P. Singh, A. Kaur, R. S. Batth, S. Kaur, and G. Gianini, "Multi-disease big data analysis using beetle swarm optimization and an adaptive neuro-fuzzy inference system," *Neural Computing & Applications*, vol. 33, no. 16, pp. 10403–10414, 2021.

[16] C. Iwendi, K. Mahboob, Z. Khalid, A. R. Javed, M. Rizwan, and U. Ghosh, "Classification of COVID-19 individuals using

Hindawi
Journal of Healthcare Engineering
Volume 2023, Article ID 9812052, 1 page
https://doi.org/10.1155/2023/9812052

Retraction

Retracted: Automatic COVID-19 Lung Infection Segmentation through Modified Unet Model

Journal of Healthcare Engineering

Received 23 May 2023; Accepted 23 May 2023; Published 24 May 2023

This article has been retracted by Hindawi following an investigation undertaken by the publisher [1]. This investigation has uncovered evidence of one or more of the following indicators of systematic manipulation of the publication process:

(1) Discrepancies in scope
(2) Discrepancies in the description of the research reported
(3) Discrepancies between the availability of data and the research described
(4) Inappropriate citations
(5) Incoherent, meaningless and/or irrelevant content included in the article
(6) Peer-review manipulation

The presence of these indicators undermines our confidence in the integrity of the article's content and we cannot, therefore, vouch for its reliability. Please note that this notice is intended solely to alert readers that the content of this article is unreliable. We have not investigated whether authors were aware of or involved in the systematic manipulation of the publication process. Wiley and Hindawi regrets that the usual quality checks did not identify these issues before publication and have since put additional measures in place to safeguard research integrity.

We wish to credit our own Research Integrity and Research Publishing teams and anonymous and named external researchers and research integrity experts for contributing to this investigation.

The corresponding author, as the representative of all authors, has been given the opportunity to register their agreement or disagreement to this retraction. We have kept a record of any response received.

References

[1] S. Shamim, M. J. Awan, A. Mohd Zain, U. Naseem, M. A. Mohammed, and B. Garcia-Zapirain, "Automatic COVID-19 Lung Infection Segmentation through Modified Unet Model," *Journal of Healthcare Engineering*, vol. 2022, Article ID 6566982, 13 pages, 2022.

Hindawi
Journal of Healthcare Engineering
Volume 2022, Article ID 6566982, 13 pages
https://doi.org/10.1155/2022/6566982

Research Article

Automatic COVID-19 Lung Infection Segmentation through Modified Unet Model

Sania Shamim[1] **Mazhar Javed Awan**[1] **Azlan Mohd Zain**[2] **Usman Naseem**[3] **Mazin Abed Mohammed**[4] **and Begonya Garcia-Zapirain**[5]

[1]*Department of Software Engineering, University of Management and Technology, Lahore, Pakistan*
[2]*School of Computing, UTM Big Data Centre, Universiti Teknologi Malaysia, Skudai 81310, Johor, Malaysia*
[3]*School of Computer Science, The University of Sydney, Sydney, Australia*
[4]*College of Computer Science and Information Technology, University of Anbar, 11, Ramadi 31001, Iraq*
[5]*eVIDA Laboratory, University of Deusto, Avda/Universidades 24, 48007, Bilbao, Spain*

Correspondence should be addressed to Mazin Abed Mohammed; mazinalshujeary@uoanbar.edu.iq

Received 12 January 2022; Revised 23 February 2022; Accepted 28 February 2022; Published 11 April 2022

Academic Editor: Sahfqat Ullah Khan

The coronavirus (COVID-19) pandemic has had a terrible impact on human lives globally, with far-reaching consequences for the health and well-being of many people around the world. Statistically, 305.9 million people worldwide tested positive for COVID-19, and 5.48 million people died due to COVID-19 up to 10 January 2022. CT scans can be used as an alternative to time-consuming RT-PCR testing for COVID-19. This research work proposes a segmentation approach to identifying ground glass opacity or ROI in CT images developed by coronavirus, with a modified structure of the Unet model having been used to classify the region of interest at the pixel level. The problem with segmentation is that the GGO often appears indistinguishable from a healthy lung in the initial stages of COVID-19, and so, to cope with this, the increased set of weights in contracting and expanding the Unet path and an improved convolutional module is added in order to establish the connection between the encoder and decoder pipeline. This has a major capacity to segment the GGO in the case of COVID-19, with the proposed model being referred to as "convUnet." The experiment was performed on the Medseg1 dataset, and the addition of a set of weights at each layer of the model and modification in the connected module in Unet led to an improvement in overall segmentation results. The quantitative results obtained using accuracy, recall, precision, dice-coefficient, F1score, and IOU were 93.29%, 93.01%, 93.67%, 92.46%, 93.34%, 86.96%, respectively, which is better than that obtained using Unet and other state-of-the-art models. Therefore, this segmentation approach proved to be more accurate, fast, and reliable in helping doctors to diagnose COVID-19 quickly and efficiently.

1. Introduction

Since December 31, 2019, COVID-19 has been identified as a new coronavirus outbreak from Wuhan, a province in China. Infected cases were reported in both the international community and other Chinese cities within a few days. Because of the virus's speed and breadth of transmission, the World Health Organization (WHO) declared the severe acute respiratory syndrome coronavirus commonly known as COVID-19 outbreak a pandemic [1]. There were 125,000 cases reported to WHO from 115 countries and territories, while the number of cases reported outside China also nearly doubled within a couple of weeks, and the number of nations affected nearly tripled [2]. Statistically, 305,914,601 people worldwide tested positive for COVID-19 and 5,486,304 people died as a result up to 10 January 2022 [3, 4].

The most common COVID-19 symptoms include respiratory ailment, cough, flu, and fever, while for its part, computer tomography (CT) is a far better form of technology in terms of reliability, speed, and usefulness. As the virus broke out rapidly, assessment of COVID-19 needed to be automatic in the case of this particular pandemic [5].

Assessment and classification of COVID-19 are quicker using CT scans, insofar as its early detection is possible using CT images, although classification takes a lot of valuable time as this is done manually by expert radiologists. RT-PCR test results for COVID-19 take more than one day for the virus to be detected in the human body [6, 7]. Ground glass opacity (GGO) in CT images is considered to be a sign of COVID-19, and GGO in CT images takes on a fuzzy appearance, with opaque cerebral lesions being either uni-partite, bilateral, cortical, or distributed invasive lesions. The immediate diagnosis of COVID-19 was initially pivotal in controlling the spread of disease [8]. Manual assessment and analysis of CT scans by expert radiologists are time-consuming procedures while the severity and spreading rate demand automatic segmentation and detection in a fast pace environment [9].

In this study, we proposed a deep learning improved model based on UNet [10] that segments the ground glass opacification areas in a COVID-19 CT image dataset that is available to the public. Some difficulties occur in the segmentation of CT scans due to varieties in surface, location, and area of tainted regions. In the case of segmentation models, very small lesions and interconnected components that appear indistinguishable in CT images effectively generate a greater likelihood of false negatives. The ground glass limitation, which results in a small difference between the region of interest and background and fuzzy appearance, leads to difficulty in distinguishing the region of interest from a normal background when the division is being measured, and these factors influence segmentation performance. Our work has two objectives. First, we ascertain whether a more weighted module can be used inside a U-Net to enhance CT images lesion segmentation for limited labeled data, which is common in COVID-19 due to a lot of time-consuming manual masking of CT images. Second, we combine our new adaption of this module and increase the number of convolving layers in standard Unet architecture. The following are the main contributions made by the study.

(1) This research addresses the problem of being unable to distinguish ROI from a normal background in deep learning segmentation and uses convolution layers and an E-D connected module in a simple and easy way.

(2) The increase in convolution layers extracts the features at a fine level and boosts the propagation of features. The E-D module enlarges the receptive field, and the gradient disappearance (indistinguishable) problem is recouped through the E-D module.

(3) The proposed Unet-like model improves the receptive field of the predicted region of interest, leading to more information being gained and the edge recognition ability of the model being magnified.

(4) The quantitative results of the proposed model compared to the basic Unet approach and other state-of-the-art models makes its performance the best one.

The rest of the paper is organized as follows: Section 2 describes related work on segmentation techniques and particular segmentation techniques for COVID-19 CT scans. Section 3 explains the method proposed and implemented. In Section 4, our model performance with state-of-the-art is discussed and Section 5 provides the conclusion drawn from our article.

2. Related Work

Deep Learning has a great capability to learn and provide solutions to state-of-the-art inventions and problems in different diseases efficiently in this new era. The segmentation of COVID-19 CT scans using deep learning approaches has a broad scope in terms of research.

2.1. Image Segmentation. Deep learning segmentation models have been matured in recent years, resulting in the development of numerous automatic systems essentially based on deep learning approaches. Semantic segmentation algorithms have also been advanced and are quick, and these algorithms are automated using medical and natural image applications. In recent years, segmentation performance of medical images has been improved from the fully convolutional network (FCN) technique to an improved convolving method version, known as dilated convolution [11]. The extensive changes in encoder-decoder pipeline architecture for image classification and segmentation has provided good results as follows: SegNet [12], ResNet [13], NnUnet [14], A2-Net [15], ShelfNet [11], and discriminative learning [16].

2.2. Segmentation Approaches for COVID-19 CT Scans. The TV-Unet model is a modified Unet model that uses regularization terms in its network and has detected and segmented pathological regions. The Basic Unet model was improved by tuning the hyperparameters and was subject to a comparative analysis of different parameters in a research study [17]. The study proposed a two-stage method to improve the Unet model by adding a residual block that was used to detect subareas and tiny lesions accurately. A two-stage cross-domain transfer learning method is proposed by applying the ResNet50. In the first stage, transfer learning is applied to the model level, while, in the second stage, data level transfer learning is applied. Each layer of Resnet50 is embedded with an enhanced channel attention component [18]. The study proposed a covTANet model to diagnose Covid-19, the severity of infection, and segmentation of infected lung lesions. A full convolution network and Unet approach were also used with few modifications to covTANet [19].

FractalCovNet architecture is proposed using fractal modules for segmentation, and this includes U-Net architecture with fractal blocks. This architecture followed the contracting and expansive path, and the contraction and expansion procedure was repeated to obtain the segmented output [20]. A Unet variation worthy of note known as CXAU-Net [21] convolution added up the value of receptive fields while the hybrid loss function improved model performance. The study [22] used progressive global perception and local polishing to build the network that could then segment infected areas in CT images. This approach applied to segmentation was in accordance with Unet architecture, with the study proposing a RTSU-Net that improved on structural relationships by introducing a nonlocal neural network module [23]. The study coped with a COVID-19 CT scans data shortage by focusing on increasing data size using the augmentation method along with the Unet model implementation for segmentation [24].

3. Proposed Methodology

3.1. Dataset Description. The annotated Medseg1 dataset from the dataset [25] contains 100 CT images of 40 COVID-19 patients. One mask class is ground glass opacity, the second is consolidation, the third is another pulmonary infection, and the fourth is the lung. Four labeled classes are used in this dataset: 1 = ground class opacity, 2 = consolidation and 3 = pulmonary effusions and 4 = lung. This dataset contains 474 images in total, including original CT scans, as shown in Figure 1. The color augmentation, noise augmentation and minoring, scaling, rotation, and elastic deformation were applied in the case of spatial augmentation.

In this dataset, there are 96 images with ground glass masks, 78 with consolidation mask images, 100 other lung and pulmonary mask images, and also 100 background mask images. According to research, ground glass opacity is the most relevant in the diagnosis of COVID-19, and so here, we focused our study on ground glass opacity mask images and other labeled classes that were not used in our work. Here in Figure 2, row 1 shows original CT scans, the second row shows ground glass opacity mask images, and the third row shows consolidation mask images.

3.2. Model Description. The proposed network design we describe in depth in this section is that of CNN model architecture. The customized CNN model features key distinctions between the previous work and the method suggested. Different techniques and models for semantic segmentation are based on convolution layers. Unet [12] architecture is comprised of an encoder and decoder symmetrically, with the encoder path involving two convolution layers at each downward step. A $3 * 3$ convolved operation was then conducted, and pooling operation of size $2 * 2$ and stride size of 2 was applied. Moreover, this process was repeated four times to collect spatial features of an image in an encoder. At first, the decoder followed the upsample operation to map the feature using the transposed convolution of size $2 * 2$, reducing the number of channels by half. Two convolution layers of size $3 * 3$ then followed the upsample operation. The feature map from the last block of the decoder undergoes a $1 * 1$ convolution operation that produces the segmentation map of the same size as the input image. Unet architecture uses the RELU activation function throughout its convolution layer, while the last convolving layer uses the Sigmoid function. Figure 3 shows the architecture of the proposed convUnet method.

Our proposed model is based on conventional Unet [12] architecture with the following enhancements:

(1) The addition of convolution layers at each block of encoder structure and the same number of convolution layers are applied at each block of the decoder pathway. Both contraction and expansion paths have more sets of weights than Unet.

(2) The set of weights in the encoder and decoder connecting module is increased from 2 to 3. The conventional Unet has 2, while our improved model has 3 sets of weights.

(3) The improved model used Batch normalization before each nonlinear function. The conventional Unet has no use for batch normalization in its network.

This research increased the convolution layers in each block of encoder and decoder architecture. To optimally handle the input image dimension $512 * 512$, we used a U-Net structure from [19], which was slightly altered by adding one more convolving layer in each block of encoderand decoder. In our proposed model, there were four blocks that made up the downsampling path, while a further four blocks comprised the upsampling path. Three times 2D convolution with a kernel size of $3 * 3$, three times batch normalization, and three times the Relu activation function is used for each block of the encoder and decoder pipeline, while a 2D convolution with kernel size $1 * 1$ is used in the last block. In order to halve the spatial dimension of the feature maps after each block, a max-pooling operation is applied for downsampling. To double the size of the spatial dimension of the concatenated feature maps, ConvTranspose2d is used in the decoder pathway. In the downsampling path, the number of feature channels is increased to 1-64-128-256-512, and in the up-sampling path, it is reduced again from channel number 512 to channel number 1. Figure 4 shows the flow of input images through the encoder pipeline. Each block shows which operation and how many convolution layers are used.

Figure 5 demonstrates the flow more clearly. The input image is convolved along with the use of batch normalization and nonlinear function, which reduces the channel number. It is then followed by a max-pooling operation to obtain a pooled feature map. Downsampling reduces the size of the input, and this sequence of operations is repeated four times in the encoder path.

Through skip connection, the output of each block comprising convolution layers that are obtained before the pooling operation in the encoder is passed to the corresponding decoder block. Furthermore, it becomes concatenated with the output of the transpose convolution layer, and feature maps are transferred to the decoder convolution layers. Feature information lost in the symmetric encoder due to the pooling operation can be obtained through skip connection, which enables the proposed model to use fine-grained details learned in the encoder part in order to construct an image in the decoder part. To summarize, the purpose of these skip connections used in the proposed model is that they provide an unvarnished or nonfluctuated

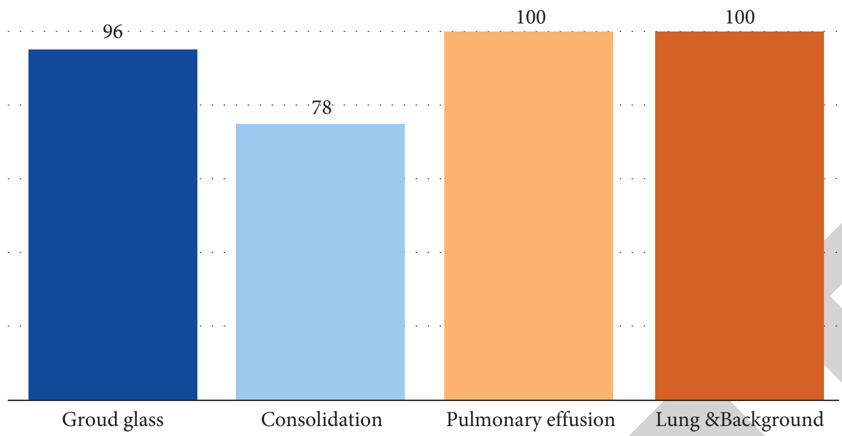

FIGURE 1: The number of each mask class segmentation in the dataset.

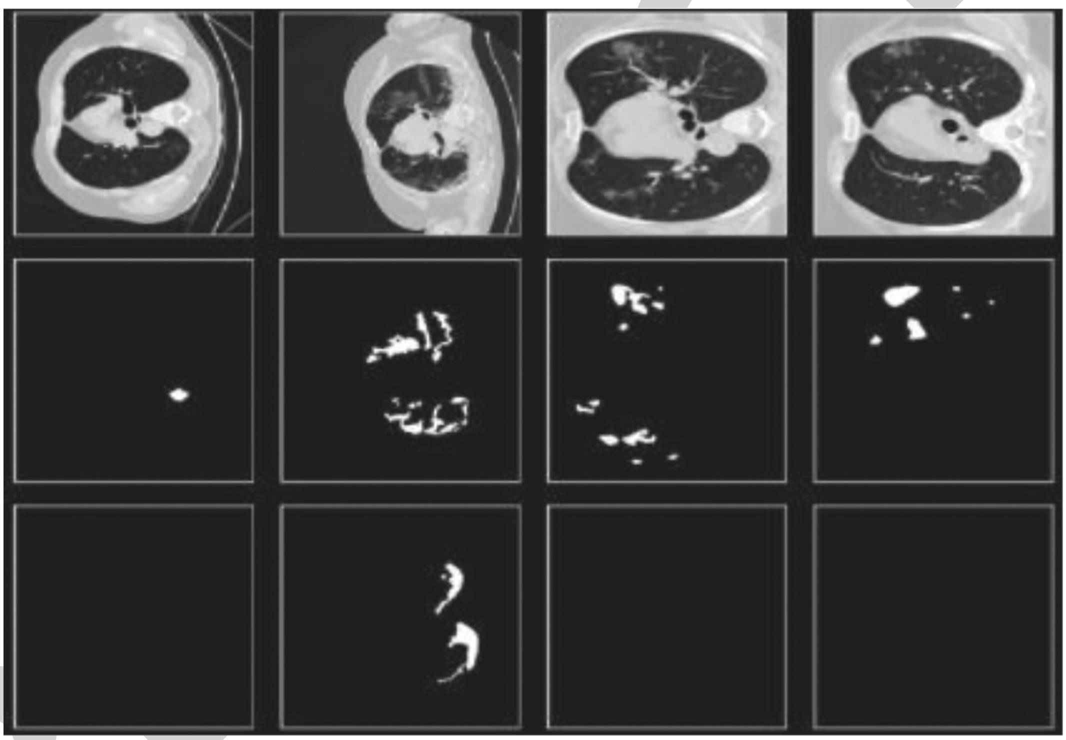

FIGURE 2: Sample dataset images.

gradient flow from the first to the final layer. The research supplemented a module in the Unet architecture as an addition to the U-bottleneck, which allowed us to gather contextual information just from the useful global context information required both proficiently and systematically, with the module structure being shown in Figure 6.

The output from the last layer of the encoder with small dimensions is taken as input to the more weighted connected module. This forms the local representation of feature maps that are produced from the final block of our proposed convUnet encoder path. The integrated module is placed into the bottleneck because the input passing through the module will have decreased in both size and dimension, reducing the amount of time spent on training and space complexity on the feature maps. Our customized model improves the segmentation performance on the COVID-19 dataset by increasing the number of convolution layers and modifying the connected encoder and decoder module that we added to the model.

Figure 6 represents the encoder-decoder-connected module. The last pooled feature map is passed through the module which has convolving layers of $3 * 3$ filter size.

The last layer feature map in our proposed model was in accordance with the soft-max classifier that generates a number of feature channels equal to the number of semantic segmentation label classes. The last layer obtained the image size $512 * 512$ equal to the actual image size with 4 channels, while the architecture had 46,773,124 parameters and

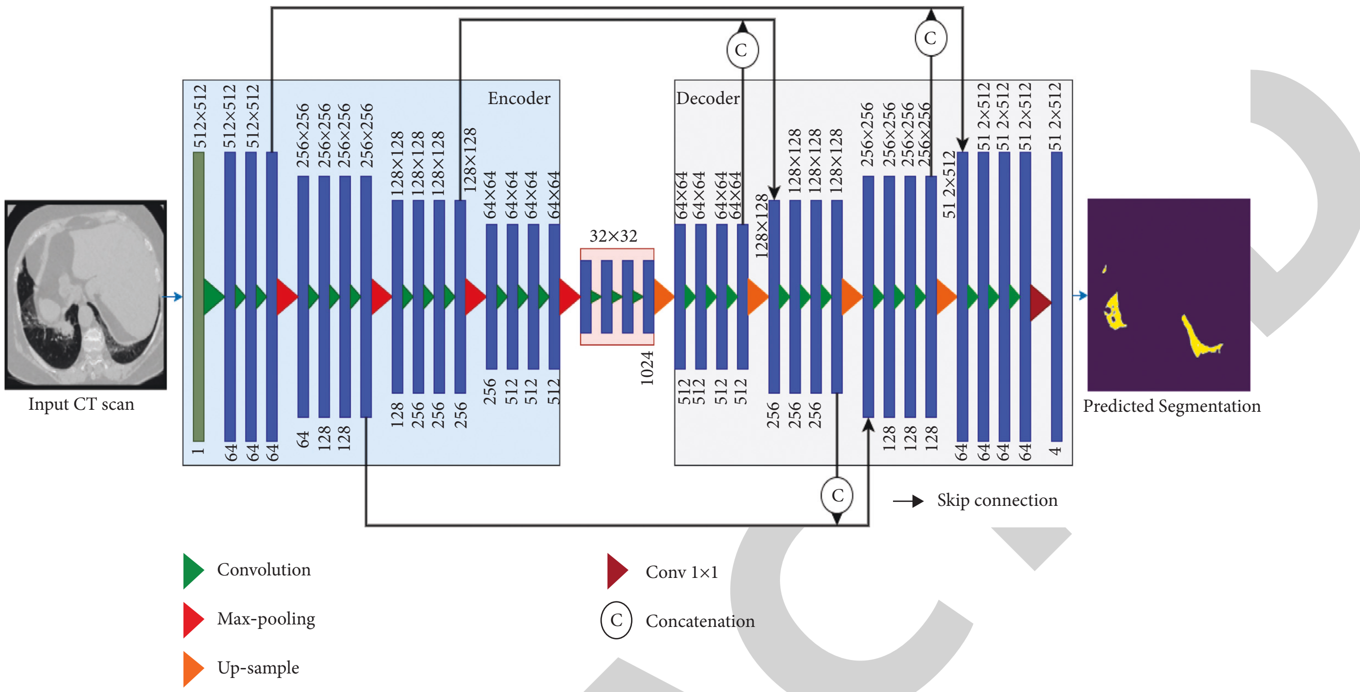

Figure 3: Architecture of proposed network.

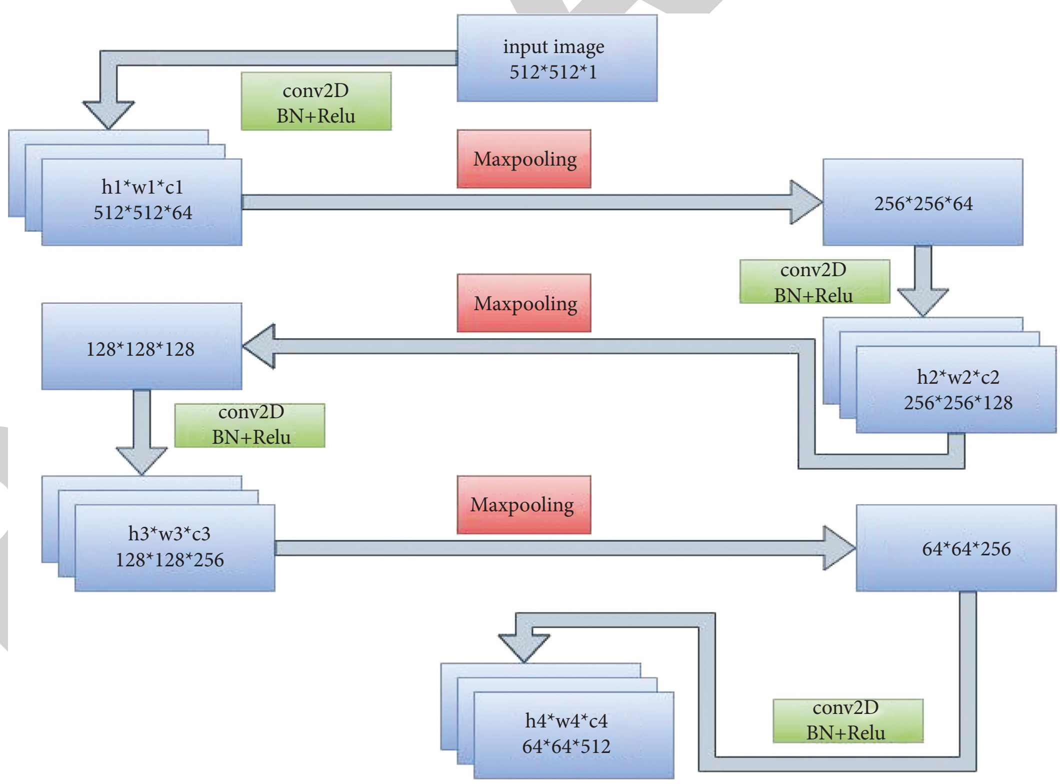

Figure 4: Encoder flow diagram.

46,755,460 trainable parameters in total. Every convolution layer comprises feature maps, C represents the convolution layer, the feature map is denoted by M, and the layer number is denoted by n. The feature map in the first layer C^1 derives from convolving the input matrix by a kernel k^1 along with the addition of bias term B^1. In this case, j denotes the feature map number and $f(y)$, a nonlinear function, is applied to the filtered output before passing it on to the convolution layer, where I denotes the input neuron. Convolution at layer one with its elements is expressed in the following equation:

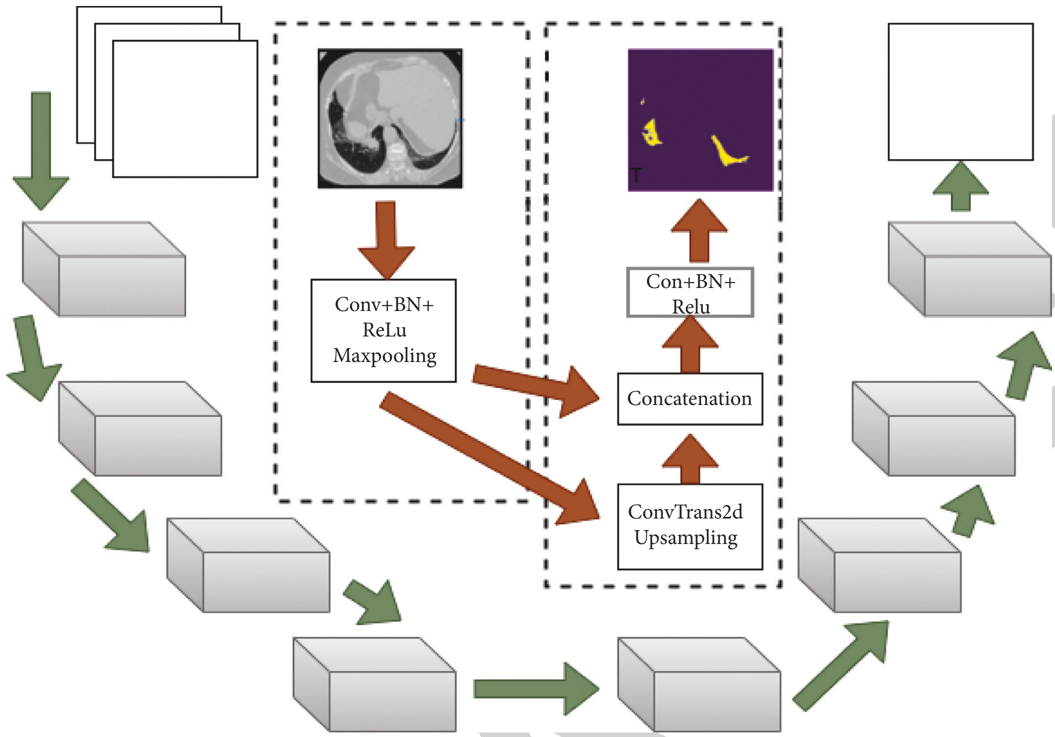

Figure 5: Encoder–decoder and concatenated skip connection flow.

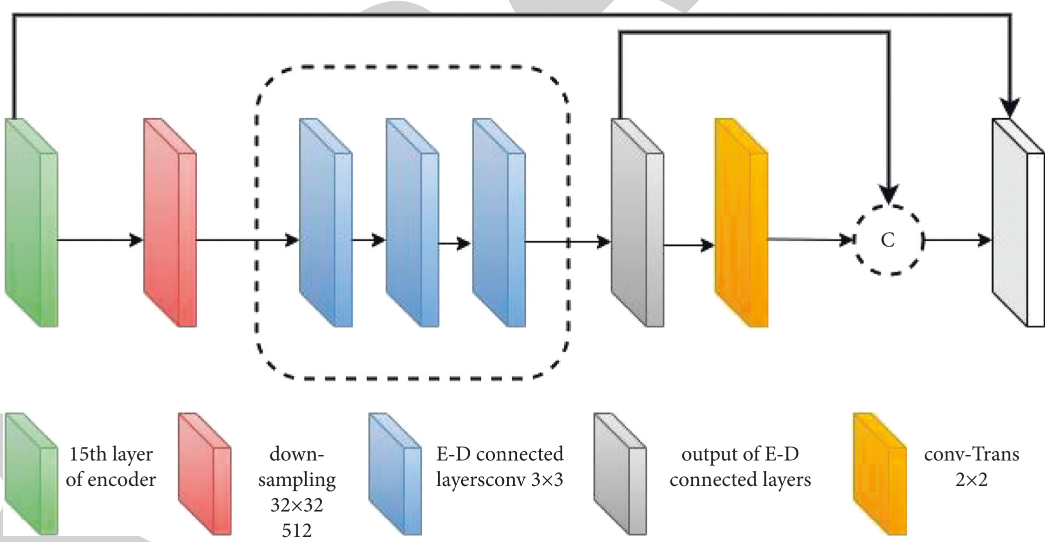

Figure 6: Encoder-decoder connected layer block.

$$C_j^{(1)} = f\left(B_j^{(1)} + K_j^{(1)} \times I\right) \text{where} \quad j = 1, \ldots, M^{(n)}. \tag{1}$$

In the first convolution layer C^1, Input I is convolved with a weight matrix to obtain a feature map. The $M1$ feature map is obtained through sliding over the different positions of the input matrix according to the set value of stride. Features are extracted in this way, and thus, the weight parameters are shared for all infection classes in the case of our dataset (ground-glass opacity, consolidation, pulmonary). Therefore, the layer acquires an equivariance property and becomes invariant to the image transformation.

It also results in a sparse weight that leads to small, fine feature detection. Further layers are added to extract fine features from starting layers. The feature map at different levels and at different layers can be expressed as follows:

$$C_j^{(n)} = f\left(B_j^{(n)} + \sum_{i=1}^{r(n-1)} K_j^{(n)} \times r_i^{(n-1)}\right) \text{where} \quad j = 1, \ldots, M^{(n)}. \tag{2}$$

Table 1 shows the difference between the conventional Unet and proposed convUnet models. In the whole network, Unet includes 16 convolution layers, while the proposed

Table 1: Conventional Unet and improved model convUnet parameters.

Method	Conv-layers	E-D module weight	Batch normalization	Total parameters	Trainable parameters	Optimizer	Learning rate
Unet	16	2	No	31,030,788	31,030,788	Adam	$1e-3$
convUnet	24	3	Yes	46,773,124	46,755,460	Adam	$1e-3$

model is comprised of 24. The Unet consists of 2 sets of weights in its connected module, while the proposed one has 3. Lastly, Unet does not include batch normalization, while the proposed model did use it.

3.3. Loss Functions. The dice coefficient-based loss function was used per 100 epochs to express dice loss, the latter also being included in the evaluation matrix.

$$\mathbf{Dice\,loss} = 1 - \mathbf{dice}(\mathbf{a}, \mathbf{c}) = 1 - 2 \times \frac{\mathbf{a} \cap \mathbf{c}}{\mathbf{a} + \mathbf{c}}. \tag{3}$$

3.3.1. Binary Cross Entropy. The last layer in our proposed model follows the Unet approach that generates a number of feature channels equal to the number of semantic segmentation label classes. Our dataset contains multilabel classes, and so we used the soft-max function with binary cross entropy for loss function. In the last layer, we obtained an image size of $512 * 512$ equal to the actual image size with 4 channels.

The binary cross entropy is used as follows:

$$\mathbf{BCE} = -\frac{1}{\mathbf{n}} \sum_{\mathbf{i}=1}^{\mathbf{n}} \left[\mathbf{y_i} \mathbf{log}\left(\mathbf{y_i'}\right) + \left(1 - \mathbf{y_i}\right) \mathbf{log}\left(1 - \mathbf{y_i'}\right)\right]. \tag{4}$$

For multilabel classes, the binary cross entropy, where $o = 4$, is as follows:

$$\mathbf{BCEM} = -\frac{1}{\mathbf{n}} \sum_{\mathbf{i}=1}^{\mathbf{n}} \sum_{\mathbf{k}=1}^{\mathbf{o}} \mathbf{y_{ik}} \mathbf{log}\left(\mathbf{y_{ik}'}\right). \tag{5}$$

3.4. Implementation Details. The convUnet model proposed in this article was implemented in Google colab using python language, while convUnet training and testing were done using an Intel(R) Core (TM) i3-4030U CPU @ 1.90 GHz 1.90 GHz 64-bit operating system. To train the data, we selected the "adam" optimizer as an optimization technique. The test size for the data was set to 20%, and the input image size for training data was $512 * 512$ with a batch size of 1 per 100 epochs and a learning rate of $1e-3$.

4. Results

This section provides the results obtained and discussion on the results in detail, providing both quantitative and qualitative results obtained using the improved model and a quantitative comparison between the improved model with other models and with the baseline approach. We used the following performance measure metrics to measure the performance of the improved model.

4.1. Segmentation Evaluation Index. Accuracy (1) is the ratio between the sum of true prediction of both (positive and negative results) and the sum of all false and true predicted values.

$$\text{accuracy} = \frac{TP + TN}{TP + TN + FP + FN}. \tag{6}$$

Sensitivity (2) is the ratio between correctly predicted segmentation and the sum of correctly predicted segmentation and false prediction as nonlesion. In medical studies, sensitivity is critical. The lower the sensitivity, the higher the occurrence of false-negative prediction. In the case COVID-19, if a person with it is predicted "negative," this can be caused by the further spread of the virus. Thus, model sensitivity must be high in the case of the efficient model.

$$\text{Senstivity} = \frac{TP}{TP + FN}. \tag{7}$$

Precision (3) is the ratio between correctly segmented prediction and total predicted segmentation.

$$\text{Precision} = \frac{TP}{TP + FP}. \tag{8}$$

Specificity (4) is the ratio between true negative and the sum of true negative and false positive.

$$\text{Specificity} = \frac{TN}{TN + FP}. \tag{9}$$

*F*1 score (5) is the ratio between the two times multiplication of precision and sensitivity multiplied result and the sum of precision and sensitivity.

$$F1\ \text{score} = 2 \times \frac{\text{Precision} \times \text{Senstivity}}{\text{Precision} + \text{Senstivity}}. \tag{10}$$

Dice coefficient is the ratio between two times multiplication of the intersected value of actual value and predicted value of the model and the sum of actual value and predicted value.

$$\text{Dice co} - \text{efficient} = 2 \times \frac{a \cap c}{a + c}. \tag{11}$$

Jaccard index: Jaccard index, which is commonly known as intersection over union (IOU), measures the similarity between actual ground truth and predicted segmentation. It refers to the intersection area of GT and PS divided by the union of both GT and PS.

$$IOU\,(a, c) = \frac{(a \cap c)}{a \cup c}. \tag{12}$$

Here, a and c show ground truth value and predicted value, respectively.

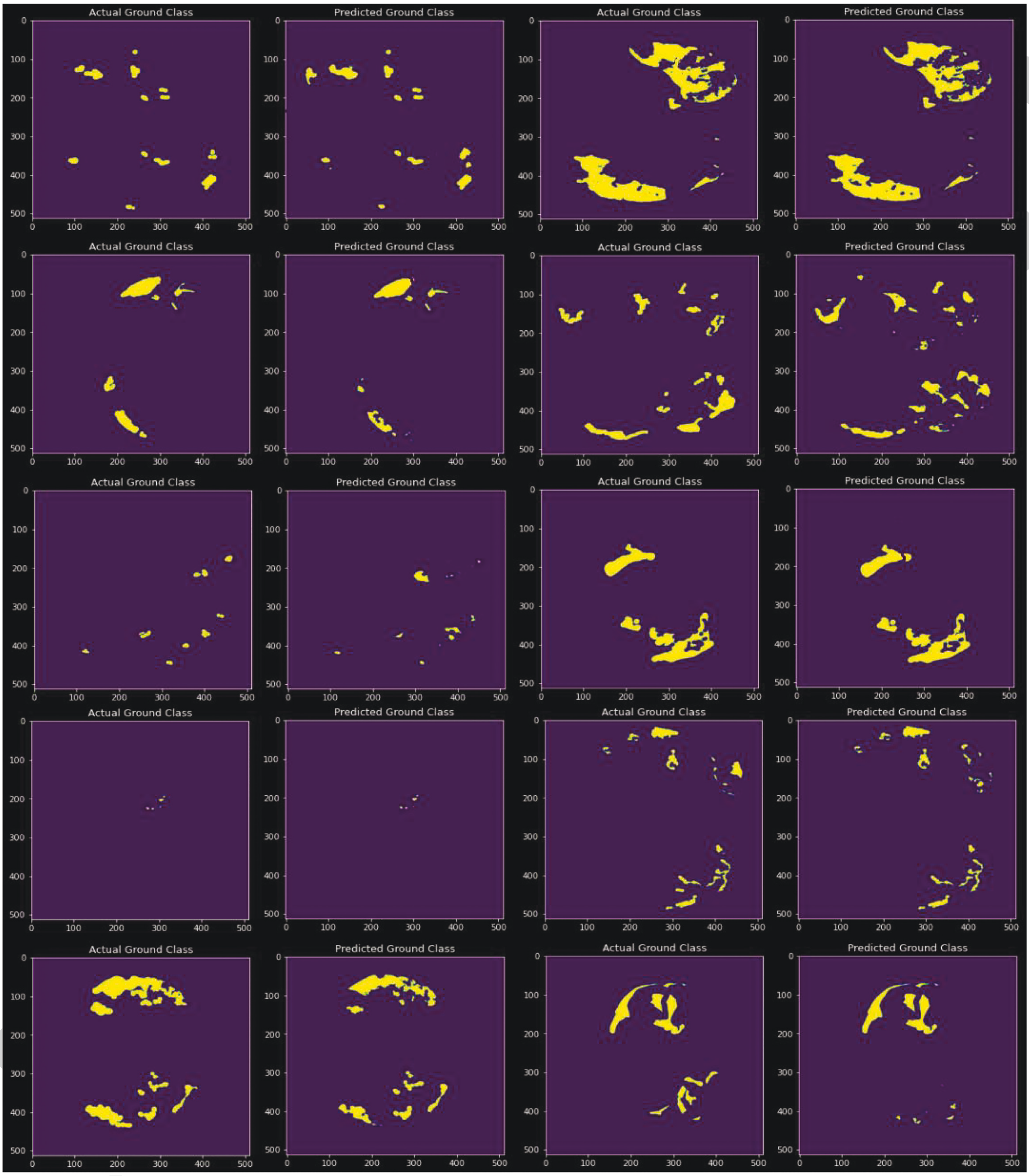

(a) (b) (c) (d)

Figure 7: Actual ground truth of ground glass opacity and predicted ground glass opacity segmentation.

In Figure 7, the a and c columns represent the actual ground truth of ground glass opacity, while the c and d columns represent predicted segmentation by our model.

4.2. Qualitative Analysis. Figure 8 shows some of the findings acquired for ground glass opacity area segmentation by displaying the ground truth and the results provided. Our suggested approach produced good segmentation results without using complex models. In addition, when compared to ground truth, we obtained good segmentation compared to other models in our study. Figure 8 shows some instances of the findings acquired with a view to evaluating the performance of the proposed approach for segmentation of the lung infection area at ground glass opacity level. In Figure 8, the first column

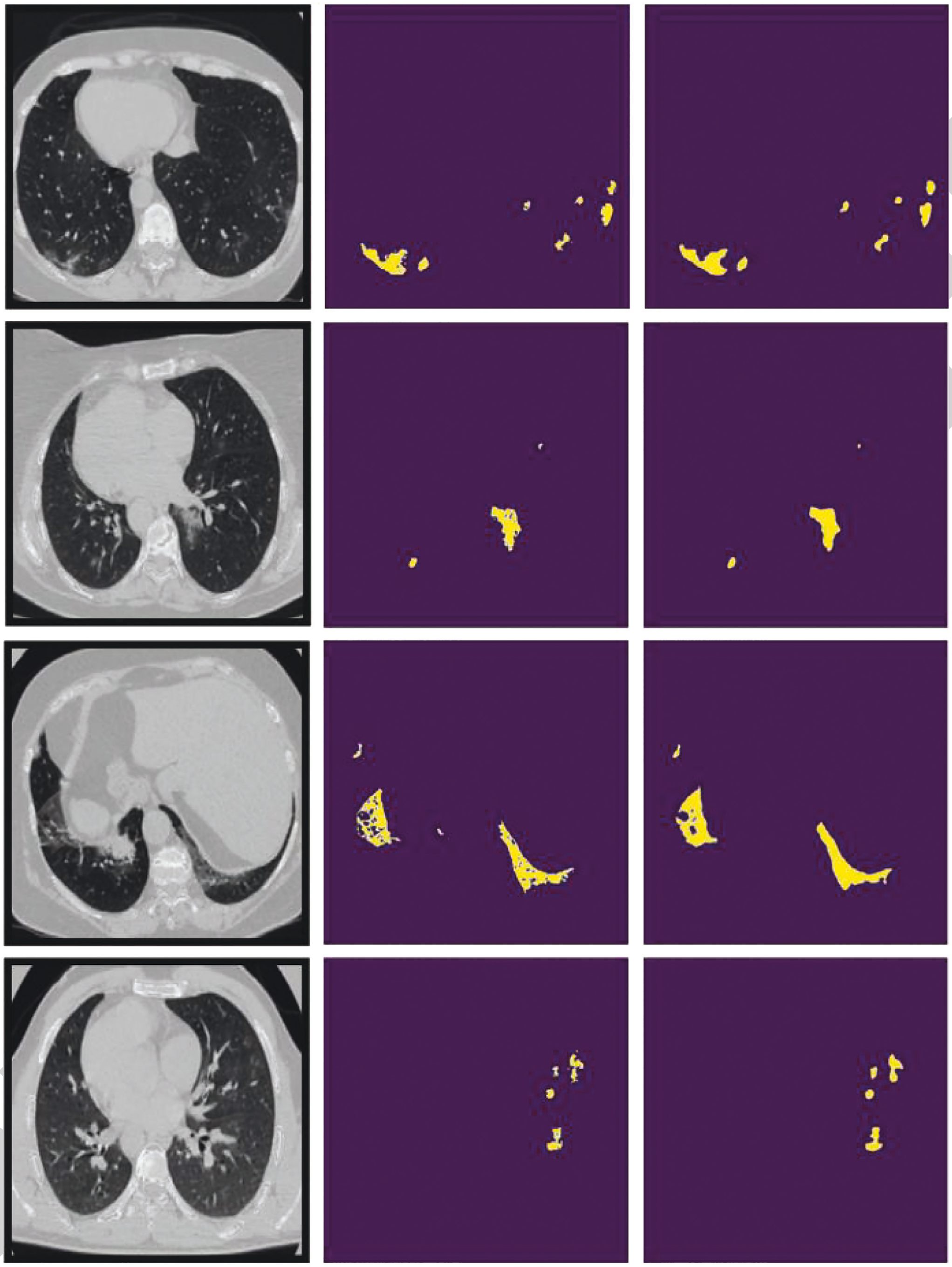

Figure 8: Our segmentation model performance.

represents the original CT scan, the second represents the actual ground truth, and the third shows our segmentation results. We can see from the data that the suggested model identified the ground glass opacity well with certain mistakes that are considered insignificant. Furthermore, as shown in Figure 7, the segmentation results obtained from our model are close to the actual ground truth.

4.3. Quantitative Results. Table 2 shows the quantitative results of the proposed model and baseline approach Unet model. Our model obtained the best results in terms of dice coefficient, Jaccard index, recall, F1 score, and precision with scores of 93.29, 92.46, 86.96, 93.01, 93.34 and 93.67, respectively. For its part, the proposed convUnet model obtained an average result over 100 epochs of 76.47%, 83.27%, 82.52%, 83.43%, 82.75%, and 84.11% in the case of IoU, accuracy, dice coefficient, $f1$-score, recall, and precision, respectively.

Figure 9 shows the box plot of the proposed model results for accuracy, dice coefficient, intersection over union,

Table 2: Best results obtained by proposed model and Unet model over 100 epochs

Method	IoU	Accuracy	Dice-coefficient	$F1$-score	Recall	Precision
Unet	82.83	91.78	90.43	91.82	91.33	92.31
convUnet average value	76.47	83.27	82.52	83.43	82.75	84.11
convUnet	86.96	93.29	92.6	93.34	93.01	93.67
Improvement in convUnet	**4.73↑**	**1.51↑**	**2.17↑**	**1.52↑**	**1.68↑**	**1.36↑**

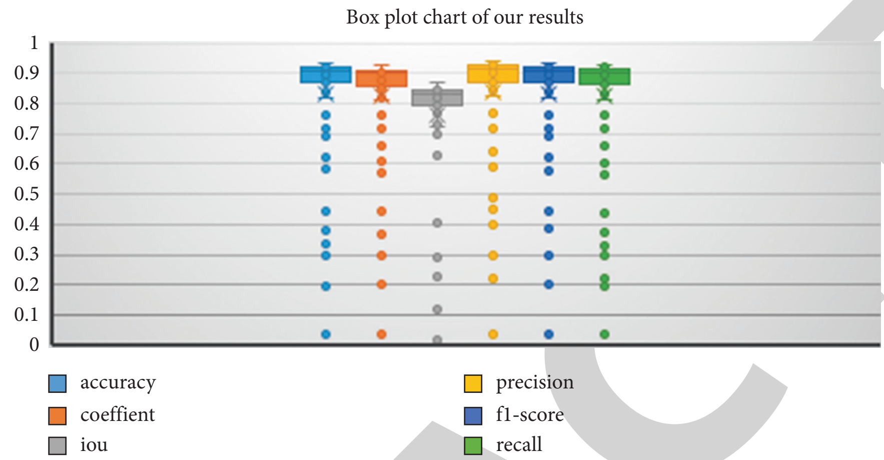

Figure 9: Box plot results.

precision, $F1$-score, and recall. Each color indicates different performance measure metrics. The boxes' upper and lower boundary represents the range of result scores, while a line in the same color inside the colored box refers to the average score, which falls between 0.8 and .09 in the case of all evaluation indexes mentioned. The results below the whiskers represent outliers, which are shown as colored dots.

Figure 10 represents the training and testing performance of the proposed model over 100 epochs. It can be noticed that in early epochs, the difference between training and testing results was high, but as the epochs increased, the difference between training and testing reached its maximum low. We obtained good segmentation results compared to other state-of-the-art models in our study.

Figures 10(a)–10(h) show training and testing performance curves for accuracy, validation loss, intersection over union, dice coefficient, dice loss, recall, precision, and $F1$ score, respectively. In early epochs, $F1$ score, precision. accuracy, recall, and IoU performance are low, but performance gradually improved without overfitting. In Figure 10(b), it can be seen that validation loss was high in the first five epochs, but after five epochs, it remained below 0 until reaching 100 epochs. In Figure 10(e), it can also be seen that dice loss was high over the first 10 epochs, but after 10 epochs, the difference between training and testing dice loss was minimized.

5. Discussion

The proposed model is a supplemented version of the Unet model and includes additional convolution layers at each step of the encoder and decoder and a more weighted connected module. These additions to the conventional Unet model improved its overall efficiency, and the corresponding improvement in results can be seen in Table 1. With the addition of convolution layers and a more weighted module, the proposed model obtained a 1.51%, 4.73%, 2.17%, 1.68%, 1.36%, 1.5% gain as compared to the conventional Unet in terms of accuracy, intersection over union, dice coefficient, recall, precision, and F1score, respectively. Overall, it achieved up to the mark segmentation results in obtaining a dice coefficient score of 92.46%, recall score of 93.01%, F1 score of 93.34%, precision of 93.67%, and Jaccard index of 86.96%. The slightly more weighted connected module obtained sufficient contextual information to ensure better segmentation. Figure 8 shows some instances of the findings acquired that were used to evaluate the performance of the proposed approach for ROI area segmentation. We can see from the data that the suggested model identified the infection well with certain mistakes that are considered insignificant. Furthermore, as shown in Figure 7, the segmentation results obtained from the proposed model are close to the actual ground truth. State-of-the-art comparison in terms of IoU, dice, recall, $F1$ score, precision, and accuracy is presented in Table 3.

The proposed approach used to segment the infection constituted a successful improvement because of the additions we included for intense learning in the baseline approach Unet. The accuracy and robustness of the technique provided were further demonstrated by the evaluation metric results obtained by the model, given in Table 1. Based on these results, we may conclude that the proposed technique outperforms the baseline Unet approach and other state-of-the-art methods. Nevertheless, the model has a large number of parameters which causes an increase in computational cost. In future work, this can be improved further

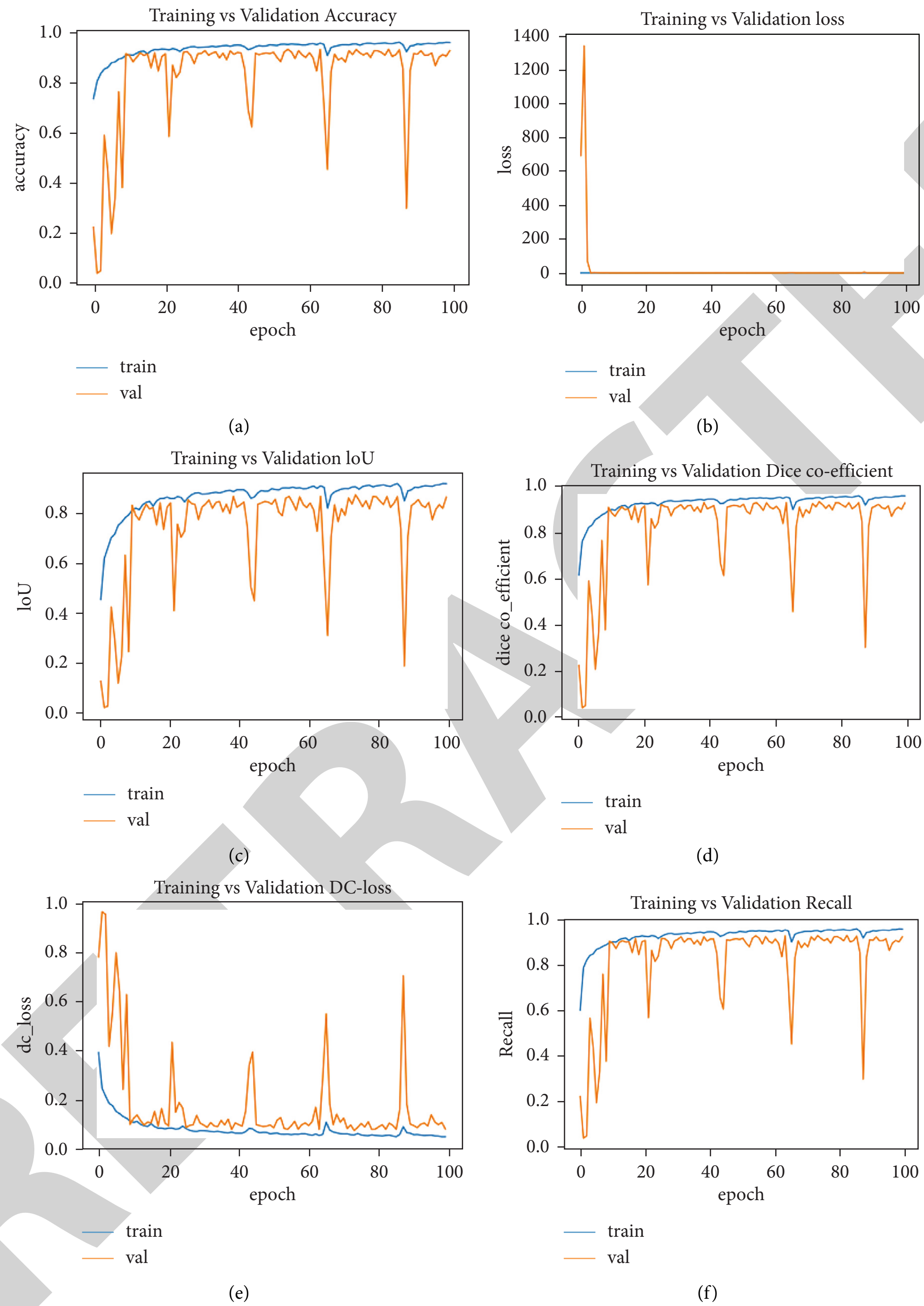

Figure 10: Continued.

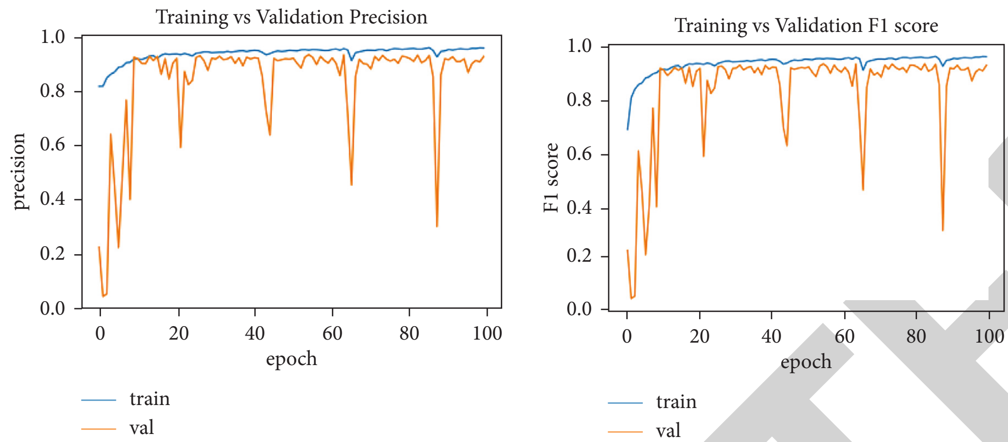

(g) (h)

Figure 10: ((a)–(h)) training and testing performance.

Table 3: State-of-the-art comparison in terms of IoU, dice, recall, $F1$ score, precision, and accuracy.

Source	Models	Acc	IoU	Dice	Recall	$F1$-score	Precision
[26]	3D Unet	—	—	61.0	62.8		74.1
[27]	Encoder-decoder method	—	—	78.6	71.1	78.4	85.6
[28]	AU-Net + FTL	—	—	69.1	81.1	—	—
[29]	Multiple deep CNN	95.23	—	88.0	90.2	—	—
[30]	Imagenet, VGG16 FCN8	—	60.0	75.0	92.0	—	63.0
[31]	DDANet	—	—	77.89	88.40	—	—
[32]	ADID-Unet	97.01	—	80.31	79.73	82.00	84.0
[33]	Semi-Inf-Net	—	—	73.01	72.00	—	—
[12]	Unet	91.78	82.83	90.43	91.33	91.82	92.31
	Ours	93.29	86.96	92.46	93.01	93.34	93.67

using different techniques involving data augmentation or tuning the hyperparameters.

6. Conclusion

This paper proposed a modified model based on Unet architecture to accurately segment COVID-19 lung infections in CT scans. The proposed model, referred to as convUnet, added supplementary convolution layers in encoder and decoder pipelines and improved the convolution module to establish a connection between encoder and decoder pipelines, giving it a major capacity to extract features from the last layer of the encoder pathway and segmentation. The addition of more sets of weights to Unet led to an improvement in its performance. The results obtained from our proposed model proved the efficiency of the convUnet model in segmenting indistinguishable and interconnected areas, as well as the fact that performance evaluation metrics achieved better quantitative results than the basic Unet approach, obtaining a gain in accuracy, intersection over union, dice coefficient, recall, precision and $F1$score of 1.51%, 4.73%, 2.17%, 1.68%, 1.36%, 1.5% respectively. As such, our proposed convUnet method can prove to be beneficial in rapid COVID-19 diagnosis, testing, and quantification of infected areas and provides an overall improvement in COVID-19 lung infection diagnosis.

Data Availability

The dataset generated during and/or analysed during the current study are available at http://medicalsegmentation.com/covid19/ and https://doi.org/10.1186/s41747-020-00173-2.

Conflicts of Interest

The authors declare no conflicts of interest.

Authors' Contributions

All authors contributed to the work. All authors read and approved the final manuscript.

Acknowledgments

The authors thank the Basque Government for supporting this work. This research was supported by the Basque Government.

References

[1] Z. A. A. Alyasseri, M. A. Al-Betar, I. A. Doush et al., "Review on COVID-19 diagnosis models based on machine learning and deep learning approaches," *Expert Systems*, vol. 39, no. 3, Article ID e12759, 2021.

Hindawi
Journal of Healthcare Engineering
Volume 2023, Article ID 9782032, 1 page
https://doi.org/10.1155/2023/9782032

Retraction

Retracted: Higher Chronic Endometritis Incidences within Infertile Polycystic Ovary Syndrome Clinical Cases

Journal of Healthcare Engineering

Received 28 November 2023; Accepted 28 November 2023; Published 29 November 2023

This article has been retracted by Hindawi, as publisher, following an investigation undertaken by the publisher [1]. This investigation has uncovered evidence of systematic manipulation of the publication and peer-review process. We cannot, therefore, vouch for the reliability or integrity of this article.

Please note that this notice is intended solely to alert readers that the peer-review process of this article has been compromised.

Wiley and Hindawi regret that the usual quality checks did not identify these issues before publication and have since put additional measures in place to safeguard research integrity.

We wish to credit our Research Integrity and Research Publishing teams and anonymous and named external researchers and research integrity experts for contributing to this investigation.

The corresponding author, as the representative of all authors, has been given the opportunity to register their agreement or disagreement to this retraction. We have kept a record of any response received.

References

[1] S. Wang, H. Zhao, F. Li, Y. Xu, H. Bao, and D. Zhao, "Higher Chronic Endometritis Incidences within Infertile Polycystic Ovary Syndrome Clinical Cases," *Journal of Healthcare Engineering*, vol. 2022, Article ID 9748041, 6 pages, 2022.

Hindawi
Journal of Healthcare Engineering
Volume 2022, Article ID 9748041, 6 pages
https://doi.org/10.1155/2022/9748041

Research Article

Higher Chronic Endometritis Incidences within Infertile Polycystic Ovary Syndrome Clinical Cases

Shuang Wang,[1] Huishan Zhao,[2] Fenghua Li,[1] Yanping Xu,[1] Hongchu Bao,[1] and Dongmei Zhao[1]

[1]*Department of Reproductive Medicine, Qingdao University Medical College Affiliated Yantai Yuhuangding Hospital, 20 Yuhuangding East Road, Yantai 264000, China*
[2]*Central Laboratory, Qingdao University Medical College Affiliated Yantai Yuhuangding Hospital, 20 Yuhuangding East Road, Yantai 264000, China*

Correspondence should be addressed to Dongmei Zhao; yhdszzx@yeah.net

Received 4 March 2022; Accepted 28 March 2022; Published 11 April 2022

Academic Editor: Liaqat Ali

Background. Clinical cases of a polycystic ovarian syndrome (PCOS) have prolonged subclinical inflammation. Hysteroscopy has revealed worsened chronic endometritis (CE), particularly endometrial diffuse hyperemia, in PCOS patients. However, the possible relationships between PCOS and CE remain largely unexplored. *Methods*. This retrospective-based investigation was conducted on 3336 infertile patients. The PCOS group consisted of 508 patients, while the non-POCS group consisted of 2828 individuals with normal ovarian function. Their clinical features and CE prevalence diagnosed with hysteroscopy were compared. The risk factors affecting the incidence of diffuse endometrial hyperemia were analyzed by binary logistic regression. *Results*. The PCOS cohort and the non-PCOS cohort showed marked variations in age, body mass index (BMI), infertility (primary, secondary), basal hormone level (bFSH, bLH, bT, and PRL), anti-Müllerian hormone (AMH), and CA125 ($P < 0.05$). The prevalence of CE in PCOS women was 41.73% (212/508), markedly higher than the 28.50% in the non-PCOS cohort (806/2828). Variations within diffuse endometrial hyperemia prevalence were especially marked ($P < 0.05$). Furthermore, we found that the variables of BMI, bLH, bT, and AMH correlated with diffuse endometrial hyperemia. *Conclusions*. CE prevalence was elevated in clinical cases of infertility associated with PCOS, and diffuse endometrial hyperemia was prevalent, as indicated by hysteroscopy. Furthermore, increased BMI, bLH, bT, and AMH levels all contribute to the risk of diffuse endometrial hyperemia.

1. Background

Chronic endometritis (CE) is characterized by mild endometrial inflammation. It is widely accepted that the presence of plasma cells inside the endometrial stroma is the most useful histologic criterion for diagnosis. Diagnosis of CE is often delayed, since it is usually asymptomatic [1]. Although CE does not manifest clinically, it interferes with embryo implantation and can result in reduced fertility. Recent studies have reported that the CE incidence rate is 14–42% within cases of recurring implantation failure (RIF), while this rate is 27–57.8% within cases of recurring pregnancy loss (RPL) [2]. CE is typically diagnosed through hysteroscopy and pathological examination of endometrium [3–5]. By hysteroscopy, CE is often diagnosed as micropolyps (<1 mm in size), stromal edema, or diffuse endometrial hyperemia [6, 7].

Polycystic ovary syndrome (PCOS) represents a highly prevalent endocrine condition and metabolic abnormality within childbearing-aged females. It is a major cause of infertility, with the phenotypes of hyperandrogenism, insulin resistance, menstrual irregularity, hirsutism, and polycystic ovarian morphology (PCOM) [8]. In addition, PCOS patients can develop several complications, such as metabolic abnormalities, cardiovascular diseases, and psychological disorders [9]. Studies have shown that serum levels of inflammatory factors, such as interleukin 17 (IL-17), in patients with endometritis are significantly increased [10].

Furthermore, serum levels of inflammation-linked cytokines, including IL-6, C-reactive protein (CRP) and tumor necrosis factor-α (TNF-α), are increased in PCOS patients [11], and such elevation may be associated with the pathological changes in the endometrium. Currently, no data are available on the incidence of CE in PCOS patients. CE may affect the expressions of endometrial cytokines, damage the endometrial receptivity, and reduce pregnancy outcomes [12]. Moreover, CE can affect the pregnancy outcomes of infertility PCOS cases who undergo in vitro fertilization/intracytoplasmic sperm injection-embryo transfer (IVF/ICSI-ET).

This investigation retrospectively probed hysteroscopic CE clinical profiles for infertile patients with PCOS treated at our hospital.

2. Methods

2.1. Participants. Herein, a retrospective, database-searched cohort study was performed that was approved by the Yantai Yuhuangding Hospital's Institutional Review Board. Overall, 3336 infertility cases experienced hysteroscopy within the Reproductive Center of Yantai Yuhuangding Hospital from January 2018 to December 2020. Among them, 508 PCOS cases were allocated into PCOS cohort. Meanwhile, 2828 patients with normal ovarian function were allocated into non-PCOS cohort. Inclusion criteria consisted of patients diagnosed with infertility, age <40 years, and medical datasets from all cohorts compiled. Exclusion criteria were set as follows: patients with hyperprolactinemia, premature ovarian failure, and abnormal parental karyotype. The underlined diagnostic criteria for PCOS were consistent with the 2018 consensus regarding PCOS theragnostics within China [13]: spare menstruation, amenorrhea, or irregular uterine bleeding is a mandatory criterion for the diagnosis; and hyperandrogenemia or polycystic change of the ovary.

2.2. Diagnostic Hysteroscopy of CE. The diagnosis of CE was performed with hysteroscopy. At 3–5 days after menstruation, all patients underwent gynecological examination and vaginal discharge examination to rule out contraindications for surgery, such as vaginitis and pelvic inflammatory disease. Throughout the menstrual cycle's follicular phase, all patients underwent a mini-hysteroscopic evaluation. Hysteroscopy was conducted through a lens-derived minitelescope (Karl Storz, Tuttlingen, Germany; OD: 2.7 mm; angle vision: 105°; OD double-flow operative sheath: 4.5 mm) [14]. After disinfection of the vagina and posterior cervix, the mirror was introduced into the vagina. Subsequently, 9% sodium chloride was used to distend the uterine cavity with an expansion pressure of 100–120 mmHg. Hysteroscopy was performed using a 300 w light source through a high-definition digital-camera and a xenon bulb (Karl Storz™, Germany). Throughout this assessment, the front/rear walls, two lateral walls, both sides of the cervix, and cervical mucosa were meticulously inspected via advancing hysteroscope in-parallel across endometrial surfaces, which helped locate possible macroscopic indications of CE, including intrauterine morphology, intima color, thickness, elasticity, smoothness, glands, stroma, and fallopian tube opening [15]. This method allowed the easy detection of surface irregularities. In brief, CE was diagnosed based on the following signs: stromal edema, isolated or diffuse micropolyps, and generalized periglandular hyperemia [6, 7, 16]. The surgery for all the enrolled patients was performed by the same surgeon, which eliminated the risk of variation.

2.3. Ethical Consideration. The study was approved by the Yantai Yuhuangding Hospital's Institutional Review Board. All participants in this study signed a written informed consent form.

2.4. Statistical Analysis. All datasets were assessed through SPSS® 22.0. Continuous variables were expressed as mean ± standard deviations (SD), whereas qualitative variables reflected case quantity (n) together with percentages (%). Intercohort comparisons of continuous variables (normally distributed) were assessed through the dependent samples t-test, whereas the intercohort differences in the categorical variables (nonnormally distributed) were analyzed through contingency tables together with the chi-square test or Fisher's exact test. Logistic regression analyses probed the independent influence of multiple variables. A P value of <0.05 was chosen to highlight statistical significance.

3. Results

3.1. Clinical Parameters. Overall, 508 cases were allocated to PCOS cohort, while 2828 cases were allocated to non-PCOS cohort. Table 1 provides backgrounds and clinical characteristics of all cases. Considerable variations were observed regarding age, BMI, infertility (primary, or secondary), basal hormone level (bFSH, bLH, bT, and PRL), AMH, CA125, cholesterol (CHOL), and triglyceride (TG) ($P < 0.05$) across both cohorts. The BMI, the proportion of primary infertility, and the levels of bLH, bT, AMH, CHOL, and TG were all significantly higher in the PCOS cohort than in the non-PCOS cohort, but the age/bFSH, PRL, and CA125 levels were significantly lower ($P < 0.05$).

3.2. Prevalence of Hysteroscopic Features. Hysteroscopy demonstrated a significant increase in the diagnostic rate of CE in the PCOS cohort compared to the non-PCOS cohort (41.73% versus 28.50%) ($P < 0.001$; Figure 1).

Incidences of various hysteroscopic features associated with CE were analyzed individually. Hyperemia was detected in 24.41% of PCOS cohort cases and 8.13% of non-PCOS cohort cases, indicating that hyperemia prevalence is significantly increased in the PCOS cohort with a P value of <0.001 and F score of 120.276. The F-statistic is the ratio of the mean squares treatment to the mean squares error. Our obtained data revealed that most of the F values were higher, which corresponded to lower P values (Table 2). The

Table 1: Clinical characteristics of patients (PCOS and non-PCOS cohorts).

	PCOS cohort ($n = 508$)	Non-PCOS cohort ($n = 2828$)	P value
Age, years	31.03 ± 3.20	31.98 ± 3.57	<0.001
Infertility duration, years	3.86 ± 2.32	3.65 ± 2.35	0.056
BMI (kg/m^2)	25.42 ± 3.65	23.40 ± 3.42	<0.001
Infertility			
Primary infertility %	280 (55.12%)	1410 (49.86%)	0.029
Secondary infertility %	228 (44.88%)	1418 (50.14%)	
bFSH (UI/L)	5.94 ± 1.41	6.84 ± 1.89	<0.001
bLH (UI/L)	8.91 ± 4.85	5.05 ± 2.01	<0.001
bE_2 (pg/ml)	35.45 ± 12.01	34.43 ± 13.86	0.128
bP (ng/ml)	0.50 ± 0.30	0.52 ± 0.25	0.055
bT (ng/ml)	0.40 ± 0.19	0.25 ± 0.12	<0.001
PRL (ng/ml)	16.30 ± 6.55	17.35 ± 6.13	0.001
AMH (ng/ml)	10.08 ± 6.36	4.14 ± 2.67	<0.001
CA125 (U/ml)	16.98 ± 7.88	23.87 ± 9.59	<0.001
CHOL (mmol/L)	4.98 ± 0.94	4.74 ± 0.83	<0.001
LDL-C (mmol/L)	2.98 ± 0.81	2.81 ± 0.67	0.241
TG (mmol/L)	1.42 ± 0.95	1.05 ± 0.84	<0.001

bFSH, basal follicle-stimulating hormone; bLH, basal luteinizing hormone; bE_2, basal estradiol; bP, basal progesterone; bT, basal total testosterone; PRL, prolactin. The limit of significance is a P value <0.05, which was evaluated on the basis of the chi-square test.

(a) (b) (c)

Figure 1: Different features of chronic endometritis at fluid hysteroscopy: (a) diffuse hyperemia endometrium, (b) micropolyps (less than 1 mm in size), and (c) edema hyperplasia.

Table 2: Hysteroscopic features in the PCOS and non-PCOS cohorts.

	PCOS cohort ($n = 508$)	Non-PCOS cohort ($n = 2828$)	F	P value
CE	212 (41.73%)	806 (28.50%)	35.557	<0.001
Hyperemic %	124 (24.41%)	230 (8.13%)	120.276	<0.001
Micropolyps %	15 (2.95%)	118 (4.17%)	1.674	0.196
Edema hyperplasia %	73 (14.37%)	458 (16.20%)	1.072	0.301
Normal %	258 (50.79%)	1656 (58.56%)	10.631	<0.001
Endometrial macropolyps %	31 (6.10%)	234 (8.27%)	2.778	0.096
Others	7 (1.38%)	132 (4.67%)	11.671	<0.001

Others are intrauterine adhesions, uterine malformations, submucosal fibroids of the uterus, and endometrium atypical hyperplasia.

prevalence of micropolyps, edema, and hyperplasia was not significantly different between the two cohorts.

3.3. Binary Logistic Regression Analysis: Clinical Characteristics of the Endometrial Hyperemia Cohort and Non-endometrial Hyperemia Cohort. Statistical analysis identified increased incidence rates for CE within PCOS cases, and most of them showed hysteroscopic features of endometrial hyperemia. A binary logistic regression analysis was performed to further explore associations across exposure factors and endometrial hyperemia. Clinical cases were segregated within two cohorts, depending upon endometrial hyperemia status. Table 3 provides the background characteristics of these patients. BMI, bLH, bT, and AMH were found to be associated with endometrial hyperemia.

Table 3: Clinical characteristics of endometrial hyperemia and nonendometrial hyperemia cohorts.

	Hyperemia cohort ($n = 354$)	Nonhyperemia cohort ($n = 2982$)	P value	95% CI
Age, years	31.19 ± 3.52	31.89 ± 3.52	0.101	0.925–1.007
Infertility duration, years	3.80 ± 2.37	3.75 ± 2.52	0.792	0.950–1.070
BMI (kg/m^2)	24.77 ± 3.39	23.64 ± 3.46	<0.001	1.064–1.164
Infertility				
Primary infertility %	192 (54.24%)	1498 (50.23%)	0.855	0.775–1.235
Secondary infertility %	162 (45.76%)	1484 (49.77%)		
bFSH (UI/L)	6.53 ± 1.77	6.71 ± 1.87	0.975	0.914–1.097
bLH (UI/L)	6.91 ± 4.10	5.57 ± 3.01	<0.001	1.058–1.149
bE$_2$ (pg/ml)	34.33 ± 13.78	34.77 ± 13.94	0.774	0.998–1.009
bP (ng/ml)	0.50 ± 0.29	0.52 ± 0.26	0.144	0.380–1.152
bT(ng/ml)	0.32 ± 0.16	0.26 ± 0.14	<0.001	4.917–19.946
PRL (ng/ml)	16.74 ± 6.59	17.30 ± 6.25	0.823	0.976–1.019
AMH (ng/ml)	7.21 ± 4.83	4.92 ± 2.78	<0.001	1.028–1.095
CA125 (U/ml)	20.89 ± 8.85	22.99 ± 7.17	0.470	0.997–1.007
CHOL(mmol/L)	4.83 ± 0.87	4.78 ± 0.86	0.880	0.559–1.647
LDL-C (mmol/L)	2.84 ± 0.78	2.85 ± 0.95	0.946	0.558–1.724
TG (mmol/L)	1.22 ± 0.92	1.08 ± 0.86	0.675	0.731–1.225

4. Discussion

For the first time, we demonstrated the common hysteroscopic characteristics linked with CE in patients with PCOS. PCOS is a multifactorial disorder of the female reproductive system that is frequently associated with metabolic disorders, such as insulin resistance, obesity, and hypertriglyceridemia [17, 18]. We found that the PCOS cohort showed higher levels of BMI (25.42 ± 3.65 vs. 23.40 ± 3.42), serum bLH (8.91 ± 4.85 vs. 5.05 ± 2.01), bT (0.40 ± 0.19 vs. 0.25 ± 0.12), AMH (0.25 ± 0.12 vs. 4.14 ± 2.67), CHOL (4.98 ± 0.94 vs, 4.74 ± 0.83), and TG (1.42 ± 0.95 vs. 1.05 ± 0.84), in comparison to the non-PCOS cohort. The findings from these datasets support previously published research. Fallopian tube blockage is the greatest driver for infertility of non-PCOS patients, which belongs to secondary infertility. Thus, age, bFSH, PRL, and CA125 levels were higher in non-PCOS cohorts compared to PCOS cohorts, indicating persistent, subclinical low-grade inflammation distinct from acute inflammation caused by bacterial or viral infections. Previous investigations demonstrated PCOS cases to have significantly upregulated chronic inflammation-linked cytokines, including IL-6, IL-8, TNF-α, and CRP, which may be attributed to the associated obesity, insulin resistance, and hyperandrogenemia [19, 20].

At present, the CE diagnoses are defined according to endometrial biopsy findings or hysteroscopy. However, the positivity rate of endometrial biopsy is very low, at only 27.1% [21]. Hysteroscopy has been shown to increase the sensitivity/accuracy of CE diagnosis [22]. This study revealed that PCOS patients have significantly increased diagnosis rates for CE using hysteroscopy. Being a pivotal CE-diagnostic measure, hysteroscopy revealed perigonadal hyperemia, micropolyps, stromal edema, and hyperplasia within CE cases. This investigation identified CE diagnosis rate to be 41.73% within PCOS cohort, with 28.50% for non-PCOS cohort ($P < 0.001$). However, hysteroscopic features of CE in PCOS patients were slightly different in this study. Diffuse endometrial hyperemia was the most prevalent feature in the study population, showing a proportion of 24.41% and 8.13% within PCOS cohort and non-PCOS cohort, accordingly. This finding might be attributed to the increment of chronic subclinical inflammatory factors. Additionally, we found that the serum levels of bLH, bT, AMH, CHOL, and TG, as well as BMI, were markedly exacerbated within PCOS cases having CE in comparison to those with normal endometrium. Some studies have suggested that the circulatory and molecular markers of inflammation observed in CE may be associated with the circulating androgens, and the luteinizing hormone may be the progenitor of chronic inflammation [23, 24]. Hence, we hypothesized that CE in PCOS patients could be a result of a persistent inflammatory state, although the pathophysiology remains mostly unknown.

Meanwhile, we found that PCOS patients had a higher diagnosis rate of CE, and endometrial hyperemia was dominant in hysteroscopy. Accordingly, a binary logistic regression analysis was performed. Variables of BMI, bLH, bT, and AMH were related to the presence of endometrial hyperemia. Several investigations highlighted detrimental influence by obesity upon natural/assisted conception, and such a hindered reproduction ambient would be inflamed within high-BMI/central fat distribution case populations [25]. It has been reported that PCOS patients have a lower pregnancy rate than non-PCOS patients [26]. Our findings speculated that the endometrial receptivity in PCOS patients with CE was damaged. CE reflects chronic and insidious inflammatory dysfunctions within the endometrium, which triggers discharging for inflammatory mediators, congestion of the uterus, proliferation of capillaries, fibrosis, gland atrophy, and destruction of the endometrial microenvironment [27]. Pietro et al. have reported that the abnormal expressions of inflammatory response factors and apoptosis-related factors, such as IL-11, chemokine ligand 4 (CCL4), insulin-like growth factor (IGF1), B cell CLL 2 (BCL2), and BCL2-associated X protein (BAX), within CE case endometria during implantation result in decreased endometrial receptivity, resulting in embryo implantation failures [12].

When evaluating this study, one of the limitations was the relatively limited sample size, as large sample sizes are required for retrospective studies. Additionally, the retrospective aspect may introduce selection bias, which should be considered.

5. Conclusion

In conclusion, CE incidence rates were significantly increased in PCOS patients, and endometrial hyperemia was the most common hysteroscopic finding in CE patients. For the first time, we showed the relationship between endometrial hyperemia and PCOS. Within this univariate analysis, BMI, bLH, bT, and AMH were the risk factors leading to endometrial hyperemia. Moreover, further investigations are needed to explore the mechanisms underlying these effects.

Abbreviations

PCOS: Polycystic ovary syndrome
CE: Chronic endometritis
IVF: In vitro fertilization
RIF: Recurrent implantation failure
RPL: Recurrent pregnancy losses
AMH: Anti-Müllerian hormone
T: Testosterone.

Data Availability

The data used to support the findings of this study are available from the corresponding author upon request.

Ethical Approval

This study protocol was approved by the Ethics Committee of Yantai Yuhuangding Hospital.

Consent

Not applicable.

Conflicts of Interest

The authors declare that they have no conflicts of interest.

Authors' Contributions

W. S was responsible for the study design and manuscript drafting. Z.H.S and L.F.H were responsible for the laboratory operation, data acquisition, and analysis. X.Y.P and B.H.C were responsible for the specimen collection, data interpretation, and critical discussion. Z.D.M was responsible for the study design, data analysis, and manuscript writing. All authors read and approved the final manuscript. Shuang Wang, Huishan Zhao, and Fenghua Li contributed equally to this work.

Acknowledgments

This study was supported by Yantai Yuhuangding Hospital of Qingdao University, Yantai, China.

References

[1] K. Kitaya, H. Matsubayashi, K. Yamaguchi, R. Nishiyama, and Y. Takaya, "Chronic endometritis: potential cause of infertility and obstetric and neonatal complications," *American journal of reproductive immunology (New York, N.Y.: 1989)*, vol. 75, pp. 13–22, 2016.

[2] J. Zolghadri, M. Momtahan, K. Aminian, F. Ghaffarpasand, and Z. Tavana, "The value of hysteroscopy in diagnosis of chronic endometritis in patients with unexplained recurrent spontaneous abortion," *European Journal of Obstetrics & Gynecology and Reproductive Biology*, vol. 155, no. 2, pp. 217–220, 2011.

[3] I. Moreno, E. Cicinelli, I. Garcia-Grau et al., "The diagnosis of chronic endometritis in infertile asymptomatic women: a comparative study of histology, microbial cultures, hysteroscopy, and molecular microbiology," *American Journal of Obstetrics and Gynecology*, vol. 218, no. 6, pp. e1–602, 2018.

[4] B.-G. Ilene, A. N. Jennifer, and K. Soheila, "Routine syndecan-1 immunohistochemistry aids in the diagnosis of chronic endometritis," *Archives of Pathology & Laboratory Medicine*, vol. 128, pp. 1000–1003, 2004.

[5] H. J. Park, Y. S. Kim, T. K. Yoon, and W. S. Lee, "Chronic endometritis and infertility," *Clinical and experimental reproductive medicine*, vol. 43, no. 4, pp. 185–192, 2016.

[6] P.-E. Bouet, H. El Hachem, E. Monceau, G. Gariépy, I.-J. Kadoch, and C. Sylvestre, "Chronic endometritis in women with recurrent pregnancy loss and recurrent implantation failure: prevalence and role of office hysteroscopy and immunohistochemistry in diagnosis," *Fertility and Sterility*, vol. 105, no. 1, pp. 106–110, 2016.

[7] E. Cicinelli, L. Resta, R. Nicoletti, V. Zappimbulso, M. Tartagni, and N. Saliani, "Endometrial micropolyps at fluid hysteroscopy suggest the existence of chronic endometritis," *Human Reproduction*, vol. 20, no. 5, pp. 1386–1389, 2005.

[8] "Revised 2003 consensus on diagnostic criteria and long-term health risks related to polycystic ovary syndrome," *Fertility and Sterility*, vol. 81, pp. 19–25, 2004.

[9] J. T. Helena, L. M. Marie, F. C. Michael, D. Anuja, and L. Joop, "Recommendations from the international evidence-based guideline for the assessment and management of polycystic ovary syndrome," *Human Reproduction*, vol. 33, pp. 1602–1618, 2018.

[10] W.-j. Wang, H. Zhang, Z.-Q. Chen et al., "Endometrial TGF-β, IL-10, IL-17 and autophagy are dysregulated in women with recurrent implantation failure with chronic endometritis," *Reproductive Biology and Endocrinology*, vol. 17, no. 1, p. 2, 2019.

[11] O. Koc, S. Ozdemirici, M. Acet, U. Soyturk, and S. Aydin, "Nuclear factor-κB expression in the endometrium of normal and overweight women with polycystic ovary syndrome," *Journal of Obstetrics and Gynaecology*, vol. 37, no. 7, pp. 924–930, 2017.

[12] C. Di Pietro, E. Cicinelli, M. R. Guglielmino, M. Ragusa, and M. Farina, "Altered transcriptional regulation of cytokines, growth factors, and apoptotic proteins in the endometrium of infertile women with chronic endometritis," *American journal of reproductive immunology (New York, N.Y.: 1989)*, vol. 69, pp. 509–517, 2013.

Hindawi
Journal of Healthcare Engineering
Volume 2023, Article ID 9869570, 1 page
https://doi.org/10.1155/2023/9869570

Retraction

Retracted: Recent Progress in Traditional Chinese Medicines and Their Mechanism in the Treatment of Allergic Rhinitis

Journal of Healthcare Engineering

Received 23 May 2023; Accepted 23 May 2023; Published 24 May 2023

This article has been retracted by Hindawi following an investigation undertaken by the publisher [1]. This investigation has uncovered evidence of one or more of the following indicators of systematic manipulation of the publication process:

(1) Discrepancies in scope
(2) Discrepancies in the description of the research reported
(3) Discrepancies between the availability of data and the research described
(4) Inappropriate citations
(5) Incoherent, meaningless and/or irrelevant content included in the article
(6) Peer-review manipulation

The presence of these indicators undermines our confidence in the integrity of the article's content and we cannot, therefore, vouch for its reliability. Please note that this notice is intended solely to alert readers that the content of this article is unreliable. We have not investigated whether authors were aware of or involved in the systematic manipulation of the publication process. Wiley and Hindawi regrets that the usual quality checks did not identify these issues before publication and have since put additional measures in place to safeguard research integrity.

We wish to credit our own Research Integrity and Research Publishing teams and anonymous and named external researchers and research integrity experts for contributing to this investigation.

The corresponding author, as the representative of all authors, has been given the opportunity to register their agreement or disagreement to this retraction. We have kept a record of any response received.

References

[1] D. Mao, Z. He, L. Li et al., "Recent Progress in Traditional Chinese Medicines and Their Mechanism in the Treatment of Allergic Rhinitis," *Journal of Healthcare Engineering*, vol. 2022, Article ID 3594210, 18 pages, 2022.

Hindawi
Journal of Healthcare Engineering
Volume 2022, Article ID 3594210, 18 pages
https://doi.org/10.1155/2022/3594210

Review Article

Recent Progress in Traditional Chinese Medicines and Their Mechanism in the Treatment of Allergic Rhinitis

Dehong Mao, Zhongmei He, Linglong Li, Yuting lei, Maodi Xiao, Huimin Zhang, and Feng Zhang

Department of Otolaryngology, Yongchuan Hospital of Traditional Chinese Medicine, Chongqing Medical University, Chongqing 402160, China

Correspondence should be addressed to Feng Zhang; fengzhang06@yeah.net

Received 18 February 2022; Accepted 17 March 2022; Published 11 April 2022

Academic Editor: Liaqat Ali

Objective. To conduct a systematic review on the mechanism of action and use of traditional Chinese medicines (TCM) in allergic rhinitis treatment. *Background*. Allergic rhinitis (AR) is a type I allergic disease of the immune system induced by immunoglobulin E mediated inflammation and is characterized by sneezing, nasal itching, paroxysmal nasal obstruction, mucosal edema, cough, and rhinorrhea. More than 500 million people have been affected by rhinitis worldwide in the past 20 years, leading to negative effects on health, quality of life, and social relationships. Currently, the trending medicines used in the case of AR include intranasal corticosteroids and oral H1 antihistamines, which are given as combinatorial medicines supplemented with immune therapy. These medications have been found to be very effective in either the short term or long term; however, they have been found to possess some serious side effects. *Search Methodology*. The information in this article on classical and traditional Chinese medications used to treat AR was derived from original papers and reviews published in Chinese and English language journals. Two Chinese databases (Wanfang and CNKI) and three English databases (Cochrane Library, PubMed, and Embase) were utilized for data gathering. *Results*. Traditional Chinese remedies have been identified to influence the production of cytokines such as IL-5 and IL-6, which are key mediators of eosinophilic inflammation, TNF-α, which stimulates TH2 cells at the site of inflammation, and NF-κB, which is required for cytokine and IgE antibody production. TCM has also been shown to be successful in lowering histamine levels, preserving histological changes by decreasing the thickness of the lamina propria, and downregulating the expression of Orai1, STIM1, and TRYC1, showing low expression of Ca^{+2} channel proteins. *Conclusion*. In this review, we discussed a series of classical, traditional Chinese medications, including *Centipeda minima*, *Scutellaria baicalensis*, licorice root (*Glycyrrhiza uralensis*), and others, as potential antiallergic agents and investigate their in vivo effect upon the production of cytokines and release of histamines for allergic rhinitis treatment.

1. Introduction

Allergic rhinitis (AR) is usually a severe condition that develops due to allergen exposure and results in IgE-mediated inflammation of the nasal membranes. The common symptoms found among patients with AR include sneezing, nasal obstruction, itching sensation in the nasal cavity, and rhinorrhea. These major symptoms may often be accompanied by fatigue from nasal discomfort, itching sensation around the eyes, swelling of the nasal mucosal membranes, postnasal dripping, and cough [1]. On the far current record, approximately 15–20% of the population around the globe is affected by AR, with a dominating ratio in western countries [2, 3]. The treatment of the condition potentially focuses on alleviating the symptoms rather than addressing the root cause of the issue. Hence, patients are often recommended to avoid direct contact with allergens such as pollen, dander, dust mites, and cockroach infestations, which can potentially stimulate the arousal of rhinitis. Considerably, the first line of treatment is solely based on (intranasal antihistamines, corticosteroids, and cromolyn) to reduce inflammation. However, some cases might require surgical intervention [4].

Using the allergen challenge test at the molecular level, several researchers have established that people with AR secrete mediators such as histamine and leukotriene (LT). These proinflammatory factors have been detected in nasal secretions of the affected individuals upon exposure to allergens, but little has been known about their secretion in natural conditions [5–7]. Previous studies have reported the secretion of cytokine (IL-1α), a proinflammatory factor, upon exposure to allergens during the early or late phase of the reaction [8–10]. Thereby, it was suggested that the cytokine might have a crucial role in activating endothelial cells long with T-lymphocytes, further stimulating the cytokine release. Recent research has also discovered the presence of IL-1Ra, a naturally occurring inhibitor, in a higher molar concentration in the nasal discharges of AR patients and controls [11]. The antagonist (IL-1Ra) binds with the IL-1 receptor, preventing the active (IL-1α) binding without affecting its respective biological response. Similar to IL-1α, another chemokine of the interleukin-8 family, interleukin-8 (IL-8), has been found to be elevated throughout the late stages of the disease and is being investigated as a possible candidate in eosinophil movement in certain conditions.

According to a seasonal study conducted to assess the effect of cytokines upon exposure to allergens, it was deduced that a constant incline in the concentration of leukotriene and Eosinophil Cationic Protein (ECP) was prominent throughout the season. According to the findings, histamine concentrations only elevated late in the season and postseasonally. Additionally, the cytokine IL-1β and its natural antagonist, IL-1Ra, were assessed. Surprisingly, there was a considerable rise in IL-1β concentrations from early in the season to postseason, corroborating the hypothesis of chronic proinflammatory upregulation in seasonal allergic rhinitis. Additionally, the same study determined a considerable decrease in IL-1Ra concentrations during the early season, indicating dysregulation of the local anti-inflammatory capacity. Similarly, nasal secretions contained a significant rise in IL-1β concentration, confirming the assumption of chronic proinflammatory regulation.

Along with IL-1β, the considerable downregulation of IL-8 and myeloperoxidase indicates disruption of localized immunity, implying a substantial connection between the two variables. Myeloperoxidase is a marker of neutrophil activation, and its lower expression means reduced IL-8 secretion. Since neutrophils account for about 40%–60% of the cells on the mucosal surface and may operate similarly to macrophages, their dysregulation may increase susceptibility to infectious diseases. To summarize, allergic rhinitis does certainly reflect chronic inflammation, as evidenced by eosinophil activity and prolonged elevation of the proinflammatory cytokine IL-1α. As a result, the release of cytokines continues for weeks after pollen contact is ceased in persistent and seasonal allergic rhinitis. Numerous components, targets, and mechanisms underlying allergen-induced inflammatory disorders remain unknown despite substantial research on allergic rhinitis. Due to the complexity of the disease, only symptomatic treatment or combined drugs treatment has been recorded to date. Although the following TCM herbs are beneficial against allergic rhinitis, no comprehensive assessment of their anti-allergic-rhinitis mechanisms information from published scientific results has yet been undertaken. As a result, the current study concentrated on using traditional Chinese medicinal herbs to treat AR. This review will cover traditional Chinese medicines (TCM) that are widely used to treat allergic rhinitis.

Studies have demonstrated certain herbs to change biological pathways implicated in allergic rhinitis, such as eosinophil cell death, adhesion molecule modulation, mast cell generation, T_{H1}/T_{H2} imbalance, nuclear factor, chemokine concentrations, and IgE regulation [12] (Table 1). Herbs that are frequently used to cure allergic rhinitis comprise *Xanthium* fruit, *Scutellaria* root (*Scutellaria baicalensis*), *Centipeda* herb (*Centipeda minima*), licorice root (*Glycyrrhiza uralensis*), and *Astragalus* roots (*Astragalus membranaceus*). These herbs are the key components in herbal prescription and other Chinese herbs [12].

2. *Xanthium* Fructus

The *Xanthii fructus* (XF) is a well-known dried fruit of *Xanthium strumarium*, also called "Cang-Erzi" in Taiwan. It has been used over the years to treat various diseases, including rheumatism, sinusitis, skin pruritus, and headaches (Figures 1(a) and 1(b)) [18]. The *Xanthii fructus* has been shown to reduce mast cell-mediated allergy reactions [19], anti-inflammatory actions in lipopolysaccharide-stimulated inflammatory responses [20], and prevention of β-cell damage in type 1 diabetes [21].

As previously stated, allergic rhinitis can be divided into two stages: early and late. The ailment manifests itself within 5–30 minutes of exposure to the antigen, such as mold, dust, or animal dander [22, 23]. Early symptoms following exposure typically include lacrimation, clear rhinorrhea, itching, and sneezing, which are commonly triggered by the production of mast cell secretions, including histamine [24]. On a molecular level, mast cells have been known to play a significant role in inflammatory processes, including the release of proinflammatory cytokines such as tumor necrosis factor (TNF-α), interleukin-1β, interleukin-8, and interleukin-6 and inflammatory factors including serotonin and histamine (Figure 2) [25–27].

Likewise, the late phase of allergic rhinitis is often characterized by the recruitment of effector cells such as basophils, eosinophils, and T-helper 2 (T_{H2}) lymphocytes, causing malaise, irritability, fatigue, and congestion within 6–24 hours after antigen exposure [28–32]. On the other hand, eosinophils have been revealed to play an essential part in the disease's late stage. The abundance of eosinophils in the nasal mucosa of the affected patients indicates the release of proinflammatory mediators such as cysteinyl leukotrienes, eosinophil peroxidase, major basic protein cation in proteins. Presently, the common treatment of AR, as mentioned earlier, includes the usage of corticosteroids, immunosuppressants, and antihistamines. However, their use is restricted due to various adverse effects, such as lipid

Table 1: A cumulative representation of traditional Chinese medicines used to treat allergic rhinitis and the respective pathways and biomarkers regulated by them.

S. no.	Traditional Chinese medicine	Status of biomarkers	Type of study	Techniques/assays used	References
01.	*Xanthi fructus*	TNF-α, IL-6, IL-5 ↓ IF-1β, MIP-1 ↓ MIP-2 ↓ Histamine, IgE ↓ Caspase-1 ↓	In vivo	Cytotoxicity assay Western blotting Optical microscopy ELISA	[13]
02.	Licorice root (glycyrrhizic acid)	IFN-γ ↑ IgE, IgG_1 ↓ β-Hexosaminidase ↓ IgE mediated Ca^{+2} influx ↓ Orai1, STIM1 ↓ IP3R, TRYC1 ↓	In vivo	Evans blue extravasion assay ELISA assay WST-8 assay β-Hex assay RT-PCR Western blot	[14]
03.	*Scutellaria baicalensis* Georgi.	IL-6, TNF-α, IL-1β ↓ STAT3 pathway ↓	In vivo	ELISA Immunohistochemical staining	[15]
04.	*Centipeda minima*	TNF-α, IL-2, IL-4 ↓ PTGS2, $MAPK_3$ ↓	In silico In vivo	ELISA Immunohistochemical staining, H&E staining	[16]
05.	Emodin	PCA, histamine ↓ LCT_4, PGD_2, LTC_4 ↓ β-Hex, Ca^{+2} influx ↓ 5-LO, MAPK, cPLA2α ↓ PDG_2 generation ↓ TNF-α, IL-6, NF-κB ↓ Syk, LAT, PLCɣ1 ↓ AKT pathway ↓	In vivo	Evans blue extravasion assay β-Hexosaminidase assay immunoblotting	[17]

(a)

Figure 1: Continued.

(b)

Figure 1: (a) and (b) Representation of the plant and fruit of *Xanthium strumarium*, also called "Cang-Erzi."

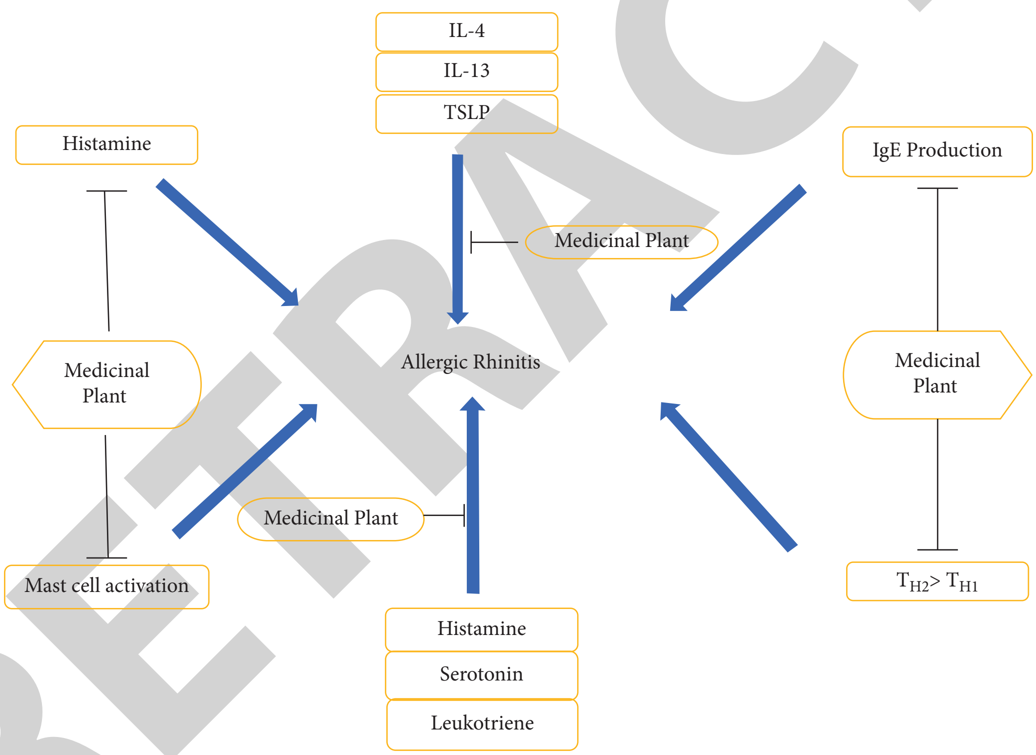

Figure 2: The diagrammatic representation of biomarkers affected during allergic rhinitis.

and glucose metabolism problems, osteoporosis, excessive sedation, and hypertension [33–35].

Over the years, multiple studies have proven the medicinal value of *Xanthii fructus* (XF) with its anti-inflammatory properties. In a survey conducted by An et al., the anti-inflammatory role of XF has been reported on liposaccharide-stimulated mouse peritoneal macrophages [20]. Another study discovered that XF extract shields pancreatic β-cells from cytokine-induced damage by inhibiting nuclear factor kappa-B (NK-κB) [21]. Another study has established that XF is responsible for inhibiting chronic inflammation found in airways among bronchial asthma patients. Additionally, the extract was found to be effective against histamine and TNF-α production in mast cell-mediated allergic responses [19, 36]. We will cover a study paper in this section which examines the mechanism of XF effects by looking at cytokine and caspase-1 levels, the thickness of nasal septum tissue, and the frequency of sneezing behavior in an *in vivo* AR model produced by ovalbumin (OVA). Additionally, the process by which XF inhibits NF-κB regulation has been explored.

2.1. Effects of Xanthii fructus over Nasal Symptoms in Allergic Rhinitis. As discussed earlier, the major symptoms of AR include rhinorrhea, itching, sneezing, and nasal congestion

[37]. An OVA-sensitized mouse model was considered to study XF's potential in vivo anti-inflammatory effects. Following sensitization, the extract of XF was injected with cetirizine (a positive control) to assess its anti-inflammatory properties. Compared to OVA-sensitized mice, a model treated with XF had a considerably lower amount of sneezing ($P < 0.01$).

2.2. Effects of Xanthii fructus on Serum Levels of Histamine, Immunoglobulin E, and OVA-Specific IgE. To investigate the effects of XF, several mice (BALB/c) were injected with OVA injections causing a significant increase in OVA-specific IgE and immunoglobulin E levels. As to our previous understanding, overexpression of IgE is a prominent marker of allergic rhinitis. In OVA-sensitized models, blood levels of histamine and total and OVA-sensitized IgE were observed to be considerably raised with time. However, treatment of mice with XF extract resulted in a significant decrease ($P < 0.05$) in histamine and total and OVA-specific IgE.

2.3. Cytokines and the Role of Xanthii fructus in Regulation. As we previously understood, cytokines play a vital role in the course of inflammation. The two groups taken under study (i.e., OVA-sensitized mice and mice treated with XF) were observed to understand the trend in the serum level of cytokines. The concentration levels of TNF-α, IL-6, IL-5, IF-1β, MIP-2, and MIP-1 significantly increased among OVA-sensitized mice. On the contrary, the XF-treated group presented an appreciable decline in the concentrations of these cytokines, indicating its anti-inflammatory function among AR models.

2.4. Eosinophil Infiltration and Histological Alterations in the Nasal Mucosa. OVA-sensitized mice groups had extensive eosinophil infiltration in the entire area of the lamina propria, increasing thickness to the nasal tissues, as per histological analyses. However, XF-treated mice groups showed a marked reduction in the thickness of the lamina propria.

2.5. Impact of Xanthii fructus on the Expression of Caspase-1. Caspase-1 is a member of a protease family also known by the name of IL-1β-converting enzyme (IL-1, BCE, or ICE). The enzyme contributes to immune-mediated inflammation by converting the precursor forms of interleukin-1β and interleukin-18 into active molecules found in the extracellular compartment [38]. Following the same trend, a significant increase in the expression of caspase-1 was observed among OVA-sensitized mice, whereas, upon treatment with XF, a prominent decrement was noted in the expression of caspase-1.

2.6. Mechanism of Action. To our knowledge, allergic illness is mediated by the increase of the Th2 cell subset and the production of particular IgE antibodies by B cells in response to diverse allergens. [39]. In such response, the IgE-sensitized mast cell begins to degranulate, secreting newly synthesized and preformed mediators including cytokines, histamines, cysteinyl leukotrienes, and prostaglandins [40, 41]. TNF-α is one of the cytokines that have been shown to have a significant role in allergic inflammation, as it is required for Th2 migration to the site of allergic inflammation and the generation of Th2 cytokines [42]. IL-1β, which has mostly been found to be elevated after allergen exposure, activates endothelial cells and T-lymphocytes, leading to further production of cytokines [43].

Similarly, IL-5 and IL-6 have been identified as major mediators of eosinophilic inflammation leading to asthma and are vital in developing nasal secretions, respectively [44]. Asthma patients' bronchoalveolar lavage fluid contains greater levels of the chemokine MCP-1, associated with the activation of eosinophils and basophils [45]. In the absence of an antigen or an anti-IgE antibody, histamine-releasing factors (HRFs) drive mast cells and basophils to release histamine.

Eosinophils move from the blood to the site of inflammation in allergic rhinitis because of the inflammatory stimulus (produced by antigen-presenting cells). This is also one of the main features of allergic rhinitis [46]. Inflammation is frequently reduced when eosinophils are decreased. Now that we know more about caspase-1, an enzyme in the cysteine-protease family, we can better understand how it affects the development of the IL-1 family and how it affects disease-causing immune responses [47]. This thickness of the lamina propria in the nasal septum and infiltration of eosinophils has been found to be conspicuously reduced after treatment with XF.

The expressions of all cytokines predominantly depend on an active transcription factor, NF-κB [48]. This activation requires phosphorylation and proteolysis and degradation of Iκ-Bα (an endogenous inhibitor of NF-κB) as its key component [49]. XF was also found to inhibit the phosphorylation and degradation of this transcription factor successfully. Hence, causing the inactivation of NF-κB leads to a substantially low level of cytokines. The treatment of AR has led to constructing an animal model in the current research strategy.

In comparison, periodic intranasal OVA treatment has induced typical AR symptoms on a physical and molecular level in the animal models (i.e., inflammatory mediators and IgE production) [48, 50, 51]. XF has drastically decreased levels and an antiallergic impact by blocking the generation of its mediators. Cetirizine, a metabolite that is a selective H1 receptor being used to treat angioedema, urticarial, and allergies [52], has been taken as a positive control. The scheme has also concluded that the effect of XF has been found similar to that of cetirizine.

3. Licorice Root

An allergic reaction is mostly regarded as a condition caused by hypersensitivity of the immune system to react with the substances normally considered harmless in all age groups, thereby leading to anaphylaxis [53]. The condition is often mediated by immunoglobulin E response with few medicines available to alleviate the allergic symptoms, including antihistamine drugs (i.e., diphenhydramine, terfenadine, and chlorpheniramine maleate), immune suppressors (hydrocortisone, dexamethasone, and adrenal cortical hormones), and mast cells stabilizers (ketotifen, sodium hydroxypropyl cromate, and disodium cromoglycate). However, as with other drugs, most of these products have been shown to possess side effects. Similarly, symptom relapse has also been observed among patients. In this regard, a suitable alternative derived from food with no side effects may serve as a possible drug of interest to overcome allergic symptoms.

Glycyrrhiza is a plant with an ancient origin and has been used over history for herbal medicine and food (Figure 3) [54]. Among other plant constituents, glycyrrhizic acid (GA) is considered one of the main components possessing several pharmacological properties. Numerous research have discovered that biologically active substances in organic foods, such as polyphenols and flavonoids, which have anti-inflammatory or antioxidant properties, lead to antiallergic action. Clinical and experimental studies have revealed the application of glycyrrhizic acid (Figure 4) with its immunomodulatory [55] and anti-inflammatory [56] characteristics. A study reduced asthma-like symptoms in mice with a Balb/c model by taking GA (2.5–20 mg/kg body weight). This was found to be an effective way to treat the mice's asthma, simultaneously preventing the reduction in total IgG2a and interferon-gamma (INF-γ) levels. Furthermore, GA (10 mg/kg body weight) has been proven to block the activation of NF-κB and STAT-317, hence reducing the onset of acute inflammation. In this section, we will discuss the antiallergic effects of glycyrrhizic acid along with its possible underlying mechanisms.

3.1. Through T-Helper Cell Development, GA Plays a Role in OVA-Induced Systemic Allergy Reactions. The antiallergic activity of GA was evaluated in an OVA-induced active systemic allergic response. Conspicuously, multiple allergic symptoms were prominent in the sensitization group, including labored respiration, scratching, and a total decrease in rectal temperature by $-1.60 \pm 0.1^{\circ}$C. However, the 100 mg/kg body weight group treated with GA showed substantial suppression of allergic symptoms and a net decrease of $-0.9 \pm 0.1^{\circ}$C in rectal temperature.

The rate of inhibition observed by 100 mg/kg of GA is comparable to that of hydrocortisone, a standard allergy treatment. As for the levels of cytokines, a significant increase was noted among T_{H2} cytokine IL-4, whereas a decreasing trend was prominent among Th1 cytokines (IFN-γ) among the OVA-sensitized group. However, after treatment with 100 mg/kg, a significant increase in the level of IFN-γ was observed. These findings indicated that an oral dose of 100 mg/kg GA might influence Th1/Th2, resulting in an attenuation of allergic reactions.

3.2. Inhibition of OVA-Specific IgE and IgG1 Production via B-Cells. Additionally, the effect of GA on the generation of IgG1 and IgE antibodies in the OVA-sensitized group was studied compared to the controls ($P < 0.05$). The results presented that only 100 mg/kg body weight of GA has significantly decreased the production of OVA-sensitized antibodies ($P < 0.05$). The inhibition effect was found to be similar to that of hydrocortisone. Hence, GA was also found to influence OVA-sensitized antibody-producing B-cells

3.3. Role of GA as a "Mast Cell Stabilizer". According to our prior knowledge, Mast cells contribute to IgE-induced allergy by producing different cytokines, a key cause of allergic conditions. Using passive cutaneous anaphylaxis (PCA) and RBL3-2H3 immunologic cell-based tests, it was further explored if GA can also influence mast cell activation.

The assay results indicate a substantial reduction in the mast cell-dependent PCA reaction in the GA-treated group (in a dose-dependent manner). Similarly, the effect of GA on degranulation was examined by quantifying β-hexosaminidase release in the absence and presence of GA. As for the cytokines, glycyrrhizic acid was found to cause substantial suppression in the release of β-hexosaminidase from 87.46% to 45.23% with the increment of dosage from 100 to 1000 μg/mL ($P < 0.05$).

3.4. Impact of GA upon Expression of Calcium Channel Proteins. According to the available literature, degranulation of RBL-2H3 cells is dependent on the release of Ca^{+2} ions from the endoplasmic reticulum (ER) and the Ca^{+2} ion influx mediated by calcium release-activated calcium channels (CRAC) [57]. Hence, the effect of GA on the influx of Ca^{+2} ions was taken under investigation. The intracellular Ca^{+2} ion concentration was determined using Fluo-3 AM (a fluorescent Ca^{+2} ion indicator). GA at a 1000 μg/mL concentration prevented Ca^{+2} influx mediated by IgE/Ag.

The activation of Ca^{+2} influx-mediated proteins such as stromal interacting molecule 1 (STIM1), Inositol 1,4,5 triphosphate receptor (IP3R), calcium release-activated calcium channel protein 1 (Orai1), and transient receptor potential channel 1 (TRPC1) was also studied. On a similar note, there was a significant decrease in the expressions of Orai1, STIM1, IP3R, and TRPC1 upon treatment with GA. These findings show that GA has no role in the depletion of the ER Ca^{+2} reservoir; instead, the stability of mast cells is predicated on Ca^{+2} influx inhibition due to decreased Orai1, STIM1, and TRPC1) expression.

3.5. Mechanism of Action. Glycyrrhizic acid (GA) has been reported to have similar effects on the immune system of Balb/c mice as other natural triterpenoids [58]. These may include anti-inflammatory, antineoplastic, antiviral, immune-regulatory, pharmacological, and antiallergic effects. The three major mechanisms by which antiallergic effect comes into play are (i) a potential role as a mast cell stabilizer, to reduce the secretion of mediators via imparting inhibitory effect over Ca^{+2} influx, (ii) modulation of TH cell development to limit cytokine (IL-4) release from T_{H2} cells, and (iii) influencing OVA-specific antibody-producing B-cells (Figure 5).

Figure 3: Presentation of a licorice plant [17].

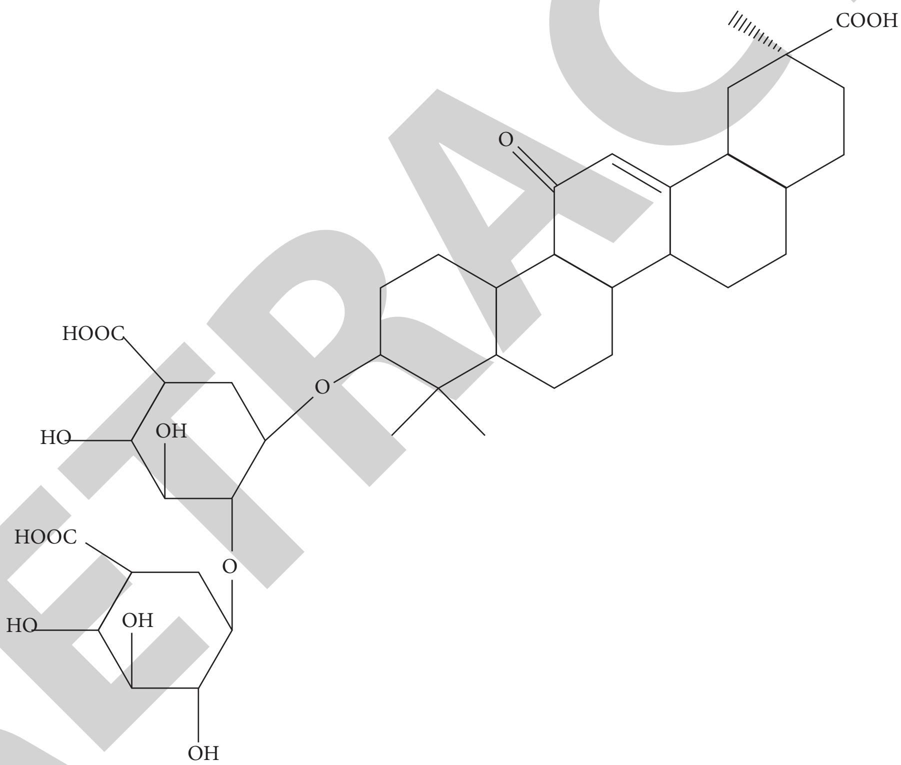

Figure 4: Structure of glycyrrhizic acid.

According to our previous understanding, GA can decrease serum total IgE and OVA-specific IgE levels [14]. In allergic rhinitis mice models, GA has been shown to elicit a considerable reduction of OVA-specific IgE antibodies in a dose-dependent way. This significant reduction could be caused by blocking T_{H1}/T_{H2} differentiation and maturation, which would impede the production of IL-4. Furthermore, GA has also been found to suppress IgG1, later leading to inhibition of basophil activation [59]. Likewise, the study has also presented the role of GA as a mast cell stabilizer, where GA treatment has led to the significant reduction of the intracellular Ca^{+2} levels. As a result, the extracellular process of Ca^{+2} influxes is inhibited. However, no variation in mRNA expression of inositol-3-phosphate receptor was identified in the absence or presence of GA, indicating that GA did not affect endoplasmic reticulum (ER) storage. On the other hand, the expressions of Orai1, STIM1, and TRYC1 were significantly reduced, suggesting that GA may regulate Ca^{+2} degranulation via decreasing calcium channel expression levels.

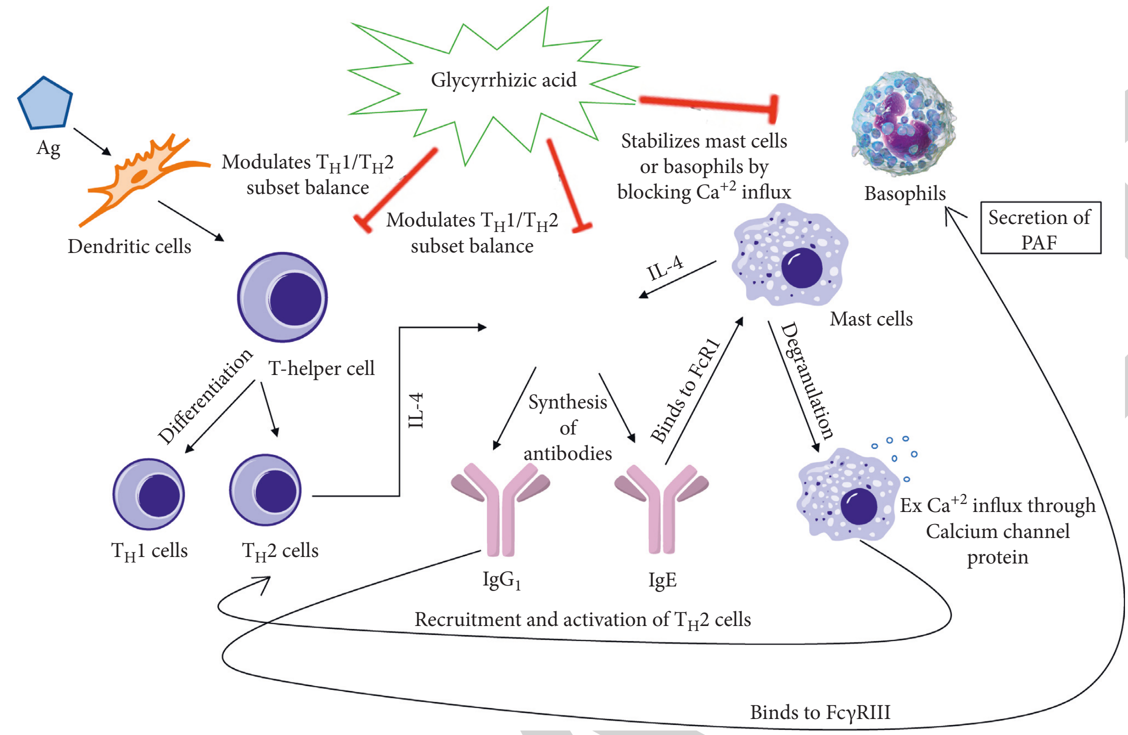

Figure 5: The mechanism through which GA exerts its antiallergic impact on IgE-mediated allergic reactions [13].

4. *Scutellariae Radix*

Scutellariae Radix (RS), also referred to as huangqin in Chinese, is the dry root of the Labiatae plant *Scutellaria baicalensis* Georgi. [60]. In English, the plant is also known as Baikal skullcap or Chinese skullcap, and it is endemic to Asia, particularly Far East Russia, Mongolia, Siberia, East Asia, and China (Figure 6). The plant is frequently used in traditional Chinese medicine to treat cardiovascular and respiratory disorders, gastrointestinal infections, inflammation, and other diseases [61]. Regardless of the whole plant, the usage of RS is more extensive in Japanese and Chinese pharmacopeia with a broad range of therapeutic effects, including detoxifying toxicosis, preventing bleeding and miscarriage, clearing away heat, and moistening aridity [62, 63]. Anti-inflammatory properties of RS have been well documented in *in vivo* and *in vitro* investigations, including inhibition of chemokine, cytokine, and growth factor production from macrophages [64–69], exhibiting potential treatment of colon cancer [70], stroke [71], and colitis [72].

The major biological compounds isolated from RS include phenylethanoid glycosides, flavonoids, diterpenes, triterpenes, phytosterols, polysaccharides, and iridoid glycosides [73]. Among these, over 40 flavonoids along with the form of glycosides have been identified as most abundant [73], which include the key bioactive components oroxylin A-7-glucuronide (OAG), oroxylin A (OA), wogonoside (wogonin-7-glucuronide, WG), baicalein (B), wogonin (W), and baicalin (baicalein-7-glucuronide, BG) [61] (Figure 7).

As previously mentioned, AR is a condition marked by significant pain and other symptoms such as respiratory obstruction, sneezing, congestion, and rhinorrhea, which can lead to ear and nasal abnormalities if left untreated [74]. A complicated allergen-induced inflammatory process within the nasal mucosa causes the condition. On a molecular level, such a process causes the release of histamine and a variety of cytokines and proinflammatory substances, which can trigger vascular dilatation and tear secretion [75]. Among all other activities, the release of IgE has been determined to have a significant part in the overproduction of basophils, eosinophils, and mast cells, as discussed in various sections [76].

Among the various flavonoids mentioned above, baicalein is one of the major constituents of RS found to regulate T_{H1}/T_{H2} balance and adjust histamine release from the mast cells [77]. Several research groups have reported the anti-inflammatory role of baicalein in mouse models, alleviating colitis, liver, and vascular inflammation [78, 79] induced by dextran sulfate sodium (DSS) and 2,4,6-trinitrobenzene sulfonic acid (TNBS) [79, 80]. Through an OVA-induced AR animal model, we will explain the regulating efficacy of baicalein derived from RS on clinical symptoms of AR, mucosal histological alterations, and inflammation *in vivo*.

4.1. Baicalein's Anti-Inflammatory Properties in AR-Infected Rats. Two major characteristic features, body weight and mass of the vital organs, were considered in OVA group, OVA + baicalein group, and OVA + clarityne group. In terms of body weight, there was no statistically significant difference between the two groups. After 30 minutes of OVA stimulation, the frequency of nasal scratching, degree of

Figure 6: A pictorial presentation of a traditional Chinese medicine herb, Scutellariae Radix [15].

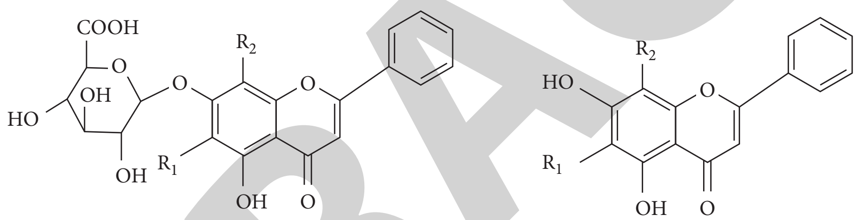

· Baicalin (R_1=OH, R_2=H)
· Wogonoside (R_1=H, R_2=OMe)
· Oroxylin A7-0-glucuronide (R_1=OMe, R_2=H)

· Baicalein (R_1=OH, R_2=H)
· Wogonin(R_1=H, R_2=OMe)
· Oroxylin A(R_1=OMe, R_2=H)

Figure 7: Active components obtained from Scutellariae Radix, including flavonoids and glycosides.

nasal outflow, and sneezing pattern in each group were recorded and then overlapped to analyze the findings.

It is worth noting that the OVA-treated group had more sneezing and nasal scratching than the control group. Furthermore, a significant reduction in the frequency of sneeze and nasal grating was found after baicalein treatment, but the inhibition mechanism is still unknown. The primary organ masses (including the spleen, kidney, liver, and heart) were also identified in the OVA-induced, OVA + baicalein-treated, and control groups. The spleen in the OVA-induced group was significantly heavier in comparison to the control group ($P < 0.05$), while the spleen in the baicalein treatment group was considerably lighter in comparison to the OVA-induced group ($P < 0.05$).

4.2. The Effect of Baicalein on Inflammatory Variables in AR Rats' Nasal Lavage Fluid and Serum. Levels of inflammatory factors such as IL-6, TNF-α, and IL-1β were assessed in the OVA-induced (AR model) and baicalein-treated groups better to understand the role of baicalein in inflammatory factor production. In the AR model, there was a considerable increase in IL-6, TNF-α, and IL-1β, which gradually decreased after treatment with baicalein.

4.3. Baicalein's Effect on Inflammatory Cell Infiltration in the Nasal Mucosa and Lung Tissue. Allergen-induced rhinitis, as we all know, results in inflammatory infiltration of the lamina propria. Three groups have been identified based on histological findings using H&E staining. Inflammatory cells were not found in the nasal cavity, lateral nasal walls, or nasal septum in the healthy one. In addition, no signs of vascular congestion or proliferation were observed while presenting normal tissue structure and mucosal glands. However, in the second group (AR model), characteristic changes were present in the histological parameters, including many inflammatory cells (eosinophils, basophils, and mast cells) inside the nasal mucosa. On the other hand, the same feature was significantly reduced in the baicalein-treated group, demonstrating a significant ability to prevent inflammatory cell formation.

Additionally, lung tissue compounds were examined, with pertinent sections stained with H&E to ascertain the extent of lung injury. Damage was visible on the surface, with interstitial edema, thickening, and infiltration of neutrophils into the alveolar wall, as well as the formation of a necrotizing ulcer. However, baicalein was found to alleviate these symptoms significantly.

4.4. Baicalein's Effect on p-STAT3 Expression in Nasal Mucosa Tissues. To further validate the impact of baicalein over the inhibition of relevant pathways, the STAT3 signaling pathway was brought into the investigation. According to the findings, baicalein inhibited the phosphorylation of the STAT3 signaling pathway in OVA-induced rats. As discussed earlier, AR can be categorized into two distinct phases. An early stage is usually characterized by IgE-induced activation of inflammatory cells, including neutrophils, eosinophils, and lymphocytes, along with the production of related cytokines (IL1β, IL-6, and TNF-α). Similarly, the late phase of the condition involves the recruitment of other inflammatory cells such as mast cells and basophils, in addition to the release of chemokines, histamine, and leukotrienes accounting for the anaphylactic shock [81–84]. Typical AR symptoms were reported in this study starting on day 15 and gradually faded after 1.5 hours. According to the present findings, baicalein reduced the frequency of nasal itching and sneezing in AR rats.

5. *Centipeda minima*

Centipeda minima (L.) A. Braun et Aschers (Compositae), sometimes known as coriander, is an annual herbaceous plant native to eastern tropical zones, Taiwan, and China (Figure 8). The plant, also known as chickweed, is drought-tolerant and spreads throughout China. *C. minima* has been known to possess a spicy taste. It has been traditionally used in Chinese folk medicine to treat sinusitis, relieve pain, reduce swelling rhinitis, and treat cancer for a very long time [86]. Medicinally, the plant has also been used to minimize cough and nasal secretions associated with respiratory complications [16]. To our current understanding, the main medicinal constituents of *C. minima* involved in treatment include polysaccharides, flavonoids, and volatile oils. Pharmacological studies of the plant represent that these therapeutic components have been conventionally used to treat antitumor, antiprotozoal, and allergic rhinitis-associated headaches.

As previously described, allergic rhinitis is a noninfectious inflammation of the nasal mucosa. Symptoms include nasal congestion, runny and itchy nose, and recurrent sneezing episodes. Work and other daily activities may be harmed due to these difficulties. *C. minima* has been

Figure 8: The plant of *Centipeda minima* [85].

demonstrated in studies to decrease eosinophil and mast cell activation, diminish degenerative alterations in nasal mucosal tissues, lower histamine levels, and minimize nasal stiffness [87].

This section will explain the experimental investigation conducted to extract volatile oil components from *C. minima* gathered from seven different geographical sites throughout China and the optimal steam distillation extraction settings. The volatile oil composition of *C. minima* was determined using gas chromatography-mass spectrometry (GC-MS) after extraction. Component-related molecular targets were investigated using network pharmacology analysis. The primary pathways and key targets of *C. minima* components were identified, as well as the overall amount of protein-disease connection. The best volatile oil extraction yield from *C. minima* was obtained at 300°C through a 10-mesh sieve.

5.1. Fingerprint and Cluster Analysis. The volatile oil-related GC-MS data from *C. minima* were integrated into the traditional Chinese medicine chromatographic fingerprints similarity evaluation method. The data reveal minor changes in the makeup of *C. minima* samples taken from seven different geographic locations.

The findings reveal that plants collected in Jiangxi, Hubei, Shanxi, and Sichuan have high similarities. We discovered roughly 30 additional volatile oil *C. minima* compounds for each location, 15 of which were identical across all plants.

5.2. C. minima and Allergic Rhinitis Target Prediction and Mapping. The Venny software tool collected the 15 volatile oil components isolated from *C. minima* specimens in seven geographic areas. 343 relevant targets for 15 components and 2155 diseases targets were identified following a database search. The Venny software was used to import the obtained component targets and disease-related targets. As a result, 117 genes with known intersections were identified. 172 intersection targets were imported into the STRING platform to study protein interactions. The circle's diameter fluctuates according to each protein's degree value, with a higher degree value suggesting that a protein interacts with more pathways. Three proteins were chosen based on their degree and centrality values: mitogen-activated protein kinase 3 (MAPK3), prostaglandin-endoperoxide synthase 2 (PTGS2), and tumor necrosis factor (TNF).

5.3. KEGG and GO Analysis. The KEGG and GO analyses of the intersection targets were performed using the R package clusterProfiler. According to the findings of the GO analysis, the biological process (BP) was linked to 1753 pathways, including response to a bacterial molecule, regulation of the inflammatory response, and cellular calcium ion homeostasis, indicating that these genes are involved in related biological processes in vivo and collaborate in the treatment of allergic rhinitis. Our study data revealed 37 cellular components (CC) pathways, including the membrane region, an important part of the resynaptic membrane transcription regulator complex, and other pathways that play a role in allergic rhinitis pathology. KEGG analysis found 137 pathways that were connected. 28 of the target proteins were found to play a role in neuroactive ligand-receptor interaction, 15 of the target proteins are involved in Th17 cell differentiation, and 12 of the target proteins are involved in the VEGF signaling process. The data analysis shows that *C. minima* active ingredients are linked to several possible allergic rhinitis pathways. People who have allergic rhinitis are more likely to get it if they go through the second Th17 cell differentiation process, according to the results of the enrichment analysis and the literature.

5.4. H&E Staining. Tissue analysis in rats demonstrated that the nasal mucosa epithelium in the "blank controls" was unaffected. There was no inflammatory cell infiltration in the submucosa of control rats. Cilia were also lost in the disease model group, and the nasal epithelium was damaged. In tissue samples from infected mice, interstitial edema and interstitial inflammatory cell infiltration were observed, as well as gland hyperplasia and swelling. *C. minima* extract-treated rats had much less damage to their nasal mucosa, with less glandular hyperplasia and less inflammatory cell infiltration into the interstitial cell layers in their noses.

5.5. ELISA. Immune cells can be activated and regulated by interleukins as second messengers, activating and regulating several inflammatory processes, such as Th17 cell differentiation. Cell proliferation and differentiation can be boosted by TNF, for example. IgE serves as a reference measure for the onset and progression of allergic rhinitis as a key inflammatory factor. Further, we measured the amounts of inflammatory and anti-inflammatory elements (IL-4, TNF-α, and IgE) in the serum to verify the network pharmacology's pathway and targets. TNF, IL-2, IgE, and IL-4 were measured in rat serum using ELISA. TNF levels in the model group were substantially higher than those in the control group ($P < 0.001$).

TNF levels were considerably lower in the treatment group compared to the model group (p 0.01). It was found that the IL-2 content in the model group was significantly lower than that in the blank group ($P < 0.01$). There was a statistically significant difference ($P < 0.01$) between the treatment and the model groups in IL-2 levels.

The model group's IL-4 levels were considerably higher ($P < 0.001$). The level of IL-4 in the treatment group was substantially lower than that in the model group ($P < 0.001$). According to the IgE study, the model group had considerably more IgE than the blank group ($P < 0.001$). Compared to the model group, the treatment group had dramatically reduced levels of IgE ($P < 0.01$). Because of this, *C. minima* can reduce inflammatory responses while increasing anti-inflammatory responses. This effect indicates the plant's ability to alleviate the symptoms of allergic rhinitis.

5.6. Immunochemistry. Immunohistochemistry results showed that the expression rates of PTGS2 and MAPK3 in inflamed tissues were much greater than those in normal tissues. Compared to the control group, the model group's average optical density of PTGS2 and MAPK3 proteins was significantly higher ($P < 0.01$). There was a big difference in the PTGS2 and MAPK3 proteins in the volatile oil-treated group compared to the model group ($P < 0.05$).

6. *Xanthium* Fruit: Emodin

As discussed previously, chronic T_{H2} allergic inflammation such as rhinitis, asthma, and atopic dermatitis affects up to 300 million people worldwide [88, 89]. With the current expansion in urbanization, there is a rise in the number of patients suffering from allergic reactions. There is an urgent need to discover alternative antiallergic medicines that can increase the quality of life while also being safer to use.

Mast cells have long been recognized as a critical player in allergic diseases, where the aggregation of high-affinity IgE receptors (FceRI) on mast cells stimulates the secretion of both preformed (e.g., proteases and histamine) and newly synthesized mediators such as prostaglandin D2 (PGD2) and leukotriene C4 (LTC4) [90, 91]. Signaling cascades are initiated when a cognate antigen (Ag) binds to FceRI. The stimulation of receptor-proximal tyrosine kinases such as Syk, Lyn, Fyn, and Btk and the phosphorylation of other adaptor molecules are examples of these pathways. Syk is essential for the activation of IgE-dependent mast cells. Once active, Syk phosphorylates adaptor proteins such as the linker for activation of T cells (LAT), resulting in the formation of a macromolecular signaling complex that allows for the diversity of downstream signaling required for the creation of various proinflammatory mediators [92–95].

Signaling pathways of such a kind include Ca^+ ion mobilization mediated through phospholipase C_g (PLC_g), a prerequisite step for LTC_4 generation and subsequent degranulation [94]. As a result, inhibiting Syk kinase may limit the release of various granule-stored and newly produced mediators [92]. Additionally, crosslinking of FceR1 has been shown to activate the mitogen-activated protein kinase (MAPK), phosphoinositol-3-kinase/Akt (PI3K/Akt), and nuclear factor-κB signaling pathways. As a result, several proinflammatory genes, such as those encoding cyclooxygenase (COX-2) and proinflammatory cytokines, are expressed [95].

Polygonum multiflorum Thunberg, *Rheum officinale* Bail, *Polygoni cuspidati* (*P. cuspidati*), *radix*, and *Cassia obtusifolia* seed have been utilized in traditional medicines in Eastern Asia for numerous centuries. These oriental plants contain various pharmacological properties, including anti-inflammatory and antiallergic properties [96–99]. Emodin (1,3,8-trihydroxy-6-methylanthraquinone), a compound found in these herbs, has been demonstrated to have a variety of biological actions (i.e., immunosuppressive, antimicrobial, anti-inflammatory, antidiabetic, and anti-atherosclerotic activities) (Figure 9) [100–104]. Additionally, Emodin has been shown to inhibit the oncogenic transformation of lung and breast cancer by inhibiting HER2/neu tyrosine kinase activity, indicating its anticancer potential. We will address the antiallergic properties of Emodin and its possible use as a natural remedy for allergic diseases in this part.

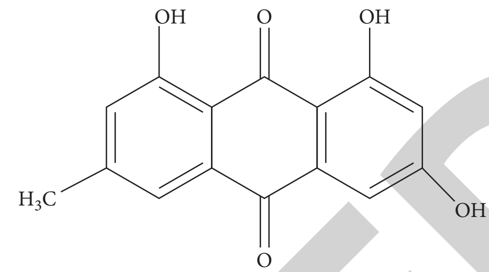

Figure 9: Structure of Emodin.

6.1. Effect of Emodin on Anaphylactic Reaction in Mice. We understand that anaphylaxis is a profound allergic reaction induced by crosslinking specific IgE bound to FceR1. This interaction between FceR1 and IgE stimulates the mediator release from mast cells, causing anaphylaxis [30, 105, 106]. Passive cutaneous anaphylaxis (PCA) and passive systemic anaphylaxis (PSA) were used to assess Emodin's antiallergic activity. PCA was considered in sensitized mice following oral treatment of 25 mg/kg and 50 mg/kg Emodin and 50 mg/kg fexofenadine-HCl for 1 h, via IV challenge with Ag (di-nitrophenyl-human serum albumin in 1% Evans blue dye).

Emodin effectively inhibited the mast cell-dependent PCA reaction in a dose-dependent manner ($n = 9$), suppressing it by 48% ($P < 0.001$) and 55% ($P < 0.001$) at 25 and 50 mg/kg, respectively. PSA levels were determined in mice sensitized with IgE or control saline through IV injection and challenged 24 hours later with an i.v. injection of DNP-HSA. Emodin dose-dependently decreased serum histamine, LTC4, and PGD2 levels ($n = 9$), suppressing LTC4 generation by 38% ($P < 0.05$) and 70% ($P < 0.05$), PGD2 generation by 41% ($P < 0.01$) and 48% ($P < 0.01$), and histamine release by 13.6% ($P < 0.05$) and 34.7% ($P < 0.01$), respectively.

6.2. Effect of Emodin on Ca^{+2} Ion Mobilization and Mast Cell Degranulation. The effect of Emodin on the degranulation of mast cells was also examined, considering them to play a major role in anaphylaxis. Initially, the cytotoxic effects of Emodin on bone marrow mast cells (BMMCs) were examined using MTT assay, and no significant effects on cell viability even at 40 mM were observed. As a result, additional studies were conducted at a concentration of <20 mM. To further study the impact of Emodin on IgE/Ag-induced BMMC degranulation, the synthesis of β-hexosaminidase (β-hex) was evaluated in the presence and absence of Emodin.

A substantial suppression of β-hex was observed in a dose-dependent manner ($P < 0.01$). Moreover, the production of cytosolic Ca^{+2} was considered, acknowledging that the release of Ca^{+2} is a key factor in mast cell degranulation [107]. Interestingly, 20 mM of Emodin completely inhibited IgE/Ag-stimulated Ca^{+2} influx ($P < 0.01$).

6.3. Effect of Emodin on the Generation of Leukotriene-C_4 (LTC_4) from Mast Cells. According to our present understanding, LTC4 production is regulated in two phases (i.e., $cPLA_{2\alpha}$ liberation of arachidonic acid (AA) from membrane phospholipids and 5-lipooxygenase oxygenation of free arachidonic acid). In response to increased Ca^{+2} levels, both molecules ($cPLA_{2\alpha}$ and 5-LO) translocate from the cytosol to the perinuclear membrane [108, 109].

Furthermore, mitogen-activated kinases (MAPK) phosphorylate cPLA2α, a mechanism necessary for optimum arachidonic acid secretion. Further, to assess the mode of action of Emodin, an immunoblot of cPLA2α, MAPK, and 5-LO was performed after treatment with IgE/IgA in the presence and absence of Emodin. The obtained results presented that the majority of cPLA2α was still in the cytosol regardless of the IgE/Ag stimulation. However, a pool of phosphorylated cPLA2α was detected in the nuclear (N-p-cPLA2α) and cytosolic (C-p-cPLA2α) regions of the activated cells where LTC4 was generated. Under these circumstances, no change was observed in the Lamin B and B-actin (internal control for nuclear and cytosolic fractions, respectively). The IgE/Ag-dependent presence of N-p-cPLA2α and C-p-cPLA2α was substantially suppressed by Emodin, indicating the potential role of Emodin in the blockage of Ca^{+2}-dependent translocation of cPLA2α as well as MAPKs (i.e., ERK1/2) dependent phosphorylation.

Similarly, whereas the majority of 5-LO was found in the cytosol (C-5-LO), a small amount was translocated into the nucleus fraction (N-5-LO) upon cell activation, resulting in the formation of LC4. Emodin and each MAPK inhibitor suppressed 5-LO's nuclear translocation effectively.

Immunoblot densitometric measurements have further demonstrated that Emodin reduced the Ag-dependent translocation of cPLA2a and 5-LO from the cytosolic to nuclear fractions. Studies have shown that intracellular Ca^{2+} influx helps regulate 5-LO translocation on multiple occasions [108, 109] and Ca^{2+}-independent 5-LO translocation into the nucleus [40]. Though 5-LO can be activated and phosphorylated by MAPKs, [110], it is unclear how MAPK

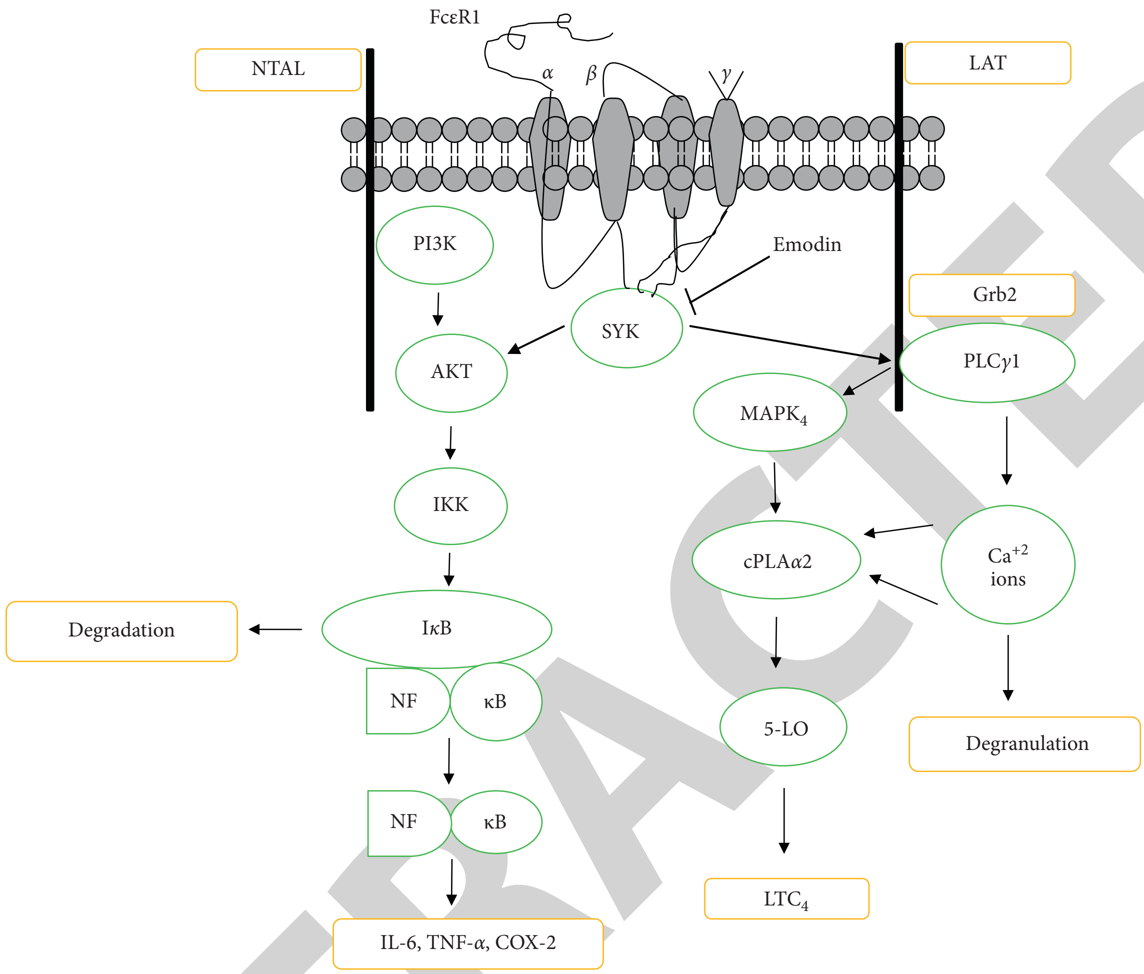

Figure 10: Emodin might stop mast cells from getting activated by FceRI. The activation of Syk, a receptor-proximal tyrosine kinase, happens when FceRI comes into contact with the right antigen. A protein called NTAL, which acts as an adaptor, helps Syk control how the PI3K pathway works. This is important because it allows NF-κB to make COX-2 and other proinflammatory cytokines. Syk also phosphorylates LAT, which leads to the formation of a macromolecular signaling complex that allows for a wide range of downstream signalings, like PLC1 and Grb2. Activated PLC1 is important for Ca^{2+} responses and activation of PKCs, which are important for degranulation and the movement of cPLA2α and 5-LO to the perinuclear membrane and the direction of cPLA2α and 5-LO to the perinuclear membrane. The Grb2-mediated pathway is important for cPLA2α to be activated properly, leading to eicosanoid hormones [17].

inhibitors prevented 5-LO translocation in IgE/Ag-stimulated BMMCs. There is some preliminary evidence to show that IgE/Ag-activated BMMCs are resistant to intracellular Ca2+ influx when treated with inhibitors of p38 and ERK. Densitometric research indicated that Emodin reduced the activation of all MAPKs evoked by IgE/Ag.

6.4. In Mast Cells, Emodin Suppresses Delayed PGD_2 Synthesis and Cytokine Production. As we are already familiar with the metabolism of arachidonic acid (AA) inside mast cells, the molecule can also opt to alternate COX pathway and thus get metabolism into prostaglandin D_2 (PGD_2). PGD_2 synthesis, in contrast to LTC_4 synthesis, is a biphasic process. LTC_4 output and PGD_2 production occur within a few minutes of each other in the immediate phase of PGD_2.

The second phase of PGD_2 synthesis, which lasts for 2–10 hours and is dependent on de novo-induced COX-2, follows the initial phase [17, 85]. IgE-sensitized BMMCs were pretreated with aspirin to eliminate any previous COX-1 activity, followed by a brief wash, and then stimulated with Ag for 7 hours with or without Emodin to examine if COX-2-mediated delayed PGD_2 production was occurring. Emodin suppressed delayed PGD_2 production dose-dependently, with a corresponding decrease in COX-2 protein. Since all MAPK inhibitors wiped out COX-2 expression, Emodin's inhibitory impact on MAPKs may be responsible for suppressing COX-2 induction.

Emodin also reduced TNF-α and IL-6 production in a dose-dependent manner. It has been found that the NF-κB is a key regulator of COX-2 and cytokine expression [111, 112]. The effect of Emodin on the NF-κB pathway was studied; results indicated that Emodin significantly inhibited the NF-κB pathway by phosphorylating IkappaB kinase (IKK-dependent phosphorylation) and degrading the inhibitory Iκ-B effects on NF-κB nuclear translocation.

After IgE/Ag activation, phosphorylation of the IKK complex (p-IκKa/b) and IκBa (p-IκBa) increased, resulting in a decrease in overall IκBa protein and nuclear translocation of NF-κB (N-NF-κB). Emodin inhibited p-IκKa/b and p-IκBa from increasing, IκBa from decreasing, and N-NF-κB from developing. Because Emodin influencess gene transcription in activated mast cells, its effect on the PI3K/Akt pathway was also studied. Emodin inhibited these reactions after IgE/Ag stimulation enhanced the phosphorylation forms of Akt.

6.5. Emodin Inhibits Syk Activation. As previously stated, Emodin has demonstrated a highly effective reaction to various mast cell functions. Thus, it would be noteworthy to assess whether it can inhibit an early regulatory step of FceRI signaling. As we know, spleen tyrosine kinase (Syk) plays a key role in initiating FceRI-dependent signaling [92, 93, 95]. Therefore, it would be essential to note whether Emodin affects the inhibition of Syk [96, 113, 114]. In addition, phosphorylated forms of LAT (linker of activated T-cells) and PLCɣ1 (phospholipase C gamma 1) were also considered. These molecules lie downstream of the Syk [115]. The experiment significantly inhibited Syk, LAT, and PLC ɣ1 by Emodin. Because PLCg1 phosphorylation is required for inositol phospholipid breakdown and subsequent Ca^{2+} signaling [116], the observed suppression of Ca^{2+} influx by Emodin is most likely due to its inhibitory action on the Syk-dependent activation of PLC1 (Figure 10).

Lastly, to determine if Emodin may also inhibit human mast cell activation, we evaluated its effect on the IgE/Ag-dependent phosphorylation of Syk, PLCɣ1, and LAT in HMC-1 cells. Emodin efficiently suppressed these receptor-proximal events in HMC-1 cells.

7. Conclusion

The current review entails a detailed discussion regarding traditional Chinese medicines used to treat allergic rhinitis. The study also outlines the limitation of the currently marketed drugs such as intranasal antihistamines and corticosteroids, which have been shown to possess multiple side effects. On the contrary, Chinese traditional medicines have been found to regulate the production of cytokines, including IL-5 and IL-6, which are the major mediators of eosinophilic inflammation, TNF-α which recruits T_{H2} cells at the site of inflammation, and NF-κB which is needed for the production of cytokines and IgE antibodies.

Similarly, traditional Chinese medicines (TCM) have also been effective in reducing histamine concentration, maintaining histological changes by reducing the thickness of the lamina propria, and downregulating the expressions of Orai1, STIM1, and TRYC1, indicating the low expression of Ca^{+2} channel proteins. Keeping in view the promising results obtained from TCM, there is a dire need to extend these medications to clinical trials further to reduce the risk ratio of the disease and contribute to society.

Data Availability

All the data are included in the main text.

Conflicts of Interest

The authors declare no conflicts of interest.

References

[1] D. V. Wallace, M. S. Dykewicz, D. I. Bernstein et al., "The diagnosis and management of rhinitis: an updated practice parameter," *The Journal of Allergy and Clinical Immunology*, vol. 122, pp. S1–S84, 2008.

[2] A Noor, "A data-driven medical decision framework for associating adverse drug events with drug-drug interaction mechanisms," *Journal of Healthcare Engineering*, vol. 2022, Article ID 9132477, 7 pages, 2022 Mar 3.

[3] R. A Settipane, "Demographics and epidemiology of allergic and nonallergic rhinitis," *Allergy and Asthma Proceedings*, vol. 22, p. 185, 2001.

[4] K. Okubo, Y. Kurono, K. Ichimura et al., "Japanese Guidelines for Allergic Rhinitis," *Allergology International*, vol. 69, pp. 331–345, 2017.

[5] S. N. Shah, R. S. Gammal, M. G. Amato et al., "Clinical utility of pharmacogenomic data collected by a health-system Biobank to predict and prevent adverse drug events," *Drug Safety*, vol. 44, no. 5, pp. 601–607, 2021 May.

[6] D. A. Nguyen, C. H. Nguyen, and H. Mamitsuka, "A survey on adverse drug reaction studies: data, tasks and machine learning methods," *Briefings in Bioinformatics*, vol. 22, no. 1, pp. 164–177, 2021 Jan.

[7] C. Y. Lee and Y.-P. P. Chen, "Prediction of drug adverse events using deep learning in pharmaceutical discovery," *Briefings in Bioinformatics*, vol. 22, no. 2, pp. 1884–1901, 2021 Mar.

[8] A. Noor and A. Assiri, "A novel computational drug repurposing approach for Systemic Lupus Erythematosus (SLE) treatment using Semantic Web technologies," *Saudi Journal of Biological Sciences*, vol. 28, no. 7, pp. 3886–3892, 2021 Jul.

[9] H. Cao, Y. Rao, L. Liu et al., "The efficacy and safety of leflunomide for the treatment of lupus nephritis in Chinese patients: systematic review and meta-analysis," *PLoS One*, vol. 10, no. 12, Article ID e0144548, 2015 Dec 15.

[10] R. Naclerio, I. J. Ansotegui, J. Bousquet et al., "International expert consensus on the management of allergic rhinitis (AR) aggravated by air pollutants," *World Allergy Organization Journal*, vol. 13, no. 3, Article ID 100106, 2020 Mar 1.

[11] J Cheng, W. J Cai, and X. M Zhang, "Study on characteristic of syndrome differentiation and therapeutic methods of traditional Chinese medicine on allergic rhinitis," *China J Tradit Chin Med Pharm*, vol. 27, no. 7, pp. 1947–1950, 2012.

[12] L Du, X Ye, M Li et al., "Mechanisms of traditional Chinese medicines in the treatment of allergic rhinitis using a network biology approach," *J Tradit Chinese Med Sci*, vol. 8, pp. 82–89, 2021.

[13] R. P Siraganian, J Zhang, K Suzuki, and K Sada, "Protein tyrosine kinase Syk in mast cell signaling," *Molecular Immunology*, vol. 38, pp. 1229–1233, 2002.

[14] R. A Isbrucker and G. A Burdock, "Risk and safety assessment on the consumption of Licorice root (Glycyrrhiza sp.), its extract and powder as a food ingredient, with emphasis on

the pharmacology and toxicology of glycyrrhizin," *Regulatory Toxicology and Pharmacology*, vol. 46, pp. 167–192, 2006.

[15] G Ciprandi, M. A Tosca, C Cosentino, A. M Riccio, G Passalacqua, and G. W Canonica, "Effects of fexofenadine and other antihistamines on components of the allergic response: adhesion molecules," *The Journal of Allergy and Clinical Immunology*, vol. 112, pp. S78–S82, 2003.

[16] F Xu, S Yu, M Qin et al., "Hydrogen-Rich Saline Ameliorates Allergic Rhinitis by Reversing the Imbalance of Th1/Th2 and Up-Regulation of CD4+CD25+Foxp3+Regulatory T Cells, Interleukin-10, and Membrane-Bound Transforming Growth Factor-β in Guinea Pigs," *Inflammation*, vol. 41, pp. 81–92, 2018.

[17] N Flamand, J Lefebvre, M. E Surette, S Picard, and P Borgeat, "Arachidonic acid regulates the translocation of 5-lipoxygenase to the nuclear membranes in human neutrophils," *Journal of Biological Chemistry*, vol. 281, pp. 129–136, 2006.

[18] N.-G Gwak, E.-Y Kim, B Lee et al., "Xanthii Fructus inhibits allergic response in the ovalbumin-sensitized mouse allergic rhinitis model," *Pharmacognosy Magazine*, vol. 11, p. 352, 2015.

[19] S Han, L Sun, F He, and H Che, "Anti-Allergic activity of glycyrrhizic acid on IgE-mediated allergic reaction by regulation of allergy-related immune cells," *Scientific Reports*, vol. 7, pp. 1–9, 2017.

[20] T Liu, J Xu, Y Wu et al., "Beneficial effects of Baicalein on a model of allergic rhinitis," *Acta Pharm*, vol. 70, pp. 35–47, 2020.

[21] Y Jia, J Zou, Y Wang et al., "Mechanism of allergic rhinitis treated by Centipeda minima from different geographic areas," *Pharmacien Biologiste*, vol. 59, no. 1, pp. 604–616, 2021.

[22] Y. Lu, J. H. Yang, X. Li et al., "Emodin, a naturally occurring anthraquinone derivative, suppresses IgE-mediated anaphylactic reaction and mast cell activation," *Biochemical Pharmacology*, vol. 82, no. 11, pp. 1700–1708, 2011 Dec 1.

[23] S. Zhao and R. Iyengar, "Systems pharmacology: network analysis to identify multiscale mechanisms of drug action," *Annual Review of Pharmacology and Toxicology*, vol. 52, no. 1, pp. 505–521, 2012 Feb 10.

[24] S. H Hong, H. J Jeong, and H. M Kim, "Inhibitory effects of Xanthii fructus extract on mast cell-mediated allergic reaction in murine model," *Journal of Ethnopharmacology*, vol. 88, no. 2-3, pp. 229–234, 2003.

[25] H. J An, H. J Jeong, E. H Lee et al., "Xanthii Fructus Inhibits Inflammatory Responses in LPS-Stimulated Mouse Peritoneal Macrophages," *Inflammation*, vol. 28, no. 5, pp. 263–270, 2004.

[26] M. Y Song, E. K Kim, H. J Lee et al., "Fructus Xanthii extract protects against cytokine-induced damage in pancreatic β-cells through suppression of NF-κB activation," *International Journal of Molecular Medicine*, vol. 23, no. 4, pp. 547–553, 2009.

[27] C Bachert, M Jorissen, B Bertrand, N Khaltaev, and J Bousquet, "Allergic Rhinitis and its Impact on Asthma Update (ARIA 2008)," *The Belgian Perspective. Acta oto-rhino-laryngologica belgica*, vol. 4, no. 4, p. 253, 2008.

[28] T. Taylor-Clark, "Histamine in allergic rhinitis," *Advances in Experimental Medicine & Biology*, vol. 709, 2010.

[29] M. F Kramer, T. R Jordan, C Klemens et al., "Factors contributing to nasal allergic late phase eosinophilia," *Am J Otolaryngol - Head Neck Med Surg*, vol. 27, no. 3, pp. 190–199, 2006.

[30] T. Wynn, "Cellular and molecular mechanisms of fibrosis," *The Journal of Pathology*, vol. 214, no. 2, pp. 199–210, 2008 Jan.

[31] B Royer, S Varadaradjalou, P Saas et al., "Autocrine regulation of cord blood-derived human mast cell activation by IL-10," *The Journal of Allergy and Clinical Immunology*, vol. 108, pp. 80–86, 2001.

[32] M Stassen, C Müller, M Arnold et al., "IL-9 and IL-13 production by activated mast cells is strongly enhanced in the presence of lipopolysaccharide: NF-κB is decisively involved in the expression of IL-9," *The Journal of Immunology*, vol. 166, no. 7, pp. 4391–4398, 2001.

[33] D. P Skoner, "Allergic rhinitis: definition, epidemiology, pathophysiology, detection, and diagnosis," *The Journal of Allergy and Clinical Immunology*, vol. 108, no. 1, pp. S2–S8, 2001.

[34] L Borish, "Allergic rhinitis: systemic inflammation and implications for management," *The Journal of Allergy and Clinical Immunology*, vol. 112, no. 6, pp. 1021–1031, 2003.

[35] S. J Galli, M Tsai, and A. M Piliponsky, "The development of allergic inflammation," *Nature*, vol. 454, pp. 445–454, 2008.

[36] E. W Gelfand, "Inflammatory mediators in allergic rhinitis," *The Journal of Allergy and Clinical Immunology*, vol. 114, no. 5, pp. S135–S138, 2004.

[37] a Jr Jc, N York, and G Science, "The Structure of a Typical Antibody Molecule," *Immunobiology*, 2001.

[38] H Schäcke, W. D Döcke, and K Asadullah, "Mechanisms involved in the side effects of glucocorticoids," *Pharmacology & Therapeutics*, vol. 96, pp. 23–43, 2002.

[39] S. K Wise, S. Y Lin, E Toskala et al., "International consensus statement on allergy and rhinology: allergic rhinitis," *International forum of allergy & rhinology*, vol. 8, no. 2, pp. 108–352, 2018.

[40] K Rifai, G. I Kirchner, M. J Bahr et al., "A new side effect of immunosuppression: high incidence of hearing impairment after liver transplantation," *Liver Transplantation*, vol. 12, no. 3, pp. 411–415, 2006.

[41] H. H Zhu, Y. P Chen, J. E Yu, M Wu, and Z Li, "Therapeutic Effect of Xincang Decoction on Chronic Airway Inflammation in Children with Bronchial Asthma in Remission Stage," *Journal of Chinese Integrative Medicine*, vol. 3, pp. 23–27, 2005.

[42] J Bousquet, P Van Cauwenberge, and N Khaltaev, "Allergic rhinitis and its impact on asthma," *The Journal of Allergy and Clinical Immunology*, vol. 108, pp. S147–S334, 2001.

[43] T. M Cunha, J Talbot, L. G Pinto et al., "Caspase-1 is involved in the genesis of inflammatory hypernociception by contributing to peripheral IL-1β maturation," *Molecular Pain*, vol. 6, pp. 1744–8069, 2010.

[44] S. N Georas, J Guo, U De Fanis, and V Casolaro, "T-helper cell type-2 regulation in allergic disease," *European Respiratory Journal*, vol. 26, pp. 1119–1137, 2005.

[45] S. T Holgate and R Polosa, "Treatment strategies for allergy and asthma," *Nature Reviews Immunology*, vol. 8, no. 3, 2008.

[46] S. A Quraishi, M. J Davies, and T. J Craig, "Inflammatory responses in allergic rhinitis: traditional approaches and novel treatment strategies," *Journal of the American Osteopathic Association*, vol. 104, pp. S7–15, 2004.

[47] M. A. McGuckin, S. K. Lindén, P. Sutton, and T. H. Florin, "Mucin dynamics and enteric pathogens," *Nature Reviews Microbiology*, vol. 9, no. 4, pp. 265–278, 2011 Apr.

[48] E. Compalati, E. Ridolo, G. Passalacqua, F. Braido, E. Villa, and G. W. Canonica, "The link between allergic rhinitis and

asthma: the united airways disease," *Expert Review of Clinical Immunology*, vol. 6, no. 3, pp. 413–423, 2010 May 1.

[49] S. Yezli and J. A. Otter, "Minimum infective dose of the major human respiratory and enteric viruses transmitted through food and the environment," *Food and Environmental Virology*, vol. 3, no. 1, pp. 1–30, 2011 Mar.

[50] S. J. Galli and M. Tsai, "IgE and mast cells in allergic disease," *Nature Medicine*, vol. 18, no. 5, pp. 693–704, 2012 May.

[51] Y. H Kim, C. S Park, D. H Lim et al., "Anti-allergic effect of anti-Siglec-F through reduction of eosinophilic inflammation in murine allergic rhinitis," *Am J Rhinol Allergy*, vol. 27, pp. 187–191, 2013.

[52] A Stutz, D. T Golenbock, and E Latz, "Inflammasomes: too big to miss," *Journal of Clinical Investigation*, vol. 119, pp. 3502–3511, 2009.

[53] A. Noor, A. Assiri, S. Ayvaz, C. Clark, and M. Dumontier, "Drug-drug interaction discovery and demystification using Semantic Web technologies," *Journal of the American Medical Informatics Association*, vol. 24, no. 3, pp. 556–564, 2017 May 1.

[54] A Azzolina, A Bongiovanni, and N Lampiasi, "Substance P induces TNF-α and IL-6 production through NFκB in peritoneal mast cells," *Biochimica et Biophysica Acta (BBA) - Molecular Cell Research*, vol. 1643, pp. 75–83, 2003.

[55] F. J Zhang, Q Wang, Y Wang, and M. L Guo, "Anti-allergic effects of total bakkenolides from Petasites tricholobus in ovalbumin-sensitized rats," *Phyther Res*, vol. 25, pp. 116–121, 2011.

[56] S. I Mayr, R. I Zuberi, and F. T Liu, "Role of immunoglobulin E and mast cells in murine models of asthma," *Brazilian Journal of Medical and Biological Research*, vol. 36, pp. 821–827, 2003.

[57] J. M Lehman and M. S Blaiss, "Selecting the Optimal Oral Antihistamine for Patients with Allergic Rhinitis," *Drugs*, vol. 66, pp. 2309–2319, 2006.

[58] S. H. Sicherer and H. A. Sampson, "Food allergy: a review and update on epidemiology, pathogenesis, diagnosis, prevention, and management," *The Journal of Allergy and Clinical Immunology*, vol. 141, no. 1, pp. 41–58, 2018 Jan 1.

[59] T Tokiwa, K Harada, T Matsumura, and T Tukiyama, "Oriental medicinal herb, Periploca sepium, extract inhibits growth and IL-6 production of human synovial fibroblast-like cells," *Biological and Pharmaceutical Bulletin*, vol. 27, pp. 1691–1693, 2004.

[60] T. J Raphael and G Kuttan, "Effect of Naturally Occurring Triterpenoids Glycyrrhizic Acid, Ursolic Acid, Oleanolic Acid and Nomilin on the Immune System," *Phytomedicine*, vol. 10, pp. 483–489, 2003.

[61] M Vig and J. P Kinet, "Calcium signaling in immune cells," *Nature Immunology*, vol. 10, pp. 21–27, 2009.

[62] E Gumpricht, R Dahl, M. W Devereaux, and R. J Sokol, "Licorice compounds glycyrrhizin and 18β-glycyrrhetinic acid are potent modulators of bile acid-induced cytotoxicity in rat hepatocytes," *Journal of Biological Chemistry*, vol. 280, pp. 10556–10563, 2005.

[63] Y Tsujimura, K Obata, K Mukai et al., "Basophils play a pivotal role in immunoglobulin-G-mediated but not immunoglobulin-E-mediated systemic anaphylaxis," *Immunity*, vol. 28, pp. 581–589, 2008.

[64] M Bruno, F Piozzi, and S Rosselli, "Natural and hemisynthetic neoclerodane diterpenoids from Scutellaria and their antifeedant activity," *Natural Product Reports*, vol. 19, pp. 357–378, 2002.

[65] C. Li, G. Lin, and Z. Zuo, "Pharmacological effects and pharmacokinetics properties of Radix Scutellariae and its bioactive flavones," *Biopharmaceutics & Drug Disposition*, vol. 32, no. 8, pp. 427–445, 2011 Nov.

[66] H. B. Li and F Chen, "Isolation and purification of Baicalein, wogonin and oroxylin A from the medicinal plant Scutellaria baicalensis by high-speed counter-current chromatography," *Journal of Chromatography A*, vol. 1074, pp. 107–110, 2005.

[67] J Ming, L Zhuoneng, and Z Guangxun, "Protective role of flavonoid baicalin from Scutellaria baicalensis in periodontal disease pathogenesis: a literature review," *Complementary Therapies in Medicine*, vol. 38, pp. 11–18, 2018.

[68] S. B. Yoon, Y. J Lee, S. K Park et al., "Anti-inflammatory effects of Scutellaria baicalensis water extract on LPS-activated RAW 264.7 macrophages," *Journal of Ethnopharmacology*, vol. 125, pp. 286–290, 2009.

[69] C. S Chen, N. J Chen, L. W Lin, C. C Hsieh, G. W Chen, and M. T Hsieh, "Effects of Scutellariae Radix on gene expression in HEK 293 cells using cDNA microarray," *Journal of Ethnopharmacology*, vol. 105, pp. 346–351, 2006.

[70] J Choi, C. C Conrad, C. A Malakowsky, J. M Talent, C. S Yuan, and R. W Gracy, "Flavones from Scutellaria baicalensis Georgi attenuate apoptosis and protein oxidation in neuronal cell lines," *Biochimica et Biophysica Acta (BBA) - General Subjects*, vol. 1571, pp. 201–210, 2002.

[71] K Kang, Y. K Oh, R Choue, and S. J Kang, "Scutellariae radix extracts suppress ethanol-induced caspase-11 expression and cell death in N2a cells," *Molecular Brain Research*, vol. 142, pp. 139–145, 2005.

[72] G. R Schinella, H. A Tournier, J. M Prieto, P Mordujovich De Buschiazzo, and J. L Ríos, "Antioxidant activity of antiinflammatory plant extracts," *Life Sciences*, vol. 70, pp. 1023–1033, 2002.

[73] J. Zielonka and B. Kalyanaraman, "Hydroethidine- and MitoSOX-derived red fluorescence is not a reliable indicator of intracellular superoxide formation: another inconvenient truth," *Free Radical Biology and Medicine*, vol. 48, no. 8, pp. 983–1001, 2010 Apr 15.

[74] C.-L. Kuo, C.-W. Chi, and T.-Y. Liu, "The anti-inflammatory potential of berberine in vitro and in vivo," *Cancer Letters*, vol. 203, no. 2, pp. 127–137, 2004 Jan 1.

[75] W Tang, X Sun, J. S Fang, M Zhang, and N. J Sucher, "Flavonoids from Radix Scutellariae as Potential Stroke Therapeutic Agents by Targeting the Second Postsynaptic Density 95 (PSD-95)/disc Large/zonula Occludens-1 (PDZ) Domain of PSD-95," *Phytomedicine*, vol. 11, pp. 277–284, 2004.

[76] H. L Chung, G. G. L Yue, K. F To, Y. L Su, Y Huang, and W. H Ko, "Effect of Scutellariae Radix extract on experimental dextran-sulfate sodium-induced colitis in rats," *World Journal of Gastroenterology*, vol. 13, p. 5605, 2007.

[77] X. Shang, X. He, X. He et al., "The genus Scutellaria an ethnopharmacological and phytochemical review," *Journal of Ethnopharmacology*, vol. 128, no. 2, pp. 279–313, 2010 Mar 24.

[78] P. W Hellings and W. J Fokkens, "Allergic rhinitis and its impact on otorhinolaryngology," *Allergy Eur J Allergy Clin Immunol*, vol. 61, pp. 656–664, 2006.

[79] P. C Bahekar, J. H Shah, U. B Ayer, S. N Mandhane, and R Thennati, "Validation of Guinea pig model of allergic rhinitis by oral and topical drugs," *International Immunopharmacology*, vol. 8, pp. 1540–1551, 2008.

[80] C Cuppari, S Leonardi, S Manti et al., "Allergen immunotherapy, routes of administration and cytokine networks: an update," *Immunotherapy*, vol. 6, pp. 775–786, 2014.

[81] T. T Bui, C. H Piao, C. H Song, C. H Lee, H. S Shin, and O. H Chai, "Baicalein, wogonin, and Scutellaria baicalensis ethanol extract alleviate ovalbumin-induced allergic airway inflammation and mast cell-mediated anaphylactic shock by regulation of Th1/Th2 imbalance and histamine release," *Anat Cell Biol*, vol. 50, pp. 124–134, 2017.

[82] S. K Ku and J. S Bae, "Baicalin, Baicalein and wogonin inhibits high glucose-induced vascular inflammation in vitro and in vivo," *BMB Rep*, vol. 48, p. 519, 2015.

[83] Y Kim, S. B Kim, Y. J You, and B. Z Ahn, "Deoxypodophyllotoxin; the cytotoxic and antiangiogenic component from Pulsatilla koreana," *Planta Med*, vol. 68, pp. 271–274, 2002.

[84] X Luo, Z Yu, C Deng et al., "Baicalein ameliorates TNBS-induced colitis by suppressing TLR4/MyD88 signaling cascade and NLRP3 inflammasome activation in mice," *Scientific Reports*, vol. 7, pp. 1–14, 2017.

[85] E. Z. M. da Silva, M. C. Jamur, and C. Oliver, "Mast cell function," *Journal of Histochemistry and Cytochemistry*, vol. 62, no. 10, pp. 698–738, 2014 Oct.

[86] X. L Fan, Q. X Zeng, X Li et al., "Induced pluripotent stem cell-derived mesenchymal stem cells activate quiescent T cells and elevate regulatory T cell response via NF-κB in allergic rhinitis patients," *Stem Cell Research & Therapy*, vol. 9, 2018.

[87] T Iinuma, Y Okamoto, Y Morimoto et al., "Pathogenicity of memory Th2 cells is linked to stage of allergic rhinitis," *Allergy Eur J Allergy Clin Immunol*, vol. 73, pp. 479–489, 2018.

[88] R Noble and D Noble, "Harnessing Stochasticity: How Do Organisms Make Choices?" *Chaos: An Interdisciplinary Journal of Nonlinear Science*, vol. 28, Article ID 106309, 2018.

[89] J Cao and G Li, "Chemical constituents of Centipeda minima," *China Journal of Chinese Materia Medica*, vol. 37, no. 15, 2012.

[90] Z. G Liu, H. M Yu, S. L Wen, and Y. L Liu, "Histopathological study on allergic rhinitis treated with Centipeda minima," *Zhongguo Zhongyao Zazhi*, vol. 30, pp. 292–294, 2005.

[91] I. V. Yang, C. A. Lozupone, and D. A. Schwartz, "The environment, epigenome, and asthma," *The Journal of Allergy and Clinical Immunology*, vol. 140, no. 1, pp. 14–23, 2017 Jul 1.

[92] H. Lehman and C. Gordon, "The skin as a window into primary immune deficiency diseases: atopic dermatitis and chronic mucocutaneous candidiasis," *Journal of Allergy and Clinical Immunology: In Practice*, vol. 7, no. 3, pp. 788–798, 2019 Mar 1.

[93] K. Amin, "The role of mast cells in allergic inflammation," *Respiratory Medicine*, vol. 106, no. 1, pp. 9–14, 2012 Jan 1.

[94] M Murakami and I Kudo, "Diversity and regulatory functions of mammalian secretory phospholipase A2s," *Advances in Immunology*, vol. 77, pp. 163–194, 2001.

[95] E. S Masuda and J Schmitz, "Syk inhibitors as treatment for allergic rhinitis," *Pulmonary Pharmacology & Therapeutics*, vol. 21, pp. 461–467, 2008.

[96] R. P Siraganian, "Mast cell signal transduction from the high-affinity IgE receptor," *Current Opinion in Immunology*, vol. 15, pp. 639–646, 2003.

[97] C Tkaczyk and A. M Gilfillan, "FcεRI-dependent signaling pathways in human mast cells," *Clinical Immunology and Immunopathology*, vol. 99, pp. 198–210, 2001.

[98] "Proximal signaling events in FcεRI-mediated mast cell activation," *The Journal of Allergy and Clinical Immunology*, vol. 119, pp. 544–552, 2007.

[99] O. L Beong, H. L Jun, Y. K Na et al., "Polygoni Cuspidati radix inhibits the activation of syk kinase in mast cells for anti-allergic activity," *Experimental Biology and Medicine*, vol. 232, pp. 1425–1431, 2007.

[100] B. Yu, J. Sun, and X. Yang, "Assembly of naturally occurring glycosides, evolved tactics, and glycosylation methods," *Accounts of Chemical Research*, vol. 45, no. 8, pp. 1227–1236, 2012 Aug 21.

[101] Z. P Liu, W. X Li, B Yu et al., "Effects of trans-resveratrol from Polygonum cuspidatum on bone loss using the ovariectomized rat model," *Journal of Medicinal Food*, vol. 8, pp. 14–19, 2005.

[102] Z Zhang and B Yu, "Total synthesis of the anti-allergic naphtho-α-pyrone tetraglucoside, cassiaside C2, isolated from Cassia seeds," *Journal of Organic Chemistry*, vol. 68, pp. 6309–6313, 2003.

[103] Y. S Lee, O. H Kang, J. G Choi et al., "Synergistic effect of Emodin in combination with ampicillin or oxacillin against methicillin-resistant *Staphylococcus aureus*," *Pharmacien Biologiste*, vol. 48, pp. 1285–1290, 2010.

[104] S. K Heo, H. J Yun, W. H Park, and S. D Park, "Emodin inhibits TNF-α-induced human aortic smooth-muscle cell proliferation via caspase- and mitochondrial-dependent apoptosis," *Journal of Cellular Biochemistry*, vol. 105, pp. 70–80, 2008.

[105] S. Z Lin, K. J Chen, H. F Tong, H Jing, H Li, and S Zheng, "Emodin attenuates acute rejection of liver allografts by inhibiting hepatocellular apoptosis and modulating the Th1/Th2 balance in rats," *Clinical and Experimental Pharmacology and Physiology*, vol. 37, pp. 790–794, 2010.

[106] G Meng, Y Liu, C Lou, and H Yang, "Emodin suppresses lipopolysaccharide-induced pro-inflammatory responses and NF-κB activation by disrupting lipid rafts in CD14-negative endothelial cells," *British Journal of Pharmacology*, vol. 161, pp. 1628–1644, 2010.

[107] Y Feng, S. L Huang, W Dou et al., "Emodin, a natural product, selectively inhibits 11β-hydroxysteroid dehydrogenase type 1 and ameliorates metabolic disorder in diet-induced obese mice," *British Journal of Pharmacology*, vol. 61, p. 113, 2010.

[108] L. A Samayawardhena and C. J Pallen, "PTPα activates Lyn and Fyn and suppresses hck to negatively regulate FcεRI-dependent mast cell activation and allergic responses," *The Journal of Immunology*, vol. 185, pp. 5993–6002, 2010.

[109] D. D Metcalfe, R. D Peavy, and A. M Gilfillan, "Mechanisms of mast cell signaling in anaphylaxis," *The Journal of Allergy and Clinical Immunology*, vol. 124, pp. 639–646, 2009.

[110] L Fischer, D Poeckel, E Buerkert, D Steinhilber, and O Werz, "Inhibitors of actin polymerization stimulate arachidonic acid release and 5-lipoxygenase activation by upregulation of Ca2+ mobilization in polymorphonuclear leukocytes involving Src family kinases," *Biochimica et Biophysica Acta (BBA) - Molecular and Cell Biology of Lipids*, vol. 1736, pp. 109–119, 2005.

[111] O Werz, E Bürkert, B Samuelsson, O Rådmark, and D Steinhilber, "Activation of 5-lipoxygenase by cell stress is calcium independent in human polymorphonuclear leukocytes," *Blood*, vol. 99, pp. 1044–1052, 2002.

[112] J. K Son, M. J Son, E Lee et al., "Ginkgetin, a biflavone from Ginko biloba leaves, inhibits cyclooxygenases-2 and 5-lipoxygenase in mouse bone marrow-derived mast

Hindawi
Journal of Healthcare Engineering
Volume 2023, Article ID 9815494, 1 page
https://doi.org/10.1155/2023/9815494

Retraction

Retracted: Research on the Mechanism of HMGB1 Regulating Autoimmune Encephalomyelitis by Regulating NF-κB

Journal of Healthcare Engineering

Received 23 May 2023; Accepted 23 May 2023; Published 24 May 2023

This article has been retracted by Hindawi following an investigation undertaken by the publisher [1]. This investigation has uncovered evidence of one or more of the following indicators of systematic manipulation of the publication process:

(1) Discrepancies in scope
(2) Discrepancies in the description of the research reported
(3) Discrepancies between the availability of data and the research described
(4) Inappropriate citations
(5) Incoherent, meaningless and/or irrelevant content included in the article
(6) Peer-review manipulation

The presence of these indicators undermines our confidence in the integrity of the article's content and we cannot, therefore, vouch for its reliability. Please note that this notice is intended solely to alert readers that the content of this article is unreliable. We have not investigated whether authors were aware of or involved in the systematic manipulation of the publication process. Wiley and Hindawi regrets that the usual quality checks did not identify these issues before publication and have since put additional measures in place to safeguard research integrity.

We wish to credit our own Research Integrity and Research Publishing teams and anonymous and named external researchers and research integrity experts for contributing to this investigation.

The corresponding author, as the representative of all authors, has been given the opportunity to register their agreement or disagreement to this retraction. We have kept a record of any response received.

References

[1] L. Liu, J. Pang, H. Yuan et al., "Research on the Mechanism of HMGB1 Regulating Autoimmune Encephalomyelitis by Regulating NF-κB," *Journal of Healthcare Engineering*, vol. 2022, Article ID 9900916, 11 pages, 2022.

Hindawi
Journal of Healthcare Engineering
Volume 2022, Article ID 9900916, 11 pages
https://doi.org/10.1155/2022/9900916

Research Article

Research on the Mechanism of HMGB1 Regulating Autoimmune Encephalomyelitis by Regulating NF-κB

Lijuan Liu,[1] Jingtao Pang,[2] Hui Yuan,[2] Shengnu Qiu,[3] Wei Zhang,[2] Zhenzhu Shang,[2] and Xiaoting Liu[2]

[1]*The Third Department of Neurology, People's Hospital of Gaomi, Weifang, China*
[2]*Second Department of Encephalopathy, Weifang Hospital of Traditional Chinese Medicine, Weifang, China*
[3]*Division of Biosciences, Faculty of Life Sciences, University College London, London, UK*

Correspondence should be addressed to Xiaoting Liu; xiaotingliu2022@163.com

Received 10 February 2022; Revised 9 March 2022; Accepted 15 March 2022; Published 11 April 2022

Academic Editor: Liaqat Ali

Background. Autoimmune encephalomyelitis is a clinical condition in which memory and cognition is affected badly and is also associated with lower levels of consciousness or even coma in worse scenarios. It is a noninfectious condition which involves immune oriented inflammation. *Objective*. The study's goal was to figure out what was causing the problem HMGB1 involved in regulating the autoimmune encephalomyelitis by regulating NF-κB. *Materials and Methods*. The expressions of HMGB1, miR-129-5p, and TLR4/NF-κB signalling pathway-related proteins were measured by qRT-PCR. To explore the differences among its control, models, and all groups, histopathology, immunohistochemistry, and immunofluorescence tests were performed. *Results*. According to the findings, miR-129-5p is in charge of suppressing HMGB1 production and inhibiting the TLR4/NF-κB signalling pathway. On development of autoimmune encephalomyelitis, neurons in the hippocampus area got injured in the miR-129-5p inhibitors class. In the miR-129-5p inhibitor class, expression of miR-129-5p reduced and HMGB1 elevated, increasing neuronal inflammation and damage. Impairment in the hippocampus, on the either side, was shown to be reduced in HMGB1 shRNA, miR-129-5p mimics, and TLR4/NF-κB classes. *Conclusion*. According to the study's findings, there is indeed a link among increased miR-129-5p and decreased HMGB1 expression and also suppression of the TLR4/NF-κB signal transduction pathway in autoimmune encephalomyelitis in the miR-129-5p inhibitors group. As a result, we may assume the autoimmune disease illness has progressed once concentrations of HMGB1, TLR4/NF-κB, and miR-129-5p have decreased.

1. Introduction

EAE (experimental autoimmune encephalomyelitis) is a CNS autoimmune illness that is utilized as a model for studying sclerosis and abnormalities in individuals [1]. New clinical therapies have elaborated the emergence of autoimmune encephalomyelitis on the basis of autoantibodies linked to the nervous tissues. Most patients who had a good outcome were promptly diagnosed and treated. Limbic encephalitis is a prominent feature in the clinical phenotypes of autoimmune encephalomyelitis–AEM. Other features are behavior changes, disabled cognition, and seizures. Combination of cerebellar symptoms, optic neuritis, brainstem linked lesions, and myelitis are reported largely.

Autoimmune encephalomyelitis is an inflammatory condition which is immune-mediated and leads to dysfunction in the CNS [2, 3]. A nonneoplastic condition is usually triggered by environmental or hereditary factors.

NF-κB (nuclear factor-κB) is a transcription factor which is responsible for regulating large array genes linked in various processes associated with the immune system and inflammatory responses [4]. The activation of NF-κB factor is linked to two main signalling pathways which are canonical and noncanonical pathways. Eventhough both have different mechanisms, but both are crucial for regulation of the inflammatory and immune responses [5, 6]. miR-129-5p, which targets the high-mobility group box 1 protein (HMGB1), has been shown to reduce renal fibrosis, according to Li Y et al. (Li et al., 2015). miR-129-5p may play a crucial role in AE-related epilepsy by regulating the TLR4/NF-κB signalling pathway and particularly targeting HMGB1, as indicated earlier. In this study, we consequently aimed to identify the mechanism of HMGB1 involved in regulating the autoimmune encephalomyelitis by regulating NF-κB.

2. Objective of Study

This study looked at the role of microRNA-129-5p (miR-129-5p) in the progression of autoimmune encephalomyelitis. A rat paradigm was used to identify HMGB1 targeted via the TLR4/NF-κB signal transduction pathway. The miR-129-5p expression and its association with inflammation, reduction of expression, apoptosis, reduction in proliferation, differentiation, and neuronal growth were evaluated.

3. Materials and Methods

3.1. Animal Selection. 70 Wistar rats, aged 10–12 weeks, have been used in this investigation, which were acquired from China Medical University's animal facility (Shenyang, China). The Laboratory Animal Ethical Committee approved the results of the experiment. Furthermore, 10 rats were included in the control group, while other random selections were selected for the induction of autoimmune encephalomyelitis via the animal model. Prior to any study, animals were permitted to acclimatize in a quality cage and were assigned unbound access to food and water. Before any therapy or surgery, a thermostat of 22–24°C was preserved, as well as a 12-hour light/dark cycle. The international guidelines for defense and analysis of pain in the laboratory animals were followed strictly. In the experimental study, the animals were divided as given in Table 1.

3.2. Establishment of the Autoimmune Encephalomyelitis Model. Wistar rats selected for the diseased group were injected subcutaneously with 0.06 ml/100 g of antigen emulsion. In the region near pad of the rear foot, a needle was inserted at 2/3 different positions for every injection leading to formation of a small bump near the foot pad. At same time, 0.05 ml pertussis bacilli (from Beijing Institute of Microbiology and Epidemiology, China) was injected intradermally in the back region of the foot pad. The region of injection was disinfected with alcohol. Immunization procedure was performed twice with a gap period of 7 days.

The behavior of rats was assessed postsensitization in accordance with the 5 criteria method via a blind study [7]. Here, 0, no sign of clinical symptom; 1, tail tension disappearance, awkward walking; 2, rear limb (weak); 3, paralysis in rear limbs; 4, hind limb paralysis/forelimb paralysis or weak muscles; 5, dead or dying. In between, symptoms were labeled via ±0.05. In the experiments conducted for the autoimmune encephalomyelitis paradigm sick class, rats scoring in the region of 2-3 were included [7].

3.3. Obtaining Tissues from Animal Models. Sections from tissues were collected after 24 hours postestablishment of the autoimmune encephalomyelitis model. Rats from both groups were anesthetized using 3 ml/kg pentobarbital sodium. The chest walls of animals were cut thus exposing the heart open. Postthoracotomy, a canula was fit in for opening aorta via ventricle (left). Furthermore, cannula implementation was performed for draining blood with help of ophthalmic scissors. Washing of the vessels was done with help of 150 ml 0.9% NaCl solution. Animals were injected with 4% polyformaldehyde fixing solution i.v at 8–10 ml/min.

After 30 minutes of the process, the body turned stiff. Heads of the rats were decapitated and kept in 0.9% NaCl for 2.5 hours. A blunt dissection was done on the right brain to isolate tissues from the hippocampal region. The sections were kept in at −80°C for IHC, histopathology, Western blotting, and qRT-PCR.

3.4. Immunohistochemistry and Immunofluorescence Analysis. Immunohistochemical histochemistry (IHC) was performed for analysis of tissue segments obtained from hippocampal region of the brain. The sections were implanted in paraffin followed by slicing into 5 μm wide slides. Furthermore, these sections were deparaffinized followed by the dehydration by implementing graded alcohols. These slices were incubated for duration of fifteen minutes in a portion of 3% hydrogen peroxide in an ambient temperature (room temperature approx. 20°C) and blocked for 30 minutes in bovine serum.

The staining of the slides was done overnight at 40°C using antibody against caspase-3 (Thermo Fisher, USA). After this process, these sliced sections were further incubated for peripheral antibodies (Thermo Fisher, USA). For duration of three minutes, the immune-reactive sections were stained using diaminobenzidine (DAB) as well as covered using a cover slip. Slides were analyzed under a light microscope (Leica Microsystems) with 20x and 100x magnification.

Immunofluorescent analysis was performed on sections obtained from hippocampus. Furthermore, these sections were cleansed using the phosphate buffer saline followed by fixing for fifteen minutes in 4% paraformaldehyde, followed by blocking the sections in 5% BSA at an ambient temperature for duration of sixty minutes. Incubation with primary antibodies caspase-3 (Thermo Fisher, USA) was done at a temperature of 4°C night. The immediate day followed the incubation of the solution using the peripheral antibodies (Sigma Aldrich). Imaging of the tissues was performed postfluorescent staining and also identification of biomarkers such as caspase, NeUN, BrdU, and GFAP.

3.5. Assay for miRNA Microarrays. RNA was extracted from sections of the brain with help of the RNA extraction kit (Lexogen) in complete accordance to protocols. RNA was then quantified using the NanoDrop 8000 spectrophotometer (Thermo Fisher Scientific, USA). A total of 250 ng RNA was labeled using fluorescent dye HY5 with help of the

Table 1: Experimental design.

S. no.	Group number	Treatment type	Number of animals (n)
1	I	Control group	10
2	II	Model group	10
3	III	miR-129-5p mimic group	10
4	IV	miR-129-5p inhibitor	10
5	V	HMGB1 shRNA	10
6	VI	TLR4/NF-κB group	10
7	VII	miR-129-5p mimics + HMGB1 shRNA group	10

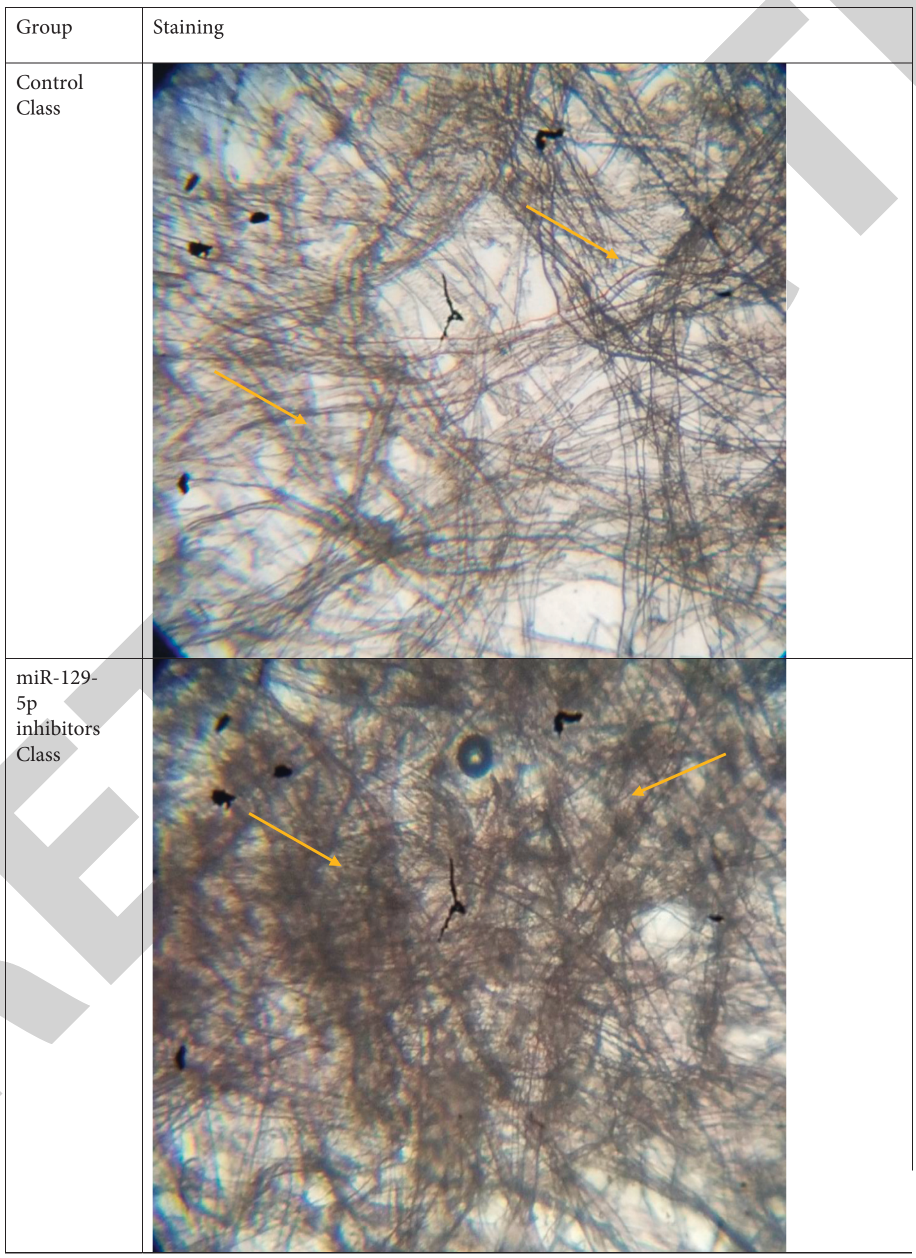

Figure 1: Histopathological analysis of the hippocampal region sectioned from the control and miR-129-5p inhibitors class.

Qubit™ microRNA Assay Kit (Thermo Fisher Scientific, USA). The labelling kit and hybridization of LNA array was designed in basis of miRBase 22, which contained probes of mice, rats, and humans.

3.6. Implementing qRT-PCR. The isolated RNA accumulation was performed followed by reverse transcription implementing the TaqMan MicroRNA (ThermoFisher) Reverse Transcription kit. The reaction system was used with

Group	Staining	
Control Group	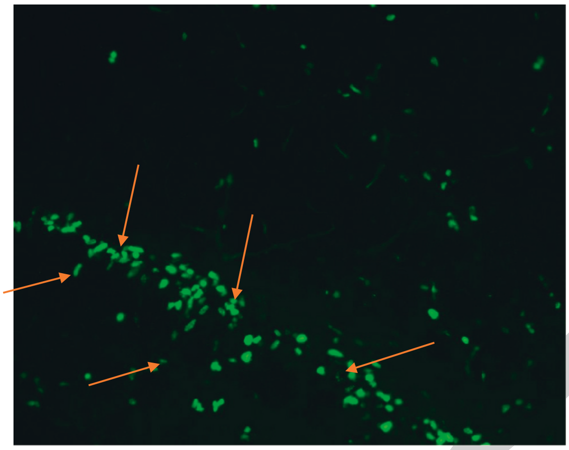	BrDU
	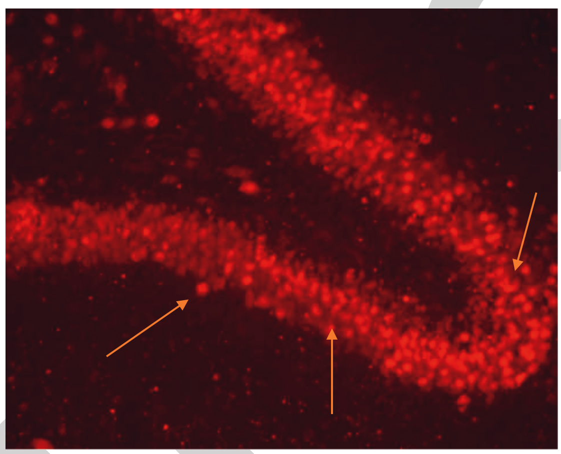	NeUN

Figure 2: Continued.

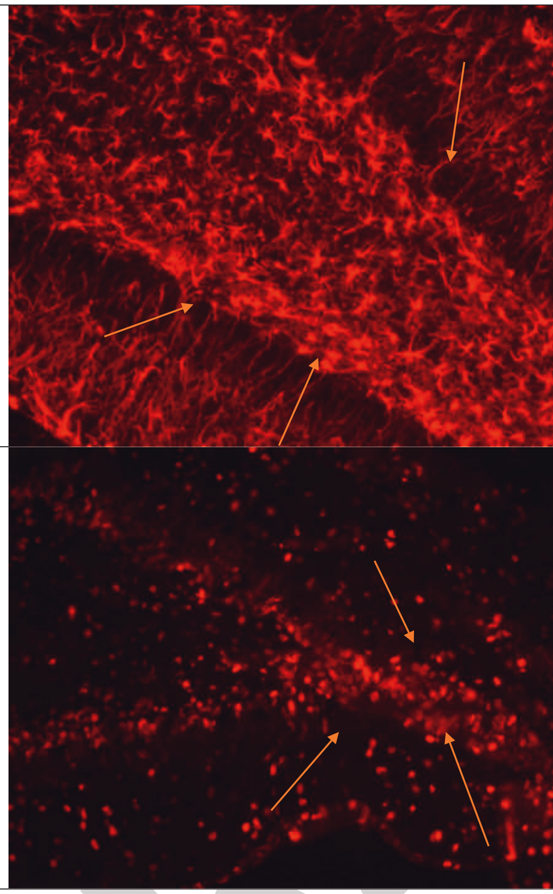

GFAP

CASPASE

Figure 2: Continued.

Group	Staining	
miR-129-5p inhibitors group	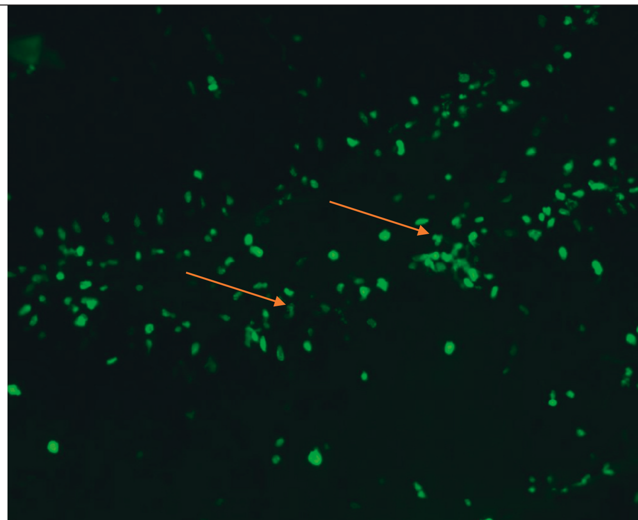	BrDU
	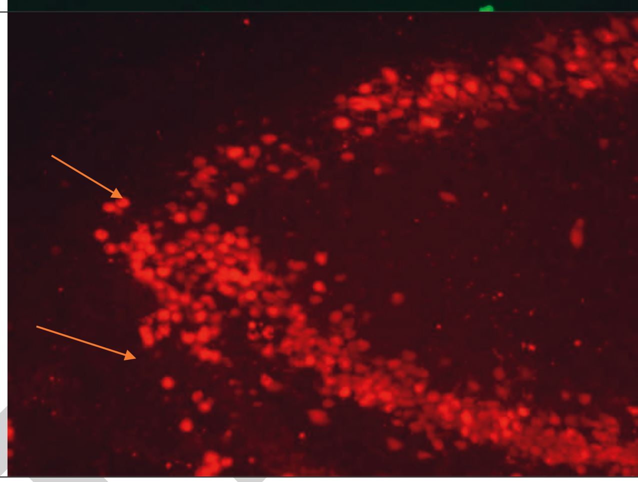	NeUN

Figure 2: Continued.

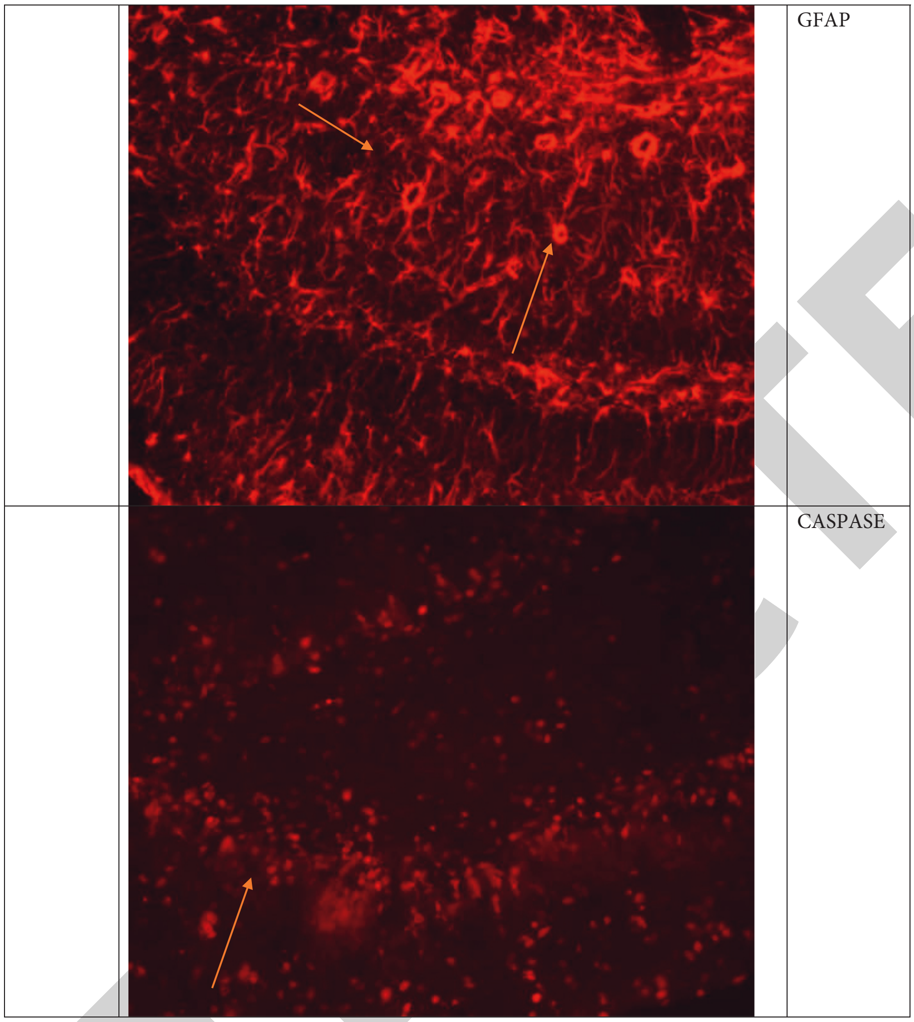

Figure 2: Immunofluorescent staining of the tissue section by antibodies for identification of biomarkers BrdU, NeUN, GFAP, and caspase.

15 μl; the conditions were maintained at 16°C for 30 minutes, 42°C for 30 min, and 85°C at 5 min. Samples were added in 5 wells. 1 gRNA was employed to make cDNA, and β-actin was employed as an internal control. The 2-Ct technique was used to identify relative quantity. To acquire the overall average, each test was done.

The primer sequence for HMGB1 was forward: 5′-AAGGAGAACATCCTGGCCTGTC-3’; reverse: 5′-TCCCAGTTTCTTCGCAACATCA-3’ and for NF-κB was forward: 5′-GCATTCTGACCTTGCCTATCT-3′; reverse: 5′-CTCCAGTCTCCGAGTGAAGC-3’. These experiments were individually carried out in a triplicate order for a final average value [8].

3.7. Western Blotting. In the hippocampal tissues isolated from all groups, a through washing done by the PBS (phosphate buffer saline) group was done using protease inhibitor. The blend was shivered at a temperature of 4°C for duration of five minutes followed by centrifugation (12000 ×g) for around ten minutes at a temperature of 4°C. The collection of supernatant fluid is performed for the protein extraction. TLR4 (Abcam, rabbit polyclonal, ab150583) and NF-κB (Abcam, rabbit monoclonal, ab32536) primary monoclonal antibodies were used to incubate the membrane overnight (1 : 1200).

3.8. Statistical Analysis. SPSS 21.0 (SPSS Inc., IL, USA) was the tool implemented for statistical analysis. The data were portrayed in terms of mean ± standard deviation. A comparative assessment between both groups was performed using the t-test. $P < 0.05$ was counted as statistically significant.

4. Results

According to the results of the experiments, the neurological injury (Figures 1–3) has been most commonly recorded in the miR-129-5p blocker class, where the neuronal in the rats' hippocampal were badly injured. In classes III, V, VI, VII, the miR-129-5p mimics group, HMGB1 shRNA, and miR-

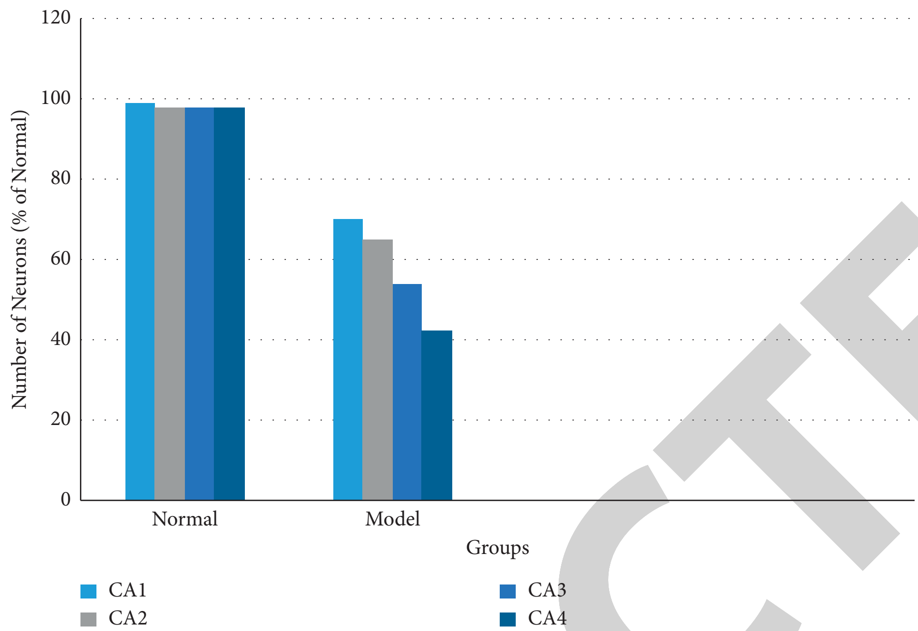

Figure 3: Percentage of normal neurons among various regions of the hippocampus in rat brain.

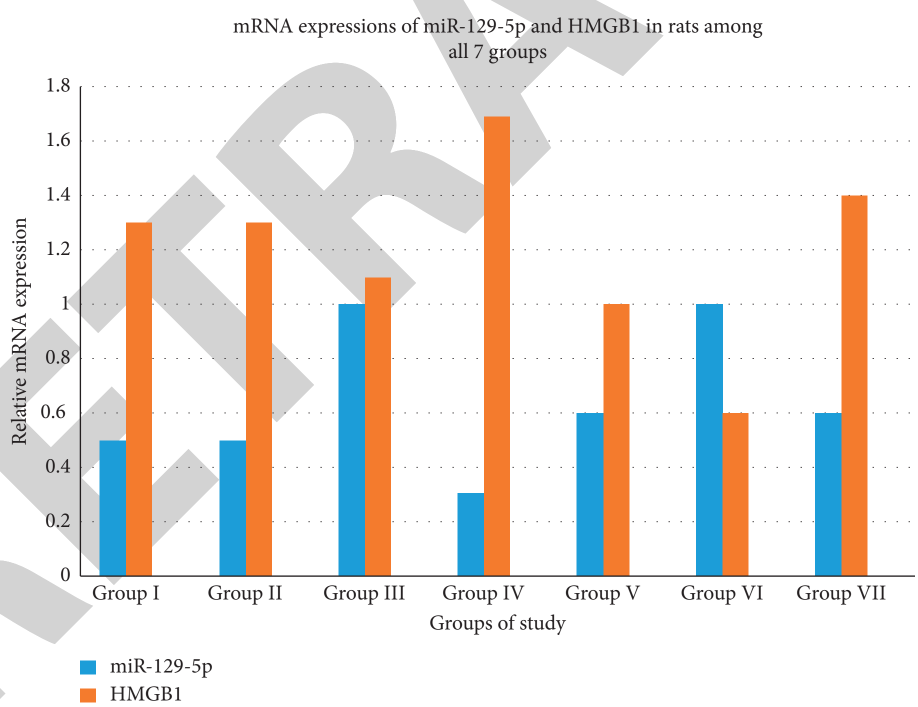

Figure 4: miR-129-5p and HMGB1 mRNA expressions in all groups.

129-5p mimics + HMGB1 shRNA class, the damages were found to be minor.

In each of the seven experimental classes, the mRNA expression of miR-129-5p and HMGB1 was examined. The finding indicated that the outcomes of the controls and TLR4/NF-κB classes were not significantly different ($P > 0.05$). The expressions of miR-129-5p in the miR-129-5p mimic + HMGB1 and miR-129-5p mimics classes, but at the other extreme, were higher than the control class (P0.05), as shown in Figure 4.

When compared to the control group and the model class, the detected expression of HMGB1 mRNA in the miR-129-5p mimics class, HMGB1 shRNA, and miR-129-5p mimics + HMGB1 shRNA class was statistically meaningful (all P0.05). The transcription of miR-129-5p was considerably lower in the miR-129-5p inhibitory league compared

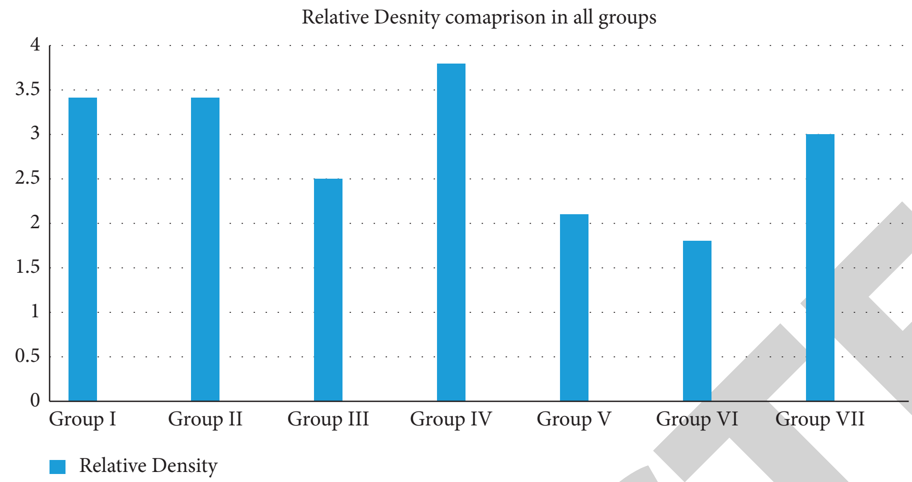

Figure 5: Comparative assessment of HMGB1 protein expressions in rats among all groups.

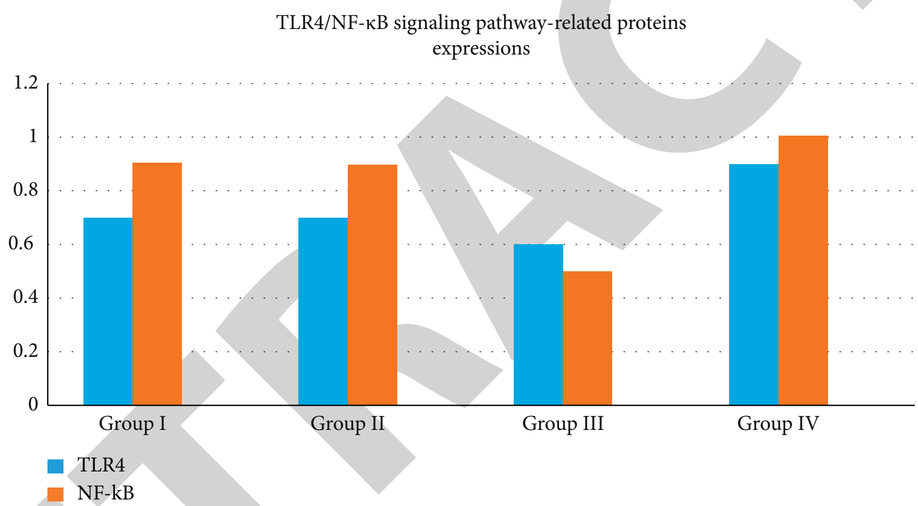

Figure 6: TLR4/NF-κB signalling pathway-associated proteins expression in all groups.

to the deterministic model (P0.05), whereas the expression of HMGB1mRNA was way greater in the miR-129-5p inhibitor class compared with the control group, prototype category (P0.05).

The expression of miR-129-5p and HMGB mRNA was shown to be inversely linked, with miR-129-5p overexpression suppressing the expression of HGMB1. The expression of mRNA HMGB1 was constant across all seven classes, according to Western blotting. The expression of HMGB1 was not substantially different in the control, TLR4/NF-κB, and model groups ($P > 0.05$). When compared to the control, prototype category, HMGB1 expressions were observed to be lower in the miR-129-5p mimics group, shRNA group, and miR-129-5p mimics + HMGB1 shRNA class (P0.05) (Figure 5).

The mRNA expression of TLR4/NF-κB related proteins was shown to be steady. The obtained expressions of proteins associated with the TLR4/NF-κB signalling pathway were not statistically significant when P0.05 was used. There was a significant drop in TLR4/NF-κB protein expression when miR-129-5p mimics, HMGB1 shRNA, and miR-129-5p mimics + HMGB1 shRNA classes were compared to the reference and model classes ($P > 0.05$) [9]. The miR-129-5p inhibitors class highly (P0.05) mirrored high levels of mRNA expressions of TLR4/NF-κB associated proteins, as shown in Figure 6 [10], (Figure 7).

Dense fibers were noted in the miR-129-5p inhibitors class in contrast to the normal group which might be due to initial inflammation subjected to evolution of autoimmune encephalomyelitis.

BrdU: this marker was responsible for identification of the generation and proliferation of neuronal cells in both control and miR-129-5p inhibitor groups. It also denotes the neuroprogenitors emerging in the BrdU injection period thus helping in evaluation of inflammation and damage. The proliferation of new formed neurons was visualized by the process of immunostaining for the marker BrdU which identifies proliferation of neurons. Expressions of BrdU were higher in control groups in contrast with the miR-129-5p inhibitors class in the hippocampal sections; thus, it can be interpreted that the proliferation declined in miR-129-5p inhibitor class. Thus, the conclusion obtained signified the

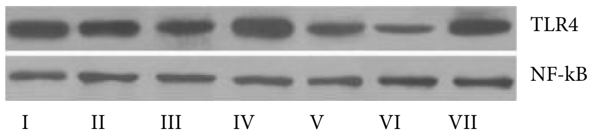

Figure 7: Expressions of TLR4/NF-κB signalling pathway-associated proteins semiquantified.

reduction in proliferation in experimental autoimmune encephalomyelitis.

Caspase: detection of dense caspase signifies of cell death via apoptosis. The domination of caspase was noted in the miR-129-5p inhibitor class, while caspase was found to be not significant in the control class. Hence, it was interpreted that inflammation due to EAE leads to early apoptosis in the hippocampal region of the brain.

NeUN: NeUN is marker for differentiation of neurons. It is mainly expressed in nuclei of most neurons. A decrease in NeUN was noted in the miR-129-5p inhibitor class, thereby signifying the degeneration as well as inflammation due to encephalomyelitis in hippocampal region of the brain.

GFAP: it is an astrocyte marker of the protein present in the neurons. In the control group, GFAP was found significant. The immune system addressed the glial fibrillary acidic proteins in the miR-129-5p inhibitor family, resulting in a decrease in their density.

5. Discussion

When compared to the control and model groups, the expression of TLR4/NF-κB group signalling pathway-related proteins in the HMGB1 shRNA category, TLR4/NF-κB group, miR-129-5p mimics group, and miR-129-5p mimics + HMGB1 shRNA group dropped, while those in the miR-129-5p inhibitors team elevated.

This study's preliminary findings confirmed the hypothesis that miR-129-5p expression improved in the miR-129-5p mimics and miR-129-5p mimics + HMGB1 shRNA groups when compared to the control and model groups. The levels of HMGB1 mRNA and protein expression in the HMGB1 shRNA, miR-129-5p mimics, and miR-129-5p mimics + HMGB1 shRNA groups, on the other hand, decreased. This revealed a negative relationship between miR-129-5p and HMGB1, as well as the possibility of miR-129-5p overexpression suppressing HMGB1 production.

HMGB1-induced stimulation of the TL4/NF-κB signal transduction pathway has also been identified as a critical stimulator of the cellular response to neuronal damage in vitro and in vivo, according to a recent research study. Studies have extensively posited a role for the HMGB1-TLR4/NF-κB interplay in enabling the neuroprotection in preclinical animals of seizures and further proposed that upregulation of HMGB1 was likely to be an intrinsic activator of the TLR4/NF-κB signalling pathway, which may advantage the remedy of neurodegeneration as well as neuroinflammatory illnesses, which is line with the observations of our study [10, 11], (Wang et al., 2010).

6. Conclusion

The study concludes by claiming that there is compelling evidence that miR-129-5p expression suppresses the TLR4/NF-κB signalling cascade and HMGB1 transcription, therefore inhibiting the progression of autoimmune encephalomyelitis. It was also discovered because when miR-129-5p is repressed, the levels of HMGB1 and TLR4/NF-κkB are elevated, meaning that when miR-129-5p is suppressed, the levels of HMGB1 and TLR4/NF-κB are elevated in autoimmune encephalomyelitis. This must be viewed as a feasible aim in generating new therapy alternatives and acquiring a better knowledge of the illness.

Abbreviations

NF-κB:	Nuclear factor-κB
miR-129-5p:	MicroRNA-129-5p
AE:	Autoimmune encephalomyelitis
EAE:	Experimental autoimmune encephalomyelitis
CNS:	Central nervous system
Caspases:	Cysteine-aspartic proteases
NeUN:	Hexaribonucleotide binding protein-3
GFAP:	Glial fibrillary acidic protein
HMGB1:	High-mobility group box 1 protein.

Data Availability

The data used to support the findings of this study are available from the corresponding author upon request.

Conflicts of Interest

The authors declare that they have no conflicts of interest.

References

[1] P. Y. Paterson and R. H. Swanborg, "Demyelinating diseases of the central and peripheral nervous systems," *Immunological diseases*, vol. 4, pp. 1877–1916, 1988.

[2] A. Venkatesan and D. R. Benavides, "Autoimmune encephalitis and its relation to infection," *Current Neurology and Neuroscience Reports*, vol. 15, no. 3, p. 3, 2015.

[3] A. Kunze, R. Drescher, K. Kaiser, M. Freesmeyer, O. W. Witte, and H. Axer, "Serial FDG PET/CT in autoimmune encephalitis with faciobrachial dystonic seizures," *Clinical Nuclear Medicine*, vol. 39, no. 10, pp. e436–e438, 2014.

[4] A. Oeckinghaus and S. Ghosh, "The NF-B family of transcription factors and its regulation," *Cold Spring Harbor Perspectives in Biology*, vol. 1, no. 4, Article ID a000034, 2009.

[5] S.-C. Sun, "Non-canonical NF-κB signaling pathway," *Cell Research*, vol. 21, no. 1, pp. 71–85, 2011.

[6] S. Vallabhapurapu and M. Karin, "Regulation and function of NF-κB transcription factors in the immune system," *Annual Review of Immunology*, vol. 27, no. 1, pp. 693–733, 2009.

[7] I. M. Stromnes and J. M. Goverman, "Active induction of experimental allergic encephalomyelitis," *Nature Protocols*, vol. 1, no. 4, pp. 1810–1819, 2006.

[8] K. J. Livak and T. D. Schmittgen, "Analysis of relative gene expression data using real-time quantitative PCR and the 2−ΔΔCT method," *Methods*, vol. 25, no. 4, pp. 402–408, 2001.

Hindawi
Journal of Healthcare Engineering
Volume 2023, Article ID 9832729, 1 page
https://doi.org/10.1155/2023/9832729

Retraction

Retracted: Optimization and Evaluation of an Intelligent Short-Term Blood Glucose Prediction Model Based on Noninvasive Monitoring and Deep Learning Techniques

Journal of Healthcare Engineering

Received 23 May 2023; Accepted 23 May 2023; Published 24 May 2023

This article has been retracted by Hindawi following an investigation undertaken by the publisher [1]. This investigation has uncovered evidence of one or more of the following indicators of systematic manipulation of the publication process:

(1) Discrepancies in scope
(2) Discrepancies in the description of the research reported
(3) Discrepancies between the availability of data and the research described
(4) Inappropriate citations
(5) Incoherent, meaningless and/or irrelevant content included in the article
(6) Peer-review manipulation

The presence of these indicators undermines our confidence in the integrity of the article's content and we cannot, therefore, vouch for its reliability. Please note that this notice is intended solely to alert readers that the content of this article is unreliable. We have not investigated whether authors were aware of or involved in the systematic manipulation of the publication process. Wiley and Hindawi regrets that the usual quality checks did not identify these issues before publication and have since put additional measures in place to safeguard research integrity.

We wish to credit our own Research Integrity and Research Publishing teams and anonymous and named external researchers and research integrity experts for contributing to this investigation.

The corresponding author, as the representative of all authors, has been given the opportunity to register their agreement or disagreement to this retraction. We have kept a record of any response received.

References

[1] Y. Zhang and G. Gao, "Optimization and Evaluation of an Intelligent Short-Term Blood Glucose Prediction Model Based on Noninvasive Monitoring and Deep Learning Techniques," *Journal of Healthcare Engineering*, vol. 2022, Article ID 8956850, 16 pages, 2022.

Hindawi
Journal of Healthcare Engineering
Volume 2022, Article ID 8956850, 16 pages
https://doi.org/10.1155/2022/8956850

Research Article

Optimization and Evaluation of an Intelligent Short-Term Blood Glucose Prediction Model Based on Noninvasive Monitoring and Deep Learning Techniques

Yongjun Zhang [1,2] and Guangheng Gao [3]

[1] *School of Information Engineering, Shandong Youth University of Political Science, Jinan, China*
[2] *Key Laboratory of Intelligent Information Processing and Information Security in Universities of Shandong, Jinan, China*
[3] *Biology Institute, Qilu University of Technology(Shandong Academy of Sciences), Key Laboratory for Biosensors of Shandong Province, Jinan, China*

Correspondence should be addressed to Yongjun Zhang; yongjunzhang@sdyu.edu.cn

Received 14 February 2022; Accepted 18 March 2022; Published 11 April 2022

Academic Editor: Liaqat Ali

Continuous noninvasive blood glucose monitoring and estimation management by using photoplethysmography (PPG) technology always have a series of problems, such as substantial time variability, inaccuracy, and complex nonlinearity. This paper proposes a blood glucose (BG) prediction model for more precise prediction based on BG series decomposition by complete aggregation empirical mode decomposition based on adaptive white noise (CEEMDAN) and the gated recurrent unit (GRU) that is optimized by improved bacterial foraging optimization (IBFO). Hierarchical clustering technology recombines the decomposed BG series according to their sample entropy and the correlations with the original BG trends. Dynamic BG trends are regressed separately for each recombined BG series by the GRU model to realize the more precise estimations, which are optimized by IBFO for its structure and superparameters. Through experiments, the optimized and basic LSTM, RNN, and support vector regression (SVR) are compared to evaluate the performance of the proposed model. The experimental results indicate that the root mean square error (RMSE) and mean absolute percentage error (MAPE) of the 15-min IBFO-GRU prediction is improved on average by about 13.1% and 18.4%, respectively, compared with those of the RNN and LSTM optimized by IBFO. Meanwhile, the proposed model improved the Clarke error grid results by about 2.6% and 5.0% compared with those of the IBFO-LSTM and IBFO-RNN in 30-min prediction and by 4.1% and 6.6% in 15-min ahead forecast, respectively. The evaluation outcomes of our proposed CEEMDAN-IBFO-GRU model have high accuracy and adaptability and can effectively provide early intervention control of the occurrence of hyperglycemic complications.

1. Introduction

Diabetes is a hyperglycemia disorder with abnormal glucose metabolism. According to the data from the WHO, there are about 450 million diabetic patients worldwide [1, 2]. By 2045, this figure may reach 700 million. The gradual maturity of continuous glucose monitoring (CGM) technology has dramatically prevented BG-related syndromes in recent years. However, the BG concentration time series includes time-variation, nonlinearity, and instability [3]. It has seriously affected the accuracy of BG level estimation and restricted the closed-loop control performance of the artificial pancreas [4].

At present, the continuous BG trend prediction systems with high and low BG alarm lines to generate timely warnings always have different degrees of deviation [5, 6]. The reason is that the injected insulin takes a particular time to reduce the BG levels. The human body consumes carbohydrates to maintain the normal physiological state by maintaining a reasonable BG level. Therefore, it is necessary to accurately predict BG levels to effectively avoid abnormal BG events in the short period ahead and ensure complementary treatment within the valid time range. If the BG prediction deviates from the actual BG trends, it will lead to a false BG alarm, which will lead to making an approximate amount of insulin injection and cannot alleviate adverse symptoms of abnormal BG changes well, even endangering the safety of patients.

With the development of noninvasive sensing and deep learning techniques, researchers use BG and other data indicators obtained by various sensors to build a data-driven BG prediction model for accurate and timely prediction of abnormal BG trends [7–11]. Alia et al. [12] constructed a blood glucose prediction model based on a neural network and studied the influence of different input characteristics on the prediction accuracy. Support vector regression is used to predict short-term blood glucose, used the differential evolution method to optimize its parameters, and achieved good prediction results [13]. In addition, some scholars have constructed BG prediction models by using ARIMA, the Gaussian mixture model, reinforcement learning, random forests, the Kalman filter, and other methods [10, 14–16]. Liu et al. [17] designed one kind of physique-based fuzzy granular modeling method for BG estimation to achieve a good prediction effect, which took PLS, SVR, random forests, AdaBoost, and the ANN as a comparison algorithm group. Wu et al. [18] proposed the accurate XGBoost-BLR model for type 2 diabetes mellitus prediction in comparison with other existing methods. These models can achieve short-term BG prediction to a certain extent, but when the time step increases, the forecasting effect will be greatly reduced. Therefore, it is necessary to study further to improve the estimation accuracy as much as possible.

Recurrent neural networks (RNNs) have more prominent advantages over other artificial neural network structures in terms of time series modeling. For the actual practice of time series prediction, RNN modeling is similar to auto-regressive analysis, but it can build models much more complex than traditional time series. Basic RNNs and its two variants, long short-term memory (LSTM) and the gated recurrent unit (GRU), have been proved to have a better prediction effect than traditional machine learning methods on time series prediction [1, 8, 19]. When the prediction step increases, its prediction effect is also significantly better than that of traditional methods. Considering the nonlinearity and complexity of the BG series, this paper applies the optimized GRU by the improved bacterial foraging algorithm to the field of BG prediction [19, 20]. The wrist was selected to acquire the pulse signals simultaneously, and body temperature series with minimally invasive extraction of BG signals from upper-arm-based subcutaneous interstitial fluid was selected to construct the training and test dataset [21, 22]. Experimental results show that our proposed method has high accuracy and adaptability and is better than similar types of deep learning methods.

The rest of this paper is organized as follows. Section 2 presents the background and previous knowledge of noninvasive BG monitoring and its feature extraction issues. The time series decomposition technologies, deep learning models, and BFO optimization algorithms are introduced to improve the prediction performance by utilizing deep learning techniques. In addition, the CEEMDAN-IBFO-GRU model is constructed through the previously sampled BG and PPG dataset. The creation and optimization process of the whole intelligent model is also described in detail in this section. Through experiments, in Section 3, the performance and accuracy of the proposed model are compared with the commonly used machine learning techniques in the actual experiments in BG-forecasting evaluations. Finally, Section 4 concludes this paper and provides possible future applications in clinical fields.

2. Materials and Methods

2.1. Dynamic Noninvasive and Minimally Invasive BG Monitoring. Photoplethysmography (PPG) is an optical measurement technique that can be used to perform noninvasive BG detection using near-infrared absorption techniques [23–26]. Specific processing of PPG signals can reveal new information about human hemodynamic characteristics and blood composition. In this study, the optical sensor with reflection mode is used to obtain high-quality PPG signals from the subjects' wrists, extract the key PPG parameters (Teager–Kaiser energy, heart rate, spectral entropy, logarithmic features of spectral energy, etc.) and body temperature, and synchronously combine with minimally invasive BG monitoring series to precisely predict the short-term BG trends. PPG signals are sampled with a frequency of 50 Hz and packaged in ATmega328P, which are more reliably harvested using ZigBee technology, and these data are sent to a backend computer using a star-type network structure. Meanwhile, the dynamic BG monitoring data are wirelessly transmitted to a smart phone by Bluetooth once every three minutes. It relies on WiFi to send these data to the backend computer for the training dataset constructions. The BG level prediction modeling process is illustrated in Figure 1.

However, the current photometric-measured signal is more unstable and imprecise, hindering the development of noninvasive BG prediction technologies. The minimally invasive BG monitoring sensors, such as Medtronic, Dexcom, and Abbott, implant the glucose sensor into the subcutaneous tissue through the skin, which dramatically reduces patients' pain and generally shows more accurate monitoring results than noninvasive technologies. Therefore, well-established training and test datasets will provides a reliable source for deep learning models to calibrate and optimize the noninvasive BG prediction modeling process by integrating the synchronous noninvasive PPG data and minimally invasive BG data. The multidimensional feature matrix is extracted as the input of deep learning models according to $S'_{\mathrm{window}}(t)$ and $S''_{\mathrm{window}}(t)$ output by the noninvasive acquisition module. The following feature matrix is used as input data for deep learning techniques. The specific definitions of the PPG features, as well as the body temperature BT, are expressed as equations (1)–(7).

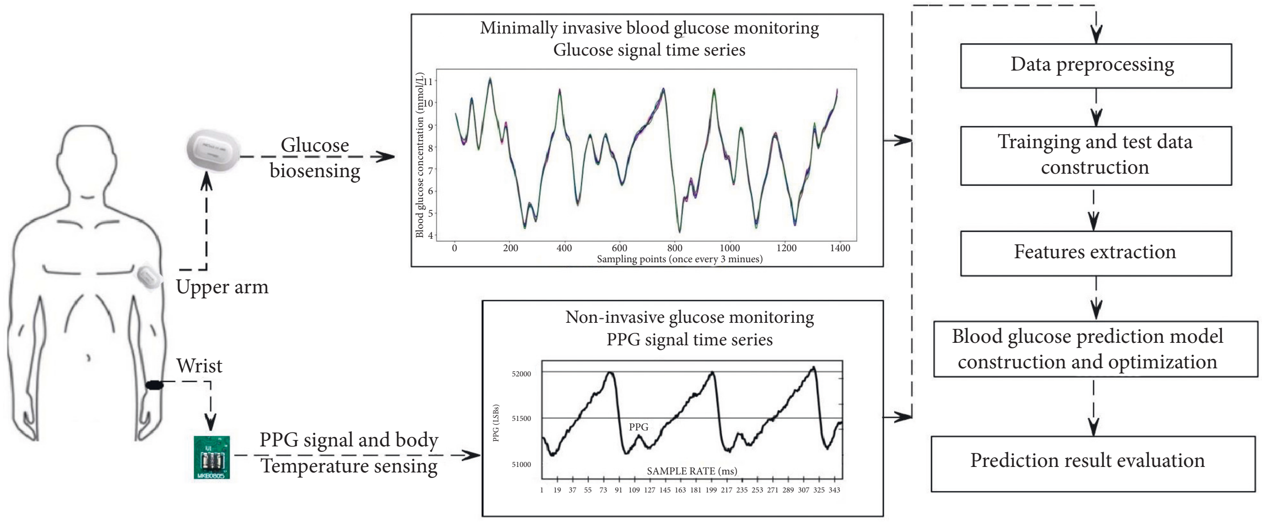

Figure 1: Overview of the BG concentration prediction modeling.

$$X_i = \left(\mathrm{KTE}^{\mu}, \mathrm{KTE}^{\sigma}, \mathrm{KTE}^{iqr}, \mathrm{KTE}^{skw}, \mathrm{HR}^{\mu}, \mathrm{HR}^{\sigma}, \mathrm{HR}^{iqr}, \mathrm{HR}^{\mathrm{skew}}, Hs^{\mu}, Hs^{\sigma}, Hs^{iqr}, Hs^{skew}, \ \log\, E^{\delta}, \ \log\, E^{iqr}, \mathrm{BT}\right). \tag{1}$$

2.1.1. Teager–Kaiser Energy Features. The Teager–Kaiser energy characteristic calculation formula is as follows:

$$\mathrm{KTE}(t) = x(t)^2 - x(t+1)x(t-1). \tag{2}$$

Using formula (3), the slice real-time energy value can be obtained:

$$\mathrm{KTE}_n(t) = S_{\mathrm{frame}}(t,n) - S_{\mathrm{frame}}(t+1,n)S_{\mathrm{frame}}(t-1,n), \tag{3}$$

where $t = 1, \ldots, L_{\mathrm{frame}-1}$.

The mean value (KTE_n^{μ}), variance (KTE_n^{σ}), interquartile spacing (KTE_n^{iqr}), and slope of a single slice ($\mathrm{KTE}_n^{\mathrm{shew}}$) can be obtained through $\mathrm{KTE}_n(t)$.

2.1.2. Heart Rate Features. The heartbeat interval can be obtained by collecting the waveform to obtain the window heart rate mean value HR^{μ}, variance HR^{σ}, interquartile spacing HR^{iqr}, and skewness $\mathrm{HR}^{\mathrm{shew}}$.

2.1.3. Spectral Entropy Futures. To apply the fast Fourier transform $S_{\mathrm{frame}}(\tau, n)$, the calculation process is as follows:

$$X_n \leftarrow \mathrm{FFT}\left(S_{\mathrm{frame}}(\tau, n), L_{\mathrm{FFT}}\right), \tag{4}$$

where $L_{\mathrm{FFT}} = 512$. X_n is regularized by the following equation:

$$P_X^n[k] \leftarrow \frac{\left|X_n[k]\right|^2}{\sum_{j=1}^{L_{\mathrm{FFT}}} \left|X_n|j\|^2}, \quad k = 1 \ldots L_{\mathrm{FFT}}. \tag{5}$$

Finally, the entropy P_X^n is calculated according to the following equation:

$$H \leftarrow P[k]\log(P[k]). \tag{6}$$

2.1.4. Logarithmic Features of Spectral Energy. According to the logarithmic formula of spectral energy,

$$H \leftarrow P[k]\log(P[k]). \tag{7}$$

The logarithmic variance of spectral energy $\log E^{\sigma}$ and interquartile difference $\log E^{iqr}$ in the window where the slice is located are calculated.

2.2. BG Series Decomposition and Recombination Processing. M. A. Colominas proposed complete ensemble empirical mode decomposition with adaptive noise (CEEMDAN) [27, 28]. This method adds adaptive white noise smoothing pulse interference to each decomposition, which can effectively solve the phenomenon of mode aliasing. This method is specifically utilized to regress modeling after signal decomposition in the fields of short-term BG estimations. The specific decomposition and denoising process is defined using steps 1–5.

Step 1. Add standard normal white noise $x(n)$ with different amplitudes to the given target signal $x(n)$, and construct the signal sequence as

$$x^i(n) = x(n) + \gamma w^i(n)\,(i = 1, \ldots, I). \tag{8}$$

Step 2. In the first stage, the empirical mode decomposition (EMD) is used to decompose the target BG signal; the first modal component is obtained, and the mean value is calculated as

$$\widehat{\mathrm{IMF}}_1(n) = \frac{1}{I}\sum_{i=1}^{I} \mathrm{IMF}_1^i(n). \tag{9}$$

The first stage margin signal is expressed as

$$r_1(n) = x(n) - \widehat{\mathrm{IMF}}_1(n). \tag{10}$$

Step 3. $E_k(\cdot)$ is defined as the IMF component after the EMD decomposition of signal data. By decomposing the sequence $r_1(n) + \gamma_1 E_1(w^i(n))$, it can be obtained that the IMF component in the second stage is as follows:

$$\widehat{\mathrm{IMF}}_2(n) = \frac{1}{I}\sum_{i=1}^{I} E_1\left\{r_1(n) + \gamma_1 E_1\left[w^i(n)\right]\right\}. \tag{11}$$

Step 4. By analogy, the $k-th$ residual component is expressed as

$$r_k(n) = r_{k-1}(n) - \widehat{\mathrm{IMF}}_k(n). \tag{12}$$

The $k+1$ IMF component is

$$\widehat{\mathrm{MF}}_{k+1}(n) = \frac{1}{I}\sum_{i=1}^{I} E_1\left\{r_k(n) + \gamma_k E_k\left[w^i(n)\right]\right\}. \tag{13}$$

Step 5. Repeat step (4) until the remaining components cannot meet the EMD decomposition conditions or the iteration ends. Finally, the target data sequence $x(n)$ is decomposed into equation (14), where $R(n)$ is the final residual component.

$$x(n) = \sum_{k=1}^{K} \widehat{\mathrm{IMF}}_k(n) + R(n). \tag{14}$$

To study changing features of the BG series, sample entropy can be used to measure the complexity of the time series [29]. It has advantages such as no self-matching problem of approximate entropy and less computation cost. Suppose $X(t)$ is a sequence with a data length n. The series $X(t)$ is constructed into a new series $Y(t)$ with m−dimension by the following expression:

$$\begin{aligned} Y(i) &= \{y(1), y(2), \ldots, y(m-1), y(m)\} \\ &= \{X(1), X(2), \ldots, X(N-m), X(N-m+1)\}. \end{aligned} \tag{15}$$

The distance $d[y(i), y(j)]$ between $y(i)$ and $y(j)$ in (16) is the absolute value of the maximum difference between all their elements.

$$d[y(i), y(j)] = \max[y(i+k) - y(j+k)]. \tag{16}$$

The sample entropy of the original series $S(m,r)$ is defined as

$$\begin{cases} S(m,r) = \lim\limits_{N\longrightarrow+\infty}\left\{-\ln\left(\left[\dfrac{A^m(r)}{B^m(r)}\right]\right)\right\}, \\ A^m(r) = (N-m+1)^{-1}\cdot\sum\limits_{i=1}^{N-m+1} A_i^m(r), B^m(r) = (N-m+1)^{-1}\cdot\sum\limits_{i=1}^{N-m+1} B_i^m(r), \end{cases} \tag{17}$$

where m represents the embedding dimension of the time series, r represents the similarity capacity, and $S(m,r)$ represents the sample entropy of the original series. Thus, $B^m(r)$ and $A^m(r)$ are the probabilities of the two-series matching $m-th$ and $(m+1)-th$ sampled points, respectively, under the similarity tolerance r. Generally, m is set to 1 or 2, and r selects a value between 0.1 and 0.25.

After the acquisition of the decomposed BG signals, it is reasonable to get the complexity of the BG series by calculating its sample entropy to avoid the problem of large error generation caused by directly applying the deep learning models for estimation training and modeling. Then, according to the correlation between the decomposed and the original BG series, the disintegrated BG series are recombined for more accurate prediction modeling by hierarchical clustering according to its complexities. The specific reconstruction process for BG signals is discussed in Section 3.3.

2.3. GRU Prediction Model. Ren [30] et al. proposed an improved recurrent neural network (LSTM) in 1997. The LSTM model uses memory cells to store and output information to solve the gradient explosion problems that easily occur in the RNN model. LSTM has good predictability for long series and is widely used to predict time series data. However, due to its complex internal structure, training of the LSTM network and its superparameters usually takes a long time. Rui [31] proposed a gated recurrent unit neural network (GRU) that is based on LSTM. Compared with LSTM, the training parameters are few, and the prediction effect is close to the LSTM. The structural unit of the GRU neural network is shown in Figure 2.

The GRU′s internal unit is similar to the internal unit of LSTM, except that the GRU combines the forgetting gate and output gate in LSTM into a single update gate. Therefore, there are only updated doors and reset doors in the GRU, and their internal relationship is as follows:

$$\begin{aligned} R_t &= \sigma(W_{rx}X_t + W_{rh}H_{t-1}), \\ Z_t &= \sigma(W_{zx}X_t + W_{zh}H_{t-1}), \\ \overline{H}_t &= \tanh(W_{sh}R_tH_{t-1} + W_{sx}X_t), \\ H_t &= (1 - Z_t)H_{t-1} + Z_t\overline{H}_t, \end{aligned} \tag{18}$$

where X_t is the input vector at time t, R_t is the reset gate vector at time t, and the gate vector Z_t is updated at t. The

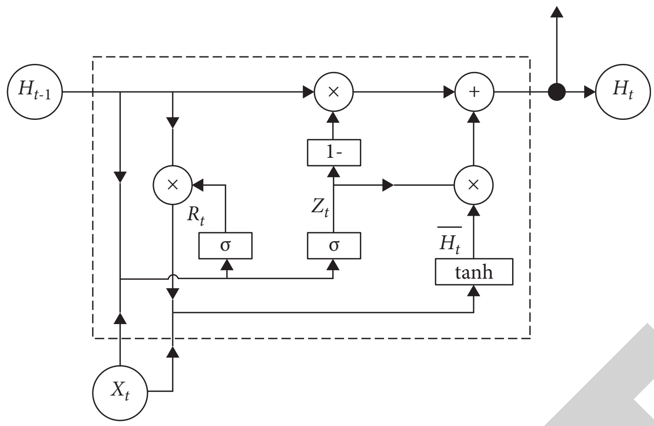

Figure 2: GRU network computing structure.

hidden layer output vector is H_t at time t. $\overline{H}_t$ is the updated candidate vector after the updation. W_{sh}, W_{sx}, W_{zx}, W_{zh}, W_{rx}, and W_{rh} are the weight matrices between the connection vectors. σ denotes the sigmoid function.

2.4. Bacterial Foraging Optimization (BFO). Bacterial foraging optimization (BFO) is a biologically inspired swarm intelligence optimization algorithm that simulates the foraging behavior of bacteria to obtain maximal energy during the searching process [32, 33]. This algorithm is designed to find the global optimal value and shows better performance than the basic PSO and genetic algorithm. Because the BFO algorithm is easy to jump out of the local minimum, its improved algorithm can accelerate the convergence speed of the algorithm. BFO simulates the behavior of *Escherichia coli* swallowing food in the human intestine and solves the problem by the following simulating behaviors.

2.4.1. Elimination and Dispersal. When the local environment of bacteria changes or mutates gradually (such as food depletion or sudden temperature increase), bacteria will randomly move to a new area with a given probability P_{ed} to cope with abnormal changes.

2.4.2. Chemotaxis. Bacteria will rotate and swim toward food-rich areas. Rotation refers to pointing in a new direction. The chemotaxis behavior is shown as follows:

$$\theta^i(j+1,k,l) = \theta^i(j,k,l) + C(i)\frac{\Delta(i)}{\sqrt{\Delta^T(i)\Delta(i)}}, \tag{19}$$

where $\theta^i(j,k,l)$ represents the position of bacteria i after the trend, $j-th$ replication, and $l-th$ dispersion; $C(i)$ is the trend step of the bacteria, and $\Delta(i)$ is a unit vector of bacteria in the random direction in the search space.

2.4.3. Swarming. When bacteria forage, there are gravitational and repulsive forces among different individuals. It makes bacteria gather more in some areas with moderate food abundance. The swarming behavior is expressed as

$$\begin{aligned} J_{cc}(\theta, P(j,k,l)) &= \sum_{i=1}^{S} J_{cc}\left(\theta, \theta^i(j,k,l)\right) \\ &= \sum_{i=1}^{S}\left[-d_{\text{attractan}}\exp\left(-w_{\text{attractant}}\sum_{m=1}^{P}\left(\theta_m-\theta_i^m\right)^2\right)\right] \\ &\quad + \sum_{i=1}^{S}\left[-h_{\text{repellant}}\exp\left(-w_{\text{repellant}}\sum_{m=1}^{P}\left(\theta_m-\theta_i^m\right)^2\right)\right]. \end{aligned} \tag{20}$$

where $d_{\text{attractant}}$ is the gravitational depth, $w_{\text{attractant}}$ is the gravitational width, $h_{\text{repellant}}$ is the repulsive height, $w_{\text{repellant}}$ is the repulsive width, θ_i^m is the $m-$th component of bacteria i, θ_m is the $m-$th component of all other bacteria, and $P(j,k,l)$ is the position of individuals in the population after the $j-$th trend operation, $k-$th replication operation, and $l-$th migration operation.

2.4.4. Reproduction. Bacteria with weak foraging ability will be eliminated, and bacteria with strong foraging ability will replicate. The following equation is called the fitness value of bacteria i:

$$J_{\text{health}}^i = \sum_{i=1}^{N_c} J(i,j,k,l), \tag{21}$$

where $J(i, j, k, l)$ is the fitness value of the $i-th$ bacterium after the $j-th$ trend operation, $k-th$ replication operation, and $l-th$ elimination and dispersal. By arranging J^i_{health}, the algorithm will discard half of the bacteria with larger fitness and copy the other half of the bacteria with smaller fitness.

In the process of BG estimation optimization, bacteria present a solution; the location of the bacterium in the search space corresponds to the solution of the optimization problem, and the fitness value of the optimization function, that is, the value of the objective function, represents the excellence of the superparameter selection for deep learning prediction modeling.

2.5. The Intelligent BG Prediction Modeling. To improve the training and tuning effect of the GRU prediction model, structure and superparameters should be reasonably selected and adjusted. Theoretically, the complexity of the network increases with the increase in the number of hidden layers and the number of neurons in the hidden layer. Meanwhile, such complexities and computation costs of deep learning networks are also increased dramatically. Therefore, scientific and reasonable optimization of models' superparameters such as the learning rate and maximum iteration times can reduce the complexity of the model to a certain extent and also improve the convergence speed as well as the prediction accuracy. The improved bacterial foraging algorithm (IBFO) that has characteristics such as good convergence performance and high optimization accuracy, which is designed in this study, learns from ideas of particle swarm optimization (PSO) [34]. It trains and optimizes the structure and superparameters of the GRU neural network according to the existing PPG and BG series to train and construct a short-term BG level prediction model with higher prediction accuracy.

In a traditional BFO algorithm, however, the invariance of step size will affect the accuracy of the optimal solution, and the invariance of elimination and dispersal probability will slow down the convergence speed in the later stage of the algorithm. In consideration of such shortcomings, the following improvements are proposed to improve the performance of the basic BFO.

The improved BFO will dynamically adjust its step size to improve the optimization accuracy. The basic rule for improvement of the convergence speed is to increase the foraging step size when the distance between the two individuals is far, and vice versa. The following equation can achieve the adaptive adjustment for foraging step size:

$$C(i)' = \lambda\left(\frac{C_{\max}}{j \times k \times l}\right)\frac{J_i}{J_{\max}}, \tag{22}$$

where J_i is the fitness value of the current bacteria i, $J_{\max}$ is the maximum fitness value of all current bacteria, $C_{\max}$ is a quarter of the sum of the maximum and minimum value of the d-dimensional optimization range, j, k, and l are the current trend, replication, and elimination and dispersal times, respectively, and λ is a random number between 0 and 1.

Learning from the idea of the learning factor of particle swarm optimization, the swimming of a bacterium is not only limited by its foraging ability but also affected by other bacteria [35]. That is to say, a bacterium's fitness function value is compared with that of the current bacteria with the best foraging ability, and its foraging ability is improved by communicating with and learning from the bacteria with better foraging ability. Its function is given by

$$\Delta(i)' = \Delta(i) + \lambda C_1 (J_{\max} - J_i) + \lambda C_2(\overline{J}_{\text{global}} - J_i), \tag{23}$$

where $\Delta(i)$ is a unit vector of bacteria in the random direction in the search space, C_1 and C_2 are learning factors, and $\overline{J}_{\text{global}}$ is the average fitness of all bacteria at that moment.

Finally, an adaptive elimination and dispersal probability of IBFO is designed to solve the drawbacks of less flexibility of the fixed migration. All bacteria migrate to a new region with fixed P_{ed}, which may lead to the loss of elite individuals and the reduction in convergence speed, accuracy, and stability of the algorithm. The improvement is realized by the following formula:

$$P'_{ed}(i) = \left[\frac{(J_{\max} - J_i)}{(J_{\max} - J_{\min})}\right] \times p_{ed}, \tag{24}$$

where $J_{\max}$ and $J_{\min}$ are the maximum and minimum fitness values of all bacteria at present and $P_{e\,d}$ and $P'_{ed}(i)$ are the fixed and adaptive elimination and dispersal probability, respectively.

Through the improvement, the bacterial migration probability with a small fitness function value is increased. This will ensure that the bacteria with the best foraging ability will be migrated to improve the stability of the algorithm. The specific algorithm for the noninvasive intelligent BG prediction modeling and evaluation is described in the following three parts, and the specific procedures are illustrated in Figure 3.

Part 1. The BG and related signal acquisition, decomposition, and recombination. The training and the test dataset are constructed by obtaining the PPG features, body temperature, and continuous real BG series simultaneously. Then, the BG signal is decomposed by CEEMDAN, and its sample entropy is also calculated to get the complexities of each decomposed signal. Afterward, the disintegrated signal is recombined into high-, medium-, and low-correlation series by hierarchical clustering. These rearranged series are proved to be more suitable for deep learning models to regress in each component and implement more accurate forecasting by reconstructing each regrouped estimation results.

Part 2. The optimization of superparameters of the prediction model. To initialize the parameters of the improved BFO algorithm, the number of output layer and input layer nodes, hidden layers, and learning rate of the GRU neural network are determined according to the original series and actual objectives. The improved BFO will dynamically adjust its step size and

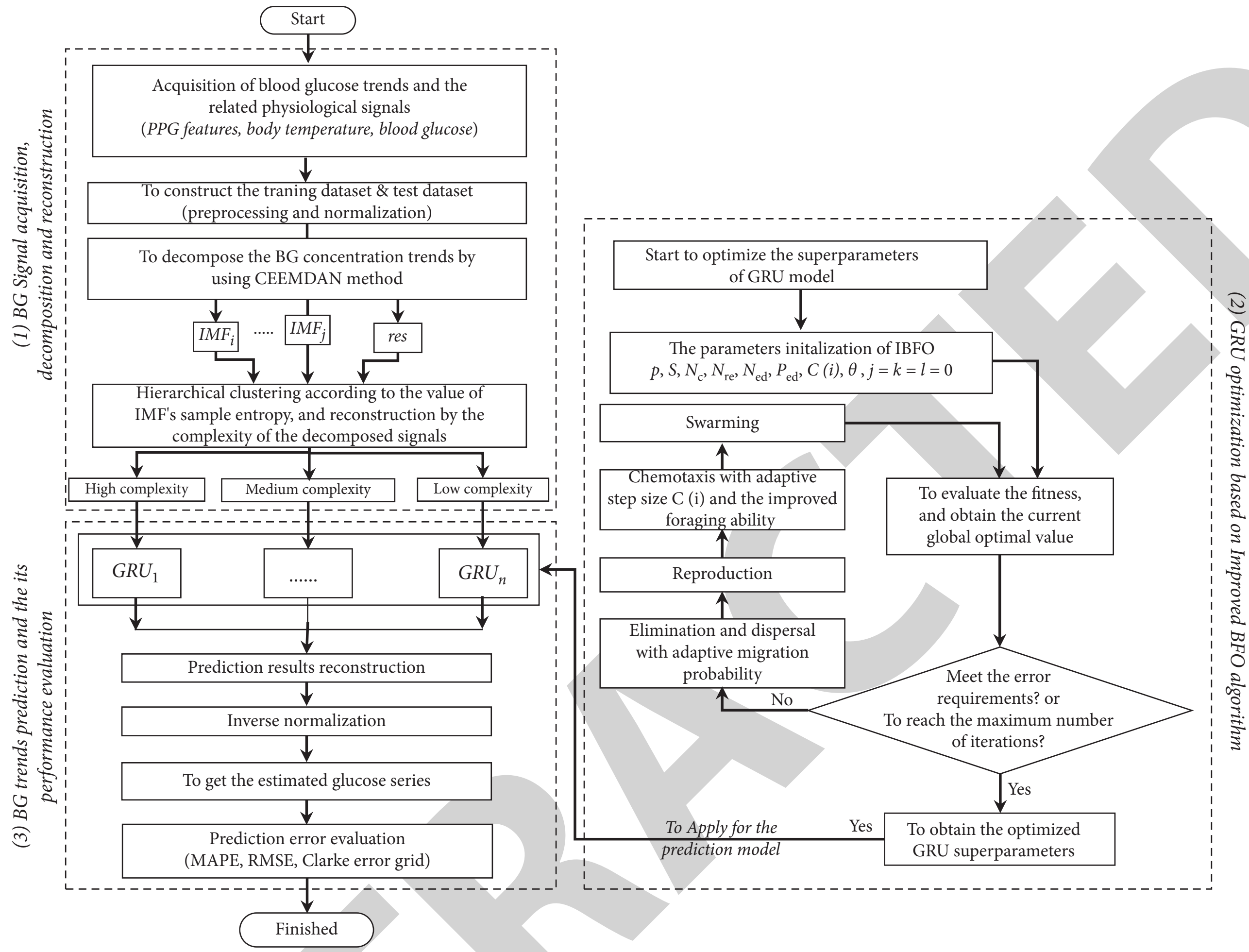

Figure 3: The process of noninvasive BG prediction and evaluation by using the CEEMDAN-IBFO-GRU model.

improve the foraging ability with adaptive migration probability to provide more optimized superparameters for the GRU model.

Part 3. The BG trend prediction and its performance evaluation. The recombined BG signals are regressed by the IBFO-optimized GRU model and to reconstruct the final estimated BG results. Consequently, the series are denormalized to get the real BG trends. Finally, the CEEMDAN-IBFO-GRU model is evaluated by MAPE, RMSE, and the Clarke error grid criterion and compared with other machine learning methods.

3. Results and Discussion

The experimental environment of this paper is Windows 10 operating system. Python 3.10 and the machine learning framework PyTorch 1.1 are used for deep learning modeling and testing. The hardware configuration is a 64-bit operating system, and the processor is Intel(R) Core (TM) i7-4900MQ CPU 2.80 GHz with 16GB RAM.

3.1. Data Source Preparation and Preprocessing. In this research, the dynamic noninvasive BG monitoring device that is worn on the wrist of patients dynamically measures BG levels by using an optical PPG acquisition module (MKB0805, YUNKEAR Ltd., Shenzhen, China). Meanwhile, the minimally invasive CGM (YUWELL Ltd., China) synchronously collects more accurate GB trends to support the construction of calibration datasets, which are collected by dynamic BG records in the Shandong rehabilitation research center, China. The real continuous BG data of 12 patients were investigated. The BG levels of diabetic patients are continuously and dynamically monitored and recorded at an interval of three minutes, and the trends are monitored for three days (about 72 hours), with a total of 1440 sampling points in our experiment, excluding the points with breakpoints, discontinuities, and serious interference during the monitoring. The sampled BG series of each patient is obtained and divided into a training dataset and test dataset, which accounts for 70% and 30%, respectively. Sliding windows and single-step prediction are used for the BG dynamic estimation processes. The acquired PPG features in the last 3 hours are utilized for GB level estimation in 15- or

30-minutes. The specific dataset construction for the intelligent BG estimation modeling is shown in Figure 4.

Due to the different dimensions between sampled feature data, in this study, the max-min standardization method is used for time series normalization as follows:

$$x_{\text{Normalization}} = \frac{x - \text{Min}(x)}{\text{Max}(x) - \text{Min}(x)}, \tag{25}$$

where $\text{Max}(x)$ and $\text{Min}(x)$ denote the maximum and the minimum value of BG series, respectively.

3.2. Model Performance Evaluation Criterion. To quantify the prediction performance of the proposed models, root mean square error (RMSE), mean absolute percentage error (MAPE), and Clarke error grid analysis (EGA) are selected as the performance measurements for the model evaluation. The calculation of RMSE and MAPE is as follows:

$$\text{RMSE} = \sqrt{\frac{1}{n}\sum_{i=1}^{n}\left(x_i - \overline{x_i}\right)^2}. \tag{26}$$

The average absolute percentage error is calculated as follows:

$$\text{MAPE} = \frac{1}{n}\sum_{i=1}^{n}\left|\frac{x_i - \overline{x}_i}{x_i}\right| \times 100. \tag{27}$$

Here, n is the number of samples, x_i is the actual value of the $i-th$ sample, and $\overline{x_i}$ is the predicted value of the $i-th$ sample.

Clarke error grid analysis was developed to evaluate the clinical accuracy of measured BG and standard reference BG data. This method can evaluate the clinical effect difference between the actual BG level and the predicted level. This method uses the Cartesian diagram principle to evaluate the accuracy of the BG prediction methods according to the probability that the predicted values fall in areas A, B, C, D, and E.

3.3. The Experimental Results. The minimally invasive BG signal is decomposed by CEEMDAN for training and modeling as shown in Figure 5, and it disassembles the intrinsic mode function (IMF) from IMF1 to IMF7 and the residuals.

According to the complexity of the decomposed signal group, the sample entropy is calculated, and the similarity is calculated by hierarchical clustering. Through clustering calculation, the signals are classified as high, medium, and low complexity (H_t, M_t, and L_t) in clusters 1 to 3. The complexity of the decomposed BG series is regrouped according to the correlation with the original BG series. The clustering process of recombined signals and its correlation with the original BG series is demonstrated in Figure 6.

The decomposed signals are clustered and reconstructed according to their complexities, and the specific combinations are demonstrated in Table 1. The Pearson correlation coefficient is used to measure how similar the rearranged GB signals and the original BG signals are. To enforce the learning and estimation results of the deep learning modeling construction, the recombined data should be more similar to the originally acquired BG series. The original BG series are reconstructed in high, medium, and low correlations, which will improve the training and estimation performance for the deep learning forecasting models.

The data series of the extracted PPG features are listed in Table 2 as a fundamental training data set for deep learning technique-based BG estimation. The values of the extracted features are normalized in order to facilitate the construction of the training data. In this case, the BG level and its corresponding PPG features are listed to support the BG estimation experiments.

After completing the decomposition of continuous BG series, the improved BFO algorithm is used to tune the deep learning models' hyperparameters. The improved BFO is initialized by the following parameters in detail. The search dimension is $d = 4$. The number of bacterial populations S, elimination and dispersal behaviors N_{ed}, and chemotaxis behaviors N_c are 50, 2, and 25, respectively. The maximum step of unidirectional motion in the trend behavior N_s is set to 4. The number of times of the copied behavior N_{re} is set to 4. The elimination and dispersal probability $P_{e\,d}$ is 0.25. The gravitational depth and width are 0.5. In addition, the repulsion depth and width are both 0.5. The local and global learning factors C_1 and C_2 are set to 2. Figure 7 demonstrates the number of iterations in the training process of IBFO-optimized models (IBFO-RNN, IBFO-LSTM, and IBFO-GRU). Through the training experiments, the number of hidden layer neurons, hidden size, learning rate, and iterations are gradually converged to the optimal value with the update of the algorithm. As can be seen from Figure 7, the number of iterations finally converges to 65, 79, and 95 in IBFO-optimized RNN, LSTM, and GRU, respectively.

Through the training process, we have obtained the optimal combination of parameters with the best performance to modify the model structure and configurations. The number of input and output layers is configured to one for the optimized deep learning models. The loss function is adopted by MSE, and the Adam technology is adopted as the optimizer. The optimized model's structure and its superparameters are described in Table 3.

3.4. Model Performance Evaluation and Discussion. This study constructed a short-term BG prediction model based on the CEEMDAN-IBFO-GRU. The whole results of 15- and 30- minute estimation are illustrated in Figure 8 and Figure 9, respectively. S1, S2, and S3 are the zoomed-in pictures in different time segments that indicate the BG estimation trends by using different machine learning methods. It can be seen that the prediction error becomes larger with the increase in prediction step size. In addition, the prediction errors of different patients may have different trends due to the different glycemic fluctuations in patients. Therefore, the BG dynamic trends and its estimation fittings are the average results with similar BMI and health levels. Among them, the best prediction effect of IBFO-GRU is in the forthcoming BG

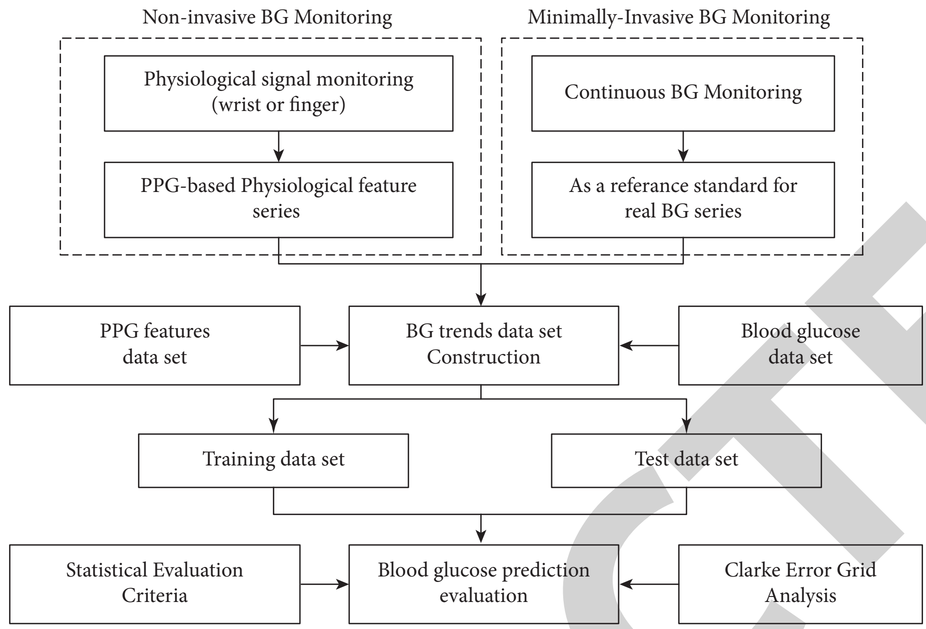

Figure 4: The specific dataset construction for BG estimation modeling.

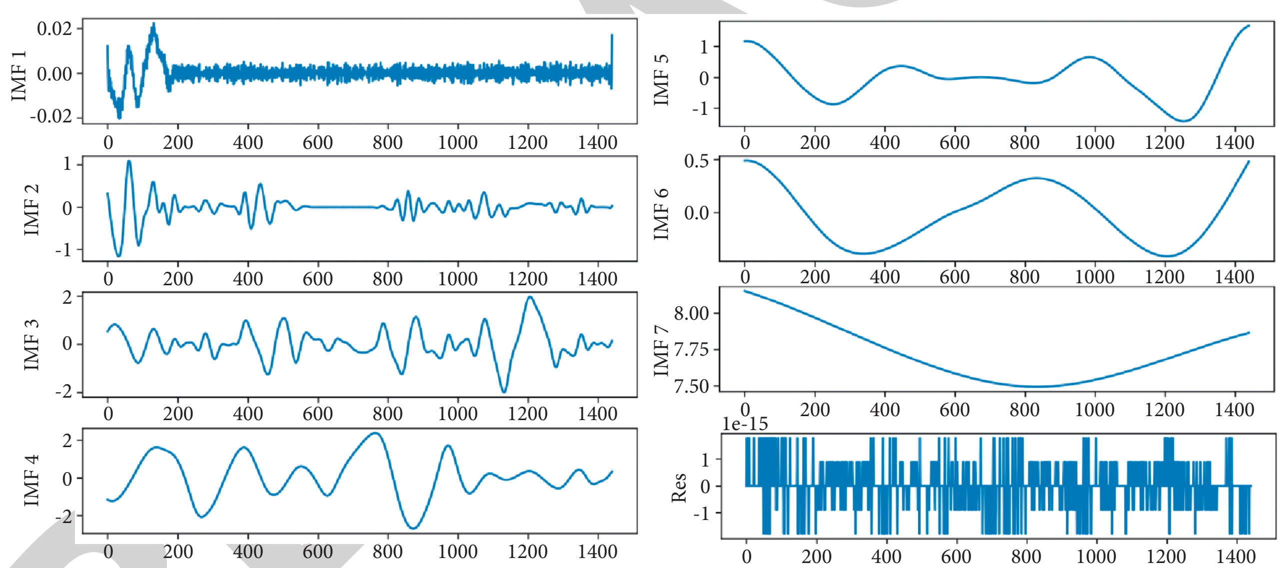

Figure 5: The BG series decomposition by CEEMDAN.

concentration 15 minutes ahead of time; its RMSE is 0.38, and the MAPE is about 6.43%. The prediction RMSE and MAPE increase obviously when the step of BG level estimation in 30-min estimation by using the IBFO-optimized GRU is increased to 0.417 and 7.82%, respectively.

To explore the prediction performance of the proposed intelligent BG prediction method, in this study, it is compared with basic deep learning models RNN, LSTM, GRU, and the support vector regression (SVR, C: 100.0; gamma: 0.01; Kernel function: RBF), and their optimized methods are measured by MAPE and RSME evaluation criteria. Figure 10 illustrates that the RMSE of IBFO-GRU has improved on average in 15-min prediction by about 3.58% and by 6.29% more than IBFO-LSTM and IBFO-RNN, respectively. In addition, the RMSE improvement is about 13.1% and 16.3% compared that of with PSO- and BFO-based GRU or LSTM. Meanwhile, the MAPE error of IBFO-GRU is increased by about 12.4%, and 18.9% more than that of IBFO-LSTM and IBFO-RNN, respectively. The effect of the CEEMDAN-IBFO-GRU-based BG estimation process has been greatly optimized and improved compared with that of other machine learning techniques.

Finally, to analyze the prediction effect more comprehensively, the Clarke error grid analysis method is purposefully utilized to evaluate the experimental results. The accuracy of the BG estimation models was evaluated by comparing the relationship between the predicted and actual BG concentration. The results are all located in areas A and

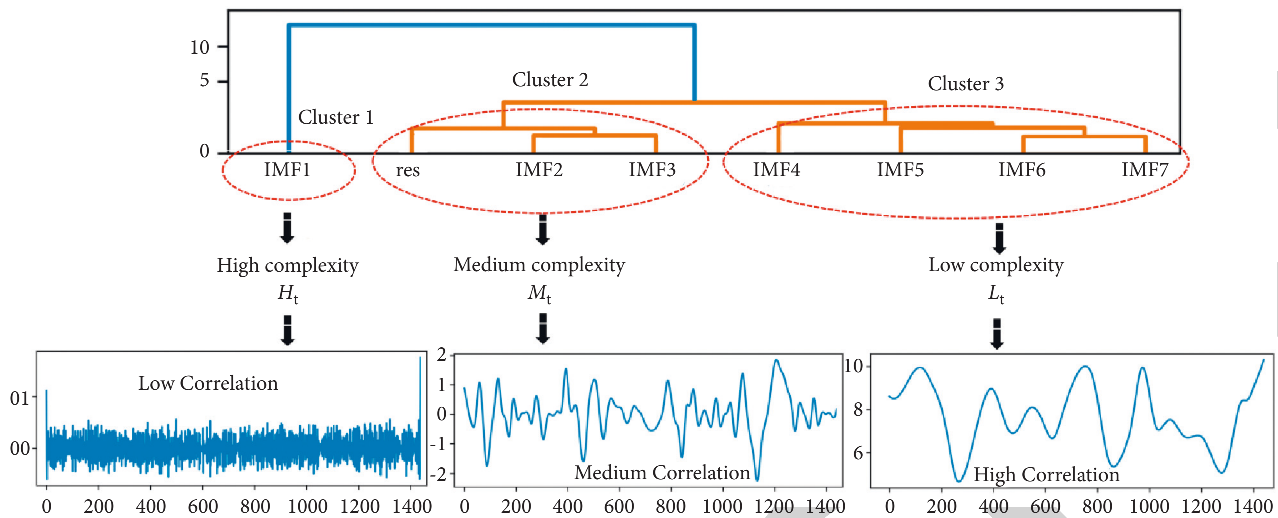

Figure 6: The recombination of decomposed BG signals and the correlation with the original BG series.

Table 1: The decomposed BG series and the correlation for reconstruction.

Clustering result	The correlation coefficient with the original BG series	Simple entropy	Decomposed signals
High complexity (H_t)	0.143, low correlation	19.121	IMF1
Medium complexity (M_t)	0.443, medium correlation	7.094	Res
		6.467	IMF2
		6.681	IMF3
Low complexity (L_t)	0.897, high correlation	5.654	IMF4
		5.157	IMF5
		5.021	IMF6
		4.553	IMF7

Table 2: The PPG features within a sampling interval.

BG level (mmol/L)	KTE^{μ}	KTE^{σ}	HR^{μ}	HR^{σ}	...	HR^{iqr}	HR^{shew}
8.9	0.804	0.615	0.861	0.725	...	0.827	0.597
8.2	0.752	0.623	0.843	0.716	...	0.801	0.571
...	...	...	...	...	...	...	...
7.4	0.644	0.578	0.832	0.703		0.793	0.512

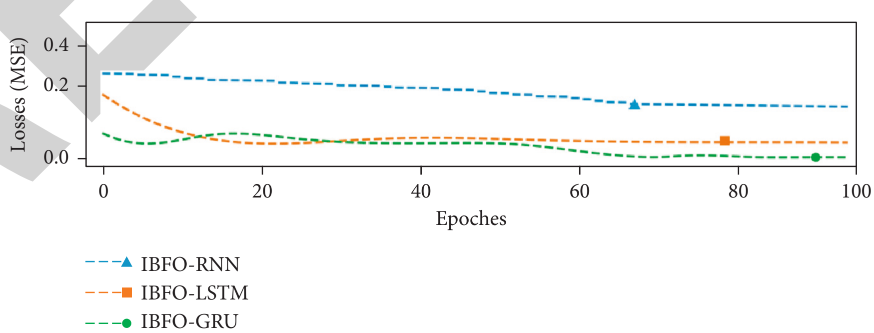

Figure 7: The number of iterations in the IBFO-based deep learning model training process.

B, indicating that the results of the analysis are acceptable in theory, that is, the predicted value of the BG level has acceptable detection accuracy in guiding clinical application. Clarke grid errors of the optimized deep learning models in 15 min predictions are shown in Figure 11.

The 15-min ahead BG predicting results are all located in area A, which were predicted by using our proposed method counts as about 98.4%, which are increased by about 4.1% and 6.6% compared to that using IBFO-LSTM and IBFO-RNN, respectively. The prediction results and

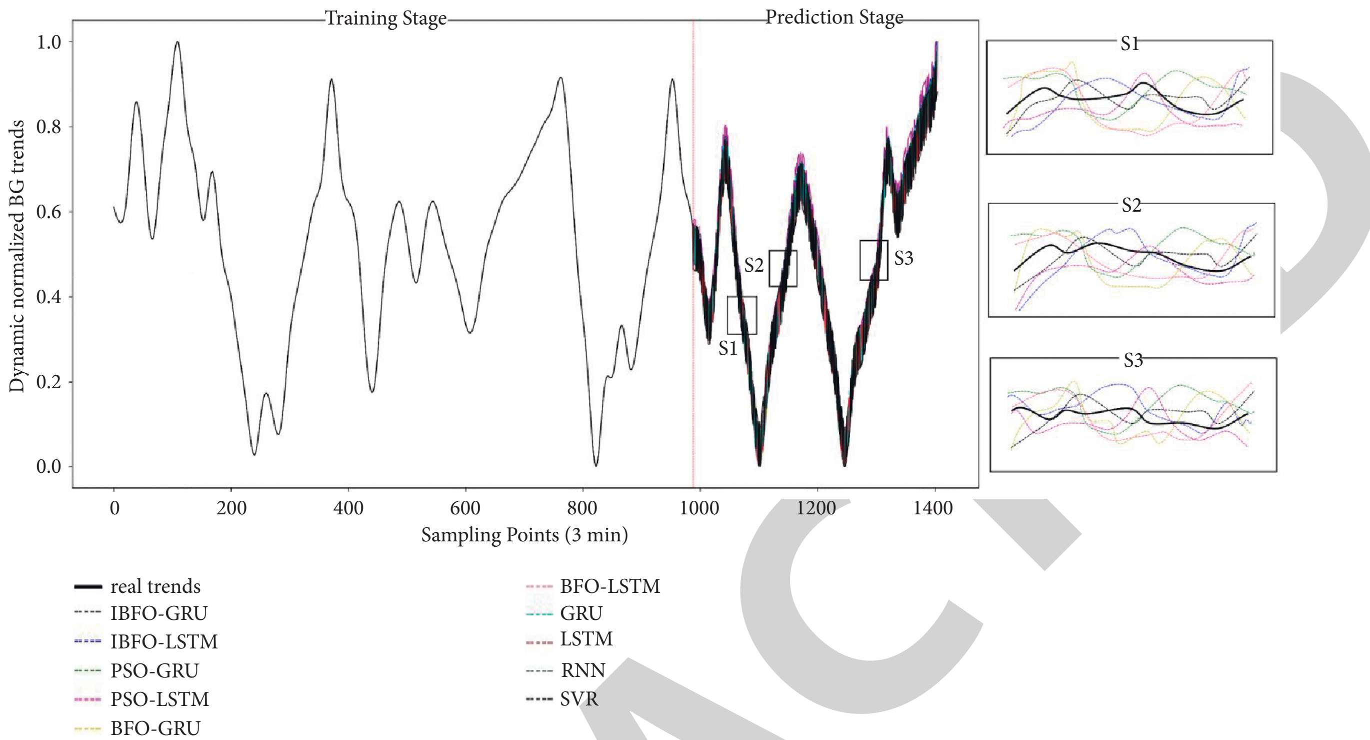

Figure 8: The short-term BG estimation results in 15 minutes.

Table 3: The optimized model's structure and its superparameters by using IBFO.

Models	Parameters	Values
IBFO-GRU	Number of hidden layer neurons	4
	Hidden size	4
	Learning rate	0.0038
	Number of iterations	95
IBFO-LSTM	Hidden size	3
	Number of hidden layer neurons	2
	Learning rate	0.0042
	Number of iterations	79
IBFO-RNN	Number of hidden layer neurons	4
	Hidden size	3
	Learning rate	0.0001
	Number of iterations	65

accuracy of BFO- and PSO-optimized GRU, LSTM, and RNN are similar when applying the dynamic BG level estimation algorithms. Figure 12 shows that the Clarke error grid results in area A of CEEMDAN-IBFO-GRU with 30-min ahead prediction are improved by about 2.7% and 5.4% when compared with those of other IBFO-optimized LSTM and RNNs and is also increased on average by about 5.4% and 6.2% compared with that of PSO- and BFO-based GRU or LSTM models, respectively. These regions quantify the accuracy of the BG reference values compared to the predicted values for different types of errors.

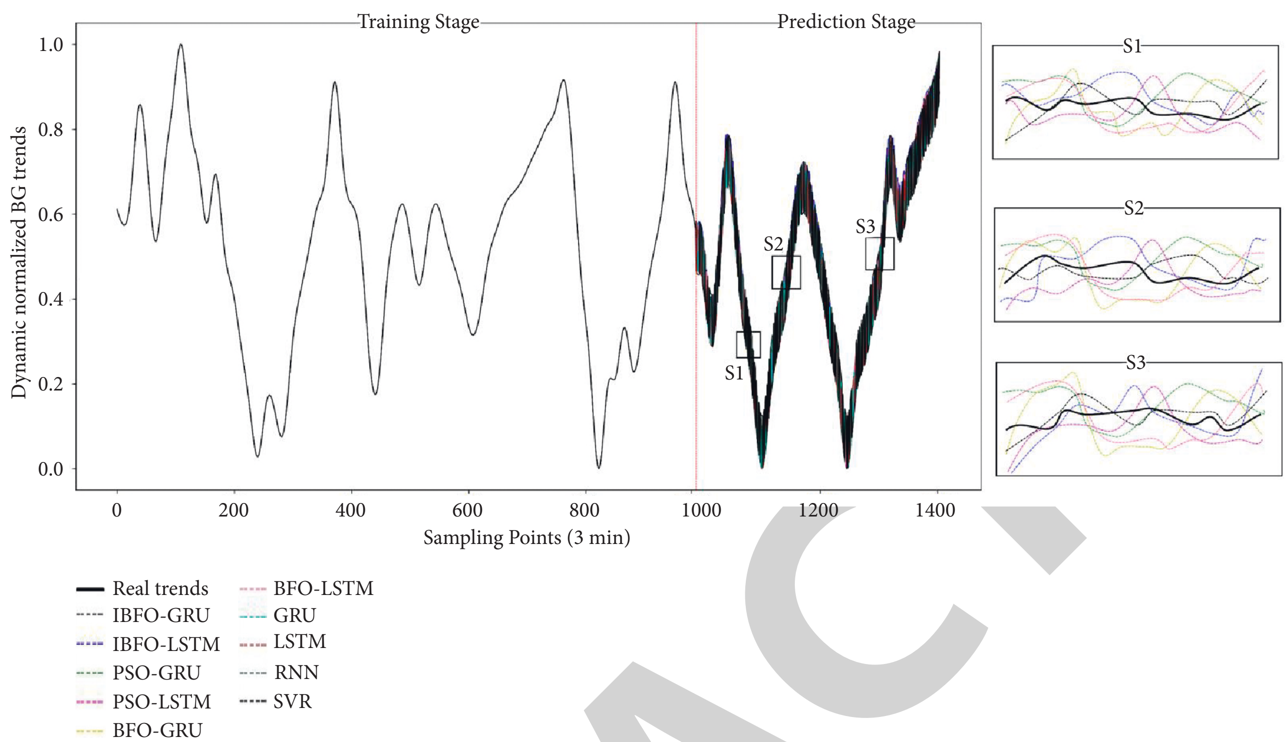

Figure 9: The short-term BG estimation results in 30 minutes.

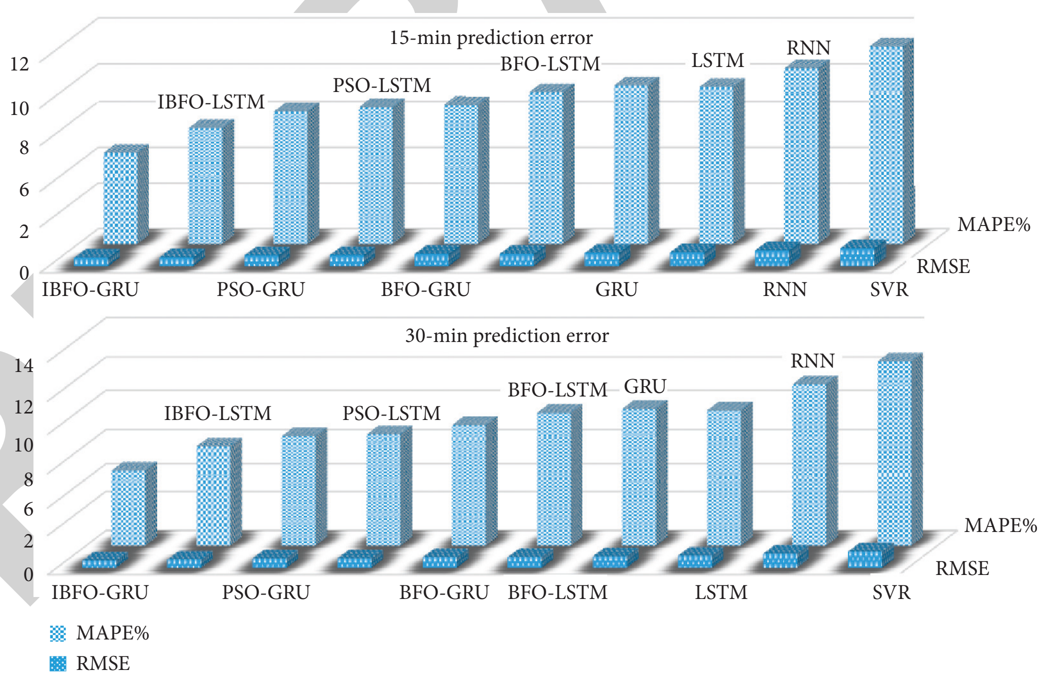

Figure 10: The short-time BG prediction errors in 15- and 30-minutes.

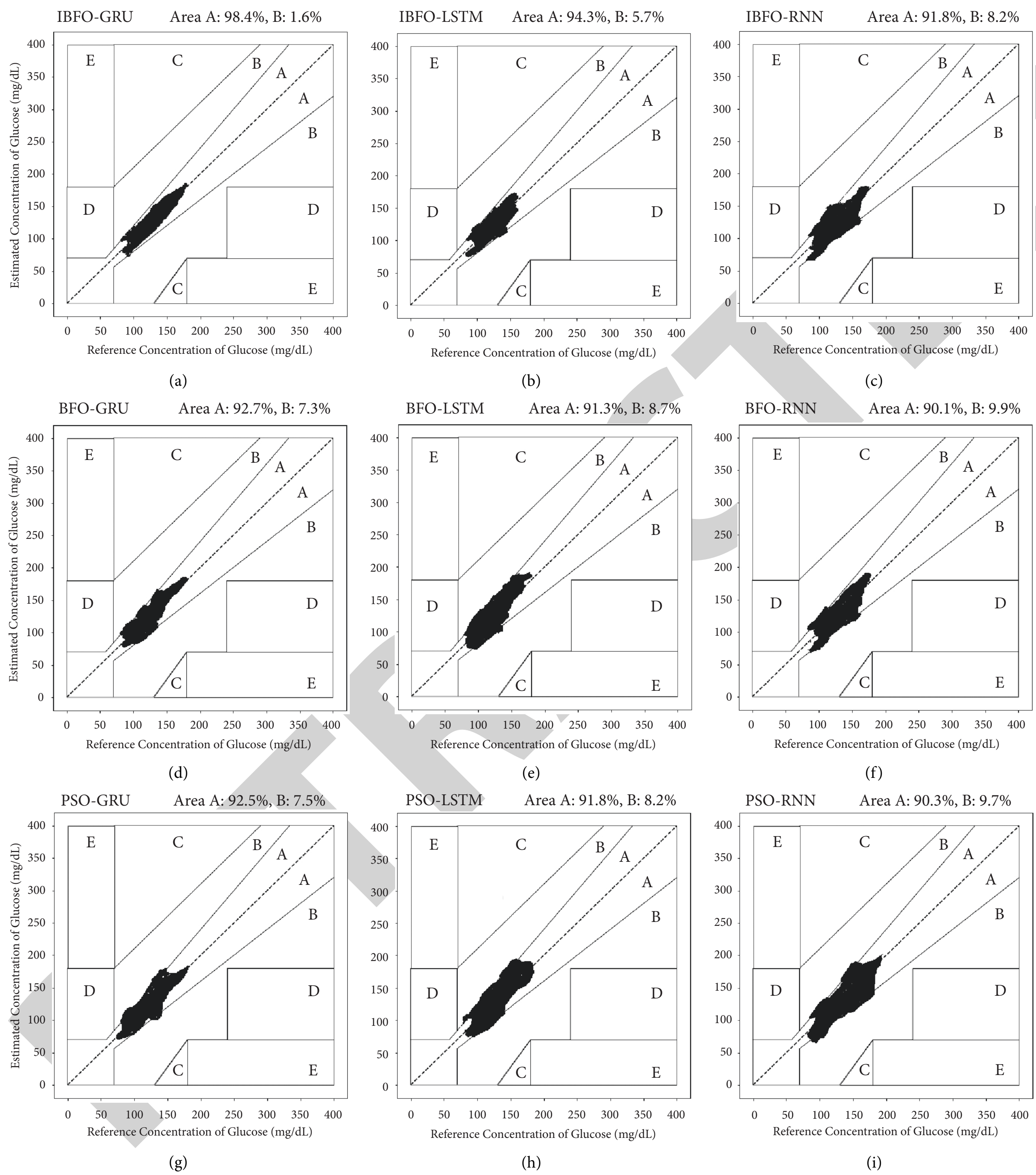

Figure 11: Clarke grid errors of the optimized deep learning models with CEEMDAN in 15 min prediction. (a) IBFO-GRU: area A: 98.4% and B: 1.6%. (b) IBFO-LSTM: area A: 94.3% and B: 5.7%. (c) IBFO-RNN: area A: 91.8% and B: 8.2%. (d) IBFO-GRU: area A: 92.7% and B: 7.3%. (e) IBFO-LSTM: area A: 91.3% and B: 8.7%. (f) IBFO-RNN: area A: 90.1% and B: 9.9%. (g) IBFO-GRU: area A: 92.5% and B: 7.5%. (h) IBFO-LSTM: area A: 91.8% and B: 8.2%. (i) IBFO-RNN: area A: 90.3% and B: 9.7%.

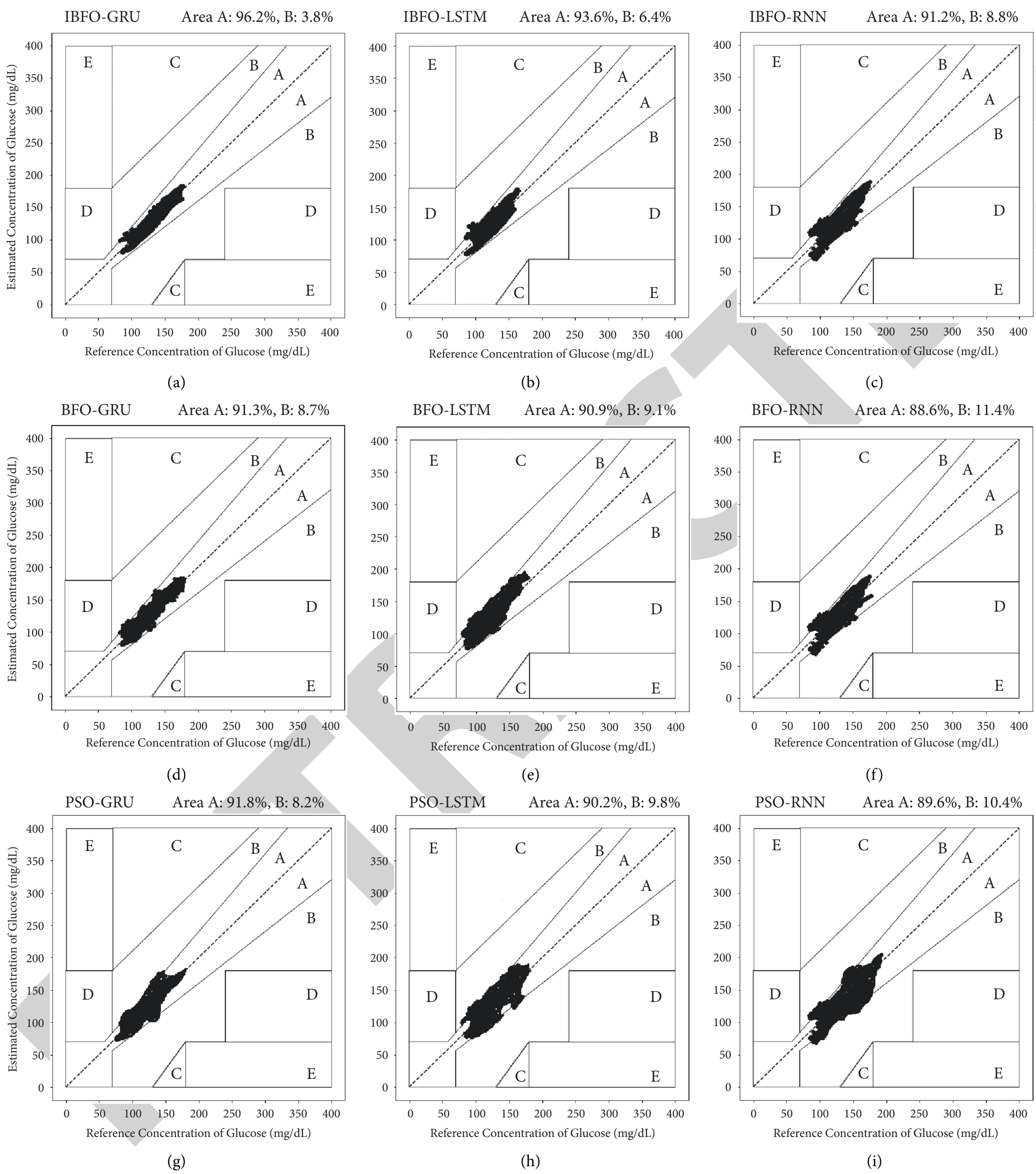

Figure 12: Clarke grid errors of the optimized deep learning models with CEEMDAN in 30 min prediction. (a) IBFO-GRU: area A: 96.2% and B: 3.8%. (b) IBFO-LSTM: area A: 93.6% and B: 6.4%. (c) IBFO-RNN: area A: 91.2% and B: 8.8%. (d) IBFO-GRU: area A: 91.3% and B: 8.7%. (e) IBFO-LSTM: area A: 90.9% and B: 9.1%. (f) IBFO-RNN: area A: 88.6% and B: 11.4%. (g) IBFO-GRU: area A: 91.8% and B: 8.2%. (h) IBFO-LSTM: area A: 90.2% and B: 9.8%. (i) IBFO-RNN: area A: 89.6% and B: 10.4%.

4. Conclusions

This research proposed an intelligent BG level prediction model (CEEMDAN-IBFO-GRU) that is well suitable for the strong time variability and complex nonlinearity of the dynamic BG changes and implements more precise BG forecasting management within short time periods. In this paper, the BG level in human subcutaneous interstitial fluid is continuously monitored through minimally invasive monitoring, and the characteristic sequence based on the PPG signal is synchronously obtained to jointly provide a better training and test dataset for the deep learning algorithm to realize noninvasive continuous BG prediction and early-warning management. BG series is decomposed by CEEMDAN and sample-entropy-based recombination by hierarchical clustering. After that, the recombined BG signals are regrouped according to their correlation with the original signals, which are regressed by the deep learning models to realize a more accurate BG estimation. Furthermore, the improved BFO algorithm is designed for increasing the performance of the deep learning models by optimizing their structures and superparameters. Through experiments, the number of training iterations is fewer, and the structures, as well as the superparameters, are also simple and reasonable for practical BG estimation application in a relatively simple hardware environment. According to the error evaluation criteria RMSE, MAPE, and Clarke error grid analysis, compared with the basic deep learning models LSTM, GRU, and RNN, the results show that the prediction accuracy of CEEMDAN-IBFO-GRU is higher than that of the nonoptimized machine learning methods. Therefore, the proposed noninvasive BG prediction model based on deep learning techniques has been proved to show good performance with relatively high accuracy. In future research, more physiological and activity characteristics should be combined to further improve the blood glucose prediction accuracy for practical clinical application.

Data Availability

The data used to support the findings of this study are included within the article.

Conflicts of Interest

The authors declare that they have no conflicts of interest.

Acknowledgments

This research was funded by the 2019 Key R&D Program of the Shandong Province public welfare project (2019GNC106079) and the Institutional Applied Scientific Research Projects (2021yyx-zd02).

References

[1] M. Rahman, D. Islam, R. J. Mukti, and I. Saha, "A deep learning approach based on convolutional LSTM for detecting diabetes," *Computational Biology and Chemistry*, vol. 88, Article ID 107329, 2020.

[2] W. Wang, M. Tong, and M. Yu, "Blood glucose prediction with VMD and LSTM optimized by improved particle swarm optimization," *IEEE Access*, vol. 8, pp. 217908–217916, 2020.

[3] S. L. Cichosz, M. H. Jensen, and O. Hejlesen, "Short-term prediction of future continuous glucose monitoring readings in type 1 diabetes: development and validation of a neural network regression model," *International Journal of Medical Informatics*, vol. 151, Article ID 104472, 2021.

[4] I. Tobore, A. Kandwal, J. Li et al., "Towards adequate prediction of prediabetes using spatiotemporal ECG and EEG feature analysis and weight-based multi-model approach," *Knowledge-Based Systems*, vol. 209, Article ID 106464, 2020.

[5] M. Boukhechba, L. Cai, C. Wu, and L. E. Barnes, "ActiPPG: using deep neural networks for activity recognition from wrist-worn photoplethysmography (PPG) sensors," *Smart Health*, vol. 14, Article ID 100082, 2019.

[6] F. D. Antoni, M. Merone, V. Piemonte, G. Iannello, and P. Soda, "Auto-regressive time delayed jump neural network for blood glucose levels forecasting," *Knowledge-Based Systems*, vol. 203, Article ID 106134, 2020.

[7] J. Huang, Y. Zhang, and J. Wu, "Review of non-invasive continuous glucose monitoring based on impedance spectroscopy," *Sensors and Actuators A: Physical*, vol. 311, Article ID 112103, 2020.

[8] S. H. Ling, P. P. San, and H. T. Nguyen, "Non-invasive hypoglycemia monitoring system using extreme learning machine for Type 1 diabetes," *ISA Transactions*, vol. 64, pp. 440–446, 2016.

[9] E. Monte-Moreno, "Non-invasive estimate of blood glucose and blood pressure from a photoplethysmograph by means of machine learning techniques," *Artificial Intelligence in Medicine*, vol. 53, no. 2, pp. 127–138, 2011.

[10] V. P. Rachim and W.-Y. Chung, "Wearable-band type visible-near infrared optical biosensor for non-invasive blood glucose monitoring," *Sensors and Actuators B: Chemical*, vol. 286, pp. 173–180, 2019.

[11] M. Zhang, X. Wang, H. Feng, Q. Huang, X. Xiao, and X. Zhang, "Wearable Internet of Things enabled precision livestock farming in smart farms: a review of technical solutions for precise perception, biocompatibility, and sustainability monitoring," *Journal of Cleaner Production*, vol. 312, Article ID 127712, 2021.

[12] J. Ben Ali, T. Hamdi, N. Fnaiech, V. Di Costanzo, F. Fnaiech, and J.-M. Ginoux, "Continuous blood glucose level prediction of type 1 diabetes based on artificial neural network," *Biocybernetics and Biomedical Engineering*, vol. 38, no. 4, pp. 828–840, 2018.

[13] T. Hamd, J. Ben Ali, V. Di Costanzo, F. Fnaiech, E. Moreau, and J.-M. Ginoux, "Accurate prediction of continuous blood glucose based on support vector regression and differential evolution algorithm," *Biocybernetics and Biomedical Engineering*, vol. 38, no. 2, pp. 362–372, 2018.

[14] J. Yang and L. Li, "An ARIMA model with adaptive orders for predicting blood glucose concentrations and hypoglycemia," *IEEE J Biomed Health Inform*, vol. 23, pp. 1251–1260, 2018.

[15] X. Yu and M. Rashid, "Online glucose prediction using computationally efficient sparse kernel filtering algorithms in type-1 diabetes," *IEEE Transactions on Control Systems Technology*, vol. 28, pp. 3–15, 2018.

[16] B. Sudharsan, M. Peeples, and M. Shomali, "Hypoglycemia prediction using machine learning models for patients with type 2 diabetes," *Journal of Diabetes Science and Technology*, vol. 9, no. 1, pp. 86–90, 2014.

Hindawi
Journal of Healthcare Engineering
Volume 2023, Article ID 9867516, 1 page
https://doi.org/10.1155/2023/9867516

Retraction

Retracted: Enamel Matrix Derivatives for Periodontal Regeneration: Recent Developments and Future Perspectives

Journal of Healthcare Engineering

Received 23 May 2023; Accepted 23 May 2023; Published 24 May 2023

This article has been retracted by Hindawi following an investigation undertaken by the publisher [1]. This investigation has uncovered evidence of one or more of the following indicators of systematic manipulation of the publication process:

(1) Discrepancies in scope
(2) Discrepancies in the description of the research reported
(3) Discrepancies between the availability of data and the research described
(4) Inappropriate citations
(5) Incoherent, meaningless and/or irrelevant content included in the article
(6) Peer-review manipulation

The presence of these indicators undermines our confidence in the integrity of the article's content and we cannot, therefore, vouch for its reliability. Please note that this notice is intended solely to alert readers that the content of this article is unreliable. We have not investigated whether authors were aware of or involved in the systematic manipulation of the publication process. Wiley and Hindawi regrets that the usual quality checks did not identify these issues before publication and have since put additional measures in place to safeguard research integrity.

We wish to credit our own Research Integrity and Research Publishing teams and anonymous and named external researchers and research integrity experts for contributing to this investigation.

The corresponding author, as the representative of all authors, has been given the opportunity to register their agreement or disagreement to this retraction. We have kept a record of any response received.

References

[1] L. Fan and D. Wu, "Enamel Matrix Derivatives for Periodontal Regeneration: Recent Developments and Future Perspectives," *Journal of Healthcare Engineering*, vol. 2022, Article ID 8661690, 10 pages, 2022.

Hindawi
Journal of Healthcare Engineering
Volume 2022, Article ID 8661690, 10 pages
https://doi.org/10.1155/2022/8661690

Research Article

Enamel Matrix Derivatives for Periodontal Regeneration: Recent Developments and Future Perspectives

Liping Fan and Dan Wu

Department of Prosthodontics, Qingdao Campus of Qilu Hospital of Shandong University, Shibei District, No. 758 Hefei Road, Qingdao 266000, Shandong, China

Correspondence should be addressed to Dan Wu; dan_wu66@126.com

Received 18 February 2022; Accepted 23 March 2022; Published 11 April 2022

Academic Editor: Liaqat Ali

In the era of the growing population, the demand for dental care is increasing at a fast pace for both older and younger people. One of the dental diseases that has attracted significant research is periodontitis. Periodontal therapy aims to regenerate tissues that are injured by periodontal disease. During recent decades, various pioneering strategies and products have been introduced for restoring or regeneration of periodontal deficiencies. One of these involves the regeneration of tissues under guidance using enamel matrix derivatives (EMDs) or combinations of these. EMDs are mainly comprised of amelogenins, which is one of the most common biological agents used in periodontics. Multiple studies have been reported regarding the role of EMD in periodontal tissue regeneration; however, the extensive mechanism remains elusive. The EMDs could promote periodontal regeneration mainly through inducing periodontal attachment during tooth formation. EMD mimics biological processes that occur during periodontal tissue growth. During root development, enamel matrix proteins are formed on the root surface by Hertwig's epithelial root sheath cells, initiating the process of cementogenesis. This article reviews the challenges and recent advances in preclinical and clinical applications of EMDs in periodontal regeneration. Moreover, we discuss the current evidence on the mechanisms of action of EMDs in the regeneration of periodontal tissues.

1. Introduction

Periodontal disease (PD) is a chronic inflammatory condition that results in the deterioration of the periodontium, or the tooth's supporting tissues [1]. PD is considered to be one of the most prevalent inflammatory oral diseases, affecting nearly 47% of individuals in the United States aged 30 years or older. If left untreated, periodontal disease severely affects periodontal tissues, resulting in tooth dislocation and eventual tooth loss [2]. Hence, there is an urgent need to prevent and treat periodontal disease, especially in an era of increasing ageing population where such diseases are dramatically increasing [3]. In 2010, the global economic cost of dental disorders was around $442 billion, of which $298 billion was spent on treatment and $144 billion on indirect expenditures associated with periodontal disease, caries, and tooth loss [4]. From an anatomic and molecular point of view, the primary characteristics of periodontitis include acute tissue inflammation, particularly those that support the tooth (periodontal ligament, gingiva, and alveolar bone), causing loss of the tooth, and it is considered to be primarily caused by dental plaque biofilm formation [5–7]. Risk factors include diabetes, smoking, genetic factors, and lack of dental care and oral hygiene. The aim of regenerative periodontal treatment is to prevent the loss of ensuing attachment loss whilst restoring the supporting structures such as the periodontal ligament and root cementum that may have been damaged, with the objective to ultimately restore the architecture and function of the tooth [8]. Regenerative periodontal therapies involve bone grafts, guided regeneration of tissues, use of matrix proteins of the enamel or their combinations.

The enamel of the tooth is an extremely complex tissue of apatite crystals arranged parallelly into prisms of enamel and possesses extraordinary mechanical strength, resistance to fracture, and physical resilience [9]. In animals, enamel is manufactured by highly specialized epithelial cells called ameloblasts only once before tooth eruption, and the capacity of the cells to form new enamel is lost permanently after eruption [10]. Bone is a unique tissue with self-regeneration capacity and unique structural and biological features. These unique features give the bone great capacity to interact with different external physicochemical modalities with potential therapeutic outcomes in bone disorders [11–14]. The characteristics of enamel which present challenges in enamel regeneration and engineering, include its unique structure and composition [15]. "Guided tissue regeneration" involves approaches for the regeneration of lost periodontal tissues employing barrier materials to facilitate space between the defect and the root surface for regeneration of the supporting tissue of the bone [16]. Graft biomaterials that are used for replacing a missing bone or assist in their growth include autografts, allografts, xenografts, and alloplasts [3]. Other biomaterials such as natural type collagen I, polylactic acid and oxidized cellulose mesh, titanium mesh, and ethylene cellulose may be easy to use, maintaining the space and reducing the possibility of bacterial infection on the graft side, but they have some drawbacks [3]. In relation to finding the right material, it is important to obtain ample stability of the primary implant in the alveolar bone to achieve predictable soft and hard dental implant tissue integration [17], while the type of defect is vital for realising successful procedures for reconstruction [18].

2. The Enamel Matrix Derivative (EMD)

The extract enamel matrix derived from porcine teeth is EMD, which comprises various proteins, 90% of which are amelogenins, which induce the attachment of the periodontium at the time of the formation of the tooth [3]. Other components of EMD are nonamelogenins *viz.* ameloblastin, tuftelin, enamelin, and amelotin. It was approved in 1996 by the USFDA for the treating defects in the periodontium and recessions in soft tissue. EMD has been extensively investigated in dental practices and has been demonstrated as an effective and safe method for the regeneration of periodontium [19]. The exact mechanism by which EMD participates in the periodontal regeneration at the cellular and molecular level is still unclear, though Emdogain® (Straumann, Basel, Switzerland), a porcine-derived tooth enamel matrix product, is commercially available with about 15 years of supportive clinical data [20]. It has a significant role in odontogenesis by upregulating Runx2 and Osterix transcription factors [21]. In addition, EMD augments the expression of markers for odontoblast-/osteoblast-like cells and upregulates dentin sialophosphoprotein, dentin matrix protein 1, and osteopontin RNA in human dentin pulp stem cells [21]. Despite the major limitation of gel-like composition in non-self-supporting abnormalities, EMD has been used alone for periodontal regeneration. To circumvent this shortcoming, EMD in combination with different biomaterials has been proposed [22]. There are many animal studies and clinical trials evaluating EMD alone or in combination with other agents in tooth regeneration, and those are listed in Table 1.

Herein, we review the recent advances (2016–present) in the application of EMD for periodontal regeneration, including *in vivo* research and clinical trials and methodologies currently in application for this purpose. We also provide novel insights into the future perspectives in this field.

2.1. Recent Developments in Applications of EMD. EMD has shown positive clinical features such as root coverage and promoting the stimulation of soft and hard tissues that surround the tooth in the scope of regeneration. EMD is considered frequently for applications in orthodontics as it has been used for over two decades in the field with positive results [3, 5, 23, 24]. EMD has been employed to improve the regeneration of alveolar bone, periodontal ligament, and new cementum [21, 31–33], as shown in Figure 1.

Another important characteristic of EMD is its inhibitory effect on the pathogenic dental plaque. EMD may promote improved early wound healing with reduced gingival fibroblast-induced inflammation. Deep intrabony periodontal abnormalities treated with EMD stimulate periodontal regeneration. Comparing EMD alone to EMD plus several forms of bone graft/bone substitute has been demonstrated to improve soft and hard tissue metrics. Compared to coronally relocated flaps alone, EMD seems to promote more keratinized tissue development and better long-term results. In mandibular class II furcations, EMD may be effective in promoting periodontal regeneration, particularly when modifying a membrane is technically difficult (Table 2) [34].

Fractures of the root of vertical teeth are associated with contained inflammation of the periodontal tissues surrounding the fracture, deepened probing depth, and bone resorption [41]. A study by Sugaya et al. in beagles was successful with Emdogain® in cementum regeneration on the surfaces of the root and also in the reduction of resorption incidences [23]. In detail, Emdogain® was applied in combination with ethylenediaminetetracetic acid to a vertically fractured root after bonding, followed by replantation. The mechanism of action was inferred to be that Emdogain® leads to cementum formation post surface resorption whilst concurrently inhibiting inflammation [23]. Additionally, Emdogain® caused the periodontal pockets to become shallow with little resorption of the roots, hence rendering the prognosis better [23]. Importantly, all the cementum that was damaged did not regenerate, and hence this approach may be considered when there is only a small fracture in the periodontal ligament.

A two-centre prospective clinical study evaluated the two-year outcome of Emdogain® in periodontal regeneration for treating intrabony defects in 42 patients and revealed a positive outcome as confirmed radiographically and also based on periodontal parameters [5]. The authors demonstrated that there were remarkable gains in clinical attachment level and reduced depth of probing. There was no correlation between the type of intrabony aberrance and

Table 1: Recent animal studies and clinical trials on EMD and other therapeutic agents.

Trial	Methods and results	References
Histopathological examination of cementum regeneration on root surfaces using the enamel derivative Emdogain®.	Roots ($n = 40$) from 24 maxillary premolars were evaluated in beagles. Emdogain® has been proven to be effective in the regeneration of cementum on root surfaces in periodontal ligament fractures.	[23]
Combining EMDs with autogenous bone graft or singly on intrabony defects in patients with chronic periodontitis.	Deep intrabony defects ($n = 30$) in 12 patients with chronic conditions were treated in a random manner with EMDs and autogenous bone graft, EMDs alone, or open flap debridement alone. The transforming growth factor beta 1 was examined in gingival crevicular fluid before and after surgery. There were no apparent clinical and radiographic differences between the combined group and EMDs, whilst the gingival curricular fluid transforming growth factor beta 1 level increased in the healing phase and was shown to be positively affected by the EMDs.	[8]
Assessment of EMD on regeneration of vertical bone around dental implants in an extra-oral model of a rabbit.	There was greater mean bone formation with EMD release from the scaffold, as well as the production of a new bone layer, increased regeneration, and increased bone density in the implant.	[17]
A study evaluating the combination of xenogenic collagen matrix and EMD.	It was found that the combinations conferred a better clinical outcome, while coronally advanced flip + EMD and coronally advanced flip + EMD + collagen matrix conferred the best results for complete root coverage.	[24]
The combination of matrix protein of the enamel and deprotenized bovine bone mineral with 1% collagen and doxycycline was evaluated in a three-year prospective cohort study in assessing bone defect regeneration related with peri-implantitis.	This combination resulted in a positive effect for bone regeneration.	[25]
Periodontal tissue regeneration with a cytokine cocktail of insulin-like growth factor-1, vascular endothelial growth factor A, and transforming growth factor-β1 assessment in a study in dogs.	The cytokine cocktail induced the formation of vascular tissues, cementum, and new bones, but was shown to be less effective at promoting osteogenesis than EMD.	[26]
A two-centre prospective clinical study evaluated the two-year outcome of EMD in the regeneration of periodontium for intrabony defects treatment.	Intrabony defect treatment of patients with EMD resulted in positive outcomes and was confirmed with radiographical and periodontal parameters.	[5]
A controlled noninferiority phase III and randomized placebo-controlled trials compared trafermin, a rhFGF 2, and EMD in periodontal regeneration in intrabony defects.	Trafermin was recognized to be a safe and effective approach, and it was also found to have superior efficacy when compared to EMD treatments.	[7]
A phase I/II trial of a 3D woven fabric scaffold with autologous bone marrow stem cell transplantation for periodontitis.	This approach may be novel for the effective regeneration of periodontitis.	[27]
A clinical study reporting on 3-year results following regenerative periodontal surgery of advanced intrabony defects with EMD alone or when combined with a synthetic bone graft.	There was not a significant advantage of comparing EMDs with synthetic bone grafts over EMD alone.	[28]
Autologous connective tissue graft or Xenogenic collagen matrix as adjunct to coronally advanced flaps to cover multiple adjacent gingival recessions: a randomized trial assessing noninferiority and superiority in root coverage, and superiority in quality of life in terms of oral health.	The xenogenic collagen matrix shortened the time to recovery and decreased morbidity. It was reported that the devices tested were inferior to the grafts of autologous connective tissue in regard to root coverage.	[29]
A clinical study evaluating the treatment results of EMD and/or hydroxyapatite/β-tricalcium phosphate (HA/β-TCP) to treat mandibular class II buccal furcations.	Clinical parameters measured were PPD, gingival index, plaque index, horizontal attachment, relative vertical level (RHCAL and RVCAL), and RGMP (relative gingival margin position). Clinical examinations at 12 months posttreatment revealed remarkable improvements in all parameters other than RGMP.	[30]

the clinical attachment level, which they attributed to the small size of the sample. The limitation of the study was that it was a single-arm study without a control group for direct comparison [5].

2.1.1. Combinations of EMD with Growth Factors. Due to its growth factor content, platelet-rich fibrin can facilitate healing of the tissue and is proven to regenerate periodontium. It acts as a regenerative scaffold and promotes the

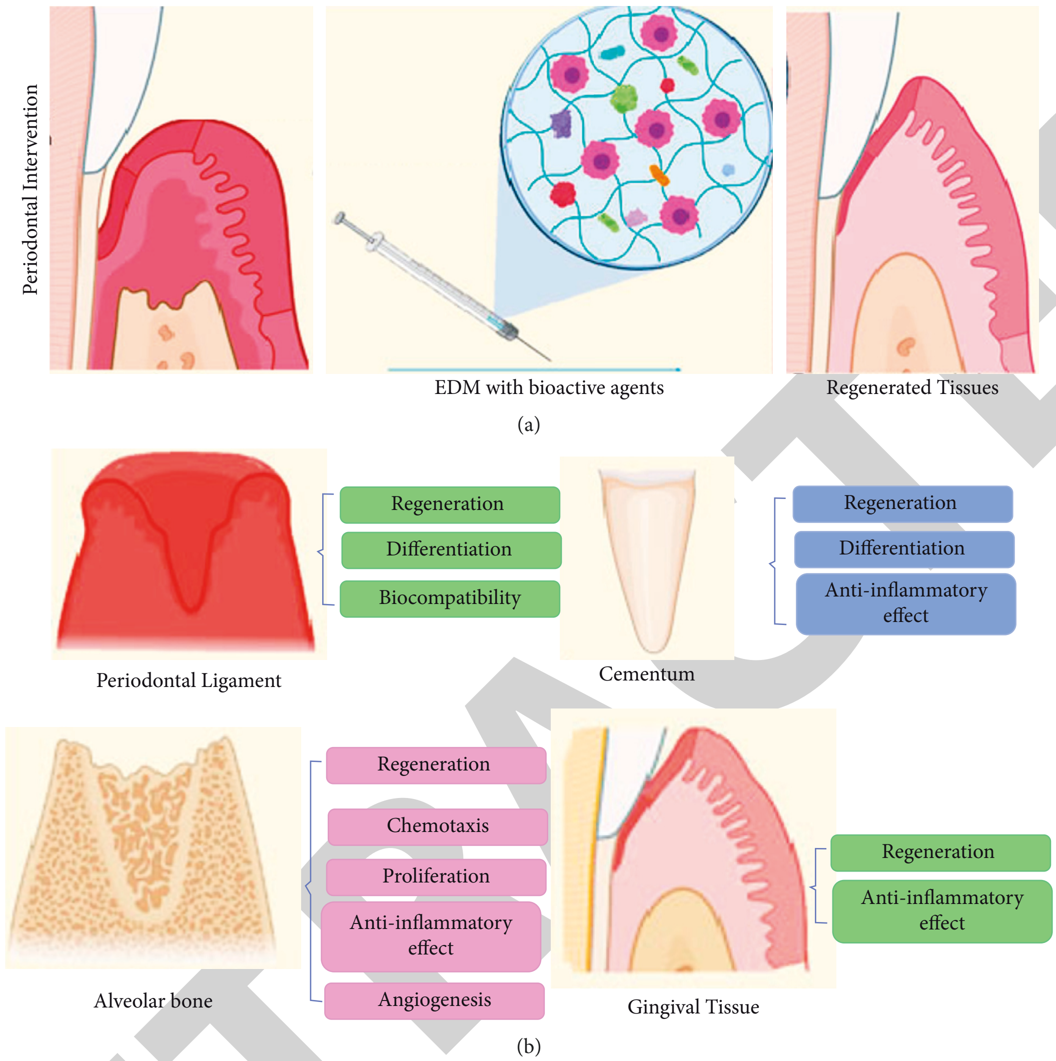

Figure 1: The regeneration of the periodontium. (a) EMD is a significant alternative to restore the structure and function of the periodontal complex. (b) EMD in periodontal cells can induce proliferation, differentiation, angiogenesis, and chemotaxis enabling the formation of new tissue.

formation of osseous and vascular tissues [5, 18]. Recently, in a randomized clinical trial, EMD + platelet-rich fibrin and EMD were compared for treating patients with chronic periodontitis having intrabony defects, and both approaches exhibited good clinical outcomes. However, the addition of fibrin rich in platelets did not appear to drastically improve the clinical outcome or the radiographic outcome [18]. Apart from platelet-derived growth factors, other growth factors that have been involved in tooth regeneration include transforming growth factors, vascular endothelial growth factors, connective tissue growth factors, insulin-like growth factors, fibroblast growth factors, and epidermal growth factor [3].

Tissue regeneration is also assumed to be promoted by human mesenchymal stem cell-produced secretomes in the medium. So, a research group made a cytokine cocktail of transforming growth factor-β1, vascular endothelial growth factor-A, and insulin-like growth factor-1, imitating the media in which the human mesenchymal stem cells were cultured [26]. In dogs, it was found that this cytokine cocktail promoted the formation of blood vessels and new cementum and bones. Interestingly, when compared with EMD, it was demonstrated that the cytokine cocktail promoted greater osteogenesis [26].

2.1.2. Combinations of EMD with Drugs/Bioactive Agents. Periodontal ligament cells were found to attach in the presence of oral pathogens such as *Streptococcus* mutants due to the addition of amoxicillin or tetracyclines and calcium phosphate in guided tissue regeneration membranes [3]. Peri-implantitis is an inflammatory condition that influences the circumventing peri-implant tissue that causes supporting bone loss. It has a similar pathogenesis to periodontitis, and thus similar management approaches are followed for both. Enamel matrix protein combined with deprotenized bovine bone mineral along with and doxycycline and 10% collagen was evaluated in a 3 year cohort

Table 2: Applications of enamel matrix derivatives (EMDs).

Application	Study	Outcome	References
Periodontal intrabony defect	A multicenter, randomized, placebo-controlled study was conducted on 33 patients with intrabony abnormalities who underwent a split-mouth operation. The effect of EMD in combination with natural bone mineral or bioactive glass was investigated in human histological tests.	The results revealed the production of root cementum and mineralization around the graft particles.	[35]
Effect on tissue inflammation	A study investigated the impact of EMD on tissue inflammation, focusing on the cellular process, mediators implicated, and soft tissue repair.	According to the findings, EMD can change inflammatory and healing responses by modifying the expression of proinflammatory markers.	[36]
Recession defects	Miller class I and II buccal gingival recessions were investigated utilizing a coronally positioned flap alone and in combination with EMD using the split-mouth method in controlled clinical research.	When compared to a coronally positioned flap alone, subsequent application of EMD resulted in a statistically larger development of keratinized tissue and root coverage that lasted for two years.	[37]
Pulp healing and dentin regeneration	An investigation using experimental pulpotomy and pulp capping in healthy premolars slated for extraction for orthodontic reasons was investigated in a blinded, randomized clinical research.	In the teeth that were evaluated, there was much greater pulpal secondary dentine development and dentine bridging, as well as significantly less inflammation.	[38]
Furcation defects	Treatment of mandibular class II furcation defects was compared to 90 equivalent defects in the contralateral molars in a multicenter, randomized, controlled, split-mouth clinical research.	Following EMD, there was a considerably higher reduction in horizontal furcation depth and a lower incidence of postoperative pain/swelling.	[39]
Wound healing	The extreme structural changes associated with a human gingival wound 10 days following the administration of EMD as an adjuvant to a laterally positioned flap in a patient with gingival recession were investigated in a quantitative study.	Both the cellular and extracellular phases of the EMD and non-EMD sites showed significant differences. At the EMD location, fibroblasts had plump cytoplasm and euchromatic nuclei, as well as a well-developed rough endoplasmic reticulum and many mitochondria. The fibroblasts at the non-EMD location, on the other hand, had a flattened, spindlelike shape.	[40]

study of osteoxonductive bone grafts in assessing bone defect regeneration in patients with peri-implantitis, and it was shown that this combination resulted in a beneficial outcome [25]. The limitation of this study is that it reported only a single treatment protocol with no control groups, and the contributions of the individual components of the mixture could not be determined. Therefore, it is important to assess the contributions of the components in long-term randomized controlled clinical trials. Furthermore, a combination of collagen matrix (xenogeneic) and EMD having a coronally advanced flap was considered in a clinical trial in order to assess whether this combination is beneficial for root coverage. It was found that the combination conferred an improved clinical outcome in comparison to the coronally advanced flap singly for coverage of the root, while the coronally advanced flap + EMD + collagen matrix and the coronally advanced flap + EMD conferred the best results for complete root coverage [24].

2.1.3. Combinations of EMD with Autogenous Bone Graft. Several preclinical animal and clinical trials have investigated the efficacy of using various bone grafts in combination with EMD for periodontal regeneration [8, 22, 28, 31, 42–45]. Studies have shown that EMD exhibited greater performance in opening flap debridement to treat the tooth intrabony impairment [46]. EMD combined with bone graft material was used in a wide intrabony defect and showed significant regenerative effect for regeneration of damaged tissue [47]. Combined EMD-bone grafts were successful in intrabony defect regeneration; the performance of the regeneration of the EMD-graft combination was comparable with the regeneration performance of human platelet-derived growth factor-BB (recombinant) with bone graft material [47, 48]. Findings of the studies have demonstrated that using EMD in combination with bovine-derived bone xenograft, freeze-dried bone allograft, and bioactive glass facilitated enhanced bone formation and improved outcomes clinically [42, 48–50]. The proof of autogenous bone grafting involves harvesting bone collected from a different site of the same individual receiving the graft [51]. The autogenous bone graft is advantageous in terms of its osteoinductivity, osteoconductivity, and osteogenic capacities [22]. On the other hand, limitations include the increase in morbidity and unpredictable resorption because of the donor site. EMD in combination with an autogenous bone graft in the regeneration of the periodontium has been reported to improve clinical outcomes, especially in promoting non-self-supporting intrabony defect regeneration [50]. In this combination, EMD initiates cementogenesis and the generation of new periodontal ligament, while autogenous bone grafts circumvent flap collapse in non-self-supporting intrabony defects because of the gel consistency of EMD.

In one controlled, randomized clinical trial, the outcome of EMD was assessed singly or combined with autogenous graft of the bone on intrabony defects in patients with chronic periodontitis. The influence on radiographic/clinical parameters and the level of gingival crevicular fluid transforming growth factor-β1 were determined and contrasted with those of open flap debridement [8]. No apparent differences were observed between the combination or the EMD alone, while the level of gingival crevicular fluid transforming growth factor-β1 was increased by EMD [8]. A limitation of this study was the sample size which might have limited the generalizability of the study.

A recent meta-analysis indicated that the EMD and autogenous bone graft combination may result in remarkable improvements in the treatment of periodontal intrabony defects in terms of the gain of the level of clinical attachment and reduction in probing depth compared with those obtained with EMD alone [22]. The application of EMD alone enables a less invasive and more manageable treatment. However, the effect of the surgical procedure or the chosen graft material on the clinical outcome is not fully understood. Another meta-analysis by Matarasso et al. demonstrated that the EMD and bone graft combination has superior clinical benefits pertaining to the gain in the clinical attachment level and the decrease in probing depth, compared to the EMD alone [52]. However, the authors did not compare the radiographic bone levels. The evidence shows that EMD proteins, when used on wide intrabony defects along with bone graft material, stimulate the self-regeneration of the impaired tissue and promote cell proliferation and ligament formation. During this process, the physicochemical properties of the bone grafts in the combination significantly influence the activity of EMD and the amount of the EMD protein precipitation. To achieve optimum self-regulation stimulated by the protein, the pH of the initial EMD formulation should be in the range of 3.9–4.2 to recompense for the pH change induced by the bone graft. Furthermore, EMD-bone graft interaction causes precipitate formation of different sizes and morphologies which envelop the grafts differently. This phenomenon could be used to improve attachment of the cell and extension of the periodontal ligament. However, further in vivo and in vitro studies are needed in this regard.

The current knowledge on the performance and interactions on combined EMD-autogenous bone graft is limited as there have been few well-designed clinical studies conducted in this regard. The clinical data on this strategy are still limited, and the therapeutic potential of the EMD-graft combination needs to be further investigated.

2.1.4. Combinations of EMD with Alloplastic Bone Grafts. The EMD surface coating of a scaffold biomaterial dramatically increases the thickness of enamel matrix proteins [17, 53]. It was also established that a formulation in the liquid could form a better coating of porous alloplastic graft materials compared to the gel form, which allowed the release of enamel matrix proteins in a controlled manner to their neighboring environment [53].

The combination of EMD with βTCP (β-tricalcium phosphate) was effective in regenerating intrabony defects [54]. The effect of EMD was comparable to that of guided tissue regeneration and demineralized freeze-dried bone allograft; it was also superior to open-flap debridement for treating intrabony defects [54].

The effect of EMD on the subgingival microbiome has been rarely assessed. Queiroz et al. analyzed the alterations in the periodontal microbiome in furcation defects of class II after treatment with hydroxyapatite graft/β-tricalcium phosphate (HA/βTCP), EMD + HA/βTCP, or EMD singly [55]. The EMD groups displayed more reductions over the long-term in a large number of species. In the EMD groups, the microbial species which are associated with periodontal disease were more reduced compared with the βTCP/HA group.

Masaeli et al. provided a comparative outlook on different combinations of biomaterials for the treatment of furcation defects. They reported that the best results were observed when EMD was used in combination with HA/β-TCP alloplastic grafts of the bone [45]. Losada et al. performed a 12-month randomized clinical trial by treating patients with uncontained infrabony defects. They were treated with EMD + calcium phosphate bone graft (biphasic) or EMD singly. No significant variations were observed in terms of CAL, bone fill, and decrease of PD [33]. Also, EMD in combination with a biphasic calcium phosphate bone graft (synthetic) and EMD alone were assessed clinically in intrabony defects. It was found that there was not a significant advantage of EMD in combination with synthetic bone graft relative to EMD alone [28].

2.1.5. Combination with Other Approaches. EMD (5–60 μg/mL) enhanced the osteogenic differentiation and proliferation of human periodontal ligament stem cells on surfaces of titanium implants [56]. It also influenced the angiogenic gene expression and proliferation in endothelial cells on the surface of the titanium implant [57]. EMD enhanced the gingival fibroblast growth on titanium surfaces along with the increased synthesis of extracellular matrix [58]. A previous report demonstrated that EMD application can be used as an adjunct to mechanical debridement in the nonsurgical treatment of peri-implant mucositis [32]. Randomized controlled trials of peri-implantitis surgical therapies proved that the adjunctive use of EMD enhanced implant survival [48, 59] and augmented marginal bone level [60].

Aggressive periodontitis (AgP) is a rare but adverse inflammatory condition, which involves periodontal tissue destruction. EMD could be effective in periodontal regeneration in individuals with generalized AgP. A systematic review evaluated various regenerative techniques used in AgP patients. The application of EMD in AgP patients offered comparable clinical improvements to the use of EMD in chronic periodontitis patients [61]. Additional prospective studies with an adequate count of AgP patients are essential to thoroughly assess the effectiveness of this approach.

Osteogain was soaked on absorbable collagen sponge in the scope of healing periodontal wounds in monkeys, and it was found that Osteogain had positive physiochemical properties, specifically in amelogenin adsorption on the collagen sponge that is absorbable and may also improve healing of periodontal wounds relative to Emdogain [44]. EMD use in combination with a coronally advanced flap led to similar outcomes in comparison to the connective tissue graft plus coronally advanced flap in individuals with several recession defects [62]. Porcine acellular dermal matrix in dogs was examined with or without EMD on recession defects of the gingiva that were treated with a coronally advanced flap; the treatment combined the coronally advanced flap along with EMD and porcine acellular dermal matrix and facilitated regeneration of the periodontium in recession defects of the gingiva [63].

2.2. Comparison of EMD with Other Approaches in Periodontal Regeneration. Studies showed that when comparing augmentation of the maxillary sinus floor with β-TCP/HA without or with EMD, it was found that the combination of Bone Ceramic® and maxillary sinus floor augmentation had resulted in high bone formation and thus installation of the implant successfully and that EMD did not lead to a significant effect [64]. Potent angiogenic and mitogenic activity is exhibited by fibroblast growth factor (FGF)-2 in mesenchymal cells inside the periodontal ligament and is found effective in periodontal tissue regeneration in animal models. Recombinant human FGF (rhFGF)-2, trafermin significantly improves the bone fill percentage in comparison to the placebo. The efficacy of trafermin was compared to that of EMD in phase III trials by Kitamura et al. for the regeneration of periodontium in intrabony defects [7]. In these phase III trials that were randomized placebo-controlled or controlled noninferiority, trafermin had superior efficacy in EMD for periodontal regeneration [7]. Yildirim et al. reported that EMD was inferior to mineral trioxide clustered as a pulpotomy agent in patients with deep caries treated with pulpotomies [65].

3. Conclusion and Future Prospects

The overall aim of regenerative orthodontics is to create and sustain an accommodating environment for tooth viability and growth, and the use of biomimetic materials is still ongoing, with advantages and disadvantages. Several factors related to the surgical site and the patient have to be accurately evaluated before applying any regenerative therapy and strictly controlled during healing postoperation. Notably, an individual's anatomy, bone fracture, site-specific factors, and materials available are some of the factors that must be considered when designing treatments for regenerative periodontology. Development in enamel tissue engineering is partially limited because of its unique structure, composition, and material properties. Tooth enamel engineering may result in novel technologies that produce new biomaterials as well as techniques for regenerative medicine and further unravel the biological mechanisms associated with tooth enamel generation.

EMD has greater evidence compared with other biomaterials and displayed similar efficacy to the guided tissue regeneration techniques. The combination of EMD with diverse materials and/or treatment strategies also demonstrated encouraging results in some studies. One issue in assessing EMD potential is that only short-term study results are presently available. Thus, long-term well-controlled trials evaluating its effectiveness in regenerative procedures relative to existing treatments are essential. The outcomes of EMD applications in endodontic therapies vary exceedingly, and hence additional research is warranted, especially in the subjects of regeneration and replantation.

Data Availability

The data are available from the corresponding author on reasonable request.

Conflicts of Interest

All authors declare that they have no conflicts of interest.

Acknowledgments

This work was funded by the Science and Technology Department of Zhejiang Province (nos. 2016C34G1360013 to FY, LGF18H140005 to LHW).

References

[1] O. Paul, P. Arora, M. Mayer, and S. Chatterjee, "Inflammation in periodontal disease: possible link to vascular disease," *Frontiers in Physiology*, vol. 11, p. 1818, 2021.

[2] Y. Liang, X. Luan, and X. Liu, "Recent advances in periodontal regeneration: a biomaterial perspective," *Bioactive Materials*, vol. 5, no. 2, pp. 297–308, 2020.

[3] M. Andrei, A. Dinischiotu, A. C. Didilescu, D. Ionita, and I. Demetrescu, "Periodontal materials and cell biology for guided tissue and bone regeneration," *Annals of Anatomy - Anatomischer Anzeiger*, vol. 216, pp. 164–169, 2018.

[4] Z. Sheikh, N. Hamdan, Y. Ikeda, M. Grynpas, B. Ganss, and M. Glogauer, "Natural graft tissues and synthetic biomaterials for periodontal and alveolar bone reconstructive applications: a review," *Biomaterials Research*, vol. 21, 2017.

[5] F. Seshima, H. Aoki, T. Takeuchi et al., "Periodontal regenerative therapy with enamel matrix derivative in the treatment of intrabony defects: a prospective 2-year study," *BMC Research Notes*, vol. 10, no. 1, p. 256, 2017.

[6] S. Liu, B. Hu, Y. Zhang, W. Li, and J. Song, "Minimally invasive surgery combined with regenerative biomaterials in treating intra- bony defects: a meta-analysis," *PLoS One*, vol. 11, no. 1, Article ID e0147001, 2016.

[7] M. Kitamura, M. Akamatsu, M. Kawanami et al., "Randomized placebo-controlled and controlled non-inferiority phase III trials comparing trafermin, a recombinant human fibroblast growth factor 2, and enamel matrix derivative in

periodontal regeneration in intrabony defects," *Journal of Bone and Mineral Research*, vol. 31, no. 4, pp. 806–814, 2016.
[8] Ö. Agrali, B. Kuru, A. Yarat, and L. Kuru, "Evaluation of gingival crevicular fluid transforming growth factor-β1 level after treatment of intrabony periodontal defects with enamel matrix derivatives and autogenous bone graft: a randomized controlled clinical trial," *Nigerian Journal of Clinical Practice*, vol. 19, no. 4, pp. 535–543, 2016.
[9] M. V. Stack, "Organic constituents of enamel," *Biochemical Journal*, vol. 50, 1952.
[10] J. P. Simmer, A. S. Richardson, Y.-Y. Hu, C. E. Smith, and J. Ching-Chun Hu, "A post-classical theory of enamel biomineralization... and why we need one," *International Journal of Oral Science*, vol. 4, no. 3, pp. 129–134, 2012.
[11] A. Yadollahpour and S. Rashidi, "A review of electromagnetic field based treatments for different bone fractures," *Biosciences Biotechnology Research Asia*, vol. 11, no. 2, pp. 611–620, 2014.
[12] A. Yadollahpour and S. Rashidi, "Therapeutic applications of low-intensity pulsed ultrasound in osteoporosis," *Asian Journal of Pharmaceutics*, vol. 11, no. 1, pp. S1–S6, 2017.
[13] J. C. Chen, A. B. Castillo, and C. R. Jacobs, "Cellular and molecular mechanotransduction in bone," in *Osteoporosis: Fourth Edition,* Elsevier Inc., Amsterdam, Netherlands, 2013.
[14] K. S. Kang, J. M. Hong, Y. H. Jeong et al., "Combined effect of three types of biophysical stimuli for bone regeneration," *Tissue Engineering. Part A*, vol. 20, no. 11–12, pp. 1767–1777, 2014.
[15] J. Kirkham, S. J. Brookes, T. G. H. Diekwisch, H. C. Margolis, A. Berdal, and M. J. Hubbard, "Enamel research: priorities and future directions," *Frontiers in Physiology*, vol. 8, p. 513, 2017.
[16] T. V. Scantlebury, "A decade of Technology development for guided tissue regeneration," *Journal of Periodontology*, vol. 64, no. 11s, pp. 1129–1137, 1993.
[17] B. Wen, Z. Li, R. Nie et al., "Influence of biphasic calcium phosphate surfaces coated with Enamel Matrix Derivative on vertical bone growth in an extra-oral rabbit model," *Clinical Oral Implants Research*, vol. 27, no. 10, pp. 1297–1304, 2016.
[18] H. Aydemir Turkal, S. Demirer, A. Dolgun, and H. G. Keceli, "Evaluation of the adjunctive effect of platelet-rich fibrin to enamel matrix derivative in the treatment of intrabony defects. Six-month results of a randomized, split-mouth, controlled clinical study," *Journal of Clinical Periodontology*, vol. 43, no. 11, pp. 955–964, 2016.
[19] F. Zepp and B. Willershausen, "Zahn- und Mundgesundheit," *Monatsschrift Kinderheilkunde*, vol. 161, no. 6, p. 499, 2013.
[20] M. Esposito, M. G. Grusovin, N. Papanikolaou, P. Coulthard, and H. V. Worthington, "Enamel matrix derivative (Emdogain) for periodontal tissue regeneration in intrabony defects: a cochrane systematic review," *European Journal of Oral Implantology*, vol. 2, no. 3, pp. 247–266, 2009.
[21] Y. Wang, Y. Zhao, and L. Ge, "Effects of the enamel matrix derivative on the proliferation and odontogenic differentiation of human dental pulp cells," *Journal of Dentistry*, vol. 42, no. 1, pp. 53–59, 2014.
[22] M. Annunziata, A. Piccirillo, F. Perillo, G. Cecoro, L. Nastri, and L. Guida, "Enamel matrix derivative and autogenous bone graft for periodontal regeneration of intrabony defects in humans: a systematic review and meta-analysis," *Materials*, vol. 12, 2019.
[23] T. Sugaya, M. Tomita, Y. Motoki, H. Miyaji, and M. Kawamami, "Influence of enamel matrix derivative on healing of root surfaces after bonding treatment and intentional replantation of vertically fractured roots," *Dental Traumatology*, vol. 32, no. 5, pp. 397–401, 2016.
[24] J. P. M. Sangiorgio, F. L. d. S. Neves, M. Rocha dos Santos et al., "Xenogenous collagen matrix and/or enamel matrix derivative for treatment of localized gingival recessions: a randomized clinical trial. Part I: clinical outcomes," *Journal of Periodontology*, vol. 88, no. 12, pp. 1309–1318, 2017.
[25] F. Mercado, S. Hamlet, and S. Ivanovski, "Regenerative surgical therapy for peri-implantitis using deproteinized bovine bone mineral with 10% collagen, enamel matrix derivative and Doxycycline—a prospective 3-year cohort study," *Clinical Oral Implants Research*, vol. 29, no. 6, pp. 583–591, 2018.
[26] K. Sakaguchi, W. Katagiri, M. Osugi, T. Kawai, Y. Sugimura-Wakayama, and H. Hibi, "Periodontal tissue regeneration using the cytokine cocktail mimicking secretomes in the conditioned media from human mesenchymal stem cells," *Biochemical and Biophysical Research Communications*, vol. 484, no. 1, pp. 100–106, 2017.
[27] S. Baba, Y. Yamada, A. Komuro et al., "Phase I/II trial of autologous bone marrow stem cell transplantation with a three-dimensional woven-fabric scaffold for periodontitis," *Stem Cells International*, vol. 2016, Article ID 6205910, 7 pages, 2016.
[28] T. Hoffmann, E. Al-Machot, J. Meyle, P.-M. Jervøe-Storm, and S. Jepsen, "Three-year results following regenerative periodontal surgery of advanced intrabony defects with enamel matrix derivative alone or combined with a synthetic bone graft," *Clinical Oral Investigations*, vol. 20, no. 2, pp. 357–364, 2016.
[29] M. S. Tonetti, P. Cortellini, G. Pellegrini et al., "Xenogenic collagen matrix or autologous connective tissue graft as adjunct to coronally advanced flaps for coverage of multiple adjacent gingival recession: randomized trial assessing non-inferiority in root coverage and superiority in oral health-related," *Journal of Clinical Periodontology*, vol. 45, no. 1, pp. 78–88, 2018.
[30] L. A. Queiroz, M. P. Santamaria, M. Z. Casati et al., "Enamel matrix protein derivative and/or synthetic bone substitute for the treatment of mandibular class II buccal furcation defects: a 12-month randomized clinical trial," *Clinical Oral Investigations*, vol. 20, no. 7, pp. 1597–1606, 2016.
[31] J.-B. Park, "The use of enamel matrix derivative for the treatment of the apically involved tooth," *Medicine*, vol. 98, no. 48, Article ID e18115, 2019.
[32] A. Kashefimehr, R. Pourabbas, M. Faramarzi et al., "Effects of enamel matrix derivative on non-surgical management of peri-implant mucositis: a double-blind randomized clinical trial," *Clinical Oral Investigations*, vol. 21, no. 7, pp. 2379–2388, 2017.
[33] M. Losada, R. González, À. P. Garcia, A. Santos, and J. Nart, "Treatment of non-contained infrabony defects with enamel matrix derivative alone or in combination with biphasic calcium phosphate bone graft: a 12-month randomized controlled clinical trial," *Journal of Periodontology*, vol. 88, no. 5, pp. 426–435, 2017.
[34] H. Seshan, *The Role of Enamel Matrix Protein Derivatives in Periodontal Tissue Regenetation: Revisited*.
[35] A. Sculean, P. Windisch, T. Keglevich, and I. Gera, "Clinical and histologic evaluation of an enamel matrix protein derivative combined with a bioactive glass for the treatment of intrabony periodontal defects in humans," *The International Journal of Periodontics & Restorative Dentistry*, vol. 25, no. 2, pp. 139–47, 2005.

[36] R. J. Miron, M. Dard, and M. Weinreb, "Enamel matrix derivative, inflammation and soft tissue wound healing," *Journal of Periodontal Research*, vol. 50, no. 5, pp. 555–569, 2015.

[37] A. Spahr, S. Haegewald, F. Tsoulfidou et al., "Coverage of miller class I and II recession defects using enamel matrix proteins versus coronally advanced flap technique: a 2-year report," *Journal of Periodontology*, vol. 76, no. 11, pp. 1871–1880, 2005.

[38] H. Olsson, J. R. Davies, K. E. Holst, U. Schroder, and K. Petersson, "Dental pulp capping: effect of Emdogain Gel on experimentally exposed human pulps," *International Endodontic Journal*, vol. 38, no. 3, pp. 186–194, 2005.

[39] S. Jepsen, B. Heinz, K. Jepsen et al., "A randomized clinical trial comparing enamel matrix derivative and membrane treatment of buccal class II furcation involvement in mandibular molars. part I: study design and results for primary outcomes," *Journal of Periodontology*, vol. 75, no. 8, pp. 1150–1160, 2004.

[40] A. Lafzi, R. M. Farahani, R. S. Tubbs, L. Roushangar, and M. M. Shoja, "Enamel matrix derivative Emdogain® as an adjuvant for a laterally-positioned flap in the treatment of gingival recession: an electron microscopic appraisal," *Folia Morphologica*, vol. 66, no. 2, pp. 100–103, 2007.

[41] A. M. Polson, "Periodontal destruction associated with vertical root fracture: report of four cases," *Journal of Periodontology*, vol. 48, no. 1, pp. 27–32, 1977.

[42] P. Potijanyakul, W. Sattayasansakul, S. Pongpanich, N. Leepong, and S. Kintarak, "Effects of enamel matrix derivative on bioactive glass in rat calvarium defects," *J Oral Implantol [Internet]*, vol. 36, pp. 195–204, 2010.

[43] S. S. Hakki, J. E. Berry, and M. J. Somerman, "The effect of enamel matrix protein derivative on follicle cells in vitro," *Journal of Periodontology*, vol. 72, no. 5, pp. 679–687, 2001.

[44] Y. Shirakata, R. J. Miron, T. Nakamura et al., "Effects of EMD liquid (Osteogain) on periodontal healing in class III furcation defects in monkeys," *Journal of Clinical Periodontology*, vol. 44, no. 3, pp. 298–307, 2017.

[45] R. Masaeli, K. Zandsalimi, Z. Lotfi, and L. Tayebi, "Using enamel matrix derivative to improve treatment efficacy in periodontal furcation defects," *Journal of Prosthodontics*, vol. 27, no. 8, pp. 733–736, 2018.

[46] M. A. Reynolds, R. T. Kao, P. M. Camargo, J. G. Caton, D. S. Clem, and J. P. Fiorellini, "Periodontal regeneration – intrabony defects: a consensus report from the AAP regeneration workshop," *Journal of Periodontology*, vol. 86, no. 2-s, pp. S105–S107, 2015.

[47] A. Apicella, P. Heunemann, L. Dejace, M. Marascio, C. J. G. Plummer, and P. Fischer, "Scaffold requirements for periodontal regeneration with enamel matrix derivative proteins," *Colloids Surfaces B Biointerfaces [Internet]*, vol. 156, pp. 221–226, 2017.

[48] P. S. Rosen and M. A. Reynolds, "A retrospective case series comparing the use of demineralized freeze-dried bone allograft and freeze-dried bone allograft combined with enamel matrix derivative for the treatment of advanced osseous lesions," *Journal of Periodontol [Internet]*, vol. 73, no. 8, pp. 942–949, 2002.

[49] E. T. Scheyer, D. Velasquez-Plata, M. A. Brunsvold, D. J. Lasho, and J. T. Mellonig, "A clinical comparison of a bovine-derived xenograft used alone and in combination with enamel matrix derivative for the treatment of periodontal osseous defects in humans," *Journal of Periodontol*, vol. 73, pp. 423–432, 2002.

[50] L. Guida, M. Annunziata, S. Belardo, R. Farina, A. Scabbia, and L. Trombelli, "Effect of autogenous cortical bone particulate in conjunction with enamel matrix derivative in the treatment of periodontal intraosseous defects," *Journal of Periodontology*, vol. 78, no. 2, pp. 231–238, 2007.

[51] R. J. Miron, E. Hedbom, N. Saulacic et al., "Osteogenic potential of autogenous bone grafts harvested with four different surgical techniques," *Journal of Dental Research*, vol. 90, no. 12, pp. 1428–1433, 2011.

[52] M. Matarasso, V. Iorio-Siciliano, A. Blasi, L. Ramaglia, G. E. Salvi, and A. Sculean, "Enamel matrix derivative and bone grafts for periodontal regeneration of intrabony defects. A systematic review and meta-analysis," *Clinical Oral Investigations*, vol. 19, no. 7, pp. 1581–1593, 2015.

[53] R. J. Miron, D. D. Bosshardt, D. Buser et al., "Comparison of the capacity of enamel matrix derivative gel and enamel matrix derivative in liquid formulation to adsorb to bone grafting materials," *Journal of Periodontology*, vol. 86, no. 4, pp. 578–587, 2015.

[54] C. W. DiGiovanni, S. S. Lin, J. F. Baumhauer et al., "Recombinant human platelet-derived growth factor-BB and beta-tricalcium phosphate (rhPDGF-BB/β-TCP): an alternative to autogenous bone graft," *Journal of Bone and Joint Surgery*, vol. 95, no. 13, pp. 1184–1192, 2013.

[55] L. A. Queiroz, R. C. V. Casarin, S. M. Dabdoub, D. N. Tatakis, E. A. Sallum, and P. S. Kumar, "Furcation therapy with enamel matrix derivative: effects on the subgingival microbiome," *Journal of Periodontology*, vol. 88, no. 7, pp. 617–625, 2017.

[56] G. Li, J. Hu, H. Chen et al., "Enamel matrix derivative enhances the proliferation and osteogenic differentiation of human periodontal ligament stem cells on the titanium implant surface," *Organogenesis*, vol. 13, no. 3, pp. 103–113, 2017.

[57] B. Shi, O. Andrukhov, S. Berner, A. Schedle, and X. Rausch-Fan, "The angiogenic behaviors of human umbilical vein endothelial cells (HUVEC) in co-culture with osteoblast-like cells (MG-63) on different titanium surfaces," *Dental Materials*, vol. 30, no. 8, pp. 839–847, 2014.

[58] Y. Wang, Y. Zhang, D. Jing, Y. Shuang, and R. J. Miron, "Enamel matrix derivative improves gingival fibroblast cell behavior cultured on titanium surfaces," *Clinical Oral Investigations*, vol. 20, no. 4, pp. 685–695, 2016.

[59] C. Isehed, B. Svenson, P. Lundberg, and A. Holmlund, "Surgical treatment of peri-implantitis using enamel matrix derivative, an RCT: 3- and 5-year follow-up," *Journal of Clinical Periodontology*, vol. 45, no. 6, pp. 744–753, 2018.

[60] C. Isehed, A. Holmlund, S. Renvert, B. Svenson, I. Johansson, and P. Lundberg, "Effectiveness of enamel matrix derivative on the clinical and microbiological outcomes following surgical regenerative treatment of peri-implantitis. A randomized controlled trial," *Journal of Clinical Periodontology*, vol. 43, no. 10, pp. 863–873, 2016.

[61] S. Eick, J. Nydegger, W. Bürgin, G. E. Salvi, A. Sculean, and C. Ramseier, "Microbiological analysis and the outcomes of periodontal treatment with or without adjunctive systemic antibiotics-a retrospective study," *Clinical Oral Investigations*, vol. 22, no. 9, pp. 3031–3041, 2018.

[62] A. Alexiou, I. Vouros, G. Menexes, and A. Konstantinidis, "Comparison of enamel matrix derivative (Emdogain) and subepithelial connective tissue graft for root coverage in patients with multiple gingival recession defects: a randomized controlled clinical study," *Quintessence International*, vol. 48, no. 5, pp. 381–389, 2017.

Hindawi
Journal of Healthcare Engineering
Volume 2023, Article ID 9865031, 1 page
https://doi.org/10.1155/2023/9865031

Retraction

Retracted: Clinical Efficacy and Safety of Anterior Cervical Decompression versus Segmental Fusion and Posterior Expansive Canal Plasty in the Treatment of Multilevel Cervical Spondylotic Myelopathy

Journal of Healthcare Engineering

Received 10 October 2023; Accepted 10 October 2023; Published 11 October 2023

This article has been retracted by Hindawi following an investigation undertaken by the publisher [1]. This investigation has uncovered evidence of one or more of the following indicators of systematic manipulation of the publication process:

(1) Discrepancies in scope
(2) Discrepancies in the description of the research reported
(3) Discrepancies between the availability of data and the research described
(4) Inappropriate citations
(5) Incoherent, meaningless and/or irrelevant content included in the article
(6) Peer-review manipulation

The presence of these indicators undermines our confidence in the integrity of the article's content and we cannot, therefore, vouch for its reliability. Please note that this notice is intended solely to alert readers that the content of this article is unreliable. We have not investigated whether authors were aware of or involved in the systematic manipulation of the publication process.

In addition, our investigation has also shown that one or more of the following human-subject reporting requirements has not been met in this article: ethical approval by an Institutional Review Board (IRB) committee or equivalent, patient/participant consent to participate, and/or agreement to publish patient/participant details (where relevant).

Wiley and Hindawi regrets that the usual quality checks did not identify these issues before publication and have since put additional measures in place to safeguard research integrity.

We wish to credit our own Research Integrity and Research Publishing teams and anonymous and named external researchers and research integrity experts for contributing to this investigation.

The corresponding author, as the representative of all authors, has been given the opportunity to register their agreement or disagreement to this retraction. We have kept a record of any response received.

References

[1] C. Xia, F. Shi, C. Chen, J. Lv, and Q. Chen, "Clinical Efficacy and Safety of Anterior Cervical Decompression versus Segmental Fusion and Posterior Expansive Canal Plasty in the Treatment of Multilevel Cervical Spondylotic Myelopathy," *Journal of Healthcare Engineering*, vol. 2022, Article ID 7696209, 9 pages, 2022.

Hindawi
Journal of Healthcare Engineering
Volume 2022, Article ID 7696209, 9 pages
https://doi.org/10.1155/2022/7696209

Research Article

Clinical Efficacy and Safety of Anterior Cervical Decompression versus Segmental Fusion and Posterior Expansive Canal Plasty in the Treatment of Multilevel Cervical Spondylotic Myelopathy

Chen Xia,[1] Fangfang Shi,[2] Chuyong Chen,[1] Jun Lv,[1] and Qi Chen[1]

[1]*Department of Orthopedics, Zhejiang Provincial People's Hospital, People's Hospital of Hangzhou Medical College, Zhejiang, Hangzhou 310014, China*
[2]*Department of Hematology, Zhejiang Provincial People's Hospital, People's Hospital of Hangzhou Medical College, Zhejiang, Hangzhou 310014, China*

Correspondence should be addressed to Qi Chen; doctor_chenqi@163.com

Received 25 February 2022; Accepted 21 March 2022; Published 11 April 2022

Academic Editor: Liaqat Ali

Objective. To compare the clinical efficacy and safety of anterior cervical decompression and segmental fusion and posterior expansive canal plasty in the treatment of multisegment cervical myelopathy. *Methods*. Retrospective analysis was performed of 56 cases of multisegment cervical myelopathy patients admitted from July 2018 to June 2021, 32 male patients and 24 females, aged 56.9 ± 12.8 years with an average duration of 10.6 ± 3.2 years. All patients' preoperative imaging examination revealed multiple-segmented cervical disc herniation and had clinical manifestations of cervical myelopathy. *Results*. No neurovascular complications occurred in both groups, and 24 to 36 months of follow-up (mean 28.6 months) were obtained. The height of the cervical spondylosis segment was higher than that 2 weeks after surgery ($p < 0.05$), and the curvature of the cervical spine was significantly lower than that before surgery. There was no statistical significance in the height of the anterior column and curvature of the cervical vertebra at 2 weeks after surgery and at the last follow-up ($p > 0.05$). There were statistically significant differences in anterior curvature of the cervical spine between the two groups at 2 weeks after surgery and the last follow-up ($p < 0.05$). Japanese Orthopaedic Association (JOA) scores in both groups recovered significantly after surgery. At 3 months and the last follow-up, the improvement rate of JOA score in the anterior approach group was significantly higher than that in the posterior approach group ($p < 0.05$), and the improvement rate of JOA score in the anterior approach group was also better than that in the posterior approach group ($p < 0.05$). *Conclusion*. This segmented anterior fusion procedure can effectively restore the anterior cervical column height and can significantly improve spinal cord function compared with posterior spinal canal enlargement plasty, thus could be considered an effective option for the treatment of multisegment cervical myelopathy.

1. Introduction

Osteophytes at the posterior edge of the vertebral body are a common cause of cervical spondylotic spondylosis, and cervical spondylosis (CS) is caused by multiple segment cervical spine degeneration which is not uncommon in clinical practice [1, 2]. For cervical spondylotic myelopathy (CSM) caused by multiple segment cervical spine degeneration, the compression of the spinal cord or nerve root is generally alleviated by direct anterior decompression or posterior indirect decompression, to achieve the purpose of improving the symptoms [3]. However, for multiple segment disc herniation of patients with CS, after anterior decompression often need to fix multiple cervical segments. Long segment cervical fusion for cervical physiological curvature is very big and is bound to affect the normal biomechanical characteristics of the cervical spine. Moreover, long-segment fusion surgery for the influence of adjacent segment degeneration is still controversial in the world [4–6].

The efficacy of anterior cervical surgery, as one of the main surgical methods of treating CS, has reached a consensus since the procedure was invented in the 1960s [7]. The principle of this operation is to achieve direct decompression through the removal of the posterior margin hyperplasia or the protruding cervical disc [8]. In addition, anterior surgery can open the diseased intervertebral space or vertebral body to restore the vertebral height, and then make the lesion segment fusion through bone grafting, thus eliminating the possibility of the continued lesion in this segment. Such surgery can not only restore the height of CS degeneration, but also restore some or all of the cervical anterior convex physiological curvature, thus holding open the folded yellow ligament, and then expanding the volume of the cervical canal and nerve root canal [9]. However, for the anterior cervical surgery with long segments, especially the anterior cervical surgery fixed with a long titanium cage and anterior long titanium plate, the normal biomechanical state of the cervical spine will be significantly changed. Therefore, it is considered to increase the risk of adjacent segment degeneration after surgery [10]. Although there are pathological changes in multiple plane vertebral body, disc, spinal canal, and spinal cord in long segment CS, there is no consistent understanding of whether they can cause clinical symptoms, whether phase I surgical decompression is needed, or which surgical choice is needed [11].

In this study, 56 patients cases with multilevel cervical spondylotic myelopathy (CSM) from July 2018 to June 2021 who were treated with anterior decompression and segmenting fusion and posterior expansive canal plasty respectively were retrospectively analyzed to evaluate the clinical efficacy and safety of these treatment options.

2. Materials and Methods

2.1. Basic Clinical Features of Patients. Inclusion criteria for the cases: Those cases that had clinical manifestations of cervical myelopathy, radiographic continuous multisegment cervical disc herniation; no serious cardiovascular and pulmonary diseases, can tolerate surgery, and can cooperate with long-term clinical follow-up were included. There were 56 cases in this group, including 32 males and 24 females. The average age was (56.9 ± 12.8) years. Preoperative CT or MRI examination showed multilevel cervical disc herniation and clinical manifestations of CSM, such as weakness of lower limbs, feeling of stepping on cotton, decreased muscle strength of lower limbs or limbs, increased muscle tension of lower limbs, active or increased antireflex of limbs, positive pathological signs such as Hoffmann's sign and Babinski's sign. Preoperative JOA scores ranged from 4 to 12, with an average of (8.2 ± 0.8) points. Thirty-four patients were treated with segmental anterior cervical interbody fusion device plus titanium cage and titanium plate internal fixation, and 22 patients were treated with posterior C_3–C_7 single-door expansion canal plasty. The follow-up period was 24–36 months (Table 1). This is a retrospective study approved by the ethical committee of the Hospital. The informed consent approval was not required as anonymized patient data was used in this study.

2.2. Therapeutic Methods

2.2.1. Anterior Group. Anterior cervical discectomy and fusion(ACDF)were performed. For example, the disc herniation of $C_{3,4}$, $C_{4,5}$, $C_{5,6}$ was introduced as an example. After general anesthesia, the supine position was taken and the towel was routinely disinfected. The right transverse incision before the neck was taken, the skin, subcutaneous tissue, and platysma myoides were cut successively, entering the gap between the tracheal and oesophageal sheath and the cervical vascular sheath, exposed to the anterior edge of the vertebral body, and oesophageal; then, a positioning needle was placed. Form X-ray, the gap was confirmed, placed open screws and automatically opened in C_3, C_4 vertebrae, open $C_{3,4}$ intervertebral space, $C_{3,4}$ disc full decompression, nerve dissection without obvious nerve compression, appropriate size cage with autologous or allogeneic bone in the $C_{3,4}$, released the moderate pressure, and then in $C_{4,5}$, $C_{5,6}$ intervertebral gap, removed $C_{4,5}$, $C_{5,6}$. The disc was subtotal with parallel C_5 vertebra, and the appropriate size cage with autologous or allogeneic bone titanium cage was placed. Then a appropriate size plate was inserted and fixed. After the X-line of the C-shaped arm confirmed that the built-in position was in good condition, the wound was fully washed with hydrogen peroxide, normal saline, and olonidazole in turn, and the smoke roll drainage strip was placed, confirming that the device dressing was correctly placed, and then the wound was closed by the layer.

2.2.2. Posterior Group. For posterior C_3–C_6 open-door dilated spinal canal plasty, a prone position was taken after general anesthesia, and a conventional disinfection blanket was used. A median incision was taken at the back of the neck, exposing cervical C_3–C_6 lamina to bilateral facet joints, grinding 1/2 of the lamina full-thickness bone at the junction of the right lamina and facet joints, grinding full-thickness lamina bone at the junction of the left lamina and facet joints, and release $C_{2,\ 3}$, The $C_{6,7}$ interlaminar ligament was connected, the left C_3, C_4, $C_5$and C_6 were fixed with small titanium plates between lamina and facet joints. After confirming that the X-line of the C-shaped arm is correct, the wound was fully washed with hydrogen peroxide, normal saline, and olonidzole, and the negative pressure drainage bottle was placed, confirming that the device dressing is correct, and then the wound was closed according to the layer.

The above two groups were followed for 3 months after postoperation, and the drainage strips (or drainage bottles) were removed from 24 to 48 h after surgery. Besides, hormones, antibiotics, and neurotrophils were routinely monitored after surgery. The lower ground activity started from 1 to 2 days after surgery.

2.3. Indicators and Methods of Observation Results. At 2 weeks after surgery, different observations at posterior-anterior, lateral, overextended flexion dynamic positions were

Table 1: Clinical features of multilevel cervical disc herniation.

Subgroup analysis	Cases (n)	Gender		Age (Year)	Time of disease	Distribution of surgical segments	
		Male	Female			C_3–C_6	C_4–C_7
Anterior group	34	24	10	56.7 ± 12.5	10.2 ± 2.7	26	8
Posterior group	22	8	14	59.1 ± 8.2	10.6 ± 3.6	15	7
t		0.212		0.425	0.771	0.562	
p		0.345		0.765	0.223	0.501	

noted. (1) Clinical observations: During the follow-up period, the subjective symptoms of the patient's subjective symptoms (mainly related to CS, such as the sensation of both limbs, muscle strength, the cotton feeling of stepping in both lower limbs) were observed. (2) Imaging observations: the height of the cervical anterior column by applying the preoperative and postoperative X-ray slices of the cervical spine was noted. The height of the anterior cervical spine column was used to measure the connection between the middle point of the upper edge. The length of the line reflects to be resected and the height of the disc to be removed. The measurement method of anterior cervical curvature was to perform the lower edge of the C_7 vertebral line and the middle point of the nodules before and after the Atlas and then do two vertical lines respectively, and the upper Angle of the two vertical lines is the anterior curvature Angle of the cervical vertebra. (3) Efficacy evaluations: JOA scores before surgery were recorded and at each follow-up, according to the orthopedic Society of Japan. The postoperative improvement rate was also calculated according to the following formula:

Improvement rate = ((follow-up score preoperative score)/(17-preoperative score)) 100%.

2.4. Imaging Observation. The fusion time and fusion rate were observed by imaging and the Cobb angle was measured. Cobb angle calculation was performed as two vertebrae with the anatomical position were selected; a straight line along the upper edge and the lower edge was drawn and made their vertical lines, and the Angle of the intersection of two vertical lines was considered as Cobb angle (Table 2).

2.5. Evaluation of Neural Function. The neural function was evaluated according to the JOA scoring standard using the formula below:

Improvement rate = (postoperative score-preoperative score)/(17 - preoperative score) × 100%. The following categories were made according to the results observed.

Excellent: 75%; good: 50%~74%; middle: 25%~49%; bad: 24%.

2.6. Statistical Analysis. SPSS 23.0 software (IBM USA) was used for statistical analysis of all data of this study. Measurement data (anterior vertebral column height, anterior cervical curvature, JOA score, and improvement rate) are expressed as the mean standard deviation of ($x \pm s$), using a two-sample mean t-test. $p < 0.05$ was considered to be statistically significant.

3. Result

3.1. Routine Clinical Outcome Index Observation. All patients were followed up for 24–36 months (28.6 months on average). The nervous system (sensory and motor function) of 56 patients was improved to varying degrees after surgery. Most patients had significant improvement in limb mobility, weakness of lower limbs, and feeling of stepping on cotton were significantly reduced, and walking was more stable and powerful than before surgery.

3.2. Imaging Observation. No built-in complications such as insert loosening, displacement, sinking, and steel plate fracture were found during the follow-up. The results of the anterior column height and anterior cervical curvature of the two preoperative procedures, 2 weeks after surgery, and at the last follow-up are presented. While the anterior post-height was slightly lost at the last follow-up, it was not statistically significant ($p > 0.05$) (Figure 1).

In the posterior approach group, there was no statistical significance in the height of an anterior column of the lesion segment 2 weeks after surgery and at the last follow-up ($p > 0.05$). There was no statistically significant difference in anterior column height between the two groups before surgery, but there was a statistically significant difference at 2 weeks after surgery and the last follow-up. In the anterior approach group, cervical curvature at 2 weeks after surgery was significantly lower than that before surgery ($p < 0.05$). Statistical difference was observed between anterior cervical curvature at 2 weeks postsurgery and the last follow-up ($p < 0.05$) (Figure 2).

3.3. Spinal Cord Function Score and Its Rate of Improvement. In terms of spinal function recovery, significant postoperative recovery was observed compared to surgery. The JOA scores at 3 months and last follow-up were also statistically significant ($p < 0.05$) (Table 3) between the two groups.

According to the subitem results of the JOA score, both the anterior fusion and posterior spinal canal enlargement groups were significantly improved in upper and lower limb movement and sensory function compared with surgery, and bladder function was not significantly different compared with surgery. By comparing the JOA subscores at 3 months after the two different postoperative procedures, the anterior fusion group was statistically significant in both the upper and lower limb motor scores compared with the posterior spinal canal enlargement group, but no difference between the two groups in sensory

Table 2: Analysis and comparison of imaging characteristics in different periods.

Time	Anterior group ($n = 34$)		Posterior group ($n = 22$)	
	Vertebral column height (mm)	Curvature of the cervical spine	Vertebral column height (mm)	Curvature of the cervical spine
Preoperative	71.2 ± 1.3	23.4 ± 7.8	70.2 ± 5.2	24.3 ± 7.8
2 weeks after surgery	73.4 ± 2.5	19.5 ± 7.8	71.4 ± 3.9	24.6 ± 6.8
Last follow-up	72.1 ± 4.2	21.4 ± 8.2	69.6 ± 3.9	25.3 ± 6.6

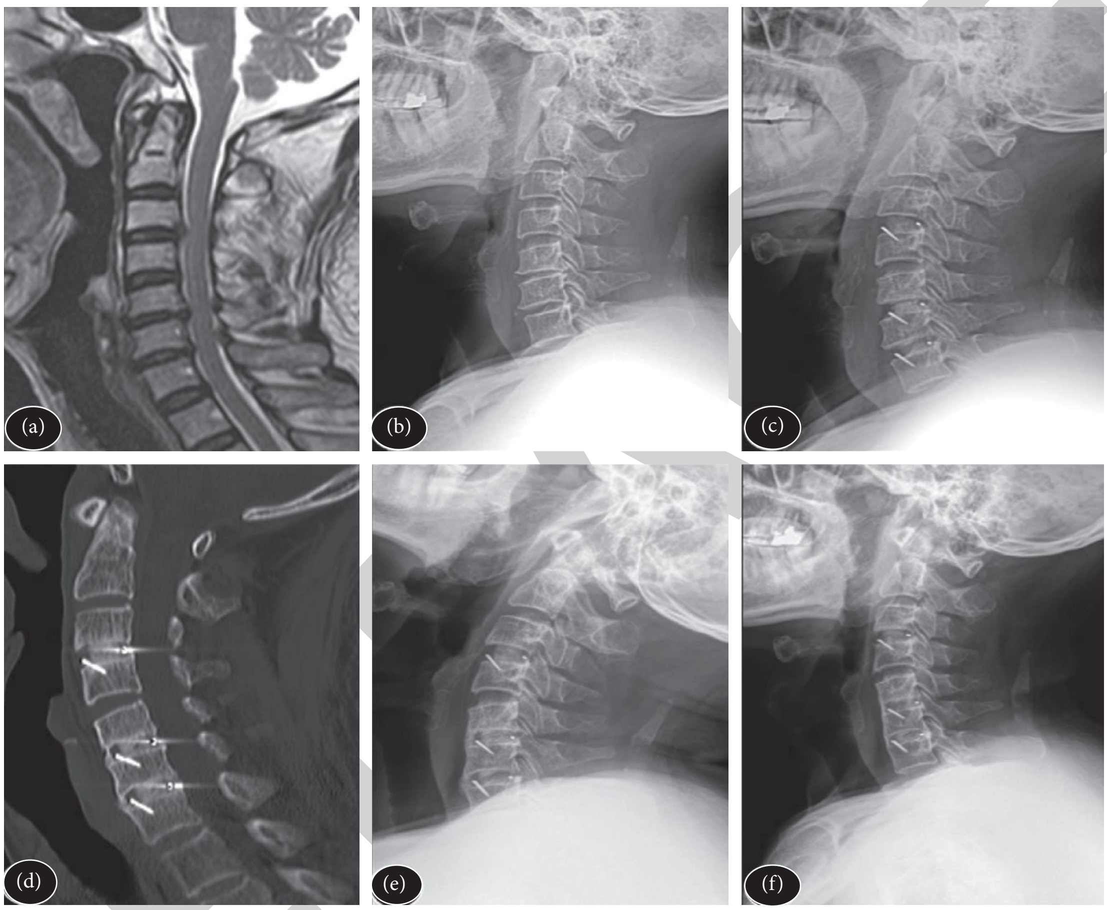

Figure 1: Sagittal MRI(T2) performed before anterior cervical decompression and segmental fusion.

function and bladder function was observed. The last follow-up result was similar to that obtained 3 months after surgery. Meanwhile, the rate of improvement of JOA scores between the two groups was also statistically significant at 3 months and the last follow-up ($p < 0.05$), and the anterior fusion group was significantly better than the posterior surgery group (Table 4).

3.4. General Observation Results. The time of surgery, intraoperative bleeding, and hospitalization of the patients in the observation group was significantly lower than those in the control group ($p < 0.01$) as shown in Table 5.

3.5. Comparison of the Preoperative and Postoperative JOA Scores. There was no significant difference in preoperative JOA scores ($p > 0.05$) of the patients as shown in Table 6. The improvement rate in JOA scores at 6 months (63.8 ± 6.6) was significantly higher than the posterior group (57.5 ± 7.1), and the two groups showed statistically significant differences ($p < 0.05$) (Figure 3).

3.6. Differences in Imaging Characteristics between ACDF and LMP. Cervical spondylotic myelopathy is caused by prolapse or degeneration of the cervical disc, causing intervertebral osteosis and compressing the spinal cord. With the acceleration of aging and the accelerated pace of life in China, the proportion of CSM patients with multiple segment involvement at medical treatment gradually increased. Except for those with perioperative complications, the X-ray showed no titanium plate and titanium mesh during the follow-up. According to postoperative X-ray follow-up,

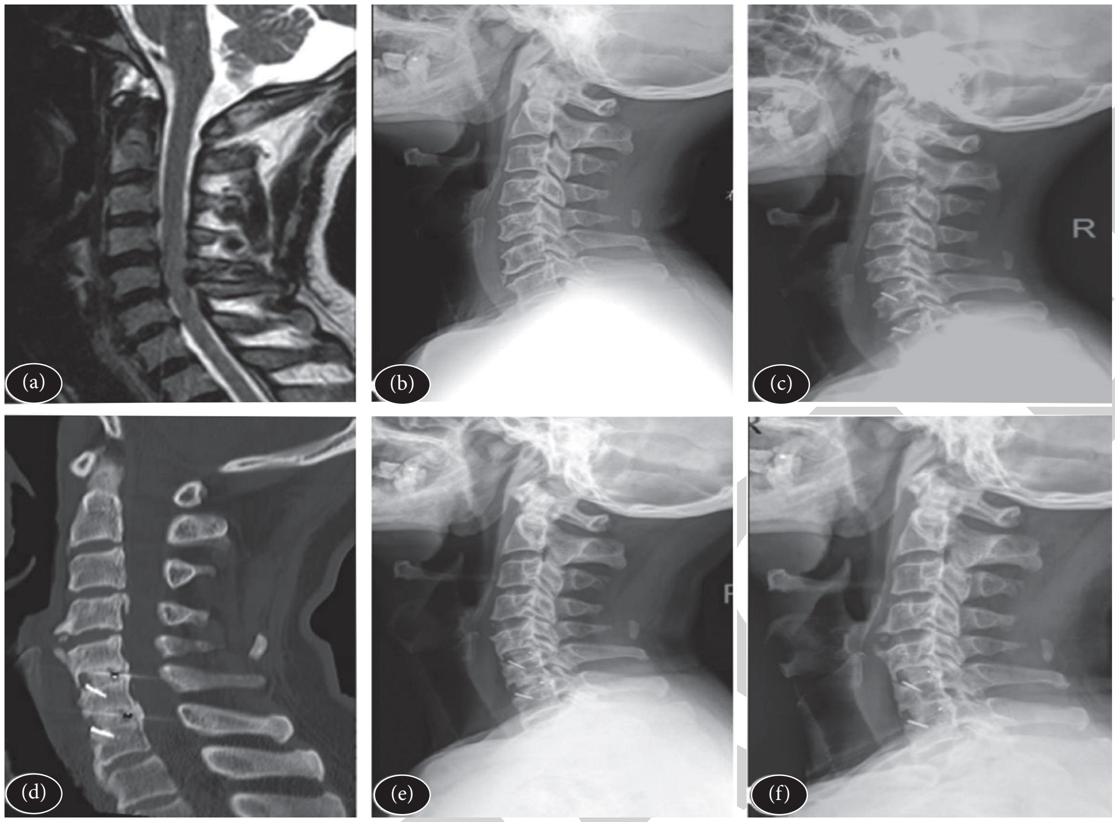

Figure 2: Sagittal MRI(T2) was performed before posterior cervical expansive canal plasty.

Table 3: Analysis and comparison of JOA scores in different periods.

Items	Anterior group ($n = 34$)		Posterior group ($n = 22$)	
	Preoperative	3 months after surgery	Preoperative	3 months after surgery
Upper limb function	1.2 ± 0.8	3.2 ± 0.8	1.1 ± 0.7	2.1 ± 0.8
Lower limb function	1.1 ± 0.8	3.0 ± 0.7	1.1 ± 0.7	2.1 ± 0.8
Sensory function	3.1 ± 0.2	5.1 ± 0.5	3.2 ± 0.3	5.2 ± 0.7
Bladder function	2.2 ± 0.6	2.1 ± 0.7	2.1 ± 0.8	2.1 ± 0.4
Total	8.4 ± 0.8	15.4 ± 0.8	8.2 ± 0.9	13.5 ± 0.2

Table 4: Comparison of JOA score before and after the operation.

Subgroup analysis	Case (n)	Preoperative	3 months after surgery	6 months after surgery
Anterior group	34	8.25 ± 0.75	16.25 ± 0.75	14.65 ± 0.46
Posterior group	22	8.25 ± 0.88	13.55 ± 0.38	12.46 ± 0.55
t		0.852	12.215	9.045
p		0.082	0.001	0.001

Table 5: Bone graft fusion and Cobb Angle fusion before and after the operation.

Subgroup analysis	Case (n)	Osteograft fusion		Fusion segment cobb angle	
		Bone fusion time	Bone fusion rate	Preoperative	3 months after the surgery
Anterior group	34	6.25 ± 1.37	40 (71.43%)	1.55 ± 0.35	8.55 ± 0.56
Posterior group	22	7.65 ± 1.87	16 (28.57%)	1.65 ± 0.22	7.82 ± 0.35
t		4.655	0.215	5.262	2.455
p		0.001	0.065	0.001	0.002

Table 6: JOA score improvement rate.

Time	Anterior group ($n = 34$)	Posterior group ($n = 22$)
Preoperative	79.4 ± 8.7	60.4 ± 7.8
6 months after the surgery	63.8 ± 6.6	57.5 ± 7.1
t	9.426	3.004
p	0.021	0.042

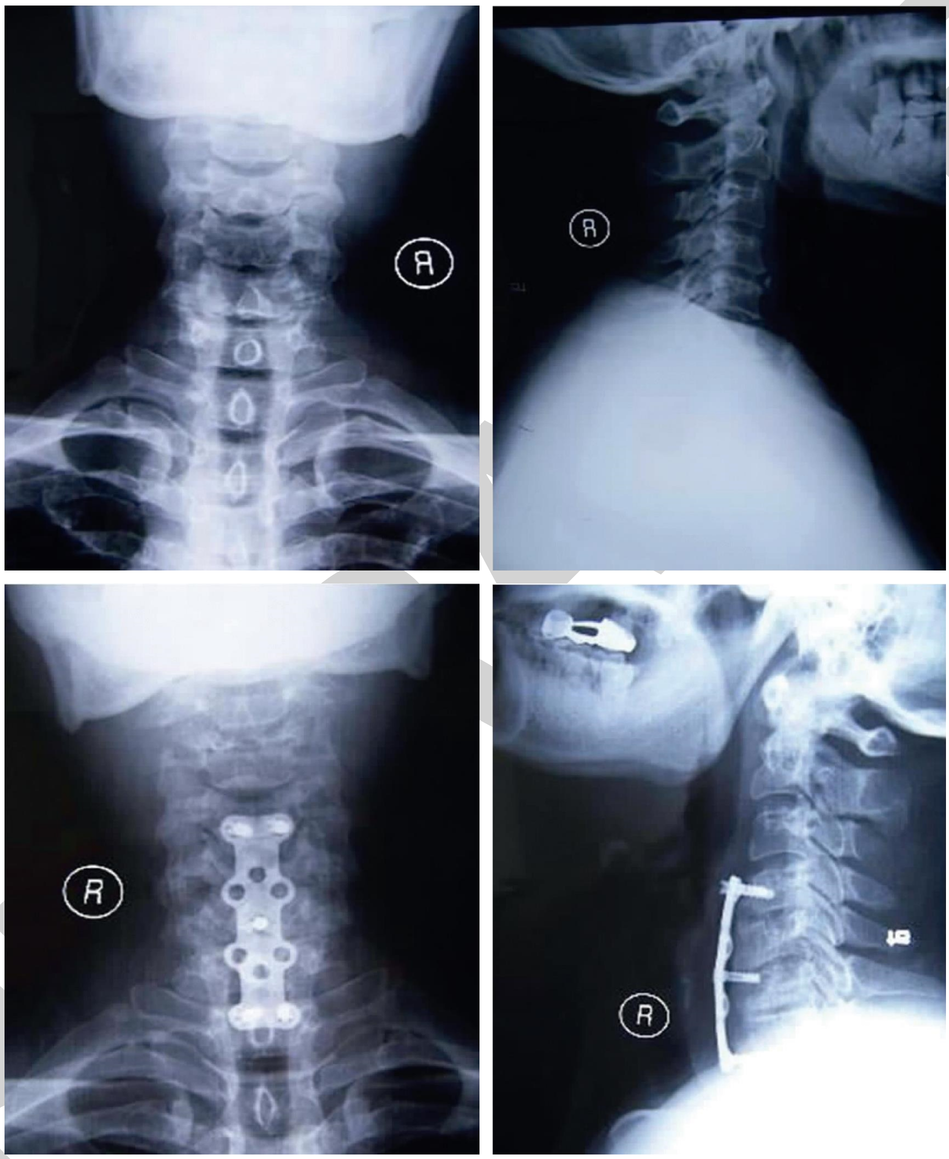

Figure 3: Preoperative and postoperative anteroposterior and lateral radiographs.

bone graft fusion was 6 to 11 months, 84.2% (16/19), 9 to 13 months, and 81.8% (27/33) (Figures 4 and 5).

4. Discussion

Multisegment cervical spondylotic myelopathy is not uncommon in clinical orthopedics, and its main clinical characteristics are extensive lesion-involved segments and more serious symptoms [12, 13]. With the development of MRI technology, the diagnosis rate of bone and disc herniated spinal diseases has been significantly improved [14–16]. However, there is still widespread international controversy about how to surgically treat multisegmented cervical pulp compression diseases [17]. Both anterior cervical discectomy and fusion and posterior cervical canal angioplasty are surgical methods for cervical myelopathy [18]. Anterior surgery indirectly expands cervical canal volume by directly relieving local compression of nerves and spinal cord and restoring cervical physiological curvature and intervertebral height, while posterior expansive canal

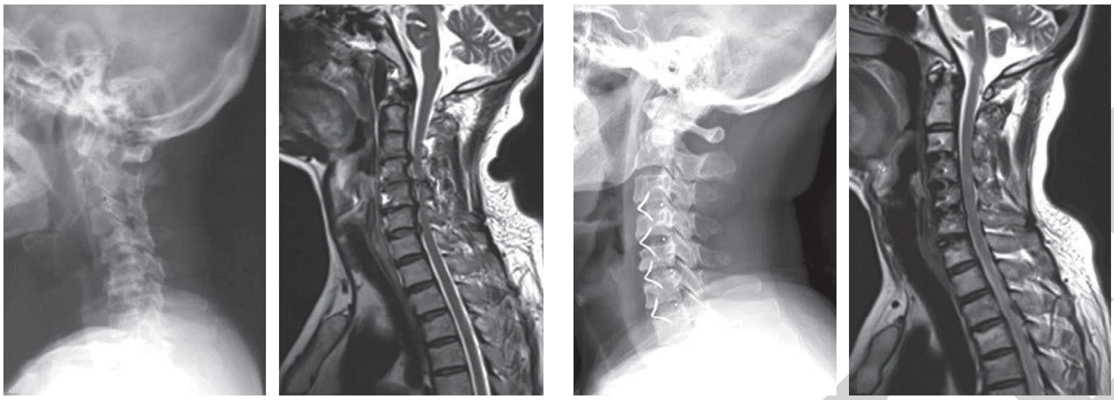

Figure 4: Comparison of preoperative and postoperative MRI and X-ray in anterior cervical decompression and fusion (ACDF) surgery.

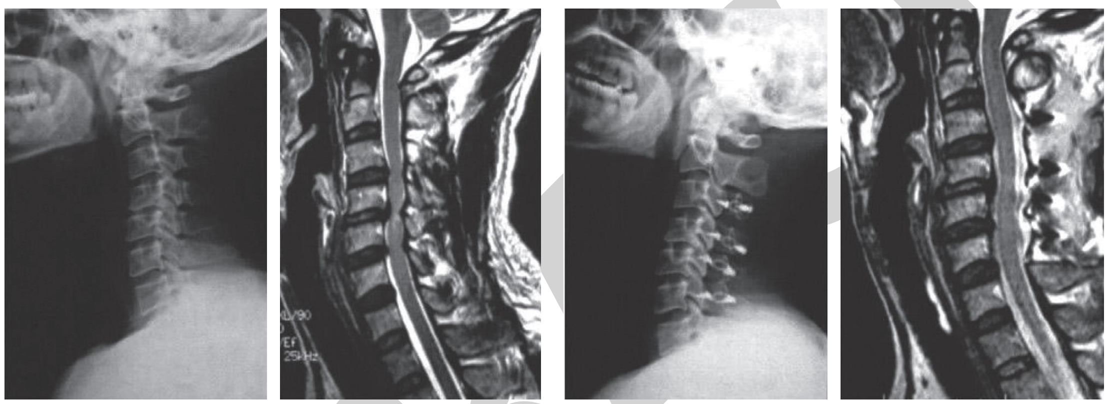

Figure 5: Comparison of preoperative and postoperative MRI and X-ray in posterior laminoplasty (LMP) surgery.

plasty indirectly achieves decompression by directly expanding cervical canal volume [19–21]. The purpose of the anterior surgery of cervical spondylosis is to relieve the spinal cord compression, expand the factors of the cervical spine canal capacity, restore normal spinal canal function, and create conditions for the recovery of the cervical spine pulp function [22]. As the gold standard of anterior cervical fusion, iliac trifacial cortical bone graft fusion has been widely used in anterior cervical surgery for various cervical diseases. Front cervical decompression often destroys the stability of the anterior column, whereas, the height of the graft and the maintenance of the early postimplantation stability is the fundamental guarantee for the recovery and correction of the cervical force lines [23]. Therefore, the recovery and maintenance of cervical physiological curvature and vertebral height are increasingly valued by spine surgery and neurosurgeons [24].

Main problems of continuous multiple segments of anterior cervical spine fusion fixation include: (1) multiple segments of cervical spondylosis due to bone hyperplasia, continuous multiple segments of disc degeneration, cervical disc stenosis, cervical physiological curvature disappear or even reverse pathological changes, continuous multisegment fusion fixation is often unable to correct or even aggravate the cervical curvature change; (2) The loss of vertebral height is inevitable. After long segments of bone absorption at the bone grafting interface (or bone intersite interface), the recovered vertebral height of the intervertebral bone graft could be lost; (3) Changes in the physiological curvature can directly affect the effective volume of the spinal canal. In addition, the loss of intervertebral height may also lead to nerve root compression and produce symptoms of nerve root compression; (4) The fusion of long segments due to the long fixed segment, there is a certain degree of micromovement between the bone grafting interface, which could have an obvious impact on the fusion of bone grafting, which can easily lead to fusion failure or false joint formation; (5) A problem in the long segment fixation may result in or accelerate the degeneration of adjacent segment, the adjacent segment degeneration is caused by natural progression, although there are controversial strategies for the problem currently, long segmental fixation will have on adjacent segment larger biomechanics changes, increased intervertebral disc pressure and facet joint stress in adjacent segments.

The ideal procedure for CSM should maintain both a high fusion rate and the cervical curvature [25–27]. The segmented fusion scheme proposed by the author, due to the use of intervertebral bone grafting and vertebral subtotal bone grafting, has an important role in increasing the stability of the bone graft segment and maintaining the physiological curvature of the cervical vertebra and has its main advantages including (1) Segmental bone grafting allows a "normal" vertebral body to be separated, so that the stress transfer between the two bone graft parts can be normal and the stress transfer after fusion can be effectively reduced; (2) When the cervical spine is extended, the anterior steel plate can play a tension band and absorb the tension of the bone-built-in interface. Whereas the cervical anterior flexion, the steel plate plays a supporting role, which can better maintain the height and physiological curvature of the vertebral space, strengthen the stability of the cervical spine, promote fusion, and improve the fusion rate.

5. Conclusion

From the JOA score data found in this study, it is evident that in 3 months after surgery, the upper and lower limb movement and sensory function are significantly improved compared with the two preoperative. Improvement in the upper and lower limb motor function and anterior decompression group has significant advantages over the posterior decompression group. In sensory function, there is no obvious difference between the two groups ($p > 0.05$). This may be associated with the reduction of anterior decompression directly beyond the cortical spinal tract compressing the anterior spinal tract [28]. It plays a vital role in restoring spinal cord function [29]. Posterior spondyloplasty, on the other hand, provides indirect decompression through flotation [30–34]. The decompression effect depends on the available buffer space of the posterior approach, and even if the posterior approach has sufficient buffer capacity, if the anterior compressor is too large, the spinal cord will still be compressed [35]. Moreover, if the spinal cord drifts back too much, it will have a certain degree of pulling effect on the nerve root, resulting in some nerve root symptoms such as numbness and pain in the upper arm [36]. To sum up, segmented anterior fusion surgery can effectively improve the symptoms of patients with multi-segmented cervical spondylosis, can restore and maintain the cervical anterior column height to a certain extent, and can have a good effect on postoperative functional recovery.

Data Availability

The labeled datasets used to support the findings of this study are available from the corresponding author upon request.

Conflicts of Interest

The authors declare no conflicts of interest.

References

[1] B. Sharifi, G. McIntosh, C. Fisher et al., “Consultation and surgical wait times in cervical spondylotic myelopathy,” *The Canadian journal of neurological sciences. Le journal canadien des sciences neurologiques*, vol. 46, no. 4, pp. 430–435, 2019.

[2] B. Wu, B. Liu, D. Sang, W. Cui, and D. Wang, “The association between cervical focal kyphosis and myelopathy severity in patients with cervical spondylotic myelopathy before surgery,” *European Spine Journal*, vol. 30, no. 6, pp. 1501–1508, 2021.

[3] D. Peng, Y. Ma, and B. Lei, “Clinical and radiological outcomes of anterior approach microscopic surgery for the pincer mechanism in cervical spondylotic myelopathy,” *BioMed Research International*, vol. 2019, Article ID 9175234, 7 pages, 2019.

[4] X. Plano, M. Ramírez, A. Matamalas et al., “30-Day unplanned surgery in cervical spondylotic myelopathy surgically treated: A single-center experience,” *European Spine Journal*, vol. 28, no. 5, pp. 1209–1216, 2019.

[5] W. H. A. Ryu, A. Platt, and H. Deutsch, “Hybrid decompression and reconstruction technique for cervical spondylotic myelopathy: Case series and review of the literature,” *Journal of Spine Surgery*, vol. 6, no. 1, pp. 181–195, 2020.

[6] S. Yabuki, K. Takatsuki, K. Otani et al., “Headache in patients with cervical spondylotic myelopathy,” *Pain Research & Management*, vol. 2020, Article ID 8856088, 6 pages, 2020.

[7] F. Meng, S. Xu, Y. Liang, Z. Zhu, K. Wang, and H. Liu, “Cervical balance and clinical outcomes in cervical spondylotic myelopathy treated by three-level anterior cervical discectomy and fusion and hybrid cervical surgery,” *Medicine*, vol. 100, no. 18, Article ID e25824, 2021.

[8] H. Abudouaini, H. Liu, B. Wang et al., “Outcome and predictive factors in rapid progressive cervical spondylotic myelopathy: A retrospective case-control study,” *Clinical Neurology and Neurosurgery*, vol. 198, Article ID 106226, 2020.

[9] S. Li, B. Zhang, Y. Shen, and Z. Wu, “Multivariate analysis of poor outcome after anterior surgery in multilevel cervical spondylotic myelopathy patients with heterotopic ossification and preoperative kyphotic alignment,” *Therapeutics and Clinical Risk Management*, vol. 15, pp. 1053–1060, 2019.

[10] W. Y. Lopez, B. C. Goh, S. Upadhyaya et al., “Laminoplasty-an underutilized procedure for cervical spondylotic myelopathy,” *The Spine Journal*, vol. 21, no. 4, pp. 571–577, 2021.

[11] M. Zileli, S. A. Borkar, S. Sinha et al., “Cervical spondylotic myelopathy: Natural course and the value of diagnostic techniques -wfns spine committee recommendations,” *Neurospine*, vol. 16, no. 3, pp. 386–402, 2019.

[12] S. Nori, N. Nagoshi, R. Aoyama et al., “Influence of intervertebral level of stenosis on neurological recovery and reduction of neck pain after posterior decompression surgery for cervical spondylotic myelopathy: A retrospective multicenter study with propensity scoring,” *Spine (Phila Pa 1976)*, vol. 47, 2021.

[13] K. Kin, T. Yasuhara, Y. Tomita, M. Umakoshi, J. Morimoto, and I. Date, “SF-36 scores predict postoperative delirium after surgery for cervical spondylotic myelopathy,” *Journal of Neurosurgery. Spine*, vol. 30, pp. 1–6, 2019.

[14] S. Borkar, R. Sreenivasan, R. Sharma et al., “Cervical rotation before and after hinge-door cervical laminoplasty for cervical spondylotic myelopathy,” *Journal of Craniovertebral Junction and Spine*, vol. 10, no. 2, pp. 114–118, 2019.

[15] A. J. Taylor, K. Combs, R. D. Kay, J. Bryman, E. Y. Tye, and K. Rolfe, “Combined motor and sensory intraoperative neuromonitoring for cervical spondylotic myelopathy surgery causes confusion,” *Spine*, vol. 46, no. 22, pp. E1185–E1191, 2021.

[16] B. M. Davies, B. Nourallah, A. Venkatesh et al., “Establishing mild, moderate and severe criteria for the myelopathy disability index in cervical spondylotic myelopathy,” *British Journal of Neurosurgery*, pp. 1–5, 2020.

[17] Z. Aljuboori and M. Boakye, “The natural history of cervical spondylotic myelopathy and ossification of the posterior

Hindawi
Journal of Healthcare Engineering
Volume 2023, Article ID 9849480, 1 page
https://doi.org/10.1155/2023/9849480

Retraction

Retracted: Prophylactic Use of Antibiotics for Postsurgical Infection in c-TACE and DEB-TACE High-Risk Patients: A Case-Control Study

Journal of Healthcare Engineering

Received 26 September 2023; Accepted 26 September 2023; Published 27 September 2023

This article has been retracted by Hindawi following an investigation undertaken by the publisher [1]. This investigation has uncovered evidence of one or more of the following indicators of systematic manipulation of the publication process:

(1) Discrepancies in scope
(2) Discrepancies in the description of the research reported
(3) Discrepancies between the availability of data and the research described
(4) Inappropriate citations
(5) Incoherent, meaningless and/or irrelevant content included in the article
(6) Peer-review manipulation

The presence of these indicators undermines our confidence in the integrity of the article's content and we cannot, therefore, vouch for its reliability. Please note that this notice is intended solely to alert readers that the content of this article is unreliable. We have not investigated whether authors were aware of or involved in the systematic manipulation of the publication process.

In addition, our investigation has also shown that one or more of the following human-subject reporting requirements has not been met in this article: ethical approval by an Institutional Review Board (IRB) committee or equivalent, patient/participant consent to participate, and/or agreement to publish patient/participant details (where relevant).

Wiley and Hindawi regrets that the usual quality checks did not identify these issues before publication and have since put additional measures in place to safeguard research integrity.

We wish to credit our own Research Integrity and Research Publishing teams and anonymous and named external researchers and research integrity experts for contributing to this investigation.

The corresponding author, as the representative of all authors, has been given the opportunity to register their agreement or disagreement to this retraction. We have kept a record of any response received.

References

[1] B. Li, "Prophylactic Use of Antibiotics for Postsurgical Infection in c-TACE and DEB-TACE High-Risk Patients: A Case-Control Study," *Journal of Healthcare Engineering*, vol. 2022, Article ID 6203817, 8 pages, 2022.

Hindawi
Journal of Healthcare Engineering
Volume 2022, Article ID 6203817, 8 pages
https://doi.org/10.1155/2022/6203817

Research Article

Prophylactic Use of Antibiotics for Postsurgical Infection in c-TACE and DEB-TACE High-Risk Patients: A Case-Control Study

Baojian Li

Department of Pharmacy, Heping Hospital Affiliated to Changzhi Medical College, Changzhi 046000, Shanxi, China

Correspondence should be addressed to Baojian Li; lbjacc@njucm.edu.cn

Received 2 February 2022; Accepted 2 March 2022; Published 11 April 2022

Academic Editor: Liaqat Ali

Objectives. According to recent reports, prophylactic use of antibiotics is not always required in conventional transarterial chemoembolization (c-TACE). However, clinical evidence of prophylactic antibiotics in drug-eluting beads transarterial chemoembolization (DEB-TACE) to prevent postsurgical infection is limited. This study is aimed to evaluate the correlation between the preoperative prophylactic application of antibiotics and postoperative infection in c-TACE or DEB-TACE, especially in a population with a high risk for postsurgical infection. *Methods*. In this retrospective study, TACE patients diagnosed with hepatic carcinoma (between January 2019 and May 2021) were examined. The case group was given 1.5 g cefuroxime sodium 0.5–1 hour before TACE, while there was no intervention in the control group. The outcomes analyzed were leukocyte count $>9.5 \times 10^9$/L on the second day after the operation and the diagnosis of infection within one month after the operation. We applied univariate, multivariate logistic regression, trend analysis, and subgroup analysis to find potential risk factors and the necessity of prophylactic antibiotics. *Results*. Among 142 eligible cases, 72 received antibiotics while 70 were kept as control, 113 cases were treated with c-TACE, and 29 were treated with DEB-TACE. Multivariate analysis showed that the increase in white blood cell count after the operation was related to diabetes (OR 5.112, 95% CI 1.229–21.264, $p = 0.025$). The occurrence of postoperative infection was negatively correlated with preoperative albumin value ($<$ 25 g/L) (OR 153.118, 95% CI 1.631–14372.331, $p = 0.030$). Trend analysis showed that the risk of postoperative infection increased with a decrease in serum albumin level ($P < 0.05$). Subgroup analysis showed that there were no significant differences in the incidence of increased leukocyte count and postoperative infection between the prophylactic and nonprophylactic treatment groups, in the case of diabetes, preoperative albumin levels, and operation mode ($P > 0.1$). *Conclusions*. Prophylactic antibiotic treatment before the c-TACE or DEB-TACE had no significant correlation with postoperative leukocyte increase and postoperative infection. Diabetes history and serum albumin levels were the prominent risk factors associated with an increase in postoperative leukocyte count and postoperative infection. Future large-scale studies and randomized-controlled trials are required to confirm and validate this association.

1. Introduction

Liver cancer especially hepatocellular carcinoma (HCC) is among the top five most common cancers. The treatment of HCC includes surgery, liver transplantation, and radiofrequency ablation with good survival benefits. However, most HCC patients having vascular involvement or multiple lesions cannot be treated with such treatment strategies [1]. Transarterial chemoembolization (TACE) is the currently known standard of care treatment of HCC in intermediate-stage patients and the most widely used nonsurgical method for the treatment of liver cancer [2]. TACE is divided into conventional TACE (c-TACE) and drug-elating beads TACE (DEB-TACE) [3, 4]. In c-TACE, a mixture of anticancer agents (e.g., cisplatin and doxorubicin) in the lipid-based formulation is administered to liver cancer patients for the treatment of intermediate-stage cancer. The foundation of this treatment is based on the recommendations of the systemic review of randomized-controlled trials (RCTs) [5]. On the other hand, in drug-eluting beads TACE, the anticancer drugs are delivered to the target site in a delivery system which combines local embolization of vasculature and release of the anticancer drug in nearby tissues [6, 7]. This procedure is specifically applied in patients with hypervascular tumors for the treatment of cancer. The administration procedure of DEB-TACE is nearly similar to c-TACE, and both are minimally invasive procedures usually carried out by radiologists [8]. The beads employed in DEB-TACE are mainly biocompatible polymers-based hydrogels including polyvinyl alcohol (PVA)-based hydrogels which are sulphonated for binding of anticancer drugs [9]. The anticancer agents are delivered to the target site upon occlusion of the beads in the vasculature, which embolizes them, and subsequently, the drug is released in the target site [10]. It is currently unclear whether DEB-TACE or c-TACE should be used for a specific patient in the absence of randomized-controlled trials. However, DEB-TACE has a safer profile than c-TACE, with fewer common side effects [3, 4, 11, 12]. Therefore, the application of DEB-TACE is becoming more and more extensive.

TACE procedures have been regarded as minimally invasive with a good curative profile and strong repeatability; thus, it is mostly used in the nonsurgical treatment of HCC. However, the chance of occurrence of infection is always there, which results will not only prolong the hospital stay and expenses but also will affect the efficacy of treatment [13]. Moreover, the majority of the TACE-treated patients are middle-aged, or they are in the advanced stage of cancer where the immune system is less active, coupled with damage to nearby tissues caused by operation and the anticancer drugs' immune function inhibition leading to postoperative infection [14, 15].

It is uncertain whether the use of antibiotics as prophylaxis before TACE is beneficial or not in the prevention of postoperative infection. The guidelines for the use of antibiotics in the China interventional radiology department believe that prophylactic use of antibiotics is generally not necessary. But if the patient has a poor physique, low immunity, and a history of biliary surgery, antibiotics can be used for prevention before the operation. The guiding principles for the clinical application of antibiotics in China suggest that antibiotics should be used to prevent infection before TACE [16]. According to Yoshihara et al., prophylactic antibiotic treatment in patients having TACE was linked to a lower risk of liver abscess necessitating surgical intervention [17]. However, recent findings show that prophylactic antibiotic medication is not always required in the TACE process for HCC patients [15, 18]. Moreover, serum albumin level, white blood cell count, length of stay, skin or mucosal ulcer, invasive operation, application of broad-spectrum antibiotics, and diabetes mellitus were independent risk factors for nosocomial infection after TACE in patients with primary liver cancer [15, 19].

The above studies on the preventive application of antibiotics refer to c-TACE or are not explicitly stated. Whether DEB-TACE needs to prevent the use of antibiotics before the operation has not been recommended by guidelines or relevant studies, and whether there are the same risk factors related to the prevention of the use of antibiotics with c-TACE has not been reported. It has been reported that postoperative infections such as a liver abscess occurred after DEB-TACE [20–22].

The abuse and unnecessary use of antibiotics has become a worldwide problem. It not only increases the occurrence and cost of adverse drug reactions but also is considered to be one of the main reasons for the emergence of more and more biological drug-resistant strains [23]. Optimizing the antibiotic prevention strategy in the TACE treatment of hepatocellular carcinoma is necessary and urgent not only for patients with hepatocellular carcinoma but also for the whole population. The value of routine prophylaxis merits justification [24].

This study aimed to explore the relationship between the use of antibiotics and postoperative infection not only in c-TACE but also in DEB-TACE, using logistic regression and trend analysis. Subgroup analysis was also conducted to study the interaction and confounding factors between high-risk factors and preventive drug use outcomes.

2. Methods

2.1. Ethical Considerations. The reports were in accordance with the Strengthening the Reporting of Observational Studies in Epidemiology (STROBE) guideline. The approval for the current retrospective study was provided by the Ethics Committee of the Heping Hospital Affiliated to Medical College, Changzhi, China. Informed consent was not required because of the retrospective nature of the study and the anonymity of the collected data.

2.2. Data Source and Patients. Between January 2019 and May 2021, the data of patients with primary liver malignancies, hepatocellular carcinoma (HCC), intrahepatic cholangiocarcinoma (ICC) [25, 26], and metastatic liver malignancies treated with TACE at Heping Hospital Affiliated with Changzhi Medical College were retrospectively analyzed. The laboratory examination data were obtained from the clinical laboratory of the hospital, and other results were accessed from the medical record system of the hospital.

2.3. Inclusion and Exclusion Criteria. The control and case inclusion criteria was based on the indications and contraindications of TACE treatment following the guidelines for diagnosis and treatment of primary liver cancer in China (Edition 2019) [25]. The cases of c-TACE were given iodized oil-based chemotherapeutic drug emulsions, supplemented with granular embolic agents. Granular embolic agents included gelatin sponge particles, blank microspheres, and polyvinyl alcohol particles. The DEB-TACE cases were given a therapeutic scheme of embolization with CalliSpheres drug-loaded microspheres (100–300 μm) preloaded with chemotherapeutic drugs. The case group was given 1.5 g cefuroxime sodium for injection only once 0.5–1 hour before TACE, while the control group had no preventive medication before TACE. Patients with incomplete or missing laboratory tests data were excluded from the analyses.

2.4. Outcomes. The outcomes assessed in this study were as follows:

(1) Increase in leukocyte count ($>9.5\times10^9$/L) on the second day after the operation

(2) The diagnosis of infection within one month after the operation was based on the diagnostic criteria of hospital infection and diagnostic criteria of nosocomial infection (China, 2001) [27].

2.5. Statistical Analysis. All statistical analyses were conducted using SPSS (V.26.0; IBM). A univariate analysis was employed for the comparison of variations in patients' baseline characteristics between the preventive medication group and the nonpreventive medication group. The Student's *t*-test was employed to evaluate if the obtained data had a homogeneous variance and a normal distribution. For nonhomogeneous variance, the comparisons were made using a one-way analysis of variance (ANOVA). In order to compare categorical variables, Fisher's exact test or Pearson's 2 test was used as applicable.

Then, univariate analysis was used to compare the clinical data which is between the WBC≤9.5×109/L group and the WBC > 9.5×109/L group and between the nonpostoperative infection group and the postoperative infection group to find associated variables, respectively. The univariate analysis included chi-square tests for categorical variables and *t*-tests for continuous variables. Significant variables ($P < 0.01$) in univariate analysis and covariates considered clinically influential were then analyzed by multivariate stepwise logistic regression (forward stepwise logistic regression) to identify significant variables. We applied univariate and multivariate logistic regression models to estimate odds ratios (ORs) with 95% confidence intervals (CIs) for significant variables for finding potential risk factors in WBC > 9.5×109/L group or postoperative infection group. In addition, dummy variables are set for grade data to test its trend.

Finally, Cochran's and mantel Haenszel tests were used for subgroup analysis of high-risk factors and surgical methods to determine whether there were important variables affecting the outcome of preoperative preventive drug treatment. *P* value less than 0.05 was considered statistically significant.

3. Results

A total of 103 patients underwent 145 TACE. Three of these patients were lacking blood sample data and were excluded from data analysis (Figure 1). The remaining 102 patients who underwent 142 procedures were included in the analysis. All the patients were diagnosed with primary liver cancer, according to the criteria mentioned earlier. The baseline characteristics of patients are listed in Table 1, and no significant difference was found between the preventive medication ($n = 72$) group and nonpreventive medication ($n = 70$) group ($p > 0.05$).

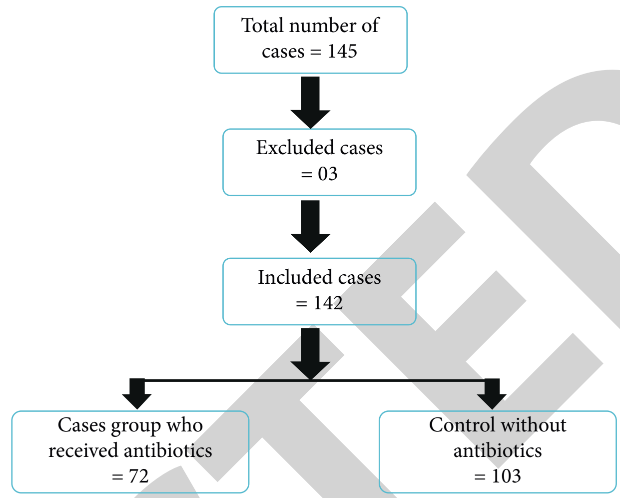

Figure 1: Allocation of subjects to case and control groups.

3.1. Univariate Analysis of Outcomes. There were 28 cases with postoperative leukocyte count $>9.5\times10^9$/L. Patients with diabetes history, age ranges, or preoperative albumin value (≥25 g/L, < 40 g/L) showed significant associations with postoperative leukocyte count >9.5 ×109/L ($P < 0.1$). There were 14 cases of postoperative infection. Patients with gallstone, number of TACE, or preoperative albumin value (< 25 g/L) showed significant associations with postoperative infection ($P < 0.1$). There was no significant correlation between preoperative prophylactic medication or operation mode and postoperative leukocyte count or postoperative infection ($P > 0.1$) as shown in Table 2.

3.2. Multivariate Analysis of Outcomes. The increase in white blood cell count after the operation was related to diabetes history (OR 5.112, 95% CI 1.229–21.264, $p = 0.025$), which was unrelated to the age of the patients ($P > 0.05$). The occurrence of postoperative infection was related to the preoperative albumin value (< 25 g/L) (OR 153.118, 95% CI1.631–14372.331, $p = 0.030$), and there was no significant correlation with gallstone (OR 3.626, 95% CI 0.843–15.597, $p = 0.084$) and number of TACE (OR 0.394, 95% CI 0.154–1.005, $p = 0.051$) as shown in Table 2.

3.3. Trend Analysis of Outcomes. The trend analysis of outcomes showed that the risk of increased leukocyte count was not related to the age of the patients with no statistically significant trend (trend $P > 0.05$). The risk of postoperative infection increased with a decrease in albumin level, which was statistically significant with or without adjustment variables ($P < 0.05$) as shown in Table 2.

3.4. Subgroup Analysis of Outcomes. Multivariate analysis revealed that the potential confounding factors were diabetes history and preoperative albumin levels. A surgical method that is considered clinically influential also needs hierarchical analysis. Two out of four patients with a history of diabetes with no prophylactic medication showed white

Table 1: Population and baseline characteristics.

Baseline characteristics	Preventive medication group	Nonpreventive medication group	P-value
Numbers	72	70	
Age (years)	61.43 ± 9.805	60.19 ± 8.742	0.426
Sex (male/female)	54/18	59/11	0.170
Diabetes history (yes/no)	9/63	4/66	0.161
History of biliary surgery (yes/no)	6/66	8/62	0.536
Gallstone (yes/no)	12/60	8/62	0.370
Operation mode (c-tace/deb-tace)	60/12	53/17	0.260
Number of TACE (n)			0.691
First time	33	29	
Second time	19	22	
Third time	10	6	
Fourth time	2	6	
Fifth time	4	3	
Sixth time	1	1	
Seventh time	1	1	
Ninth time	1	1	
Tenth time	1	0	
Eleventh time	0	1	
Preoperative albumin value (g/L)	34.654 ± 5.0938	34.817 ± 4.4169	0.839
Preoperative leukocyte count (10^9/L)	5.193 ± 2.2486	5.268 ± 1.8230	0.831

blood cells' count of $>9.5 \times 10^9$/L as shown in Table 3. On the other hand, 3 out of 9 patients with diabetic history and prophylactic medication showed an increase in leukocyte count. The effect of albumin level and different surgical methods on the preoperative infection was analyzed, and the results are shown in Table 4. It is evident from the table that the maximum number of patients with albumin levels below 25 g/L experienced postoperative infection. The surgical method applied had no effect on the postoperative infection. The effect of diabetes mellitus, preoperative albumin levels, and operation mode on the increase in WBC count or postoperative infection was also assessed. The results are shown in Table 5 which indicates that there was no significant difference in postoperative infection or increase in WBC counts between the prophylactic and nonpreventive treatment groups, diabetes mellitus, preoperative albumin levels, or operation mode ($P > 0.1$).

4. Discussion

This study retrospectively analyzed the need for preoperative prophylactic use of antibiotics in patients who underwent c-TACE and DEB-TACE. The results showed that there were no significant differences in the incidence of increased leukocytes count and postoperative infection with both applied surgical methods. However, the history of diabetes and preoperative serum albumin level were risk found factors for postoperative leukocyte elevation and postoperative infection. However, these factors cannot alter the effect of prophylactic use of antibiotics before c-TACE or DEB-TACE on postoperative leukocyte elevation and postoperative infection.

The need for prophylactic use of antibiotics before c-TACE is consistent with the previous research results [18, 28, 29]. The risk factors for postoperative infection, such as diabetes history [19] and preoperative serum albumin level [15], are also consistent with previous studies. Some studies have shown that the risk of postoperative infection increases with the increase of age [30], but our results show there was no significant difference between age and postoperative leukocyte count or postoperative infection. This may be related to fewer positive cases of postoperative infection, and more cases are needed to prove it. Some studies have shown that biliary surgery is a risk factor for postoperative infection [31]. TACE can be performed without antibiotics in patients with intact biliary anatomy [24]. Our study did not find that biliary surgery is related to postoperative infection, which may be related to fewer cases of biliary surgery. Our study found that cholecystolithiasis is an independent risk factor for postoperative infection, but it cannot change the effect of preoperative medication on postoperative infection.

We clearly distinguished between therapeutic and prophylactic antibiotics and control the dose and timing of prophylactic antibiotics. The cases we included did not undergo pathological typing screening, which is applicable to all patients with liver malignant tumors treated with TACE. It can also be used as a reference for the preoperative preventive medication of DEB-TACE (CalliSpheres drug-loaded microspheres 100–300 um). This research was carried out at Changzhi, China, where the minimum inhibitory concentration of cefuroxime sodium for most *Escherichia coli* (E Coli), *Staphylococcus aureus*, and *Klebsiella* pneumonia is low. Keeping the above-mentioned points in mind, the findings of our study may not be applicable to places where resistant bacteria are prevalent in high or low numbers. More instances should be included in the future to better understand the need for antibiotics to be used as a prophylactic measure.

Table 2: Univariate, multivariate, and trend analysis of outcomes.

Variables	Postoperative leukocyte count $>9.5 \times 10^9$/L group ($n = 28$)				Postoperative infection group ($n = 14$)			
	Univariate analysis		Multivariate analysis		Univariate analysis		Multivariate analysis	
	p value	Odds ratio (95% CI)	p value	Odds ratio (95% CI)	p value	Odds ratio(95% CI)	p value	Odds ratio(95% CI)
Age (years)	0.093*	0.705(0.470–1.060)	0.152*	0.720(0.460–1.128)				
≤ 39	0.050	14.677(0.999–215.310)	0.073	16.087(0.776–333.645)	0.176	4.444(0.512–38.611)		
40–49	0.139	6.000(0.557–64.576)	0.126	7.462(0.568–98.016)	0.581	0.513(0.048–5.477)		
50–59	0.094	6.286(0.730–54.099)	0.073	8.022(0.825–78.002)	0.823	0.833(0.169–4.118)		
60–69	0.088	6.160(0.762–49.793)	0.061	8.257(0.909–75.019)	0.314	0.444(0.092–2.518)		
70+	Reference		Reference		Reference		Reference	
Sex (male/female)	0.883	0.927(0.337–2.549)			0.223	3.640(0.456–29.039)		
Diabetes history (yes/no)	0.085	2.880(0.863–9.610)	0.025	5.112(1.229–21.264)	0.488	1.773(0.351–8.954)		
History of biliary surgery (yes/no)	0.593	0.654(0.138–3.104)			0.999	0.000(0.000–0.000)		
Gallstone (yes/no)	0.973	1.021(0.313–3.332)			0.003	6.107(1.848–20.179)	0.084	3.626(0.843–15.597)
Operation mode (c-tace/deb-tace)	0.504	1.394(0.526–3.691)			0.922	1.070(0.278–4.116)		
Number of TACE (n)	0.919	0.988(0.788–1.240)			0.075	0.515(0.248–1.068)	0.051	0.394(0.154–1.005)
Preoperative albumin value (g/L)	0.270*	0.566(0.206–1.556)	0.289*	0.5610.192–1.633)	0.011*	11.097(1.738–70.873)	0.046 *	8.824(1.041–74.773)
≥40 g/L	Reference				Reference		Reference	
≥25 g/L, < 40 g/L	0.037	0.326(0.114–0.934)	0.082	0.364(0.117–1.136)	0.642	1.651(0.199–13.693)	0.455	2.332(0.253–21.472)
< 25 g/L	0.626	1.714(0.196–15.019)	0.821	1.335(0.110–16.147)	0.010	54.000(2.611–11116.898)	0.030	153.118(1.631–14372.331)
Preoperative preventive medication (yes/no)	0.614	0.808(0.353–1.850)			0.290	1.857(0.590–5.847)		

* = p for trend.

Table 3: Number of subgroup cases in diabetes and in operation mode.

Diabetes history/operation mode	Whether preventive medication	Postoperative leukocyte count normal	Postoperative leukocyte count >9.5 ×109/L	Total
	N	53	13	66
Nondiabetes history	Y	53	10	63
	Total	106	23	129
	N	2	2	4
Diabetes history	Y	6	3	9
	Total	8	5	13
	N	55	15	70
Total	Y	59	13	72
	Total	114	28	142
	N	42	11	53
c-TACE	Y	50	10	60
	Total	92	21	113
	N	13	4	17
DEB-TACE	Y	9	3	12
	Total	22	7	29
	N	55	15	70
Total	Y	59	13	72
	Total	114	28	142

Table 4: Number of subgroup cases in preoperative albumin value and in operation mode.

Preoperative albumin value (g/L)/operation mode	Whether preventive medication	Non postoperative infection	Postoperative infection	Total
	N	8	0	8
≥40	Y	10	1	11
	Total	18	1	19
	N	56	4	60
≥25- < 40	Y	53	6	59
	Total	109	10	119
	N	1	1	2
< 25	Y	0	2	2
	Total	1	3	4
	N	65	5	70
Total	Y	63	9	72
	Total	128	14	142
	N	49	4	53
c-TACE	Y	53	7	60
	Total	102	11	113
	N	16	1	17
DEB-TACE	Y	10	2	12
	Total	26	3	29
	N	65	5	70
Total	Y	63	9	72
	Total	128	14	142

5. Limitations of the Study

In this study, fewer cases, especially very less cases with positive outcomes, were included. To generalize the results of this study, more case studies and randomized-controlled trials are needed.

In addition, this study was carried out in an area where the minimum inhibitory concentration of the antibiotic (cefuroxime sodium) is very low against E. Coli, K. pneumonia, and *S. aureus*. Therefore, the results of this study may not be applicable to places where resistant bacterial strains are prevalent. Moreover, in this study, the cases of DEB-TACE were CalliSpheres 100–300 μm microsphere preloaded with chemotherapeutic drugs. According to Prajapati et al., the use of 100–300 m sized particles is associated with a much-improved survival rate and fewer problems when compared to the use of 300–500 and 500–700 m sized DEB [32]. Therefore, it cannot represent other drug-loaded microspheres precisely. Thus, it is suggested to conduct and include cases of DEB size 300–500 and 500–700 m in other large studies to get conclusive and evidence-based results.

Table 5: Subgroup analysis of preventive medication group and nonpreventive medication group.

Outcome event	High risk factors	Cochran's		Mantel-Haenszel			Mantel-Haenszel common odds ratio	
		Chi-squared	Asymptotic significance (2-sided)	Chi-squared	Asymptotic significance (2-sided)	Odds ratio (95% CI)	Odds ratio (95% CI)	Asymptotic significance (2-sided)
Postoperative leukocyte count $>9.5\times10^9$/L	Diabetes history (yes/no)	0.534	0.465	0.261	0.61	0.808 (0.353–1.850)	0.730 (0.312–1.706)	0.467
	Operation mode (c-tace/deb-tace)	0.198	0.657	0.053	0.818	0.808 (0.353–1.850)	0.829 (0.361–1.903)	0.658
Postoperative infection	Preoperative albumin value (g/L)	1.256	0.262	0.649	0.420	1.857 (0.590–5.847)	1.886 (0.593–6.000)	0.282
	Operation mode (c-tace/deb-tace)	1.177	0.278	0.634	0.426	1.857 (0.590–5.847)	1.864 (0.593–5.857)	0.287

6. Conclusion

This study was aimed to analyze the effect of prophylactic use of antibiotics on the postoperative leukocytes count in a population with high risk factors for postsurgical infection undergoing c-TACE and DEB-TACE. Results of this study showed that prophylactic antibiotic treatment before the c-TACE or DEB-TACE had no significant correlation with the postoperative increase in leukocyte count and postoperative infection. Diabetes history and serum albumin levels were the prominent risk factors associated with an increase in postoperative leukocyte count and postoperative infection. If a patient has a history of diabetes during the c-TACE treatment or a serum albumin level <25 g/L during DEB-TACE treatment, antibiotics are recommended to prevent postoperative infection. Future large-scale studies and randomized-controlled trials are required to confirm and validate this association.

Data Availability

The data will be provided upon request to the authors.

Conflicts of Interest

The authors declare that they have no conflicts of interest.

References

[1] W.-H. Chan, S.-F. Huang, C.-W. Lee et al., "Incorporation of biochemical factors for survival analysis of transarterial chemoembolization in patients with hepatocellular carcinoma: a retrospective cohort study," *Journal of International Medical Research*, vol. 47, no. 10, pp. 4862–4871, 2019.

[2] W. Sieghart, F. Hucke, and M. Peck-Radosavljevic, "Transarterial chemoembolization: modalities, indication, and patient selection," *Journal of Hepatology*, vol. 62, no. 5, pp. 1187–1195, 2015.

[3] J. H. Zou, L. Zhang, Z. G. Ren, and S. L. Ye, "Efficacy and safety of cTACEversusDEB-TACE in patients with hepatocellular carcinoma: a meta-analysis," in *Journal of Digestive Diseases*vol. 17, no. 8, pp. 510–517, Wiley Online Library, 2016.

[4] F. Melchiorre, F. Patella, L. Pescatori et al., "DEB-TACE: a standard review," *Future Oncology*, vol. 14, no. 28, pp. 2969–2984, 2018.

[5] J. Llovet and J. Bruix, "Systematic review of randomized trials for unresectable hepatocellular carcinoma: chemoembolization improves survival," *Hepatology*, vol. 37, no. 2, pp. 429–442, 2003.

[6] A. L. Lewis, R. R. Taylor, B. Hall, M. V. Gonzalez, S. L. Willis, and P. W. Stratford, "Pharmacokinetic and safety study of doxorubicin-eluting beads in a porcine model of hepatic arterial embolization," *Journal of Vascular and Interventional Radiology*, vol. 17, no. 8, pp. 1335–1343, 2006.

[7] A. L. Lewis, M. V. Gonzalez, A. W. Lloyd et al., "DC bead: in vitro characterization of a drug-delivery device for transarterial chemoembolization," *Journal of Vascular and Interventional Radiology*, vol. 17, no. 2, pp. 335–342, 2006.

[8] Q. Shi, D. Chen, C. Zhou et al., "Drug-eluting beads versus lipiodol transarterial chemoembolization for the treatment of hypovascular hepatocellular carcinoma: a single-center retrospective study," *Cancer Management and Research*, vol. 12, pp. 5461–5468, 2020.

[9] Y. Tang, R. Taylor, M. Gonzalez, A. Lewis, and P. Stratford, "Evaluation of irinotecan drug-eluting beads: a new drug–device combination product for the chemoembolization of hepatic metastases," *Journal of Controlled Release*, vol. 2, no. 116, pp. 55-56, 2006.

[10] K.-C. Liu, W.-F. lv, D. Lu et al., "Initial experience of drug-eluting bead-transcatheter arterial chemoembolization after lipiodol-based transcatheter arterial chemoembolization failure for patients with advanced hepatocellular carcinoma," *Cancer Management and Research*, vol. 13, pp. 7973–7980, 2021.

[11] A. Facciorusso, "Drug-eluting beads transarterial chemoembolization for hepatocellular carcinoma: current state of the art," *World Journal of Gastroenterology*, vol. 24, no. 2, pp. 161–169, 2018.

[12] A. Fohlen, J. P. Tasu, H. Kobeiter, J. M. Bartoli, J. P. Pelage, and B. Guiu, "Transarterial chemoembolization (TACE) in the management of hepatocellular carcinoma: results of a French national survey on current practices," *Diagnostic and interventional imaging*, vol. 99, no. 9, pp. 527–535, 2018.

[13] S. J. Kang, U. J. Kim, S. E. Kim et al., "Predictive value of procalcitonin for bacterial infection after transarterial chemoembolization or radiofrequency ablation for hepatocellular

Hindawi
Journal of Healthcare Engineering
Volume 2023, Article ID 9892301, 1 page
https://doi.org/10.1155/2023/9892301

Retraction

Retracted: Anti-DDI Resource: A Dataset for Potential Negative Reported Interaction Combinations to Improve Medical Research and Decision-Making

Journal of Healthcare Engineering

Received 23 May 2023; Accepted 23 May 2023; Published 24 May 2023

This article has been retracted by Hindawi following an investigation undertaken by the publisher [1]. This investigation has uncovered evidence of one or more of the following indicators of systematic manipulation of the publication process:

(1) Discrepancies in scope
(2) Discrepancies in the description of the research reported
(3) Discrepancies between the availability of data and the research described
(4) Inappropriate citations
(5) Incoherent, meaningless and/or irrelevant content included in the article
(6) Peer-review manipulation

The presence of these indicators undermines our confidence in the integrity of the article's content and we cannot, therefore, vouch for its reliability. Please note that this notice is intended solely to alert readers that the content of this article is unreliable. We have not investigated whether authors were aware of or involved in the systematic manipulation of the publication process. Wiley and Hindawi regrets that the usual quality checks did not identify these issues before publication and have since put additional measures in place to safeguard research integrity.

We wish to credit our own Research Integrity and Research Publishing teams and anonymous and named external researchers and research integrity experts for contributing to this investigation.

The corresponding author, as the representative of all authors, has been given the opportunity to register their agreement or disagreement to this retraction. We have kept a record of any response received.

References

[1] A. Assiri and A. Noor, "Anti-DDI Resource: A Dataset for Potential Negative Reported Interaction Combinations to Improve Medical Research and Decision-Making," *Journal of Healthcare Engineering*, vol. 2022, Article ID 8904342, 6 pages, 2022.

Hindawi
Journal of Healthcare Engineering
Volume 2022, Article ID 8904342, 6 pages
https://doi.org/10.1155/2022/8904342

Research Article

Anti-DDI Resource: A Dataset for Potential Negative Reported Interaction Combinations to Improve Medical Research and Decision-Making

Abdullah Assiri [1] and Adeeb Noor [2]

[1]Department of Clinical Pharmacy, College of Pharmacy, King Khalid University, Abha 62529, Saudi Arabia
[2]Information Technology Department, Faculty of Computing and Information Technology, King Abdulaziz University, Jeddah 21589, Saudi Arabia

Correspondence should be addressed to Adeeb Noor; arnoor@kau.edu.sa

Received 16 February 2022; Revised 3 March 2022; Accepted 8 March 2022; Published 9 April 2022

Academic Editor: Sahfqat Ullah Khan

Potential drug-drug interactions (DDIs) are a core concern across medical decision support systems. Among healthcare practitioners, the common practice for screening these interactions is via computer software. However, as real-world negative reporting is missing, counterexamples that serve as contradictory evidence may exist. In this study, we have developed an anti-DDI resource, a set of drug combinations having negative reported interactions. This resource was created from a set of the top 200 most-used drugs, resulting in 14365 prospective negative reported DDI pairs. During analysis and filtering, 2110 DDIs (14.69%) were found in publicly free DDI resources, another 11130 (77.48%) were filtered by a rule-based inference engine incorporating ten mechanisms of interaction, and 208 were identified through commercial resources. Additionally, 90 pairs were removed due to recent FDA approvals or being unapplicable in clinical use. The final set of 827 drug pairs represents combinations potentially having negative reported interactions. The anti-DDI resource is intended to provide a distinctly different direction from the state of the art and establish a ground focus more centered on the evaluation and utilization of existing knowledge for performing thorough assessments. Our negative reported DDIs resource shall provide healthcare practitioners with a level of certainty on DDIs that is worth investigating.

1. Introduction

In the course of primary care, patients often are prescribed drugs that might have a risk of interaction, and the majority of such interactions are of major relevance [1]. Adverse interaction of drugs may lead to hospital admission and serves to increase morbidity and mortality. Additionally, several studies have reported an increase in patient hospital stay when DDIs are identified, suggesting that DDIs have a significant clinical and economic burden. Accordingly, ensuring quality pharmacotherapy requires the selection of appropriate drug combinations considering the condition being treated [2]. As concerns patient factors, this means considering cost, dosage, administration method, contraindications, and possible adverse reactions; but the prospect of one drug impacting another in terms of its safety or efficacy—that is, a drug-drug interaction (DDI)—is also not to be ignored [2, 3].

Conceptually, it is common practice to screen potential interactions via computer software, and numerous programs developed for identifying drug interactions presently see wide use in detecting interactions of clinical significance. For example, the commercial resources Lexicomp [4] and Micromedex [5] have been utilized by healthcare practitioners in detecting and determining the risk of interactions. Other publicly available free resources, such as DrugBank [6] and Drugs.com [7], are also widely leveraged for reporting known and potential interactions. However, despite the importance of DDI detection, existing DDI resources have a low level of overlap and a high level of diversity in reported interactions. For example, a recent study conducted by our group [8] demonstrated considerable variation among five commercial and free resources when used in reporting chemotherapy agent interactions.

As a result, it is common that available resources, whether commercial or publicly free, fail to detect all significant interactions, yield alerts whose significance is questionable, and do not supply information on risk factors for adverse reactions [9–11]. One reason for the diversity in these resources is that each software has been developed to employ a different algorithm and database combination [12–14]. Another is that the determination of related literature primarily depends on expert evaluation, ultimately leading to discrepancies in the references that different utilities incorporate. A third is the lack of a robust validation process for algorithms [9]. Consequently, this problem may be alleviated, at least in part, by instituting precise, clear instructions for algorithm development and validation.

In fact, the lack of overlap among DDI resources seems to be more due to specialization of resources than to negative consideration (i.e., no reported interaction = potential safe interaction combination). While originally a larger number of utilities and resources were considered for input, the actual resources that ended up being used are those with clinical/research backing. Furthermore, investment in thoughtful research and clinical trials proves the worthiness of the reported DDIs. This does not consider information that was "omitted" for whatever reason (i.e., any found DDI is assumed to be reported). In healthcare practice, on the other hand, it is essential to be both selective and transparent when choosing drug interactions for inclusion in such resources. Nonetheless, among the abundance of available utilities, no particular resource has yet emerged as a groud-truth for healthcare practitioners.

Here, we present the development of a potentially negatively reported DDI dataset, the anti-DDI resource, containing the most commonly prescribed drug pairs for which no DDIs have been reported. This resource is created as a means of differentiation from the state of the art and to provide a different direction, establishing a ground focus centered more on evaluation than on the generation and utilization of expanded knowledge and resources to perform evaluations. To the best of our knowledge, this represents the first study to construct such a list by employing a data-driven approach in conjunction with widely-employed DDI-screening software, and with the output further reviewed by healthcare practitioners. This robustly-resourced, trustworthy dataset has the potential to benefit both healthcare practitioners and researchers in the course of their work; being comprised of the most frequently prescribed drugs, it serves to summarize common safe combinations along with those least utilized due to safety concerns. Finally, the anti-DDI resource can enable stratification of patients receiving multiple drugs according to risk for DDIs, and so benefit practitioners in reducing unwanted effects.

2. Materials and Methods

2.1. Data Baseline. All possible pairwise drug combinations were generated for a set of the top 200 drugs, which include those most commonly used to treat several conditions. The list of top drugs was obtained from [15]. The rationale was to develop the initial dataset from the most-used drugs, with which patients might be at higher risk of being exposed to DDIs. The list can vary slightly from year to year and country to country according to national health policies. When generating drug combinations, consideration was given to reasons other than DDIs that preclude drugs being used together, such as having similar indications or belonging to the same pharmacological group.

2.2. Drug List Curation and Drug Mapping. From the top 200 most-used drugs, we generated 14365 prospective negative reported DDI pairs. The steps of pair creation are detailed below:

(i) Step 1: we normalized each drug name in the list to the corresponding UMLS concept unique identifier (CUI) through UMLS terminology services (UTS) [16]. For each drug, we utilized the text search box provided by the UTS tool to extract the equivalent CUI. We also ensured that the retrieved CUI was grouped correctly in the UMLS semantic network, i.e. as a drug. This yielded 192 drugs, as there were eight drugs with no CUIs.

(ii) Step 2: we mapped the UMLS CUI of each drug to its STITCH ID using Anatomical Therapeutic Chemical (ATC) identifiers. This step was necessary to enable checking for interactions as reported and represented by the publicly free DDI resources. This step reduced the set to 170 recognized drugs.

(iii) Step 3: we created pairwise combinations of the 170 unique drugs as follows:

For each drug in the list:
Create a list of all possible pairs of drugs that could interact as a result of any combination.

This produced 14365 prospective negative reported DDI pairs.

2.3. Checking Prospective Negative Reported DDI Pairs against Publicly-Free DDI Resources. To ensure our final list consisted of only potential negative reported DDI pairs, we intended to remove any pair having been recorded in either clinical or computational DDI resources. Accordingly, we downloaded the potential drug-drug interaction (PDDI) knowledge base of Ayvaz et al. [17] from https://github.com/dbmi-pitt/public-PDDI-analysis, obtained on 01/02/2022. This database consisted of two files. The first, labeled "Conservative," featured mappings based on both

International Chemical Identifiers and either the drug preferred term or synonym. It contained the following DDI sources and corresponding potential DDI counts, for 200159 potential DDIs in total: Drugbank-24103, NDF-RT-1876, KEGG-52104, CredibleMeds-83, DDI Corpus 2011-334, DDI Corpus 2013-787, NLM Corpus-238, PK Corpus-146, ONC High-Priority-1930, ONC Non-Interuptive-2101, OSCAR-10325, HIV-19198, HEP-11194, FRENCH-62047, and World Vista-13693. The second file, labeled "Non-conservative," featured mappings based just on International Chemical Identifiers or either the drug preferred term or synonym. It contained the following DDI sources and corresponding potential DDI counts, for 219617 potential DDIs in total: Drugbank-24103, NDF-RT-2606, KEGG-52104, CredibleMeds-83, DDI Corpus 2011-733, DDI Corpus 2013-1780, NLM Corpus-328, PK Corpus-184, ONC High-Priority-1930, ONC Non-Interuptive-2101, OSCAR-10325, HIV-19198, HEP-11194, FRENCH-62047, and World Vista-30901.

We integrated both sets and removed duplicate entries, which yielded a set of 40631 DDIs. After that, we tested our prospective negative reported DDI pairs as follows:

For each DDI in the possible negative set:

Check for the interaction in all integrated DDI resources

Retrieve all resources that report an interaction

Remove the pair with the identified interaction

Continue

This filtering reduced the list from 14365 to 12255, so 2110 of the prospective negative pairs were reported as interacting in the free resources.

2.4. Eliminating False-Positive Prospective Negative DDI Pairs Based on Mechanisms of Interaction. Following our construction of the list of prospective negative reported DDI pairs and testing it against publicly free DDI resources, we took the remaining 12255 pairs and annotated them with interaction mechanisms using the Drug-drug Interaction Discovery and Demystification (D3) inference framework by Noor et al. [14]. D3 applies rules on a knowledge graph to distinguish the following mechanisms of interaction: protein binding, metabolic induction & inhibition, transporter induction & inhibition, multiple pathways, competitive pharmacological, additive pharmacodynamic, indication similarity, and side-effect similarity. We removed any DDI from the prospective negative list that was identified as having a mechanistic interaction by the D3 system as follows:

For each DDI in the negative set:

Apply D3 rules on the DDI pair

If at least one rule is retrieved (a mechanism of interaction is found), remove the pair

Else keep it

After this evaluation, the number of prospective negative pairs decreased to 1125. Therefore, more than 70% (11130) were found to be false positives, i.e. were explained by at least one mechanism of interaction included in the D3 framework.

2.5. Technical Validation by Experts and FDA Approval Cutoff for Quality Assurance of Prospective Negative Reported DDI Pairs. After generation and filtering of the set of pairwise combinations, two experts (trained, licensed pharmacists) reviewed the list for repetition and unapplicable drug combinations. Multiple criteria were established for the reviewers to follow. First, each pharmacist reviewed all generated combinations for repetitions in which the same two drugs were combined in different directions. Second, each pharmacist assessed the applicability of every drug pair to clinical practice and its clinical appropriateness or lack thereof. Lastly, agreement between the two pharmacists was assessed, with consensus being required for the removal of any pair from the dataset. Additionally, all drugs approved after 2018 were removed due to lacking sufficient reported DDI studies or DDI-associated adverse reactions.

2.6. Eliminating False Positives from Prospective Negative Reported DDI Pairs Based on Commercial DDI Resources. Finally, the list was checked for previously-reported potential DDIs by entering each pair into the well-known software Lexicomp [5]. The rationale for using Lexicomp over other resources was that it is considered a reliable resource for clinical information, and therefore is the most commonly used drug software among clinical and research institutions. DDI risk in Lexicomp is classified as follows: no known interaction (A), no action needed (B-minor), monitor therapy (C-moderate), consider therapy modification (D-major), and avoid combination (X-major). Drug pairs were considered as detected DDIs and removed from the dataset when classified in any class from B to X. Pairs labeled with class A were retained. All removed pairs were collected and reported as shown in Figures 1 & 2, after which a similar check was performed against Drugs.com [7]. DDI risk in Drugs.com is classified as follows: minor, moderate, or major interaction. Any pairs labeled with any of these classes were recorded and removed from the final dataset. Lastly, the final filtered list was reviewed by two trained and licensed pharmacists, in which process each pharmacist respectively reentered the drug pairs into one of the commercial DDI resources (either Lexicomp or Drugs.com) to confirm the absence of DDI risk among those included in the final list.

3. Data Records

The final list of potential negative reported DDI pairs evaluated in this study is publicly available as tab-delimited files upon request. Table 1 gives a summary of the drug pairs, their validation, DDI risks, and risk stratifications, along with an outline of the available data files, which can be accessed directly through the corresponding URLs. Of the 14365 total drug pairs constructed from the set of 200 drugs, 827 (5.76%) were retained to comprise the final list, those

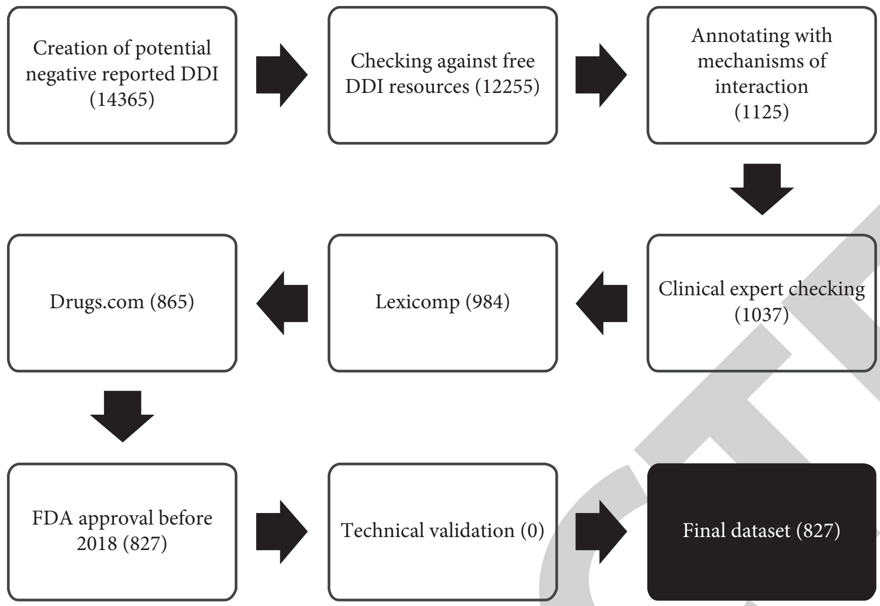

Figure 1: Flowchart of dataset construction and validation processes.

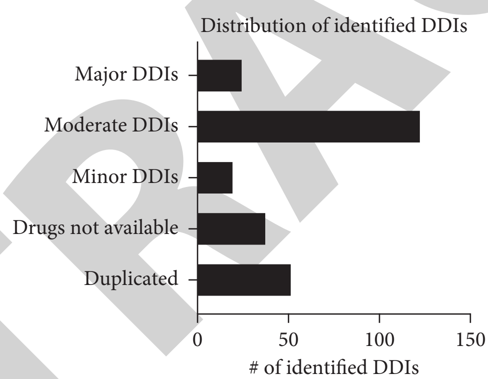

Figure 2: Type distribution of DDIs identified through the dataset construction and validation processes.

Table 1: Description of anti-DDI resource.

Parameter	(n)	Comments
Total number of drugs	172	
Total number of drug combinations	827	
Technical validation	52	Duplication
Lexicomp	89	Known DDI
Drugs.com	119	Known DDI
Approved after 2018	38	Recent approval
Checker 1	0	
Checker 2	0	
Total	298	
Detected DDIs		
Minor	20	
Moderate	123	
Major	25	
Medications most frequently appearing		
Sevelamer	152	
Ustekinumab	140	
Levetiracetam	78	
Atenolol	77	
Liraglutide	72	

having no potential risk for DDIs. In the course of the filtering process, 2110 DDIs (14.69%) were excluded based on available resources, and 11130 (77.48%) were identified by the D3 algorithm. Checking against Lexicomp and Drugs.com yielded 208 DDIs between them, of which 20 were reported in Lexicomp as requiring therapy modification, while 5 in Drugs.com were classed as major DDIs.

4. Limitations

The accuracy of this work is constrained by the data resources and by the computation methods. First, not all potential DDI mechanisms are incorporated into the D3 algorithm that was used for filtering potential DDIs, hence some DDIs might be missing. This limitation was moderated by checking the filtered list against two commonly-used resources, Lexicomp and Drugs.com. However, these resources have their own limits in being based on results from clinical studies that cannot be generalized to all populations. As such, the obtained list might be subjected to modifications as more clinical data become available. Our set of drug combinations represents a comprehensive list of pairwise combinations of the top 200 most-used drugs. In addition, validation of this dataset utilized all resources presently available; that said, future studies may produce new findings and new reports of DDIs that disqualify some of the "risk-free" combinations identified here. To help minimize this prospect, we only considered drugs that were approved before 2018 and so had enough data available to be confident in their safety. Furthermore, our study group will continue to annually update this list to ensure its ongoing accuracy.

5. Data Utility (Usage Notes)

5.1. Validation of DDI Prediction Software. As no negative reported DDI dataset is available for validation of DDI research, our group was inspired to develop a different means of validating newly-developed DDI prediction algorithms. Researchers can use this dataset, available upon request, alongside current validation methods to assess developed algorithms in terms of false-positive DDIs. Approaching validation from two directions will undoubtedly provide more precise and accurate assessments of prediction accuracy for new software.

5.2. Comprehensive List of Drug Combinations for Healthcare Practitioners. Given the discrepancies in reported DDIs among available public free and noncommercial resources, healthcare practitioners must have other means of detecting potential DDIs or confirming the safety of a given combination of drugs. Such capability enables the provision of appropriate patient care and the minimization of unwanted effects that stem from concurrent treatment with multiple drugs. Our dataset presented here represents an excellent first step towards a comprehensive list of drugs that can be safely utilized in combination, assuring the absence of DDI risk in patients. Additionally, it can guide healthcare practitioners by providing potential safe alternatives for interacting drugs. Notably, several drugs occurred with high frequency among drug pairs included in the final dataset, as shown in Table 1, indicating to some extent a degree of safe use for these drugs in clinical practice. Further extension of this work would have a significant impact in minimizing the frustrations that available DDI software poses for healthcare practitioners. In addition, a simplified version of this dataset can be made publicly available to patients as a reputable, trustworthy resource, reducing reliance on free resources of dubious validity that could mislead and provide imprecise information regarding drugs.

6. Discussion and Conclusions

In clinical pharmacy, understanding, and managing DDI events poses a major challenge. Several algorithms and strategies have been proposed by healthcare practitioners and researchers alike in attempts to address this perplexing subject. Our group previously developed a DDI prediction algorithm incorporating ten potential mechanisms [14, 18]; other algorithms have been developed to predict DDIs and stratify risk based on available DDI resources [19–21]. A persistent challenge in all of these endeavors is the lack of proper validation data for the developed algorithms [9].

This study extracted the top 200 most-used drugs from available resources and assessed all possible pairwise combinations of those drugs. Distinct from the state of the art, we filtered the generated list to identify those pairs having no risk of interaction. As no negative dataset of DDIs is yet available, we leveraged multiple resources for evidence of potential negative DDIs. In addition, the list was reviewed manually by experts to ensure the logic of generated combinations and the plausibility of their use in healthcare practice. The rigor of this filtering and review process ensures the resulting dataset is precise and well-constructed, and that it is appropriate for utilization in diverse situations.

As this approach of singling out safe drug combinations is unique in current DDI research, which predominantly focuses on the negative aspects of interactions and associated adverse events, it has the potential to open up new avenues and perspectives. Therefore, a wide range of researchers would significantly benefit from this work in many ways. Additionally, we plan to continue developing this work by integrating data from additional resources and considering all drugs with clinical use, not solely the most-used. We additionally plan to validate the clinical safety of all drug resources by connecting the generated combinations with data on their actual use.

In summary, the method employed here approaches research into DDIs and associated events from a new perspective and opens a new avenue for considering concurrently-used drugs on multiple levels. Further research is merited to address the challenges that yet limit DDI prediction algorithms and to improve clinical decision-making and patient safety in meaningful ways.

Data Availability

The data generated by this work are available on supplementary 1.

Hindawi
Journal of Healthcare Engineering
Volume 2023, Article ID 9795025, 1 page
https://doi.org/10.1155/2023/9795025

Retraction

Retracted: Ten Hotspot MicroRNAs and Their Potential Targets of Chondrocytes Were Revealed in Osteoarthritis Based on Bibliometric Analysis

Journal of Healthcare Engineering

Received 23 May 2023; Accepted 23 May 2023; Published 24 May 2023

This article has been retracted by Hindawi following an investigation undertaken by the publisher [1]. This investigation has uncovered evidence of one or more of the following indicators of systematic manipulation of the publication process:

(1) Discrepancies in scope
(2) Discrepancies in the description of the research reported
(3) Discrepancies between the availability of data and the research described
(4) Inappropriate citations
(5) Incoherent, meaningless and/or irrelevant content included in the article
(6) Peer-review manipulation

The presence of these indicators undermines our confidence in the integrity of the article's content and we cannot, therefore, vouch for its reliability. Please note that this notice is intended solely to alert readers that the content of this article is unreliable. We have not investigated whether authors were aware of or involved in the systematic manipulation of the publication process. Wiley and Hindawi regrets that the usual quality checks did not identify these issues before publication and have since put additional measures in place to safeguard research integrity.

We wish to credit our own Research Integrity and Research Publishing teams and anonymous and named external researchers and research integrity experts for contributing to this investigation.

The corresponding author, as the representative of all authors, has been given the opportunity to register their agreement or disagreement to this retraction. We have kept a record of any response received.

References

[1] W. Hu, Q. Zhang, S. Li, S. Ai, and Q. Wu, "Ten Hotspot MicroRNAs and Their Potential Targets of Chondrocytes Were Revealed in Osteoarthritis Based on Bibliometric Analysis," *Journal of Healthcare Engineering*, vol. 2022, Article ID 8229148, 11 pages, 2022.

Hindawi
Journal of Healthcare Engineering
Volume 2022, Article ID 8229148, 11 pages
https://doi.org/10.1155/2022/8229148

Research Article

Ten Hotspot MicroRNAs and Their Potential Targets of Chondrocytes Were Revealed in Osteoarthritis Based on Bibliometric Analysis

Wei-Shang Hu[1] **Qi Zhang**[1,2] **Si-Hui Li**[1] **Shuang-Chun Ai**[3] **and Qiao-Feng Wu**[1,4,5]

[1]*Acupuncture and Moxibustion College, Chengdu University of Traditional Chinese Medicine, Chengdu, Sichuan, China*
[2]*Chongqing Traditional Chinese Medicine Hospital, Chongqing, China*
[3]*Mianyang Hospital of Traditional Chinese Medicine, Mianyang, Sichuan, China*
[4]*Institute of Acupuncture and Homeostasis Regulation, Chengdu University of Traditional Chinese Medicine, Chengdu, Sichuan, China*
[5]*Acupuncture & Chronobiology Key Laboratory of Sichuan Province, Chengdu, Sichuan, China*

Correspondence should be addressed to Qiao-Feng Wu; wuqiaofeng@cdutcm.edu.cn

Received 13 February 2022; Accepted 2 March 2022; Published 9 April 2022

Academic Editor: Liaqat Ali

Background. Osteoarthritis (OA) is one of the most common joint disorders and debilitating diseases. Current evidence suggests that microRNAs (miRNAs) play a critical role in the pathogenesis of OA and have great potential as new biomarkers and therapeutic targets. We aimed to analyze the trends and research status on miRNAs in OA and further demonstrate the hotspot miRNAs in OA via CiteSpace and VOSviewer. *Methods*. Publications regarding miRNAs and OA were extracted from the Web of Science (WOS) database on October 30, 2021. We assessed the number of publications, institutions, countries, authors, journals, cited references, and keywords with the help of the software tools CiteSpace and VOSviewer. *Results*. A total of 1109 articles were included. Research related to miRNAs and OA began to appear in 2008, and the overall trend is increasing. Chinese institutions have a leading advantage in the number of publications but lack high-quality and high-cited research and are laggard in co-cited literature. Ten miRNAs including miR-140, miR-146, miR-34, miR-181, miR-27, miR-9, miR-29, miR-21, miR-26, and miR-155 and chondrocytes were revealed as the most obvious miRNAs and a potential target for OA based on bibliometric analysis. More focus will be placed on a comprehensive study on chondrocytes regulated by miRNAs, which may accelerate possible diagnostic biomarkers and diagnostic biomarkers of OA in the future.

1. Introduction

Osteoarthritis (OA) is the most common joint disease, affecting an estimated more than 300 million people worldwide, and the increase of the age-standardized prevalence and annual incidence rate was 9.3% and 8.2%, respectively, from 1990 to 2017 [1–4]. With the increase of population aging and obesity, as well as the change of lifestyle, the prevalence of OA has also increased, and it has gradually become a joint disease that has the greatest impact on the quality of life of middle-aged and elderly people [3, 5]. The etiology of OA remains enigmatic, which may involve genetic susceptibility, metabolism, trauma, inflammation, biomechanics, aging, epigenetics, and other factors [2, 6]. Researchers have attempted to intervene in the out-of-control molecular pathways of OA in recent years, including bisphosphonates, catabolic enzymes targeting articular cartilage degradation, inducible nitric oxide synthase (iNOS), and NF-κB inhibitors, but the experimental and clinical effects are not ideal [7, 8]. The main clinical treatments for OA are still limited to physiotherapy, NSAIDs, and eventual arthroplasty [9].

MicroRNA (miRNA) is a type of endogenous noncoding small RNA [10]. It affects the regulation of gene expression by degrading or inhibiting target gene mRNA translation to control target gene expression [11]. Current studies have established the role of miRNAs in regulating gene expression in articular chondrocytes and their significance to the pathogenesis of OA [12, 13]. Methods for maintaining or suppressing the expression of critical miRNAs involved in the pathogenesis of OA have the potential to find new diagnostic and therapeutic targets [12]; Zhang et al. [14]. However, there are more than 100 miRNAs found differentially expressed in OA cartilage [15]; Nugent [16]. Therefore, investigating the current research status, hotspots, and frontiers of miRNAs in OA is meaningful and necessary.

This study focused on the network of authors, countries, and institutions, as well as the analysis of co-cited references, co-occurring keywords, cluster analysis, and keyword burst, to explore the global trends and hotspots of the past research on miRNAs in OA. And further this study excavates the hotspot miRNAs, related mechanisms, and targets to provide a reference for follow-up research.

2. Methods

2.1. Search Strategy. Data were collected from the Science Citation Index Expanded (SCI-E) of the Web of Science Core Collection (WoSCC), including Science Citation Index Expanded (SCI-EXPANDED), Conference Proceedings Citation Index-Science (CPCI-S), Current Chemical Reactions (CCR-EXPANDED), and Index Chemicus (IC). The data retrieval strategy included the topic "microRNAs or miRNAs or microRNA or miRNA" and the topic "osteoarthritis". Publication type and language had no restriction. The search year is limited to 1900 to 31 October 2021. WoS export information function is used to download the information including the author, affiliation, title, abstract, keywords, journal, publication year, WoS category, and citation of each publication.

2.2. Visualization Analysis Based on CiteSpace and VOSviewer. CiteSpace 5.8.R3 was used to analyze the knowledge graph and study burst detection [1]. The parameters of CiteSpace were set as follows: time: 1900–2021; interval year: 1; selection criteria: select the top 100 levels with the most citations or occurrences. In the network diagram generated by CiteSpace, nodes represent countries, institutions, cited references, or keywords. When the third node references two nodes together, a link would be created between the two nodes. In co-occurrence network clustering, the clustering module value Q was used to evaluate the significance of the modular clustering structure of the network. The greater the network's modularity value, the better the network's clusters. The value interval of Q was [0, 1], and $Q > 0.3$ indicates that the clustering structure is significant; S is the average contour value of the cluster, which is used to determine the network's uniformity. It is generally considered that $S > 0.5$ clustering is reasonable. $S > 0.7$ means that the clustering is convincing. VOSviewer 1.6.16 was used to extract the keyword co-occurrence analysis of documents. To simplify the co-occurrence network, we set the co-occurrence threshold to 3 to perform the keywords co-occurrence analysis.

3. Results

3.1. Distribution of Publication Output. A total of 1109 publications were included in the study. In general, the number of publications of miRNA in OA has been increasing significantly since 2008, as the number of publications increased from 4 in 2008, to 207 in 2020, and 199 in 2021 as of the retrieval date, as shown in Figure 1(a). According to this trend, the total number in 2021 is likely to exceed that in 2020. Figure 1(b) shows that 78.22% of the total publications are articles and 12.51% of them are reviews, the rest are meeting abstract, early access, proceedings paper, correction and others. Figure 1(c) shows OSTEOARTHRITIS AND CARTILAGE published the most articles, with 85 publications. There were 34 articles in MOLECULAR MEDICINE REPORTS, 29 articles in INTERNATIONAL JOURNAL OF MOLECULAR SCIENCES, and 26 articles in EXPERIMENTAL AND THERAPEUTIC MEDICINE on miRNAs in OA. The annual citations of publications have been also increased from 11 in 2008 to 5378 in 2020, and 6041 as of 31 October 2021 (Figure 1(d)).

3.2. Countries, Institutions, and Authors' Analysis. As shown in Table 1, the country with the most publications was China (690 publications), contributing 58.97% of the total publications, followed by the US (140 publications), England (64 publications), Italy (47 publications), and South Korea (41 publications). Among the top 10 publishing institutions, 6 of them were located in China, 3 in Canada, and 1 in England (Table 1).

In the atlas of institutional cooperation networks, node size represented the number of literature published by countries or institutions, and the connection between nodes reflected the strength of the cooperative relationship. As shown in Figure 2(a), except for the relatively frequent cooperation between the US and Japan, there were few links between different countries and institutions, but within a certain country, there was more cooperation among institutions (Figure 2(b)). The top 20 most prolific authors who published on miRNAs in OA are shown in Table 1, contributed 345 (31.10%) of the total publications. Kapoor M from the University of Toronto had the highest number of publications (30 publications), followed by Wang Y (27 publications), Gandhi R (21 publications), Li J (20 publications), Young DA, and Zhang ZQ (19 publications). 9 of the top 20 most prolific authors are from China. Miyaki S from Hiroshima University had the highest co-citation count (293), followed by Goldring MB (248), Bartel DP (214), Iliopoulos D (189), and Loeser RF (180). As presented in Figure 2(c), prolific authors frequently work in close collaboration with other authors.

3.3. Distribution of Co-Cited References. The co-citation network shows the correlation between articles and reflects the knowledge structure of this field. In this study, the top 100 co-cited publications were selected to form a co-citation network. The combined network contains 256,916 references and 65 clusters, 632 nodes, and 3,672 connections. The

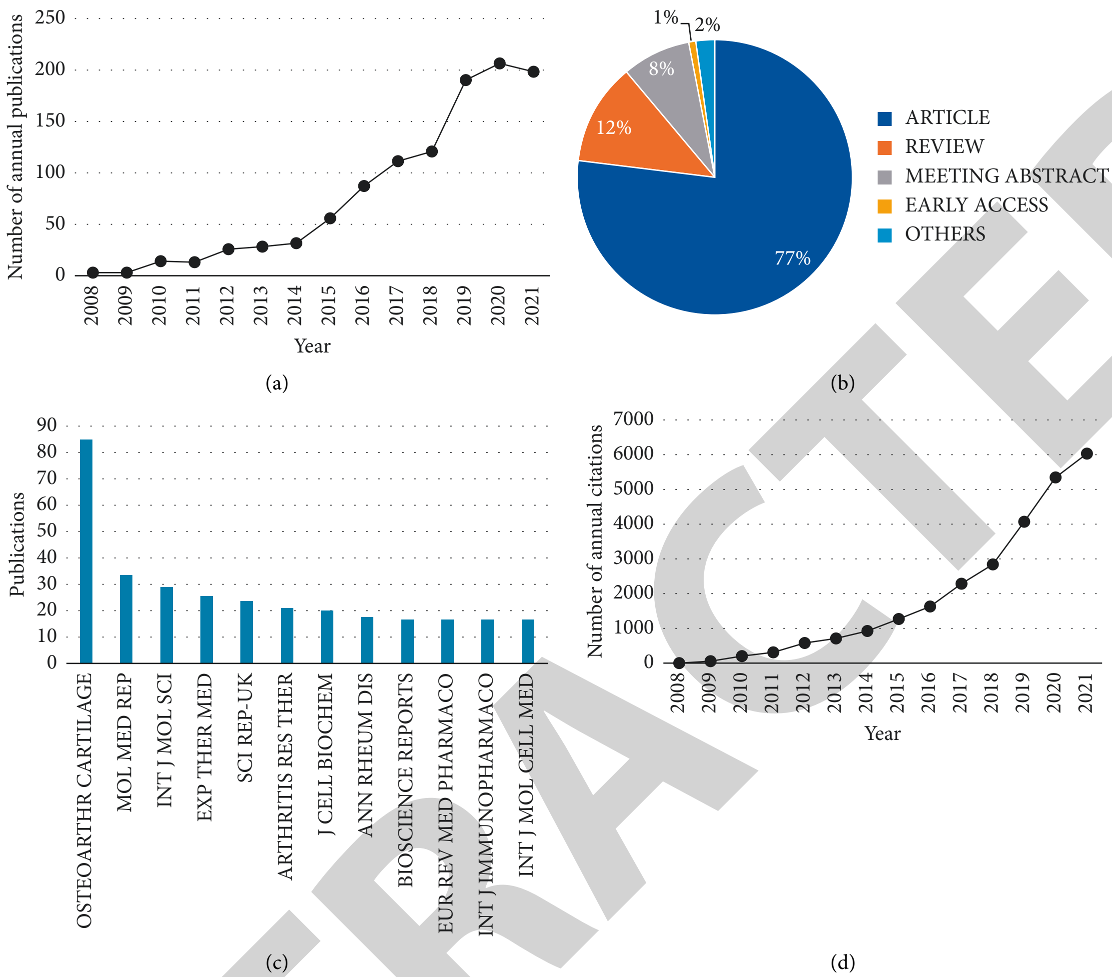

Figure 1: Citation of publications related to osteoarthritis. (a) The number of annual publications till 2021, (b) types of publications, (c) number of publications having osteoarthritis with most citations in different journals, and (d) the annual citations of publications till 2021 with osteoarthritis.

Table 1: Countries, institutions, and authors' analysis.

Country	Publications (%)	Institution	Publications (%)	Author	Publications	Cited author	Counts
China	690 (58.97%)	Sun Yat-sen University	40 (3.61%)	Kapoor M	30	Miyaki S	293
United States	140 (12.62%)	Xi'an Jiaotong University	34 (3.07%)	Wang Y	27	Goldring MB	248
England	64 (5.77%)	University of Toronto	33 (2.98%)	Gandhi R	21	Bartel DP	214
Italy	47 (4.24%)	Shanghai Jiaotong University	30 (2.71%)	Li J	20	Iliopoulos D	189
South Korea	41 (3.70%)	University Health Network Toronto	30 (2.71%)	Young DA	19	Loeser RF	180
Japan	39 (3.52%)	Krembil Research Institute	29 (2.61%)	Zhang ZQ	19	Akhtar N	154
Canada	39 (3.52%)	Newcastle University UK	24 (2.16%)	Kang Y	18	Jones SW	154
Germany	20 (1.80%)	Jilin University	23 (2.07%)	Zhang Y	18	Yamasaki K	148
Spain	18 (1.62%)	Nanjing Medical University	22 (1.98%)	Barter MJ	16	Swingler TE	128
Netherland	18 (1.62%)	Shandong University	22 (1.98%)	Clark IM	16	Song J	125

modular Q of the network is 0.6007, indicating that the cluster structure is acceptable. The average contour value is 0.8377, indicating that the network has good uniformity. The labels of the cluster are extracted from the most commonly used headings in the articles of the cluster group. A total of 65 clusters were generated in this network. Figure 2(d) shows the top 11 largest cluster tags. The cluster tags were #0 chondrogenesis, #1 knee osteoarthritis, #2 ADAMTS5, #3 circular RNA, osteoporosis, #4 apoptosis, #5 DNA methylation, #6 exosomes, #7 bone, #8 MiR-1, #9 embryonic development, and #10 resistin.

We extracted the top 10 co-cited publications and found that Miyaki's article [17] on the dual role of miRNA-140 in chondrogenesis and homeostasis published in Gene &

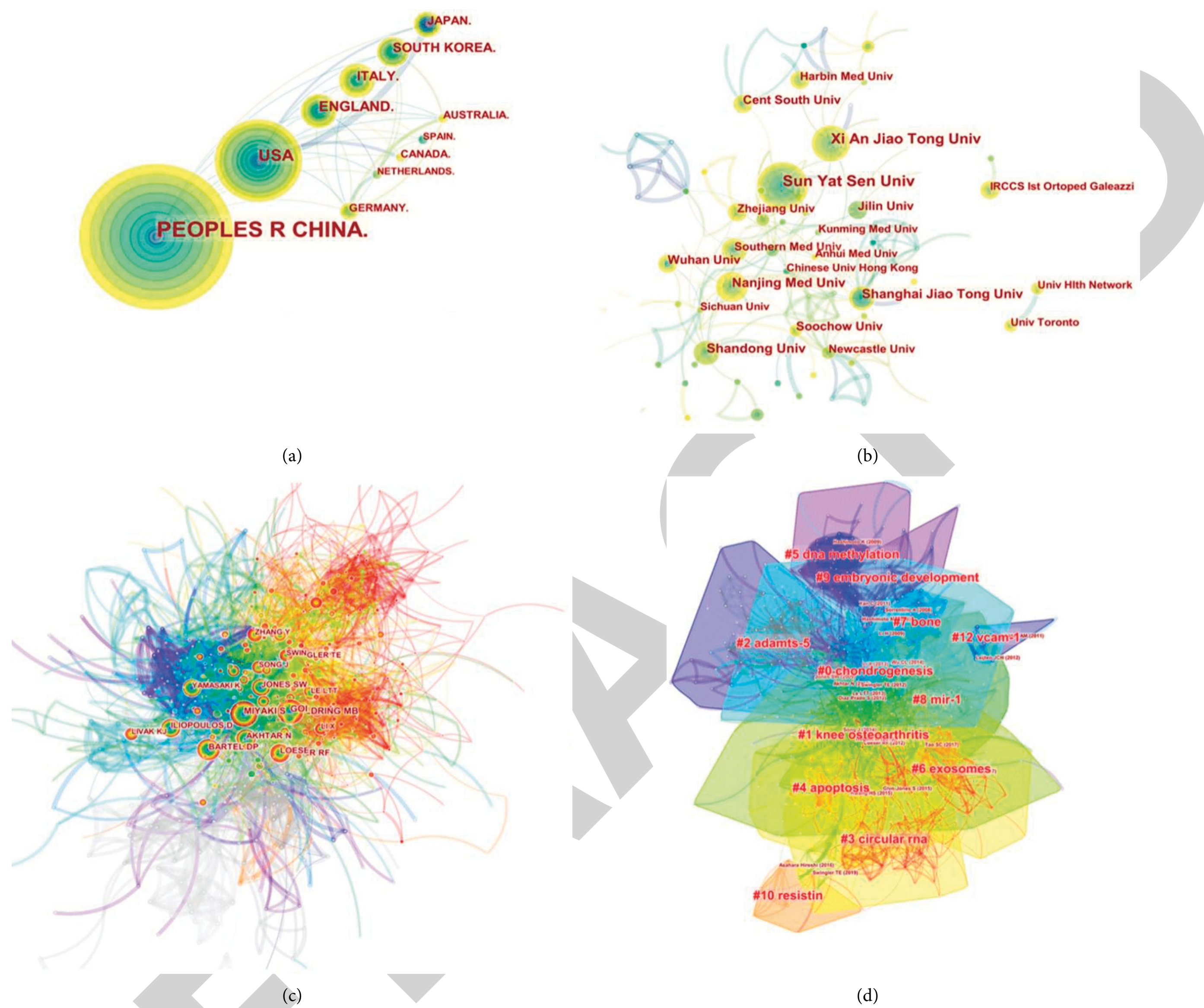

Figure 2: Literature published by countries and institutions regarding OA. (a) Relative cooperation and links between countries for publications in the same area, (b) relative cooperation and links between different institutions for publications in the same area in China, (c) prolific authors frequently work in close collaboration with other authors, and (d) most commonly used headings in articles, which were used as labels in the cluster network.

Development in 2010 and Jones's article [18] on the regulation of TNF-α and MMP-13 by differentially expressed miRNAs in OA and cartilage tissues were the foundation work of miRNAs in OA research (Table 2).

3.4. Co-Occurring Keywords and Cluster Analysis. The analysis of keywords indicates the theme of the publication and the hotspots in the research field. A keyword co-occurrence network composed by the association of these keyword pairs is formed by counting the frequency of the occurrence of keywords in the publications (Figure 3). The frequency of two keywords appearing in the same publication shows the strength between these two keywords. In VOSviewer, we combined keywords with different but identical meanings or singular or plural forms to get a clear network and then classify according to the co-occurrence frequency. A total of 1627 keywords were obtained. In order to simplify the co-occurrence network, keywords with co-occurrence time greater than 3 were selected as the co-occurrence network, and a co-occurrence network composed of 362 keywords was finally obtained (Figure 3). The co-occurrence network has 13 clusters and 7917 connections. The node size in the figure is positively correlated with co-occurrence frequency, and different colors represent different clusters. According to the co-occurrence frequency of keywords, screening and classification were performed (Figure 3), and we found that these publications mainly involved miRNAs, cytokines, signaling pathways, and gene expression. Cytokines involved in the co-occurrence

Table 2: Distribution of co-cited references of the published articles.

Rank	Co-cited publications	First author (year)	Counts
1	MicroRNA-140 plays dual roles in both cartilage development and homeostasis [17]	Miyaki S (2010)	113
2	The identification of differentially expressed microRNA in osteoarthritic tissue that modulates the production of TNF-alpha and MMP-13 [18]	Jones SW (2009)	101
3	MicroRNA-27b regulates the expression of matrix metalloproteinase 13 in human osteoarthritis chondrocytes [19]	Akhtar N (2010)	98
4	Macro view of microRNA function in osteoarthritis [12]	Miyaki S (2012)	96
5	MicroRNA-140 is expressed in differentiated human articular chondrocytes and modulates interleukin-1 responses [20]	Miyaki S (2009)	95
6	Integrative microRNA and proteomic approaches identify novel osteoarthritis genes and their collaborative metabolic and inflammatory networks [21]	Iliopoulos D (2008)	88
7	Characterization of microRNA expression profiles in normal and osteoarthritic human chondrocytes [22]	Diaz-Prado S (2012)	88
8	The expression and function of microRNAs in chondrogenesis and osteoarthritis [23]	Swingler TE (2012)	87
9	Expression of microRNA-146a in osteoarthritis cartilage [24]	Yamasaki K (2009)	86
10	Osteoarthritis: a disease of the joint as an organ [25]	Loeser R. (2012)	76

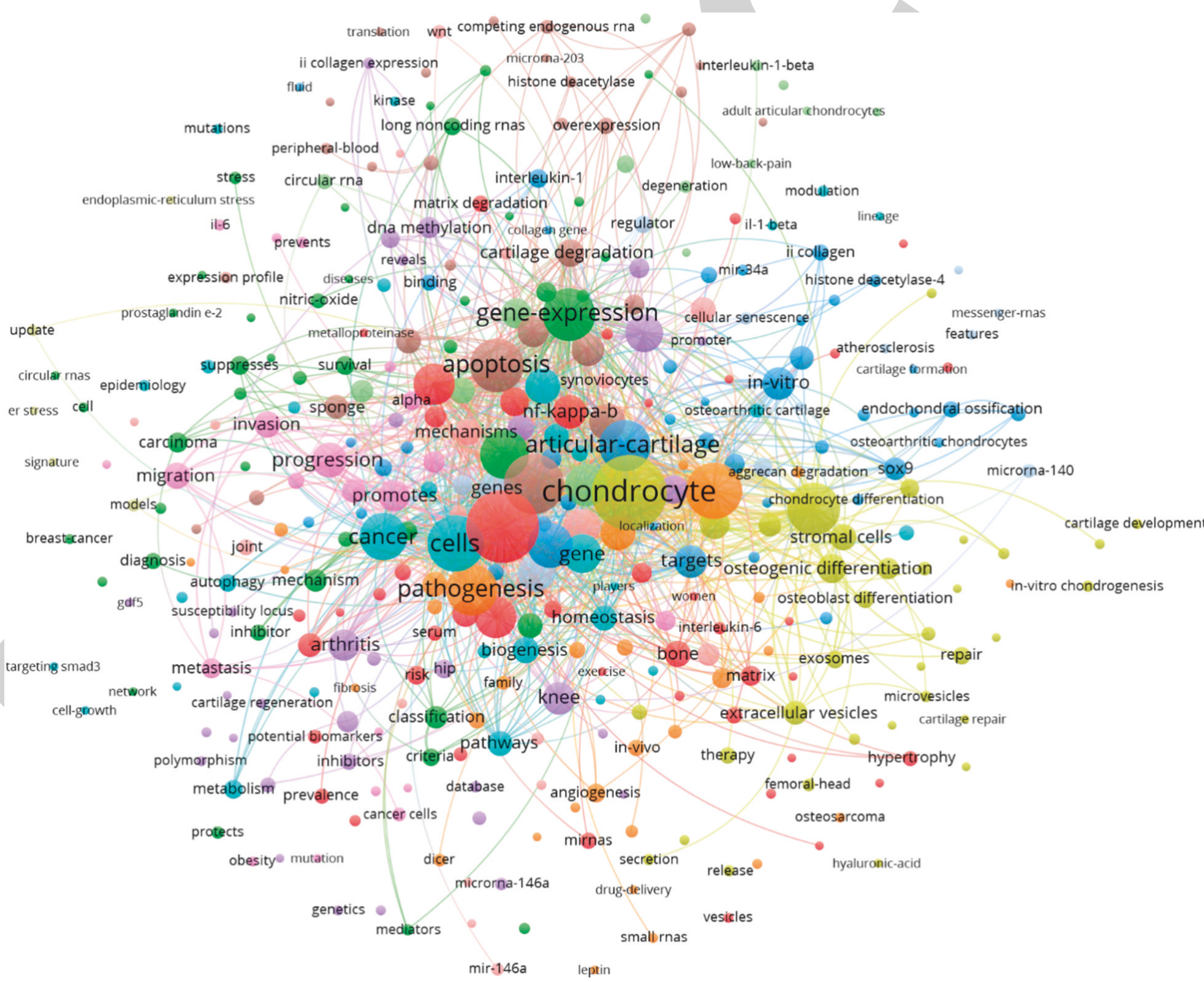

Figure 3: Co-occurring keywords and cluster analysis of reported literature.

network were IL-1β, IL-6, TNF-α, TGF-β, and MMP-13. The involved signaling pathways and genes included Wnt/β-catenin, NF-κ B, RUNX2, ADAMTS5, PTEN, SMad4, SIRT1, PI3k/AKT, p53, IRAK1, Bcl-2, C-MYC, and SOX9. The mechanisms involved in OA are apoptosis, proliferation, differentiation, chondrogenesis, degradation, osteogenic differentiation, autophagy, oxidative stress, DNA methylation, inflammation, long noncoding RNA CPG site, and histone deacetylase 4. The cells related to the field of study were cartilage/chondrocyte, mesenchymal stem cells, synovial fibroblast, extracellular matrix, and stromal cell. Furthermore, we found that the chondrocyte was the core of this co-occurrence network (Figure 3), mainly including proliferation, apoptosis, and chondrogenesis, indicating that the function of these miRNAs may be related to chondrocytes and involved the mechanism of cell proliferation and apoptosis.

According to the frequency of occurrence, we combined the repeated miRNAs in the keyword co-occurrence network and found that the number of miRNAs in the network exceeded 100. After merging miRNAs of the same category (merging miR-XA with miR-Xb, miR-XA-3p, and miR-XA-5p), the top 10 miRNAs were miR-140, miR-146, miR-34, miR-181, miR-27, miR-9, miR-29, miR-21, miR-26, and miR-155 (Table 3), suggesting that these miRNAs may be the hotspot miRNAs in this field.

3.5. Keywords with Citation Bursts. Burst detection is used to detect keywords that change rapidly in a certain period. Figure 4 shows the burst keywords in this research area. The blue line indicates the time interval, while the red line indicates the time of the keyword outbreak from start to completion. Keywords with citation bursts first appeared in 2008 (gene), along with the strongest keyword (human articular chondrocyte). The most recent keyword with bursts of citations appeared in 2019 (proliferation, NF-κB, and regeneration). And 4 keywords with citation bursts continue to 2021 (sponge, proliferation, NF-κB, and regeneration). These mutation words reflect the change of research trend in this field in a certain time interval.

4. Discussion

4.1. Global Description of the Trends of miRNAs in OA Research. According to Figure 1(a), the annual publications of miRNAs in OA research increased rapidly from 2008 to 2020 and after peaked in 2020 to 209, and the publication number is likely to continue increasing in the future based on current trends. This suggested that miRNA has attracted considerable attention in OA research.

The analysis of countries and institutions revealed that Chinese researchers constitute the majority of publications in this area (58.97%, Table 1). This finding could be explained by China's increasing prevalence of OA, which has resulted in a significant increase in demand for health care, which has been complicated by rising healthcare expenses and an aging population (Huibin Long et al.). With the expansion of China's expenditure on OA research, Chinese researchers have shown significant research productivity. However, there was no publication from China in the top 10 highest co-cited publications (Table 2), indicating more work should be done for Chinese researchers. This may be due to being the late mover of this field and the lack of high-quality exploratory research. Meanwhile, Japan occupies the majority of the top 10 most cited publications with a rather small total number of publications [12, 17, 19, 20, 24], indicating that Japanese researchers may play a critical role in the area as well. What's more, the cooperation networks revealed that domestic institutions cooperated frequently, while international cooperation was lacking and needs to be strengthened. Unfortunately, we are not optimistic about future international cooperation under the impact of the global epidemic.

By burst detection in emerging keywords in mRNA research of OA (Figure 4), we found the burst keywords from the beginning of "Genes," "Rheumatoid Arthritis," "Tissue." "Cartilage," "Differentiation," and "Human Chondrocytes," to "Messenger RNA," "DNA methylation," "in vitro," "Gene Expression," "Transcription Factor," "Matrix metalloproteinase 13," "Regulation," and "NF-κB." This reflects that the research on miRNAs in OA has gradually begun to focus on the role of tissue cells and molecular mechanisms, and the experimental research methods have shifted from in vivo animal experiments to cell experiments, and from the role of correlation research to molecular mechanism exploration, and the research level has gradually deepened.

4.2. The Hotspot miRNAs in OA Research. After merging miRNAs of the same category in the keyword co-occurrence network, we found that the hotspot miRNAs in OA included miR-140, miR-146, miR-21, miR-34, miR-155, miR-203, miR-26, miR-29, miR-125, and miR-141 as shown in Table 3. With different target genes and signaling pathways, they play various roles in early diagnosis, pathogenesis, and potential treatment (Table 3).

MiR-140 is closely related to cartilage homeostasis including chondrocyte proliferation, differentiation, apoptosis, autophagy, and inflammatory responses [26, 27, 29, 53]. In detail, miR-140 is indicated to influence chondrocyte degradation via chondrogenic factor transcription factor SRY-box-containing gene 9 (SOX9), ADAMTS, fucosyltransferase (FUT), and runt-related transcription factor (Runx2) regulators and pathways [26, 27, 29, 53]. Furthermore, miR-140 plays a critical role in E2-mediated cartilage homeostasis, as it allows E2 to suppress the production of MMP-13, thereby protecting chondrocytes from degradation [30]. Therefore, miR-140 could be a target for OA therapeutic interventions.

MiR-146a, as the main member of the miR-146 family, is found promoting chondrocyte autophagy through Bcl-2, which is induced by hypoxia [31]. It also promotes chondrocyte apoptosis by increasing the level of vascular endothelial growth factor (VEGF) in cartilage via Smad4 [33] and participates in inflammation [54]. Additionally, miR-146a is inferred regulating MMP-13 through IRAK1, TLR4, and TRAF6 to maintain the delicate balance of ECM homeostasis [34].

MiR-34 promotes chondrocyte death and OA progression via DLL1 and PI3K/AKT pathway modulation [36]. Similarly, earlier research has demonstrated that silencing miR-34a with LNA-modified antisense can significantly inhibit rat chondrocyte apoptosis produced by IL-1β [36].

Table 3: Different pathways and their function.

miRNAs	Frequency (Strength)		Pathways (Genes)	Functions
miR-140	**12** (99)	miR-140 [23–26]	SOX9/ADAMTS5/FUT/RUNX2	↑chondrocyteproliferation/differentiation
		miR-140 [27]	E2/MMP-13	↓chondrocyte apoptosis/autophagy
		miR-140 [28]	ADAMTS5/TIMP1/SP1/MMP13	↓chondrocyte degradation ↓matrix degradation
miR-146	**4** (30)	miR-146a [29]	Bcl-2	↑chondrocyte autophagy
		miR-146a [30]	VEGF /SMAD4/TGF-b	↑chondrocyte apoptosis
		miR-146a [31]	TLR4/TRAF6/IRAK1/MMP-13	↓ECM homeostasis
		miR-146a [32]	IRAK1/TRAF6	↑Inflammation
miR-34	**6 (42)**	miR-34 [65]	DLL1/PI3K/AKT	↑chondrocyte apoptosis
		miR-34a [33]	IL-1β	↑chondrocyte apoptosis
		miR-34a-5p [34]	SYVN1	↑chondrocyte proliferation/apoptosis/autophagy
miR-181	**5 (42)**	mir-181 [35]	PTEN/Caspase-3/PARP/MMP-2/MMP-9	↓cell proliferation ↑chondrocyte apoptosis
		mir-181 [36]	NF-κB/TNF-α/IL-6	↑inflammatory
miR-27	**4 (32)**	miR-27 [37]	NF-κB/IL-6/IL-8	↓inflammatory
		miR-27-3p/miR-27b [38, 39]	MMP13	↓ECM degradation ↓chondrocyteapoptosis
miR-9	**4 (33)**	miR-9-5p [40]	SDC1	↓Inflammatory ↓oxidative stress injury
		miR-9-3p [41]	ADAMTS5/IL-1β	↓apoptosis ↓ECM degradation
		miR-9 [42]	MALAT1/NF-κB	↑chondrocyte's growth
miR-29	**3 (25)**	miR-29 [43]	SMAD/NF-κB/WNT/TGF-β1/IL-1	↑chondrocyte apoptosis
		miR-29b-3p [44]	PGRN	↑chondrocyte apoptosis
		miR-29a [45]	BAX	↑chondrocyte apoptosis
miR-21	**3 (27)**	miR-21 [46]	GAS5/MMPs	↑chondrocyte apoptosis ↓chondrocyte autophagy
		miR-21-5p [47]	IL-1β	↑chondrocyte degradation
		mir-21 [48, 49]	Spry1/ GDF-5/SOX5/NF-κB	↑chondrocyte degradation ↑angiogenesis
miR-26	**2 (18)**	miR-26a/26b [50, 51]	FUT4/NF-κB	↓inflammatory ↓cartilage injury
miR-155	**2 (18)**	miR-155 [51]	NF-κB/JNK AP-1/MMP-13	↑chondrocyte degradation
		miR-155-5p [52]	IL-6/TNF-α	↑chondrocyte degradation and hypertrophy

Additionally, miR-34a-5p has been shown to affect chondrocyte proliferation, autophagy, and apoptosis by targeting SYVN1 [37], providing a novel insight into the OA pathogenesis.

MiR-181 could be a potential biomarker to screen OA patients [51]; it also upregulates caspase-3, PARP, MMP-2, and MMP-9 expression, inhibiting cell proliferation and promoting apoptosis in OA chondrocytes via PTEN targeting [38]. Furthermore, the study found that decreasing miR-181 expression can lower the inflammatory factors TNF-α and IL-6 expression by downregulating the NF-κB signaling pathway, thereby suppressing the occurrence of OA [39].

MiR-27 upregulation inhibits OA pathogenesis through targeting leptin and inhibiting the NF-κB signaling pathway [40]. It exerts protective effects against OA. MiR-27 is also thought to be a target of lncRNA-CIR and MMP-13, both of which are involved in chondrocyte extracellular matrix (ECM) degradation in OA [27, 41].

MiR-9 is a potential therapeutic target for OA. Exosomal miR-9-5p, which is secreted by bone marrow-derived mesenchymal stem cells, has been shown to alleviate OA by inhibiting syndecan-1 [42]. And inhibition of LncRNA MIR22HG ameliorated IL-1β-induced apoptosis and ECM degradation of human chondrocytes through miR-9-3p/ADAMTS5 pathway (Hui Long et al.). Furthermore, resveratrol is also reported to have a therapeutic effect in OA by regulating the MALAT1/miR-9/NF-κB signaling pathway [43].

The miR-29 family negatively regulated SMAD, NF-κB, and canonical WNT signaling pathways, and they are also regulated by TGF-β1 and IL-1 in chondrocytes [44]. WNT-related genes, such as FZD3, FZD5, DVL3, FRAT2, and CK2A2, are validated as direct targets of the miR-29 family. Moreover, miR-29b-3p promotes chondrocyte apoptosis and facilitates the occurrence and development of OA by targeting PGRN [45]. And Bax targeted by miR-29a regulates chondrocyte apoptosis as well [46].

MiR-21 is identified as a regulator of growth arrest-specific 5 (GAS5) during OA pathogenesis, by increasing the expression levels of MMPs, thus stimulating apoptosis and suppressing autophagic responses [47]. Likewise, miR-21-5p promotes hyaline cartilage production, protecting IL-1β-induced chondrocytes from degradation [48], and regulates ECM degradation and angiogenesis by targeting Spry1 [49]. Moreover, the recent study showed that the novel NF-κB inhibitor sc75741 mitigates chondrocyte degradation and prevents

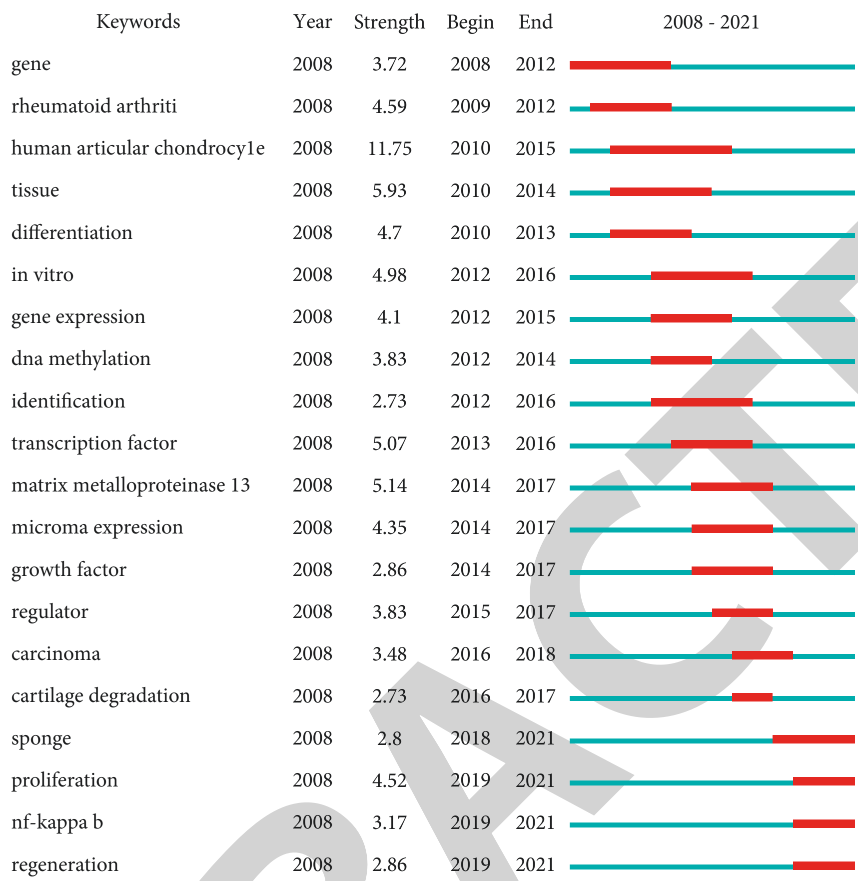

FIGURE 4: Keywords with citation bursts.

activated fibroblast transformation by modulating miR-21/gdf-5/sox5 signaling [55], which may be a potential treatment for OA.

MiR-26a and miR-26b mediate OA progression by targeting FUT4 via the NF-κB signaling pathway [52]. Furthermore, miR-26a reduces cartilage injury and synovial inflammation in OA of knee joints by inhibiting the activation of the NF-B signaling pathway [56].

It has been shown that miR-155 plays an important role in chondrocyte degradation via the upstream MAPK pathway. Furthermore, recent studies indicate that frugoside (FGS) inhibits macrophage M1 polarization by partially downregulating miR-155 levels, so decreasing IL-6 and TNF-α secretion, thereby delaying ECM and cartilage degradation and chondrocyte hypertrophy [50]. Besides, exosomes produced from synovial mesenchymal stem cells overexpressing miR-155-5p prevent OA by promoting proliferation and migration, inhibiting apoptosis, and regulating ECM secretion in chondrocytes. Therefore, miR-155 is most likely a potential OA therapeutic target [50].

4.3. Chondrocytes are Potential Targets for Most miRNAs in OA. According to the keywords co-occurrence network, chondrocytes are most closely linked to miRNAs in the research field of OA, as well as the core elements of the co-occurrence network. Chondrocytes are responsible for synthesizing ECM components and maintaining cartilage homeostasis. A strong relationship between miRNAs and chondrocytes has been reported in prior studies. The top 10 miRNAs we found were also closely related to chondrocytes. They mainly correlate with the apoptosis, degradation, autophagy, proliferation, and differentiation of chondrocytes. In detail, most of the miRNAs in the list are found to promote chondrocyte apoptosis and exacerbates the progression of OA, while miR-140 is essential for normal endochondral bone development, accelerating chondrocyte proliferation and differentiation [16, 57]. Furthermore, miR-140 and miR-34a are closely involved in the dynamic balance between proliferation and apoptosis of chondrocytes, thus maintaining the stability of cartilage quantity and function [18, 32]. Meanwhile, due to the protective and antiapoptotic functions of chondrocyte autophagy [28, 54], miRNAs like miR-146 [58] and miR-155 [59] regulate the expression of the autophagy-associated gene (ATG) in chondrocytes during this process to balance of material and energy metabolism of chondrocytes.

Moreover, the pathology of MMP transcription concerning proinflammatory cytokines as IL-1β, IL-6, TNF-α, TGF-β, and NF-κB was also involved in the co-occurrence network. Much of the literature we retrieved on miRNAs in OA showed that miR-140, miR-146a, miR-155, and miR-124 can mediate MMP-13 through TNF-α, IL-1β, and NF-κB, which may affect chondrocyte degradation. The keywords co-occurrence network includes involving signaling pathways and genes Wnt/β-catenin, NF-κB, RUNX2, ADAMTS5, PTEN, SMad4, SIRT1, PI3k/AKT, p53, IRAK1, Bcl-2, C-MYC, and SOX9.

5. Strengths and Limitations

Our study used bibliometric and visual analyses to assess the status and trends of miRNA research in OA. The following limitations, however, must be mentioned. The data were retrieved only from the databases of the Web of Science, and other databases like PubMed, MEDLINE, EMBASE, and Google Scholar were not included. Although we found that China was the leading country in the total number of publications, we did not have data from major Chinese databases like the China National Knowledge Infrastructure Database (CNKI), Wanfang Data Journal Database, Chinese Biomedical Literature Database, and Chongqing VIP database. And the limited terms were used in the publication retrieval strategy, so we may not have identified all the relevant studies in the field. Furthermore, differences between the real world and the current results may exist. For example, different literature types may cause bias to our study because reviews may have higher citations than original studies. Additionally, some recently published high-quality papers might not be highlighted due to low citation frequency for the short time in publication.

6. Conclusion

This study showed the current status and global trends of miRNAs in OA research. Furthermore, the study showed miR-140, miR-146, miR-34, miR-181, miR-27, miR-9, miR-29, miR-21, miR-26, and miR-155 were hotspot miRNAs in OA; besides, chondrocytes could be a potential target for OA treatment. More studies should be focused on the relationship between miRNAs and chondrocytes in the future [17, 60–64].

Data Availability

Data will be provided upon request to the authors.

Ethical Approval

This article does not contain any studies with human participants or animals performed by any of the authors.

Conflicts of Interest

The authors declare that they do not have any conflicts of interest.

Authors' Contributions

Wei-Shang Hu and Qi Zhang conceived and designed the study. Wei-Shang Hu and Si-Hui Li searched the publications from Web of Science and decided which paper to be included. Wei-Shang Hu drafted the manuscript. Qiao-Feng Wu was in charge of the fund program. Qiao-Feng Wu and Shuang-Chun Ai made the most contribution to the manuscript revision.

Acknowledgments

This work was supported by the National Key R&D Program of China (No. 2019YFC1709001); Innovation Team and Talents Cultivation Program of National Administration of Traditional Chinese Medicine. (No: ZYYCXTD-D-202003), and Fund of Science and Technology Department of Sichuan Province, China (Nos. 2021ZYD0081 and 2022ZDZX0033).

References

[1] C. Chen and M. Song, "Visualizing a field of research: a methodology of systematic scientometric reviews," *PLoS One*, vol. 14, no. 10, Article ID e0223994, 2019.

[2] D. J. Hunter and S. Bierma-Zeinstra, "Osteoarthritis," *The Lancet*, vol. 393, no. 10182, pp. 1745–1759, 2019.

[3] S. Safiri, A.-A. Kolahi, E. Smith et al., "Global, regional and national burden of osteoarthritis 1990-2017: a systematic analysis of the global burden of disease study 2017," *Annals of the Rheumatic Diseases*, vol. 79, no. 6, pp. annrheumdis–2019, 2020.

[4] T. Vos, A. D. Flaxman, M. Naghavi et al., "Years lived with disability (YLDs) for 1160 sequelae of 289 diseases and injuries 1990-2010: a systematic analysis for the Global Burden of Disease Study 2010," *Lancet (North American Edition)*, vol. 380, no. 9859, pp. 2163–2196, 2012.

[5] D. Prieto-Alhambra, A. Judge, M. K. Javaid, C. Cooper, A. Diez-Perez, and N. K. Arden, "Incidence and risk factors for clinically diagnosed knee, hip and hand osteoarthritis: influences of age, gender and osteoarthritis affecting other joints," *Annals of the Rheumatic Diseases*, vol. 73, no. 9, pp. 1659–1664, 2014.

[6] R. F. Loeser, U. Gandhi, D. L. Long, W. Yin, and S. Chubinskaya, "Aging and oxidative stress reduce the response of human articular chondrocytes to insulin-like growth factor 1 and osteogenic protein 1," *Arthritis & Rheumatology*, vol. 66, no. 8, pp. 2201–2209, 2014.

[7] F. C. Grandi and N. Bhutani, "Epigenetic therapies for osteoarthritis," *Trends in Pharmacological Sciences*, vol. 41, no. 8, pp. 557–569, 2020.

[8] M. A. Karsdal, M. Michaelis, C. Ladel et al., "Disease-modifying treatments for osteoarthritis (DMOADs) of the knee and hip: lessons learned from failures and opportunities for the future," *Osteoarthritis and Cartilage*, vol. 24, no. 12, pp. 2013–2021, 2016.

[9] B. Abramoff and F. E. Caldera, "Osteoarthritis," *Medical Clinics of North America*, vol. 104, no. 2, pp. 293–311, 2020.

[10] D. P. Bartel, "MicroRNAs," *Cell*, vol. 116, no. 2, pp. 281–297, 2004.

[11] D. P. Bartel, "MicroRNAs: target recognition and regulatory functions," *Cell*, vol. 136, no. 2, pp. 215–233, 2009.

[12] S. Miyaki and H. Asahara, "Macro view of microRNA function in osteoarthritis," *Nature Reviews Rheumatology*, vol. 8, no. 9, pp. 543–552, 2012.

[13] G. R. Sondag and T. M. Haqqi, "The Role of microRNAs and their targets in osteoarthritis," *Current Rheumatology Reports*, vol. 18, no. 8, p. 56, 2016.

[14] M. Zhang, K. Lygrissea, and J. Wanga, "Role of MicroRNA in osteoarthritis," *Journal of Arthritis*, vol. 06, no. 02, 2017.

[15] L. Cong, Y. Zhu, and G. Tu, "A bioinformatic analysis of microRNAs role in osteoarthritis," *Osteoarthritis and Cartilage*, vol. 25, no. 8, pp. 1362–1371, 2017.

[16] M. Nugent, "MicroRNAs: exploring new horizons in osteoarthritis," *Osteoarthritis and Cartilage*, vol. 24, no. 4, pp. 573–580, 2016.

[17] S. Miyaki, T. Sato, A. Inoue et al., "MicroRNA-140 plays dual roles in both cartilage development and homeostasis," *Genes & Development*, vol. 24, no. 11, pp. 1173–1185, 2010.

[18] S. W. Jones, G. Watkins, N. Le Good et al., "The identification of differentially expressed microRNA in osteoarthritic tissue that modulate the production of TNF-α and MMP13," *Osteoarthritis and Cartilage*, vol. 17, no. 4, pp. 464–472, 2009.

[19] N. Akhtar, Z. Rasheed, S. Ramamurthy, A. N. Anbazhagan, F. R. Voss, and T. M. Haqqi, "MicroRNA-27b regulates the expression of matrix metalloproteinase 13 in human osteoarthritis chondrocytes," *Arthritis & Rheumatism*, vol. 62, no. 5, pp. 1361–1371, 2010.

[20] S. Miyaki, T. Nakasa, S. Otsuki et al., "MicroRNA-140 is expressed in differentiated human articular chondrocytes and modulates interleukin-1 responses," *Arthritis & Rheumatism*, vol. 60, no. 9, pp. 2723–2730, 2009.

[21] D. Iliopoulos, K. N. Malizos, P. Oikonomou, and A. Tsezou, "Integrative microRNA and proteomic approaches identify novel osteoarthritis genes and their collaborative metabolic and inflammatory networks," *PLoS One*, vol. 3, no. 11, Article ID e3740, 2008.

[22] S. Díaz-Prado, C. Cicione, E. Muiños-López et al., "Characterization of microRNA expression profiles in normal and osteoarthritic human chondrocytes," *BMC Musculoskeletal Disorders*, vol. 13, no. 1, p. 144, 2012.

[23] T. E. Swingler, G. Wheeler, V. Carmont et al., "The expression and function of microRNAs in chondrogenesis and osteoarthritis," *Arthritis & Rheumatism*, vol. 64, no. 6, pp. 1909–1919, 2012.

[24] K. Yamasaki, T. Nakasa, S. Miyaki et al., "Expression of MicroRNA-146a in osteoarthritis cartilage," *Arthritis & Rheumatism*, vol. 60, no. 4, pp. 1035–1041, 2009.

[25] R. F. Loeser, S. R. Goldring, C. R. Scanzello, and M. B. Goldring, "Osteoarthritis: a disease of the joint as an organ," *Arthritis & Rheumatism*, vol. 64, no. 6, pp. 1697–1707, 2012.

[26] T. A. Karlsen, R. B. Jakobsen, T. S. Mikkelsen, and J. E. Brinchmann, "microRNA-140 targets RALA and regulates chondrogenic differentiation of human mesenchymal stem cells by translational enhancement of SOX9 and ACAN," *Stem Cells and Development*, vol. 23, no. 3, pp. 290–304, 2014.

[27] C. Li, Z. Chen, J. Yang, and D. O. Orthopedics, "Expression and function of miR-140 in different stage chondrocytes of patients with osteoarthritis," *Journal of Practical Orthopaedics*, vol. 23, no. 11, pp. 995–999, 2017.

[28] V. Vijayan and P. Verstreken, "Autophagy in the presynaptic compartment in health and disease," *Journal of Cell Biology*, vol. 216, no. 7, pp. 1895–1906, 2017.

[29] X. H. Zhou, M. Wang, J. I. Yan-Hui et al., "Expression of miRNA-140 in chondrocytes of patients with early osteoarthritis and its function," *Academic Journal of Second Military Medical University*, 2014.

[30] X. Li, L. Duan, Y. Liang et al., "Human umbilical cord blood-derived mesenchymal stem cells contribute to chondrogenesis in coculture with chondrocytes," *BioMed Research International*, vol. 2016, no. 1, pp. 1–9, Article ID 3827057, 2016.

[31] F. Zhang, J. Wang, J. Chu et al., "MicroRNA-146a induced by hypoxia promotes chondrocyte autophagy through Bcl-2," *Cellular Physiology and Biochemistry*, vol. 37, no. 4, pp. 1442–1453, 2015.

[32] Z.-j. Liang, H. Zhuang, G.-x. Wang et al., "MiRNA-140 is a negative feedback regulator of MMP-13 in IL-1β-stimulated human articular chondrocyte C28/I2 cells," *Inflammation Research*, vol. 61, no. 5, pp. 503–509, 2012.

[33] L. Jin, J. Zhao, W. Jing et al., "Role of miR-146a in human chondrocyte apoptosis in response to mechanical pressure injury in vitro," *International Journal of Molecular Medicine*, vol. 34, no. 2, pp. 451–463, 2014.

[34] K. D. Taganov, M. P. Boldin, K.-J. Chang, and D. Baltimore, "NF-κB-dependent induction of microRNA miR-146, an inhibitor targeted to signaling proteins of innate immune responses," *Proceedings of the National Academy of Sciences*, vol. 103, no. 33, pp. 12481–12486, 2006.

[35] W. Zhang, P. Hsu, B. Zhong et al., "MiR-34a enhances chondrocyte apoptosis, senescence and facilitates development of osteoarthritis by targeting DLL1 and regulating PI3K/AKT pathway," *Cellular Physiology and Biochemistry*, vol. 48, no. 3, pp. 1304–1316, 2018.

[36] M. M. Abouheif, T. Nakasa, H. Shibuya, T. Niimoto, W. Kongcharoensombat, and M. Ochi, "Silencing microRNA-34a inhibits chondrocyte apoptosis in a rat osteoarthritis model in vitro," *Rheumatology*, vol. 49, no. 11, pp. 2054–2060, 2010.

[37] F. Tian, J. Wang, Z. Zhang, and J. Yang, "LncRNA SNHG7/miR-34a-5p/SYVN1 axis plays a vital role in proliferation, apoptosis and autophagy in osteoarthritis," *Biological Research*, vol. 53, no. 1, pp. 9–11, 2020.

[38] X.-F. Wu, Z.-H. Zhou, and J. Zou, "MicroRNA-181 inhibits proliferation and promotes apoptosis of chondrocytes in osteoarthritis by targeting PTEN," *Biochemistry and Cell Biology*, vol. 95, no. 3, pp. 437–444, 2017.

[39] L. Zhu and M. Yang, "The suppression of miR-181 inhibits inflammatory responses of osteoarthritis through NF-kappaB signaling pathway," *European Review for Medical and Pharmacological Sciences*, vol. 23, no. 13, pp. 5567–5574, 2019.

[40] B. Zhou, H. Li, and J. Shi, "miR-27 inhibits the NF-κB signaling pathway by targeting leptin in osteoarthritic chondrocytes," *International Journal of Molecular Medicine*, vol. 40, no. 2, pp. 523–530, 2017.

[41] S. Chen, Z. Luo, and X. Chen, "Andrographolide mitigates cartilage damage via miR-27-3p-modulated matrix metalloproteinase13 repression," *The Journal of Gene Medicine*, vol. 22, no. 8, Article ID e3187, 2020.

[42] Z. Jin, J. Ren, and S. Qi, "Exosomal miR-9-5p secreted by bone marrow-derived mesenchymal stem cells alleviates osteoarthritis by inhibiting syndecan-1," *Cell and Tissue Research*, vol. 381, no. 1, pp. 99–114, 2020.

[43] G. Zhang, H. Zhang, W. You, X. Tang, X. Li, and Z. Gong, "Therapeutic effect of Resveratrol in the treatment of osteoarthritis via the MALAT1/miR-9/NF-κB signaling pathway," *Experimental and Therapeutic Medicine*, vol. 19, no. 3, pp. 2343–2352, 2020.

[44] L. T. T. Le, T. E. Swingler, N. Crowe et al., "The microRNA-29 family in cartilage homeostasis and osteoarthritis," *Journal of Molecular Medicine (Berlin)*, vol. 94, no. 5, pp. 583–596, 2016.

[45] L. Chen, Q. Li, J. Wang et al., "MiR-29b-3p promotes chondrocyte apoptosis and facilitates the occurrence and development of osteoarthritis by targeting PGRN," *Journal of Cellular and Molecular Medicine*, vol. 21, no. 12, pp. 3347–3359, 2017.

Hindawi
Journal of Healthcare Engineering
Volume 2023, Article ID 9850297, 1 page
https://doi.org/10.1155/2023/9850297

Retraction

Retracted: Data on the Impact of Epidemic on Nursing Staff's Mental Health in the Context of Wireless Network

Journal of Healthcare Engineering

Received 10 October 2023; Accepted 10 October 2023; Published 11 October 2023

This article has been retracted by Hindawi following an investigation undertaken by the publisher [1]. This investigation has uncovered evidence of one or more of the following indicators of systematic manipulation of the publication process:

(1) Discrepancies in scope
(2) Discrepancies in the description of the research reported
(3) Discrepancies between the availability of data and the research described
(4) Inappropriate citations
(5) Incoherent, meaningless and/or irrelevant content included in the article
(6) Peer-review manipulation

The presence of these indicators undermines our confidence in the integrity of the article's content and we cannot, therefore, vouch for its reliability. Please note that this notice is intended solely to alert readers that the content of this article is unreliable. We have not investigated whether authors were aware of or involved in the systematic manipulation of the publication process.

Wiley and Hindawi regrets that the usual quality checks did not identify these issues before publication and have since put additional measures in place to safeguard research integrity.

We wish to credit our own Research Integrity and Research Publishing teams and anonymous and named external researchers and research integrity experts for contributing to this investigation.

The corresponding author, as the representative of all authors, has been given the opportunity to register their agreement or disagreement to this retraction. We have kept a record of any response received.

References

[1] D. Guo, Y. Guo, and Y. Xing, "Data on the Impact of Epidemic on Nursing Staff's Mental Health in the Context of Wireless Network," *Journal of Healthcare Engineering*, vol. 2022, Article ID 3413815, 11 pages, 2022.

Hindawi
Journal of Healthcare Engineering
Volume 2022, Article ID 3413815, 11 pages
https://doi.org/10.1155/2022/3413815

Research Article

Data on the Impact of Epidemic on Nursing Staff's Mental Health in the Context of Wireless Network

Dan Guo,[1] Yi Guo,[2] and YanJi Xing[3]

[1]*Department of Operating Room, Central South University Xiangya School of Medicine Affiliated Haikou Hospital, Haikou 570208, Hainan, China*
[2]*Department of Haikou Administrative Center Outpatient, Central South University Xiangya School of Medicine Affiliated Haikou Hospital, Haikou 570208, Hainan, China*
[3]*Department of Health Medicine, Central South University Xiangya School of Medicine Affiliated Haikou Hospital, Haikou 570208, Hainan, China*

Correspondence should be addressed to YanJi Xing; 13211010333@stu.cpu.edu.cn

Received 21 January 2022; Revised 29 January 2022; Accepted 5 February 2022; Published 7 April 2022

Academic Editor: Liaqat Ali

The research was aimed to analyze the impact of epidemic pneumonia on nursing personnel's mental health under wireless network background and to improve the selection of random forest classification (RFC) algorithm parameters by the whale optimization algorithm (WOA). Besides, a total of 148 in-service nursing personnel were selected as the research objects, and 148 questionnaires were recycled effectively. The collected data were analyzed by the improved RFC algorithm. In addition, the research investigated the impacts of demographic factors on nursing personnel's mental health by the one-way variance method. The results demonstrated that the accuracy of the improved algorithm in training samples and test samples reached 83.3% and 81.6%, respectively, both of which were obviously higher than those of support vector machine (SVM) (80.1% and 79.3%, respectively) and back-propagation neural network (BPNN) (78.23% and 77.9%, respectively), and the differences showed statistical meanings ($P < 0.05$). The *Patient Health Questionnaire-9* (PHQ-9) showed that the depression levels of 9.46% of the included personnel were above moderate. The *Generalized Anxiety Disorder* (GAD-7) demonstrated that the anxiety levels of 3.38% of the included personnel were above moderate. The insomnia severity index (ISI) indicated that the insomnia levels of 3.38% of the included personnel were above moderate. The average score of male personnel (3.65) was obviously lower than that of female personnel (3.71). Besides, the average scale score of married personnel (3.78) was significantly higher than that of unmarried personnel (3.65). The average scale scores of personnel with bachelor's (3.66) and master's degrees (3.62) were obviously lower than those of personnel with junior college (3.77) and technical secondary school (3.75) diplomas. The average scale score of personnel with over 5-year work experience (3.68) was significantly lower than that of personnel working for less than five years (3.72). The average scale score of personnel with experience in responding to public emergencies (3.65) was obviously lower than that of personnel without related experience (3.74). The differences all showed statistical meaning ($P < 0.05$). The results of this research revealed that the accuracy of the improved RFC algorithm was remarkably higher than that of the SVM and BPNN algorithms. Furthermore, many nursing personnel suffered from mental diseases at different levels with the impact of the epidemic. Gender, marital status, education level, and experience in responding to public emergencies were the main factors affecting nursing personnel's mental health.

1. Introduction

Health emergencies refer to sudden serious infectious diseases that cause (may cause) damage to the health of the vast majority of people, as well as mass diseases of unknown cause [1]. The outbreak of pneumonia in December 2019 was a type of health emergency, and this outbreak was lethal. Due to the suddenness of the disease, the relevant departments did not formulate effective solutions, resulting in a surge in the number of infections at home and abroad in a short period of time [2, 3]. According to relevant investigations and studies, the incubation period is generally 3 to 7 days, and some can even incubate for 14 days. The clinical presentation of this epidemic is similar to that of the common cold, with some atypical symptoms, including dry cough and fever [4–7]. Advances in wireless networking technology have allowed researchers to rapidly collect data on global infections [8, 9]. According to big data statistics, as of May 2021, there had been more than 140 million confirmed cases worldwide, with a case fatality rate of about 2.1%, causing serious harm to the country and its people [10, 11]. Mental health refers to the promotion and maintenance of people's psychological states through positive and beneficial measures to adapt to changes in the natural and social environment [12]. However, people's mental health has been greatly harmed by the epidemic. As front-line personnel in the fight against the pneumonia epidemic, medical staff shoulder the great responsibility of curing diseases and promoting health. They were hurt the most. Therefore, research on the psychological and stress responses of medical staff has become a hotspot [13, 14].

Traditional mental health survey methods are passive and inaccurate. Patients' mental health states can be determined only by the active consultation with psychologists and the implementation of professional detection [15]. Psychologists diagnose and treat patients' diseases mainly by communicating with patients and giving out questionnaires, which is greatly affected by the subjective factors of doctors, and the diagnosis and treatment based on this method are inaccurate [16]. With the development of medical treatment, science, and technology, the active description is not the only method of diagnosing patients' mental states. Some scholars detect brain waves, heart rate, and electrical signals by apparatuses designed by wireless networks and artificial intelligence (AI) technology to reflect the current mental state of patients. As result, there are the intersection and combination between AI technology and psychology [17]. With the background of big data, AI promotes the rapid development of Internet technology as well as generates massive data. The extraction of useful information from these massive data is a major difficulty in the current development of Internet technology [18]. The decision tree (DT) algorithm is a kind of typical single classifier among many classification algorithms, which is applied in a great many fields [19]. However, the issues needed to be tackled by classifiers have become gradually complex with the development of human society. Hence, DT algorithm-based classifiers are significantly limited [20]. Random forest classification (RFC) is a kind of common combined classification method, which adopts DT as basic classifiers, and it is usually applied in mental diagnostic classification [21]. RFC is pervasive, and the excellent anti-noise capacity as well as the tolerance of abnormal values are advanced in data mining. Nevertheless, the classification results are affected by the artificial setting of the RFC algorithm parameters. Therefore, the methods of reducing the generalization errors of the RFC algorithm need to be improved [22, 23]. The whale optimization algorithm (WOA) is a new nature-inspired metaheuristic optimization algorithm that simulates the social behaviors of humpback whales and introduces a bubble net hunting strategy. The algorithm has a simple structure, few parameters, strong search capability, and is easy to implement. However, the research and application of WOA is still in its initial stage, and the algorithm itself still has the disadvantages of low solution accuracy, slow convergence speed, and is easy to fall into local optimum. The BP neural network is the most basic neural network, whose output is propagated forward and the error is propagated backward, and the BPNN is widely used in classification and regression problems due to its strong nonlinear mapping ability and high self-learning and adaptive capabilities. BP neural networks can automatically extract the "reasonable rules" between the output and the output data and adaptively memorize the learning content in the network weights. BP neural networks have a high degree of self-learning and self-adaptive ability, and it is difficult to solve the contradiction between the size of the application problem and the size of the network, which involves the relationship between the possibility of network capacity and feasibility, i.e., the problem of learning complexity.

To sum up, the research was based on the random forest (RF) algorithm, which was improved and applied in data analysis to investigate the impact of the epidemic on nursing personnel's mental health under the background of wireless network. In addition, nursing personnel's mental health states were studied and analyzed by survey to offer an effective decision analysis to nursing personnel's mental health and clinical work.

2. Materials and Methods

2.1. Research Objects. A total of 148 in-service nurses working at Central South University Xiangya School of Medicine Affiliated Haikou Hospital from May 2020 to August 2020 were selected as the research objects in the research, which included 42 male cases and 106 female cases aged between 19 and 54. Their average age was 34.23. Besides, the general data on the included nurses were collected. The research objects were included in the research based on the following standards: the included cases must be the front-line nurses with more than 1-year work experience, and they should be equal to or over 18 years old. The nurses were excluded by the research based on the following standards: those on further training or internship were excluded from the research, and those with previous neurasthenia and mental trauma were also excluded from the research. The implementation of this research has been approved by the Central South University Xiangya School of Medicine Affiliated Haikou Hospital Medical Ethics Committee, and all research objects have been informed about the research and volunteered to engage in the research.

2.2. Survey Tools. Questionnaires mainly consisted of the following several types of data (Table 1). Including the first one was the general data of the research objects, *Patient Health Questionnaire-9* (PHQ-9), *Generalized Anxiety Disorder* (GAD-7), and Insomnia Severity Index (ISI).

Table 1: Specific items of questionnaire.

Questionnaire item type	Explanations
General data statistics	The collected general data on the research objects included gender, age, marital status, education level, working years, and experience in responding to public emergencies.
PHQ-9	The survey scale consisted of 9 items, including pleasure loss, depression, sleep disorder, energy lack, eating disorder, low self-evaluation, difficulty in concentration, dysphoria, and negative ideas. Each item was scored between 0 and 3. 0 referred to no occurrence, 1 represented an occasional occurrence, 2 meant that more than half of the above symptoms occurred, and 3 indicated an everyday occurrence. The total score between 0 and 4 stood for no depression, that between 5 and 9 referred to mild depression, that between 10 and 14 was moderate depression, and that over 15 denoted severe depression.
GAD-7	The survey scale consisted of 7 items, including dysphoria, control concern, concern about this kind of thing, tension without relaxation, fidget, irritability, and the fear that something bad would happen. Each item was scored between 0 and 3.0 referred to no occurrence, 1 represented an occasional occurrence, 2 meant that more than half of the above symptoms occurred, and 3 indicated an everyday occurrence. The total score between 0 and 4 represented no depression, that between 5 and 9 meant mild depression, that between 10 and 14 referred to moderate depression, and that over 15 denoted severe depression.
ISI	The survey scale consisted of 7 items, including difficulty in falling asleep, difficulty in maintaining sleep, early weakening, dissatisfaction with sleep, impacts on daily activities, impacts on living quality, and worry/pain. The full score for each item was 4. 0 referred to no insomnia, 1 represented mild insomnia, 2 denoted moderate insomnia, 3 stood for severe insomnia, and 4 meant extremely severe insomnia. The total score between 0 and 7 represented no insomnia, that between 8 and 14 referred to mild insomnia, that between 15 and 21 denoted moderate insomnia, and that between 22 and 28 indicated severe insomnia.

2.3. Survey Methods. The online questionnaire method was adopted in the research. All questionnaires were shared in the form of quick response (QR) code onto the electronic communication devices of 148 nursing personnel through WeChat. All the survey items designed in the research were compulsory. To avoid repeat answers, each case was allowed to answer each item once only, and relevant staff were arranged to answer questions raised by confused nursing personnel. In the research, a total of 148 questionnaires were handed out, and 148 valid questionnaires were recycled with the recycling efficiency reaching 100%.

2.4. AI Algorithm and Its Improvement. The RF algorithm was introduced as follows: DT consisted of nodes and directed edges. Nodes contained root nodes, internal nodes, and leaf nodes (root nodes were the assembly of the whole training data, internal nodes referred to a certain feature or property, and leaf nodes represented a certain category). Each node could be split into DT, and leaf nodes could be viewed as the data sets containing classification labels. As a result, DT could be regarded as the exploration of the path to the classification. However, DT could not process continuous variables effectively, and the classification rules were complex. In addition, overfitting occurred if there were few training data. The RFC algorithm was a classification algorithm based on the combination of multiple DT, and it was a kind of typical classifier among ensemble learning algorithms. Ensemble learning refers to the assembly of excellent performances to solve complex tasks by adopting different combined algorithms. The structure of classifiers consisted of n corresponding functions generated by n classifiers, and these functions were combined with others according to certain rules to generate a combined classifier. The RFC algorithm was the combined form of multiple classifications (Figure 1).

It was assumed that α referred to random parameter vectors, α_1 was the corresponding vector of α in the DT T, m represented test samples, and lead nodes were expressed as $e(m,\alpha)$, and then the RFC algorithm was further discussed in this study.

Bootstrap resampling was adopted to generate x training sets, which were marked with $\alpha_1, \alpha_2, \alpha_3, \ldots, \alpha_x$, respectively. In each training set, the corresponding DT was generated and marked as $\{T(m,\alpha_1)\}, \{T(m,\alpha_2)\}, \{T(m,\alpha_3), \ldots, \{T(m,\alpha_x)\}$, respectively. If features had P dimensions, p features were selected randomly from P dimensions as the classification feature set of the node. The nodes were classified by the classification method with the best effect among p features to make each DT grow to the maximum size. F was set to be test samples, and the trained DT were adopted in tests to generate the corresponding categories, including $\{T(f,\alpha_1)\}, \{T(f,\alpha_2)\}, \{T(f,\alpha_3)\} \ldots \{T(f,\alpha_x)\}$. The voting method was utilized to set the category with the most output in x DT as the category of the test set sample F.

The improvement of the RFC algorithm was as follows: the results predicted by RFC were susceptible to the number of DT in forests, feature subsets, and leaf nodes, which reduced the classification accuracy. To reduce the forecast errors by the RFC algorithm, a whale optimization algorithm (WOA) [24] was introduced in the research to improve the RFC algorithm. The classification accuracy A was selected as fitness function, which was expressed by (1) as follows:

$$A = \frac{R}{T} \times 100\%\#. \tag{1}$$

In (1), R refers to the number of samples correctly classified, and T denotes the total number of samples. The process of the optimized RFC algorithm was explained as follows: the evaluation indexes of nursing personnel's mental health were set as the initial data, and then the

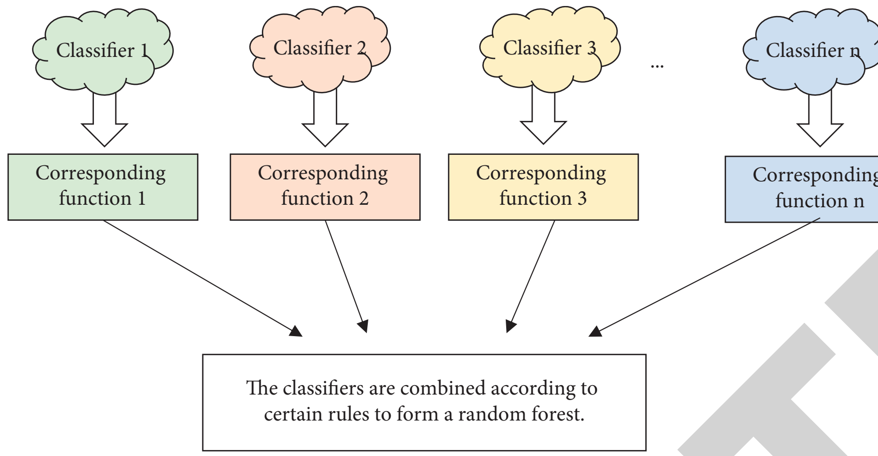

Figure 1: Classifier composition diagram.

training set (M) and the test set (F) of the RFC algorithm were obtained. After that, data were normalized as shown in (2) as follows:

$$m^1 = q + \left(\frac{m - m_{min}}{m_{max} - m_{min}}\right) \times (w - q). \tag{2}$$

In equation (2), m^1 represents the training set data after normalization, m refers to the initial data, $m_{\min}$ denotes the minimum value of the initial data, $m_{\max}$ means the maximum value of the initial data, q represents for the minimum value after normalization, and w refers to the maximum value after normalization. In the research, q was assigned with the value −1, and w was assigned with the value 1.

The colony size and the number of iterations were set to be Y and s, respectively. Besides, the position of whales was randomly initialized as $M_i\,(i = 1, 2, 3, \ldots, n)$. The number of DT, feature subsets, and the number of leaf node samples were also initialized. Based on (1), the fitness of each individual in whales was obtained. The best number of whales M^1 were selected and saved. In addition, the best fitness of individuals in whales and the corresponding spatial position were output to obtain the parameters of the optimal colony, including the number of DT, feature subsets, and leaf nodes (Figure 2). In addition, a 17 : 3 ratio of test data to training data was used in this study.

2.5. Observation Indexes. Figure 3 demonstrates the evaluation of the classification effects of two types of classifier algorithms, including back-propagation neural network (BPNN) [25] and support vector machine (SVM) [26] by confusion matrix. BP neural networks are the most basic neural networks, with forward propagation of the output and backward propagation of the error. It imitates the activation and transmission processes of human neurons. Taking the three-layer neural network as an example, the BP neural network contains three layers of structure: an input layer, a hidden layer, and an output layer. The input layer receives data, the output layer outputs data, and the neurons in the previous layer are connected to the neurons in the next layer, collecting information from the neurons in the previous layer and passing the values to the next layer after "activation." BPNN has nonlinear mapping capability, self-learning and self-adaptive capability, generalization capability, and fault tolerance.

TP denotes positive real values, *TN* refers to negative real values, *FP* represents positive forecast values, and *FN* represents for negative forecast values. The accuracy was expressed by (3) as follows:

$$accuracy = \frac{TP + TN}{TP + TN + FP + FN}. \tag{3}$$

2.6. Statistical Analysis. In the research, Statistical Product and Service Solutions (SPSS) 19.0 statistical software was adopted to analyze and process data. The measurement data were expressed by the mean ± deviation ($\overline{X} \pm S$), and the enumeration data were denoted by percentage mark (%). Besides, one-way variance analysis was adopted in pairwise comparison, and $P < 0.05$ indicated that the differences showed statistical meanings.

3. Results

3.1. Experimental Test. To test the application effects of the improved RFC algorithm (n-RFC), nurse mental health questionnaires from 2018 to 2019 at Central South University Xiangya School of Medicine Affiliated Haikou Hospital were retrospectively analyzed in the research, and the survey results were included as the research objects. Besides, 85% of data were selected randomly from the sample data as the training data, and the rest were set as the test data. In addition, BPNN and SVM classifiers were compared, and the forecast accuracy of the results (three health dimensions including anxiety, depression, and fear) by three types of algorithms was compared based on expert judgment (Figure 4).

According to the abovementioned three results, the accuracy of three algorithms in training samples and test samples could be calculated. The accuracy of the n-RFC algorithm, SVM algorithm, and BPNN algorithm in training

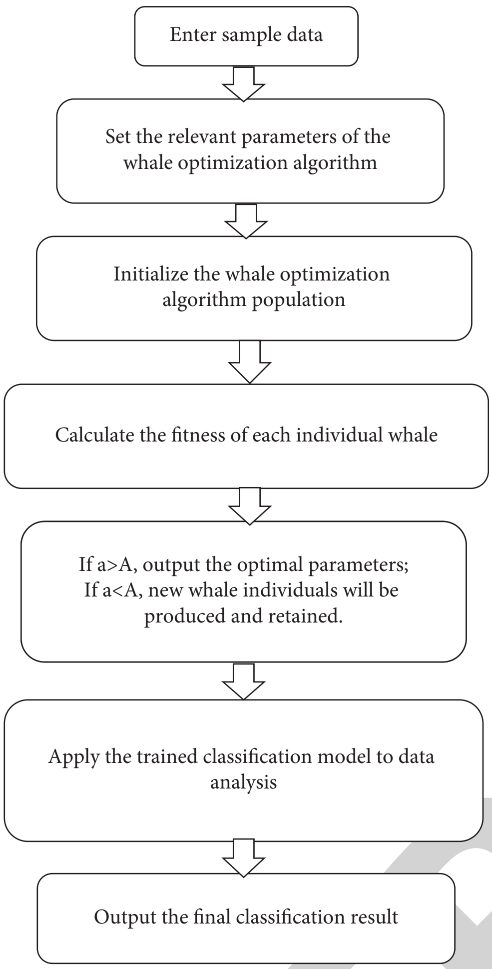

Figure 2: Optimized RFC algorithm framework after introduction of WOA algorithm.

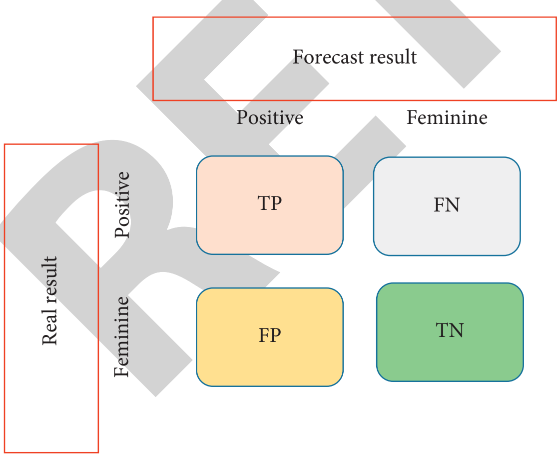

Figure 3: Confusion matrix diagram.

samples was 83.3%, 80.1%, and 78.23%, respectively, while those in test samples were 81.6%, 79.3%, and 77.9%, respectively (Figure 5). Obviously, the accuracy of the n-RFC algorithm in training samples was significantly higher than that of the SVM and BPNN algorithms, and the differences showed statistical meaning ($P < 0.05$).

3.2. Basic Data Statistics. A total of 148 research objects were included in the research, and 148 valid questionnaires were obtained, including 42 and 106 statistical results of data on males (28.37%) and females (71.63%), respectively. Most of the included research objects were aged between 27 and 45 (50.67%), and the proportion of the research objects with bachelor's degrees in the research objects at different education levels was the highest (52.03%) (Table 2).

3.3. Statistics Results of Each Scales

3.3.1. PHQ-9. Figure 6 demonstrates the survey results of depression of 148 nursing personnel in the past 2 weeks. Among depression-related symptoms in PHQ-9, most of the cases suffered from A (pleasure loss), C (sleep disorder), D (energy lack), E (eating disorder), and G (difficulty in concentration) for more than half the time in the past 2 weeks, and the proportion of the incidence of the above 5 symptoms in that of all symptoms in the past 2 weeks reached 6.08%, 8.78%, 6.76%, 6.76%, and 8.1%, respectively.

3.3.2. GAD-7. Figure 7 shows the survey results of the depression of 148 nursing personnel in the past 2 weeks. Among depression-related symptoms in GAD-7, A2 (dysphoria), B2 (failure to control concern), C2 (energy lack), and F2 (fidget) occurred over half the time in the past 2 weeks among most of the cases, and the proportion of the incidence of the above 4 symptoms in that of all symptoms in the past 2 weeks amounted to 4.05%, 4.05%, 4.73%, and 3.38%, respectively.

3.3.3. ISI. Figure 8 reveals the survey results of the sleep status of 148 nursing personnel in the past 2 weeks. Among the insomnia-related symptoms in ISI, A3 (difficulty in falling asleep), B3 (difficulty in maintaining sleep), C3 (early awakening), D3 (satisfaction with sleep), E3 (impacts on daily activities), F3 (impacts on living quality), and G3 (worry/pain) manifested at moderate levels among 9.23%, 8.66%, 7.25%, 22.61%, 8.02%, 5.01%, and 7.57% of the included research objects in the past 2 weeks. Among all the symptoms manifesting at severe and extremely severe levels, the proportions of dissatisfaction with sleep among the included research objects were the highest, reaching 7.43% and 2.03%, respectively.

3.4. Overview of Anxiety, Depression, and Insomnia. Based on the abovementioned statistical results, the data were analyzed by the n-RFC algorithm in the research, which is shown in Figure 9. According to the statistical results, the average scores of 148 nursing personnel by PHQ-9, GAD-7, and ISI were 4.01 ± 4.09, 4.12 ± 4.27, and 2.87 ± 3.08, respectively. According to PHQ-9, the depression levels of 14 cases were above moderate; GAD-7 revealed that the anxiety levels of 5 cases were above moderate; and ISI showed that the insomnia levels of 5 cases were above moderate. To reflect the grading of different levels in different scales more

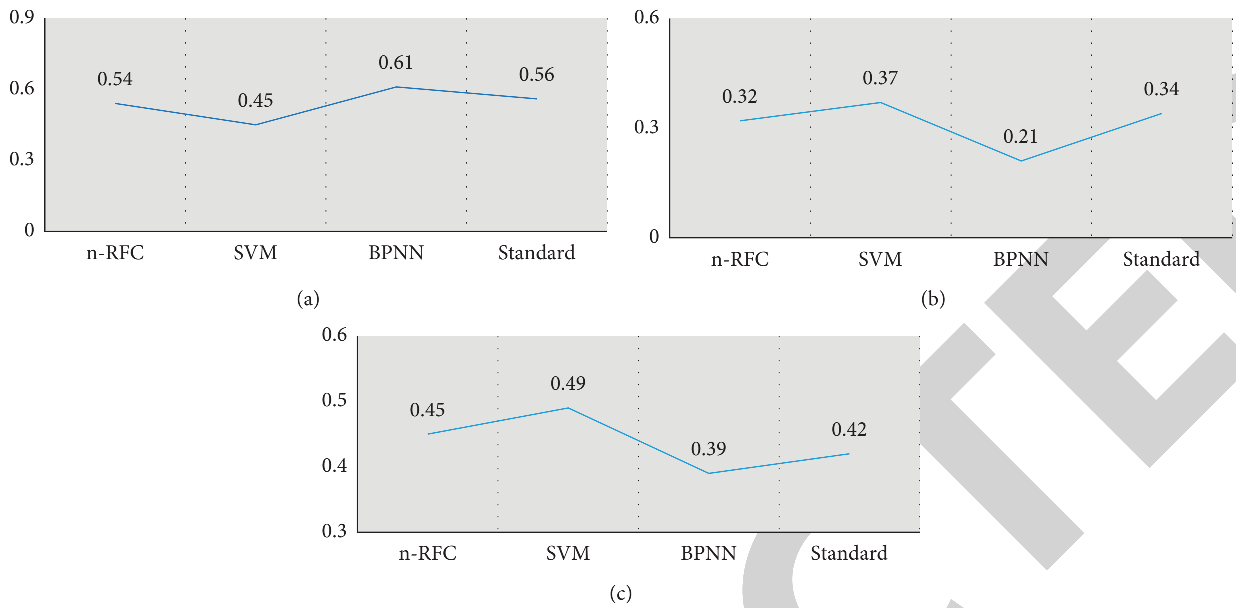

Figure 4: Comparison results of mental health dimensions and algorithms based on nurse mental health questionnaires from 2018 to 2019 as research objects. (a) The health dimensions of depression. (b) The health dimensions of depression. (c) The health dimensions of fear.

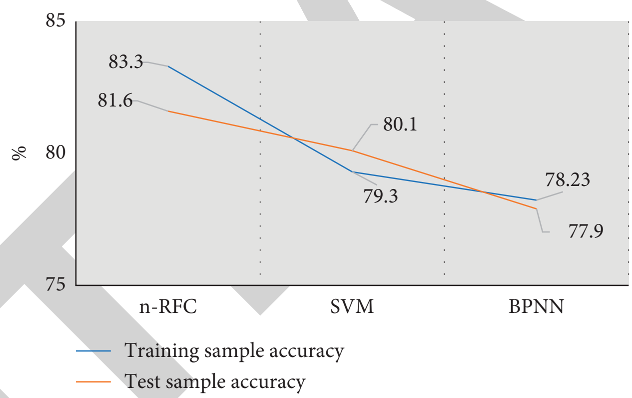

Figure 5: Comparison of the accuracy of n-RFC, SVM, and BPNN algorithms in training samples and test samples based on nurse mental health questionnaires from 2018 to 2019 as research objects. Note: *indicates that the comparison with the accuracy of the n-RFC algorithm showed statistical meaning $(P < 0.05)$.

Table 2: Basic data statistics of nursing personnel.

Items		Number of cases	Proportion (%)
Gender	Male	42	28.37
	Female	106	71.63
Age group (years)	19~26	45	30.41
	27~45	75	50.67
	46~54	28	18.92
Marital status	Married	78	52.7
	Unmarried	70	47.3
Education level	Technical secondary school diploma	6	4.05
	Junior college diploma	62	41.89
	Bachelor's degree	77	52.03
	Master's degree	3	2.03
Working years	More than 5 years	62	41.89
	Less than 5 years	86	58.11
Experience in responding to public emergencies	Experienced	71	47.97
	No experience	77	52.03

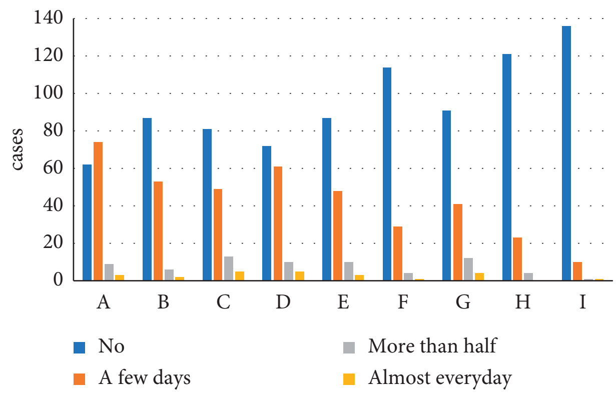

Figure 6: Statistics results of 148 nursing personnel in the past 2 weeks by PHQ-9 questionnaires. A refers to pleasure loss, B indicates depression, C represents for sleep disorder, D represents energy lack, E denotes to eating disorder, F means low self-evaluation, G refers to difficulty in concentration, H represents dysphoria, and I means negative ideas.

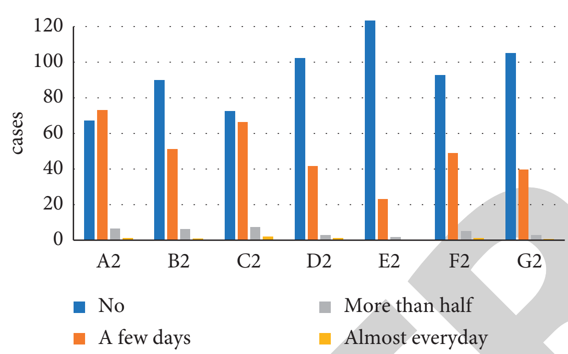

Figure 7: Statistics results of 148 nursing personnel in the past 2 weeks by GAD-7 questionnaires. A2 refers to dysphoria, B2 represents failure to control concern, C2 denotes the concern about this kind of thing, D2 means tension without relaxation, E2 represents for fidget, F2 represents irritability, and G2 indicates the fear that something bad would happen.

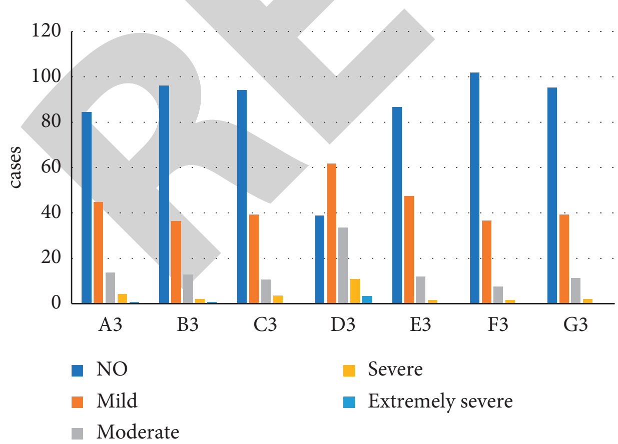

Figure 8: Statistics results of 148 nursing personnel in the past 2 weeks by ISI questionnaires. A3 refers to difficulty in falling asleep, B3 denotes difficulty in maintaining sleep, C3 represents early awakening, D3 denotes for dissatisfaction with sleep, E3 indicates impacts on daily activities, F3 means impacts on living quality, and G3 refers to worry/pain.

intuitively, the proportions of different levels were presented (Figure 9(c)).

3.5. Single Factor Analysis of Factors Affecting Nursing Personnel's Mental Health. Figure 10 demonstrates the single factor analysis of the factors affecting nursing personnel's mental health. According to the results, the average score of males (3.65) was lower than that of females (3.71), the average score of scales of married nursing personnel (3.78) was obviously higher than that of the unmarried (3.65), and the average scores of nursing personnel with bachelor's (3.66) and master's (3.62) degree were obviously lower than those of nursing personnel with junior college diploma (3.77) and technical secondary school diploma (3.75). Besides, the average score of nursing personnel with more than 5-year work experience (3.68) was significantly lower than that of those working for less than 5 years (3.72). The average score of nursing personnel with experience in responding to public emergencies (3.65) was obviously lower than that of those without related experience (3.74), and the differences all demonstrated statistical meaning ($P < 0.05$).

4. Discussion

The pneumonia outbreak that occurred in 2019 is an acute respiratory disease that is highly contagious. This is another health emergency following the 2003 SARS and the 2009 infection of the A hemagglutinin 1 neuraminidase 1 (H1N1) population [27]. It not only directly threatens physical life and health but also greatly affects people's mental health [28]. As the front-line team in the fight against the epidemic, the mental health of nursing staff has received much attention. Therefore, the study used the RFC algorithm to analyze the impact on the mental health of nursing staff in the context of wireless networks [29]. Traditional RFC algorithms were susceptible to the number of DT, feature subsets, and leaf nodes, which resulted in significant errors in forecast results [30]. Weng et al. [31] improved the forecast accuracy of cardiovascular risks by adopting the RFC algorithm in wireless network technology and machine learning. In this research, the WOA algorithm was introduced, and the selection of RFC algorithm parameters by the self-adaptability of the WOA algorithm. To verify the forecast performance of the improved algorithms, SVM and BPNN algorithms were introduced in the research. Besides, the data on nurse mental health questionnaires from 2018 to 2019 were included as the research objects to analyze the accuracy of three types of algorithms. The results demonstrated that the scores of three health dimensions, including anxiety, depression, and fear, were 0.56, 0.34, and 0.42, respectively, according to the experts' analysis. In contrast, the forecast scores of anxiety, depression, and fear by the n-RFC algorithm were 0.54, 0.32, and 0.46, respectively. Compared with those by SVM and BPNN, the forecast scores generated by n-RFC algorithm were more similar to the results of expert analysis. In addition, expert analysis results were set as the standard for the comparison of the forecast accuracy of the n-RFC, SVM, and BPNN

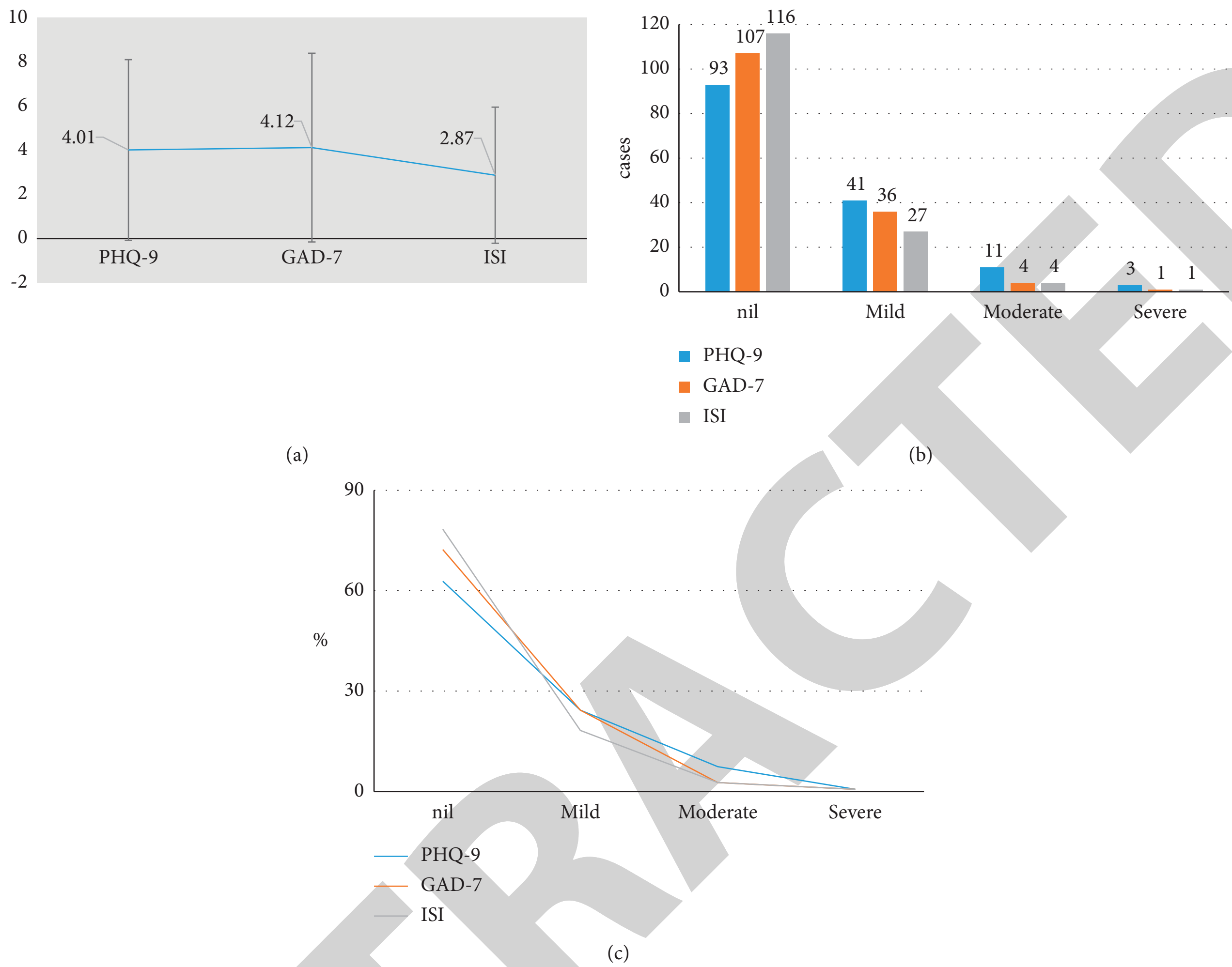

Figure 9: n-RFC data analysis diagram of the general results of 148 nursing personnel in the past 2 weeks by PHQ-9, GAD-7, and ISI, respectively. (a) The average scores of three scales, and error bars denoted the average score standard deviation of each scale of 148 nursing personnel. (b) The population statistics. (c) The general proportion of each level.

algorithms. The results showed that the accuracy of the n-RFC algorithm in training and test samples was 83.3% and 81.6%, respectively, which was significantly higher than those of the SVM algorithm (80.1% and 79.3%) and the BPNN algorithm (78.23% and 77.9%), and the differences demonstrated statistical meaning ($P < 0.05$). The above results revealed that the improved algorithm was more accurate and had potential in data analysis to some degree.

In the research, a total of 148 in-service nursing personnel were included as the research objects, and 148 questionnaires were recycled effectively. To collect more specific data, 3 scales were introduced in the questionnaire designed in the research in total. The PHQ-9 scale mainly reflected the degree of depression, the GAD-7 scale mainly reflected the degree of anxiety, and the ISI scale mainly reflected insomnia. The results of the research showed that most included cases suffered from pleasure loss, sleep disorder, energy lack, eating disorder, and difficulty in concentration over half the time of the past 2 weeks among depression-related symptoms in PHQ-9, and the proportions of the above cases in all cases with each symptom were 6.08%, 8.78%, 6.76%, 6.76%, and 8.1%, respectively. Among depression-related symptoms in GAD-7, most of the cases suffered from dysphoria, failure to control concern, energy lack, and fidgeting over half the time in the past 2 weeks, and the proportions of the above cases in all cases with each symptom were 4.05%, 4.05%, 4.73%, and 3.38%, respectively. Among the insomnia-related symptoms in ISI, most of the cases suffered from difficulty in falling asleep, difficulty in maintaining sleep, early awakening, dissatisfaction with sleep, impacts on daily activities, impacts on living quality, and worry/pain at moderate levels in the past 2 weeks, and the proportions of the above cases in all cases with different levels of each case were 9.23%, 8.66%, 7.25%, 22.61%, 8.02%, 5.01%, and 7.57%, respectively. In addition, the n-RFC algorithm was adopted to analyze the collected data in the research, which revealed that the average scores of the PHQ-9, GAD-7, and ISI scales of 148 nurses were 4.01 ± 4.09, 4.12 ± 4.27, and 2.87 ± 3.08, respectively. According to PHQ-9, the depression levels of 14 cases (9.46%) were above moderate. GAD-7 indicated that the anxiety levels of 5 cases (3.38%) were above moderate, and the insomnia levels of 5

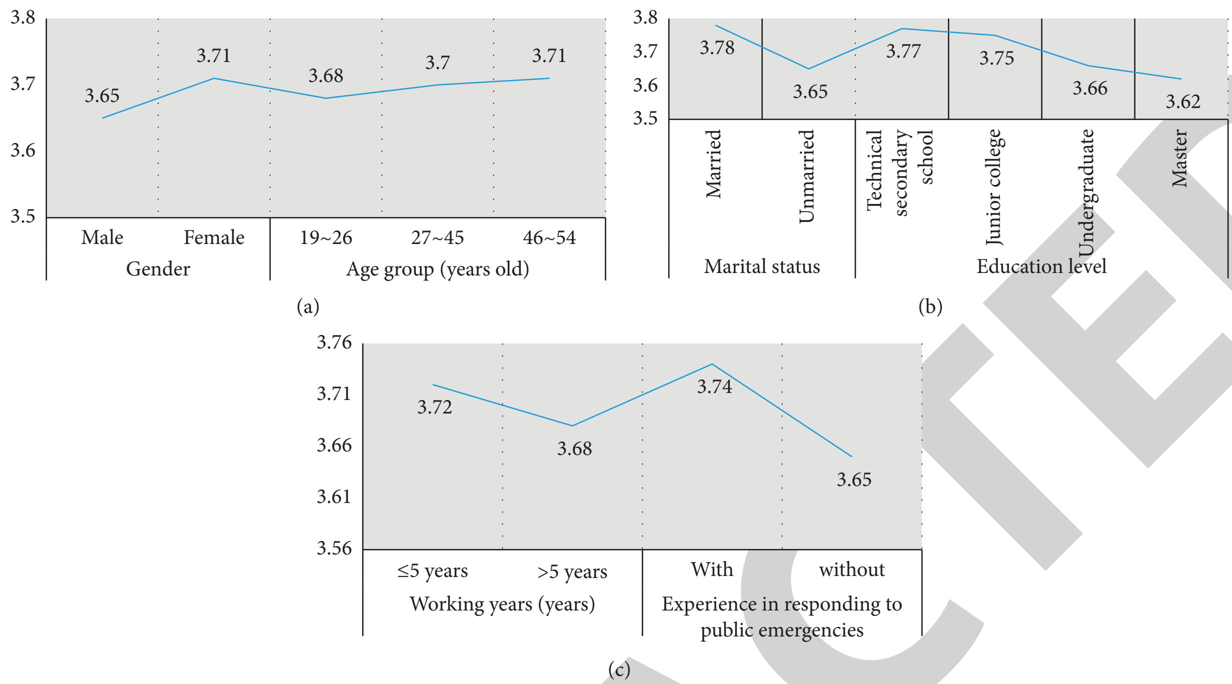

Figure 10: Single factor analysis of factors affecting 148 nursing personnel's mental health. (a) Gender and age groups. (b) Marital status and education levels. (c) Working years and experience in responding to public emergencies. Note: *indicated that the comparison with the average scores of other factors in the same group showed statistical meaning ($P < 0.05$).

cases (3.38%) were above moderate. The epidemic broke out suddenly and was extremely contagious. The constant growth of the infected population and clinical infected cases caused certain mental pressure for medical care personnel, and few of them ever got involved in large-scale sudden sanitation events like this. With the lack of related solutions, they often felt anxious and depressed. According to the study conducted by Pollock et al. [32], antistress ability could be enhanced by workplace interventions, interventions to support basic and daily needs, mental support interventions, and drug interventions during the epidemic. With the current advanced wireless network technology, people can know about real-time epidemic development by intelligent devices. Regular epidemic prevention training and mental training for nursing personnel need to be provided. Besides, nursing personnel's mental pressure could be alleviated by mental preparation for emergencies at any time.

In addition, the factors that affected nursing personnel's mental health were analyzed in the research, which showed that the differences of the impacts of age on nursing personnel's mental health demonstrated no statistical meaning ($P > 0.05$), and the average score of a male (3.65) was obviously lower than that of a female.

The results of the research also indicated that the scale average score of married nursing personnel (3.78) was significantly higher than that of unmarried. The average scores of nursing personnel with bachelor's (3.66) or master's (3.62) degree were obviously lower than those of nursing personnel with junior college or technical secondary school diplomas. Besides, the average scores of nursing personnel with more than 5-year work experience (3.68) were obviously lower than those of nursing personnel with less than 5-year work experience. The average score of nursing personnel with experience in responding to public emergencies (3.65) was significantly lower than that of nursing personnel without related experience, and the differences showed statistical meaning ($P < 0.05$). The differences resulted mainly from females' sensitivity compared with males. Besides, the antistress ability of females was significantly poorer than that of males because of body hormones. Because married nursing personnel often needed to care for their families and spouses, they felt more stressed compared with unmarried nursing personnel. The professional and mental qualities of nursing personnel with higher education levels were both higher than those of nursing personnel with lower education levels. Besides, the mental enduring capacity of nursing personnel with more working years was stronger than that of nursing personnel with fewer working years. According to the survey and study conducted by Spoorthy et al. [33], some sociodemographic variables were related to the pressure on medical care personnel, anxiety, depression, and insomnia, such as gender, occupation, age, workplace, and department. Furthermore, some mental variables, such as social support and self-efficacy, were also related to the pressure on medical care personnel, anxiety, depression, and insomnia. In addition, the nursing personnel with experience in responding to public emergencies showed less anxiety and fear than those without related experience in coping with them. Therefore, nursing staff should be encouraged to share their clinical nursing experience in responding to the pneumonia epidemic and praise the value of their experience in fighting the epidemic with positive actions.

5. Conclusion

In the research, the selection of the RFC algorithm parameters was improved by the WOA algorithm. Besides, a total of 148 in-service nursing personnel were included as the research objects, and 148 questionnaires were recycled effectively. The collected data were analyzed by the improved RFC algorithm. In addition, the single factor analysis method was adopted to investigate the impacts of demographic factors on nursing personnel's mental health in the research. The results demonstrated that the accuracy of the improved RFC algorithm was obviously higher than that of the SVM and BPNN algorithms. Under the impact of the epidemic, many nursing personnel suffered from mental diseases at different levels. Gender, marital status, education levels, and experience in responding to sudden sanitation events were the main factors affecting nursing personnel's mental health. Nevertheless, the sample size was small compared with the global epidemic. Furthermore, the results of the research were incomprehensive, such as the lack of research results of the factors affecting nursing personnel's mental health. In future research, the sample size needs to be enlarged, and the impact of job factors on mental health should be increased. In general, the research offered data support to the elimination of the adverse impact of the epidemic on medical care personnel's mental health.

Data Availability

The data used to support the findings of this study are included within the article.

Disclosure

Dan Guo and Yi Guo are co-first authors of this paper.

Conflicts of Interest

The authors declare no conflicts of interest.

Authors' Contributions

Dan Guo and Yi Guo have contributed equally to this study.

References

[1] J. Torales, M. O'Higgins, J. M. Castaldelli-Maia, and A. Ventriglio, "The outbreak of COVID-19 coronavirus and its impact on global mental health," *International Journal of Social Psychiatry*, vol. 66, no. 4, pp. 317–320, 2020.

[2] G. Giorgi, L. I. Lecca, F. Alessio et al., "COVID-19-Related mental health effects in the workplace: A narrative review," *International Journal of Environmental Research and Public Health*, vol. 17, no. 21, p. 7857, 2020.

[3] D. Talevi, V. Socci, M. Carai et al., "Mental health outcomes of the CoViD-19 pandemic," *Rivista di Psichiatria*, vol. 55, no. 3, pp. 137–144, 2020.

[4] M. M. Hossain, S. Tasnim, A. Sultana et al., "Epidemiology of mental health problems in COVID-19: A review," *F1000Research*, vol. 9, p. 636, 2020, Published Jun 23, 2020.

[5] J. Gao, P. Zheng, Y. Jia et al., "Mental health problems and social media exposure during COVID-19 outbreak," *PLoS One*, vol. 15, no. 4, Article ID e0231924, 2020, Published, 2020.

[6] L. Kang, Y. Li, S. Hu et al., "The mental health of medical workers in Wuhan, China dealing with the 2019 novel coronavirus," *The Lancet Psychiatry*, vol. 7, no. 3, 2020.

[7] J. Heitzman, "Impact of COVID-19 pandemic on mental health," *Psychiatria Polska*, vol. 54, no. 2, pp. 187–198, 2020.

[8] S. B. Guessoum, J. Lachal, R. Radjack et al., "Adolescent psychiatric disorders during the COVID-19 pandemic and lockdown," *Psychiatry Research*, vol. 291, Article ID 113264, 2020.

[9] J. Shigemura, R. J. Ursano, J. C Morganstein, M. Kurosawa, and D. M. Benedek, "Public responses to the novel 2019 coronavirus (2019-nCoV) in Japan: mental health consequences and target populations," *Psychiatry and Clinical Neurosciences*, vol. 74, no. 4, pp. 281-282, 2020.

[10] L. Dong and J. Bouey, "Public mental health crisis during COVID-19 pandemic, China," *Emerging Infectious Diseases*, vol. 26, no. 7, pp. 1616–1618, 2020.

[11] F. Nearchou, C. Flinn, R. Niland, S. S. Subramaniam, and E. Hennessy, "Exploring the impact of COVID-19 on mental health outcomes in children and adolescents: A systematic review," *International Journal of Environmental Research and Public Health*, vol. 17, no. 22, p. 8479, 2020.

[12] F. F. Ren and R. J. Guo, "Public mental health in post-COVID-19 era," *Psychiatria Danubina*, vol. 32, no. 2, pp. 251–255, 2020.

[13] Y. Zhai and X. Du, "Addressing collegiate mental health amid COVID-19 pandemic," *Psychiatry Research*, vol. 288, Article ID 113003, 2020.

[14] The Lancet Psychiatry, "COVID-19 and mental health," *The Lancet Psychiatry*, vol. 8, no. 2, p. 87, 2021.

[15] A. B. R. Shatte, D. M. Hutchinson, and S. J. Teague, "Machine learning in mental health: A scoping review of methods and applications," *Psychological Medicine*, vol. 49, no. 9, pp. 1426–1448, 2019.

[16] S. A. Graham, E. E. Lee, D. V. Jeste et al., "Artificial intelligence approaches to predicting and detecting cognitive decline in older adults: A conceptual review," *Psychiatry Research*, vol. 284, Article ID 112732, 2020.

[17] E. Lin, C. H. Lin, and H. Y. Lane, "Precision psychiatry applications with pharmacogenomics: Artificial intelligence and machine learning approaches," *International Journal of Molecular Sciences*, vol. 21, no. 3, p. 969, 2020.

[18] E. K. Unger, J. P. Keller, M. Altermatt et al., "Directed evolution of a selective and sensitive serotonin sensor via machine learning," *Cell*, vol. 183, no. 7, pp. 1986–2002, 2020.

[19] Y. Mao, Y. He, L. Liu, and X. Chen, "Disease classification based on eye movement features with decision tree and random forest," *Frontiers in Neuroscience*, vol. 14, p. 798, 2020.

[20] A. Alabdulkarim, M. Al-Rodhaan, T. Ma, and Y. Tian, "PPSDT: a novel privacy-preserving single decision tree algorithm for clinical decision-support systems using IoT devices," *Sensors (Basel)*, vol. 19, no. 1, p. 142, 2019.

[21] H. Esmaily, M. Tayefi, H. Doosti, M. Ghayour-Mobarhan, H. Nezami, and A. Amirabadizadeh, "A comparison between decision tree and random forest in determining the risk factors associated with type 2 diabetes," *Journal of Research in Health Sciences*, vol. 18, no. 2, 2018.

[22] W. Chen, Y. Li, W. Xue et al., "Modeling flood susceptibility using data-driven approaches of naïve Bayes tree, alternating decision tree, and random forest methods," *The Science of the Total Environment*, vol. 707, Article ID 134979, 2020.

Hindawi
Journal of Healthcare Engineering
Volume 2023, Article ID 9789870, 1 page
https://doi.org/10.1155/2023/9789870

Retraction

Retracted: Impact of Yiqi Huoxue Decoction on the Relationship between Remodeling of Cardiac Nerves and Macrophages after Myocardial Infarction in Rats

Journal of Healthcare Engineering

Received 23 May 2023; Accepted 23 May 2023; Published 24 May 2023

This article has been retracted by Hindawi following an investigation undertaken by the publisher [1]. This investigation has uncovered evidence of one or more of the following indicators of systematic manipulation of the publication process:

(1) Discrepancies in scope
(2) Discrepancies in the description of the research reported
(3) Discrepancies between the availability of data and the research described
(4) Inappropriate citations
(5) Incoherent, meaningless and/or irrelevant content included in the article
(6) Peer-review manipulation

The presence of these indicators undermines our confidence in the integrity of the article's content and we cannot, therefore, vouch for its reliability. Please note that this notice is intended solely to alert readers that the content of this article is unreliable. We have not investigated whether authors were aware of or involved in the systematic manipulation of the publication process. Wiley and Hindawi regrets that the usual quality checks did not identify these issues before publication and have since put additional measures in place to safeguard research integrity.

We wish to credit our own Research Integrity and Research Publishing teams and anonymous and named external researchers and research integrity experts for contributing to this investigation.

The corresponding author, as the representative of all authors, has been given the opportunity to register their agreement or disagreement to this retraction. We have kept a record of any response received.

References

[1] Y. Liu, S. Guo, Y. Zhang et al., "Impact of Yiqi Huoxue Decoction on the Relationship between Remodeling of Cardiac Nerves and Macrophages after Myocardial Infarction in Rats," *Journal of Healthcare Engineering*, vol. 2022, Article ID 4441603, 13 pages, 2022.

Hindawi
Journal of Healthcare Engineering
Volume 2022, Article ID 4441603, 13 pages
https://doi.org/10.1155/2022/4441603

Research Article

Impact of Yiqi Huoxue Decoction on the Relationship between Remodeling of Cardiac Nerves and Macrophages after Myocardial Infarction in Rats

Yunke Liu,[1] Shunwen Guo,[2] Yuqin Zhang,[1,3] Hui Wang,[1] Jiani Wu,[4] Wang'ou Lin,[5] Binyue Zhang,[6] Jie Chen,[1] Yufei Li,[1] Yunshu Zhang,[1] Fanyu Wei,[1] and Tianhui Du[1]

[1]*School of Traditional Chinese Medicine, Beijing University of Chinese Medicine, Beijing 100029, China*
[2]*Fangshan Hospital Beijing University of Chinese Medicine, Beijing 102499, China*
[3]*School of Acupuncture-Moxibustion and Tuina, Beijing University of Chinese Medicine, Beijing 100029, China*
[4]*Wang Jing Hospital of CACMS, Beijing 100102, China*
[5]*Yantai Puhui Hospital of Integrated Traditional Chinese and Western Medicine, Yantai 264004, Shandong, China*
[6]*Guang'anmen Hospital China Academy of Chinese Medical Science, Beijing 100053, China*

Correspondence should be addressed to Shunwen Guo; guo1163@163.com

Received 27 February 2022; Accepted 18 March 2022; Published 7 April 2022

Academic Editor: Liaqat Ali

Sympathetic nerve remodeling after myocardial infarction (MI) has an indispensable role in cardiac remodeling. Numerous works have shown that sympathetic nerve remodeling can be delayed by inhibition of inflammatory response. Earlier studies have shown improvement in ventricular remodeling and inhibited chronic stage neural remodeling by Yiqi Huoxue decoction (YQHX). Therefore, the current study looked at the inhibitory effect of YQHX prescription on proinflammatory mediators and macrophages and the effect on neural remodeling at 3 and 7 days after MI. YQHX inhibited the expression of Toll-like receptor 4 (TLR4) and nuclear factor kappa B (NF-κB) proteins and macrophage infiltration within 7 days after myocardial infarction. YQHX could decrease Th-positive nerve fiber density in the area around infarction and reduce the expression of growth-associated protein 43 (GAP43), nerve growth factor (NGF), and tyrosine hydroxylase (TH) proteins, which was associated with the remodeling of sympathetic nerves. Thus, the nerve remodeling inhibition after MI due to YQHX may be through its anti-inflammatory action. These data provide direct evidence for the potential application of traditional Chinese medicine (TCM) in the remodeling of sympathetic nerves after MI.

1. Introduction

In the past 20 years, MI (myocardial infarction) has been among the main causes of heart failure [1], and persistent arrhythmia after MI is also the main cause of sudden death [2]. In recent years, many investigations have demonstrated that sympathetic remodeling after MI is a crucial factor and the mode of triggering, initiating, and even maintaining malignant arrhythmias. Nerve repair and rearrangement occur in the infarcted area with the occurrence of ventricular remodeling after MI, which is called cardiac nerve remodeling. After MI, sympathetic nerves involved in cardiac innervation are damaged, and various local and circulating neurotrophic factors, for instance, GAP43 (growth-related protein 43) and NGF (nerve growth factor), participate in the repair process, resulting in excessive nerve sheath cells and axon regeneration around the infarcted tissue [3, 4]. Factors related to the remodeling of neurons play essential roles in reflecting sympathetic nerve function [5], promoting sympathetic nerve injury repair [6], and avoiding excessive growth [7]. However, cardiac remodeling is in a dynamic process, not a single repair or inhibition effect; it is also affected by a variety of factors, at different times or locations, or mutually promotes or antagonizes each other.

Increasing evidence indicates that the budding of a sympathetic nerve is closely associated with inflammation, mainly at the edge of infarction, where there are a large number of macrophages and inflammatory factors [8, 9]. Cytokines in the inflammatory environment can induce macrophage activation [10], thus promoting the expression of NGF [11], indicating that macrophages may also be involved in the regeneration and remodeling of sympathetic nerves. Wernli et al. [12] reported that chemical knockout of macrophages significantly reduces sympathetic nerve regeneration and NGF content after MI in rats. Hasan et al. [13] found that, after left ventricular myocardial tissue infarction in rats caused by left coronary artery ligation, sympathetic nerve remodeling and regeneration occur in the aggregation area harboring macrophages and fibroblasts. Through immunohistochemistry and in situ hybridization, NGF was found to be mainly synthesized and released by fibroblasts A and activated M-type macrophages, thus promoting sympathetic nerve remodeling. Macrophages generate a substantial count of proinflammatory cytokines and high levels of oxide metabolites, while M2 macrophages have an essential role in the repair of infarction by inhibiting destructive immune responses [14]. Anti-inflammatory treatment can reduce sympathetic remodeling after MI [15–17]. Thus, an anti-inflammatory drug is a promising approach for preventing sympathetic remodeling.

YQHX (Yiqi Huoxue decoction) is widely used to treat myocardial conditions considering its safety and efficacy. The formula comprises *Angelica Sinensis*, *Astragalus membranaceus*, *ginseng*, *Ligusticum chuanxiong*, and *Panax notoginseng*. According to the qi and blood theory of traditional Chinese medicine, YQHX can nourish the heart and qi, promote blood circulation, and clear veins. YQHX has been shown to improve ventricular remodeling in rats [18], improve mitochondrial function [19], regulate energy metabolism [20, 21], block the expressions of neural remodeling factor and cardiac hypertrophy protein within the chronic stage, and reduce cardiac hypertrophy and nerve remodeling [22], to achieve the effect of alleviating MI injury.

Although YQHX can reduce nerve remodeling, whether it can improve sympathetic remodeling of the heart by regulating the phenotypic transformation of macrophages needs more research. Hence, in the current work, the function of macrophages in sympathetic remodeling after MI was evaluated, and the potential of YQHX to inhibit sympathetic remodeling after MI was determined by regulating the differentiation of macrophages.

2. Reagents and Methods

2.1. Ethical Approval. The current study was approved by the Medical and Laboratory Animal Ethics Committee, Beijing University of Chinese Medicine (ETHICS No.: BUCM-4-2018071701-3002). All the animal studies were carried out following the National Institutes of Health Guidelines for the Care and Use of Laboratory Animals (NIH Publication No. 85-23 and revised in 1996) guidelines.

2.2. Herb Preparation. YQHX comprises five herbs: *Angelica sinensis*, *Astragalus membranaceus*, *Ligusticumchuanxiong Hort*, *Panax ginseng* C. A. Meyer, and *Panax notoginseng*. Each of these herbs was procured from Dongzhimen Hospital, Beijing University of Chinese Medicine. The high-performance liquid chromatography coupled with linear ion trap quadrupole Orbitrap high-resolution mass spectrometry (HPLC-LTQ-Orbitrap MS) method was applied with DDA-MS2 information acquisition and earlier studies for examining the components of YQHX aqueous extracts systematically, and 87 compounds were inferred, in addition to the structural types of flavonoids and triterpenoid saponins, including panaxosides, ginsenosides, floralginsenoside, astragaloside, and quinquenoside. As per the recommended active pharmaceutical ingredients (API) dose for the human body (of 96 g/d), the rat dose was six times the relative dose ratio for the human body. Hence, a drug dose equal to 8.2 g/kg was selected; earlier studies have furnished sufficient evidence for the effectiveness of this dose [19].

2.3. Animal Model Establishment and Group Administration. Adult male specific-pathogen free (SPF) Sprague Dawley (SD) rats (200 ± 20 g) were procured from Beijing Weitong Lihua Laboratory Animal Science and Technology Co., Ltd. (Certificate Number: SCXK2016-0006). Adaptive feeding for three days before MI surgery was performed in the Animal Experimental Center, Beijing University of Chinese Medicine. In the period for feeding, the rats were freely provided with distilled water and a regular diet. A constant humidity and temperature were maintained in the laboratory. An earlier published method was followed to establish the rat MI model [23]. Experimental surgery was performed aseptically with pentobarbital sodium (1%, 40 mg/kg) for abdominal anesthesia. Postendotracheal intubation, an animal ventilator of small size, was connected (breathing rate of 85 times/min) at a breathing ratio of 1 : 2. To make the model, ligation of the descending anterior branch of the left coronary artery was performed through 5-0 nylon suture, and the thoracic cavity was closed layerwise. The same procedure was performed on the control rats except for left anterior descending (LAD) ligation. The significant elevation of the ST segment under electrocardiogram (ECG) limb lead monitoring confirmed the successful modeling of MI (Shanghai Medical Electronic Instrument Factory).

The rats were arbitrarily categorized into the sham operation group ($n = 10$) and the infarction group ($n = 10$). In the infarction group, ECG examination was carried out on day 2 after operation, and more than four Q-wave numbers met the requirements of the experiment. Rats having identical Q-wave numbers were arbitrarily categorized into two groups. Ten rats without ligature were selected as the sham operation group. SD rats with successful ligation were arbitrarily categorized into three groups: the MI model (MI, $N = 10$), the MI model + invigorating qi, and promoting blood circulation (YQHX, $N = 10$), and the MI model + metoprolol (METO, $N = 10$). On day 2 after MI surgery, a dose of 8.2 g/kg/d YQHX and 5 mg/kg/d metoprolol (AstraZeneca Pharmaceutical Co., Ltd., National Drug

Standard H32025391, Batch no. 1805A23) was administered. The same amount of water (distilled) was given to both groups of MI and sham operations. Allergic reactions were checked on days 3 and 7 after intragastric administration.

2.4. Echocardiogram. Before sampling, echocardiography (Visual Sonic, Vevo770, Canada) was conducted to examine the rats. For this, an injection of pentobarbital sodium (1%) was used as anesthesia, with the chest skin of the rats being supine. At the time of ultrasound, a state of normal physiology was maintained. For each mouse, 3 consecutive cardiac cycles were considered. FS (left ventricular short-axis ratio), left ventricular EF (ejection fraction), LVIDd (left ventricular end-diastolic diameter), and LVIDs (left ventricular end-systolic diameter) were measured.

2.5. Staining with Hematoxylin and Eosin (HE). The myocardium tissue was fixed, dehydrated, embedded, sliced (4 μm thick), and stained with HE. Then, through gradient down ethanol, sections were dewaxed and dehydrated. Staining of nuclei was performed using hematoxylin, followed by differentiation in HCL ethanol (1%). Then, a solution of red ethanol (1%) was used, followed by dehydration using gradient ethanol. The sections were microscopically observed, and images were acquired for evaluation.

2.6. Immunohistochemical Analyses. After dewaxing, paraffin sections were positioned in a repair chamber containing ethylenediaminetetraacetic acid (EDTA) antigen extraction buffer (pH 8.0) for the extraction of antigen in a steamer. The slides, after being inserted in phosphate-buffered saline (PBS, pH 7.4), were rinsed three times, followed by shaking on a decolorizing shaker, each time for 5 min. Endogenous peroxidase was blocked, a circle was drawn, and serum was used to seal it. This was followed by the addition of a primary antibody to the slides after gently discarding the blocking solution, placed in a damp box, and incubated at 4°C overnight. Next, the slides were inserted in PBS (pH 7.4) on a decoloring shaker and rinsed three times, each for 5 min. The slices were allowed to dry slightly, and a secondary antibody specific for the primary antibody was poured dropwise into the circle for covering the tissue and incubated at ambient temperature for 60 min. Then, the tissue was rinsed and incubated in horseradish peroxidase (HRP). After rinsing, DAB (3, 3′-diaminobenzidine) staining was continued; for this, the solution of PBS was eliminated, and a fresh solution of DAB (50–200 μL) was added to individual pieces for dyeing the nuclei.

2.7. Western Blotting. The tissue samples were homogenized with a 1 mL radioimmunoprecipitation assay (RIPA) lysis buffer. For the extraction of proteins, the samples were dissolved for 30 minutes on ice, and the obtained proteins were quantified by employing a bicinchoninic acid (BCA) protein assay kit. The total load protein was 40 μg and 20 μL. The target protein's molecular weight was detected by gel isolation with appropriate proportions, and then electrophoresis and electrical conversion were performed. The polyvinylidene difluoride (PVDF) membrane following electroporation was submerged in Tris Buffer Saline Tween20 (TBST) sealing solution containing 5% milk. Antibodies against GAP43 (AB75810, Abcam), NGF (ab52918, Abcam), Semaphorin3A (SEMA-3A, AB11370, Abcam), tyrosine hydroxylase (TH, AB112, Abcam), actin (AB8226, Abcam), CD68 (AM25212, Abcam), CD163 (Ab82422, Abcam), CD86 (GTX34569, GeneTex), TLR4 (Proteintech, 19811-1-AP), and NF-κB antibody (Ab16502, Abcam) were added and kept overnight. Relative expressions of proteins were determined by grayscale scanning gel imaging and electrochemiluminescence.

2.8. Statistical Analysis. All data were processed by SPSS22.0 software. The comparisons between multiple groups were in accordance with normal distribution, and a one-way assessment of variance was employed. If the variance was uniform, multiple comparisons between multiple groups were analyzed by least significant difference (LSD) to test the level. If the variance was uneven, Games–Howell is used for analysis. If the normal distribution was not met, nonparametric k independent samples were tested and $P < 0.05$ was deemed significant considering statistical standards.

3. Results

3.1. Alterations in Cardiac Function and Structure in MI Rats. Echocardiography is an effective and common technique to assess changes in cardiac activity. As shown in Figure 1(a), there was a significant decrease in EF and FS of rats in the MI group, an increase in LVIDs, and severely impaired cardiac function 3 and 7 days after MI. At 7 days, YQHX and METO groups exhibited a higher EF than that in the MI group and lower LVIDs levels than that in the MI group. HE staining is one of the common and intuitive methods for observing tissue morphology. HE staining showed (Figure 1(b)) that 3 days after MI, relative to the sham group, the MI group had structurally damaged and disordered myocardial cells with inflammatory cell infiltration. The pathological alterations in the YQHX intervention group were slightly fewer than those in the METO intervention group. Seven days after MI, the structure of myocardial cells in the group of sham was neat and occasionally broken. Regarding the MI group, the myocardial cell number at the edge of infarction decreased, the arrangement of myocardial tissue was disordered, and a large, remarkably high number of inflammatory cells were observed in the interstitium. In comparison to the MI group, myocardial cells in the YQHX intervention group were arranged continuously and neatly, and inflammatory infiltration of the extracellular interstitium was reduced. The pathological changes of the METO intervention group were similar to those of the Y group. In conclusion, YQHX can cause improvement in cardiac function after MI in rats and also decrease the impairment at the infarction area edge.

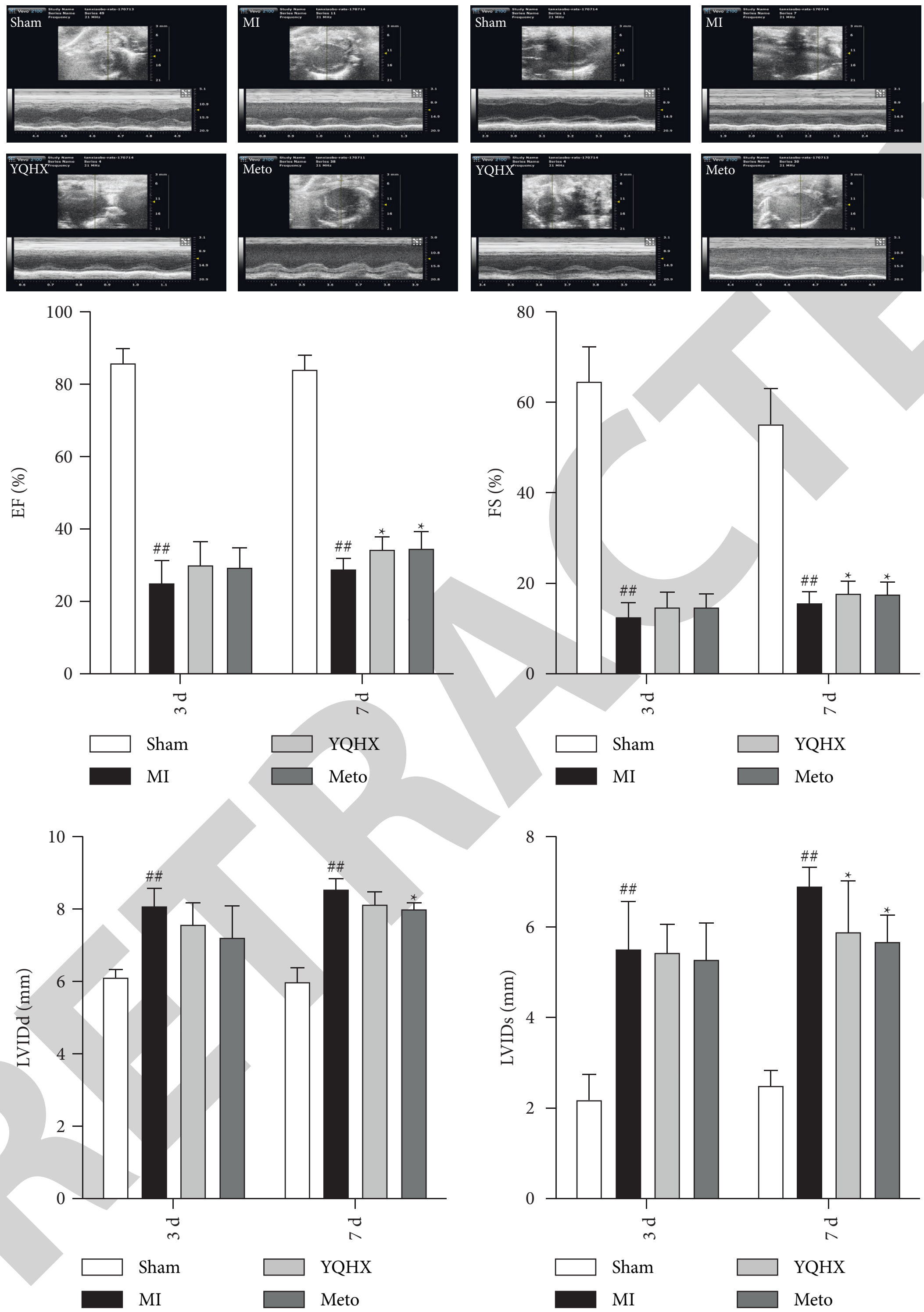

(a)

Figure 1: Continued.

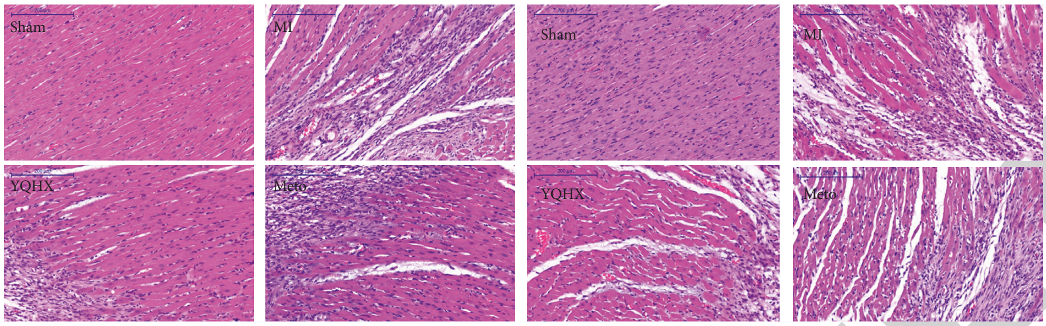

(b)

Figure 1: (a) Cardiac function and echocardiogram of rats in each group after days 3 and 7 of MI (myocardial infarction) ($N = 9$). $^{\#\#}P < 0.01$, vs. the sham operation group; $^{*}P < 0.01$, vs. the MI model group. (b) Histopathological staining using hematoxylin and eosin of the tissue in the infarct marginal area of rats with MI in each group (scale bar = 200 μm).

3.2. Function of YQHX on Factors for Nerve Remodeling in the Marginal Area of MI Rats. The study of NORI by Wang et al. [22] on MI rats showed that most of the regenerated nerve fibers were positive for TH, indicating that the regenerated nerve was mainly a mature sympathetic nerve. TH is a sympathetic nerve-specific marker, extensively distributed in the cytoplasm of norepinephrine nerve axons. It takes part in catecholamine synthesis, being a ring-ring-speed enzyme of catecholamine synthesis with remarkable specificity [24], and its positive detection can depict the sympathetic nerve distribution. The increase in nerve fibers leads to the increase in catecholamine release and the increase in sympathetic nerve activity, which is unbalanced with parasympathetic innervation. The positive distribution of TH in myocardia is associated closely with nerve remodeling after MI.

Immunohistochemical analyses in the MI marginal area showed (Figure 2(a)) that, 3 days after MI, there was a notable or complete reduction in the nerve fibers positive for TH in the sham group, with a uniform and consistent distribution among myocardial fibers in the direction of myocardial cells. In the MI group, nerve fibers positive for TH were increased significantly in density, coarse in shape, with random distribution. After treatment with METO and YQHX, the density and morphology distribution of nerve fibers positive for TH decreased relative to that in the MI group. The nerve growth factors, NGF and GAP43, can lead to uncontrolled regeneration and uneven density of cardiac nerves following MI. An inhibitor of nerve growth, SEMA-3A, impedes sympathetic overgrowth. As shown in Figure 2(b), on days 3 and 7, the expression of TH, NGF, and GAP43 in group *M* was higher at significant levels relative to those in group S, while SEMA-3A expression was low. On days 3 and 7, the expression of TH, GAP43, and NGF in the YQHX group and the METO group decreased relative to that in group *M*. At day 7, both YQHX and METO upregulated SEMA-3A expression. Therefore, after METO and YQHX intervention, TH, GAP43, and NGF expressions were downregulated, and SEMA-3A expression could be upregulated 7 days later as shown in Figure 2(c).

3.3. Effects of YQHX on Macrophages and Inflammation-Related Proteins in the Marginal Area of Myocardial Infarction Rats. Macrophages are differentiated mainly into two subtypes after activation [25]: the classical activated macrophage M1 and the selective activated macrophage M2 subtypes. Molecular markers on the surface of macrophages are also an important basis for the classification of macrophages. CD68 and CD86 are the second surface markers of M-type macrophages, which can secrete inflammatory factors like tumor necrosis factor (TNF)-α, interleukin (IL)-1, and IL-6 after activation. Activation of M2-type macrophages increases the expression of CD68 and CD163 and secretion of transforming growth factor-β (TGF-β), IL-10, IL-4, and other anti-inflammatory factors [26, 27]. Toll-like receptors (TLR), mainly distributed on the surface of immune cells, for instance, mononuclear macrophages, lymphocytes, and dendritic cells, are also expressed in the heart and are considered a bridge between immune response and inflammatory response [28, 29]. Nuclear factor kappa B (NF-κB) is an essential regulating factor for the transcription of inflammatory genes and is essential for the macrophage inflammatory response. After activation, NF-κB is transferred from the cytoplasm into the nucleus and is essential for regulating inflammatory factors [30]. The activated macrophage surface TLR4 receptor is activated and binds to the corresponding ligand to activate NF-κB.

According to Figure 3(a), relative to the sham group, other groups had significantly increased CD86 on day 3 and decreased in group YQHX and METO in comparison to the group of MI on day 7 (Figure 3(b)). The change of CD163 was not obvious at 3 days (Figure 3(c)) but increased at 7 days (Figure 3(d)).

Western blot results showed (Figure 4) that, on day 3, CD86 content underwent an increase in the model group and enhanced in the MI group on day 7. In comparison with the group of MI, the protein content of CD163 in the myocardial tissue at the edge of infarction in the medication group had a substantial increment. In addition, the CD163 expression in the medication group increased significantly on the 7th day compared to that on the 3rd day. On day 3 after MI, a significantly higher expression of TLR4 and NFκB was detected in the group of MI than in the group of sham, but the change was not obvious in the medication group. On day 7 after MI, TLR4 and NF-κB expressions were lower in the medication group than in the MI group.

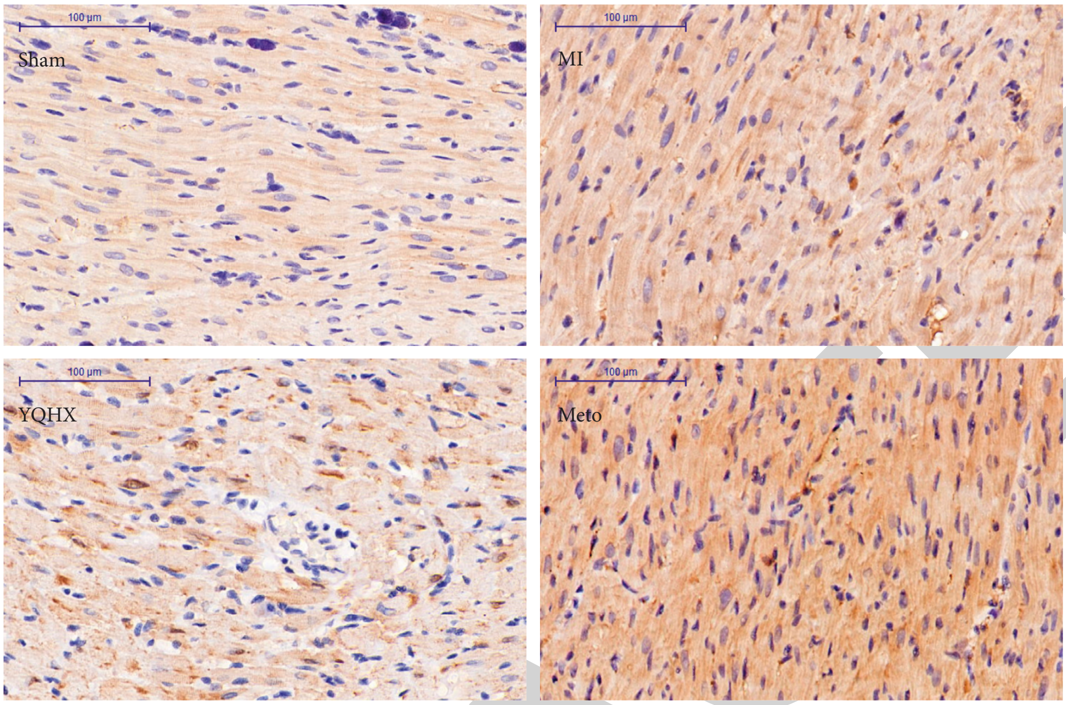

(a)

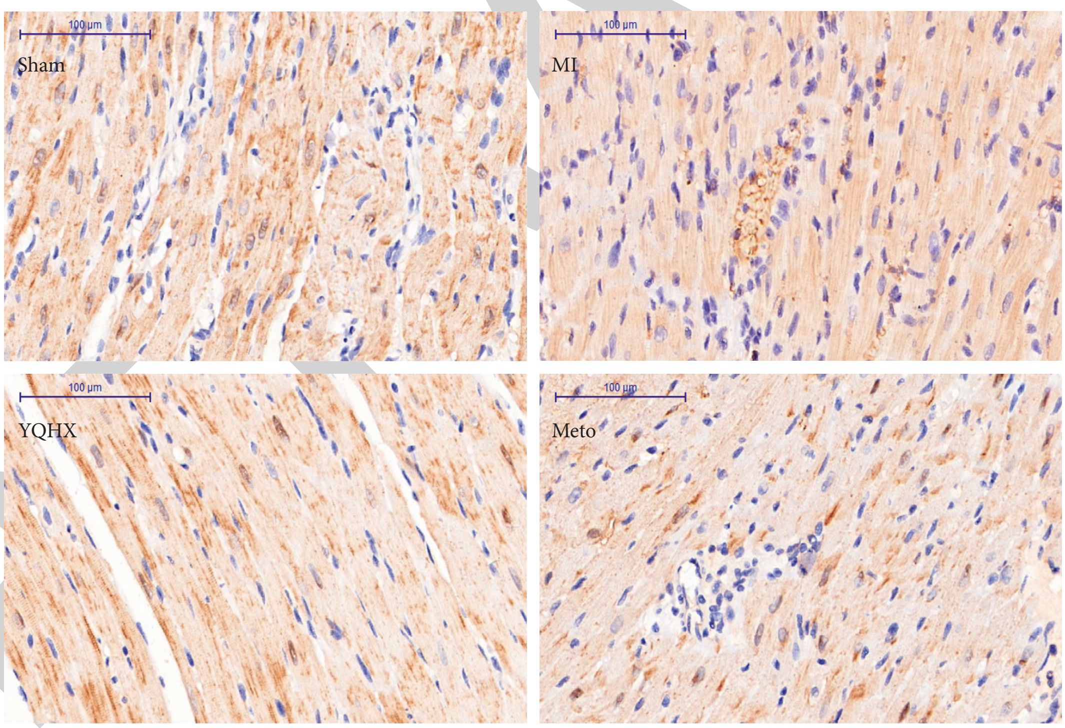

(b)

Figure 2: Continued.

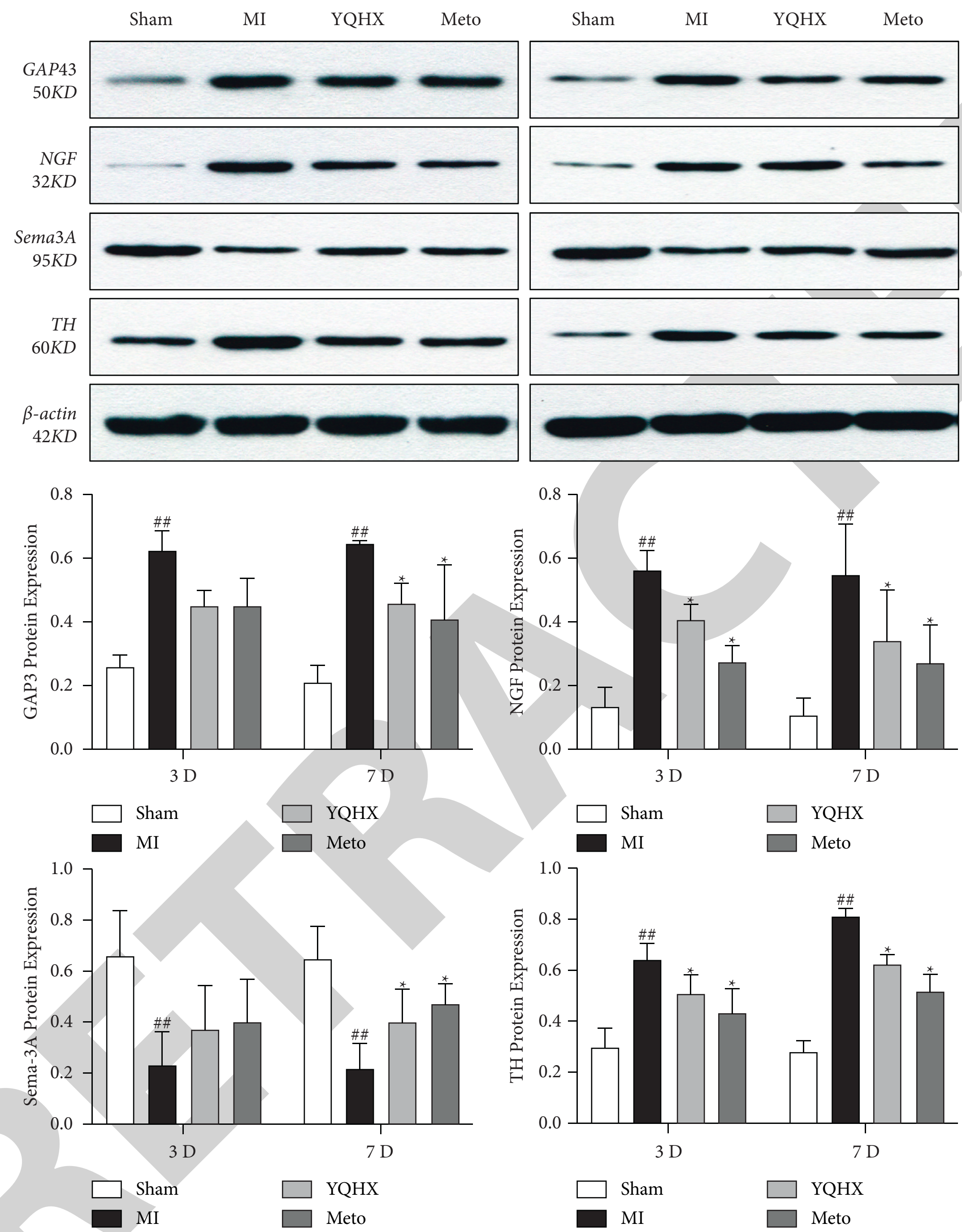

(c)

Figure 2: (a) Immunohistochemical staining for examining the positive, sympathetic nerve fibers at the edge of MI (myocardial infarction) in rats 3 days after MI (scale). (b) Immunohistochemical staining was used to observe the positive, sympathetic nerve fibers at the edge of myocardial infarction in rats 7 days after MI (myocardial infarction). (c) The influence of YQHX on GAP43, TH, SEMA-3A, and NGF expression. $^{\#\#}P < 0.01$, vs. the sham operation group; $^{*}P < 0.01$, vs. MI.

According to the above results, M1-type CD86 macrophages promoting inflammation increased significantly on day 3 after MI. On day 7, macrophages of M2-type CD163, which inhibits inflammation, increased, consistent with the differentiation process of macrophages after inflammation. It is noteworthy that, after 7 days of continuous administration, CD86 expression in the medication group decreased relative to that in the model group, while the content of CD163 increased superior to that in the model group. Concurrently, the levels of inflammatory factors TRL4 and NFκB also decreased. Combined with immunohistochemical findings, further clarification proves that YQHX can promote M2-type macrophage secretion and decrease MI breakdown cell to minimize MI in the rat with myocardial

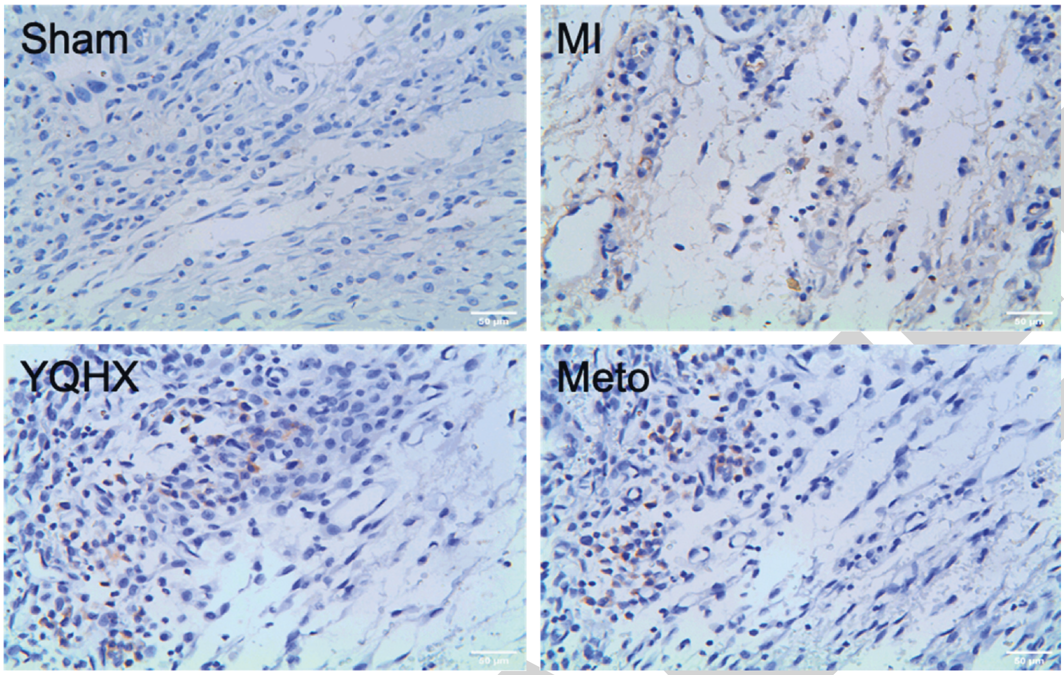

(a)

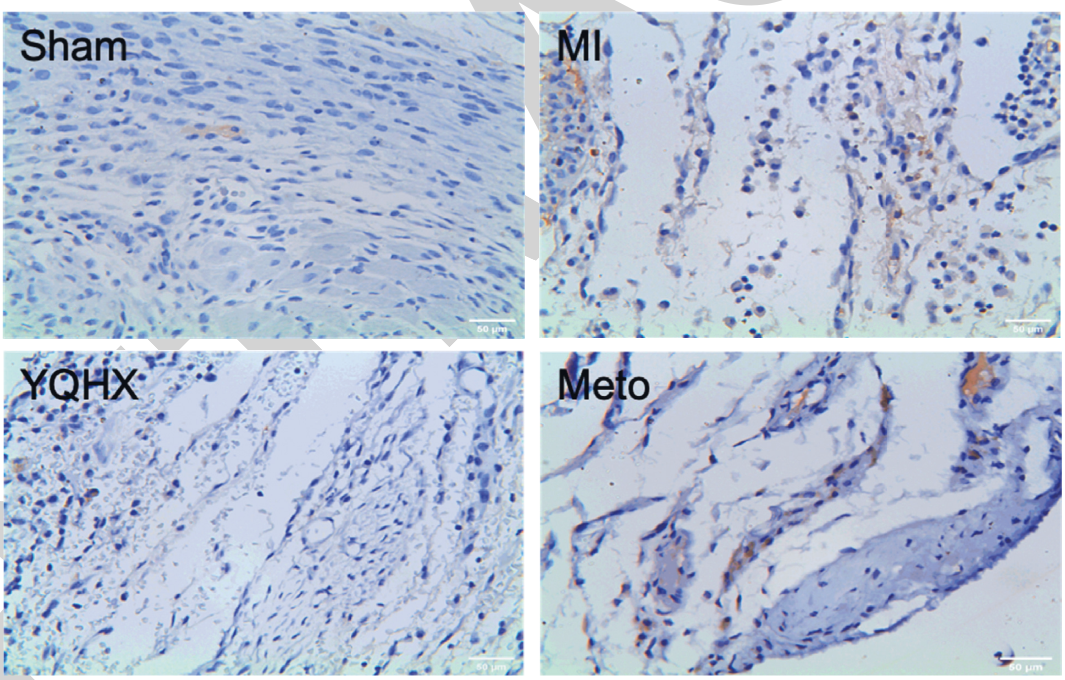

(b)

Figure 3: Continued.

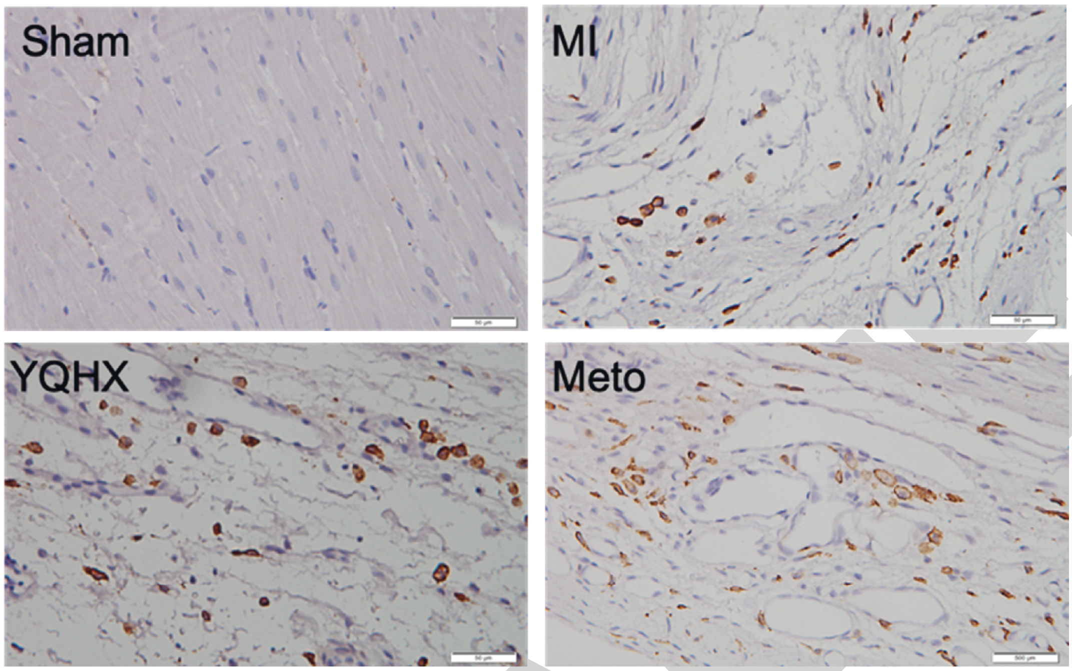

(c)

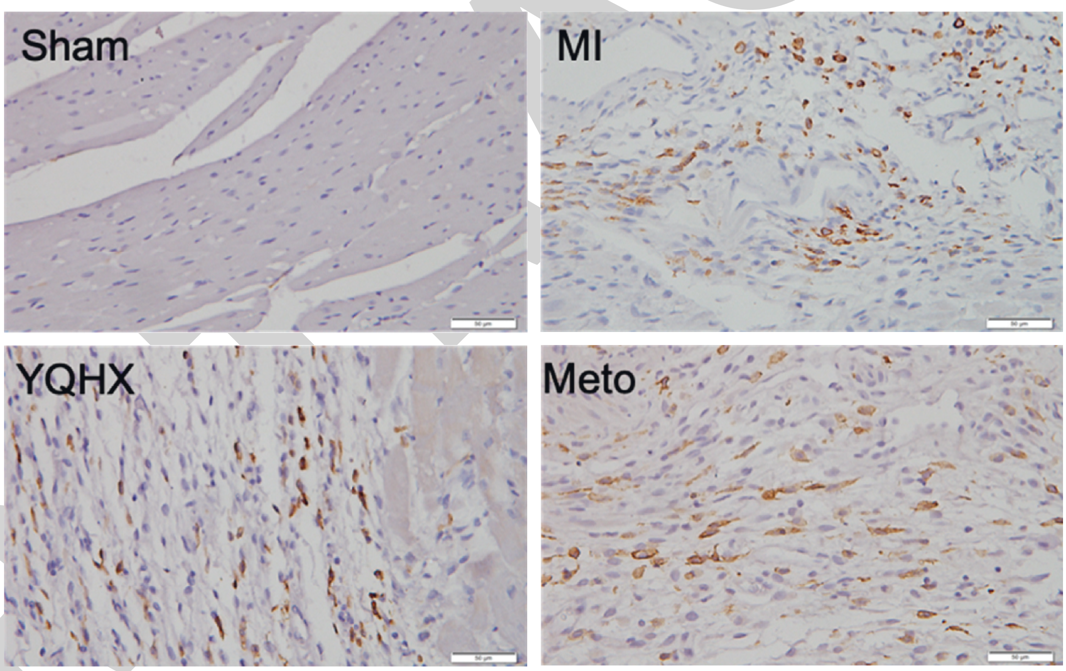

(d)

Figure 3: (a) Immunohistochemical analysis to detect the CD86 macrophages at the edge of myocardial infarction (MI) in rats 3 days after myocardial infarction. (b) Immunohistochemical analysis to observe the CD86 macrophages at the edge of MI in rats 7 days after myocardial infarction. (c) Immunohistochemical analysis to observe the CD163 macrophages at the edge of MI in rats 3 days following myocardial infarction. (d) Immunohistochemical analysis to observe the CD163 macrophages at the edge of MI in rats 7 days after myocardial infarction.

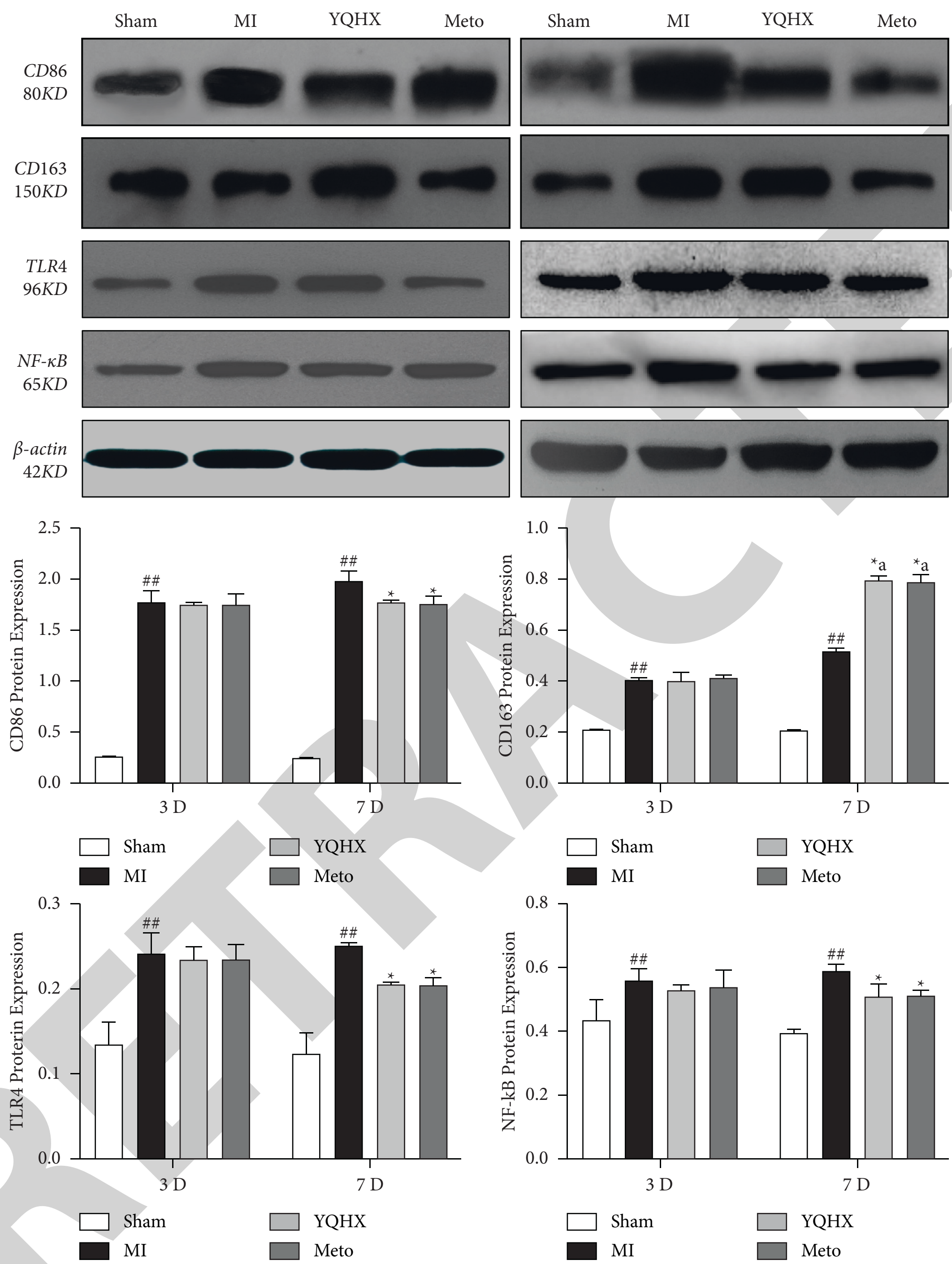

FIGURE 4: The expression of CD86, CD163, TLR4, and NFκB in each group of rats; the tissue of the infarct marginal area was examined. $^{\#\#}P < 0.01$, vs. the sham operation group; $^{*}P < 0.01$, vs. the MI model group; a$P < 0.01$, vs. the model group of 3 days.

inflammatory response in the edge area of infarction to reduce the myocardial injury, promote the freshmen, reshape myocardial tissue, and improve heart function and recovery.

4. Discussion

In this study, we examined the mechanism by which YQHX inhibits MI-induced sympathetic nerve regeneration. Sympathetic nerve remodeling after MI may result in arrhythmias and sudden death. YQHX downregulates the expression of TLR4 and NFκB in MI rats, induces macrophage phenotype transformation from M1 to M2, and reduces the expression of nerve growth factors, thus improving sympathetic nerve germination and innervation, consistent with previous findings. TH-positive nerve fiber clusters were found at the edge of MI, and YQHX treatment improved sympathetic remodeling by decreasing TH-positive nerve fiber density, decreasing NGF and GAP43 expression, and increasing SEMA-3A expression.

The pathogenesis of MI is closely associated with the acute inflammatory response. The inflammatory response due to MI aggravates tissue damage and functional impairment, and the inflammatory response is also the prerequisite for healing and tissue scar formation. Anti-inflammatory therapy can reduce the scope of infarction in treating MI to prevent cardiac remodeling and further cardiac failure [31]. At the same time, sympathetic nerve germination after MI is closely related to inflammatory processes [8, 9, 32, 33] that lead to NGF synthesis locally by inflammatory cells, including myofibroblasts and macrophages. Nerve growth factor (NGF) is a powerful neurochemokine that is essential for sympathetic nerve germination, survival, differentiation, and synaptic functions during heart injury [34]. Studies have shown that direct intracardial transduction lentivirus vectors carry NGF-targeted siRNA (short interfering RNA) to downregulate NGF. It can significantly improve the remodeling and budding of the sympathetic nerve [35]. Moreover, Hasan et al. [13] opined that NGF is a necessary condition for the germination of the sympathetic nerve, and NGF is widely expressed in the area around infarction and is associated with the aggregation of a large number of filtered macrophages and myofibroblasts. Wernli et al. [12] confirmed that macrophage consumption after MI significantly reduced NGF content and inhibited sympathetic overregulation.

As reported in previous studies, this study data also showed that after MI, NGF, and GAP-43 expressions were upregulated, SEMA-3A expressions were downregulated, TH-positive nerve fiber density was increased, and sympathetic overinnervation selectively occurred in regions containing a large number of macrophages. YQHX downregulates NGF expression by inhibiting the differentiation of macrophages; therefore, it is like that macrophages may be involved in the relationship between inflammation and cardiac sympathetic innervation induced by MI through the regulation of NGF expression.

At the early stage of 1–3 days after myocardial infarction, M1-type macrophages mainly secreted TNF-α, inducible nitric oxide synthase (iNOS), IL-6, and additional factors involved in inflammation response, which mainly phagocytosed apoptotic and necrotic cell fragments. However, long-term inflammatory reactions lead to poor ventricular remodeling. From 3 to 7 days (middle and late stage), M2 macrophages are the primary type, and type 2 predominantly secretes arg-1, TGF-β, etc., which mainly promote angiogenesis and degradation of extracellular matrix, stimulate fibroblasts into myofibroblast differentiation, participate in the occurrence of myocardial fibrosis [36, 37], and participate in anti-inflammatory and tissue repair [38,39]. CD68 macrophages and α fibroblasts are important sources of NGF synthesis and release. In MI rat models, clodronate liposomes can reduce the density of sympathetic axons and NGF expression by 69% without affecting the number of T cells; hence, macrophages are considered the main cause of sympathetic nerve regeneration after MI [12, 13]. The activation of P2X purinoceptor 7 (P2X7R) of M1-type macrophages promotes the generation of NLR family pyrin domain containing 3 (NLRP3)/IL-1β, increases the generation of NGF, and causes the pathological process of sympathetic nerve regeneration after MI [40]. Blocking P2X7R can inhibit NLRP3/IL-1β pathway and reduce sympathetic nerve regeneration after MI. Therefore, it is speculated that M1-type macrophages of the heart promote the formation of NGF, participate in cardiac nerve remodeling, and impact arrhythmia after MI, concurrent with the results of this study.

Herein, the infiltration of M1 and M2 macrophages in the injured myocardial tissue was observed by immunohistochemical and western blotting. CD86 macrophages were more infiltrated in the myocardial tissue after MI. Further analysis was made on the classification of infiltrated macrophages. A decrease in inflammatory cells was observed. Compared with the MI group, the inflammatory M1-type CD86 macrophages decreased, while the anti-inflammatory M2-type CD163-positive macrophages increased significantly, thus indicating that YQHX can alleviate myocardial inflammation in the infarct margin of MI rats by promoting the secretion of M2-type macrophages and inhibiting the secretion of M1-type macrophages to alleviate myocardial injury, promote the regeneration and remodeling of myocardial tissue, and facilitate the recovery of cardiac function.

This study suggests that YQHX can affect the phenotypic changes of macrophages after MI, which may downregulate NGF expression. YQHX was confirmed to polarize macrophages into the M2 phenotype, and the levels of TLR4 and NFKB are downregulated. Meanwhile, GAP-43 and NGF expressions and the TH and positive nerve fibers density also decreased, and the expression of SEMA-3A increased. Thus, we hypothesize that the phenotype of macrophages is important for sympathetic regeneration.

5. Conclusion

In summary, through these experimental results, we confirm that YQHX can affect the phenotypic changes of macrophages after MI and regulate the expression of neuro-associated factors after MI. It is speculated that the phenotype of macrophages is essential for sympathetic nerve regeneration, and YQHX has an effect on sympathetic nerve regeneration. However, the regulatory mechanisms of YQHX with macrophages and sympathetic nerves should be studied further in cellular and animal experiments. With the deepening of the investigation on sympathetic nerves and inflammation after MI, the early intervention of inflammation and factors associated with nerve remodeling and the application of traditional Chinese medicine in the convalescence stage of MI may be a significant target and therapy plan to diminish and treat cardiovascular diseases in the next years.

Abbreviations

MI: Myocardial infarction
YQHX: Yiqi Huoxue decoction
TLR4: Toll-like receptor 4

NF-κB: Nuclear factor kappa B
GAP43: Growth-associated protein 43
NGF: Nerve growth factor
TH: Tyrosine hydroxylase
TCM: Traditional Chinese medicine
HPLC-LTQ-Orbitrap MS: The high-performance liquid chromatography coupled with linear ion trap quadrupole Orbitrap high-resolution mass spectrometry
API: Active pharmaceutical ingredients
SPF: Specific pathogen free
LAD: Left anterior descending
ECG: Electrocardiogram
METO: Metoprolol
EF: Ejection fraction
LVIDd: Left ventricular end-diastolic diameter
LVIDs: Left ventricular end-systolic diameter
HE: Hematoxylin and eosin
EDTA: Ethylenediaminetetraacetic acid
PBS: Phosphate buffered saline
HRP: Horseradish peroxidase
DAB: 3, $3'$-diaminobenzidine
PVDF: Polyvinylidene difluoride
TBST: Tris buffer saline tween20
TNF: Tumor necrosis factor
IL: Interleukin
TGF-β: Transforming growth factor-β definition
iNOS: Inducible nitric oxide synthase
siRNA: Short interfering RNA
SEMA-3A: Semaphorin3A
NLRP3: NLR family pyrin domain containing 3
P2X7R: P2X purinoceptor 7
LSD: Least significant difference
BCA: Bicinchoninic acid
RIPA: Radioimmunoprecipitation assay.

Data Availability

The data employed to support the achievements of the present survey can be obtained from the corresponding author upon request.

Conflicts of Interest

The authors declare that they have no conflicts of interest.

Acknowledgments

This work was supported by the National Natural Science Foundation of China (81774031).

References

[1] D. Jenča, V. Melenovský, J. Stehlik et al., "Heart failure after myocardial infarction: incidence and predictors," *ESC Heart Failure*, vol. 8, no. 1, pp. 222–237, 2021 February.

[2] T. M. Kolettis, "Autonomic function and ventricular tachyarrhythmias during acute myocardial infarction," *World Journal of Experimental Medicine*, vol. 8, no. 1, pp. 8–11, 2018.

[3] R. Li, J. Wu, Z. Lin et al., "Single injection of a novel nerve growth factor coacervate improves structural and functional regeneration after sciatic nerve injury in adult rats," *Experimental Neurology*, vol. 288, pp. 1–10, 2017.

[4] C. Cabo and P. A. Boyden, "Electrical remodeling of the epicardial border zone in the canine infarcted heart: a computational analysis," *American Journal of Physiology - Heart and Circulatory Physiology*, vol. 284, no. 1, pp. H372–H384, 2003.

[5] S. D. Skaper, "The neurotrophin family of neurotrophic factors: an overview," *Neurotrophic Factors*, vol. 846, pp. 1–12, 2012.

[6] J. Hu, C.-X. Huang, P.-P. Rao et al., "Inhibition of microRNA-155 attenuates sympathetic neural remodeling following myocardial infarction via reducing M1 macrophage polarization and inflammatory responses in mice," *European Journal of Pharmacology*, vol. 851, pp. 122–132, 2019.

[7] M. Ieda, H. Kanazawa, K. Kimura et al., "Sema3a maintains normal heart rhythm through sympathetic innervation patterning," *Nature Medicine*, vol. 13, no. 5, pp. 604–612, 2007.

[8] L. I. Benowitz and P. G. Popovich, "Inflammation and axon regeneration," *Current Opinion in Neurology*, vol. 24, no. 6, pp. 577–583, 2011.

[9] Y. Wang, F. Suo, J. Liu et al., "Myocardial infarction induces sympathetic hyperinnervation via a nuclear factor-κB-dependent pathway in rabbit hearts," *Neuroscience Letters*, vol. 535, pp. 128–133, 2013.

[10] A. J. Mouton, X. Li, M. E. Hall, and J. E. Hall, "Obesity, hypertension, and cardiac dysfunction:novel roles of immunometabolism in macrophage activation and inflammation," *Circulation Research*, vol. 126, no. 6, pp. 789–806, 2020.

[11] M. C. Caroleo, N. Costa, L. Bracci-Laudiero, and L. Aloe, "Human monocyte/macrophages activate by exposure to LPS overexpress NGF and NGF receptors," *Journal of Neuroimmunology*, vol. 113, no. 2, pp. 193–201, 2001.

[12] G. Wernli, W. Hasan, A. Bhattacherjee, N. Rooijen, and P. G. Smith, "Macrophage depletion suppresses sympathetic hyperinnervation following myocardial infarction," *Basic Research in Cardiology*, vol. 104, no. 6, pp. 681–693, 2009.

[13] W. Hasan, A. Jama, T. Donohue et al., "Sympathetic hyperinnervation and inflammatory cell NGF synthesis following myocardial infarction in rats," *Brain Research*, vol. 1124, no. 1, pp. 142–154, 2006.

[14] F. O. Martinez, A. Sica, A. Mantovani, and M. Locati, "Macrophage activation and polarization," *Frontiers in Bioscience*, vol. 13, no. 13, pp. 453–461, 2008.

[15] P. Xin, Y. Pan, W. Zhu, S. Huang, M. Wei, and C. Chen, "Favorable effects of resveratrol on sympathetic neural remodeling in rats following myocardial infarction," *European Journal of Pharmacology*, vol. 649, no. 1-3, pp. 293–300, 2010.

[16] V. El-Helou, C. Proulx, H. Gosselin et al., "Dexamethasone treatment of post-MI rats attenuates sympathetic innervation of the infarct region," *Journal of Applied Physiology*, vol. 104, no. 1, pp. 150–156, 2008.

[17] M. J. Yuan, C. X. Huang, Y. H. Tang et al., "A novel peptide ghrelin inhibits neural remodeling after myocardial infarction in rats," *European Journal of Pharmacology*, vol. 618, no. 1-3, pp. 52–57, 2009.

[18] J. Wu, S. Guo, X. Chen et al., "Yiqi Huoxue prescription can prevent and treat post-MI myocardial remodeling through promoting the expression of AMPK signal pathway," *Journal of Traditional Chinese Medical Sciences*, vol. 4, no. 3, pp. 235–244, 2017.

Hindawi
Journal of Healthcare Engineering
Volume 2023, Article ID 9849835, 1 page
https://doi.org/10.1155/2023/9849835

Retraction

Retracted: Exploring the Effect of Enbrel Softgels on PWI Indicators in VCIND Patients

Journal of Healthcare Engineering

Received 19 September 2023; Accepted 19 September 2023; Published 20 September 2023

This article has been retracted by Hindawi following an investigation undertaken by the publisher [1]. This investigation has uncovered evidence of one or more of the following indicators of systematic manipulation of the publication process:

(1) Discrepancies in scope
(2) Discrepancies in the description of the research reported
(3) Discrepancies between the availability of data and the research described
(4) Inappropriate citations
(5) Incoherent, meaningless and/or irrelevant content included in the article
(6) Peer-review manipulation

The presence of these indicators undermines our confidence in the integrity of the article's content and we cannot, therefore, vouch for its reliability. Please note that this notice is intended solely to alert readers that the content of this article is unreliable. We have not investigated whether authors were aware of or involved in the systematic manipulation of the publication process.

In addition, our investigation has also shown that one or more of the following human-subject reporting requirements has not been met in this article: ethical approval by an Institutional Review Board (IRB) committee or equivalent, patient/participant consent to participate, and/or agreement to publish patient/participant details (where relevant).

Wiley and Hindawi regrets that the usual quality checks did not identify these issues before publication and have since put additional measures in place to safeguard research integrity.

We wish to credit our own Research Integrity and Research Publishing teams and anonymous and named external researchers and research integrity experts for contributing to this investigation.

The corresponding author, as the representative of all authors, has been given the opportunity to register their agreement or disagreement to this retraction. We have kept a record of any response received.

References

[1] L. Cui, P. Li, J. Zhang, and X. Li, "Exploring the Effect of Enbrel Softgels on PWI Indicators in VCIND Patients," *Journal of Healthcare Engineering*, vol. 2022, Article ID 9681235, 7 pages, 2022.

Hindawi
Journal of Healthcare Engineering
Volume 2022, Article ID 9681235, 7 pages
https://doi.org/10.1155/2022/9681235

Research Article

Exploring the Effect of Enbrel Softgels on PWI Indicators in VCIND Patients

Lei Cui,[1] Pan Li,[2] Jingchen Zhang,[1] and Xiaofang Li[1]

[1]*Department of Neurology, Affiliated Hospital of Hebei University, Baoding, Hebei 071000, China*
[2]*Department of Neurology, Baoding No. 1 Central Hospital, Baoding, Hebei 071000, China*

Correspondence should be addressed to Xiaofang Li; lxf2530@hbu.edu.cn

Received 22 January 2022; Revised 21 February 2022; Accepted 26 February 2022; Published 6 April 2022

Academic Editor: Liaqat Ali

Objective. To investigate the effect of Enbrel softgels on the head nuclear magnetic (PWI) indices in patients with vascular cognitive impairment-no dementia (vascular cognitive impairment-no dementia, VCIND). *Methods*. Patients with confirmed VCIND hospitalized in the Department of Neurology of the Affiliated Hospital of Hebei University from April 2017 to April 2019 were included in the study, and they were divided into experimental and control groups (30 patients in each group) according to the difference of interventions. The PWI examination and neuropsychological assessment were performed at the beginning of the experiment, 12 w after treatment, and 48 w after treatment in the two groups. Score differences between the two groups and the preliminary demonstration of the clinical value of the MMSE and ADAS-Cog in the diagnosis of VCIND. *Results*. (1) The difference in PWI positivity rate between the two groups at the beginning of the experiment was not statistically significant ($P > 0.05$); the PWI positivity rate in the experimental group at 12 W was significantly lower than that in the control group ($P < 0.05$); the difference in PWI positivity rate between the two groups at 48 W was not statistically significant ($P < 0.05$); (2) the MMSE scores of patients in the experimental group at 12 W and 48 W were higher than those in the control group, and the ADAS-Cog scores were lower than those in the control group ($P < 0.05$). (3) The diagnostic AUCs of MMSE and ADAS-Cog for VCIND were 0.7960 (95% CI = 0.6411–0.9508, $P = 0.0037$) and 0.9291 (95% CI = 0.8390), respectively (95% CI = 0.8390–1.000, $P < 0.0001$). *Conclusion*. The addition of Enbrel softgels to concomitant therapy in VCIND patients can lead to changes in their PWI imaging indicators, which in turn can have a significant impact on their neuropsychological indicators, and quantitative analysis scales such as the MMSE and ADAS-Cog can be considered for the diagnostic treatment of VCIND.

1. Introduction

Vascular cognitive impairment-no dementia (VCIND) is a cognitive dysfunction due to cerebrovascular disease, generally ischaemic cerebrovascular lesions [1]. Patients can present with dysfunction in multiple or single cognitive domains such as visuospatial and executive abilities, memory, attention, language, abstraction, calculation, and orientation [2, 3]. These cognitive dysfunctions are often partially impaired and do not meet the diagnostic criteria for dementia, and the patient's ability to perform daily life is generally unaffected [4]. With the development of an ageing population and longer life expectancy in our society, the incidence of cerebrovascular disease is increasing, and the corresponding incidence of vascular cognitive dysfunction is also on the rise [5].

There is no effective drug to cure vascular cognitive dysfunction, but the symptoms of cognitive impairment can be further improved by controlling the risk factors of cerebrovascular disease and carrying out postischemic neuroprotective treatment to improve the quality of survival and delay the progression of the disease [6, 7]. Enbrel soft capsule is a new class I drug developed independently in China for the treatment of ischaemic stroke, and has been widely used in the acute clinical treatment of ischaemic cerebrovascular disease in recent years [8]. PWI is the most important clinical test for the diagnosis of intracranial lesions, which can calculate cerebral blood volume (rCBV), local cerebral blood flow (rCBF), and mean time to passage (MTT). It shows the blood flow in the capillary network, which in turn provides the functional status of oxygen and nutrients in the surrounding tissues and is used in the diagnosis and assessment of disease [9, 10]. In this paper, we propose to investigate the changes in PWI indicators after the application of Enbrel softgels to patients with VCIND by setting up a control group in order to provide a new reference for the clinical treatment and diagnostic assessment of these patients.

2. Materials and Methods

2.1. General Information. Patients with confirmed VCIND hospitalized in the Department of Neurology of the Affiliated Hospital of Hebei University from April 2017 to April 2019 were included in the study, and they were distinguished into experimental and control groups (30 patients in each group) according to the differences in interventions.

2.1.1. Inclusion Criteria. The inclusion criteria were as follows: (1) neuropsychological assessment of patients with cognitive impairment but not at the level of dementia; (2) MMSE ≥24 in the junior high school and above group and ≥20 in the primary school group (MMSE ≤28); (3) MRI of the head showing subcortical ischaemic vascular disease; and (4) age 60–75 years.

2.1.2. Exclusion Criteria. The exclusion criteria were as follows: (1) those with severe psychiatric or neurological disorders who cannot cooperate with the neuropsychological assessment examination; (2) those with other disorders affecting cognitive function or cognitive impairment due to drug dependence; (3) those with severe psychiatric disorders; (4) those with new cerebral infarction within 3 months prior to enrolment; (5) those with severe gastrointestinal, circulatory, urinary, and immune system disorders; (6) those who are allergic to the investigational drug; and (7) those who are unable to complete the head MRI.

2.2. Research Method. After admission, patients in both groups received conventional interventions, such as the application of drugs to improve cerebral blood flow, the start of hyperbaric oxygen chamber therapy, and the application of neurotrophic factors. Meanwhile, the control group was given nimodipine (manufacturer: Yabao Pharmaceutical Group Co., Ltd., specification 20 mg/tablet, and approval number: State Drug Quantifier H14022821) 30 mg/time, 3 times daily, for 90 days. The experimental group was supplemented with Enbep Soft Capsules (trade name: Butylphthalein Soft Capsules, manufacturer: Shiyang Pharmaceutical Group, Enbep Pharmaceutical Co., Ltd., specification 0.1 g/capsule, and approval number: Guo medicine quantity H20050299) 200 mg/dose, 3 times daily for 90 days.

2.3. Observational Indicators and Rubrics

2.3.1. Neuropsychological Scores. Neuropsychological scores were administered before the start of the trial, at 12 weeks of treatment, and at 48 weeks after treatment, using the MMSE and ADAS-cog scales, respectively. The staff conducting the assessments were trained and tested before the start of the trial to ensure the objectivity of the results. The scales were assessed in a dedicated neurology laboratory in a quiet and relaxed environment. The MMSE scale [11] is the most widely used cognitive screening scale both nationally and internationally, covering orientation, memory, attention, numeracy, language skills, and visuospatial abilities. The scale covers a wide range of topics but is relatively simple to administer and easy for the assessing practitioner to master. The total score ranges from 0 to 30, with higher scores indicating better cognitive functioning. However, the MMSE scale has limitations in differentiating normal elderly people from those with mild cognitive impairment. Therefore, this experiment also assessed patients on the ADAS-cog scale [12], which consists of 12 items covering memory, orientation, language, use, and attention and can assess the severity of cognitive symptoms and treatment changes in patients. In this trial, five subtests reflecting attention/executive function, including digit breadth (backwards recall), digit scratching, symbolic digit conversion, verbal fluency, and maze test, were added to it to further assess vascular cognitive impairment.

2.3.2. Head MRI (PWI). PWI (PWI parameters: SE-EPI sequence, TR 1500 ms, TE 16 ms, layer thickness set to 4 mm, spacing set to 0 mm, contrast agent injected via elbow vein using a high-pressure syringe, 0.15 ml/kg injected according to body weight, and flow rate set to 4 ml/s) was used to investigate brain perfusion in the two groups of patients at the beginning of the experiment, 12 W of the experiment, and at 48 W of the experiment. The patients with reduced perfusion in the PWI study area were defined as positive, and the difference in the rate of positive PWI between the two groups at different observation times was recorded.

2.4. Statistical Methods. The SPSS22.0 statistical software was chosen to analyse the data collected in the study, in which the measures were expressed as mean ± standard deviation, and the tests of normal distribution and chi-square were carried out. The difference between groups was tested using the chi-square test and the diagnostic value was analyzed using the ROC curve, with $P < 0.05$ being taken as a statistically significant difference. Graphpad prism 8.3 was used for this study [13].

3. Results

3.1. Comparison of the Differences in Baseline Clinical Information between the Two Groups. The gender, age, and previous disease history of the two groups were included in the study, and a comparison of the differences between the groups was implemented. The results showed that the differences between the groups in terms of the above baseline clinical information were not statistically significant ($P > 0.05$), suggesting that the two groups were comparable (Table 1).

3.2. Analysis of the Changes in PWI Indicators before and after the Intervention in the Two Groups. The PWI test was carried out at the beginning of the experiment at w 12 and w 48 for the two groups of patients, respectively, and the positive rate of PWI in the group at different observation times was recorded and compared between the groups (0.05). At 12 w after treatment, there was 1 positive PWI case in the experimental group, with a positive rate of 3.33%, and 7 positive PWI cases in the control group, with a positive rate of 23.33%, with a significant difference between the two groups ($P < 0.05$). At 48 w after treatment, there was 1 positive PWI case in the experimental group, with a positive rate of 3.33%, and 5 positive PWI cases in the control group, with a positive rate of 16.67%, with no significant difference between the two groups ($P > 0.05$) (Table 2 and Figure 1) and Figure 2.

3.3. Comparison of Neuropsychological Scores between the Two Groups of Patients before and after the Intervention. The neuropsychological functioning of the two groups was assessed using the MMSE and ADAS-Cog scores at the beginning of the experiment, at experiment 12 W and at experiment 48 W, respectively, and the differences between the groups were compared. The results showed that the difference between the two groups of patients' MMSE scores at the beginning of the experiment was not statistically significant ($P > 0.05$), and the MMSE scores of the patients in the experimental group were significantly higher than those of the control group at both the 12th W and 48th W of the experiment, and the difference between the groups was statistically significant ($P < 0.05$). The MMSE scores were higher in the experimental group than at the beginning of the experiment at both the 12th W and 48th W of the experiment ($P < 0.05$), while the difference was not statistically significant in the control group before and after the comparison ($P > 0.05$). The difference in ADAS-cog scores between the two groups at the beginning of the experiment was not statistically significant ($P > 0.05$), while the ADAS-cog scores of patients in the experimental group were significantly lower than those in the control group at both the 12th W and 48th W of the experiment, and the difference between the groups was statistically significant ($P < 0.05$). The ADAS-cog scores were lower in the experimental group than at the beginning of the experiment at both the 12th W and 48th W of the experiment in the within-group comparison ($P < 0.05$), while the difference was not statistically significant in the control group before and after the comparison ($P > 0.05$) (Table 3 and Figure 3).

3.4. Analysis of the Diagnostic Value of MMSE and ADAS-Cog Scores for VCIND. The diagnostic ROC curves for the MMSE and ADAS-cog scores for VCIND were plotted separately, and their AUCs were calculated, showing AUCs of 0.7960 (95% CI = 0.6411–0.9508, $P = 0.0037$) and 0.9291 (95% CI = 0.8390–1.000, $P < 0.0001$) for the above scales, respectively (Figure 4).

4. Discussion

In recent years, the incidence of dementia has increased year by year as the population ages [14]. Currently, approximately about 30 million people worldwide suffer from dementia, and it is expected that this number will increase to 42 million by 2021 [15]. Vascular injury is the second most common cause of dementia, with subcortical ischaemic cerebrovascular disease, typically caused by lacunar infarction or white matter injury, being the most common cause of vascular cognitive impairment [16]. Vascular nondementia cognitive impairment (VCIND) refers to early or mild cognitive impairment due to vascular injury, a state of cognitive impairment between normal individuals and dementia, and is generally considered to be the early stage of vascular cognitive impairment, with a variety of risk factors that are highly intervenable. The incidence of dementia is also significantly reduced if appropriate interventions are provided [17, 18]. Studies have shown that approximately 40% of patients with VCIND progress to vascular dementia within 2 years, and those who have progressed to vascular dementia experience irreversible deterioration [19], so appropriate intervention and treatment of patients with VCIND can help improve the prognosis and quality of life of older people with vascular injury.

Enbep softgel is a butanol-based soft gel capsule commonly used in the treatment of mild to moderate acute ischaemic stroke. It has been shown to have a variety of pharmacological effects and to be a comprehensive treatment for the symptoms of neurological deficits caused by ischaemic stroke, with positive implications for improving the patient's ability to live [20]. In this study, the effect of Enbrel soft gelatin capsules on the PWI index of VCIND patients was analyzed by establishing a control group. The results showed that compared to the control group, the experimental group with Enbrel soft gelatin capsules showed a significant decrease in the PWI positivity rate at 12 weeks of treatment compared to the beginning of the experiment, and the PWI positivity rate at 12 weeks of treatment was significantly lower than that of the control group, which This suggests that the intervention effect of Enbrel softgels was significant, which is consistent with the findings of other scholars. A study conducted on 58 patients with chronic cerebral insufficiency showed that Enbep Soft Capsules had a good clinical intervention effect on chronic cerebral insufficiency, and patients treated with the drug showed significant improvement in transcranial Doppler ultrasound indices [21]. The authors of this paper analyzed that butylphenol is a chemical component that can protect brain tissue in multiple ways. This substance can use the increase of nitric oxide and prostaglandin in the cerebrovascular endothelium to reduce intracellular calcium concentration, thus achieving the effect of inhibiting glutamate release and inhibiting oxygen free radical damage to brain cells, and also

Table 1: Comparison of baseline information between the two groups of patients $(\overline{x} \pm s)/[n(\%)]$.

General clinical information		Experimental group ($n = 30$)	Control group ($n = 30$)	t/χ^2	P
Gender	Male	18	17	0.069	0.793
	Female	12	13		
Average age (years)		69.57 ± 3.41	69.17 ± 3.01	0.482	0.632
Average weight (kg)		70.19 ± 2.39	69.98 ± 3.01	0.229	0.766
With or without medical insurance	Yes	27	28	0.218	0.64
	None	3	2		
High blood pressure	Yes	6	5	0.111	0.739
	None	24	25		
Diabetes	Yes	4	5	0.131	0.718
	None	26	25		
High blood cholesterol	Yes	7	8	0.089	0.766
	None	23	22		
Coronary heart disease	Yes	4	7	1.002	0.317
	None	26	23		

Table 2: Analysis of the changes in PWI indicators before and after the intervention in the two groups $[n(\%)]$.

Group	Number of examples	Start of the experiment	Experiment 12 w	Experiment 48 w
Experimental group	30	6(20.00)	1(3.33)	1(3.33)
Control group	30	7(23.33)	7(23.22)	5(16.67)
χ^2	—	0.098	5.192	2.963
P	—	0.754	0.023	0.085

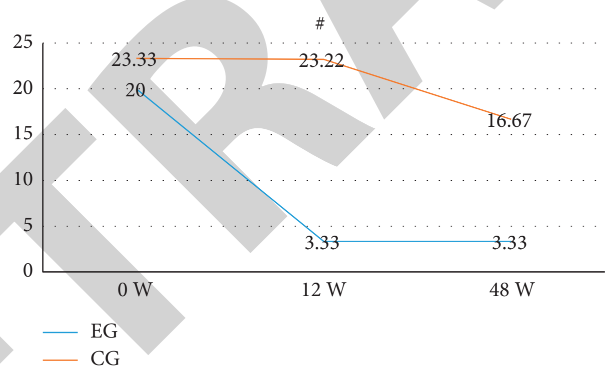

Figure 1: Analysis of the changes in PWI indicators before and after the intervention in the two groups The difference in DWI positivity between the two groups at the beginning of the experiment was not statistically significant ($P > 0.05$), the DWI positivity rate in the experimental group was significantly lower than that in the control group at the 12th W of the experiment ($P < 0.05$), and the difference in DWI positivity between the two groups at the 48th week of the experiment was not statistically significant ($P > 0.05$).

improving ischaemic and hypoxic symptoms by increasing microcirculation and blood flow in the ischaemic areas of brain tissue, with multiple mechanisms. It can also improve the symptoms of ischemia and hypoxia by increasing microcirculation and blood flow in the ischaemic area of brain tissue and improving the impaired functional state of brain tissue brought about by vascular injury through multiple mechanisms [22].

The paper further demonstrates the effect of Enbrel softgels on the neurobiological indicators of VCIND patients. The data show that the MMSE scores of the patients in the experimental group were higher than those of the control group, and the ADAS-cog scores were lower than those of the control group at both time points, 12 and 48 weeks after receiving the experiment, suggesting that the use of Enbrel softgels effectively improved the neurological function of VCIND patients and also improved the clinical manifestations of Alzheimer's disease. A randomized controlled study conducted on 178 acute stroke patients found that the application of Enbrel capsules reduced the incidence of poststroke dementia from 14.61% to 5.62% and improved the patients' cognitive function scores from (24.20 ± 4.43) to (25.30 ± 2.79) and behavioral ability scores from (52.40 ± 17.70) to (57.10 ± 13.30), a significant change [23]. Current animal experiments have demonstrated that butanol has a strong anti-cellular ischaemic-hypoxic effect, reduces the infarct area of local cerebral ischemia in rats, inhibits neuronal apoptosis, and inhibits thrombus

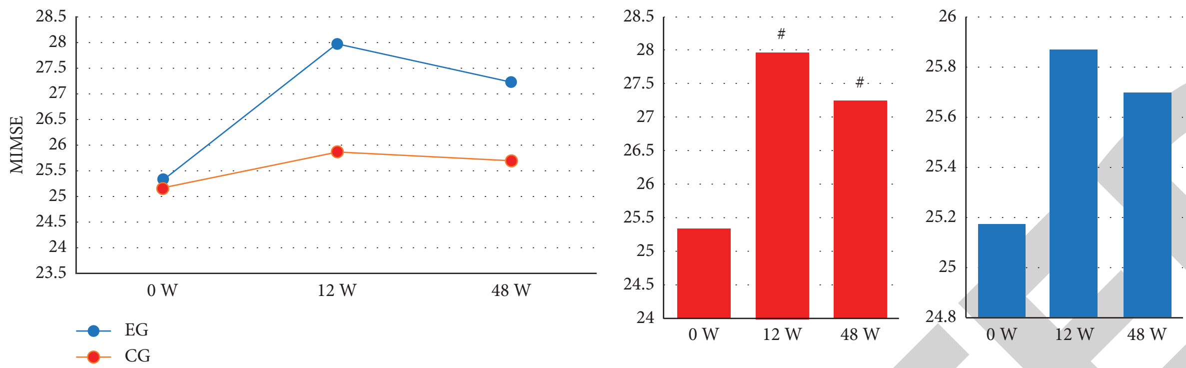

(a) (b) (c)

FIGURE 2: Comparison of MMSE scores between the two groups before and after the intervention. The comparison showed that the difference between the two groups of patients' MMSE scores before the experiment was not statistically significant ($P > 0.05$), while the MMSE scores of the experimental group were higher than those of the control group at both the 12th W and 48th W of the experiment ($P < 0.05$) (a). Within the group, prepost variability was compared, with the experimental group (b) having higher MMSE scores at both the 12th W and 48th W than at the beginning of the experiment ($P < 0.05$), while the control group (c) did not have statistically significant differences in prepost comparisons ($P > 0.05$). # represents a statistically significant difference (Table 4).

TABLE 3: Comparison of MMSE scores between the two groups before and after the intervention ($\overline{x} \pm s$).

Group	Number of examples	Start of the experiment	Experiment 12 w	Experiment 48 w
Experimental group	30	25.33 ± 1.09	$27.97 \pm 0.96^{\#}$	$27.23 \pm 1.19^{\#}$
Control group	30	25.17 ± 1.02	25.87 ± 0.94	25.70 ± 0.99
T	—	0.587	7.827	5.414
P	—	0.559	<0.001	<0.001

Note. Comparison with the beginning of the experiment, $^{\#}P < 0.05$

TABLE 4: Comparison of ADAS-cog scores before and after intervention between the two groups ($\overline{x} \pm s$).

Group	Number of examples	Start of the experiment	Experiment 12 w	Experiment 48 w
Experimental group	30	16.40 ± 0.93	$14.93 \pm 1.31^{\#}$	$15.00 \pm 1.17^{\#}$
Control group	30	16.37 ± 0.93	16.53 ± 0.94	16.90 ± 1.24
T	—	0.125	5.435	6.104
P	—	0.901	<0.001	<0.001

Note. Comparison with the beginning of the experiment, $^{\#}P < 0.05$.

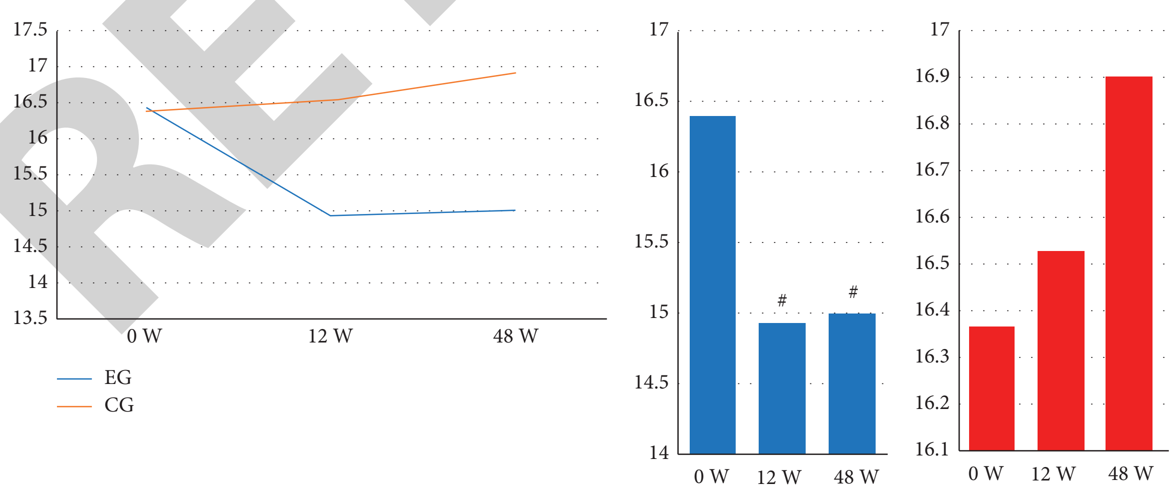

(a) (b) (c)

FIGURE 3: Comparison of ADAS-cog scores between the two groups before and after the intervention. The comparison showed that the difference between the two groups in ADAS-cog scores before the experiment was not statistically significant ($P > 0.05$), and the ADAS-cog scores in the experimental group were lower than those in the control group at both the 12th W and 48th W of the experiment ($P < 0.05$) (a) Within-group, prepost variability was compared, with the experimental group (b) having lower ADAS-cog scores at both the 12th W and 48th W than at the beginning of the experiment ($P < 0.05$), while the control group (c) had no statistically significant differences in prepost comparisons ($P > 0.05$). # represents a statistically significant difference.

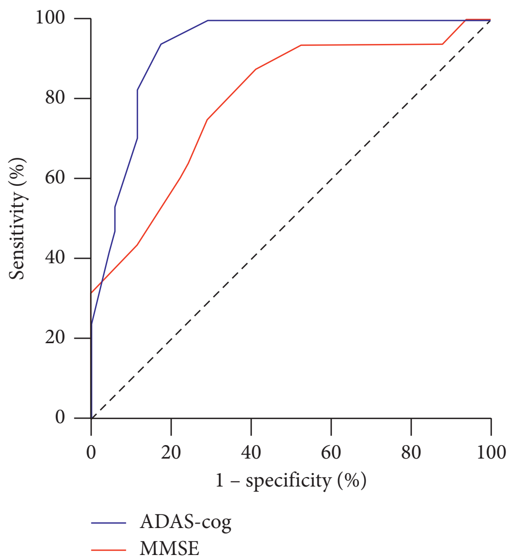

Figure 4: Analysis of the diagnostic value of MMSE and ADAS-cog scores for VCIND. The diagnostic AUC for VCIND was 0.7960 (95% CI = 0.6411–0.9508, $P = 0.0037$) and 0.9291 (95% CI = 0.8390–1.000, $P < 0.0001$) for MMSE and ADAS-cog scores, respectively.

formation, which the authors of this paper suggest is an important reason why Enbrel capsules can improve neurobiological scores in VCIND patients [24]. Finally, the paper also verified the value of MMSE and ADAS-cog scores in VCIND patients by plotting ROC curves, and the results suggested a better diagnostic value, which may provide a new reference for the clinical identification of VCIND patients.

In summary, the addition of Enbrel softgels to concomitant therapy in VCIND patients can lead to changes in their PWI imaging indicators, which in turn can have a significant impact on their neuropsychological indicators, and quantitative analysis scales such as the MMSE and ADAS-Cog can be considered for use in the diagnostic treatment of VCIND.

Data Availability

The data used to support the findings of this study are available from the corresponding author upon request.

Conflicts of Interest

The author declares that there are no conflicts of interest.

Authors' Contributions

The authors Lei Cui and Pan Li contributed equally to this work.

Acknowledgments

This work in this paper was supported by Department of Neurology, Affiliated Hospital of Hebei University.

References

[1] C. Iadecola, M. Duering, V. Hachinski et al., "Vascular cognitive impairment and dementia," *Journal of the American College of Cardiology*, vol. 73, no. 25, pp. 3326–3344, 2019.

[2] W. M. Van der Flier, I. Skoog, J. A. Schneider et al., "Vascular cognitive impairment," *Nature Reviews Disease Primers*, vol. 4, no. 1, p. 18003, 2018.

[3] M.-K. Sun, "Potential therapeutics for vascular cognitive impairment and dementia," *Current Neuropharmacology*, vol. 16, no. 7, pp. 1036–1044, 2018.

[4] V. Frantellizzi, A. Pani, M. Ricci, N. Locuratolo, F. Fattapposta, and G. De Vincentis, "Neuroimaging in vascular cognitive impairment and dementia: a systematic review," *Journal of Alzheimer's Disease*, vol. 73, no. 4, pp. 1279–1294, 2020.

[5] M. U. Farooq, J. Min, C. Goshgarian, and P. B. Gorelick, "Pharmacotherapy for vascular cognitive impairment," *CNS Drugs*, vol. 31, no. 9, pp. 759–776, 2017.

[6] D. G. Loughrey, M. E. Kelly, G. A. Kelley, S. Brennan, and B. A. Lawlor, "Association of age-related hearing loss with cognitive function, cognitive impairment, and dementia," *JAMA Otolaryngology-Head & Neck Surgery*, vol. 144, no. 2, pp. 115–126, 2018.

[7] F. Lyu, D. Wu, C. Wei, and A. Wu, "Vascular cognitive impairment and dementia in type 2 diabetes mellitus: an overview," *Life Sciences*, vol. 254, Article ID 117771, 2020.

[8] T. Yang, Y. Sun, Z. Lu, R. K. Leak, and F. Zhang, "The impact of cerebrovascular aging on vascular cognitive impairment and dementia," *Ageing Research Reviews*, vol. 34, pp. 15–29, 2017.

[9] G. J. Biessels and F. Despa, "Cognitive decline and dementia in diabetes mellitus: mechanisms and clinical implications," *Nature Reviews Endocrinology*, vol. 14, no. 10, pp. 591–604, 2018.

[10] J. O. Kim, S. J. Lee, and J.-S. Pyo, "Effect of acetylcholinesterase inhibitors on post-stroke cognitive impairment and vascular dementia: a meta-analysis," *PLoS One*, vol. 15, no. 2, Article ID e0227820, 2020.

[11] M. Simonetto, M. Infante, R. L. Sacco, T. Rundek, and D. Della-Morte, "A novel anti-inflammatory role of omega-3 PUFAs in prevention and treatment of atherosclerosis and vascular cognitive impairment and dementia," *Nutrients*, vol. 11, no. 10, p. 2279, 2019.

[12] N. Kandiah, P. A. Ong, T. Yuda et al., "Treatment of dementia and mild cognitive impairment with or without cerebrovascular disease: expert consensus on the use of Ginkgo biloba extract, EGb 761," *CNS Neuroscience and Therapeutics*, vol. 25, no. 2, pp. 288–298, 2019.

[13] L. Vinciguerra, G. Lanza, V. Puglisi et al., "Transcranial Doppler ultrasound in vascular cognitive impairment-no dementia," *PLoS One*, vol. 14, no. 4, Article ID e0216162, 2019.

[14] G. A. Rosenberg, "Binswanger's disease: biomarkers in the inflammatory form of vascular cognitive impairment and dementia," *Journal of Neurochemistry*, vol. 144, no. 5, pp. 634–643, 2018.

[15] M. R. Azarpazhooh and V. Hachinski, "Vascular cognitive impairment: a preventable component of dementia," *Handbook of Clinical Neurology*, vol. 167, pp. 377–391, 2019.

[16] R. O. Akinyemi, M. O. Owolabi, M. Ihara et al., "Stroke, cerebrovascular diseases and vascular cognitive impairment in Africa," *Brain Research Bulletin*, vol. 145, pp. 97–108, 2019.

[17] C. Czakó, T. Kovács, Z. Ungvari et al., "Retinal biomarkers for Alzheimer's disease and vascular cognitive impairment and

Hindawi
Journal of Healthcare Engineering
Volume 2023, Article ID 9876973, 1 page
https://doi.org/10.1155/2023/9876973

Retraction

Retracted: Performance Evaluation of Hospital Economic Management with the Clustering Algorithm Oriented towards Electronic Health Management

Journal of Healthcare Engineering

Received 10 October 2023; Accepted 10 October 2023; Published 11 October 2023

This article has been retracted by Hindawi following an investigation undertaken by the publisher [1]. This investigation has uncovered evidence of one or more of the following indicators of systematic manipulation of the publication process:

(1) Discrepancies in scope
(2) Discrepancies in the description of the research reported
(3) Discrepancies between the availability of data and the research described
(4) Inappropriate citations
(5) Incoherent, meaningless and/or irrelevant content included in the article
(6) Peer-review manipulation

The presence of these indicators undermines our confidence in the integrity of the article's content and we cannot, therefore, vouch for its reliability. Please note that this notice is intended solely to alert readers that the content of this article is unreliable. We have not investigated whether authors were aware of or involved in the systematic manipulation of the publication process.

In addition, our investigation has also shown that one or more of the following human-subject reporting requirements has not been met in this article: ethical approval by an Institutional Review Board (IRB) committee or equivalent, patient/participant consent to participate, and/or agreement to publish patient/participant details (where relevant).

Wiley and Hindawi regrets that the usual quality checks did not identify these issues before publication and have since put additional measures in place to safeguard research integrity.

We wish to credit our own Research Integrity and Research Publishing teams and anonymous and named external researchers and research integrity experts for contributing to this investigation.

The corresponding author, as the representative of all authors, has been given the opportunity to register their agreement or disagreement to this retraction. We have kept a record of any response received.

References

[1] T. Tian and D. Deng, "Performance Evaluation of Hospital Economic Management with the Clustering Algorithm Oriented towards Electronic Health Management," *Journal of Healthcare Engineering*, vol. 2022, Article ID 3603353, 15 pages, 2022.

Hindawi
Journal of Healthcare Engineering
Volume 2022, Article ID 3603353, 15 pages
https://doi.org/10.1155/2022/3603353

Research Article

Performance Evaluation of Hospital Economic Management with the Clustering Algorithm Oriented towards Electronic Health Management

Tian Tian[1] and Dixin Deng[2]

[1]*Youth League Committee, The First Affiliated Hospital, University of South China, Hengyang 421001, Hunan, China*
[2]*Finance Department, The First Affiliated Hospital of University of South China, Hengyang 421001, Hunan, China*

Correspondence should be addressed to Dixin Deng; 2021010001@usc.edu.cn

Received 23 December 2021; Revised 11 January 2022; Accepted 15 January 2022; Published 6 April 2022

Academic Editor: Liaqat Ali

In order to study the clustering algorithm based on density grid, the performance evaluation index system of hospital economic management under the application of electronic health management system is constructed. Firstly, this work designs the basic architecture of electronic health management system, classifies and screens the process of index system of electronic health management system, compares the clustering algorithm based on density grid with the simple clustering algorithm based on density or grid, and then applies it to the performance evaluation index system of hospital economic management. According to the principle of Mitchell scoring method, the expert questionnaire of hospital economic management performance evaluation index system was designed, and Delphi method was used to evaluate the candidate indexes from the three dimensions of right, legitimacy, and urgency. The results show that, compared with simple network clustering algorithm and density clustering algorithm, the clustering algorithm based on density network produces higher purity (94% VS 73% VS 67%) and lower entropy (0.9 VS 1.4 VS 1.54), which effectively saves memory consumption, and the difference is statistically significant ($P < 0.05$). The core indicators with scores above 4.5 in both dimensions include budget revenue implementation rate, budget expenditure implementation rate, implementation rate of special financial appropriation, asset-liability ratio, hospitalization income cost rate, medical insurance settlement rate, average cost of discharged patients, and drug proportion. The coefficient of variation of the first grade index is between 0.05 and 0.14 and that of the second grade index is between 0.05 and 0.15. Clustering algorithm based on density network has higher purity and lower entropy, which can effectively save memory consumption. The performance evaluation index system of hospital economic management finally determines 6 first-level indexes: budget management, financial fund management, cost management, medical expense management, medical efficiency, medical quality, and 25 second-level indexes.

1. Introduction

In the era of big data today, the public social activities on the Internet become continuous and comprehensive gradually, and more and more people are willing to upload personal health information to the cloud. Electronic health management has become a key social issue. In recent years, new network information technology has been mainly developed on artificial intelligence, databases, and fifth-generation (5G) networks, and the rudiment of a complex and comprehensive digital society has been gradually shown. Therefore, the development of electronic health management becomes an inevitable phenomenon [1–3]. A latest survey report released by the Global Web Index (GWI) shows that social media users account for 98% of global Internet users. With the ever-increasing social media users, people face with the biggest opportunity and challenge of information disclosure globally in the personal electronic health management. In some developed countries, such as the United States, the United Kingdom, and Japan, the management of personal health information is stressed, and the specific protective laws have been issued. There is a similar history of information protection laws in electronic health management in these countries, all of which show a transition from the health information protection to the construction of a health information system [4–7]. China is an important economic entity in the world, but there are still many shortcomings in the laws on electronic health management. The personal health information cannot be protected essentially, as it mainly relies on relevant laws. In addition, the needs of some institutions for electronic health management cannot be satisfied due to the lack of effective laws. It is necessary to resolve the conflict reasonably between the public needs for electronic health management and its safety and keep the balance between the relevant institutions and the public needs, for the stable development of society and the improvement of the electronic health management.

The Guidelines on the Establishment of a Modern Hospital Management System of the General Office of the State Council (No. 67 [2017]) was issued by the General Office of the State Council on July 14, 2017, pointed out that the establishment of a comprehensive hospital management system can be started with the financial asset management system and the performance assessing system. The *Guidelines on Strengthening the Operation and Management of Public Hospitals* (No. 27 [2020]) was issued by the National Health Commission on December 25, 2020. It was stated that it is necessary to accelerate the transformation of management model and operating mechanism to promote the high-quality development of public hospitals so that the hospitals could meet the scientific, refined, and informatized standard and meet the relevant requirements of the public hospital operation and management system. The most important thing in the reform of public hospitals is to improve the hospital economic management comprehensively. The public hospital reform can be reflected through changes in the economic management [8–10]. In addition, for comprehensive improvement of the economic management of hospitals, it is required to innovate the operating mechanism of public hospitals and improve the financial management system and economic operation system. The hospital economic management is mainly reflected in its performance evaluation, and the feasibility of performance plan depends on the performance evaluation indicator system of hospital economic management.

Hospital economic management refers to the strengthening of hospital economic activities with economic means in accordance with objective laws of economic development, through improving hospital management systems and hospital management methods continuously [11, 12]. Manpower, property, and resources should be reasonably used to reduce labour costs as much as possible, and the medical and health service technology should also be continuously improved to achieve the greatest economic outcome. Thus, the healthcare-centred teaching and research could be better completed and the increasing medical needs of people could be satisfied. Performance evaluation refers to a comprehensive evaluation of the implementation degree and results of hospital management goals, using specific evaluation methods with the evaluation standards and quantitative indicators. Ohio University Research puts forward two aspects, including internal evaluation and external evaluation, as the overall framework of performance measurement of medical and health institutions, each of which includes two dimensions of financial performance and quality performance [13]. Sana mentioned that the hospital performance management system mainly includes three aspects: first, the management analysis, the implementation of branch management in hospitals, daily analysis and comparison of operating results, and regular review. Second, the quantity can be checked, and all personnel have a reward mechanism. Third, personnel management, the labour cost accounts for about half of the total hospital cost, and poor personnel management will cause adverse effects [14]. With the issuance of Bitcoin, blockchain, the underlying core technology of the Bitcoin system has gradually come into people's life as a database technology with the advantages of openness, flatness, and equality. Blockchain technology takes the trust security as the core, not only innovating the pattern of traditional Internet but also promoting efficient operation in transactions, authentication, and other aspects. Blockchain technology can also promote the synergy of multiple energies and various participating entities, the rapid integration of information and physical systems, the diversification of transactions, and cost minimization. Data mining is an interdisciplinary subject including artificial intelligence, pattern recognition, statistics, database, and neural network, including prediction verification function and description function. Among them, the prediction verification function includes association analysis, sequence pattern mining, and regression analysis. Functions include classification, clustering, feature analysis, and deviation analysis. The team led by the professor of Stanford University focuses on data stream management, continuous query, and clustering. Clustering algorithm is an important data mining method, which divides an object set into several clusters according to some similarity measure criterion, and the objects in the same cluster have high similarity in some aspects. The purpose of clustering algorithm is to divide a data set into unconnected clusters with the same attributes. Clustering algorithm is widely used, and it has been developed in many fields such as commerce, medical care, geography, insurance industry, Internet application, and e-commerce [15–21]. Combining the advantages of the density-based and the grid-based clustering algorithms, the clustering algorithm is an important data mining method, which divides an object set into several clusters according to some similarity measure criterion, and the objects in the same cluster have high similarity in some aspects. Grid-based algorithm is a clustering algorithm based on multiresolution idea, which divides the data sample space into a limited number of cells to form a grid structure, and finally all clustering operations are carried out on the grid. The main advantage of this method is that the processing speed is fast, and the clustering process is independent of the number of original data samples and only depends on the maximum number of grid cells.

Combining the advantages of density-based clustering algorithm and grid-based clustering algorithm, this study uses density-grid-based clustering algorithm to cluster data samples and uses blockchain technology to apply it to hospital economic management performance evaluation system and achieves ideal results.

At present, academic performance evaluation in different fields has achieved remarkable results, but there is no sufficient theoretical support for hospital economic management performance evaluation under electronic health management [22]. Extensive economic management generally exists in public hospitals, which directly affects the overall operation effect of the hospital. In order to maintain the normal survival and development of the hospital, hospital managers increase hospital revenue by constantly expanding the scale of the hospital, adding large-scale equipment and increasing charging items. Although this relieves the pressure of the hospital to a certain extent, the algorithm still covers up the real situation of poor internal management of the hospital, which is not conducive to the self-adjustment and improvement of hospital management direction, and at the same time, it harms the interests of patients to a certain extent. From the perspective of economic management, this work formulates the performance evaluation index system of hospital economic management, which is beneficial to the hospital to clarify the key points of economic management, adjust the development of operation mode from extensive to refined, and enable the hospital construction to enter the benign track of sustainable development, thus fully reflecting the value orientation of public welfare, efficiency, and fairness of public hospitals, meeting the medical needs of the broad masses of people and completing other related tasks of public hospitals.

2. Technologies and Methods

2.1. Basic Architecture of the Electronic Health Management System. The basic architecture of the management platform mainly included the host terminal structure, client/server (C/S) structure, browser/server (B/S) structure, and file server structure. With the development of the network computing and the rapid increase of social media users, the B/S structure gave a highly stable technical platform with C/S structure. The B/S structure itself had diversified modes, and its client was a very convenient browser, while the server was responsible for complex data processing. The major advantage of the B/S structure was the convenient configuration of the client, which was conducive to the development and maintenance of the system.

Client users could complete the information publishment through simple and flexible operations. In this study, a three-tier B/S structure was taken as the development tool for the basic architecture design. The first tier was the client, mainly providing basic services for doctor workstations and individual users. The second tier was the application server to operate the business processing of the hospital system with two servers. The data storage, replacement, management, and other operations could be done through the tier. The third tier was the data tier consisting of database and other systems, and it was designed for the storage and management of information data. The architecture is shown in Figure 1.

According to the main business steps of electronic health management, the flow of health data information was taken as the major direction of system operation, and the preliminary software framework of electronic health management system was designed. The framework included 5 main parts, which were data collection and transmission, health check, health risk assessment, automatic intervention measures, and interfaces, as shown in Figure 2.

2.2. Construction Process of Electronic Health Management Index System. At the initial stage of the index system construction, it is necessary to collect relevant literature materials of health information management and performance evaluation to provide theoretical support for the establishment of electronic health management index evaluation index system. Through on-the-spot investigation, questionnaire survey, symposium, and other forms, it can understand the development of medical services, investigate the situation of health information management in depth, and build the performance evaluation index system of health information management. To construct the performance evaluation index system of health information management, relevant principles should be followed, and scientific evaluation methods should be selected to construct it. At this stage, different standards should be set for the main contents that affect the performance of health information management, the factors that affect health information management should be refined and quantified, and the relevant weights should be determined. In order to test the rationality of the health information management performance evaluation index system, it is necessary to optimize and test it. Finally, after passing the relevant tests, before formally establishing the performance evaluation index of health information management, actual testing is a necessary procedure to ensure the operability of the index system, and the established index system is revised through the test results, as shown in Figure 3.

2.3. Blockchain Technology. Blockchain network is a point-to-point network. The whole network has no centralized hardware structure (central server) and management mechanism (central router). Each node in the blockchain network has equal status and can be used as both a client and a server. Each node retains all data resources of the entire blockchain network, and all network data have multiple backups. The more the nodes participating in the network, the more the data backup. In the prior art, the backup of blockchain is completed by each node by itself, and when the backup conditions are met, the blockchain node uploads data to the designated server, which may result in repeated backup, wasting network, and server resources, and the backup efficiency is not high. On the other hand, in the prior art, backup information needs to be maintained by blockchain nodes or blockchain networks themselves, which also brings a burden to blockchain networks and wastes resources, and self-maintenance of backup information will also lead to security problems of backup information.

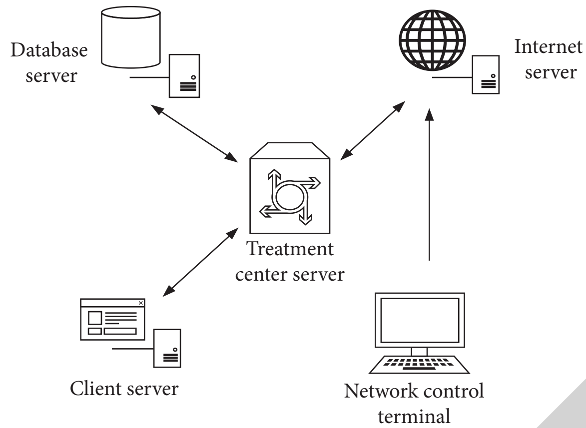

Figure 1: Basic architecture of the electronic health management platform.

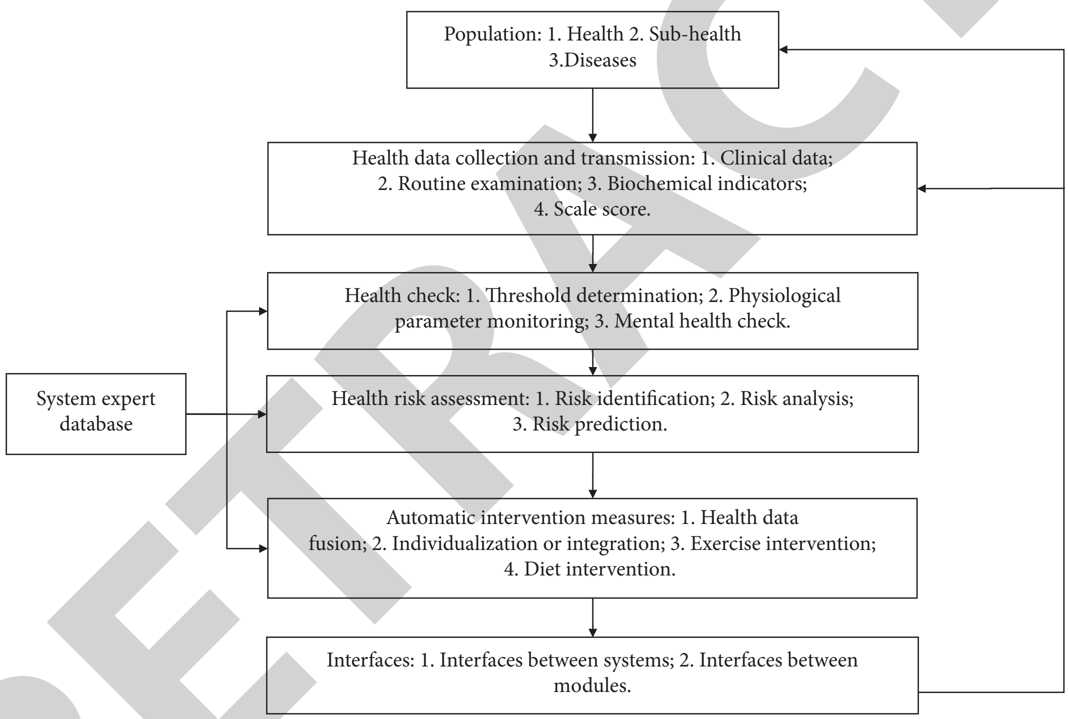

Figure 2: Framework diagram of the electronic health management system based on business processes.

Therefore, this study optimizes the backup method of blockchain data so that each node can enter or leave the network at will to maintain the stability of the network. In addition, the possibility of data modification is reduced.

In the encryption system of blockchain network, an asymmetric encryption algorithm was adopted to deal with the trust issue among network users. The asymmetric encryption algorithm is run with two types of keys: the public key and a private key, which were matched one to one. As the public key was used to encrypt the processed data, only the matched private key could decrypt it. In the same way, if the processed data were encrypted through the private key, only the corresponding public key could decrypt it. Each user in the blockchain had a unique public key and private key, of which the public key was public to all users on the network. Users on the blockchain network used the same encryption algorithm, and the private key was owned by its user alone. The user encrypted the information with the private key, and other users could decrypt the information with the public key.

2.4. Operating Environment of the Electronic Health Management System. The server adopted Windows 10.0 operating system, and it was more advanced than Microsoft SQL2005. The processor was of P4 3.0 GHz, and the hard disk capacity was 120G. The Windows 10.0 operating system was also adopted for the client with Microsoft Office 2013; the P4 3.0 GHz processor and the 1920×1080 resolution of display screen were applied as well.

2.5. The Density-Grid Clustering Algorithm. In the density-grid clustering algorithm, the density threshold of grid cells was generally used to distinguish dense grid cells from sparse grid cells. Then, the neighbouring dense grid cells were merged into a grid cluster to achieve the clustering effect. Thus, the parameters of the density threshold affected the clustering results directly. If the density threshold was set too small, the algorithm might not be able to distinguish the dense areas from sparse areas accurately in the data space. There would be a lot of noises in the final clustering results obtained, which reduced the quality of clustering. If it was set too large, the algorithm would recognize a large number of evenly distributed clusters as sparse grid cells. Even in the Gaussian distributed clusters, only a few high-density independent grid cells could be found [23]. The idea of mean density was adopted in this study, so part of the data was collected for the statistics of data density distribution, and then the grid cell density threshold of the algorithm was determined with the basic statistical information.

In the process of data flow processing, N, the amount of data in the network unit, is firstly, and then grid cells with the data are counted to calculate the maximum value $U_{\max}$, mean value U_{mean}, and minimum value $U_{\min}$ of the cell density.

The equation for the mean value of network cell density is as follows:

$$U_{\text{mean}} = \frac{\sum_{i=1}^{N} U_i}{N}. \tag{1}$$

In (1), U_i represents the density of the network cell density f, and N is the number of network grid cells.

The dense grid cell threshold is computed through

$$U_d = \frac{U_{\max} + U_{\text{mean}}}{2}. \tag{2}$$

In (2), U_d stands for the dense grid cell threshold and $U_{\max}$ and U_{mean} are the maximum value and the mean value of the network cell density, respectively.

The sparse grid cell threshold is calculated via

$$U_s = \frac{U_{\min} + U_{\text{mean}}}{2}. \tag{3}$$

In (3), U_s is the sparse grid cell threshold, and $U_{\min}$ represents the maximum value of the cell density.

At some time, the mean density of clusters in the data flow is very high, but it may change to be very low at the next moment. It means that the density of clusters in the data flow is changing constantly over time.

As time goes by, new data samples in the data flow would be input into the computer system continuously and mapped to the corresponding data unit. If the dense grid cell had not received new data samples for a long time, it might degenerate into a sparse grid. On the contrary, if the sparse grid cell received a batch of new data samples in a certain period of time, it might be upgraded to a dense grid [24–26]. Therefore, it was necessary to monitor the network density regularly and the clusters that had been generated should also be adjusted. The grid density detection period (P) was related to the clustering result directly, so it cannot be too long or too short.

Theorem 1. *The minimum time required for a dense grid to degenerate into a sparse grid is represented as ΔT^{-}_{min}, which is calculated by the following*

$$\Delta T^{-}_{\min} = \frac{1}{\gamma} \log \frac{\delta}{\delta - 1}. \tag{4}$$

In (4), the parameter δ is the density threshold, and $\delta > 0$; and $0 < \gamma < 1$.

Theorem 2. *The minimum time required for a sparse grid to be upgraded into a dense grid is ΔT^{+}_{min}, which is expressed as*

$$\Delta T^{-}_{\min} = \left| \frac{1}{\gamma} \log \frac{G(f,t)\left(1 - 2^{-\delta}\right) - 1}{\delta\left(1 - 2^{-\delta}\right) - 1} \right|. \tag{5}$$

In (5), $G(f,t)$ represents the density of grid cell f at t; δ is the density threshold, and $\delta > 0$; and $0 < \gamma < 1$. The density detection period P should be the smallest integer between $\Delta T^{-}_{\min}$ and $\Delta T^{+}_{\min}$.

Proof. Assuming that grid element f is a sparse grid, it is upgraded to a dense grid after time ΔT. Therefore, because of the set $S(f,t) \subseteq S(f,t+\Delta T)$, the data samples of $S(f,t+\Delta T)$ in the set can be divided into two categories: one is the data sample points of the set $S(f,t)$, and the other is the data samples that arrive between time t and time $t + \Delta T$. The necessary condition for a sparse grid F to be upgraded to a dense grid is that all data samples arriving between t and $t + \Delta T$ are mapped to the F grid. This means that from the time of t and $t + \Delta T$, a new data sample is mapped to F at each time. Based on the above analysis, the following equation can be obtained:

$$G(f,t+\Delta T) \leq \sum_{x \in s(f,t)} g(x,t+\Delta T) + \sum_{t=0}^{\Delta T - 1} 2^{-\delta i} = \sum_{x \in s(f,t)} 2^{-\delta \Delta T} g(x,t) + \frac{1 - 2^{-\delta \Delta T}}{1 - 2^{-\delta}} = 2^{-\delta \Delta T} G(x,t) + \frac{1 - 2^{-\delta \Delta T}}{1 - 2^{-\delta}}. \tag{6}$$

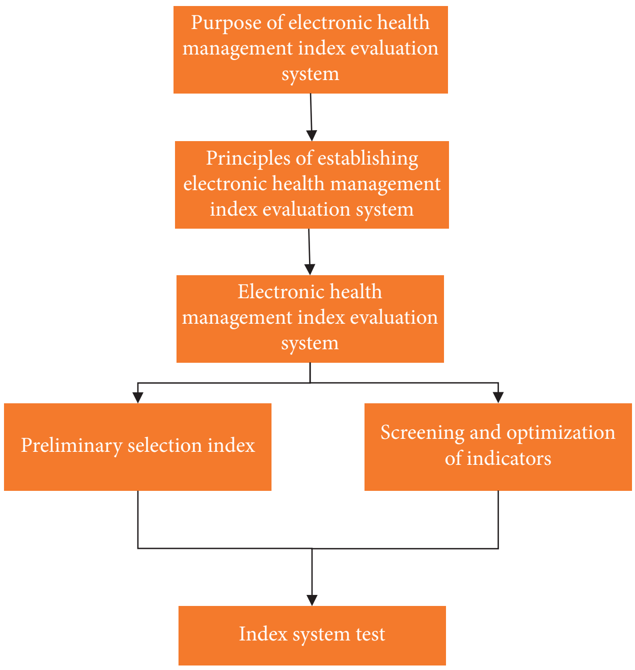

Figure 3: Construction process of electronic health management index system.

Suppose

$$2^{-\delta\Delta T}G(x,t)+\frac{1-2^{-\delta\Delta T}}{1-2^{-\delta}}=\sigma, \tag{7}$$

can get

$$2^{-\delta\Delta T}=\frac{S(x,t)\left(1-2^{-\delta}\right)-1}{\sigma\left(1-2^{-\delta}\right)-1}. \tag{8}$$

The density detection period should take the minimum integer value between $\Delta T^{-}_{\min}$ and $\Delta T^{+}_{\min}$. According to Theorems 1 and 2, the following (3) was worked out:

$$P=\left\lfloor \min\left\{\frac{1}{\gamma}\log\frac{\delta}{\delta-1},\left|\frac{1}{\gamma}\log\frac{G(x,t)\left(1-2^{-\delta}\right)-1}{\delta\left(1-2^{-\delta}\right)-1}\right|\right\}\right\rfloor. \tag{9}$$

□

Theorem 3. *When the parameter is greater than a certain critical value, the sparse grid cannot be upgraded to the dense grid.*

It is proved that the sum of densities of data sample points in the set $S(f,t)$ at time t is $\sum_{x\in S(f,t)}g(x,t)$, and the sum of densities at time $t+\Delta T$ is $\sum_{x\in s(f,t)}g(x,t+\Delta T)$. If the decreasing speed of the sum of density of data sample points in the set $S(f,t)$ is greater than the increasing speed of the sum of density of all newly arrived data samples within ΔT time interval, then the sparse grid f cannot be upgraded to a dense grid, and the equation is as follows:

$$\sum_{x\in s(f,t)}g(x,t)-\sum_{x\in s(f,t)}g(x,t+\Delta T)>\sum_{t=0}^{\Delta T-1}2^{-\delta i}. \tag{10}$$

Calculate

$$\left(1-2^{-\delta\Delta T}\right)g(x,t)>\frac{1-2^{-\delta\Delta T}}{1-2^{-\delta}},$$
$$\delta>\log\frac{G(x,t)}{G(x,t)-1}. \tag{14}$$

According to Theorem 3, when the parameter δ satisfies $\delta>\log G(x,t)/G(x,t)-1$, where $G(f,t)$ represents the density of sparse grid unit f at time t, grid unit f will not be upgraded to dense grid.

2.6. Simulation Experiment and Performance Evaluation under the Density-Grid Clustering Algorithm. In this study, the performance of the density-grid clustering algorithm was verified through the experiment, and it was compared with the single density-based clustering algorithm and the single grid-based clustering algorithm. The hardware platform used in the experiment was a personal computer with Intel® Core$^{(\mathrm{TM})}$ i3-2100 3.10GH central processing unit (CPU) and 4 GB random access memory (RAM). The software environment adopted Visual Studio 2020 and MATLAB R2008a. The experimental parameters were set as $\delta=2.5$ and $\gamma=0.24$. In the data set in this experiment, each data sample had 40 attributes, of which 32 continuous attributes constituted a subdata set. For the more accurate experimental results, the data used were standardized before the experiment.

The clustering effects of the three algorithms were evaluated by the purity and the entropy.

The calculation method of cluster purity is as follows:

$$\text{cluster purity}=\frac{\sum_i^N\left|\mathrm{M}_i^h\right|/\left|\mathrm{M}_i\right|}{N}\times 100\%. \tag{12}$$

In (12), N represents the number of classes in the clustering result, $|\mathrm{M}_i^h|$ represents the number of all cluster labels in the ith cluster, and $|\mathrm{M}_i|$ represents the data of the data in the ith cluster. The higher the purity of the cluster, the more similar the data in the cluster, and the greater the similarity between the data.

The calculation method of clustering entropy is as follows:

$$\text{clustering entropy}=\sum_{i}^{N}\sum_{x\in M_i}I^2(x,p_i). \tag{13}$$

In (13), M_i represents the number of all data in the ith cluster, and $I^2(x,p_i)$ represents the distance from data x to the center of the cluster p to which it belongs. The smaller the clustering entropy, the higher the clustering degree of data in the cluster, and the better the clustering quality. The higher the clustering entropy, the more scattered the data in the cluster, and the lower the clustering quality.

2.7. Construction Methods and Contents of the Performance Evaluation Indicator System. Key performance indicators referred to that after an organization analysed the characteristics of individual work performance; the indicators that represented the performance best were taken as key indicators for performance evaluation [27]. The balanced scorecard mainly emphasized that there was a balance between various indicators. Because of its simple and reasonable evaluation indicators and weight design, it is easy to operate in use and the most widely used in the performance evaluation of major enterprises and organizations [28]. The stakeholder theory explained the core of business management and performance assessment in details and provided a theoretical basis for performance evaluation [29]. The stakeholder theory was introduced as the main research method in this study, and key performance indicators and balanced scorecard were the auxiliary methods to construct a performance evaluation indicator system.

Any performance evaluation tool had its advantages and disadvantages. When choosing an evaluation tool, it should be considered whether it met the organization's own conditions. Various evaluation tools were widely used in the performance evaluation of hospital economic management, but they did not form a comprehensive and unified evaluation mode. The performance evaluation indicators of well-defined hospital economic management were listed out one by one, to obtain the best evaluation indicators as candidate indicators, with integrity, relevance, countability, and independence as the attribute principles for selection. The questionnaire was designed based on the Mitchell scoring method mainly in this study, and these selected candidate indicators were taken as the source of performance evaluation indicators of public hospital economic management. Then, the Delphi method was adopted to determine the final evaluation indicators and their weights.

2.8. Research Process and Quality Control. Mitchell scoring method scores stakeholders from three aspects: legitimacy, power, and urgency. According to the scoring results, stakeholders are divided into three types: decisive stakeholders, that is, they have three attributes: legitimacy, power, and urgency. Stakeholders of this type are the first objects that organizations pay close attention to and contact. Expected stakeholders are with any two of the above attributes; potential stakeholders have one of the above three attributes. Mitchell scoring method optimizes the limitations of multicone subdivision method, which makes the classification of stakeholders more scientific and easier to operate. According to the Mitchell scoring method, the expert consultation form for the performance evaluation indicator system of hospital economic management was designed with the candidate indicators. The survey objects of the expert consultation form were mainly health administration staff, medical college tutors, technologists in hospital, hospital management personnel, and hospital financial management personnel. The candidate indicators belonging to the performance evaluation indicators of hospital economic management were scored in entitlement, legitimacy, and urgency. The total score was 5 points, which indicated the strongest entitlement, legitimacy, and urgency, while 1 point suggested the weakest. Then, the weights of the indicators were obtained according to the results of expert consultation questionnaire survey.

Delphi method is based on the professional knowledge, experience, and subjective judgment ability of many experts and is especially suitable for analysis that lacks information and historical data and is influenced by many other factors. Among them, the survey consultation form uses the anonymity of experts, and the consultation experts only contact with the investigators, and there is no horizontal contact between the experts, which can well avoid the interference of experts on the results and reflect the real thoughts of experts. The Delphi method was used for the quality control of the experts participating in the scoring, aiming to ensure the quality of the expert consultation form. The prescribed procedures were strictly followed, and independent consultations of each expert were carried out. Experts finished the questionnaire surveys in strict accordance with the procedures to fully guarantee the scoring. After multiple questionnaire surveys, the expert opinions were collected, and finally the performance evaluation indicator system was formed. The system of hospital economic management was divided in the importance, mainly including core indicators, potential indicators, and marginal indicators, and the weights of relevant indicators were determined finally.

2.9. General Information of Experts. 16 experts from the practical and academic fields related to hospital economic management were invited to participate in the performance evaluation of hospital economic management. They were from health administration, medical colleges, hospital technologies, hospital management, and hospital financial management.

Table 1 shows the general information of the experts. In the first round of consultation, there were 9 experts (56.25%) who were 35–55 years old, accounting for the most of all experts. 7 experts (43.75%) were graduated with a master degree, which was the most; and there was no junior college graduate. It was proved that the experts had the high cultural literacy with a great understanding of the contents in consultation form. There were 13 experts (52.25%) with deputy senior titles or above, and 13 experts (81.25%) had worked for more than 10 years. 1 (6.25%), 6 (37.50%), 3 (18.75%), 4 (25.00%), and 2 (12.50%) experts were working in the health administration, medical colleges, medical technologies, hospital management, and hospital financial management, respectively. In the types of the work units, the distribution of experts was relatively reasonable. These experts were all capable in the actual work so that they could contact and deal with problems as soon as they encountered.

Two rounds of expert questionnaire surveys were conducted in this study. The survey content includes the importance and feasibility evaluation of indicators at all levels, comparison score, modification, and supplementary opinions on the importance of indicators at the same level. The response rates of the two rounds of questionnaire surveys were 100%, indicating that the experts were highly motivated to participate in and concern about the study.

Table 1: General information of experts.

Items	Classification	Number (proportion)
Age	<35 years old	3 (18.75%)
	35–55 years old	9 (56.25%)
	≥56 years old	4 (25.00%)
Highest education qualification	Doctor	6 (37.50%)
	Master	7 (43.75%)
	Bachelor	3 (18.75%)
Professional title	Junior	0 (0.00%)
	Medium grade	3 (18.75%)
	Deputy senior	8 (20.00%)
	Senior	5 (31.25%)
Type of work unit	Health administration	1 (6.25%)
	Medical colleges	6 (37.50%)
	Medical technologies	3 (18.75%)
	Hospital management	4 (25.00%)
	Hospital financial management	2 (12.50%)
Working years	<10 years	3 (18.75%)
	10–20 years	2 (12.50%)
	20–30 years	5 (31.25%)
	>30 years	6 (37.50%)
Regent's canal	Completely unfamiliar	0 (0.00%)
	Basically unfamiliar	0 (0.00%)
Familiarity of hospital management	Generally familiar	1 (6.25%)
	Relatively familiar	6 (37.50%)
	Very familiar	9 (56.25%)

2.10. Coordination Degree of Expert Opinions. The coordination degree of expert opinions referred to the degree of disagreement among experts on the stakeholder evaluation indicator scoring in entitlement, legitimacy, and urgency. It was assumed that C represented the coordination coefficient, and the value range of C was [0, 1]. The larger the value of C, the better the coordination degree of expert opinions on the stakeholder evaluation indicator scoring. If the coordination coefficient C was different after check, it meant a good coordination degree of expert opinions and the result was advisable; otherwise, it was unadvisable.

3. Results and Discussion

3.1. Comparison Results of Simulation Experiment. Figure 4 shows the comparison of the purity, entropy, and memory consumption of three clustering algorithms. In this section, real data sets are used to test and compare network-based clustering algorithm, density-based clustering algorithm, and network density-based clustering algorithm. The parameter setting data flow rate $v = 1000$, and other parameters are the same as those in the dynamic evolution operation experiment of data stream. With the density-grid clustering algorithm, the parameter γ could be compared with the grid density. Then, the density detection period was selected adaptively, which could capture the changes of the data flow at any time. The results showed that, compared with simple network clustering algorithm and density clustering algorithm, the clustering algorithm based on density network produces higher purity (94% VS 73% VS 67%) and lower entropy (0.9 VS 1.4 VS 1.54), which effectively saved memory consumption, and the difference is statistically significant ($P < 0.05$).

The density-based clustering algorithm mainly dealt with static data sets. Lee et al. [30] found that the algorithm could search for clusters in different shapes and then process the noise in the data set effectively. The grid-based clustering algorithm mainly dealt with the multiresolutions. He et al. [31] illustrated that the algorithm could classify the data set space, which was dispersed into some units and formed a grid shape gradually. Then, all clustering operations were performed on the grid. The major advantages of the grid-based algorithm were the short time and fast speed for processing the data sets. In this study, the two clustering algorithms were integrated into the density-grid clustering algorithm, and then the data flow was clustered. It turned out that the data flow sample space could be divided into many small grids, and each data sample in the data flow was mapped to a corresponding small grid. Then, the data flow sample was clustered through the density of these grids. In addition, the density-grid clustering algorithm was also optimized in its density detection period of grid cells and sparse grid detection.

3.2. Construction Results of Performance Evaluation Indicator System. With two rounds of expert consultation questionnaire surveys, the performance evaluation indicator system of hospital economic management was finally established. There were 6 first-level indicators, namely, budget management, financial fund management, cost control, medical expense management, medical efficiency,

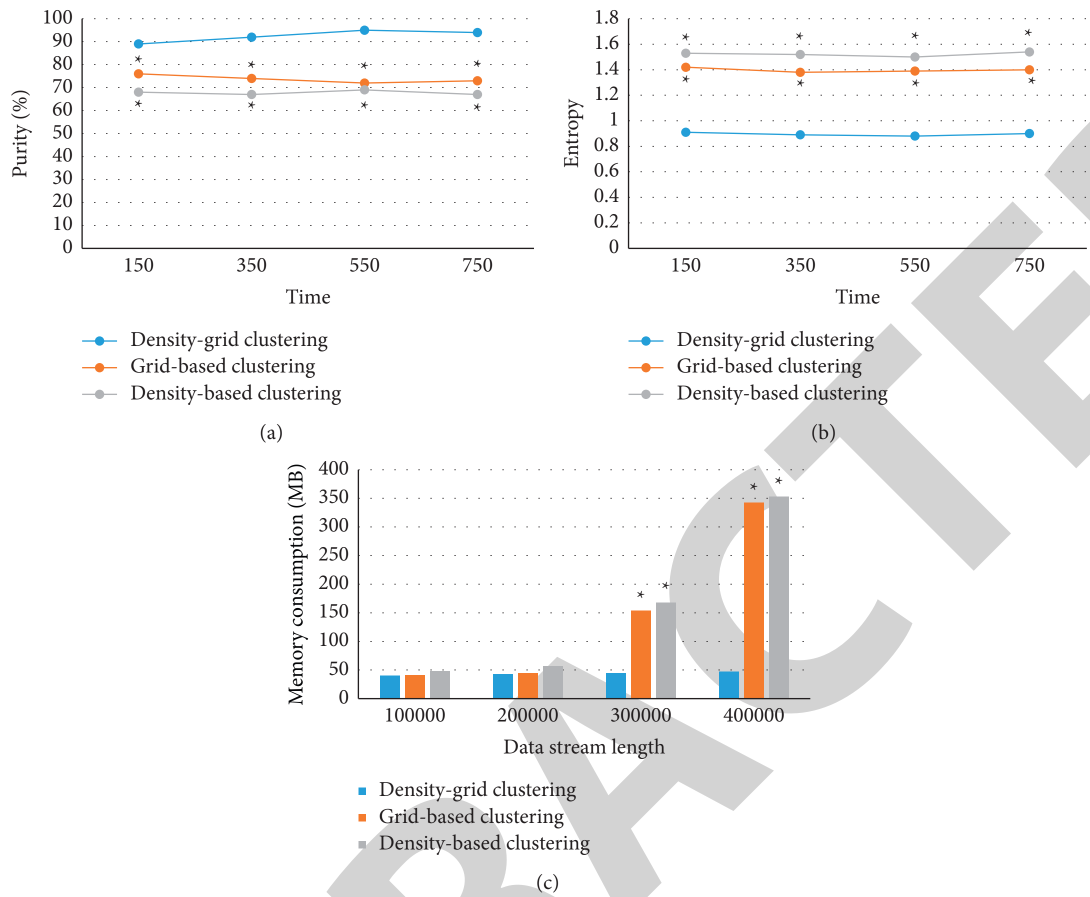

Figure 4: Comparison of purity, entropy, and memory consumption of the three algorithms. (a) Clustering purity comparison. (b) Clustering entropy comparison. (c) Memory consumption comparison. $*$ indicates the differences statistically significant compared with results of the density-grid clustering algorithm ($P < 0.05$).

and medical quality, respectively. There were also 25 second-level indicators, which are shown in Figure 5 in details.

3.3. Classification Results of Performance Evaluation Indicators. According to the Mitchell's scoring method, the performance evaluation indicators were classified in three dimensions of entitlement, legitimacy, and urgency.

Entitlement referred to the indictors directly related to the status and capability of hospital economic management. As shown in Figure 6, the larger the score, the greater the influence on the hospital, while the smaller the score, the slighter the influence.

The indicators that had a greater influence on the hospital economic management were listed as follows with the score greater than 4.5 points. The second-level indicators in the first-level budget management included the budget revenue implementation efficiency (4.91 points), the budget expenditure implementation efficiency (4.85 points), and the implementation efficiency of special appropriation (4.89 points). In financial fund management, the second-level indicators above 4.5 points were balance ratio of payments (4.52 points) and asset-liability ratio (4.67 points). In cost control, outpatient service income cost rate (4.52 points) was included. In medical expense management, those consisted of the medical insurance accounting rate (4.65 points), the average cost of discharged patients per time (4.52 points), the average cost of outpatient emergency per visit (4.58 points), the drug expenditure ratio (4.78 points), and the consumables ratio (4.63 points).

With the score between 4 and 4.5 points, the following indicators had the moderate influence on hospital economic management. In financial fund management, the liquidity ratio (4.12 points) was on the list. In cost control, inventory turnover ratio (4.31 points), hospitalization income cost rate (4.35 points), and consumption of drugs and health consumables in 100 RMB income (4.34 points) were included. In medical efficiency, outpatient emergency visits (4.39 points), number of discharged patients (4.32 points), number of surgeries (4.31 points), average length of stay (4.42 points), and utilization rate of beds (4.32 points) were all in this score range. In medical quality, coincidence of admission and discharge diagnoses (4.12 points),

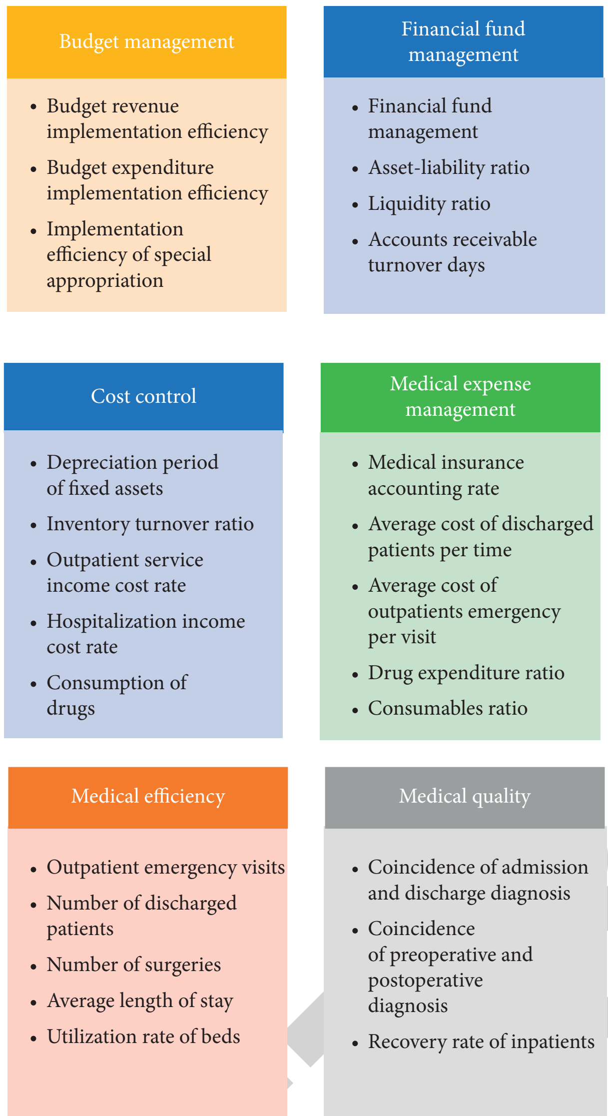

Figure 5: Performance evaluation index system of hospital economic management.

coincidence of preoperative and postoperative diagnoses (4.05 points), and recovery rate of inpatients (4.04 points) were also included.

Only accounts receivable turnover days (3.78 points) and depreciation period of fixed assets (3.95 points) had the score less than 4 points, as well as little influence on hospital economic management.

Legitimacy referred to the influence of some indicators in legal benefits, morality, or special hospital economic management. The larger the score, the higher the legitimacy of an indicator. It could be observed in Figure 7 for details.

The indicators, with the score more than 4.5 points and high legitimacy, were listed as follows. In the first-level indicator budget management, all of the budget revenue implementation efficiency (4.91 points), budget expenditure implementation efficiency (4.86 points), and implementation efficiency of special appropriation (4.78 points) met the situation. In financial fund management, only asset-liability ratio (4.92 points) was listed. In cost control, outpatient service income cost ratio (4.67 points), hospitalization income cost ratio (4.85 points), and consumption of drugs and health consumables in 100 RMB income (4.82 points) were included. In medical expense management and medical efficiency, medical insurance accounting rate (4.87 points), average cost of discharged patients per time (4.67 points), average cost of outpatient emergency per visit (4.86 points), drug expenditure ratio (4.62 points), and outpatient emergency visits (4.75 points) were on the list.

The indicators with the score between 4 and 4.5 points had a moderate legitimacy. In financial fund management, balance ratio of payments (4.43 points) and liquidity ratio (4.24 points) were in the range. In cost control, depreciation period of fixed assets (4.32 points) and inventory turnover ratio (4.25 points) were also included in the range. In medical efficiency, outpatient emergency visits (4.25 points), number of discharged patients (4.27 points), number of surgeries (4.26 points), average length of stay (4.35 points), and utilization rate of beds (4.41 points) were listed. In medical quality, all of the coincidence of admission and discharge diagnoses (4.36 points), coincidence of preoperative and postoperative diagnoses (4.25 points), and recovery rate of inpatients (4.12 points) went with the moderate legitimacy as well.

The indicators with less legitimacy had a score below 4 points, including the accounts receivable turnover days (3.87 points) only.

Urgency referred to whether the indicators could attract attention of the hospital and related administrative department managers immediately. The larger the score, the stronger the urgency; and the scores of various second-level indicators are shown in Figure 8.

As the score was above 4.5 points, the indicators had a greater urgency. Such second-level indicators included budget revenue implementation efficiency (4.67 points), budget expenditure implementation efficiency (4.58 points), and implementation efficiency of special appropriation (4.75 points) in the first-level indicator budget management. The medical insurance accounting rate (4.81 points) and the drug expenditure ratio (4.71 points) in medical expense management were also included.

Scored 4–4.5 points, the indicators had a moderate urgency. In financial fund management, the balance ratio of payments was 4.35 points, and the asset-liability ratio was 4.37 points. In cost control, outpatient service income cost rate, hospitalization income cost rate, and consumption of drugs and health consumables in 100 RMB income were 4.12 points, 4.26 points, and 4.41 points, respectively. In medical expense management, the average cost of discharged patients per time (4.35 points), the average cost of outpatient emergency per visit (4.41 points), and the consumables ratio (4.23 points) were on the list. In medical efficiency, all of the outpatient emergency visits (4.35 points), the number of discharged patients (4.37 points), the number of surgeries (4.41 points), average length of stay (4.28 points), and utilization rate of beds (4.36 points) were in this range. Besides, coincidence of admission and discharge diagnoses in medical quality reached 4.3 points.

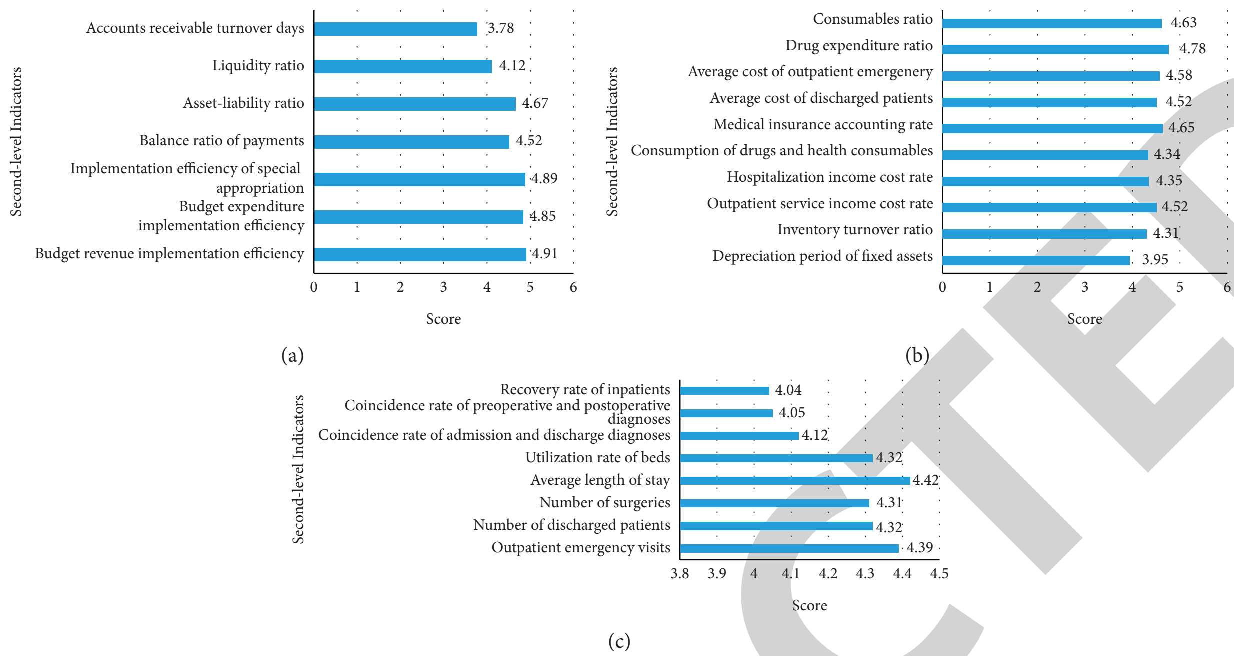

Figure 6: Entitlement evaluation of second-level indicators. (a) Entitlement evaluation of second-level indicators in budget management and financial fund management; (b) entitlement evaluation in cost control and medical expense management; (c) entitlement evaluation in medical efficiency and medical quality.

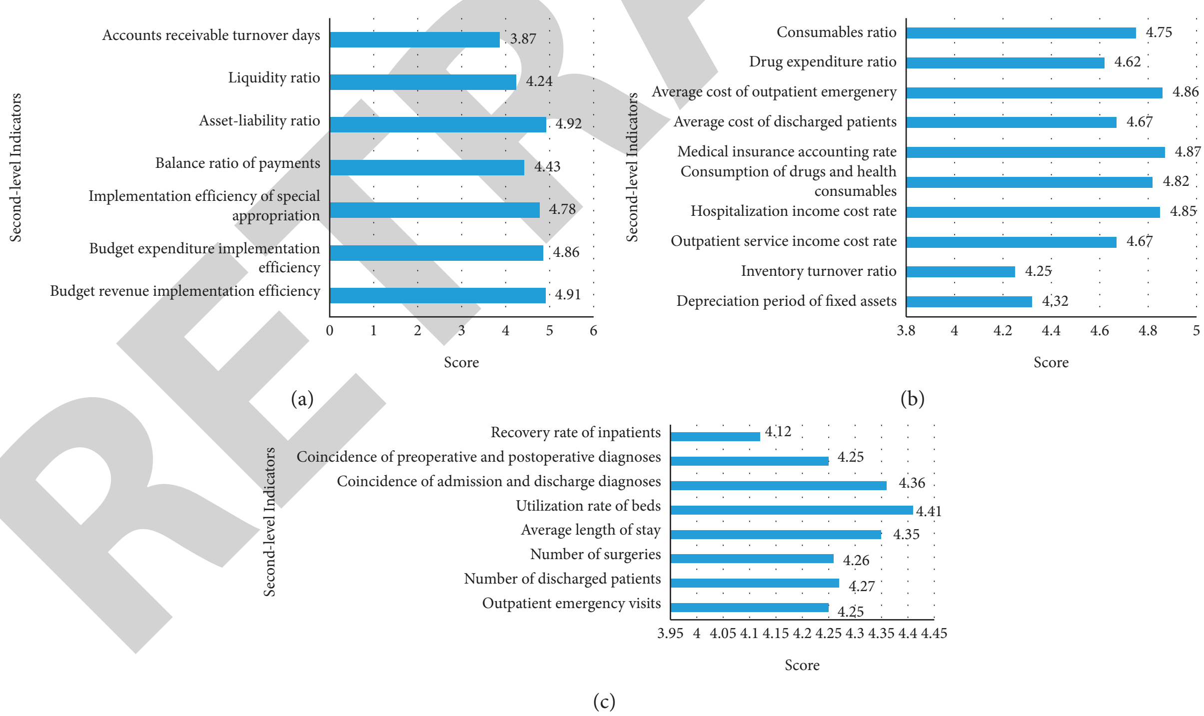

Figure 7: Legitimacy evaluation of second-level indicators. (a) Legitimacy evaluation of second-level indicators in budget management and financial fund management; (b) legitimacy evaluation in cost control and medical expense management; (c) legitimacy evaluation in medical efficiency and medical quality.

Liquidity ratio (3.78 points), accounts receivable turnover days (3.56 points), depreciation period of fixed assets (3.86 points), inventory turnover ratio (3.95 points), coincidence of preoperative and postoperative diagnoses (3.78 points), and recovery rate of inpatients (3.76 points) had a less urgency with the score less than 4 points.

According to the classification of stakeholder theory, those with scores above two dimensions (including two dimensions)

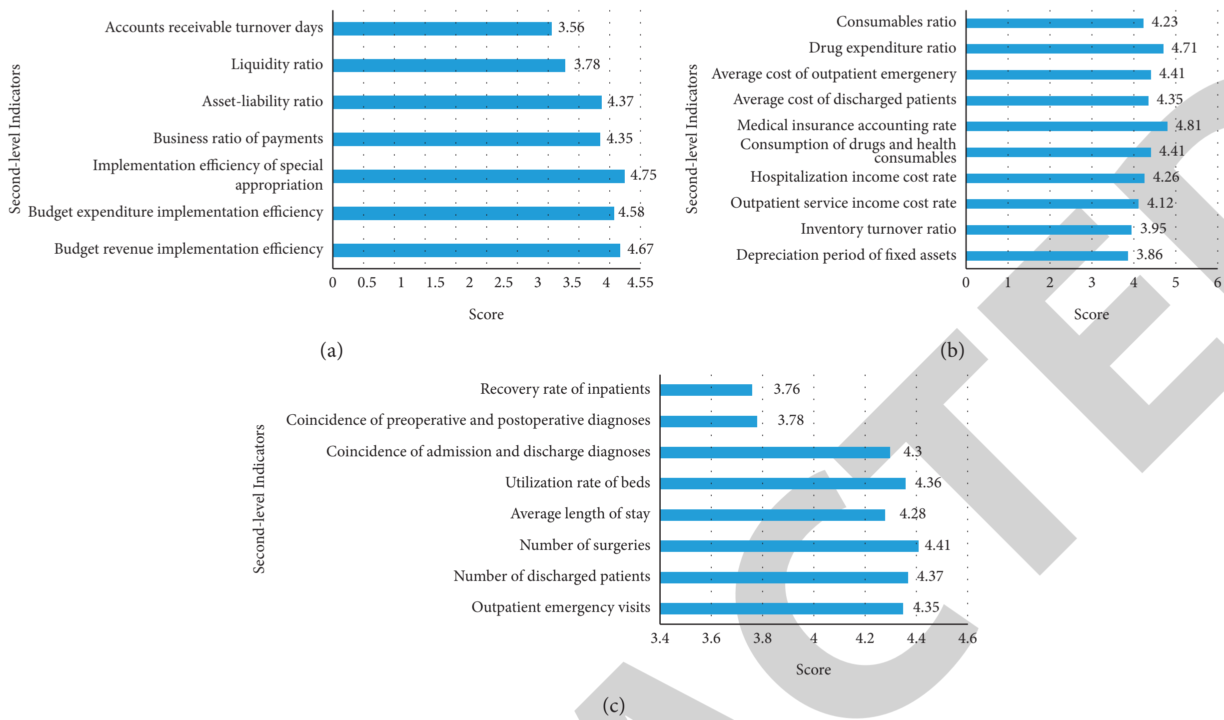

Figure 8: Urgency evaluation of second-level indicators. (a) Urgency evaluation of second-level indicators in budget management and financial fund management; (b) urgency evaluation in cost control and medical expense management; (c) urgency evaluation in medical efficiency and medical quality.

above 4.5 points can be considered as core indicators, mainly including budget revenue implementation rate, budget expenditure implementation rate, financial special allocation implementation rate, asset-liability ratio, hospitalization revenue cost rate, medical insurance settlement rate, average cost of discharged patients, and drug proportion. If the score of more than two dimensions (including two dimensions) is more than 4 points, it can be considered as a potential index, mainly including business balance rate, current rate, depreciation period of fixed assets, outpatient income cost rate, consumption of sanitary consumables, consumables ratio, outpatient and emergency visits, discharge visits, operation visits, average hospitalization days, bed utilization rate, diagnosis coincidence rate of admission and discharge visits, diagnosis coincidence rate before and after operation, and hospitalization mixed cure and improvement rate. Those with more than two dimensions (including two dimensions) below 4 points can be considered as marginal indicators, including average collection period and inventory turnover rate.

The listed candidate indicators were evaluated from the three dimensions of entitlement, legitimacy, and urgency, aiming to determine whether the indicators should be taken into the performance evaluation indicator system of hospital economic management. 5 points represented the greatest entitlement, legality, and urgency, while 1 point meant the least. The numerical results of the entitlement, legality, and urgency were basically similar to the definition of comprehensive relevance scores. It was indicated that the scoring results in this study were more reliable, and it was more complete than the indicator system of Li and Hao (2018) [32].

3.4. Determination of the Weights of Performance Evaluation Indicators. 6 first-level indicators with 25 second-level indicators were determined finally. The weights of the 6 first-level indicators are shown in Table 2, and those of the 25 second-level indicators are shown in Table 3.

After the determination of the performance evaluation indicators of hospital economic management, the Delphi method was used again for two rounds of expert consultation questionnaires of weighted indicators. With statistics on the standard deviation and mean of each indicator, it was finally determined that the coefficient of variation of first-level indicators was between 0.05 and 0.14 and that of second-level indicators was in the range of 0.05–0.15. It was suggested that experts gave the higher credibility in scoring the weights of indicators after two rounds of questionnaires. The total score of weight was 100 points in this study; but actually, it was calculated as a percentage. Therefore, the indicator system could be used for comparative research, which was slightly different from the research of Wei et al. [33].

There was a strong economic management performance of this study itself. In the process of constructing the performance evaluation indicator system, special attention was paid to the orientation of economic indicators. The ultimate goal of the performance evaluation was to optimize the hospital running efficiency and enhance the hospital's role in improving health of people, which reflected the social responsibility that the hospital should be born. Although a relatively complete and practical performance evaluation indicator system of hospital economic management was

Table 2: Weights of first-level indicators.

First-level indicators	Indicator number	Indicated number	Standard deviation	Mean	Coefficient of variation	Weight
Budget management	A	1	1.26	16.89	0.12	16.9
Financial fund management	B	2	1.36	17.37	0.05	17.4
Cost control	C	3	2.16	15.44	0.13	15.4
Medical expense management	D	4	2.28	13.58	0.08	13.6
Medical efficiency	E	5	1.45	15.37	0.14	15.4
Medical quality	F	6	2.26	21.35	0.07	21.3
Total score						100 points

Table 3: Weights of second-level indicators.

Second-level indicators	Indicator number	Indicated number	Units	Standard deviation	Mean	Coefficient of variation	Weight
Budget revenue implementation efficiency	A1	1	%	1.56	8.61	0.15	8.6
Budget expenditure implementation efficiency	A2	2	%	1.52	1.12	0.09	1.1
Implementation efficiency of special appropriation	A3	3	%	1.78	7.23	0.12	7.2
Balance ratio of payments	B1	4	%	2.56	3.71	0.08	3.7
Asset-liability ratio	B2	5	%	2.78	3.72	0.11	5.3
Liquidity ratio	B3	6	%	2.45	2.83	0.13	2.8
Accounts receivable turnover days	B4	7	Day	2.67	5.61	0.16	5.6
Depreciation period of fixed assets	C1	8	Year	2.67	5.62	0.14	2.9
Inventory turnover ratio	C2	9	%	2.43	3.63	0.08	3.6
Outpatient service income cost rate	C3	10	%	1.71	3.71	0.05	3.7
Hospitalization income cost rate	C4	11	%	2.56	2.52	0.07	2.5
Consumption of drugs and health consumables in 100 RMB income	C5	12	RMB	1.89	2.73	0.13	2.7
Medical insurance accounting rate	D1	13	%	1.45	3.39	0.12	3.4
Average cost of discharged patients per time	D2	14	RMB	1.23	2.08	0.07	2.1
Average cost of outpatient emergency per visit	D3	15	RMB	2.45	2.07	0.13	2.7
Drug expenditure ratio	D4	16	%	2.67	3.09	0.08	3.1
Consumables ratio	D	17	%	1.89	2.28	0.12	2.3
Outpatient emergency visits	E1	18	Case	1.12	2.47	0.16	2.5
Number of discharged patients	E2	19	Case	2.13	4.09	0.07	4.1
Number of surgeries	E3	20	Case	2.14	2.68	0.06	2.7
Average length of stay	E4	21	Day	2.67	3.77	0.14	3.8
Utilization rate of beds	E5	22	%	1.81	2.25	0.07	2.3
Coincidence of admission and discharge diagnoses	F1	23	%	2.86	7.21	0.08	7.3
Coincidence of preoperative and postoperative diagnoses	F2	24	%	1.57	5.75	0.15	5.8
Recovery rate of inpatients	F3	25	%	2.89	8.16	0.09	8.2
Total score							100 points

proposed, it remained at the level of theoretical inquiry for some indicators without being tested and verified by comprehensive practice. Therefore, it needed to be further explored in related fields, especially in practical management.

4. Conclusion

The framework of the electronic health management system was designed in this study under the density-grid clustering algorithm. Meanwhile, the included candidate indicators were taken to design the expert questionnaire for the performance evaluation indicator system of hospital economic management. With the Delphi method, 16 experts in related fields and hospital administration were chosen for the questionnaire survey, which was to evaluate the included candidate indicators in entitlement, legitimacy, and urgency. After two rounds of expert questionnaire surveys, the weight of each indicator in the system was determined. The density-grid clustering algorithm gave higher purity and lower entropy, which saved memory massively. 6 first-level indicators were finally brought into the performance evaluation indicator system of hospital economic management, including budget management, financial fund management, cost control, medical expense management, medical efficiency, and medical quality. There were also 25 second-level indicators affiliated to the first-level indicators who were ascertained. In budget management, there were budget revenue implementation efficiency, budget expenditure implementation efficiency, and implementation efficiency of special appropriation. In financial fund management, there were balance ratio of payments, asset-liability ratio, liquidity ratio, and accounts receivable turnover days. Cost control was composed of depreciation period of fixed assets, inventory turnover ratio, outpatient service income cost rate, hospitalization income cost rate, and consumption of drugs. In medical expense management, the medical insurance accounting rate, average cost of discharged patients per time, average cost of outpatient emergency per visit, drug expenditure ratio, and consumables ratio were included. Medical efficiency consisted of the outpatient emergency visits, number of discharged patients, number of surgeries, average length of stay, and utilization rate of beds. Medical quality was made up of the coincidence of admission and discharge diagnoses, the coincidence of preoperative and postoperative diagnoses, and the recovery rate of inpatients. The results of the two following rounds of expert consultation questionnaires found that the scoring of indicator weights by experts were highly credible. The deficiency of this study lies in the fact that the indicators are screened in combination with the background of big data, which may lead to the imperfect index system. Therefore, it is necessary to broaden the field of evaluation indicators in the later period to meet the needs of performance evaluation of hospital economic management in China.

Data Availability

All data included in this study are available upon request by contact with the corresponding authors.

Conflicts of Interest

The authors declare that they have no financial and personal relationships with other people or organizations that can inappropriately influence this work. There is no professional or other personal interest of any nature or kind in any product, service, and/or company that could be construed as influencing the position presented in, or the review of, the manuscript entitled.

References

[1] Y. H. Yun, E. Kang, Y. M. Cho et al., "Efficacy of an electronic health management program for patients with cardiovascular risk: randomized controlled trial," *Journal of Medical Internet Research*, vol. 22, no. 1, Article ID e15057, 2020.

[2] E. Kang, S. M. Park, K. Lee et al., "Efficacy of health coaching and an electronic health management program: randomized controlled trial," *Journal of General Internal Medicine*, vol. 36, no. 9, Article ID 21-06671-2, 2021.

[3] H. J. Baer, B. A. De La Cruz, R. Rozenblum et al., "Integrating an online weight management program with population health management in primary care: design, methods, and baseline data from the PROPS randomized controlled trial (Partnerships for Reducing Overweight and Obesity with Patient-centered Strategies)," *Contemporary Clinical Trials*, vol. 95, Article ID 106026, 2020.

[4] M. H. Stanfill and D. T. Marc, "Health information management: implications of artificial intelligence on healthcare data and information management," *Yearbook of medical informatics*, vol. 28, no. 1, pp. 56–64, 2019.

[5] M. Bloomrosen and E. S. Berner, "Section editors for the IMIA yearbook section on health information management. Findings from 2017 on health information management," *Yearb Med Inform*, vol. 27, no. 1, pp. 67–73, 2018.

[6] X. Zhou, Y. Ni, G. Xie et al., "Analysis of the health information needs of diabetics in China," *Studies in Health Technology and Informatics*, vol. 264, pp. 487–491, Article ID 190269, 2019.

[7] W. Zhao, P. Lu, S. Yu, and L. Lu, "Consumer health information needs in China - a case study of depression based on a Social Q&A community," *BMC Medical Informatics and Decision Making*, vol. 20, no. Suppl 3, p. 130, 2020.

[8] Y. Zhao, L. Liu, Y. Qi, F Lou, J Zhang, and W Ma, "Evaluation and design of public health information management system for primary health care units based on medical and health information," *Journal of infection and public health*, vol. 13, no. 4, pp. 491–496, Article ID 2019.11.004, 2020.

[9] X. Zhao, X. Li, W. Yang, Q Feng, Y Zhou, and Q Wang, "Primary health information standard system based on semantic interoperability," *BMC Medical Informatics and Decision Making*, vol. 18, no. Suppl 5, p. 112, Article ID 018-0696-5, 2018.

[10] D. Gu, J. He, J. Sun et al., "The global infectious diseases epidemic information monitoring system: development and usability study of an effective tool for travel health management in China," *JMIR Public Health Surveill*, vol. 7, no. 2, Article ID e24204, 2021.

[11] M. Stedman, M. Lunt, M. Davies et al., "Cost of hospital treatment of type 1 diabetes (T1DM) and type 2 diabetes (T2DM) compared to the non-diabetes population: a detailed economic evaluation," *BMJ Open*, vol. 10, no. 5, Article ID e033231, 2020.

[12] A. Ismail, L. S. Suddin, S. Sulong, Z Ahmed, N. A Kamaruddin, and N Sukor, "Economic burden of managing type 2 diabetes mellitus: analysis from a teaching hospital in Malaysia," *Indian Journal of Public Health*, vol. 61, no. 4, pp. 243–247, Article ID 24_16, 2017.

[13] M. R. Amin, J. P. Gentile, B. Edwards, and M. Davis, "Evaluation of health care disparities for individuals with intellectual and developmental disabilities in Ohio," *Community Mental Health Journal*, vol. 57, no. 3, pp. 482–489, 2021.

[14] S. Rouis, A. Ben Abdelaziz, H. Nouira, M. Khelil, C. Zoghlami, and A. Ben Abdelaziz, "Development of a balanced scorecard for the monitoring of hospital performance in the countries of the greater maghreb. Systematic review," *La Tunisie medicale*, vol. 96, no. 10-11, pp. 774–788, 2018.

[15] Z. Zhang, X. Liu, and L. Wang, "Spectral clustering algorithm based on improved Gaussian kernel function and beetle antennae search with damping factor," *Computational Intelligence and Neuroscience*, vol. 2020, Article ID 1648573, 9 pages, 2020.

[16] A. Diamond, M. Schmuker, and T. Nowotny, "An unsupervised neuromorphic clustering algorithm," *Biological Cybernetics*, vol. 113, no. 4, pp. 423–437, 2019.

Hindawi
Journal of Healthcare Engineering
Volume 2023, Article ID 9858470, 1 page
https://doi.org/10.1155/2023/9858470

Retraction

Retracted: Opioid-Free Labor Analgesia: Dexmedetomidine as an Adjuvant Combined with Ropivacaine

Journal of Healthcare Engineering

Received 26 September 2023; Accepted 26 September 2023; Published 27 September 2023

This article has been retracted by Hindawi following an investigation undertaken by the publisher [1]. This investigation has uncovered evidence of one or more of the following indicators of systematic manipulation of the publication process:

(1) Discrepancies in scope
(2) Discrepancies in the description of the research reported
(3) Discrepancies between the availability of data and the research described
(4) Inappropriate citations
(5) Incoherent, meaningless and/or irrelevant content included in the article
(6) Peer-review manipulation

The presence of these indicators undermines our confidence in the integrity of the article's content and we cannot, therefore, vouch for its reliability. Please note that this notice is intended solely to alert readers that the content of this article is unreliable. We have not investigated whether authors were aware of or involved in the systematic manipulation of the publication process.

Wiley and Hindawi regrets that the usual quality checks did not identify these issues before publication and have since put additional measures in place to safeguard research integrity.

We wish to credit our own Research Integrity and Research Publishing teams and anonymous and named external researchers and research integrity experts for contributing to this investigation.

The corresponding author, as the representative of all authors, has been given the opportunity to register their agreement or disagreement to this retraction. We have kept a record of any response received.

References

[1] W. Gao, J. Wang, Z. Zhang et al., "Opioid-Free Labor Analgesia: Dexmedetomidine as an Adjuvant Combined with Ropivacaine," *Journal of Healthcare Engineering*, vol. 2022, Article ID 2235025, 7 pages, 2022.

Hindawi
Journal of Healthcare Engineering
Volume 2022, Article ID 2235025, 7 pages
https://doi.org/10.1155/2022/2235025

Research Article

Opioid-Free Labor Analgesia: Dexmedetomidine as an Adjuvant Combined with Ropivacaine

Wei Gao,[1] Jie Wang,[1] Zhiguo Zhang,[1] Haiying He,[2] Huiwen Li,[1] Ruili Hou,[3] Liping Zhao ,[4] and Daniel Muthee Gaichu [5]

[1]*Department of Anesthesiology, Baotou Obstetrics and Gynecology Hospital, Inner Mongolia (the Third Hospital of Inner Mongolia Baotou Iron and Steel Group), Gaotou 014010, China*
[2]*Department of Neonatal Pediatrics, Baotou Obstetrics and Gynecology Hospital, Inner Mongolia (the Third Hospital of Inner Mongolia Baotou Iron and Steel Group), Gaotou 014010, China*
[3]*School of Public Health Baotou Medical College, Gaotou 014010, China*
[4]*Department of Gynecology and Obstetrics, Baotou Obstetrics and Gynecology Hospital, Inner Mongolia (the Third Hospital of Inner Mongolia Baotou Iron and Steel Group), Gaotou 014010, China*
[5]*Chuka University, Chuka 60400, Kenya*

Correspondence should be addressed to Liping Zhao; 657664025@qq.com and Daniel Muthee Gaichu; dgaichu@chuka.ac.ke

Received 17 February 2022; Revised 9 March 2022; Accepted 11 March 2022; Published 29 March 2022

Academic Editor: Liaqat Ali

Background. Side effects of the use of opioid analgesics during painless delivery are the main factors that affect rapid postpartum recovery. Opioid use can result in dangerous respiratory depression in the patient. Opioids can also disrupt the baby's breathing and heart rate. The nonopioid analgesic dexmedetomidine, a new a2-adrenergic agonist, possesses higher selectivity, greater analgesic effects, and fewer side effects. Moreover, epidural administration of dexmedetomidine also reduces local anesthetic consumption. *Objective*. Our study aims to compare the analgesic effects as well as the side effects of ropivacaine with dexmedetomidine against sufentanyl as an epidural labor analgesia. *Methods*. This study is a randomized, double-blinded, controlled trial (registration no. ChiCTR2200055360) involving 120 primiparous (a woman who has given birth once), singleton pregnancy women who are greater than 38 weeks into gestation and have requested epidural labor analgesia. The participants were randomized to receive 0.1% ropivacaine with sufentanyl (0.4 μg/ml) or dexmedetomidine (0.4 μg/ml). The primary outcomes included Visual Analogue Score (VAS), duration of first epidural infusions, the requirement of additional PCEA bolus, and adverse reactions during labor analgesia. *Results*. Of the 120 subjects who consented, 91 parturient women (women in the condition of labor) had complete data for analysis. Demographics and VAS, as well as maternal and fetal outcomes, were similar between the groups. The duration of first epidural infusions in dexmedetomidine was significantly longer than sufentanyl (median value: 115 vs 68 min, $P < 0.01$); the parturient women who received dexmedetomidine and who required additional PCEA bolus were fewer in comparison to those who received sufentanyl (27.5% vs 49.0%, $P < 0.05$). Furthermore, the incidence of pruritus in the dexmedetomidine group was lower in comparison to the sufentanyl group (0% vs 11.8%, $P < 0.05$). *Conclusions*. Dexmedetomidine, a nonopioid, is superior to the opioid analgesic sufentanyl in providing a prolonged analgesic effect as an epidural during labor. It also reduces local anesthetic consumption and has fewer side effects. The trial is registered with ChiCTR2200055360.

1. Introduction

The pain of childbirth is severe and unbearable to most primiparous women, hence effective labor analgesia options are necessary to improve the intrapartum maternal-fetal well-being [1]. A combination of local anesthetic and an opioid is often administered for the management of severe pain to ensure that a minimal dose of each is used. Ropivacaine, combined with low-dose sufentanyl, has been widely and effectively used to provide analgesia for epidural labor [2]. However, opioids can produce side effects themselves, including vomiting, nausea, pruritus, respiratory depression, urinary retention, and reduced variability in the fetal heart rate [3].

Opioid-free anesthesia (OFA) is a multimode anesthesia strategy that combines multiple nonopioid drugs and/or techniques to obtain high-quality anesthesia and has recently gained increasing attention [4]. The impact of OFA has been investigated in the case of transthoracic oesophagectomy in comparison with opioid-based anesthesia technique (OBA) on postoperative analgesia and recovery criteria (hemodynamics, respiratory rate, and hemoglobin oxygen saturation) [5].

As a new agonist of the a2-adrenergic receptor, the nonopioid, dexmedetomidine, is characterized by its high selectivity and greater analgesic effects [6, 7]. Dexmedetomidine-based OFA in cardiac surgery patients is feasible and could be associated with lower postoperative morphine consumption and better postoperative outcomes, reducing local anesthetic consumption, as well as producing fewer side effects [8]. Dexmedetomidine has been shown to protect numerous organs in recent studies (such as the heart, kidney, lung, intestine, liver, and nervous system). This mechanism is thought to primarily relate to the regulation of neurotransmitters and singling pathways, as well as having anti-apoptotic and anti-inflammatory properties [9]. Previous studies have indicated that epidural ropivacaine in combination with dexmedetomidine is an effective method of reducing postoperative pain, prolonging the analgesic effect [10]. The purpose of this study was to carry out a randomized, double-blinded, controlled trial for evaluating the maternal and fetal safety, analgesic effects, and adverse effects of dexmedetomidine in comparison to sufentanyl used as an adjuvant to local anesthetics during epidural labor analgesia.

2. Materials and Methods

This study is a randomized, double-blinded, controlled clinical trial with registration no. ChiCTR2200055360 and is approved by the Inner Mongolia Baotou Maternity Hospital's Ethics Committee. Between January 2021 and August 2021, written informed permission was received from 120 study participants who requested epidural labor analgesia. Parturients were enrolled if they were considered as a physical status I or II (according to the American Society of Anesthesiologists), aged between 20 and 36 years, weighed less than 100 kg, carried a single fetus ≥38 weeks, and experienced cervical dilation ≥3 cm and ≤5 cm. The study exclusion criteria included patients with hypertensive disease, multiple gestations, and history of premature labors and patients with contraindications to epidural analgesia or allergies to opioids/local aesthetics, a history of chronic opioid analgesic use, and VAS ≥4 30 min after epidural labor analgesia.

120 patients were randomized in a balanced manner into two groups via a computer-generated random-number table: the sufentanyl group (Group S, $n = 60$) and the dexmedetomidine group (Group D, $n = 60$). All parturients who met the inclusion criteria were established with venous access and had their vital signs monitored (blood pressure, heart rate, blood oxygen saturation (SpO_2), and cardiotocography (CTG)) after entering the delivery room. Analgesia was administered in the left lateral decubitus position at the estimated level of the L2 to L3 interspace. The epidural space was identified using a loss-of-resistance approach with an 18-gauge Tuohy needle. An epidural catheter was inserted 3 cm cephaladly into the epidural space. After a negative cerebrospinal fluid and blood aspiration test, a test dose of 3 mL (1% lidocaine) was administered for 5 minutes. As the first epidural infusion dosage, Group S participants received 12 mL 0.4 μg/mL sufentanyl in combination with 0.1% ropivacaine, while Group D participants received 12 mL 0.4 μg/ml dexmedetomidine in combination with 0.1% ropivacaine. These mixed solutions were infused by a patient-controlled-analgesia pump (PCEA) when VAS ≥4. The PCEA pump was set to 8 mL/80 min with an 8 mL rescue bolus (lockout 30 minutes) (Group S: PCEA with ropivacaine (0.1%) + sufentanyl (0.4 μg/mL); Group D: PCEA with 0.1% ropivacaine + 0.4 μg/ml dexmedetomidine). Another anesthetist prepared local anesthetic solutions for epidural labor analgesia. The investigators were blind to these solutions.

3. Outcome Measures and Data Collection

During labor, heart rate, blood pressure, SpO_2, and cardiotocography (CTG) were continuously monitored and recorded; the parturient's pain level was determined using a 10 cm Visual Analogue Score (VAS: 0 cm = no pain; 10 cm = worst possible pain); the enhanced Bromage score is used to grade the motor block caused by intraspinal anesthesia in parturient women. 0, there is no obstruction to movement; 1, the straight leg cannot be lifted and that the feet and knees cannot be moved; 2, inability to straighten a leg or move the knee, as well as the inability to move the feet; 3, limb movement is completely blocked; additionally, the Ramsay Sedation Scale is used to determine a patient's sedation level: 1, anxiety, irritation, and uneasiness; 2, oriented, calm, and cooperative; 3, responsive only to commands; 4, a brisk reaction to a stimulus; 5, a sluggish reaction to a stimulus; 6, no reaction to a stimulus (T0: prior to the block; T1: 30 min after the block; T2: at the start of the second stage of labor).

The duration of the first epidural infusions, requiring additional PCEA bolus and adverse reactions during analgesia, was observed. The adverse reactions included fever, nausea or vomiting, and pruritus.

Neonatal data including Apgar scores at 1 and 5 minutes, immediate umbilical arterial blood gas analysis (pH, lactic acid), and the Neonatal Behavioral Neurological Assessment (NBNA) on the third day and two weeks after birth were also analyzed. Physicians from our hospital's Department of Children Health examined NBNA scores, which included general condition, muscular tension, action behavior, and primitive reflex. Each parameter received a point value between 0 and 2. All parameters were evaluated before sample collection, given that the consent of family members was obtained.

4. Statistical Analysis

SPSS (Windows Version 20.0) was used to conduct statistical analysis. The median, mean, percentage, and standard deviation are all used to depict the data. Comparisons between groups were made using the Mann–Whitney *U* test or independent samples *t*-test. The categorical variables were compared between groups using the Fisher's exact probability test and chi-square detection. The repeated data were analyzed using the analysis of repeated measurements of variance.

5. Results

5.1. Maternal Characteristics and Neonatal Outcomes. A total of 120 parturients were recruited in this study. Ultimately, 91 parturient women were enrolled (Figure 1), who shared similar bodily characteristics, such as age and weight, as well as similar labor characteristics, such as gestational age. Furthermore, the immediate umbilical arterial blood gas findings (pH, lactic acid), Apgar scores, and NBNA scores between the two groups were also similar (Table 1).

5.2. Quality of Labor Analgesia. There was no significant difference between the VAS and maternal or fetal heart rate between the two groups at T0, T1, and T2 ($P > 0.05$) (Table 2, Figure 2). Furthermore, the requirement of additional PCEA bolus (27.5%) by the parturient women in Group D was less than in Group S (49.0%) ($P < 0.05$, Table 3) (Figure 4).

However, compared with Group S, the duration of the first epidural infusions in Group D (median 115 min, 90–130) was greater than in Group S (median 68 min, 60–80) ($P < 0.001$) (Figure 3).

5.3. Maternal Side Effects. The incidence of pruritus in Group D was significantly lower than in Group S (0% vs 11.8%, $P < 0.05$); fever, nausea, or vomiting in Group D (2.5% and 2.5%) was reported lower compared to Group S (7.8% and 5.9%) (Table 3, Figure 4).

6. Discussion

Opioid-free anesthesia (OFA) is a new concept of analgesic therapy. OFA is fully in line with the concept of accelerated rehabilitation surgery (ERAS), using multimode anesthesia and pain management to significantly improve patient outcomes and reduce the incidence of postoperative adverse reactions and promote patient recovery [11]. As a result, the optimal labor analgesia not only provides adequate analgesia to parturients but also reduces opioid intake without causing adverse effects, allowing for rapid neonatal or maternal postpartum recovery. Such an analgesic agent has a low risk of motor block, vomiting, nausea, pruritus, bradycardia, and most importantly fetal distress [12].

Sufentanyl, an opioid, has been widely utilized as an adjuvant for epidural labor analgesia in combination with ropivacaine. Opioids are well known to produce side effects themselves, such as nausea, vomiting, pruritus, urinary retention, respiratory depression, and decreased fetal heart rate variability.

As a new a2-adrenergic agonist, dexmedetomidine, a nonopioid, possesses a highly selective, sedative, anxiolytic, sympatholytic, and analgesic effect. Its antinociceptive action is a result of stimulation of a2-adrenoreceptors situated throughout the spinal cord and central nervous system [13]. It has been used as an adjuvant in anesthesia and multimodal analgesia because it can enhance sedation and prolong analgesic effects whilst reducing the risk of adverse reactions opioids can cause [10, 14]. Dexmedetomidine decreases heart rate as its concentration increases in the plasma. This is assumed to be caused by the activation of a2-receptors in vascular smooth muscles, resulting in hypertension and peripheral vasoconstriction. This is presumably caused by the baroceptor reflex [15, 16]. Human studies have shown that a small intravenous bolus of dexmedetomidine decreases blood pressure (0.25–1 μg/kg), whereas larger boluses (1–4 μg/kg) lead to a transient increase in blood pressure and occasionally profound reflex bradycardia [17]. Dexmedetomidine's sedative effect is concentration-dependent; plasma concentrations of 0.2–0.3 μg/mL produce considerable and rousable sedation. Deep sedation is thought to occur at plasma concentrations above 1.9 μg/mL, where a patient is not rousable [15].

In this work, Group S received sufentanyl and ropivacaine for epidural labor analgesia and Group D received dexmedetomidine 0.4 μg/mL plus 0.1% ropivacaine for epidural labor analgesia.

Compared with Group S, Group D participants did not experience pruritus (0% vs 11.8%) and had fewer complications of nausea and vomiting (2.5% vs 5.9%) in concordance with the study [10]. However, this effect may be related to opioid-free anesthesia rather than the specific antiemetic activity of dexmedetomidine [18].

When comparing the use of sufentanyl, we found that the incidence of fever in dexmedetomidine was lower (7.8% vs 5.9%). Fever during labor analgesia is unknown; it could be caused by heat loss, suppression of the thermoregulatory mechanism of the body, or heat redistribution throughout the body. However, intrathecal dexmedetomidine has the potential to impair the body's thermoregulatory center by impairing the transfer of body temperature signals at the spinal cord level [19].

Patients receiving dexmedetomidine received a longer initial infusion time (115 vs 68) compared to patients administered with sufentanyl. Furthermore, Group D parturient women required fewer additional PCEA boluses (27.5% vs 49%) whist experiencing similar analgesic effects, such as the VAS. In addition, the group's patients and fetuses did not experience significant cardiovascular or sedative side effects, which could be because we used 0.4 μg/mL intrathecal dexmedetomidine, which resulted in a relatively lower plasma concentrations [15, 17, 20].

The immediate umbilical arterial blood gas analysis is an important criterion referenced for the clinical evaluation of fetal acid-base balance. Umbilical artery blood gas analysis and lactic measurements can accurately, objectively, and directly reflect fetal intrauterine oxygenation and stay of

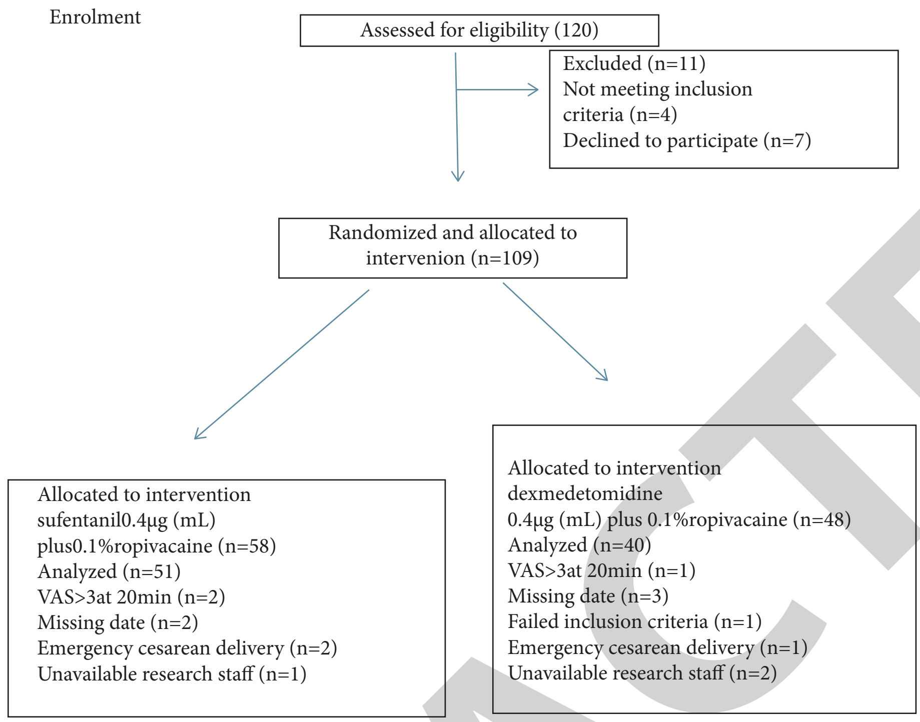

Figure 1: Participant flow diagram.

Table 1: Maternal characteristics and neonatal outcomes.

	Group S ($n = 51$)	Group D ($n = 40$)	P value
Age (years)	27.73 ± 3.13	28.68 ± 2.32	0.113
Body mass index (kg/m^2)	27.70 ± 3.03	27.81 ± 3.13	0.862
Gestational age (d)	276.70 ± 6.89	276.00 ± 6.27	0.615
Apgar score			
1 min	9.57 ± 0.92	9.55 ± 0.96	0.925
5 min	9.96 ± 0.19	9.98 ± 0.15	0.710
Umbilical artery pH	7.29 ± 0.08	7.31 ± 0.05	0.057
Lactic acid (mmol/L)	3.68 ± 1.15	3.81 ± 1.22	0.628
NBNA score			
Three days	38.12 ± 1.35	37.70 ± 0.99	0.105
Two weeks	38.96 ± 1.17	38.65 ± 0.89	0.166

Data are reported as mean ± SD or numbers. Group S received sufentanyl 0.4 μg/mL plus 0.1%.

Table 2: VAS and maternal or fetal heart rate.

	Group S ($n = 51$)	Group D ($n = 40$)	P value
VAS			
T0	7.78 ± 1.17	7.38 ± 0.83	0.065
T1	1.06 ± 1.25	0.93 ± 0.79	0.559
T2	2.93 ± 1.01	2.85 ± 0.53	0.688
Maternal heart rate			
T0	82.88 ± 9.69	81.43 ± 8.715	0.459
T1	81.24 ± 8.24	79.28 ± 8.32	0.265
T2	83.59 ± 8.54	82.98 ± 6.98	0.714
Fetal heart rate			
T0	140.18 ± 6.65	142.58 ± 8.53	0.135
T1	141.57 ± 7.25	142.75 ± 9.35	0.499
T2	143.04 ± 9.61	144.15 ± 9.05	0.576

Date are reported as mean ± SD or numbers.

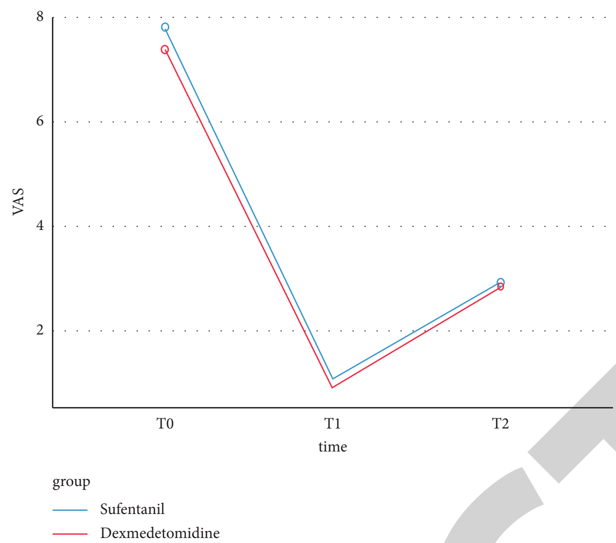

FIGURE 2: VAS of two groups at T0, T1, and T2. $P < 0.05$ was considered statistically significant.

TABLE 3: Quality of labor analgesia and adverse reactions.

	Group S ($n = 51$)	Group D ($n = 40$)	P value
The duration of first epidural infusions (min)	68 (60 to 80)	115 (90 to 130)	<0.01
Requiring additional PCEA bolus, n (%)	25 (49.0)	11 (27.5)	0.037
Pruritus, n (%)	6 (11.8)	0 (0)	0.033
Nausea or vomiting, n (%)	3 (5.9)	1 (2.5)	0.682
Fever, n (%)	4 (7.8)	**1 (2.5)**	0.380

Date are reported as median (interquartile range) or n (%) of the group. $P < 0.05$ is considered statistically significant.

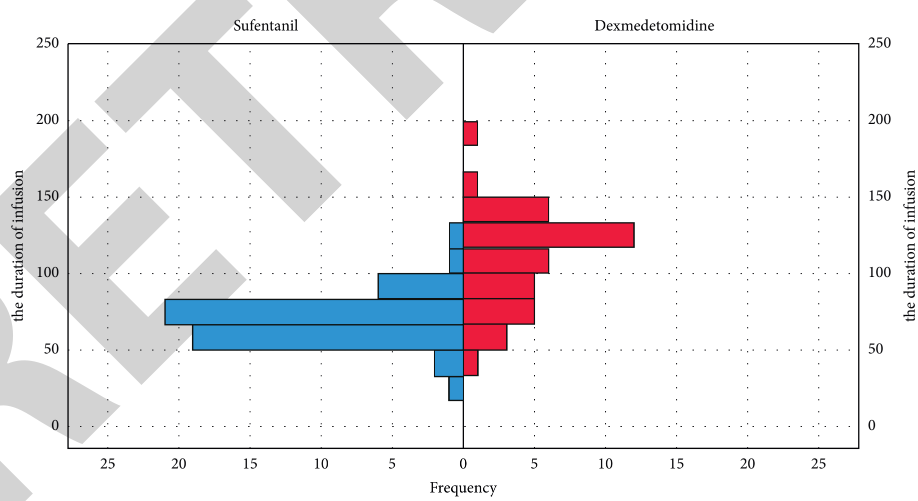

FIGURE 3: Duration of the first epidural infusions of the two groups.

ischemia; moreover, this method avoids the disadvantages of using the Apgar scoring system alone. In newborns, the reference range for umbilical cord arterial blood gas is pH 7.10~7.42, and lactic acid 3.0 ± 1.8. According to relevant clinical study results, the factors affecting neonatal asphyxia levels are directly related to lactic acid changes [21, 22]. The Apgar score, another important criterion of neonatal health, assesses a neonate's physiological reflexes, respiration, muscular tension, and circulation status after delivery. NBNA is a scoring system comprising inspection methods and scoring standards pertaining to 20 neurobehavioral tests in China. It has a total score of 40 points, which comprises 5 segments assessing the ability of newborns to adapt to their external environments as well as external stimuli. Passive and active muscle tone, in addition to original reflex status and general response, are also assessed. A newborn with a score of 37 or higher, within one week of birth, is considered normal [23]. In regards to our study findings, there was no

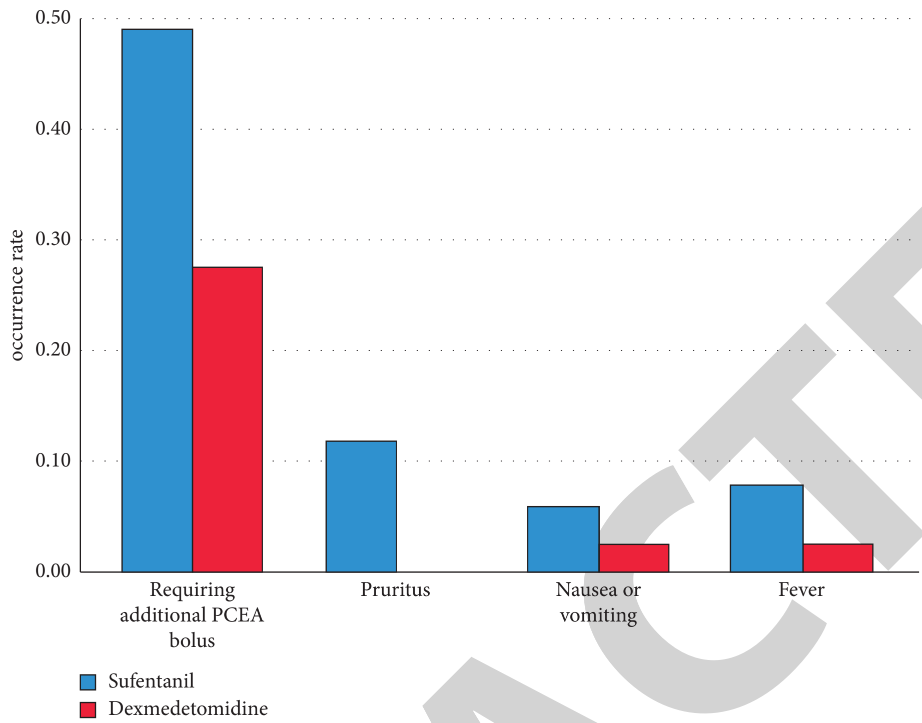

Figure 4: Maternal side effects and those requiring additional PCEA bolus from the two groups.

significant difference between the group's immediate umbilical arterial blood pH and lactate. Neither was a difference between the groups' Apgar scores at 1.5 min nor NBNA on the third day and two weeks after birth. This showed that the two methods of anesthesia had little impact on the newborn.

Therefore, the results of this study show that both sufentanyl (0.4 μg/mL) and dexmedetomidine (0.4 μg/mL) as adjuvants to ropivacaine could provide satisfactory epidural labor analgesia. Moreover, dexmedetomidine is superior to sufentanyl in providing prolonged analgesic effects and also reduces local anesthetic consumption and fewer side effects. It is fully in line with the concept of opioid-free anesthesia (OFA) as a basis for successful fast-track surgery.

It is necessary to mention some limitations of the current study. The most important being the limited number of participants involved. Also, the validity of the results requires the study to be performed at multiple sites. Therefore, the effects of dexmedetomidine on the mother and newborn needs further research using multicenter randomized controlled trials as well as a larger sample size.

7. Conclusion

0.4 μg/mL intrathecal dexmedetomidine combined with ropivacaine as an opioid-free epidural labor analgesia therapy can provide satisfactory analgesia effective with lower local anesthetic consumption and fewer side effects. It can also accelerate postpartum recovery during delivery.

Data Availability

The data used to support the findings of this study will be provided upon request to authors.

Conflicts of Interest

All authors declare that they have no conflicts of interest.

Acknowledgments

This study was supported by the Inner Mongolia Baotou Science and Technology Bureau Fund (w.jwk.2020066). The authors would like to thank their colleagues for their help in this study.

References

[1] E. T. C. Miles and J. P. Stone, "Pain relief during labour," *The Lancet*, vol. 394, no. 10198, p. e14, 2019.

[2] V. A. Arkoosh, C. M. Palmer, E. M. Yun et al., "A randomized, double-masked, multicenter comparison of the safety of continuous intrathecal labor analgesia using a 28-gauge catheter versus continuous epidural labor analgesia," *The Journal of the American Society of Anesthesiologists*, vol. 108, no. 2, pp. 286–298, 2008.

[3] M. Zhi, Y. Diao, S. Liu et al., "Sufentanil versus fentanyl for pain relief in labor involving combined spinal-epidural analgesia: a systematic review and meta-analysis of randomized controlled trials," *European Journal of Clinical Pharmacology*, vol. 76, no. 4, pp. 501–506, 2020.

[4] P. Lirk and J. P. Rathmell, "Opioid-free anaesthesia: Con: it is too early to adopt opioid-free anaesthesia today," *European Journal of Anaesthesiology*, vol. 36, no. 4, pp. 250–254, 2019.

[5] T. N. Abdelrahman and W. S. Algharabawy, "Opioid-free general anaesthesia for transthoracic oesophagectomy: does it improve postoperative analgesia and other recovery criteria? A prospective randomised study," *Ain-Shams Journal of Anaesthesiology*, vol. 13, no. 1, pp. 1–10, 2021.

Hindawi
Journal of Healthcare Engineering
Volume 2023, Article ID 9806864, 1 page
https://doi.org/10.1155/2023/9806864

Retraction

Retracted: Clinical Observation and Pharmacoeconomic Evaluations of Original Research Drug and Generic Drug Bortezomib in the Treatment of Multiple Myeloma

Journal of Healthcare Engineering

Received 26 September 2023; Accepted 26 September 2023; Published 27 September 2023

This article has been retracted by Hindawi following an investigation undertaken by the publisher [1]. This investigation has uncovered evidence of one or more of the following indicators of systematic manipulation of the publication process:

(1) Discrepancies in scope
(2) Discrepancies in the description of the research reported
(3) Discrepancies between the availability of data and the research described
(4) Inappropriate citations
(5) Incoherent, meaningless and/or irrelevant content included in the article
(6) Peer-review manipulation

The presence of these indicators undermines our confidence in the integrity of the article's content and we cannot, therefore, vouch for its reliability. Please note that this notice is intended solely to alert readers that the content of this article is unreliable. We have not investigated whether authors were aware of or involved in the systematic manipulation of the publication process.

In addition, our investigation has also shown that one or more of the following human-subject reporting requirements has not been met in this article: ethical approval by an Institutional Review Board (IRB) committee or equivalent, patient/participant consent to participate, and/or agreement to publish patient/participant details (where relevant).

Wiley and Hindawi regrets that the usual quality checks did not identify these issues before publication and have since put additional measures in place to safeguard research integrity.

We wish to credit our own Research Integrity and Research Publishing teams and anonymous and named external researchers and research integrity experts for contributing to this investigation.

The corresponding author, as the representative of all authors, has been given the opportunity to register their agreement or disagreement to this retraction. We have kept a record of any response received.

References

[1] Y. Liang, Y. Zhu, Y. Zhang et al., "Clinical Observation and Pharmacoeconomic Evaluations of Original Research Drug and Generic Drug Bortezomib in the Treatment of Multiple Myeloma," *Journal of Healthcare Engineering*, vol. 2022, Article ID 5201354, 7 pages, 2022.

Hindawi
Journal of Healthcare Engineering
Volume 2022, Article ID 5201354, 7 pages
https://doi.org/10.1155/2022/5201354

Research Article

Clinical Observation and Pharmacoeconomic Evaluations of Original Research Drug and Generic Drug Bortezomib in the Treatment of Multiple Myeloma

Yongchao Liang,[1,2] Ying Zhu,[2] Ying Zhang,[2] Ziwei Chen,[2,3] Boyang Li,[2,4] Aijun Liu,[5] and Lihong Liu[2]

[1]*Capital Medical University, Beijing 100069, China*
[2]*Department of Pharmacy, Beijing Chao-yang Hospital, Capital Medical University, Beijing 100020, China*
[3]*Jianguomen Community Health Service Center, Dongcheng District, Beijing 100005, China*
[4]*Xiaotangshan Hospital, Beijing 102211, China*
[5]*Department of Hematology, Beijing Chao-yang Hospital, Capital Medical University, Beijing 100020, China*

Correspondence should be addressed to Aijun Liu; aijun.liu72@yahoo.com and Lihong Liu; liulihong@bjcyh.com

Received 8 February 2022; Accepted 1 March 2022; Published 29 March 2022

Academic Editor: Liaqat Ali

Background. Multiple myeloma (MM) is one of the hitherto incurable malignant blood tumors. Bortezomib plays an important role in the treatment of MM. *Objective*. We aimed to compare effectiveness, safety, and pharmacoeconomic evaluations of the original research drug and the generic drug Bortezomib in the treatment of MM, so as to provide a reasonable basis for the selection of drugs in clinical diagnosis and treatment. *Methods*. A collection of 374 patients with MM were diagnosed and treated with combined Bortezomib in our hospital from July 2019 to January 2020.Two hundred and sixty nine cases met the criteria for inclusion and discharge. According to the different drug manufacturers, divided into the original research drug group ($n = 149$) and the generic drug group ($n = 120$). The effectiveness and safety were separately counted, and use the cost-minimization analysis to make the pharmacoeconomic evaluations. *Results*. Compared with the results of the two groups, there was no statistical difference between the two groups of treatment efficacy or adverse reaction rates ($P > 0.05$). The average daily cost of the original research drug group was 2954.38 Chinese yuan (CNY), the average treatment cost per cycle was 32967.69 CNY, the average daily cost of the generic drug group was 2697.29 CNY, and the average treatment cost per cycle was 29129.57 CNY. The price of the generic drug group is lower than the original drug group, and there was a statistical difference between the two groups ($P < 0.05$). *Conclusion*. There was no difference between the two groups of effectiveness or safety, and the generic drug is more economical in the treatment.

1. Introduction

Multiple myeloma (MM) is caused by multiple locus plasma cells which proliferate abnormally in the bone marrow, resulting in multiple tissue and organ damage and making it one of the hitherto incurable malignant blood tumors [1, 2]. Bortezomib plays an important role in the treatment of MM. The importance of Bortezomib in various regimens of MM therapy is reflected in the guidelines of the International Myeloma Working Group, the US National Comprehensive *Cancer* Network, and the cellular and molecular genetics (mSMART) criteria established by the Mayo Clinic research group. However, the price of imported original research drug is very expensive, leading to a huge economic burden on patients. In this study, the efficacy and safety between original research drug and generic drug Bortezomib was compared based on an observational study. The pharmacoeconomic analysis was carried out to provide reasonable reference for variable alternative selection in clinical diagnosis and treatment, so as to make a little contribution for the early realization of "Value-based Healthcare" in China [3].

1.1. Aim of the Study. We aimed to compare effectiveness, safety, and pharmacoeconomic evaluations of the original research drug and the generic drug Bortezomib in the treatment of MM, so as to provide a reasonable basis for the selection of drugs in clinical diagnosis and treatment.

1.2. Ethics Approval. The study/data collection was conducted after approval by the Ethics Committee of Beijing Chao-yang Hospital, Capital Medical University (Approval reference number: 2019-4-15–4).

2. Methods

2.1. Inclusion and Exclusion Criteria. Patients with multiple myeloma treated with Bortezomib chemotherapy regimen in our hospital from July 2019 to January 2020 were followed up and collected. Inclusion criteria: (1) diagnosed MM, (2) with the result of FISH, and (3) treatment with Bortezomib. Exclusion criteria: (1) combined treatment with Bortezomib was less than 2 weeks, (2) insufficient clinical data, and it was unable to perform treatment efficacy and adverse reaction rates, and (3) both original research drug and generic drug were applied.

2.2. Study Subjects. There were 374 patients diagnosed with MM which was collected in this study. One case was of smoldering myeloma, 4 cases died within 2 cycles in the treatment, 7 cases with no Bortezomib in the treatment regimen, and 5 cases used both drugs. Eighty eight cases, whose treatment information was unable to be collected, were transferred to other hospitals or returned to local hospitals due to residential area and economic problems. According to inclusion and exclusion criteria, patients who met the criteria were 269 cases. They were divided into the original research drug group ($n = 149$) and the generic drug group ($n = 120$) based on the different drug manufacturers. Baseline date of patients were collected: gender, age, disease staging (ISS stage, traditional DS stage, and revised R-ISS stage) [4–6], and basic diseases (hypertension, diabetes, coronary heart disease, atrial fibrillation, cerebral hemorrhage, cerebral infarction, atherosclerosis, vein thrombosis of lower limb, hyperlipidemia, high uric acid hematic disease, hypothyroidism, thyroid nodules, chronic respiratory system disease, digestive system diseases, rheumatoid immune-related diseases, history of orthopaedical surgery, allergies, etc.). Test and examination information of patients before each cycle of treatment (blood routine, urine routine, biochemistry, blood $\beta 2$ microglobulin, serum free light chain (FLC) test, serum immunofixation electrophoresis, serum M protein electrophoresis, 24-hour urine M protein, bone marrow puncture, bone marrow flow MRD test, etc.). All medical expenses incurred during hospitalization were collected.

2.3. Treatment Method. After diagnosing with MM, patients were treated with the chemotherapy regimen combined with Bortezomib. The recommended dose of Bortezomib was 1.3 mg/m^2, subcutaneously injected twice weekly for two weeks (i.e., injected on days 1, 4, 8, and 11), followed by 10 days of withdrawal as a treatment cycle. The actual dose was appropriately reduced to 1.0 mg/m^2 according to the tolerance level of patients or changed to once a week according to the tolerance level of patients, with continuous 4 weeks of administration (i.e., injection on the 1st, 8th, 15th, and 22nd days), followed by 13 days of withdrawal, namely, a treatment cycle. Continuous treatment for at least 2 cycles, followed up for 6 cycles. During the treatment, according to the condition and the occurrence of adverse reactions, timely symptomatic treatment, program adjustment, and drug dose adjustment were performed.

Drugs used: Bortezomib in the original research drug development group was VELCADE (manufacturer: BSP Pharmaceuticals S.p.A, specification: 3.5 mg/dose, approval no.: J20171067, and price: 5639.50 CNY/dose), and Bortezomib in the generic drug group was Xintai (manufacturer: Jiangsu Hausen Pharmaceutical Group Co., LTD., specification: 3.5 mg/branch, approval no.: National Drug Approval WORD H20173306, and price: 3929.20 CNY/branch).

Drugs for combined use include Lenalidomide (Remifamide) (Celgene Intenational Sarl, specification: 25 mg/tablet, approval no.: H20171348, and price: 1030.68 CNY/tablet), Lenalidomide (Zipuyi) (manufacturer: Qilu Pharmaceutical Co., LTD., specification: 25 mg/tablet, approval no.: National Drug Approval H20193115, and price: 182.8571 CNY/tablet), Thalidomide (manufacturer: Changzhou Pharmaceutical Co., LTD., specification: 25 mg/tablet, approval no.: National drug Approval H3202619, and price: 1.91 CNY/tablet), Cyclophosphamide (manufacturer: specification: 0.2 g/tablet, approval no.: H20160467, and price: 24.8 CNY/tablet), Dexamethasone (manufacturer: Tianjin Lisheng Pharmaceutical Co.,Ltd., specification: 0.75 mg/tablet, approval no.: H12020686, and price: 0.0869 CNY/tablet), and Etoposide (manufacturer: Qilu Pharmaceutical Co., LTD., specification: 5 ml:0.1 g/piece, approval no.: National Drug approval WORD H20143143, and price: 7.79 CNY/piece).e2.4. Outcomes' Index

2.3.1. Treatment Efficacy Index. According to the uniform efficacy standard of the International Myeloma Working Group (IMWG), the efficacy of the patients after each cycle of treatment was evaluated. Efficacy was divided into strict complete response (sCR), complete response (CR), very good partial response (VGPR), partial response (PR), disease stabilization (SD), disease progression (PD), and relapse after complete response (relapse after CR). Define therapeutic effectiveness = sCR + CR + VGPR. Adverse reaction indicators: the occurrence of peripheral neuritis in treated patients was tracked and recorded in this experiment.

2.3.2. Cost Index. Total expenses = hospitalization expenses + examination expenses + medicine expenses, hospitalization expenses = bed expenses + nursing expenses, examination fee = ultrasound fee + radiation fee + laboratory fee, medicine fee = Chinese medicine fee + western medicine fee, average daily cost = total expenses/days of hospitalization, and average treatment cost per cycle = total cost/number of treatment cycles. In this pharmacoeconomic evaluation, we only considered direct medical cost among direct costs. Due to the complexity of patient sources, direct nonmedical costs, including patient meals, patient transportation, patient wage loss, and family care, were not included in the cost calculation [4, 5]. The two groups were compared using *t*-test for statistical differences, and *P* value less than 0.05 was considered statistically significant.

3. Results

3.1. Baseline Characteristics of Included Patients. There was no statistical significance in gender, age, disease staging (ISS stage, traditional DS stage, and revised R-ISS stage) [6–8], and basic diseases (hypertension, diabetes, coronary heart disease, atrial fibrillation, cerebral hemorrhage, cerebral infarction, atherosclerosis, vein thrombosis of lower limb, hyperlipidemia, high uric acid hematic disease, hypothyroidism, thyroid nodules, chronic respiratory system disease, digestive system diseases, rheumatoid immune-related diseases, history of orthopedic surgery, allergies, etc.) ($P > 0.05$). See Table 1, for details.

3.2. Comparison of Treatment Efficacy and Safety

3.2.1. Comparison of Treatment Efficacy and Safety in All Patients. Evaluated efficacy after each cycle of treatment: the effective cases were summarized and statistically analyzed. There was no statistical difference between the original drug research group and the generic drug group. The statistical results of each cycle are shown in Table 2 ($P > 0.05$).

There was no statistical difference between the evaluation groups for each treatment cycle, indicating equivalence. The incidence of peripheral neuritis during treatment is shown in Table 3 ($P > 0.05$). There was no statistical difference in the incidence of peripheral neuritis among the included patients.

One hundred and twenty seven patients were in the newly treated original research drug group and 102 patients were in the newly treated generic drug group. The occurrence and grading of peripheral neuritis in the two groups were compared, and the specific comparison results are shown in Table 4 ($P > 0.05$). There was no statistical difference in the incidence of peripheral neuritis among the newly treated patients.

3.2.2. Comparison of Efficacy according to Different Starting States. Subgroup comparative analysis was conducted for patients with different initial states of disease, and they were divided into initial treatment MM group and recurrence/progression MM group. The effective cases were summarized and statistically analyzed, and there was no difference between initial treatment MM group and recurrence/progression MM group. Statistical results of each cycle are shown in Table 5 ($P > 0.05$). There was no statistical difference in the comparison between the subgroups of the included patients according to their different initial states, and the subgroup analysis was still equivalent [9].

3.2.3. Comparison of Efficacy in the Treatment of VRD Regimen. Each MM patient included in the experiment with each course of treatment was considered as a unit, and the highest number of treatments was VRD (Bortezomib + Lenalidomide + Dexamethasone) regimen, with a total of 323 treatment units. The partial data were still divided into VRD original research drug group and VRD generic drug group, and their curative effect evaluation was statistically analyzed. Among them, 145 patients in the original research drug group were treated with 88 patients above VGPR, and the effective rate was 60.69%. There were 178 patients in the generic drug group, and 94 patients were treated with VGPR or above. The treatment effective rate was 52.81%. The treatment effective rate between the two groups was 0.155, $P > 0.05$. In the subgroup analysis with VRD as the treatment plan, there was no statistical difference between the original drug group and the generic drug group, and the subgroup analysis was still equivalent. The statistical results are shown in Table 6.

3.2.4. Cost-Minimization Analysis of Treatment Costs. There was no statistical significance of efficacy and safety between original research drug and generic drug Bortezomib; therefore, cost-minimization analysis can be used for pharmacoeconomic analysis. Excluding the cases participating in clinical trials and data loss, 11 cases in the original research drug group and 8 cases in the generic drug group, the remaining 138 cases in the original drug group and 112 cases in the generic drug group were analyzed and compared during hospitalization. The average daily cost and average cycle cost of patients in the two groups were compared. The average daily cost of the original research drug group was 2954.38 CNY, and the average daily cost of the generic drug group was 2697.29 CNY, ($P < 0.05$). The average treatment cost per cycle was 32967.69 CNY, and the average treatment cost per cycle was 29129.57 CNY, ($P < 0.05$). The price of the average daily cost and the average treatment cost per cycle in the generic drug group were lower than the original drug group. Therefore, the generic drug group is more economical. The results were shown in Table 7.

4. Discussion

Our study results showed that there was no statistical significance of efficacy or safety between original research drug and generic drug Bortezomib. Compared with the original research drug, the generic drug has an obvious price advantage. Currently, the treatment of multiple myeloma is mainly induced by the proteasome inhibitor Bortezomib combined with glucocorticoid, plus the "three-drug combination" regimen with the immunomodulator thalidomide or lenalidomide, until autologous stem cell transplantation or disease progression [10, 11]. The treatment can obviously

Table 1: Comparison of baseline date in included patients.

	Original research drug group ($n = 149$)			Generic drug group ($n = 120$)			P
Median age		61			61		0.466
$\bar{X} \pm S$		60.55 ± 9.434			60.33 ± 8.665		
Gender							
Male		88 (0.59)			66 (0.55)		0.503
Female		61 (0.41)			54 (0.46)		
Basic disease species							
No basic disease		35 (0.23)			15 (0.13)		
1 basic disease		41 (0.28)			28 (0.23)		
2 basic diseases		33 (0.22)			25 (0.21)		
3 basic diseases		20 (0.13)			29 (0.24)		0.068
4 basic diseases		8 (0.05)			13 (0.11)		
5 basic diseases		5 (0.03)			5 (0.04)		
6 or more basic diseases		7 (0.05)			5 (0.04)		
Disease staging	I	II	III	I	II	III	
ISS	37 (0.25)	36 (0.24)	71 (0.48)	24 (0.20)	25 (0.21)	68 (0.57)	0.359
DS	5 (0.03)	16 (0.11)	125 (0.84)	5 (0.04)	14 (0.12)	98 (0.82)	0.902
R–ISS	14 (0.09)	58 (0.39)	29 (0.19)	13 (0.11)	51 (0.43)	28 (0.23)	0.435

Table 2: Comparison of treatment efficacy and safety in included patients.

Treatment cycle	Original research drug group			Generic drug group			P
	>=VGPR	Sample	Total efficacy rate (%)	>=VGPR	Sample	Total efficacy rate (%)	
1	20 (0.13)	149	13.42	22 (0.18)	120	18.33	0.270
2	44 (0.30)	149	29.53	31 (0.26)	120	25.83	0.501
3	80 (0.54)	147	54.42	65 (0.57)	114	57.02	0.676
4	92 (0.66)	139	66.19	75 (0.71)	105	71.43	0.383
5	91 (0.66)	137	66.42	69 (0.73)	95	72.63	0.315
6	90 (0.67)	134	67.16	71 (0.79)	90	78.89	0.056

Table 3: Comparison of peripheral neuritis among the included patients.

Peripheral neuritis	Original research drug group	Generic drug group	P
Cases	59	42	0.439
Incidence rate	39.60%	35.00%	

Table 4: Comparison of peripheral neuritis grades in newly treated patients.

Peripheral neuritis grade	Newly treated original research drug group ($n = 127$)	Newly treated generic drug group ($n = 102$)	P
1	9 (0.07)	7 (0.07)	0.595
2	20 (0.16)	10 (0.10)	
3	13 (0.10)	10 (0.10)	
4	0	0	

prolong the survival time and improve the quality of life. In application of Bortezomib for MM which is inevitable in the process of adverse reaction, hematology-related adverse reactions are mainly for neutropenia and nonhematology-related adverse reactions mainly include peripheral neuritis and cardiac toxicity [12, 13] and also include other herpes zoster, gastrointestinal reaction, paralytic ileus, venous thrombosis, and severe infections [14]. However, in all serious adverse reactions, peripheral neuritis has been confirmed to be the key factor for the dose limitation of Bortezomib application [15, 16]. It has a clear evaluation criterion, which has a significant effect on patients' life. Other serious adverse reactions require symptomatic treatment, which can be indirectly reflected in the treatment cost. In this study, the effectiveness of Bortezomib was compared between the original study and the generic Bortezomib, and there was no statistical difference between the groups. The collected data were used for subgroup analysis and were divided into initial treatment MM group and recurrence/progression MM group; there was no statistical difference of efficacy comparison between the groups. The effectiveness of all extracted drugs was compared between the original research drug and generic drug using VRD regimen, and there was no statistical difference

Table 5: Comparison of efficacy according to different starting states in included patients.

Subgroups	Treatment cycle	Original research drug group			Generic drug group			P
		>=VGPR	Sample	Total efficacy rate (%)	>=VGPR	Sample	Total efficacy rate (%)	
Initial treatment MM	1	17 (0.13)	127	13.39	21 (0.21)	102	20.59	0.145
	2	38 (0.30)	127	29.92	30 (0.29)	102	29.41	0.933
	3	72 (0.57)	126	57.14	62 (0.63)	98	63.27	0.354
	4	82 (0.68)	121	67.77	69 (0.76)	91	75.82	0.200
	5	80 (0.67)	119	67.23	63 (0.78)	81	77.78	0.105
	6	79 (0.71)	111	71.17	62 (0.82)	76	81.58	0.105
Recurrence/progression MM	1	3 (0.14)	22	13.64	1 (0.06)	18	5.56	0.397
	2	6 (0.27)	22	27.27	1 (0.06)	18	5.56	0.072
	3	8 (0.38)	21	38.10	3 (0.19)	16	18.75	0.202
	4	10 (0.56)	18	55.56	6 (0.43)	14	42.86	0.476
	5	11 (0.61)	18	61.11	6 (0.43)	14	42.86	0.305
	6	11 (0.85)	13	84.62	9 (0.64)	14	64.29	0.228

Table 6: Comparison of efficacy in the treatment of VRD regimen.

Subgroups	>=VGPR	Sample	Total efficacy rate (%)	P
VRD original research drug group	88	145	60.69	0.155
VRD generic drug group	94	178	52.81	

Table 7: Comparison of treatment costs for each cycle in included patients.

	Groups	Cases	Average	Standard deviations	Standard error mean	P
Average daily cost	Original research drug group	138	2954.38 CNY/day	955.22	81.31	0.044
	Generic drug group	112	2697.29 CNY/day	1053.41	99.54	
Average treatment cost per cycle	Original research drug group	138	32967.69 CNY/cycle	16374.99	1393.93	0.044
	Generic drug group	112	29129.57 CNY/cycle	12957.72	1224.39	
Average cycle length of stay	Original research drug group	138	12.52 days	6.67	0.57	0.816
	Generic drug group	112	12.35 days	3.90	0.37	

between the groups. At the same time, the safety of the drugs was analyzed and compared. By comparing the occurrence of peripheral neuritis between the original research drug and generic drug in all the included patients, it was concluded that there was no difference in the occurrence of peripheral neuritis between the two groups. There was no difference in the occurrence of peripheral neuritis between the two groups. In summary, in this study, the efficacy and incidence of peripheral neuritis of the original and generic Bortezomib were analyzed and compared through multiangle and multi-subgroup analysis, which can prove that there is no difference in the efficacy and safety of the generic and the original research drugs in China, which can provide strong support for clinical drug selection.

In the data of this experiment, the average daily cost of the original research drug was 257.09 CNY/day higher than that of the generic drug, and the average treatment cost per cycle was 3838.12 CNY/cycle higher. The unit price difference of the two drugs was 1710.03 CNY/dose. Four doses of Bortezomib were applied in each cycle, and the difference was 6840.12 CNY/cycle, which was less than the difference of average treatment cost per cycle. There was a difference of 0.17 days/cycle between patients in hospital, indicating that the price difference was not completely derived from Bortezomib. The expenses included were hospitalization expenses, examination expenses, and drug expenses. It can be seen that, in the case of small hospitalization time difference, the drug expenses of Bortezomib original research group, the main chemotherapy drug, were 6,840.12 CNY/cycle higher than the generic drug group. The price difference of 6840.12 CNY/cycle -3838.12 CNY/cycle = 3002 CNY/cycle may be derived from the examination fee during hospitalization and the drug fee for symptomatic treatment when adverse reactions occur. Although part of the treatment cost of the original research drug group was lower than that of the generic drug group, the overall treatment cost of the generic drug group was significantly lower than that of the original research drug group.

There were also some limitations in our experiment, such as limited sample size and record content amd short tracking record time. In order to get more accurate conclusions, it is still necessary to accumulate more cases, conduct long-term follow-up, and establish an accurate database.

Compared with America and Japan, the consistency evaluation of generic drugs in China started late. However, China is a big country of generic drugs; about 95% or above chemicals are generic drugs. It can be seen that it is important for Chinese national health to obtain generic drugs with high purity of active ingredients, good stability, and good safety. In 2018, the National Medical Products Administration issued the Notice on Matters Related to The Consistency Evaluation of Generic Drug Quality and Efficacy and, in May 2020, issued a series of technical guidelines, including The Technical Requirements for consistency Evaluation of Generic Drug Quality and Efficacy of Chemical Injections, to further carry out the consistency evaluation of generic drugs in China. Nowadays, more and more generic drugs are coming to people's side, and the threshold of generic drug consistency evaluation should be strictly regulated so that people can use high-quality and inexpensive drugs [17].

The Harvard Business School Management Professor Michael Porter puts forward the concept of "value-based healthcare." Different countries and teams have different interpretations of value-based healthcare. Under the social environment with serious aging trend of population, high incidence of chronic diseases, and rising medical costs, how to solve the "difficult and expensive medical treatment" has been a concern of the country, hospitals, and the masses. For patients with multiple myeloma, it is the embodiment of value medicine to improve the consistency evaluation standard of domestic generic drugs, ensure the effectiveness and safety of Bortezomib, reduce the price of generic drugs, improve the quality of life for patients with chronic cancer, and strive for longer survival time and material support.

5. Conclusion

We compared the original research drug and the generic drug Bortezomib in the treatment of MM. There was no difference between the two groups of effectiveness or safety, and the generic drug is more economical in treatment.

Data Availability

The data used to support the findings of the study can be obtained from the corresponding author upon request.

Conflicts of Interest

The authors declare that there are no conflicts of interest associated with this manuscript.

Acknowledgments

Yongchao Liang and Ying Zhu contributed equally to this study.

References

[1] S. Wang, L. Xu, J. Feng et al., "Prevalence and incidence of multiple myeloma in urban area in China : A national population-based analysis," *Frontiers Oncology*, vol. 24, 2020.

[2] W. Liu, J. Liu, J. Liu et al., "Mortality of lymphoma and myeloma in China, 2004-2017: an observational study : an observational study," *Journal of Hematology & Oncology*, vol. 12, no. 1, 2019.

[3] C. L. Jin, H. Y. Wang, and H. Sun, "The concept, progress and practice path of value-based healthcare," *Health Economics Research*, vol. 36, no. 2, pp. 6–8, 2019.

[4] G. Liu, S. Hu, J. Wu, H. Dong, and H. Li, "China guidelines for pharmacoeconomic evaluations, China," *China Journal of Pharmaceutical Economic*, vol. 6, no. 3, pp. 9+11–48, 2011.

[5] S. F. Wang, F. Zhou, and X. D. Pan, "Analysis of curative effect, hospitalization cost and cost-effect of different treatments for patients with multiple myeloma," *Chinese Journal of Evidence-Based Medicine*, vol. 20, no. 7, pp. 764–768, 2020.

[6] S. V. Rajkumar, M. A. Dimopoulos, A. Palumbo et al., "International Myeloma Working Group updated criteria for the diagnosis of multiple myeloma," *The Lancet Oncology*, vol. 15, no. 12, pp. e538–e548, 2014.

[7] B. G. M. Durie and S. E. Salmon, "A clinical staging system for multiple myeloma correlation of measured myeloma cell mass with presenting clinical features, response to treatment, and survival," *Cancer*, vol. 36, no. 3, pp. 842–854, 1975.

[8] A. Palumbo, H. Avet-Loiseau, S. Oliva et al., "Revised international staging system for multiple myeloma: a report from international myeloma working group," *Journal of Clinical Oncology*, vol. 33, no. 26, pp. 2863–2869, 2015.

[9] R. Q. Liao, X. J. Lin, X. L. Li et al., "Short-term efficacy and safety profile of generic bortezomib in the treatment of multiple myeloma," *Journal of Experimental Hematology*, vol. 29, no. 1, pp. 137–144, 2021.

[10] N. K. Z. Z. Zhonghua, "The guidelines for the diagnosis and management of multiple myeloma in China(2020 revision)," *Chinese Journal of Internal Medicine*, vol. 59, no. 5, pp. 341–346, 2020.

[11] Y. C. Liang, Z. X. Zhao, and Y. Zhu, "Research status of bortezomib in the treatment of multiple myeloma," *The Chinese Journal of Clinical Pharmacology*, vol. 37, no. 15, pp. 2096–2099, 2021.

[12] R. Fonseca, S. Abouzaid, M. Bonafede et al., "Real-world trends in treatment use, healthcare costs, and overall survival among patients with multiple myeloma," *Blood*, vol. 128, no. 22, p. 3558, 2016.

[13] C. Y. Sun, J. Y. Li, Z. B. Chu, L. Zhang, L. Chen, and Y. Hu, "Efficacy and safety of bortezomib maintenance in patients with newly diagnosed multiple myeloma: a meta-analysis," *Bioscience Reports*, vol. 37, no. 4, 2017.

[14] Q. Wang, C. X. Zhang, and J. Fu, "Clinical efficacy of domestic Bortezomib in the treatment of multiple myeloma and its safety," *Journal of Chinese Physician*, vol. 22, no. 08, pp. 1275–1278, 2020.

Hindawi
Journal of Healthcare Engineering
Volume 2023, Article ID 9841704, 1 page
https://doi.org/10.1155/2023/9841704

Retraction

Retracted: Unilateral Sciatic Nerve Crush Induces White Blood Cell Infiltration of the Contralateral Nerve

Journal of Healthcare Engineering

Received 23 May 2023; Accepted 23 May 2023; Published 24 May 2023

This article has been retracted by Hindawi following an investigation undertaken by the publisher [1]. This investigation has uncovered evidence of one or more of the following indicators of systematic manipulation of the publication process:

(1) Discrepancies in scope
(2) Discrepancies in the description of the research reported
(3) Discrepancies between the availability of data and the research described
(4) Inappropriate citations
(5) Incoherent, meaningless and/or irrelevant content included in the article
(6) Peer-review manipulation

The presence of these indicators undermines our confidence in the integrity of the article's content and we cannot, therefore, vouch for its reliability. Please note that this notice is intended solely to alert readers that the content of this article is unreliable. We have not investigated whether authors were aware of or involved in the systematic manipulation of the publication process. Wiley and Hindawi regrets that the usual quality checks did not identify these issues before publication and have since put additional measures in place to safeguard research integrity.

We wish to credit our own Research Integrity and Research Publishing teams and anonymous and named external researchers and research integrity experts for contributing to this investigation.

The corresponding author, as the representative of all authors, has been given the opportunity to register their agreement or disagreement to this retraction. We have kept a record of any response received.

References

[1] J. Cheng, L. Ding, M. Yang, Y. Zhu, Z. Gu, and G. Lv, "Unilateral Sciatic Nerve Crush Induces White Blood Cell Infiltration of the Contralateral Nerve," *Journal of Healthcare Engineering*, vol. 2022, Article ID 1101383, 6 pages, 2022.

Hindawi
Journal of Healthcare Engineering
Volume 2022, Article ID 1101383, 6 pages
https://doi.org/10.1155/2022/1101383

Research Article

Unilateral Sciatic Nerve Crush Induces White Blood Cell Infiltration of the Contralateral Nerve

Jia Cheng, Lingtao Ding, Minlie Yang, Yugang Zhu, Zaiqiu Gu, and Guozhong Lv

Department of Burn and Plastic Surgery, Affiliated Hospital of Jiangnan University, Wuxi, Jiangsu, China

Correspondence should be addressed to Guozhong Lv; lv_gzh126@126.com

Received 13 February 2022; Revised 27 February 2022; Accepted 12 March 2022; Published 29 March 2022

Academic Editor: Liaqat Ali

Nerve injury leads to the accumulation of white blood cells derived from the bone marrow in the lesioned nerve, but it is still unknown whether there are similar responses in unlesioned nerves. To address this question, sciatic nerves of mice expressing enhanced green fluorescent protein (EGFP) in their bone marrow were crushed unilaterally to observe the invasion of bone marrow-derived cells into the contralateral unlesioned nerve. Two days after surgery, $EGFP^+$ cells began to infiltrate both the damaged and undamaged nerves. These cells gradually amplified to the highest point within 14 days and slowly lowered. In ipsilateral (lesioned) and contralateral (unlesioned) nerves, the time course of infiltration of $EGFP^+$ cells was similar, but the magnitude was much less for the unlesioned one. Through CD68 staining, some cells were identified as macrophages. Transmission electron microscopy revealed slight demyelination and phagocytosing macrophages in the contralateral nerve. The data showed that infiltration by white blood cells is a response to nerve injury, even in uninjured nerves.

1. Introduction

Peripheral nerve degeneration after an injury is characterized by the breakdown of axons and myelin sheaths, glial cell proliferation, blood-nerve barrier compromise, and dramatically, phagocytosis by macrophages of Schwann cells in the distal nerve which is called Wallerian degeneration [1–4]. There are two kinds of macrophages within the Wallerian degeneration: hematogenous macrophages derived from the bone marrow and resident endogenous macrophages. Cámara-Lemarroy et al. [5] and Koltzenburg et al. [6] have found that, in addition to the phagocytosing axon and myelin remnants, macrophages could promote proliferation of Schwann cells and fibroblasts and release neurotrophic factors and cytokines [7, 8].

The nervous system of mammals has a high degree of bilateral symmetry [9]. There is a wide range of examples in which unilateral interventions produce bilateral effects [10–12]. In the center nerve system, unilateral injury to the lateral fimbria resulted in bilateral gliosis in the septum and hippocampus. Some cellular and molecular changes in the contralateral DRG and sciatic nerve after unilateral peripheral nerve injury have also been described [9, 13]. There is no study showing whether there are changes or not in the contralateral sciatic nerve after unilateral injury, nor has any report discussed the differences between cell infiltration patterns in the contralateral nerve compared with the ipsilateral side.

The aim of this research was to find out whether white blood cells derived from the bone marrow invade the contralateral sciatic nerve after unilateral injury and analyze the pattern of such infiltration. To track bone marrow-derived cell infiltration, we utilized irradiated bone marrow chimera mice that expressed EGFP in all bone marrow-derived cells [5, 14]. Preparations were counterstained with an antiserum against CD68, a marker of macrophages, to visualize hematogenous macrophages infiltration from the systemic circulation. Two days, sciatic nerves were extracted at 1, 2, 4, 8, 12, and 30 weeks following the crush injury and tested through immunofluorescent staining and transmission electron microscopy.

2. Materials and Methods

2.1. Bone Marrow-Irradiated Chimeric Mice. The Animal Ethics Committee of the Chinese Academy of Medical Sciences and Peking Union Medical College approved all experimental methods. As previously stated, chimeric mice were created [13–15]. On a C57BL/6J genetic background, EGFP transgenic mice expressing the enhanced green fluorescent protein gene were utilized (Model Animal Research Central of Nanjing University, Nanjing, China). 9 Gray was used to irradiate wild-type C57BL/6J mice (Shanghai SLAC Laboratory Animal Co., Ltd., Shanghai, China). Following that, donor bone marrow cells were extracted from the long bones of $EGFP^+$ mice, and 8106 cells were injected into the tail vein by injection. Only chimeras with >95 percent $EGFP^+$ leukocytes were used for additional studies after 3 months. Fluorescence microscopy was used to measure the percentage of $EGFP^+$ leukocytes in chimera mice.

2.2. Sciatic Nerve Injury and Tissue Processing. Intraperitoneal injection of ketamine/xylazine was used to deeply anesthetize mice. Only the epineurium remained intact after the right sciatic nerve was crushed for 15 seconds distal to the sciatic notch using forceps. Six mice from each group were allowed to survive for 2 days, 1, 2, 4, 8, 12, and 30 weeks after crush injury. Sciatic nerves were then extracted and fixed for 2 hours in a 10% sucrose solution with 4% paraformaldehyde, then submerged in a 30% sucrose solution at 4°C overnight. Samples were embedded in optimal cutting temperature compound (OCT) for frozen sections, and 10 mm thick cryosections were produced with a cryostat-microtome (Thermo, Cheshire, USA). The contralateral transverse sections were obtained at a site that was roughly comparable to the crash damage.

2.3. Immunofluorescence Analysis. The slides were rinsed with PBS and masked in a solution that contains 10% goat serum at ambient temperature, followed by an incubation period at 4°C with rat anti-CD68 antibody (1 : 250, Serotec, Oxford, UK). Finally, the sections were treated with Alexa Fluor 555-donkey anti-rat IgG for 45 minutes at 37°C (1 : 1000, Invitrogen, Carlsbad, USA). 4′,6-diamidino-2-phenylindole (DAPI; 1 : 500, Invitrogen) was used to counterstain the nuclei for 30 seconds. A confocal microscope was used to capture the fluorescent pictures (Leica SP5, Germany). The intensity of immunofluorescence staining was measured using the Image-Pro Plus 6.0 software (Media Cybernetics, USA) to calculate the integrated optical density (IOD) of positive expression from six randomly selected sections, as described previously [16].

2.4. Transmission Electron Microscopy. Sciatic nerves were preserved in 2% glutaraldehyde for 2 hours at 4°C then in 1% osmic acid (diluted with PBS) for 2 hours at 4°C. Sciatic neurons were dehydrated to use a graded series of alcohol solutions in the sequence shown below after being washed with PBS. The sciatic nerve cells were washed with PBS and dehydrated with the gradient series of alcohol solution as shown in the following sequence: 30%–50%–70% and 80%–95%–100% alcohol 10 min each. After that, the alcohol was replaced with epoxypropane for 10 minutes, followed by epoxy resins 618 and epoxypropane (1 : 1) for 2 hours, and then the mixture was heated to 60°C for 48 hours. Using an LKB-V ultramicrotome (LKB ProdukterB, Stockholm; Sweden), semithin sections (1 mm thickness) and ultrathin sections (50 nm thickness) were cut, stained with lead citrate, and examined under CM-120 transmission electron microscopy (Philips, Netherlands).

2.5. Statistical Analysis. All of the data were presented as means with standard deviations (SD). When applicable, values were established using paired *t*-tests between two groups and one-way analysis of variance (ANOVA) among three or more groups using SPSS version 19.0 (Chicago, IL, USA) for quantitative comparison and analysis. Statistical significance was defined as a P value of less than 0.05.

3. Results

3.1. Bone Marrow-Derived $EGFP^+$ Cells Invade the Contralateral Uninjured Nerve. Very few $EGFP^+$ cells were detected in normal sciatic nerve (Figure 1(a), control). To observe whether the uninjured nerve had any changes of bone marrow-derived $EGFP^+$ cells after unilateral nerve crush, both nerves were harvested at 2 days and 1, 2, 4, 8, 12, and 30 weeks after injury. Similar to the injury site, on day 2, $EGFP^+$ cells began invading the contralateral neuron, which steadily grew to a peak at 2 weeks before gradually decreasing (Figure 1(a)). Interestingly, $EGFP^+$ cells of the injured side dropped to a normal level within 12 weeks; but on the contralateral side, they were still elevated (Figure 1(b)). In addition, most $EGFP^+$ cells were arranged in a longitudinal direction within the entire nerve (Figure 2). Contralateral nerve segment $EGFP^+$ cell infiltration patterns were identical to ipsilateral nerve segment infiltration patterns. The number of $EGFP^+$ cells in contralateral nerve segments, on the other hand, was lower than in ipsilateral nerve segments. The contralateral: the ipsilateral ratio was around 1 : 11.5 at 2 weeks (Figure 1(b)).

3.2. Variation of Macrophages on the Contralateral Side. Macrophages are the crucial effector cells in neuropathies [17]. To identify and localize bone marrow-derived macrophages, EGFP autofluorescence was combined with a CD68 antibody. In normal sciatic nerve, very few resident macrophages ($EGFP^-/CD68^+$) were observed in either nerve (Figure 3(a), Control). Two days, 1, 2, 4, 8, 12, and 30 weeks after crush injury, numerous hematogenous macrophages ($EGFP^+/CD68^+$) as well as resident macrophages were present in the injured nerve (Figure 3(a)), and hematogenous macrophages increased more obviously than resident macrophages (Figure 3(b)). On the contrary, on the contralateral side, only a few $EGFP^+$ cells were macrophages (Figure 3(a)), and hematogenous macrophages were significantly less than resident macrophages (Figure 3(b)). When the total number of $EGFP^+$ cells and macrophages

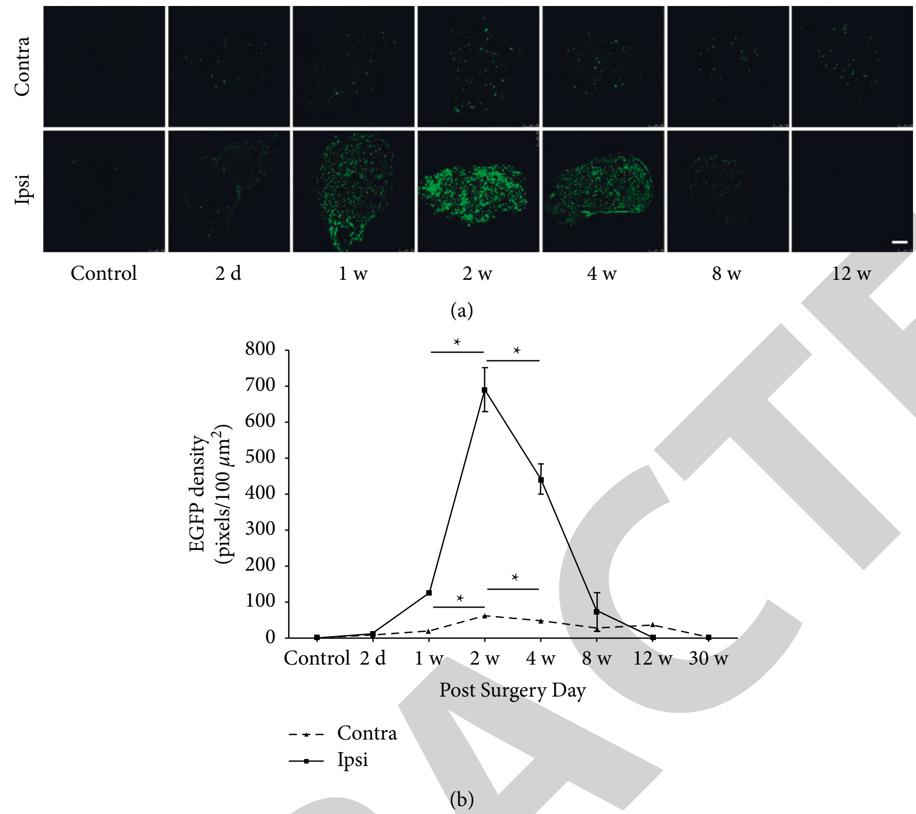

FIGURE 1: EGFP$^+$ cells infiltration in the contralateral and ispilateral sciatic nerves after unilateral injury. (a) EGFP$^+$ cells in the contralateral (contra) and ispilateral nerves (Ipsi). (b) Quantification of EGFP$^+$ cells at different time points. Control: normal sciatic nerve. Bar = 100 μm. $^*P < 0.05$.

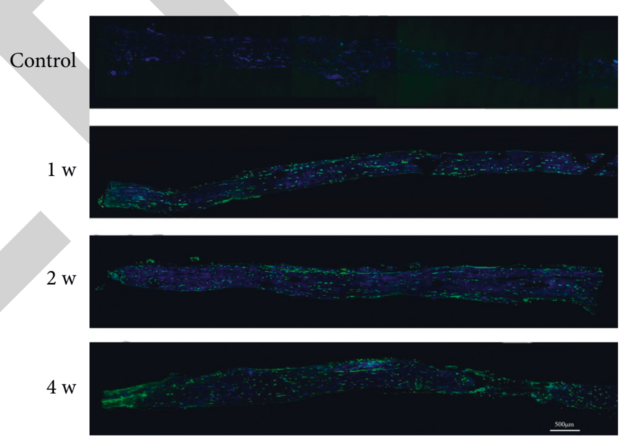

FIGURE 2: EGFP$^+$ cells distribution in the whole entire contralateral nerves. The longitudinal distribution of EGFP$^+$ cells within contralateral and ispilateral nerves 1 week, 2 weeks, and 4 weeks after injury. Bar = 500 μm.

(Total M) in the crush-injured nerve was compared to the contralateral nerve, the total number of EGFP$^+$ cells and macrophages (Total M) was found to be significantly higher in the crush-injured nerve (Figures 1(b), 3(b), and 3(c)).

3.3. Ultrastructure of the Contralateral Nerve. After nerve injury, macrophages penetrate the Schwann cell basal lamina to reach and phagocytose the myelin. To assess whether there was the same phenomenon in the contralateral uninjured nerve, we examined the nerves after 2 weeks of crush injury by electron microscopy. The results demonstrated that most myelin sheaths were normal and complete in the contralateral nerve (Figure 4(a)). However, typical degenerative Schwann cell alterations were also observed (Figures 4(b) and 4(c)). In addition, motile macrophages with elongated cytoplasmic processes located outside the Schwann cell basal lamina were noticed to be sparsely

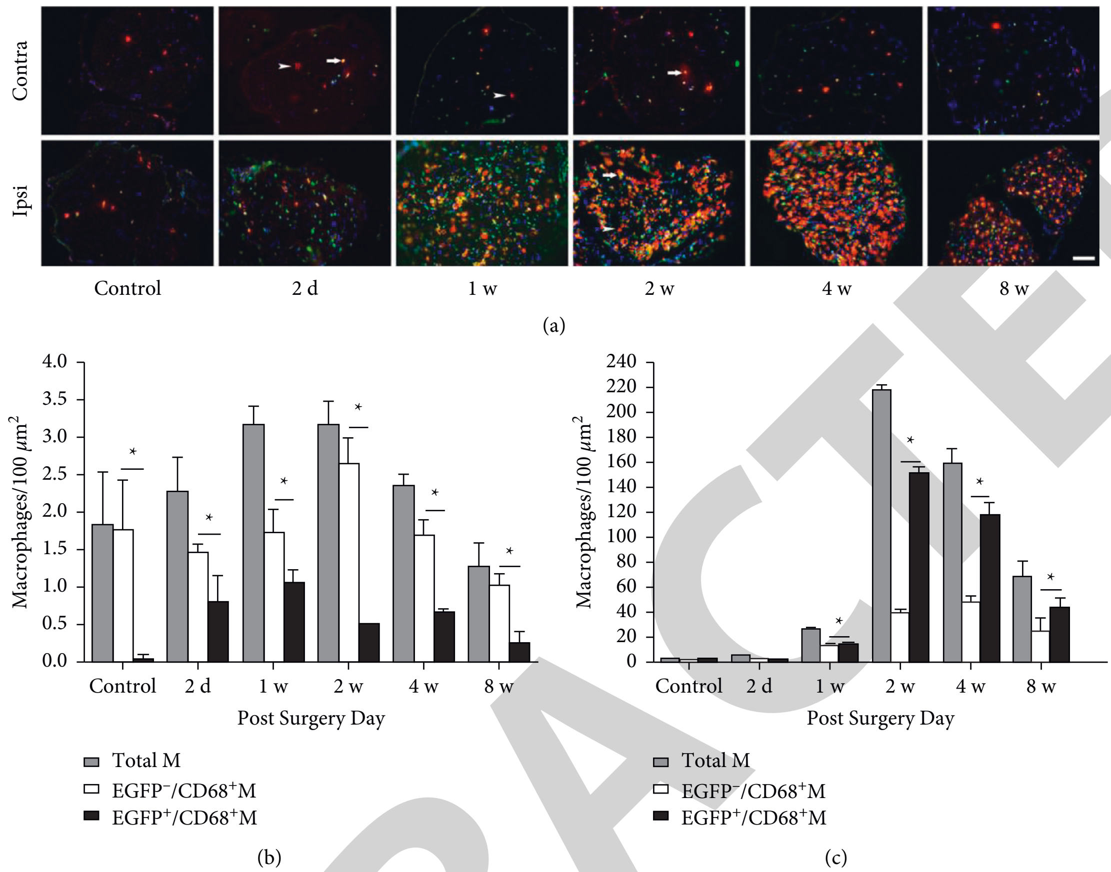

Figure 3: Localization of endogenous and hematogenous macrophages at different time points. (a) CD68 staining (red) and EGFP$^+$ cells within the contralateral and ispilateral nerves. (b) Quantification of macrophages at different time points. Total M: total macrophages; EGFP$^-$/CD68$^+$ M: endogenous macrophages (arrowhead, red); EGFP$^+$/CD68$^+$ M: hematogenous macrophages (arrow, yellow). Bar = 100 μm. $^*P < 0.05$.

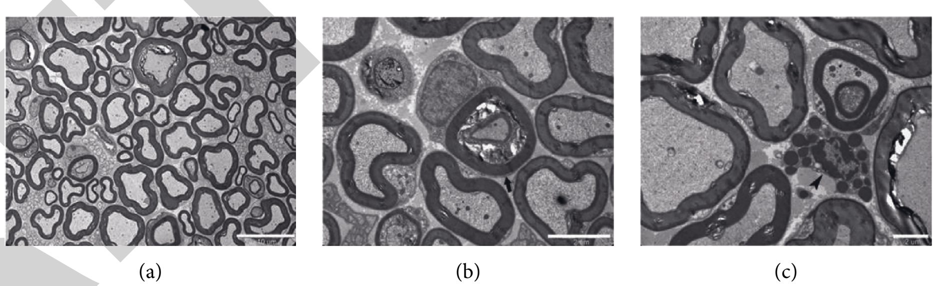

Figure 4: Ultrastructure of the contralateral sciatic nerves 2 weeks after injury. (a) Normal and complete myelin sheaths in the contralateral nerve. Demyelinating phenomenon ((b), arrow) and active macrophages with elongated cytoplasmic processes and deris filled the cytoplasm ((c), arrowhead) were present in the contralateral nerve. Bar (a) = 10 μm. Bar (b, c) = 2 μm.

distributed (Figure 4(c)). Some macrophages with lipid droplets and end products of myelin-degradation were presented as phagocytosing macrophages (Figure 4(c)). These data provided strong evidence that the contralateral nerve also undertook slight demyelination and inflammatory reaction after unilateral sciatic nerve crush.

4. Discussion

When the peripheral nervous system is damaged, a complicated cellular immune response emerges. Neutrophils are the first immune cells to assemble in the distal stump, and they do so within 8 hours. Hematogenous macrophages take over as the main leukocyte population as a result. In addition, local macrophages have been discovered to have a role in Wallerian degeneration. In peripheral nerves, resident macrophages makeup 2–9 percent of total cells and are known to be phagocytic. To date, whether hematogenous immune cells are recruited into the contralateral sciatic nerve has never been investigated. Our study corroborated that the infiltration by white blood cells in one nerve also appears in the contralateral uninjured nerve at the same time [18].

In our study, bone marrow chimeric animal models were used to detect bone marrow-derived cells. Together with the colocalization of CD68, resident and hematogenous macrophages could be separated from other cells easily. In our mice, rapid $EGFP^+$ cell infiltration and macrophages activation were found in the injured nerve. A similar time course of infiltration of $EGFP^+$ cells was also seen on the contralateral side, but many fewer infiltrating cells were seen. Interestingly, in the contralateral nerve, only a few bone-derived marrow-derived cells were $EGFP^+/CD68^+$, which was in sharp contrast to the injured nerve. This may be because other hematogenous immune cells have a more important role than macrophages in the contralateral response. These available data indicated that macrophage reaction patterns had a close relationship with the severity of damage in the peripheral nerve system. Only under the circumstance of more severe damages, an additional influx of macrophages is initiated, together with resident macrophages to exert their functions [19].

Macrophages will efflux out of the lesioned Schwann cell basal lamina and nerve once phagocytosis is done, allowing for effective repair and regeneration [18, 19]. In addition, Fry et al. [20] have demonstrated that the presence of new myelin promotes macrophage outflow from the Schwann cell basal lamina and impacts their final exit from the lesioned nerve. In our experiment, $EGFP^+$ cells moved out of the contralateral nerve more slowly than from the injured nerve. This might be due to less newly synthesized myelin, so fewer signals were sent to $EGFP^+$ cells to migrate out of the nerve [21].

One explanation for contralateral involvement is that the lesion-induced signals from the spinal commissural interneurons where hematogenous macrophages and the retrograde signal could be transported from the injury site during Wallerian degeneration could induce cellular and molecular changes in the contralateral side. Another possible reason is the blood transmission of the damage-induced signals to the contralateral side. During Wallerian degeneration, the blood-nerve barrier becomes more permeable for large molecules. Therefore, blood flow might deliver factors from the injured nerve to the contralateral nerve which could initiate the invasion of $EGFP^+$ cells. However, some limitations and shortcomings of our research still need to be improved in our further experimentation, such as the exact mechanism responsible for contralateral involvement and how the contralateral nerve can get information from the injured nerve remain unknown. Our data describe for the first time unilateral sciatic nerve crush induces white blood cell infiltration of the contralateral nerve. That is, is this increase in infiltration, and the associated slight disruption of myelin, a general response of all peripheral nerves to local lesions, or a specific response to uninjured sciatic nerves [22]?

5. Conclusion

In this study, we concluded that an immunologically mediated hematogenous cells response could take place in the uninjured nerves, which had a similar infiltration trend with the injured side. Studies focusing on the contralateral nerves may also have implications for our comprehensive understanding of peripheral nerve pathophysiology [23].

Data Availability

The data used to support this study are available from the corresponding author upon request.

Disclosure

Jia Cheng is the first author.

Conflicts of Interest

The authors declare that there are no conflicts of interest.

Acknowledgments

This research was supported by the National Natural Science Foundation of China (81571921), Major Program of Wuxi Municipal Health and Family Planning Commission (Z201710), and Capital Characteristic Key Project of Beijing Municipal Science and Technology Commission (Z141107002514007).

References

[1] W. Brück, “The role of macrophages in Wallerian degeneration,” *Brain Pathology*, vol. 7, no. 2, pp. 741–752, 1997.

[2] M. P. Coleman and M. R. Freeman, “Wallerian degeneration, wld(s), and nmnat,” *Annual Review of Neuroscience*, vol. 33, no. 1, pp. 245–267, 2010.

[3] H. Lee, J. Baek, H. Min, I. H. Cho, S. W. Yu, and S. J. Lee, “Toll-like receptor 3 contributes to wallerian degeneration after peripheral nerve injury,” *Neuroimmunomodulation*, vol. 23, pp. 209–216, 2016.

[4] E. Ydens, A. Cauwels, and B. Asselbergh, “Acute injury in the peripheral nervous system triggers an alternative macrophage response,” *Journal of Neuroinflammation*, vol. 9, p. 176, 2012.

[5] C. R. Cámara-Lemarroy, F. J. Guzmán-de la Garza, and N. E. Fernández-Garza, “Molecular inflammatory mediators in peripheral nerve degeneration and regeneration,” *Neuroimmunomodulation*, vol. 17, no. 5, pp. 314–324, 2010.

[6] M. Koltzenburg, P. D. Wall, and S. B. McMahon, “Does the right side know what the left is doing?” *Trends in Neurosciences*, vol. 22, pp. 122–127, 1999.

[7] J. A. Lindborg, M. Mack, and R. E. Zigmond, “Neutrophils are critical for myelin removal in a peripheral nerve injury model of wallerian degeneration,” *Journal of Neuroscience*, vol. 37, pp. 10258–10277, 2017.

Hindawi
Journal of Healthcare Engineering
Volume 2023, Article ID 9871960, 1 page
https://doi.org/10.1155/2023/9871960

Retraction

Retracted: Consistency Analysis of CTLM Imaging and Mammography in the Diagnosis of Breast Tumor Lesions

Journal of Healthcare Engineering

Received 26 September 2023; Accepted 26 September 2023; Published 27 September 2023

This article has been retracted by Hindawi following an investigation undertaken by the publisher [1]. This investigation has uncovered evidence of one or more of the following indicators of systematic manipulation of the publication process:

(1) Discrepancies in scope
(2) Discrepancies in the description of the research reported
(3) Discrepancies between the availability of data and the research described
(4) Inappropriate citations
(5) Incoherent, meaningless and/or irrelevant content included in the article
(6) Peer-review manipulation

The presence of these indicators undermines our confidence in the integrity of the article's content and we cannot, therefore, vouch for its reliability. Please note that this notice is intended solely to alert readers that the content of this article is unreliable. We have not investigated whether authors were aware of or involved in the systematic manipulation of the publication process.

In addition, our investigation has also shown that one or more of the following human-subject reporting requirements has not been met in this article: ethical approval by an Institutional Review Board (IRB) committee or equivalent, patient/participant consent to participate, and/or agreement to publish patient/participant details (where relevant).

Wiley and Hindawi regrets that the usual quality checks did not identify these issues before publication and have since put additional measures in place to safeguard research integrity.

We wish to credit our own Research Integrity and Research Publishing teams and anonymous and named external researchers and research integrity experts for contributing to this investigation.

The corresponding author, as the representative of all authors, has been given the opportunity to register their agreement or disagreement to this retraction. We have kept a record of any response received.

References

[1] Z. Song, H. Wang, X. Feng, X. Yang, P. Han, and J. Zhao, "Consistency Analysis of CTLM Imaging and Mammography in the Diagnosis of Breast Tumor Lesions," *Journal of Healthcare Engineering*, vol. 2022, Article ID 5391636, 8 pages, 2022.

Hindawi
Journal of Healthcare Engineering
Volume 2022, Article ID 5391636, 8 pages
https://doi.org/10.1155/2022/5391636

Research Article

Consistency Analysis of CTLM Imaging and Mammography in the Diagnosis of Breast Tumor Lesions

Zhangjun Song ,[1] Huxia Wang,[2] Xiaorui Feng,[3] Xiaomin Yang,[2] Pihua Han,[2] and Jing Zhao[2]

[1]*Department of Oncology, Shaanxi Provincial People's Hospital, Xi'an 710068, China*
[2]*Department of Breast, Shaanxi Provincial Cancer Hospital, Xi'an 710061, China*
[3]*Department of Radiation Oncology, Xi'an High-tech Hospital, Xi'an 710000, China*

Correspondence should be addressed to Zhangjun Song; szj2017006@xjtu.edu.cn

Received 9 February 2022; Accepted 7 March 2022; Published 29 March 2022

Academic Editor: Liaqat Ali

Objective. To analyze the consistency of preoperative CTLM imaging in the diagnosis of breast cancer lesions and postoperative pathological examination. Methods. The clinical data of 225 patients with breast tumor in our breast surgery department were collected. All patients underwent mammography, CTLM, and pathological examination. To analyze the image characteristics of breast CTLM imaging, calculate the diagnostic efficacy of CTLM imaging for breast tumors, and compare the image characteristics of CTLM imaging for benign and malignant tumors. Results. (1) Postoperative pathological examination showed that 136 cases (60.44%) of lesions were benign tumors, and 89 cases (39.56%) were malignant tumors. (2) The "spokes distribution" of normal breast CTLM images was interrupted. In the 3D reconstructed images, the morphology of the abnormal angiogenesis area is mostly irregular nonbanded structure, which is manifested as slab structure, spindle structure, spherical structure, diverticulum structure, inverted conical structure, rings structure, branched structure, and dumbbell structure. (3) The detection rate of breast tumor by CTLM imaging was 84.44%. The specificity and coincidence rate of CTLM imaging were higher than that of mammography ($P < 0.05$). (4) The features of CTLM imaging images of breast malignant tumors are mostly bright white locally, with irregular edges and obvious attenuation of laser signal, and the reconstructed shape of 3D images is mostly like a slab structure. Conclusion. CTLM imaging can provide related information of neovascularization in breast cancer lesions, which is basically consistent with pathologically confirmed lesions.

1. Introduction

According to the global cancer incidence and death rates released by the International Agency for Research on *Cancer* in 2020 [1], female breast cancer has surpassed lung cancer as the most common cancer. Factors such as women's age [2], fertility [3], hormone use [4], and family history of breast cancer [5] affect the incidence of breast cancer. For example, the incidence of breast cancer increases with age. Annual physical examination is recommended for women younger than 40 years of age and can help patients screen for abnormalities early in the disease [6]. Physical examination of the breast usually involves routine imaging examinations, such as mammography [7]. There are some limitations to this examination. Breast density affects the rate of disease detection. For women between 40 and 79 years with fatty breasts, the sensitivity is 80–87%. However, for women with dense breasts, the sensitivity of the examination is significantly decreased [8]. Early detection of breast cancer lesions and accurate measurement of tumor size in abnormal lesions can help to develop accurate treatment protocols and improve patient prognosis. Radiologists are often unable to make an accurate diagnosis with only the results of routine imaging tests. Computed tomographic laser mammography (CTLM) is an optical imaging method [9]. The near-infrared laser with a wavelength of 808 nm can be used as the laser source, the oxygenated hemoglobin in the blood vessels of patients can be used as the natural contrast agent of human body, and the stimulated light can be absorbed and scattered [10]. Finally, abnormal vascular information was obtained by 3D image reconstruction. Abnormal angiogenesis plays a key role in tumor growth, nourishing the lesion and promoting the proliferation and migration of abnormal cells. In the examination of breast cancer, monitoring abnormal angiogenesis is of great significance. Therefore, 225 patients with breast tumors in this study were examined by routine mammography, CTLM imaging, and pathological examination, with mammography as the contrast, aiming to analyze the image characteristics of breast tumor measured by CTLM imaging and the consistency between the diagnosis of lesions and postoperative pathological examination.

2. Materials and Methods

2.1. General Data. A retrospective analysis was performed on breast tumor patients admitted to the Mammary Department of Shaanxi Provincial *Cancer* Hospital from January 2018 to February 2020. All patients were examined by mammography and CTLM. The treatment was operation, and the diagnosis was based on the results of operation and pathology. The inclusion criteria were as follows: (1) patients between 18 and 80 years; (2) patients with complete clinical data and confirmed breast lesions; and (3) all patients with single lesions received mammography, CTLM imaging, and postoperative pathological examination. The exclusion criteria were as follows: (1) had received breast lesions related treatment one month before examination; (2) had breast augmentation surgery with implants in the breast; (3) a history of allergic symptoms to light; (4) pregnant or nursing patients; and (5) incomplete clinical data, lack of mammography, CTLM imaging, and postoperative pathological examination. The final total included 225 patients. All were females, including 89 patients with malignant breast tumor, aged 24–79 years, with a mean age of 50.33 ± 10.58 years, and 136 patients with benign breast lesions, aged 31–70 years, with a mean age of 46.62 ± 6.98 years. The study was a retrospective analysis with no informed written consent from the patients. Before analysis, all records are anonymized and stripped of identity.

2.2. Instruments and Methods. (1) Mammography: the full digital mammography machine (Selenia Dimensions, Hologic, USA) was used for breast examination. The patient was placed in a standing position, and radiographs of both breasts were taken in the head and tail and in the external oblique position, with point compression and other views as appropriate. The main calculation of breast density, observation of calcification, and lesion location. (2) CTLM imaging: Imaging Diagnostic Systems of model 1020 CTLM is used for detection. The patient lies flat on the examination table in a prone position, fully exposing the examination area. A scan ring of an appropriate size is selected, and the laser source detector surrounds the area to be inspected. The section thickness is set to 2 mm by default, which can be adjusted according to the size of the patient's breast. If the breasts are too large, it is set to 4 mm. If the breasts are too small, it is set to 1 mm. After scanning, 3D image reconstruction is carried out using special software. Image interpretation is performed by radiologists with at least 5 years of working experience.

2.3. Observation Indexes

(1) The results of the postoperative pathological examination of 225 patients were recorded and the image characteristics of CTLM were analyzed
(2) The patients were divided into benign tumor group and malignant tumor group. The differences of general clinical data and image features of CTLM imaging were compared between the two groups
(3) Compared with the pathological results, the detection rate of benign and malignant tumors and abnormal lesions on mammography and CTLM were analyzed, and the sensitivity, specificity, positive predictive value (PPV), and negative predictive value (NPV) of the two methods were calculated and also comparative diagnostic efficacy was carried out
(4) To explore whether the classification of different clinical indicators can affect the detection rate of abnormal lesions by CTLM imaging

2.4. Statistical Analysis. SPSS 25.0 statistical software package was used for data analysis. Quantitative parameters in this paper were expressed in the form of the mean $\pm$ standard deviation ($X \pm S$). Intergroup analysis was performed using the independent sample *t*-test. The images were drawn using the GradPad Prism 7.0 software package. Enumeration data were presented in the form of (%), and differences between groups were compared using χ^2 analysis. The significance level was 0.05.

3. Results

3.1. Pathological Results and General Clinical Data of Enrolled Patients. According to the inclusion criteria and exclusion criteria established according to the purpose of the study, a total of 225 patients were included as research objects. Pathological results showed that 136 cases (60.44%) of breast tumors were benign tumors. There were 74 (32.89%) fibroadenomas, 38 (16.59%) adenopathy, 19 (8.44%) intraductal papilloma, 2 (0.89%) chronic inflammation, and 3 (1.33%) lobulated tumors of the breast. 89 patients (39.56%) were found with malignant tumors, including 40 (17.78%) with invasive lobular carcinoma, 36 (16%) with invasive ductal carcinoma, 2 (0.89%) with invasive ductal lobular carcinoma, 3 (1.33%) with ductal carcinoma in situ, 2(0.89%) with lobular carcinoma in situ, 2(0.89%) with micro-infiltrating carcinoma, and 4 (1.78%) with other tumors. The patients were divided into the benign tumor group and the malignant tumor group. There were significant differences in age, BMI, and menstrual status between the two groups ($P < 0.05$). There was no significant difference between groups with hormone use history and family history of breast lesions ($P > 0.05$). The results are in Table 1 and 2.

Table 1: Pathological results of 225 patients with breast tumor.

Benign and malignant	Category	Ratio of patients N (%)
	Fibroadenoma	74 (32.89)
	Adenopathy	38 (16.89)
Benign tumour, $n = 136$ (60.44%)	Intraductal papilloma	19 (8.44)
	Chronic inflammation	2 (0.89)
	Lobulated tumor of the breast	3 (1.33)
	Invasive lobular carcinoma	40 (17.78)
	Invasive ductal carcinoma	36 (16.00)
	Invasive ductal lobular carcinoma	2 (0.89)
Malignant tumor, $n = 89$ (39.56%)	Ductal carcinoma in situ	3 (1.33)
	Lobular carcinoma in situ	2 (0.89)
	Microinfiltrating carcinoma	2 (0.89)
	Others	4 (1.78)
Total		225 (100)

Table 2: Comparison of general clinical features of 225 patients with breast tumor.

Classification	Benign tumor ($n = 136$)	Malignant tumors ($n = 89$)	*P Value*
Age (years)	46.62 ± 6.98	50.33 ± 10.58	0.001
BMI (kg/m^2)	23.26 ± 3.51	24.10 ± 3.13	0.021
Menstrual status n (%)			
Premenopausal	96 (70.59)	41 (46.07)	0.000
Postmenopausal	40 (29.41)	48 (53.93)	
Hormone use, n (%)	1 (0.74)	2 (2.25)	0.397
History of benign breast lesions, n (%)	8 (5.88)	4 (4.49)	0.578
Family history of breast malignancy, n (%)	22 (16.18)	18 (20.22)	0.740

Note. BMI is body mass index.

3.2. CTLM Image Features of Normal and Abnormal Breast. In CTLM imaging, blood hemoglobin is the body's natural contrast agent. By comparing the image features of normal and abnormal blood vessels, the image features of attenuation signal of abnormal blood vessels were summarized in Figure 1. In CTLM imaging, the normal vascular signal structure of the breast was mainly manifested as banded, branched, and stellate structures. The branching or stellate structures are usually formed by intersecting veins. In this study, the normal CTLM images of blood vessels are thicker near the chest wall and converge toward the nipple, and gradually become thinner when converging, and when converging in the areola region, a flat round high signal intensity region (or bright region) is formed. The blood distribution of normal glandular lobules in the coronal image is shown as multiple cone-shaped regions with tips pointing to the center, showing a "spoke-like" distribution. The image can be observed layer by layer on the coronal image, and this image representation is continuously changing. Abnormal vascular morphology in coronal images is usually manifested as round or oval bright signal or high signal intensity areas, and is often accompanied by a layer-by-layer interruption of the "hub-like distribution" of the glandular lobules. In the 3D reconstruction images, the abnormal angiogenic areas were mostly irregular nonbanded structures, manifested as slab structure, spindle structure, spherical structure, diverticulum structure, inverted conical structure, rings structure, branched structure and dumbbell structure, and were shown in MIP mode, but rarely appeared in FTB mode. The angiogenic area of malignant tumors is also shown as an isolated area of high signal intensity, which is less associated with the surrounding areas of low signal intensity.

3.3. Comparison of CTLM Image Features of Benign and Malignant Breast Tumor. Benign and malignant tumors have different CTLM image characteristics. The classification and summary of the image features of benign and malignant tumors are helpful to the diagnosis of benign and malignant breast tumors. Compared with CTLM images of normal patients, the abnormal focus image signal area has a significant bright area, interrupting the regular distribution, color for bright white or yellow-green. The results of the 3D reconstruction showed that the shape of the abnormal area was more like a slab structure, a spindle structure, a spherical structure, and a diverticulum structure. The areas of malignant lesions were bright white ($P < 0.001$), and the margins with surrounding normal tissue were irregular ($P < 0.001$). The laser signal attenuation was obvious ($P < 0.001$), and the probability of 3D reconstruction shapes resembling slab structure, branch structure, ring structure, and dumbbell structure is higher than that of benign tumor lesions ($P < 0.001$). The high-intensity signal areas of benign lesions were yellow-green ($P < 0.001$), and the margins with surrounding normal tissue were regular ($P < 0.001$). The laser signal attenuation was moderate ($P < 0.001$), and the probability of the 3D reconstruction structure being spindle structure, spherical structure, and diverticulum structure is higher than that of the malignant tumor focus ($P < 0.001$). The results are in Table 3.

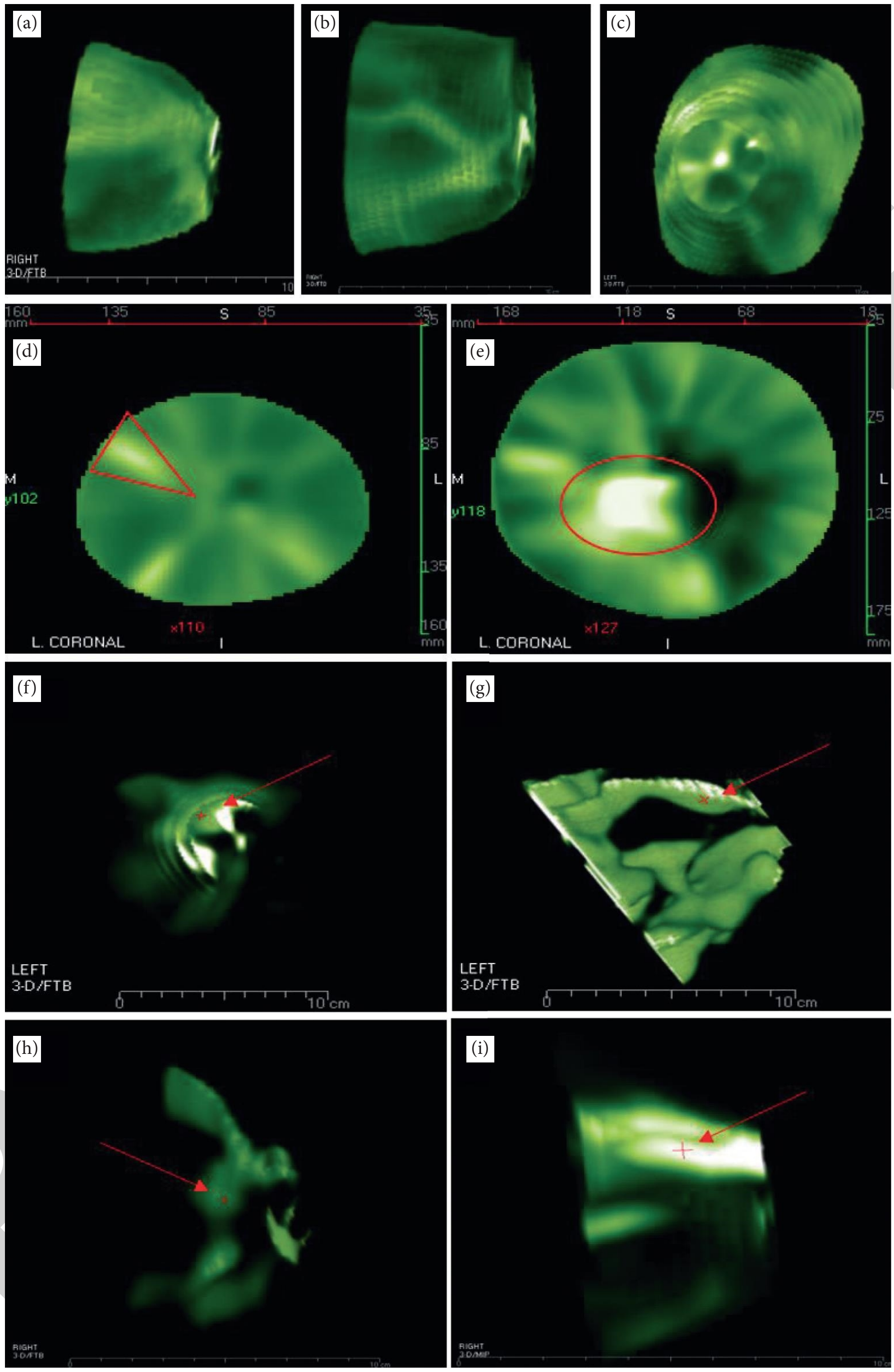

Figure 1: CTLM image features of normal and abnormal breast (A–C) normal vascular signal structure of the breast: banded structure (a), branched structure (b), and stellate structure (c); (d) Coronal plane normal glandular lobules "spokes" distribution; (e) Oval-shaped bright signal area on the coronal plane of CTLM, showing abnormal angiogenesis and "spoke-like" distribution interruption; F–I : the abnormal vascular signal structures in the breast are indicated by the red arrow: ring structure (f), spindle structure (g), diverticulum structure (h), and plate structure (i).

Table 3: Comparison of CTLM image features of benign and malignant breast tumors.

Image characteristics	Benign tumour ($n = 105$)	Malignant tumor ($n = 85$)	*P value*
Region color			
Bright white	49 (46.67)	72 (84.71)	0.000
Green and yellow	56 (53.33)	13 (15.29)	
Focal edge			
Regular	34 (32.38)	7 (8.24)	0.000
Irregular	71 (67.62)	78 (91.76)	
Laser signal attenuation			
Weak	8 (7.62)	2 (2.35)	
Medium	76 (72.38)	24 (28.24)	0.000
Obvious	21 (20.00)	59 (69.41)	
3D structure			
Slab structure	13 (12.38)	29 (34.12)	
Spindle structure	34 (32.38)	21 (24.71)	
The spherical structure	25 (23.81)	3 (3.53)	
Diverticulum structure	23 (21.90)	16 (18.82)	
Inverted conical structure	7 (6.67)	1 (1.18)	0.000
Rings structure	1 (0.95)	6 (7.06)	
Branched structure	1 (0.95)	4 (4.71)	
Dumbbell structure	1 (0.95)	5 (5.88)	

Table 4: Comparison of the detection rate of benign and malignant lesions by mammography and CTLM imaging.

Inspection method		Pathological result		Total	*P*
		Benign	Malignant		
Mammography	Malignant	26	75	101	0.000
	Benign	61	8	69	
	Not detected	49	6	55	
	Total	136	89	225	
CTLM	Malignant	27	78	105	0.000
	Benign	78	7	85	
	Not detected	31	4	35	
	Total	136	89	225	

3.4. Consistency Analysis between CTLM Imaging and Pathological Examination. 225 cases of patients with mammography and CTLM imaging, according to the image characteristics of the two detection methods, for the diagnosis of patients with lesions. Mammography diagnosis of breast showed that 101 cases were malignant (75 cases were pathologically malignant, 26 cases were benign), 69 cases were benign (8 cases were pathologically malignant and 61 cases were benign), and 55 cases were undetected (6 cases were pathologically malignant and 49 cases were benign). The total detection rate of breast tumors by mammography is 75.5% (170/225), and the detection rate of breast malignant tumors is higher than that of breast benign tumors, with a benign detection rate of 63.97% (87/136) and a malignant detection rate of 93.26% (83/89). CTLM imaging diagnosed 105 cases as malignant (78 cases as pathological malignant and 27 cases as benign), 85 cases as benign (7 cases as pathological malignant and 78 cases as benign), and 35 cases as undetected (4 cases as pathological malignant and 31 cases as benign). The total detection rate of CTLM imaging for breast tumors was 84.44% (190/225), and the detection rate for breast malignant tumors was higher than that for breast benign tumors, with the benign detection rate of 77.20% (105/136) and the malignant detection rate of 95.50% (85/89). The sensitivity, specificity, PPV, and NPV of the two assays were calculated. The specificity and diagnostic coincidence rate of CTLM imaging were higher than those of mammography ($P < 0.05$). The results are in Table 4, Table 5, and Figure 2.

Table 5: Comparison of diagnostic performance of mammography and CTLM imaging in 225 breast patients.

	Breast X-ray	CTLM imaging	*P*
Sensitivity (%)	84.26 (75/89)	87.64 (78/89)	0.518
Specificity (%)	44.85 (61/136)	57.35 (78/136)	0.039
NPV (%)	88.41 (61/69)	91.76 (78/85)	0.484
PPV (%)	74.26 (75/101)	74.29 (78/105)	0.622
Coincidence rate	60.44 (136/225)	69.33 (156/225)	0.048

Note. NPV is negative predictive value, and PPV is positive predictive value.

3.5. Influences of Different Clinical Indicators on the Detection Rate of CTLM Lesions. Different clinical indicators may affect the diagnostic results of CTLM imaging. 89 patients were classified, and the detection rates of CTLM imaging in different breast densities, tumor sizes, estrogen receptor (ER), progesterone receptor (PR), and human epidermal growth factor receptor -2 (HER2) expression were compared. The results showed that there was no statistical difference in the detection rate of CTLM imaging in the classification of different breast densities, tumor focus sizes, ER, PR, HER2, and other markers ($P > 0.05$). The results are in Table 6.

4. Discussion

Breast cancer is the most common cancer in women, with a higher mortality rate. For breast cancer, the prevention and treatment are mainly regular screening, early detection of abnormal lesions, according to the type of lesions and tumor

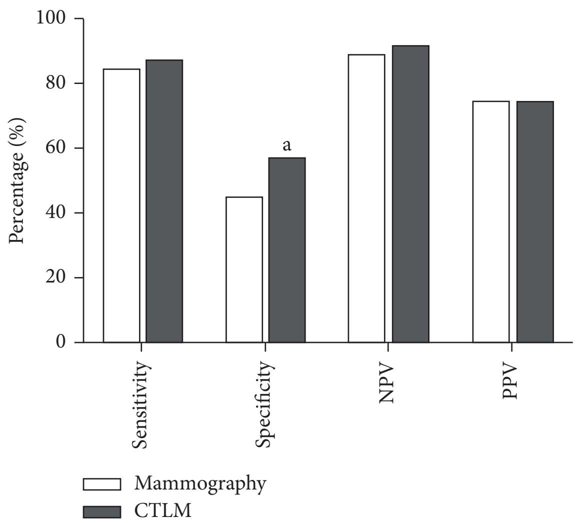

Figure 2: Comparison of diagnostic efficacy between mammography and CTLM in 225 breast patients.

Table 6: Influence of different clinical indicators on the detection rate by CTLM in 89 breast cancer.

Index	Type	CTLM imaging		P
		Detection n (%)	Not detected n (%)	
Breast density	Dense type	69 (81.2)	4 (100)	0.202
	Lard type	16 (18.8)	0 (0.0)	
Tumor size	≤2 cm	47 (55.3)	2 (50.0)	0.659
	2–5 cm	31 (36.5)	2 (50.0)	
	>5 cm	7 (8.2)	0 (0.0)	
ER	+	70 (82.4)	2 (50.0)	0.153
	-	15 (17.6)	2 (50.0)	
PR	+	46 (54.1)	3 (75.0)	0.399
	-	39 (45.9)	1 (25.0)	
HER2	+	34 (40.0)	2 (50.0)	0.693
	-	51 (0.0)	2 (50.0)	
Ki67	<14	7 (8.2)	0 (0.0)	0.413
	≥14	78 (91.8)	4 (100.0)	

size to formulate the corresponding treatment plan [11]. The early detection of abnormal lesions is mainly due to regular physical examination, which mainly includes clinical palpation and routine imaging examinations such as mammography, MRI, and B-ultrasound [12, 13]. Accurate diagnosis of lesion types and measurement of primary tumor size can help doctors make appropriate treatment plans before operation, and accurately evaluate the progress of lesions and the efficacy of neoadjuvant therapy in the course of treatment.

In this study, 225 patients with breast tumors were analyzed retrospectively. CTLM imaging and mammography were performed in all patients. Mammography was used as the routine imaging control, and postoperative pathological examination was taken as the gold standard. The CTLM image characteristics of breast lesions by CTLM imaging were analyzed, and the consistency of CTLM imaging in the diagnosis of breast lesions was calculated. The image characteristics of CTLM imaging were analyzed, the differences of image features between benign and malignant breast tumors were compared, and the common points of image identification were summarized. Use different clinical indicators to classify patients and explore the impact of different clinical indicators on the detection rate of CTLM imaging. To further discuss the clinical value of CTLM imaging in breast cancer.

Mammography is a common method for screening breast cancer. Mammography includes two positions: head-tail position and internal and external oblique positions. Breast density will affect the radiographic results. On mammograms, low-density tissue appears to be translucent, a dark gray shadow close to a black background. When the patient has a dense breast, the breast tissue density increases, and the film looks whiter on a gray background. The tumor in the focal area is also composed of dense tissue, so the film will also show white [14]. As a result, the tissue in the focus area of dense breast patients cannot form an obvious contrast with the surrounding normal tissues, which leads to measurement errors [15]. In this study, we compared the tumor detection rate of CTLM imaging in patients with dense breast and fatty breast. The results showed that there was no statistical difference in the detection rate between the two groups. It shows that the breast density of the patient will not interfere with the diagnostic structure of CTLM imaging.

If the tumor in abnormal breast lesions is to grow into a mass larger than $1\,mm^3$, new blood vessels need to be generated [16]. Neovascularization in tumor cannot only nourish the surrounding tumor tissues [17], but also secrete various factors to induce the proliferation and migration of tumor cells. Therefore, it is of great clinical significance to monitor abnormal angiogenesis in the lesion. CTLM imaging is an optical imaging technology characterized by noninvasive and nonradiation. In CTLM imaging, there is no need to inject additional contrast agents, and deoxyhemoglobin in blood can be used as the natural contrast agent of the human body. Therefore, the high-density deoxyhemoglobin region can be quickly found. Three-dimensional image reconstruction is carried out on the image of this area, and the image features are analyzed. By analyzing the abnormal hemoglobin generation in the diseased area, it is judged whether there is abnormal angiogenesis in this area.

In this study, according to the results of postoperative pathological examination, among 225 breast patients, 136 cases were benign tumors and 89 cases were malignant tumors. Analysis of CTLM imaging results showed that 190 patients (84.44%) were abnormal, and the detection rate of benign breast lesions was 77.20%, and the detection rate of malignant breast lesions was 95.50%. The consistency between CTLM imaging and postoperative pathological examination was calculated. The results showed that the sensitivity, specificity, NPV, PPV, and diagnostic coincidence rate of CTLM imaging were 87.64%, 57.35%, 91.76%, 74.29%, and 69.33%, respectively. The consistency of CTLM imaging in diagnosis and pathological examination of breast tumors is higher than that of mammograms, which is considered to be related to the high proportion of heterogeneous dense breast and extremely dense breast in the population of this study.

CTLM imaging is mainly aimed at tumor neovascularization in the focus area. The vascular structure of benign and malignant lesions is different [18], partly influenced by tumor angiogenesis factors. Tumor cells in malignant lesions grow faster and need a more abundant blood supply. Therefore, the secretion of angiogenic factors in malignant lesions increases, which increases the speed of vascular growth. There are many new blood vessels, but the basic structure of blood vessels is incomplete, lacking vascular endothelial cells, smooth muscle cells, and nerve endings [19]. The systolic and diastolic function of malignant blood vessels is lost, the wall of blood vessels is thin, and the diameter of blood vessels is increased. When CTLM imaging is performed, there are areas with high local hemoglobin content, which appear as local bright white on the image, destroying the original regular radial distribution. Irregular edges of lesions and surrounding normal tissues, obvious attenuation of laser signals, and the shape of 3D reconstruction similar to plate-like structures are also interpreted as signs of malignant lesions. Image features are consistent with those reported by researchers such as Qi [20]. When CTLM imaging is performed on benign and malignant lesions, the two lesions will show different image features. In this study, the detection rate of malignant tumors by CTLM imaging was higher than that of benign tumors. Nevertheless, since CTLM is a functional examination, there are some limitations in accurately locating the lesions.

In conclusion, CTLM can reflect the information of breast cancer neovascularization to some extent, and the results of image identification are consistent with the results of pathological examination. CTLM imaging can be used as an auxiliary examination in the diagnosis of breast cancer lesions with a certain clinical value.

Data Availability

All the data including statistical analysis has been presented in this paper.

Conflicts of Interest

The authors declare no conflicts of interest.

Acknowledgments

This work was supported by Xi'an "Science and Technology +" Action Plan-Medical Research Project (No. 2019115213YX007SF040(3)).

References

[1] H. Sung, J. Ferlay, and R. L. Siegel, "Global cancer statistics 2020: globocan estimates of incidence and mortality worldwide for 36 cancers in 185 countries," *CA: A Cancer Journal for Clinicians*, vol. 68, 2021.

[2] E. Bidoli, S. Virdone, M. Hamdi-Cherif et al., "Worldwide age at onset of female breast cancer: a 25-year population-based cancer registry study," *Scientific Reports*, vol. 9, no. 1, Article ID 14111, 2019.

[3] M. G. Andarieh, M. A. Delavar, D. Moslemi, M. H. Ahmadi, E. Zabihi, and S. Esmaeilzadeh, "Infertility as a risk factor for breast cancer: results from a hospital-based case-control study," *Journal of Cancer Research and Therapeutics*, vol. 15, no. 5, pp. 976–980, 2019.

[4] Y. Vinogradova, C. Coupland, and J. Hippisley-Cox, "Use of hormone replacement therapy and risk of breast cancer: nested case-control studies using the QResearch and CPRD databases," *BMJ*, vol. 371, Article ID m3873, 2020.

[5] H. R. Brewer, M. E. Jones, M. J. Schoemaker, A. Ashworth, and A. J. Swerdlow, "Family history and risk of breast cancer: an analysis accounting for family structure," *Breast Cancer Research and Treatment*, vol. 165, no. 1, pp. 193–200, 2017.

[6] A. Shahabaz and M. Afzal, "Implementation of high dose rate brachytherapy in cancer treatment," *Science Progress and Research*, vol. 1, no. 3, pp. 77–106, 2021.

[7] M. S. Fuller, C. I. Lee, and J. G. Elmore, "Breast cancer screening," *Medical Clinics of North America*, vol. 99, no. 3, pp. 451–468, 2015.

[8] K. Kerlikowske, R. Hubbard, and D. Miglioretti, "Comparative edversus film-screen mammography in community practice in the United States," *Annals of Internal Medicine*, vol. 155, no. 8, pp. 493–502, 2011.

[9] A. Jalalian, S. Mashohor, R. Mahmud, B. Karasfi, M. Iqbal Saripan, and A. R. Ramli, "Computer-assisted diagnosis system for breast cancer in computed tomography laser mammography (CTLM)," *Journal of Digital Imaging*, vol. 30, no. 6, pp. 796–811, 2017.

[10] D. Floery, T. H. Helbich, C. C. Riedl et al., "Characterization of benign and malignant breast lesions with computed tomography laser mammography (CTLM)," *Investigative Radiology*, vol. 40, no. 6, pp. 328–335, 2005.

[11] A. Javeed, S. S. Rizvi, S. Zhou, R. Riaz, S. U. Khan, and S. J. Kwon, "Heart risk failure prediction using a novel feature selection method for feature refinement and neural network for classification," *Mobile Information Systems*, vol. 2020, Article ID 8843115, 11 pages, 2020.

[12] S. Iranmakani, T. Mortezazadeh, and F. Sajadian, "A review of various modalities in breast imaging: technical aspects and clinical outcomes," vol. 51, no. 1, 2020.

[13] T. Cortadellas, P. Argacha, J. Acosta et al., "Estimation of tumor size in breast cancer comparing clinical examination, mammography, ultrasound and MRI-correlation with-- the pathological analysis of the surgical specimen," *Gland Surgery*, vol. 6, no. 4, pp. 330–335, 2017.

[14] S. S. Nazari and P. Mukherjee, "An overview of mammographic density and its association with breast cancer," *Breast Cancer*, vol. 25, no. 3, pp. 259–267, 2018.

[15] I. V. Gruber, M. Rueckert, K. O. Kagan et al., "Measurement of tumour size with mammography, sonography and magnetic resonance imaging as compared to histological tumour size in primary breast cancer," *BMC Cancer*, vol. 13, no. 1, p. 328, 2013.

[16] S. Gupta, S. Goyal, M. Arora, and D. Gupta, "Role of miRNAs in urological cancers," *SPR*, vol. 1, no. 2, pp. 1–7, 2021.

[17] Y. Yuan, Y.-C. Jiang, C.-K. Sun, and Q.-M. Chen, "Role of the tumor microenvironment in tumor progression and the clinical applications (Review)," *Oncology Reports*, vol. 35, no. 5, pp. 2499–2515, 2016.

Hindawi
Journal of Healthcare Engineering
Volume 2023, Article ID 9816857, 1 page
https://doi.org/10.1155/2023/9816857

Retraction

Retracted: Clinical Application of Artificial Intelligence: Auto-Discerning the Effectiveness of Lidocaine Concentration Levels in Osteosarcoma Femoral Tumor Segment Resection

Journal of Healthcare Engineering

Received 10 October 2023; Accepted 10 October 2023; Published 11 October 2023

This article has been retracted by Hindawi following an investigation undertaken by the publisher [1]. This investigation has uncovered evidence of one or more of the following indicators of systematic manipulation of the publication process:

(1) Discrepancies in scope
(2) Discrepancies in the description of the research reported
(3) Discrepancies between the availability of data and the research described
(4) Inappropriate citations
(5) Incoherent, meaningless and/or irrelevant content included in the article
(6) Peer-review manipulation

The presence of these indicators undermines our confidence in the integrity of the article's content and we cannot, therefore, vouch for its reliability. Please note that this notice is intended solely to alert readers that the content of this article is unreliable. We have not investigated whether authors were aware of or involved in the systematic manipulation of the publication process.

In addition, our investigation has also shown that one or more of the following human-subject reporting requirements has not been met in this article: ethical approval by an Institutional Review Board (IRB) committee or equivalent, patient/participant consent to participate, and/or agreement to publish patient/participant details (where relevant).

Wiley and Hindawi regrets that the usual quality checks did not identify these issues before publication and have since put additional measures in place to safeguard research integrity.

We wish to credit our own Research Integrity and Research Publishing teams and anonymous and named external researchers and research integrity experts for contributing to this investigation.

The corresponding author, as the representative of all authors, has been given the opportunity to register their agreement or disagreement to this retraction. We have kept a record of any response received.

References

[1] S. Ni, X. Li, and X. Yi, "Clinical Application of Artificial Intelligence: Auto-Discerning the Effectiveness of Lidocaine Concentration Levels in Osteosarcoma Femoral Tumor Segment Resection," *Journal of Healthcare Engineering*, vol. 2022, Article ID 7069348, 12 pages, 2022.

Hindawi
Journal of Healthcare Engineering
Volume 2022, Article ID 7069348, 12 pages
https://doi.org/10.1155/2022/7069348

Research Article

Clinical Application of Artificial Intelligence: Auto-Discerning the Effectiveness of Lidocaine Concentration Levels in Osteosarcoma Femoral Tumor Segment Resection

Shuqin Ni,[1] Xin Li,[2] and Xiuna Yi[1]

[1]*Department of Anesthesiology, Yantaishan Hospital, Yantai 264003, Shandong, China*
[2]*Department of Surgery, Jinyintan Hospital, Wuhan, Hubei 430022, China*

Correspondence should be addressed to Xiuna Yi; 120212202029@ncepu.edu.cn

Received 14 February 2022; Revised 23 February 2022; Accepted 28 February 2022; Published 28 March 2022

Academic Editor: Liaqat Ali

Adolescents and children worldwide are threatened by osteosarcoma, a tumor that predominantly affects the long bone epiphysis. Osteosarcoma is the most common and highly malignant bone tumor in youngsters. Early tumor detection is the key to effective treatment of this disease. The discovery of biomarkers and the growing understanding of molecules and their complex interactions have improved the outcome of clinical trials in osteosarcoma. This article describes biomarkers of osteosarcoma with the aim of positively influencing the progress of clinical treatment of osteosarcoma. Femoral bone tumor is a typical condition of osteosarcoma. Due to the wide range of femoral stem types, complexities in the distal femur, and tumors in the rotor part of femur, physicians following the traditional clinical approach face difficulties in removing the lesion and fixing the femur with resection of the tumor segment. In this paper, the effect of small doses of different concentrations of lidocaine anesthesia in patients undergoing lumpectomy for osteosarcoma femoral tumor segments is investigated. A computer-based artificial intelligence method for automated determination of different concentration levels of lidocaine anesthesia and amputation of osteosarcoma femoral tumor segment is proposed. Statistical analysis is carried on the empirical data including intraoperative bleeding, intraoperative and postoperative pain scores, surgical operation time, postoperative complications, patient satisfaction, and local anesthetic dose. The results showed that the patients in the study group had low intraoperative bleeding, short operation time, low postoperative hematoma formation rate, high patient satisfaction, higher dosage of anesthetic solution, and low dosage of lidocaine. Results revealed that mean arterial pressure and heart rate in extubating and intubating were significantly lower in the observation group than in the control group, and a significant difference ($P < 0.05$) was observed between the two groups. This proves that the proposed algorithm can adequately reduce bleeding, alleviate postoperative pain, shorten operation time, reduce complications, accelerate recovery, and ensure better treatment results.

1. Introduction

Osteosarcoma is a disease of the bone first described in 1807 in the Boyle Lectures [1]. Osteosarcoma is the most common malignant bone tumor in this age group, with a higher incidence in males than in females. Osteosarcoma most often occurs in the long bone epiphysis (43% in the distal femur, 23% in the proximal tibia, and 10% in the proximal humerus). The main symptoms of osteosarcoma include swelling of the affected area, joint pain, and limitation of movement. Pathological examination provides definitive information on the diagnosis and tumor grading. Most osteosarcomas develop early pulmonary metastases. The five-year survival rate is higher in patients without metastases compared to those with pulmonary metastases. Neoadjuvant chemotherapy as well as surgical resection has increased the 5-year survival rate for such patients from 10% before 1970 to 50%–70%. microRNAs or miRNAs are highly conserved, endogenous, tightly regulated noncoding small RNAs (18–25 nucleotides) that target and inhibit mRNA transcription by direct degradation or inhibition of translation. Their expression is strictly regulated by epigenetics (e.g., DNA methylation, histone deacetylation, and other transcriptional regulatory mechanisms) [2–5]. miRNAs can inhibit the expression of oncogenes that play an important role in tumorigenesis. Taking osteosarcoma as an example, several studies have reported the expression profiles of different miRNAs in cell lines or samples. For example, miR-195, miR-99, miR-181, and miR-148a are upregulated in osteosarcoma, while others such as miR-539, miR-145, and miR-335 are downregulated in MG-63 human osteosarcoma cell line. As miRNA is a bone tumor marker, studies from the literature found that miR-195 levels in serum of osteosarcoma patients were lower than normal controls by real-time quantitative RT-PCR assay [6]. This indicates that miRNA has the potential to be used as a marker of osteosarcoma and can be used effectively for screening and monitoring of osteosarcoma. Serum miR-199a-5p was found at higher concentrations in osteosarcoma samples. miRNA (miR-21, miR-199a-3p, miR-143, miR-34, miR-140, and miR-132) expression levels were found to be higher in osteosarcoma patients, while miR-199a-3p and miR-143 in osteosarcoma patients had lower expression levels. Cytokines are small proteins secreted by monocytes and macrophages, among others, which are regulators of the host's response to trauma, infection, and immunity. Abnormally elevated plasma levels of proinflammatory cytokines have been associated with obesity, type 2 diabetes, atherosclerosis, rheumatoid arthritis, and cancer. Several studies have shown elevated levels of transforming growth factor (TGF-β) in patients with osteosarcoma compared to healthy controls. Osteosarcoma cells stimulate the production of protumor cytokines by mesenchymal stem cells (MSCs). The cells stimulate the production of IL-6 and vascular endothelial growth factor (VEGF) in MSCs through the medium of Saos-2 and U2 osteosarcoma cell lines. The stimulation effect can be neutralized by TGF-β antibodies. Drugs that inhibit TGF-β have also been used in preclinical studies and clinical trials. In contrast, VEGF has also been observed to be upregulated in several types of cancer, including osteosarcoma. The involvement of VEGF in angiogenesis has been used as a biomarker of prognosis in patients with osteosarcoma [7–9]. In addition, VEGF expression was also associated with overall disease-free survival, whereas patients with high VEGF expression had lower disease-free survival and overall survival, suggesting that VEGF may serve as a valid biomarker for osteosarcoma prognosis. Cytokine levels in osteosarcoma patients, including ILS-6, TGF-β, growth-related oncogenes, hepatocyte growth factor, chemokine ligand 16, end proteinase, matrix metalloproteinase-9, and platelet-derived growth factor-AA, were upregulated in the test group compared with normal controls. It was observed that enzyme-linked immunosorbent assay (ELISA) with MSC-based ILS-6, osteosarcoma proliferation, and metastasis was promoted. In [6] β-isomerized C-terminal peptide (β-CTx) and total type 1 procollagen aminoterminal peptide (tP1NP) were found to be significantly elevated by immunoassay of sera from osteosarcoma patients. Therefore, it is believed that these proteins could be used as osteosarcoma biomarkers. Abnormal TIM3 expression is associated with a variety of cancers, belongs to the family of molecules containing the immunoglobulin and mucin structural domains of T cells (TIM), and is expressed by a variety of immune cells including T cells, macrophages, dendritic cells, and natural killer cells. TIM3 is also expressed in human osteosarcoma cell lines. In addition, TIM3 has been found to be coexpressed with Slug, Snail, and Smad, which have been detected in osteosarcoma patients [10–12]. Therefore, TIM3 is expected to be used as a tool for the diagnosis and treatment of osteosarcoma. Matrix metalloproteinases (MMPs) belong to a family of zinc-dependent endopeptidases that are secreted by macrophages and neutrophils and are involved in a variety of physiological and pathological processes including extracellular matrix (ECM) degradation and remodeling, morphogenesis, wound healing, tissue repair, and remodeling. In addition, MMPs play a key role in tumor progression by activating cell growth, migration, invasion, metastasis, and angiogenesis. A study showed a significant correlation between MMP-9 expression and osteosarcoma risk in Asian and non-Asian populations [13].

Lidocaine is a local anesthetic with anesthetic and analgesic effects. Intravenous lidocaine can increase the risk of cardiac arrhythmias due to elevated blood concentrations. Transdermal topical administration, on the other hand, avoids hepatic first-pass effects, increases local drug concentrations at the site of pain, decreases systemic plasma concentrations of lidocaine, and reduces systemic adverse effects while also improving patient safety and compliance. Topical lidocaine formulations have been shown to exert analgesic effects by blocking voltage-gated sodium channels (Nav), effectively reducing abnormal peripheral nerve discharge, and decreasing peripheral sensitization. Lidocaine gel/ointment can be applied directly to the painful skin area, and in order to keep the gel in contact with the skin and enhance permeability, it is often used in combination with a closed dressing; however, the closed dressing is less tolerable due to the lack of breathability, easy to cause local burning sensation, and troublesome to use, so the lidocaine patch with a protective backing layer was created [14, 15]. The molecular formula of lidocaine is shown in Figure 1.

In March 1999, the U.S. Food and Drug Administration (FDA) approved lidocaine patch 5% for the treatment of postherpetic neuralgia (PHN). In Europe, the product was approved for marketing in the EU in 2007 under the name lidocaine patch 5%, and generic versions of lidocaine topical patches have been introduced into the market since then. In February 2018, the 1.8% lidocaine topical transdermal system was also approved by the FDA for PHN, and in the same year, lidocaine gel patches were marketed in China, filling a therapeutic gap in this area in China. The use of topical lidocaine patches (collectively, the above dosage forms) for the treatment of PHN has been supported by the consensus of clinical practice guidelines in China and abroad but has not been approved for other indications. Based on its effectiveness and safety in the treatment of PHN, lidocaine topical patches have also been widely used for other peripheral neuropathic pain conditions, such as diabetic peripheral neuropathic pain (DPNP) and postoperative or posttraumatic neuropathic pain, and even for localized injury-sensitive pain. However, the safety and efficacy in the

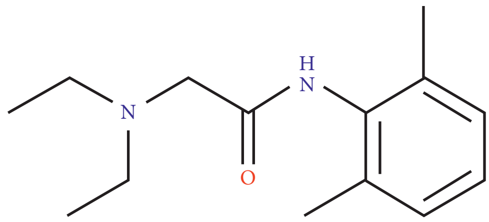

Figure 1: Lidocaine molecular formula.

treatment of other types of pain disorders are unclear, and there are few relevant studies in China.

The heterogeneity of osteosarcoma is a major factor in treatment outcome. Biomarkers can be used to diagnose patients with osteosarcoma, especially those with metastatic osteosarcoma, and biomarkers may be an effective way to diagnose osteosarcoma early and to identify potential therapeutic targets. Therefore, this paper reviews the research on biomarkers in cellular experiments, animal models, and histological specimens of osteosarcoma in this direction. Moreover, we study the dosage form characteristics, pharmacokinetics, safety, and efficacy of currently marketed lidocaine topical patches and their applications in the field of pain treatment, taking into account the latest advances, to provide a reference basis for its further in-depth research application. In this paper, a computer-based artificial intelligence method is proposed for the automated determination of different concentrations of lidocaine anesthesia in osteosarcoma femoral tumor segment resection, and the effectiveness of this method for determining different concentrations of lidocaine anesthesia applied in tumor resection surgery is demonstrated by experimental validation in relevant data.

The paper is organized into 4 sections. Section 2 is about the literature review. The proposed method is discussed in Section 3. Experimentation and analysis are performed in Section 4 whereas conclusion is presented in the last section, Section 5.

2. Related Work

Pain has been listed as the "fifth vital sign" of the human body, yet the treatment of pain still faces great challenges in clinical practice. Among them, neuropathic pain is the common clinical pain caused by somatosensory system injury or disease. Chronic pain not only affects the patient's ability to sleep, work, and live, but also increases the incidence of depression, anxiety, and other emotional disorders, seriously affecting human health and quality of life. Therefore, early, adequate, and aggressive treatment of chronic neuropathic pain can effectively relieve pain and its accompanying symptoms, restore physical function, and improve quality of life. Although many drugs (e.g., anticonvulsants, antidepressants, and opioids) are available, systemic administration is often limited by adverse drug reactions, especially in elderly and frail groups. In contrast, topical administration has low systemic exposure and high safety [16], so topical dosage forms available for topical administration (e.g., gels, ointments, and patches) are receiving increasing attention from clinicians.

The femur is a favored site for bone tumors and tumor-like lesions in children, with diverse disease types, more homozygous lesions, and the site is deep, without obvious specific clinical symptoms, making differential diagnosis difficult. In children, benign lesions are common in the femur, including osteochondroma, osteoid osteoma, and osteoblastoma. The incidence is higher in males than females, and some literature reports that the most common benign bone tumor in children is osteochondroma, which accounts for 10% to 15% of bone tumors [6]. The incidence of benign tumors was higher in children with a wide variety of femoral tumors and tumor-like lesions, and the top three were osteoid osteoma, osteosarcoma, and osteochondroma, which were basically consistent with those reported in the literature [17–19]. Common signs of femoral tumors or tumor-like lesions in children include cystic expansion bone destruction, osteoblastoma, chondroblastoma, aneurysmal bone cyst, giant cell tumor of bone, bone cyst, and abnormal proliferation of bone fibers. Similarly, osteolytic bone destruction is a common sign of malignant bone tumors.

2.1. Tumor Segment of Femoral Bone. Common signs of bone destruction in children with femoral tumors or tumor-like lesions: cystic distensible bone destruction is the most common benign bone tumors and tumor-like lesions in children, including osteoblastoma, chondroblastoma, aneurysmal bone cyst, giant cell tumor of bone, bone cyst, and abnormal bone fiber proliferation disorder, while osteolytic bone destruction is a common sign of malignant bone tumors. Figure 2 [20, 21] shows X-ray of right femoral neck osteoid osteoma of a male, 8 years old with cystic distensible bone destruction, all of which are benign bone tumors and tumor-like lesions with well-defined lesion extent.

Osteoblastic osteoma is most seen in adolescents under 25 years of age. The disease is more common in males and is more common in the lower extremities. Attack of the disease in childhood may lead to skeletal deformities. In children, endogenous chondrosarcoma and stromal ossification are rare, and the "fan-shaped sign" can be seen in their bone. Osteolytic destruction is a kind of malignant tumors; hence, osteosarcoma is characterized by osteolytic bone destruction with indistinct borders and worm-like or sieve-like destruction of the bone cortex, accompanied by tumor bone formation. When the lesion breaks through the articular surface, the continuity of the epiphyseal plate can be interrupted, and pathological fractures can sometimes occur in osteosarcoma that invades the epiphyseal plate and epiphysis. This increases the difficulty of diagnosis in children with osteosarcoma. In [22], image fusion technique based on advanced AI classifiers is proposed to diagnose osteosarcoma using the data of both CT and MRI images.

2.1.1. Periosteal Reaction. When the outer periosteum of long bones is stimulated by a granulation tissue mass that breaks through the bone cortex, it can manifest as a periosteal reaction, such as laminar and onion skin-like. Malignant tumors, including osteosarcoma and lymphoma, can be seen with varying degrees of periosteal reaction, forming

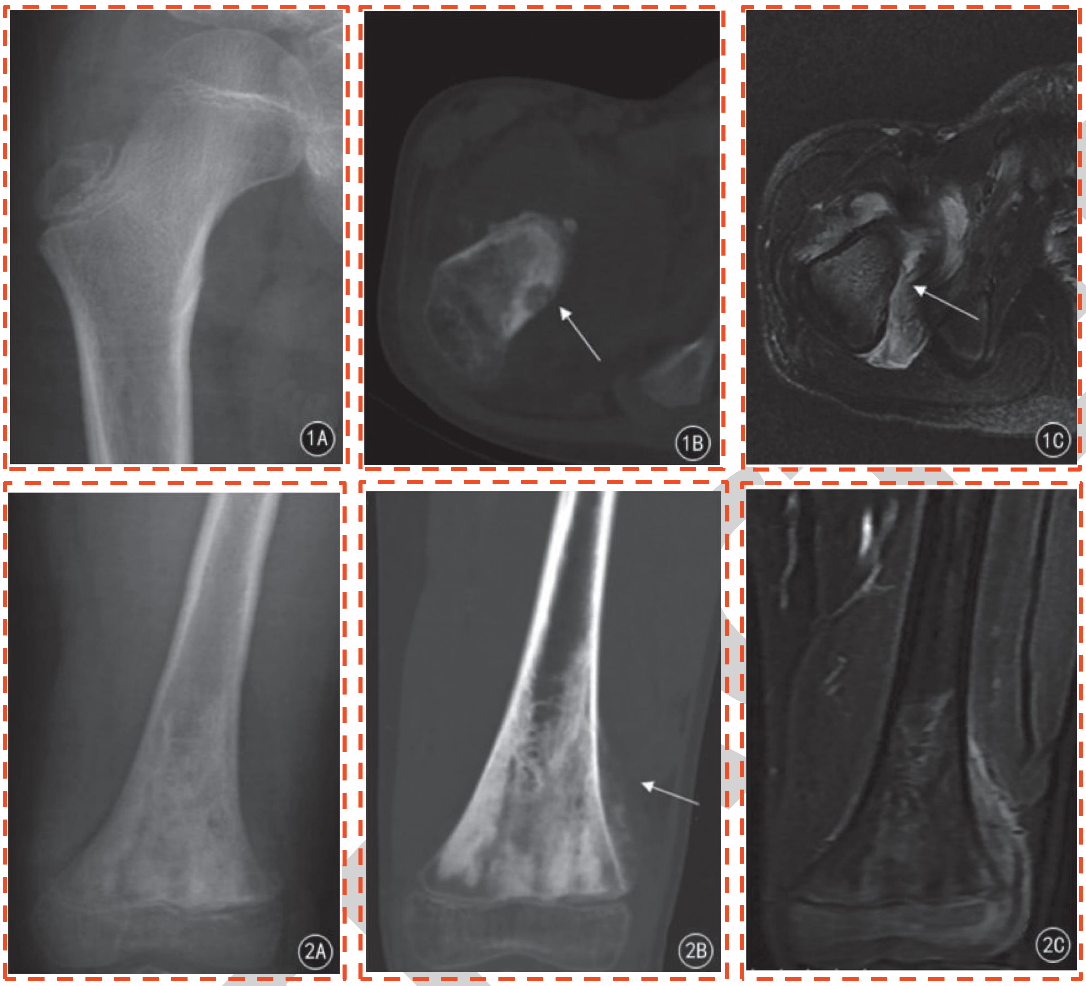

Figure 2: Male, 8 years old, X-ray of osteoid osteoma of the right femoral neck.

the Codman triangle. Typical eosinophilic granulomas in benign bone diseases may also show onionskin-like periosteal reaction with high density, no radiolucent bone pins, and well-defined margins. In case of eosinophilic granulomas, it is common that the extent of the bone destruction area exceeds limits and may be accompanied by a wide range of soft tissue masses or swelling, usually occurring in the epiphysis or bone ends of long bones. Malignant bone tumors have an incomplete periosteal response with radiolucent bone [23]. When the neoplastic periosteum is broken by the tumor, it can be deformed and disrupted, forming Codman's triangle, which can then be easily distinguished. In benign tumors and tumor-like lesions combined with pathological fractures, typically a thin periosteal reaction may appear.

2.1.2. Intratumoral Calcification. When cartilage matrix calcium salt deposition or intratumoral tissue necrosis occurs, calcification signs may appear. Among benign tumors, chondroblastoma and osteoblastoma may show speckled calcification, which can be better visualized by high-resolution CT. Osteoblastoma and osteoblastoma can show speckled calcification in the nest. Among benign bone tumors, chondroblastoma is most often found in the epiphysis of long bones and can involve the epiphysis across the epiphyseal plate. Chondroblastoma can be differentiated from malignant bone tumors such as chondrosarcoma with incomplete circumferential calcification, low density, and indistinct margins.

2.1.3. Fluid-Fluid Plane. Benign tumor-like lesions of aneurysmal bone cysts often show fluid-fluid plane. The principle is due to the separation of plasma and cells in the blood of the cyst and the formation of a partition interface after the bottom of cell precipitation. Aneurysmal bone cysts show typical fluid-fluid plane in CT and MRI, but fluid-fluid plane is not unique like that of aneurysmal bone cysts. The giant cell tumor of bone, osteoblast, and/or hemorrhage may cause this phenomenon.

2.1.4. Focal Boundaries. Benign bone tumors and tumor-like lesions have clear boundaries due to slow development. The obvious sclerotic edges are often seen on X-ray and CT, while malignant tumors, such as osteosarcoma, chondroblastoma, and nonossifying fibroma, have clear sclerotic edges [24]. Osteochondroma is the most common benign bone tumor in children, preferably in boys, with the femur being the most common. Retrospective analysis of patients likewise revealed that osteochondroma is the most prevalent benign tumor. Osteochondroma occurs near the epiphysis of the long bones and presents as a bony redundancy with a cartilaginous cap and a well-defined lesion. The diagnosis of osteochondroma is established by X-ray plain film before surgery. Bone fibro dysplasia and aneurysmal bone cysts can be seen with clear sclerotic edges and internal segregation-like changes. CT and MRI are more advantageous in showing details of the lesion.

2.1.5. Soft Tissue Changes. Benign bone tumors or tumor-like lesions may show soft tissue changes, including edema or mass formation, such as osteoid osteoma, chondroblastoma, and eosinophilic granuloma. Soft tissue swelling can be seen around osteoid osteoma and simple bone cysts combined with pathologic fractures, consistent with the literature. Typical childhood eosinophilic granuloma can be seen as soft tissue mass formation, but unlike malignant tumors, soft tissue masses have clear and smooth borders. The tissues are generally thin, elongated, and evenly encircle areas of bone destruction. Eosinophilic granuloma can be seen as an obvious elongated soft tissue mass that evenly encases the bone destruction area and can be seen as soft tissue swelling of varying degrees. Osteosarcoma is the most common malignant bone tumor of the long bones of the extremities in children, preferably in the epiphysis, and is characterized by osteolytic destruction and soft tissue masses within the verrucous bone. Osteosarcoma can be seen as soft tissue masses of varying sizes, with poorly defined borders and progressive enlargement [24].

2.2. Lidocaine Anesthesia. Local anesthetic lidocaine is a sodium channel blocker with membrane stabilizing effects and is used in antiventricular arrhythmias. In recent years, as pharmacological research and clinical applications continue to advance, lidocaine also has immune system regulatory functions and exerts anti-inflammatory effects in several parts of the inflammatory response. Its significant inhibitory effects on the inflammatory response, acute lung injury, sensitizing effects on anticancer drugs, bacterial inhibition, cerebral protection, and reduction of postoperative cognitive dysfunction (POCD) have received attention from clinical scholars and are reviewed below. Lidocaine has broad-spectrum antiarrhythmic effects. Ventricular arrhythmias include ventricular asystole, ventricular tachycardia, ventricular flutter, and ventricular fibrillation. The latter three characteristics are known as malignant arrhythmias and are an independent risk factor for sudden cardiac death, and malignant ventricular arrhythmias often lead to hemodynamic deterioration, accelerated progression, and even life-threatening conditions. Lidocaine is a class IB antiarrhythmic drug, which selectively acts on Purkinje fibroblasts and ventricular myocytes, slowing down the rate of 4-phase depolarization, reducing the autoregulation of Purkinje fibroblasts, promoting K+ efflux, shortening the action potential time course, and relatively prolonging the effective induction period. It is often used in the prevention and treatment of ventricular arrhythmias. Lidocaine slows cardiac conduction, inhibits cardiac contractility, and decreases cardiac output. Lidocaine has been used for a long time and has more experience in clinical antiarrhythmic use. In the face of ventricular arrhythmias, clinicians often choose lidocaine to control them, and its effectiveness and safety are high. Lidocaine can prevent excessive inflammatory responses. Many studies have shown that lidocaine is very effective in preventing and combating trauma or endotoxin-induced inflammatory responses [25]. Lidocaine is a membrane stabilizer that inhibits neutrophil (PMN) adhesion and aggregation, reduces oxygen radical and protein hydrolase release, stabilizes cell membranes, regulates cytokines, and suppresses excessive inflammatory responses. Inflammatory mediators LB4 and interleukin 1α (IL-1α) are strong PMN chemotactic agents, inducing PMN edge, degranulation, exudation, superoxide production, and increasing vascular permeability in concert with prostaglandin E2 [24, 26]. In vitro incubation of monocytes with different concentrations (2–20 mol/L) of lidocaine significantly inhibited the release of LB4 and IL-1α, and micromolar concentration levels of lidocaine inhibited the release of histamine from leukocytes, mast cells, and basophils, suggesting that lidocaine can inhibit the release of some key inflammatory mediators and exert anti-inflammatory effects. In clinical applications, several studies have found that intraoperative intravenous infusion of lidocaine can modulate patients' immune function and accelerate their postoperative recovery. Intraoperative lidocaine infusion in patients undergoing colorectal surgery was found to accelerate the recovery of enhanced gastrointestinal function and significantly shorten the length of hospital stay, while intravenous lidocaine infusion significantly reduced the expression levels of IL-6 and IL-8, complementing C3a, CD-11b, etc. in plasma. In [27], it is reported that in a prospective randomized double-blind controlled trial, intravenous lidocaine infusion was given to outpatient laparoscopic patients, and it was found that the postoperative recovery index was significantly higher in the lidocaine group. Besides, it was observed that intravenous lidocaine infusion significantly reduced the length of hospital stay and reduced the dose of opioids used by the patients. There are complications that prevent the occurrence of phlebitis during Patient-Controlled Intravenous Analgesia (PCIA) while adding lidocaine to the intravenous analgesic pump. It may be due to the action of lidocaine on vascular endothelial cells and peripheral nerve receptors near the venipuncture site, which dilates the blood vessels and inhibits the irritation response of the vein wall to the cannula needle and the release of inflammatory factors from vascular endothelial cells. The dilated blood vessels accelerate blood flow and make platelets less likely to aggregate, thus preventing the formation of microthrombi and the occurrence of phlebitis. Chemotherapy-induced phlebitis often occurs in clinical practice, and some studies have shown that the use of low-dose lidocaine plus dexamethasone in the perioperative period to prevent chemotherapeutic phlebitis has significant efficacy [28]. In conclusion, perioperative low-dose intravenous lidocaine can reduce the inflammatory response due to surgery, reduce the amount of anesthesia and analgesics used during surgery, and relieve postoperative pain. Lidocaine, a commonly used amide local anesthetic, has been shown to have anti-inflammatory effects, and perioperative intravenous infusion of lidocaine can reduce postoperative pain, decrease the use of opioid analgesics, reduce the inflammatory response of the body, accelerate the recovery of gastrointestinal function, and shorten the hospital stay of patients. Further study on the protective effect and mechanism of lidocaine on the decrease of immune function caused by surgical trauma can provide a new theoretical basis for the application of lidocaine in clinical anti-inflammatory treatment.

2.3. Artificial Intelligence Healthcare. Deep learning models can be flexibly scaled to huge data resources and improved by distributed dedicated hardware resources. The migration strategies can be introduced to easily improve the performance on more types and domains of data. Deep learning models have gradually replaced the traditional machine learning methods to effectively implement and utilize AI technology in healthcare. On the other hand, deep learning models have the flexibility to encode heterogeneous data, catering to the heterogeneous nature of medical data. In [24], a deep learning algorithm is trained using more than 17,000 facial images of patients to identify rare genetic syndromes with high accuracy. The research is based on the idea that various genetic syndromes exhibit unique facial features that can help clinicians make a diagnosis. Google Inc. released a model based on a deep learning approach that uses current and historical CT images of patients to predict lung cancer risk [29]. The block diagram of the intelligent medical system is shown in Figure 3. The model has been shown to achieve the best current results on 6,716 cases, outperforming human radiologists' diagnoses, especially in cases where historical CT image data are not available. The model provides an overall prediction of lung cancer malignancy and identifies less visible malignant tissue in the lung. The model also effectively incorporates historical scans to help predict lung cancer risk, given that historical data on the growth rate of malignant tissue in the lung can help predict malignancy.

DeepMind has released a new circulating neural network-based artificial intelligence algorithm [30] that can predict acute kidney injury lesions 48 hours before they occur. By incorporating AI algorithms and intelligent medical assistants, the system proposes a shift from a reactive to a preventive model of care. The AI-based model proposed in [26] can help improve patient care and reduce healthcare spending. Researchers at the Massachusetts Institute of Technology have developed a system to predict the characteristics of vocal cord disease [31]. Built on a dataset of more than 100 medical subjects, the system uses features automatically extracted from this data and then trained with high precision to classify patients with and without vocal cord nodules. The study takes full advantage of the data from the rise of wearable devices, with approximately one week of voice monitoring data and billions of samples for each subject in the dataset. The corresponding signals captured from small accelerometers and sensors mounted on the subject's neck overcome many of the drawbacks of traditional feature engineering methods for mining disease-causing features. The research aims to improve medical decision-making by replacing some of the steps with excessive manual input through the application of artificial intelligence in medicine. The greatest achievement of deep learning for image analysis is reflected in the field of computer vision research. Accordingly, medical image analysis technology has become the brightest calling card of artificial intelligence technology in the current medical field. The related technology excels in processing convolutional neural network models with spatially invariant data. Relying on image video analysis and parsing technology, it handles tasks such as target classification, target detection, and target segmentation, which are very effective in determining whether a patient's CT image contains malignant tumors and other diseases. Such computer vision-based image classification and target detection applications are useful in complex diagnoses in dermatology, radiology, and pathology as well [32]. For instance, in [33] a fully automated tool is proposed to assess viable and necrotic tumor in osteosarcoma, by utilizing 40 digitalized slide images and 13 machine learning models. Apart from the above-mentioned clinical decision-making systems, a large number of artificial intelligence-based clinical and healthcare systems have been proposed and simulated in clinical and wellbeing setups for cancer [34], diabetes mellitus [35], and wellness recommendations [36, 37].

3. Method

At present, the depth of anesthesia is monitored in a subjective way by observing the patient's signs that are more affected by drugs, surgical stimulation, and primary diseases, such as respiration, circulation, eyes, skin, digestive tract, and skeletal muscle tone. It can also be monitored in an objective way with the help of monitors, certain vital signs of the patient, etc., and a quantitative evaluation index is given. With this research work, an objective method is proposed utilizing AI classifiers on EEG data to accurately predict the depth of anesthesia. The approach is feasible to understand the current state of anesthesia of the patient and requires no advanced skill or professionalism. Detail of the model is presented in the following subsections.

3.1. Model Architecture. The method proposed in this paper is based on EEG signals and neural networks, which has the advantage of reflecting conscious activity and noninvasive characteristics and is one of the most promising methods in detecting the depth of anesthesia at present. The method architecture is shown in Figure 4.

3.2. Data Preprocessing. In places such as operating rooms, electroencephalogram (EEG) signals are susceptible to pulse interference caused by equipment such as high-frequency

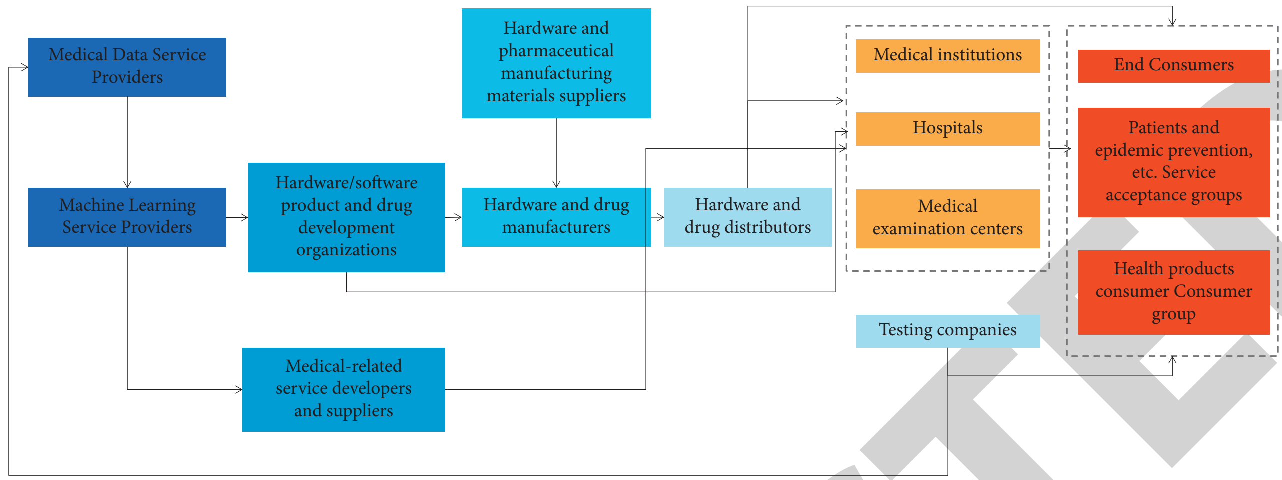

Figure 3: Intelligent medical system.

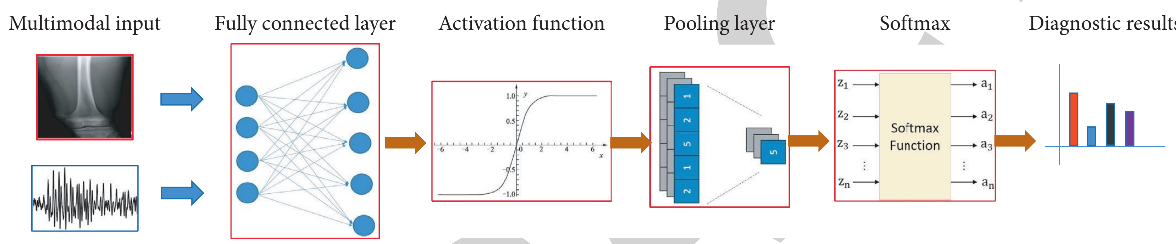

Figure 4: Model structure.

electric knives. The EEG signal is a low frequency signal, and the signal frequency band is generally 0.5~35.0 Hz. According to the characteristics of EEG signal, the high frequency noise signal can be filtered out. For doing so, a corresponding low-pass filter is designed to retain the effective EEG signal. In the proposed method, the adaptive thresholding method is used to better overcome the pulse interference. The threshold is continuously adjusted to accommodate the whole signal change. The adaptive thresholding method first segments the EEG signal with each segment containing 0.5 s of data. The variance of one segment of data is multiplied by the scale factor and is used as a threshold value for the next segment of data. If the computed variance of the next segment of data is less than the threshold value, the data is modified and the threshold value is updated; otherwise, the segment of data is deleted. A 4^{th} order 47 Hz Butterworth low-pass filter is used to filter out the high frequency interference signal based on retaining the low frequency effective signal of EEG signal. As the EEG signals acquisition process is susceptible to the interference of 50 Hz industrial frequency signal, a 4^{th} order 50 Hz trap is used to filter out the interference of the industrial frequency signal. During the EEG signal acquisition process, it is also susceptible to interference from human movement, which generates baseline drift. The baseline drift will cause the EEG signal to drift up and down. However, the interference generated by human movement can be effectively removed by designing a high-pass filter with a 2^{nd} order 0.5 Hz Butterworth filter. The EEG signal processing flow is shown in Figure 5.

Periodogram spectrum estimation, when the signal sequence is of finite length, is given as

$$\widehat{P}(w) = \frac{1}{N}\left|\sum_{n=1}^{N} x(n)e^{-jwn}\right|^2. \quad (1)$$

The periodogram method has low frequency resolution and simple calculation because of the power spectrum estimation. Given the poor spectral performance of the periodogram method, the variance characteristics of the periodogram are improved using the averaging method. To obtain the weighted overlapping averaging, the Welch averaging periodogram method is used. For L independent random variables $X_1, X_2 \cdots X_L$ with same mean μ and variance δ^2, the new random variable $X = (X_1 + X_2 + \cdots + X_L)/L$ has mean μ and variance reduced by a factor of L. With the Welch averaging method segments $x_N(n)$, the data in each segment overlap by M points for the number of segments L given as

$$L = \text{floor}\left(\frac{N - \text{lap}}{M - \text{lap}}\right), \quad (2)$$

where lap is the number of overlapping data points to add a window $w(n)$ to each segment of data and adding a Hanning window to improve the spectral distortion occurred due to a large side flaps of the rectangular window. The power spectrum is computed as

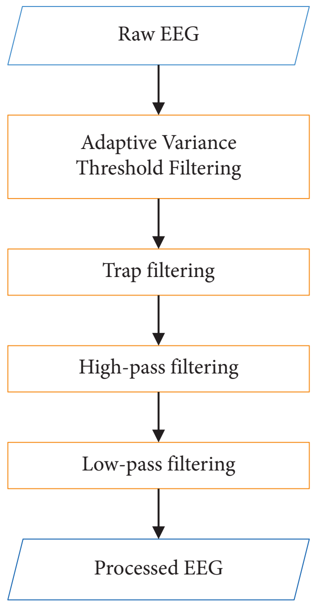

Figure 5: EEG signal preprocessing flow chart.

$$\widehat{P}^{i}_{\mathrm{PER}}(k) = \frac{1}{MU}\left|\sum_{n=1}^{M-1} X^{i}_{N}(n)w(n)W_{M}^{-kn}\right|^{2}. \tag{3}$$

Thus, the average power spectrum obtained by the Welch averaging method is given as

$$\widehat{P}_{PER}(k) = \frac{1}{MUL}\sum_{i=1}^{L}\left|\sum_{n=1}^{M-1} X^{i}_{N}(n)w(n)W_{M}^{-kn}\right|^{2}. \tag{4}$$

The Welch averaging method has the characteristics of data overlapping and increasing number of segments and is, therefore, more computationally intensive. Let $P(k)$ be the power spectrum of the Fourier transform of N points, and the formula to find the total power of the waveform from 0 to 30 Hz is given as

$$\text{Total\_Power} = \sum_{k=1}^{30\times N/s} P(k). \tag{5}$$

3.3. Neural Networks. The back propagation (BP) neural network consists of an input layer, an implicit layer, and an output layer. The forward propagation of the working signal and the backward propagation of the error signal are continuously cycled to make the output of the network closer to the expectation until the error between the output of the network and the expected output is small enough or the iteration steps reach the preset limit. The construction of the BP network structure mainly includes the determination of the number of layers and hidden layer nodes of the BP network and the design of the input and output nodes. Through the determination of the number of hidden layers of BP, Hecht Nielsen proved that when each node has different thresholds, a continuous function in the closed region can be approximated by a network with one hidden layer [38]. Therefore, a three-layer BP neural network can accomplish any n-dimensional to m-dimensional mapping.

If the number of nodes in the hidden layer is too small, the training effect is poor and the training accuracy is not achieved, which reduces the prediction ability of the network, i.e., "underfitting". Too many nodes in the hidden layer will lead to "overfitting". In order to find a suitable number of nodes in the hidden layer, a smaller number of nodes in the hidden layer are used to train the network first. In case sufficient accuracy is not achieved, the number of nodes in the hidden layer is gradually increased, and then the network is retrained. Different numbers of hidden layer nodes have little effect on the generalization ability of the network. In the proposed method, the three-layered network is followed because of two main reasons: (1) in order to improve the generalization ability of the network, the training process uses validation method to check the generalization ability. After setting the max-failure times, if the parameter values during validation cause a continuous rise in the prediction error, the training is stopped. (2) A simpler anesthesia depth exponential function is used, which can be fitted by a three-layer BP network using a smaller number of nodes. Therefore, to reduce the network structure, a smaller network is used and the number of nodes in the hidden layer is set to 5.

The number of input and output nodes of the BP network is selected such that the number of input nodes depends on the dimensionality of the data source and the input feature vector. The anesthesia depth index is fitted by 3 parameters, spectral edge frequency (SEF), BETA-RATIO, and burst-suppression ratio (BSR); thus, the number of network input nodes is set to 3. The output of the network has only one parameter, i.e., the anesthesia depth evaluation value, which is a dimensionless value from 0 to 100, so the number of nodes in the output layer of the network is set to 1.

One of the considerations of this paper is to find out whether different excitation functions influence the generalization ability of the network or not; key focus is paid on the selection of the network excitation function. Since the bispectral index (BIS) function is a linear function, the final choice in this paper is the linear excitation function, PURELINE. The activation function is expressed as

$$y = f\left(\sum_{i=1}^{r} w_i x_i\right). \tag{6}$$

The effect of different learning functions on the generalization ability of the network was examined. It was observed that training algorithms of the BP neural networks have a great impact on the generalization ability, convergence rate, and stability of the network. As it is difficult to predict how much time a training method consumed in training, the correlation coefficient of BIS was computed to select a suitable training function. Different training functions have different values of the correlation coefficient r between the fitted BIS and nonfitting BIS values. If the r values obtained for each validation sample of a certain training function are, as a whole, larger than the r values obtained for other training functions, it is assumed that the

Table 1: Comparison of mean arterial pressure (MAP) and heart rate (HR) between the two groups at different time points ($x \pm s$).

Group	Number of cases	MAP/mmHg			HR/(times/min-1)		
		T1	T2	T3	T1	T2	T3
Observation group	58	80.2 ± 11	81.6 ± 12.4	81.3 ± 12.1	80.7 ± 12.4	79.3 ± 12.9	82.2 ± 14.1
Control group	57	80.2 ± 11	109.8 ± 13.4	100.3 ± 12.7	81.2 ± 12.6	90.1 ± 13.5	93.6 ± 14.2
t		0.824	7.236	5.043	0.721	5.526	6.137
P		0.217	0.000	0.002	0.342	0.003	0.001

training function has a strong generalization ability. Although the algorithm with variable learning rate converges slowly, in some specific cases, the algorithm converges too fast. In such case, the training ends earlier and the obtained results do not reach the required target, thus missing the point that minimizes the error. Therefore, as a result it was decided to use the momentum BP algorithm trained with variable learning rate, which is one of the most commonly used training algorithms in BP networks.

4. Experimentation and Evaluation

The proposed method is evaluated by real data obtained from the patients suffering from osteosarcoma in the Yantaishan Hospital, Zhifu District, China. Details of the experiment and evaluation are presented in the following subsections.

4.1. Dataset. One hundred and five patients undergoing osteosarcoma femoral tumor segment amputation from January 2020 to January 2021 in Yantaishan Hospital were randomly divided into an observation group (58 patients) and a control group (57 patients). Inclusion criteria: both groups were patients undergoing osteosarcoma femoral tumor segment resection; patients were willing to cooperate with the study; patients had good communication skills; and patients were assessed as grade I to III by the American Society of Anesthesiologists. Exclusion criteria: patients with mental disorders; patients <18 years of age; patients with other serious diseases; patients with long-term sedation; patients with an operation time longer than 3 h; and patients with intraoperative accidents. The general data of the two groups were not significantly different ($P > 0.05$) and were comparable.

4.2. Experimental Setup. This experiment uses a hardware platform to collect dental data from the patient's mouth. First, the tongue depressor with camera is inserted into the patient's oral cavity, the high brightness LED is used for both the groups, the multifunctional monitor was connected after admission to the operating room, and intravenous inhalation anesthesia was given by tracheal intubation. In both groups, no sedative drugs were used before induction of anesthesia, and intravenous midazolam (dose 0.04 mg/kg), sufentanil (dose 0.4 μg/kg), etomidate (dose 0.2 mg/kg), and cis-atracurium (dose 0.2 mg/kg) were given to patients for induction of anesthesia. After the disappearance of the lash reflex and general relaxation of patients, tracheal intubation was given, and the ventilator was connected. Anesthesia was maintained, using lidocaine every hour as per the proposed AI algorithm to automatically calculate the use of intermittent additional. Intraoperative additional lidocaine was used to maintain the EEG bispectrality index (BIS) at 40–55; the infusion of lidocaine was stopped 10 min before the end of surgery, and the infusion of sufentanil was stopped after the completion of skin sealing. At the end of surgery, when the patient's BIS was ≥80, he was resuscitated in the anesthesia resuscitation room. In the observation group, dexmedetomidine hydrochloride was given by intravenous pump at a dose of 0.5 μg/kg for 15 min before the end of surgery. The control group was given an equal amount of saline in the same way. SPSS 20.0 software was applied for data analysis, and the measurement data were expressed as mean ± standard deviation. The t-test was used for comparison between the groups and the count data were expressed as number of cases (in %). The χ^2 test was used for comparison where a value of $P < 0.05$ was considered significantly different.

4.3. Evaluation Metrics. The mean arterial pressure (MAP) and heart rate (HR) at different time points: the time of anesthesia, recovery time of spontaneous respiration, extubating time, and awakening time; the occurrence of agitation; and the incidence of complications in the two groups were used as observation indexes. Patients' agitation was evaluated by the following methods: patients who were able to cooperate quietly were evaluated as grade 0, patients who moaned intermittently were evaluated as grade 1, patients who moaned continuously were evaluated as grade 2, and patients who shouted and struggled were evaluated as grade 3 and were evaluated as severe agitation. Complications included hypoxemia, chills, hypotension, and choking cough.

4.4. Experimental Results. The MAP and HR of the two groups at different time points were compared before extubating at the end of surgery (T1). There was no significant difference between MAP and HR of the observation group and the control group ($P > 0.05$). However, MAP and HR of the observation group were significantly lower than those of the control group at the time of extubating (T2) and 5 min after extubating (T3) ($P < 0.05$); see Table 1.

Comparison of anesthesia-related indexes between the two groups: there was no significant difference in the anesthesia time, recovery time of spontaneous breathing, and extubating time in the observation group compared with the control group ($P > 0.05$), but the awakening time in the

Table 2: Comparison of anesthesia-related indicators between the two groups [$(x \pm s)$, min].

Group	Number of cases	Duration of anesthesia	Recovery time of spontaneous breathing	Time to extubation	Time to awaken
Observation group	58	138.3 ± 15.5	11.3 ± 2.2	8.4 ± 2.3	19.2 ± 4.9
Control group	57	139.6 ± 16.8	11.2 ± 2.4	8.5 ± 2.6	35.4 ± 6.1
t		0.915	1.118	0.853	10.024
P		0.162	0.132	0.225	0.000

Table 3: Comparison of the occurrence of agitation during the awakening period between the two groups (cases, %).

Group	Number of cases	Level 0	Grade 1	Level 2	Grade 3	Total
Observation group	58	23 (39.7)	24 (41.4)	8 (13.8)	3 (5.2)	35 (60.3)
Control group	57	10 (17.5)	23 (40.3)	16 (28.1)	8 (14.0)	47 (82.5)
t						6.869
P						0.009

Table 4: Comparison of the occurrence of complications between the two groups (cases, %).

Group	Number of cases	Chills	Hypoxemia	Hypotension	Choking cough	Total
Observation group	58	2 (3.4)	4 (6.9)	3 (5.2)	3 (5.2)	12 (20.7)
Control group	57	3 (5.3)	3 (5.3)	2 (3.5)	3 (5.3)	11 (19.3)
t						0.035
P						0.852

observation group was significantly shorter than that in the control group ($P < 0.05$); see Table 2.

The incidence of agitation in the observation group (60.3%) was significantly lower than that in the control group (82.5%) ($P < 0.05$); see Table 3.

There was no significant difference in the incidence of complications in the observation group (20.7%) compared with that in the control group (19.3%) ($P > 0.05$); see Table 4.

5. Conclusion

In the limb-preserving surgical treatment of femoral bone tumor, complete resection of the tumor segment, local bone graft, allograft or reimplantation after inactivation of the tumor segment, and fixation of the femur with appropriate internal fixation are required to restore lower limb function. In this study, patients with osteosarcoma femoral tumor segment amputation in Yantaishan Hospital were treated with lidocaine definite injection, and the results showed that MAP and HR in T2 and T3 were significantly lower in the observation group than in the control group, suggesting that lidocaine definite injection contributes to the hemodynamic stability of patients after general anesthesia. The analgesic effect may promote the stabilization of theophylline and aldosterone in patients' bodies after surgery and reduce the effect on patients' cardiovascular system. The awakening time of the observation group was significantly shorter than that of the control group, suggesting that the lidocaine definitive injection promoted the awakening of the patients, and its analgesic and sedative effects may have played an important role in the awakening of the patients. The incidence of agitation in the observation group was significantly lower than that in the control group, which further showed that lidocaine definitive injection helped to reduce the incidence of agitation in patients. This result has some differences with other types of postoperative patients under general anesthesia in the data, but the ability of lidocaine definitive injection to reduce the incidence of agitation in patients is consistent. The reason may be related to the type of surgery selected in this study and the selection of cases. The incidence of complications in the observation group was the same as that in the control group, suggesting that lidocaine definitive injection promotes patients' awakening through analgesia and sedation and reduces the incidence of agitation in patients, but has no significant side effects on patients, which is of great value in the clinical application for patients under general anesthesia. To summarize, the AI algorithm based on the automated determination of different concentrations of lidocaine dine injection applied to patients with osteosarcoma femoral tumor segment amputation proposed in this paper can help maintain the stability of MAP and HR of patients, reduce the incidence of agitation of patients, and have no significant side effects on patients. The method is significant for further promotion and application.

Data Availability

The datasets used during the current study are available from the corresponding author on reasonable request.

Conflicts of Interest

The authors solemnly declare that there are no conflicts of interest.

Authors' Contributions

Shuqin Ni and Xin Li contributed equally to this work.

References

[1] M. F. Hansen, M. Seton, and A. Merchant, "Osteosarcoma in Paget's disease of bone," *Journal of Bone and mineral Research*, vol. S2, pp. 58–63, 2006.

[2] J. Lee, J.-Y. Lee, H. J. Kim, and K.-S. Seo, "Dental anesthesia for patients with allergic reactions to lidocaine: two case reports," *Journal of dental anesthesia and pain medicine*, vol. 16, no. 3, pp. 209–212, 2016.

[3] H. J. Park and M. R. Prausnitz, "Lidocaine-ibuprofen ionic liquid for dermal anesthesia," *AIChE Journal*, vol. 61, no. 9, pp. 2732–2738, 2015.

[4] B. Ji, Y. Li, D. Cao, C. Li, S. Mumtaz, and D. Wang, "Secrecy performance analysis of UAV assisted relay transmission for cognitive network with energy harvesting," *IEEE Transactions on Vehicular Technology*, vol. 69, no. 7, pp. 7404–7415, 2020.

[5] J. Li, X. Zhu, S. Yang et al., "Lidocaine attenuates cognitive impairment after isoflurane anesthesia by reducing mitochondrial damage," *Neurochemical Research*, vol. 44, no. 7, pp. 1703–1714, 2019.

[6] H. Cai, H. Zhao, J. Tang, and H. Wu, "Serum miR-195 is a diagnostic and prognostic marker for osteosarcoma," *Journal of Surgical Research*, vol. 194, no. 2, pp. 505–510, 2015.

[7] X Lin, J Wu, S. Mumtaz, S. Garg, J. Li, and M. Guizani, "Blockchain-based on-demand computing resource trading in IoV-assisted smart city," *IEEE Transactions on Emerging Topics in Computing*, vol. 9, no. 3, pp. 1373–1385, 2020.

[8] D. J. Kim, R. Bengali, and T. A. Anderson, "Opioid-free anesthesia using continuous dexmedetomidine and lidocaine infusions in spine surgery," *Korean journal of anesthesiology*, vol. 70, no. 6, p. 652, 2017.

[9] D. Giordano, M. G. Raso, C. Pernice, V. Agnoletti, and V. Barbieri, "Topical local anesthesia: focus on lidocaine–tetracaine combination," *Local and Regional Anesthesia*, vol. 8, p. 95, 2015.

[10] R. G. Wade, J. Crawfurd, D. Wade, and R. Holland, "Radial artery blood gas sampling: a randomized controlled trial of lidocaine local anesthesia," *Journal of Evidence-based Medicine*, vol. 8, no. 4, pp. 185–191, 2015.

[11] Y. Zhang, Z. He, Y. Li et al., "Selection of surgical methods in the treatment of upper tibia osteosarcoma and prognostic analysis," *Oncology Research and Treatment*, vol. 40, no. 9, pp. 528–532, 2017.

[12] Y. Yang, L. Han, Z. He et al., "Advances in limb salvage treatment of osteosarcoma," *Journal of bone oncology*, vol. 10, pp. 36–40, 2018.

[13] Y. Liu, Y. Wang, Z. Teng et al., "Matrix metalloproteinase 9 expression and survival of patients with osteosarcoma: a meta-analysis," *European Journal of Cancer Care*, vol. 26, no. 1, 2017.

[14] M. Szewczyk, R. Lechowski, and K. Zabielska, "What do we know about canine osteosarcoma treatment? - review," *Veterinary Research Communications*, vol. 39, no. 1, pp. 61–67, 2015.

[15] M. Xu, M. Xu, S. Zhang et al., "Comparative efficacy of intraoperative extracorporeal irradiated and alcohol-inactivated autograft reimplantation for the management of osteosarcomas—a multicentre retrospective study," *World Journal of Surgical Oncology*, vol. 19, no. 1, pp. 1–10, 2021.

[16] A. F. Kamal and P. Rubiansyah, "Clinical outcome of various limb salvage surgeries in osteosarcoma around knee: m," *Annals of Medicine and Surgery*, vol. 42, pp. 14–18, 2019.

[17] T. Liu, X. Zhang, Q. Zhang, X. Zhang, and X. Guo, "Total femoral reconstruction with custom prosthesis for osteosarcoma," *World Journal of Surgical Oncology*, vol. 14, no. 1, pp. 1–6, 2016.

[18] M. Xu, Z. Wang, X. C. Yu, J. H. Lin, and Y. C. Hu, "Guideline for limb-salvage treatment of osteosarcoma," *Orthopaedic Surgery*, vol. 12, no. 4, pp. 1021–1029, 2020.

[19] W. Yao, Q. Cai, J. Wang, and S. Gao, "Treatment of osteosarcoma around the knee in skeletally immature patients," *Oncology Letters*, vol. 14, no. 5, pp. 5241–5248, 2017.

[20] D. A. Hashimoto, E. Witkowski, L. Gao, O. Meireles, and G. Rosman, "Artificial intelligence in anesthesiology," *Anesthesiology*, vol. 132, no. 2, pp. 379–394, 2020.

[21] C. W. Connor, "Artificial intelligence and machine learning in anesthesiology," *Anesthesiology*, vol. 131, no. 6, pp. 1346–1359, 2019.

[22] X.-h. Du, H. Wei, P. Li, and W.-T. Yao, "Artificial intelligence (AI) assisted CT/MRI image fusion technique in preoperative evaluation of a pelvic bone osteosarcoma," *Frontiers in Oncology*, vol. 10, p. 1209, 2020.

[23] P. Gambus and S. L. Shafer, "Artificial intelligence for everyone," *Anesthesiology*, vol. 128, no. 3, pp. 431–433, 2018.

[24] M. R. Mathis, S. Kheterpal, and K. Najarian, "Artificial intelligence for anesthesia: what the practicing clinician needs to know," *Anesthesiology*, vol. 129, no. 4, pp. 619–622, 2018.

[25] H. Hermanns, M. W. Hollmann, M. F. Stevens et al., "Molecular mechanisms of action of systemic lidocaine in acute and chronic pain: a narrative review," *British Journal of Anaesthesia*, vol. 123, no. 3, pp. 335–349, 2019.

[26] C. Matava, E. Pankiv, L. Ahumada, B. Weingarten, and A. Simpao, "Artificial intelligence, machine learning and the pediatric airway," *Pediatric Anesthesia*, vol. 30, no. 3, pp. 264–268, 2020.

[27] M. Kaszyński, D. Lewandowska, P. Sawicki, P. Wojcieszak, and I. Pągowska-Klimek, "Efficacy of intravenous lidocaine infusions for pain relief in children undergoing laparoscopic appendectomy: a randomized controlled trial," *BMC Anesthesiology*, vol. 21, no. 1, 1 page, 2021.

[28] D. Zhou, L. Wang, Q. Cui, R. Iftikhar, Y. Xia, and P. Xu, "Repositioning lidocaine as an anticancer drug: the role beyond anesthesia," *Frontiers in Cell and Developmental Biology*, vol. 8, p. 565, 2020.

[29] C. Jacobs, A. A. Setio, E. T. Scholten et al., "Deep learning for lung cancer detection on screening CT scans: results of a large-scale public competition and an observer study with 11 radiologists," *Radiology: Artificial Intelligence*, vol. 3, no. 6, 2021.

[30] N. Tomašev, X. Glorot, J. W. Rae et al., "A clinically applicable approach to continuous prediction of future acute kidney injury," *Nature*, vol. 72, no. 7767, pp. 116–119, 2019.

[31] R. Matheson, "Automating artificial intelligence for medical decision-making," 2019.

[32] J. Bowness, O. Varsou, L. Turbitt, and D. Burkett-St Laurent, "Identifying anatomical structures on ultrasound: assistive artificial intelligence in ultrasound-guided regional anesthesia," *Clinical Anatomy*, vol. 34, no. 5, pp. 802–809, 2021.

[33] H. B. Arunachalam, R. Mishra, O. Daescu et al., "Viable and necrotic tumor assessment from whole slide images of osteosarcoma using machine-learning and deep-learning models," *PLoS One*, vol. 14, no. 4, Article ID e0210706, 2019.

[34] M. Hussain, M. Afzal, T. Ali et al., "Data-driven knowledge acquisition, validation, and transformation into HL7 Arden

Hindawi
Journal of Healthcare Engineering
Volume 2023, Article ID 9807182, 1 page
https://doi.org/10.1155/2023/9807182

Retraction

Retracted: Effect of Carbon Dioxide on Bispectral Index of EEG under Intravenous Target-Controlled Anesthesia Based on Intelligent Medical Treatment

Journal of Healthcare Engineering

Received 10 October 2023; Accepted 10 October 2023; Published 11 October 2023

This article has been retracted by Hindawi following an investigation undertaken by the publisher [1]. This investigation has uncovered evidence of one or more of the following indicators of systematic manipulation of the publication process:

(1) Discrepancies in scope
(2) Discrepancies in the description of the research reported
(3) Discrepancies between the availability of data and the research described
(4) Inappropriate citations
(5) Incoherent, meaningless and/or irrelevant content included in the article
(6) Peer-review manipulation

The presence of these indicators undermines our confidence in the integrity of the article's content and we cannot, therefore, vouch for its reliability. Please note that this notice is intended solely to alert readers that the content of this article is unreliable. We have not investigated whether authors were aware of or involved in the systematic manipulation of the publication process.

In addition, our investigation has also shown that one or more of the following human-subject reporting requirements has not been met in this article: ethical approval by an Institutional Review Board (IRB) committee or equivalent, patient/participant consent to participate, and/or agreement to publish patient/participant details (where relevant).

Wiley and Hindawi regrets that the usual quality checks did not identify these issues before publication and have since put additional measures in place to safeguard research integrity.

We wish to credit our own Research Integrity and Research Publishing teams and anonymous and named external researchers and research integrity experts for contributing to this investigation.

The corresponding author, as the representative of all authors, has been given the opportunity to register their agreement or disagreement to this retraction. We have kept a record of any response received.

References

[1] A. Li, Q. He, R. Li, Y. Chen, and W. Xu, "Effect of Carbon Dioxide on Bispectral Index of EEG under Intravenous Target-Controlled Anesthesia Based on Intelligent Medical Treatment," *Journal of Healthcare Engineering*, vol. 2022, Article ID 4696128, 10 pages, 2022.

Hindawi
Journal of Healthcare Engineering
Volume 2022, Article ID 4696128, 10 pages
https://doi.org/10.1155/2022/4696128

Research Article

Effect of Carbon Dioxide on Bispectral Index of EEG under Intravenous Target-Controlled Anesthesia Based on Intelligent Medical Treatment

Aizhi Li,[1] Qunhui He,[1] Rulin Li,[2] Yu Chen,[1] and Weiwei Xu[1]

[1]*Yantai Yuhuangding Hospital, Anesthesiology Department, 264000 Shan Dong, China*
[2]*Yantai Zhifu Hospital, Anesthesiology Department, 264000 Shan Dong, China*

Correspondence should be addressed to Weiwei Xu; 2014061@qhnu.edu.cn

Received 28 January 2022; Revised 18 February 2022; Accepted 21 February 2022; Published 27 March 2022

Academic Editor: Liaqat Ali

Laparoscopic surgery has the advantages of less trauma and quick recovery, and it is more and more favored by surgeons and patients in clinical practice. However, the impact of carbon dioxide pneumoperitoneum on the body during laparoscopic surgery has attracted the attention of many scholars. Pneumoperitoneum can cause increased cerebral blood flow and increased intracranial pressure, cerebral metabolic rate is highly correlated with blood carbon dioxide partial pressure, and cerebral metabolism without cardiopulmonary bypass is linearly correlated with the depth of anesthesia. Electroencephalographic (EEG) bispectral index (BIS) is a signal analysis method, which can directly measure the effect of drugs on the cerebral cortex and reflect the depth of anesthesia. Based on this, this study takes smart medical treatment as the background and uses the improved BP neural network as a tool to explore the effect of carbon dioxide on EEG bispectral index under intravenous target-controlled anesthesia. The main purpose is to observe the correlation between arterial blood carbon dioxide partial pressure and EEG bispectral index under propofol target-controlled anesthesia during retroperitoneal laparoscopic surgery. The experimental results show that the model proposed in this study can efficiently and accurately obtain the size of the influencing factors, which provides a clinical basis for the anesthesia management and anesthesia depth regulation of carbon dioxide pneumoperitoneum laparoscopic surgery.

1. Introduction

Anesthesia depth assessment is always an important issue with the development of anesthesiology. It is directly related to the safety of patients during operation and postoperative outcome [1]. There are many methods to monitor the depth of general anesthesia. However, there is no method that can directly, accurately, and dynamically reflect the depth of anesthesia. In the past, the depth of anesthesia was indirectly reflected by monitoring the changes in hemodynamics. It was also useful to use primitive electroencephalogram (EEG), auditory evoked potential, electromyography, changes in esophageal contractility, pupillary reflex, comprehensive analysis of various variations, and multifactor logic equation analysis of microcomputer. However, there has been no direct method to determine the effect of anesthetics on the central nervous system. Taking the clinical use of muscle relaxants as the boundary, its development can be divided into two stages: in the former stage, anesthetists evaluate the depth of anesthesia by observing the changes in patients' autonomic nervous system (heart rate, blood pressure, tears, pupil size, etc.) and somatic reaction during anesthesia [2]. It is often necessary to meet the muscle relaxant effect required by surgery at the cost of deepening anesthesia. Therefore, there is a risk of too deep anesthesia; in the latter stage, the use of muscle relaxants may mask some clinical signs (such as body movement reaction) of patients during anesthesia, so that some "inadequate anesthesia" cannot be found in time, resulting in intraoperative awareness, which will cause physical and mental damage to patients [3].

So far, the purpose and content of anesthesia depth monitoring include preventing potentially dangerous hemodynamic changes, preventing intraoperative body movement, eliminating intraoperative awareness, and regulating the number of anesthetic drugs [4]. In recent years, the focus of anesthesia depth monitoring has turned to electroencephalogram (EEG) analysis. Conventional EEG can reflect the activity of the cerebral cortex and subcortical nervous system, but the operation is complicated, susceptible to external interference, difficult to analyze data, and difficult to routinely apply to Clinical determination of anesthetic effects [5]. In recent years, with the application of microcomputers and the development of EEG analysis technology, the application of EEG technology in clinical anesthesiology has received attention again, and different EEG parameters such as bi-frequency index have been derived, which can reflect the brain more accurately and timely [6]. Among them, the electric bispectral index (BIS), which has been widely studied, is known as a useful index to reflect the depth of anesthesia, and it has its own characteristics in clinical applications [7]. A large number of studies have shown that the bispectral index (BIS) is currently a very reliable indicator for evaluating the depth of sedation in anesthesia. BIS has received much attention and research in the field of clinical anesthesia [8]. This article intends to evaluate its application in anesthesia depth monitoring.

At present, the research on carbon dioxide (CO_2) pneumoperitoneum mostly focuses on the impact on physiology, and few people pay attention to the impact of CO_2 pneumoperitoneum on the depth of anesthesia. This research study is conducted to explore whether CO_2 pneumoperitoneum has a synergistic or antagonistic effect on the depth of anesthesia and draw a statistically significant difference, which is an exploration in a new direction.

2. Related Work

2.1. Research Status of Monitoring Mechanism. There are two forms of electrical activity, spontaneous EEG activity and induced EEG activity. The main differences between the two are as follows: (1) spontaneous EEG is the EEG activity in a quiet state without any external stimulation, which often shows continuous rhythmic potential changes; evoked EEG is a relatively limited potential change generated in a certain area of the skin layer under external stimuli such as sound, light, and electricity. (2) The amplitude of spontaneous EEG is high, 50–100 Hz, no signal stimulation is required, and the waveform is continuous, so there is no time-phase relationship [9]. The recording adopts direct amplification, and its waveform has only physiological significance; the evoked EEG intensity is weak, only 0.3~20 V, and there must be signal stimulation. The waveform is limited and has a time-locked relationship with the stimulation. The recording adopts synchronous superposition, and its waveform has not only physiological significance but also specific anatomical positioning and psychological significance. BIS belongs to spontaneous EEG monitoring [10].

The shape of brain wave shows the spontaneous and rhythmic electrical activity of brain cell group, which is generally described by the characteristics of amplitude, frequency, and phase. During general anesthesia, EEG frequency changes sequentially with the deepening or shallowing of anesthesia and has a functional relationship with anesthetic concentration, so it can be used to reflect the depth of anesthesia [11]. However, in the early stage, the time-domain characteristics of EEG were mostly used to reflect the depth of anesthesia, mainly analyzing the geometric properties of EEG waveform. With the maturity of fast Fourier transform technology, more and more EEG frequency domain features can be used to reflect the depth of anesthesia, convert the original EEG signal with time-to-amplitude relationship into frequency-to-power relationship, and derive multiple digital quantization parameters, such as dual frequency index (BIS), edge frequency (SEF), and intermediate frequency (MF). The phase-locking energy is subtracted from energy and expressed as the ratio of double-wave spectral density in 0~30 Hz band. Finally, a quantitative index is obtained [12]. On the one hand, the EEG characteristics of PBIS are reflected in the amplitude and frequency characteristics, and on the other hand, they are reflected in the waveform and phase characteristics. Accordingly, EEG analysis methods are also divided into frequency-domain analysis and time threshold analysis [13]. The traditional processing method is to use fast Fourier transform (FFT) to convert the change in EEG amplitude into the change in EEG power, that is, spectrum analysis. However, FFT is a typical linear analysis method, which is suitable for stable and nonrandom normal distribution signals, while EEG activity is a random skew distribution signal. Therefore, there are some limitations in analyzing EEG with this linear analysis method. BIS is a quantitative analysis index of EEG including frequency, amplitude, and phase [14]. The advantage of its monitoring is to maintain and quantify the nonlinear relationship of the original EEG, so it can better retain the functional information of the original EEG. The observation is simple and easy to use. Bispectral analysis is to quantify the phase coupling between EEG frequencies [15]. Figure 1 shows the schematic diagram of EEG signal and bispectral index.

Including frequency and amplitude information, phase coupling is the characteristic of nonlinear behavior. Therefore, bispectral analysis can accurately control and quantify the linear and nonlinear changes between signals, and it can more accurately reflect the changes in anesthesia depth. The changes in frequency and power of many anesthetics do not form a simple relationship with dose [16]. Low doses of benzodiazepines or propofol usually cause high-frequency activation, showing a net increase in frequency in the power spectrum, while higher doses of thiopental or isoflurane can cause explosive inhibition and a net decrease in power. BIS decreased during natural sleep, but it was impossible to achieve the degree of inhibition caused by high-dose propofol, sodium thiopental, or volatile anesthetics [17]. Many studies have found that with the deepening of anesthesia, the electrophysiological activities of central nerve cells change significantly. Therefore, BIS has an important value in EEG signal analysis. BIS is a dimensionless simple variable, representing fully awake state and completely no EEG activity state, respectively.

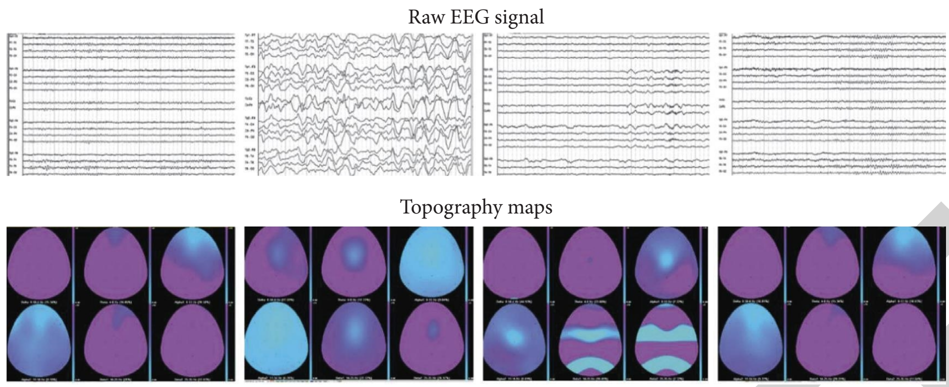

Figure 1: Schematic diagram of EEG signal and bispectral index.

2.2. Clinical Application. It is found that BIS can better reflect different sedation (sleep) depths. Whether there is awareness, memory, and implicit memory in anesthesia depends on the sedation depth in anesthesia. It is found that the BIS value is 75~90 in light sleep, 75~92 in rapid eye movement, and 20~70 in slow-wave sleep [18]. It is more advantageous to distinguish the existence and disappearance of consciousness. The sedation level depends on the inhibition degree of drugs on the cerebral cortex, which is related to the concentration of sedative and hypnotic drugs in the effective part (brain). BIS has a good correlation with the plasma concentrations of propofol and sevoflurane, which provides a theoretical basis for monitoring the depth of anesthesia (sleep). Because BIS has the above advantages in monitoring the depth of sleep (anesthesia), it helps to reduce blindness and improve safety in clinical anesthesia. Figure 2 represents the basic EEG monitoring [19].

However, more attention should be paid to the body movement in the anesthesia maintenance stage: on the one hand, due to the complex relationship between anesthesia factors (sedation, analgesia, and muscle relaxation) and surgical stimulation factors, and the existence of individual differences in patients, it is more difficult to manage body movement at this stage [20]. On the other hand, the body movement management at this stage is more necessary: because at this time, the body movement not only affects the surgical operation but also may cause accidents for some fine operations. Unfortunately, there are few studies on this stage [21]. The results of the above studies show that BIS monitoring improves the quality of anesthesia and is convenient for drug control, but BIS evaluation of anesthesia depth obviously depends on the anesthesia method used, mainly reflecting the patient's sedation or sleep depth. Patients with high-dose opioids may still show shallow anesthesia when there is no obvious somatic reaction to skin incision, indicating that BIS is different in evaluating the effects of analgesics and sedatives [22]. In conclusion, BIS changes with the increase or decrease in anesthetic concentration and dose and with the increase or decrease in surgical stimulation intensity.

2.3. Research Status of Impact Assessment Algorithm. The machine learning algorithm is an important content in the field of data analysis. We have frequent contact with the machine learning algorithms in our daily work. The machine learning algorithm classification is to subdivide the samples to be detected into the most appropriate class. The following introduces the common machine learning classification algorithms. The decision tree classification algorithm is widely used in our daily life because of its simple implementation principle. The decision tree algorithm uses tree structure for classification and decision-making. The important content of the decision tree algorithm is to improve the accuracy and reduce the scale of the algorithm [23]. The following describes the construction steps of the decision tree, which mainly includes two parts. The first is the generation of the decision tree, which is generally obtained from the training sample set, in which the sample data set has high requirements [24].

The Bayesian classification is a statistical classification method, which involves the knowledge of probability. It mainly achieves the classification effect by successfully classifying a given set of test elements into a specific category [25]. Among them, the most commonly used method in the Bayesian algorithm is the naive Bayesian algorithm. The naive Bayesian method is a classification method that assumes the independence of feature conditions under the condition of the Bayesian algorithm. It is the simplest and most commonly used Bayesian classification algorithm. The advantage of the naive Bayesian algorithm is that it needs less estimated parameters and is not sensitive to missing data; however, its accuracy mainly depends on the assumption of independence between attributes, and the algorithm has no classification rule output [26].

An artificial neural network is an algorithm that imitates the neural structure of the biological brain and its information transmission and processing. It is composed of input and output units organized together, and any connection of each unit has a weight. In the e-learning stage, the one-to-one correspondence among various categories is realized through the continuous adjustment of the weight [27]. BP neural network is the most widely used form of neural network at present. BP neural network is a network trained based on an error back propagation algorithm. Its advantage is that it has a strong nonlinear mapping ability. Secondly, the number of hidden layers and the number of neural units in each layer of the network can be unlimited, but the performance will be different with the different structures.

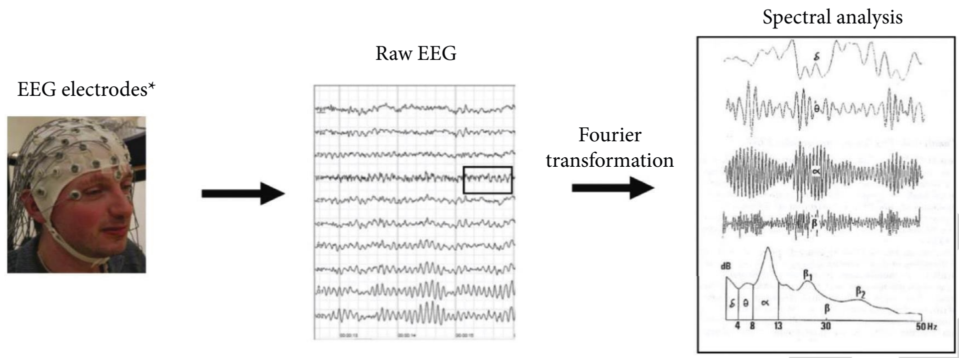

Figure 2: Representation of basic EEG monitoring [19].

This study focuses on the research of BP neural network algorithm, which will be further elaborated in the following chapters [28].

Apart from the use of AI models in different domains, intelligent models have been proposed for identifying the ways how to reduce CO_2 in the environment to be safe from its bad impacts on the human health [29]. Similarly, intelligent decision models have been proposed and implemented to realize the scenario of physical activities recommendations and diabetes' type prediction using multimodal hybrid reasoning [30] and roughest reasoning [31], respectively.

3. Impact Assessment Model

This section introduces the overall structure of the impact assessment model of optimizing BP neural network based on the improved grey wolf algorithm. Firstly, it introduces the basic principle of grey wolf algorithm, then introduces how to improve grey wolf algorithm, and finally introduces how to optimize BP neural network based on the improved grey wolf algorithm.

3.1. Principle of Grey Wolf Algorithm. Grey wolf optimization algorithm is a new swarm intelligence optimization algorithm, which imitates the leadership and hunting mode of grey wolf group in nature. According to the fitness value, GWO algorithm divides wolves into four categories: α, β, δ, and ω. Among them, α is the leader of the grey wolf, responsible for the decision-making of the whole wolf group: β is the second best Grey wolf, follows the orders issued by α in the wolf group, and also leads the subordinate wolf group. δ is the third grey wolf to help make decisions and is responsible for assisting α and β wolves to complete the hunting of prey: other grey wolves belong to ω, which is the basis of the wolf group and must obey the decision of the leadership. When catching prey, grey wolves α, β, and δ chase prey directly. The remaining grey wolves follow the first three types of grey wolves to track and surround their prey. In the GWO algorithm, the position of prey corresponds to the solution of the problem. The research shows that the GWO algorithm is obviously superior to particle swarm optimization algorithm, genetic algorithm, and other intelligent optimization algorithms in finding the global optimal solution. The mathematical model of grey wolf optimization algorithm is as follows:

$$\begin{aligned} D &= \left|K \cdot X_P(t) - X(t)\right|, \\ X(t+1) &= X_p(t) - A \cdot D, \end{aligned} \tag{1}$$

where t represents the current number of iterations. X_P is the location of prey; X is the position vector of grey wolves in the wolf pack; and A represents the convergence factor. A and K are calculated as follows:

$$\begin{aligned} A &= 2a \cdot d_1 - a, \\ K &= 2d_2, \end{aligned} \tag{2}$$

where components of a are linearly decreased from 2 to 0 over the course of iterations and d_1 and d_2 are random vectors in [0, 1]. When the location of the prey is determined, grey wolf α leads grey wolves β and δ to guide the wolves to surround the prey. Since α, β, and δ are closest to the prey, the approximate position of the prey can be judged from the position of the three wolves. The mathematical expression is as follows:

$$D_\alpha = \left|K_1 \cdot X_\alpha(t) - X(t)\right|, \tag{3}$$

$$D_\alpha = \left|K_2 \cdot X_\beta(t) - X(t)\right|, \tag{4}$$

$$D_\delta = \left|K_3 \cdot X_\delta(t) - X(t)\right|. \tag{5}$$

Among them, X_α, X_β, and X_δ represent the current positions of grey wolves α, β, and δ, respectively. K_1, K_2, and K_3 are random vector coefficients, and X represents the current position vector of grey wolf. The following equation represents the forward distance and direction of other grey wolves ω towards grey wolves α, β, and δ, respectively:

$$X_1 = X_\alpha - A_1 \cdot D_\alpha$$
$$X_2 = X_\beta - A_2 \cdot D_\beta$$
$$X_3 = X_\delta - A_3 \cdot D_\delta \qquad (6)$$
$$X(t+1) = \frac{(X_1 + X_2 + X_3)}{3}.$$

Among them, X_1 refers to the position update of ω wolves led by grey wolf α, X_2 refers to the position update of ω wolves led by grey wolf β, and X_3 refers to the position update of ω wolves led by grey wolf β, and equations (3) and (4) represent the updated grey wolf position, and equation (6) represents the final position of prey. According to the above equation (especially the calculation of forward distance and direction), the grey wolf group gradually approaches the prey and catches the prey. The implementation process of grey wolf algorithm is as follows:

(1) Firstly, the grey wolf population is initialized to generate n grey wolf positions. Then, A, a, and K are initialized, and the maximum number of iterations $t_{\max}$ is determined.
(2) The fitness value of each Grey wolf individual is calculated, the position of the grey wolf according to equations (4)–(6) is updated, the fitness values of each grey wolf individual is compared, and the optimal solution of the fitness value, the suboptimal solution, and the third optimal solution are found.
(3) The values of A, a, and K are updated.
(4) Whether the current number of iterations t is within the maximum number of iterations is compared. If $t < t_{\max}$, step 2 is processed.
(5) Otherwise, process should be ended.

The grey wolf algorithm flow is shown in Figure 3.

Many researchers have proved that grey wolf optimization algorithm is superior to particle swarm optimization algorithm, genetic algorithm, and other intelligent optimization algorithms in forming the global optimal solution of the problem. However, because the grey wolf algorithm itself is easy to fall into local optimization, its convergence accuracy is not high. At present, the grey wolf algorithm belongs to a new swarm intelligence algorithm, which has a good room for improvement in convergence accuracy and efficiency. Therefore, the improvement of grey wolf algorithm plays a very important role in the further research of grey wolf algorithm in the future. The improvement of grey wolf algorithm will be described in detail as follows.

3.2. Improved Grey Wolf Algorithm. Grey wolf algorithm is proposed and more and more applied to real life because of its convenient parameter setting, good robustness, and good optimization effect. However, because it is easy to fall into local optimization in the later stage, the accuracy is affected. This disadvantage is not only a problem in grey wolf algorithm, but also a common consistency problem in general swarm intelligence optimization algorithm. The common problem of swarm intelligence optimization algorithm is the disharmony between global and local search performance. This will lead to the reduction in convergence accuracy and performance. A swarm intelligence optimization algorithm with strong generalization ability and wide applicability must have a strong coordination mechanism of global and local search performance.

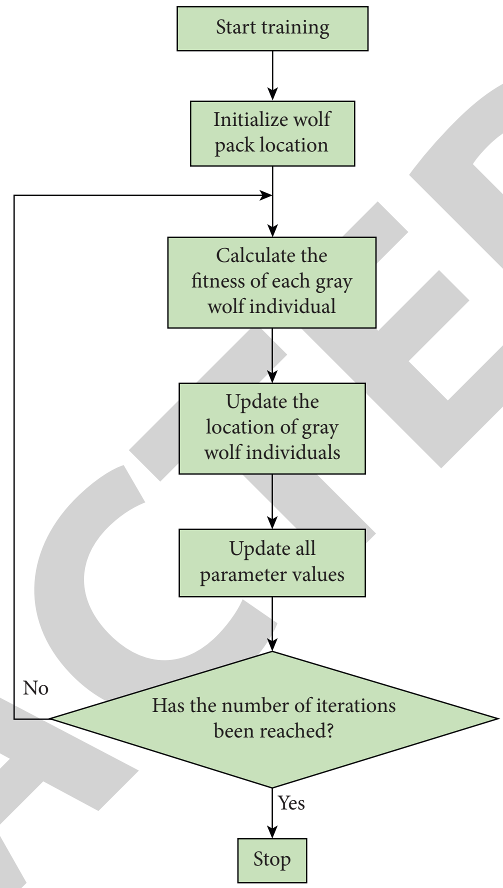

Figure 3: Grey wolf algorithm flow chart.

The control factor A in grey wolf algorithm is a very important factor for coordinating the performance of global search and local search. Therefore, this section mainly introduces the optimization of control factor a. Therefore, the calculation of control factor needs to be optimized and improved. In this section, a nonlinear control factor algorithm based on logarithmic function is proposed for the control factor of grey wolf algorithm, and its equation is shown as follows:

$$a = \log_2\left(4 - \frac{3t}{t_{\max}}\right), \qquad (7)$$

where parameter t is the number of iterations, and parameter $t_{\max}$ is the maximum number of iterations. The improved control factor A has changed from linear decline to nonlinear decline. The initial control factor A is monotonic, and the rate in the decline process is consistent. The improved control factor a changes according to the law of logarithmic decline. This can better coordinate the global and local search capabilities and more in line with the change trend and convergence process of control factors in the experiment.

The first three types of wolves in the grey wolf algorithm are α, β, and δ, respectively. During the implementation of the grey wolf algorithm, the three types of wolves α, β, and δ led other wolves to ω track prey. In the experiment, the three types of wolves play the same guiding and leading role, regardless of grade. However, in terms of the principle of the grey wolf algorithm itself, the three types of wolves α, β, and δ should be limited by hierarchical order; that is, wolf α, wolf β, and wolf δ have different degrees of guidance for other wolves ω. Grey wolf α is the leader, and grey wolves β and δ mainly help wolf α make decisions. This leadership role is closely related to the appetite level. In the implementation process of grey wolf algorithm, the corresponding fitness values of α, β, and δ calculated through the fitness function are equivalent to the three optimal solutions of the function, which does not reflect the leadership degree between grey wolves, which also reduces the convergence speed of grey wolf algorithm, and then, it is easy to form a local optimal problem. In view of this, this section realizes the dynamic follow-up of grey wolf leadership through variable proportional weight and improves the generalization ability of grey wolf algorithm. The specific calculation formula of variable proportional weight is as follows.

Firstly, the proportional weight calculated according to the grey wolf fitness value is as follows:

$$W_\alpha = \frac{F_\alpha}{F_\alpha + F_\beta + F_\delta}$$

$$W_\beta = \frac{F_\beta}{F_\alpha + F_\beta + F_\delta} \tag{8}$$

$$W_\delta = \frac{F_\delta}{F_\alpha + F_\beta + F_\delta}.$$

Among them, F_α, F_β, and F_δ represent the fitness values of grey wolves α, β, and δ, respectively. W_α, W_β, and W_δ represent the proportional weight of grey wolves α, β, and δ, respectively. Since the above proportional weights W_α, W_β, and W_δ are dynamically variable in each iteration process of the algorithm, the improved grey wolf algorithm can dynamically change the proportional weight according to different experimental environments, and the optimization performance and generalization are improved.

3.3. Neural Network Based on Improved Grey Wolf Algorithm. In the process of practical application of BP neural network, the selection of hidden layers and nodes has a great impact on the accuracy of prediction results, so it is very important to determine the number of hidden layers and nodes for the use of BP neural network. The following describes how to determine the number of hidden layers and nodes of BP neural network:

(1) *Determination of Hidden Layers.* In general, 1 layer is selected for the number of hidden layers; that is, the BP neural network is a 3-layer network, which is ideal. At the same time, overfitting may also occur. Therefore, at present, selecting the number of hidden layers can achieve the ideal training effect and accuracy.

(2) *Determination of the Number of Hidden Layer Nodes.* Compared with the selection of the number of hidden layers, the selection of the number of hidden layer nodes will be easier to achieve. Moreover, the determination of the number of hidden layer nodes is more important. Improper selection of the number of hidden layer nodes will make the neural network fall into local minimum, resulting in overfitting phenomenon, which will affect the prediction performance of the model. Because the improved grey wolf algorithm can effectively find the global optimal solutions of many problems and further improve the convergence speed and accuracy of the model, this study selects algorithm to optimize BP neural network. The structure diagram of BP neural network optimized by improved grey wolf algorithm is shown in Figure 4 [32].

With the continuous change in Grey wolf's position, the weight and threshold of BP neural network algorithm are constantly updated. The best position of grey wolf is the optimal solution sought by BP neural network. Through the optimization of algorithm, compared with the standard grey wolf algorithm, the effect of optimizing BP neural network is further improved. At the same time, the convergence speed and accuracy of BP neural network are further improved. The specific steps of optimizing BP neural network by algorithm are as follows:

(1) The first is the selection of the structure of BP neural network itself. The most important thing is to determine the number of nodes in the network hidden layer.

(2) Initialization of Basic Parameters: the grey wolf population is initialized, grey wolf position is generated, the grey wolf population size and initialization parameters a and K are calculated according to the network structure, and the maximum number of iterations is determined.

(3) The fitness function of neural network and the excitation function of output node are determined.

(4) The individual fitness value of grey wolf is calculated, and the optimal solution of fitness value is found.

(5) Training samples and test samples for experiments are selected, and the error and its corresponding optimal solution are recorded.

(6) Whether the maximum number of iterations or the set error value is met is judged, such as meeting the conditions to terminate the cycle.

(7) Finally, the returned results are the position of grey wolf α, that is, the position of the optimal solution,

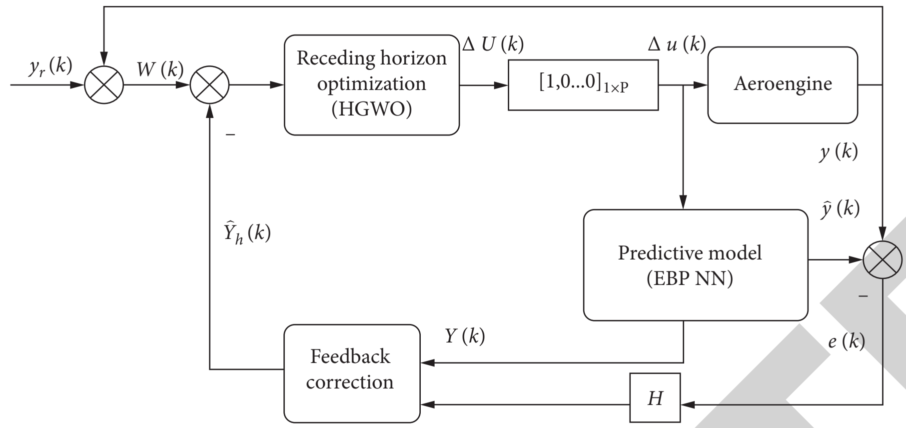

Figure 4: Improved grey wolf algorithm to optimize BP neural network structure diagram [29].

the position of Grey wolf α in each iteration of the training process, the minimum error of the position of Grey wolf α, and the error of training samples and test samples.

Through the optimization of IMGWO algorithm, the feasible initial weight and the threshold of BP neural network are generated, so as to properly solve the problems of local minimum and slow convergence.

4. Experiments and Results

4.1. General Information. Sixty (60) cases of gynecological laparoscopic surgery under general anesthesia were selected in our hospital. The patient's family members before operation are informed, and signed informed consent was obtained from the patient or family members. There was no significant difference in the composition of general data such as age, body mass index, and ASA grade among the three groups ($P > 0.05$) (Table 1).

Table 1: Comparison of general conditions and indexes of three groups of patients.

Group	Age	Body mass index	Hierarchical structure
C	49 ± 9	23 ± 3	9/11
D1	52 ± 7	23 ± 4	12/8
D2	50 ± 6	22 ± 3	10/10

The patients were randomly divided into three groups: control group (group C), low-dose carbon dioxide group (group D1), and high-dose carbon dioxide group (group D2). Groups D1 and D2: the doses of carbon dioxide were 0.3 g and 0.6 g, respectively, diluted to 10 ml with normal saline. Group C was the control group, without carbon dioxide and 10 ml of normal saline. All patients were fasting solid food 12 hours before operation, drinking 6 hours before operation, and no preoperative drugs. After entering the room, the upper limb was opened for intravenous infusion of lactate Ringer's solution, and the Philips MP60 multifunctional monitoring system (Philips, the Netherlands) was used to monitor ECG, BP, SpO_2, and RR. The bispectral index (BIS) module equipped with the system (Philips, the Netherlands) and aspect standard four-electrode sensor (aspect, the USA) was used to monitor BIS.

BIS monitoring method: the patient's forehead to the left temple is wiped with an alcohol cotton ball to increase the sensitivity of the sensor. No. 1 electrode of the disposable signal sensor about 5 cm is stuck above the central nasal root of the patient's forehead, a direction indication line on No. 1 electrode is made to face the nasal root, No. 2 and No. 4 electrodes are stuck above the corresponding eyebrow arch along the direction of the sensor, and finally No. 3 electrode is stuck to the Taiyang point on the same side. The sensor and power cable are connected, and self-test is started and monitored after passing the electrode impedance test.

4.2. Results and Analysis. The depth of sedation was assessed according to the improved OAA score. The BIS value, propofol effect chamber concentration, and hemodynamic parameters were recorded before entering the room, after pumping dexmedetomidine or normal saline and when the OAA score was stable at 4, 3, 2, and 1. Data and OAA scores were collected by the same anesthesiologist. After entering the room and before medication, the OAA score of the three groups was 5, and the BIS was greater than 94. After pumping dexmedetomidine, the OAA score of two cases and five cases in groups D1 and D2 decreased to 4 points and the BIS decreased to the range of 84 to 77. When the OAA score was stable at 4, 3, 2, and 1, the BIS values in groups D1 and D2 were significantly lower than those in group C (see Table 2). When the OAA score was 3 and 2, the BIS value of group D1 was also lower than that of group C. The value of group D2 is less than that of group D1. At OAA scores of 4, 3, and 2, group D2 was lower than group D1, and it can be seen in Table 2.

When OAA score was 4, 3, 2, and 1, the concentration of carbon dioxide effector chamber in groups D1 and D2 was lower than that in group C ($P < 0.05$) (see Table 3), and the concentration of carbon dioxide effector chamber in group D2 was lower than that in group D1 ($P < 0.05$), as shown in Figure 5.

Table 2: Comparison of BIS values and OAA scores among the three groups.

			OAA score			
	T0	T1	1	2	3	4
C	97 ± 1	96 ± 3	82 ± 4	65 ± 3	59 ± 4	46 ± 5
D1	96 ± 1	93 ± 3	80 ± 4	59 ± 6	54 ± 4	42 ± 3
D2	97 ± 1	91 ± 3	73 ± 4	53 ± 3	48 ± 4	39 ± 3

Table 3: Comparison of BIS values and OAA scores among the three groups.

	4	3	2	1
C	1.11 ± 0.38	1.52 ± 0.37	1.70 ± 0.25	1.88 ± 0.06
D1	0.82 ± 0.26	1.14 ± 0.19	1.33 ± 0.11	1.62 ± 0.08
D2	0.25 ± 0.11	0.45 ± 0.15	0.66 ± 0.07	0.73 ± 0.03

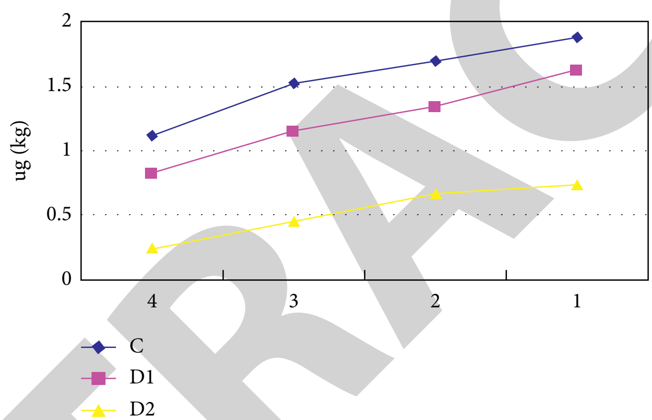

Figure 5: Propofol effect chamber concentration corresponding to different OAA scores in group A.

Forearm isolation technology was prospectively studied. BIS monitoring was used to predict the recovery of consciousness after anesthesia induction. BIS was continuously monitored after intravenous injection of a single dose of propofol or thiopental, and patients were required to grasp the researcher's fingers intermittently. The results showed that although the drug concentration and duration were very inconsistent, it was consistent that consciousness began to recover when BIS increased more than 60; the BIS value below 65 indicates that the possibility of consciousness recovery within 50 seconds is not N5%. No patient who responded to the command can recall this episode. This study supports that BIS value is a good indicator to judge whether the patient's consciousness is restored. The incidence of respiratory depression and hypotension in group C was significantly higher than that in groups D1 and D2. Compared with group C, the incidence of bradycardia in groups D1 and D2 is higher, and the incidence of bradycardia in group D2 is higher than that in group D1 (see Figure 6).

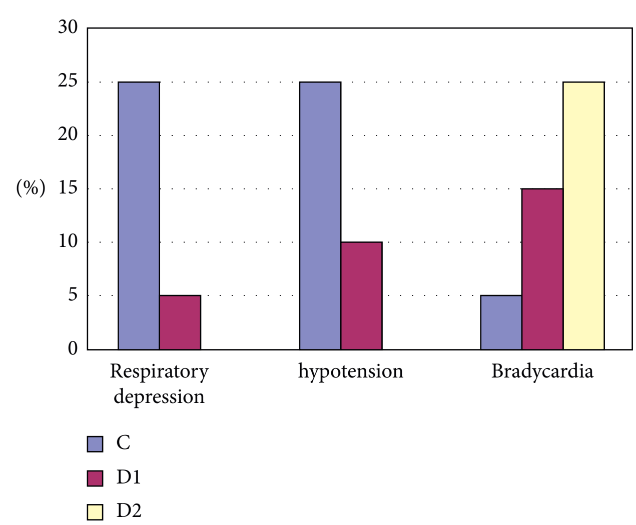

Figure 6: Comparison of adverse events of respiration and circulation among the three groups.

5. Conclusion

Anesthesiology is developing rapidly. The diversification of anesthetics, the renewal of anesthesia equipment, and the improvement of operation methods have put forward new challenges and requirements for anesthesiologists. The rationalization, refinement, and individualization of drug use have also become the common goal of anesthesiologists. Good anesthesia has several elements: sufficient sedation, reasonable analgesia, and satisfactory muscle relaxation. Among them, adequate sedation is an important premise to ensure the comfort and safety of patients and the smooth completion of surgery. Patients have a higher and higher demand for "painless," not only in routine surgery but also in some interventional radiotherapy and endoscopy. Good sedation and analgesia have also become an urgent demand for patients.

The traditional evaluation method cannot meet the needs of clinical work. Studies have shown that there is no direct correlation between changes in consciousness and hemodynamic parameters such as heart rate and blood pressure. In particular, in the case of combined medication, the changes in hemodynamics cannot accurately reflect the sedation degree of drugs. At present, many evaluation methods of sedation depth are widely used in clinics, and alert sedation score (OAA/s) is one of the commonly used methods in clinic. As a commonly used sedation depth monitoring index in clinics, the results of BIS are very useful for the judgment of sedation depth. However, it cannot be called an ideal sedation depth detection index.

This study also has some limitations. The sample size is relatively small. We are patients who choose gynecological laparoscopic surgery under certain conditions, which can eliminate the tension and anxiety caused by patients without ideological preparation. In this study, the method of single administration of carbon dioxide is adopted, so we can only see the influence of carbon dioxide on BIS value after single administration. Then, when the constant load dose of carbon dioxide is given and continuously pumped, we have not done research.

Data Availability

The datasets used during this study are available from the corresponding author on reasonable request.

Conflicts of Interest

The authors declare that there are no conflicts of interest.

Authors' Contributions

Aizhi Li and Qunhui He are contributed equally to this work.

References

[1] H. C. Lee, H. G. Ryu, Y. Park et al., "Data driven investigation of bispectral index algorithm," *Scientific Reports*, vol. 9, no. 1, pp. 13769–13778, 2019.

[2] L. Yin, J. Xu, J. Wu et al., "Effect of acute normovolemic hemodilution autologous blood transfusion on the EEG bispectral index and muscle relaxation in elderly patients undergoing orthopedic surgery," *Chinese Journal of Clinical Pharmacology and Therapeutics*, vol. 26, no. 10, Article ID 1153, 2021.

[3] J. Haesen, W. Eertmans, C. Genbrugge et al., "The validation of simplified EEG derived from the bispectral index monitor in post-cardiac arrest patients," *Resuscitation*, vol. 126, pp. 179–184, 2018.

[4] K. Ni, M. Cooter, D. K. Gupta et al., "Paradox of age: older patients receive higher age-adjusted minimum alveolar concentration fractions of volatile anaesthetics yet display higher bispectral index values," *British Journal of Anaesthesia*, vol. 123, no. 3, pp. 288–297, 2019.

[5] W. Tiefenthaler, J. Colvin, B. Steger et al., "How bispectral index compares to spectral entropy of the EEG and A-line ARX index in the same patient," *Open Medicine*, vol. 13, no. 1, pp. 583–596, 2018.

[6] Y.-H. Liu, D.-J. Qiu, L. Jia et al., "Depth of anesthesia measured by bispectral index and postoperative mortality: a meta-analysis of observational studies," *Journal of Clinical Anesthesia*, vol. 56, pp. 119–125, 2019.

[7] A. A. Dahaba, "Thinking outside the box. Off-label use of Bispectral Index within context and limitations for conditions other than depth of anesthesia," *Minerva Anestesiologica*, vol. 85, no. 2, pp. 189–193, 2018.

[8] D. Shi, C. Shen, J. Wu et al., "Evaluation of prognosis of coma patients with acute brain injury by electroencephalogram bispectral index monitoring," *Journal of Trauma Nursing*, vol. 28, no. 5, pp. 298–303, 2021.

[9] K. Hayashi and T. Sawa, "The fundamental contribution of the electromyogram to a high bispectral index: a postoperative observational study," *Journal of Clinical Monitoring and Computing*, vol. 33, no. 6, pp. 1097–1103, 2019.

[10] D. Kim, J. H. Ahn, G. Heo, and J. S. Jeong, "Comparison of Bispectral Index and Patient State Index values according to recovery from moderate neuromuscular block under steady-state total intravenous anesthesia," *Scientific Reports*, vol. 11, no. 1, pp. 5908–5917, 2021.

[11] S. Avci, B. Bayram, G. Inanç et al., "Evaluation of the compliance between EEG monitoring (Bispectral IndexTM) and Ramsey Sedation Scale to measure the depth of sedation in the patients who underwent procedural sedation and analgesia in the emergency department," *Ulusal travma ve acil cerrahi dergisi*, vol. 25, no. 5, pp. 447–452, 2019.

[12] A. A. Dahaba, H. Lin, X. F. Ye et al., "Propofol-bispectral index (BIS) electroencephalography (EEG) pharmacokinetic-pharmacodynamic model in patients with post-cerebral hemorrhage hydrocephalus," *Clinical EEG and Neuroscience*, vol. 52, no. 5, pp. 351–359, 2021.

[13] A. L. Ferreira, J. G. Mendes, C. S. Nunes, and P. Amorim, "Evaluation of Bispectral Index time delay in response to anesthesia induction: an observational study," *Brazilian Journal of Anesthesiology (English Edition)*, vol. 69, no. 4, pp. 377–382, 2019.

[14] T. W. Schnider, C. F. Minto, T. D. Egan, and M. Filipovic, "Relationship between propofol target concentrations, bispectral index, and patient covariates during anesthesia," *Anesthesia & Analgesia*, vol. 132, no. 3, pp. 735–742, 2021.

[15] M. Sargin, M. S. Uluer, and B. Şimşek, "The effect of bispectral index monitoring on cognitive performance following sedation for outpatient colonoscopy: a randomized controlled

Hindawi
Journal of Healthcare Engineering
Volume 2023, Article ID 9835702, 1 page
https://doi.org/10.1155/2023/9835702

Retraction

Retracted: Role of miR-181b/Notch1 Axis in circ_TNPO1 Promotion of Proliferation and Migration of Atherosclerotic Vascular Smooth Muscle Cells

Journal of Healthcare Engineering

Received 26 September 2023; Accepted 26 September 2023; Published 27 September 2023

This article has been retracted by Hindawi following an investigation undertaken by the publisher [1]. This investigation has uncovered evidence of one or more of the following indicators of systematic manipulation of the publication process:

(1) Discrepancies in scope
(2) Discrepancies in the description of the research reported
(3) Discrepancies between the availability of data and the research described
(4) Inappropriate citations
(5) Incoherent, meaningless and/or irrelevant content included in the article
(6) Peer-review manipulation

The presence of these indicators undermines our confidence in the integrity of the article's content and we cannot, therefore, vouch for its reliability. Please note that this notice is intended solely to alert readers that the content of this article is unreliable. We have not investigated whether authors were aware of or involved in the systematic manipulation of the publication process.

In addition, our investigation has also shown that one or more of the following human-subject reporting requirements has not been met in this article: ethical approval by an Institutional Review Board (IRB) committee or equivalent, patient/participant consent to participate, and/or agreement to publish patient/participant details (where relevant).

Wiley and Hindawi regrets that the usual quality checks did not identify these issues before publication and have since put additional measures in place to safeguard research integrity.

We wish to credit our own Research Integrity and Research Publishing teams and anonymous and named external researchers and research integrity experts for contributing to this investigation.

The corresponding author, as the representative of all authors, has been given the opportunity to register their agreement or disagreement to this retraction. We have kept a record of any response received.

References

[1] M. Chen, F. Li, Q. Jiang, W. Zhang, Z. Li, and W. Tang, "Role of miR-181b/Notch1 Axis in circ_TNPO1 Promotion of Proliferation and Migration of Atherosclerotic Vascular Smooth Muscle Cells," *Journal of Healthcare Engineering*, vol. 2022, Article ID 4086935, 12 pages, 2022.

Hindawi
Journal of Healthcare Engineering
Volume 2022, Article ID 4086935, 12 pages
https://doi.org/10.1155/2022/4086935

Research Article

Role of miR-181b/Notch1 Axis in circ_TNPO1 Promotion of Proliferation and Migration of Atherosclerotic Vascular Smooth Muscle Cells

Mingxiang Chen, Fuping Li, Qilong Jiang, WeiMin Zhang, Zhiping Li, and Wenshuai Tang

Department of Cardiovascular Surgery, The Third Affiliated Hospital Of Chongqing Medical University, Chongqing, China

Correspondence should be addressed to Wenshuai Tang; 651094@hospital.cqmu.edu.cn

Received 11 February 2022; Revised 19 February 2022; Accepted 4 March 2022; Published 27 March 2022

Academic Editor: Liaqat Ali

Background. The role and expression level change in circ_TNPO1 (hsa_circ_0072951) in atherosclerosis (AS) and VSMC dysfunction remain unknown. In this study, we try to explore the effects of circ_TNPO1 on oxidized low-density lipoprotein (ox-LDL)-induced human vascular smooth muscle cell (VSMC) excessive proliferation and migration, and the potential molecular mechanism. *Methods*. Quantitative real-time polymerase chain reaction (RT-qPCR) and western blot experiment were used to detect the serum samples from AS patients and healthy controls. CCK-8, Transwell, and the dual-luciferase reporter gene assay were used to detect the cell biology. *Results*. In human AS serum and ox-LDL-induced VSMCs, circ_TNPO1 was increased, whereas miR-181b was decreased. Silencing circ_TNPO1 inhibited proliferation and migration activity and reduced protein expression of PCNA, Ki-67, MMP2, and E-cadherin and promoted N-cadherin protein expression in ox-LDL induced VSMCs. Remarkably, miR-181b knockdown or Notch1 overexpression could efficiently offset the proliferation and migration inhibiting effect of circ_TNPO1 knockdown in ox-LDL-induced VSMCs. Furthermore, a molecular mechanism study pointed out that circ_TNPO1 and Notch1 are direct-acting targets of miR-181b. *Conclusions*. In conclusion, our study indicated that circ_TNPO1 promotes the proliferation and migration progression of VSMCs in atherosclerosis through the miR-181b/Notch1 axis.

1. Introduction

In recent years, the incidence of atherosclerosis (AS) had an increasing trend worldwide year by year [1]. Atherosclerotic plaque rupture following a lead to acute thrombosis is an important cause of cerebral infarction and acute myocardial infarction [2]. Numerous studies have pointed out that the proliferation, invasion, and migration of VSMCs originating from the middle arterial layer are playing a significant role in the pathological processes of atherosclerotic plaque formation [3, 4]. In normal arteries, VSMCs regulate the contraction of arteries and modulate the synthesis of the extracellular matrix. In AS, VSMCs migrate from the media layer to the intima and switch from a "contractile" phenotype to an activated "synthetic" phenotype. Synthetic VSMCs generally demonstrate enhanced viability in cell proliferation and migration and could exacerbate inflammatory response and intimal calcification, ultimately promoting the process of atherosclerosis [5, 6]. The abnormal proliferation and migration of VSMCs are critical events of atherosclerosis. Thus, it is extremely important to investigate the molecular mechanisms of excessive proliferation and migration of VSMCs to treat and prevent AS.

Circular RNAs (circRNAs) are a class of noncoding RNAs characterized by covalently linked 5' and 3′ ends with a closed circular structure. Current studies point out that some upstream regulators of circRNA biogenesis or stability have been studied already before the rediscovery of circRNAs in the context of AS [7, 8]. circRNA plays an indirect role in regulating mRNA translation. mRNA translation contains miRNA response elements and acts as a miRNA sponge to inhibit miRNA-mediated repression of target mRNA , thus regulating the pathologic process of AS [9]. circRNAs are the latest focus of atherosclerotic pathology and are involved in regulating the proliferation and migration process of VSMCs. However, the key circRNAs regulating the proliferation and migration process of VSMCs cells and their precise mechanism remain unclear. circ_TNPO1 (hsa_circ_0072951) is located on chromosome 5. No research has yet been reported on the regulatory effect of circ_TNPO1 in AS and the dysfunction of VSMCs. In this study, we investigated the expression level variation of circ_TNPO1 in the serum of AS patients and correlations between circ_TNPO1 and VSMC dysfunction.

MicroRNA (miRNA) is an important post-transcriptional level regulator, which can bind to the $3'$ untranslated region ($3'$-UTR) of mRNA, leading to translation inhibition or degradation of mRNA. Recent studies have pointed out that the decreased expression level of miR-181b may be an important cause of AS plaque formation and vascular endothelial injury [10, 11]. The reason for reduced expression levels of miR-181b in AS is not known. Prior studies have suggested that miR-181b exerted these biological effects by directly repressing Notch1. The Notch1 proteins are evolutionarily conserved transmembrane receptor proteins that are widely distributed in a variety of tissue [12]. Recent research indicated that Notch1 signaling is significantly activated in AS plaques, and overexpression of Notch1 can promote proliferation, migration, survival, and extracellular matrix synthesis of VSMCs [13–15].

In this study, we investigated the expression level variation of circ_TNPO1 in the serum of AS patients and correlations between circ_TNPO1 and VSMCs dysfunction and to verify whether it exerts its biological effects by targeting the miR-181b/Notch1 axis.

2. Methods

2.1. Serum Samples. The 37 patients with AS were included from the clinic and inpatient department of The Third Affiliated Hospital of Chongqing Medical University between June 2019 and June 2020. Written informed consent was obtained from all patients before collecting their serum samples. Additionally, 40 serum samples from healthy individuals were collected during the same period as the control group. For all patients, 5 ml of morning fasting venous blood was collected and centrifuged at 4,000 r/min for 10 min, and the separated serum was stored in a refrigerator at -80°C.

2.2. circRNA Sequence. circRNA sequences were conducted as in the literature [10]. The sequencing experiments were performed by Shanghai Yuansong Biotechnology Co., Ltd.

2.3. RT-qPCR Experiment. Serum samples from AS patients and healthy controls were collected. Then, total RNA was extracted from serum samples using TRIzol reagent (TRIzol reagent, Sigma-Aldrich, St. Louis, Missouri). Total RNA was precipitated with isopropanol and then dissolved with DEPC-H2 (General Biotech). cDNA was synthesized by M-MLV-reverse transferase using an RT-PCR kit (Promega) according to the kit instructions. qPCR amplification was performed using ABI 7300 real-time PCR system (Applied Biosystems) using 2X Power SYBR-Green PCR Master Mix (Applied Biosystems) according to the kit instructions (Table 1). The relative expression of mRNA was determined by the relative standard curve method ($2^{-\Delta\Delta Ct}$) using GAPDH as an internal reference.

2.4. Western Blot Experiment. The protein samples were prepared and stored at -80°C. After denaturation, the proteins were separated by 10% SDS-PAGE gel electrophoresis. Then, the proteins were transferred to the PVDF membrane (Millipore, USA) by the wet transfer method. Subsequently, PVDF membrane was incubated with 5% skimmed milk powder for 2 h, washed three times with TBST, incubated overnight at 4°C with primary antibody, incubated for 1h at room temperature with secondary antibody, washed four times with TBST, and detected by Odyssey two-color infrared fluorescence imaging system (LI-COR Company, USA). The immunoreactive bands on the membrane were detected using the Odyssey two-color IR imaging system.

2.5. Cell Culture. Human VSMCs (ScienCell, no. 6,110) were cultured in a DMEM medium (GIBCO, USA) containing 10% fetal bovine serum (GIBCO, USA) at 37°C in a humidified incubator with 5% CO_2. When cell density grew to 80%, the supernatant was discarded and the digestion proceeded with 0.25% trypsin-EDTA for cell passages. The ox-LDL-induced AS model was conducted as shown in the literature and is briefly described here as follows. VSMCs of the experimental group were treated with 30, 60, 90, or 120 μg/mL ox-LDL for 24 h, while VSMCs of the control group with the same volume of solution without ox-LDL.

2.6. CCK-8 Assay. After transfection, cells in each group were cultured for 48 h, then, 10 μL CCK-8 reagent (Dojindo, Japan) was added into each well, and the absorbance at 570 nm was measured by microplate reader after 2-h incubation.

2.7. Transwell Assay. After transfection, cells in each group were collected. Then, 1×10^5 cells suspended in 200 μl serum-free DMEM media were inoculated into the upper layer of Transwell (Corning, USA) for 24 h. After the VSMCs had been cultured for 24 h, the upper layer of cells was gently wiped off with a cotton swab, subsequently, were washed with PBS, fixed with 4% paraformaldehyde for 30 min, and then stained with 0.1% crystal violet (Nakaraitesk, Kyoto, Japan) for 10 min. Finally, 3 fields of view were randomly selected under an inverted microscope for photographing and counting. The experiment was repeated 3 times.

Table 1: The primers of RT-qPCR.

Name	Sequence (5′-3′)
circ_TNPO1	AGCTGCTGAATTTTAAAGAGAGT
	AGGCTCCCTTATAGTCTCCA
miR-181b	ACACTCCAGCTGGGAACATTCATTGCTGTCGG
	TGGTGTCGTGGAGTCG
Notch1	GGTGAACTGCTCTGAGGAGATC
	GGATTGCAGTCGTCCACGTTGA

2.8. Dual-Luciferase Reporter Gene Assay. The wild sequence or mutant sequence of Notch1 (3′-UTR) and circ_TNPO1 containing miR-181b binding site was cloned into the psi-CHECK plasmid to construct dual-luciferase reporter plasmids. Afterward, miR-181b mimic or miR-NC (GenePharma, China) was cotransfected with WT or MUT plasmids into VSMCs, respectively. Cells were collected 48 h after transfection, and luciferase activity was detected using a dual-luciferase reporter gene assay kit (Promega, USA).

2.9. Cell Transfection. The VSMCs were seeded in a T-25 cm^2 flask and related si-RNAs, and pcDNA plasmid was transfected with Lipofectamine 3000 (Invitrogen, USA) after reaching a density of 50%–60% confluence. These si-RNA and pcDNA plasmids included si-circ_TNPO1, miR-181b mimic, miR-181b inhibitor, pcDNA plasmid (Notch1), and the negative controls (si-NC, miR-NC, and empty pcDNA plasmid). The sequence of oligonucleotides is depicted below as follows: si-circ_TNPO1, 5′-AAGTTGTTTAACTATAGTCCTTC-3′; si-NC, 5′-GCAAGCTGACCCTGAAGTT-3′; miR-181b mimic, 5′-AACAUUCAUUGCUGUCGGUGGGU-3′; miR-181b inhibitor, 5′–ACCCACCGACAGCAAUGAAUGUU–3′; miR-NC, 5′-GCUUCAUACGUGGACUAAUCU-3′; miR-inhibitor NC, 5′-CAGCACUCAUGUAUGGUACGG-3′.

2.10. Statistical Analysis. SPSS 17.0 statistical software was used for statistical analysis. Quantitative data were expressed as mean ± standard deviation (mean ± SD). The t-test was used for comparison between two groups, and $P < 0.05$ was considered a statistically significant difference.

3. Results

3.1. Expression Level of circ_TNPO1 Was Increased in AS Patients' Serum and Ox-LDL-Treated VSMCs. By circular RNA sequence method, overall 33 circRNAs were significantly differentially expressed with the screening criteria: $P < 0.05$, fold change>2.0, or fold change < −2.0. Among them, circ_TNPO1 was the most significantly upregulated circRNA, as shown in Figure 1(a). Subsequently, an RT-qPCR assay was performed to validate the reliability of the results of the circRNA sequencing experiment. Consistent with the result of circRNA sequence, RT-qPCR assay pointed out that the expression of circ_TNPO1 was significantly increased in the serum of AS patients compared with the control group, as shown in Figure 1(b).

A large number of research indicated that ox-LDL is a potential inducer of VSMC dysfunction in AS. Thus, we treated VSMCs with different doses of ox-LDL. These results indicated that, *in vitro* level, ox-LDL promoted the expression of circ_TNPO1 in a dose-dependent manner. In summary, our study suggests that circ_TNPO1 expression is significantly increased in the serum of AS patients and ox-LDL-treated VSMC and may be a key pathogenic determinant of AS.

3.2. The Knockdown of circ_TNPO1 Inhibited Proliferation and Migration Progression of Ox-LDL-Induced VSMCs. To investigate the functional role of circ_TNPO1 in ox-LDL-induced proliferation and migration of VSMCs, we applied si-RNA transfection to artificially knockdown circ_TNPO1 expression level in VSMCs. RT-qPCR identified that the expression level of circ_TNPO1 was significantly reduced in VSMCs transfected with si-circ_TNPO1, as shown in Figure 2(a). Subsequently, loss function experiments were performed in ox-LDL-treated VSMCs. CCK-8 assay revealed that the si-circ_TNPO1 treatment dramatically attenuates proliferation activity of ox-LDL-treated VSMCs at 24 h, as shown in Figure 2(b). Moreover, si-circ_TNPO1 treatment dramatically reduced Ki-67 and PCNA protein expression levels in ox-LDL-treated VSMCs, which was consistent with the results of the CCK-8 assay, as shown in Figure 2(d). Transwell assay indicated that the number of migrating VSMCs in the si-circ_TNPO1-treated group was significantly lower compared with the si-NC-treated group, as shown in Figure 2(c). Consistent with the results of the Transwell assay, Western blot analysis also indicated that si-circ_TNPO1 treatment dramatically reduced MMP2 and N-cadherin protein expression level, while the expression levels of E-cadherin proteins were significantly promoted, as shown in Figure 2(d). In summary, our study suggests that knockdown of circ_TNPO1 could significantly inhibit ox-LDL-induced proliferation and migration of VSMCs.

3.3. miR-181b Directly Interacted with circ_TNPO1 in VSMCs. Previous studies have shown that the knockdown of circ_TNPO1 inhibited proliferation and migration progression of ox-LDL-induced VSMCs. To further explore the molecular mechanism of circ_TNPO1, we predicted the potential targets of circ_TNPO1 based on the TargetScan database. The results showed that circ_TNPO1 has a miR-181b binding site, as shown in Figure 3(a). Pearson's correlation coefficient analysis showed that circ_TNPO1 was negatively correlated with miR-181b, as shown in Figure 3(b). RT-qPCR assay pointed out that the expression of miR-181b was significantly decreased in the serum of AS patients compared with the control group, as shown in Figure 3(c).

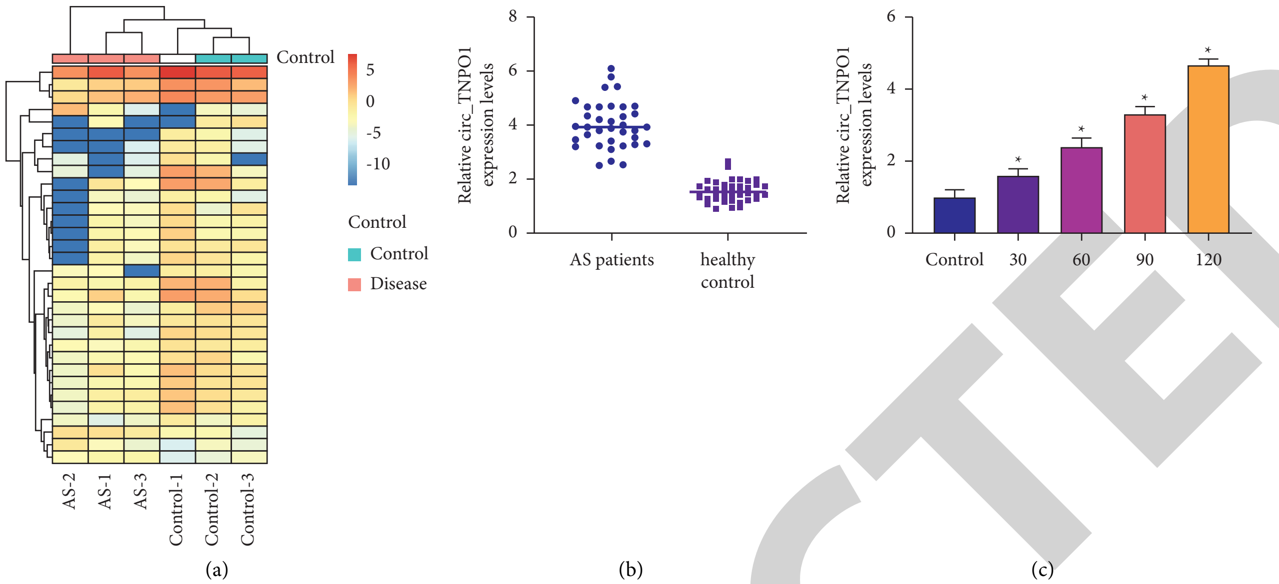

Figure 1: circ_TNPO1 expression was significantly increased in serum of AS patients and ox-LDL-treated VSMCs. (a) A heat map with hierarchical clustering of 33 differentially expressed circRNAs between AS serum and healthy controls serum. (b) Relative circ_TNPO1 expression levels in AS sample and control sample were determined by RT-qPCR. (c) The expression level of circ_TNPO1 in VSMCs treated by different doses of ox-LDL was detected by RT-qPCR. $^*P < 0.05$.

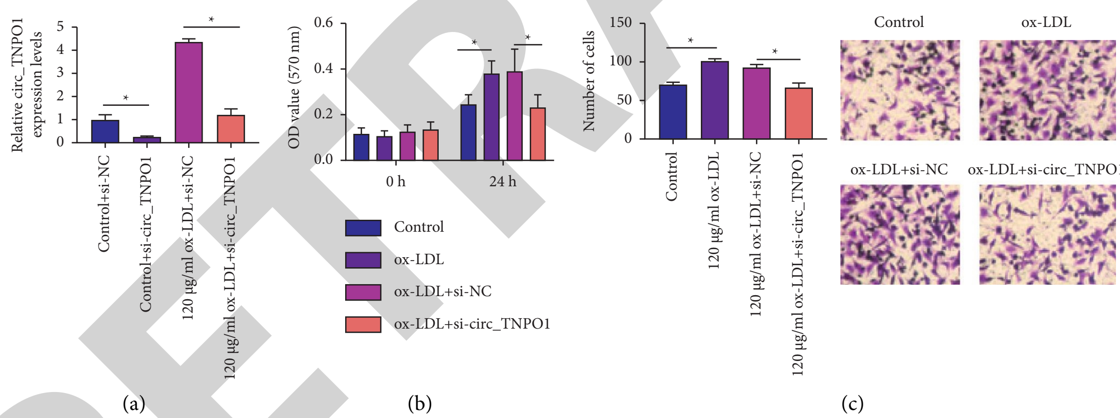

Figure 2: Continued.

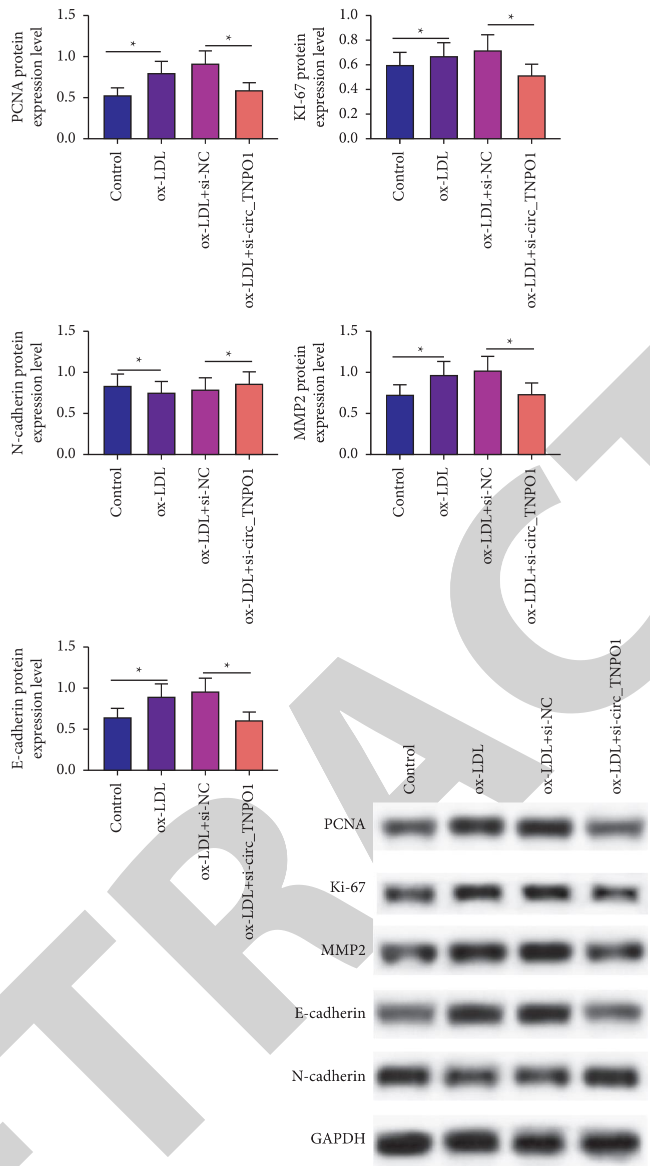

(d)

Figure 2: The knockdown of circ_TNPO1 inhibited proliferation and migration progression of ox-LDL-induced VSMCs. (a) Relative expression levels of circ_TNPO1 were measured in VSMCs transfected with si-circ_TNPO1 or si-NC by RT-qPCR assay. (b) CCK-8 assay monitored proliferation activity of VSMCs after cotreatment with si-circ_TNPO1 or si-NC and ox-LDL. (c) Transwell assay monitored migration activity of VSMCs after cotreatment with si-circ_TNPO1 or si-NC and ox-LDL. (d) Western blot assay detected the protein expression levels of Ki67, PCNA, MMP2, E-cadherin, and N-cadherin in VSMCs after cotreatment with si-circ_TNPO1 or si-NC under ox-LDL stress. $^{*}P < 0.05$.

Finally, a dual-luciferase reporter assay was used to verify the direct interaction between circ_TNPO1 and miR-181b. The results showed that miR-181b mimic cotransfected with WT plasmid was able to significantly reduce luciferase activity in VSMCs. However, miR-181b mimics cotransfected with MUT plasmid did not reduce luciferase activity in VSMCs, as shown in Figure 3(d). These outcomes illuminated that circ_TNPO1 may exert its biological function by targeting miR-181b.

3.4. The Blockage of miR-181b Counteracted Proliferation and Migration Suppressing Effects of circ_TNPO1 Knockdown in Ox-LDL-Induced VSMCs. Our studies have shown that miR-181b is a direct target of circ_TNPO1, and si-circ_TNPO1 treatment dramatically promotes the expression level of miR-181b in VSMCs, yet whether circ_TNPO1 exerts its biological effects by targeting miR-181b is not directly verified. To further prove whether the proliferation and migration suppressing effects of circ_TNPO1 knockdown rely on overexpression of miR-181b, we carried out a rescue experiment.

RT-qPCR assay indicated that miR-181b inhibitor transfection can significantly suppress the expression level of miR-181b , as shown in Figure 4(a). Rescue experiment

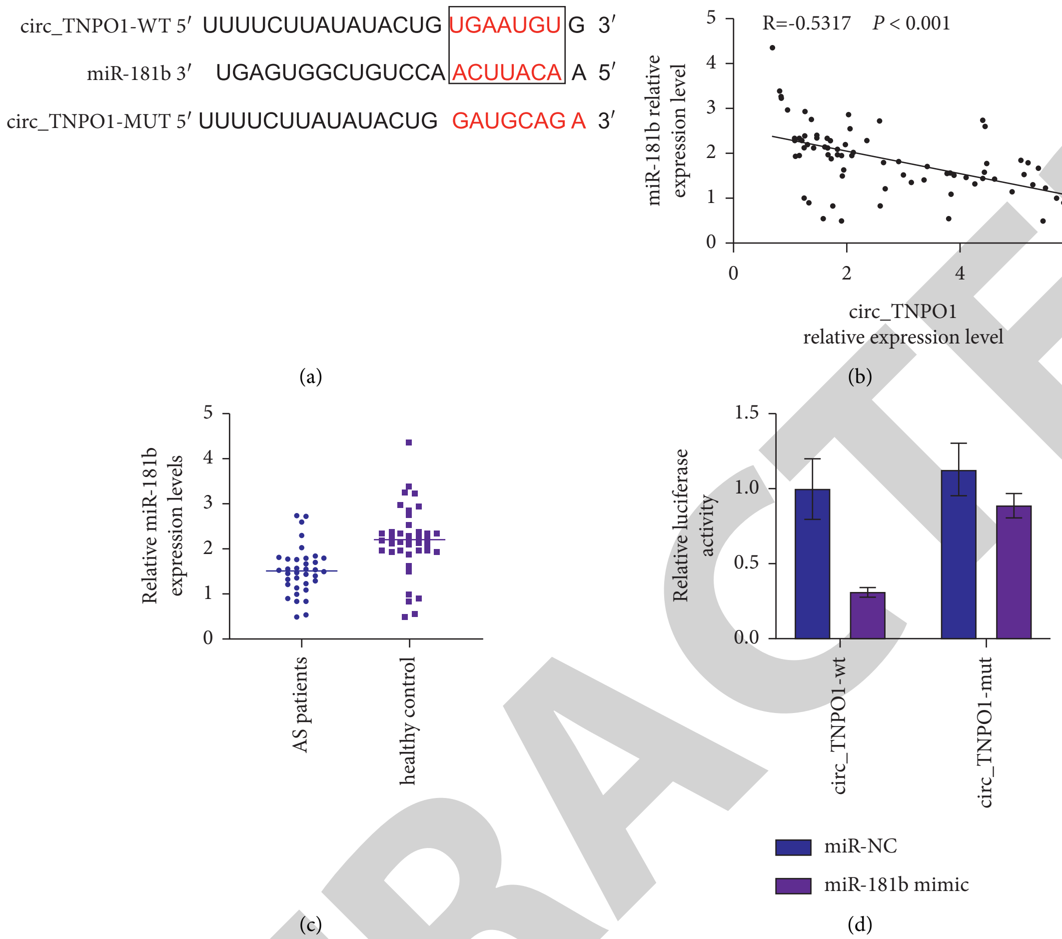

FIGURE 3: miR-181b directly interacted with circ_TNPO1 in VSMCs. (a) TargetScan database predicts the binding sequence between circ_TNPO1 and miR-181b. (b) Pearson's correlation coefficient determined the correlations between circ_TNPO1 and miR-181b in AS patients' serum. (c) Relative expression levels of miR-181b were measured in AS patients' serum and control healthy serum. (d) Dual-luciferase reporter assay determined the direct interaction of circ_TNPO1 with miR-181b in VSMCs. $^*P < 0.05$.

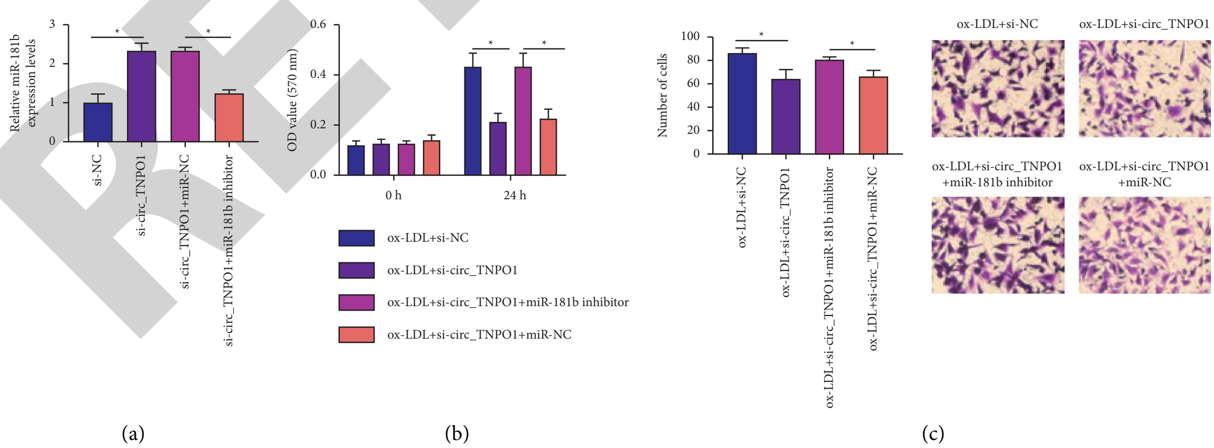

FIGURE 4: Continued.

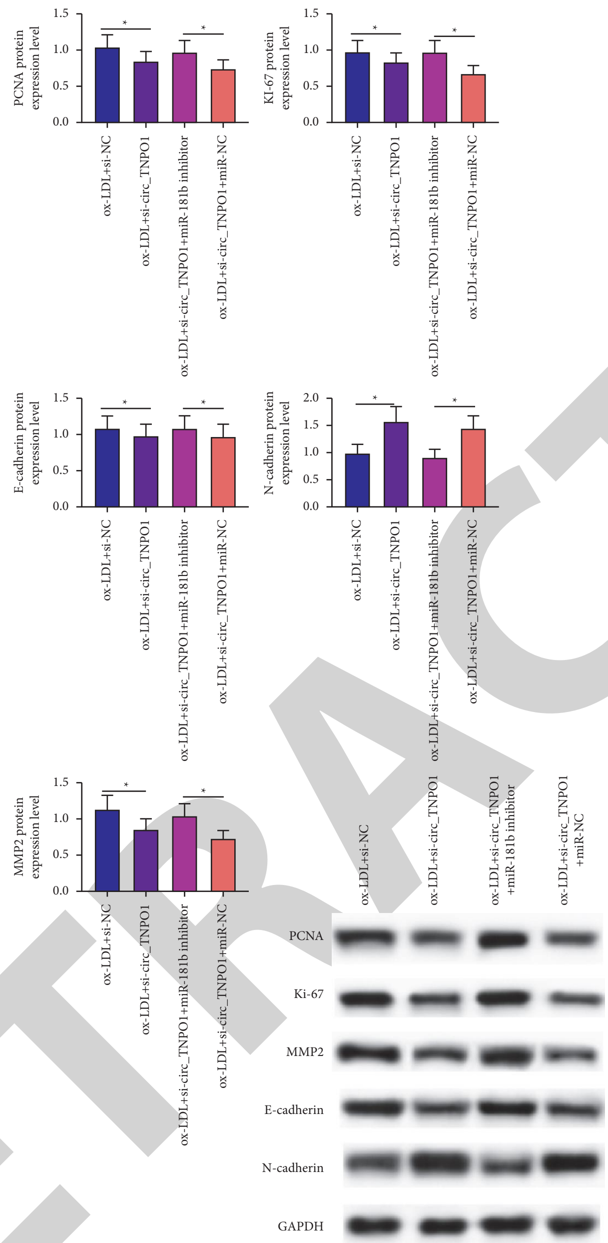

(d)

Figure 4: The blockage of miR-181b counteracted proliferation and migration suppressing effects of circ_TNPO1 knockdown in ox-LDL-induced VSMCs. (a) Relative expression levels of miR-181b were measured in VSMCs transfected with si-circ_TNPO1 alone, si-NC alone, or together with miR-181b inhibitor or miR-NC. (b) CCK-8 assay monitored proliferation activity of VSMCs transfected with si-circ_TNPO1 alone, si-NC alone, or together with miR-181b inhibitor or miR-NC under ox-LDL stress. (c) Transwell assay detected the migration activity of VSMCs transfected with si-circ_TNPO1 alone, si-NC alone, or together with miR-181b inhibitor or miR-NC under ox-LDL stress. (d) Western blot assay detected the protein expression levels of Ki67, PCNA, MMP2, E-cadherin, and N-cadherin in VSMCs transfected with si-circ_TNPO1 alone, si-NC, or together with miR-181b inhibitor or miR-NC under ox-LDL stress. $^*P < 0.05$.

Notch1-WT 5' UAUUUUACACAGAA ACACUGCC U 3'

miR-181b 3' UGGUCGAUUGUUA UGUGACGG U 5'

Notch1-MUT 5' UAUUUUACACAGAA GAUGCAGU U 3'

(a)

Figure 5: Continued.

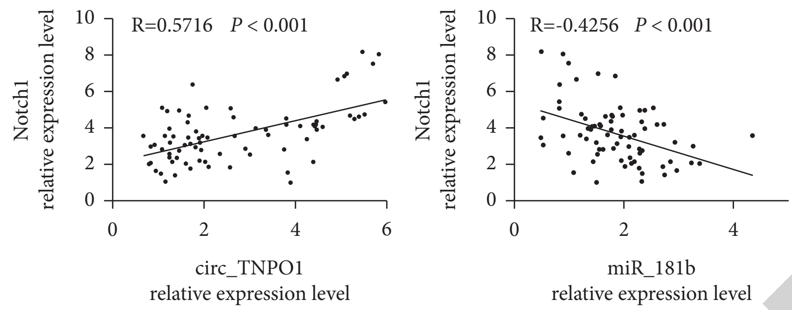

(b)

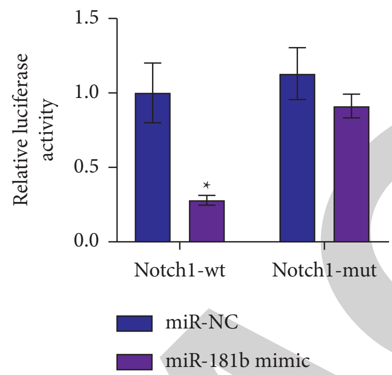

(c)

(d)

FIGURE 5: miR-181b directly interacted with Notch1 in VSMCs. (a) TargetScan database predicts the binding sequence between Notch1 and miR-181b. (b) Pearson's correlation coefficient determined the correlations between Notch1 and circ_TNPO1 or miR-181b in AS patients' serum. (c) Dual-luciferase reporter assay determined the direct interaction of Notch1 with miR-181b in VSMCs. $^*P < 0.05$. (d) Effects of miR-181b mimic and miR-181b inhibitor on Notch1 protein expression levels in VSMCs.

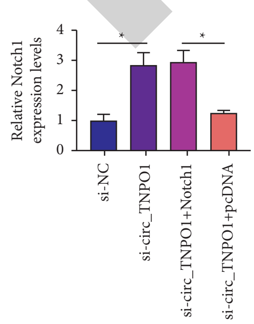

(a)

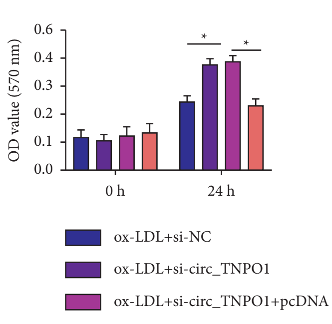

(b)

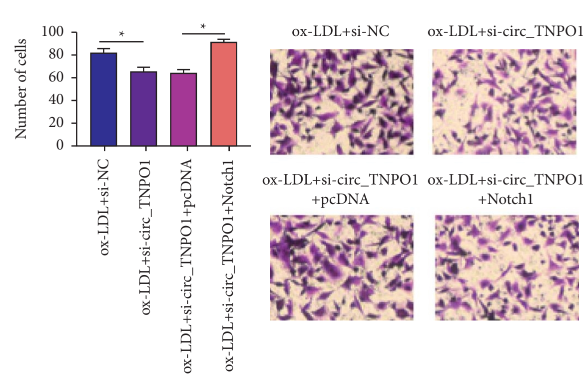

(c)

FIGURE 6: Continued.

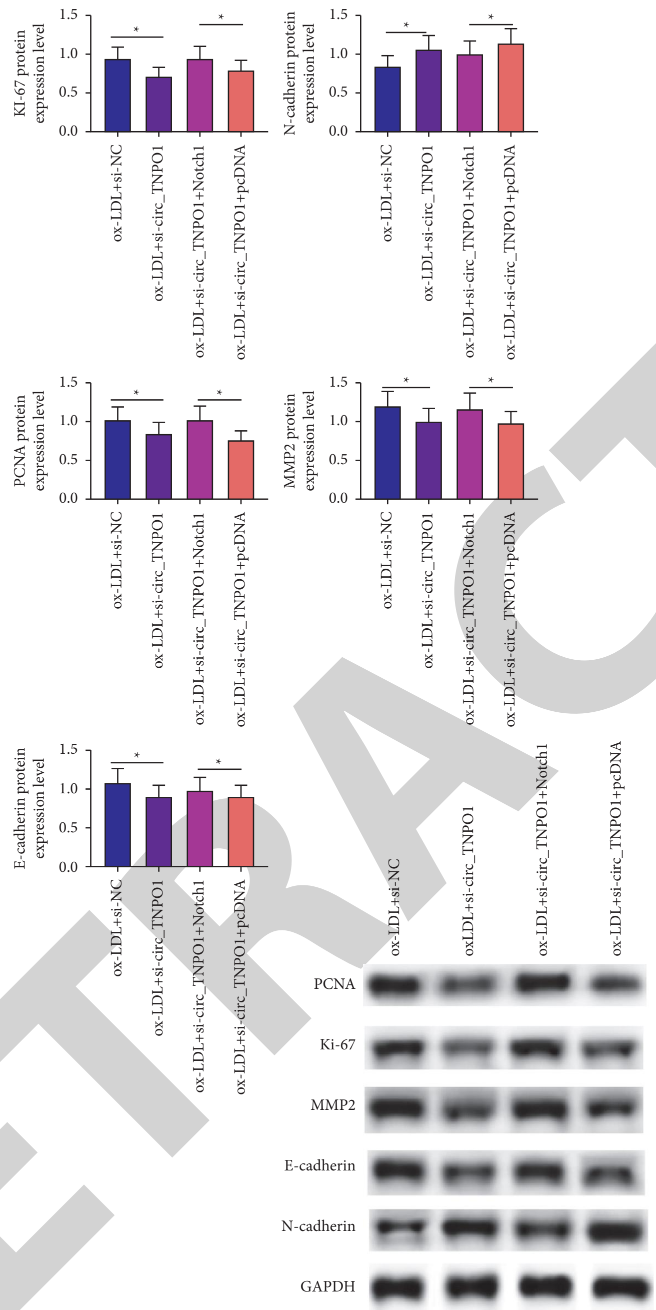

(d)

Figure 6: Overexpression of Notch1 counteracted inhibition effects of proliferation and migration of circ_TNPO1 knockdown in ox-LDL-induced human VSMCs. (a) RT-qPCR assay determined Notch1 mRNA expression level in VSMCs transfected with si-NC, or si-circ_TNPO1, or si-circ_TNPO1 along with pcDNA plasmid or si-circ_TNPO1 along with pcDNA-Notch1 plasmid. (b) The effect of Notch1 overexpression on the proliferative activity of ox-LDL-induced VSMCs transfected with si-circ_TNPO1 was determined by the CCK-8 assay. (c) The effect of Notch1 overexpression on the migrating activity of ox-LDL-induced VSMCs transfected with si-circ_TNPO1 was determined by Transwell assay. (d) The effect of Notch1 overexpression on protein expression of Ki67, PCNA, MMP2, E-cadherin, and N-cadherin in ox-LDL-induced VSMCs transfected with si-circ_TNPO1 was determined by Western blot assay. $^{*}P < 0.05$.

indicated that miR-181b inhibitor transfection can significantly facilitate the activity of proliferation and migration in VSMCs with circ_TNPO1 depletion under ox-LDL stress , as shown in Figures 4(b) and 4(c). Subsequently, consistent with the results of CCK-8 assay and Transwell assay, Western blot analysis also indicated that miR-181b inhibitor transfection can significantly promote protein expression level of Ki-67, PCNA, MMP2, and E-cadherin while inhibiting protein expression level of N-cadherin in VSMCs with circ_TNPO1 depletion under ox-LDL stress, as shown in Figure 4(d). These outcomes indicated that the blockage of miR-181b counteracted proliferation and migration suppressing effects of circ_TNPO1 knockdown in ox-LDL-induced VSMCs.

3.5. miR-181b Directly Interacted with Notch1 in VSMCs. It has been shown that miR-181b has a direct interaction with Notch1 in other cell lines. In this study, we predicted the potential targets of miR-181b based on the TargetScan database. The results showed that miR-181b had binding sites with Notch1, as shown in Figure 5(a). Pearson's correlation coefficient analysis showed that miR-181b was negatively correlated with Notch1, while Notch1 was positively correlated with circ_TNPO1, as shown in Figure 5(b). Moreover, RT-qPCR assay indicated that the expression level of Notch1 was dramatically increased in ox-LDL-induced VSMCs and VSMCs transfected with si-circ_TNPO1, as shown in Figure 5(c). Subsequently, RT-qPCR assay indicated that miR-181b inhibitor can dramatically promote mRNA and protein expression levels of Notch1. All these findings suggest that Notch1 may be a direct target of miR-181b. Finally, a dual-luciferase reporter assay was used to verify the direct interaction between Notch1 and miR-181b. Dual-luciferase reporter assay showed that miR-181b mimic cotransfected with Notch1 WT plasmid was able to significantly reduce luciferase activity in VSMCs. However, miR-181b mimic cotransfected with Notch1 MUT plasmid did not inhibit luciferase activity, as shown in Figure 5(d). These outcomes illuminated that miR-181b directly interacted with Notch1 in VSMCs.

3.6. Overexpression of Notch1 Counteracted Inhibition Effects of Proliferation and Migration of circ_TNPO1 Knockdown in Ox-LDL-Induced Human VSMCs. Notch1 has been well demonstrated to promote cell proliferation and migration in a variety of cell lines. Previous studies have well demonstrated that circ_TNPO1 may promote Notch1 expression by targeting miR-181b in ox-LDL-treated VSMCs; however, whether circ_TNPO1 exerts its pro-proliferative and migratory effects on VSMCs through overexpression of Notch1 is unclear. The overexpression experiment indicated that Notch1 overexpression can restore the content of Notch1 in VSMCs transfected with si-circ_TNPO1, as shown in Figures 6(a) and 6(b). In addition, CCK-8 and Transwell assay indicated that restoring Notch1 expression also can augment the activity of proliferation and migration in VSMCs with circ_TNPO1 depletion under ox-LDL stress, as shown in Figures 6(c) and 6(d). Subsequently, Western blot analysis also indicated that si-circ_TNPO1 lowered protein expression of Ki-67, PCNA, MMP2, and E-cadherin and enhanced protein expression of N-cadherin in ox-LDL-induced VSMCs, which was rescued by Notch1 overexpression plasmid, as shown in Figure 6(e). These outcomes indicated that overexpression of Notch1 counteracted inhibition effects of proliferation and migration of circ_TNPO1 knockdown in ox-LDL-induced human VSMCs.

4. Discussion

circRNAs are endogenous noncoding RNAs, which are a hot topic of current research. Currently, with the continuous progress of detection technology, more and more circRNAs are discovered and their mechanisms of action are gradually revealed. A large number of studies have shown that circRNAs can play an important role in the development and progression of VSMC dysfunction and AS by acting as molecular sponges for miRNAs and exerting ceRNA mechanisms to indirectly regulate the expression of target genes. For example, Ding [16] et al. showed that in ox-LDL-induced VSMCs, circ_0010283 promoted the proliferation and migration of VSMCs through the miR-370-3p/HMGB1 axis. Wang et al. [17] showed that circ_CHFR was able to promote the proliferation, invasion, and migration of VSMCs through the miR-149-5p/NRP2 axis under the induction of PDGF-BB. VSMCs are the major cellular components of arteries, a special class of multiphenotypic and multifunctional cellular taxa. When the blood vessels are stimulated by pathological factors, multiple signaling pathways on VSMCs are activated and the number of "synthetic" phenotypes of VSMCs gradually increases. While synthetic VSMCs have the functions of secretion, migration, and proliferation, the excessive proliferation and migration of VSMCs are the pathophysiological basis of atherosclerosis and vascular stenosis diseases [18, 19].

circRNAs can be used as early predictors of AS development and provide more effective biomarkers for the diagnosis and treatment of AS [20]. However, the expression of profile regulatory mechanisms of most circRNAs in the pathological process of AS remains poorly known. No study has been conducted to investigate the effect of circ_TNPO1 on the proliferation and migration of VSMCs and potential mechanisms. In this study, circRNA sequencing technology was used to detect the differentially expressed circRNAs between the AS patients' serum and healthy controls, and from them, we found that circ_TNPO1 expression levels were significantly increased in the serum of AS patients. Subsequent RT-qPCR results further indicated that circ_TNPO1 expression was significantly increased in ox-LDL-treated VSMCs and the serum of AS patients. Subsequently, the function studies indicated that knockdown of circ_TNPO1 significantly inhibited proliferation and migration progression of ox-LDL-induced VSMCs. Subsequently, a molecular mechanism study indicated that, under ox-LDL stress, circ_TNPO1 could indirectly regulate the expression level of Notch1 by targeting miR-181, thus promoting the proliferation and migration progression of VSMCs.

In this study, the results of the RT-qPCR assay pointed out that expression levels of miR-181b were significantly downregulated in the serum of AS patients. Consistent with our findings, the results of Li and Cao and Zhong et al. [21, 22] pointed out that expression levels of miR-181b were significantly reduced in the serum of patients with atherosclerosis. In addition, our study also demonstrated that miR-181b expression levels were also significantly downregulated in ox-LDL-treated VSMCs, which is consistent with the previous findings [23].

Subsequently, the dual-luciferase reporter assay indicated that miR-181b directly interacted with circ_TNPO1 in VSMCs. Regarding the effect of miR-181b on the proliferation and migration of VSMCs, our results pointed out that miR-181b knockdown significantly promoted abilities of proliferation and migration of ox-LDL induced VSMCs transfected with si-circ_TNPO1 and promoted Ki67, PCNA, MMP2, and E-cadherin protein expressions. Consistent with our findings, the results of Ghasempour et al. [23] indicated that miR-181b was able to inhibit the proliferation and migration of VSMCs by regulating the β-ARR2/p-ERK1/2 signaling pathway. Also, the results of Ghasempour et al. [24] indicated that miR-181b could inhibit the proliferation and migration of VSMCs by targeting HCK, and in addition, the results of Zhong et al. [21] indicated that miR-181b could inhibit cell proliferation by targeting STAT3 in an ox-LDL-induced AS cell model and inhibiting cell cycle to promote apoptosis. Taken together, miR-181b may provide a new therapeutic target for alleviating the disease process of AS.

In our study, further molecular mechanism study indicated that miR-181b directly binds to the 3′-UTR of Notch1 mRNA and thus inhibits Notch1 expression on mRNA and protein level in VSMCs. Currently, the interactive relationship between miR-181b and Notch1 has been widely reported in a variety of cell lines. In addition, our results showed that Notch1 expression levels were increased in serum samples from AS patients and showed a trend toward a positive association with circ_TNPO1 expression level and a negative association with miR-181b expression level. Our results align with the findings from previous studies. For instance, Bassani et al. [25] pointed out that miR-181b was able to target Notch1 and inhibit Notch1 expression in human NK cells. Moreover, An et al. and Sun et al. [10, 11] also pointed out that the presence of a direct interact relationship between miR-181b and Notch1 and miR-181b/Notch1 axis plays a significant role in the pathogenesis of AS. Subsequently, function studies indicated that the overexpression of Notch1 counteracted the knockdown of circ_TNPO1 induced inhibitory effects of proliferation and migration of VSMCs under ox-LDL stress. Notch1 plays an important regulatory role in the proliferation and migration of VSMCs, and its possible mechanisms include the CBF-1/RBP-Jκ-dependent pathway and the non-CSL-dependent pathway [26]. Consistent with our findings, Chen et al. [27] showed that miR-34a was able to inhibit VSMCs cell proliferation and migration by targeting the 3′-UTR of Notch1.

Our study also indicated that si-circ_TNPO1 lowered protein expression of Ki-67, PCNA, MMP2, and E-cadherin and enhanced protein expression of N-cadherin in ox-LDL-induced VSMCs , which was rescued by Notch1 overexpression plasmid. Ki-67 and PCNA are the most common markers reflecting cell proliferation. MMP2 and E-cadherin are molecular markers of cell migration. E-cadherin is a transmembrane glycoprotein that binds normal and polarized epithelial cells together at adhesion junctions, thereby inhibiting abnormal cell proliferation and migration. MMP2 is a protein with type IV collagen degradation properties that has a biological function in promoting cell migration. The correlation between Notch1, MMP2, and E-cadherin protein expressions has been investigated. For example, Fujiki et al. [26] noted that the application of si-RNA to inhibit Notch1 expression significantly promoted E-cadherin protein expression in the BEAS-2B cell line. In addition, Wang et al. [27] noted that inhibition of suppression of Notch1 expression in skin cancer cell lines was able to significantly promote E-cadherin protein expression. Meanwhile, Zou et al. [28] pointed out that promoting Notch1 activation promotes MMP2 protein expression levels in Jurkat and Sup-T1 cell lines. However, there are also limitations of this study. There are no animal experiments in this study, which made this study not so scientific.

Taken together, our study shows that circ_TNPO1 knockdown can inhibit the abnormal proliferation and migration of ox-LDL-induced VSMCs through the miR-181b/Notch1 axis. The results of this study suggest that circ_TNPO1, miR-181b, and Notch1 may be potential therapeutic targets in AS [29, 30].

Data Availability

The data used to support this study are available from the corresponding author upon request.

Conflicts of Interest

The authors declare that they have no conflicts of interest.

Acknowledgments

This work was supported by Science and Technology Research Project of Chongqing Education Commission Project No. KJQN202000437.

References

[1] Y. Zhao, M. A. Evans, M. A. Allison et al., "Multisite atherosclerosis in subjects with metabolic syndrome and diabetes and relation to cardiovascular events: the Multi-Ethnic Study of Atherosclerosis," *Atherosclerosis*, vol. 282, pp. 202–209, 2019.

[2] T. Sugiyama, E. Yamamoto, K. Bryniarski et al., "Nonculprit plaque characteristics in patients with acute coronary syndrome caused by plaque erosion vs. plaque rupture," *JAMA Cardiology*, vol. 3, no. 3, pp. 207–214, 2018.

[3] U. Kansakar, S. S. Jankauskas, J. Gambardella, and G. Santulli, "Targeting the phenotypic switch of vascular smooth muscle cells to tackle atherosclerosis," *Atherosclerosis*, vol. 324, pp. 117–120, 2021.

[4] S. Huang, W. Luo, and G. Wu, "Inhibition of CDK9 attenuates atherosclerosis by inhibiting inflammation and phenotypic switching of vascular smooth muscle cells," *Aging*, vol. 13, no. 11, pp. 14892–14909, 2021.

[5] R. Gurung, A. M. Choong, C. C. Woo, R. Foo, and V. Sorokin, "Genetic and epigenetic mechanisms underlying vascular smooth muscle cell phenotypic modulation in abdominal aortic aneurysm," *International Journal of Molecular Sciences*, vol. 21, no. 17, p. 6334, 2020.

[6] A. Jaminon, K. Reesink, A. Kroon, and L. Schurgers, "The role of vascular smooth muscle cells in arterial remodeling: focus on calcification-related processes," *International Journal of Molecular Sciences*, vol. 20, no. 22, p. 5694, 2019.

Hindawi
Journal of Healthcare Engineering
Volume 2023, Article ID 9756286, 1 page
https://doi.org/10.1155/2023/9756286

Retraction

Retracted: Signal-to-Noise Ratio Comparison of Several Filters against Phantom Image

Journal of Healthcare Engineering

Received 23 May 2023; Accepted 23 May 2023; Published 24 May 2023

This article has been retracted by Hindawi following an investigation undertaken by the publisher [1]. This investigation has uncovered evidence of one or more of the following indicators of systematic manipulation of the publication process:

(1) Discrepancies in scope
(2) Discrepancies in the description of the research reported
(3) Discrepancies between the availability of data and the research described
(4) Inappropriate citations
(5) Incoherent, meaningless and/or irrelevant content included in the article
(6) Peer-review manipulation

The presence of these indicators undermines our confidence in the integrity of the article's content and we cannot, therefore, vouch for its reliability. Please note that this notice is intended solely to alert readers that the content of this article is unreliable. We have not investigated whether authors were aware of or involved in the systematic manipulation of the publication process. Wiley and Hindawi regrets that the usual quality checks did not identify these issues before publication and have since put additional measures in place to safeguard research integrity.

We wish to credit our own Research Integrity and Research Publishing teams and anonymous and named external researchers and research integrity experts for contributing to this investigation.

The corresponding author, as the representative of all authors, has been given the opportunity to register their agreement or disagreement to this retraction. We have kept a record of any response received.

References

[1] M. H. Siddiqi and Y. Alhwaiti, "Signal-to-Noise Ratio Comparison of Several Filters against Phantom Image," *Journal of Healthcare Engineering*, vol. 2022, Article ID 4724342, 11 pages, 2022.

Hindawi
Journal of Healthcare Engineering
Volume 2022, Article ID 4724342, 11 pages
https://doi.org/10.1155/2022/4724342

Research Article

Signal-to-Noise Ratio Comparison of Several Filters against Phantom Image

Muhammad Hameed Siddiqi and Yousef Alhwaiti

College of Computer and Information Sciences, Jouf University, Sakaka, Aljouf 2014, Saudi Arabia

Correspondence should be addressed to Muhammad Hameed Siddiqi; mhsiddiqi@ju.edu.sa

Received 27 December 2021; Revised 21 January 2022; Accepted 10 March 2022; Published 26 March 2022

Academic Editor: Sahfqat Ullah Khan

Image denoising methods are important in order to diminish various kinds of noises, which are presented either capturing the image or distorted during image transmission. Signal-to-noise ratio (SNR) is one of the main barriers which avoids the theoretical observations to be accomplished in practice. In this study, we have utilized various kinds of filtering operators against three various noises, which are the signal-to-noise ratio comparison against the phantom image in spatial and frequency domain. In frequency domain, the average filter is used to smooth the image and frequency domain, and Gaussian low-pass filter is applied with empirically determined cutoff frequency. This work has six major parts such as applying average filter, determining the SNR of region of interest, transforming the image in frequency domain by discrete Fourier transform, obtaining the rectangular Gaussian low-pass filter along with a cutoff frequency, multiplying them, and carrying out the inverse Fourier transform. These steps are repeated accordingly until the resulting image SNR is equal to or greater than the spatial domain SNR. In order to achieve the goal of this study, we have analyzed the proposed approach against some of complex phantom images. The performances of these filters are compared against signal-to-noise ratio.

1. Introduction

Signal-to-noise ratio (SNR) has a significant role in many research fields such as signal and image processing, computer vision, artificial intelligence, and machine learning. Occasionally, SNR might be the main barrier which avoids theoretical observations to be accomplished in practice. Conservative filtering and optimization methods [1] are the general techniques for SNR enhancement. Commonly, the Gaussian filtering technique is more effective but less efficient, and the regularization technique is more efficient but less effective. Moreover, SNR is utilized to illustrate the quality of image. Basically, the sensitivity of the imaging approach is explained in the terms of the signal level that yields a threshold level of SNR. In imaging approaches, the image quality enhancement and noise reduction are the major steps. Image denoising efficiently conserves the edges of the image to a higher range in the smooth areas [2].

Image denoising is a significant process for reinstating the noise-free pictures from the noisy annotations which aid in conserving the texture and edges located in the corresponding pictures [3, 4]. Image denoising is measured as an important stage in color examination, segmentation, and feature extraction and selection [5]. There are lots of denoising approaches presented for diminishing noise from the various images.

A state-of-the-art approach was proposed by [6] for denoising which increases the image resolution through a model network assessed on identical data. First, this approach extracted the frames from video clips and then screened them using a trigonometric-Gaussian operator to reduce noise from the image. After this, the adaptive histogram equalization was employed in order to revise the contrast of the image that finally improved the resolution of the image [6]. However, the major limitation of adaptive histogram equalization is the propensity to over-intensify noise in comparatively homogeneous image areas [7].

Similarly, an adaptive and efficient method was proposed by [8] for image denoising, where they utilized the updated version of cuckoo search approach. In this method, two-sided filtering noisy image is enhanced through unsharp window and then utilized as the supervision image for the developed optimum supervised filtering method. However, the cuckoo searching method has the clear phenomenon of the early conjunction issue that is simply stuck into local optimum [9].

Therefore, the contribution of this study is described as

(i) This study compares the signal-to-noise ratio of a phantom image in spatial and frequency domain.

(ii) In frequency domain, average filter is utilized to smooth the picture and frequency domain, and Gaussian low-pass filter is applied with empirically determined cutoff frequency.

(iii) This work has five major parts:

  (1) Apply average filter
  (2) Determine the SNR of region of interest
  (3) Transform the image in frequency domain by discrete Fourier transform
  (4) Obtain the rectangular Gaussian low-pass filter along with a cutoff frequency
  (5) Multiply them and do the inverse Fourier transform.

(iv) These steps are repeated accordingly until the resulting image SNR is equal to or greater than the spatial domain SNR.

(v) (v)In order to achieve the goal of this study, we have analyzed the proposed approach against some of complex phantom images.

The remaining article is arranged as follows. Section 2 prescribes a comprehensive literature review against the proposed approach. Section 3 explains the details of the proposed methodology. Section 4 presents the performance evaluation of the developed approach against phantom images. Finally, the study is concluded with some forthcoming directions in Section 5.

2. Literature Review

Image denoising is a significant process for reinstating the noise-free pictures from the noisy annotations which aid in conserving the texture and edges located in the corresponding pictures. The authors of [10] developed an integrated method for image denoising. In this system, they combined two-dimensional disparity decomposition and nonlocal reprojection methods, in which the corresponding image is decomposed into a series of variational mode functions to make the denoising step easier. However, this approach considered synthetic images for validation that cannot be employed in real domains. Likewise, in [11], the authors introduced a new framework for image denoising. This framework has the ability to separate the signals from noise through a learning set of renovation in the feature space. After the separation, the denoising might be attained by choosing the conforming base of the signal subspace and projecting the input into such space. However, they lost much information during the separation process that make the denoising process a challenging task. Furthermore, the authors of [12] performed a correlative examination of various noise removal techniques against different operators in spectral images. These images are presented with various kinds of noise and further operators are employed to denoise the corresponding image. They utilized different group of filters such as Gaussian filter, Prewitt filter, Wiener filter, and Sobel filter for denoising. However, Prewitt and Sobel filters are sensitive to noise in edge detection and orientation, which means that if we increase noise of the image, then the accuracy will be decreased [13].

On the other side, different denoising methods such as nonlocal mean operator, wavelet transform, and median operator were proposed by [14, 15]. In their experiments, they added various types of noises such as Gaussian, salt and pepper, and speckle noise on X-ray and MRI images. However, these filters not only smooth the data to diminish noise but also blur the corresponding edges of the image as well [16]. A multilayered wavelet transform-based methodology was investigated by [17] for denoising under the presence of crop images. In their wavelet-based algorithm, they ignored low-frequency coefficients, while expanded high-frequency coefficients on, respectively, horizontal, vertical, and diagonal directions. However, wavelet transform has one of the common disadvantages such as poor directionality and shift invariance [18]. Similarly, in [19], the authors proposed a new deep generative network coupled with several target images and adaptive termination situation. They generated two clear target images by using a normal denoising technique that enabled best guidance during conjunction step and improved its speed. However, this approach suffered from overfitting problem.

An integrated method in [20] was based on the combination of bilateral operator and anisotropic diffusion method. This method performed the smoothing of the homogeneous areas without disturbing the edges of the corresponding image. However, the bilateral filter does not provide good results at higher noise levels. Also, one of the general limitations of the anisotropic diffusion method does not have the ability to preserve the shrill edges and details of the denoised image [21]. Similarly, the authors of [22] proposed a data augmentation technique in order to resolve the problem of overfitting that was due to the absence of the truth image. However, this approach is not applicable in real-world domains because of low processing speed. A multilevel wavelet transform was proposed by [23] for the image denoising that was distorted by selecting the horizontal coefficients for processing, which was based on tristate median and switching median operators, respectively. Different types of rules were employed for each operator against various levels of salt-and-pepper noise. However, wavelet transform has one of the common disadvantages such as poor directionality and shift invariance [18].

A recent work has been presented by [24], which exposed a missing edge in order to integrate various approaches. The main advantage of this approach is to process the image without preprocessing step to find the mode of the following distribution. However, this approach works only in controlled environment. Likewise, a new integrated denoising system was proposed in [25], where they utilized various kinds of evaluation metrics such as structural similarity index measure, mean square error, contrast to noise, signal-to-noise ratio, and cross correlation. However, the image structure data might not properly be preserved by these noising methods [26]. Similarly, a latest denoising method was proposed [27] that relied on immoral images alone for approach training. It is an unsupervised technique which employed a design of blind-spot network. It needs only a single noisy image as its input and, hence, is well-matched for medical settings. However, this approach needs the accessibility of pairs of noisy images, and the gaining of these pairs along with some constants is only possible for static domains [28]. A robust method was designed by [29] for CT image denoising, which was the combination of various filters such as Gaussian and median filters. The effect of the shadow from CT images was removed by employing the Sobel method that detected the pixels of the edges and then assigned them to grain stages based on threshold. However, this approach does not efficiently work when the noise of spatial density is high [30].

An edge aware denoising method was recommended by [31] in order to get the goal of conserving the material of the original picture when utilizing the features of the noisy picture. However, this approach has a generalized issue such as weak antinoise capacity and false edge [32]. Another denoising scheme was developed in [33] that was based on different wavelet transforms against the threshold value. They selected the threshold value and wavelet structure with the help of spatial adaptivity and hybrid techniques, respectively. However, the wavelet transform has one of the common disadvantages such as poor directionality and shift invariance [18]. Moreover, this scheme is heuristic because of the manual selection of threshold. On the contrary, a deep neural network-based model was proposed in [34, 35] in order to observe the quality of the image from the denoising of a complete viewpoint of the CT image. In their respective work, first, they generated a library having innovative denoising styles of deep neural network. This library was included of denoising styles that was demonstrated and trained one by one to predict the best performance. However, this method showed some concerns such as complex optimization and computational expenses during denoising [36]. Similarly, a Haar wavelet transform-based method was developed in [37] for image denoising. First, analyze the memory necessities of the algorithm and computational complexity. To improve the significance, an integration of the convolution and recursion methods are utilized in order to understand the Haar filter bank, and gradient ancestry technique is employed to determine the reduction factors. However, the main limitation of the Haar wavelet transform is the features' disjointedness which leads to problems for simulating continuous signals [38]. Likewise, the authors of [39, 40] employed statistical features in order to diminish the noise from the image; however, their performances degrade against naturalistic domains.

3. Proposed and Ensembled Denoising Approach

In the proposed approach, we utilized various kinds of operators for denoising. The overall flow diagram is presented in Figure 1.

3.1. Averaging Filter. Averaging filter is diminishing the total intensity differences among the pixels. Generally, the averaging filter is used to substitute the value of every pixel within an image based on the average value of its surroundings, which has the effect of removing the value of the pixels that are misleading of their neighbors. For this filter, the template functions are the union such that 1/9 to confirm that the output of averaging nine white pixels is white but not in excess of white. It depends on the window that presents the size and shape of the region for the expected sample during the mean estimation. In this filter, 3×3 square mask is utilized as described in Figure 2.

For a common execution, we explained the size of the filter as "W_S is the size of window" and the size of template is $W_S\times W_S$. Then, we create the average of the entire pixels inside the region enclosed through the template, which is divided by the amount of points in the mask of the template. This is a straight execution of a common averaging filter instead of utilizing the convolution of the template filter as

$$A(I,W_s) := \left| \begin{array}{l} \text{New}\leftarrow \text{zero}(I), \\ \text{Partial}\leftarrow \text{floor}\left(\dfrac{W_s}{2}\right), \\ \text{for } i \in \text{ Partial..Col}(I) - \text{Partial} - 1, \\ \text{for } j \in \text{ Partial..Row}(I) - \text{Partial} - 1, \\ \text{New}_{j,i}\leftarrow \text{floor}\left[\dfrac{\sum_{x=0}^{W_s}\sum_{y=0}^{W_s} I_{j+x-\text{Partial},i+y-\text{Partial}}}{W_s\times W_s}\right], \end{array}\right. \tag{1}$$

where I is the corresponding image, W_s is the size of the window, and Col represents the number of the columns, respectively.

We need to design a template to execute the averaging filter by utilizing the convolution of the template filter, although the ease of the direct averaging filter typically prevents such types of executions. This diminishes the noise that is one the advantage of the averaging filter. However, the averaging filter may cause blurring that diminishes the features of the image. Therefore, we utilized Fourier transform to permit the components of the low frequencies and stop the components of the high frequencies.

3.2. Fourier Transform. The Fourier transform contains a set of K points p_i (tested through a frequency that is equal to the rate of testing) in the tested frequencies F_{pv} and is given as

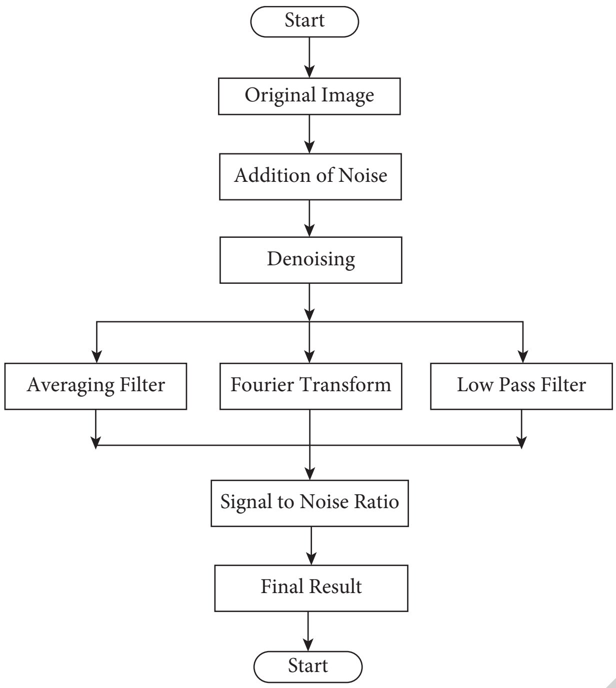

Figure 1: The flow diagram of the proposed approach.

1/9	1/9	1/9
1/9	1/9	1/9
1/9	1/9	1/9

Figure 2: 3×3 averaging kernel commonly employed in the averaging filter.

$$Fp_v = \frac{1}{\sqrt{K}} \sum_{i=0}^{K-1} p_i e^{-j(2\pi/K)iv}. \tag{2}$$

This explains the discrete correspondent Fourier transform that is substituted through a group of samples, the consecutive frequencies of the samples, and the summation of the frequencies. If the Fourier transform is applied to the pulse samples in a mask having range 0~K/2–1, when the pulsation finishes, then equation (1) becomes as follows:

$$Fp_v = \frac{1}{\sqrt{K}} \sum_{i=0}^{k/2-1} S e^{-j(2\pi/K)iv}. \tag{3}$$

The summation of the geometric evolution might be assessed as

$$\sum_{k=0}^{K} s_0 r^k = \frac{s_0\left(1 - r^{k+1}\right)}{1 - r}. \tag{4}$$

The sampled pulsation of the Fourier transform is given below:

$$Fp_v = \frac{S}{\sqrt{K}} \left(\frac{1 - e^{-j^{(2\pi/K)(K/2)v}}}{1 - e^{-j^{(2\pi/K)v}}} \right). \tag{5}$$

Through reordering, we can obtain

$$Fp_v = \frac{S}{\sqrt{K}} e^{-j^{(\pi v/K)(1-2/K)}} \frac{\sin(\pi v/2)}{\sin(\pi v/K)}. \tag{6}$$

Hence,

$$\left|Fp_v\right| = \frac{S}{\sqrt{K}} \left| \frac{\sin(\pi v/2)}{\sin(\pi v/K)} \right|, \tag{7}$$

as the scale of the exponential is 1.

The spatial frequency is represented by the ratio of the pixels' intensity variations. Figure 3 indicates various frequencies of an image, where the higher frequencies are focused throughout the axis distributing the image in quad. Higher frequencies are described by the attentions of high amplitude waves in small checker board outline; while, the bends have lesser frequencies that are described by large regions of closer constant points.

When we employed the digital images, the continuous function has never been utilized; however, we just considered a limited number of samples that are made by the number of pixels. In order to analyze an image, we need Fourier transform that is inherited from continuous FT and is represented by

$$H(u,v) = \frac{1}{MN} \sum_{x=0}^{M-1} \sum_{y=0}^{N-1} h(x,y) e^{-j2\pi(ux/M + vy/N)}. \tag{8}$$

Equation (8) is converted to spatial domain and is represented by

$$h(u,v) = \sum_{x=0}^{M-1} \sum_{y=0}^{N-1} H(u,v) e^{j2\pi(ux/M + vy/N)}. \tag{9}$$

It is obvious that both the processes of discrete Fourier transforms and inverse Fourier transforms are equivalent. Actually, the code which performs these processes might be the similar considering the route of the transform and accordingly sets up the symbol of the exponential. Figure 4 shows an example of the Fourier transformed image.

3.3. Gaussian Low-Pass Filter. This filter describes the region from which we can collect spectral components, and the size of the region presents the range of the retained frequencies. If we collect the points from the center of the circular area and inverse Fourier transform is the filtered transform, then the output will be distorted. The features who have higher frequencies are located at sharp edges, and diminishing them may cause distortion.

Gaussian low-pass filters have significant roles in various applications of pattern recognition, communication, and image processing, which are categorized through bandwidths, cutoff, and overshoots, respectively. One of the important features of these filters is that the Gaussian of such filters is Gaussian as well due to which it has the same

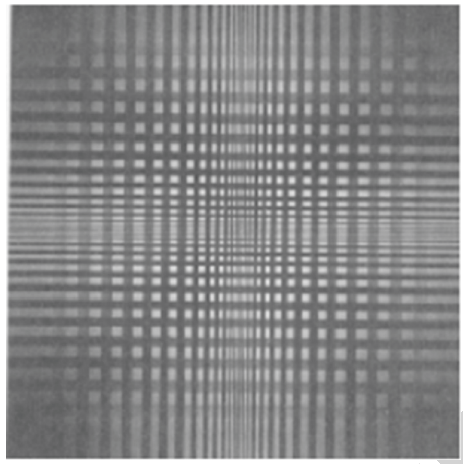

Figure 3: Frequency variations of an image.

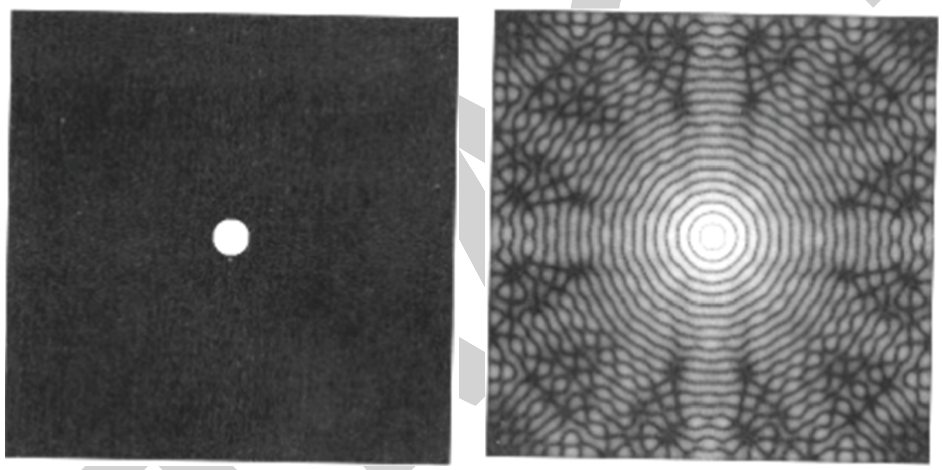

(a) (b)

Figure 4: Processing of the corresponding image: (a) original image and (b) result of the FT.

response pattern in both spatial and frequency domains, respectively, which is represented as

$$H(u, v) = e^{-D^2\left(u,v/2\sigma^2\right)}. \quad (10)$$

In the frequency level at the origin, the distance is indicated by $D(u, v)$; the scattering of the Gaussian curvature is calculated by σ. If the value of σ is higher, then cutoff frequency will be high. For instance, if $\sigma = r_0$, then equation (10) will be re-written as

$$H(u, v) = e^{-D^2\left(u,v/2r_0^2\right)}. \quad (11)$$

If $D(u, v) = r_0$, then value of the filter is 0.671, which has the maximum value equal to 1.

A perception scheme to display an image and circular view is presented in Figure 5.

More specifically, the Gaussian low-pass filtering function for a 2D image can be written as

$$H(u, v) = e^{-u^2/2u_c^2} e^{-v^2/2u_c^2}, \quad (12)$$

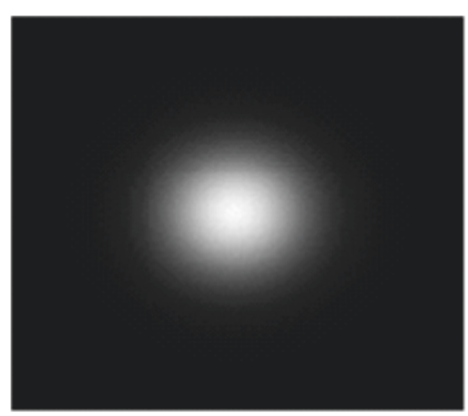

Figure 5: Filter displayed as an image.

where u_c represents the cutoff frequency.

3.4. Signal-to-Noise Ratio (SNR). SNR of an image is the ratio between the original intensity value and the noise. As we know that the mean of the random noise in an image is zero, thus, the SNR of the image might be measured with the help of its mean and standard deviation. Let an image be given as $C\ (x,\ y)$. Therefore, the SNR of $C\ (x,\ y)$ is

$$\mathrm{SNR}_{C(x,y)} = \frac{\mathrm{mean}\,(C\,(x,\,y))}{\sigma_{c\,(x,y)}}. \tag{13}$$

4. Performance Assessment

In order to accomplish the proposed approach, we have sequentially done the 5×5 averaging filter, discrete Fourier transform, and Gaussian low-pass filtering with appropriate cutoff frequency so that the SNR of the frequency domain filtered image is the same as the spatial domain image. The entire procedures are implemented in Matlab with the specification of 1.9 Hz processor and 8 GB RAM. The step-by-step procedures of the proposed approach are described as

4.1. Acquiring the Phantom Image. A phantom image is created with the size of 512×512, as shown in Figure 6.

4.2. Results of an Averaging Filter on the Phantom Image. As presented before, we have applied an averaging filter on the spatial domain of the image. The mask size of the filter was 5×5, as shown in Figure 7. Furthermore, after applying the average filter, we have obtained a smoothed image as Figure 8.

The SNR calculated for both the spatially smoothed phantom image was 37.65270.

4.3. Results of Discrete Fourier Transform on the Phantom Image. For such experiment, we are going to apply the frequency domain processing. In order to convert the spatial phantom image into its frequency domain, we utilized the *fft*$_2$ function. However, after applying this function, the values of the resultant image are too high; thus, we took the log values. On the contrary, the low frequencies were at the corner that require a shifting the corner. For shifting the corner, we exploited *fft*$_2$ function. Figures 9 and 10 demonstrate the logged image of the frequency domain representation and shifted image of the logged image. In Figure 10, the low-frequency components stay near the center, and then, it spreads out to higher frequencies.

4.4. Results of Gaussian Low-Pass Filter on the Phantom Image. For this experiment, we designed a rectangular low-pass Gaussian filter that takes the midposition of 512×512 as center. We started the cutoff frequency from 10 Hz until we get the equal and larger SNR than the spatial domain smoothed image. At last, when the cutoff frequency was 55, then we got the desired SNR and break the loop of searching the equal SNR. Figure 11 shows the filter image with the cutoff frequency of 55.

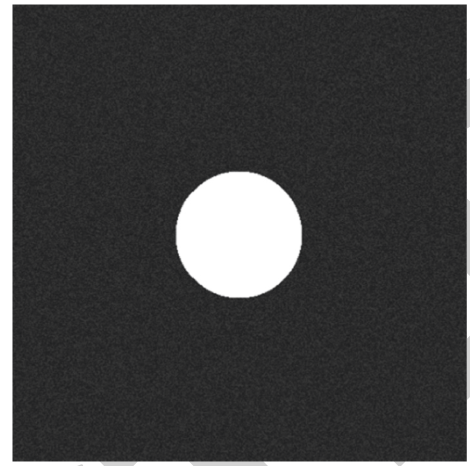

Figure 6: The overall flow of the proposed and ensembled method.

1/25	1/25	1/25	1/25	1/25
1/25	1/25	1/25	1/25	1/25
1/25	1/25	1/25	1/25	1/25
1/25	1/25	1/25	1/25	1/25
1/25	1/25	1/25	1/25	1/25

Figure 7: 5×5 averaging kernel often used in average filtering.

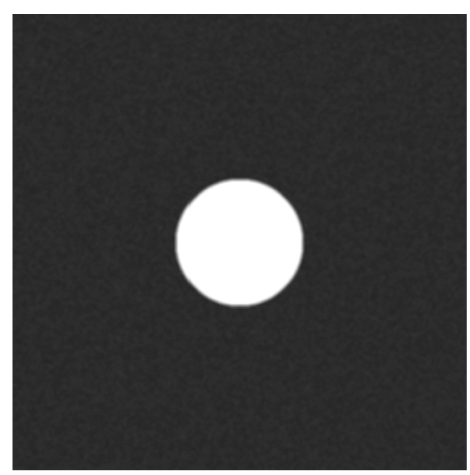

Figure 8: Smoothed image after average filtering by 5×5 window.

After the first step, we multiplied the filtered image with the shifted frequency-domain transformed image. We utilized the inverse Fourier transform by *ifft*$_2$ function against the smoothed image in order to see the filtered image in spatial domain. Hence, it gives the high-frequency removed and smoothed image, as shown in Figure 12. Moreover, Table 1 depicts the SNR for the cutoff frequency from 40 to 55.

Figure 13 shows 12 Gaussian low-pass filter images with 12 different cutoff frequencies, and Figure 14 represents the smoothing result applying the 12 different Gaussian low-pass filters shown in Figure 13.

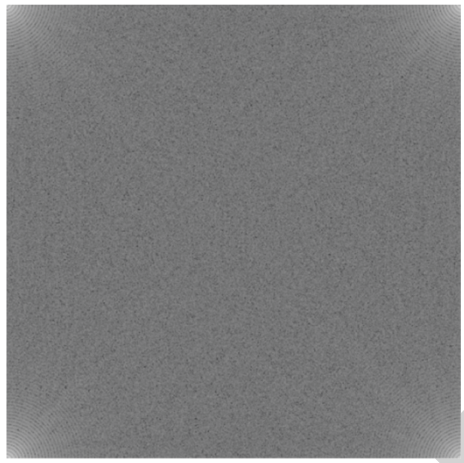

Figure 9: Logged frequency image of the phantom image.

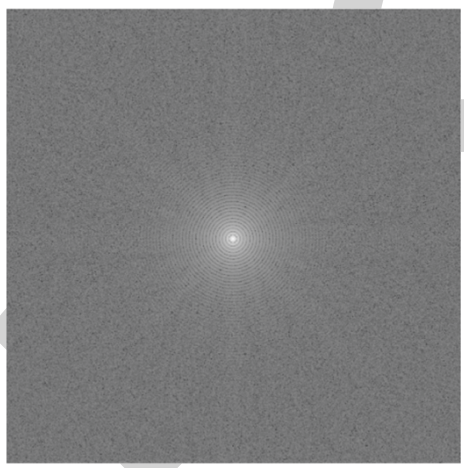

Figure 10: Shifted image of the logged frequency image of the phantom image.

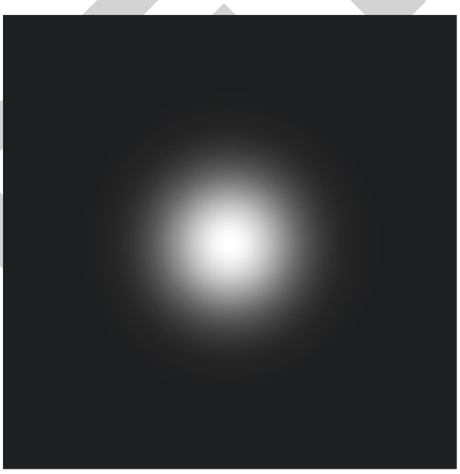

Figure 11: Rectangular Gaussian low-pass filter image with cutoff frequency of 55.

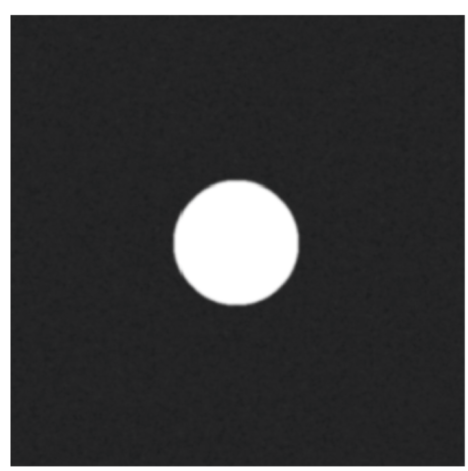

Figure 12: Smoothed image after the inverse Fourier transform of the frequency-domain filtered image.

4.5. Discussion. After applying the smoothing operation both in spatial and frequency domain, it is seen that the frequency domain filtering shows better smoothing than the spatial on where the SNRs are almost the same. In Figure 15, the smoothed image in frequency domain shows better edges and less noise representation than the smoothing in spatial

Table 1: SNR of the filtered image for the cutoff frequency from 40 to 55.

Cutoff freq.	SNR
40	35.51455
41	35.74032
42	35.95237
43	36.15139
44	36.33805
45	36.51296
46	36.67671
47	36.82986
48	36.97293
49	37.10641
50	37.23078
51	37.34648
52	37.45393
53	37.55354
54	37.64570
55	37.73075

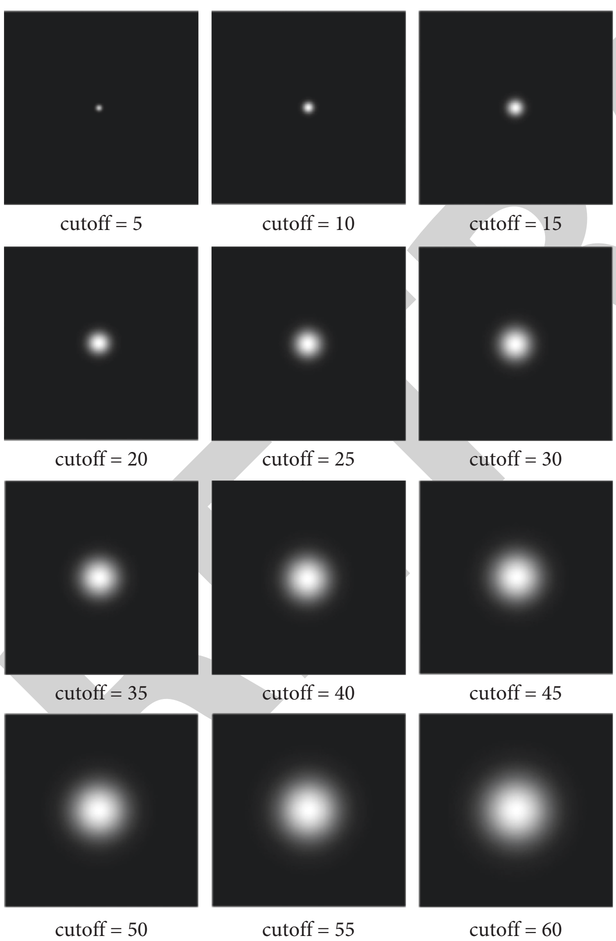

Figure 13: Gaussian low-pass filter image with different cutoff frequencies.

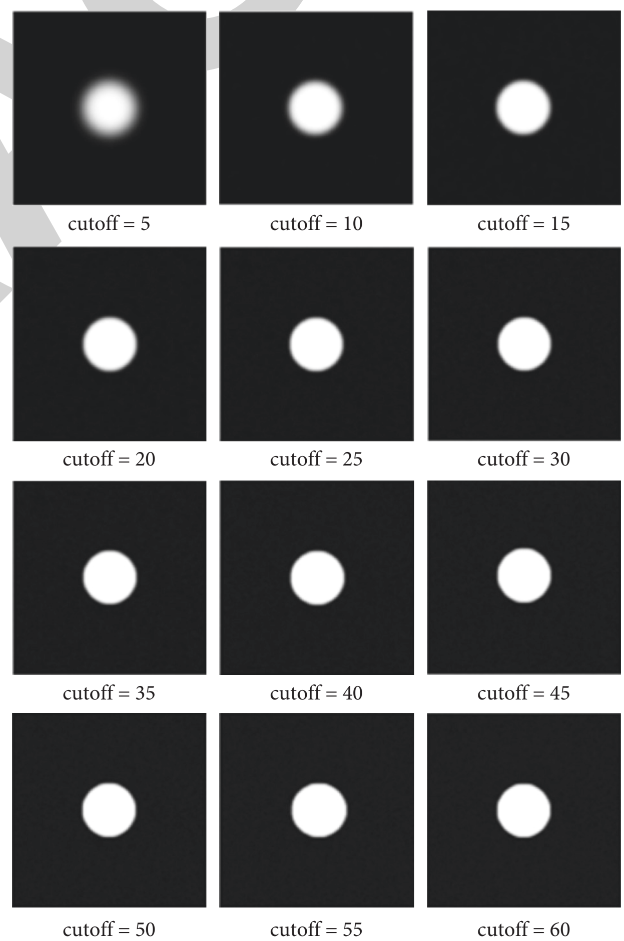

Figure 14: The smoothing result using different Gaussian low-pass filters with different frequencies.

domain. However, it may vary from time to time and depends on the types of filtering and choosing different criteria such as cutoff frequency or SNR in frequency-domain filtering. Thus, we can say that the SNR improvement of an image is very much dependent of the characteristics of the image.

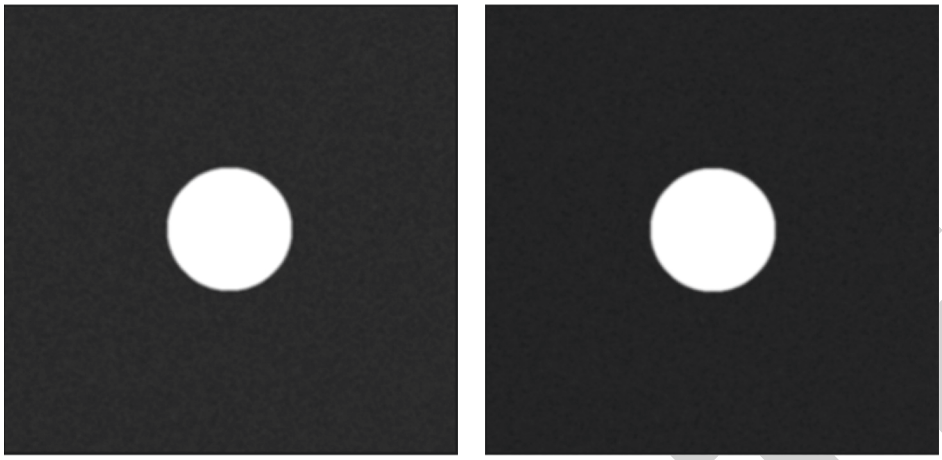

(a) (b)

Figure 15: Smoothed phantom image after (a) spatial domain average and (b) frequency domain Gaussian low-pass filtering.

Table 2: Comparison of the proposed approach with existing methods under the presence of quality measurement techniques against the phantom image (as shown in Figure 6).

Methods	Noise level	SSIM	MSE	RMSE	PSNR
[41]	0.2	0.88	19.85	13.08	22.64
	0.4	0.84	26.66	18.61	18.91
[42]	0.2	0.80	24.76	14.72	15.28
	0.4	0.90	19.01	16.99	23.05
[43]	0.2	0.85	23.89	13.91	18.89
	0.4	0.80	18.94	15.76	16.58
[44]	0.2	0.83	22.67	11.90	22.75
	0.4	0.86	18.41	14.84	18.41
Proposed approach	0.2	0.65	14.89	11.33	13.78
	0.4	0.72	15.30	12.88	16.38

Furthermore, qualitywise, the performance of the proposed approach is compared with some of the existing work [41–44] against quality measurement techniques such as SSIM, MSE, RMSE, and PSNR. The overall performance is presented in Table 2.

As can be seen from Table 1 that, after denoising, we measured the quality of the denoised images through SSIM, MSE, RMSE, and PSNR metrics. In Table 2, most of the existing methods gave consistent results against the phantom image. When the noise level increases the quality measurement matrices increase as well, the result of the proposed approach is much better than existing methods against the phantom image.

5. Conclusion

In medical images, noise diminishing is a challenging task for the research community in image processing. Noise produces supreme critical instabilities and degrades the quality of the medical images such as ultrasound, X-ray, and CT in healthcare. Generally, the image is considered as the collection of data and the quality of image may degrade under the presence of noises. It has to be vigorous to regenerate the noises of the original images for achieving supreme data from images. Signal-to-noise ratio (SNR) is one of the main barriers which avoids the theoretical observations to be accomplished in practice. Phantom images are generated that have well-known noises such as Gaussian noise, salt and pepper, and speckle noise. In this study, we have tried to discuss about spatial- and frequency-domain smoothing operation of a phantom image. For this purpose, several image processing methods have been utilized here such as average filtering, discrete Fourier transform, and Gaussian low-pass filtering. This work has six major parts such as applying the average filter, determining the SNR of region of interest, transforming the image in frequency domain by discrete Fourier transform, obtaining the rectangular Gaussian low-pass filter with a cutoff frequency, multiplying them, and carrying out the inverse Fourier transform. These steps are repeated accordingly until the resulting image SNR is equal to or greater than the spatial domain SNR. In order to achieve the goal of this study, we have analyzed the proposed approach against some of complex phantom images. The significances of these operators are compared against signal-to-noise ratio.

In the future research, we will deploy the proposed approach in healthcare domains such as hospitals to facilitate the physicians in various radiology domains. This approach may help the experts to accurately diagnose the corresponding disease from various radiology domains such as X-ray, CT, ultrasound, and MRI.

Data Availability

The data used to support the findings of the study and simulation can be obtained from the corresponding author upon request.

Conflicts of Interest

The authors declare that they have no conflicts of interest.

Acknowledgments

This work was funded by the Deanship of Scientific Research at Jouf University, under Grant no. DSR–2021–02–0348.

References

[1] Y. Xie, “Improving the quality of low snr images using high snr images,” *PeerJ Preprints*, Article ID e27800v1, 2019.

[2] A. Suneetha and E. Srinivasa Reddy, “Robust Gaussian noise detection and removal in color images using modified fuzzy set filter,” *Journal of Intelligent Systems*, vol. 30, no. 1, pp. 240–257, 2021.

[3] H. Hu, J. Froment, and Q. Liu, “A note on patch-based low-rank minimization for fast image denoising,” *Journal of Visual Communication and Image Representation*, vol. 50, pp. 100–110, 2018.

[4] A. Siddig, Z. Guo, Z. Zhou, and B. Wu, “An image denoising model based on a fourth-order nonlinear partial differential equation,” *Computers & Mathematics with Applications*, vol. 76, no. 5, pp. 1056–1074, 2018.

[5] H. A. Jalab and R. W. Ibrahim, “Fractional Alexander polynomials for image denoising,” *Signal Processing*, vol. 107, pp. 340–354, 2015.

[6] A. K. Cherian, E. Poovammal, N. S. Philip, K. Ramana, S. Singh, and I.-H. Ra, “Deep learning based filtering algorithm for noise removal in underwater images,” *Water*, vol. 13, no. 19, p. 2742, 2021.

[7] V. Magudeeswaran and J. F. Singh, “Contrast limited fuzzy adaptive histogram equalization for enhancement of brain images,” *International Journal of Imaging Systems and Technology*, vol. 27, no. 1, pp. 98–103, 2017.

[8] H. Singh, S. V. Raghavendra Kommuri, A. Kumar, and V. Bajaj, “A new technique for guided filter based image denoising using modified cuckoo search optimization,” *Expert Systems with Applications*, vol. 176, Article ID 114884, 2021.

[9] W. Wang and C. Xie, “A cuckoo search algorithm based on self-adjustment strategy,” *Journal of Physics: Conference Series*, vol. 1087, no. 2, Article ID 022003, 2018.

[10] H. Badre, Y. Tounsi, M. S. Rachafi, H. Bioud, and A. Nassim, “SAR images denoising using bidimensional variational mode decomposition and nonlocal means reprojection with minimizing variance,” *Geosciences*, vol. 11, no. 1, pp. 1–9, 2021.

[11] S. Cheng, Y. Wang, H. Huang, D. Liu, H. Fan, and S. Liu, “NBNet: noise basis learning for image denoising with subspace projection,” in *Proceedings of the IEEE/CVF Conference on Computer Vision and Pattern Recognition*, pp. 4896–4906, IEEE, Nashville, TN, USA, June 2021.

[12] S. Annam and S. Anshu, “Correlative analysis of denoising methods in spectral images embedded with different noises,” in *Proceedings of the 2020 6th International Conference on Parallel, Distributed and Grid Computing (PDGC)*, pp. 318–323, IEEE, Himachal Pradesh, India, November 2020.

[13] G. T. Shrivakshan and C. Chandrasekar, “A comparison of various edge detection techniques used in image processing,” *International Journal of Computer Science Issues (IJCSI)*, vol. 9, no. 5, p. 269, 2012.

[14] S. Kavitha and I. Hannah, “COVID-19 and MRI image denoising using wavelet transform and basic filtering,” in *Proceedings of the 2021 5th International Conference on Intelligent Computing and Control Systems (ICICCS)*, pp. 792–799, IEEE, Madurai, India, May 2021.

[15] K. Huang and H. Zhu, “Image noise removal method based on improved nonlocal mean algorithm,” *Complexity*, vol. 2021, Article ID 5578788, 11 pages, 2021.

[16] R. Anutam and F. Rajni, “Performance analysis of image denoising with wavelet thresholding methods for different levels of decomposition,” *The International Journal of Multimedia & Its Applications*, vol. 6, no. 3, pp. 35–46, 2014.

[17] R. Wang, W. Cai, and Z. Wang, “A new method of denoising crop image based on improved SVD in wavelet domain,” *Security and Communication Networks*, vol. 2021, Article ID 9995813, 9 pages, 2021.

[18] S. K. Mohideen, “Denosing of images using complex wavelet transform,” *International Journal of Advance Sci Tech Res*, vol. 1, no. 2, pp. 176–184, 2012.

[19] S. Chen, S. Xu, X. Chen, and F. Li, “Image denoising using a novel deep generative network with multiple target images and adaptive termination condition,” *Applied Sciences*, vol. 11, no. 11, p. 4803, 2021.

[20] S. Budhiraja, B. Goyal, A. Dogra, and S. Agrawal, “An efficient image denoising scheme for higher noise levels using spatial domain filters,” *Biomedical and pharmacology journal*, vol. 11, no. 2, pp. 625–634, 2018.

[21] V. Kamalaveni, R. A. Rajalakshmi, and K. A. Narayanankutty, “Image denoising using variations of Perona-Malik model with different edge stopping functions,” *Procedia Computer Science*, vol. 58, pp. 673–682, 2015.

[22] T. Pang, H. Zheng, Y. Quan, and J. Hui, “Recorrupted-to-recorrupted: unsupervised deep learning for image denoising,” in *Proceedings of the IEEE/CVF Conference on Computer Vision and Pattern Recognition*, pp. 2043–2052, IEEE, Nashville, TN, USA, June 2021.

[23] M. M. Laftah, “Image denoising using multiwavelet transform with different filters and rules,” *International Journal of Interactive Mobile Technologies*, vol. 15, p. 15, 2021.

[24] K. Kim and Y. Jong Chul, “Noise2Score: tweedie’s approach to self-supervised image denoising without clean images,” 2021, https://arxiv.org/abs/2106.07009.

[25] A. S. Ahmed, W. H. El-Behaidy, and A. A. A. Youssif, “Medical image denoising system based on stacked convolutional autoencoder for enhancing 2-dimensional gel electrophoresis noise reduction,” *Biomedical Signal Processing and Control*, vol. 69, Article ID 102842, 2021.

[26] L. I. U. Baozhong and L. I. U. Jianbin, “Overview of image noise reduction based on non-local mean algorithm,” in *Proceedings of the MATEC Web of Conferences*, p. 03029, EDP Sciences, Cape Town, South Africa, November 2018.

[27] T.-A. Song, F. Yang, and J. Dutta, “Noise2Void: unsupervised denoising of PET images,” *Physics in Medicine and Biology*, vol. 66, no. 21, Article ID 214002, 2021.

[28] A. Krull, T. O. Buchholz, and F. Jug, “Noise2void-learning denoising from single noisy images,” in *Proceedings of the IEEE/CVF Conference on Computer Vision and Pattern Recognition*, pp. 2129–2137, Long Beach, CA, USA, June 2019.

[29] A. Moslemipour, S. Sadeghnejad, and J. Gostick, “A hybrid image processing approach to enhance signal to noise ratio of carbonate micro CT-images,” in *Proceedings of the 82nd EAGE Annual Conference & Exhibition*, no. 1, pp. 1–5, European Association of Geoscientists & Engineers, Amsterdam, Netherlands, October 2020.

[30] H. Soni and D. Sankhe, “Image restoration using adaptive median filtering,” *Image*, vol. 6, p. 10, 2019.

[31] X. Zhang, Y. Yang, and L. Lin, “Edge-aware image denoising algorithm,” *Journal of Algorithms & Computational Technology*, vol. 13, Article ID 1748301818804774, 2018.

Hindawi
Journal of Healthcare Engineering
Volume 2023, Article ID 9838676, 1 page
https://doi.org/10.1155/2023/9838676

Retraction

Retracted: Critical Retrospection of Performance of Emerging Mobile Technologies in Health Data Management

Journal of Healthcare Engineering

Received 23 May 2023; Accepted 23 May 2023; Published 24 May 2023

This article has been retracted by Hindawi following an investigation undertaken by the publisher [1]. This investigation has uncovered evidence of one or more of the following indicators of systematic manipulation of the publication process:

(1) Discrepancies in scope
(2) Discrepancies in the description of the research reported
(3) Discrepancies between the availability of data and the research described
(4) Inappropriate citations
(5) Incoherent, meaningless and/or irrelevant content included in the article
(6) Peer-review manipulation

The presence of these indicators undermines our confidence in the integrity of the article's content and we cannot, therefore, vouch for its reliability. Please note that this notice is intended solely to alert readers that the content of this article is unreliable. We have not investigated whether authors were aware of or involved in the systematic manipulation of the publication process. Wiley and Hindawi regrets that the usual quality checks did not identify these issues before publication and have since put additional measures in place to safeguard research integrity.

We wish to credit our own Research Integrity and Research Publishing teams and anonymous and named external researchers and research integrity experts for contributing to this investigation.

The corresponding author, as the representative of all authors, has been given the opportunity to register their agreement or disagreement to this retraction. We have kept a record of any response received.

References

[1] S. Vyas, D. Bhargava, J. Bhola, J. A. Ujjan, S. Eswaran, and A. W. Rahmani, “Critical Retrospection of Performance of Emerging Mobile Technologies in Health Data Management,” *Journal of Healthcare Engineering*, vol. 2022, Article ID 8903604, 12 pages, 2022.

Hindawi
Journal of Healthcare Engineering
Volume 2022, Article ID 8903604, 12 pages
https://doi.org/10.1155/2022/8903604

Research Article

Critical Retrospection of Performance of Emerging Mobile Technologies in Health Data Management

Sonali Vyas[1] **Deepshikha Bhargava**[2] **Jyoti Bhola**[3] **Javed Ahmed Ujjan**[4] **Sathyapriya Eswaran**[5] **and Abdul Wahab Rahmani**[6]

[1]*University of Petroleum and Energy Studies, Dehradun, India*
[2]*School of Computing, DIT University, Dehradun, India*
[3]*Electronics & Communication Engineering Department, National Institute of Technology, Hamirpur, India*
[4]*College of Animal Sciences & Technology, Northwest A&F University, Xianyang, China*
[5]*Agricultural Extension, Amrita School of Agricultural Sciences, Arasampalayam, Coimbatore, Tamil Nadu, India*
[6]*Isteqlal Institute of Higher Education, Kabul, Afghanistan*

Correspondence should be addressed to Deepshikha Bhargava; deepshikhabhargava@gmail.com and Jyoti Bhola; jyotib@nith.ac.in

Received 8 December 2021; Revised 16 January 2022; Accepted 16 February 2022; Published 25 March 2022

Academic Editor: Hafiz Tayyab Rauf

The recent advancement in mobile technologies has led to opening a new paradigm in the field of medical healthcare systems. The development of WBAN sensors, wearable devices, and 5G/6G wireless technology has made real-time monitoring and telecare of the patient feasible. The complex framework to secure sensitive data of the patient and healthcare professionals is critical. The fast computation of health data generated is crucial for disease prediction and trauma-related services; the security of data and financial transactions is also a major concern. Various models, algorithms, and frameworks have been developed to tame critical issues related to healthcare services. The efficiency of these frameworks and models depends on energy and time consumption. Thus, the review of recent emerging technologies in respect of energy and time consumption is required. This paper reviews the developments in recent mobile technologies, their application, and the comparative analysis of their performance parameters to explicitly understand the utility, capacity, and limitations. This will help to understand the shortcomings of the recent technologies for the development of better frameworks with higher performance capabilities as well as higher quality of services.

1. Introduction

Mobile phones are playing an important role in this modern era. In this period of digitalization, the importance of mobiles has been increasing day by day in every field, such as schools, colleges, companies, healthcare services, and manufacturing. The wireless communication technology in mobile phones helps in the prevention of unwanted visits. There are various types of mobile applications which are used in various fields; especially, they have played a vital role in the medical field for the last 5–10 years. According to Liquid State (2018), there were about 318,000 mobile healthcare applications available for patients, about 200 apps are built every day, and we can assume that the number of healthcare apps will increase during the COVID-19 pandemic [1], the period in which all individuals prevent or avoid unnecessary or unwanted visits, especially hospitals, medical stores, and so on. Individuals want the facilities to be delivered to their doors, and it is possible by these applications; by medical id, we can share information about our health including blood type, whole physical statement, and diabetes that provides the exact information of blood sugar level and insulin. These apps are available for Android as well as iOS devices; Apple Health is available only for iPhone and all Apple devices, which is helpful in the monitoring of sleep, daily activities, food, heart rate, respiratory rate, and so on; it can be able to identify the location of patients by the GPS address in case of emergency and able to reach at the time of emergency. Eyecare Live helps in the treatment of problems related to the eyes within an hour, doctors can recognize the real-time condition of your eyes online and live, and this app is available on Android as well as iOS.

WebMD Baby app is helpful in taking care of babies such as feeding, sleep, diapers, and growth because it can detect the essential things for their growth [2]. This app is available for Android as well as iOS devices. Recently, in the COVID-19 pandemic, the Cova app and Aarogya Setu app played an important role in digital or online communication with the relevant knowledge about corona [3,4]. The experts and medical staff are available for providing proper guidance when no one knows the effects of the SARS COVID-19. The fruitful knowledge is provided by the doctors and volunteers. Similarly, there are more applications, such as dminder, Medisafe Pill, Minder, MyFitnessPal, AliveCor drugs, and Comedication guide, which are available for mobiles [5–7].

The advancement has emerged in this modern era in the healthcare system by wireless mobile communication (5G) with high-speed network and high data rates, and we can say that there is explosive growth in the mobile network [8]. According to the review of 2014, the predictable progress in mobile data will rise up to 15.8 Exabyte 2018-19 [9]. Mobile phones provide a number of facilities for expanding the capabilities by overcoming their limitations like battery life, limited memory, CPU, and big data analytical methods able to abstract values from the four Vs: volume, variety, velocity, and veracity. Mobile phones provide facilities for multiple tasks such as meetings, food, and online booking, which control unwanted visits; real-time navigation helps to find the exact way of suitable visiting places, especially for suitable hospitals and medical stores, online meetings with disease specialists, which helps in proper treatments and future medications, online bookings of appointment with doctors with good knowledge of diseases, online flights for the transportation, and so on. Healthcare applications require the bulk of computational and communicational resources. Some researchers discussed the dynamic access and collected a large amount of data of the patients, and this can be done by using mobile cloud systems and clouds in some cities.

In the modern era, the death rates with noncommunicable chronic diseases such as heart diseases, diabetes, cancer, stroke, respiratory diseases, and genetic disorders increase day by day all over the world. We can say that a large amount of earnings of individuals goes to health treatments; data of loss of national income per year in different countries are shown in Table 1.

According to the EU, the number of deaths with chronic diseases is about two million throughout the year. To overcome the increased mortality rate, various organizations are trying to cure these heart diseases through organizing a number of programs, but these are done in the hospitals under the supervision of medical staff. People have less participation in these programs due to long distances and limited time, but there is a need to recognize the real-time condition of the patients. In these cases, mobile communication and mobile cloud computing play an important role in curing these noncommunicable chronic diseases [10].

Wireless mobile communication and digital clinics play a pivotal role in mental health, especially in pandemic COVID-19; these are used routinely in daily life. The cognitive situation can be identified by smartphones apps which recognize the mental condition by measuring the depression level, anxiety, hours of sleep, and so on. These data can also help in the recovery of patients through shared decision-making. The symptoms of the disease can be collected by the digital clinic. Digital clinic for mental health is a new paradigm in the modern healthcare system. The digital clinic for mental healthcare includes synchronous health visits (by video, in person, or by phone call) for measurement-based healthcare, shared decision-making, and personalized medicine for health mental illness patients [11]. This hybrid mode of care includes discreet and/or real-time data collection of the patient using WBAN sensors. The successful implementation of the digital clinic has been observed at Beth Israel Deaconess Medical Center using an app, namely, mindLAMP, for serving patients with mood, anxiety disorder, and posttraumatic stress disorder. Similar types of digital clinics for mental health are established in the USA [12].

Mobile phones have been used as a powerful tool for providing primary healthcare services in low- and middle-income countries, which includes the usage of short message services (SMS), multimedia messaging services, interactive voice response, video clips, audio clips, and images. These methods help to address logistics-related issues, patient education, clinical decision-making, and many more. In Ghana and Uganda, the use of mobile phones has helped to improve the performance of community health workers. A similar approach has been used in Indonesia, Columbia, some rural parts of India, Bangladesh, Nepal, Kenya, Tanzania, and Zambia, to name a few. However, certain challenges require special attention, such as the lack of proper training of the community health worker for using mobile Internet and network issues and weak technical back-end support. Other issues such as poor sustainability of pilot projects, cost of operations, maintenance, investment, management, age, technology proficiency, education level, and years of experience of the community health worker affect the mobile health services. The careful implementation and operation of mHealth services can mitigate these challenges [13].

Mobile became a life savior tool in the time of the COVID-19 outbreak. During the COVID-19 pandemic, person-to-person contact and isolation became the critical parameters to tackle the pandemic. Mobile telehealth facilitates the contactless and real-time interaction of healthcare professionals, doctors, and patients for patient diagnosis, case discussion, decision-making, and personalized medicine. With the development of WBAN and BAN sensors, it has become possible to monitor and diagnose the patient in real time. Mobile telehealth also poses the risk of sensitive data theft and data misuse. To tackle the security, continuous efforts have been put to mitigate risks; blockchain and cloud security are the recent advancements [14].

Mobile-based technology became a promising tool for hastening patient-doctor communication about sexual health concerns. Breast cancer is the leading cause of death in the female population. The distress related to emotional, physical, and mental health makes the problem and patient condition more complex. Mobile-based application is used

Table 1: Loss of national income per year in different countries.

Country	Loss of income in 2005	Loss of income in 2015	Accumulated loss
Brazil	2.7	9.3	49.2
Canada	0.5	1.5	8.5
China	18.3	131.8	557.7
India	8.7	54	236.6
Nigeria	0.4	1.5	7.6
Pakistan	1.2	6.7	30.7
Russian Federation	11.1	66.4	303.2
UK	1.6	6.4	32.8
Tanzania	0.1	0.5	2.5

for breast cancer patients for routine clinic encounters to boost patient confidence. This application also provides educational material related to breast cancer. The pilot test of this app certainly faces challenges such as scalability and availability of limited studies, which can be tamed in the near future [15].

Telemedicine, along with other emerging mobile technologies such as e-diaries, remote patient monitoring, digital inhalers, and Bluetooth-connected wearable devices, is used as an effective measure for timing allergy, asthma adherence doctors, and healthcare consultation on mobile audio-video methods for general medicine. Also, the tracking of clinical information status in digital record for asthma, allergy, and anxiety disorder patients and autoreminders of medicine and severity of disorder alert can be done. The synchronized e-diary with mobile and smartwatches helps to maintain the digital record of medicine/inhaler. The increased frequency of medicine intake will alert the patient and healthcare professionals about the severity of the patient's condition, suggest preventive measures, customize medication, and book doctor appointments [16].

A similar approach has been implemented for patients suffering from chronic kidney disease, which affects the society disproportionally and is costly to society; telenephrology was found to be effective for CKD patients where time and distance between patients and healthcare professionals are critical. Telenephrology is able to decrease the mortality rate in CKD patients who were isolated demographically from the renal health services. Small-scale trials of telenephrology were found to be successful in some states of the USA and Canada; however, large-scale studies are still lacking [17].

After the outbreak of the COVID-19 pandemic, the importance of smart health monitoring, telemedicine, and mobile health services has been globally realized. The Industry 5.0 and 5G technology have led to the emergence of WBAN and BAN sensors as well as devices that made the modern healthcare system possible [18–20]. The application of emerging mobile technologies has been shown in Figure 1.

The rigorous comparative analysis helps us to accurately select the model for different applications in medical as well as nonmedical fields. Thus, there is a need to review the recently emerging mobile technologies for their performance parameters such as energy, time, and memory consumption, as most of the frameworks are focused on WBAN sensors and devices whose performance capabilities are directly related to connectivity and available energy/power/battery. The present work summarizes the comparative studies of various mobile-based emerging technologies with their shortfalls and applications.

Thus, the review of recent emerging technologies in respect of energy and time consumption is required. The present work reviews the developments in recent mobile technologies, their application, and the comparative analysis of their performance parameters to explicitly understand the utility, capacity, and limitations. This will help to understand the shortcoming of the recent technologies for the development of better frameworks with higher performance capabilities as well as higher quality of services.

2. State-of-the-Art Review

The selection and optimization of the user-defined parameters are made for easy access. Smart healthcare involves a variety of parties, including physicians and patients, hospitals, and research organizations. It is a multifaceted organism that encompasses sickness prevention and monitoring, diagnosis and treatment, hospital management, health decision-making, and medical research. Smart healthcare is based on information technologies, including Internet of Things, mobile Internet, cloud computing, big data, 5G, microelectronics, and artificial intelligence, as well as modern biotechnology. These technologies are widely used in all aspects of smart healthcare. Chronic noncommunicable diseases are mostly spread in the elderly population, the hospitals cannot be able to provide quick services, and care seems to be difficult among them because most of the population are elder; hence, their care and treatment are challenging. This can be done by using the mobile-medical system, which uses effective data decision-making modules, wireless mobile communication, and deep learning model 2014, combined sparse autoencoders (CSAE). The CSAE algorithm is the best for the detection of patients' conditions; this is proved by the comparison between the four machine learning algorithms in terms of accuracy, sensitivity, and specificity, as shown in Figure 2. The experimental results have shown the superiority of the CSAE algorithm with accuracy and specificity of more than 85% and sensitivity not more than 75%.

Figure 2 shows that the use of CSAE and KNN is better than the use of other methods, proving the graphical representation with an accuracy of 93.03% and 91.66%, and NB and LDA show

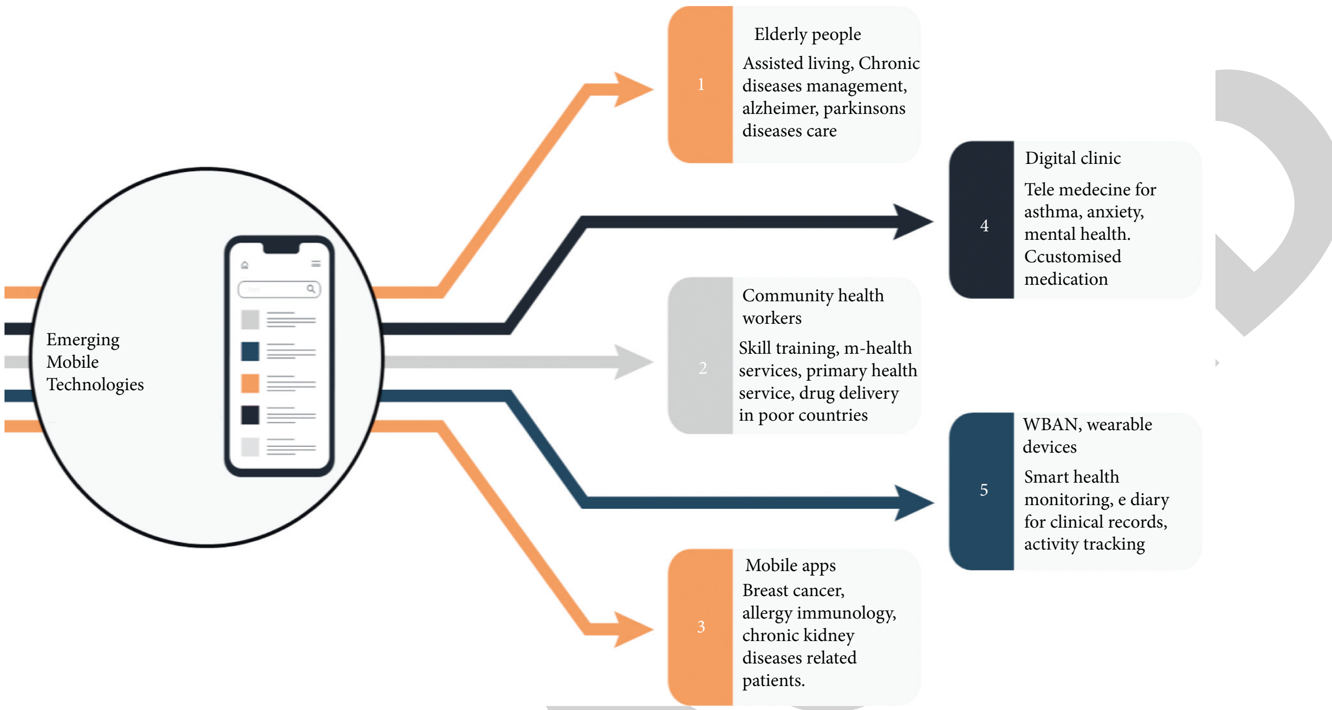

Figure 1: Applications of emerging mobile technologies in the medical field.

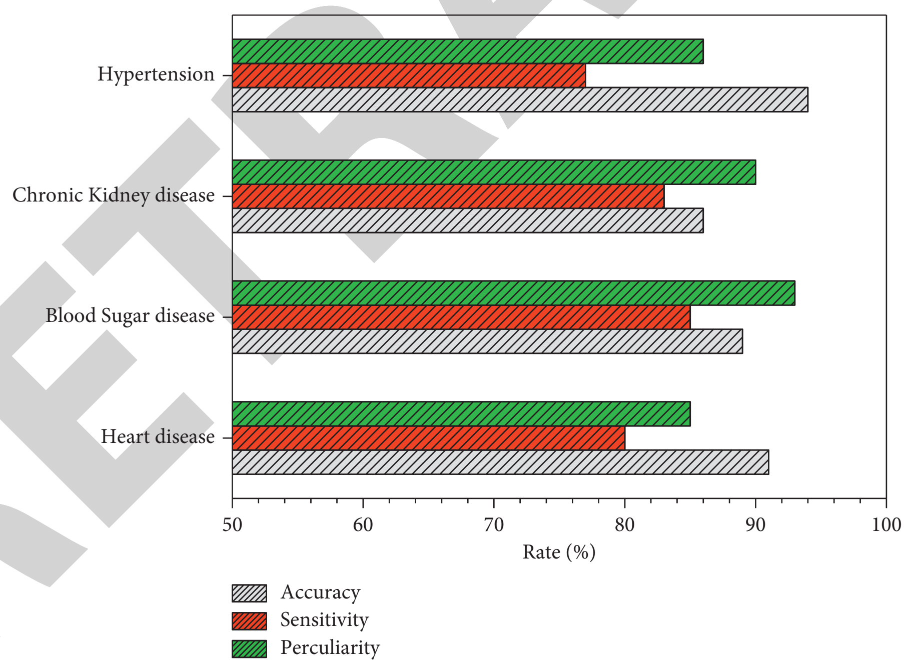

Figure 2: The performance indicator for four chronic diseases showing the second validation of the CSAE algorithm.

poor accuracy. Figure 3 shows the probability of exceeding standard values (gradual decline); exceeding the standard values indicates that the patients have multiple diseases. The accuracy of all algorithms is dropped by 30%. When multiple diseases are identified, the performance of algorithms is also most stable [3].

IoTs play a vital role in the detection of diseases and communication with medical staff with the help of Wi-Fi ZigBee, which are interconnected by various types of devices. Sometimes, during the communication, the smart devices undergo cyberattacks like insider attacks, DDoS, and so on, which are responsible for vulnerabilities. There are several programs that are developed to overcome these attacks because the extended Coverage GSm protocols emerge with wide frag mouth protocol into the IoMT sectors. This scalability of the security model is evaluated by increasing the security nodes and by observing time changes. The protocol

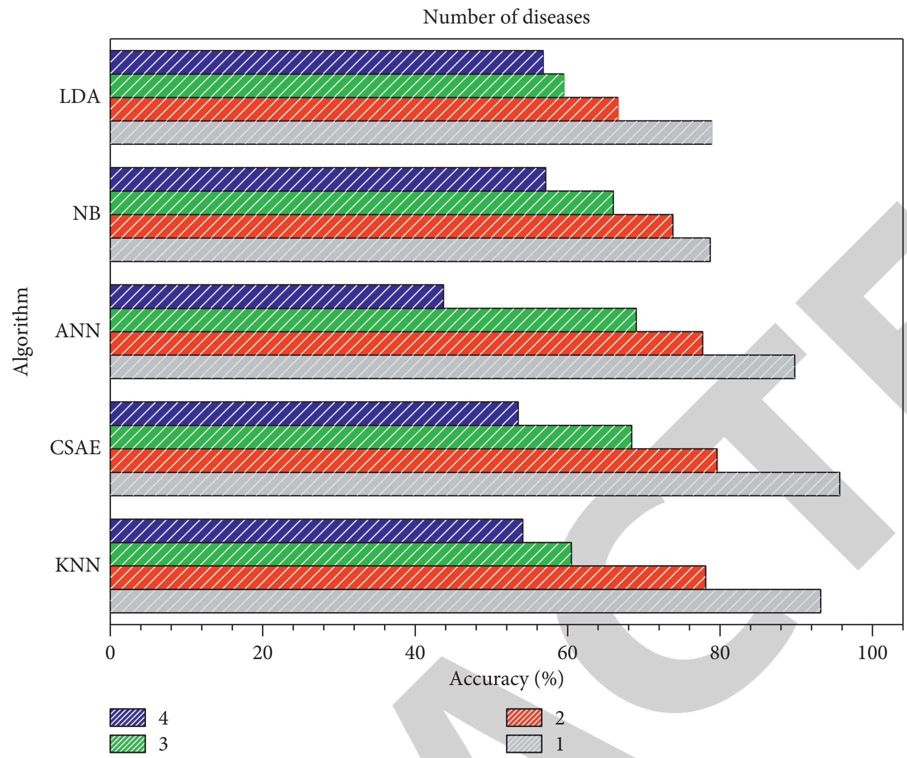

FIGURE 3: The comparative analysis of the accuracy performance of the proposed algorithm when the prediction of the number of diseases is varying.

EC-GSM helps increase the speed of response time for every single task. In Figure 4, it is shown that EC-GSM IoT consumes the minimum time of 423 ms to 2897 ms for up to 25 nodes. It shows that the wide-mouth frag protocol-based authentication schemes utilize less number of packets [21].

As we know about COVID-19, coronavirus disease is caused by the severe acute respiratory syndrome virus (SARS-CoV (2)), which is announced as a pandemic by WHO. During the pandemic, there were very few speculations about the disease. A mobile application has been developed to track COVID-19 symptoms. The COPE consortium was established to bring together scientists all over the world with expertise in the field of big data research and epidemiology of COVID-19 symptoms. The proposed method was implemented in the UK in March 2020 and was successful in the real-time collection of population-level data.

The time-domain-based biometric feature also plays an important role in IoTs-based healthcare devices. Some researchers collect data by applying mobile healthcare things. They are able to prove the security of these types of equipment, which also talks about the secure transformation of data from patients to doctors or medical staff. The IoTs are made up of various types of intelligent nodes which are interconnected with each other to visualize the data and for equations. The IoMTs are associated with many medical nodes and applications which are having the goal of providing better medical services.

There are many devices that transfer the patient's data through wireless communication, and therefore people are scared of security. According to the Health Insurance Portability and Accountability Act, wireless communications are responsible for providing the secure transformation of data from patients to medical staff. The IoTs consist of three layers, perception, network, and application. Figure 5 shows that the generated biometrics keys, which are formed from different subjects, can be used for security purposes. From Figure 5, we can say that the IoT-based healthcare protocols consume less time and energy [22].

Guo et al. have proposed a framework for efficient privacy promising mobile healthcare named FEEL-"federated edge learning system." The proposed framework is targeted to improve training efficiency, interference performance, and privacy protection. The edge-based training task offloading design has been evaluated for performance and comparative analysis with existing models. The proposed model helps to collect patient data from mobile and other WBAN devices and then process the data at a local hospital server instead of uploading the whole data to the cloud. This will help to reduce the burden of data security, and only processed information is uploaded to the cloud after the addition of noise to the data. The noise addition to the data prevents data misuse by unauthorized users. The implementation of the neural network at the edge servers helps in the training of patient data. The proposed framework has been evaluated for energy, memory, and time consumption with an increasing number of offload layers and presented in Figure 6.

As shown in Figure 6, the training time includes local training time, communication time, and third-party aggregations time. The gradual decreasing trend in time

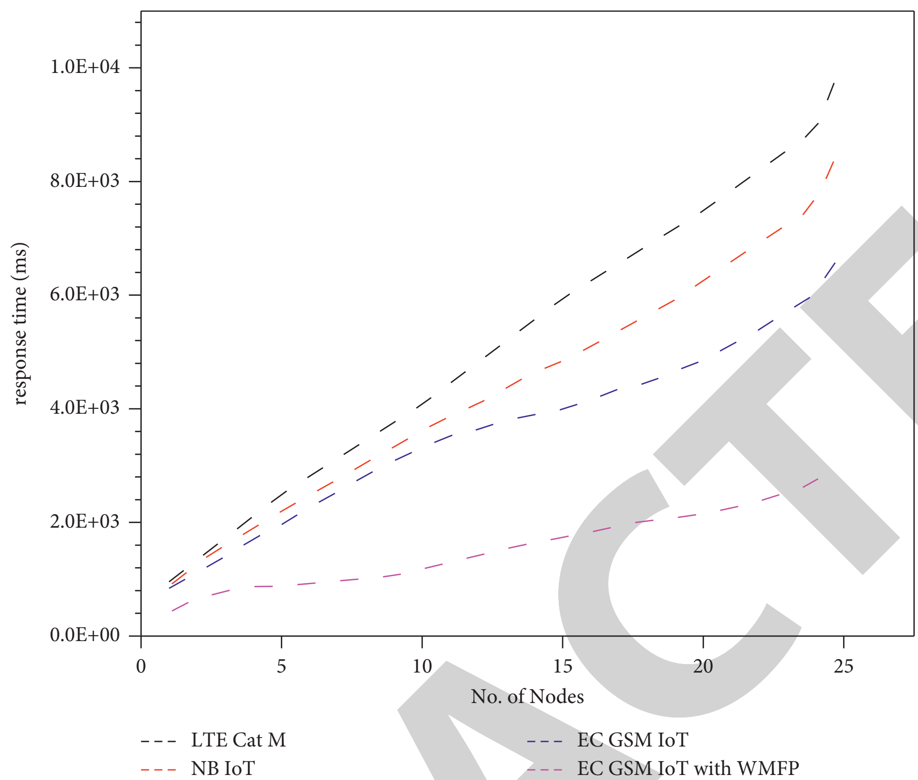

FIGURE 4: Scalability rate for a number of nodes.

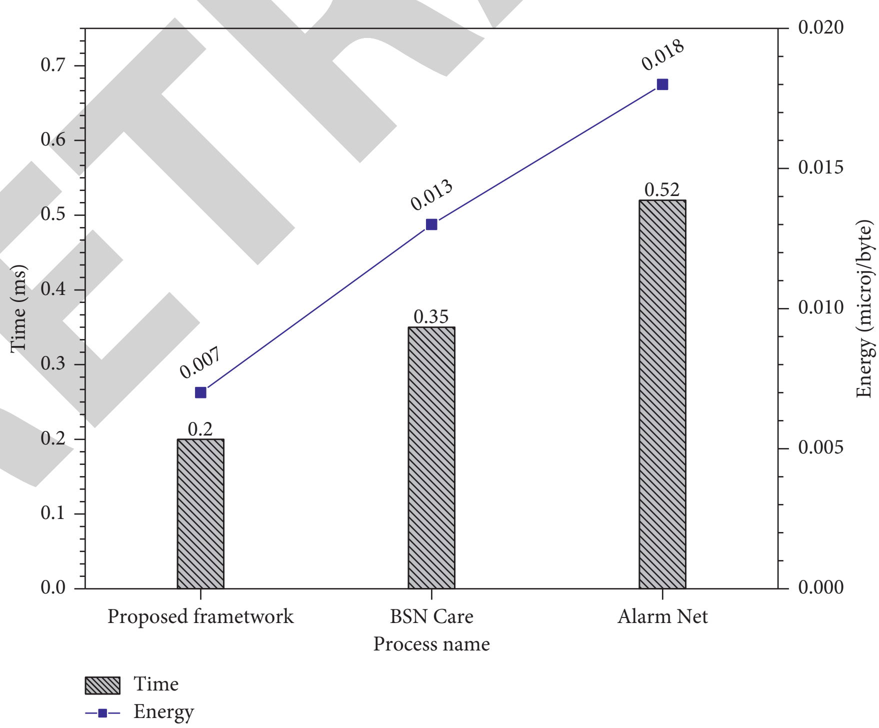

FIGURE 5: Total energy and time consumption comparison of the proposed framework with similar existing models.

consumption is observed with an increasing number of offloading layers. A similar trend is observed in energy and memory consumption. In the proposed network, only one offloading layer is directly connected to mobile devices, and the remaining are connected to servers which help in reduction in CPU consumption, memory, and energy by

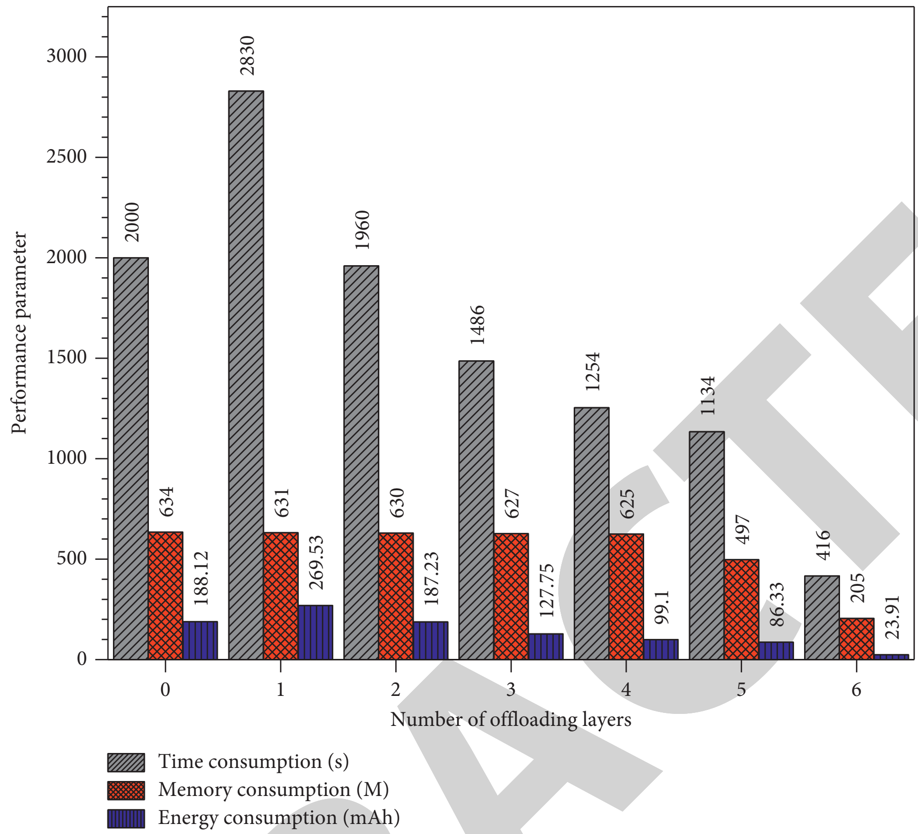

FIGURE 6: The variation of energy, time, and memory consumption with changing number of offloading layers for FEEL framework.

79.23%, 54.43%, and 51.4%, respectively, when compared to the conventional federal learning system along with improved accuracy and high data security [23].

In this modern era, advanced computing systems and mobile-based technologies inspired the development of cloud-based real-time health monitoring. There are some limitations of transfer of data of patient's health to the clouds, which is responsible for the latency consuming more time and energy. It can be reduced or overcome by using some algorithms fog-based computing systems in the healthcare system. This is based on the gigabit passive optical network (GPON) access network and energy-efficient fog computing model (EEFC), which is based on mixed-integer linear programming (MILP). Mohamad O.I. Musa et al. observed that 36% to 52% of energy is consumed. By this, we can also develop a real-time experimental heuristic, energy-optimized fog computing (EOFC) heuristic.

The use of EEFC minimizes the energy and time consumption; as shown in Figure 7, the energy consumption used in the processing of the EOFC heuristic is the same as that in the EEFC model. The energy consumption of both decreases as the ideal consumption decreases. This is due to the domination of energy consumption of networking equipment. Figure 7 also shows the comparison of energy savings between both models, which shows that the energy consumption of the model decreases from 83.1% to 0.3% when increasing the percentage reduction of ideal power from 0% to 100% [24].

As we know, mobile applications and wireless communications are more prominent nowadays and increase the use of IT and increase the cyberspace. This is expected to increase in the future, and in this pandemic, IoMT is a necessity for the coming days; hence, cybersecurity is basically assumed to be a challenge.

The data of patients are very sensitive and need protection from cyberattacks. For example, the government of the US establishes the data security act, Health Insurance Portability and Accountability Act (HIPPA ACT 2020). There are many healthcare industries that are unable to accept healthcare cybersecurity by increasing the trends of cyberspace, fraud, theft, and cyberattack. In Figure 7, the author shows the comparison of energy consumption in the author's protocol with others. The energy consumption by using the AES algorithm is 1.21 microjoule/byte. Figure 7 clearly shows the scheme outperformance from others based on the same platform, which is effective in securing the patient`s confidential data [25].

For the improvement in chronic diseases diagnosis, the mobile healthcare system provides bilateral solutions, also offers the real-time monitoring of chronic diseases, and

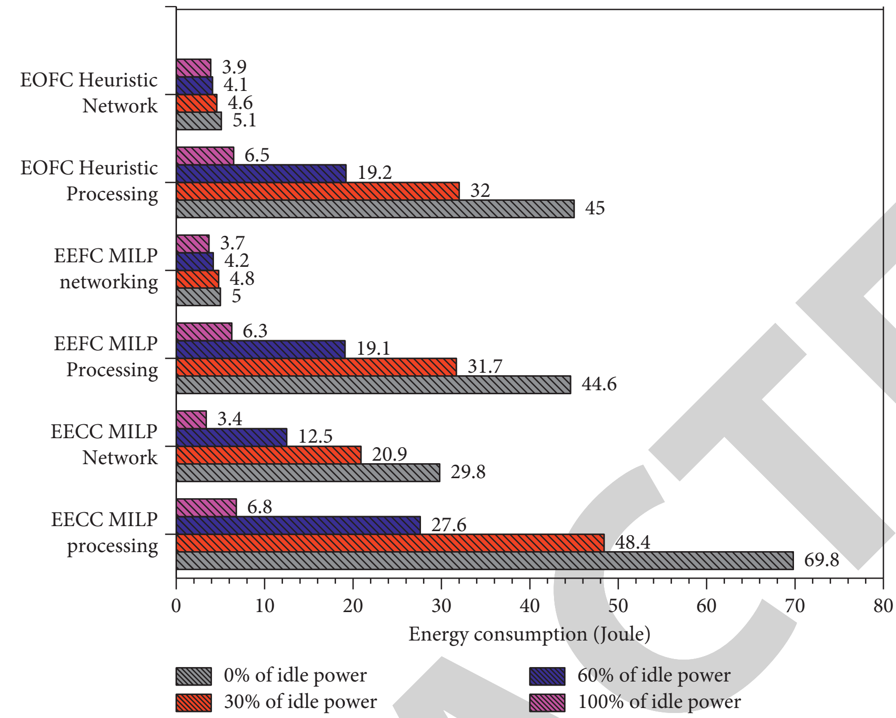

Figure 7: Energy consumption of various equipment and processing of EECCC model, EEFC model, and EOFC heuristic with various idling conditions.

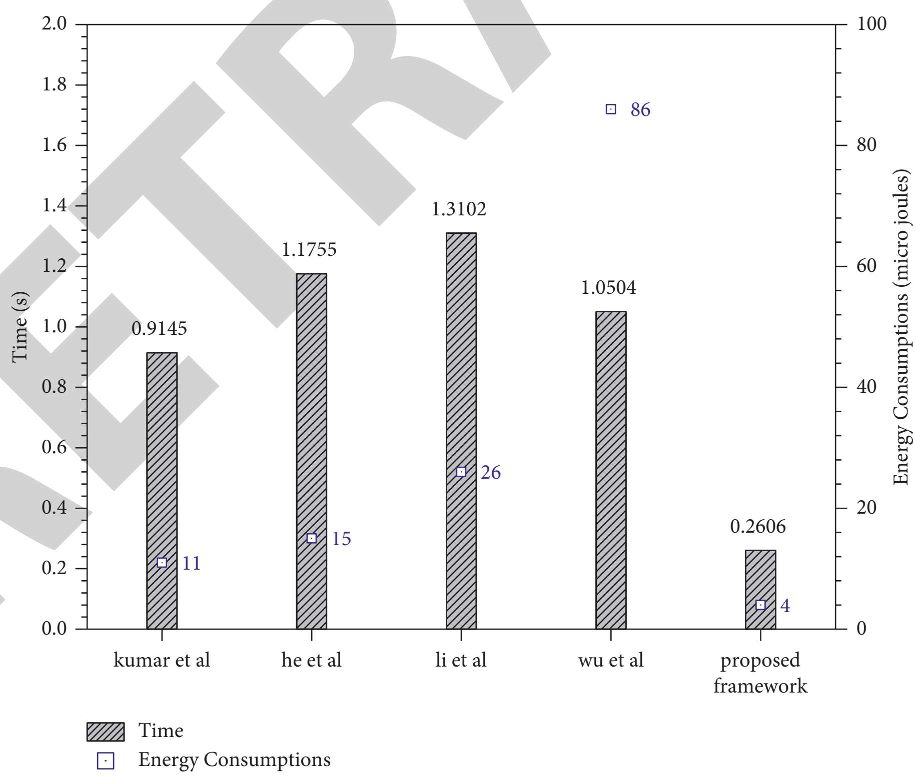

Figure 8: Energy and time consumption comparison for various models with the proposed model during login and authentication model.

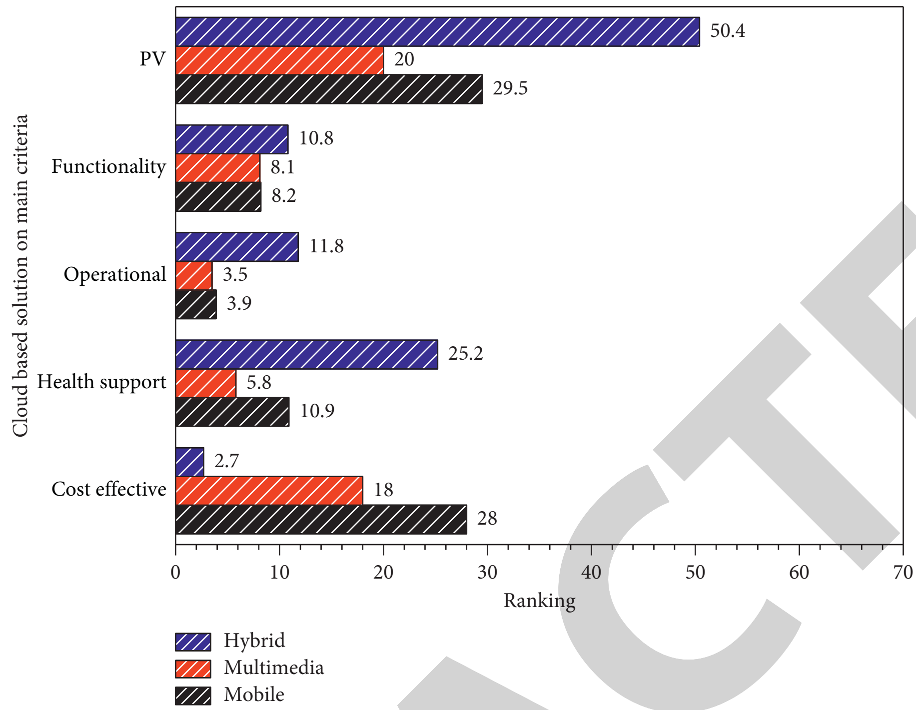

Figure 9: Ranking of cloud-based solutions for various platforms based on the main criteria.

helps to support the maintenance of a healthy lifestyle and immediate diagnosis of health conditions. Figure 8 shows the solution based on the cloud and shows how the framework is suitable and has higher priority vectors.

Figure 9 also shows the weakness and strengths of every solution. The strength of the hybrid solution is located in between the support factors. Qurishi et al. at least have focused on two things—the first is the development of the architectural framework and the second one is the development of new evolutionary models—and focused on developing the best solution for decision-making which is based on multimedia decision-making methods (MCDM) which are also known as analytical hierarchy process (AHP). With the help of graphical representation, there is a try to find the best results by using the best hybrid frameworks, and it is observed that the AHP method is the best method to solve the problems [10].

Smartphones play a pivotal role in the detection of daily life human activities of patients, especially old, aged, and children. According to the survey of some researchers in this modern era, the number of deaths or mortality rate with chronic diseases increases because the elder ones prefer to live alone. Therefore, it is necessary to provide care for them, which is possible through the detection of daily activities using some wearable smart devices or smartphones, and by applying human activity recognition (HAR) algorithms; however, the HAR algorithm lacks classifying accuracy, which requires high computation.

Group-based context human activity recognition (GCHAR) has been implemented for achieving high accuracy without requiring high computation. GCHAR system is made up of two different stages, trading stage and classifying stage, which is further trifurcated into three categories; the first is sensing and processing, the second is feature extraction, and the third is group-based context-aware method. GCHAR algorithm is able to recognize the accurate activities as shown in Figure 10, in which the value of GCHAR for each activity is accurate when compared with other algorithms. This is the proof of the accuracy of GCHAR for each daily activity, and the KNN algorithm achieves the second highest rank. The recognition of human activity by using the GCHAR algorithm is able to recognize and advance in the overall performance and real time. This is due to the use of a two-level hierarchical model, which can improve classification accuracy [26].

Jongs et al. have given information about the use of mobile technologies in the study of biological mechanisms, metabolism, human behavior, phenotypic and genotypic characters, brain activity pattern, brain structures, and so on. For better performance of these Android functions, they used various protocols. The assessments are near to real-time conditions.

Hussian et al. have proposed the security among mobile health applications and the protection of privacy of users, which is possible by the use of a framework that provides security policies. The framework is composed of two different layers: the security module layer (SML) and the system interface layer (SIL). The framework is based on effectiveness and efficiency. The effectiveness is evaluated by the presentation of the framework in contrast to the security attack, and efficiency is evaluated by the comparison of performances such as memory, energy consumption, and CPU utilization. Due to highly advanced working and capabilities, smartphones replaced computers, as shown in Figure 11.

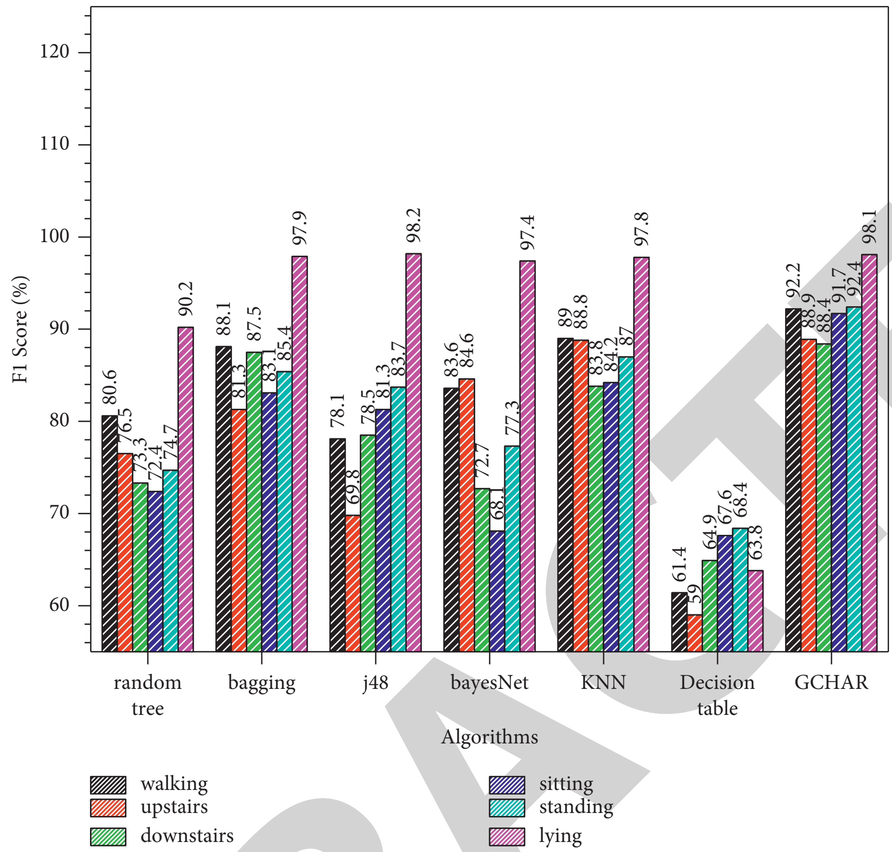

Figure 10: Comparison of F1 score for various activities among GCHAR and other algorithms.

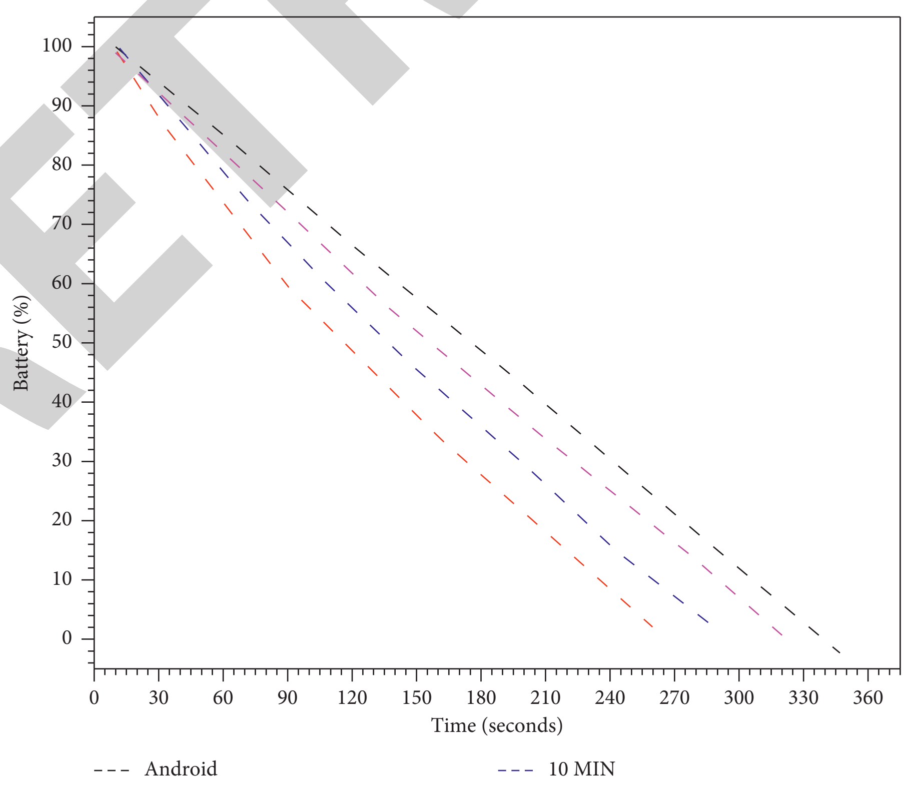

Figure 11: Comparison of device battery consumption when checking the context update.

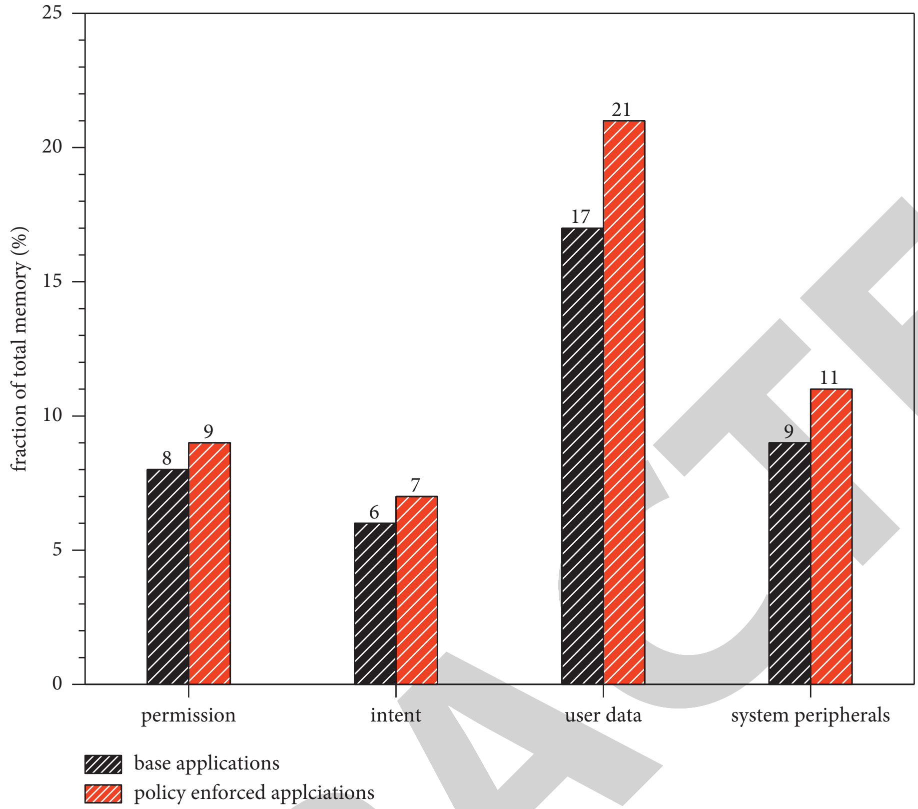

Figure 12: Total memory overhead comparison with and without MASF algorithm.

According to some specialists, the Android operating system is at the topmost position, it has a market share of more than 85%, and more than 3.5 million mobile applications are available on Google Play. Out of them, many applications have emerged in the medical field. Hussian et al. projected the use of the mHealth apps security framework (MASF), which has been added to the system and provides security from data threats, DNB attacks, data leakages, and so on. Figure 12 shows the experimental proof about the use of MASF against cyberattacks that is very effective.

It also gives fruitful results in other terms such as time, energy consumption, and memory usage. It can prove that the framework MASF is compatible with both the Android ecosystem and the healthcare community. This is due to the fact that it is incorporated into the Android system with minimal changes [27].

3. Conclusion and Future Scope

Various emerging mobile bases technologies, their application domain, and framework have been discussed thoroughly with the application domain and application range, along with their limitations. This work focuses on the performance parameters of the proposed framework as most of them deal with WBAN sensors and devices where power consumption and energy-based performance are major constraints. The rigorous comparative analysis helps us to accurately select a model for different applications in the medical as well as nonmedical filed. The latency issue and time consumption of the various emerging frameworks have been analyzed and compared with other similar models. The comparison of the various models and frameworks has been made on various platforms, which needs more standardization. However, the availability of several functions can sometimes make a system difficult to use and discourage healthcare workers from learning how to use it. The thorough review of the emerging mobile-based technologies helps to lay the foundation and benchmark for future research to develop more efficient models, frameworks, and algorithms and achieve higher performance capabilities as well as better quality of services.

Data Availability

The data used to support the findings of this study are available from the corresponding author upon request.

Conflicts of Interest

The authors declare that there are no conflicts of interest regarding the publication of this paper.

References

[1] J. Fang, "Health data at your fingertips: federal regulatory proposals for consumer-generated mobile health data," *Georgetown Law Technology Review*, vol. 4, no. 125, 2019.

Hindawi
Journal of Healthcare Engineering
Volume 2023, Article ID 9892756, 1 page
https://doi.org/10.1155/2023/9892756

Retraction

Retracted: Curative Effect of Foraminal Endoscopic Surgery and Efficacy of the Wearable Lumbar Spine Protection Equipment in the Treatment of Lumbar Disc Herniation

Journal of Healthcare Engineering

Received 3 October 2023; Accepted 3 October 2023; Published 4 October 2023

This article has been retracted by Hindawi following an investigation undertaken by the publisher [1]. This investigation has uncovered evidence of one or more of the following indicators of systematic manipulation of the publication process:

(1) Discrepancies in scope
(2) Discrepancies in the description of the research reported
(3) Discrepancies between the availability of data and the research described
(4) Inappropriate citations
(5) Incoherent, meaningless and/or irrelevant content included in the article
(6) Peer-review manipulation

The presence of these indicators undermines our confidence in the integrity of the article's content and we cannot, therefore, vouch for its reliability. Please note that this notice is intended solely to alert readers that the content of this article is unreliable. We have not investigated whether authors were aware of or involved in the systematic manipulation of the publication process.

In addition, our investigation has also shown that one or more of the following human-subject reporting requirements has not been met in this article: ethical approval by an Institutional Review Board (IRB) committee or equivalent, patient/participant consent to participate, and/or agreement to publish patient/participant details (where relevant).

Wiley and Hindawi regrets that the usual quality checks did not identify these issues before publication and have since put additional measures in place to safeguard research integrity.

We wish to credit our own Research Integrity and Research Publishing teams and anonymous and named external researchers and research integrity experts for contributing to this investigation.

The corresponding author, as the representative of all authors, has been given the opportunity to register their agreement or disagreement to this retraction. We have kept a record of any response received.

References

[1] Z. Meng, J. Zheng, K. Fu, Y. Kang, and L. Wang, "Curative Effect of Foraminal Endoscopic Surgery and Efficacy of the Wearable Lumbar Spine Protection Equipment in the Treatment of Lumbar Disc Herniation," *Journal of Healthcare Engineering*, vol. 2022, Article ID 6463863, 12 pages, 2022.

Hindawi
Journal of Healthcare Engineering
Volume 2022, Article ID 6463863, 12 pages
https://doi.org/10.1155/2022/6463863

Research Article

Curative Effect of Foraminal Endoscopic Surgery and Efficacy of the Wearable Lumbar Spine Protection Equipment in the Treatment of Lumbar Disc Herniation

ZhaoWu Meng, JinYang Zheng, Kai Fu, YiZhao Kang, and Liang Wang

Sunshine Union Hospitai,Spinal Surgery, Weifang, Shandong 261000, China

Correspondence should be addressed to Liang Wang; 201904217133@stu.zjsru.edu.cn

Received 28 January 2022; Revised 11 February 2022; Accepted 12 February 2022; Published 25 March 2022

Academic Editor: Liaqat Ali

Lumbar disc herniation is a common and frequently-occurring disease in pain clinics. The incidence rate of affliction is increasing with every passing year. Besides the aged, young people also suffer from long-term pain, which not only affects their daily routines but may also lead to serious impairment. The causes of chronic low back and leg pain caused by lumbar disc herniation are mainly related to mechanical compression, the adhesion of epidural space, intervertebral space, and aseptic inflammatory reaction. The treatment of lumbar disc herniation should follow the principle of step-by-step treatment. An appropriate treatment scheme needs to be adopted according to the patient's condition. About 80% of patients received nonsurgical treatment to get relief from the pain symptoms. However, 10% to 15% of patients still need traditional open surgery. Spinal foraminal surgery is a new method for the treatment of lumbar disc herniation, lumbar surgery failure syndrome, and lumbar spinal stenosis. However, there are only scattered clinical reports on the efficacy of spinal foraminal surgery. Based on it, this paper proposes a method to explore the efficacy of spinal foraminal mirror surgery in the treatment of lumbar disc herniation. Besides, postoperative wearable lumbar protective equipment is proposed to ensure a seamless rehabilitation effect on the patients. Statistical analysis performed using a t-test revealed that there was a significant difference between the visual analog scales (VAS) scores of the two groups after 3 and 6 months of treatment ($P < 0.05$). The paper analyzes and summarizes the cases with definite and poor curative effects, which not only provides the basis for clinical practice but also paves the way to multicenter clinical research.

1. Introduction

Pain is a signal of human body damage or disease invasion. Pain is considered one of the factors affecting the routine mode of living. It is also the main reason for patients to see a doctor and the main complaint of the first diagnosis. As a symptom, chronic pain has attracted great attention all over the world [1]. The world pain conference defined pain as "the fifth vital sign of mankind" after respiration, pulse, body temperature, and blood pressure. 80% of adults have experienced low back and leg pain. The incidence rate of lumbar disc herniation is 7.62% in China [2]. The proportion of surgical treatment for lumbar disc herniation in China has reached 0.12%. Likewise, the incidence rate of affliction is on the rise. The cost of treatment increases economic burdens and may lead to depression in patients and families. Anxiety and bad mood caused by pain seriously affect the work and life of patients [3].

The mechanism and etiology of lumbar disc herniation include the mechanical stimulation of nerve endings outside the fibrous ring, direct compression of nerve roots, and inflammatory stimulation induced by the compression of the nucleus pulposus [4]. It results in a series of symptoms, such as radiation pain. Other studies have shown that it is related to autoimmunity, smoking, gender, obesity, weight-bearing degree, and other factors. The treatment of lumbar disc herniation follows the principle of step-by-step treatment. Conservative treatment should be considered in the early stage [5]. If the formal treatment is ineffective or the symptoms are aggravated, minimally invasive treatment or open surgery should be considered. Of course, the surgical effect is the most accurate one. Because of the relatively large surgical incision, more muscle stripping and more bone tissue resection may destroy the stable structure of the spine. The treatment cycle of affliction is relatively long, which most of the patients find difficult to follow [6].

There are many surgical methods for the treatment of lumbar disc herniation, which can be summarized as traditional open surgery and minimally invasive surgery. The laminectomy and decompression of the nucleus pulposus with traditional open surgery is still a common surgical method in clinics. However, compared with minimally invasive surgery, open surgery causes greater trauma and damage to the posterior column of the spine [7]. Although the decompression range is larger than minimally invasive surgery, it can lead to nerve root adhesion. Because of the large wound and scar formation, the surgery takes a longer time in postoperative recovery, besides other complications [8]. With the progress of science and technology, the concept of minimally invasive surgery has been enhanced and has attracted the research community. Therefore, surgeons will have more consideration in the choice of surgical methods. With the rapid development and wider adaptation of technology, minimally invasive technology with less intraoperative and postoperative complications has become possible. With rapid postoperative recovery, little trauma, and less harm to spinal stability, minimally invasive technology is favored by surgeons and patients [9]. At the same time, with the continuous improvement of minimally invasive surgery technology, its scope of adaptation is also expanding, which can be well-applied to clinical practice. Hence, in recent years, minimally invasive surgery has been applied in clinics, and the promising results of the method have been reported in the treatment of lumbar disc herniation [10]. The schematic diagram of the lumbar intervertebral disc is shown in Figure 1.

Foraminal endoscopic surgery is a minimally invasive approach that preserves the multifidus muscle and delays the need for fusion. Unlike open surgery, the approach treats foraminal stenosis and requires only a small incision for the operation.

This paper presents a method to explore the curative effect of foraminal endoscopic surgery in the treatment of lumbar disc herniation. The original data are analyzed by the machine learning algorithm, and the curative effect analysis results are obtained. The research studies the wearable lumbar protective device after operation to further ensure the rehabilitation effect of the patients. Subsequently, the paper summarizes and analyzes the cases with definite and bad curative effects. The experimental results have laid a foundation for clinical research.

The remaining of the paper is organized into 5 sections. Section 2 deals with the literature review. Details about the efficacy methods are presented in Section 3. The design and application of the wearable lumbar spine protection device are elaborated in Section 4. In Section 5, the experimental method is discussed with numerical findings and analysis. The last section, Section 6, is about the conclusion and future work.

2. Related Work

Low-back pain (LBP) is a prevailing affliction. It is reported that about 2 to 3 of adults suffer from LBP [11, 12]. The patients face difficulties to maintain healthy a lifestyle. According to [13], lumbar flexion and rotation are major causes of LBP. Though one of the main causes of LBP is lumbar disc herniation (LDH), 10-year research is necessary for the surgical approach to gain widespread popularity [14]. Details about the pain and treatment methods of LDH are discussed in the following subsections.

2.1. Research Status of Pain Mechanism of Lumbar Disc Herniation. Lumbar disc herniation is a low back and leg pain disease characterized by the degenerative changes of the lumbar disc, the rupture of the fibrous ring, the protrusion of the nucleus pulposus, and the stimulation or compression of the nerve root. Other causes include inflammatory reaction, low back pain, and radiation pain of the lower limb sciatic nerve under the action of external force [15]. The pain-causing mechanism of lumbar disc herniation is mainly related to the mechanical compression theory, inflammatory chemical stimulation theory, and autoimmune theory. The patient's bad mood, excessive body mass index, smoking, educational level, and blood circulation disorder may also be the causes of pain [16].

The theory of mechanical oppression comes first in the discussion of lumbar disc impairment. The lumbar intervertebral disc is composed of the fibrous ring and the nucleus pulposus. The fibrous ring is tough because of type I collagen. The nucleus pulposus has type II collagen and rich proteoglycan. Hence, it has good elasticity and fluidity under normal conditions. The prone lumbar segments are L4 ~ 5 and L5 ~ S1, accounting for more than 90% of the whole section. These two segments are located at the lumbosacral junction, with high mobility and high pressure [17]. Nerve root compression is the main cause of chronic pain in the lower limbs. As the spinal nerve root lacks the protection of the nerve sheath, slight compression will have obvious compression symptoms. With the extension of compression time, the normal metabolism of the nerve root is destroyed, and thus, the pain symptoms are obvious [18]. Yet, there is another theory, i.e., the theory of inflammatory chemical stimulation. Nerve roots compressed by the surrounding tissues are more likely to induce pain than the noncompressed nerve roots. Some nerve roots are not compressed. In such cases, patients have the symptoms of lower limb pain [19]. Oral nonsteroidal anti-inflammatory drugs or hormones can alleviate the pain, suggesting that chronic lower limb pain in patients with lumbar disc herniation is related to inflammatory response stimulation. This inflammation is not caused by pathogenic microorganisms like bacteria, however, aseptic inflammation is caused by ischemia or immunity. Long-term inflammation will inevitably produce fibrosis, leading to extensive tissue adhesion in the epidural space [20]. Finally, it is pertinent to discuss the immune response theory. The immune response theory of lumbar disc herniation holds that the extract of the intervertebral

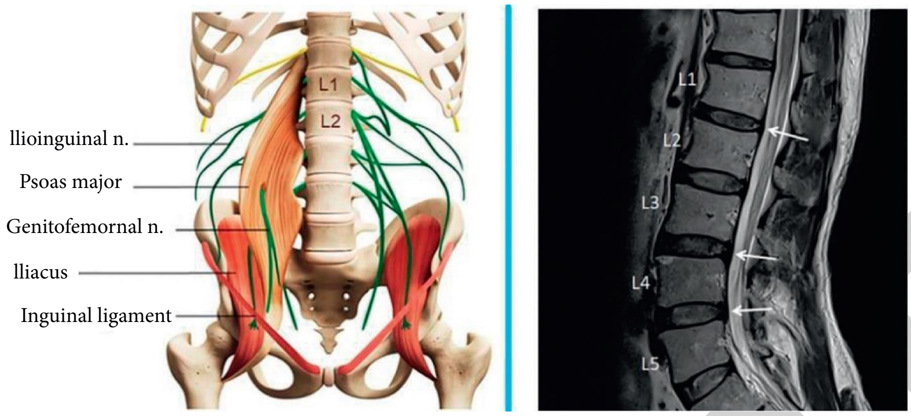

Figure 1: Schematic diagram of the lumbar intervertebral disc.

disc tissue has immunogenicity. Under normal circumstances, the nucleus pulposus tissue is wrapped in the annulus fibrosus. However, when the annulus fibrosus is broken, the nucleus pulposus protrudes from the disconnected position of the annulus fibrosus and even falls out of the annulus fibrosus [21]. The body considers the detached nucleus pulposus as "alien" and produces an immune response. The degree of immune response is positively correlated with the degree of the rupture of the annulus fibrosus and the prolapse of the nucleus pulposus [22]. The degree of pain is also related to the severity of the immune response. When the nerve without inflammation is simply compressed, its feeling and movement will be affected, however, there will be no pain. Only when the nerve with inflammatory stimulation is mechanically compressed, there will be pain. It can be seen that the autoimmune response plays an important role in chronic lower limb radiation pain [23]. The main factors of lumbar disc herniation are shown in Figure 2.

As observed in Figure 2, the main factors of low back and leg pain caused by lumbar disc herniation are mechanical compression, epidural adhesion, and inflammation. The compression of nerve roots plays an initiating role in the pain of patients with LDH, activating inflammatory chemical stimulation. Inflammatory stimulation leads to epidural adhesion, and epidural adhesion causes inflammatory stimulation and pain.

2.2. Research Status of Diagnostic Methods of Lumbar Disc Herniation. The diagnosis of the herniated lumbar disc (HLD) is rarely difficult and complicated. It can be diagnosed according to the patient's symptoms, positive signs, and imaging examination. Positive straight leg raise (SLR) test, sensory segmental pain, hypoesthesia, hyporeflexia or disappearance, and decreased muscle strength are some of the symptoms [24]. HLD can be diagnosed if three of the four criteria are met. The pain characteristics of HLD are as follows: the sensory changes and muscle strength changes of lower limb pain are consistent with the distribution characteristics of the nerve root segments. The cauda equina syndrome is an indication for immediate surgery. CT: in the past, it was considered that computed tomography (CT) was inferior to magnetic resonance imaging (MRI) in the diagnosis of HLD. CT discography can replace MRI in the diagnosis of lumbar disc herniation [25]. X-Ray film: it is a necessary examination for the diagnosis of HLD. It is recommended to give hyperextension and hyperflexion examination on the basis of frontal and lateral position to evaluate the stability of the lumbar spine.

Research shows that the results of CT and MRI are not positively correlated with the clinical symptoms of patients. Imaging suggests that the severity of HLD is serious; however, the pain symptoms of patients are not obvious, or there is no pain performance. Some patients have severe pain symptoms; however, the results of CT and MRI suggest that the severity of HLD is not obvious [26]. In [27], an SLR is performed to compare the efficacy of various treatment methods followed for lumbar disc herniation. The meta-analysis showed that lumbar discectomy LD is more effective than conservative care CC in treating herniation.

2.3. Treatment of Lumbar Disc Herniation. With the rapid development of China's economy and the popularization and improvement of medical insurance and rural cooperative medical care policies, people pay more attention to health. As a common disease, low back has attracted medical practitioners and researchers to treat low back and leg pain with a low cost and few side effects [28].

The early stage of HLD is mainly conservative treatment. It mainly includes bed rest, manual therapy, drug therapy, patient education, physical therapy, and nerve block. The traditional view is that bed rest is an effective treatment for both acute and chronic lumbar disc herniation. If conditions permit, they should be encouraged to go to the ground early. The curative effect of the patients is better than that of the nonexercise group. Patients with high exercise frequency and lower frequency of exercise have lower incidence rate of pain. Lumbar traction is effective in the treatment of sciatica [29]. The two methods can reduce the incidence of sciatica.

An epidural injection is a short-term outpatient operation, which can be carried out in doctors' clinics, hospitals, or surgical centers. It is highly effective and is a relatively safe and effective nonsurgical treatment option. One of the signs of success of epidural puncture depends on the sense of

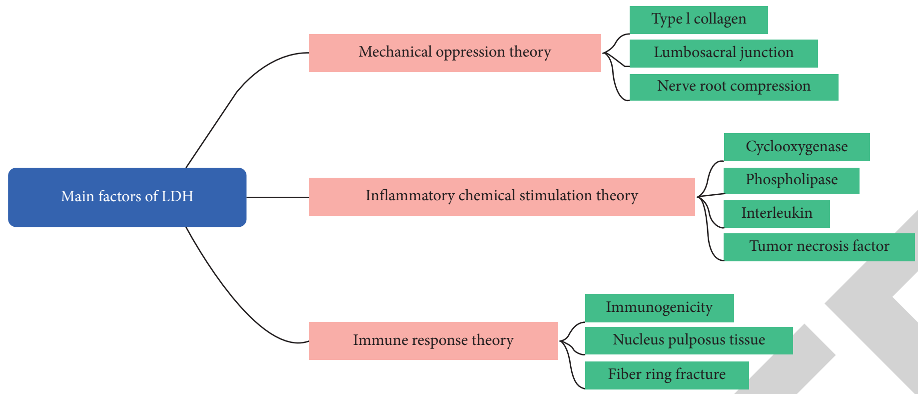

Figure 2: The main factors of lumbar disc herniation.

breakthrough. However, 30% of epidural puncture has no sense of the disappearance of resistance. Hence, imaging should be used to assist in positioning [30]. The needle entry path of epidural injection is carried out through the sacral hiatus approach, lamina space approach, and intervertebral foramen approach. The puncture through the sacral hiatus path is relatively easy to succeed and relatively safe. Its disadvantage is that the injection dose is the largest, usually 10 ml to 20 ml [31].

With the continuous development of clinical minimally invasive technology and the continuous improvement of imaging technology, the treatment of lumbar disc herniation is no exception. Clinicians pay more attention to minimally invasive treatment. Minimally invasive treatment methods are continuously improved [32]. Its advantages include small injury, fast postoperative recovery, and imaging guidance. Minimally invasive technology is suitable to accurately locate and improve the curative effect. Therefore, some patients can avoid the risk of open operation. Currently, minimally invasive treatment is performed through one or several small incisions through a percutaneous puncture or spinal endoscopy. Percutaneous transluminal endoscopic discectomy is a minimally invasive treatment that is widely used in clinical practice [33]. Surgical operation with microsystem has the advantages of short operation time, less intraoperative bleeding, rapid recovery, significantly shorter hospital stay, and higher pain relief rate of patients after hand surgery. The recurrence rate of postoperative pain within one year is between 2% and 10%. However, the technical route of the intervertebral foraminal mirror is steep, which has high requirements for the operator's technology, operating room machinery, and operating room environment [34]. A number of treatment approaches have been proposed so far in the literature. In the study [35], M. S. Kabil studied the far lateral lumbar disc herniation of 33 patients. The outcomes of the study suggest that the microendoscopic approach is safe and effective for treating back pain and lower limb symptoms. Waters et al. used the mathematical approach to estimate the LBP risks in manual lifting tasks [36], whereas assessed the risks factors involved in industries [37]. With EMG signals [38], the lumbar vertebrae pressure is computed during lying, sitting, and walking [39]. With lightweight bend sensors, Milea measured joint motion [40]. Some studies suggest the multimodal approach to treating LDH, including anti-inflammatory medications and physical therapy [41]. The research of Kim et al. compared the common treatments and preferred nerve injections [42] for affliction.

Tumor necrosis factor-alpha (TNF-α) is another widely used clinical treatment [43]. According to [44], TNF-α is effective in treating the sciatica of LDH patients. Intradiscal injection, however, has no benefit in such cases [45]. Thackeray et al. evaluated the profile of patients utilizing formal PT and their outcomes [46].

3. Efficacy Evaluation Method

This section, firstly, introduces the relevant theoretical knowledge of efficacy evaluation, and then the basic mathematical principle of support vector machine (SVM) is introduced. Following that, a method of efficacy evaluation of intervertebral foraminal endoscopic surgery for lumbar disc herniation based on SVM is discussed.

3.1. Correlation Theory. As a subjective discomfort, pain can usually clarify the location, nature, onset time, and inducement of pain. However, the severity of pain is an important reference index for assessing pain treatment. The key issue is how to measure subjective pain with objective indicators. Patients can evaluate themselves by representing different types of sensory scales. These methods are simple, feasible, and reliable. In clinical research, visual analog scales (VAS) are a measurement tool commonly used in pain assessment. However, the reliability of using it alone in pain research has been questioned by scholars. The Oswestry disability index (ODI) is a widely used low back pain evaluation index. The scoring table includes 10 observation items, including the degree of low back pain and leg pain, personal life and cooking, lifting heavy objects, walking, sitting, standing, sleeping, sexual life, social life, travel, etc. Each item is divided into 6 options from normal to abnormal, and the corresponding score of each option is from 0 to 5. Patients can choose according to their own situation and add the scores of 10 options. The calculation method of ODI score is given as follows:

$$\mathrm{ODI} = \frac{\text{Actual Score}}{5 \times \text{Number of questions answered}} \times 100\%. \quad (1)$$

The lower the score percentage, the better the functional status, and the higher the score, the worse the functional status.

Patients' global impressions of change (PGIC) can reflect whether the patients' subjective pain is alleviated after the intervention of pain treatment. It can respond to the changes in the intensity and nature of subjective pain. It can also eliminate the patient's subjective misunderstanding that the reduction of pain is the improvement of the disease. According to the improvement of patients' condition, PGIC is divided into "1" for obvious improvement, "2" for slight improvement, "3" for no change, and "4″ for pain plus reuse. Patients with chronic low back and leg pain suffer from pain for a long time, and their work and life are affected to varying degrees. In the clinical study of chronic low back and leg pain, it is necessary to evaluate the changes of pain in combination with the patients' overall feeling and satisfaction with the treatment. The reason is that some research on the treatment of pain only aims to observe the changes of pain, however, it cannot treat the disease itself. Therefore, PGIC was selected as the evaluation standard for the efficacy of the two methods in the treatment of lumbar disc herniation. Then, the sample size estimation algorithm is introduced. Based on the difference test of two independent sample rates, the sample size calculation formula is as follows:

$$n_1 = \frac{\left[Z_{1-a/s}\sqrt{\overline{\pi}(1-\overline{\pi})(1+1/\gamma)} + Z_{1-\beta}\sqrt{\pi_1(1-\pi_1)+\pi_2/\gamma(1-\pi_2)}\right]^2}{(\pi_1-\pi_2)^2/\gamma}. \quad (2)$$

Among them, γ is the proportion of the sample size of the two groups, $n_1 \colon n_2 = \gamma$. $\overline{\pi}$ is the weighted average rate of two samples, and π_1 and π_2 are the two population rates, respectively. Z is the normal distribution. The research flow of the experiment is shown in Figure 3.

SPSS 21.0 was used for the statistical analysis of data. The measurement data are expressed by mean and standard deviation. The general data of the two groups were analyzed by chi-square test and analysis of variance. Paired t-test was used for intragroup comparison. Two independent sample t-tests were used for comparison between groups. The other measurement data were compared between groups by an independent sample t-test. The chi-square test was used to compare the gender composition ratio. The proportion of ineffective cases decreased the muscle strength, and hypoesthesia in the ENP group was tested by Fisher's exact test. The proportion of ineffective cases decreased the muscle strength, and hypoesthesia in the TFSI group was tested by approximate chi-square test. The test levels were all $P < 0.05$, with a statistical difference.

3.2. Efficacy Evaluation Method Based on SVM. The development of SVM theory is relatively mature. The SVM theory minimizes structural risk. Moreover, it can take into account the training ability and generalization ability. Moreover, it has very obvious advantages in solving the problems of nonlinearity, local minimum, small samples, and high dimension. It can be said that support vector machine provides a basic framework for machine learning. The basic principle of SVM is depicted in Figure 4.

When extending linear SVM to nonlinear SVM, we need to extend the linear partition to a general linear partition. Set the original training set as follows:

$$T = \{(x_i, y_i), (i = 1, 2, \ldots, l)\} \in (R^n \times y)^l. \quad (3)$$

Then, spatial transformation is introduced, which is given as

$$\begin{aligned} \Phi\colon R^n &\longrightarrow H, \\ x &\longrightarrow z = \Phi(x). \end{aligned} \quad (4)$$

After transformation, the training set T becomes

$$T_\Phi = \{(z_i, y_i), (i = 1, 2, \ldots, l)\} \in (H \times y)^l. \quad (5)$$

The linear partition hyperplane is finding out in the space. Next, the partition hypersurface and decision function on the original space are derived.

$$\begin{aligned} f(x) &= \mathrm{sgn}((w^* \cdot z) + b^*) \\ &= \mathrm{sgn}((w^* \cdot \Phi(x)) + b^*). \end{aligned} \quad (6)$$

It is noted that the distance between two hyperplanes in Hilbert space can still be expressed as w^*, which can be obtained as

$$\begin{aligned} &\min_{w,b,\xi} \frac{1}{2}\|w\|^2 + C\sum_{i=1}^{l}\xi_i \\ &\text{s.t.}\, y_i((w \cdot \Phi(x_i)) + b) \geq 1 - \xi_i,\ i = 1, 2, \ldots, l \\ &\xi_i \geq 0,\ i = 1, 2, \ldots, l. \end{aligned} \quad (7)$$

In the above formula, w is the vector weight, while C and ξ_i are the penalty coefficient and relaxation variable, respectively. Introduce the Lagrange function.

$$\begin{aligned} L(w, b, \xi, \alpha, \beta) = {} & \frac{1}{2}\|w\|^2 + C\sum_{i=1}^{l}\xi_i \\ & - \sum_{i=1}^{l}\alpha_i((y_i(w \cdot \Phi(x_i)) + b) - 1 + \xi_i) - \sum_{i=1}^{l}\beta_i\xi_i. \end{aligned} \quad (8)$$

For support vector machine, the kernel function is the key factor. Different kernel functions and selected parameters can affect the performance of support vector machine. For the theoretical research of support vector machine and for the application of SVM, the selection of kernel function and its parameters are particularly important. At present, among all classification algorithms, the most advanced is the kernel function method. The kernel function of SVM performs well in solving classification problems. In the selection of kernel function, there are two specific parts: one is to select the specific type of kernel function and the other is to select relevant

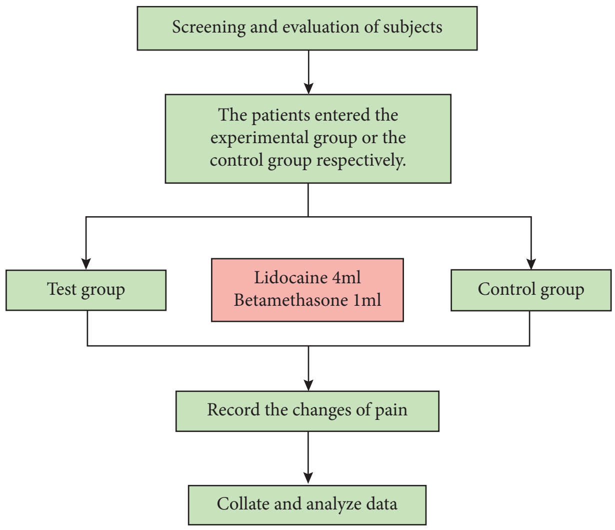

Figure 3: Research flow chart of experiment.

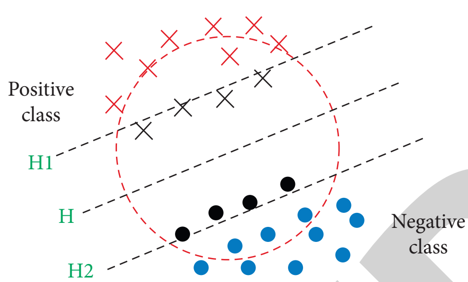

Figure 4: Basic principle diagram of support vector machine.

parameters. Therefore, in the application field of SVM, one of the difficult problems is how to select the appropriate kernel function parameters according to the specific problems, which is also the focus of researchers. However, so far, there is no theory to guide the development of these two aspects.

In the field of kernel method, kernel function plays a very important role, which can effectively resolve nonlinearity and overcome the disaster of dimension. This part will focus on the basic properties and characteristics of kernel function. It is important in the construction of new kernel function and the implementation of SVM algorithm. A hybrid kernel function method is proposed, which can improve the performance of SVM. The form of hybrid kernel function is usually written as follows:

$$K_{\text{mixed}}(x, x') = \sum_{i=1}^{n} \rho_i K_i(x, x'). \tag{9}$$

where n refers to the weight of n different kernel functions, ρ_i is the weight, which refers to the weight of the i^{th} kernel function, and $K_i(x, x')$ is the mixed kernel function. According to the kernel function theory, the mixed kernel function satisfies the Mercer condition. The kernel function constructed by the combination of different types of kernel functions can take into account the characteristics of its basic kernel function. In addition, the performance can be improved by adjusting the model parameters. To sum up, it can be considered to use the kernel function with strong generalization ability and the kernel function with strong learning ability for linear weighting to construct the hybrid kernel SVM algorithm. The combination of polynomial kernel function and sigmoid kernel function can theoretically improve the generalization ability and learning ability of SVM. The constructed hybrid kernel function has the characteristics of the above two basic kernel functions. Under some conditions, the properties of the sigmoid kernel function and RBF function are similar.

After normalizing the data, it is used as input data. Finally, the form of the mixed kernel function, the value range of parameters, and the method of parameter optimization are determined. The polynomial kernel with strong generalization ability and sigmoid kernel with strong learning ability are linearly weighted to construct the mixed kernel functioned SVM. In the training model, the grid search algorithm is used to optimize the parameters of the hybrid kernel SVM algorithm. Finally, the constructed hybrid kernel SVM algorithm is applied to the pulmonary nodule recognition to improve the accuracy and sensitivity of pulmonary nodule recognition.

4. Wearable Lumbar Spine Protection Device

After comprehensively comparing the existing equipment at home and abroad, it is found that almost all traction equipment cannot carry out lumbar push massage. A number of such devices have been designed with varying intrinsic issues. The device of extensible sensors is proposed by [47] to monitor lumbar flexion and rotation and to help diagnosticians in assessing the risk of low-back pain. However, because of the cumbersome setup, the device has wearability issues. Similarly, the inertial measurement unit (IMU) has also been utilized for measuring body motions [48]. Similarly, the inexpensive bend sensors-based equipment of [40] fails to detect three-axis motions of the lumbar joints. The lumbar-motion monitoring tool of [49] is heavy enough to be worn for a long time. The combined treatment scheme of traction and lumbar push cannot be realized. Therefore, this paper introduces the designs of a lumbar pushing traction treatment device that uses the combination of motor and hydraulic pressure to complete the treatment of the combination of traction and lumbar pushing. With the cooperation of a multisensor, it can realize the accurate control of traction force, traction distance angle, amplitude, and frequency of the push massage. The tool supports the cooperative treatment of push and traction. Moreover, the modular design and software design of the control system of the lumbar pushing traction treatment device is introduced. The effectiveness of the control system is proved by a prototype test. The overall results of the lumbar spine protection device are shown in Figure 5.

The lumbar pushing and traction device is a rehabilitation training system for the treatment of lumbar diseases. The device decomposes the lumbar back extension method,

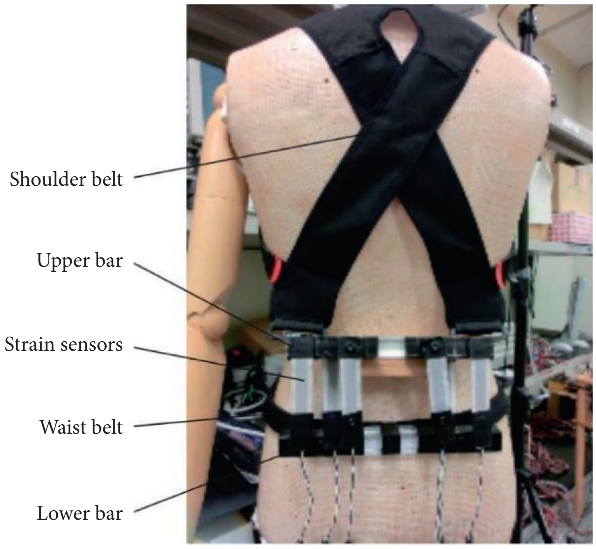

Figure 5: Overall structure diagram of lumbar protection equipment.

lumbar oblique pulling method, and pelvic traction method in massage manipulation into five actions: longitudinal traction, left and right rotation, left and right swing angle, up and down angle, and lumbar pushing and massage. The device design is mainly divided into the head chest plate and hip leg plate. The waist pushing device is located near the hip leg plate of the head chest plate. The whole bed can be pulled longitudinally, rotated left and right, swung left and right, and angled up and down.

The hydraulic system of the lumbar pushing traction treatment device is mainly composed of power components, executive components, control components, auxiliary components, and hydraulic oil. The power element adopts an internal gear pump, which can convert the mechanical energy output by the motor into liquid pressure energy, with low noise and high efficiency. The actuating elements include hydraulic cylinders and a hydraulic motor. The hydraulic cylinder is used to cooperate with the mechanical structure to drive the bed movement. The control components are various hydraulic valves, including directional valve, overflow valve, proportional valve, and one-way valve. With this setup, it becomes quite feasible to control and regulate the flow, pressure, and direction of liquid in the system. The lumbar pushing traction treatment device needs to complete longitudinal traction, left and right swing angle, left and right rotation, up and down angle, and lumbar pushing massage. To ensure the stability and safety of the system operation, the control system adopts the idea of modular design. The system is mainly composed of a power module, waist pushing module, traction module, and human-computer interaction module. The treatment posture is shown in Figure 6.

To realize the adjustable frequency and amplitude of waist pushing, it is necessary to control the speed of the DC motor and the displacement of the other two motors driving the mechanism. The speed of a DC motor determines the frequency of lumbar pushing, and the displacement of the motor mechanism determines the amplitude of lumbar pushing. By controlling two DC motors at the same time, the alternating movement or joint movement of two waist pushing mechanisms can be realized. In the process of lumbar pushing massage, aiming at the control problems of the left and right pushing devices, the system uses the PWM voltage regulation method to change the voltage of the two DC motors. Moreover, the system supports effortless changes in the speed of the motor through voltage regulation and alterations in the lumbar pushing frequency and realizes the adjustable lumbar pushing frequency.

5. Experiments and Results

To systematically evaluate the proposed approach, data about the patients suffering from LDH was collected and analyzed. Details about the experimental setup and analysis are discussed in the following subsections.

5.1. Relevant Preparations for the Experiment. Patients with lumbar disc herniation (LDH) were recruited from the pain clinic of the Department of Anesthesiology of Hospital. This study followed the requirements and principles of clinical research. The subjects were completely voluntary, and the information was kept confidential. After the study, privacy-related information was deleted from the patient's name, gender, age, ID number, and so on. Patients were kept unaware of the treatment cycle and general process to reduce their fear of treatment and enhance their confidence in treatment. Patients were demonstrated to correctly use the pain assessment scale for pain scoring.

After the first injection, the patients who received epidural injection through the intervertebral foramen reported that the pain relief was less than 50%. The patients were suggested to avoid taking painkillers, strenuous activities, and exercises that aggravate the load on the waist during treatment. As shown in Table 1, there is no statistically significant difference in gender, age, body mass index, and course of disease between the ENP group and TFSI group. It implies that the data of the two groups meet the requirements of clinical research, and the test data are comparable, as shown in Table 1.

Similar to the impact of demographic information on body weight and obesity [50, 51], there are different opinions on the influence of gender, age, weight, occupation, and other factors on pain score. Compared with other data, the p value is closer to 0.05. We further analyze the body mass index (BMI) and gender of the two groups to determine whether the BMI and gender have an impact on the pain score of the two groups in this study. BMI is a number obtained by dividing the weight in kilograms by the square of the height in meters. BMI is a neutral and reliable indicator. The BMI index of the domestic population is different from that of other countries in Europe and the United States. Table 2 shows the changes of the VAS scores of BMI within and beyond the normal range in the ENP group before and after treatment.

Table 2 shows the changes in the VAS scores of BMI within and beyond the normal range in the ENP group

Figure 6: Treatment posture diagram of lumbar spine protection equipment after lying down.

Table 1: General information of two groups of patients.

Observation items	ENP	TFSI	T	P
Gender	15/12	23/28	0.773	0.379
Age	51.07 ± 16.13	47.78 ± 15.15	0.892	0.375
Body mass index	23.61 ± 1.81	22.93 ± 1.44	1.799	0.076
Course of disease	9.52 ± 5.65	8.84 ± 4.61	0.573	0.569

Table 2: Effect of BMI on VAS score.

Time	ENP			TFSI		
	BMI	T	P	BMI	T	P
Zero	5.36 ± 1.03	0.918	0.368	5.81 ± 1.38	0.757	0.453
One	2.09 ± 1.04	0.828	0.415	2.56 ± 1.67	0.883	0.382
Three	2.09 ± 1.14	0.384	0.704	2.25 ± 1.00	0.112	0.911
Six	2.82 ± 1.60	0.010	0.992	2.81 ± 1.42	0.031	0.975

before and after treatment. The VAS scores at each follow-up point after treatment were lower than those before treatment. The VAS score at each time point after treatment was compared between the groups. After the t-test, the results showed that there was no statistical significance between the groups ($P > 0.05$). In the TFSI group, whether BMI was within the normal range or beyond the normal range, it was improved compared with the same group before treatment. For the intergroup comparison, the VAS scores of the two groups before treatment, 1 month after treatment, 3 months after treatment, and 6 months after treatment were tested by the t-test for the two independent samples. The results showed that the difference was not statistically significant.

5.2. Experimental Result and Analysis. The intergroup comparison revealed that there was no significant difference between the two groups after treatment ($P > 0.05$). There was a significant difference between the two groups after 3 months of the treatment ($P < 0.05$). The VAS score of the ENP group was lower than that of the TFSI group. Six months after treatment, there was a significant difference between the two groups ($P < 0.05$). The VAS score of the ENP group was lower than that of the TFSI group. The VAS score changes of the two groups before and after treatment and at each follow-up point are shown in Figure 7.

The figure shows the change trend of VAS in the two groups at each follow-up time point before and after treatment. There was a significant difference between the two groups at three and six months after treatment ($P < 0.05$). Over time, the VAS score of the ENP group was lower than that of the TFSI group. Two independent sample t-tests showed that there was no significant difference in VAS between the two groups after treatment ($P > 0.05$). The changes of VAS between the two groups, 3 months, and 6 months after the treatment showed that the change range of the ENP group was significantly higher than that of the TFSI group (all $P < 0.05$). Table 3 shows the changes in the number of people in the ENP group and TFSI group before, after, and at each follow-up time point compared with before treatment. It makes a comparative analysis between the groups, as illustrated in the table.

It is clear from Table 3 that there is no change in VAS in the TFSI and ENP groups after one month of treatment. No significant difference was reported between the two groups. The table also shows that there is no significant difference between the two groups in patients whose VAS score decreases ≥ 2 cm at one time after treatment. The comparison of the number of patients with VAS reduction ≥ 2 cm 1 month after treatment is shown in Figure 8.

It was observed that after treatment, the VAS pain score of the two groups decreased significantly as compared with

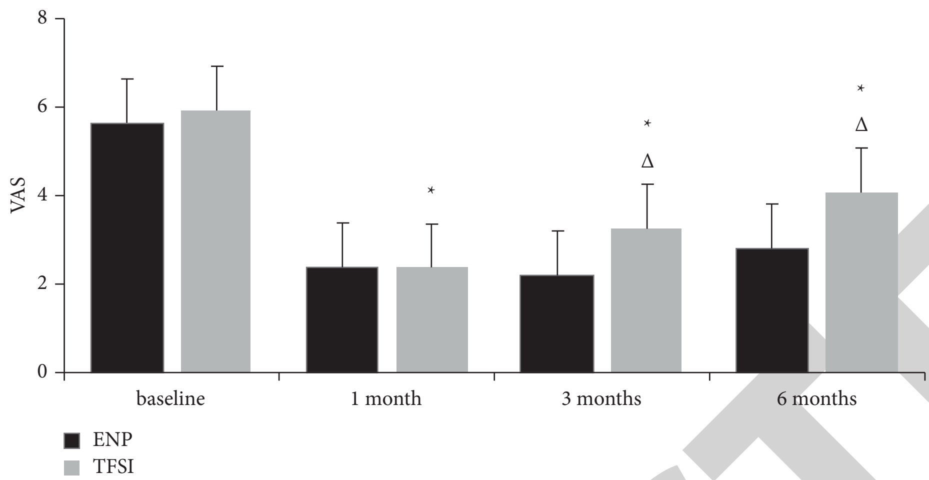

Figure 7: VAS score changes of the two groups before and after treatment.

Table 3: Comparison results of the proportion of people with changes in the VAS score.

Time	Unchanged		Rise		Reduce	
	TFSI	ENP	TFSI	ENP	TFSI	ENP
1 month	1 (51)	0 (27)	0 (51)	1 (27)	38 (51)	18 (27)
3 months	5 (51)	1 (27)	0 (51)	0 (27)	27 (51)	21 (27)
6 months	7 (15)	3 (27)	2 (15)	0 (27)	15 (15)	15 (27)

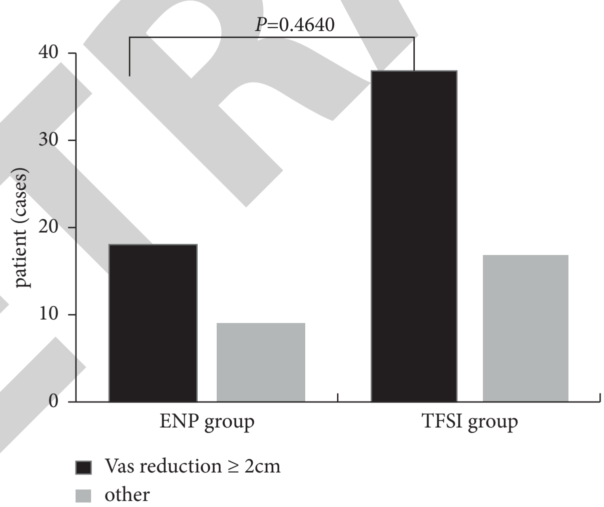

Figure 8: Comparison of patients with VAS reduction ≥ 2 cm 1 month after treatment.

that before treatment. The VAS score of the ENP group decreased more significantly than that of the TFSI group at 3 and 6 months of the follow-up. After treatment, the ODI scores of the two groups were significantly lower than those before the treatment. At 1 month, 3 months, and 6 months after treatment, the ODI value of the ENP group was lower than that of the TFSI group. During the whole study, two patients temporarily stopped treatment because they could not cooperate with local surgery. One patient complained of dizziness and nausea during treatment. After adjusting body position and fluid, the symptoms were relieved. However, the other patients had no adverse reactions.

6. Conclusion and Future Work

At present, domestic and foreign scholars are still exploring the influencing factors of intraoperative and postoperative complications of the efficacy of percutaneous transformational endoscopic discectomy (PTED) in the treatment of lumbar disc herniation. Combined with the experience of our department in PTED surgery, it is suggested that doctors who are about to carry out intervertebral foraminal endoscopy should have rich experience in open surgery and solid anatomical knowledge. The physician, on the basis of formal training, should gradually expand the indications of surgery. Initially, the main goal should be clinical efficacy with fewer complications. At present, local anesthesia is still the main anesthesia method for PTED. After accumulating rich clinical experience, our department found that general anesthesia is a feasible anesthesia method through a clinical test in the interlaminar approach. Local anesthesia combined with intravenous anesthesia can be selected in the lateral approach to reduce patients' pain and improve pain tolerance. In the current era of technology, medical surgery ought to make full use of the development of science and technology. The cutting edge-research studies suggest that spine surgeons should follow evidence-based medicine besides the concept of minimally invasive surgery. Moreover, as PTED has broader development prospects, the approach needs to be adopted to serve the human race in the best possible way. In this perspective, this research work proposes a method to explore the curative effect of foraminal endoscopic surgery in the treatment of lumbar disc herniation. The SVM machine learning classifier is utilized for the analysis of the curative effect. The findings of the experimentation reveal that the VAS pain score of the two groups decreases significantly after treatment. Moreover, it was observed that the ODI scores of the two groups were significantly lower than those before the treatment. Besides, this research work suggests the use of the wearable lumbar protective device for the effective rehabilitation of patients. To the authors' knowledge, this study is the first of its kind to apply ENP technology in treating HLD in China. Although the research is single-centered with a small sample, it provides preliminary, reliable, and scientific experimental data for the further study of ENP in the treatment of HLD.

This study is not free from limitations. The research targets only a follow-up of six months after the operation. After six months of pain relief, it is not known whether the patients treated with ENP will form epidural adhesion again. The research at this stage is quiet on such questions. In the future, we are planning to use other machine learning classifiers and a hybrid approach to further enhance the research work. Moreover, we look forward to the results of multicenter and large sample studies to further confirm the clinical significance of ENP in the treatment of HLD-derived chronic low back and leg pain [52].

Data Availability

The datasets used during the current study are available from the corresponding author on reasonable request.

Conflicts of Interest

The authors declare that there are no conflicts of interest.

References

[1] F. Salaffi, P. Sarzi-Puttini, and F. Atzeni, "How to measure chronic pain: new concepts," *Best Practice & Research Clinical Rheumatology*, vol. 29, no. 1, pp. 164–186, 2015.
[2] N. Shepard and W. Cho, "Recurrent lumbar disc herniation: a review," *Global Spine Journal*, vol. 9, no. 2, pp. 202–209, 2019.
[3] Y. Wang, G. Dai, L. Jiang, and S. Liao, "The incidence of regression after the non-surgical treatment of symptomatic lumbar disc herniation: a systematic review and meta-analysis," *BMC Musculoskeletal Disorders*, vol. 21, no. 1, pp. 1–12, 2020.
[4] H. Kanno, T. Aizawa, K. Hahimoto, and E. Itoi, "Minimally invasive discectomy for lumbar disc herniation: current concepts, surgical techniques, and outcomes," *International Orthopaedics*, vol. 43, no. 4, pp. 917–922, 2019.
[5] M. Brooks, A. Dower, M. F. A. Jalil, and S. Kohan, "Radiological predictors of recurrent lumbar disc herniation: a systematic review and meta-analysis," *Journal of Neurosurgery: Spine*, vol. 34, no. 3, pp. 481–491, 2020.
[6] X. Chen, U. Chamoli, S. Lapkin, J. V. Castillo, and A. D. Diwan, "Complication rates of different discectomy techniques for the treatment of lumbar disc herniation: a network meta-analysis," *European Spine Journal*, vol. 28, no. 11, pp. 2588–2601, 2019.
[7] M. Yao, B. Xu, Z. Li et al., "A comparison between the low back pain scales for patients with lumbar disc herniation: validity, reliability, and responsiveness," *Health and Quality of Life Outcomes*, vol. 18, no. 1, pp. 1–12, 2020.
[8] S. B. Andersen, R. Birkelund, M. Ø. Andersen, L. Y. Carreon, A. Coulter, and K. D. Steffensen, "Factors affecting patient decision-making on surgery for lumbar disc herniation," *Spine*, vol. 44, no. 2, pp. 143–149, 2019.
[9] A. Wirries, F. Geiger, A. Hammad, L. Oberkircher, I. Blümcke, and S. Jabari, "Artificial intelligence facilitates decision-making in the treatment of lumbar disc herniations," *European Spine Journal*, vol. 30, no. 8, pp. 2176–2184, 2021.
[10] B. B. Carlson and T. J. Albert, "Lumbar disc herniation: what has the spine patient outcomes research trial taught us?" *International Orthopaedics*, vol. 43, no. 4, pp. 853–859, 2019.
[11] C. Leboeuf-Yde, N. Klougart, and T. Lauritzen, "How common is low back pain in the nordic population?" *Spine*, vol. 21, no. 13, pp. 1518–1525, 1996.
[12] R. A. Deyo, J. G. Jarvik, and R. Chou, "Low back pain in primary care," *BMJ*, vol. 349, Article ID g4266, 2014.
[13] W. E. Hoogendoorn, P. M. Bongers, H. C. W. De Vet et al., "Flexion and rotation of the trunk and lifting at work are risk factors for low back pain," *Spine*, vol. 25, no. 23, pp. 3087–3092, 2000.
[14] R. M. Amin, N. S. Andrade, and B. J. Neuman, "Lumbar disc herniation," *Current reviews in musculoskeletal medicine*, vol. 10, no. 4, pp. 507–516, 2017.
[15] L. Yu, J.-K. Wen, S. Wang, W.-H. Wang, J.-M. Yu, and X.-J. Ye, "Removal of calcified lumbar disc herniation with endoscopic-matched ultrasonic osteotome - our preliminary experience," *British Journal of Neurosurgery*, vol. 34, no. 1, pp. 80–85, 2020.
[16] M. R. Konieczny, J. Reinhardt, M. Prost, C. Schleich, and R. Krauspe, "Signal intensity of lumbar disc herniations: correlation with age of herniation for extrusion, protrusion,

and sequestration," *International journal of spine surgery*, vol. 14, no. 1, pp. 102–107, 2020.

[17] A. R. El-Zayat, W. Gomah, and A. H. Aldesouky, "Spinal decompression therapy as an alternative modality for management of low back pain and radicular pain caused by lumbar disc herniation or protrusion," *Egyptian Rheumatology and Rehabilitation*, vol. 46, no. 3, pp. 183–188, 2019.

[18] A. D. Mendelow, B. A. Gregson, P. Mitchell et al., "Lumbar disc disease: the effect of inversion on clinical symptoms and a comparison of the rate of surgery after inversion therapy with the rate of surgery in neurosurgery controls," *Journal of Physical Therapy Science*, vol. 33, no. 11, pp. 801–808, 2021.

[19] L. Favaro, R. G. Boggs, and M. C. Geraci, "Conservative management of a foraminal lumbar disc herniation[J]," *JOSPT Cases*, vol. 1, no. 1, pp. 49-50, 2021.

[20] A. Boado, A. Nagy, and S. Dyson, "Ultrasonographic features associated with the lumbosacral or lumbar 5-6 symphyses in 64 horses with lumbosacral-sacroiliac joint region pain (2012-2018)," *Equine Veterinary Education*, vol. 32, pp. 136–143, 2020.

[21] M. H. Shin, J. S. Bae, H. L. Cho, and I. T. Jang, "Extradiscal epiduroscopic percutaneous endoscopic discectomy for upper lumbar disc herniation A technical note," *Clinical Spine Surgery: A Spine Publication*, vol. 32, no. 3, pp. 98–103, 2019.

[22] S. Bashir, S. Maryam, M. Zakir et al., "Correlation between magnetic resonance imaging and clinical diagnostic findings of lumbar degenerative Disc Disease," *Ophthalmology Update*, vol. 19, no. 3, pp. 240–243, 2021.

[23] D.-M. Seo and Y. Cho, "Risk factors for disc height loss in conservatively treated symptomatic lumbar disc herniation in elderly patients," *Journal of Korean Society of Geriatric Neurosurgery*, vol. 17, no. 2, pp. 58–63, 2021.

[24] M. Mahmoud, A. Almelesy, and M. A. Mohamed, "Endoscopic management of lumbar disc prolapse," *International Journal of Medical Arts*, vol. 3, no. 3, pp. 1689–1693, 2021.

[25] I. Y. J. Hung, T. T. F. Shih, B. B. Chen, S. H. Liou, I. K. Ho, and Y. L. Guo, "The roles of lumbar load thresholds in cumulative lifting exposure to predict disk protrusion in an Asian population," *BMC Musculoskeletal Disorders*, vol. 21, no. 1, pp. 1–13, 2020.

[26] V. M. Butenschoen, L. Hoenikl, M. Deschauer, B. Meyer, and J. Gempt, "Bilateral thoracic disc herniation with abdominal wall paresis: a case report," *Acta Neurochirurgica*, vol. 162, no. 9, pp. 2055–2059, 2020.

[27] M. P. Arts, A. Kuršumović, L. E. Miller et al., "Comparison of treatments for lumbar disc herniation: systematic review with network meta-analysis," *Medicine*, vol. 98, no. 7, Article ID e14410, 2019.

[28] F. Dai, Y. X. Dai, H. Jiang, P. Y. Fei, and J. L. Tao, "Non-surgical treatment with XSHHD for ruptured lumbar disc herniation: a 3-year prospective observational study," *BMC Musculoskeletal Disorders*, vol. 21, no. 1, pp. 1–8, 2020.

[29] C. Cunha, A. J. Silva, P. Pereira, R. Vaz, and R. M. Gonçalves, "The inflammatory response in the regression of lumbar disc herniation," *Arthritis Research & Therapy*, vol. 20, no. 1, pp. 1–9, 2018.

[30] R. Qin, B. Liu, J. Hao et al., "Percutaneous endoscopic lumbar discectomy versus posterior open lumbar microdiscectomy for the treatment of symptomatic lumbar disc herniation: a systemic review and meta-analysis," *World neurosurgery*, vol. 120, pp. 352–362, 2018.

[31] Y.-K. Kim, D. Kang, I. Lee, and S.-Y. Kim, "Differences in the incidence of symptomatic cervical and lumbar disc herniation according to age, sex and national health insurance eligibility: a pilot study on the disease's association with work," *International Journal of Environmental Research and Public Health*, vol. 15, no. 10, p. 2094, 2018.

[32] S. Tang, Z. Mo, and R. Zhang, "Acupuncture for lumbar disc herniation: a systematic review and meta-analysis," *Acupuncture in Medicine*, vol. 36, no. 2, pp. 62–70, 2018.

[33] Z. Chen, L. Zhang, J. Dong et al., "Percutaneous transforaminal endoscopic discectomy compared with microendoscopic discectomy for lumbar disc herniation: 1-year results of an ongoing randomized controlled trial," *Journal of Neurosurgery: Spine*, vol. 28, no. 3, pp. 300–310, 2018.

[34] J. Chen, X. Jing, C. Li, Y. Jiang, S. Cheng, and J. Ma, "Percutaneous endoscopic lumbar discectomy for L5S1 lumbar disc herniation using a transforaminal approach versus an interlaminar approach: a systematic review and meta-analysis," *World neurosurgery*, vol. 116, pp. 412–420, 2018.

[35] M. S. Kabil, "The microendoscopic approach for far lateral lumbar disc herniation: a preliminary series of 33 patients," *Egyptian Journal of Neurosurgery*, vol. 34, no. 1, pp. 1–8, 2019.

[36] T. R. Waters, V. Putz-Anderson, A. Garg, and L. J. Fine, "Revised NIOSH equation for the design and evaluation of manual lifting tasks," *Ergonomics*, vol. 36, no. 7, pp. 749–776, 1993.

[37] R. Norman, R. Wells, P. Neumann et al., "A comparison of peak v s cumulative physical work exposure risk factors for the reporting of low back pain in the automotive industry," *Clinical Biomechanics*, vol. 13, no. 8, pp. 561–573, 1998.

[38] H. J. Wilke, P. Neef, M. Caimi, T. Hoogland, and L. E. Claes, "New in vivo measurements of pressures in the intervertebral disc in daily life," *Spine*, vol. 24, no. 8, pp. 755–762, 1999.

[39] A. L. Nachemson, "The lumbar spine an orthopaedic challenge," *Spine*, vol. 1, no. 1, pp. 59–71, 1976.

[40] L. Milea, M. Dascalu, E. Franti et al., "Detection and telereplication of human hand motions by a robotic hand," *American Journal of Aerospace Engineering*, vol. 2, no. 4, pp. 30–35, 2015.

[41] J. J. Wong, P. Côté, D. A. Sutton et al., "Clinical practice guidelines for the noninvasive management of low back pain: a systematic review by the Ontario Protocol for Traffic Injury Management (OPTIMa) Collaboration," *European Journal of Pain*, vol. 21, no. 2, pp. 201–216, 2017.

[42] J. Kim, J. W. Hur, J.-B. Lee, and J. Y. Park, "Surgery versus nerve blocks for lumbar disc herniation : quantitative analysis of radiological factors as a predictor for successful outcomes," *Journal of Korean Neurosurgical Society*, vol. 59, no. 5, 478 pages, 2016.

[43] B. J. C. Freeman, G. L. Ludbrook, S. Hall et al., "Randomized, double-blind, placebo-controlled, trial of transforaminal epidural etanercept for the treatment of symptomatic lumbar disc herniation," *Spine*, vol. 38, no. 23, pp. 1986–1994, 2013.

[44] T. Korhonen, J. Karppinen, A. Malmivaara et al., "Efficacy of infliximab for disc herniation-induced sciatica," *Spine*, vol. 29, no. 19, pp. 2115–2119, 2004.

[45] S. P. Cohen, D. Wenzell, R. W. Hurley et al., "A double-blind, placebo-controlled, dose-response pilot study evaluating intradiscal etanercept in patients with chronic discogenic low back pain or lumbosacral radiculopathy," *Anesthesiology*, vol. 107, no. 1, pp. 99–105, 2007.

[46] A. Thackeray, J. M. Fritz, J. D. Lurie, W. Zhao, and J. N. Weinstein, "Nonsurgical treatment choices by individuals with lumbar intervertebral disc herniation in the United States," *American Journal of Physical Medicine & Rehabilitation*, vol. 96, no. 8, pp. 557–564, 2017.

Hindawi
Journal of Healthcare Engineering
Volume 2023, Article ID 9758310, 1 page
https://doi.org/10.1155/2023/9758310

Retraction

Retracted: Efficacy of Human Adipose Derived Mesenchymal Stem Cells in Promoting Skin Wound Healing

Journal of Healthcare Engineering

Received 26 September 2023; Accepted 26 September 2023; Published 27 September 2023

This article has been retracted by Hindawi following an investigation undertaken by the publisher [1]. This investigation has uncovered evidence of one or more of the following indicators of systematic manipulation of the publication process:

(1) Discrepancies in scope
(2) Discrepancies in the description of the research reported
(3) Discrepancies between the availability of data and the research described
(4) Inappropriate citations
(5) Incoherent, meaningless and/or irrelevant content included in the article
(6) Peer-review manipulation

The presence of these indicators undermines our confidence in the integrity of the article's content and we cannot, therefore, vouch for its reliability. Please note that this notice is intended solely to alert readers that the content of this article is unreliable. We have not investigated whether authors were aware of or involved in the systematic manipulation of the publication process.

Wiley and Hindawi regrets that the usual quality checks did not identify these issues before publication and have since put additional measures in place to safeguard research integrity.

We wish to credit our own Research Integrity and Research Publishing teams and anonymous and named external researchers and research integrity experts for contributing to this investigation.

The corresponding author, as the representative of all authors, has been given the opportunity to register their agreement or disagreement to this retraction. We have kept a record of any response received.

References

[1] L. Zhou, H. Wang, S. Yao, L. Li, and X. Kuang, "Efficacy of Human Adipose Derived Mesenchymal Stem Cells in Promoting Skin Wound Healing," *Journal of Healthcare Engineering*, vol. 2022, Article ID 6590025, 5 pages, 2022.

Hindawi
Journal of Healthcare Engineering
Volume 2022, Article ID 6590025, 5 pages
https://doi.org/10.1155/2022/6590025

Research Article

Efficacy of Human Adipose Derived Mesenchymal Stem Cells in Promoting Skin Wound Healing

Lingcong Zhou,[1] Hui Wang,[2] Sidi Yao,[3] Li Li,[1] and Xin Kuang[4]

[1] *Department of Plastic and Cosmetic Surgery, The Central Hospital of Yueyang, Yueyang, Hunan 414000, China*
[2] *Department of Burn and Plastic Surgery, The First Affiliated Hospital of University of South China, Hengyang, Hunan 421000, China*
[3] *Hunan Industrial Technician College, Yueyang, Hunan 414000, China*
[4] *Department of Anesthesia,Affiliated Longhua People's Hospital, Southern Medical University, Longhua People's Hospital, Shenzhen 518000, China*

Correspondence should be addressed to Xin Kuang; kuangxin221@126.com

Received 13 February 2022; Revised 4 March 2022; Accepted 7 March 2022; Published 24 March 2022

Academic Editor: Liaqat Ali

Background. The aim of this pilot clinical study is to evaluate the efficacy of human adipose derived mesenchymal stem cells (HAMSCs) treatment for the wound healing with patients. *Methods*. This study was a clinical trial to investigate the efficacy of human adipose derived mesenchymal stem cells treatment for the wound healing with patients. 346 patients with skin wounds attending the central hospital of Yue Yang were enrolled in the study, setting in the period from January 2016 to January 2021. Patients were randomly allocated into two groups: experimental group received treatment with human adipose derived mesenchymal stem cells for each 10 cm^2 of wound and control group received conventional dressing with normal saline for each 10 cm^2 of wound. *Results*. No adverse events were recorded during the period of treatment. The granulation tissue coverage rate and thickness of granulation tissue after 10 days of treatment in experimental group were significantly improved compared with control group. Furthermore, the occurrence of bleeding of wound and suppurative wounds between two groups had significant difference ($P < 0.05$). *Conclusion*. The data in this pilot study indicated that human adipose derived mesenchymal stem cells may be a safe and effective alternative therapy for wound healing. Moreover, larger, placebo-controlled, perspective studies are necessity to evaluate the efficacy and safety of human adipose derived mesenchymal stem cells treatment for wound healing patients.

1. Introduction

Wound healing is complex progress, containing hemostasis, epithelization, angiogenesis, granulation tissue formation, and collagen deposition [1]. In the United States, chronic wounds affect approximately 6.5 million patients, and approximately $25 billion is spent annually on treatment of these wounds. Furthermore, it severely affects people's life quality [2]. Therefore, effective treatments to improve wound healing will be of great social significance.

Wound healing is accomplished through the cooperation of a variety of cells and factors in the body, and their respective numbers need to be controlled within a balanced range [3]. In this process, any factors that break the balance will affect the wound healing speed and even leave abnormal scar [4]. The factors affecting wound healing can be divided into systemic factors and local factors. Systemic factors include nutritional status and complications, while local factors mainly refer to tissue hypoxia and wound infection [5, 6].

Mesenchymal stem cells (MSCs) are derived from mesoderm. As an adult stem cell, they exist in organ stroma and connective tissue with strong proliferation ability [7]. When in a suitable environment, they can differentiate into a variety of cells, such as osteoblasts [8, 9]. Therefore, they also show a certain multidirectional differentiation potential and can be separated from bone marrow and other tissues [10]. Compared with embryonic stem cells, MSCs have the advantages of no ethical disputes, wide sources, strong migration ability, and low immunogenicity [11]. Based on these advantages, it has been widely used in biomedicine. The International Society for Cell Therapy has put forward a general standard for MSCs: (1) under standard culture conditions, MSCs can adhere and grow on tissue culture vessels, that is, they must have viscoplasticity [12]; (2) MSCs must be able to express specific surface markers such as CD105, CD90, and CD34 [13]; (3) MSCs have the ability of osteogenic and adipogenic differentiation in vitro. This standard provides identification basis for preclinical and clinical studies of MSCs [14, 15].

Therefore, the aim of this protocol study was to assess the efficacy of human adipose derived mesenchymal stem cells treatment for the wound healing with patients.

2. Method

2.1. Study Design. This study was a clinical trial to investigate the efficacy of human adipose derived mesenchymal stem cells treatment for the wound healing with patients. 346 patients with skin wounds attending the central hospital of Yue Yang were enrolled in the study, setting in the period from January 2016 to January 2021.

The procedures of this clinical trial are presented in Figure 1. All patients were recorded full medical history: cause, onset, course, and duration of wound(s), present extension or complication, history of smoking, and previous and present medications that could affect the healing process (Table 1). The treatment result and complications were recorded to detect the treatment efficacy.

2.2. Inclusion Criteria. The patients met the inclusion criteria as follows: (1) acute wounds (burns or crush wounds); (2) age ≤75 years old.

2.3. Exclusion Criteria. The exclusion criteria were as follows: (1) age >75 years old, or diabetes mellitus; (2) pregnancy; (3) patients had blood systemic diseases; (4) patients had immunosuppressive therapy; (5) complicated wounds (e.g., bleeding or infection); (6) take medications likely to affect the outcome of the study; (7) cardiovascular diseases; (8) renal and hepatic failure; (9) peripheral arterial disease.

2.4. Ethics. This clinical study was approved by the Ethical Committee of The Central Hospital of Yue Yang Hospital, and written informed consent was obtained from all participants. This study completely complied with the recommendations of the Declaration of Helsinki.

2.5. Preparation. Before starting the therapeutic procedure, all wounds were fully washed with physiologic serum (i.e., saline 0.9%). Dirty or crusted wounds were debrided using a surgical blade (bistori) and local anesthesia. Postdebridement bleeding was controlled using sterile gauze packing. Meanwhile, we measure the length of the wound and confirm that there is no active bleeding and exposure of important blood vessels, nerves, and tendons.

2.6. Treatment. The 316 eligible patients enrolled in this study were randomly allocated into two groups: the insulin group ($n = 158$) and the control group ($n = 158$).

Experimental group patients received human adipose derived mesenchymal stem cells for promoting wound healing. Control group patients received 1 ml saline 0.9% for each 10 cm^2 of wound. The topical treatment was applied twice daily in both groups, left to dry for 30 minutes, and covered with sterile cotton gauze. All patients were positioned to prevent solution run-off from the wound. Neither the patient nor the physician was informed about treatment groups and solutions for ensuring blinding. The enrolled subjects accepted successive treatment until wound healing.

The dead necrotic tissue attached to the wound was surgically debrided. All the wounds were thoroughly washed with 0.9% normal saline before applying the dressing. Systemic antibiotics were given based on pus culture and sensitivity. During the course of dressing, the wound was observed for granulation tissue, wound discharge, and control of infection. The outcome was measured in terms of reduction in wound size between the two groups.

2.7. Assessment of Efficacy. The primary end point of this research was total wound closure. Rate of wound healing was calculated as (the primary area-final wound area) (in mm^2)/healing time (in days) and reported as (mm^2/day) [16]. A wound was considered completely healed when wound was completely closed and epithelialized. Moreover, we investigate the granulation tissue coverage rate and thickness of granulation tissue to assess the progress of wound healing.

Another primary end point was safety and adverse effect. General adverse effects were recorded as headache, palpitation, and vertigo (due to hypoglycemia). All adverse events were recorded during follow-up and evaluated by an independent committee.

2.8. Statistical Analysis. SPSS 22.0 software (SPSS Inc., Chicago, IL, USA) was used for the statistical analysis. The *t*-test was conducted to calculate the statistical significance between the groups. $P \leq 0.05$ was considered statistically significant.

3. Results

3.1. Characteristics of the Subjects. Among the 338 patients enrolled, 13 patients did not meet inclusion criteria and 9 were not willing to participate in this clinical study. Finally, 316 eligible patients were enrolled in this pilot study; they were randomly allocated into two groups: the insulin group ($n = 158$) and the control group ($n = 158$) (Figure 1). In the progress, the experimental group excluded 12 patients and the control group excluded 8 patients. Finally, 146 patients were analyzed in the experimental group, and 150 patients

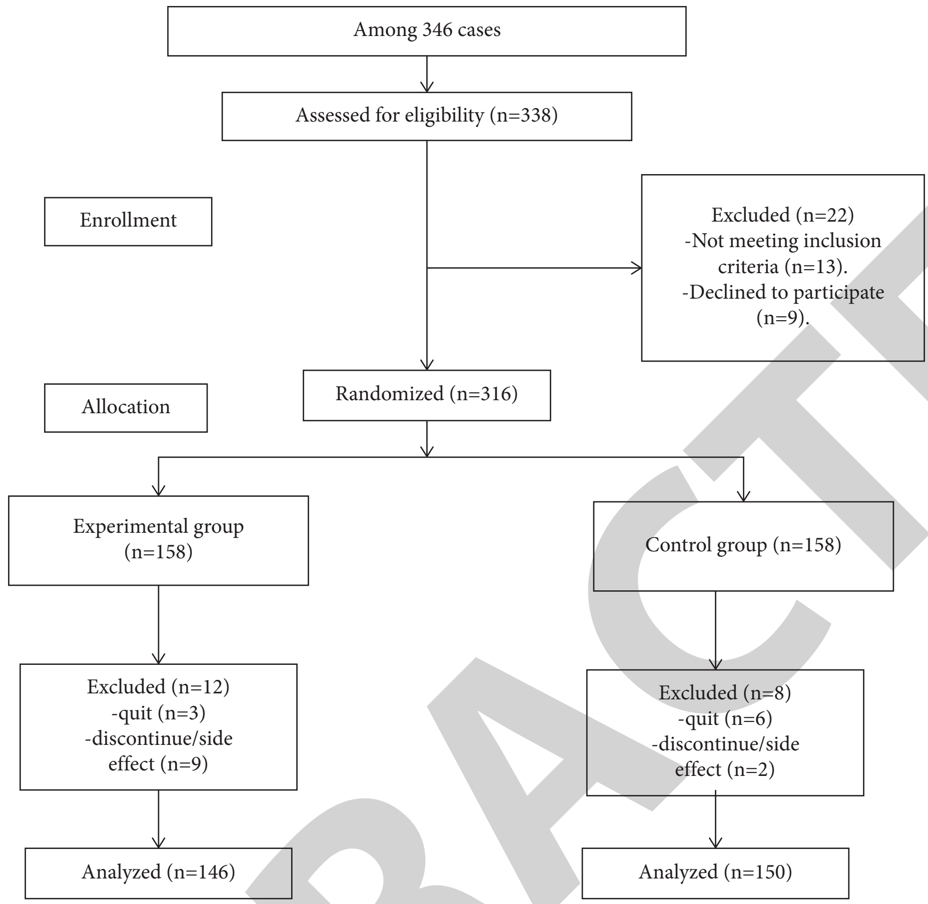

Figure 1: Flow chart showing recruitment.

Table 1: Clinical characteristics of wounded patients in the experimental group and in control group.

	Experimental group ($n = 150$)	Control group ($n = 150$)	t	P value
Age (years)	57.4 ± 5.27	55.4 ± 5.46	0.35	0.213
Female	63 (43.2%)	88 (58.7%)	—	—
Male	83 (56.8%)	62 (41.3%)	—	—
Weight (kg)	66.4 ± 8.96	61.53 ± 7.96	0.24	0.576
BMI (kg/m^2)	22.73 ± 1.39	22.87 ± 1.86	0.28	0 .78
Size of the wound (cm^2)	323.53 ± 147.24	299.56 ± 105.15	0.77	0.89
Area of the body affected				
Upper extremity	48 (32.9%)	53 (35.3%)	—	—
Lower limb	57 (39%)	45 (30%)	—	—
Back	11 (7.5%)	14 (9.3%)	—	—
Face	3 (2%)	5 (3.3%)	—	—
Anterior thorax	9 (6.2%)	10 (6.7%)	—	—
Abdomen	12 (8.2%)	13 (8.7%)	—	—
Sacrum	2 (1.4%)	4 (2.7%)	—	—
Head	4 (2.7%)	6 (4%)	—	—
Cause of the wound				
Trauma	79 (54.1%)	94 (62.7%)	—	—
Burn	10 (6.8%)	13 (8.7%)	—	—
Pressure	33 (22.6%)	29 (19.3%)	—	—
Scald	24 (16.4%)	14 (9.3%)	—	—
Wound classification				
Clean	40 (27.4%)	37 (24.7%)		
Clean contaminated	32 (21.9%)	39 (26%)		
Contaminated	39 (26.7%)	42 (28%)		
Dirty	35 (24.4%)	32 (21.3%)		
Healing rate (mm^2/day)	48.7 ± 19.52	32.47 ± 14.10	0.91	0.006
Time to healing (days)	34.4 ± 14.24	32.7 ± 9.38	1.44	0.39

Note. significant difference as $P < 0.05$.

Table 2: Comparison of the growth of granulation tissue in the two groups after 10 days of treatment.

	Experimental group ($n = 146$)	Control group ($n = 150$)	t	P value
Granulation tissue coverage rate (%)	32.6 ± 10.1	21.4 ± 8.9	10.78	<0.05
The thickness of granulation tissue (mm)	3.47 ± 0.84	2.60 ± 1.92	25.37	<0.05

Note. Significant difference as $P < 0.05$.

Table 3: Comparison of complications in the two groups after treatment.

	Experimental group ($n = 146$)	Control group ($n = 150$)	t	P value
Bleeding of wound (%)	10 (6.8%)	16 (10.7%)	5.843	0.041
Wound infection (%)	6 (4.1%)	11 (7.3%)	4.931	0.054
Suppurative wounds	2 (1.4%)	8 (5.3%)	6.172	0.045
Malnutrition	8 (5.5%)	16 (10.7%)	5.624	0.059
Hypoproteinemia	9 (6.2%)	15 (10%)	5.361	0.054
Osteomyelitis	1 (0.7%)	4 (2.7%)	3.128	0.143
Septicemia	3 (2.1%)	7 (4.7%)	2.195	0.642

Note. Significant difference as $P < 0.05$.

were analyzed in the control group. The demographic characteristics of the subjects are showed in Table 1; there was no significant difference in age, weight, BMI, size of the wound, wound classification, and time to healing between the two groups ($P > 0.05$). Interestingly, the healing rates were significantly improved in the experimental group ($P < 0.05$).

3.2. Safety Evaluation of Therapy. No adverse events were reported during the period of our research. No significant adverse effects from wound such as sweating, palpitations, and headache were observed. No serious adverse events such as allergic reactions and fever were observed.

3.3. The Growth of Granulation Tissue. The clinical wound healing rate of patients was improved after treatment. The rate of wound healing significantly increased ($P = 0.008$) (Table 1). Table 2 indicates that the granulation tissue coverage rate and thickness of granulation tissue after 10 days of treatment in experimental group were $32.6 \pm 10.1\%$ and 3.47 ± 0.84 mm, which were significantly improved compared with control group ($P < 0.05$).

3.4. Complications of Therapy. As demonstrated in Table 3, the occurrence of bleeding of wound and suppurative wounds between two groups had significant difference ($P < 0.05$), and the occurrence of other complications (such as wound infection, malnutrition, hypoproteinemia, osteomyelitis, and septicemia) had no significant difference between two groups ($P > 0.05$).

4. Discussion

This pilot research demonstrated that HAMSCs treatment could promote wound healing in patients, such as the granulation tissue coverage rate, the healing rate, and thickness of granulation tissue, which were improved. Furthermore, the results in this protocol study also showed that there were no serious adverse events observed during the period of study, which indicated the safety of HAMSCs treatment in patients.

ADMSCs come from mesoderm [17]. They are isolated from adipose tissue around blood vessels and cultured. They can differentiate into a variety of cells, including bone cells, chondrocytes, and nerve cells [18]. Compared with other MSCs, ADMSCs are not only easy to obtain but also show multidirectional differentiation potential, and there is no ethical dispute [19]. Secondly, ADMSCs are homing after transplantation, mainly distributed in the injury site. Many literatures show that ADMSCs have good immunomodulatory effect, inhibit dendritic cell (DC) maturation, and induce immune tolerance by negatively regulating immunity [20, 21]; Induce macrophage (M2) polarization and downregulate immune response [49]; Inhibit the proliferation of NK cells and keep them in the tissue for enough time to balance the immune response before clearance; inhibit the proliferation of B cells and T cells [22]. ADMSCs did not express major histocompatibility complex II, which help promote the release of factors such as PGE2 and control the mixed lymphocyte reaction after transplantation [23]. Therefore, ADMSCs can effectively inhibit the acute immune response of the host. There are also limits of this study. First, the evaluation index of the result is a little simple, which needs more complex comparison. Second, the mechanism is not detected, which is not so scientific. Furthermore, the basic concept needs more verification in future.

5. Conclusion

This protocol clinical trial suggested that HAMSCs injections may be a safe and feasible therapy for wound healing in patients. A larger, placebo-controlled, perspective, multicenter studies are necessity to further study the efficacy and safety of HAMSCs treatment for wound healing patients.

Data Availability

The data used to support this study are available from the corresponding author upon request.

Hindawi
Journal of Healthcare Engineering
Volume 2023, Article ID 9821301, 1 page
https://doi.org/10.1155/2023/9821301

Retraction

Retracted: Biometric Authentication for Intelligent and Privacy-Preserving Healthcare Systems

Journal of Healthcare Engineering

Received 23 May 2023; Accepted 23 May 2023; Published 24 May 2023

This article has been retracted by Hindawi following an investigation undertaken by the publisher [1]. This is investigation has uncovered evidence of one or more of the following indicators of systematic manipulation of the publication process:

(1) Discrepancies in scope
(2) Discrepancies in the description of the research reported
(3) Discrepancies between the availability of data and the research described
(4) Inappropriate citations
(5) Incoherent, meaningless and/or irrelevant content included in the article
(6) Peer-review manipulation

The presence of these indicators undermines our confidence in the integrity of the article's content and we cannot, therefore, vouch for its reliability. Please note that this notice is intended solely to alert readers that the content of this article is unreliable. We have not investigated whether authors were aware of or involved in the systematic manipulation of the publication process. Wiley and Hindawi regrets that the usual quality checks did not identify these issues before publication and have since put additional measures in place to safeguard research integrity.

We wish to credit our own Research Integrity and Research Publishing teams and anonymous and named external researchers and research integrity experts for contributing to this investigation.

The corresponding author, as the representative of all authors, has been given the opportunity to register their agreement or disagreement to this retraction. We have kept a record of any response received.

References

[1] D. Nigam, S. N. Patel, P. M. D. Raj Vincent, K. Srinivasan, and S. Arunmozhi, "Biometric Authentication for Intelligent and Privacy-Preserving Healthcare Systems," *Journal of Healthcare Engineering*, vol. 2022, Article ID 1789996, 15 pages, 2022.

Hindawi
Journal of Healthcare Engineering
Volume 2022, Article ID 1789996, 15 pages
https://doi.org/10.1155/2022/1789996

Review Article

Biometric Authentication for Intelligent and Privacy-Preserving Healthcare Systems

Dhananjay Nigam,[1] **Shilp Nirajbhai Patel**,[1] **P. M. Durai Raj Vincent**,[2] **Kathiravan Srinivasan**,[1] **and Sinouvassane Arunmozhi**[3]

[1]*School of Computer Science and Engineering, Vellore Institute of Technology, Vellore, India*
[2]*School of Information Technology and Engineering, Vellore Institute of Technology, Vellore, India*
[3]*Department of Electronics and Communication Engineering, Manakula Vinayagar Institute of Technology, Puducherry, India*

Correspondence should be addressed to Kathiravan Srinivasan; kathiravan.srinivasan@vit.ac.in

Received 11 January 2022; Revised 27 February 2022; Accepted 8 March 2022; Published 24 March 2022

Academic Editor: Sahfqat Ullah Khan

Secure identification is a critical system requirement for patients seeking health-related services. In the event of critical, aged, or disabled patients who require frequent health treatments, quick and easy identification is vital. Researchers describe the notion of the unprotected environment in this study, in which patients can receive health services from the hospital's smart and intelligent surroundings without the use of explicit equipment. Patients would interact directly with the environment and be identified through it. We suggest a biometric-based authentication technique for the unprotected hospital environment that also safeguards the patient's identity privacy. Furthermore, we demonstrate that this authentication technique is resistant to many well-known assaults, including insider attacks, replay attacks, and identity privacy. Doctors and other staff members showed enthusiastic responses after installing 2-factor authentications, as it makes their workflow efficient and makes things easier for patients. It also lets them focus on other factors rather than worrying about data security; hence, we need biometric authentication in intelligent and privacy-preserving healthcare systems. The paper deals with two-factor biometric authentication, and despite the added security, two-factor authentication adoption is said to be poor. It is due to a lack of awareness and difficulty to use and configure two-factor authentication (2FA) into a particular application by some individuals who struggle with the concept of authentication and its technology. Also, many 2FA methods in widespread use today have not been subjected to adequate usability testing. Research focuses on the point that there is still a large section of people unaware of the use of biometric systems to protect their online data. Researchers collected quantitative and qualitative data from 96 individuals during a two-week between-subjects usability survey of some common and rarely used 2FA approaches. The survey allowed the researcher to investigate which authentication methods are given higher priority and why, along with the relationship between different usage patterns and perceived usability, and identify user misconceptions and insecure habits to determine ease of use. It was observed that the biometric-based method was given the utmost preferability.

1. Introduction

Due to recent breakthroughs in Internet of things (IoT) and wireless sensor networks, there is a new digital paradigm shift. These technologies prove to be very useful, especially in the case of healthcare systems, thereby enhancing the well-being of people. With the help of this technology, the doctors and the hospital staff can continuously monitor their patients without even being present with them. Elderly patients can be automatically identified based on their surroundings and thus receive the appropriate services [1]. Electronic prescriptions for restricted medicines are heavily regulated and require a strong authentication system. Imprivata, a healthcare company, developed a biometric-powered confirmation ID system that enables healthcare institutions to meet their Drug Enforcement Administration criteria for electronic prescriptions of restricted medicines. Ghana's Health Ministry has already joined with Gavi to begin its biometric-based national vaccination programs by the end of 2021.

External devices such as laptops, cell phones, and tablets can interact with the system; the user interface provided by these devices is pertinent. On the contrary, the wearable category is far better and more advanced than other devices. The goal is to develop an intelligence technology in which services are incorporated through sensors and are available when needed and disappear when not, removing the need for the user to engage with the device. These cutting-edge technologies supply customers with a plethora of new options while also providing new revenue streams. Lightweight security solutions are required to implement these devices because they include various sensitive resources. Figure 1 shows the architecture of a digital healthcare services.

Identifying a valid patient/user is a significant difficulty in this type of unprotected setting. Traditional password-based single-factor authentication systems are not suitable and have some limitations. They are substantially weak when it comes to incorporating security in smart systems. As they contain only a single factor, which consists of a pin or a password, it can be easily breached by brute-forcing or simply guessing the password. Hence, a more transparent method such as biometric authentication should be incorporated, including face and speech recognition.

The unique property of biometrics expands its use in authentication protocols. Some important advantages of biometric keys are as follows:

(i) A user cannot lose or forget the key
(ii) They are difficult to copy or forge
(iii) They are tough to duplicate and transfer
(iv) It cannot be guessed easily when compared to low-entropy passwords

Password breaches, whether due to multiple password database leaks or increasingly sophisticated phishing attacks, dramatically increase the risk of authentication credential vulnerability [2]. Worse, poor user password hygiene, such as using passwords that are easily discovered such as birth dates, names, relatives' names, and phone pins, or repeating them across several accounts, exacerbates these flaws [3]. Figure 2 depicts the healthcare IT topology for medical devices.

Two-factor authentication (2FA), commonly known as two-step verification or dual-factor authentication, is a security feature in which users must authenticate their identity using two different authentication factors [4]. 2FA is used to protect a user's credentials and the resources to which they have access. Single-factor authentication (SFA), in which the user provides only one factor (usually a password), provides a lower level of security than 2FA [5]. 2FA gives the user a second factor that is either something they have (such as a hardware token or a phone) or something they are (referring to biometrics, such as facial recognition or fingerprint) [6]. It is the successor step after one has entered their credentials, which corresponds to something they know (traditionally a password and a username), so even though an attacker steals or guesses a user's password, they must compromise the user's phone or steal a physical device to gain access to the account [7]. As a result, compromising an account protected by a second authentication factor is far more difficult for a remote attacker [8, 9]. However, these technologies still reside in an external gadget that might be stolen and hence exploit the technology. So, we need a more transparent technology such as biometric authentication, which stays with the user all the time and is very difficult to exploit.

Many biometric services are now under development and testing, to be widely used in a few years. Plastic cards will soon be a thing of the past, and biometric scans will become the norm. The publicity of biometrics appears to be a concern. You have fingers, eyes, and a face, as everyone knows. On the other hand, open biometric data are only the tip of the iceberg. Every imaginable attribute is being studied, from heart rate monitoring to implanting chips under your skin, as well as examining intraocular veins, the structure of your earlobes, and more.

Two-factor authentication is a vast area, but this study focuses on biometric authentication: facial and speech recognition. The research is conducted because many people are unaware of the password-related risks and do not use 2FA for security. This hypothesis will be proved with the help of a survey further in the paper. A two-week survey was done using the Google Form, circulated among people using different social platforms. The survey measures the awareness of people from both technical and nontechnical backgrounds and people from all age brackets. The participants were from different parts of India. Researchers tried to determine which of the following two-factor authentication methods were popular and easy to use. The study focuses on the following:

(i) Presents the increasing need for 2FA
(ii) Expounds the concept of biometric authentication using face and speech recognition
(iii) Explains the integration of this technology into intelligent and smart healthcare systems
(iv) Presents diagrammatically the functioning of smart wireless sensors integrated with biometric authentication
(v) Presents a survey analysis conducted in India, which gives insight into the awareness and usability of biometrics

The study covers a literature survey of various research articles and journals, survey analysis, scope: present scenario and future opportunities, open challenges, and future research directions.

1.1. Biometric Recognition. Humans normally identify between persons using their faces, and recent advances in computer vision capacity have enabled similar recognitions to be made automatically [10]. Face recognition algorithms used simple geometric models in the past, but they have evolved into a science of complex mathematical models and representations throughout time, putting face and speech recognition in the spotlight for verification and

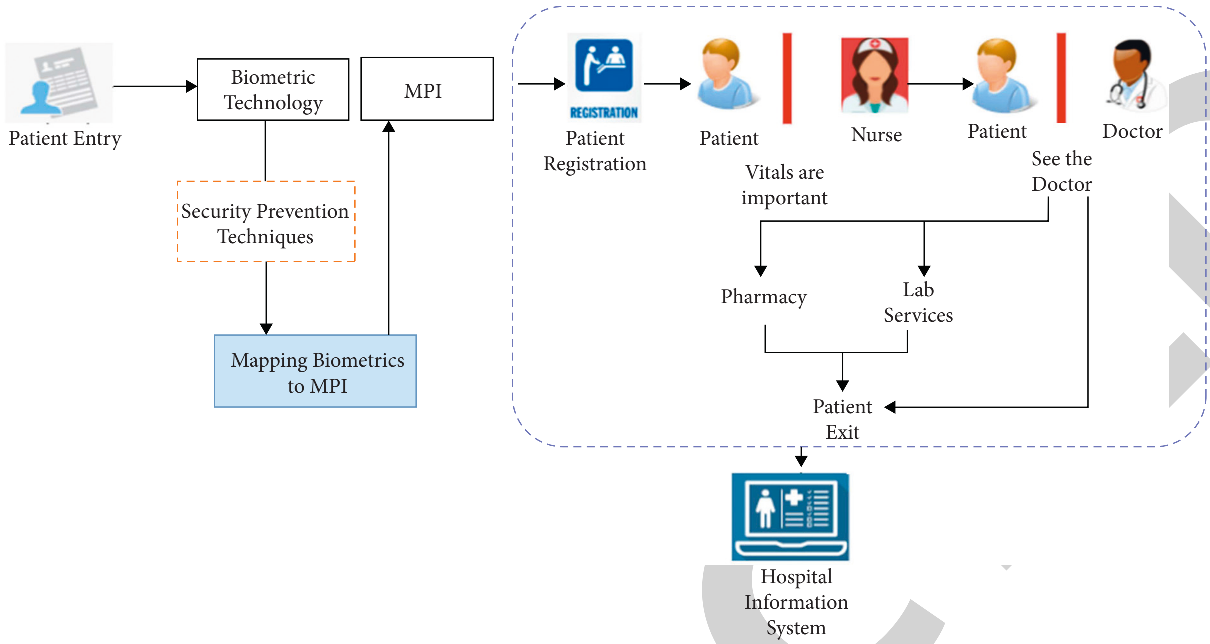

Figure 1: Architecture of biometric authentication for digital healthcare services.

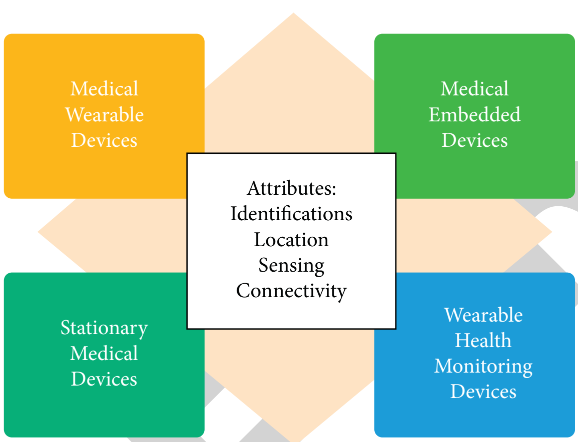

Figure 2: Healthcare IT topology for medical devices.

identification [11]. The practice of comparing one biometric pattern to another to determine whether it should be rejected or accepted is known as verification. Figure 3 shows the steps for authentication and verification.

2. Literature Review

Previous research has looked into using extremely low-resolution photographs to accomplish activity recognition while maintaining anonymity. Low-resolution action recognition based on the shape of the human head to guide body position estimate is proposed in one paper (Privacy-Preserving Action Recognition for Smart Hospitals Using Low-Resolution Depth Images). Inverse super-resolution (ISR) employs a network that generates several low-resolution recommendations and employs MCMC and entropy measure techniques to find the best action recognition transformation. Two comparable approaches use two-stream neural networks to aggregate data and build a cross representation between high- and low-resolution images to learn an appropriate feature mapping.

Significant investment is needed in biometrics for security. Machine learning and algorithms must be very advanced to minimize biometric demographic bias. Some biometric systems can face scanning issues if there is a slight change, especially if the company is using retina scanning. Hard biometrics consists of authentication using face, fingerprints, or signature. It is very easy nowadays to forge another person's fingerprint or signature. Getting a facial snapshot of a person is very easy, and by that way, face recognition can be easily breached. Soft biometrics include voice recognition, eye color, and scars, which provide ancillary information but are not fully distinctive and permanent [12].

Numerous symmetric key techniques have been proposed in the literature for smart card-based authentication on single-server and multi-server architectures. In addition to smart card-based authentication, the literature describes three-factor authentication techniques that involve biometrics. However, biometric information integration is bound to be a fixed string and implemented similarly to password introduction. These smart card-based procedures can easily be transformed into the biometric form and vice versa. Most of the suggested smart card-based and biometric-based authentication methods are unsafe for well-known attacks such as stolen smart card attacks, replay attacks, user impersonation attacks, and insider attacks. A novel security system with identity privacy and untraceability is offered. Fuzzy extractors, fuzzy vaults, and fuzzy commitments, on the other hand, are commonly used to facilitate reusability and unlinkability in the practical integration of biometric data. These techniques use a template and assistance data to retrieve the secret material.

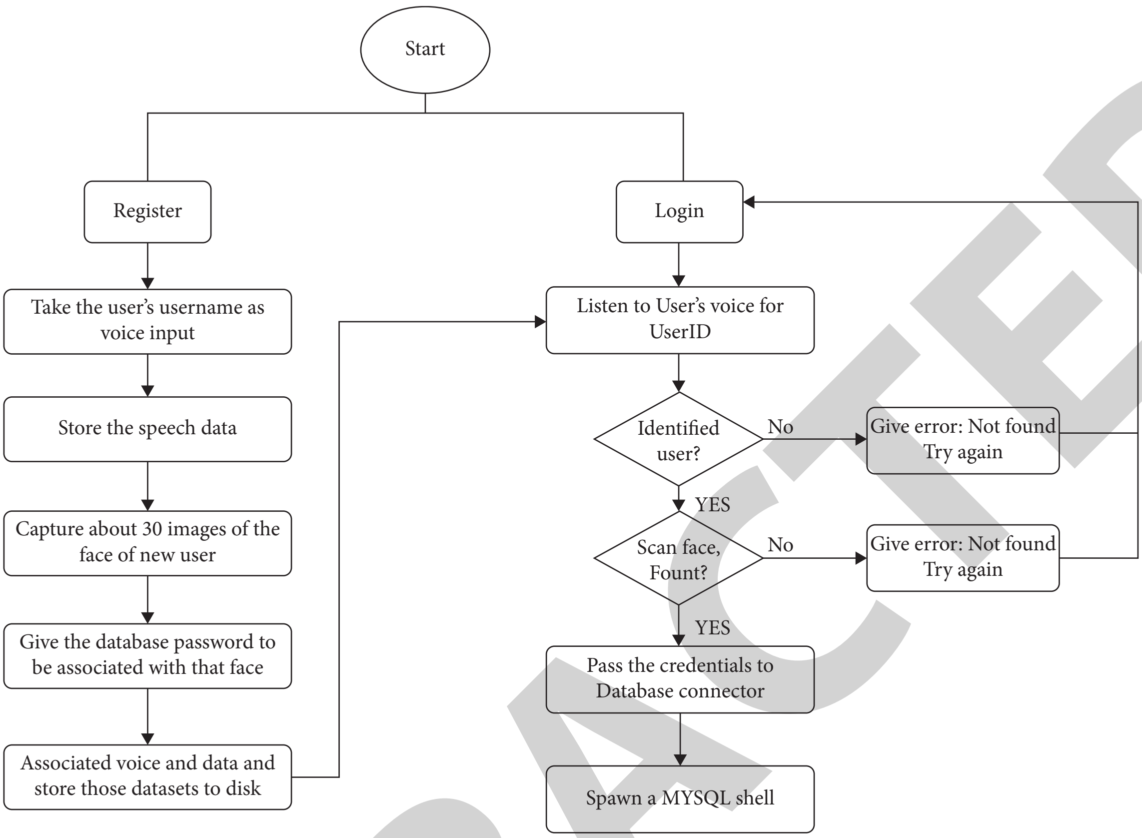

Figure 3: Flow of authentication.

Unfortunately, these approaches come at a considerable cost in terms of complexity and performance. The use of a pseudorandom number generator (PRNG) is proposed in "Identity Privacy-Preserving Biometric-Based Authentication Scheme for Unprotected Healthcare Environment" to develop a safe and computationally efficient remote biometric authentication technique, which adds robust biometric data security to a wide range of existing authentication protocols. Because it protects templates and the user's privacy, the technique is known as a blind biometric authentication protocol. The protocol is blind since it does not display any information about the user other than their identification. On the server side, it also employs a PRNG.

Many current 2FA approaches are being called into question. Two-factor authentication enabled using one-time password (OTP), or SMS has one major disadvantage. As long as the device on which the OTP has been configured is in possession, it is convenient, but sometimes when the person does not have the device with him/her, although his account is secure, he is not able to log in or get access. It becomes a matter of convenience and hence is not used sometimes. For example, according to "Transparent two-factor authentication" [13] paper, certain methods of 2FA can be turned against a user's system. One such case is when McAfee and Guardian Analytics released a joint report titled "Dissecting Operation High Roller." It mentioned an international criminal group that used an automated operation and stole large sums of money through unauthorized and fraudulent transfers. By infesting malicious software, they were able to get hold of the user's system, and hence, they could even verify the two-factor tokens required for the bank account. Hence, this study suggested a more transparent method so that users can easily verify themselves and save themselves from different frauds. "Overview of fingerprint recognition system" states that the fingerprint system will be unavailable to certain segments of the population. People who have lost fingers or hands would be excluded, while older adults who are indulged in manual labor for so many years may struggle to record worn prints into a system. Many laptops do not support fingerprint recognition; hence, they cannot be used for online databases.

According to the "Five methods of usability of 2FA," many users disliked hardware code generators; in fact, a few people switched banks because the tokens were so difficult to use. We also found out that the most common 2FA methods used were email or SMS for financial or personal sites [14]. According to another survey, these common methods have certain limitations. An attacker may pose as somebody while speaking to the victim, somebody from a particular bank, and by taking advantage of the user's distraction, which may get hold of the one-time password from that user [15, 16]. This way, the user might lose every penny he owns, further affecting his/her business or professional life. According to one paper on cryptography known as "multifactor authentication," integrating credible and new solutions has always been a huge hurdle for developers and managers. User acceptance is low and a very serious part of adopting multifactor authentication. For example, a method known as deoxyribonucleic acid (DNA) recognition has very high performance, universality, and uniqueness, but the acceptability rate is quite low, although it is not prone to spoof attacks and is an assuring method. On the other hand, this study supports using face and speech recognition as a part of 2FA. They suggest it is more transparent and easier to use and configure for people from almost every age bracket [17].

There are different ways with the help of which can optimize this method and make it more and more secure [18]. We can enable three-dimensional face recognition, i.e., by asking the user to move the head during the authentication process in a specific manner. User expressions can also be detected, making it less prone to any attacker or breach. According to a survey done at Carnegie Mellon University [19], many people were satisfied and thought that one-factor authentication is secure. The conclusion followed in the paper deduces that two-factor authentication now has become a necessity, regardless of the petty limitations that will be fixed in due time. Table 1 presents the list of existing methods with their approaches and limitations.

3. Methodology

The researchers have opted for the empirical way of research and are using the survey to prove the above hypothesis. The survey was conducted through Google Forms with 96 responses from different age groups and aspects of the society, which gave the researcher a vivid idea of the hypothesis. The survey was carried out for two weeks, and the participants were from different professions and different parts of India. For those who did not know the meaning of 2FA, researchers explained the meaning and usage to get their views. They were asked to use a simple biometric 2FA to get a clear idea.

4. Survey Analysis

Researchers got thoughtful opinions on where exactly the technology should be incorporated, which areas need immediate attention to this kind of technology, etc. Most people voted in favor of the companies that handle finances and online payment systems using the 2FA system. Although many people know about two-factor authentication, more people need to be aware of this technology as it will be fruitful soon.

This was an investigational study to see how people interpreted, adopted, and used 2FA. The researchers focused their efforts on gathering data that may be used to guide future deployments and improve specific procedures. In particular, the researchers were interested in users' impressions of 2FA and the factors that encourage and inhibit adoption. The survey was conducted through Google Form with 96 responses, including people from all the age brackets. In some questions, multiple-choice can be selected.

Analysis 1: the majority of the people, about 86.5%, i.e., 83 of the 96 participants, belonged to the 16–30 age group. Less than 9.4% (9 people) were people above 45 years. Only 2.1% (2 people) belonged to the age bracket of 5–15 and 31–45 years. This shows the targeted audience. People from age groups 5–15 are too young to understand the concept of 2FA and use it properly. Due to the generation gap and technical knowledge gap, not many people above the age of 40 use 2FA. Researchers did not circulate the Google Form to the people who did not know about 2FA because some questions required knowing 2FA and authentication. That is why there are fewer people in this age group. Currently, the main users of 2FA are people from 16 to 30 years. This gap will fade away in a few years, and people above 30 years will also actively use 2FA. Figure 4 illustrates the survey query 1.

Analysis 2: researchers found out that 35.8%, i.e., 34 of the 95 people, fall into indecision in the case of a password compromise. They are not aware of how to recover and restore their account by changing their passwords so that the attacker may not control their account for too long. Figure 5 depicts the survey query 2.

Analysis 3: 63.5%, i.e., 61 of the 96 people, use the same passwords everywhere. Hence, if one of their accounts gets compromised, it is very likely that other accounts will also get attacked, and they may lose a huge amount of sensitive information. Even if your password is leaked, attackers still need the 2nd factor to authenticate successfully. Using biometric factors makes it difficult to steal face or speech factors. Thus, the need for two-factor authentication is very high. Figure 6 portrays the survey query 3.

Analysis 4: participants selected multiple options. 68.1% of people (64 people) prefer biometric authentication such as face and speech recognition for security. One-time password through SMS is the most common and used method. However, it is observed that participants wanted to switch to technologies such as face and speech recognition, which is more secure and not easily stolen or imitated. Researchers focus on "biometric 2FA for online database"; therefore, face and speech recognition is the most feasible options. OTP and PIN codes are not biometric, and fingerprints are difficult to use for online databases on the laptop. Figure 7 shows the survey query 4, and Figure 8 represents the survey query 5.

Analysis 5: 23.2%, i.e., 22 of the 95 people, still think that a single authentication system is enough for the security of their accounts. One reason for this could be that they find it difficult to carry hardware tokens everywhere to authenticate themselves repeatedly, which is a tedious task. 58.9%, i.e., 56 of the 95 people, think 2FA is the highest level of security, which cannot be surpassed and is more than enough to secure their data, while 21.1% of people (20 people) want 2FA to be optimized and more factors should be added to strengthen the security. Few people feel like multifactor is a time-consuming process. Figure 9 illustrates the survey query 6, and Figure 10 depicts the survey query 7.

Analysis 6: 84.9%, i.e., 79 of the 93 people, want to incorporate 2FA into online payment apps and other financial consultancies operating online and where the exchange of money is taking place. Figure 11 portrays the survey query 8.

Analysis 7: in the survey, researchers found that 60.3% of people (38 people) find 2FA easy to use. 7.9% of people (5 people) reported it being difficult, out of which most people

Table 1: List of existing methods with their approaches and limitations.

Scheme	Year	Approach	Limitations
[20]	2012	Asymmetric	Forgery attacks are possible
[21]	2015	Cryptographic hash function	Vulnerable to impersonation attacks and insider attacks
[22]	2012	Symmetric encryption	User tracking attacks are possible
[23]	2016	Cryptographic hash function	Experiencing issues with transmitting secrecy and revocability
[13]	2018	Fingerprint verification	Fingerprints can also be stolen by capturing your prints without you knowing
[18]	2015	Hardware tokens	Many people find it difficult to carry hardware tokens and may lose them sometimes
[24]	2020	Bloom filter and format-preserving encryption	The primary downside is its probabilistic nature

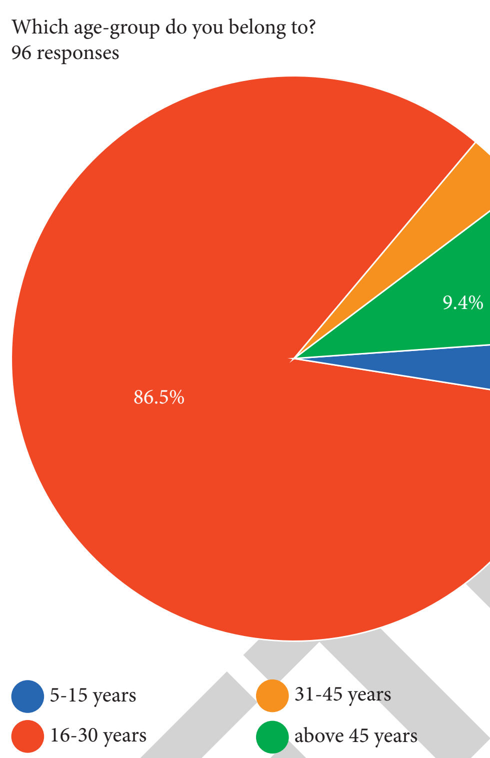

Figure 4: Survey query 1.

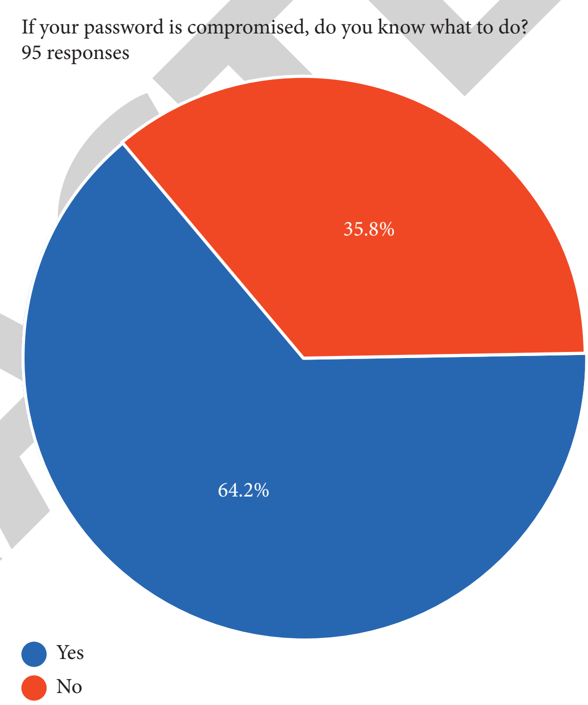

Figure 5: Survey query 2.

were above 45 years old. 14.3% of people (9 people) feel like it is unnecessary, and 17.5%, i.e., 11 of the 63 people, feel like it is very time-consuming and annoying. With this small-scale survey, researchers could figure out the qualitative and quantitative aspects of two-factor authentication technology. From these data, researchers can undoubtedly infer that although the preponderance of the people is aware of the technology and its logistics, there are still many people who are entirely oblivious to the use of this technology. Figure 12 represents the survey query 9. Table 2 presents the comparison results for privacy and security characteristic features.

5. Scope

5.1. Present Scenario. There are some limitations of this technology. It has been observed that two-factor authentication brings inconvenience to users when a physical entity is used as a second authentication factor, where many additional operation steps are added [28]. The main barriers to this technique are the data collecting and data storage processes. There is a chance the platform will crash or get an authentication problem. The possibility of technology duplication by other companies is a concern. New technologies could put this platform and technology to the challenge. After completing the password recovery process, many services will automatically log you into your account. When you use social media to log in to your account, 2FA may be ignored [29].

Patient records, data from clinical trials, radiological images, and genetic sequencing data are among the sources of the ever-increasing healthcare data. These data are predicted to have grown to a size of 25,000 petabytes by 2020. Virtualization and cloud computing are two new technologies that may acquire, manipulate, and store massive amounts of data. Healthcare data management thus involves the issues of storage and retrieval of vast amounts and types of data and the integration and exchange of such data across numerous sites. Aside from that, the construction of a scalable system that provides continuous connectivity

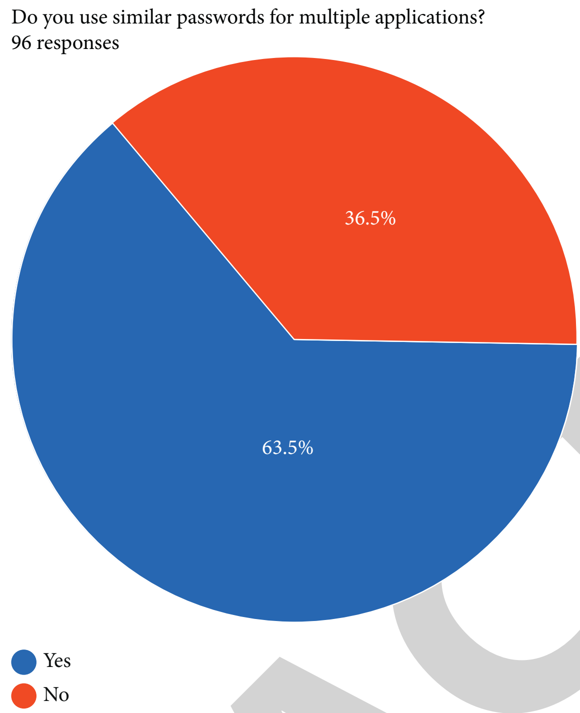

Figure 6: Survey query 3.

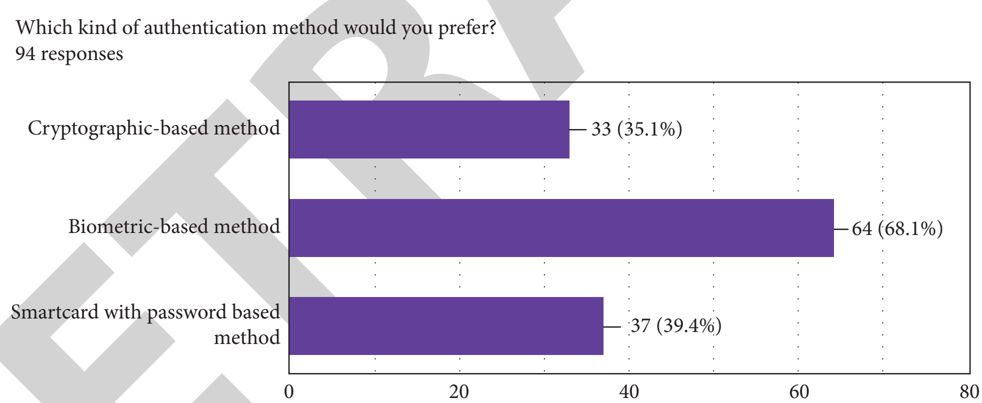

Figure 7: Survey query 4.

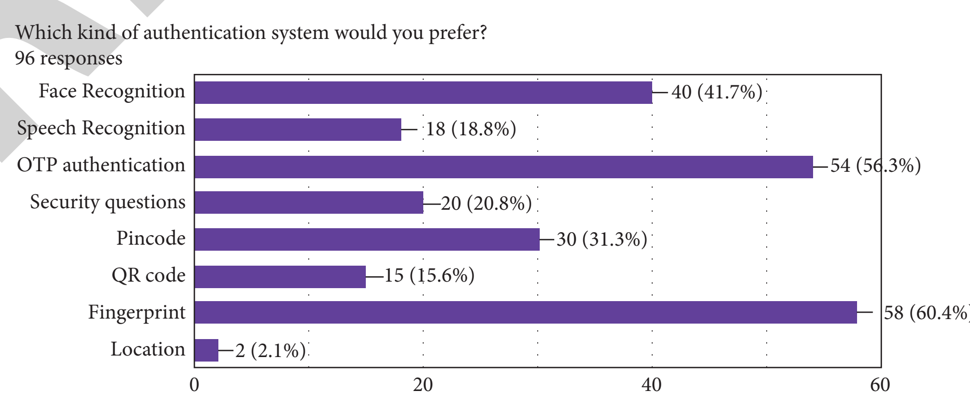

Figure 8: Survey query 5.

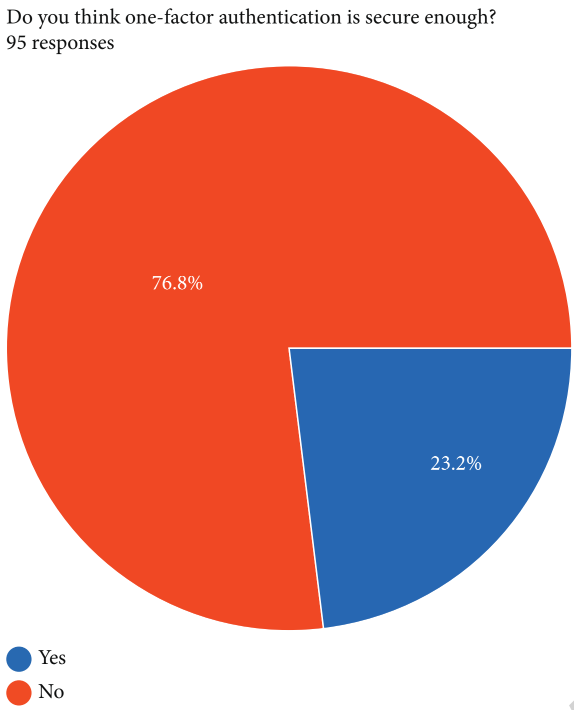

Figure 9: Survey query 6.

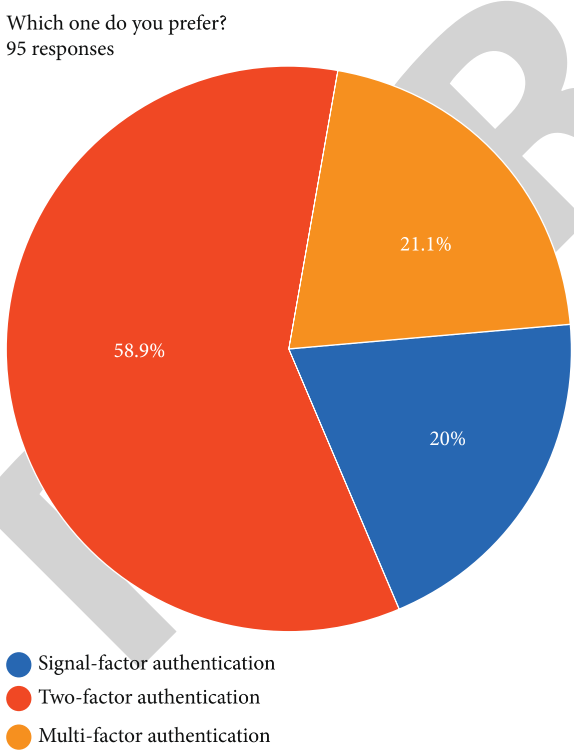

Figure 10: Survey query 7.

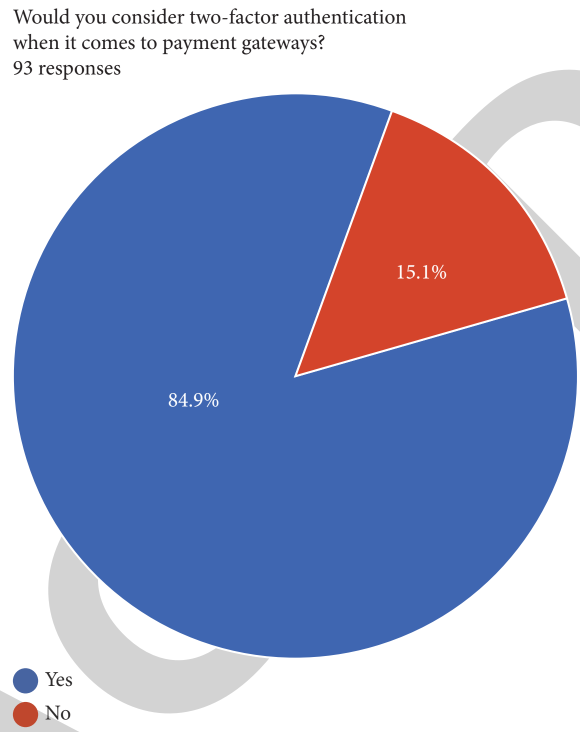

Figure 11: Survey query 8.

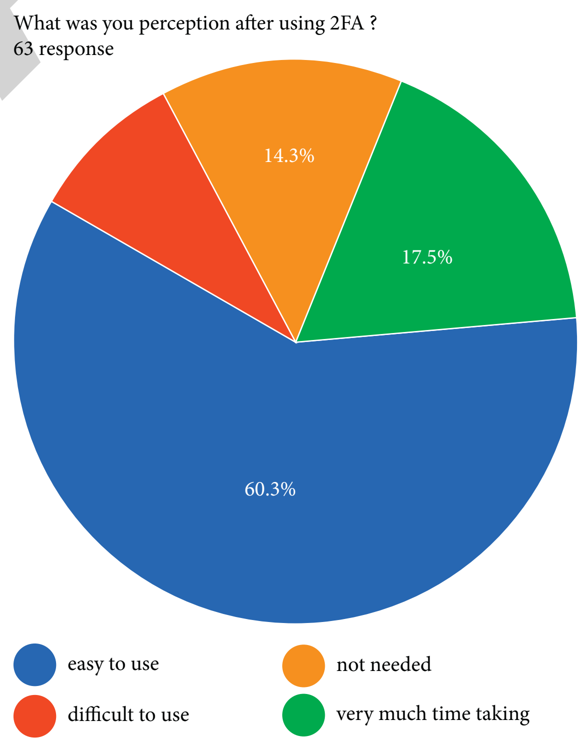

Figure 12: Survey query 9.

between the healthcare management system and its users is required [30].

5.2. Case Study: Healthcare Facilities. In a case such as healthcare data storage and retrieval, a biometric system can provide authentication. The fundamental motivation for implementing biometrics in the healthcare industry is to ensure the privacy and security of patient records. Health Insurance Portability and Accountability Act (HIPAA), the European Data Protection Directive, and the Australian

Table 2: Comparison results for privacy and security characteristic features.

Features	[25]	[26]	[27]	[10]
User anonymity	Yes	Yes	No	No
Mutual authentication	Yes	Yes	Yes	Yes
Off-line PW guessing attack	Yes	No	No	No
Impersonation attack	Yes	Yes	Yes	No
Replay attack	Yes	No	No	Yes
Provides formal security	Yes	Yes	No	No

Privacy Principles Act are examples of the international rules that mandate a high level of security, sensitive data exchange, and access control [30].

"Two-factor authentication platform helps healthcare institutions and health information networks secure remote access to confidential health information in a cost-effective and scalable manner, without disrupting provider workflow" [31]. The security of patient data is legal and an ethical obligation of the medical sector. Complete security is difficult to achieve, especially in the medical domain, where disclosing information regarding the patient is a significant part of treating the patient. As dangers to the patient's health data rise, suitable technical, administrative, and physical protection measures must be taken to protect the privacy of protected health information (PHI). Hackers consistently target user credentials to gain access to the healthcare system [32]. Figure 13 shows the functional platform for the healthcare system.

According to the Protenus Breach Barometer, these types of incidents compromised 3.8 million medical records in 2019. An increase in health data available electronically implies more risks. For example, it is usually these days for family members and the provider's office to share usernames and passwords. Employees may be given these personal credentials to gain legitimate access. They are occasionally written down and picked up by curious individuals. It may be guessed or detected by malicious software. This increased exposure has resulted in a significant increase in information leakage, theft of personal information, and numerous violations of HIPAA's privacy and security regulations [33]. Using a static password to prevent unauthorized or unlawful access to your personal or sensitive information is no longer deemed sufficient [34]. Also, there are important data of healthcare departments such as information related to where particular medicine is kept and how many doses can be harmful, or research information needed to be protected at any cost. The leakage of such data can prove fatal and affect the masses.

Two-factor authentication provides a higher level of security and reliability. According to "[31]" by William Braithwaite, it is accepted and understood widely that to provide sufficient security to protect access of sensitive data and personal information of the patient, two-factor authentication needs to be implemented. Allowing access only after face and speech recognition verification will help keep intruders from hacking or logging in and stealing important healthcare data. Keeping factors such as face detection and speech verification prevent robots or other systems [7]. Figure 14 shows the healthcare data breach record in the past years.

According to HealthTech, a company that deals with software requirements of healthcare facilities, doctors and other staff members showed enthusiastic response after the installation of 2-factor authentications as it makes their workflow efficient and makes things easier for patients. It also lets them focus on other factors rather than worrying about data security. It saves money and time.

For example, many healthcare companies ask their employees to strengthen their passwords, which may sometimes be complicated. They also require users to change their passwords periodically to ensure the security of their sensitive data, which makes passwords hard to remember but very easy to lose. Based on studies by Microsoft, the account becomes 99.9% less likely to be compromised or attacked if you use MFA. Table 3 presents a summary of the protocol, results, and key contributions from authentication and privacy-preserving healthcare systems. Table 4 presents the details on the classification of healthcare apps for authentication and privacy-preserving healthcare systems. Table 5 shows the different types of attacks for authentication and privacy-preserving healthcare systems.

6. Open Challenges: Authentication and Privacy-Preserving Healthcare Systems

Figure 15 illustrates the open challenges for authentication and privacy-preserving healthcare systems. Some of the open challenges are as follows:

(i) If only one parameter is impacted, the accuracy of the entire system will suffer
(ii) Cost and technical complexity to implement
(iii) 2FA for many platforms can be circumvented
(iv) Creating procedural delays in the system
(v) Susceptible to social engineering
(vi) Access codes can be stolen; vulnerable to phishing attacks
(vii) Poses advanced threats such as a 3D modeling of a face or finger
(viii) The influence of the technical issues is significant
(ix) Usability issues in Google's 2FA setup processes

7. Future Research Directions: Authentication and Privacy-Preserving Healthcare Systems

Face recognition (FR) is becoming a key study area due to the wide range of applications in commercial and law

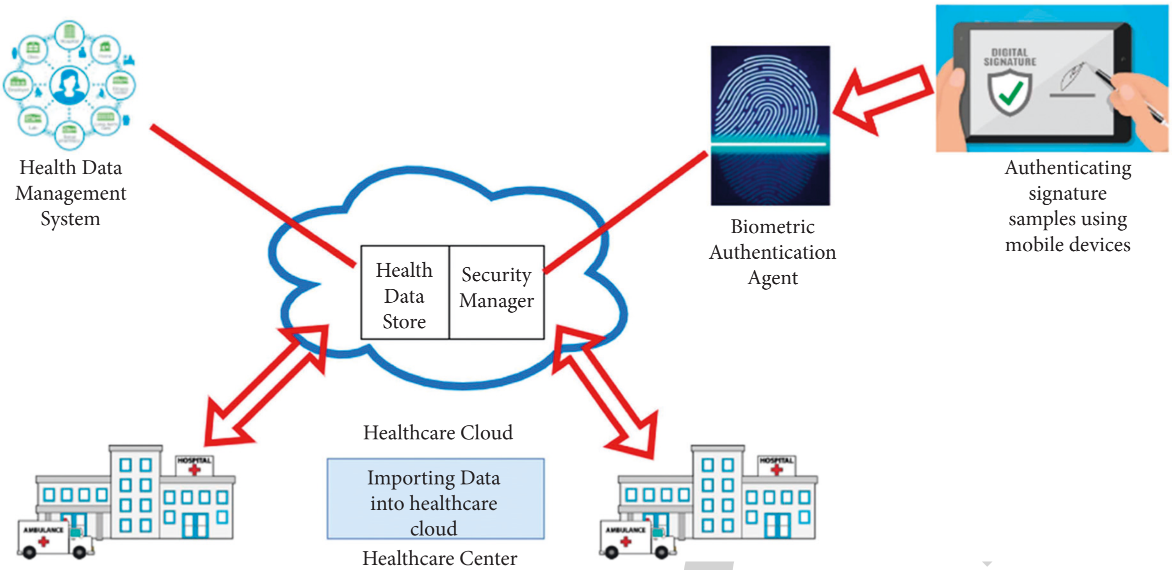

FIGURE 13: Functional platform of the intelligent and privacy-preserving healthcare system.

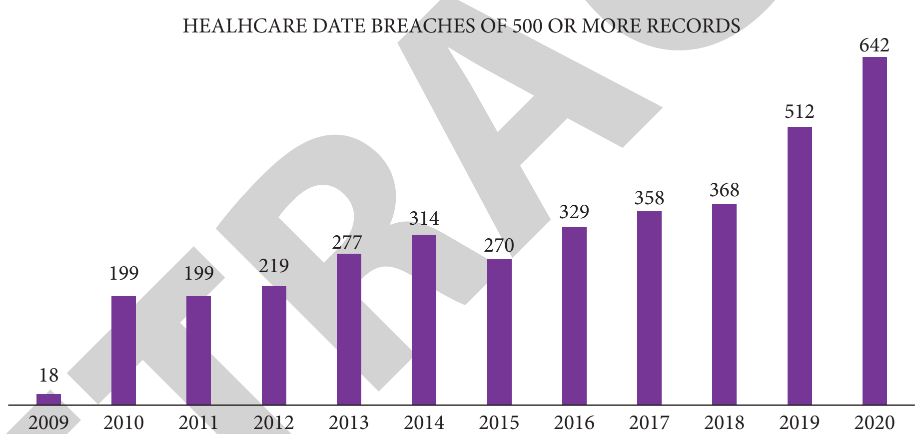

FIGURE 14: Healthcare data breach record.

TABLE 3: A summary of the protocol, results, and key contributions from authentication and privacy-preserving healthcare systems.

Reference	Year	Protocol	Results	Key contributions
[1]	2019	Health screening for people who have diabetes	Smart services do the whole screening autonomously	They do not describe how a procedure is performed but why, when, where, and by whom the care is given
[27]	2015	Security	Promotes public confidence in healthcare services	Provides a secure environment for people using the services
[35]	2019	Decentralized privacy-preserving healthcare blockchain for IoT	Secures data transfers and logging of data and storage on the blockchain	Security through blockchain
[36]	2017	Radiofrequency identification	Tracks hospital supplies, medical equipment, medications	Privacy-preserving access controls
[12]	2013	Wireless medical sensor network	Sensitive patient information is sent through the open air.	The lightweight encryption algorithm is proposed to secure communication between the sensor node and the Sharemind system.

Table 4: A classification of healthcare apps: authentication and privacy-preserving healthcare systems.

Category	Common apps	Description
Medicine delivery app	Netmeds, PharmEasy, Medlife	Delivery anywhere
Telenursing applications	Practo	Online doctor consultation
Medicine reminders app	Medisafe Pill reminder, Bedside Reminders	Alerting with push notification
Appointment scheduling apps	AppointmentPlus, PatientPop	Set online scheduler with doctor
Mindfulness, health, and fitness apps	MyFitnessPal, Headspace	Records your heart rate, water level, sugar level, and gives you a full report at the end
Patient health education apps	CardioTech, Simply Sayin'	Educates patients about different diseases, what causes them, and what are the symptoms

Table 5: Different types of attacks: authentication and privacy-preserving healthcare systems.

Reference	Year	Attacks	Description
[37]	2012	Dictionary and password guessing attack	Guessing the password from a password list
[38]	2013	Denial of service	Denying service to the user by creating unnecessary traffic
[20]	2012	Impersonation attacks	Impersonating to be someone and stealing information
[39]	2013	Patient anonymity violation	Exploiting the hidden identity of the patient
[40]	2014	Spoofing	The act of misrepresenting a communication from an unknown source as coming from a recognized, reliable source.
[22]	2012	Malware infusion	Ingesting malware into the system so that it does not work properly
[23]	2016	Man in the middle	Capturing and listening to the information being passed from the sender to the receiver and vice versa.
[21]	2015	Tracing attacks	In each session, the patient uses the same identifier, leading to the disclosure of private information.

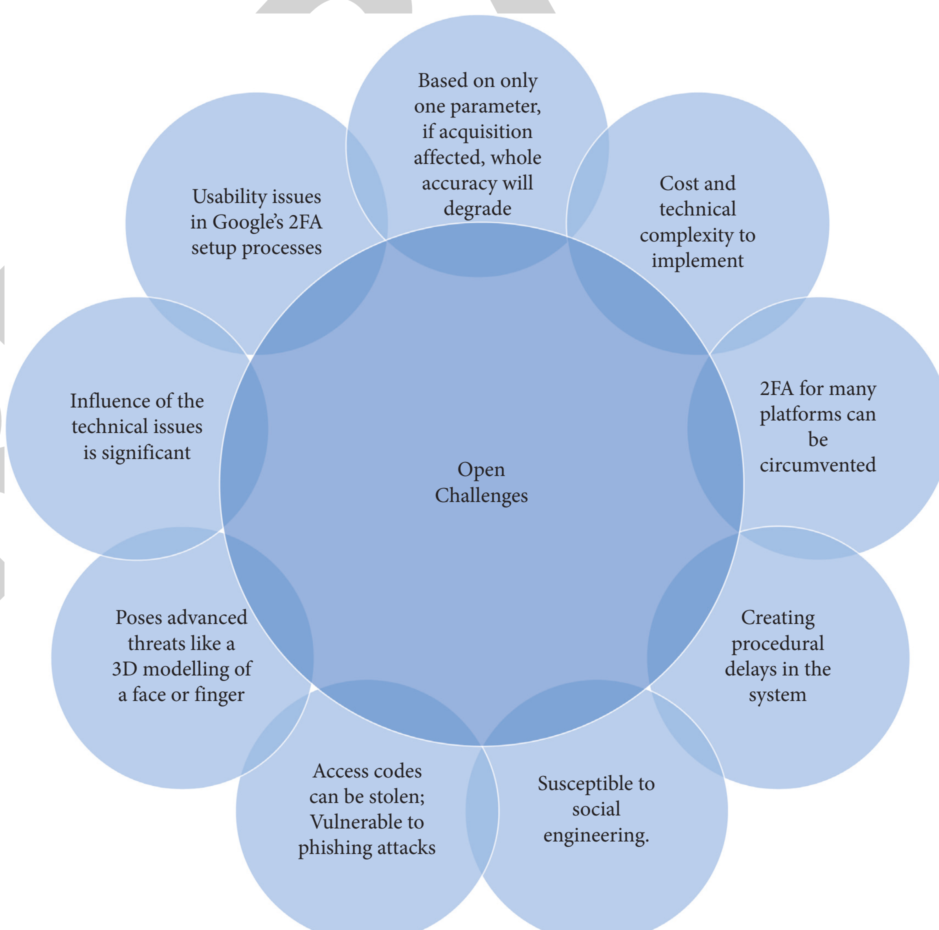

Figure 15: Open challenges: authentication and privacy-preserving healthcare systems.

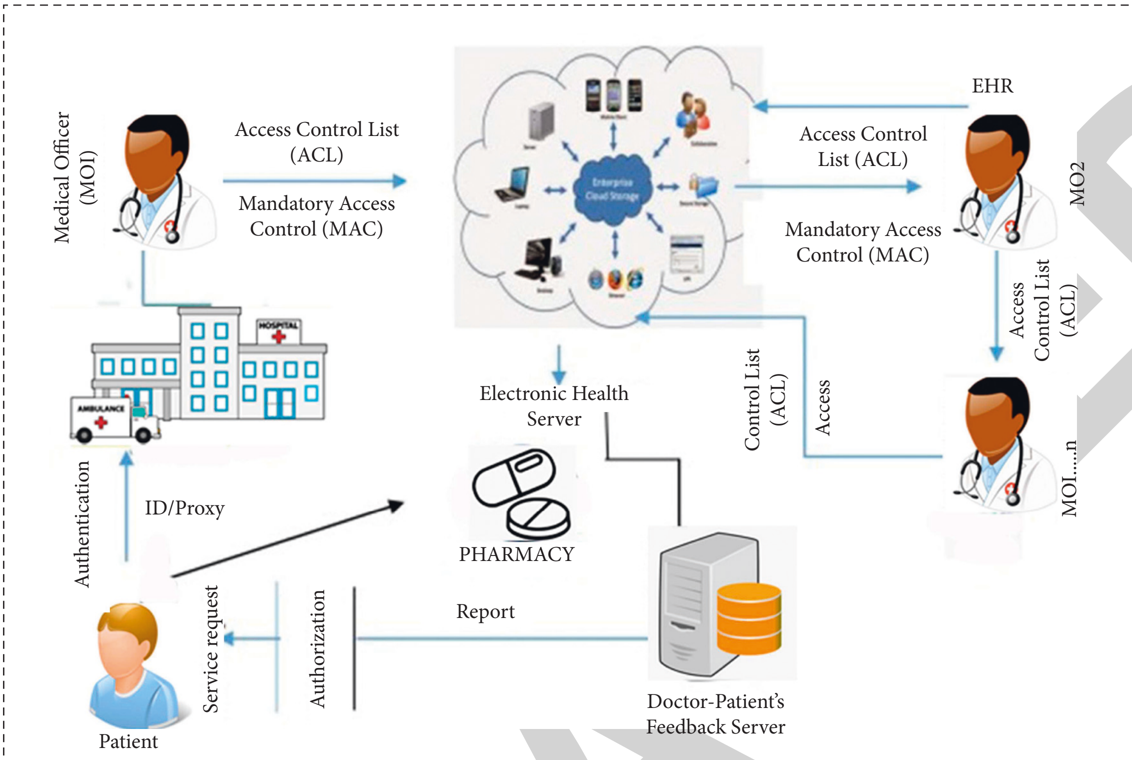

Figure 16: Operating model: authentication and privacy-preserving healthcare systems.

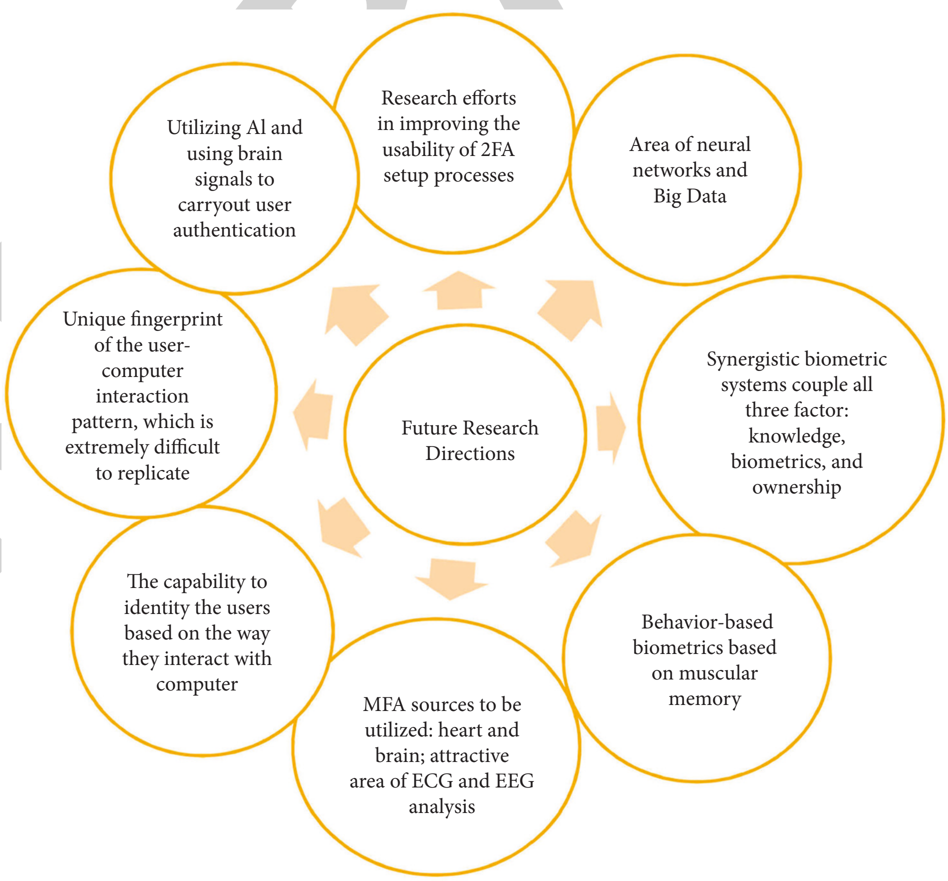

Figure 17: Future research directions: authentication and privacy-preserving healthcare systems.

enforcement industries. Figure 16 represents the operating model for authentication and privacy-preserving healthcare systems. Object lighting, pose variation, expression variations, and facial disguises are all issues for traditional FR approaches based on visible spectrum (VS). Unfortunately, these constraints reduce object identification and verification performance. Figure 17 shows the future research directions for authentication and privacy-preserving healthcare systems. The infrared spectrum (IRS) may be employed in human FR to circumvent these constraints. Some of the future research directions are as follows:

(i) In India, preventing ATM fraud is a priority. It is possible to construct a database of all ATM cardholders in India with facial and speech recognition technologies.

(ii) It can also identify candidates during examinations such as the Civil Services Exam, SSC, IIT, MBBS, and others.

(iii) This technology can verify and track attendance at various government offices and businesses.

(iv) It can also be implemented in bank lockers and vaults for access control verification and authentication of authentic users.

(v) More biometric authentication-enabled items, such as computers and cell phones, can be manufactured.

(vi) Consumers' growing security concerns result in increased demand for biometric services.

(vii) Research efforts in improving the usability of 2FA setup processes.

(viii) Area of neural networks and big data.

(ix) Synergistic biometric systems couple all three factors: knowledge, biometrics, and ownership.

(x) Behavior-based biometrics based on muscular memory.

(xi) MFA sources to be utilized: heart and brain; attractive area of ECG and EEG analysis.

(xii) The capability to identify the users based on the way they interact with the computer.

(xiii) Unique fingerprint of the user-computer interaction pattern, which is extremely difficult to replicate.

(xiv) Utilizing AI and using brain signals to carry out user authentication.

8. Conclusions

It is no surprise that various digital accounts have become a magnet for fraudsters because people spend so much of their time on their phones and laptops. Malicious attacks on governments, businesses, and individuals are becoming increasingly widespread. Moreover, there are no indicators that hacking, data breaches, or other forms of cybercrime will slow down anytime soon. Fortunately, two-factor authentication, often known as 2FA, is a simple way for organizations to add an extra layer of security to user accounts.

Many existing approaches are vulnerable to insider attacks and off-line password guessing attacks, resulting in increased security risks and the inability to provide user anonymity. Secure authentication is required to overcome the problem of timely updating patient data in the medical system. The discussion above makes us believe that the new scheme meets the following requirements: smart health care is good. The Proposed Intelligent and Privacy-Preserving Healthcare Systems scheme provides mutual authentication between patient and authentication server. The patient can also change their password freely without the help of the registration server. Researchers have demonstrated that the proposed scheme has more security features and a greater security level than similar schemes.

Some people still do not use 2FA, making them vulnerable to security threats. The company's responsibility is to endeavor to make people aware of the process and benefits of 2FA and biometric systems.

A very recent example of the same is WhatsApp. They have started their end-to-end encryption; they have used various media platforms to spread awareness about the same and influence people to use it more as it is the safer way, and this shall prevent them from various sorts of data breaches. So, even now, if people are not technically aware of end-to-end encryption, they still know this will protect their data. The same efforts are needed in the field of biometric 2FA.

Biometric authentication is undoubtedly gaining popularity and is commonly used by mobile users, but its popularity has been restricted to phones only. People are unaware of its usage on online databases, which is too vulnerable to security breaches. It should be user-friendly, with terms and conditions explained in a layman's way and the threats of not using it.

Data Availability

The article's original contributions generated for this study are included; further inquiries can be directed to the corresponding author.

Conflicts of Interest

The authors declare that there are no conflicts of interest regarding the publication of this study.

References

[1] S. Khatoon, S. M. M. Rahman, M. Alrubaian, and A. Alamri, "Privacy-preserved, provable secure, mutually authenticated key agreement protocol for healthcare in a smart city environment," *IEEE Access*, vol. 7, pp. 47962–47971, 2019.

[2] S. Pandey, T. Taffese, M. Huang, and M. D. Byrne, "Human performance in google's two-factor Authentication setup process," *Proceedings of the Human Factors and Ergonomics Society - Annual Meeting*, vol. 63, no. 1, pp. 2221–2225, 2019.

[3] A. Abuarqoub, "D-FAP: dual-factor authentication protocol for mobile cloud-connected devices," *Journal of Sensor and Actuator Networks*, vol. 9, no. 1, p. 1, 2020.

[4] O. Persson and E. Wermelin, *A Theoretical Proposal of Two-Factor Authentication in Smartphones*, 2017, http://www.bth.se.

[5] R. Bruzgiene and K. Jurgilas, "Securing remote access to information systems of critical infrastructure using two-factor authentication," *Electronics (Switzerland)*, vol. 10, no. 15, 2021.

[6] M. H. Barkadehi, M. Nilashi, O. Ibrahim, A. Zakeri Fardi, and S. Samad, "Authentication systems: a literature review and classification," *Telematics and Informatics*, vol. 35, no. Issue 5, pp. 1491–1511, 2018.

[7] M. K. Sharma and M. J. Nene, "Two-factor authentication using biometric-based quantum operations," *Security and Privacy*, vol. 3, no. 3, 2020a, https://doi.org/10.1002/spy2.102.

[8] G. Ali, M. A. Dida, and A. E. Sam, "Two-factor authentication scheme for mobile money: a review of threat models and countermeasures," *Future Internet*, vol. 12, no. Issue 10, pp. 1–27, 2020.

[9] A. J. Mohammed and A. A. Yassin, "Efficient and flexible multi-factor authentication protocol based on fuzzy extractor of administrator's fingerprint and smart mobile device," *Cryptography*, vol. 3, no. 3, pp. 1–222, 2019.

[10] A. Ometov, S. Bezzateev, N. Mäkitalo, S. Andreev, T. Mikkonen, and Y. Koucheryavy, "Multi-factor authentication: a survey," *Cryptography*, vol. 2, no. 1, pp. 1–31, 2018.

[11] U. Sharma, P. Tomar, S. S. Ali, N. Saxena, and R. S. Bhadoria, "Optimized authentication system with high security and privacy," *Electronics (Switzerland)*, vol. 10, no. 4, pp. 1–23, 2021.

[12] X. Yi, J. Willemson, and F. Nait-Abdesselam, "Privacy-preserving wireless medical sensor network," in *Proceedings of the 12th IEEE International Conference on Trust, Security and Privacy in Computing and Communications, TrustCom 2013*, pp. 118–125, 2013.

[13] J. Zhang, X. Tan, X. Wang, A. Yan, and Z. Qin, "T2FA: transparent two-factor Authentication," *IEEE Access*, vol. 6, pp. 32677–32686, 2018.

[14] S. Yu, K. Park, and Y. Park, "A secure lightweight three-factor authentication scheme for IoT in the cloud computing environment," *Sensors*, vol. 19, no. 16, 2019.

[15] M. Obaidat, J. Brown, S. Obeidat, and M. Rawashdeh, "A hybrid dynamic encryption scheme for multi-factor verification: a novel paradigm for remote authentication," *Sensors*, vol. 20, no. 15, pp. 1–32, 2020.

[16] G. Xu, S. Qiu, H. Ahmad et al., "A multi-server two-factor authentication scheme with un-traceability using elliptic curve cryptography," *Sensors*, vol. 18, no. 7, 2018.

[17] K. David Biaru, *University of Nairobi School of Computing and Informatics A Model of Two-Factor Authentication Using Facial Recognition in Automated Teller Machines*, 2014.

[18] I.-P. Chang, T.-F. Lee, T.-H. Lin, and C.-M. Liu, "Enhanced two-factor authentication and key agreement using dynamic identities in wireless sensor networks," *Sensors*, vol. 15, no. 12, pp. 29841–29854, 2015.

[19] J. Colnago, S. Devlin, M. Oates et al., "It's not actually that horrible: Exploring Adoption of Two-Factor Authentication at a University," in *Proceedings of the 2018 CHI Conference on Human Factors in Computing Systems*, pp. 1–11, 2018.

[20] Z. Zhu, "An efficient authentication scheme for telecare medicine information systems," *Journal of Medical Systems*, vol. 36, no. 6, pp. 3833–3838, 2012a.

[21] A. K. Das, V. Odelu, and A. Goswami, "A secure and robust user authenticated key agreement scheme for Hierarchical multi-medical server environment in TMIS," *Journal of Medical Systems*, vol. 39, no. 9, p. 92, 2015.

[22] Z.-Y. Wu, Y.-C. Lee, F. Lai, H.-C. Lee, and Y. Chung, "A secure authentication scheme for telecare medicine information systems," *Journal of Medical Systems*, vol. 36, no. 3, pp. 1529–1535, 2012.

[23] M. Wazid, A. K. Das, S. Kumari, X. Li, and F. Wu, "Design of efficient and provably secure anonymity preserving three-factor user authentication and key agreement scheme for TMIS," *Security and Communication Networks*, vol. 9, no. 13, pp. 1983–2001, 2016.

[24] V. Bansal and S. Garg, "A cancelable biometric identification scheme based on bloom filter and format-preserving encryption," *Journal of King Saud University - Computer and Information Sciences*, 2022.

[25] A. Irshad, M. Sher, O. Nawaz, S. A. Chaudhry, I. Khan, and S. Kumari, "A secure and provable multi-server authenticated key agreement for TMIS based on Amin et al. scheme," *Multimedia Tools and Applications*, vol. 76, no. 15, pp. 16463–16489, 2017.

[26] R. Amin and G. P. Biswas, "An improved RSA based user authentication and Session key agreement protocol useable in TMIS," *Journal of Medical Systems*, vol. 39, no. 8, p. 79, 2015.

[27] D. Giri, T. Maitra, R. Amin, and P. D. Srivastava, "An efficient and robust RSA-based remote user authentication for telecare medical information systems," *Journal of Medical Systems*, vol. 39, no. 1, p. 145, 2015.

[28] Z. Siddiqui, O. Tayan, and M. Khurram Khan, "Security analysis of smartphone and cloud computing authentication frameworks and protocols," *IEEE Access*, vol. 6, pp. 34527–34542, 2018.

[29] M. K. Sharma and M. J. Nene, "Dual factor third-party biometric-based authentication scheme using quantum one-time passwords," *Security and Privacy*, vol. 3, no. 6, 2020b.

[30] K. A. Shakil, F. J. Zareen, M. Alam, and S. Jabin, "BAM-HealthCloud: a biometric authentication and data management system for healthcare data in cloud," *Journal of King Saud University - Computer and Information Sciences*, vol. 32, no. 1, pp. 57–64, 2020.

[31] W. R. Braithwaite, *Why Two-Factor Authentication in Healthcare?*, 2009, http://www.anakam.com.

[32] A. Acar, W. Liu, R. Beyah, K. Akkaya, and A. S. Uluagac, "A privacy-preserving multi-factor authentication system," *Security and Privacy*, vol. 2, no. 5, 2019.

[33] X. Yin, J. He, Y. Guo, D. Han, K. C. Li, and A. Castiglione, "An efficient two-factor authentication scheme based on the Merkle tree," *Sensors*, vol. 20, no. 20, pp. 1–19, 2020.

[34] H. Khalid, S. J. Hashim, S. M. S. Ahmad, F. Hashim, and M. A. Chaudhary, "Selamat: a new secure and lightweight multi-factor authentication scheme for cross-platform industrial IoT systems," *Sensors*, vol. 21, no. 4, pp. 1–32, 2021.

[35] A. D. Dwivedi, G. Srivastava, S. Dhar, and R. Singh, "A decentralized privacy-preserving healthcare blockchain for IoT," *Sensors*, vol. 19, no. 2, 2019.

[36] F. Rahman, M. Z. A. Bhuiyan, and S. I. Ahamed, "A privacy preserving framework for RFID based healthcare systems," *Future Generation Computer Systems*, vol. 72, pp. 339–352, 2017.

[37] H.-M. Chen, J.-W. Lo, and C.-K. Yeh, "An efficient and secure dynamic ID-based authentication scheme for telecare medical information systems," *Journal of Medical Systems*, vol. 36, no. 6, pp. 3907–3915, 2012.

[38] H. Y. Lin, "On the security of a dynamic ID-based authentication scheme for telecare medical information systems," *Journal of Medical Systems*, vol. 37, no. 2, p. 9929, 2013.

Hindawi
Journal of Healthcare Engineering
Volume 2023, Article ID 9767585, 1 page
https://doi.org/10.1155/2023/9767585

Retraction

Retracted: Evaluation of the Effect of Comprehensive Nursing Interventions on Plaque Control in Patients with Periodontal Disease in the Context of Artificial Intelligence

Journal of Healthcare Engineering

Received 3 October 2023; Accepted 3 October 2023; Published 4 October 2023

This article has been retracted by Hindawi following an investigation undertaken by the publisher [1]. This investigation has uncovered evidence of one or more of the following indicators of systematic manipulation of the publication process:

(1) Discrepancies in scope
(2) Discrepancies in the description of the research reported
(3) Discrepancies between the availability of data and the research described
(4) Inappropriate citations
(5) Incoherent, meaningless and/or irrelevant content included in the article
(6) Peer-review manipulation

The presence of these indicators undermines our confidence in the integrity of the article's content and we cannot, therefore, vouch for its reliability. Please note that this notice is intended solely to alert readers that the content of this article is unreliable. We have not investigated whether authors were aware of or involved in the systematic manipulation of the publication process.

In addition, our investigation has also shown that one or more of the following human-subject reporting requirements has not been met in this article: ethical approval by an Institutional Review Board (IRB) committee or equivalent, patient/participant consent to participate, and/or agreement to publish patient/participant details (where relevant).

Wiley and Hindawi regrets that the usual quality checks did not identify these issues before publication and have since put additional measures in place to safeguard research integrity.

We wish to credit our own Research Integrity and Research Publishing teams and anonymous and named external researchers and research integrity experts for contributing to this investigation.

The corresponding author, as the representative of all authors, has been given the opportunity to register their agreement or disagreement to this retraction. We have kept a record of any response received.

References

[1] J. Xu, L. Wang, H. Sun, and S. Liu, "Evaluation of the Effect of Comprehensive Nursing Interventions on Plaque Control in Patients with Periodontal Disease in the Context of Artificial Intelligence," *Journal of Healthcare Engineering*, vol. 2022, Article ID 6505672, 11 pages, 2022.

Hindawi
Journal of Healthcare Engineering
Volume 2022, Article ID 6505672, 11 pages
https://doi.org/10.1155/2022/6505672

Research Article

Evaluation of the Effect of Comprehensive Nursing Interventions on Plaque Control in Patients with Periodontal Disease in the Context of Artificial Intelligence

Juan Xu,[1] Lingling Wang,[2] Hongxia Sun,[3] and Shanshan Liu[4]

[1]*Department of Stomatology, First People's Hospital of Yongkang City, Yongkang City, Zhejiang Province, China*
[2]*Department of Internal Medicine-Cardiovascular Department Xiangyang No. 1 People'sHospital, Hubei University of Medicine, Xiangyang 441000, China*
[3]*Qingdao Jimo District Tongji Health Center and Medical Nursing, Qingdao, Shandong 266228, China*
[4]*Department of Stomatology, Fourth Affiliated Hospital, Hebei Medical University, Shijiazhuang 050017, Hebei, China*

Correspondence should be addressed to Shanshan Liu; 2015003@qhnu.edu.cn

Received 28 January 2022; Revised 11 February 2022; Accepted 12 February 2022; Published 23 March 2022

Academic Editor: Liaqat Ali

Plaque is a bacterial biofilm that adheres to each other and exists on the tooth surface, and new plaque can continuously reform after removing it from the tooth surface. The pathogenesis of periodontal disease is related to the bacteria, the host and the environment, with the bacteria and bacterial products in plaque being the main initiators of periodontal disease. The effective control of plaque is an effective method for the treatment and prevention of periodontal disease and is often underappreciated in clinical practice. For the traditional diagnostic method through experience and visual observation, it may lead to misdiagnosis and underdiagnosis. In order to accurately diagnose plaque disease, this study designed a convolutional neural network-based oral dental disease diagnosis system for oral care interventions to improve oral health awareness. Thus motivate patients to implement proper oral health care measures, and continuously and lifelong insist on thorough daily plaque removal to improve patients' physical health and quality of life in periodontal disease patients.

1. Introduction

With the continuous improvement of people's living standard, oral diseases are getting more and more attention. Some patients with malocclusion are accompanied by periodontal diseases of different degrees, and periodontal disease treatment and orthodontic treatment are becoming more and more closely integrated. Periodontal disease is one of the most common oral diseases with a high prevalence worldwide, which seriously endangers periodontal health, oral health and general health conditions. Patients with periodontal disease suffer from the destruction of periodontal supporting tissues leading to fan shifting and spreading of front teeth and gaps, which seriously affects the aesthetics and creates occlusal trauma, which in turn further aggravates the loss of periodontal supporting tissues and eventually leads to tooth loss. China is a country with a high prevalence of periodontal disease, and the results of the third national oral health survey show that the prevalence of periodontal disease in China is not optimistic and has become the primary cause of tooth loss in adults. For the treatment of periodontal disease in adults, an orderly, perfect, multidisciplinary and systematic treatment plan needs to be formulated, among which orthodontic treatment occupies an important position. On the one hand, orthodontic treatment can establish a good occlusal relationship for patients with periodontal disease, which is important for promoting the health of periodontal tissues [1–4]. On the other hand, improving the periodontal condition while improving fan-shifted anterior teeth and closing the gap between teeth also helps to restore the aesthetics and function and promoting the psychological and general health of patients. Orthodontic treatment has become an important tool in the comprehensive treatment of periodontal disease in adults. Periodontal disease leading to secondary malocclusion should be treated with a comprehensive treatment plan before taking orthodontic treatment, especially a comprehensive periodontal treatment. Orthodontic treatment on the basis of periodontal treatment can achieve good orthodontic treatment effect. As shown in Figure 1, we plotted the global hot trend of dental plaque in Google, and we can find that it has consistently shown a high level of hotness in recent years.

Dental plaque and its bacterial metabolites are the initiating factors of caries and periodontal disease. It has been found that some oral diseases are closely related to systemic diseases such as cardiovascular diseases, diabetes and premature low birth weight infants." Through large-scale epidemiological surveys and case-control studies, it has been confirmed that there is a relationship between dental plaque and systemic diseases. Dental plaque biofilm (biofilm) refers to microorganisms that adhere firmly to the surface of a host or growth vehicle, forming clonal colonies surrounded by a large amount of extracellular matrix, in which the individuals exhibit a phenotype that differs significantly from the planktonic state. Dental plaque is a biofilm adhering to the tooth surface, consisting of bacteria and matrix, surviving in a holistic manner as a microbial ecological community [5–7]. Microscopically, dental plaque is visible as a population of bacteria of different biomass wrapped by an acquired film and an extracellular matrix, with internal intervals of aqueous channels of varying size and fluid flow within the channels. The bacteria in the plaque are tightly adhered to each other by virtue of the unique structure of the biofilm, which can resist the killing effect of host defenses and external harmful factors. The rate and composition of plaque formation are influenced by many factors, including oral hygiene, quality and quantity of saliva, surface finish, local pH, oxygen and carbon dioxide tension, dietary composition, immune response at the gingival-dental bonding site, and dependent synergy or competitive antagonism between bacteria. Plaque disease caries and periodontal disease are common oral diseases in humans, and dental plaque is closely related to the development of these two diseases. The supragingival plaque is composed of sticky matrix and bacteria embedded in it, and its acid-producing metabolic activity plays a continuous role locally, leading to enamel demineralization, which is the direct cause of caries; the subgingival plaque is divided into adherent plaque and nonadherent plaque, and adherent plaque is related to the formation of subgingival tartar, root surface caries and root surface resorption; nonadherent plaque is closely related to the occurrence and development of periodontitis. Nonadherent plaque is closely related to the development of periodontitis and is considered to be the progress front of periodontitis [8]. In the past, people regarded dental caries and periodontal disease as two unrelated diseases, but modern etiological research reveals that dental plaque plays an important role in the occurrence and development of both diseases, therefore, from the etiological point of view, caries and periodontal disease and other oral diseases caused by them are called plaque diseases. The plaque biofilm is the initiating factor of caries and periodontal diseases. As a typical bacterial biofilm, it consists of microbial cells and extracellular polysaccharide matrix of Streptococcus spp., Lactobacillus spp., Lactobacillus spp [9] and other bacteria. Various bacteria exist in a three-dimensional 3-dimensional structure surrounded by host and bacterial extracellular polysaccharide matrix, adhering to each other or attaching and colonizing the tooth surface and interface. Through a dynamic developmental cycle, the dental plaque biofilm becomes the site of survival and intercellular signal exchange for the bacterial flora. At present, the main studies include the spatial structure of plaque biofilm microorganisms, the population distribution of plaque biofilm microorganisms and the information exchange of plaque biofilm bacteria. There are sites in the oral cavity that are difficult to reach by periodontal instruments, scraping is difficult to be complete, and residual inflammation is not easily controlled [10–12]; pathogenic microorganisms that invade periodontal tissues cannot be removed by simple mechanical treatment; the oral cavity is a bacterial environment, and periodontal pathogenic microorganisms may exist in different sites, which can cause reinfection. Pharmacological treatment can be used as a complement to scaling and scraping. Some patients with clinically aggressive periodontitis, severe or persistent periodontitis prone to recurrence do not respond well to basic treatment, and pharmacotherapy has an important adjunctive therapeutic role. Ultrasonic subgingival scraping with simultaneous pharmacological rinsing has a superior therapeutic effect than conventional subgingival scraping followed by rinsing with a rinse. Topical application of minocycline hydrochloride gel as an adjunctive treatment for Scaling and Root Planing (SRP) was effective in inhibiting the recolonization and growth of periodontopathogen bacteria, suggesting that this method can reduce the risk of recurrence of chronic periodontitis. Adjunctive application of 400 mg or 250 mg of metronidazole plus 500 mg of amoxicillin three times a day for 14 d resulted in better clinical outcomes compared to patients with severe periodontitis treated with SRP only [13].

In recent years, oral dental diseases are gradually becoming younger and more prevalent, such as children of five- or six-years old suffering from dental caries and middle-aged and elderly people suffering from tooth loss. At the same time, oral dental diseases can also induce a variety of high-risk diseases, such as plaque in patients with periodontal disease. The traditional method of oral disease diagnosis is to use tongue depressor and flashlight to examine the lesions of teeth inside the mouth and make a diagnosis of the observation based on the doctor's clinical experience. Since the oral environment is affected by the lighting conditions, the observation results are biased, which can easily lead to misdiagnosis and missed diagnosis, resulting in improper treatment. In the past few years, deep learning has received much attention, for example, in scenarios such as image object recognition and classification, video target tracking and speech recognition, which are widely used, and convolutional neural networks are an important part of it. Compared with BP neural networks and recurrent neural

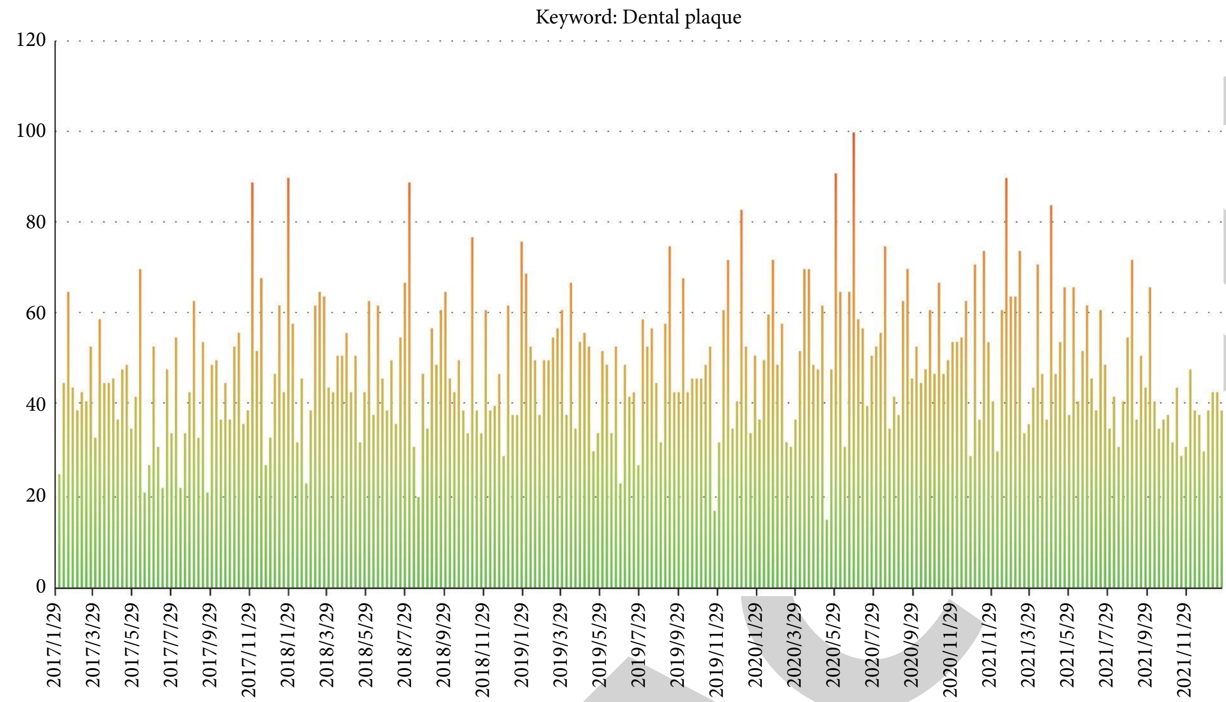

Figure 1: Dental plaque in Google global hot trend.

networks, convolutional networks have developed more rapidly and are more intensively studied. Due to the shortage of data resources and insufficient computing speed in the early days, convolutional network models with high performance could not be trained. After the rapid development of big data and the emergence of GPU, the research progress of convolutional neural networks has been accelerated to some extent. In order to better prevent and accurately diagnose oral dental diseases, this paper designs a comprehensive care intervention based on convolutional neural network for plaque control and diagnosis system for periodontal disease patients, which uses a camera to collect oral dental data, and then extracts oral dental features layer by layer using a trained GoogleNet network model, and finally performs recognition and classification [14, 15]. Extended experiments were conducted in the relevant dataset to prove the effectiveness of the method in this paper.

2. Related Work

2.1. Comprehensive Nursing Intervention for Plaque Control. The study of the three-dimensional structure and formation process of dental plaque biofilm is the basis of dental plaque biofilm research. At present, the structure and bacterial activity of dental plaque biofilm are mainly studied by various advanced biotechnologies at home and abroad. The plaque biofilm is a small mushroom-like or rod-like colony containing a pipeline system formed by the adhesion and aggregation of oral planktonic bacteria on the acquired membrane, which has a complex three-dimensional structure and a certain thickness. The cells, matrix, voids and duct system are unevenly distributed in the plaque biofilm [13, 16–18]. Nutrients, metabolic wastes, enzymes, metal ions and oxygen are transported to the plaque biofilm through the matrix. The voids in the membrane vary in size, some of which can lead from the enamel surface to the outside through the entire plaque biofilm, and the nutrients required by bacteria can reach the inside of the biofilm through the voids, suggesting that antibacterial plaque drugs can also reach the membrane through the voids to prevent and control the plaque biofilm. Fluorescent brightener staining and permeation experiments on dental plaque biofilms revealed that glucosyltransferase C-deficient Streptococcus pyogenes could not form an extracellular matrix that could retard the permeation of macromolecules, and macromolecular dextrose passed through the plaque biofilm formed by the defective strain at 16 times the rate involved in the wild strain group, confirming that the canal system in the dental plaque biofilm was filled with extracellular polymers [19,20]. The thickness of the in vitro and ex vivo biofilm models ranged from 0 to 65 μm, depending on the plaque site, the nutritional environment, and the extent and frequency of oral hygiene measures involved. The process of plaque biofilm formation is dynamic in space and time. The plaque biofilm formation was dominated by cocci such as Streptococcus at the early stage, and mainly by filamentous bacteria, bacilli, actinomycetes and Wyomia at the later stage. Different species adsorbed to the acquired film at different rates, and the ratio of each group showed spontaneous and regular transformation. Streptococcus mutans and Streptococcus dastans are the common bacteria of plaque biofilm and the main caries-causing bacteria; Streptococcus haematobium is the pioneer bacteria of plaque biofilm formation, and the above three bacteria play a role in the process of plaque biofilm formation on the enamel surface. Streptococcus spp. were the main constituents of plaque biofilm formation on day 1, and their thickness in plaque biofilm decreased after 7 days; Clostridium perfringens decreased on day 2 and then gradually increased; the thickness of Actinomyces nervous biofilm was thinner on day 7 than on day 2; the thickness of Meningococcus biofilm did not change significantly during the whole observation period. In addition, domestic and international studies found that dead bacteria are one of the components of dental plaque biofilm, competing with live bacteria for contact sites, participating in the initial formation process of natural dental plaque biofilm, and having the role of promoting the formation of dental plaque biofilm. Laser confocal scanning microscopy combined with multiplex fluorescence in situ hybridization was applied to the structural study of dental plaque biofilm. The Confocal Laser Scanning Microscopy (CLSM) combined with multiplex FISH technique was used to study the spatial distribution and composition of plaque biofilms formed by six common oral bacteria in vitro, and it was shown that the integrity of plaque biofilms was not destroyed and the spatial distribution of plaque biofilms could be studied simultaneously by several sequential hybridization steps. The spatial distribution of G+ and G- bacteria in plaque biofilms formed by a variety of bacteria could be analyzed by multiple staining of Gram-positive and negative bacteria simultaneously in several consecutive hybridization steps [21]. Structure of in vivo dental plaque biofilm models and changes in the distribution of different oral strains in dental plaque biofilms. The application of CLSM combined with multiplex FISH technique can truly reflect the three-dimensional structure and formation process of dental plaque biofilm and provide in-depth morphological and kinetic study of dental plaque biofilm. CLSM combined with dead and live bacteria fluorescence staining technique can quickly compare the efficacy of antibacterial drugs or treatments and observe their depth of action in dental plaque biofilm. Main characteristics and visualization of dental plaque is shown in Figure 2.

Periodontal disease is a chronic infectious disease of the periodontal supporting tissues caused by the interaction between bacterial infection and the host immune response. The pathogenic mechanism is the long-term action of plaque microorganisms and their products on periodontal support tissues, which induces the immune response of the body, leading to progressive destruction of gingiva, periodontal membrane, dental bone and alveolar bone, resulting in gingival inflammation, loss of periodontal attachment, alveolar bone resorption and periodontal pocket formation, which can lead to loosening and even loss of teeth in severe cases, and is the main cause of tooth loss in adults. The key to the treatment of periodontal disease is to remove the plaque and bacterial products planted on the root surface, remove the diseased periodontal tissues, stop the progress of the disease, and promote the regeneration of periodontal tissues. Periodontal nonsurgical treatment for plaque control is the most widely used and effective treatment for periodontal disease and is the basis of periodontal sequential treatment. This article reviews the content and research progress of nonsurgical treatment of periodontal disease. Periodontal basic treatment is the first stage of periodontal sequential treatment, which is the basic treatment necessary for patients with periodontal disease, mainly including: plaque control: personalized oral hygiene education and guidance of self-oral health care techniques; periodontal mechanical treatment (supragingival scaling, subgingival scraping and root surface leveling); and dental treatment: occlusal relationship adjustment, and loose tooth fixation. Supragingival scaling is divided into manual scaling and ultrasonic scaling. Whether manual scaling or ultrasonic scaling, the operating instruments will leave small scratches on the tooth surface or root surface, making the tooth surface or root surface rough and unsmooth, resulting in easy redeposition of plaque and pigment on the tooth surface; some tooth surfaces and root surfaces have a lot of smoke and pigment, which are closely combined with the tooth surface and not easy to remove, and the scaling efficiency is low. Therefore, polishing is an essential step after scaling, which can remove the tiny tartar debris, residual plaque and pigment on the tooth surface or root surface, make the tooth surface or root surface polished, and reduce the speed and degree of plaque reattachment. At present, most of the clinical use is sub-regional scraping. However, the treatment period of this method is longer, and the number of visits is more frequent, and the follow-up rate is not easily guaranteed for patients with poor compliance. Also, due to the long interval, periodontal pathogenic bacteria may be transplanted from the non-SRP site to the newly completed SRP site, leading to the recurrence of periodontitis. Therefore, some scholars support the whole-mouth one-time scraping treatment method. However, full-mouth one-time scraping treatment has disadvantages such as high operator requirements, long operation time, poor acceptance by some patients, and possible induction of bacteremia. Recent studies suggest that both treatment methods can significantly improve the clinical index of periodontal tissues, and there is no difference between them. Therefore, the selection of periodontal nonsurgical treatment options needs to take into account the patient's inclination, the patient's consultation time, the actual situation during treatment, the surgeon's operating skills and the cost-effectiveness of the treatment. The role of traditional manual scraping in removing subgingival tartar, plaque, diseased dental bone and pocket lining granulation tissue has been widely recognized. It has a good feel when used by the surgeon and is more easily tolerated by patients with root sensitivity. However, manual scraping takes a long time to operate, the number of visits is high, the labor intensity of the surgeon is easy to cause operator fatigue and patients may experience discomfort, such as intraoperative pain, postoperative sensitivity, and swelling; at the same time, manual scraping requires high operator skill, especially for root bifurcation, irregular root surfaces and deep periodontal pocket areas, which are all examined and scraped by the operator's fingertips to remove subgingival tartar. Inexperienced operators are prone to soft tissue damage and poor root surface leveling due to wrong choice of instruments or improper use. Subgingival ultrasound instruments have a smaller diameter and longer working length with a modified tip shape and a more varied curved design, making

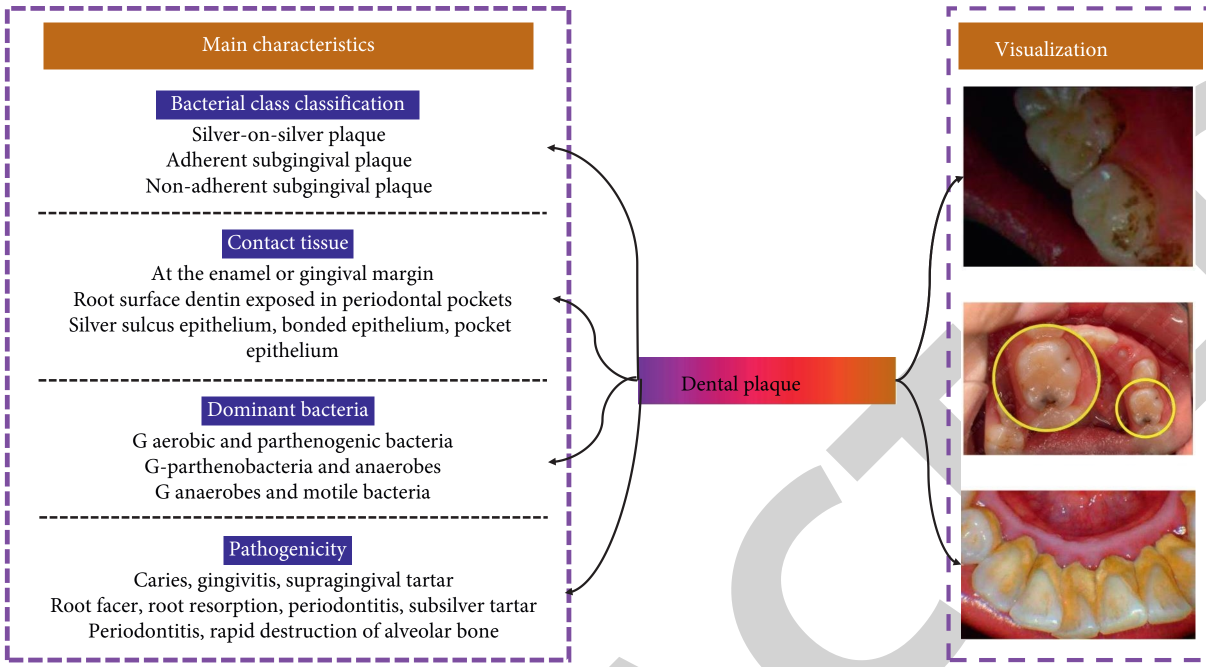

Figure 2: Main characteristics and visualization of dental plaque.

it easier to access deeper areas that are difficult to reach with manual scraping instruments, such as the root bifurcation zone. Subgingival scraping with ultrasound instruments is easy to perform, effortless, and can be done in a single pass, with little tremor during treatment, making it more acceptable to the patient.

2.2. Artificial Intelligence Algorithms. Artificial intelligence (AI) is a brand-new field that has been developing rapidly for more than a decade, in which deep learning algorithms have received more and more attention from researchers, and it has obvious advantages over shallow models in both feature extraction and modeling. Deep learning is good at mining increasingly abstract feature representations from raw input data, and these representations have good generalization ability. It overcomes some of the problems that have been considered intractable in AI in the past. And with the significant growth in the number of training data sets and the dramatic increase in chip processing power, it has been effective in areas such as target detection and computer vision, natural language processing, speech recognition, and semantic analysis, and therefore has contributed to the development of artificial intelligence. Deep learning is a hierarchical machine learning method that includes multilevel nonlinear transformations, and deep neural networks are the main form at present [14, 15]. The connection pattern between neurons is inspired by the organization of animal visual cortex, and convolutional neural networks are one of the classical and widely used structures. The local connectivity, weight sharing, and pooling operations of convolutional neural networks enable them to effectively reduce the complexity of the network, reduce the number of training parameters, make the model invariant to translation, distortion and scaling to a certain degree, and have strong robustness and fault tolerance, and are also easy to train and optimize. Based on these superior properties, it outperforms standard fully connected neural networks in a variety of signal and information processing tasks. The structure of a convolutional neural network, including convolutional, pooling, and fully connected layers, plays different roles [22]. Figure 3 shows the basic structure of convolutional neural network. Net-in-net models, spatial transformation networks and other improved convolutional neural networks and supervised learning and unsupervised learning training methods for convolutional neural networks as well as some common open source tools. The applications of convolutional neural networks mainly include image classification, face recognition, audio retrieval, ECG classification and target detection.

Studies of the visual cortex of the cat brain have revealed a series of complexly constructed cells in the visual cortex that are sensitive to local areas of visual input space, called “receptive fields.” The receptive fields, which cover the entire visual field in some way, play a local role in the input space and are thus better able to uncover the strong local spatial correlations present in natural images. The classifies these cells, called receptive fields, into two types: simple and complex cells. According to Hubel-Wiesel’s hierarchical model, there is a hierarchical structure of neural networks in the visual cortex: lateral geniculate bodies, simple cells, complex cells, low-order hypercomplex cells, and high-order hypercomplex cells. The neural network structure between low-order hypercomplex cells and high-order super complex cells is similar to the neural network structure between simple cells and complex cells. In this hierarchical structure, cells at higher stages usually have a tendency to: selectively respond to more complex features of the stimulus pattern; and also have a larger receptive field that is more insensitive to changes in the location of the stimulus pattern. The

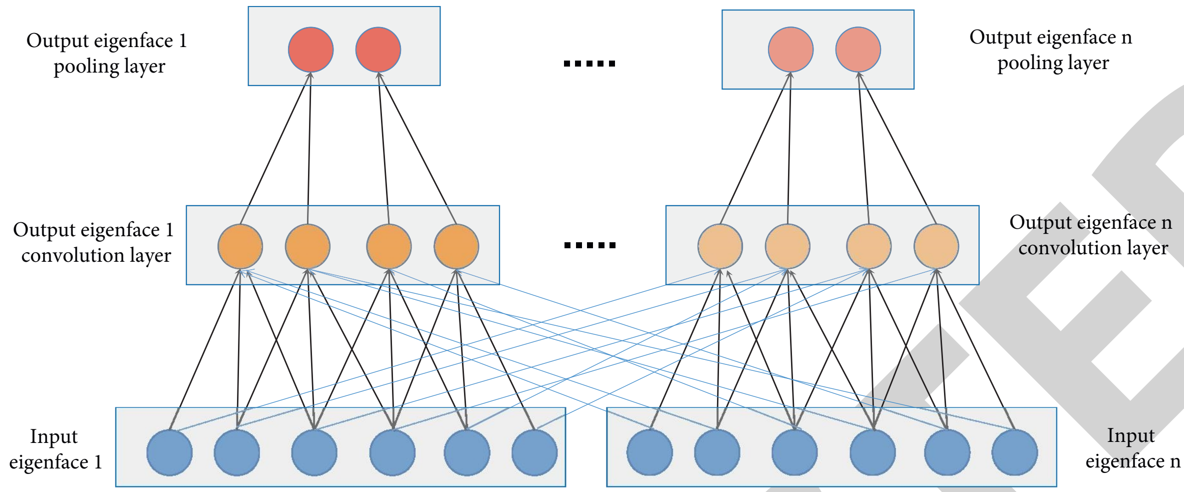

Figure 3: Convolutional neural network structure.

hierarchical model proposes a neurocognitive machine with a similar structure [23]. The neurocognitive machine is composed of alternating simple cell layers (S-layer, S-layer) and complex cell layers (C-layer, C-layer), where S-layer corresponds to the simple cell layer or low-order super complex cell layer in the Huble-Wiesel hierarchical model, and C-layer corresponds to the complex cell layer or high-order super complex cell layer. The S-layer can extract local features of its input layer in response to specific edge stimuli in the receptive field, and the C-layer is locally insensitive to stimuli from the exact location. Although there is no globally supervised learning process available in neurocognitive machines like the BP algorithm, it can still be considered as the first engineered implementation of CNNs, with convolution and pooling (also called downsampling) inspired by the Hubel-Wiesel concept of simple and complex cells, respectively, which can accurately recognize input patterns with displacement and slight deformation. Based on Fukushima's work, a CNN was designed and trained using the BP algorithm (the model is called LeNet-5), a classical CNN structure on which many subsequent works have been based and which has achieved good classification results in several pattern recognition fields. The basic structure of a CNN consists of an input layer, a convolutional layer (convolutional layer, pooling layer (also called sampling layer), fully connected layer and output layer. The convolutional and pooling layers are generally taken several, and the convolutional and pooling layers are set alternately, i.e., a convolutional layer is connected to a pooling layer, a pooling layer is connected to another convolutional layer, and so on. Since each neuron of the output eigenface in the convolutional layer is locally connected to its input, and the corresponding connection weights are weighted and summed with the local input plus the bias value to obtain the input value of the neuron, the process is equivalent to the convolutional process, which gives the CNN its name. The convolutional layer consists of multiple eigenfaces, each of which consists of multiple neurons, each of which is connected to a local region of the previous eigenface through a convolutional kernel. The convolution kernel is a matrix of weights (e.g., 3×3 or 5×5 matrix for a 2D image.) The convolutional layers of a CNN extract different features of the input through convolutional operations, with the first layer of convolution extracting low-level features such as edges, lines, and corners, and the higher layers extracting higher-level features. junure 3 shows the schematic structure of the convolutional and pooling layers of the 1-D CNN, with the top layer being the pooling layer, the middle layer being the convolutional layer, and the bottom layer being the input layer of the convolutional layer. The neurons in the convolutional layer are organized into individual eigenfaces, and each neuron is connected to a local region of the eigenface in the previous layer through a set of weights, i.e., the neurons in the convolutional layer are locally connected to the eigenfaces in its input layer. The output value of each neuron in the convolutional layer is then obtained by passing the local weighted sum to a nonlinear function such as the ReLU function. In the same input eigenface and the same output eigenface, the weights of the CNN are shared, and the weight sharing occurs in the same color, but not in different colors. By sharing weights, the complexity of the model can be reduced, and the network can be trained more easily [24].

3. Method

3.1. Model Architecture. Model Architecture Convolutional neural network is a multilayer supervised learning neural network that is extremely adaptive and adept at mining local features of data and combining high-level semantic information for classification. The network includes a convolutional layer, an excitation layer, a pooling and a fully connected layer. The convolutional layer and pooling layer are the core modules to realize the feature extraction function of the convolutional neural network; the gradient descent method is used to minimize the loss function, and the weight parameters in the network are adjusted in reverse layer by layer to improve the accuracy of the network through multiple iterations of training, and the structure of the proposed convolutional network is shown in Figure 4.

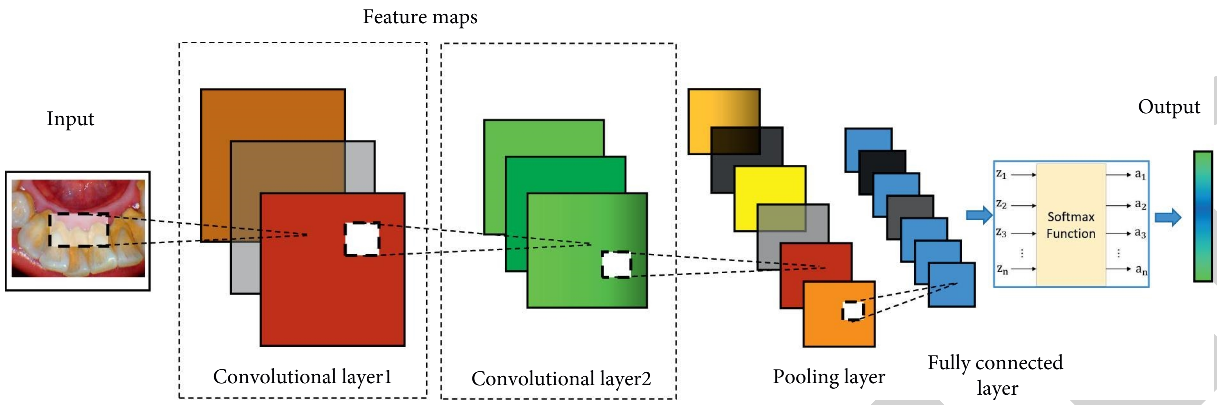

Figure 4: Model structure.

3.2. Technical Details. The convolutional layer is a special neuronal network layer, which is used to scan the image by convolutional operation with convolutional kernel to obtain the corresponding features with local sensing and weight sharing. The output equation of the convolutional layer is

$$y_i = \sum_i k_{ij} * x_i + b_i, \tag{1}$$

where y_i is the output of the convolutional layer; k_{ij} is the convolutional kernel; $*$ is the convolutional operation; x_{i} is the input image; b_{i} is the bias term. In convolutional neural networks, the neuron nodes between layers are no longer in the form of full connections, but the local spatial correlation between layers is used to connect the neuron nodes of each adjacent layer only to the neuron nodes of the upper layer it is close to, i.e., local sensing, thus reducing the parameter scale of the neural network architecture. The convolutional layer has a shared weight mechanism where each convolutional kernel parameter is repeatedly applied to the whole perceptual field to convolve the input image, and the convolution result constitutes the feature map of the input image. This mechanism not only extracts image features, but also reduces the number of convolutional neural network model parameters.

The excitation layer is a nonlinear unit after the output of the convolution layer. Since the multilayer neural network model is highly nonlinear and the convolutional layer is a linear computational process, an excitation layer (i.e., nonlinear unit) needs to be introduced to ensure the nonlinearity. The excitation layer is calculated as

$$f = \sigma(y_i), \tag{2}$$

where y_i is the output of the convolutional layer; the excitation function σ is the mapping relationship between input and output. In order to make the model learn more quickly, the correction unit is introduced in the excitation layer. The commonly used correction functions include Logistic function, tanh function, Sigmoid function, and ReLU function.

The pooling layer, also known as downsampling, has the important function of feature compression of the feature map. By selecting the maximum value or average value of a region instead of that region, the purpose of feature map compression is achieved. The pooling layer uses the Maxpool method, which is calculated as

$$y_j = f\left(\frac{1}{n}\sum_j x_j + b\right), \tag{3}$$

where y_j is the output of the pooling layer; n denotes the window size from the convolution layer to the pooling layer; x_j is a region of size $n \times n$; and b_j is the bias term. Since the pooling layer significantly reduces the spatial dimension of the input feature map, which results in a 75% reduction in the number of weight parameters, reduces the computational cost, and allows control of system overfitting.

In the fully connected layer, the neuron nodes are linear one-dimensional arrangement structure, and each neuron node in the layer is interconnected with each other. The output of the fully connected layer is given by

$$y_i = f\left(\sum_{j=1}^{n} w_{ij}x_j - \theta_i\right), \tag{4}$$

where x_j is the input signal from the neuron in the upper layer; w_{ij} is the connection weight from neuron j to neuron i; θ_i is the threshold value; and f is the activation function. Since the final layer of pooling, the output is high-level features of each region of the image, the fully connected layer is needed to combine these nonlinear features, in an easy way, to classify the input image using a SoftMax or Support Vector Machine (SVM) classifier.

3.3. Intelligent Detection System. The emergence of Bitcoin not only solves the problem of value transfer in a detrusted peer-to-peer network, but also its PoW consensus algorithm combined with economic incentives and crypto the intelligent oral detection system proposed in this paper is based on STM32 chip as the core, using image display module to complete real-time display of image data and instantaneous capture, and wireless transmission through WiFi module to realize the functions of processing and classification of oral dental images. The system mainly consists of controller module, image acquisition module, image display module, image storage and transmission module, image detection platform and power supply module. The block diagram of the system structure is shown in Figure 5.

The controller module is composed of STM32f103 chip, crystal circuit and reset circuit which form the minimum system of the controller. The controller module performs operations such as lighting LEDs, camera data acquisition and wireless data transmission based on user key inputs. The image acquisition module is the basic link of the system.

The module is a tongue depressor IC board consisting of camera, LED light source, and membrane keypad. The camera is mounted on the top of the board, and when it reaches into the mouth to acquire images, the LED light provides the light source, and then the camera is controlled by the membrane button for image data acquisition. In this case, the camera acquires oral data in real time at 30 fps and 300 000pixel clarity. The image display module is a real-time observation of the images captured by the camera through the Liquid Crystal Display (LCD), which can help the doctor to observe and understand the internal environment of the patient's mouth more carefully. Image storage and transmission module is composed of SD card, WiFi transmission module and other parts. When the camera is aimed at the oral and dental parts, the photos are taken by key control and can be optionally saved in the SD card in JPG or BMP format; at the same time, the captured images are transmitted to the image detection network through the WiFi module. The image detection network module is the core unit of the intelligent oral disease detection system, which is a Googlenet detection network composed of Inception units and determines whether there is a disease in the oral teeth through feature extraction and recognition and classification of the collected images by convolutional neural network. The power supply module is composed of MP2359 chip, AMS1117-3.3V chip and its peripheral circuits. This module converts the 12V DC input voltage into 5 and 3.3V DC voltages to power the other modules in the system and ensure the normal operation of the system.

4. Experimentation and Evaluation

4.1. Dataset. The oral dental images used in this paper are all real oral dental images, a total of 400 images. The images were divided into two (2) categories, the first category is the healthy teeth total 200 data, marked as 1; the second category is the existence of periodontal disease patients' plaque disease total 200 data, marked as 2.

4.2. Experimental Setup. This experiment uses a hardware platform to collect dental data from the patient's mouth. First, the tongue depressor with camera is inserted into the patient's oral cavity, the high brightness LED is lit by the 1st button, the oral environment is observed using the LCD monitor, the key parts are photographed, and the data is transmitted to the image detection network module through the WiFi transmission module. The image detection module uses the trained GoogLeNet network model to extract and classify the features of the received oral dental data, and finally obtains the category probability, and the highest probability value is its category. Among the 64 feature maps extracted from the oral teeth image after the convolutional layer of layer 1, the feature map of the first channel is selected. The feature maps from the extracted oral teeth show that this layer mainly extracts the edge contours of the input image. In this paper, we use the TensorFlow framework for GPU accelerated computation under GTX1050TI. When training the GoogLeNet model, the backpropagation is performed using the Gradient Descent method, setting the initial value of the learning rate to 0.01 and adjusting it once every 2000 iterations. The recognition rates of the training sample set and the test sample set are shown in Table 1, and the recognition rates of both sample sets increase as the number of training iterations continues to increase. At 2000 iterations, the test samples reached the highest recognition rate of 71.95% for this experiment.

To verify the performance of the network used in this experiment, a 3-layer fully connected network was also built to compare with it. The 2nd layer of the fully connected neural network takes 500 neurons and learns them at a fixed learning rate of 0.01. The comparison results are shown in Table 2. Table 2 shows that the recognition rate of GoogLeNet exceeds that of the fully connected network by about 10%. And there are about 75×106 parameters in the fully connected network, while there are about 25×106 in GoogLeNet.

4.3. Clinical Experiments. Eighty patients with periodontal disease admitted from June 2017 to May 2018 were selected. Inclusion criteria: gingival index ≥2, no less than 4 loci with periodontal probe depth ≥4 mm; alveolar bone resorption up to 1/3–1/2 of the root length, periodontal attachment loss ≥3 mm; chronic gingivitis or periodontitis, oral odor, gingival redness, bleeding and other symptoms; normal communication ability; informed consent to this study. The patients were randomly divided into observation and control groups using the random number table method, with 40 cases each. In the observation group, there were 25 male cases and 15 female cases; age ranged from 26 to 68 years, with an average of (44.73 ± 10.21) years; disease duration ranged from 2 months to 3 years, with an average of (10.37 ± 6.95) months. In the control group, there were 24 male and 16 female cases; age ranged from 27 to 69 ears old, average (44.80 ± 10.48) years old; disease duration ranged from 2 months to 3 years, average (10.43 ± 6.76) months. there was no statistically significant difference in the general data of gender and age between the two groups ($P > 0.05$), which was comparable. Treatment method Basic treatment of periodontal disease was performed in both groups. After complete removal of calculus, polishing, periodontal rinsing, and topical medication were given by the treating physician. The treatment lasted for 7 d. During the treatment period, nursing intervention was given by specially trained nursing staff. Nursing method: the control group was given routine nursing care, including health education, oral hygiene nursing guidance, and medication guidance. The

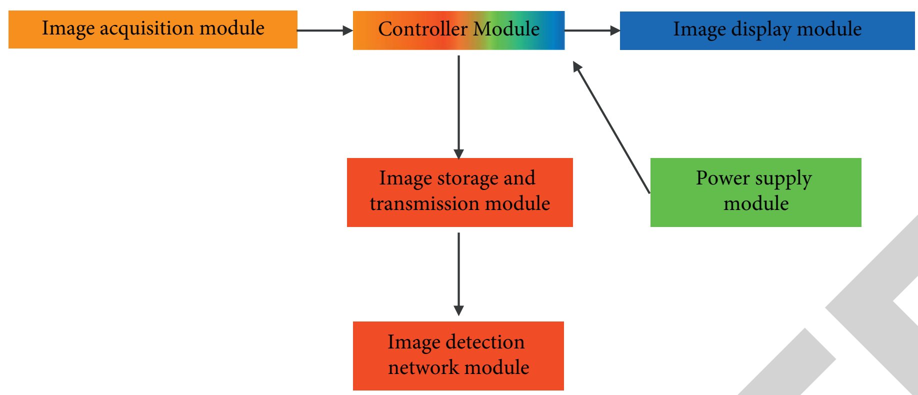

Figure 5: Intelligent diagnostic architecture.

Table 1: Recognition rate of training sample set and test sample set.

Number of training	1200 (%)	1400 (%)	1600 (%)	1 800	2 000 (%)
Training samples	83.67	84.32	85.71	85.94%	86.21
Test samples	64.73	66.28	68.49	70.11%	71.95

Table 2: Comparison of recognition performance of fully connected neural networks and GoogLeNet.

Type	Fully connected (%)	GoogLeNet
Recognition rate	60.36	71.95%

Table 3: Comparison of plaque control effect before and after intervention in 2 groups ($x \pm s$).

Time	Group	Gingival index	Gingival bleeding index	Periodontal pocket probing depth (mm)	Plaque index
Preintervention	Observation group ($n = 40$)	2.15 ± 0.33	3.67 ± 0.35	3.17 ± 2.08	2.59 ± 0.96
	Control group ($n = 40$)	2.12 ± 0.37	3.59 ± 0.32	3.14 ± 2.10	2.60 ± 0.93
Postintervention	Observation group ($n = 40$)	1.02 ± 0.65	0.46 ± 0.20	2.09 ± 2.35	0.98 ± 0.77
	Control group ($n = 40$)	1.57 ± 0.59	0.67 ± 0.25	2.76 ± 2.42	1.49 ± 0.85

observation group was given systematic oral care interventions based on conventional interventions. The patients' lack of professional knowledge and insufficient attention to the importance of following medical advice and correcting poor oral hygiene habits were the main reasons affecting the efficacy of periodontal disease. To address this situation, comprehensive health education measures such as detailed explanation of the pathogenesis of periodontal disease and oral health care behaviors, distribution of periodontal disease health brochures, oral health care lectures, and on-site demonstrations were used to enhance patients' correct understanding of periodontal disease and make them pay full attention to the implementation of medical prescriptions and improvement of personal oral hygiene. Statistical methods were used with SPSS22.0 software, and the measurement data were expressed as mean ± standard deviation ($x \pm s$), and t-test was used for comparison between groups, and the count data were expressed as rate (%), and $\chi 2$ test was used, and the test level $\alpha = 0.05$, and $P < 0.05$ was considered statistically significant. After the intervention, the gingival index, gingival bleeding index, periodontal pocket probing depth and plaque index of the two groups were significantly improved compared with those before the intervention ($P < 0.05$), and the observation group was better than the control group ($P < 0.05$). See Table 3.

5. Conclusion

Plaque control is a basic principle in the treatment of periodontal disease. However, plaque, as a bacterial biofilm, is difficult to be rinsed off by water, and it is also easy to be recreated after short-term removal, which makes the treatment of periodontal disease extremely difficult. Therefore, the ability to achieve ideal plaque control is of great importance to the therapeutic effect of periodontal disease. Although plaque can be removed by mechanical measures and chemical means, only short-term removal can be achieved. Instead, fundamentally, patients need to develop healthy oral hygiene habits. After the systematic oral care intervention, patients have a more correct understanding of the pathogenesis of periodontal disease, and their willingness and ability to participate in the care are improved, so they can provide better conditions for plaque control. Systematic oral care interventions are conducive to increasing the rate of patient awareness of oral health care knowledge, starting from a change in the level of ideology, so that patients understand the importance of healthy oral behavior. From a practical point of view, the demonstration as the focus of health education and the continuous strengthening of patients' capacity for healthy oral health care behaviors provide the conditions for improving patients' oral health care behaviors. In this paper, a convolutional neural network-based plaque diagnosis system for oral periodontal patients is designed to address the problem of plaque susceptibility to misdiagnosis and omission in oral periodontal patients. Its GoogLeNet model is used to analyze the oral dental health condition, and the recognition rate of diseased teeth is 86.21% and 71.95% on the training set samples and test set samples, respectively. Meanwhile, the GoogLeNet model is compared with the fully connected network, and it has better accuracy and higher recognition rate. This design has two aspects of work outlook, on the one hand, to accurately identify dental disease categories, such as caries and plaque, based on the continuous expansion of valid labeled data; on the other hand, to increase the regression loss function to calibrate the specific location of diseased teeth.

Data Availability

The datasets used during the current study are available from the corresponding author on reasonable request.

Conflicts of Interest

The authors declare that he has no conflicts of interest.

Authors' Contributions

Juan Xu and Lingling Wang contributed equally to this work.

References

[1] A. M. Valm, "The structure of dental plaque microbial communities in the transition from health to dental caries and periodontal disease," *Journal of Molecular Biology*, vol. 431, no. 16, pp. 2957–2969, 2019.

[2] J. Lee, Y. H. Nho, S. K. Yun, and Y. S. Hwang, "Use of ethanol extracts of terminalia chebula to prevent periodontal disease induced by dental plaque bacteria," *BMC Complementary and Alternative Medicine*, vol. 17, no. 1, pp. 1–10, 2017.

[3] V. Lazar, L. M. Ditu, C. Curutiu et al., "Impact of Dental Plaque Biofilms in Periodontal Disease: Management and Future therapy," in *Periodontitis: A Useful Reference*, P. Arjunan, Ed., InTech Open, London, UK, pp. 11–42, 2017.

[4] F. A. Scannapieco and E. Gershovich, "The prevention of periodontal disease—an overview," *Periodontology 2000*, vol. 84, no. 1, pp. 9–13, 2020.

[5] K. A. Overmyer, T. W. Rhoads, A. E. Merrill et al., "Proteomics, lipidomics, metabolomics, and 16S DNA sequencing of dental plaque from patients with diabetes and periodontal disease," *Molecular & Cellular Proteomics*, vol. 20, Article ID 100126, 2021.

[6] D. Liccardo, A. Cannavo, G. Spagnuolo et al., "Periodontal disease: a risk factor for diabetes and cardiovascular disease," *International Journal of Molecular Sciences*, vol. 20, no. 6, p. 1414, 2019.

[7] S. Sälzer, C. Graetz, C. E. Dörfer, D. E. Slot, and F. A. Van der Weijden, "Contemporary practices for mechanical oral hygiene to prevent periodontal disease," *Periodontology 2000*, vol. 84, no. 1, pp. 35–44, 2020.

[8] J. D. Harvey, "Periodontal microbiology," *Dental Clinics of North America*, vol. 61, no. 2, pp. 253–269, 2017.

[9] C. E. FloresBTreviño, V. H. Urrutia Baca, R. Gómez Flores, M. A. D. L. Garza Ramos, M. M. Sánchez Chaparro, and M. A. Garza Elizondo, "Molecular detection of helicobacter pylori based on the presence of caga and vaca virulence genes in dental plaque from patients with periodontitis," *Journal of dental sciences*, vol. 14, no. 2, pp. 163–170, 2019.

[10] J. Sun, M. Zhou, C. R. Salazar et al., "Chronic periodontal disease, periodontal pathogen colonization, and increased risk of precancerous gastric lesions," *Journal of Periodontology*, vol. 88, no. 11, pp. 1124–1134, 2017.

[11] M. A. Nazir, "Prevalence of periodontal disease, its association with systemic diseases and prevention," *International Journal of Health Sciences*, vol. 11, no. 2, p. 72, 2017.

[12] F. A. Pieri, M. C. de Castro Souza, L. L. R. Vermelho et al., "Use of β-caryophyllene to combat bacterial dental plaque formation in dogs," *BMC Veterinary Research*, vol. 12, no. 1, pp. 1–8, 2016.

[13] A. Sakanaka, M. Kuboniwa, E. Hashino, T. Bamba, E. Fukusaki, and A. Amano, "Distinct signatures of dental plaque metabolic byproducts dictated by periodontal inflammatory status," *Scientific Reports*, vol. 7, no. 1, pp. 1–10, 2017.

[14] R. Yamashita, M. Nishio, R. K. G. Do, and K. Togashi, "Convolutional neural networks: an overview and application in radiology," *Insights into imaging*, vol. 9, no. 4, pp. 611–629, 2018.

[15] R. Ali, S. Lee, and T. C. Chung, "Accurate multi-criteria decision making methodology for recommending machine learning algorithm," *Expert Systems with Applications*, vol. 71, pp. 257–278, 2017.

[16] I. M. Velsko, J. A. F. Yates, F. Aron et al., "Microbial differences between dental plaque and historic dental calculus are related to oral biofilm maturation stage," *Microbiome*, vol. 7, no. 1, pp. 1–20, 2019.

[17] A. Jindal, A. S. Parihar, M. Sood, P. Singh, and N. Singh, "Relationship between severity of periodontal disease and control of diabetes (glycated hemoglobin) in patients with type 1 diabetes mellitus," *Journal of International Oral Health: JIOH*, vol. 7, no. 2, p. 17, 2015.

[18] J. D. Pereira dos Santos, E. Cunha, T. Nunes, L. Tavares, and M. Oliveira, "Relation between periodontal disease and systemic diseases in dogs," *Research in Veterinary Science*, vol. 125, pp. 136–140, 2019.

[19] J. T. Newton and K. Asimakopoulou, "Managing oral hygiene as a risk factor for periodontal disease: a systematic review of psychological approaches to behaviour change for improved plaque control in periodontal management," *Journal of Clinical Periodontology*, vol. 42, pp. S36–S46, 2015.

[20] S. Sujatha, U. M. Jalihal, and S. Sharma, "Association between periodontal disease and oral and gastric Helicobacter pylori infection," *Indian Journal of Gastroenterology*, vol. 34, no. 4, pp. 343-344, 2015.

[21] P. Eswar, C. G. Devaraj, and P. Agarwal, "Anti-microbial activity of Tulsi {Ocimum sanctum (Linn.)} extract on a

Hindawi
Journal of Healthcare Engineering
Volume 2023, Article ID 9848967, 1 page
https://doi.org/10.1155/2023/9848967

Retraction

Retracted: Effect of Uterine Artery Ligation and Uterine Artery Embolization on Postpartum Hemorrhage Due to Uterine Asthenia after Cesarean Section and Its Effect on Blood Flow and Function of Uterine and Ovarian Arteries

Journal of Healthcare Engineering

Received 26 September 2023; Accepted 26 September 2023; Published 27 September 2023

This article has been retracted by Hindawi following an investigation undertaken by the publisher [1]. This investigation has uncovered evidence of one or more of the following indicators of systematic manipulation of the publication process:

(1) Discrepancies in scope
(2) Discrepancies in the description of the research reported
(3) Discrepancies between the availability of data and the research described
(4) Inappropriate citations
(5) Incoherent, meaningless and/or irrelevant content included in the article
(6) Peer-review manipulation

The presence of these indicators undermines our confidence in the integrity of the article's content and we cannot, therefore, vouch for its reliability. Please note that this notice is intended solely to alert readers that the content of this article is unreliable. We have not investigated whether authors were aware of or involved in the systematic manipulation of the publication process.

Wiley and Hindawi regrets that the usual quality checks did not identify these issues before publication and have since put additional measures in place to safeguard research integrity.

We wish to credit our own Research Integrity and Research Publishing teams and anonymous and named external researchers and research integrity experts for contributing to this investigation.

The corresponding author, as the representative of all authors, has been given the opportunity to register their agreement or disagreement to this retraction. We have kept a record of any response received.

References

[1] W. Liu and W. Yin, "Effect of Uterine Artery Ligation and Uterine Artery Embolization on Postpartum Hemorrhage Due to Uterine Asthenia after Cesarean Section and Its Effect on Blood Flow and Function of Uterine and Ovarian Arteries," *Journal of Healthcare Engineering*, vol. 2022, Article ID 1337234, 6 pages, 2022.

Hindawi
Journal of Healthcare Engineering
Volume 2022, Article ID 1337234, 6 pages
https://doi.org/10.1155/2022/1337234

Research Article

Effect of Uterine Artery Ligation and Uterine Artery Embolization on Postpartum Hemorrhage Due to Uterine Asthenia after Cesarean Section and Its Effect on Blood Flow and Function of Uterine and Ovarian Arteries

Wufen Liu and Wei Yin

Obstetrics and Reproductive Center, Affiliated Hospital of Yunnan University, Kunming 650021, China

Correspondence should be addressed to Wei Yin; 20201910304@nxmu.edu.cn

Received 8 February 2022; Accepted 4 March 2022; Published 21 March 2022

Academic Editor: Liaqat Ali

Objective. To investigate the efficacy of uterine artery ligation (UAL) and uterine artery embolization (UAE) in the treatment of uterine asthenia postpartum hemorrhage (PPH) after cesarean section and its effect on uterine and ovarian artery blood flow and function. *Methods*. 100 patients with uterine asthenia PPH after cesarean section in our hospital from January 2018 to November 2020 were randomly divided into 50 cases in the UAL group and 50 cases in the UAE group. They were followed up for 12 months. The bleeding volume, operation time, immediate hemostasis rate, and hemostasis effective rate; lochia clearance time and menstrual rehydration time; RI and S/D; and serum FSH, E2, and LH levels were compared between the two groups. *Results*. Compared with the UAL group, the amount of bleeding in the UAE group was significantly increased and the operation time was significantly shortened ($p < 0.05$). There was no significant difference in the immediate hemostatic rate and hemostatic effective rate between the two groups ($p > 0.05$). There was no significant difference in lochia clearance time and menstrual rehydration time between the two groups ($p > 0.05$). There was no significant difference in RI and S/D between the two groups ($p > 0.05$). Compared with before the operation, the levels of FSH and LH in the two groups decreased significantly, and the level of E2 increased significantly ($p < 0.05$). There was no significant difference between the two groups ($p > 0.05$). *Conclusion*. The efficacy of UAL and UAE in the treatment of PPH with uterine asthenia after cesarean section and its effect on the blood flow and function of uterine and ovarian arteries are equivalent, but the amount of bleeding in UAL is less and the operation time of UAE is shorter. The appropriate operation method can be selected according to the actual situation.

1. Introduction

Within 24 h of delivery of a fetus, when a hemorrhage of more than 500 mL or a cesarean section of more than 1000 mL occurs, it is called PPH. Clinical manifestations are mainly hypotension, vaginal bleeding, and other symptoms, which can cause severe anemia and hemorrhagic shock in severe cases and are one of the important causes of maternal death [1, 2]. PPH can be caused by coagulation dysfunction, rupture of the soft birth canal, placental factors, and uterine contraction weakness, among which uterine contraction weakness is the most common [3]. Cesarean section is an effective measure to rescue puerpera, fetal life and solve dystocia, and the risk of postoperative PPH is significantly higher than that of vaginal delivery [4]. At present, PPH patients are mainly treated by drugs and surgery, and for those whose hemostatic effect is not obvious, surgery is used for treatment [5]. As an effective and rapid treatment for PPH, hysterectomy is suitable for all kinds of PPH that have failed to be rescued. However, it can lead to the loss of fertility of patients and seriously damage the physical and mental health of patients. Therefore, in the treatment of PPH, more and more attention has been paid to the preservation of the uterus [6]. UAL and UAE are based on vascular treatments, which block the blood supply of the uterine artery through ligation or embolization and thus have a hemostatic effect. Both can effectively treat PPT, but both have limitations [7, 8]. At present, there are few studies on which is better than UAL or UAE in the treatment of PPH after cesarean section, which is worthy of further study. Therefore, the purpose of this study is to explore the efficacy of UAL and UAE in the treatment of postcesarean delivery PPH with uterine contraction weakness and its influence on the blood flow and function of uterine and ovarian arteries in order to provide some reference for improving the quality of life of patients with postcesarean delivery PPH with uterine contraction weakness.

2. Data and Methods

2.1. General Information. A total of 100 patients with PPH after cesarean section in our hospital from January 2018 to November 2020 were selected as the study subjects, and they were divided into the UAL group ($n = 50$) and the UAE group ($N = 50$) according to the random number table method. This study was approved by the hospital's ethics committee.

2.2. Inclusion and Exclusion Criteria. The inclusion criteria were as follows: (1) after examination, the blood loss of all patients was 1000 mL within 24 h after fetal delivery; (2) patients who did not respond to drug treatment; (3) patients with stable vital signs; (4) patients with normal heart, liver, and kidney function; and (5) informed consent was signed by patients or their families.

The exclusion criteria were as follows: (1) patients with contraindications to UAL or UAE or who could not tolerate surgery; (2) PPH patients caused by coagulation dysfunction, soft birth canal laceration, placental factors, and other factors were excluded; (3) combined with premature ovarian failure, ovarian function decline, polycystic ovary syndrome, and other patients; and (5) patients with scar uterus.

2.3. Methods. In the UAL group, the uterus was pulled out to the abdominal cavity by a cesarean section incision, and the uterus was pulled to one side, so that the artery was completely exposed. At the same time, the round ligament was avoided, the surgeon placed the left hand on the posterior wall of the lower uterine segment, and the round needle was passed through the outermost vascularless area of the arteriovenous plexus of the patient's uterine margin by 2~3 cm. The distal end of the uterine artery was carefully observed with local compressions. If the distal end pulsated, the uterine artery on the contralateral side was also treated with UAL.

UAE group: patients were subjected to local anesthesia under digital subtraction angiography (GE, Innova IGS 530) until the puncture was successful. The 5 F arterial sheath (Termao, Japan) was inserted into the femoral artery, and the left uterine artery was angiographed by a 5 F Cobra catheter (Cook, USA) to ensure no extravasation of contrast media. Then, sodium chloride (H51021158), gentamicin (H42021503), and contrast agent (Chenxin Pharmaceutical Co., Ltd., H42021503) were injected into the uterine artery under fluoroscopy. Chinese medicine (approval H20063128), gelatin sponge particles (Hangzhou Ailekon Pharmaceutical Technology Co., Ltd.) of the mixture, in the embolization at the same time, pay attention to the mixture of reflux, the contralateral artery using the same method for embolization.

Patients in both groups were followed up for 12 months.

2.4. Observation Indicators. The observation indicators are as follows: (1) Operating-related indicators: the amount of blood loss (calculated by weighing method, visual method, and volume method), operation time, immediate hemostasis rate (bleeding stopped within 30 min after surgery), and hemostatic efficiency (no bleeding within 48 h after surgery and stable condition) were observed and compared between the two groups. (2) Postoperative recovery index: the time of lochia excretion and the time of menstrual revulsion were compared between the two groups. (3) Uterine and ovarian arterial blood flow: color Doppler ultrasonography (Mindray DC-25) was used to evaluate the vascular resistance index of the left and right uterine arteries of the 2 groups at 3–7 days after menstruation and 12 months after operation (RI, peak systolic velocity/peak diastolic velocity, and S/D). (4) Ovarian function: 3 ml of venous blood was extracted from the patients on the 2nd to 3rd day after the first menstruation before surgery and placed in the EP tube. The enzyme-linked immunosorbent assay was adopted to detect serum follicle stimulating hormone (FSH), estradiol (E2), and luteinizing hormone (LH) levels. All the kits were provided by Shanghai Fusheng Industrial Co., Ltd.

2.5. Statistical Methods. SPSS 18.0 was used for statistical analysis. The measurement data were expressed as the mean ± standard deviation ($\pm S$) and tested by T. The enumeration data were expressed by example (n) or percentage (%) and tested by χ^2. $p < 0.05$ indicated statistically significant difference.

3. Results

3.1. Comparison of General Data between the Two Groups. There was no statistically significant difference between the two groups in age, gestation time, gestation number, newborn weight, and maternal type ($p > 0.05$), indicating comparability, as shown in Table 1.

3.2. Comparison of Surgical Indicators between the Two Groups. The amount of blood loss in the UAL group was significantly less than that in the UAE group, and the operation time was significantly longer than that in the UAE group, with statistical significance ($p < 0.05$). There was no significant difference in immediate hemostasis rate and hemostasis efficiency between the two groups ($p > 0.05$), as shown in Table 2.

Table 1: Comparison of general information of the two groups of patients.

The general information	Group UAL ($n = 50$)	Group UAE ($n = 50$)	T	p
Average age (years)	29.49 ± 4.40	28.83 ± 4.73	0.372	0.708
Average gestation time (weeks)	35.56 ± 8.09	35.13 ± 8.82	0.459	0.639
Average number of pregnancies	2.62 ± 0.73	2.70 ± 0.92	1.116	0.125
Average newborn weight (kg)	3.86 ± 0.86	3.96 ± 0.97	0.854	0.397
Type of puerpera (n (%))	Unipara	36 (72.00)	35 (70.00)	0.454
	Multipara	14 (28.00)	15 (30.00)	0.501

Table 2: Comparison of operation related indexes between the two groups.

Indicators	Group UAL ($n = 50$)	Group UAE ($n = 50$)	t	p
Blood loss (mL)	1627.63 ± 403.62	1778.49 ± 429.16	5.182	0.039
Operation time (min)	60.46 ± 13.70	44.49 ± 7.43	5.867	0.032
Immediate hemostasis rate (N (%))	46 (92.00)	47 (94.00)	0.838	0.405
Effective rate of hemostasis (N (%))	48 (96.00)	49 (98.00)	0.383	0.721

3.3. Comparison of Postoperative Recovery Indicators between the Two Groups. There was no significant difference in the net time of lochia excretion and the time of menstrual revulsion between the two groups ($p > 0.05$), as shown in Table 3.

3.4. Comparison of Uterine and Ovarian Arterial Blood Flow Indexes between the Two Groups. There were no significant differences in RI and S/D between the two groups ($p > 0.05$), as shown in Table 4.

3.5. Comparison of Ovarian Function Indexes between the Two Groups before and after Surgery. Before the operation, there were no significant differences in FSH, E2, and LH levels between the two groups ($p > 0.05$). After surgery, the levels of FSH and LH in the two groups were significantly decreased, while the level of E2 was significantly increased, with statistical significance ($p < 0.05$). There was no significant difference between the two groups ($p > 0.05$), as shown in Table 5 and Figure 1.

4. Discussion

PPH is a common complication after cesarean section, and uterine weakness is one of the main causes of PPH [9]. PPH is urgent and develops rapidly, requiring active and effective treatment; otherwise it may cause functional ischemia of multiple organs, hypovolemic shock, etc., and seriously affect the maternal quality of life [10]. Conservative treatment and surgical treatment are currently the main means of clinical management of PPH, and surgical treatment is performed if conservative treatment fails [11]. UAL is the most commonly used surgical method in the clinical treatment of PPH, although it has good blood control effects. However, it may block the blood supply of the uterine body, and then block the blood supply of the corresponding ovarian branches, which can cause serious damage to ovarian function and is limited in clinical application [12]. UAE is when a catheter is inserted into the femoral artery, deep into the uterine artery, and a stent, or gelatin sponge, is inserted into the artery. At the same time, it causes little trauma and can effectively preserve the body's fertility and uterus, but there are many contraindications [13]. Both UAL and UAE have certain limitations. At present, few studies have explored the efficacy of UAL and UAE in the treatment of hysteroconstrictive PPH after cesarean section and their effects on uterine and ovarian artery blood flow and function.

Eggel et al. [14] showed that the effective rate in UAE treatment of PPH reached 93.50%, and the menstrual cycle recovery time was 5.6 months. Sanket and Herendael [15] showed that uterine artery ligation can effectively reduce intraoperative blood loss. In this study, the immediate hemostatic rate and hemostatic effective rate of the two groups reached more than 90%, and the time of lochia excretion and menstrual revulsion was similar in the two groups, which was basically consistent with the results of Eggel and Sanket studies, indicating that UAL and UAE have significant efficacy in the treatment of hysterostatic PPH after cesarean section. UAL can block most of the uterine blood supply, cause ischemic stimulation, promote smooth muscle contraction, and finally achieve hemostatic effect [16]. UAE is a minimally invasive surgery, which can determine the site and scope of bleeding through angiography, and perform embolization on the proximal and distal sides of the bleeding artery to timely block uterine blood supply and have an immediate hemostatic effect [17]. In addition, this study found more blood loss in the UAE group than in the UAL group. However, the operation time is shortened, and the possible reasons are analyzed: compared with UAL, UAE is simpler, but the implementation of UAE often requires the cooperation of interventional departments, thus prolonging the preoperative preparation time and resulting in increased blood loss of patients. Therefore, it is suggested that the preparation time before UAE should be shortened as much as possible [18].

RI and S/D are common hemodynamic indexes in clinical practice. RI reflects the characteristic quantity of vascular resistance. The greater the value is, the greater the vascular resistance and the more serious the blood circulation disorder. S/D is generally maintained at a dynamic equilibrium, and abnormal changes can be caused once abnormal blood flow occurs [19]. Garg [20] showed that

Table 3: Comparison of postoperative recovery indexes between the two groups.

Indicators	Group UAL ($n = 50$)	Group UAE ($n = 50$)	t	p
Lochia removal time (D)	31.68 ± 2.54	31.83 ± 2.20	0.029	0.972
Period of menstruation (weeks)	41.31 ± 7.10	42.40 ± 6.73	0.245	0.784

Table 4: Comparison of blood flow indexes of uterine and ovarian arteries between the two groups ($\overline{x} \pm s$).

Indicators		Group UAL ($n = 50$)	Group UAE($n = 50$)	t	p
Left uterine artery	RI	0.81 ± 0.01	0.83 ± 0.02	1.861	0.081
	S/D	12.30 ± 3.06	12.50 ± 2.82	1.525	0.116
Right uterine artery	RI	0.82 ± 0.02	0.80 ± 0.02	0.949	0.203
	S/D	12.89 ± 2.13	12.63 ± 2.86	1.316	0.354

Table 5: Comparison of ovarian function indexes between the two groups before and after operation ($\overline{x} \pm s$).

Project		Group UAL ($n = 50$)	Group UAE ($n = 50$)
FSH (IU/L)	Before the operation	5.10 ± 1.20	5.13 ± 1.26
	After the operation	$3.25 \pm 0.51^*$	$3.16 \pm 0.62^*$
E2 (pmol/L)	Before the operation	18.57 ± 1.11	17.86 ± 1.10
	After the operation	$33.25 \pm 2.13^*$	$32.87 \pm 2.18^*$
LH (IU/L)	Before the operation	4.48 ± 0.84	4.68 ± 0.78
	After the operation	$2.40 \pm 0.56^*$	$2.23 \pm 0.51^*$

Note. Compared with that before the operation, $^*p < 0.05$.

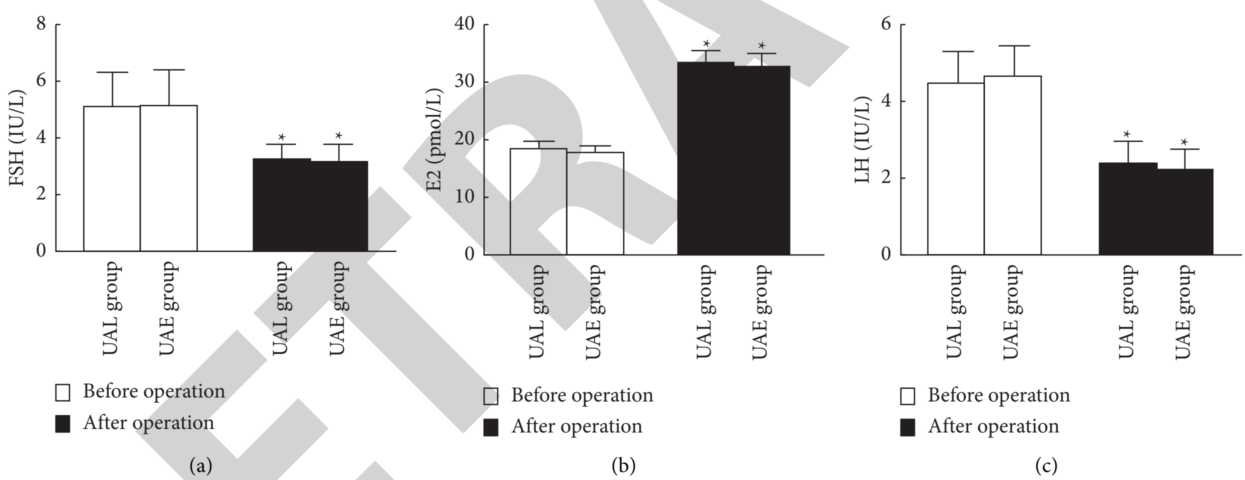

Figure 1: Comparison of ovarian function indexes between the two groups before and after operation.

laparoscopic uterine vascularization can maintain the stability of patients' blood flow. In this study, RI and S/D of the left and right uterine arteries in the two groups showed no significant difference. Combined with the results of Menderes' study, it was found that neither UAL nor UAE had a significant impact on the uterine and ovarian artery blood flow in patients with PPH after cesarean section. After UAL, the uterine blood supply can return to normal due to the establishment of collateral circulation. In addition, intraoperative sutures can be absorbed and have a certain tension at a certain time, which has a hemostatic effect. With proteolytic hydrolysis and uterine involution and shrinkage, sutures are gradually hydrolyzed, and the uterine artery and other blood vessels ligated will recalculate, thus having no significant influence on blood circulation [21]. After UAE, blood perfusion can be restored from the communication branch to the ovarian branch of the uterine artery. At the same time, the embolization material is absorbable gelatin sponge particles, which can reach the peripheral artery and keep the blood supply of pelvic organ collateral, so as not to affect the blood supply of uterus and ovary [22].

The ovary is located in the female pelvic cavity, and its main function is to discharge and produce egg cells and secrete sex hormones so as to effectively promote and maintain the development of female characteristics. Therefore, sex hormones can effectively reflect the ovarian function of the body. FSH, E2, and LH are common sex hormones in clinical practice, and FSH plays a role in promoting follicular development and maturation. At the same time, it can cooperate with LH to induce mature follicles to secrete estrogen and ovulation, which play a role in promoting the formation of normal menstruation. FSH can be up-regulated in patients with ovarian hypoplasia, primary amenorrhea, hyporeproductive function, and so on. E2 is the most abundant and most active steroid hormone, mainly secreted from ovarian follicular granulosa cells. Once menopause, amenorrhea, ovariectomy, and ovarian dysfunction occur, the E2 level will be reduced. LH can secrete estrogen and progesterone and promote luteogenesis, and an abnormal increase of LH level may occur when menopause, oophorectomy, and premature ovarian failure occur [23]. In this study, the levels of FSH and LH decreased and E2 increased in both groups after the operation, but there was no significant difference between the two groups, indicating that UAL and UAE can promote the recovery of ovarian function in patients with PPH after cesarean section. UAL, by ligation of the uterine arcuate artery with absorbable suture, not only has an obvious hemostasis effect, but also has simple operation and little trauma, which will not have a significant impact on the uterus and promote uterine rejuvenation and functional recovery [24]. UAE can clearly observe the uterine artery variation through angiography, which provides a good display of the uterine blood supply network. At the same time, hyperselective embolization of blood supply through a microcatheter or catheter can preserve the integrity of the uterus and normal physiological function [8].

5. Conclusion

In conclusion, both UAL and UAE can effectively treat PPH with uterine contraction after cesarean section and have a significant hemostatic effect. Both have similar effects on uterine and ovarian arterial blood flow and can effectively improve ovarian function. However, with less blood loss and a short UAE operation time, appropriate surgical procedures can be selected according to the specific situation of patients.

Data Availability

The data used to support the findings of this study are available from the corresponding author upon request.

Conflicts of Interest

The authors declare that they have no conflicts of interest.

Acknowledgments

This work was supported by Tangshan Gongren Hospital.

References

[1] O. Karlsson, A. Jeppsson, and M. Hellgren, "Factor XIII activity at onset of labour and association with postpartum haemorrhage: an exploratory post-hoc study," *International Journal of Obstetric Anesthesia*, vol. 47, no. 1, Article ID 103174, 2021.

[2] N. L. Ambounda, S. H. Woromogo, F. E. Yagata-Moussa et al., "Primary postpartum haemorrhage at the libreville university hospital centre: epidemiological profile of women," *PLoS One*, vol. 16, no. 9, Article ID e0257544, 2021.

[3] D. Habek, I. Marton, and M. Prka, "Transvaginal perpendicular cervical wafeform sutures in the treatment of early postpartum hemorrhage caused by lower uterine segment atony," *Taiwanese Journal of Obstetrics and Gynecology*, vol. 60, no. 3, pp. 577-578, 2021.

[4] Z. Ling, L. Yao, Z. Cui, and C Lifan, "Effect of carboprost tromethamine in prevention of postpartum hemorrhage in cesarean section," *Pakistan Journal of Pharmaceutical Sciences*, vol. 31, no. 5, pp. 2257–2262, 2018.

[5] A. Javeed, S. S. Rizvi, S. Zhou, R. Riaz, S. U. Khan, and S. J. Kwon, "Heart risk failure prediction using a novel feature selection method for feature refinement and neural network for classification," *Mobile Information Systems*, vol. 202011 pages, 2020.

[6] D. Xavier, V. Marie, W. Ingrid, F. Goffinet, and L. Sentilhes, "Maternal outcome after abdominal packing for uncontrolled postpartum hemorrhage despite peripartum hysterectomy," *PLoS One*, vol. 12, no. 6, Article ID e0177092, 2017.

[7] S. N. X. Shamima, S. K. Kundu, and M. D. Hossain, "Ultrasonographic assessment of retroverted gravid uterus and first trimester pregnancy loss of women in a semi-urban area of dhaka, Bangladesh," *Science Progress and Research*, vol. 1, no. 3, pp. 70–76, 2021.

[8] M. Toguchi, Y. Iraha, J. Ito et al., "Uterine artery embolization for postpartum and postabortion hemorrhage: a retrospective analysis of complications, subsequent fertility and pregnancy outcomes," *Japanese Journal of Radiology*, vol. 38, no. 3, pp. 240–247, 2020.

[9] A. Javeed, S. U. Khan, L. Ali, S. Ali, Y. Imrana, and Y. Imrana, "Machine learning-based automated diagnostic systems developed for heart failure prediction using different types of data modalities: a systematic review and future directions," *Computational and Mathematical Methods in Medicine*, vol. 2022, Article ID 9288452, 30 pages, 2022.

[10] I. M. Whlk-Hansen, T. Bergholt, and K. Ekelund, "Adherence to guidelines on red blood cell transfusions in women having post-partum haemorrhage," *Dan Med J*, vol. 67, no. 5, Article ID A10190569, 2020.

[11] C. Y. Wang, H. H. Pan, C. C. Chang, and C. K. Lin, "Outcomes of hypogastric artery ligation and transcatheter uterine artery embolization in women with postpartum hemorrhage," *Taiwanese Journal of Obstetrics and Gynecology*, vol. 58, no. 1, pp. 72–76, 2019.

[12] R. Cabrera, A. Vigeras, R. Ribeiro, M. T. Zomer, and W. Kondo, "Laparoscopic variants of temporary uterine artery ligation," *Journal of Minimally Invasive Gynecology*, vol. 27, no. 4, pp. 811-812, 2019.

[13] M. Aoki, H. Tokue, M. Miyazaki, K. Shibuya, S. Hirasawa, and K. Oshima, "Primary postpartum hemorrhage: outcome of uterine artery embolization," *British Journal of Radiology*, vol. 91, no. 1087, Article ID 20180132, 2018.

[14] B. Eggel, M. Bernasconi, T. Quibel et al., "Gynecological, reproductive and sexual outcomes after uterine artery embolization for post-partum haemorrage," *Scientific Reports*, vol. 11, no. 1, p. 833, 2021.

[15] P. Sanket and B. Herendael, "Temporary ligation of the uterine artery at its origin using a removable "Shoelace" knot," *Journal of Minimally Invasive Gynecology*, vol. 27, no. 1, p. 26, 2020.

[16] M. K. Paul, B. Rupen, D. Natalya, L. Q. V. D. Does, L. R. Haworth, and N. Kazi, "Laparoscopic-assisted myomectomy with bilateral uterine artery occlusion/ligation," *Journal of Minimally Invasive Gynecology*, vol. 26, no. 5, pp. 856–864, 2018.

Hindawi
Journal of Healthcare Engineering
Volume 2023, Article ID 9785132, 1 page
https://doi.org/10.1155/2023/9785132

Retraction

Retracted: Differential Prognostic Analysis of Higher and Lower PEEP in ARDS Patients: Systematic Review and Meta-Analysis

Journal of Healthcare Engineering

Received 3 October 2023; Accepted 3 October 2023; Published 4 October 2023

This article has been retracted by Hindawi following an investigation undertaken by the publisher [1]. This investigation has uncovered evidence of one or more of the following indicators of systematic manipulation of the publication process:

(1) Discrepancies in scope
(2) Discrepancies in the description of the research reported
(3) Discrepancies between the availability of data and the research described
(4) Inappropriate citations
(5) Incoherent, meaningless and/or irrelevant content included in the article
(6) Peer-review manipulation

The presence of these indicators undermines our confidence in the integrity of the article's content and we cannot, therefore, vouch for its reliability. Please note that this notice is intended solely to alert readers that the content of this article is unreliable. We have not investigated whether authors were aware of or involved in the systematic manipulation of the publication process.

Wiley and Hindawi regrets that the usual quality checks did not identify these issues before publication and have since put additional measures in place to safeguard research integrity.

We wish to credit our own Research Integrity and Research Publishing teams and anonymous and named external researchers and research integrity experts for contributing to this investigation.

The corresponding author, as the representative of all authors, has been given the opportunity to register their agreement or disagreement to this retraction. We have kept a record of any response received.

References

[1] M. Liang and X. Chen, "Differential Prognostic Analysis of Higher and Lower PEEP in ARDS Patients: Systematic Review and Meta-Analysis," *Journal of Healthcare Engineering*, vol. 2022, Article ID 5399416, 8 pages, 2022.

Hindawi
Journal of Healthcare Engineering
Volume 2022, Article ID 5399416, 8 pages
https://doi.org/10.1155/2022/5399416

Research Article

Differential Prognostic Analysis of Higher and Lower PEEP in ARDS Patients: Systematic Review and Meta-Analysis

Min Liang [1] **and Xin Chen** [2]

[1]*Department of Intensive Care Unit, Sir Run Run Shaw Hospital, Affiliated to School of Medicine, Zhejiang University, Hangzhou, China*
[2]*Department of Intensive Care Unit, Hangzhou Tumor Hospital, Affiliated to School of Medicine, Zhejiang University, Hangzhou, China*

Correspondence should be addressed to Min Liang; bldwlm@zju.edu.cn

Received 11 February 2022; Revised 25 February 2022; Accepted 2 March 2022; Published 21 March 2022

Academic Editor: Liaqat Ali

Background. Positive end-expiratory pressure (PEEP) refers to the positive pressure in the respiratory tract at the end of the exhalation when we use a ventilator. The differences of higher PEEP and lower PEEP on clinical outcomes in acute respiratory distress syndrome (ARDS) patients are less well known. *Methods*. A comprehensive literature search of all randomized control trials (RCTs) was conducted using PubMed, Embase, World Health Organization (WHO) Global Index Medicus, WHO clinical trial registry, and Clinicaltrials.gov. Inclusion criteria included RCTs comparing the clinical outcomes of higher and lower PEEP in ARDS patients. *Results*. Eleven studies were included in the final analysis. In the higher PEEP group, the hospital mortality, 28-day mortality, and ICU mortality showed no significantly lower risk compared to the lower PEEP group (RR = 0.92, 95% CI 0.80–1.05, $p = 0.22$; RR = 0.88, 95% CI 0.73–1.05, $p = 0.15$; RR = 0.84, 95% CI 0.67–1.05, $p = 0.12$; respectively). High certainty could be obtained that there is no significant difference between the clinical outcomes of higher PEEP and lower PEEP in ARDS patients. *Conclusions*. There is no significant difference of the hospital mortality, 28-day mortality, and ICU mortality between higher and lower PEEP in ARDS patients.

1. Introduction

Acute respiratory distress syndrome (ARDS) is caused by intrapulmonary and/or extrapulmonary causes. It is a clinical syndrome characterized by refractory hypoxemia and has attracted much attention due to its high mortality [1]. The etiology of ARDS is various, and the pathogenesis of ARDS caused by different etiology is different. The clinical manifestations are acute onset, respiratory distress, and hypoxemia which is difficult to be corrected by conventional oxygen therapy. At present, "Berlin definition" is used to make diagnosis and stratification of severity of ARDS, and it is necessary to make differential diagnosis with many diseases [2].

Etiology of ARDS includes intrapulmonary cause and extrapulmonary cause [3]. Intrapulmonary causes include pneumonia, aspiration, pulmonary contusion, drowning, and inhalation of toxic substances. Extrapulmonary factors include severe systemic infection, severe multiple injuries (multiple fractures, flail chest, severe brain trauma, and burns), shock, high-risk surgery (cardiac surgery, major artery surgery, etc.), massive blood transfusion, drug poisoning, pancreatitis, and cardiopulmonary bypass. In addition, the etiology of ARDS can be divided into biological pathogenic agents and abiotic pathogenic agents. Biological pathogenic agents mainly include a variety of pathogens, such as bacteria, viruses, fungi, atypical pathogens, DAMPs, and malignant tumors. Abiotic pathogenic agents mainly include acid substances, drugs, toxic gas inhalation, and mechanical ventilation-related injury [4, 5].

At present, in addition to actively treating the primary disease, respiratory support technology is the main treatment method for ARDS, which aims to correct intractable hypoxemia, prevent alveolar collapse, reduce the degree of pulmonary edema, improve oxygenation, and relieve ventilator fatigue [6]. The treatment of ARDS includes mechanical ventilation and nonmechanical ventilation. Mechanical ventilation is the main treatment for ARDS patients. According to the different modes of mechanical ventilation, it can be divided into noninvasive ventilation and invasive ventilation [7]. Noninvasive ventilation relies on mask for ventilation, while invasive ventilation relies on endotracheal intubation or tracheotomy catheter for ventilation. The choice of the two depends on the specific condition and the timing [8, 9].

Positive end-expiratory pressure (PEEP) refers to the positive pressure in the respiratory tract at the end of the exhalation when we use a ventilator (usually positive pressure is applied only on the inhale and drops to zero on the exhalation). In this way, early alveolar closure can be avoided, and some alveoli that lose ventilation function due to exudation, atelectasis, and other reasons will expand so that the reduced functional residual volume will increase, and the purpose of improving blood oxygen can be achieved [10]. PEEP is similar to intermittent positive pressure respiration, but because of its longer duration of action, it has a wider range of effects on the respiratory and circulatory systems [11]. PEEP is the external pressure applied to the airway by the ventilator at the end of the patient's expiratory breath during mechanical ventilation. PEEP helps the lungs to expand and dilate collapsed alveoli. Acute lung injury reduces lung volume, lung compliance, ventilation/blood flow imbalance, and intrapulmonary shunt, leading to persistent hypoxemia and life-threatening complications. Appropriate PEEP is selected to reopen poorly ventilated alveoli, thereby improving lung compliance, ventilation/flow imbalance, and pulmonary shunt.

Many randomized controlled trials (RCTs) have compared the effect of higher PEEP and lower PEEP on reducing mortality in ARDS patients with inconsistent results [12–22], most likely due to variations in experiment design and methodological measurements. The differences of higher PEEP and lower PEEP on clinical outcomes in acute respiratory distress syndrome (ARDS) patients are less well known. Therefore, an explicit systematic review and meta-analysis were demanded to evaluate the difference of higher PEEP and lower PEEP on clinical outcomes in ARDS patients.

2. Materials and Methods

2.1. Study Selection. All RCTs to compare the effect of higher PEEP and lower PEEP on preventing mortality in ARDS patients were searched using PubMed (1966–2021), Embase (1980–2021), and World Health Organization (WHO) Global Index Medicus. Unpublished or ongoing studies were identified by checking clinical trials registers through Clinicaltrials.gov and WHO clinical trial registry. Literature in all languages was included in the search. Meta-analyses and systematic reviews were also hand-searched to find relevant literature that might have been missed by the initial search. The keywords used for search were "Positive end-expiratory pressure," "acute respiratory distress syndrome," "PEEP," "ARDS," "Mortality." Furthermore, records from relevant searches were eventually hand-searched for further research. The asymmetry associated with the inclusion parameters of the published studies was finalized via discussion. The full set of published studies that were identified to be relevant for systematic review and meta-analysis were finalized according to the following set of inclusion parameters: (1) authentic research works, (2) documented in English language, (3) consisting of patients diagnosed with heart failure, and (4) includes details of patients taking medication for cardiovascular disease. As per the aim of the given study, prime attention was provided to the data where the patient cases related to heart failure were involved. There were multiple studies with the following category which were discarded: (1) insufficient data of the patients, (2) duplicity in published works, (3) nonclinical studies, (4) abstracts, conference papers, editorials, letters, or review studies, (5) research studies with no conclusions, and (6) insufficient patient data.

2.2. Data Extraction. Articles retrieved from the searches were evaluated independently by 2 reviewers using predefined standardized data extraction forms, and then, the data were evaluated by a third reviewer independently based on the US National Institute of Health National Heart, Lung, and Blood Institute (NHLBI) study quality assessment tool for controlled intervention studies [23]. Clinical outcome of interest was the hospital mortality, 28-day mortality, and ICU mortality as defined by the trial authors. The data pertaining to patients, the kinds of treatment, and methodology were abstracted (Table 1).

2.3. Meta-Analysis. The Preferred Reporting Items for Systematic Reviews and Meta-Analyses statement methodology [24] was adhered to. Relative risks (RRs) with a 95% CI for postoperative infectious complications of each trial were calculated to estimate treatment effects. Meta-analysis of the pooled data was performed using the fixed-effect model or random-effect model, depending on the heterogeneity of the included studies. If clinical heterogeneity was observed, data were analyzed using a random-effect model. Heterogeneity was quantified using the Cochrane's Q statistic and I^2 statistic, with the values of 25%, 50%, and 75% signifying the limits of low, moderate, and high statistical heterogeneity, respectively [25]. A funnel plot was used to explore publication bias for the studies. All statistical analyses were performed using RevMan 5.4.

The risk of bias was evaluated using the Cochrane risk of bias tool. It was used to evaluate the selection bias, performance bias, detection bias, attrition bias, reporting bias, and other bias. The evidence quality was evaluated using the GRADEPro based on the results of systematic evaluation. To achieve transparency and implicity, the GRADE system classifies the certainty of evidence in one of four grades: high: further research is very unlikely to change our confidence in the estimate of effect; moderate: further research is likely to have an important impact on our confidence in the estimate of effect and may change the estimate; low: further research is very likely to have an important impact on our confidence

Table 1: Characteristics of all randomized control trials comparing the effect of higher PEEP and lower PEEP on mortality (1966–2021).

Study name	No. of participants (high PEEP)	No. of participants (low PEEP)	Higher PEEP	Lower PEEP	Outcome of interest
Amato et al. [12]	29	24	Lower inflection point + 2 cm H_2O	FiO_2-PEEP	①②③
Ranieri et al. [13]	18	19	Lower inflection point + 2 cm H_2O	FiO_2-PEEP	②
Brower et al. [14]	276	273	FiO_2-PEEP (ARDSnet)	FiO_2-PEEP	①
Villar et al. [15]	50	45	Lower inflection point + 2 cm H_2O	FiO_2-PEEP	①③
Meade et al. [16]	475	508	FiO_2-PEEP	FiO_2-PEEP	①②③
Mercat et al. [17]	385	382	P_{plat}	FiO_2-PEEP	①②
Talmor et al. [18]	30	31	Transpulmonary pressure	FiO_2-PEEP	②
Huh et al. [19]	30	27	Saturation decrease more	FiO_2-PEEP	②③
Hodgson et al. [20]	10	10	$PFiO_2$-PEEP	FiO_2-PEEP	①
Kacmarek et al. [21]	99	101	PEEP + 35–45 cm H_2O	FiO_2-PEEP	①②③
Cavalcanti et al. [22]	501	509	PEEP + 2 cm H_2O	FiO_2-PEEP	① ②③

①: hospital mortality; ②: 28-day mortality; ③: ICU mortality.

in the estimate of effect and is likely to change the estimate; very low: any estimate of effect is very uncertain.

3. Results

3.1. Demographic Characteristics of the Studies. The literature search process, shown in Figure 1, identified 221 potential studies for full analyses. Eleven studies were finally included for further quantitative meta-analyses after exclusion [12–22] (Figure 1), involving a total of 3832 patients. Clinical outcome of interest was the hospital mortality, 28-day mortality, and ICU mortality. Of the 11 studies identified in the present analysis, 8 studies reported the hospital mortality, 8 studies reported the 28-day mortality, and 6 studies reported the ICU mortality. Only 4 studies included in the analysis reported all the three outcomes (Table 1).

3.2. Comparison of Hospital Mortality during Higher PEEP or Lower PEEP. Of the 11 studies identified in the present analysis, 8 studies reported the hospital mortality, including 3683 patients. Among these patients, higher PEEP was performed in 1827 patients, 766 patients died, and the hospital mortality was 41%, while lower PEEP was performed in 1856 patients, 805 patients died, and the hospital mortality was 43%. There was moderate heterogeneity between trials and it was significant ($I^2 = 55\%$, $p = 0.03$; Figure 2), so the random-effect model was applied. In the higher PEEP group, the hospital mortality showed no significant lower risk relative to the lower PEEP group (RR = 0.92, 95% CI 0.80–1.05, $p = 0.22$; Figure 2). In the funnel plot, all points are symmetrically distributed, indicating that there is no obvious publication bias (Figure 3).

3.3. Comparison of 28-Day Mortality during Higher PEEP or Lower PEEP. Of the 11 studies identified in the meta-analysis, 8 studies reported the 28-day mortality, including 3168 patients. Among these patients, higher PEEP was performed in 1567 patients, 576 patients died, and the hospital mortality was 37%, while lower PEEP was performed in 1601 patients, 610 patients died, and the hospital mortality was 38%. There was moderate heterogeneity between trials, and it was significant ($I^2 = 59\%$, $p = 0.02$; Figure 4), so the random-effects model was applied. In the higher PEEP group, the hospital mortality showed no significantly lower risk relative to the lower PEEP group (RR = 0.88, 95% CI 0.73–1.05, $p = 0.15$; Figure 4). In the funnel plot, all points are symmetrically distributed, indicating that there is no obvious publication bias (Figure 5).

3.4. Comparison of ICU Mortality during Higher PEEP or Lower PEEP. Of the 11 studies included in the final analysis, 6 studies reported the ICU mortality, including 2405 patients. Among these patients, higher PEEP was performed in 1186 patients, 514 patients died, and the hospital mortality was 43%, while lower PEEP was performed in 1219 patients, 549 patients died, and the hospital mortality was 45%. There was moderate heterogeneity between trials, and it was significant ($I^2 = 69\%$, $p = 0.006$; Figure 6), so the random-effects model was applied. In the higher PEEP group, the hospital mortality showed no significant lower risk relative to the lower PEEP group (RR = 0.84, 95% CI 0.67–1.05, $p = 0.12$; Figure 6). In the funnel plot, all points are symmetrically distributed, indicating that there is no obvious publication bias (Figure 7).

3.5. Publication Bias. Publication bias was assessed and visualized by using a funnel plot (Figure 5). A funnel plot is a simple scatter plot that reflects the estimated intervention effect of a single study with a given sample size or accuracy. The most common funnel plot is the estimated effect of each study on the horizontal axis and the sample size on the vertical axis. If there is bias, the funnel diagram will be asymmetrical and the bottom corner of the graph will be blank. In such cases, the effects calculated by meta-analysis may overestimate the efficacy of the intervention. The more pronounced the asymmetry, the more likely there is to be substantial bias. From Figures 3, 5, and 7, all points are symmetrically distributed, indicating that there is no obvious publication bias.

3.6. Risk of Bias Analysis. The risk of bias of the studies included is summarized in Figure 8. The selection bias, performance bias, detection bias, attrition bias, and other bias were evaluated by using the Cochrane risk of bias tool. Of the

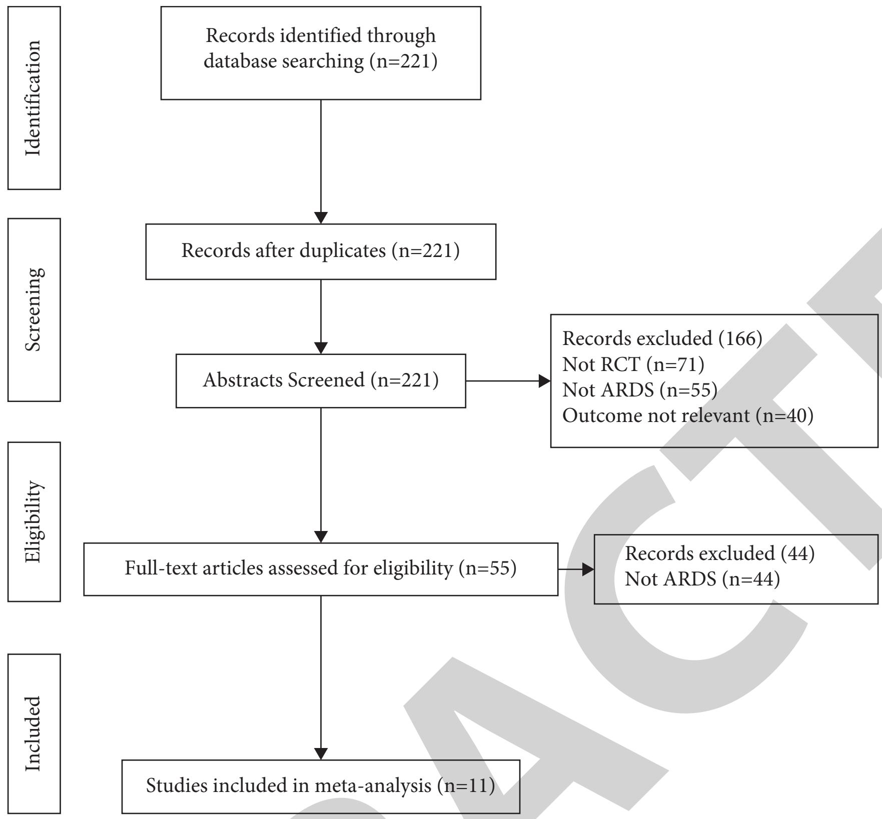

Figure 1: PRISMA flow diagram showing the process of literature screening, study selection, and reasons for exclusion. PRISMA, preferred reporting items for systematic reviews and meta-analyses.

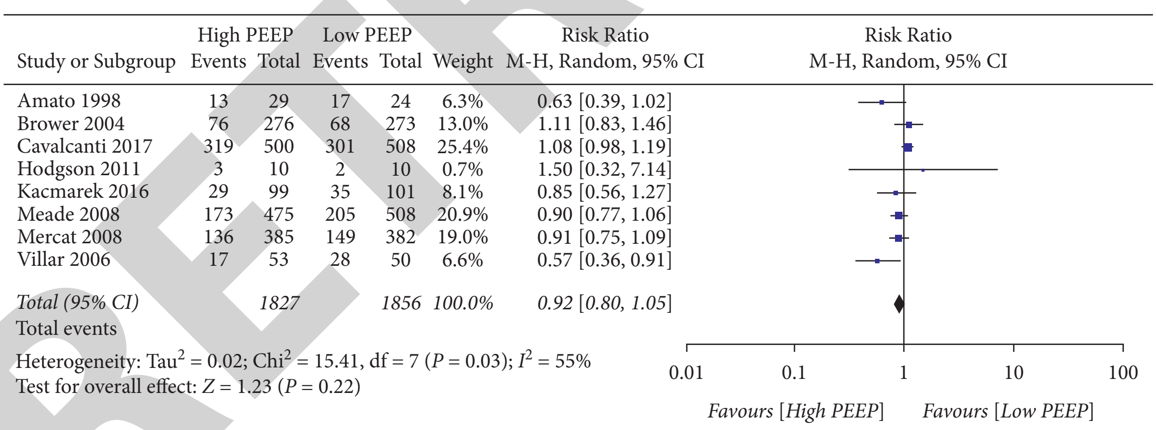

Figure 2: Forest plot of comparison of hospital mortality during higher PEEP or lower PEEP.

11 studies, 2 had incomplete outcome data and 4 had selection reporting bias (18% and 36%, respectively). Attrition bias occurred during the study follow-up due to loss of follow-up, withdrawal, and no response. Use of appropriate statistical methods, such as intention-to-treat (ITT) analysis, can reduce this bias. Reporting bias occurs when research results are reported and can be avoided by registering research.

3.7. Evaluation of the Quality of Evidence. The GRADE system classifies the certainty of evidence in one of four grades: high, moderate, low, and very low.

The three clinical outcomes (hospital mortality, 28-day mortality, and ICU mortality) were all critical. High certainty could be obtained that there is no significant difference between the clinical outcomes of higher PEEP and lower PEEP in ARDS patients (Table 2).

4. Discussion

With the rapid increase of the ARDS incidence, the burden of ARDS diseases is gradually increasing. PEEP has been the common treatments for ARDS patients worldwide. It can be used in patients with spontaneous breathing through a face

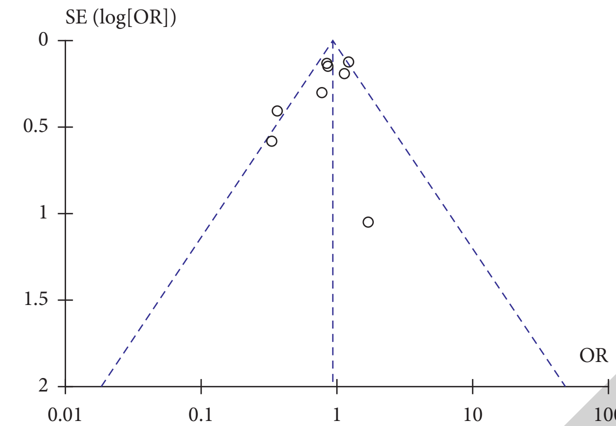

Figure 3: Funnel plot of included studies demonstrating the risk ratios of hospital mortality in the higher PEEP group compared to the lower PEEP group. SE indicates standard error.

Study or Subgroup	High PEEP Events	High PEEP Total	Low PEEP Events	Low PEEP Total	Weight	Risk Ratio M-H, Random, 95% CI
Amato 1998	11	29	17	24	8.4%	0.54 [0.31, 0.91]
Cavalcanti 2017	277	501	251	509	25.4%	1.12 [1.00, 1.26]
Huh 2009	12	30	9	27	5.7%	1.20 [0.60, 2.39]
Kacmarek 2016	22	99	27	101	9.4%	0.83 [0.51, 1.36]
Meade 2008	135	475	164	508	21.8%	0.88 [0.73, 1.06]
Mercat 2008	107	385	119	382	20.2%	0.89 [0.72, 1.11]
Ranieri 1999	7	18	11	19	5.6%	0.67 [0.34, 1.35]
Talmor 2008	5	30	12	31	3.5%	0.43 [0.17, 1.07]
Total (95% CI)		*1567*		*1601*	*100.0%*	*0.88 [0.73, 1.05]*
Total events	576		610			

Heterogeneity: $Tau^2 = 0.03$; $Chi^2 = 17.14$, df = 7 ($P = 0.02$); $I^2 = 59\%$
Test for overall effect: $Z = 1.42$ ($P = 0.15$)

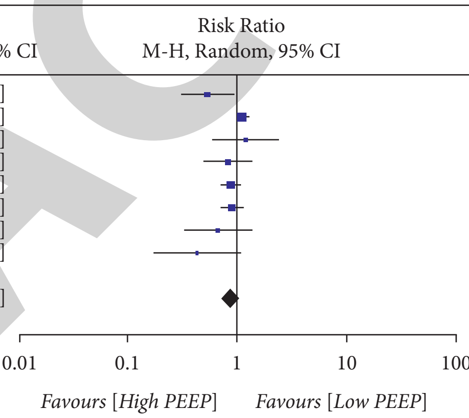

Figure 4: Forest plot of comparison of 28-day mortality during higher PEEP or lower PEEP.

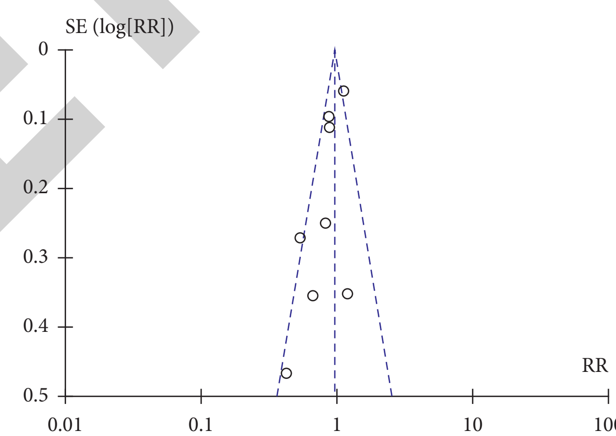

Figure 5: Funnel plot of included studies demonstrating the risk ratios of 28-day mortality in the higher PEEP group compared to the lower PEEP group. SE indicates standard error.

mask or endotracheal intubation. PEEP in this case is called continuous positive airway pressure. PEEP can also be used in conjunction with intermittent positive pressure mechanical ventilation to produce what is known as continuous positive pressure ventilation. The extent to which either form of PEEP may improve the oxygenation state depends on the degree to which the mean airway pressure increases. However, the difference between higher PEEP and lower

Study or Subgroup	High PEEP Events	High PEEP Total	Low PEEP Events	Low PEEP Total	Weight	Risk Ratio M-H, Random, 95% CI
Amato 1998	11	29	17	24	10.9%	0.54 [0.31, 0.91]
Cavalcanti 2017	303	500	284	509	28.2%	1.09 [0.98, 1.21]
Huh 2009	14	30	13	27	10.5%	0.97 [0.56, 1.68]
Kacmarek 2016	25	99	30	101	13.2%	0.85 [0.54, 1.34]
Meade 2008	145	475	178	508	25.0%	0.87 [0.73, 1.04]
Villar 2006	16	53	27	50	12.3%	0.56 [0.34, 0.91]
Total (95% CI)		*1186*		*1219*	*100.0%*	*0.84 [0.67, 1.05]*
Total events	514		549			

Heterogeneity: $Tau^2 = 0.04$; $Chi^2 = 16.28$, df = 5 ($P = 0.006$); $I^2 = 69\%$
Test for overall effect: $Z = 1.56$ ($P = 0.12$)

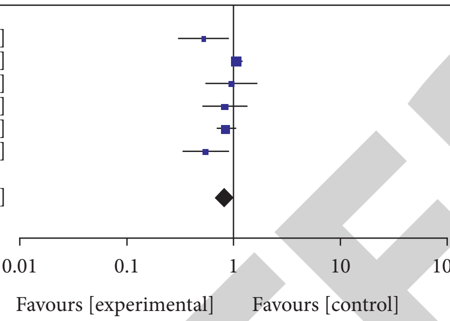

Figure 6: Forest plot of comparison of ICU mortality during higher PEEP or lower PEEP.

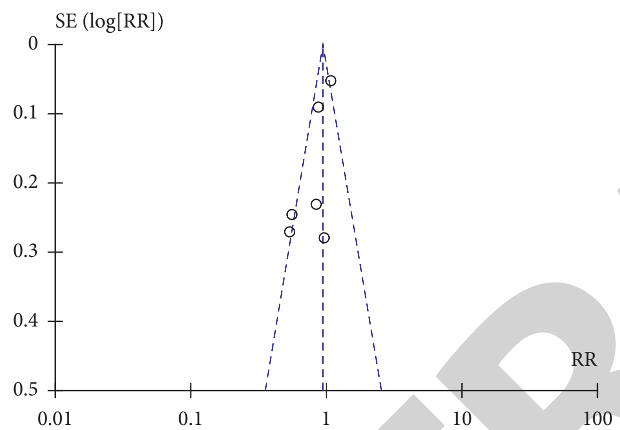

Figure 7: Funnel plot of included studies demonstrating the risk ratios of ICU mortality in the higher PEEP group compared to the lower PEEP group. SE indicates standard error.

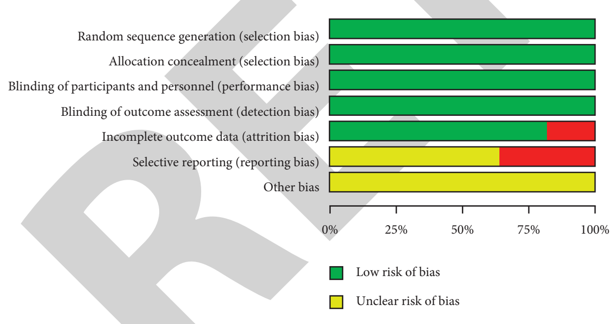

Figure 8: Risk of bias analysis for the studies included.

PEEP was less known. In the present study, we evaluated the difference of them on clinical outcomes in ARDS patients systematically.

PEEP should be applied early in patients who have failed to respond to oxygen therapy. During mechanical ventilation, the inspiratory airway and alveoli are under positive pressure, and the airway and alveolar pressure are higher than atmospheric pressure when the airway opens at the end of expiratory. PEEP can improve the ventilation function of ARDS. Low levels of PEEP are often used in supine intubated patients [26]. Some researchers believe that low-pressure PEEP allows patients to maintain higher lung volume while breathing through a tracheal tube, thus helping to wean them off mechanical ventilation [27]. Hypoxemia in pulmonary diseases is mainly caused by intrapulmonary shunt, and adequate oxygenation is often not achieved even at FiO_2 1.0. When used at more than 5 cm H_2O, PEEP generally improves PaO_2 in these patients. PEEP also reduced FiO_2 by 0.6 or less, thereby reducing the risk of oxygen poisoning [28].

Eleven studies were identified in the meta-analysis. In the higher PEEP group, the hospital mortality, 28-day mortality, and ICU mortality showed no significantly lower risk compared to the lower PEEP group. In all the funnel plots, all points are symmetrically distributed, indicating that there is no obvious publication bias. Attrition bias and reporting bias are the main two bias existed in the study. High certainty could be obtained that there is no significant difference between the clinical outcomes of higher PEEP and lower PEEP in ARDS patients. The complications of PEEP are related to lung volume and airway pressure. Air is pushed into the lungs at high pressure throughout the ventilation cycle to increase the volume of the lungs. Not only is air pumped into the lungs at high pressure during inhalation, it is more likely to cause barotrauma, or “volume injury,” but it is also more likely to reduce venous blood flow to the chest, lowering blood pressure and cardiac output.

There are some limitations should be acknowledged. First, there was significant clinical heterogeneity between studies. Therefore, the random-effects model was applied. Second, definitions of clinical outcomes were not specified among these studies, and differences in the definition of them can affect estimation of effect size. Third, differences in the treatment used between studies may account for heterogeneity, which may have influenced our results. Despite these limitations, the findings support higher PEEP is not different from lower PEEP when considering the incidence of clinical outcomes, including the hospital mortality, 28-day mortality, and ICU mortality as defined by each study. Further studies are required to be conducted to confirm the findings due to large clinical heterogeneity.

Table 2: Higher PEEP compared lower PEEP in ARDS patients with different clinical outcomes of interest.

		Certainty assessment					No. of patients		Effect			
No. of studies	Study design	Risk of bias	Inconsistency	Indirectness	Imprecision	Other considerations	Higher PEEP	Lower PEEP	Relative (95% CI)	Absolute (95% CI)	Certainty	Importance
Hospital mortality												
8	Randomized trials	Not serious	Not serious	Not serious	Not serious	Strong association	766/1827 (41.9%)	805/1856 (43.4%)	RR 0.97 (0.89 to 1.04)	13 fewer per 1,000 (from 48 fewer to 17 more)	High	Critical
28-day mortality												
8	Randomized trials	Not serious	Not serious	Not serious	Not serious	None	576/1567 (36.8%)	610/1601 (38.1%)	RR 0.96 (0.88 to 1.05)	15 fewer per 1,000 (from 46 fewer to 19 more)	High	Critical
ICU mortality												
6	Randomized trials	Not serious	Not serious	Not serious	Not serious	None	514/1186 (43.3%)	549/1219 (45.0%)	RR 0.96 (0.88 to 1.04)	18 fewer per 1,000 (from 54 fewer to 18 more)	High	Critical

CI: confidence interval; RR: risk ratio.

Hindawi
Journal of Healthcare Engineering
Volume 2023, Article ID 9862546, 1 page
https://doi.org/10.1155/2023/9862546

Retraction

Retracted: Two Different Transplant Preconditioning Regimens Combined with Irradiation and Chemotherapy in the Treatment of Childhood Leukemia: Systematic Review and Meta-Analysis

Journal of Healthcare Engineering

Received 26 September 2023; Accepted 26 September 2023; Published 27 September 2023

This article has been retracted by Hindawi following an investigation undertaken by the publisher [1]. This investigation has uncovered evidence of one or more of the following indicators of systematic manipulation of the publication process:

(1) Discrepancies in scope
(2) Discrepancies in the description of the research reported
(3) Discrepancies between the availability of data and the research described
(4) Inappropriate citations
(5) Incoherent, meaningless and/or irrelevant content included in the article
(6) Peer-review manipulation

The presence of these indicators undermines our confidence in the integrity of the article's content and we cannot, therefore, vouch for its reliability. Please note that this notice is intended solely to alert readers that the content of this article is unreliable. We have not investigated whether authors were aware of or involved in the systematic manipulation of the publication process.

Wiley and Hindawi regrets that the usual quality checks did not identify these issues before publication and have since put additional measures in place to safeguard research integrity.

We wish to credit our own Research Integrity and Research Publishing teams and anonymous and named external researchers and research integrity experts for contributing to this investigation.

The corresponding author, as the representative of all authors, has been given the opportunity to register their agreement or disagreement to this retraction. We have kept a record of any response received.

References

[1] X. Wang, D. Mu, A. Geng, A. Zhao, and Y. Song, "Two Different Transplant Preconditioning Regimens Combined with Irradiation and Chemotherapy in the Treatment of Childhood Leukemia: Systematic Review and Meta-Analysis," *Journal of Healthcare Engineering*, vol. 2022, Article ID 2825712, 9 pages, 2022.

Hindawi
Journal of Healthcare Engineering
Volume 2022, Article ID 2825712, 9 pages
https://doi.org/10.1155/2022/2825712

Review Article

Two Different Transplant Preconditioning Regimens Combined with Irradiation and Chemotherapy in the Treatment of Childhood Leukemia: Systematic Review and Meta-Analysis

Xiangwen Wang, Dan Mu, Anyang Geng, Anqi Zhao, and Yiyuan Song

Inner Mongolia People's Hospital Pediatric Hematology, Hohhot, China

Correspondence should be addressed to Xiangwen Wang; 18047192454@163.com

Received 19 February 2022; Revised 23 February 2022; Accepted 25 February 2022; Published 18 March 2022

Academic Editor: Liaqat Ali

Objective. To observe the therapeutic effect and the incidence of adverse reactions of total body irradiation plus cyclophosphamide (TBI/CY) and busulfan plus cyclophosphamide (BU/CY) in the treatment of pediatric hematopoietic stem cell transplantation. *Methods*. By searching the Cochrane Library, PubMed, Web of Knowledge, Embase, Chinese Biomedical Literature Database (CBM), and screening randomized controlled trials (RCTs), quality evaluation and data extraction were performed for the included literature, and meta-analysis was performed for RCTs included at using Review Manager 5.2 software. *Results*. A total of 10160 patients were enrolled in 15 RCTs, including 5211 patients in the TBI/CY group and 4949 patients in the BU/CY group. Meta-analysis showed that there was a statistical difference in transplant failure rate (OR = 1.56, 95% CI (1.23, 1.97), $P = 0.0002$, $I^2 = 56\%$, $Z = 3.69$), transplant mortality (OR = 1.45, 95% CI (1.24, 1.68), $P < 0.00001$, $I^2 = 76\%$, $Z = 4.80$), transplantation long-term disease-free survival rate (OR = 1.52, 95% CI (1.09, 2.12), $P = 0.01$, $I^2 = 0\%$, $Z = 2.50$), and transplantation adverse reactions (OR = 1.28, 95% CI (1.08, 1.52), $P = 0.004$, $I^2 = 0\%$, $Z = 2.85$). *Conclusion*. Meta-analysis showed that TBI/CY combined pretreatment regimen was more effective than BU/CY regimen alone in the treatment of pediatric hematologic transplantation, with a lower incidence of adverse reactions and significant long-term survival efficacy.

1. Introduction

Acute leukemia (AL) is a heterogeneous malignant clonal disease of hematopoietic stem cells, with a high recurrence rate and mortality rate [1]. Leukemia is mainly because of hematopoietic stem cells during differentiation and infiltrating the tissues and organs of the human body. Then, it caused different degrees of fever, anemia, and bleeding symptoms [2–5]. Leukemia has a high incidence of pediatric malignant tumors, mostly presented as acute leukemia. Nowadays, with the gradual improvement of clinical hematopoietic stem cell technology and hematopoietic stem cell source, the success rate of transplantation is significantly improved, making more children with leukemia have the desire for long-term survival [6].

Pediatric leukemia is a high incidence of malignant tumor in China [7]. Currently, although allogeneic hematopoietic stem cell transplantation (allo-HSCT) can serve as an effective treatment for AL, patients of leukemia still face various complications after transplantation, including graft-versus-host disease(GVHD), venoocclusive disease (VOD), thrombotic microvascular disease (TMA), and fungal infection that have caused adverse effects on the survival and prognosis of AL patients after transplantation. The main measures for the clinical treatment of the disease include chemical therapy, targeted therapy, and hematopoietic stem cell transplantation. For children with refractory and recurrent leukemia, conventional chemotherapy is short [8]. Nowadays, with the continuous in-depth research of the clinical characteristics of hematopoietic stem cells and transplantation immune technology and the continuous promotion of new anti-infectious drugs and immunosuppressors, bone marrow transplantation has been gradually developed and improved, and now, it has become one of the main means for the treatment of hematological diseases. Acute leukemia is characterized by abnormal proliferation of leukemia cells, abnormal primitive cells, and naive cells in the bone marrow, which can be widely infiltrated into the extramedullary organs, and is clinically manifested by different degrees of anemia, bleeding, infection, and other symptoms. Allogeneic HSCT is currently the main treatment for hematological malignancies, but the recurrence rate after acute leukemia transplantation is still not significantly reduced. Studies at home and abroad show that if small residual disease can be detected before transplantation, the recurrence rate of patients is significantly increased after transplantation, but there are few survival studies on myeloablative HSCT [9].

Allogeneic hematopoietic stem cell transplantation (Allo-HSCT) is the preferred method for treating AML in middle and high-risk patients, and the quality of the pretreatment regimen directly affects the prognosis of patients. Traditional busulfan combined with cyclophosphamide (BU/CY) and total body irradiation combined with cyclophosphamide (TBI/CY) protocol. Guolo et al. [10] showed that overall and leukemia-free survival had significant advantages for patients undergoing pretreatment with systemic radiotherapy in remission, but large meta-analysis showed similar survival for the two regimens. Therefore, for relapsed/refractory acute myeloid leukemia resistant to multiple chemotherapy drugs, a systemic radiotherapy myelination-based regimen might be needed. Whether conditioning regimen, it has an advantage that has not been explicitly recommended.

Therefore, in this study, relevant randomized controlled trials in recent years were systematically searched, and meta-analysis was used to evaluate the efficacy and safety of two different transplant preconditioning regiments combined with radiotherapy and chemotherapy in the treatment of childhood leukemia, providing reliable evidence for clinical treatment.

2. Materials and Methods

2.1. Search Strategy. In this study, Cochrane Library, PubMed, Web of Science, Embase, and CBM were searched and other databases and related websites search. Subject words such as "Transplant," "Total body irradiation," "Busulfan," "Childhood leukemia," "Cyclophosphamide," and related drug trade names were retrieved as subject words and free words, respectively. In order to avoid bias caused by language limitations, this study searched both Chinese and English literature. In order to avoid missing relevant studies, relevant references listed in the article and conference abstracts found in the search were traced (Figure 1).

2.2. Data Extraction. Data extraction was completed independently by two evaluators. First, read the title of the literature, read the abstract of the literature related to the content of this study, and further read the full text of the literature if it is a randomized controlled trial. The studies that met the inclusion and exclusion criteria were classified and evaluated, and the data were extracted. If there is any disagreement between the two reviewers in the selection of literature, the problem will be solved through discussion within the group. The authors of studies for which detailed data were not available were contacted by e-mail or by reviewing the literature referencing the candidate study. The inclusion criterion is childhood diagnosed with leukemia, aged 1–14 years. The exclusion criterion is patients treated with irradiation and chemotherapy before.

2.3. Literature Quality Assessment. 2 reviewers used the Jadad rating scale to independently evaluate 15, mainly to evaluate the randomized controlled experimental design of the included literature, including generation of random sequence ("yes" = 2, "unclear" = 1," no" = 0); random hiding ("yes" = 2, "unclear" = 1," no" = 0); blind ("yes" = 2, "unclear" = 1," no" = 0); and exit ("yes" = 1, "no" = 0). A score of 1–3 is considered low quality, while a score of 4–7 is considered high quality. Data extraction of information mainly includes the author information, country, Jadad score, types and patient's age and gender, study drug dosage, number of cycles, effective treatment before and after treatment, and adverse reaction condition, after data extraction, two commentators' data comparison, discuss the inconsistencies, and supplement the missing information as much as possible.

2.4. Bias Analysis. Heterogeneity between studies was assessed using I^2 statistics, 25%, 50%, and 75% representing low, medium, and high heterogeneity, respectively; $I^2 < 50\%$ and $P > 0.1$ between studies using fixed effect models and $I^2 > 50\%$ and $P < 0.1$ from chi-square analysis showed study heterogeneity. Meta-analysis was done by random effects models and searched for possible heterogeneity by subgroup analysis source. The sensitivity analysis removed the included literature one by one to see whether the pooled effect values were stable and reliable (Figures 2 and 3).

2.5. Statistical Analysis. Consolidated effect size analysis of indicators of concern for this system evaluation was analyzed using STATA 12.0 software. For measurement data, the weighted mean difference (WMD) is the same; the standard mean difference (SMD) and its 95% CI are the effect amount. Relative hazard (relative risk, RR) and its 95% CI were used as the effect size, and $P < 0.05$ was used as the statistical difference. Intertest heterogeneity was performed using a 2-test, $P > 0.1$, and I^2 <50%. If there is no heterogeneity, the fixed effect model is used for data pooled analysis, and the random effect model for pooled analysis and subgroup analysis was to detect the reasons for possible clinical heterogeneity and statistical heterogeneity. Publication bias was detected by the rank correlation test (Begg method) and the linear regression method (Egger method). Finally, the sensitivity analysis was conducted by the elimination method to test the stability of the results level. For the meta-analysis, there must be treatment effects and their standard deviation.

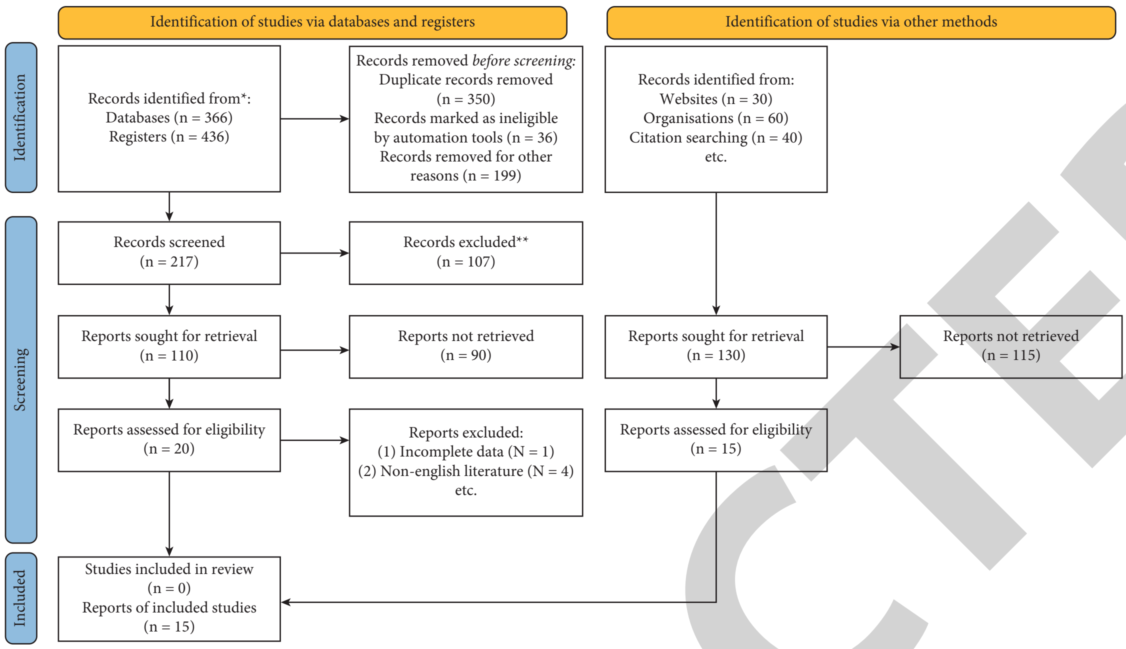

Figure 1: Flowchart of the literature screening.

3. Result

3.1. Basic Characteristics of Literature. A total of 802 documents were initially retrieved, and duplicates were removed by software with 692 remaining. After reading of the topic, abstract, and full text, 15 literature [11–25] were obtained, and a total of 10160 patients were included in the meta-analysis, including 5211 in the TBI/CY group and 4949 in the BU/CY group. Final included general features of the 15 literature are given in Table 1.

3.2. Transplant Failure Rate. Among the 15 RCTs literature included in transplant failure rate, the heterogeneity test was carried out, and it was found that the heterogeneity of the selected studies was small, so meta-analysis with fixed models could be performed. The results of meta-analysis showed that the rhombus plot and vertical line not intersected in the forest map of transplant failure rate for 4 included literature, so there was a statistical difference in the comparison of transplant failure rate between the BU/CY group and the TBI/CY group (OR = 1.56, 95% CI (1.23, 1.97), $P = 0.0002$, $I^2 = 56\%$, $Z = 3.69$) (Figure 4).

3.3. Transplant Mortality. Among the 15 RCTs literature included in transplant mortality, the heterogeneity test was carried out, and it was found that the heterogeneity of the selected studies was small, so meta-analysis with fixed models could be performed. The results of meta-analysis showed that the rhombus plot and vertical line not intersected in the forest map of transplant mortality for 4 included literature, so there was a statistical difference in the comparison of transplant mortality between the BU/CY group and the TBI/CY group (OR = 1.45, 95% CI (1.24, 1.68), $P < 0.00001$, $I^2 = 76\%$, $Z = 4.80$) (Figure 5).

3.4. Transplantation Long-Term Disease-Free Survival Rate. Among the 15 RCTs literature included in the transplantation long-term disease-free survival rate, the heterogeneity test was carried out, and it was found that heterogeneity of the selected studies was small, so meta-analysis with fixed models could be performed. The results of meta-analysis showed that the rhombus plot and vertical line not intersected in the forest map of transplantation long-term disease-free survival rate for 4 included literature, so there was a statistical difference in the comparison of transplantation long-term disease-free survival rate between the BU/CY group and the TBI/CY group (OR = 1.52, 95% CI (1.09, 2.12), $P = 0.01$, $I^2 = 0\%$, $Z = 2.50$) (Figure 6).

3.5. Incidence of Transplantation Adverse Reactions. Among the 15 RCTs literature included in incidence of transplantation adverse reactions, the heterogeneity test was carried out, and it was found that the heterogeneity of the selected studies was small, so meta-analysis with fixed models could be performed. The results of meta-analysis showed that the rhombus plot and vertical line not intersected in the forest map of incidence of transplantation adverse reactions for 4 included literature, so there was a statistical difference in the comparison of incidence of transplantation adverse reactions between the BU/CY group and the TBI/CY group (OR = 1.28, 95% CI (1.08, 1.52), $P = 0.004$, $I^2 = 0\%$, $Z = 2.85$) (Figure 7).

4. Discussion

Pretreatment protocol of allo-HSCT for AML, retrospective analysis, and meta-analysis had no clear answer as to whether TBI treatments are superior to BU treatment. It has been shown that oral BU in TBI-MAC patients reduced

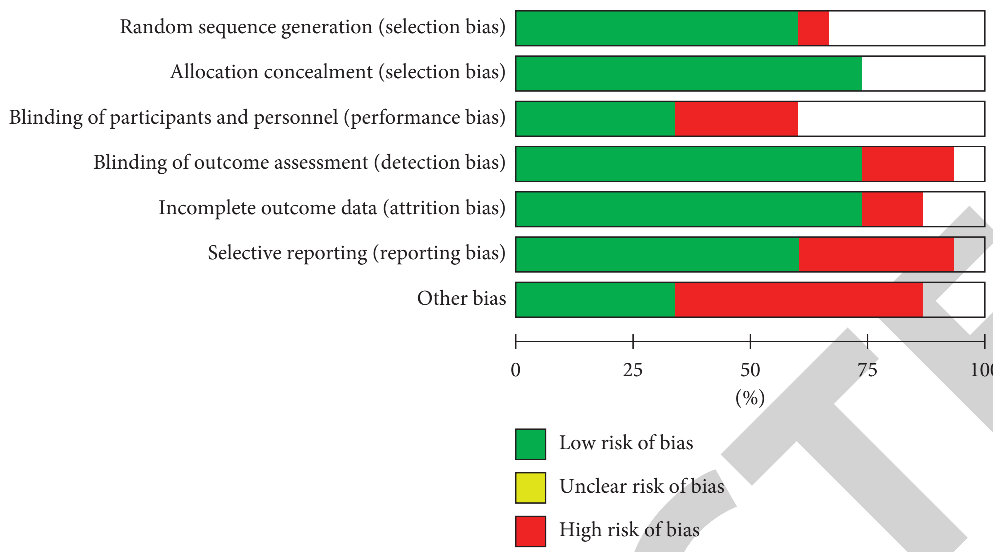

(a)

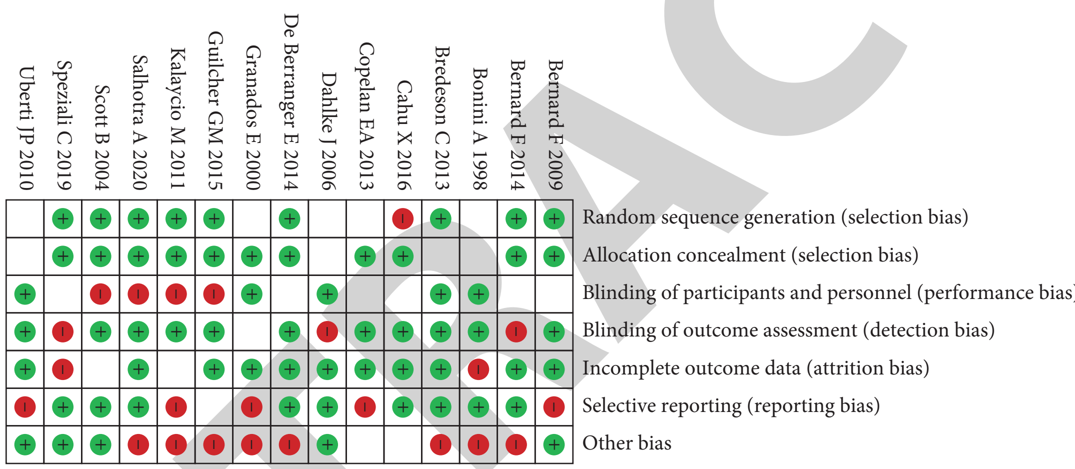

(b)

FIGURE 2: Literature quality evaluation chart. (a) Risk of bias graph. (b) Risk of bias summary.

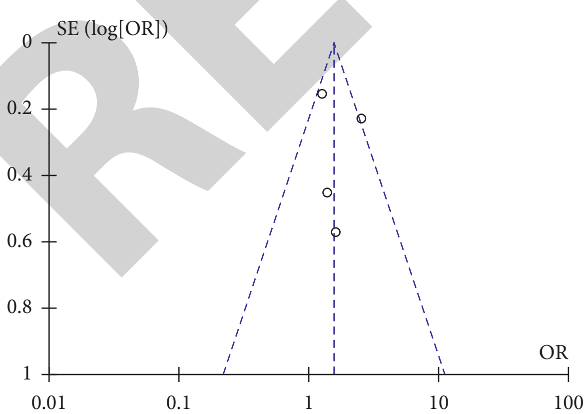

(a)

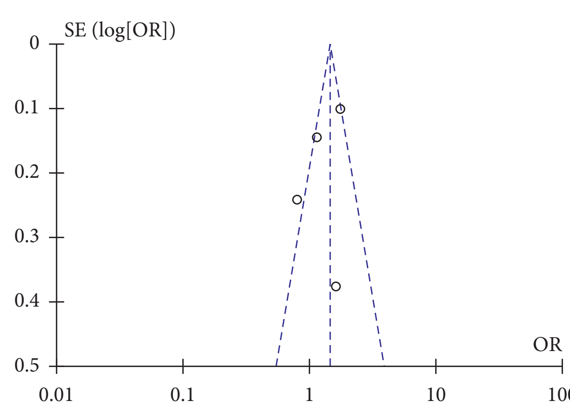

(b)

FIGURE 3: Continued.

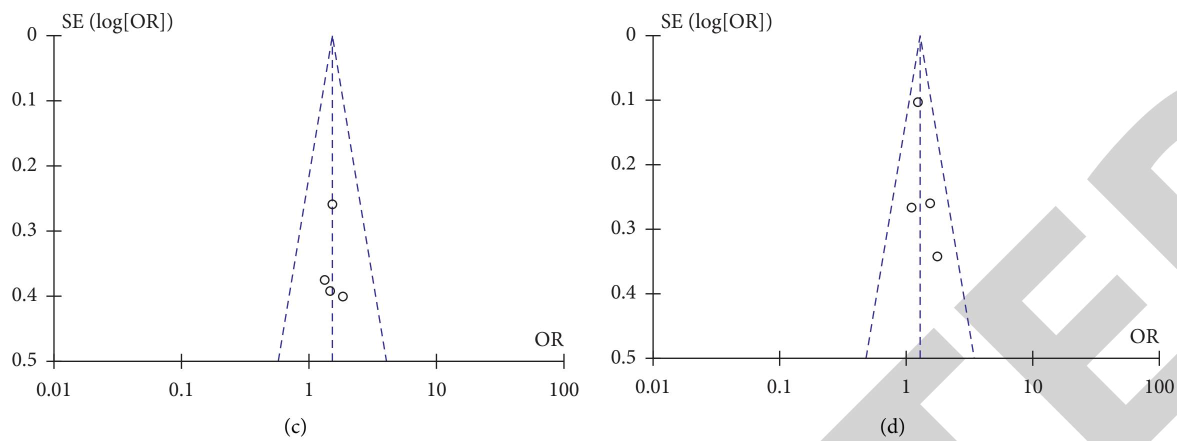

Figure 3: (a)–(d) Funnel plot of literature publication bias.

Table 1: Basic clinical features of 15 literature included in our study.

Study	Age	Gender (male) (%)	Hospitalization days	BU/CY group (*N*)	TBI/CY group (*N*)	NOS score	Research type
Speziali et al. [11]	6.71 ± 2.2	44.25	17.8 ± 1.1	26/146	16/146	8	RCT
Uberti et al. [12]	6.65 ± 3.4	59.12	12.2 ± 1.3	240/1593	200/1593	7	RCT
Bernard et al. [13]	6.12 ± 4.5	45.72	12.4 ± 3.9	174/240	66/130	7	RCT
Salhotra et al. [14]	7.15 ± 1.5	44.12	12.9 ± 4.9	47/167	34/167	7	RCT
Kalaycio et al. [15]	6.85 ± 2.4	51.89	9.8 ± 3.4	19/86	14/86	8	RCT
Copelan et al. [16]	6.36 ± 3.2	63.45	11.2 ± 5.1	311/1230	197/1230	7	RCT
Bernard et al. [17]	9.62 ± 12.2	78.10	10.9 ± 2.1	16/42	14/46	9	RCT
Guilcher et al. [18]	6.61 ± 3.0	48.75	19.9 ± 1.4	21/78	17/78	9	RCT
Scott et al. [19]	7.25 ± 1.51	59.23	13.4 ± 4.1	43/128	40/128	7	RCT
De Berranger et al. [20]	6.22 ± 1.21	56.22	17.8 ± 1.5	56/226	41/142	8	RCT
Bredeson et al. [21]	11.35 ± 2.12	53.16	16.1 ± 5.9	121/458	102/458	8	RCT
Cahu et al. [22]	9.25 ± 1.01	66.34	17.5 ± 1.6	125/601	112/601	8	RCT
Dahlke et al. [23]	8.51 ± 2.61	48.34	15.0 ± 5.6	23/76	16/76	7	RCT
Bonini et al. [24]	12.34 ± 3.51	53.12	12.4 ± 1.7	12/26	9/26	9	RCT
Granados et al. [25]	9.25 ± 4.21	67.22	11.1 ± 1.2	45/114	11/42	9	RCT

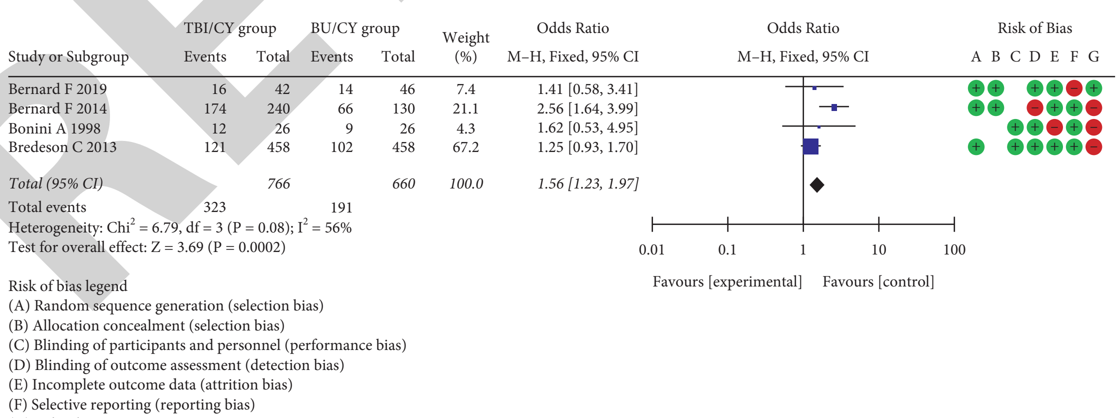

Figure 4: Meta-analysis of transplant failure rate between two groups.

relapse rate and disease-free survival is high; while, patients treated with intravenous BU, with improved survival due to reduced side effects of BU, obtained similar results to that of TBI-MAC. Analysis from the International Blood and Bone Marrow Transplantation Research Center showed that for AML patients in remission, disease-free and overall survival in the BU group outperformed the TBI group, with similar relapse rates and low nonrelapse mortality [26]. No large

Study or Subgroup	TBI/CY group Events	TBI/CY group Total	BU/CY group Events	BU/CY group Total	Weight (%)	Odds Ratio M–H, Fixed, 95% CI
Cahu X 2016	125	601	112	601	31.1	1.15 [0.86, 1.52]
Copelan EA 2013	311	1230	197	1230	51.7	1.77 [1.45, 2.17]
Dahlke J 2006	23	76	16	76	3.9	1.63 [0.78, 3.40]
De Berranger E 2014	56	226	41	142	13.3	0.81 [0.51, 1.30]
Total (95% CI)		*2133*		*2049*	*100.0*	*1.45 [1.24, 1.68]*
Total events	515		366			

Heterogeneity: $Chi^2 = 12.45$, df = 3 (P = 0.006); $I^2 = 76\%$
Test for overall effect: Z = 4.80 (P < 0.00001)

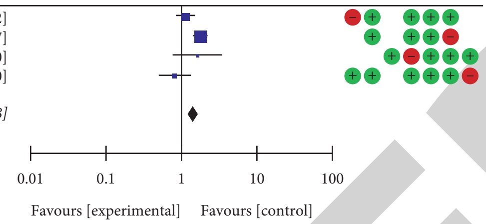

Risk of bias legend
(A) Random sequence generation (selection bias)
(B) Allocation concealment (selection bias)
(C) Blinding of participants and personnel (performance bias)
(D) Blinding of outcome assessment (detection bias)
(E) Incomplete outcome data (attrition bias)
(F) Selective reporting (reporting bias)
(G) Other bias

Figure 5: Meta-analysis of transplant mortality between two groups.

Study or Subgroup	TBI/CY group Events	TBI/CY group Total	BU/CY group Events	BU/CY group Total	Weight (%)	Odds Ratio M–H, Fixed, 95% CI
Granados E 2000	45	114	11	42	16.9	1.84 [0.84, 4.02]
Guilcher GM 2015	21	78	17	78	21.6	1.32 [0.63, 2.76]
Kalaycio M 2011	19	86	14	86	19.0	1.46 [0.68, 3.14]
Salhotra A 2020	47	167	34	167	42.5	1.53 [0.92, 2.54]
Total (95% CI)		*445*		*373*	*100.0*	*1.52 [1.09, 2.12]*
Total events	132		76			

Heterogeneity: $Chi^2 = 0.38$, df = 3 (P = 0.95); $I^2 = 0\%$
Test for overall effect: Z = 2.50 (P = 0.01)

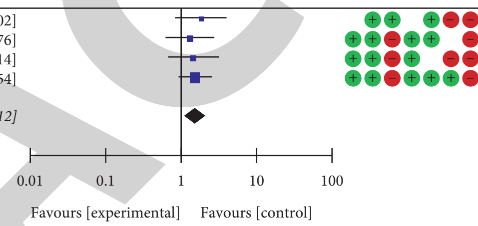

Risk of bias legend
(A) Random sequence generation (selection bias)
(B) Allocation concealment (selection bias)
(C) Blinding of participants and personnel (performance bias)
(D) Blinding of outcome assessment (detection bias)
(E) Incomplete outcome data (attrition bias)
(F) Selective reporting (reporting bias)
(G) Other bias

Figure 6: Meta-analysis of transplantation long-term disease-free survival rate between two groups.

Study or Subgroup	TBI/CY group Events	TBI/CY group Total	BU/CY group Events	BU/CY group Total	Weight (%)	Odds Ratio M–H, Fixed, 95% CI
Salhotra A 2020	47	167	34	167	10.4	1.53 [0.92, 2.54]
Scott B 2004	43	128	40	128	11.4	1.11 [0.66, 1.88]
Speziali C 2019	26	146	16	146	5.6	1.76 [0.90, 3.44]
Uberti JP 2010	240	1593	200	1593	72.6	1.24 [1.01, 1.51]
Total (95% CI)		*2034*		*2034*	*100.0*	*1.28 [1.08, 1.52]*
Total events	356		290			

Heterogeneity: $Chi^2 = 1.75$, df = 3 (P = 0.63); $I^2 = 0\%$
Test for overall effect: Z = 2.85 (P = 0.004)

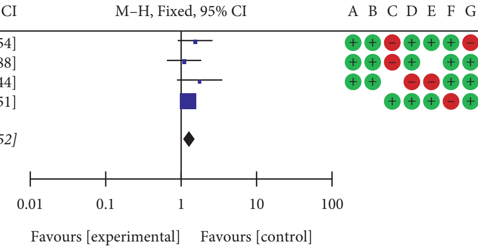

Risk of bias legend
(A) Random sequence generation (selection bias)
(B) Allocation concealment (selection bias)
(C) Blinding of participants and personnel (performance bias)
(D) Blinding of outcome assessment (detection bias)
(E) Incomplete outcome data (attrition bias)
(F) Selective reporting (reporting bias)
(G) Other bias

Figure 7: Meta-analysis of incidence of transplantation adverse reactions between two groups.

sample size has been reported in treating similar results in AML patients with relapse/refractory. The statistical results from this study showed that relapse was the main cause of death in the two groups of relapsed/refractory AML patients. In addition to applying new drugs and new technologies to reduce the pretransplant tumor load, the improved pretreatment protocol can also reduce the nonrelapse mortality and improve survival. In recent years, it has been reported that pretreatment with TBI combined with BU or mafalan has reduced nonrelapse mortality and improved disease-free survival in patients. At the same time, the residual leukemia was detected regularly after transplantation, and the early withdrawal of immunosuppressant and immunotherapy also improved according to the patient's disease status and patient prognosis [27].

Hematopoietic stem cell transplantation can cure childhood leukemia, aplastic anemia, hemoglobin disease, and congenital immune deficiency [28]. The pretreatment regiments for pediatric transplantation include total body irradiation (TBI) and chemotherapy alone [29–32]. The most classical pretreatment regiments are TBI/CY and BU/CY. Preconditioning is one of the important factors affecting the curative effect of hematopoietic stem cell transplantation [33]. The BU/CY-based pretreatment protocols are two of which are considered classical pretreatment options for HSCT [34]. However, there is little literature on the impact of different pretreatment protocols on pediatric HSCT [35]. The results show that children in hematopoietic stem cell transplantation, TBI/CY and BU/CY two pretreatment methods, implant failure rate, no significant difference between the BU/CY group-related increased mortality after transplantation, might be more prone to this group of patients after transplantation of complications such as complicated with hepatic vein occlusion disease, hemorrhagic cystitis, and lead to the early death of increase after transplantation. The long-term disease-free survival rate in the TBI/CY group was significantly better than that in the BU/CY group [36–39].

This study has some limitations: the number of RCTs included and the number of cases is small, which may have a certain publication bias; the number of included literature was small, and no subgroup analysis was performed to compare the efficacy; this study only evaluated the efficacy at the end of treatment, but did not evaluate the maintenance of the medium and long-term efficacies.

5. Conclusion

The available evidence tentatively demonstrates the safety and efficacy of BU/CY in pediatric HSCT [40], and TBI/CY combined pretreatment regimen was more effective than BU/CY regimen alone in the treatment of pediatric hematologic transplantation, with a lower incidence of adverse reactions and significant long-term survival efficacy.

Data Availability

The data used to support the findings of this study are available from the corresponding author upon request.

Conflicts of Interest

The authors declare that they have no conflicts of interest.

Acknowledgments

This study was funded by Inner Mongolia Autonomous Region People's Hospital in Hospital Fund Project (2019YN06).

References

[1] I. Cunningham, "Post-transplant leukemia relapse in organs: biology. and behavior in 585 reports," *Critical Reviews in Oncology*, vol. 157, Article ID 103170, 2021.

[2] C. Rautenberg, U. Germing, R. Haas, G. Kobbe, and T. Schroeder, "Relapse of acute myeloid leukemia after allogeneic stem cell transplantation: prevention, detection, and treatment," *International Journal of Molecular Sciences*, vol. 20, no. 1, p. 228, 2019.

[3] B. Dholaria, B. N. Savani, B. K. Hamilton et al., "Hematopoietic cell transplantation in the treatment of newly diagnosed adult acute myeloid leukemia: an evidence-based review from the American society of transplantation and cellular therapy," *Transplantation and Cellular Therapy*, vol. 27, no. 1, pp. 6–20, 2021.

[4] K. K. Yeo, K. Kayser, A. S. Margol et al., "Clinical and neuropsychological outcome of pediatric non-midline central nervous system germinoma treated with chemotherapy and reduced dose/volume irradiation: the Children's Hospital Los Angeles experience," *Pediatric Blood & Cancer*, vol. 66, 2019.

[5] P. D. Lulla, S. Naik, S. Vasileiou et al., "Clinical effects of administering leukemia-specific donor T cells to patients with AML/MDS after allogeneic transplant," *Blood*, vol. 137, no. 19, pp. 2585–2597, 2021.

[6] S. Scobioala and H. T. Eich, "Risk stratification of pulmonary toxicities in the combination of whole lung irradiation and high-dose chemotherapy for Ewing sarcoma patients with lung metastases: a review," *Strahlentherapie und Onkologie*, vol. 196, no. 6, pp. 495–504, 2020.

[7] T. Guillaume, F. Malard, L. Magro et al., "Prospective phase II study of prophylactic low-dose azacitidine and donor lymphocyte infusions following allogeneic hematopoietic stem cell transplantation for high-risk acute myeloid leukemia and myelodysplastic syndrome," *Bone Marrow Transplantation*, vol. 54, no. 11, pp. 1815–1826, 2019.

[8] C. Li, W. Ni, X. Wang et al., "A phase I/II radiation dose escalation trial using simultaneous integrated boost technique with elective nodal irradiation and concurrent chemotherapy for unresectable esophageal Cancer," *Radiation Oncology*, vol. 14, no. 1, p. 48, 2019.

[9] A. L. Olson, R. M. Saliba, and B. Oran, "Cytogenetics and blast count determine transplant outcomes in patients with active acute myeloid leukemia," *Acta Haematologica*, vol. 144, no. 1, pp. 74–81, 2021.

[10] F. Guolo, C. Di Grazia, and P. Minetto, "Pre-transplant minimal residual disease assessment and transplant-related factors predict the outcome of acute myeloid leukemia patients undergoing allogeneic stem cell transplantation," *European Journal of Haematology*, vol. 107, no. 5, pp. 573–582, 2021.

[11] C. Speziali, A. Daly, M. Abuhaleeqa et al., "Fludarabine, busulfan, and low-dose TBI conditioning versus cyclophosphamide and TBI in allogeneic hematopoietic cell transplantation for adult acute lymphoblastic leukemia," *Leukemia and Lymphoma*, vol. 60, no. 3, pp. 639–648, 2019.

[12] J. P. Uberti, M.-A. Agovi, S. Tarima et al., "Comparative analysis of BU and CY versus CY and TBI in full intensity unrelated marrow donor transplantation for AML, CML and myelodysplasia," *Bone Marrow Transplantation*, vol. 46, no. 1, pp. 34–43, 2011.

[13] F. Bernard, P. Auquier, I. Herrmann et al., "Health status of childhood leukemia survivors who received hematopoietic

cell transplantation after BU or TBI: an LEA study," *Bone Marrow Transplantation*, vol. 49, no. 5, pp. 709–716, 2014.

[14] A. Salhotra, S. Hui, D. Yang et al., "Long-term outcomes of patients with acute myelogenous leukemia treated with myeloablative fractionated total body irradiation TBI-based conditioning with a tacrolimus- and sirolimus-based graft-versus-host disease prophylaxis regimen: 6-year follow-up from a single center," *Biology of Blood and Marrow Transplantation*, vol. 26, no. 2, pp. 292–299, 2020.

[15] M. Kalaycio, B. Bolwell, L. Rybicki et al., "BU- vs TBI-based conditioning for adult patients with ALL," *Bone Marrow Transplantation*, vol. 46, no. 11, pp. 1413–1417, 2011.

[16] E. A. Copelan, B. K. Hamilton, B. Avalos et al., "Better leukemia-free and overall survival in AML in first remission following cyclophosphamide in combination with busulfan compared with TBI," *Blood*, vol. 122, no. 24, pp. 3863–3870, 2013.

[17] F. Bernard, P. Bordigoni, M.-C. Simeoni et al., "Height growth during adolescence and final height after haematopoietic SCT for childhood acute leukaemia: the impact of a conditioning regimen with BU or TBI," *Bone Marrow Transplantation*, vol. 43, no. 8, pp. 637–642, 2009.

[18] G. M. T. Guilcher, R. Moorjani, T. H. Truong, and V. A. Lewis, "Myeloablative BU, fludarabine, antithymocyte globulin and low-dose TBI in the treatment of juvenile myelomonocytic leukaemia with allogeneic haematopoietic cell transplantation," *Bone Marrow Transplantation*, vol. 50, no. 3, pp. 455-456, 2015.

[19] B. Scott, H. J. Deeg, B. Storer et al., "Targeted busulfan and cyclophosphamide as compared to busulfan and TBI as preparative regimens for transplantation in patients with advanced MDS or transformation to AML," *Leukemia and Lymphoma*, vol. 45, no. 12, pp. 2409–2418, 2004.

[20] E. De Berranger, A. Cousien, A. Petit et al., "Impact on long-term OS of conditioning regimen in allogeneic BMT for children with AML in first CR: TBI+CY versus BU+CY: a report from the Société Française de Greffe de Moelle et de Thérapie Cellulaire," *Bone Marrow Transplantation*, vol. 49, no. 3, pp. 382–388, 2014.

[21] C. Bredeson, J. LeRademacher, K. Kato et al., "Prospective cohort study comparing intravenous busulfan to total body irradiation in hematopoietic cell transplantation," *Blood*, vol. 122, no. 24, pp. 3871–3878, 2013.

[22] X. Cahu, M. Labopin, M. Labopin et al., "Impact of conditioning with TBI in adult patients with T-cell ALL who receive a myeloablative allogeneic stem cell transplantation: a report from the acute leukemia working party of EBMT," *Bone Marrow Transplantation*, vol. 51, no. 3, pp. 351–357, 2016.

[23] J. Dahlke, N. Kröger, T. Zabelina et al., "Comparable results in patients with acute lymphoblastic leukemia after related and unrelated stem cell transplantation," *Bone Marrow Transplantation*, vol. 37, no. 2, pp. 155–163, 2006.

[24] A. Bonini, G. Bandini, G. Rosti et al., "Big BU/CY is associated with a favorable long-term outcome in patients allo-transplanted for chronic myelogenous leukemia in chronic phase," *Bone Marrow Transplantation*, vol. 21, no. 11, pp. 1085–1089, 1998.

[25] E. Granados, R. de La Cámara, L. Madero et al., "Hematopoietic cell transplantation in acute lymphoblastic leukemia: better long term event-free survival with conditioning regimens containing total body irradiation," *Haematologica*, vol. 85, pp. 1060–1067, 2000.

[26] L. Marino, V. Lancellotta, P. Franco et al., "Loco-regional adjuvant radiation therapy in breast cancer patients with positive axillary lymph-nodes at diagnosis (CN2) undergoing preoperative chemotherapy and with complete pathological lymph-nodes response. Development of GRADE (Grades of recommendation, assessment, Development and Evaluation) recommendation by the Italian Association of radiation therapy and Clinical Oncology (AIRO)," *The Breast*, vol. 55, pp. 119–127, 2021.

[27] T. Lehrnbecher, D. Averbuch, E. Castagnola et al., "8th European Conference on Infections in Leukaemia. 8th European Conference on Infections in Leukaemia: 2020 guidelines for the use of antibiotics in paediatric patients with cancer or post-haematopoietic cell transplantation," *The Lancet Oncology,*vol. 22, pp. e270–e280, 2021.

[28] E. Al-Shaibani, S. Cyriac, S. Chen et al., "Comparison of the prognostic ability of the HCT-CI, the modified EBMT, and the EBMT-ADT pre-transplant risk scores for acute leukemia," *Clinical Lymphoma, Myeloma & Leukemia*, vol. 21, no. 6, pp. e559–e568, 2021.

[29] A. H. Groll, D. Pana, F. Lanternier et al., "8th European Conference on Infections in Leukaemia: 2020 guidelines for the diagnosis, prevention, and treatment of invasive fungal diseases in paediatric patients with cancer or post-haematopoietic cell transplantation," *The Lancet Oncology*, vol. 22, no. 6, pp. e254–e269, 2021.

[30] J. Burgos-Burgos, V. Vega, D. Macias-Verde et al., "Hypofractionated whole breast irradiation after IORT treatment is safe in patients receiving adjuvant chemotherapy," *Clinical and Translational Oncology*, vol. 23, no. 12, pp. 2579–2583, 2021.

[31] Y. Lu, J. Hua, F. Yan et al., "Combined radiotherapy and chemotherapy versus radiotherapy alone in elderly patients with nasopharyngeal carcinoma," *Medicine*, vol. 100, no. 29, Article ID e26629, 2021.

[32] Z. A. Yegin, F. Can, S. Gökçen et al., "The impact of pre-transplant cell-free DNA levels on leukemia relapse and transplant-related complications in allogeneic hematopoietic stem cell transplant recipients," *Balkan Medical Journal*, vol. 37, no. 3, pp. 138–143, 2020.

[33] V. T. Ho, A. S. Martin, W. S. Pérez et al., "Prior gemtuzumab ozogamicin exposure in adults with acute myeloid leukemia does not increase hepatic veno-occlusive disease risk after allogeneic hematopoietic cell transplantation: a center for international Blood and marrow transplant research analysis," *Biology of Blood and Marrow Transplantation*, vol. 26, no. 5, pp. 884–892, 2020.

[34] R. El Fakih, B. Savani, M. Mohty, and M. Aljurf, "Hematopoietic cell transplant consideration for philadelphia chromosome-like acute lymphoblastic leukemia patients," *Biology of Blood and Marrow Transplantation*, vol. 26, no. 1, pp. e16–e20, 2020.

[35] R. Elsharawi, E. Antonucci, A. Sukari, and J. D. Cramer, "Quality metrics for head and neck cancer treated with definitive radiotherapy and/or chemotherapy," *Head & Neck*, vol. 43, no. 6, pp. 1788–1796, 2021.

[36] J. Loke, R. Buka, and C. Craddock, "Allogeneic stem cell transplantation for acute myeloid leukemia: who, when, and how?" *Frontiers in Immunology*, vol. 12, Article ID 659595, 2021.

[37] M. Q. Salas, S. Prem, E. G. Atenafu et al., "Reduced intensity allogeneic stem cell transplant with anti-thymocyte globulin and post-transplant cyclophosphamide in acute myeloid leukemia," *European Journal of Haematology*, vol. 103, no. 5, pp. 510–518, 2019.

Hindawi
Journal of Healthcare Engineering
Volume 2023, Article ID 9894304, 1 page
https://doi.org/10.1155/2023/9894304

Retraction

Retracted: Regulatory Mechanism of circEIF4G2 Targeting miR-26a in Acute Myocardial Infarction

Journal of Healthcare Engineering

Received 26 September 2023; Accepted 26 September 2023; Published 27 September 2023

This article has been retracted by Hindawi following an investigation undertaken by the publisher [1]. This investigation has uncovered evidence of one or more of the following indicators of systematic manipulation of the publication process:

(1) Discrepancies in scope
(2) Discrepancies in the description of the research reported
(3) Discrepancies between the availability of data and the research described
(4) Inappropriate citations
(5) Incoherent, meaningless and/or irrelevant content included in the article
(6) Peer-review manipulation

The presence of these indicators undermines our confidence in the integrity of the article's content and we cannot, therefore, vouch for its reliability. Please note that this notice is intended solely to alert readers that the content of this article is unreliable. We have not investigated whether authors were aware of or involved in the systematic manipulation of the publication process.

Wiley and Hindawi regrets that the usual quality checks did not identify these issues before publication and have since put additional measures in place to safeguard research integrity.

We wish to credit our own Research Integrity and Research Publishing teams and anonymous and named external researchers and research integrity experts for contributing to this investigation.

The corresponding author, as the representative of all authors, has been given the opportunity to register their agreement or disagreement to this retraction. We have kept a record of any response received.

References

[1] Z. Zhang, J. Li, C. Long et al., "Regulatory Mechanism of circEIF4G2 Targeting miR-26a in Acute Myocardial Infarction," *Journal of Healthcare Engineering*, vol. 2022, Article ID 5308372, 10 pages, 2022.

Hindawi
Journal of Healthcare Engineering
Volume 2022, Article ID 5308372, 10 pages
https://doi.org/10.1155/2022/5308372

Hindawi

Research Article

Regulatory Mechanism of circEIF4G2 Targeting miR-26a in Acute Myocardial Infarction

Zaiyong Zhang [1,2] Jianhao Li,[1,2] Cheng Long,[3,4] Yuanyuan Han,[5] Jun Fan,[1,2] Afzal Misrani,[3] and Xiangyu Ji[4]

[1]*Department of Cardiology, Panyu Central Hospital, Guangzhou 511400, China*
[2]*Cardiovascular Institute of Panyu District, Guangzhou 511400, China*
[3]*South China Normal University-Panyu Central Hospital Joint Laboratory of Translational Medical Research, Panyu Central Hospital, Guangzhou 511400, China*
[4]*School of Life Sciences, South China Normal University, Guangzhou 510630, China*
[5]*Department of Radiology, Panyu Central Hospital, Guangzhou 511400, China*

Correspondence should be addressed to Zaiyong Zhang; zaiyong@sina.cn

Received 26 January 2022; Accepted 17 February 2022; Published 16 March 2022

Academic Editor: Liaqat Ali

Background. Acute myocardial infarction (AMI) involves a series of complex cellular and molecular events, including circular RNAs (circRNAs), microRNAs (miRNAs) and other noncoding RNAs. *Objective*. In this study, the regulation mechanism of circEIF4G2 acting on miR-26a on HUVECs (Human Umbilical Vein Endothelial Cells) proliferation, cell cycle and angiogenesis ability was mainly explored in the vascular endothelial growth factor induced (VEGF-induced) angiogenesis model. *Methods*. VEGF induced HUVECs angiogenesis model was constructed, and the expression of circEIF4G2 and miR-26a in VEGF model was detected by qRT-PCR. When circEIF4G2 and miR-26a were knocked down or overexpressed in HUVECs, qRT-PCR was used to detect the expression of circEIF4G2 and miR-26a, CCK-8 was used to detect cell proliferation, flow cytometry was used to detect the cell cycle transition of HUVECs, and cell formation experiment was used to detect the ability of angiogenesis. MiRanda database and Targetscan predicted the binding site of circEIF4G2 and miR-26a, lucifase reporting assay and RNA pull down assay verified the interaction between circEIF4G2 and miR-26a. *Results*. After HUVECs were treated with VEGF, circEIF4G2 was significantly upregulated. After circEIF4G2 was knocked down, the proliferation and angiogenesis of HUVECs cells were decreased, and the process of cell cycle G0/G1 phase was blocked. The overexpression of miR-26a reduced the proliferation and angiogenesis of HUVECs cells and blocked the cell cycle progression of G0/G1 phase. Double lucifase reporter gene assay verified that circEIF4G2 could directly interact with miR-26a through the binding site, and RNA Pull down assay further verified the interaction between circEIF4G2 and miR-26a. When circEIF4G2 and miR-26a were knocked down simultaneously in HUVECs, it was found that knocking down miR-26a could reverse the inhibition of circEIF4G2 on cell proliferation, cycle and angiogenesis. *Conclusion*. In the VEGF model, circEIF4G2 was highly expressed and miR-26a was low expressed. MiR-26a regulates HUVECs proliferation, cycle and angiogenesis by targeting circEIF4G2.

1. Introduction

Acute myocardial infarction (AMI) is a common cardiovascular disease. How to maximize the benefits of patients is the direction that needs to be explored and studied in the field of AMI diagnosis and treatment [1–3]. AMI involves a series of complex cellular and molecular events, and various molecules in cells coordinate with each other to respond to AMI. Studies have shown that noncoding RNAs (ncRNAs) such as circRNA, miRNA and long noncoding RNA (lncRNA) can play a key role in the occurrence and progression of heart disease [4, 5]. Noncoding RNAs usually regulate protein gene expression through competing endogenous RNAs (ceRNAs) and affect disease progression [6].

CircRNA is a novel type of RNA whose unique structure is generated by a $3'$–$5'$ end joining event (reverse splicing).

Once circular RNA is produced, it may remain in the nucleus as observed with intron-retaining multiexon rings, and most of it will be exported to the cytoplasm. Regardless of location, the unique structure of circRNAs ensures that the molecule is protected from exonuclear dissolution decay and thus remains very stable [7]. Apoptosis of AMI cells involves a variety of apoptosis signals, including cytokines, hypoxia, increased oxidative stress and DNA damage, and circrNa-miRNA-mRNA axis is no exception [8]. Li et al. [9] suggested that circNCX1 gene transcribed from sodium/calcium exchanger 1 (ncx1) plays a key role in the regulation of cardiomyocyte apoptosis by regulating miR-133a-3p and its target cell death inducing protein CDIP1. Liu et al. [10] suggested that after circZNF609 was knocked out, endothelial cell migration level was increased and resistance to oxidative stress was enhanced, while overexpressed circZNF609 showed the opposite effect. CircZNF609 inhibited the activity of miR-133a-3p and increased the expression level of MEF2A, which could inhibit the effect of circZNF609 silencing on endothelial cells. Myocardial cell proliferation and neovascularization are two major biological processes of AMI cardiac repair. The synergistic effect between the two is essential for cardiac regeneration and repair, and circRNA is also involved [11].

MiRNA is a large class of small noncoding RNA molecules that can be widely recognized early [12, 13]. The vast majority of these molecules originate from noncoding genes with a length of about 22nt, and were thought to be functionally antisense modulators of other RNAs in the early stage [14]. MiRNA genes are often expressed singly, but many occur in clusters of 2–7 genes with small intervention sequences. Experimental results suggest that these genes exhibit simultaneous transcription, suggesting that they may be controlled by common upstream gene sequences [15, 16]. Other miRNA genes were excised from introns of protein-coding genes [17, 18] and exons of noncoding genes [19], or even from 3′-UTR of protein-coding genes [20]. In mammalian genomes, miRNAs may also be found in repetitive regions. However, translocation factors may be involved in the generation of new miRNAS [21]. MiRNA can inhibit the mRNA translation of target genes on the basis of certain base pairing, thus participating in the regulation of target protein expression. In recent years, a number of studies have shown that some miRNAs protect the heart by going up or down by altering key signaling elements. These effects play a protective role through miRNAs and/or antagonists in ischemic preconditioning, regulation of heat shock proteins, antihypoxia and pharmacological preconditioning [22].

In this study, the molecular regulatory mechanism of AMI related circRNA was studied, providing a new theoretical basis for the molecular mechanism of myocardial infarction, and thus providing a new intervention strategy for the treatment of myocardial infarction.

2. Materials and Methods

2.1. Abbreviation and Full Title. All abbreviations and full titles are shown in Table 1.

Table 1: Abbreviation and full title.

Abbreviation	Full title
AMI	Acute myocardial infarction
circRNAs	Circular RNAs
miRNAs	MicroRNAs
HUVECs	Human umbilical vein endothelial cells
VEGF	Vascular endothelial growth factor
ncRNAs	Noncoding RNAs
lncRNA	Long noncoding RNA
ceRNAs	Competing endogenous RNAs
FBS	Foetal bovine serum

2.2. Establishment of VEGF-Induced HUVECs Angiogenesis Model. HUVECs were cultured with DMEM medium containing 10% FBS. HUVECs were treated with VEGF to promote angiogenesis, and VEGF induced angiogenesis model of HUVECs were established.

2.3. Transfection. SiRNA for circEIF4G2, mimics and siRNA for miR-26a and NC were purchased from Shanghai Jikai gene Chemical Technology Co., Ltd. Transfection was performed according to the instructions of Lipofectamine 2000 Reagent (Shanghai Qifa Experimental Reagent Co., Ltd.). The detailed operations were as follows. 24 well cell culture plate was prepared and cells were cultured in DMEM medium with 10% FBS. The corresponding inoculation density was controlled as 2×10^4 per well for one day. It was observed that when the cells were fully fused, the culture medium was removed and fully rinsed with the phosphate buffer. Then, 0.3 mL OPTI-MEM was added into each well, and the culture was transferred to standard conditions for full cultivation. 1 μL lipofectamine 2000 reagent was diluted by the above medium and diluted 50 times to get 50 μL. The reagent was placed at room temperature for 10 minutes. 1 μL of 20 μM miRNA mimics, inhibitors, and 0.5 μg plasmid were added to OPTI-MEM medium, and put it at room temperature for 5 minutes. Concentrations of miRNA mimics and inhibitors were eventually adjusted to 50 nM. They were mixed with lipofectamine 2000 reagent which diluted 50 times and put at room temperature for 20 minutes. 0.1 mL of transfection mixture was added into each well. After proper mixing, it was cultured under standard environmental conditions for 5 hours. Finally, the transfection reagent was moved away and DMEM medium with fresh 10% FBS was added.

2.4. qRT-PCR. Total RNA was extracted from HUVECs, and the RNA was reversely transcribed into cDNA using reverse transcriptase (Thermo, USA), which was used as a template for PCR amplification. According to the design principle of real-time quantitative PCR primers, circRNA sequences were downloaded from circBase database and PCR primers designed for hSA_CIRC_0021245 (circEIF4G2) reverse splices were as follows:

circEIF4G2:

F:CAAGTCATGTTCATGCCCTGA, R:TCCATGTCATAGAAGTGCACA

EIF4G2:

F:CCACAAGTGACAACTTCATGC, R: TCTGAAATGCTCACCAGCTCT

β-Actin:

F:CATGTACGTTGCTATCCAGGC, R: CTCCTTAATGTCACGCACGAT

2.5. CCK-8. HUVECs, which were transfected for 48 hours were inoculated in a 96-well culture plate with 1.5 × 103 cells/mL, 100 μL per well. The 96-well plates were placed in an incubator for 1, 2, 3, 4, and 5 days, respectively (the blank control group was medium without cells). 10 μL CCK-8 reagent (APExBIO, USA) was added to each well and cultured in an incubator for 4 hours. At the absorption wavelength of 450 nm, the absorbance value of each well was recorded with a microplate reader, and the growth curve of cells was plotted.

2.6. Flow Cytometry. Transfected HUVECs for 48 hours after digested with trypsin, terminated digestion and centrifuged. The cells were washed with phosphate buffer twice, centrifuged at 1000 rpm for 5 minutes, and collected. Suspended cells by adding 500 μL binding buffer (Shanghai QianChen Biotechnology Co., Ltd.). Annexinv-fitc (Shanghai Qianchen Biotechnology Co., Ltd.) was added to 500 μL cell suspension, mixed and incubated for 15 minutes. 5 μL Propidium Iodide dye (Shanghai Qianchen Biological Co., Ltd.) was added to cell suspension, mixed well, and incubated for 15 minutes under dark conditions. The fluorescence intensity was determined by flow cytometry.

2.7. Tube Formation Assay. Matrigel glue was put on ice to melt, and the gun head and 96-well plate were put at −20°C refrigerator to precool. The precooled gun heads were used to take Matrigel glue 100 μL/well and added it to the precooled 96 well plate. Pay attention to avoid the formation of bubbles. Place it on ice for 5 minutes to make the Matrigel level, and then put the plate into 37°C cell incubator for 30 minutes to solidify the gel. The 100 μL HUVECs (1.5 × 104 cells/well) were added to the well containing Matrigel gel. At the same time, the tested compounds diluted into different concentrations with M199 medium and DMSO control were added and cultured at 37°C for 8 hours. Observed and photographed under a microscope. Five fields were randomly selected to take photos and image Pro Plus software was used to calculate the length of cavity formation.

2.8. Double Luciferase Reporting Experiment. The luciferase reaction reagent (5 mL + 1 vial) were dissolved, repacked and stored it under dark conditions. Mix as required to obtain luciferase reaction reagent II, and then stored it in dark after subpackaging. Lysis buffer and double distilled water were mixed for treatment. After transfecting for 48 hours, the culture medium was absorbed and discarded, and the cells were fully rinsed with phosphate buffer. Then, the cells were placed in the wells of cell lysis buffer at room temperature for 10 minutes. After full pyrolysis, took the pyrolysis solution and added it into the sterilized centrifuge tube. Then centrifuged at high speed at 4°C for 10 minutes, and took the supernatant for determination. Turn on the fluorometer according to relevant operating specifications, with an interval of 2 seconds and test for 10 seconds. Taking out the preserved reaction reagent and balanced it at room temperature. Then took out 20 μL of sample, added 100 μL of luciferase reaction reagent (Hanheng Bioengineering (Shanghai) Co., Ltd.), and detected RLU after appropriate mixing. The control test group was reporter gene cell lysate. Taking an appropriate amount of luciferase reaction reagent II and balanced it to room temperature. After the above tests were completed, then added 0.1 mL of luciferase II into each tube, and detected RLU after sufficient mixing. Set luciferase as the internal parameter, divided its RLU value by the RLU value determined by detection, and reflected the activation degree of the target gene based on the obtained results.

2.9. RNA Pull down. Biotin labeled wt-miR-26a and mut-miR-26a RNA fragments were synthesized and transfected into HUVECs using Lipofectamine 2000 (Thermo Fisher Scientific (Shanghai) Co., Ltd.), respectively. After 48 hours of transfection, the 100 μL RIP solution which containing protease inhibitor (Roche) and RNase inhibitor (Promega) were added for cracking according to Magna RIP Kit (Millipore). Cell lysates were collected and incubated with RNase-free BSA and TRNA-coated streptavidin agarose beads, and ice bath for 2 hours. It was centrifuged and washed with buffer. Then according to the kit instructions, RNA was extracted using TRIzol Regent (Invitrogen), and circEIF4G2 was detected by qRT-PCR. The antagonist miR-26a probe was set as a negative control.

2.10. Statistical Analysis. Statistical analysis was performed by using the GraphPad Prism 8.0 software. The *t*-test was used between the two groups, ANOVA between multiple groups, and $P < 0.05$ was statistically significant. Repeat three times for each set.

3. Results

3.1. Expression of circEIF4G2 in the Angiogenesis Model of HUVECs. We have known the expression of circEIF4G2 and miR-26a in peripheral blood of patients with myocardial infarction through previous studies, but their regulatory mechanism in myocardial infarction is still unclear. In order to investigate the role of circEIF4G2 in promoting angiogenesis, HUVECs were treated with corresponding VEGF, and the expression of circEIF4G2 was detected by amplification method. It was found that circEIF4G2 was upregulated by 7.54 ± 0.53 in VEGF treatment group, which was significantly different from that in control group (Figure 1(a)). Compared with the control group, the expression of miR-26a in VEGF treatment group was down regulated (Figure 1(b)). These results suggest that circEIF4G2 may be regulated by angiogenic factor VEGF.

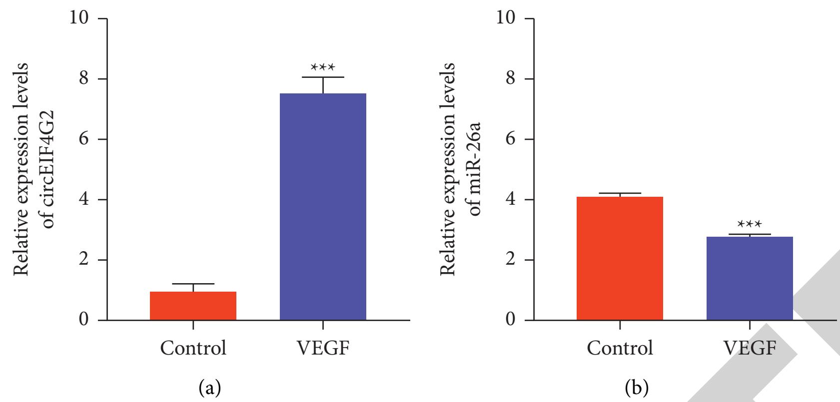

Figure 1: CircEIF4G2 was upregulated and miR-26a was downregulated. (a) The expression levels of circEIF4G2. (b) The expression levels of miR-26a. $^{***}P < 0.001$ vs. control group.

3.2. Effects of Knockdown of circEIF4G2 on Proliferation, Cell Cycle, and Angiogenesis of HUVECs. After knockdown circEIF4G2 with siRNA, the proliferation ability of HUVECs was detected by CCK-8. The proliferation ability of the interference group decreased significantly from day 3 (Figure 2(a)). Flow cytometry was used to detect the cell cycle process of HUVECs after circEIF4G2 knockdown. The results showed that the G1/G0 phase was blocked after knockdown of circEIF4G2 (48% and 66%, respectively) (Figure 2(b)). The results of angiogenesis experiment showed that knockdown of circEIF4G2 significantly inhibited the angiogenesis of HUVECs, and the complete vascular network structure could not be obtained (Figure 2(c)). These results suggest that knockdown of circEIF4G2 inhibits the proliferation, cycle progression and angiogenesis of HUVECs.

3.3. Effects of Overexpression or Knockdown of miR-26a on Proliferation, Cycle, and Angiogenesis of HUVECs. After miR-26a was overexpressed or knocked down, the expression rates of miR-26a and circEIF4G2 were detected by qRT-PCR. When miR-26a was overexpressed in HUVECs, compared with the control group, the expression of miR-26a was upregulated (Figure 3(a)), while the expression of circEIF4G2 was downregulated (Figure 3(b)). When miR-26a was knocked down in HUVECs, compared with the control group, the expression of miR-26a was downregulated (Figure 3(c)), while the expression of circEIF4G2 was upregulated (Figure 3(d)). After miR-26a was overexpressed by transfecting miR-26a mimics into HUVECs, the proliferation ability, cell cycle progression and angiogenesis ability of HUVECs were detected. Compared with the control group, its proliferation ability was reduced (Figure 3(e)). The cell cycle was also arrested in G1/G0 phase (47% and 80%, respectively) (Figure 3(f)). The results of angiogenesis experiment showed that overexpression of miR-26a significantly inhibited the angiogenesis ability of HUVECs, and the complete vascular network structure could not be obtained (Figure 3(g)). This suggests that overexpression of miR-26a also inhibits HUVECs proliferation, cycle progression and angiogenesis.

3.4. circEIF4G2 Interacts with miR-26a. MiRanda database and Targetscan were used to predict the binding sites of circEIF4G2 and miR-26a, and the results showed that circEIF4G2 had binding sites with miR-26a (Figure 4(a)). The direct interaction between circEIF4G2 and miR-26a was verified by dual lucifase reporter gene and RNA-pull down (RIP) assay. The results showed that when wild-type circEIF4G2 was cotransfected with miR-26a mimics, the fluorescence value of lucifase reporter gene was decreased. After the combination of circEIF4G2 mutant with miR-26a, the fluorescence value increased, and there was no difference between the two groups (Figure 4(b)). The results indicated that circEIF4G2 could directly interact with miR-26a through binding sites. To further verify the interaction between circEIF4G2 and miR-26a, HUVECs cells were transfected with biotin marking the wild type 3′ end and mutant 3′ end of miR-26a mimics. RNA molecules bound to biotin-labeled miR-26a were captured by magnetic beads coated with streptomycin, and the abundance of circEIF4G2 was detected by qPCR. The results showed that circEIF4G2 molecules were significantly enriched in IP group compared with the control group (Figure 4(c)). These results indicated that circEIF4G2 had direct interaction with miR-26a.

3.5. miR-26a Is an Important Component that Mediates circEIF4G2 to Promote HUVECs Proliferation, Cell Cycle, and Angiogenesis. The plasmid with knockdown miR-26a and knockdown circEIF4G2 were cotransfected into HUVECs. The experimental groups were NC plasmid group, si circEIF4G2 plasmid group and si miR-26a + si circEIF4G2 plasmid group. The proliferation ability of the si circEIF4G2 plasmid group and the si miR-26a + si circEIF4G2 plasmid group were significantly reduced compared with the control group. Moreover, the cell proliferation ability of the si circEIF4G2 plasmid group was weaker than that of the si miR-26a + si circEIF4G2 plasmid group (Figure 5(a)). Compared with the control group, the cell cycle of the si circEIF4G2 plasmid group and the si miR-26a + si circEIF4G2 plasmid group were arrested in G1/G0 phase. Moreover, more cells were blocked in G1/G0 phase in the si circEIF4G2 plasmid group than in the si miR-26a + si

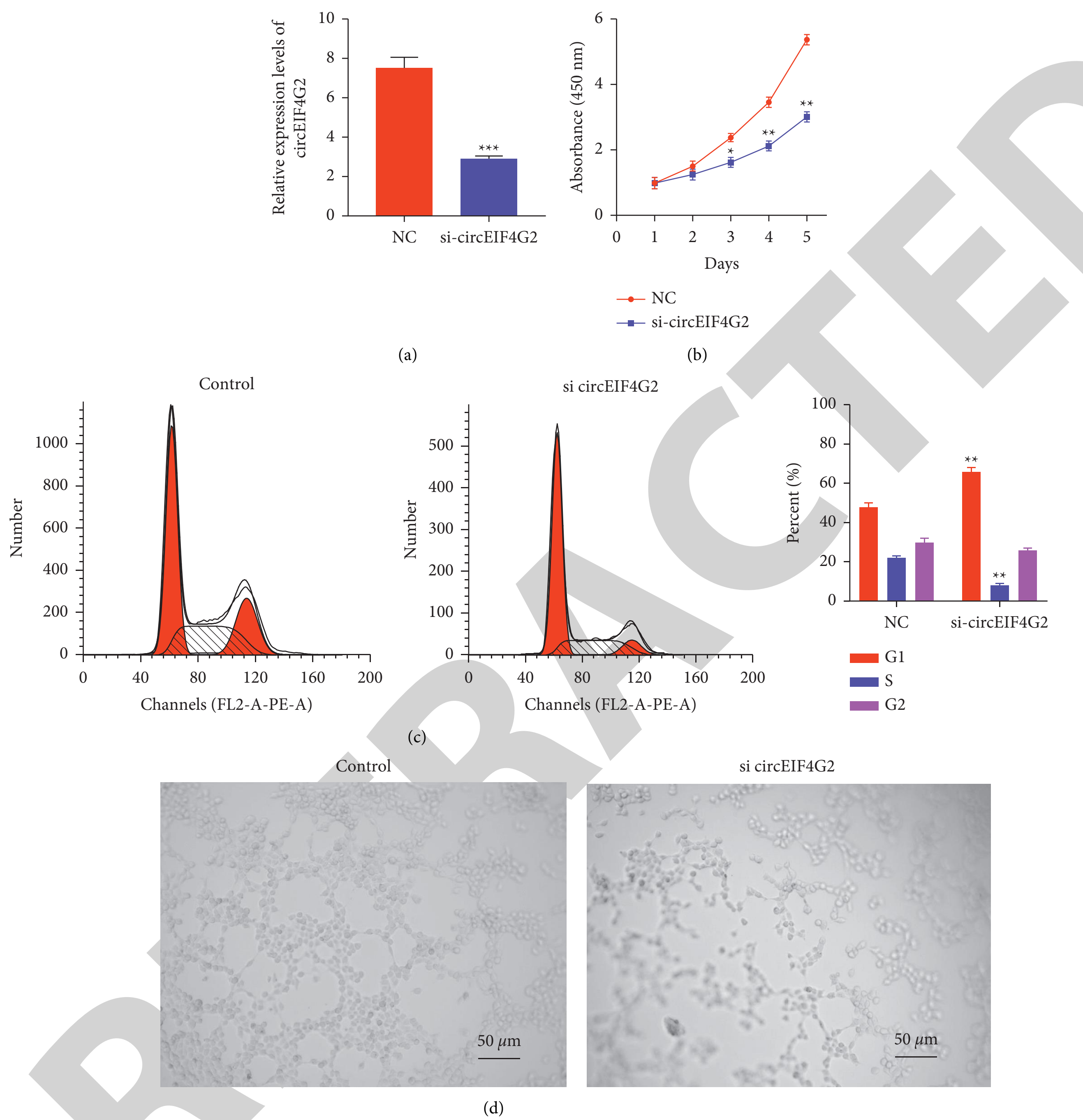

Figure 2: Downregulation of circEIF4G2 inhibited HUVECs proliferation, blocked cell cycle and inhibited angiogenesis. (a) The expression levels of circEIF4G2 were detected by qRT-PCR after knockdown of circEIF4G2. (b) CCK-8 was used to detect cell proliferation after knockdown of circEIF4G2. (c) Cell cycle transformation was detected by flow cytometry after knockdown of circEIF4G2. (d) Detection of angiogenesis by cell formation assay after knockdown of circEIF4G2. $^{**}P < 0.01$ and $^{***}P < 0.001$ vs. control group.

circEIF4G2 plasmid group (Figure 5(b)). In the angiogenesis experiment, compared with the control group, the si circEIF4G2 plasmid group and the si miR-26a + si circEIF4G2 plasmid group could not obtain the complete vascular network structure. However, the ability of promoting angiogenesis in the si miR-26a + si circEIF4G2 plasmid group was stronger than that in the si circEIF4G2 plasmid group (Figure 5(c)). The above results suggest that miR-26a knockdown can partially reverse the inhibitory effects of circEIF4G2 knockdown on the proliferation, cell cycle and angiopoiesis of HUVECs. It is suggested that miR-26a is an important component that mediates circEIF4G2 to promote HUVECs proliferation, cell cycle and angiogenesis.

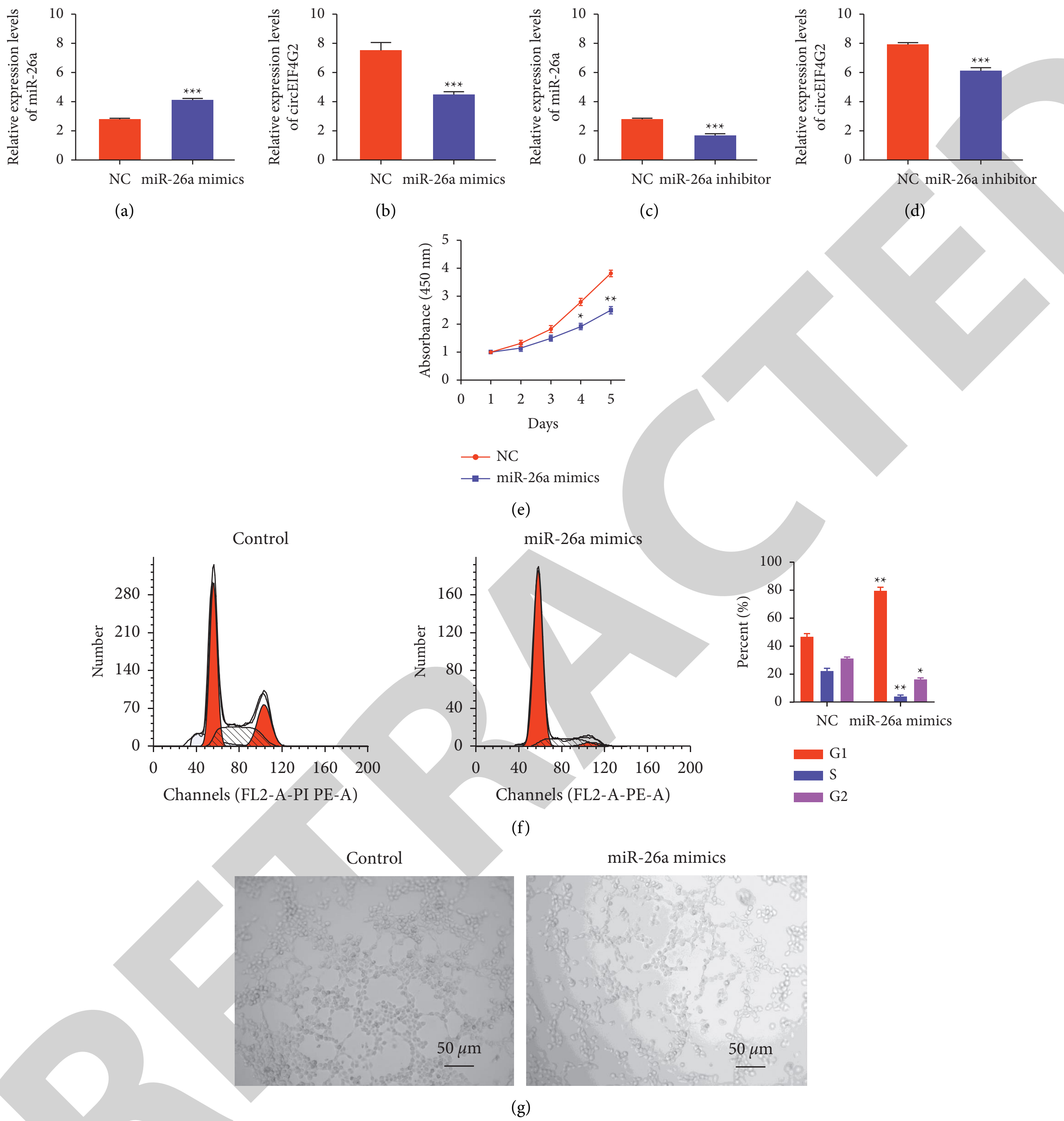

Figure 3: Overexpression of miR-26a inhibited HUVECs proliferation, blocked cell cycle, and inhibited angiogenesis. (a, b) The expression levels of miR-26a and circEIF4G2 were detected by qRT-PCR after overexpressing miR-26a. (c, d) The expression levels of miR-26a and circEIF4G2 were detected by qRT-PCR after knockdown of miR-26a. (e) The proliferation ability of HUVECs were detected by CCK-8 after overexpression of miR-26a. (f) The cell cycle progression of HUVECs was detected by flow cytometry after overexpression of miR-26a. (g) Angiogenesis of HUVECs was detected by cell formation assay after overexpression of miR-26a. $^{**}P < 0.01$ and $^{***}P < 0.001$ vs. NC group.

4. Discussion

Acute myocardial infarction is a common heart disease. In the process of treatment, the myocardial blood supply in the ischemic area should be restored as soon as possible, which is of great significance to improve the prognosis [23, 24]. The proliferation and neovascularization of myocardial cell are two major biological processes of AMI cardiac repair. The synergistic effect between the two is essential for cardiac regeneration and repair, and circRNA is also involved [11]. Regulating circRNA expression may be a potential strategy to promote cardiac function and remodeling after myocardial infarction.

Angiogenesis is a complex process of producing new capillaries. The regulation of angiogenesis includes

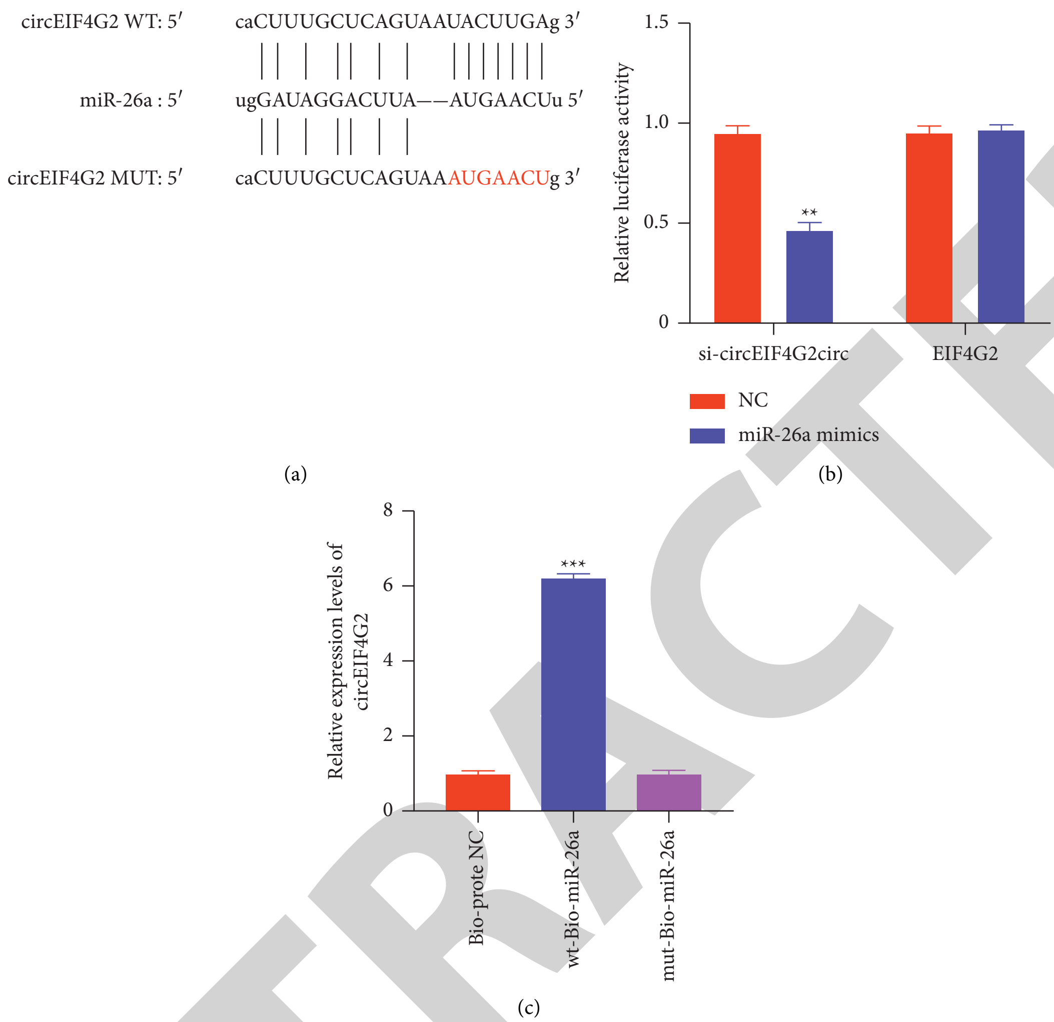

Figure 4: CircEIF4G2 can bind to miR-26a directly. (a) MiRanda database and Targetscan predicted the binding sites of circEIF4G2 and miR-26a. (b) Lucifease reporter gene assay verified that circEIF4G2 could directly target miR-26a. (c) Detection of interaction between circEIF4G2 and miR-26a by RNA pulldown assay. $^{**}P < 0.01$ and $^{***}P < 0.001$ vs. NC group.

endothelial cells' proliferation, migration, basement membrane rupture and relates growth factors, such as VEGF and FGF-2 [25–27]. Inhibiting the proliferation of this type of cells can improve the antiangiogenic activity. AMI caused severe damage to the coronary microcirculation, resulting in the collapse of blood vessels and thinning of capillaries in the infarct area. Tissue repair after MI involves a powerful angiogenic response that begins at the infarct boundary and extends to the necrotic infarct core. Advances in several areas have provided novel mechanologic understanding of postinfarction angiogenesis and how it may be targeted to improve cardiac function after MI. Currently, it is generally accepted that angiogenesis is derived from tissue-derived signaling pathways, among which VEGF pathway is the most important [28, 29]. This factor is a glycoprotein that play an important role in promoting angiogenesis by promoting endothelial cell growth. VEGF-b, VEGF-c, and VEGF-d are the main members of the VEGF family. VEGF-c and VEGF-d are mainly involved in the regulation of lymphangiogenesis. VEGF downstream signaling pathways include JAK2, PLCγ1, etc., which can regulate the proliferation of vascular endothelial cells based on these pathways. In addition, Src and FAK signaling pathways can promote their migration, while JAK2 and Akt pathways are closely related to their apoptosis. According to Garikipati's analysis [30], overexpression of circFndc3b in cardiac endothelial cells could increase the expression of VEGF-A, enhance the angiogenesis activity, and reduced apoptosis of cardiomyocytes and endothelial cells. After myocardial infarction, adeno-associated virus-9 mediated myocardial overexpression of circFndc3b reduced myocardial apoptosis, enhances neovascularization and improved left ventricular function. CircFndc3b interacts with fused RNA-binding proteins in sarcomas to regulate VEGF expression and signal transduction. Therefore, understanding the mechanisms underlying the improvement of infarct angiogenesis may yield multiple therapeutic opportunities. During preclinical development, possible angiogenesis promotion strategies will be tested to provide mechanistic insights into treatment options for myocardial infarction patients.

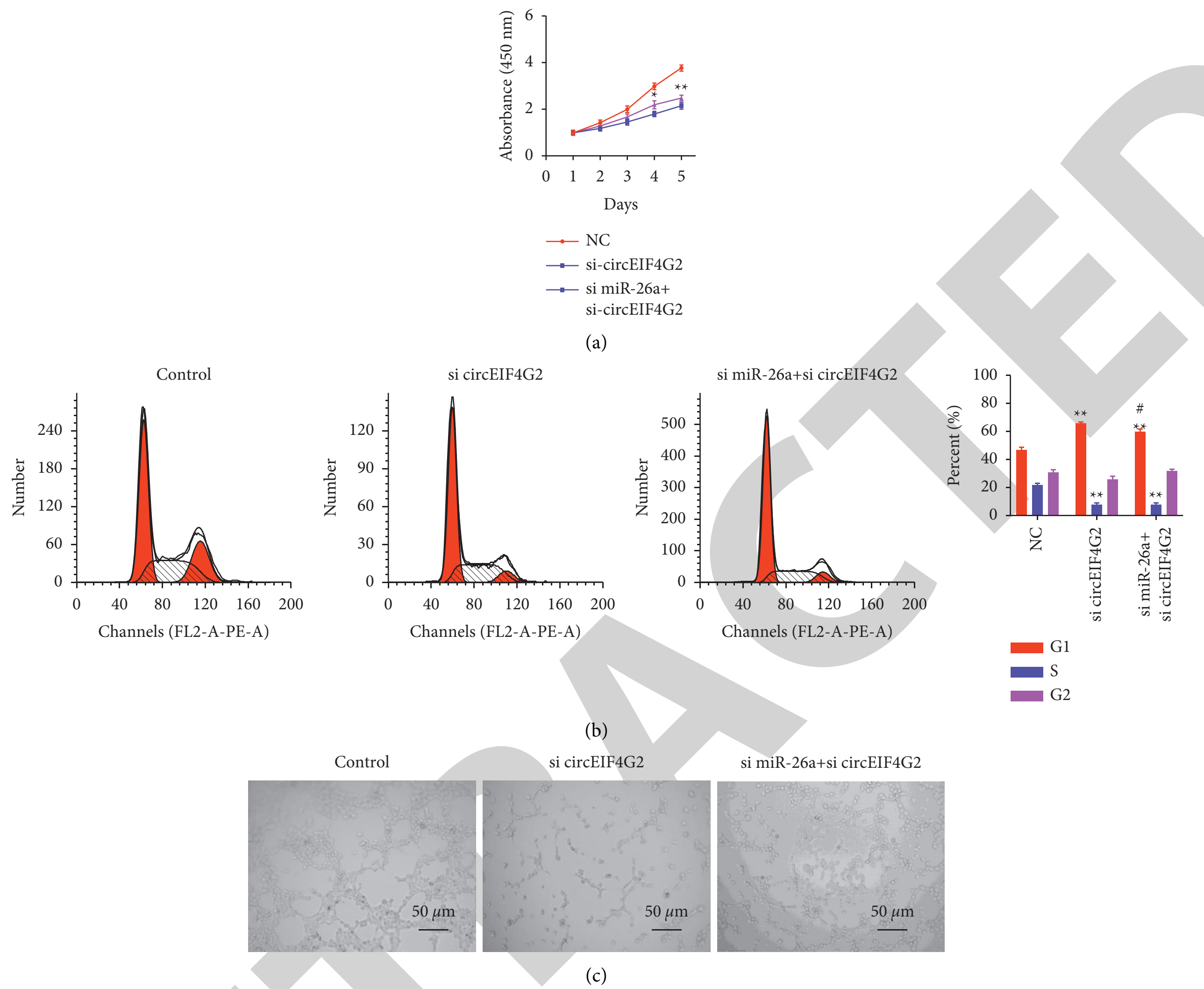

Figure 5: Downregulation of miR-26a partially reversed the inhibition of circEIF4G2 downregulation on proliferation, cell cycle and angiogenesis of HUVECs. (a) The proliferation ability of cells was detected by CCK-8. (b) The cycle progression of HUVECs were detected by flow cytometry. (c) The angiogenesis was detected by cell formation assay. $^{*}P < 0.05$ and $^{**}P < 0.01$ vs. control group. $^{\#}P < 0.05$ vs. si circEIF4G2 group.

In our study, HUVECs were treated with VEGF to establish the angiogenesis promoting model, and the effect of circRNA on angiogenesis of vascular endothelial cells was discussed. qPCR showed that the expression level of circEIF4G2 was significantly upregulated after VEGF induction. After siRNA knockdown circEIF4G2, CCK-8 detected the proliferation of HUVECs. It was found that down regulating circEIF4G2 could block the proliferation of HUVECs stimulated by VEGF. The detection of cell cycle suggests that interference with circEIF4G2 may lead to the weakening of cell proliferation and angiogenesis by blocking the process of G0/G1 phase in the metaphase of HUVECs. In the cell model, miR-26a mimics were transfected into HUVECs, and overexpression of miR-26a obtained a similar functional phenotype. This negative correlation between circEIF4G2 and miR-26a in expression level and functional phenotype. Next, the results of double luciferase reporter gene experiment and RNA pull down experiment showed that there was a direct interaction between circEIF4G2 and miR-26a. SiRNA targeting miR-26a was co-infected with circEIF4G2 interfering cells. It was found that knockdown of miR-26a could partially reverse the inhibitory effects of knockdown of circEIF4G2 on the proliferation, cycle and angiogenesis of HUVECs.

This article has its limitations. Firstly, we constructed a VEGF-induced angiogenesis model, and verified the regulatory effect of circEIF4G2 and miR-26a on the VEGF-induced model and the interaction between circEIF4G2 and miR-26a. However, the signal pathway of its action has not been studied. We will continue to improve it in future studies.

5. Conclusion

After HUVECs were treated with the VEGF, the expression of circEIF4G2 was significantly upregulated and the expression of miR-26a was downregulated. miR-26a is an important component that mediates circEIF4G2 to promote HUVECs proliferation, cell cycle and angiogenesis. These results provide a new theoretical basis for the molecular mechanism of myocardial infarction and provide a new intervention strategy for the treatment of myocardial infarction.

Data Availability

The data used to support the findings of this study are included within the article.

Conflicts of Interest

The authors declare that they have no conflicts of interest.

Acknowledgments

This work was supported by the Natural Science Foundation of Guangdong Province General Project (no. 2020A1515010277), Guangzhou Science And Technology Planning Project (no. 202002030012), and Guangzhou Medical and Health Science and Technology General Guidance Project (no. 20201A011120);

References

[1] D. Mozaffarian, E. J. Benjamin, A. S. Go et al., "Heart disease and stroke statistics--2015 update: a report from the American Heart Association," *Circulation*, vol. 131, pp. e29–322, 2015.

[2] B. Ibanez, S. James, S. Agewall et al., "ESC Scientific Document Group. 2017 ESC Guidelines for the management of acute myocardial infarction in patients presenting with ST-segment elevation: The Task Force for the management of acute myocardial infarction in patients presenting with ST-segment elevation of the European Society of Cardiology (ESC)," *Eur Heart J*, vol. 39, no. 2, pp. 119–177, 2018.

[3] G. Tao, P. C. Kahr, Y. Morikawa et al., "Pitx2 promotes heart repair by activating the antioxidant response after cardiac injury," *Nature*, vol. 534, no. 7605, pp. 119–23, 2016.

[4] R. C. Lee, R. L. Feinbaum, and V. Ambros, "The C. elegans heterochronic gene lin-4 encodes small RNAs with antisense complementarity to lin-14," *Cell*, vol. 75, no. 5, pp. 843–854, 1993.

[5] R. C. Lee and V. Ambros, "An extensive class of small RNAs in Caenorhabditis elegans," *Science*, vol. 294, no. 5543, pp. 862–4, 2001.

[6] R. Fiore and G. Schratt, "MicroRNAs in synapse development: tiny molecules to remember," *Expert Opin Biol Ther*, vol. 7, no. 12, pp. 1823–31, 2007.

[7] S. Starke, I. Jost, O. Rossbach et al., "Exon circularization requires canonical splice signals," *Cell Reports*, vol. 10, no. 1, pp. 103–111, 2015.

[8] T. Kalogeris, C. P. Baines, M. Krenz, and R. J. Korthuis, "Cell biology of ischemia/reperfusion injury," *International Review of Cell and Molecular Biology*, vol. 298, pp. 229–317, 2012.

[9] M. Li, W. Ding, M. A. Tariq et al., "A circular transcript of ncx1 gene mediates ischemic myocardial injury by targeting miR-133a-3p," *Theranostics*, vol. 8, no. 21, pp. 5855–5869, 2018.

[10] C. Liu, M.-D. Yao, C.-P. Li et al., "Silencing of circular RNA-znf609 ameliorates vascular endothelial dysfunction," *Theranostics*, vol. 7, no. 11, pp. 2863–2877, 2017.

[11] Y. Wang, R. Zhao, C. Shen et al., "Exosomal CircHIPK3 released from hypoxia-induced cardiomyocytes regulates cardiac angiogenesis after myocardial infarction," *Oxidative Medicine and Cellular Longevity*, vol. 2020, p. 8418407, 2020.

[12] R. C. Lee and V. Ambros, "An extensive class of small RNAs in Caenorhabditis elegans," *Science*, vol. 294, no. 5543, pp. 862–864, 2001.

[13] R. Fiore and G. Schratt, "MicroRNAs in synapse development: tiny molecules to remember," *Expert Opinion on Biological Therapy*, vol. 7, no. 12, pp. 1823–1831, 2007.

[14] V. Ambros, "microRNAs," *Cell*, vol. 107, no. 7, pp. 823–826, 2001.

[15] Y. Lee, K. Jeon, J. T. Lee, S. Kim, and V. N. Kim, "MicroRNA maturation: stepwise processing and subcellular localization," *The EMBO Journal*, vol. 21, no. 17, pp. 4663–4670, 2002.

[16] S. Baskerville and D. P. Bartel, "Microarray profiling of microRNAs reveals frequent coexpression with neighboring miRNAs and host genes," *RNA*, vol. 11, no. 3, pp. 241–247, 2005.

[17] E. C. Lai, P. Tomancak, R. W. Williams, and G. M. Rubin, "Computational identification of Drosophila microRNA genes," *Genome Biology*, vol. 4, no. 7, p. R42, 2003.

[18] L. Sun, L. Zhi, S. Shakoor, K. Liao, and D. Wang, "microRNAs involved in the control of innate immunity in Candida infected Caenorhabditis elegans," *Scientific Reports*, vol. 6, no. 1, p. 36036, 2016.

[19] Y. Wang and P. Zhang, "Recent advances in the identification of the host factors involved in dengue virus replication," *Virologica Sinica*, vol. 32, no. 1, pp. 23–31, 2017.

[20] X. Cai, C. H. Hagedorn, and B. R. Cullen, "Human microRNAs are processed from capped, polyadenylated transcripts that can also function as mRNAs," *RNA*, vol. 10, no. 12, pp. 1957–1966, 2004.

[21] N. Smalheiser and V. Torvik, "Mammalian microRNAs derived from genomic repeats," *Trends in Genetics*, vol. 21, no. 6, pp. 322–326, 2005.

[22] R. C. Kukreja, C. Yin, and F. N. Salloum, "MicroRNAs: new players in cardiac injury and protection," *Molecular Pharmacology*, vol. 80, no. 4, pp. 558–564, 2011.

[23] U. Zeymer, "Hat der Patient einen Herzinfarkt?" *MMW - Fortschritte der Medizin*, vol. 161, no. 4, pp. 34–36, 2019.

[24] I. Cavallari and M. P. Bonaca, "Antiplatelet therapy for secondary prevention after acute myocardial infarction," *Interventional Cardiology Clinics*, vol. 6, no. 1, pp. 119–129, 2017.

[25] R. S. Apte, D. S. Chen, and N. Ferrara, "VEGF in signaling and disease: beyond discovery and development," *Cell*, vol. 176, no. 6, pp. 1248–1264, 2019.

[26] E. Ikpegbu, L. Basta, D. N. Clements et al., "FGF-2 promotes osteocyte differentiation through increased E11/podoplanin expression," *Journal of Cellular Physiology*, vol. 233, no. 7, pp. 5334–5347, 2018.

[27] J. Kinoda, M. Ishihara, S. Nakamura et al., "Protective effect of FGF-2 and low-molecular-weight heparin/protamine nanoparticles on radiation-induced healing-impaired wound repair in rats," *Journal of Radiation Research*, vol. 59, no. 1, pp. 27–34, 2018.

[28] C. S. Melincovici, A. B. Boşca, S. Şuşman et al., "Vascular endothelial growth factor (VEGF) - key factor in normal and pathological angiogenesis," *Romanian journal of morphology*

Hindawi
Journal of Healthcare Engineering
Volume 2023, Article ID 9816836, 1 page
https://doi.org/10.1155/2023/9816836

Retraction

Retracted: Clinical Observation of Laser Peripheral Iridoplasty with Number of Laser Shots in the Treatment of Acute Angle-Closure Glaucoma

Journal of Healthcare Engineering

Received 10 October 2023; Accepted 10 October 2023; Published 11 October 2023

This article has been retracted by Hindawi following an investigation undertaken by the publisher [1]. This investigation has uncovered evidence of one or more of the following indicators of systematic manipulation of the publication process:

(1) Discrepancies in scope
(2) Discrepancies in the description of the research reported
(3) Discrepancies between the availability of data and the research described
(4) Inappropriate citations
(5) Incoherent, meaningless and/or irrelevant content included in the article
(6) Peer-review manipulation

The presence of these indicators undermines our confidence in the integrity of the article's content and we cannot, therefore, vouch for its reliability. Please note that this notice is intended solely to alert readers that the content of this article is unreliable. We have not investigated whether authors were aware of or involved in the systematic manipulation of the publication process.

In addition, our investigation has also shown that one or more of the following human-subject reporting requirements has not been met in this article: ethical approval by an Institutional Review Board (IRB) committee or equivalent, patient/participant consent to participate, and/or agreement to publish patient/participant details (where relevant).

Wiley and Hindawi regrets that the usual quality checks did not identify these issues before publication and have since put additional measures in place to safeguard research integrity.

We wish to credit our own Research Integrity and Research Publishing teams and anonymous and named external researchers and research integrity experts for contributing to this investigation.

The corresponding author, as the representative of all authors, has been given the opportunity to register their agreement or disagreement to this retraction. We have kept a record of any response received.

References

[1] C. Ma, Z. Liu, W. Zhao, L. Hei, and S. Yao, "Clinical Observation of Laser Peripheral Iridoplasty with Number of Laser Shots in the Treatment of Acute Angle-Closure Glaucoma," *Journal of Healthcare Engineering*, vol. 2022, Article ID 7968999, 6 pages, 2022.

Hindawi
Journal of Healthcare Engineering
Volume 2022, Article ID 7968999, 6 pages
https://doi.org/10.1155/2022/7968999

Research Article

Clinical Observation of Laser Peripheral Iridoplasty with Number of Laser Shots in the Treatment of Acute Angle-Closure Glaucoma

Cheng Ma, Zengye Liu, Wei Zhao, Luning Hei, and Shuang Yao

Department of Ophthalmology, Tianjin First Central Hospital, School of Medicine, Nankai University, Tianjin 300192, China

Correspondence should be addressed to Zengye Liu; 5020201153@nankai.edu.cn

Received 26 January 2022; Accepted 22 February 2022; Published 15 March 2022

Academic Editor: Liaqat Ali

Objective. To quantitatively study the intraocular pressure (IOP) control and chamber angle opening degree of patients with acute angle-closure glaucoma (stage of attack) treated by laser peripheral iridoplasty (LPIP) with different numbers of laser shots, and to evaluate the efficacy and safety of different numbers of laser shots. *Methods*. Fifty-five patients (60 eyes) with acute angle-closure glaucoma treated in our hospital from May 2019 to December 2020 were selected as the research subjects. All patients had poor intraocular pressure control (≥40 mmHg) after IOP-lowering drug therapy. The patients were randomly divided into three groups, 20 eyes in each group, and underwent laser peripheral iridoplasty (LPIP) with different numbers of laser shots (group I: 35 laser shots, group II: 45 laser shots, and group III: 60 laser shots). The best-corrected visual acuity, IOP, corneal condition, and opening degree of anterior chamber angle (ACA), namely, the trabecular-iris angle (TIA), angle opening distance at 500 μm (AOD_{500}), and complications of patients before LPIP, 2 hours after LPIP, and 24 hours after LPIP were observed, and the opening degree of ACA were quantitatively measured. *Results*. The corrected visual acuity of the three groups after LPIP was improved to varying degrees, and the IOP decreased, TIA and AOD_{500} were increased compared with those before operation, and the differences were statistically significant ($P < 0.05$). There were statistically significant differences between group II and group I ($P < 0.05$). Four eyes in group I underwent LPIP again due to increased IOP. In group III, iris hemorrhage occurred in one eye and iris depigmentation occurred in one eye, and there was no statistical difference compared with group II ($P > 0.05$). *Conclusions*. LPIP can effectively reduce preoperative IOP and increase ACA width in patients with persistent high IOP that failed to respond to drug therapy, and moderate numbers of laser shots can achieve satisfactory results and highest safety.

1. Introduction

Glaucoma is a progressive optic neuropathy having specific pattern of visual field defects and characteristic appearances of the optic discs. It is classified into open-angle or closed-angle glaucoma based on appearance of anterior chamber angle. An elevated intraocular pressure (IOP) is built as a result of the obstruction of the outflow pathway located in the anterior chamber angle by peripheral iris [1, 2]. Many individuals with appositional anterior chamber angle closure have normal IOP and no glaucoma symptoms. They have "narrow angles" or "primary angle closure suspects" (PACs). If the IOP is high and/or there is synechial closure (but no glaucomatous damage), the phrase "primary angle closure" (PAC) is recommended. Primary angle-closure glaucoma (PACG) is defined as angle closure with glaucomatous optic disc injury and/or visual field loss. Angle closure refers to patients with narrow angles, PAC, or PACG [1]. Glaucoma is the main cause of permanent blindness worldwide. Glaucoma affects 67 million individuals globally. PACG is more prevalent than OAG, although it is more likely to cause bilateral blindness [3, 4]. The disease affects Asians and women more than Caucasians [5]. In China, Foster et al. found 28.2 million people have narrow angles [6], whereas 9.1 million have closed angles [7]. Moreover, PACG causes 91 percent of the 1.7 million bilaterally blinded Chinese glaucoma patients. PACG may be the main cause of glaucoma blindness today, according to Foster and Johnson [8].

The acute attack of primary acute angle-closure glaucoma is an ocular emergency. If it is not treated in time and effectively, the optic nerve will be irreversibly damaged, which will greatly affect the prognosis of vision [9]. Clinically, many patients cannot effectively control intraocular pressure (IOP) even with the combined use of topical and systemic IOP-lowering drugs. For many years, laser iridoplasty can successfully open the angle-closure glaucoma [10]. Laser peripheral iridoplasty (LPIP) can reduce IOP effectively by photocoagulation of iris root to make iris tissue shrink and open the angle of the chamber to increase the outflow of aqueous humor. In this study, the postoperative effects of LPIP with different numbers of laser shots were observed in three groups of patients, and the appropriate number of laser shots was explored to obtain the best therapeutic effect and maximum safety.

2. Materials and Methods

2.1. General Information. From May 2019 to December 2020, 55 patients (60 eyes) with acute primary acute angle-closure glaucoma who were admitted to our department and emergency department for outpatient, emergency, and inpatient treatment and whose IOP still could not be controlled after IOP-lowering drugs were selected. There were 21 males (22 eyes) and 34 females (38 eyes), aged from 55 to 72 years, with an average of 63.4 years.

2.2. Inclusion Criteria. Patients with an onset time of 12–72 hours, all had been treated with local or systemic IOP-lowering drugs for 1–3 days, and the IOP was not well controlled (≥40 mmHg) were included in the study. No IOP-lowering drugs were used before onset. There was no other primary disease in the eye and no history of eye surgery.

2.3. Methods. The affected eyes were randomly divided into three groups, with 20 eyes in each group; all LPIP were completed by the same doctor who was proficient in LPIP. The three groups were respectively applied with different numbers of laser shots, with 35 in group I, 45 in group II, and 60 in group III. The patients were treated with the Sitron 532 laser produced by LUMENIS Medical Laser Company. Half an hour before the operation, 1% pilocarpine eye drops were given to reduce pupil, and proparacaine hydrochloride eye drops were used for topical anesthesia. After the iris microscope was placed, 360° photocoagulation was performed on the iris root with spot diameter of 300 μm, energy of 180–200 mw, and exposure time of 0.2–0.4 s. After operation, pranoprofen eye drops and fluorometholone eye drops were given.

2.4. Observation Indicators. The best-corrected visual acuity, corneal condition, and opening degree of anterior chamber angle (ACA), namely, the trabecular-iris angle (TIA), angle opening distance at 500 μm (AOD500), and complications of the three groups of patients before LPIP, 2 hours after LPIP, and 24 hours after LPIP were observed. The IOP changes were measured with a noncontact tonometer, and the opening degree of ACA was quantified by OCT.

2.5. Statistical Methods. Statistical software SPSS (version 22.0) was used to analyze the data. Completely random grouping design was adopted. The data of all indicators were expressed as mean ± standard deviation ($\bar{x} \pm s$). One-way ANOVA was used to compare the difference in decrease of IOP, increase of degree of TIA, and increase of distance of TOD_{500} among the three groups at each time point. If there were differences, the LSD-T test was used for further pairwise comparison between the three groups. $P < 0.05$ was considered statistically significant.

3. Results

3.1. The Distribution of Best-Corrected Visual Acuity before and after Surgery in the Three Groups of Patients. The best-corrected visual acuity of the three groups of patients before surgery was less than 0.5, which was improved to varying degrees after surgery (Table 1).

3.2. The IOP of the Three Groups of Patients. The average preoperative IOP of patients in the three groups were 55.4 ± 10.2 mmHg, 57.7 ± 7.6 mmHg, and 56.2 ± 8.3 mmHg, respectively; the average IOP 2 hours after the operation were 20.3 ± 5.6 mmHg, 17.2 ± 6.3 mmHg, and 18.9 ± 4.9 mmHg, respectively; the average IOP 24 hours after surgery were 19.2 ± 8.3 mmHg, 17.9 ± 4.9 mmHg, and 17.6 ± 8.4 mmHg, respectively (Table 2, Figure 1).

3.3. TIA of the Three Groups of Patients. The average preoperative TIA of the three groups of patients were 7.4 ± 3.2°, 7.7 ± 5.4°, and 7.2 ± 4.3°, respectively; the average TIA 2 hours after operation were 23.3 ± 4.1°, 25.2 ± 2.3°, and 26.9 ± 4.6°, respectively; the average TIA 24 hours after operation was 25.2 ± 3.8°, 27.3 ± 4.7°, and 27.6 ± 8.2°, respectively (Table 3).

3.4. TOD_{500} of the Three Groups of Patients. The average preoperative TOD_{500} of the three groups of patients were 105 ± 064 μm, 114 ± 054 μm, and 109 ± 043 μm, respectively; the average TOD_{500} 2 hours after surgery were 273 ± 041 μm, 325 ± 083 μm, and 330 ± 046 μm, respectively; the average TOD_{500} 24 hours after surgery were 285 ± 110 μm, 331 ± 050 μm, and 329 ± 042 μm, respectively (Table 4, Figure 2).

3.5. Comparison of Postoperative Changes in IOP, TIA, and TOD_{500} among the Three Groups. The changes in IOP, TIA, and TOD_{500} were compared among the three groups. The results showed that there were differences among the three groups ($P < 0.05$), the increase degree of TIA and TOD_{500} in group II and III was significantly higher than that in group I ($P < 0.05$), while there was no statistically significant difference between group II and group III ($P > 0.05$) (Table 5).

Table 1: The distribution of best-corrected visual acuity before and after surgery in the three groups of patients (number of eyes).

Time point	Group I			Group II			Group III		
	< 0.1	0.1–0.5	> 0.5	< 0.1	0.1–0.5	> 0.5	< 0.1	0.1–0.5	> 0.5
Before surgery	15	5	0	13	7	0	14	6	0
2 hours after surgery	2	8	12	0	4	16	0	5	15
24 hours after surgery	2	7	11	0	3	17	0	4	16

Table 2: Preoperative and postoperative IOP of patients in the three groups (mmHg) ($\bar{x} \pm s$).

Time point	Different numbers of laser shots		
	Group I (30–40)	Group II (40–50)	Group III (> 60)
Before surgery	55.4 ± 10.2	57.7 ± 7.6	56.2 ± 8.3
2 hours after surgery	20.3 ± 5.6	17.2 ± 6.3	18.9 ± 4.9
24 hours after surgery	19.2 ± 8.3	17.9 ± 4.9	17.6 ± 8.4

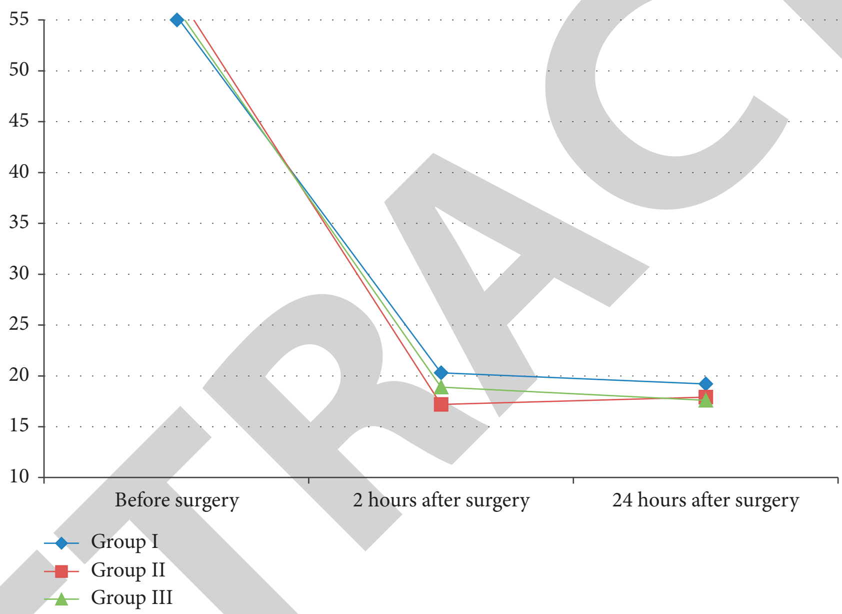

Figure 1: Comparison of preoperative and postoperative IOP among the three groups.

Table 3: Preoperative and postoperative ACA opening degree of three groups of patients (°) ($\bar{x} \pm s$).

Time point	Different numbers of laser shots		
	Group I (30–40)	Group II (40–50)	Group III (> 60)
Before surgery	7.4 ± 3.2	7.7 ± 5.4	7.2 ± 4.3
2 hours after surgery	18.3 ± 4.1	21.2 ± 2.3	22.9 ± 4.6
24 hours after surgery	20.2 ± 3.8	23.3 ± 4.7	24.6 ± 8.2

Table 4: Preoperative and postoperative TOD_{500} of the three groups (μm) ($\bar{x} \pm s$).

Time point	Different numbers of laser shots		
	Group I (30–40)	Group II (40–50)	Group III (> 60)
Before surgery	105 ± 064	114 ± 054	109 ± 043
2 hours after surgery	273 ± 041	325 ± 083	330 ± 046
24 hours after surgery	285 ± 110	331 ± 050	329 ± 042

3.6. Intraoperative and Postoperative Complications and Treatment. In group I, four eyes were treated with LPIP again due to increased IOP, and postoperative IOP was controlled. The IOP in group II was well controlled, and no abnormal condition was found. In group III, iris depigmentation was observed in one eye after the operation, IOP

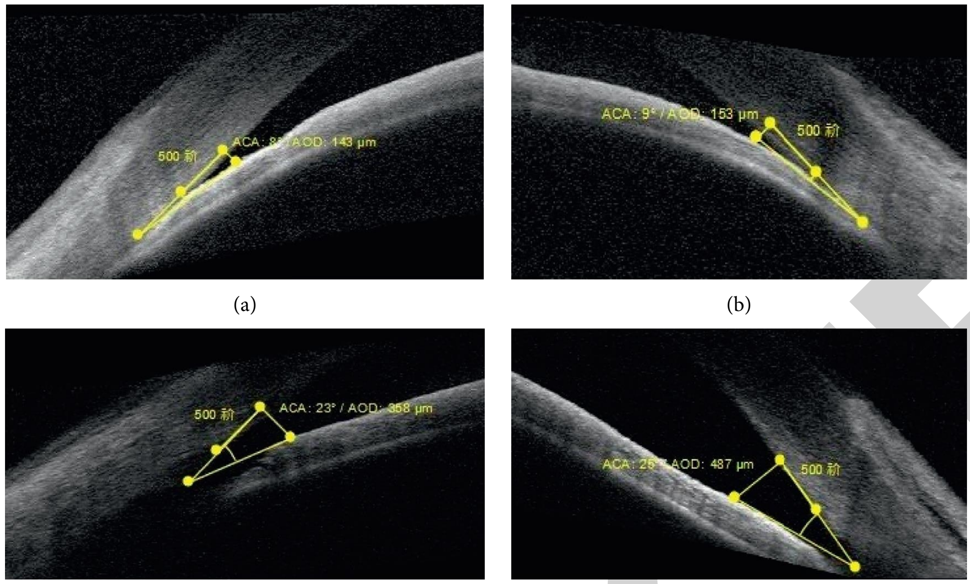

(a) (b) (c) (d)

Figure 2: (a, b) TIA (ACA) at 3 o'clock and 9 o'clock before LPIP were 8° and 9°, respectively, and TOD_{500} were 143 μm and 153 μm, respectively; (c, d) TIA (ACA) at 3 o'clock and 9 o'clock after LPIP were 23° and 25°, respectively, and TOD_{500} were 358 μm and 487 μm, respectively; suggesting that TIA (ACA) and TOD_{500} increased after LPIP compared with before surgery.

Table 5: Changes in IOP, TIA, and TOD_{500} were compared among the three groups.

Group	Decrease in IOP (mmHg)		Increase in TIA (°)		Increase in TOD_{500} (μm)	
	2 hours after surgery	24 hours after surgery	2 hours after surgery	24 hours after surgery	2 hours after surgery	24 hours after surgery
Group I	34.9 ± 5.3	35.9 ± 4.6	12.2 ± 5.6	13.2 ± 3.6	181 ± 064	202 ± 106
Group II	38.6 ± 5.9	37.9 ± 4.8	15.2 ± 8.1	16.3 ± 4.8	223 ± 012	252 ± 129
Group III	38.8 ± 7.4	38.1 ± 6.1	16.9 ± 3.4	17.1 ± 2.2	243 ± 105	256 ± 047
F	4.512	3.462	5.101	4.547	3.689	5.478
P value	< 0.05	< 0.05	< 0.05	< 0.05	< 0.05	< 0.05
t group I vs. group II	9.105	10.231	8.342	7.115	7.412	6.532
P value group I vs. group II	< 0.05	< 0.05	< 0.05	< 0.05	< 0.05	< 0.05
t group I vs. group III	8.143	7.450	9.145	8.542	6.543	8.141
P value group I vs. group III	< 0.05	< 0.05	< 0.05	< 0.05	< 0.05	< 0.05
t group II vs III	0.356	0.245	1.435	0.657	1.230	0.856
P value group II vs III	> 0.05	> 0.05	> 0.05	> 0.05	> 0.05	> 0.05

was normal, and no special treatment was given except local application of pranoprofen eye drops and fluorometholone eye drops. In group III, one eye had iris hemorrhage after operation, and Zhikang capsule was given orally for 3 days. The hematocele was absorbed, and the IOP was normal (Figure 3).

4. Discussion

With the aging of the population, glaucoma is still the first irreversible blinding eye disease in the world [11]. Therefore, timely and effective control of IOP and maintenance of stable target IOP value is of great importance. The occurrence of angle-closure glaucoma is closely related to the anatomy of anterior segment of the eyeball and the state of the lens. Short ocular axis, shallow anterior chamber, narrow chamber angle, thick lens, and its anterior position are all predisposition factors. In addition to the traditional pupillary block factors, there are still a variety of nonpupil block factors, including peripheral iris accumulation, anterior position of the ciliary body, and anterior displacement of lens. In acute onset of acute angle-closure glaucoma, the sudden closure of ACA causes a sharp increase in IOP. If the IOP is not controlled in time, it will cause irreversible damage to the optic nerve. Therefore, early and rapid reduction of IOP is very important for patients with acute attack.

The traditional treatment method for acute angle-closure glaucoma in acute attack stage is local application of IOP-lowering drugs, combined with systemic application of hypertonic agents and carbonic anhydrase inhibitors, and the IOP of most patients can be effectively controlled [12]. However, for some patients and some patients with cardiac

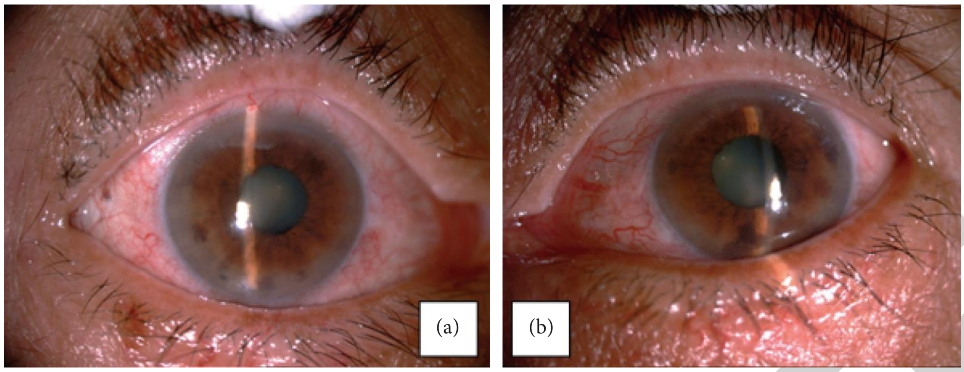

Figure 3: (a, b) appearance of the right eye and left eye at the attack stage of acute angle-closure glaucoma after treatment with IOP-lowering drugs, showing ciliary hyperemia, corneal edema, and slightly dilated pupil.

and renal insufficiency who cannot use hypertonic agents, the IOP is often not effectively controlled. Although anterior chamber puncture and discharge can temporarily reduce IOP, the stable IOP-lowering effect cannot be maintained due to the continuous closure of ACA. Due to severe corneal edema and extremely shallow anterior chamber during acute attack, peripheral iridotomy is not the best treatment method. Besides, trabeculectomy under high IOP is a risky operation, which is prone to serious complications such as malignant glaucoma and explosive suprachoroidal hemorrhage during and after operation. Therefore, it is necessary to seek an effective and safe treatment to reduce IOP before glaucoma filtration surgery.

In previous reports, laser treatment is mostly LPIP, but it mainly relieves angle-closure glaucoma caused by pupillary block factors and has no obvious effect on angle-closure glaucoma caused by other factors [5, 13]. LPIP has become one of the important methods for the treatment of acute angle-closure glaucoma in recent years and has been widely used in clinical practice. LPIP is applied to the peripheral iris by laser photocoagulation, which causes the iris matrix to shrink, mechanically pulls open the ACA, reopens the closed ACA, and increases aqueous humor outflow [14]. Although the laser operation is simple and convenient, it can quickly open the ACA and reduce the IOP, but the unreasonable laser energy and exposure time can produce complications such as corneal injury, aggravation of anterior chamber inflammation, iris hemorrhage or atrophy, and pupil dilation. Therefore, it is our focus to explore the reasonable numbers of laser shots and obtain the most effective and safe therapeutic effect through the minimum laser energy, that is, the minimum damage.

Previous studies mostly observed the effectiveness of LPIP surgery, but there was no report on how much total laser energy could achieve the best therapeutic effect with the highest safety and minimum complications. In this study, the basic parameters of laser treatment, namely, spot diameter, single laser energy, and action time were relatively fixed, and the number of laser shots was set as a variable. Also, the number of laser shots from 35 to 60 was selected through clinical experience and the subjects were divided into three groups (group I: 35 laser shots, group II: 45 laser shots, and group III: 60 laser shots). The results showed that IOP in all three groups decreased at 2 and 24 hours after surgery, and TIA and TOD_{500} increased at different degrees compared with before surgery. Compared with group I, IOP decreased significantly in group II and group III, and the opening degree of ACA increased, the difference was statistically significant. Four eyes in group I underwent LPIP again due to increased IOP, and postoperative IOP was controlled. This suggested that with the increase of the number of laser shots, that is, the total laser energy, the decrease in IOP increased, and the opening degree of ACA increased, and the treatment effect was obvious. However, there was no statistically significant difference between group III and group II. In addition, with the increase in number of laser shots from 45 to 60, one eye had iris depigmentation and one eye had iris hemorrhage after surgery, suggesting that the opening degree of ACA will not increase infinitely after the increase in number of laser shots, and there will be complications related to laser treatment in the eye. Therefore, moderate laser shots, that is, the total laser energy of about 45 laser shots, is safer, more effective, and has less side effects.

5. Conclusion

In conclusion, LPIP should be actively performed for patients with acute angle-closure glaucoma who are ineffective in local and systemic drug treatment. The moderate laser shots, that is, about 45 laser shots, can effectively reduce IOP, which is safe and effective, creating opportunities for glaucoma surgery and avoiding the risk of glaucoma filtration surgery under high IOP. However, the number of cases observed in this study was limited, and trabeculectomy was performed in some patients within one week after LPIP, and the observation time was only 24 hours after LPIP. Therefore, long-term clinical observation with large samples is still needed for the observation of long-term effect of LPIP.

Data Availability

The data will be available from the corresponding author upon request.

Conflicts of Interest

The authors declare that they have no conflicts of interest regarding the publication of this paper.

Hindawi
Journal of Healthcare Engineering
Volume 2023, Article ID 9840958, 1 page
https://doi.org/10.1155/2023/9840958

Retraction

Retracted: A Research Study to Measure the Efficacy of Terminating Cervical Cancer via Customized Optimum Pathway

Journal of Healthcare Engineering

Received 10 October 2023; Accepted 10 October 2023; Published 11 October 2023

This article has been retracted by Hindawi following an investigation undertaken by the publisher [1]. This investigation has uncovered evidence of one or more of the following indicators of systematic manipulation of the publication process:

(1) Discrepancies in scope
(2) Discrepancies in the description of the research reported
(3) Discrepancies between the availability of data and the research described
(4) Inappropriate citations
(5) Incoherent, meaningless and/or irrelevant content included in the article
(6) Peer-review manipulation

The presence of these indicators undermines our confidence in the integrity of the article's content and we cannot, therefore, vouch for its reliability. Please note that this notice is intended solely to alert readers that the content of this article is unreliable. We have not investigated whether authors were aware of or involved in the systematic manipulation of the publication process.

Wiley and Hindawi regrets that the usual quality checks did not identify these issues before publication and have since put additional measures in place to safeguard research integrity.

We wish to credit our own Research Integrity and Research Publishing teams and anonymous and named external researchers and research integrity experts for contributing to this investigation.

The corresponding author, as the representative of all authors, has been given the opportunity to register their agreement or disagreement to this retraction. We have kept a record of any response received.

References

[1] X. Zhang, H. Ma, X. Lu, and Z. Zhang, "A Research Study to Measure the Efficacy of Terminating Cervical Cancer via Customized Optimum Pathway," *Journal of Healthcare Engineering*, vol. 2022, Article ID 7872915, 6 pages, 2022.

Hindawi
Journal of Healthcare Engineering
Volume 2022, Article ID 7872915, 6 pages
https://doi.org/10.1155/2022/7872915

Research Article

A Research Study to Measure the Efficacy of Terminating Cervical Cancer via Customized Optimum Pathway

Xianyu Zhang, Huan Ma, Xiurong Lu, and Zhilin Zhang

Department of Radiotherapy, The First Affiliated Hospital of Hebei North University, Zhangjiakou, Hebei, China

Correspondence should be addressed to Zhilin Zhang; zhangxy@hebeinu.edu.cn

Received 13 January 2022; Revised 27 January 2022; Accepted 2 February 2022; Published 15 March 2022

Academic Editor: Liaqat Ali

Background. To develop a precise prognostic model of overall survival in patients with terminating cervical cancer based on surveillance, epidemiology, and end results (SEER) program. *Methods*. The patients were retrieved from SEER data who are diagnosed with terminating cervical cancer from 2004 to 2016. The data were performed using univariate and multivariate analyses and constructed nomograms for predicting survival. Use C-index to validate the model accuracy. *Results*. Totally 15839 patients diagnosed with cervical cancer were independently allocated into the training set ($n = 11088$) and validation set ($n = 4751$). The multivariate analysis results indicated that age, race, stage_T, stage_M, and stage_N were confirmed as independent risk predictors, and those factors are applied to construct this clinical model. The C-index of overall survival in the training set was 0.6816 (95% confidence intervene (CI), 0.694–0.763) and that in the validation set was 0.6931(95% CI, 0.613–0.779). All calibration curves of various factors were consistent with predicted and actual survival. *Conclusion*. The nomogram provides a novel method for predicting the survival of patients with terminating cervical cancer, assisting in accurate therapeutic methods for patients with primary terminating cervical cancer.

1. Introduction

Cervical cancer is the most common malignancy in female genital tract [1]. The incidence rate of cervical cancer is second in women and even in some underdeveloped countries and regions [2, 3]. The latest data show that there are about 500000 new cases of cervical cancer worldwide every year, of which more than 80% are in developing countries [4]. More than 260000 women die of cervical cancer every year, mainly in low and middle-income countries [5]. In China, the incidence rate of cervical cancer accounts for 11.9% of the total worldwide, and the death rate accounts for 11.1% [6]. The age of onset is younger. At present, gene expression microarray has been widely used to study gene expression profile [7]. Gene expression microarray is a credible and high-efficiency way to identify target genes. These microarray spectra not only provide a new method for studying various disease-related genes but also provide a good prospect for molecular prediction, drug-based molecular targeting, and molecular therapy [8, 9]. With the wide application of gene expression chip technology, a large number of data are published on the public database platform [10]. Using these databases can further study the molecular mechanisms related to diseases [11].

Nomograms have been applied on various disorders [12–16], and surveillance, epidemiology, and SEER data served as an all-around database to search cancers. By using all-around SEER database to assess different factors, the nomograms could predict survival prognosis [17]. Nomogram is a mathematical model based on multivariate regression analysis. Through this model, a variety of independent prognostic factors can be gathered together to make the predictive value more individualized and intuitive [18, 19].

In our study, we develop a precise prognostic model of overall survival in patients with terminating cervical cancer based on surveillance, epidemiology, and end results (SEER) program, which aimed to help clinical patients to relieve their disease.

2. Materials and Methods

2.1. Patients and Ethic. The patients were retrieved from the SEER data, which included information related to cancer prevalence, incidence, race, histological types, pathological types, survival time, and treatment at 18 registries in the USA. All the participants were diagnosed with cervical cancer by histopathological examination. The experiments were approved by the clinical research ethics committee hospital. All patients wrote the informed consent, in accordance with the provisions of the Helsinki Declaration of 1975.

Inclusive standard: patients were diagnosed with cervical cancer by histopathological means, age ≥18 years old, and patient's clinical information is complete.

Exclusion criteria: patients were with more primary carcinomas or secondary tumor and data about survival time or other clinical characteristics were missing.

2.2. Study Variables. The basic patient data were collected. The survival time (1 year, 3 years and 5 years) is related to invasive depth of tumor (T stage) (1 = T0, 2 = T1, 3 = T2, 4 = T3 and T3a and T3b, 5 = T4 and T4a and T4b, and 6 = TX), the number of involved lymph node (N stage) (1 = N0, 2 = N1, 3 = N2, 4 = N3, and 5 = Nx), and distant metastasis (M stage) (1 = M0, 2 = M1).

2.3. Construction and Validation of the Nomogram. All statistical data were conducted using R software 3.3.0 (R Foundation for Statistical Computing, Vienna, Austria, www.r-project.org). Second, we constructed a nomogram used the multivariate Cox regression-the area under the curve (AUC) by R software to confirm the factors; furthermore, we used concordance index and calibration curves to assess the accuracy. The Kaplan–Meier method is applied to verify the accuracy of survival curves [20]. The prognostic value of the factors was confirmed by Cox regression analyses [21]. Value of $P < 0.05$ was considered statistically significant.

2.4. Statistical Analyses. The data were compiled using with SPSS 19.0 statistical software. Values are presented as means ± SEM. The results were compared using Student's *t*-test. Kaplan–Meier survival analyses were used to analyze the clinicopathologic features. All experiments were performed in triplicate and a P value.

3. Results

3.1. Clinicopathological Characteristics of the Training and Validation Sets. Totally, 15839 qualified subjects were independently allocated into the training group ($n = 11088$) and validation group ($n = 4751$). As given in Table 1, there was no statistical significance between two groups in race, age, stage_T, stage_N, and stage_M ($P > 0.05$).

Table 1: Clinicopathological characteristics of the training and validation sets.

	Training set ($n = 11088$)	Validation set ($n = 4751$)	P value
Age (years)			
<50	8425 (76%)	3515 (74%)	0.584
50–69	1774 (16%)	730 (15.4%)	
≧70	889 (8%)	506 (10.6%)	
Race			
White	6376 (57.5%)	2755 (58%)	
Black	3060 (27.6%)	1235 (26%)	
Others	1652 (14.9%)	761 (16%)	
Stage_T			
T0	3880 (35%)	1615 (34%)	
T1	3215 (27%)	1377 (29%)	
T2	2106 (19%)	997 (21%)	0.196
T3	887 (8%)	332 (7%)	
T4	665 (6%)	237 (5%)	
TX	665 (5%)	157 (4%)	
Stage_M			
M0	8532 (77%)	3563 (75%)	0.881
M1	2556 (23%)	1188 (25%)	
Stage_N			
N0	4546 (41%)	1852 (29%)	
N1	3659 (33%)	1615 (34%)	
N2	1108 (10%)	855 (18%)	0.304
N3	1219 (11%)	570 (12%)	
NX	665 (5%)	332 (7%)	

$P < 0.05$, significant difference.

3.2. Survival Analysis in the Training Set. As shown in Figure 1, age, stage_T, stage_N, and stage_M were significantly associated with overall survival (OS) in Kaplan–Meier mean.

3.3. Prognostic Factors in the Training Set. Univariate analysis and multivariate analysis are given in Table 2. The results showed that factors such as age, race, invasive depth of tumor (T stage), the number of involved lymph node (N stage), and distant metastasis (M stage) were related to survival time. Mostly, stage_T, stage_N, and stage_M were important factors. Furthermore, we did further analyze binary logistic regression analysis to identify factors potentially predict cervical cancer development. Race, stage_T, stage_N, and stage_M were conformed as independent predictors for individual with cervical cancer.

3.4. Construction of the Nomogram. The nomogram was constructed by collecting all independent predictors for OS in the training cohort [22]. The model indicated that age ≧70 years old was most associated with survival for individual with cervical cancer, followed by TX stage and distant metastasis. Race and NX had moderate impacts on survival outcomes (Figure 2).

3.5. The Internal Validation of Nomogram. The nomogram had an exact prediction in cervical cancer development, and the unadjusted concordance index in the training set showed

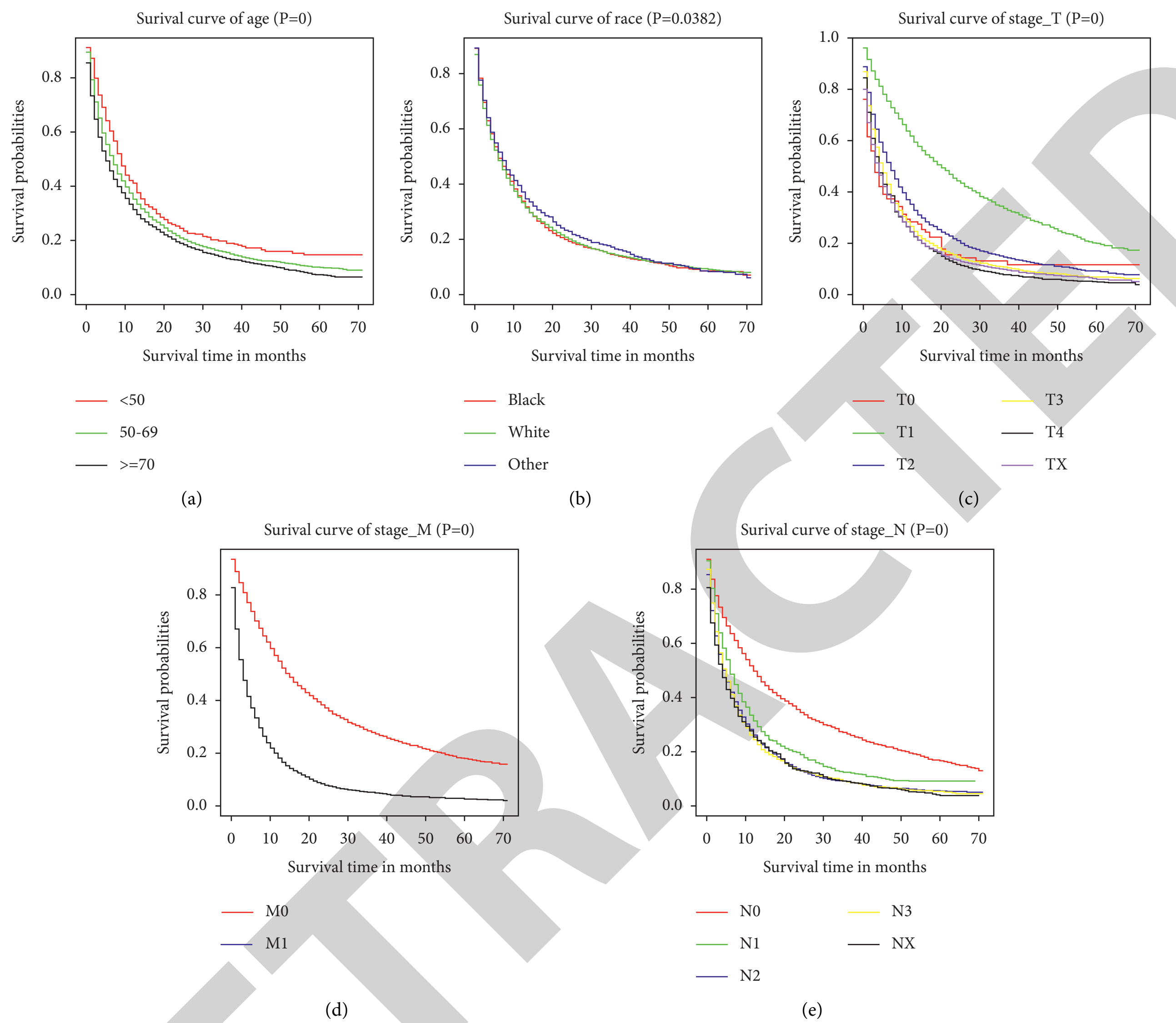

Figure 1: Kaplan–Meier survival curves for overall survival in the training cohort as stratified by (a) age, (b) race, (c) stage_T, (d) stage_M, and (e) stage_N.

0.6816 (95% CI, 0.694–0.763) and that in the validation set was 0.6931 (95% CI, 0.613–0.779). It indicated that the nomogram precisely predicts OS. Area under the curves (AUCs) are used to predict overall survival at 3 years and 5 years using the internal validation cohort (Figure 3). The 3 years and 5 years of AUCs were, respectively, 0.758, 0.788, and 0.792. This indicated that this nomogram model had a good predictive performance.

3.6. The External Validation of Nomogram. The external validation set result demonstrated that the model was exact. As shown in Figures 4 and 5, the proper consistency is between the predicted and observed OS for 3 and 5 years.

4. Discussion

Cervical cancer is one of the three most common gynecological tumors and has become the fourth leading cause of cancer-related death in women all over the world. Early screening and prevention of cervical cancer are of great importance in reducing the incidence rate and mortality of cervical cancer in China. Therefore, it is still worth to explore the pathological mechanism and find the genes related to the development of cervical cancer.

In our study, 15839 subjects were retrieved from the SEER data and construct the survival prognosis model. Age, race, stage_T, stage_N, and stage_M were confirmed as the inde-

Table 2: Risk factors for OS according to the Cox proportional hazards regression model.

	Univariate analysis			Multivariate analysis		
	HR	95% CI	*P* value	HR	95% CI	*P* value
Age (years)						
<50	Reference					
50–69	1.3174	1.1744–1.4778	<0.001	1.2767	1.1593–1.4060	<0.001
≧70	1.7925	1.5980–2.0108	<0.001	1.7058	1.5491–1.8784	<0.001
Race						
Black	Reference					
White	1.7911	0.9266–1.0537	<0.001	0.9952	0.9435–1.0497	<0.001
Others	0.9881	0.7178–0.8719	0.7142	0.8000	0.7375–0.8677	0.85994
Stage_T						
T0	Reference					
T1	0.9497	0.5843–0.9619	0.0235	0.7225	0.5844–0.8932	0.00266
T2	1.0924	0.8552–1.3953	0.0193	1.0626	0.8627–1.3087	0.00323
T3	1.2169	0.9528–1.5542	0.1158	1.1750	0.9539–1.4474	0.12949
T4	1.2521	0.9810–1.5981	0.0710	1.2163	0.9880–1.4973	0.06487
TX	1.3546	1.0580–1.7344	0.0161	1.3164	1.0664–1.6249	0.01052
Stage_M						
M0	Reference					
M1	2.4121	2.3003–2.5293	<0.001	2.3545	2.2632–2.4495	<0.001
Stage_N						
N0	Reference					
N1	1.2549	1.1513–1.3678	<0.001	1.2307	1.1448–1.3231	<0.001
N2	1.3563	1.2851–1.4314	<0.001	1.3810	1.3199–1.4449	<0.001
N3	1.3033	1.2172–1.3954	<0.001	1.3537	1.2779–1.4341	<0.001
NX	1.3443	1.2324–1.4663	<0.001	1.3919	1.2932–1.4981	<0.001

$P < 0.05$, significant difference. HR, hazard ratio.

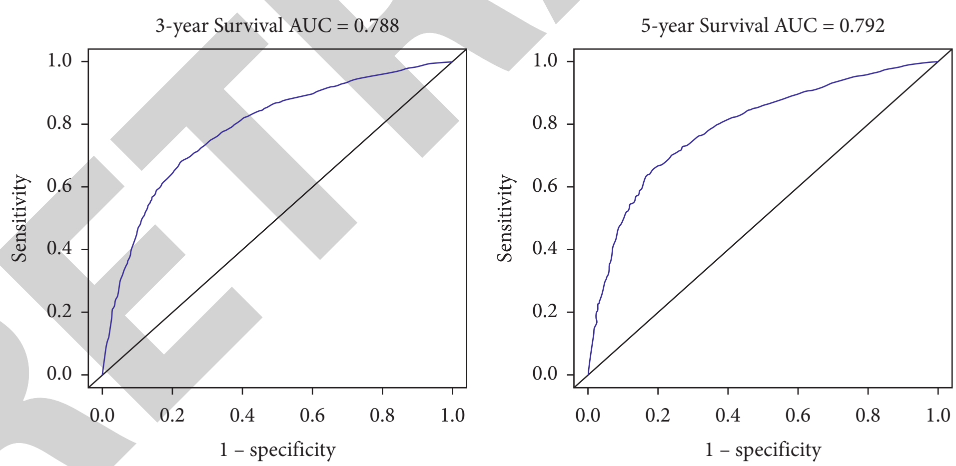

(a) (b)

Figure 2: Area under the curves to predict overall survival at 3 years (a) and 5 years (b) using the internal validation cohort.

pendent prognostic factors. The nomogram displays a comparably higher C-index value and calibration, which indicated that it had a better appraise survival prediction performance.

The nomogram model contains more prediction factors, so that it has higher prediction accuracy than the traditional staging model [23]. In our study, a nomogram was developed with 15839 patients which is based on the SEER database, and we predicted that the overall survival time relied on the independently factors: age, race, stage_M, stage_N, and stage_T.

This research has some limitations. First, the nomogram model is based on the SEER database. Although the database covers 28% of the population in the United States and collects clinical data from multiple medical centers in the United States, it lacks some information, for example, treatment details and so on. Second, this study confirmed that the prognosis of cervical cancer patients is related with metastasis sites, but the SEER database only contains four specific distant metastasis sites. However, adrenal

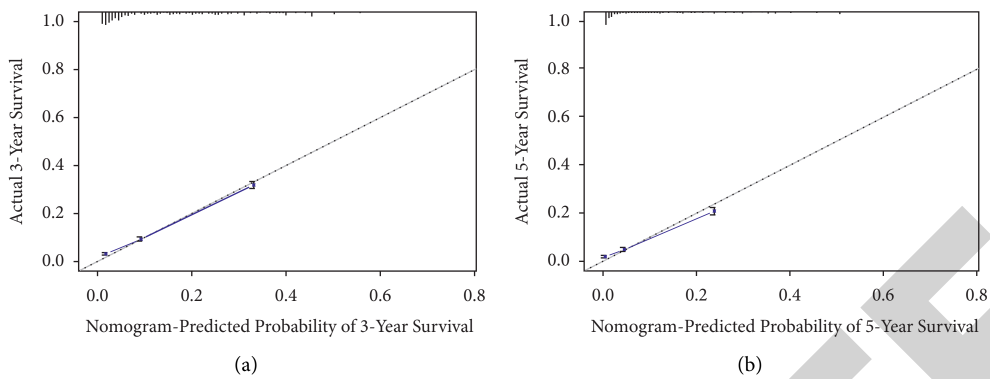

Figure 3: (a) Te calibration curves for predictions of overall survival in the training set at 3 years and (b) 5 years after diagnosis. Te dashed line represents perfect agreement between the nomogram-predicted probability (x-axis) and the actual probability, calculated from a Kaplan–Meier analysis (y-axis).

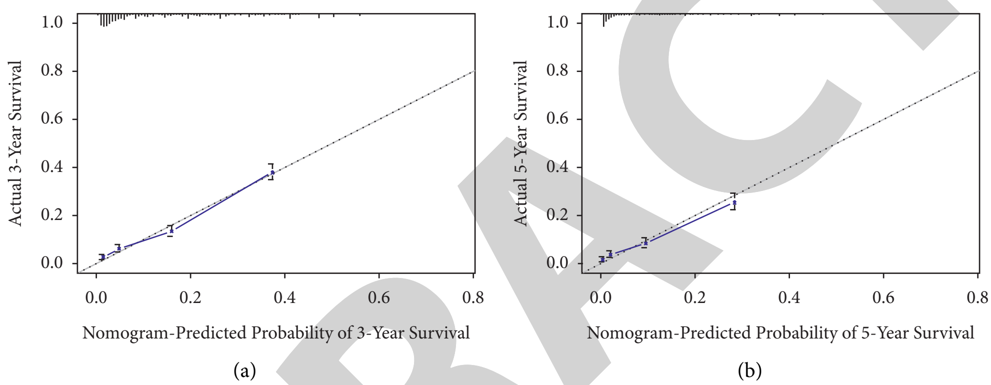

Figure 4: (a) Te calibration curves for predictions of overall survival in the validation set at 3 years and (b) 5 years after diagnosis. Te dashed line represents perfect agreement between the nomogram-predicted probability (x-axis) and the actual probability, calculated from a Kaplan–Meier analysis (y-axis).

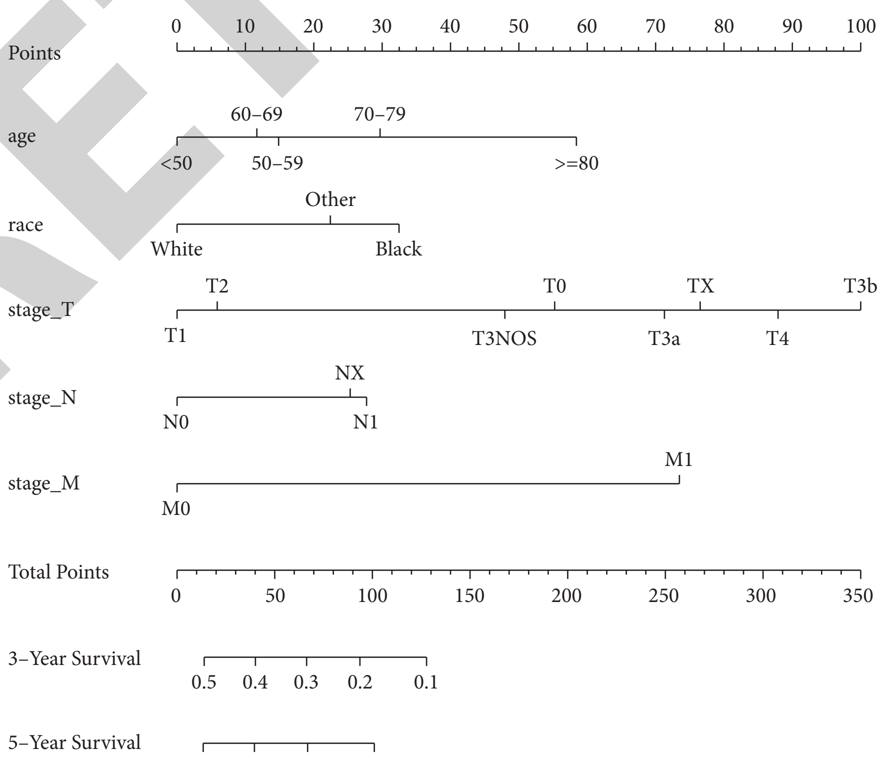

Figure 5: Nomogram predicting 3 and 5-year overall survival for patients with cervical cancer.

Hindawi
Journal of Healthcare Engineering
Volume 2023, Article ID 9896325, 1 page
https://doi.org/10.1155/2023/9896325

Retraction

Retracted: Effects of Four Types of Watermelon Frost Combination Medications for the Treatment of Oral Ulcers: A Network Meta-Analysis

Journal of Healthcare Engineering

Received 23 May 2023; Accepted 23 May 2023; Published 24 May 2023

This article has been retracted by Hindawi following an investigation undertaken by the publisher [1]. This investigation has uncovered evidence of one or more of the following indicators of systematic manipulation of the publication process.

(1) Discrepancies in scope
(2) Discrepancies in the description of the research reported
(3) Discrepancies between the availability of data and the research described
(4) Inappropriate citations
(5) Incoherent, meaningless and/or irrelevant content included in the article
(6) Peer-review manipulation

The presence of these indicators undermines our confidence in the integrity of the article's content and we cannot, therefore, vouch for its reliability. Please note that this notice is intended solely to alert readers that the content of this article is unreliable. We have not investigated whether authors were aware of or involved in the systematic manipulation of the publication process. Wiley and Hindawi regrets that the usual quality checks did not identify these issues before publication and have since put additional measures in place to safeguard research integrity.

We wish to credit our own Research Integrity and Research Publishing teams and anonymous and named external researchers and research integrity experts for contributing to this investigation.

The corresponding author, as the representative of all authors, has been given the opportunity to register their agreement or disagreement to this retraction. We have kept a record of any response received.

References

[1] Z. Liu and H. Dou, "Effects of Four Types of Watermelon Frost Combination Medications for the Treatment of Oral Ulcers: A Network Meta-Analysis," *Journal of Healthcare Engineering*, vol. 2022, Article ID 2712403, 7 pages, 2022.

Hindawi
Journal of Healthcare Engineering
Volume 2022, Article ID 2712403, 7 pages
https://doi.org/10.1155/2022/2712403

Research Article

Effects of Four Types of Watermelon Frost Combination Medications for the Treatment of Oral Ulcers: A Network Meta-Analysis

Zhenhua Liu [1] and Huiqin Dou [2]

[1]Department of Stomatology, Zhongguancun Hospital, Beijing 100080, China
[2]Department of Oral Medicine, Qilu Hospital of Shandong University, Jinan 250012, China

Correspondence should be addressed to Huiqin Dou; douhuiqin@qiluhospital.com

Received 1 February 2022; Revised 17 February 2022; Accepted 18 February 2022; Published 12 March 2022

Academic Editor: Liaqat Ali

Objective. The aim of this study is to identify the effectiveness of the four different watermelon frost combination medications in the treatment of oral ulcers through network meta-analysis and rank them based on their performances. *Methods*. Five randomized controlled studies of four distinct types of a combination medication for the treatment of oral ulcers were observed in numerous databases, and a network meta-analysis was conducted to evaluate the odds ratio (OR) and sequence of the diverse treatments using Stata software (version 13.0). The underlined studies were categorized into two groups: the control group (watermelon frost alone) and the observation group (one of four watermelon frost combinations). *Results*. The study comprised of 598 cases and the findings indicated that the pooled OR and 95% CI of oral ulcers that improved relative to watermelon frost alone were 3.26 (1.28 to 8.30) for watermelon frost and Kangfuxin fluid, 8.74 (2.94 to 26.02) for watermelon frost and erythromycin, 6.53 (1.81 to 23.50) for watermelon frost and metronidazole, and 2.62 (0.63 to 10.95) for watermelon frost and cydiodine buccal tablets. The study showed the significant efficacy of watermelon frost combination medications. In terms of clinical efficacy, the combination of watermelon frost and erythromycin was the most promising concomitant medication. It had an 86.3 surface under cumulative ranking (SUCRA). *Conclusion*. All the studied watermelon frost combinations were effective against oral ulcers validating the use of watermelon frost for oral ulcers. The combination of watermelon frost and erythromycin is the most promising candidate among the four combinations for the treatment of oral ulcers.

1. Introduction

Oral ulcer is a common oral disease in clinics. It is a superficial ulcer that occurs on the oral mucosa. The ulcer is mainly round or oval. The common symptom is local oral pain. This disease has the highest incidence among oral mucosal diseases and has a certain periodicity and self-limitation [1]. At present, the etiological mechanism of the disease is not very clear, and may be closely related to heredity and infection. The disease will affect the patient's normal diet and even language function and cause great pain to the patient [2]. Improper treatment after the onset of the disease will significantly reduce the quality of life. If it is not treated timely and effectively, it is easy to involve diseases of the nervous, cardiovascular, digestive, and respiratory systems [3]. Therefore, the timely and effective clinical treatment of oral ulcer patients with scientific and reasonable treatment plans has very important clinical significance for enhancing the quality of life.

The meta-analysis, which is based on direct comparisons of well-planned randomized controlled trials, has been considered as the gold standard for determining the effectiveness of interventions [4]. In clinical practice, there is no evidence of direct comparative studies on the efficacy of many different interventions. The biggest advantage of network meta-analysis (NMA) is that distinct interventions for the treatment of the same disease can be indirectly compared and sorted according to the effect of a certain outcome index, and then, the optimal treatment plan can be selected [5, 6].

The current study aimed to identify the effectiveness of four types of watermelon frost combination medications for the treatment of oral ulcers using NMA and to rank them according to their performances. These four schemes are most widely used to treat oral ulcers. Watermelon frost spray is an anti-inflammatory Chinese patent medicine. This included combinations of watermelon frost with Kangfuxin fluid, erythromycin, metronidazole, and cydiodine buccal tablets. This study may provide critical guidance for therapeutic medication selection in the treatment of oral ulcers.

2. Methods

2.1. Search Strategy. The databases conducted for this research included EMBASE, PubMed, Web of Science, China Science and Technology Journal, SciFinder, Sino Med, Wan fang, China National Knowledge Index, China Academic Journal Network Publishing, Chinese Science Citation, Cochrane Library, China Biomedical Medicine, Chongqing VIP Network, and BIOSIS Previews. Each database has its own set of search algorithms, which include variations on the search keywords, wildcard symbols, and Boolean operators that combine words. The searching date is from the establishment of the database to February 17, 2021. The searched words are "watermelon frost," "combination therapy," "Kangfuxin fluid," "erythromycin," "metronidazole," "cydiodine buccal tablets," "oral ulcer," "mouth ulcer," "aphthous," "randomized controlled trials," "efficacy," and "drug therapy."

2.2. Inclusion and Exclusion Criteria. The following were the inclusion criteria: (1) randomly controlled trials, (2) subjects with oral ulcers who met the requirement of diagnosis of oral ulcers [7]: the integrity of the oral mucosal epithelium is continuously damaged or destroyed, and the surface layer is necrotic and sloughed to form a depression [8], (3) patients aged 18 years and above, (4) the results of the effective number of cases of both the observation group and the control group are provided, (5) absence of seriously malignant ulcers, and (6) studies in which watermelon frost alone was used as the control group and watermelon frost combinations were utilized to treat oral ulcers as the observation group.

The following were the exclusion criteria: (1) subjects with tuberculous ulcer, traumatic ulcer, oral mucosa herpes simplex, or mental illness, (2) individuals with serious tumor, heart, kidney, lung, or liver damage, as well as those with autoimmune illnesses (3) studies that are entirely descriptive and do not include a control group, (4) types of studies that were theoretical reviews, discussions of case reports, and summaries of experience, and (5) studies in which incomplete data are provided.

2.3. Efficacy Evaluation Criteria. The efficacy was assessed using the integral value of clinical signs and indicators pre- and post-treatment: (1) healed: the ulcer surface was completely healed, and the clinical symptoms and signs disappeared; (2) markedly effective: the ulcer surface was obviously healed. Moreover, the clinical symptoms and indications had improved noticeably; (3) effective: the ulcer surface was partially healed, and the clinical symptoms and signs were partially improved; (4) ineffective: the ulcer surface was not healed or even enlarged, and the clinical symptoms and signs remained unchanged or even worsened. The total effective cases were the sum of effective, markedly effective, and healed cases.

2.4. Data Extraction and Quality Evaluation. Two reviewers read the literature independently and searched all titles and abstracts of potentially eligible trials based on the inclusion and exclusion criteria, and then they extracted all relevant information including numerical results, sample size (control and observation) in each arm, characteristics of participants and interventions, outcomes reported and collected, and quality indicators of publications in each included study. The information extracted was cross-checked and disagreements were transferred to a third reviewer. The quality of the publications in this study was assessed using the Jadad quality scoring system.

2.5. Statistical Evaluations. The network meta-analysis was used by using Stata software 13.0 version to construct the network commands network package was used to construct evidence contribution, forest plot, funnel, and ranking plots. The value of the SUCRA curve was used to rank the efficacy of the interventions. SUCRA values were shown in percentages. The greater the SUCRA value, the better the intervention. The selected indicators were count data, while ORs were used as the concomitant effect, and CIs were set at 95%. The probability value of $P < 0.05$ was regarded as statistically considerable.

2.6. Ethical Approval and Consent to Participate. Each study was based on a previously published research study. As a result, there was no need for ethical approval or patient consent.

3. Results

3.1. Characteristics of Included Studies. This study eventually identified 5 eligible publications published between 2016 and 2020. A total of 598 cases including 299 observation cases and 299 control cases were included. The basic classification of included papers is shown in Table 1.

3.2. Network Meta-Analysis

3.2.1. Network Plot of Four Types of Integrated Chinese and Western Medicines. Of the 5 studies, the combination of watermelon frost with Kangfuxin fluid was the most common one, while watermelon frost with erythromycin, metronidazole, and cydiodine buccal tablets were the least, all were one. Figure 1 showed that the watermelon frost

Table 1: Classification of included studies.

Author	Comparison	Year	Area	Dose		Observation group		Control group		Duration (days)	Jadad quality score
				A	Combined medication	Total effective cases	Total cases	Total effective cases	Total cases		
Chen HZ	B vs A	2016	China	4 time/day	20 ml/day	37	40	32	40	7	3
You Ying	B vs A	2018	China	4 time/day	12–20 ml/day	36	40	29	40	7	4
Xu HF	C vs A	2013	China	4 time/day	4 time/day	101	105	78	105	7–14	3
Li XY	D vs A	2020	China	3 time/day	3 time/day	71	74	58	74	14	3
Shan HZ	E vs A	2014	China	6time/day	7.5 mg/day	37	40	33	40	7	3

A, watermelon frost; B, watermelon frost + Kangfuxin fluid; C, watermelon frost + erythromycin; D, watermelon frost + metronidazole; E, watermelon frost + cydiodine buccal tablets.

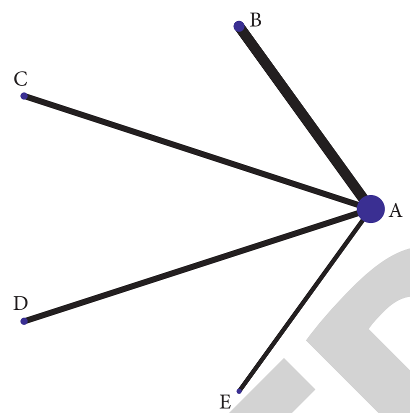

Figure 1: Network plot of different interventions for treatment of acute cerebral infarction. The size of the point in the network graph is proportional to the number of subjects, while the thickness of the line is proportional to the number of studies. A, watermelon frost; B, watermelon frost + Kangfuxin fluid; C, watermelon frost + erythromycin; D, watermelon frost + metronidazole; E, watermelon frost + cydiodine buccal tablets.

alone group had the largest number of participants, while watermelon frost with cydiodine buccal tablets had the least number of subjects.

3.2.2. Evidence Contribution Plot. The direct comparison of watermelon frost alone and the combination of watermelon frost + Kangfuxin fluid had a 100% impact on the combined results. The direct comparison between watermelon frost alone and watermelon frost + Kangfuxin fluid had a 50% effect on the indirect comparison between watermelon frost + Kangfuxin fluid and watermelon frost + erythromycin. The direct comparison of watermelon frost alone and watermelon frost + Kangfuxin fluid had a 16.7% effect on the results of the meta-analysis (Figure 2).

3.2.3. Forest Plot. The pooled OR and 95% CI of oral ulcers improvement compared with watermelon frost alone was 3.26 (1.28 to 8.30) for watermelon frost + Kangfuxin fluid, 8.74 (2.94 to 26.02) for watermelon frost + erythromycin, 6.53 (1.81 to 23.50) for watermelon frost + metronidazole, and 2.62 (0.63 to 10.95) for watermelon frost + cydiodine buccal tablets, considerably, which shows considerable variations in efficacy. For the comparison between watermelon frost combinations, no considerable variations were observed. The OR for the network estimates along with 95% CI is shown in Figure 3.

3.2.4. Publication Bias. In terms of publishing bias, all of the study's outcomes were nearly symmetrical (Figure 4), implying that there was no publication bias.

3.3. Ranking Plot. Table 2 and Figure 5 illustrate the distribution of probability for each treatment that was ranked for its efficacy in treating oral ulcers based on SUCRA values. The following was the order of SUCRA values for various watermelon frost combinations: watermelon frost + erythromycin (86.3), watermelon frost + metronidazole (75.0), watermelon frost + Kangfuxin fluid (46.8), and watermelon frost + cydiodine buccal tablets (39.4). As a result, the combination of watermelon frost and erythromycin had the best chance of being the most effective intervention in terms of clinical efficacy.

4. Discussions

Traditional meta-analysis is a direct head-to-head comparison of the treatment or safety of two treatment methods [9]. However, in practice, there are often many drugs to treat the same disease. Decision-makers, doctors, and patients need to be able to choose the best treatment method among a variety of treatment measures or programs [2]. Network meta-analysis is an extension of traditional meta-analysis and can be used to compare any number of treatments at the same time. Even if the two treatments to be compared have never been directly compared, this analysis method can still summarize the data of random clinical trials of different treatments, and then estimate the point and confidence interval for a given treatment endpoint [1,10].

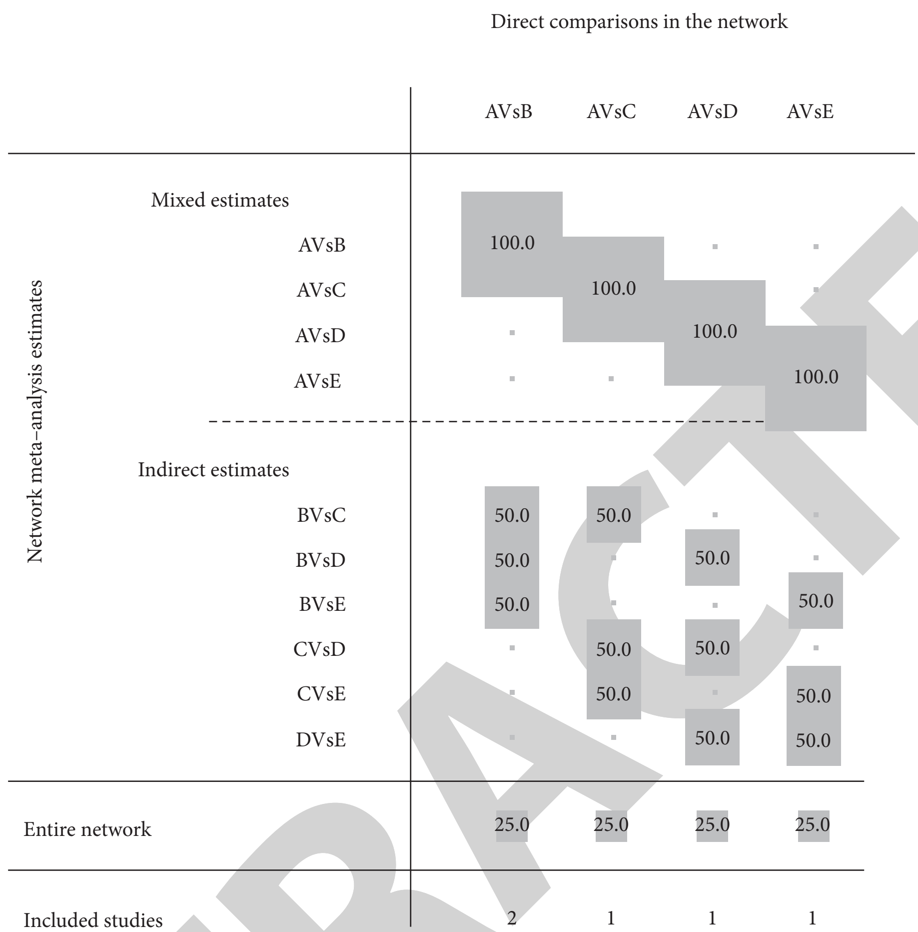

Figure 2: Evidence contribution plot. The matrix showed the effect of comparing the results of different control measures directly against the results of their network meta-analysis. A, watermelon frost; B, watermelon frost + Kangfuxin fluid; C, watermelon frost + erythromycin; D, watermelon frost + metronidazole; E, watermelon frost + cydiodine buccal tablets.

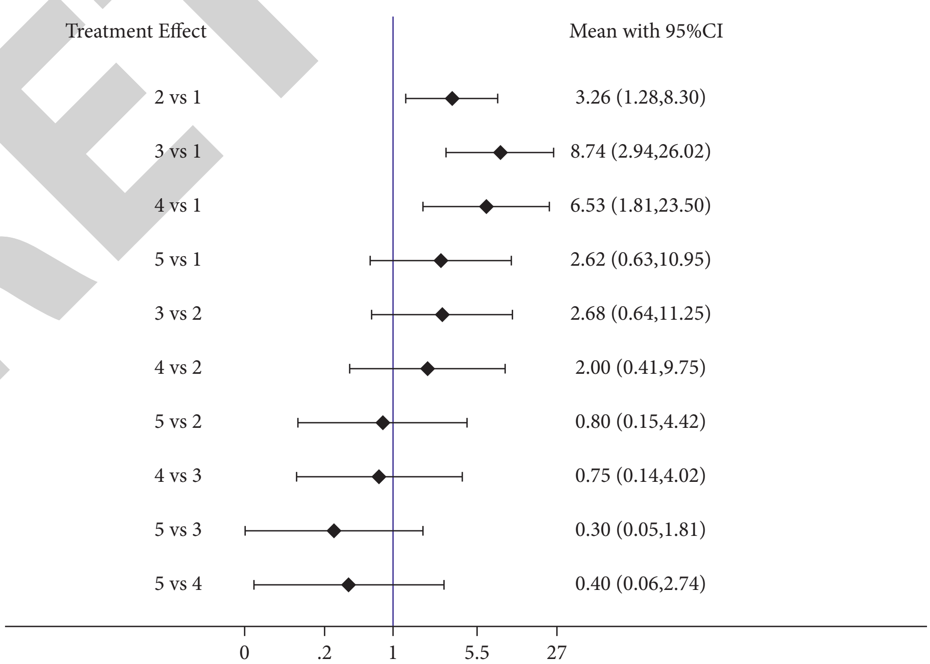

Figure 3: Network estimates of mean OR, their 95% Cis, and prediction intervals (red extensions). A, watermelon frost; B, watermelon frost + Kangfuxin fluid; C, watermelon frost + erythromycin; D, watermelon frost + metronidazole; E, watermelon frost + cydiodine buccal tablets.

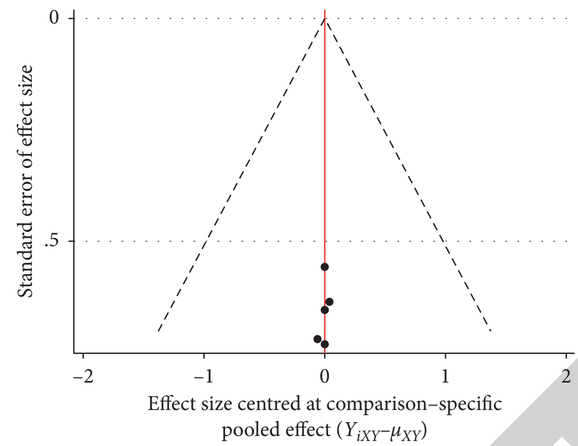

Figure 4: Funnel plot for publication bias in selected studies.

Table 2: SUCRA rankings of acute cerebral infarction treatments.

Treatment	SUCRA	PrBest	Mean rank
Watermelon frost	2.5	0.0	4.9
Watermelon frost + erythromycin	86.3	58.2	1.5
Watermelon frost + metronidazole	75.0	33.6	2.0
Watermelon frost + Kangfuxin fluid	46.8	3.1	3.1
Watermelon frost + cydiodine buccal tablets	39.4	5.1	3.4

Notes: SUCRA: surface under the cumulative ranking.

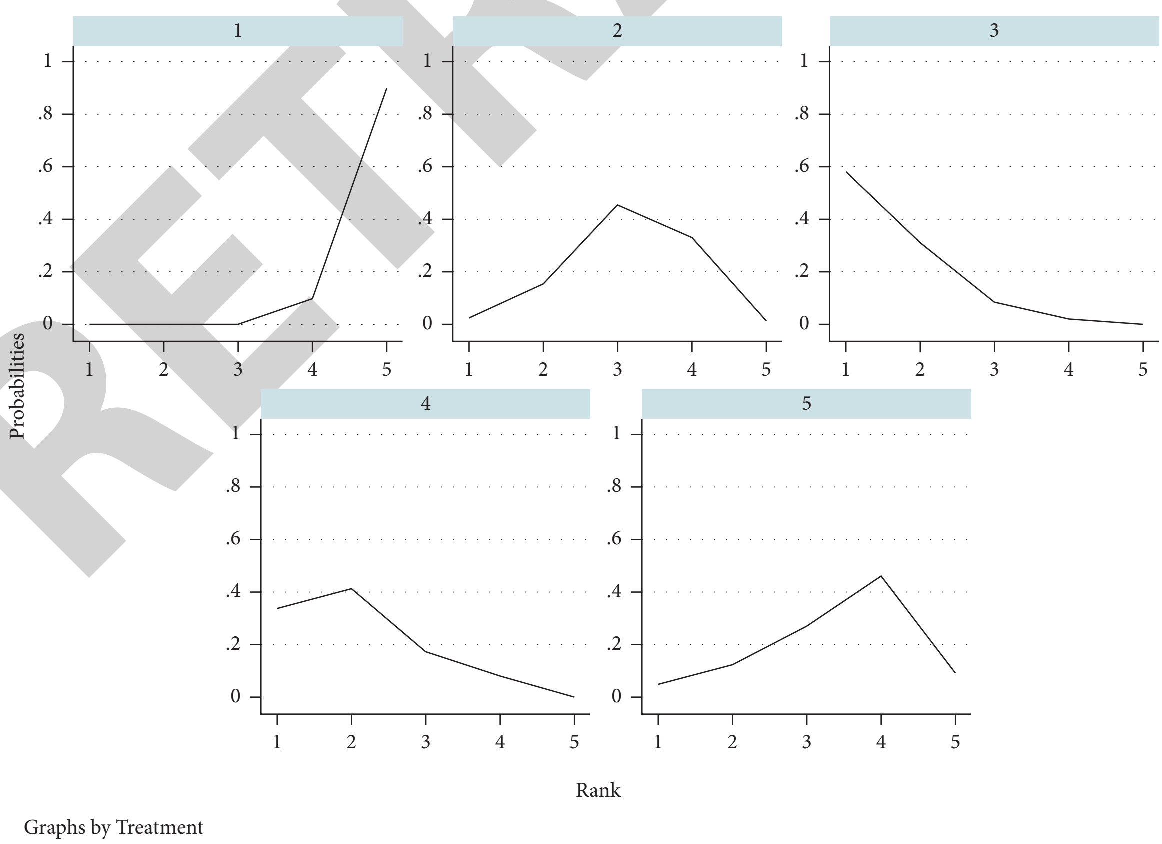

Figure 5: SUCRA for the cumulative probabilities. Notes: A, watermelon frost; B, watermelon frost + Kangfuxin fluid; C, watermelon frost + erythromycin; D, watermelon frost + metronidazole; E, watermelon frost + cydiodine buccal tablets.

In this research, four types of combined medicines with watermelon frost for treatment of oral ulcers were analyzed and pairwise comparison was performed to draw a network diagram, which showed a more intuitive result. The combinations of watermelon frost with Kangfuxin fluid, erythromycin, metronidazole, and cydiodine buccal tablets were more effective relative to watermelon frost alone in the treatment of oral ulcers. Watermelon frost combined with erythromycin had the greatest SUCRA value and was most likely to be the optimal treatment option.

The oral ulcer is a common oral mucosal disease in the hospital's oral departments [11]. It has the characteristics of recurring attacks, which make the patient feel very painful and has a serious impact on the daily life, study, and work of the patient [12]. The causes of oral ulcers mainly include two points: the first is that the oral cavity is infected by bacteria or viruses, which leads to oral mucosal erosion and ulcers; the second is that the patient's immune response causes oral mucosal ulcers [13, 14].

At present, the methods of clinical treatment of oral ulcers include traditional Chinese medicine treatment, western medicine treatment, and integrated traditional Chinese and western medicine treatment [15]. Clinically, watermelon frost sprays are often used to treat patients. The watermelon frost spray is made from traditional Chinese medicine, which contains 14 kinds of Chinese medicine including cork, sophora tonkinensis, scutellaria, coptis, menthol, fritillaria thunbergii, borneol, and borax. Borax in the composition has detoxification and antiseptic effects; fritillaria thunbergii can reduce swelling and anti-inflammatory; menthol and borneol have the effects of reducing swelling and pain, detoxification, and purging fire; the three herbs of phellodendron chinense, coptis, and scutellaria can be anti-inflammatory in action; sophora tonkinensis can also reduce swelling, relieve pain, and detoxify [16]. A variety of Chinese medicinal materials are mixed, so watermelon frost has a good effect of clearing heat and detoxification, reducing swelling and pain, clearing the throat and throat, promoting mucosal regeneration, and has a good therapeutic effect on oral ulcers.

However, a single drug cannot achieve the ideal therapeutic effect for the treatment of oral ulcers. In clinical practice, a combination of drugs is often used to improve the therapeutic effect and quickly relieve the pain of patients. Kangfuxin liquid belongs to a kind of traditional Chinese medicine biological preparation, which contains abundant mucosine, peptides, polyols, and other biologically active substances [17]. Metronidazole can affect the DNA metabolism process of bacteria, promote cell death, and has a good antibacterial effect. Cydiodine buccal tablets are mainly active iodine, which is quickly released after reacting with saliva, halogenating the protein of the bacteria, thereby achieving the effect of eliminating microorganisms [18]. This article found that the combination of watermelon frost and erythromycin is the best treatment option for oral ulcers. The combination regimen is putting erythromycin and watermelon frost together in a mortar, pounding it into a fine powder, then putting it in a powder spray bottle, shaking it evenly, and spraying it on the surface of the ulcer. Erythromycin is a macrolide antibiotic extracted from the culture medium of Streptomyces erythreus [19]. From the analysis of pharmacological effects, it is the use of erythromycin to bind to the 50S subunit of the bacterial ribosome, inhibit peptide acyltransferase, and then affect the translocation of ribonucleosome. The process hinders the growth of the peptide chain and ultimately inhibits the synthesis of bacterial protein to control secondary infections [20].

4.1. Limitations of the Study. Although this study has the potential to be highly useful in the clinical treatment of oral ulcers, it has certain limitations. The side effects of the four concomitant drugs with watermelon frost were not reported in studies. Therefore, their results were not analyzed. The research only looks at Chinese studies and there is no quantitative analysis of immune system cytokines. Therefore, high-quality randomized controlled trials are needed in the future to evaluate the efficacy of combining medicines and watermelon frost in oral ulcers.

5. Conclusion

The oral ulcer is a common oral disease-causing superficial round or oval ulcer that occurs on the oral mucosa with a common symptom of local oral pain. Watermelon frost has traditionally been used for the treatment of oral ulcers. This study was designed to identify the effectiveness of four types of watermelon frost combination medications for the treatment of oral ulcers using NMA and to rank them according to their performances. These four schemes are most widely used to treat oral ulcers. Watermelon frost spray is an anti-inflammatory Chinese patent medicine. This included combinations of watermelon frost with Kangfuxin fluid, erythromycin, metronidazole, and cydiodine buccal tablets. Five randomized controlled studies of four distinct types of a combination medication for the treatment of oral ulcers were evaluated using network meta-analysis (NMA). The underlined studies were categorized into two groups: the control group (watermelon frost alone) and the observation group (one of four watermelon frost combinations). The study showed the significant efficacy of watermelon frost combination medications. In terms of clinical efficacy, the combination of watermelon frost and erythromycin was the most promising concomitant medication with 86.3 surfaces under cumulative ranking (SUCRA). This study may provide critical guidance for therapeutic medication selection in the treatment of oral ulcers. A combination of watermelon frost with erythromycin is the most promising candidate among four combinations for the treatment of oral ulcers.

Data Availability

The data used to support the findings of this study are available from the corresponding author upon request..

Conflicts of Interest

The authors declare that they have no conflicts of interest.

Hindawi
Journal of Healthcare Engineering
Volume 2023, Article ID 9836767, 1 page
https://doi.org/10.1155/2023/9836767

Retraction

Retracted: Facile Synthesis of NaYF4:Yb Up-Conversion Nanoparticles Modified with Photosensitizer and Targeting Antibody for In Vitro Photodynamic Therapy of Hepatocellular Carcinoma

Journal of Healthcare Engineering

Received 23 May 2023; Accepted 23 May 2023; Published 24 May 2023

This article has been retracted by Hindawi following an investigation undertaken by the publisher [1]. This investigation has uncovered evidence of one or more of the following indicators of systematic manipulation of the publication process:

(1) Discrepancies in scope
(2) Discrepancies in the description of the research reported
(3) Discrepancies between the availability of data and the research described
(4) Inappropriate citations
(5) Incoherent, meaningless and/or irrelevant content included in the article
(6) Peer-review manipulation

The presence of these indicators undermines our confidence in the integrity of the article's content and we cannot, therefore, vouch for its reliability. Please note that this notice is intended solely to alert readers that the content of this article is unreliable. We have not investigated whether authors were aware of or involved in the systematic manipulation of the publication process. Wiley and Hindawi regrets that the usual quality checks did not identify these issues before publication and have since put additional measures in place to safeguard research integrity.

We wish to credit our own Research Integrity and Research Publishing teams and anonymous and named external researchers and research integrity experts for contributing to this investigation.

The corresponding author, as the representative of all authors, has been given the opportunity to register their agreement or disagreement to this retraction. We have kept a record of any response received.

References

[1] J. Ding, Y. Jin, F. Zhu et al., "Facile Synthesis of NaYF4:Yb Up-Conversion Nanoparticles Modified with Photosensitizer and Targeting Antibody for In Vitro Photodynamic Therapy of Hepatocellular Carcinoma," *Journal of Healthcare Engineering*, vol. 2022, Article ID 4470510, 12 pages, 2022.

Hindawi
Journal of Healthcare Engineering
Volume 2022, Article ID 4470510, 12 pages
https://doi.org/10.1155/2022/4470510

Research Article

Facile Synthesis of NaYF4:Yb Up-Conversion Nanoparticles Modified with Photosensitizer and Targeting Antibody for In Vitro Photodynamic Therapy of Hepatocellular Carcinoma

Jingyi Ding,[1] Yan Jin,[1] Fengqi Zhu,[1] Cunle Zhu,[1] Jiang Peng,[1] Tiantian Su,[2] and Jinzhen Cai[3]

[1]*The Institute of Transplantation Science, Qingdao University, Qingdao 266000, China*
[2]*Department of Human Anatomy, Histology and Embryology, Key Laboratory of Carcinogenesis and Translational Research (Ministry of Education) and State Key Laboratory of Natural and Biomimetic Drugs, Peking University Health Science Center, Beijing 100086, China*
[3]*Organ Transplantation Center, The Institute of Transplantation Science, The Affiliated Hospital of Qingdao University, Qingdao 266000, China*

Correspondence should be addressed to Tiantian Su; sutiantian@bjmu.edu.cn and Jinzhen Cai; cai_jinzhen@126.com

Received 20 January 2022; Revised 3 February 2022; Accepted 7 February 2022; Published 8 March 2022

Academic Editor: Liaqat Ali

Rare Earth up-conversion nanoparticles NaYF4:20%Yb,2%Er@PEI (UCNPs) were generated via a one-step hydrothermal technique at relatively reduced temperatures. Photosensitizer Ce6 and anti-EpCAM, a highly expressed monoclonal antibody in cancer stem cells of hepatocellular carcinoma, were linked to UCNP surfaces via the formation of amide linkage between carboxyl from Ce6 or anti-EpCAM and abundant amino from PEI, leading to the formation of Ps-Ce6 and anti-EpCAM-UCNPs-Ce6 nanoparticles. The synthesized nanoparticles characterized by XRD, TEM, and IR, and their zeta potential, ROS generation ability, Ce6 loading rate, and up-conversion fluorescence properties were investigated. It has been revealed that all the products were uniformly dispersed nanoparticles (25–32 nm), which crystallized primarily as hexagonal structures, and their up-conversion fluorescence spectra were similar to that of NaYF4:20%Yb,2%Er. The Ce6 loading rate in the anti-EpCAM-UCNPs-Ce6 nanoparticles was about 2.9%, thereby resulting in good ROS generation ability. For anti-EpCAM-UCNPs-Ce6, the biosafety, targeting effect, and PDT effect exposed under near-infrared (NIR) laser (980 nm) were evaluated using human liver cancer cells (BEL-7404). The results showed that it has good biocompatibility and biosafety as well as high targeting and PDT treatment efficiencies, which renders it a potential experimental material for the near-infrared PDT study.

1. Introduction

As one of the most common malignant tumors globally, morbidity and mortality rates for hepatic tumors rank 6th and 4th, respectively, from all clinically observed tumor models [1]. Due to the insidious condition progression, it is typically not detected until such an illness is in the middle or advanced stages, and the 5-year survival rate is as low as 10.1%, accompanied by a poor life quality of patients [2]. Currently, chemotherapy, radiotherapy, immunotherapy, and arterial chemoembolization are the major available options for treating middle-advanced liver cancer [3]. However, there are quite a few disadvantages of these methods, such as systemic toxicity, radiation damage, low selectivity as well as drug resistance [4, 5]; hence, developing safe and efficient treatment plans for malignant tumors is a major need.

Recently, nanomaterial-based photodynamic therapy (PDT) has received wide attention and has become an important research niche for cancer treatment [6, 7]. PDT is a noninvasive treatment, and its basic principle is as follows: after the photosensitizer ingested by the tumor cells is excited by light of a certain wavelength, it is capable of transferring the absorbed energy to the ambient oxygen present, developing reactive oxygen species (ROS) that can lead to oxidation-driven dysfunction within mitochondria and DNA, causing cell apoptosis and necrosis, thereby curing cancer [8]. In comparison to traditional cancer treatments, PDT has several advantages, such as less trauma, good applicability, accurate targeting, low toxicity, and low cost, and is well established in treating esophageal tumors, skin cancer, and other tumors with excellent curative effect [9–11]. However, most photosensitizers used in traditional PDT treatment are porphyrins or phthalocyanine derivatives, which suffer from poor hydrophilicity and biocompatibility, and cannot be easily transported to the tumor site [12, 13]. Furthermore, the ultraviolet-visible (UV-Vis) light for exciting the photosensitizer is easily absorbed or quenched by biological tissues, thus the depth of penetration is minimized, and it can easily cause light damage to biological tissues. Therefore, PDT treatment is now limited to the treatment of superficial or tiny tumors, but the impact of the treatment of traditional PDT for deep tumors is rather unsatisfactory [14, 15].

Up-conversion luminescent materials can convert long-wave radiation with lower energy to short-wave radiation with higher energy mediated by two-/multi-photon techniques, also referred to as antiStokes shift [16]. For example, hexagonalβ-NaYF4:Yb, Er is a well-known up-conversion luminescent material with high efficiency, which can generate UV-Vis fluorescence with high intensity and low-nonspecific fluorescence background under the excitation of near-infrared (NIR) laser [17]. More importantly, the infrared band (700–1000 nm) lies inside a bio-optical window, which can reduce the extent of light absorption by biological tissues. In addition, the penetrability of NIR into tissue is stronger, and the light damage of NIR to the organism is relatively less in comparison to that of ultraviolet light [18]. The up-conversion nanoparticles (UCNPs) suitable for biological application can be synthesized with many chemical methods together with further surface functional modification by photosensitizers, hydrophilic groups, targeting agent, specific antibodies, and so on, to facilitate the PDT for deep-tissue cancers, improving selectivity and biocompatibility and reducing side effects [19–21].

The materials used in PDT must be very small monodisperse nanoparticles having good water solubility. Monodisperse β-NaYF4:Yb, Er nanoparticles, having a high intensity of up-conversion fluorescence, were usually synthesized through pyrolysis method comprising dissolution, precursor formation (150°C), distillation for the removal of methanol (70°C), and pyrolysis (300–320°C) for promoting the cubic-to-hexagonal phase transformation [22]. However, there are some obvious disadvantages of this method, such as complicated and long procedure, production of large amount refractory waste solvent due to the oxidation, polymerization, and pyrolysis of octadecene and oleic acid upon attaining elevated temperatures. Furthermore, the oleic acid linked to β-NaYF4:Yb, Er surfaces is highly hydrophobic; thus, it needs to be removed and subsequently substituted by hydrophilic groups through various kinds of physical and chemical methods.

Polyethyleneimine (PEI) has a large number of amino groups with high reactivity and polarity and an abundance of positive charges. Accordingly, surface modification of the β-NaYF4:Yb, Er nanoparticles by PEI could not only increase the hydrophilicity but also conveniently increment the reactive activity for further functionalization. At the same time, the positive charge on the PEI surface can adhere to negatively charged residues upon cellular surfaces and penetrate via endocytosis for promoting drug uptake, a phenomenon known as enhanced permeability and retention effect (EPR) [23, 24].

However, relying only on the EPR causes passive accumulation of UCNP in the body, reducing the overall therapeutic effect. If some specific molecules are conjugated onto the surface of UCNPs, such as the monoclonal antibody anti-EpCAM, which can target the surface marker epithelial cell adhesion molecule (EpCAM) of the cancer stem cells of hepatocellular carcinoma, the nanosystem would possess an active targeting effect. EpCAM consists of a transmembrane glycoprotein that is mainly present within epithelial/progenitor/normal/malignant stem cells and a variety of tumor cells [25]. EpCAM expression profile changes dynamically throughout hepatic maturation. It can be detected in both bile duct plate cells and liver parenchyma cells within fetal/neonatal livers, particularly in the former, then decreases significantly with age till it practically disappears in the liver of healthy adults [26, 27]. However, during the occurrence and development of hepatocellular carcinoma, liver pathological changes are linked to potent EpCAM reexpression, and EpCAM expression by liver cancer cells is significantly higher in comparison to that in normal epithelial cells [28]. If the anti-EpCAM and photosensitizer are assembled on the surface of UCNPs via chemical reactions, it would presumably result in a good NIR-PDT method with high targeting ability and low side effects for hepatocellular carcinoma. There are a few reports on the conjugation of specific antibodies with UCNPs; however, most of them were coated with mesoporous silica. Surface modification of UCNPs with both specific antibodies and photosensitizer by using PEI as a bridge has been rarely reported [29, 30].

In this study, monodisperse UCNPs (β-NaYF4:Yb, Er@PEI) were generated via one-step hydrothermal technique at a relatively reduced temperature. The photosensitizer chlorin e6 (Ce6) and anti-EpCAM were further assembled over UCNP surfaces through the formation of amide linkage, constructing an anti-EpCAM-UCNPs-Ce6 nanoplatform, which was identified through X-ray diffraction (XRD), transmission electron microscopy (TEM), infrared spectrum (IR), and UV-Vis spectrum. In addition, the cell line BEL7404 was used to evaluate the biosafety of anti-EpCAM-UCNPs-Ce6, and in-cell PDT and cell-targeted uptake experiments were conducted to provide basic data for the clinical application of the system. The principle of PDT for liver cancer cells based on upconversion nanoparticles modified by Ce6 and anti-EpCAM is shown in Scheme 1.

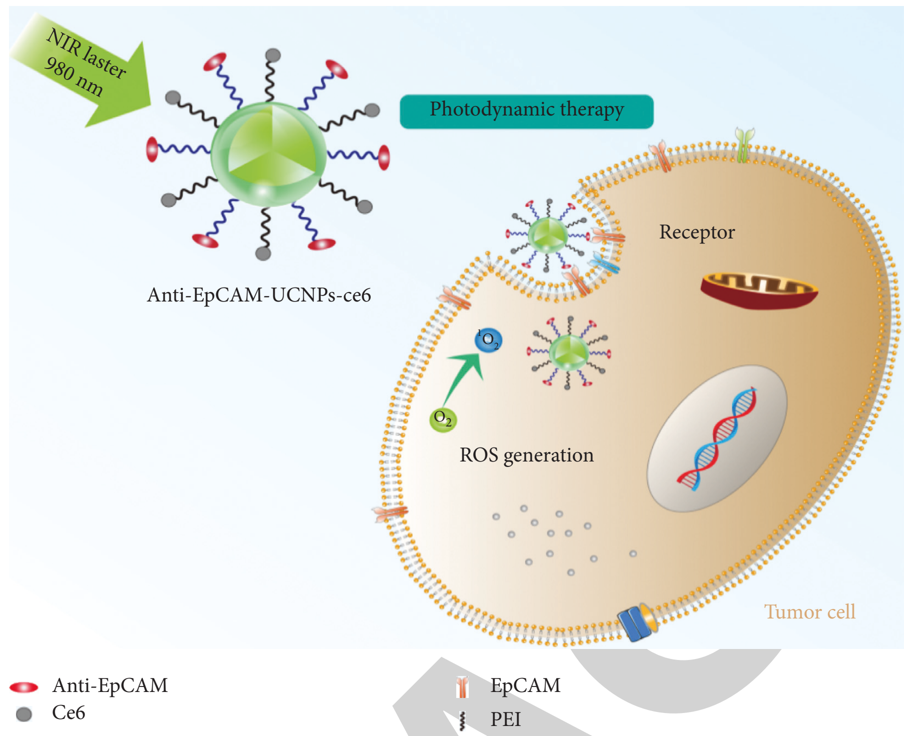

Scheme 1: Schematic diagram depicting PDT therapy of anti-EpCAM-UCNPs-Ce6 nanoplatform in vivo. After binding with EpCAM-expressing hepatoma cells, PDT could be achieved after irradiation at 980 nm.

2. Methodology

2.1. Materials and Cell Lines. $Er(NO_3)_3 \cdot 5H_2O$ (99.9%), $Yb(NO_3)_3 \cdot 5H_2O$ (99.9%), $Y(NO_3)_3 \cdot 6H_2O$ (99.9%), NaOH (analytical purity AR), absolute ethanol (AR), hydroxyethyl cellulose (AR, viscosity of 20,000 mPa s), polyethyleneimine (PEI, M.W. = 10000, 99%), NH4F (98%), concentrated hydrochloric acid (AR, 37%), dimethyl sulfoxide (DMSO, AR), 1-(3-dimethylamino propyl)-3-ethyl-carbodiimide hydrochloride (EDC, 98%), N-hydroxysuccinimide (NHS, 98%), phosphate-buffered saline (PBS, pH = 7.2–7.4), chlorin E6 (Ce6, 94%), and 1,3-diphenylisobenzofuran (DPBF, 99.9%) were procured through Sigma-Aldrich™ (St. Louis, USA). Anti-EpCAM monoclonal antibody was procured through eBioscience (San Diego, USA). A cellular proliferation kit (CCK-8) was procured through Abcam™ (Shanghai, China). 4′,6-Diamidino-2-phenylindole, dihydrochloride (DAPI) was procured through Sigma-Aldrich Chemicals™ (Sydney, Australia).

The human hepatocellular carcinoma cell line BEL-7404 was obtained from ATCC (Shanghai, China), and the LO_2 cell line was obtained from the Affiliated Hospital of Qingdao University, China. BEL-7404 cultures were grown within RPMI-1640 medium, and LO_2 cells were grown within DMEM augmented by 10% fetal bovine serum (FBS)/1% penicillin-streptomycin at 37°C within a humidified atmosphere carrying 5% CO_2.

2.2. Generation of Targeted UCNPs

2.2.1. Generation of NaYF4:20%Yb,2%Er@PEI (UCNPs). For creating UCNPs, 0.5 g NaOH, 0.5 g $YCl_3.7H_2O$ (1.56 mmol), 0.15 g $YbCl_3.6H_2O$ (0.4 mmol), 0.015 g $ErCl_3.6H_2O$ (0.04 mmol), 1.0 g polyethylene imine (PEI, AR, $M = 20{,}000$), 0.5 g NH_4F, 0.2 g hydroxyethyl cellulose (AR, viscosity of 20,000 mpa s), and 40 ml deionized water were added to the inner tank of a polytetrafluoroethylene reactor and stirred evenly to yield a viscous semifluid. The pH was optimized for 6.5–7.0 using 6 M HCl, and then the stainless reactor shell was applied to seal the reactor. The reactor was placed in a homogeneous reactor with a rotating shaft at 80 rpm, allowed to react at 150°C for 10 hours, and left to cool down naturally after the reaction. The initial product was centrifuged at 5,000 rpm (5 minutes), mother liquor was removed, with the precipitate washed three times using 5 mL deionized water (5,000 rpm). Subsequently, 5 ml DMSO was added to the washed precipitate for ultrasonic dispersion and centrifuged at 14,000 rpm, and the mother liquor was discarded. The precipitate was centrifuged again and washed with DMSO thrice, and the solid products were freeze dried.

2.2.2. Synthesis of UCNPs-Ce6. The activated Ce6 solution was obtained by dispersing 5 mg Ce6, 15 mg EDC, and 15 mg NHS within 25 mL DMSO, with the solution mixed at ambient temperature for 120 minutes. Consequently, 20 mg UCNPs were added into 10 mL DMSO and dispersed by ultrasonication to obtain a uniform solution. The solution was mixed with the activated Ce6 solution, stirred at room temperature, and reacted in dark for 12 hours. After the reaction, the product was centrifuged (14,000 rpm), and the mother liquor was removed, with crude solid product washed using 5 mL DMSO thrice and subsequently freeze dried.

2.2.3. Synthesis of Anti-EpCAM-UCNPs-Ce6. The mixture of UCNPs-Ce6 (2 mg) and PBS buffer (10 ml) was shaken for 30 minutes, centrifuged, with precipitate washed four times using PBS (14,000 rpm). Then 10 mL PBS and 40 μg anti-EpCAM were introduced into obtained solid, and the mixture was shaken completely (30 minutes) and then centrifuged. Precipitate was washed thrice using PBS for removing unreacted antibodies, with such product being ultrasonically dispersed in PBS. The schematic diagram of the material synthesis is shown in Figures 1 and 2.

2.3. Characterization of Nanomaterials. An X-ray diffractometer was used to record the XRD patterns to characterize the phase of the materials, using Cu Kα ($\lambda = 1.54056$ Å) as the radiation source at a functional voltage of 40 kV, a functional current of 100 mA, a scanning rate of 8°/min, and a step size of 0.02°.

IR spectrums of the materials were recorded using the potassium bromide pressed-disk method to detect the characteristic functional groups across material surfaces. Scanning range was 650–4000 cm^{-1}, and the resolution was 4 cm^{-1}.

TEM images were taken by JEM-2100F TEM in bright-field mode at an operating voltage of 200 kV to determine the morphology and size of the materials. The sample preparation for TEM microscopy is as follows: the freeze-dried materials were dispersed in ethanol solution at a concentration of about 0.1 mg/mL, which were ultrasonicated for 10 minutes. Then, 10 μL of the solution was dropped onto the carbon film microgrid and dried naturally.

The nanoparticles were ultrasonically dispersed in deionized water for 15 minutes to record the fluorescence spectrums by using a fluorescence spectrophotometer with a 980 nm laser (IR range) as an excitation source. Test condition is as follows: 1 kW of the power of the laser, 0.2 nm of the emission slit, and 450–700 nm of the scanning range.

The zeta potentials of the nanoparticles, which were dispersed into de-ionized water to render a solution (2 mg/mL), were measured with a zeta potentiometer (SOE-070) at 25°C.

2.4. ROS Generation Ability Detection. After DPBF captured the ROS generated by the photosensitizer, the absorption intensity between 350 and 470 nm weakened. UCNPs-Ce6 was dispersed in DPBF-ethanol as a solution of 50 mg/L standing in the dark for 1 hour allowing DPBF to adsorb UCNPs-Ce6. The solution was irradiated using a 980 nm laser (power density = 1.0 W/cm^2) and sampled every 5 minutes. UV-Vis absorption spectra for this solution were determined using UV-Vis spectrophotometry. Test conditions were as follows: scanning range: 200 nm–1100 nm; slit width: 2.0 nm, and sampling interval: 0.5 nm. The absorption peak intensity-time curve was drawn at 420 nm.

3. Cellular Experiments

3.1. Nanoparticle Cytotoxicity Test. As a potential material for use in human therapy, the nanoparticles must have low toxicity. Normal human liver cells (LO_2) were employed for evaluating in vitro cytotoxicity by synthesized nanoparticles. LO_2 cultures were introduced into a 96-well plate (2×103 cells/well) and placed into incubation at 37°C and 5% CO_2 (approximately 12 hours). The UCNPs/UCNPs-Ce6/anti-EpCAM-UCNPs-Ce6 were divided into two groups, cultured with DMEM medium, and used to prepare solutions at different concentrations (3.9–500 μg/mL). Each group was tested in three wells, along with the blank control group, and cultured at 37°C and 5% CO_2 (24 and 48 h, respectively). Experimental cultures and 100 μL CCK-8 were incubated for 4 hours. Optical density value (OD value) for individual wells was calculated through a microplate reader at 450 nm, using the following formula for cellular inhibition rates: inhibition rate = ((OD value of control group − OD value of treatment group)/OD value of control group) × 100%.

3.2. Targeting Uptake Ability of Anti-EpCAM-UCNPs-Ce6. In order to probe the targeting ability for generated nanoparticles, we used human liver cancer cell line BEL-7404 (2×103 cells/well), in which the EpCAM expression rate as measured by flow cytometry was 51.55%. The BEL-7404 cells (2×103 cells/well) were inoculated into 6-well plates until the adherent growth reached about 80%. The cells were exposed to 200 μg/mL anti-EpCAM-UCNPs together with nontargeted UCNPs (not combined with anti-EpCAM) and pretreated with 20 μL of free anti-EpCAM (0.1 μg/mL) for the blocking test. In the next step, cultures were washed thrice using PBS for removing free nanoparticles. Cultures were placed again into incubation with 2 μg/mL DAPI for nuclear staining. Then, samples were observed and detected using an external 980 nm light source under an inverted fluorescence microscope. Image J software was employed for semiquantitative calculation of the green fluorescence intensity of the cytoplasm in each group.

3.3. Effect of External PDT of Anti-EpCAM-UCNPs-Ce6. Bel-7404 cells were plated into 6-well plates (105 cells/well) and cultured at 37°C and 5% CO_2 for 24 hours. Cultures were divided into a NIR group, Ce6 group, UCNPs-Ce6 group, anti-EpCAM-UCNPs-Ce6 group, and UCNPs group. An RPMI1640 (medium) group served as control group. The concentration gradient for Ce6 was 1 μg/mL. Cultures were irradiated through a 980 nm NIR laser (power density = 320 mW/cm^2 for 5 minutes) and then placed in a cell incubator for further culturing for 24 hours. The survival rate of the cells was determined (450 nm) in a microplate

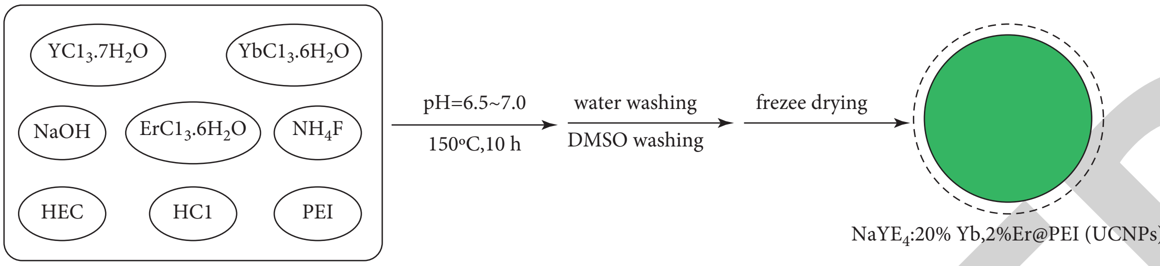

Figure 1: Schematic diagram illustrating the hydrothermal generation of NaYF4:20%Yb,2%Er@PEI(UCNPs).

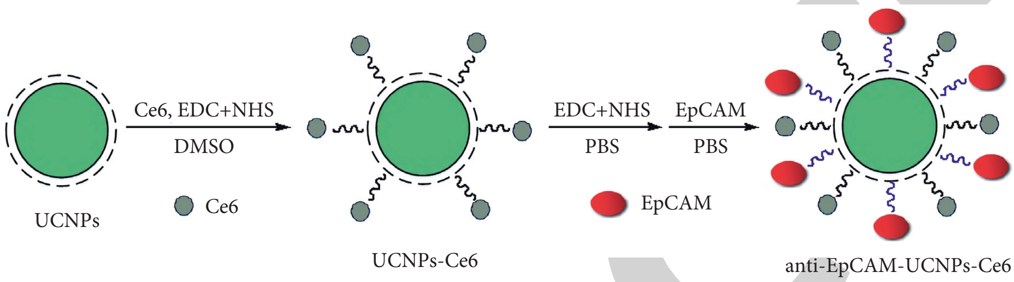

Figure 2: Schematic diagram illustrating UCNPs surface modification.

reader. The CCK-8 was used to measure cellular proliferation in this experiment.

4. Results and Discussion

4.1. Phase and Morphology Analysis. The XRD patterns of UCNPs and UCNPs-Ce6 are shown in Figure 3. The results show that the two exist in similar phases, indicating that the crystal structure of the UCNPs did not change following the attachment of Ce6 to the surface. The main phase was isomorphic to hexagonal NaYF4 (β-NaYF4, JCPDS 16-0344), and some were isomorphic to cubic NaYF4 (β-NaYF4, JCPDS 77-2042), with a small amount of unknown impurities.

Figures 4(a)–4(c) are TEM photos of UCNPs, UCNPs-Ce6, and anti-EpCAM-UCNPs-Ce6. Their particle sizes are approximately 25 nm, 28 nm, and 32 nm, respectively. All nanoparticles had good dispersibility and are suitable for biological applications.

UCNPs nanoparticles that mainly crystallized in a hexagonal structure, in this study, were generated using one-step hydrothermal technique through hydroxyethyl cellulose serving as a crystal growth inhibitorandPEI as a surface modifier. The products had a high polarity and good water dispersion properties. The reaction temperature (150°C) for this method was significantly lower than that used in the high-temperature thermal decomposition method [22]. Besides, the synthesis step was simple, without employing any long-chain fatty acids, thereby avoiding the complicated postprocessing process, which thus opens new paths for the research and application of β-$NaYF_4$-based up-conversion fluorescent materials.

4.2. IR and Zeta Potential Analysis. Figure 5 shows the IR spectra for UCNPs, UCNPs-Ce6, and anti-EpCAM-UCNPs-Ce6. Regarding IR spectrum for UCNPs, the peaks occurring at 3427, 2957, 1470, and 1314 cm^{-1} correspond to N-H stretching vibrations, C-H stretching/bending vibrations, and C-N stretching vibrations, respectively, which all originated from PEI, indicating that PEI successfully modified NaYF4:20%Yb, 2%Er nanoparticle surfaces, and abundant amino groups increased the polarity of the UCNPs, resulting in good hydrophilicity. On the other hand, no C-O stretching vibration peaks (strong and wide peak between 1000 and 1200 cm^{-1}) were observed, indicating that hydroxyethyl cellulose is only used as a reaction medium during the synthesis process, whose role was to probably form a uniform dense gel inhibiting the growth of UCNPs particles.

Regarding IR spectrum for UCNPs-Ce6, peaks appearing at 3422, 2967, 1652, 1541, 1455, 1267, and 1116 cm^{-1} corresponded to N-H and O-H and/or C-H stretching vibrations, C=O stretching vibrations, N-H bending vibrations in amide, C-H stretching vibrations, C-N stretching vibrations, and C-O stretching vibrations, respectively. Besides absorption peaks for characteristic PEI groups, there were also characteristic peaks for C=O, C-O, and amide N-H bending vibrations, which indicated that amide bond formation reaction occurred between -NH2 from PEI on the surface of UCNPs and -COOH from Ce6; thereupon, then the photosensitizer Ce6 was firmly and chemically bonded to the surface of the upconversion nanomaterial. However, the conjugate structure of Ce6 itself did not change, thus it still could generate ROS under the excitation of visible light at a certain wavelength and can be used as the active component of PDT.

In the IR spectrum of anti-EpCAM-UCNPs-Ce6 the peaks at 3357, 2936, 1642, 1557, 1445, 1267, 1197, 1121, 909 cm^{-1} were in line with N-H stretching vibrations and O-H stretching vibrations, C-H stretching vibrations, C=O stretching vibrations in amide, N-H bending vibrations in

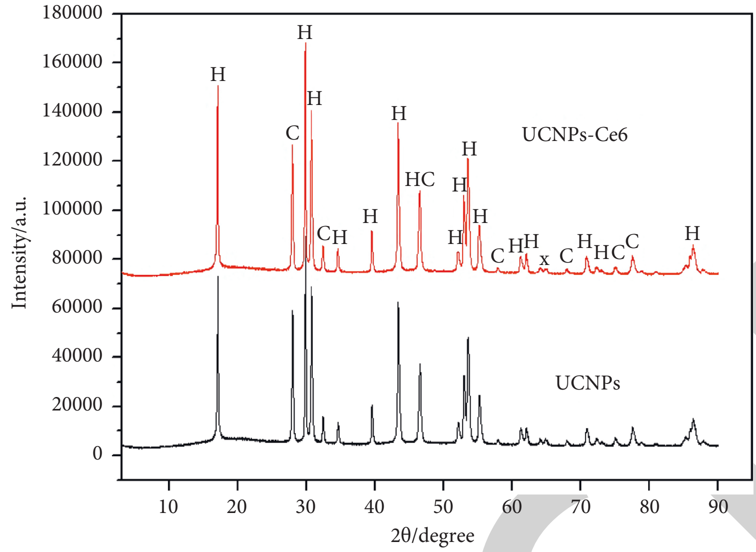

Figure 3: XRD patterns of UCNPs and UCNPs-Ce6 nanoparticle powders, in which *H* is the diffraction peak for hexagonal phase, *C* is the diffraction peak for cubic phase, and *X* is the diffraction peak of unknown impurities.

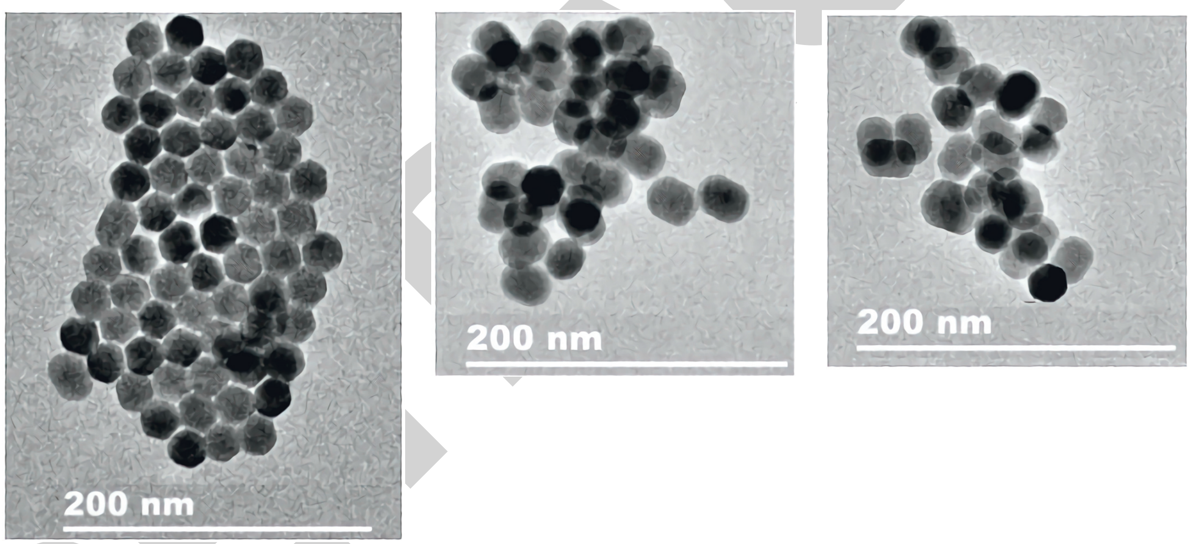

(a) (b) (c)

Figure 4: TEM images of powdered nanoparticles. (a) UCNPs. (b) UCNPs-Ce6. (c) Anti-EpCAM-UCNPs-Ce6.

amide, C-H stretching vibrations, C-N stretching vibrations, P=O stretching vibrations, C-O stretching vibrations, and P-O-C stretching vibrations. In addition to the IR absorption peaks of the characteristic groups of UCNPs-Ce6, there were also P=O stretching vibrations and P-O-C stretching vibrations, which came from the phospholipid acyl group in the anti-EpCAM antibody, indicating that anti-EpCAM was successfully loaded onto the surface of the nanoparticles.

UCNPs, UCNPs-Ce6, and anti-EpCAM-UCNPs-Ce6 had zeta potentials of 32.1, 17.5, and 10.2 mV, respectively. Due to the abundance of positive charges on the surface of PEI, UCNPs treated simply with PEI have a rather high zeta potential. The zeta potentials of Ce6 and anti-EpCAM were reduced to 17.5 mV and 10.2 mV, respectively, when they chemically bound to the amino groups on the PEI surface, substantially reducing the damage caused by positive charges on cell membranes. The modest amount of positive charge on the surface of nanoparticles, on the other hand, prevents nanoparticle aggregation and allows them to penetrate cells.

4.3. ROS Generation Ability. DPBF is a commonly used ROS-capture agent. After it is oxidized by ROS, the characteristic absorption peak in the 350~450 nm range would be significantly weakened. Therefore, DPBF can be used to detect the ability of materials to generate ROS. To 5 mL of anti-EpCAM-UCNPs-Ce6 ethanol solution (2 mg/mL), 0.5 mg DPBF were introduced, with such mixture stirred in dark conditions. The mixed solution was simultaneously

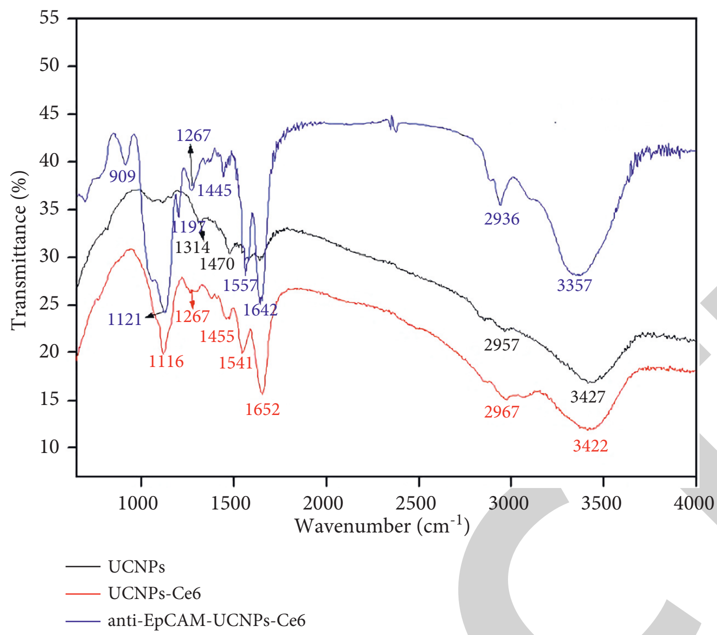

Figure 5: IR spectra of UCNPs, UCNPs-Ce6, and anti-EpCAM-UCNPs-Ce6.

irradiated with a 980 nm laser (1.0 W/cm^2) for various timeframes. Postirradiation, the mixture solution was centrifugated at 13,000 rpm for 5 minutes to discard the anti-EpCAM-UCNPs-Ce6 nanoparticles, with UV-Vis spectra of the supernatant determined. Figure 6 shows the UV-Vis spectra of eight samples subjected to the same treatment process and irradiation for 0, 5, 10, 15, 20, 25, and 35 minutes, respectively. The results show that, with the prolongation of irradiation time, the intensity of the characteristic absorption peaks in the 350~450 nm range gradually decreased, indicating that anti-EpCAM-UCNPs-Ce6 generated ROS under 980 nm infrared laser irradiation, which demonstrates its potential for application in PDT research fields.

4.4. Ce6 Loading Rate Testing. A predetermined amount of Ce6 was dissolved in ethanol to form a series of solutions of 1, 5, 10, 15, and 20 μg/mL. The absorbance of these solutions at the maximum absorption wavelength of Ce6 (404 nm) was determined through UV-Vis spectrophotometry, and the standard curve of Ce6 absorbance against concentration was drawn, as shown in Figure 7. The linear regression equation for the standard curve was $A = 0.216c - 0.001$, and the correlation coefficient was $R = 0.9929$. Then, 2 mg anti-EpCAM-UCNPs-Ce6 was added to 5 mL ethanol and dispersed uniformly via ultrasonication to form the solution of nanoparticles, and its absorbance at 404 nm was determined through UV-Vis spectrophotometry. According to such calculation, [Ce6] in anti-EpCAM-UCNPs-Ce6 was 11.56 (μg/mL) $\times$ 5 mL/2 mg = 2.9%.

4.5. Up-Conversion Fluorescence Properties. The nanoparticles were dispersed in deionized water and homogenized ultrasonically for 15 minutes to produce an aqueous nanoparticle dispersion of 1 mg/mL to record their up-conversion fluorescence spectrum under the excitation of a 980 nm infrared laser having 1.0 kW power. As shown in Figure 8, the emission spectra for UCNPs, UCNPs-Ce6, and anti-EpCAM-UCNPs-Ce6 were quite similar to the up-conversion fluorescence spectra of NaYF4:20%Yb,2%Er reported in many previous reports [17, 22], which indicates that the surface modifications of UCNPs by Ce6 and anti-EpCAM do not change their up-conversion fluorescence properties but decrease the fluorescence intensity of the materials. Ce6 can produce ROS under the excitation of the up-conversion fluorescence, which demonstrates their potential for use in PDT.

4.6. Nanomaterial Toxicity Tests. The cytotoxicity of the UCNPs, UCNPs-Ce6, and anti-EpCAM-UCNPs-Ce6 nanoparticles on human normal hepatocytes (LO_2) was demonstrated by CCK-8 testing. PEI has a large amount of positive charge on its surface, which is destructive to cell membranes and has a demonstrated cytotoxicity. However, as evident from Figure 9, UCNPs have low toxicity, which is presumably because the protonated amino nitrogen atoms on the PEI surface replace some of the Na+ in β-NaYF4:Yb, Er, thus reducing the number of surface positive charges. With the surface modification of UCNPs by Ce6 and anti-EpCAM, the positive charge on the surface of the entire nanoparticle is further reduced. This observation is also quite consistent with the zeta potential values (32.1, 17.5, and 10.2 mV) recorded for the above three materials. The PEI coated on the surface of anti-EpCAM-UCNPs-Ce6 material contains an abundance of polar groups, which confers increased water solubility. Meanwhile, the coupling of the photosensitizer and specific antibody with amino groups on the surface of PEI not only introduces photoactive and targeting groups but also significantly reduces its

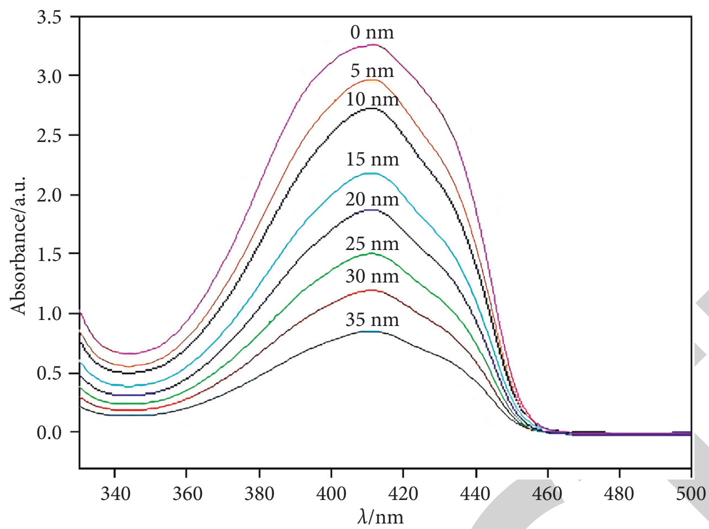

Figure 6: Anti-EpCAM-UCNPs-Ce6 after being adsorbed, the variation of the characteristic absorption peak of the ultraviolet spectrum (350–450 nm) of DPBF with the irradiation time of infrared laser (980 nm).

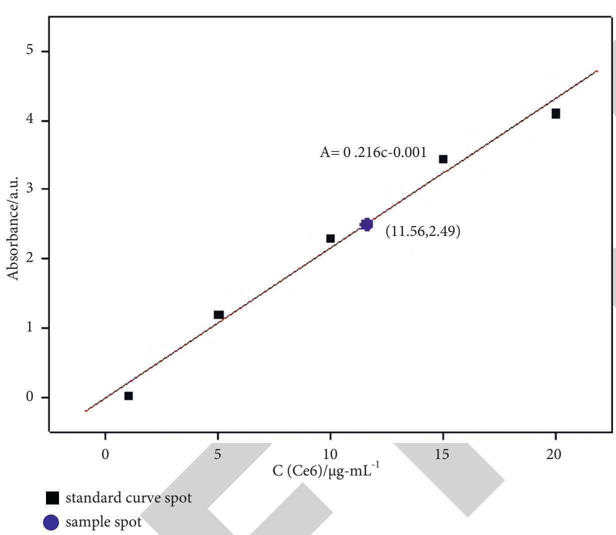

Figure 7: Standard curve and the load rate of Ce6.

cytotoxicity, thus rendering good biocompatibility. The cell survival rate was highest when anti-EpCAM-UCNPs-Ce6 was applied at the highest concentration (500 μg/mL).

4.7. In Vitro Targeting Ability of the Nanomaterial. The anti-EpCAM monoclonal antibody was used to label the BEL-7404 cell line. The flow cytometric analysis revealed that the EpCAM expression rate of this cell line was 51.5%, as shown in Figure 10. Inverted fluorescence was employed for monitoring potential by anti-Epti-EpCAM-UCNPs to target the EpCAM-positive hepatoma cell BEL-7404. As seen in Figure 10, the targeted group's cytoplasm had a strong green, fluorescent signal, indicating that the EpCAM antibody conjugated to the targeted material group had interacted with the EpCAM antigen on the cell surface, enhancing the cells' absorption capacity for the materials. However, there was a small amount of fluorescent signal in the cytoplasm of the nontargeted group, which could be because the nontargeted material only entered the cells through nonspecific endocytosis. This implies that its intake was markedly reduced in comparison to targeted material. Cultures in the blocking group were first treated with an anti-EpCAM monoclonal antibody for 4 hours before being incubated with anti-EpCAM-UCNPs. After washing, the intensity of the green, fluorescent signal in the cytoplasm was the lowest among the three groups. This is because, after pretreatment with an anti-EpCAM monoclonal antibody, the antigen-binding site on the cell was blocked, resulting in a significant reduction in the uptake of targeted nanomaterials by the cell and a weak green signal. The semiquantitative analysis of the green fluorescence signal of each group by Image J showed that the results were consistent with the observations under an inverted fluorescence microscope, and the fluorescent signal values of each group were significantly different statistically. The results showed that the EpCAM antibody ligand enhanced the uptake of nanoparticles by hepatocellular carcinoma cells.

4.8. In Vitro Antitumor Effect Study. To test the antitumor influence by nanoparticles when excited at 980 nm NIR light in vitro, a 980 nm NIR laser (power density of 320 mW/cm^2) was used to irradiate the material, and cells in the NIR group, control group (RMPI1640), Ce6 (100 μg, concentration: 1 μg/ml), Ce6-UCNPs group (100 μg), anti-EpCAM-UCNPs-Ce6 group (100 μg), and UCNPs (100 μg) group were analyzed with the CCK-8. As shown in Figure 11, 980 nm NIR irradiation alone had no significant cell-killing ability, the cell death rate in the anti-EpCAM-UCNPs-Ce6 group was markedly elevated in comparison to other groups, and the apoptotic rate was 87.57% for 100 μg/mL anti-EpCAM-UCNPs-Ce6.

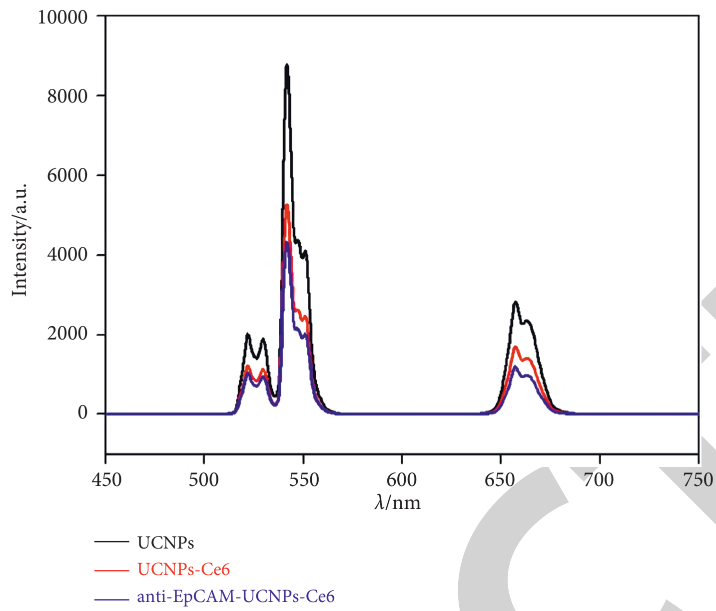

Figure 8: Up-conversion fluorescence spectra for UCNPs, UCNPs-Ce6, and anti-EpCAM-UCNPs-Ce6 under the excitation of 980 nm infrared laser.

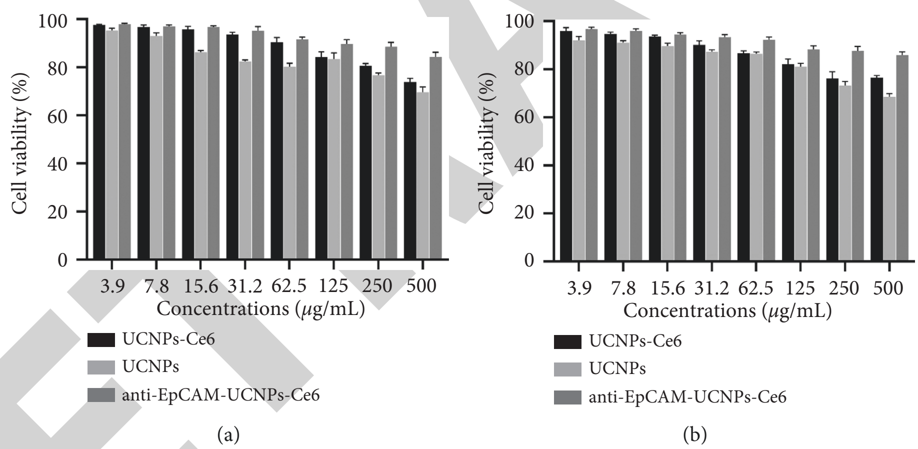

Figure 9: Cytotoxicity assay results of the anti-EpCAM-UCNPs-Ce6 nanoplatform. (a) Cell viability of LO_2 cells following 24 h coincubation with different concentrations of anti-EpCAM-UCNPs-Ce6/UCNPs/UCNPs-Ce6. (b) Cell viability of LO_2 cells incubated with differing doses of anti-EpCAM-UCNPs-Ce6/UCNPs/UCNPs-Ce6 for 48 h.

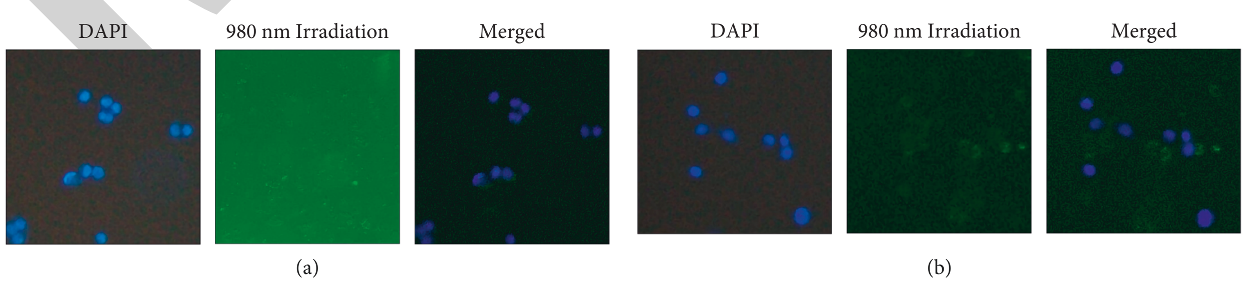

Figure 10: Continued.

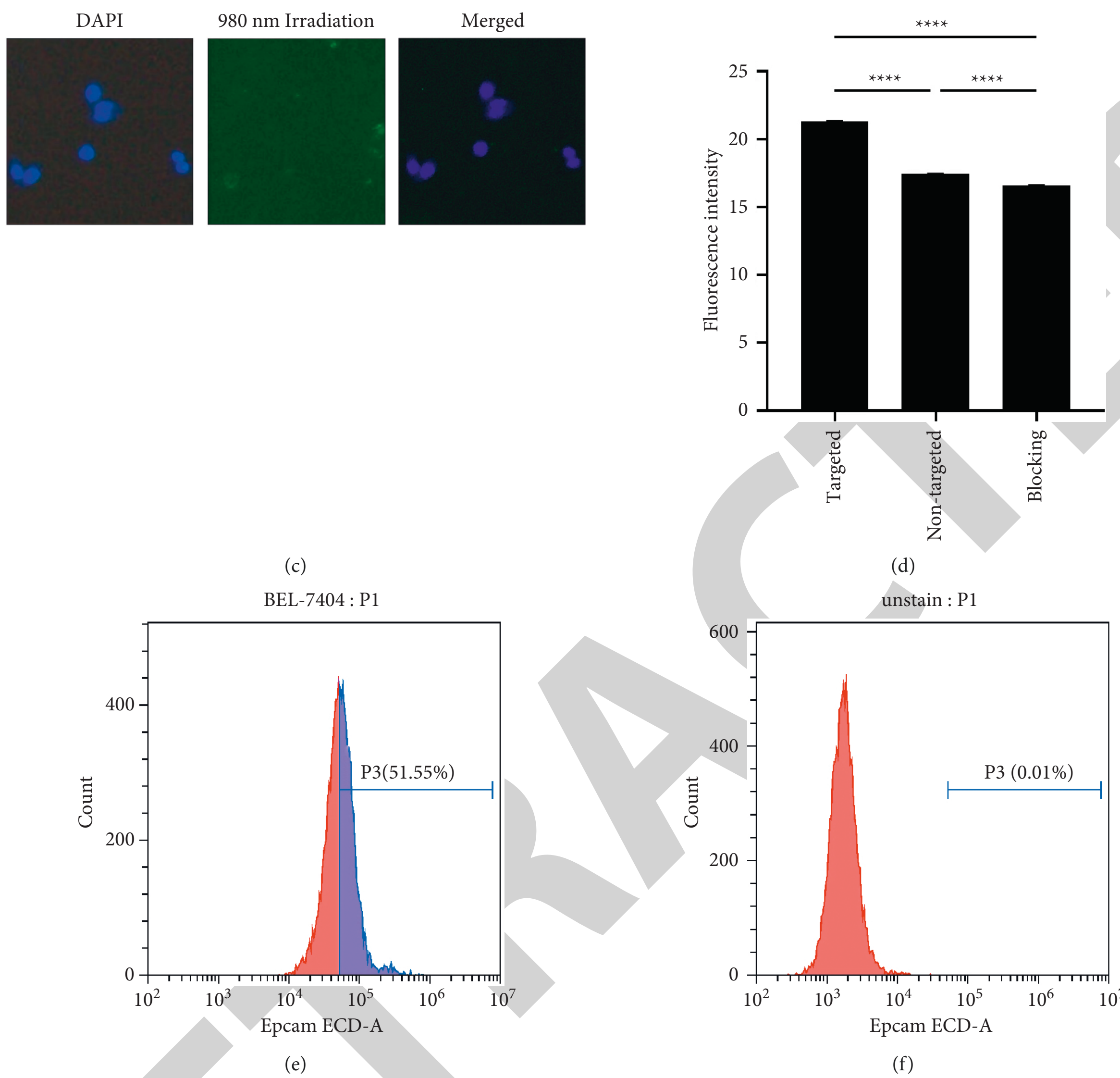

Figure 10: Results of in vitro targeting of materials evaluated by fluorescence inversion. (a) Results of UCNPs-ce6 coincubation with BEL-7404 cells after 4 h. (b) Results of BEL-7404 cells photographed after 4 h incubation with anti-EpCAM-UCNPs-ce6. (c) The result after coincubation of BEL-7404 cells with an anti-EpCAM monoclonal antibody, followed by coincubation with anti-EpCAM-UCNPs-ce6 for 4 h. (d) Semiquantitative plots of cellular fluorescence values in different treatment groups ($^{****}P < 0.0001$). EpCAM expression in the BEL-7404 cell line. (e) Flow cytometric plot of cells and anti-EpCAM monoclonal antibody after coculture. (f) Blank control: graph of the flow results of cells without any labeling.

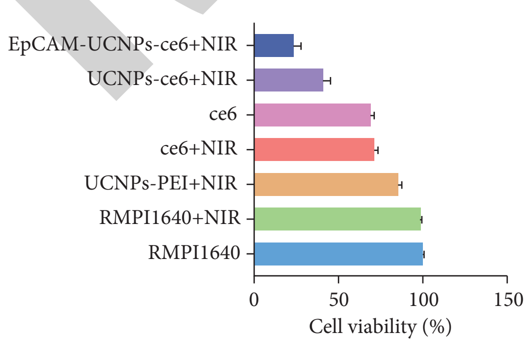

Figure 11: Results of the PDT effect study of the anti-EpCAM-UCNPs-Ce6 nanoplatform. The figure shows the survival of BEL-7404 after being given different conditions.

5. Conclusion

In this research, an up-conversion nanoplatform (anti-EpCAM-UCNPs-Ce6) comodified by Ce6 and anti-EpCAM was successfully fabricated. The preparation process avoided the traditional high-temperature pyrolysis as well as solvent wastage This platform organically combines the effects of NIR PDT—low light damage and deep tissue penetration—with the targeting properties of anti-EpCAM and shows good biocompatibility and excellent up-conversion fluorescence performance. In vitro experiments showed that the platform has good biosafety, targeting, and PDT tumor treatment effects under the action of NIR light (980 nm).

Abbreviations

UCNPs: Up-conversion nanoparticles
PDT: Photodynamic therapy
PEI: Polyethyleneimine
Ce6: Chlorin e6
Anti-EpCAM: Epithelial cell adhesion molecule antibody
XRD: X-ray diffraction
TEM: Transmission electron microscope
IR: Infrared spectrum
ROS: Reactive oxygen species
NIR: Near infrared
UV-Vis: Ultraviolet-visible
AR: Analytical purity
DMSO: Dimethyl sulfoxide
EDC: 1-(3-Dimethylamino propyl)-3-ethylcarbodiimide hydrochloride
NHS: N-Hydroxysuccinimide
DPBF: 1,3-Diphenylisobenzofuran
CCK-8: Cell counting kit-8
DAPI: 4′,6-Diamidino-2-phenylindole, dihydrochloride
PBS: Phosphate-buffered saline
FBS: Fetal bovine serum
OD value: Optical density value.

Data Availability

The data that support the findings of this study are available from the corresponding author upon reasonable request.

Consent

Not applicable.

Conflicts of Interest

The authors declare no conflicts of interest.

Authors' Contributions

Conceptualization was carried out by J. C. and T. S.; methodology was designed by J. D. and J. Y.; software was provided by J. D. and F. Z.; validation was done by C. Z. and P. J.; investigation was carried out by J. D. and J. Y.; original draft preparation was done by J. D.; review and editing were carried out by J. D.; supervision was performed by J. C.; project administration was conducted by J. C. All authors have read and agreed to the published version of the manuscript.

Acknowledgments

This research was supported by the National Natural Science Foundation of China (grant number: 81900575).

References

[1] B. Freddie, F. Jacques, I. Soerjomataram, R. L. Siegel, L. A. Torre, and A. Jemal, "Global Cancer Statistics 2018: GLOBOCAN Estimates of Incidence and Mortality Worldwide for 36 Cancers in 185 Countries," *CA Cancer*, a cancer journal for clinicians, vol. 68, no. 6, , 2018.

[2] H. Zeng, R. Zheng, Y. Guo et al., "Cancer survival in China, 2003-2005: a population- based study," *International Journal of Cancer*, vol. 136, no. 8, 2013.

[3] D. Anwanwan, S. K. Singh, S. Singh, V. Saikam, and R. Singh, "Challenges in liver cancer and possible treatment approaches," *Biochimica et Biophysica Acta (BBA) - Reviews on Cancer*, vol. 1873, no. 1, Article ID 188314, 2019.

[4] L. Wang, X. Lin, J. Wang et al., "Novel insights into combating cancer chemotherapy resistance using a plasmonic nanocarrier: enhancing drug sensitiveness and accumulation simultaneously with localized mild photothermal stimulus of femtosecond pulsed laser," *Advanced Functional Materials*, vol. 24, no. 27, 2014.

[5] Q. Y. Zhang, F. X. Wang, K. K. Jia, and L. D. Kong, "Natural product interventions for chemotherapy and radiotherapy-induced side effects," *Frontiers in Pharmacology*, vol. 9, 2018.

[6] J. P. Celli, B. Q. Spring, I. Rizvi et al., "Imaging and photodynamic therapy: mechanisms, monitoring, and optimization," *Chemical Reviews*, vol. 110, no. 5, pp. 2795–2838, 2010.

[7] L. Cheng, C. Wang, L. Feng, K. Yang, and Z. Liu, "Functional nanomaterials for phototherapies of cancer," *Chemical Reviews*, vol. 114, no. 21, pp. 10869–10939, 2014.

[8] A. P. Castano, T. N. Demidova, and M. R. Hamblin, "Mechanisms in photodynamic therapy: part one-photosensitizers, photochemistry and cellular localization," *Photodiagnosis and Photodynamic Therapy*, vol. 1, no. 4, pp. 279–293, 2004.

[9] X. Wang, R. R. Valiev, T. Y. Ohulchanskyy, H. Ågren, C. Yang, and G. Chen, "Dye-sensitized lanthanide-doped upconversion nanoparticles," *Chemical Society Reviews*, vol. 46, no. 14, pp. 4150–4167, 2017.

[10] A. Sedlmeier and H. H. Gorris, "Surface modification and characterization of photon-upconverting nanoparticles for bioanalytical applications," *Chemical Society Reviews*, vol. 44, 2015.

[11] J. Wang, T. Wei, X. Li et al., "Inside back cover: near-infrared-light-mediated imaging of latent fingerprints based on molecular recognition (angew. Chem. Int. Ed. 6/2014)," *Angewandte Chemie International Edition*, vol. 53, no. 6, p. 1709, 2014.

[12] W. Mo, D. Rohrbach, and U. Sunar, "Imaging a photodynamic therapy photosensitizerin vivowith a time-gated fluorescence tomography system," *Journal of Biomedical Optics*, vol. 17, no. 7, Article ID 071306, 2012.

[13] A. P. Castano, P. Mroz, and M. R. Hamblin, "Photodynamic Therapy and Anti-tumour immunity," *Nature Reviews Cancer*, vol. 6, no. 7, 2006.

[14] M. Meinhardt, R. Krebs, A. Anders, U. Heinrich, and H. Tronnier, "Wavelength-dependent penetration depths of ultraviolet radiation in human skin," *Journal of Biomedical Optics*, vol. 13, no. 4, p. 5, 2008.

[15] T. Gambichler, S. Boms, M. Stücker et al., "Acute skin alterations following ultraviolet radiation investigated by optical coherence tomography and histology," *Archives of Dermatological Research*, vol. 297, no. 5, pp. 218–225, 2005.

[16] C. Li, Z. Quan, P. Yang, S. Huang, H. Lian, and J. Lin, "Shape-controllable synthesis and upconversion properties of lutetium fluoride (doped with Yb3+/Er3+) microcrystals by hydrothermal process," *Journal of Physical Chemistry C*, vol. 112, no. 35, 2008.

[17] W. Yang, L. Fengqi, X. Zhang, and D. Chen, "Synthesis of Oil-Dispersible Hexagonal-phase and Hexagonal-Shaped NaYF4:

Hindawi
Journal of Healthcare Engineering
Volume 2023, Article ID 9789750, 1 page
https://doi.org/10.1155/2023/9789750

Retraction

Retracted: Estimation of Soft and Hard Tissue Revolutionization Surrounding Dental Implant: A 2-Year Retrospective Study

Journal of Healthcare Engineering

Received 26 September 2023; Accepted 26 September 2023; Published 27 September 2023

This article has been retracted by Hindawi following an investigation undertaken by the publisher [1]. This investigation has uncovered evidence of one or more of the following indicators of systematic manipulation of the publication process:

(1) Discrepancies in scope
(2) Discrepancies in the description of the research reported
(3) Discrepancies between the availability of data and the research described
(4) Inappropriate citations
(5) Incoherent, meaningless and/or irrelevant content included in the article
(6) Peer-review manipulation

The presence of these indicators undermines our confidence in the integrity of the article's content and we cannot, therefore, vouch for its reliability. Please note that this notice is intended solely to alert readers that the content of this article is unreliable. We have not investigated whether authors were aware of or involved in the systematic manipulation of the publication process.

Wiley and Hindawi regrets that the usual quality checks did not identify these issues before publication and have since put additional measures in place to safeguard research integrity.

We wish to credit our own Research Integrity and Research Publishing teams and anonymous and named external researchers and research integrity experts for contributing to this investigation.

The corresponding author, as the representative of all authors, has been given the opportunity to register their agreement or disagreement to this retraction. We have kept a record of any response received.

References

[1] M. M. Al-Ahmari, "Estimation of Soft and Hard Tissue Revolutionization Surrounding Dental Implant: A 2-Year Retrospective Study," *Journal of Healthcare Engineering*, vol. 2022, Article ID 1540668, 6 pages, 2022.

Hindawi
Journal of Healthcare Engineering
Volume 2022, Article ID 1540668, 6 pages
https://doi.org/10.1155/2022/1540668

Research Article

Estimation of Soft and Hard Tissue Revolutionization Surrounding Dental Implant: A 2-Year Retrospective Study

Manea Musa Al-Ahmari

Department of Periodontics and Community Dental Sciences, College of Dentistry, King Khalid University, Abha, Saudi Arabia

Correspondence should be addressed to Manea Musa Al-Ahmari; ieeemtech@gmail.com

Received 24 December 2021; Accepted 9 February 2022; Published 7 March 2022

Academic Editor: Liaqat Ali

A dental implant is an idyllic mode of operandi for oral rehabilitation for complete and partially edentulous patients. The success of an implant is based on the health of its surrounding tissues. Therefore, the biological and clinical aspects of implant prosthesis and their surrounding tissues must persist to be investigated. A two-year retrospective clinical-radiological study was conducted to estimate peri-implant soft and hard tissue revolutionization after the placement of implants. A clinical-radiological investigation was carried out to determine the amount of soft and hard tissue revolutionization that occurred following the implantation of 200 implants. From October 2020 to March 2021, the research was carried out in the College of Dentistry at King Khalid University in Saudi Arabia. It was decided to conduct this study using a retrospective clinical record, which involved gathering information about patients who had previously received dental implants within the previous two years. Plaque index (PI), gingival index (GI), bleeding index (BI), peri-implant probing depth (PD), and peri-implant crestal bone level were measured at baseline and three months after implant placement in adult patients ranging in age from 20 to 50 years. The results were compared to the full-mouth index (FMI). Ethical clearance and written informed consent were obtained from all the study participants. The statistical analysis was done by using Statistical Package for Social Sciences (SPSS-23.0 version) (IBM; Chicago). The present study concluded that plaque accumulation, gingival bleeding, and probing depth were increased around implants during the follow-up, but it would not affect crestal bone loss. Still, it is essential to conduct a similar study with a larger sample size and a long follow-up period to give more precise results.

1. Introduction

A dental implant is an idyllic mode of operandi for oral rehabilitation for complete and partially edentulous patients, since 1965 it has been recognized as a consistent and conventional means for dental reformation, long-term treatment success, and esthetics [1]. Peri-implant tissue firmness is the prime concern. It can affect the esthetics, success, and survival rates of implant restorations [2]. Peri-implantitis is defined as an inflammation and demolition of soft and hard tissues adjacent to dental implants [3].

Bleeding on probing upon pressure <0.25 N is the key indicator for the diagnosis of peri-implant mucositis. It is supposed that peri-implant mucositis is the forerunner of peri-implantitis, like gingivitis for periodontitis. For that reason, prevention of the translation of peri-implant mucositis into peri-implantitis is most important (Salvi and Zitzmann 2014) [4].

According to Howe and others, the 10-year survival rate of dental implants was 96.4% [5]; similarly, one retrospective long-term study documented that the survival rates for dental implants up to 27 years of function were 92.6% [6]. Due to higher survival rates, dental implants are measured as an expected alternative for oral rehabilitation for edentulous or partially edentulous patients. On the other hand, due to repeated tooth-borne pathologies, lack of tissue coverages in both quality and quantity, and horizontal bone loss and vertical bone loss are common complications in implants' long-term survival rates [7]. Several authors accounted for a midfacial gingival recession in the region of a single implant with an average loss of 0.5 to 1 mm or more [8–10]. A mean diminution of the facial bone thickness of 0.4 to 0.7 mm has also been reported around the peri-implant area over one year [11].

Visual inspection, monitoring inflammatory changes by plaque accumulation, bleeding on probing from soft tissues, and determining the amount of probable loss of hard tissue structures are all methods for evaluating the state of the peri-implant site clinically [12]. However, because it is an ideal treatment for oral rehabilitation, the biological and clinical aspects of this work of fiction involving dental implants and their surrounding tissues must be continued to be explored in order to fully understand them. Consequently, the goal of this study was to evaluate peri-implant soft and hard tissue revolutionization following the placement of dental implants using tools such as plaque index, gingival index, bleeding index, peri-implant probing depth, and peri-implant crestal bone at baseline and three months after the placement of the dental implant.

2. Methodology

A clinical-radiological study was conducted to estimate peri-implant soft and hard tissue transformations after the placement of 200 implants. The study was conducted in the College of Dentistry, King Khalid University, from October 2020 to March 2021. This study utilized a 2-year retrospective clinical record that implicated assembling information about patients who were formerly treated with dental implants in the last 2 years. The method of sampling was convenient sampling; thus, patients who underwent dental implant were included as the final sample size. 200 dental implants were placed in adult patient's age range from 20 to 50 years, and soft and hard tissue changes were evaluated by plaque index (PI), gingival index (GI), bleeding index (BI), peri-implant probing depth (PD), and peri-implant crestal bone level at baseline and three months and the results were compared with the full-mouth index. Ethical clearance was obtained from the institutional ethical committee, and treatment was completed as per the principles of the Declaration of Helsinki regarding involving human subjects. Written informed consent was obtained from all the study participants.

2.1. Patient Selection. Patient selection was done according to the following selection criteria: good systemic health, nonsmokers ≤10 cigarettes/day, good oral cleanliness, ≤ 25% full-mouth plaque score at baseline, ≤ 25% full-mouth bleeding of probing at baseline, ≤ 3 mm probing pocket depth around six facets of the teeth adjacent to the implant, ≤ 2 mm periodontal attachment level around six facets of the teeth adjacent to the implant site, absence of any vigorous infection around the implant site, and absence of parafunctional habits (bruxism and clenching).

The exclusion criteria were as follows: patients with any local or systemic disease, smoking habits, a habit of betel nut or tobacco chewing, alcoholism, pregnancy or breastfeeding, continuing oral medications, oral parafunctional habits, ignored periodontal disease, and insufficient bone density, and patients who are reluctant to provide informed consent [13]. An estimation of gingival and periodontal status around the implant sites was done at baseline and after 3 months and the results were compared with the full-mouth index. A cone-beam computed tomography (CBCT) was used to evaluate bone density at the implant site. All measurements were performed by a single investigator to minimize the bias.

2.2. Statistical Analysis. The data were entered into spreadsheets and analyzed by using Statistical Package for Social Sciences (SPSS-23.0 version) (IBM; Chicago). Parameters are expressed as mean and standard deviation. Paired t-test was used to determine the difference between baseline and 3 months in both groups. Student's t-test was used to find intergroup differences for all variables. The results were analyzed with a p value less than 0.05 as significant.

3. Results

A clinical-radiological, two-year retrospective study was conducted to estimate peri-implant soft and hard tissue transformation after the placement of 200 implants. In this study, the mean age of the study population was 39.0 ± 9.78 years for both males and females.

Table 1 and Figure 1 show the comparison of the mean values of plaque index at the implant site and full mouth at baseline and 3 months. Figure 1 shows the comparison of the mean plaque index for the implant site and for the full mouth as well. The plaque index score at the implant site was $0.387 + 0.024$ at the start of the study and $0.536 + 0.045$ at the end of the study, resulting in a mean difference of 0.1492 that was statistically significant ($p = 0.042$). Initially, the baseline plaque index score for complete mouth was $0.638 + 0.568$, and after three months, the score had improved to $0.510 + 0.059$, with a mean difference of 0.12760, which did not reach statistical significance ($p = 0.639$).

Table 2 and Figure 2 show the comparison of mean values of the gingival index at the implant site and full mouth at baseline and 3 months. The baseline gingival index score at the implant site was 0.456 ± 0.034 and after 3 months was 0.599 ± 0.119, with a mean difference of 0.1430 which was significant ($p = 0.02$), whereas the baseline gingival index score for the full mouth was 0.595 ± 0.039 and after 3 months was 0.490 ± 0.077, with a mean difference of 0.1051 which was nonsignificant ($p = 0.218$).

Table 3 and Figure 3 show the comparison of the mean values of the bleeding index at the implant site and full mouth at baseline and 3 months. The baseline bleeding index score at the implant site was 0.479 ± 0.087 and after 3 months was 0.599 ± 0.559, with a mean difference of 0.1204 which was nonsignificant ($p = 0.385$), whereas the baseline bleeding index score for the full mouth was 0.632 ± 0.060 and after 3 months was 0.500 ± 0.084, with a mean difference of 0.1321, which was nonsignificant ($p = 0.914$).

Table 1: Comparison of the mean plaque index for a 3-month interval.

Parameter		Time interval	Mean + SD	Mean difference from baseline	t value	p value
Plaque index	Implant site	Baseline	0.387 ± 0.024	0.1492	7.657	0.042*
		3 months	0.536 ± 0.045			
	Full mouth	Baseline	0.638 ± 0.568	0.12760	15.957	0.639 (NS)
		3 months	0.510 ± 0.059			

*Approximate value.

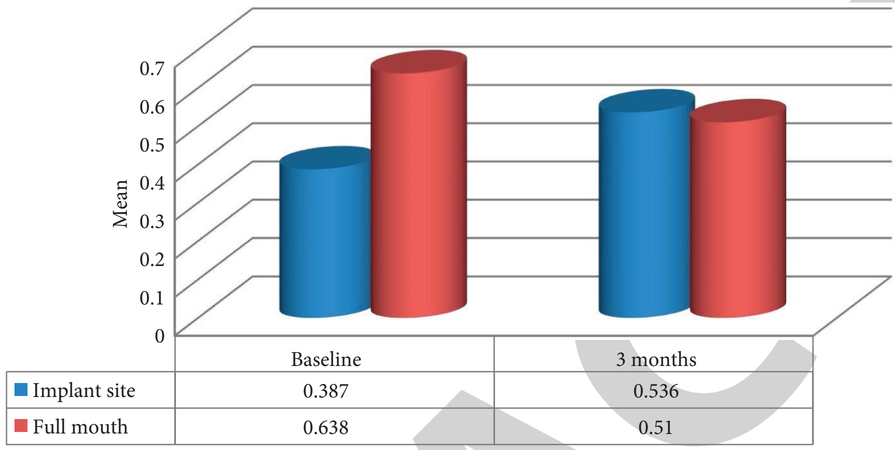

Figure 1: Comparison of the mean plaque index for a 3-month interval.

Table 2: Comparison of the mean gingival index for a 3-month interval.

Parameter		Time interval	Mean + SD	Mean difference from baseline	t value	p value
Gingival index	Implant site	Baseline	0.456 ± 0.034	0.1430	10.120	0.02*
		3 months	0.599 ± 0.119			
	Full mouth	Baseline	0.595 ± 0.039	0.1051	4.399	0.218 (NS)
		3 months	0.490 ± 0.077			

*Approximate value.

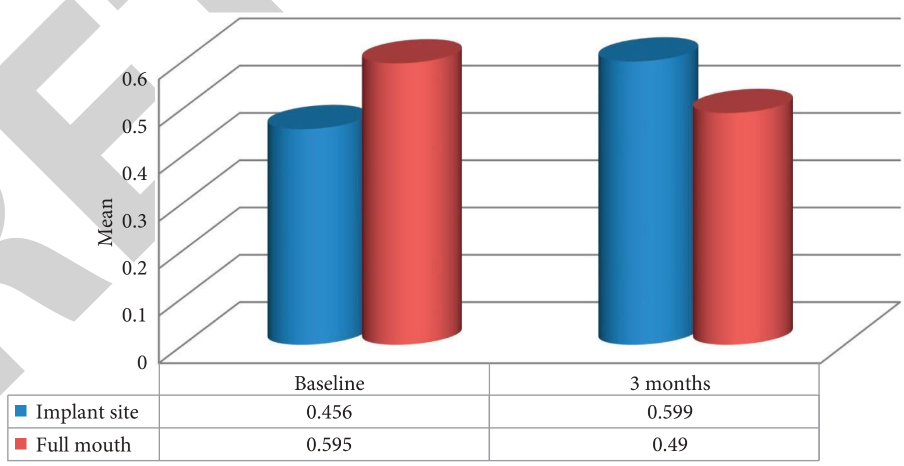

Figure 2: Comparison of the mean gingival index for a 3-month interval.

The comparison of the mean values of peri-implant probing depth at the implant site at baseline and 3 months showed that the baseline peri-implant probing depth score at the implant site was 3.00 ± 0.010 and after 3 months was 3.80 ± 0.44, with a mean difference of 0.8000, which was nonsignificant ($p = 0.161$), as shown in Table 4 and Figure 4.

The comparison of the mean values of peri-implant crestal bone at the implant site at baseline and 3 months showed that the baseline peri-implant crestal bone score at the implant site was 13.77 ± 1.67 and after 3 months was 13.51 ± 1.66, with a mean difference of -0.2604, which was significant ($p = 0.013$), as shown in Table 5 and Figure 5.

TABLE 3: Comparison of the mean bleeding index for a 3-month interval.

Parameter		Time interval	Mean + SD	Mean difference from baseline	t value	p value
Bleeding index	Implant site	Baseline 3 months	0.479 ± 0.087 0.599 ± 0.559	0.1204	6.875	0.385 (NS)
	Full mouth	Baseline 3 months	0.632 ± 0.060 0.500 ± 0.084	0.1321	9.697	0.914 (NS)

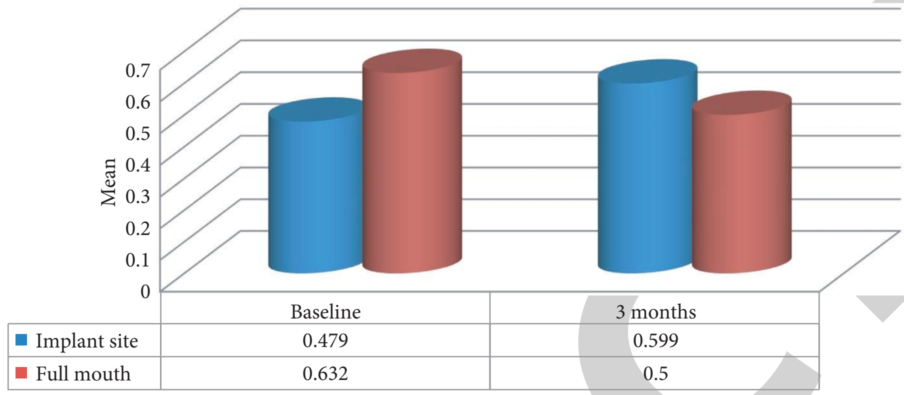

FIGURE 3: Comparison of the mean bleeding index for a 3-month interval.

TABLE 4: Comparison of peri-implant probing depth for a 3-month interval.

Parameter		Time interval	Mean + SD	Mean difference from baseline	t value	p value
Peri-implant probing depth	Implant site	Baseline 3 months	3.00 ± 0.010 3.80 ± 0.44	0.8000	4.812	0.161 (NS)

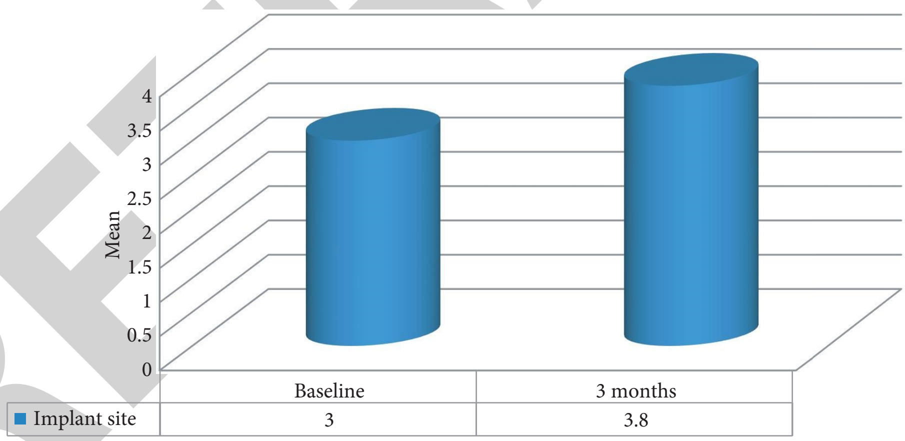

FIGURE 4: Comparison of peri-implant probing depth for a 3-month interval.

TABLE 5: Comparison of peri-implant bone height for a 3-month interval.

Parameter		Time interval	Mean + SD	Crestal bone loss (3 months–baseline)	t value	p value
Peri-implant crestal bone	Implant site	Baseline 3 months	13.77 ± 1.67 $13.51 + 1.66$	−0.2604	17.835	0.013*

*Approximate value.

4. Discussion

This was a clinical-radiological retrospective study, conducted to estimate peri-implant soft and hard tissue transformations after the placement of 200 implants. In this study, the mean age of the study population was 39.0 ± 9.78 years for both males and females. However, in a study by Seung-Mi Jeong et al., 432 implants were placed in 241 patients and soft and hard tissues changes around peri-implant sites and radiographic marginal bone were assessed

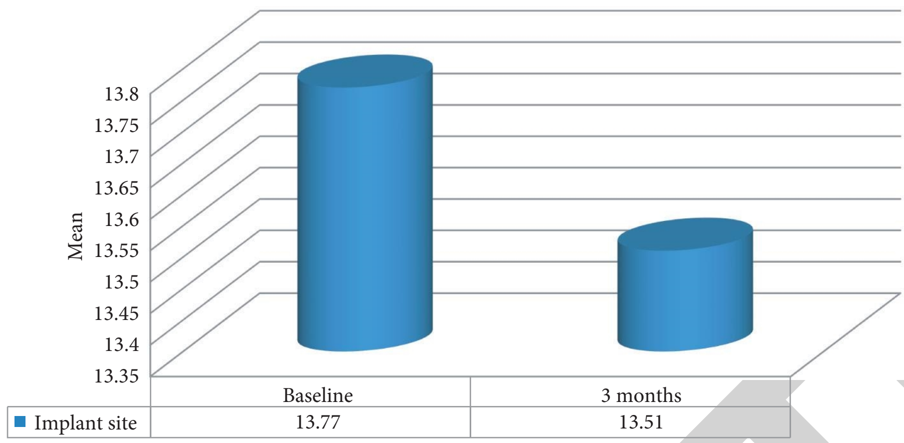

Figure 5: Comparison of peri-implant bone height for a 3-month interval.

after 1 year [14]. A similar study was conducted by Gopalakrishnan and others [15, 16] to examine the periodontal status affecting soft and hard tissues surrounding laser microtextured single tooth implants. This study was conducted among 13 patients (8 males (40%) and 5 females (60%)) and 20 implants were placed.

In this study, the mean value of the plaque index at the implant site was 0.387 ± 0.024 at baseline and 0.536 ± 0.045 after 3 months, which showed plaque accumulation increased from baseline to 3 months with a significant p value ($p = 0.042$). Similarly, according to Guarnieri and others, the number of sites with a plaque at baseline and after 5 years increased. In contrast to that, Gopalakrishnan and others found that the plaque index reduced from baseline to 6 months with a statistically significant p value [16].The baseline plaque index score for full mouth was 0.638 ± 0.568 and after 3 months was 0.510 ± 0.059, with a mean difference of 0.12760, which was nonsignificant ($p = 0.639$). However, Paolo De Angelis et al. [17] found that 92% (44/48) patients had no plaque at 12-month follow-up.

According to the present study, the mean values of the gingival index at the implant site at baseline were low (0.456 ± 0.034) as compared to after 3-month (0.599 ± 0.1190) follow-up, with a significant p value ($p = 0.02$). However, a study by Gopalakrishnan found that the gingival index score reduced from baseline to 6 months with a statistically significant p value [15]. In contrast, BOP was negative around the implant site in 83% (40/48) of the participants in the Paolo De Angelis et al.'s study [17]. As per Jeong et al., the average gingival index score was 0.1 (SD 0.3), which was utilized for peri-implant mucosal health and inflammation assessment.

In the present study, the baseline bleeding index score at the implant site was 0.479 ± 0.087 and after 3 months was 0.599 ± 0.559, with a mean difference of 0.1204, which was nonsignificant ($p = 0.385$). Similar results were found by Guarnieri and others; in their study, the number of sites with BOP increased from baseline to 5 years [16]. According to Mehrotra N and others, the modified sulcus bleeding index reduced from baseline to 6 months with a statistically significant p value.

This study found that the baseline peri-implant probing depth score at the implant site was 3.00 ± 0.010 and after 3 months was $3.80 + 0.44$, which showed peri-implant probing depth was increased from baseline to 3 months, but the difference was not statistically significant. As per Jeong et al., the mean probing depth was 2.1 mm (SD 0.7) on one-year follow-up. In the present study, the baseline peri-implant crestal bone score at the implant site was 13.77 ± 1.67 and after 3 months was 13.51 ± 1.66, with a mean difference of -0.2604 which was significant ($p = 0.013$). As per Jeong et al. [14], in their study, the peri-implant crestal bone loss was 2.1 mm (SD 0.7) on one-year follow-up (0.3 ± 0.4). Thus, according to the trend in this study, the plaque index, bleeding index, and probing depth at the implant site were increased during the follow-up. For this reason, effective plaque control measures should be recommended after implant surgery.

5. Conclusion and Recommendations

An investigation of soft and hard tissue around the peri-implant site was carried out using the plaque index, gingival index, and sulcus bleeding index, and a 2-year retrospective approach was used in this study. It revealed plaque collection, gingival bleeding, and probing depth increased in the area around the implant, but it had no effect on crestal bone loss, according to the study. Nonetheless, it is necessary to undertake a similar study with a larger sample size and a longer follow-up period in order to obtain more accurate results [4].

Data Availability

The data shall be made available on request.

Conflicts of Interest

The authors declare that they have no conflicts of interest.

Acknowledgments

This research work is self-funded.

Hindawi
Journal of Healthcare Engineering
Volume 2023, Article ID 9850271, 1 page
https://doi.org/10.1155/2023/9850271

Retraction

Retracted: A Data-Driven Medical Decision Framework for Associating Adverse Drug Events with Drug-Drug Interaction Mechanisms

Journal of Healthcare Engineering

Received 23 May 2023; Accepted 23 May 2023; Published 24 May 2023

This article has been retracted by Hindawi following an investigation undertaken by the publisher [1]. This investigation has uncovered evidence of one or more of the following indicators of systematic manipulation of the publication process:

(1) Discrepancies in scope
(2) Discrepancies in the description of the research reported
(3) Discrepancies between the availability of data and the research described
(4) Inappropriate citations
(5) Incoherent, meaningless and/or irrelevant content included in the article
(6) Peer-review manipulation

The presence of these indicators undermines our confidence in the integrity of the article's content and we cannot, therefore, vouch for its reliability. Please note that this notice is intended solely to alert readers that the content of this article is unreliable. We have not investigated whether authors were aware of or involved in the systematic manipulation of the publication process. Wiley and Hindawi regrets that the usual quality checks did not identify these issues before publication and have since put additional measures in place to safeguard research integrity.

We wish to credit our own Research Integrity and Research Publishing teams and anonymous and named external researchers and research integrity experts for contributing to this investigation.

The corresponding author, as the representative of all authors, has been given the opportunity to register their agreement or disagreement to this retraction. We have kept a record of any response received.

References

[1] A. Noor, "A Data-Driven Medical Decision Framework for Associating Adverse Drug Events with Drug-Drug Interaction Mechanisms," *Journal of Healthcare Engineering*, vol. 2022, Article ID 9132477, 7 pages, 2022.

Hindawi
Journal of Healthcare Engineering
Volume 2022, Article ID 9132477, 7 pages
https://doi.org/10.1155/2022/9132477

Research Article

A Data-Driven Medical Decision Framework for Associating Adverse Drug Events with Drug-Drug Interaction Mechanisms

Adeeb Noor

Information Technology Department, Faculty of Computing and Information Technology, King Abdulaziz University, Jeddah 21589, Saudi Arabia

Correspondence should be addressed to Adeeb Noor; arnoor@kau.edu.sa

Received 10 January 2022; Revised 1 February 2022; Accepted 15 February 2022; Published 3 March 2022

Academic Editor: Hafiz Tayyab Rauf

Adverse drug events (ADEs) occur when multiple drugs interact within an individual, thus causing effects that were not initially predicted. Such toxic interactions lead to morbidity and mortality. Contemporary research surrounding ADEs has tended to focus on the detection of potential ADEs without great concern for elucidating the associations of drug-drug interaction (DDI) mechanisms that can predict potential adverse drug reactions (ADRs). Such associations are of great practical importance for everyday pharmacovigilance efforts. This study presents a data-driven framework for conducting knowledge-driven data analysis that combines a semantic inference system and enrichment analysis in order to identify potential ADE mechanisms. The framework was used to rank mechanisms according to their relevance for DDIs and also to categorize ADEs based on the number of DDI mechanism associations identified through enrichment analysis. Its validity is demonstrated through using both commercial and publicly available DDI resources. The results of this study solidly prove the framework's effectiveness and highlight potential for future research by way of incorporating additional and broader data to deepen and expand its capabilities.

1. Introduction

One type of medical error is adverse drug events (ADEs), the occurrence of which is recognized as among the greatest concerns in cases of drug-drug interaction (DDI). ADEs occur when multiple drugs interact within an individual to cause unanticipated toxic effects, which lead to morbidity and mortality. As reported in multiple studies [1–3], ADEs cause considerable illness and death; they kill over 770,000 patients in U.S. hospitals each year, with an estimated annual cost of $5.6 million per hospital [4, 5]. While additional ADEs may be prevented by contraindicating drug pairs that have been observed to generate toxic interactions in a clinical setting, new approaches are required to predict and prevent never-before-seen ADEs.

Fundamentally, multiple avenues can be pursued when endeavoring to study and understand ADEs. Traditional ADE research efforts are bench-science-based, i.e., conducted either in vivo (in living organisms) or in vitro (outside living organisms). While such studies are important, their scope is narrow; effective avoidance of ADEs requires the collection and integration of comprehensive knowledge regarding diseases, targets, drugs, drug effects, and underlying interaction mechanisms. Accordingly, the field of pharmacovigilance (PhV) was introduced by the World Health Organization to monitor, collect, and synthesize research information from multiple resources, the better to prevent short-term and long-term side effects resulting from ADEs [6]. PhV implementations have shown promising results in studying and predicting ADEs before their occurrence, for example, through data extraction, collection, and creation [7–10]. Other applications have focused on predicting ADEs using computational methods such as text mining [11], machine learning [12], deep learning [13], and network models [14]. Such methods often employ inputs that are clinically based, such as electronic patient records [15], clinical notes [16], disease characteristics [17], or drug features [18]; other nonclinical inputs consist of personal messages [19], social media posts [20], and advice from human experts [21]. Overall, these studies have concentrated more strongly on identifying new potential ADEs rather than providing support for determination of the mechanisms of drug interaction.

Examining ADEs within the context of their defining mechanisms, which stem from DDIs, is one of the most potent methods for advancing our understanding. In that regard, two main approaches have been undertaken. The first is a drug-based approach, in which the features or relations of drugs related to ADEs are studied and analyzed in order to uncover ADE mechanisms; for example, studies have examined drugs and their molecular targets [22], drug properties such as chemical substructure [23], and drug-target relationships [24]. The second approach centers on ADEs and is geared toward studying and understanding disease/phenotype profiles and gene-pathway interactions [25]. Both approaches have shown promising outcomes in terms of advancing prediction of ADEs prior to their occurrence, but they also share two important limitations, focusing on either drug-ADE or phenotype-ADE relations and considering only pharmacokinetic or pharmacodynamic mechanisms. In addition, discovery of ADEs involves a careful combination of analyses, integrating data from diverse sources with knowledge of underlying interaction mechanisms [26]. Combining established approaches with knowledge of the many possible DDI mechanisms is essential to informing strategies for ADE prevention [27]. The ultimate aim of this work is to illustrate the potential for advancement of ADE research by leveraging the data and knowledge regarding DDI mechanisms contained within multiple biomedical repositories to fill gaps and potentially predict ADEs.

Here, we present a data-driven medical decision framework developed to perform knowledge-driven data analysis to associate mechanisms of ADEs together with DDIs. Specifically, our framework relies on structured knowledge and ontology-based annotations in conjunction with a semantic inference system to associate ADEs with ten correlated DDI mechanisms, allowing for categorization of ADEs through enrichment analysis. We conducted two demonstrative experiments with this framework, first, ranking mechanisms according to their relevance for DDIs and, second, generating ten corresponding ADE datasets and using them in enrichment analysis. We also demonstrate our framework using both commercial and publicly available DDI resources and show how it can aid clinicians in identifying patients at risk of ADEs stemming from DDIs, including ADEs that have yet to be fully characterized.

2. Materials and Methods

The framework is designed around utilizing experimental data from the Human Phenotype Ontology (HPO) [28] in conjunction with the drug-drug interaction discovery and demystification (D3) inference framework by Noor et al. [29]. It ranks the predictive significance of DDI mechanisms and explores the associations of ADEs with potentially correlated DDI mechanisms, allowing categorization of ADEs. Table 1 shows the mechanisms of interaction covered by the D3 framework. Two experiments are presented here, each employing the system in a different capacity to showcase some of the inferences it could be used to draw and each designed to yield outcomes of potential direct benefit to clinicians. These are not intended to exhibit the full capacity of what is possible with this system, leaving room for future expansion beyond the framework presented herein.

2.1. Experiment (1): Rank the Predictive Significance of DDI Mechanisms. The first experiment was designed to first construct annotations that associate interacting drug pairs with DDI mechanisms and then apply an extra trees' classifier to rank those mechanisms (features) according to predictive significance. A total of 146 drug pairs (73 interacting and 73 noninteracting) were retrieved manually from Micromedex, a well-known commercial DDI repository, without consideration for potentially applicable DDI mechanisms. A pharmacist was then asked to review all 146 drug pairs. Each drug was then manually mapped to its respective concept unique identifier (CUI) in Unified Medical Language System (UMLS) [37] as required by the D3 inference framework, which was used to confirm and annotate the interactivity or noninteractivity of each pair. Next, a feature matrix was constructed in which rows contained drug pairs and columns contained the applicability of distinct DDI mechanisms. Finally, the extra trees' classifier was applied to the matrix, with 70% of the set used for training and 30% for testing.

An extra trees' classifier is akin to a random forest, but more extreme. In this classifier, several randomized decision trees are fitted to multiple independent subsamples, the results of which are averaged to limit overfitting and increase prediction accuracy. As with a random forest classifier, extra trees select a random sample from among the candidate features. Rather than identifying thresholds that provide greatest discrimination, however, extra trees randomize the threshold for each feature and use the best-performing threshold to define the splitting rule. This approach typically enables the model's variance to be reduced somewhat further, though with the tradeoff of slightly increasing bias.

In the classifier, the relative rank (i.e., depth) of any given decision node (i.e., feature) represents its relative importance in predicting the target variable; that is, features positioned higher in the tree contribute to prediction decisions for a greater portion of the input dataset. Accordingly, a feature's relative importance can also be estimated in terms of the expected fraction of samples for which it contributes to prediction decisions (i.e., the expected activity rate). Generating multiple randomized trees and averaging a feature's expected activity rates across them reduces the variance of its estimated importance, which is useful in feature selection. Figure 1 shows the workflow for ranking features (mechanisms) using the extra trees classifier.

2.2. Experiment (2): Categorize ADEs by the Count of DDI Mechanism Associations. In this second scenario, the semantic inferences from experiment (1) and an ontology were used to associate DDI mechanisms with ADEs and categorize them via enrichment analysis. Specifically,

Table 1: Proposed mechanisms of drug-drug interaction according to the D3 framework [29].

#	Mechanism	Definition
1	Protein binding [30]	Displacement reactions between two drugs
2	Metabolic induction [31]	Induction is caused by one of two drugs
3	Metabolic inhibition [31]	Inhibition is caused by one of two drugs
4	Transporter induction [32]	Induction is caused by one of two drugs
5	Transporter inhibition [32]	Inhibition is caused by one of two drugs
6	Multiple pathways [33]	Both drugs share enzymes and transporters
7	Competitive pharmacological [34]	Both drugs share a target
8	Additive pharmacodynamic [35]	Both drugs share mechanisms of action
9	Indication similarity [36]	Both drugs treat the same disease
10	Side-effect similarity [31]	Both drugs share side effects

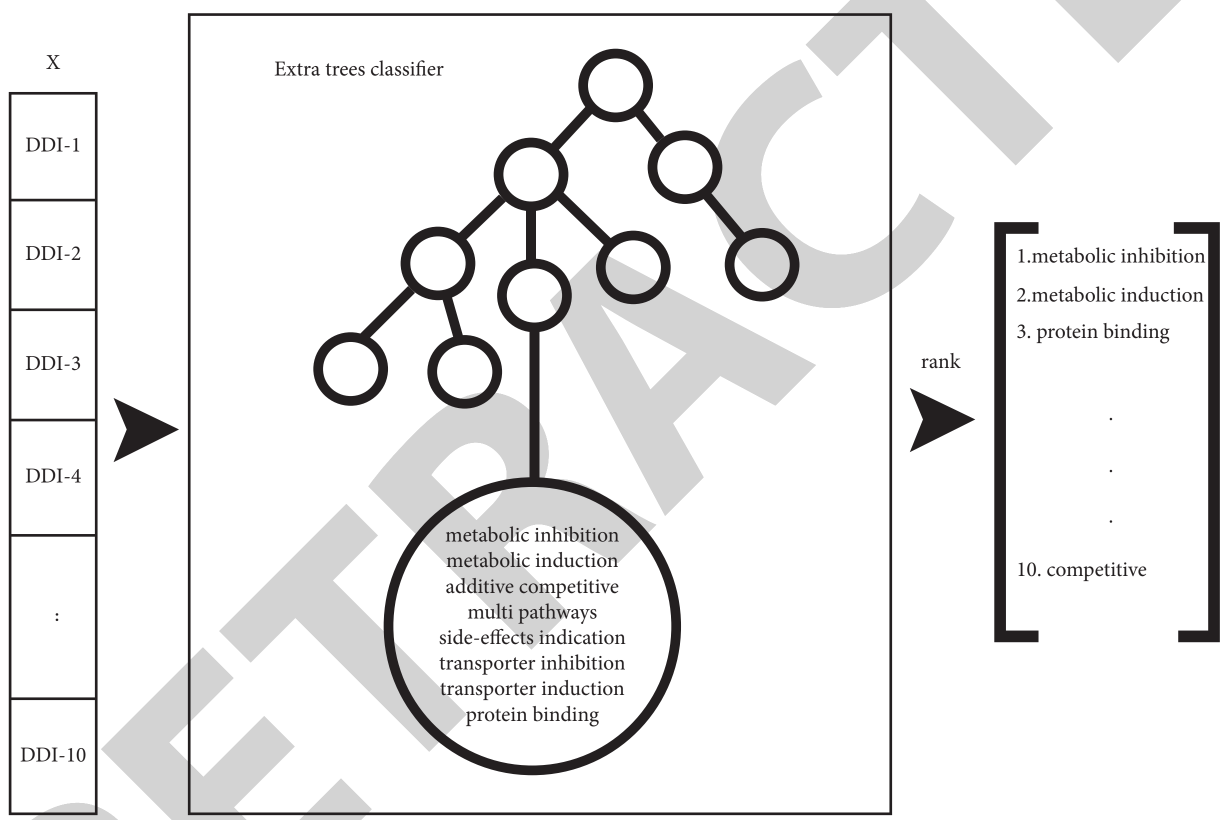

Figure 1: Overall steps in the process of ranking DDI mechanisms.

enrichment analysis was carried out over the HPO, where each term explains a phenotype deviation, and ADEs in the ontology were examined for enrichments of the ten DDI mechanisms from the D3 inference framework. This experiment was comprised of four essential steps (Figure 2).

(1) First, TWOSIDES [9], a repository of FDA-recognized spontaneous ADEs containing 63,473 unique interacting drug pairs (645 drugs and 1318 ADEs), was chosen as a dataset due to being freely available to the public and providing a sufficient number of DDI-ADE associations with corresponding likelihood values (p values).

(2) Second, TWOSIDES was annotated with DDI mechanism information using the D3 inference framework; specifically, all drugs listed in TWOSIDES were mapped to UMLS CUIs; then, each drug pair was fed through the D3 framework. The recall rate for the overall inferential coverage of TWOSIDES was computed, with the result being above 79% (49,915 inferred interactions out of 62,886 verified interactions). This value is critical for computing the recall rates associated with individual DDI mechanisms.

(3) Third, enrichment analysis was used to rank the predictive significance of the associations between DDI mechanisms and ontological annotations in the HPO. The ADEs in TWOSIDES (represented by UMLS identifiers) were mapped to HPO terms using a Java OWL script. ADE test sets were then constructed for each of the ten DDI mechanisms, with

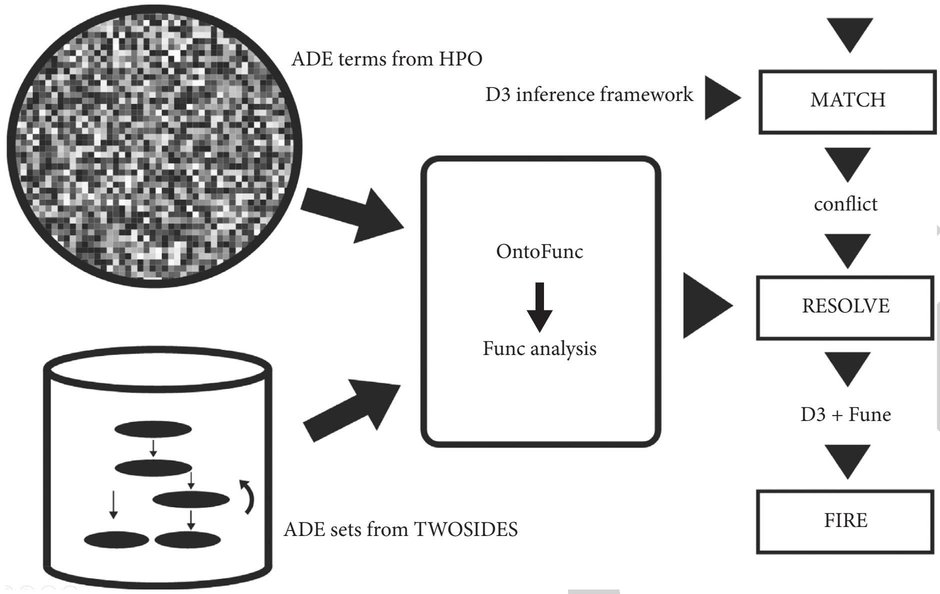

Figure 2: Workflow for applying enrichment analysis over ADEs with semantic inference to identify mechanisms.

each having a Boolean outcome based on detection of a DDI within the set by the D3 framework. Subsequently, the ontology analysis tools FUNC [38] (used to find associations specifically with Gene Ontology terms) and OntoFunc [39] (used for different ontologies) were leveraged to carry out enrichment analysis and rank associations between the ten DDI mechanisms and the HPO annotations for ADEs. This yielded ten annotated sets, each consisting of three columns: DDI, phenotype (ADE) from the HPO, and the Boolean result of the inference drawn by the D3 framework.

(4) Finally, a hypergeometric test was performed on the ten annotated records to assess the probability of "drawing" the observed number of differentially expressed ADEs for each mechanism.

We also employed the Wilcoxon signed-rank test to identify the quality of the ten mechanisms in terms of distinguishing between positive and negative DDIs in TWOSIDES. For each DDI pair found to be associated with multiple ADEs, we chose the association having the smallest nonzero p value. The Wilcoxon test was run in *R* and a W value of 3843500 and a median difference between positive and negative DDIs of 0.04692435 (95% confidence interval 0.0377504–0.0541043 and p value < 2.2e-16) were returned.

3. Results and Discussion

3.1. Ranking Mechanisms according to Their Relevance for DDIs. The first experiment considered a total of 146 drug pairs (73 interacting and 73 noninteracting; 70% used for training and 30% for testing) and ranked the predictive significance of DDI mechanisms. Table 2 summarizes the results of this experiment.

In this ranking of predictive significance, the framework demonstrated good capability overall: average precision

Table 2: Performance metrics obtained when using the extra trees' classifier on 146 commercially recognized DDI pairs.

	Precision	Recall	F1 score
Interacting drug pairs (73)	0.79	0.88	0.83
Noninteracting drug pairs (73)	0.92	0.85	0.88

0.855, average recall 0.866, and average F1 score 0.855. The F1 scores obtained for each DDI mechanism were metabolic inhibition, 0.281019, metabolic induction, 0.242089, protein binding, 0.168295, multipathway, 0.109771, side-effect similarity, 0.091208, indication similarity, 0.047006, transporter inhibition, 0.034505, transporter induction, 0.022949, additive pharmacodynamic, 0.003157, and competitive pharmacological, 0.000000.

3.2. Enrichment Analysis over HPO terms to Identify Which ADEs Are Associated with Each DDI Mechanism. Before running the enrichment analysis, we examined the individual recall rates of the ten mechanisms for ADEs in TWOSIDES. Mutual exclusivity of the asserted DDIs was not incorporated, that is, in the event of multiple mechanistic explanations for a given DDI, that DDI was counted towards all relevant inferences. The F1 scores per mechanism were side-effect similarity, 0.76, metabolic inhibition, 0.29, protein binding, 0.21, transporter inhibition, 0.13, metabolic induction, 0.11, multipathway, 0.08, indication similarity, 0.06, transporter induction, 0.03, competitive pharmacological, 0.02, and additive pharmacodynamic, 0.01.

We next performed enrichment analysis over HPO terms to identify which ADEs among the ontology associate with each mechanism. This analysis yielded several examples of significant ADEs involving medications that share one or more of the listed mechanisms; for example, thrombocytopenia ($p = 6.13$E-06) was identified as a common ADE that

Table 3: Selected potentially significant ADEs and corresponding counts of associated DDI mechanisms.

No. of associations	ADEs (HPO)
6 mechanisms	Abnormal inflammatory response
	Neurological speech impairment
	Dysphonia
	Abnormality of body weight
	Pancreatitis
	Abnormality of leukocytes
5 mechanisms	Abnormality of bone marrow cell morphology
	Abnormality of erythrocytes
	Abnormality of cells of the erythroid lineage
	Pancytopenia
	Abnormality of multiple cell lineages in the bone marrow
	Thrombocytopenia
	Abnormality of higher mental function
4 mechanisms	Growth abnormality
	Decreased body weight
	Abnormal emotion/affect behaviour
	Restlessness
	Thrombophlebitis
3 mechanisms	Venous thrombosis
	Diabetes mellitus
	Increased body weight
	Seizure
	Sleep disturbance
	Ketosis
2 mechanisms	Abnormal platelet count
	Rheumatoid arthritis
	Hematological neoplasm
	Abnormality of carbohydrate metabolism/homeostasis
	Abnormal glucose homeostasis
	Hypoglycemia
	Abnormal thrombosis
	Diabetic ketoacidosis
	Excessive daytime somnolence
	Reduced consciousness/confusion
	Psychosis
	Abnormality of the urinary system physiology
	Leukopenia
	Acute kidney injury
	Renal insufficiency
	Abnormality of neutrophils
1 mechanism	Abnormality of prenatal development or birth
	Hepatomegaly
	Skin rash
	Multiple myeloma
	Metrorrhagia
	Menstrual irregularities
	Puberty and gonadal disorders
	Abnormality of female internal genitalia
	Abnormality of the cardiovascular system
	Arteriosclerosis
	Abnormality of the systemic arterial tree
	Lymphadenopathy
	Abnormality of the lymph nodes

can be a direct risk for medications sharing the same indication (cf. Tirofiban and abciximab, or quinine and quinidine) [40–42].

To further characterize the associations of DDI mechanisms with ADEs, we categorized ADEs based on the number of associated mechanisms. From each DDI mechanism, we picked the top ten associations having the lowest p values, which yielded 55 examples of potentially significant ADEs. We then tabulated the number of DDI mechanisms associated with each ADE (Table 3). The most prominent was "abnormality of inflammatory response," which was associated with six DDI mechanisms; another eleven ADEs were each associated with five mechanisms. The complete per-mechanism results are reported in Supplementary 1.

In addition to potentially predicting ADEs that could result in noxious ADRs, this approach opens avenues for providing some indication of their frequency, which could aid clinicians in identifying at-risk patients. However, an important limitation to consider is data availability. When designing a data-driven system, the quantity of training data can potentially be limited by available financial and material resources, as well as the scope of the design. In regard to commercial repositories of DDI mechanisms, readily available data can be quite constrained by factors including limited sharing, limited research, and private control of information. Such limitations are a driving force behind the construction of computational systems; this study was impelled by the apparent lack of an automated resource for evaluating the effectiveness of such systems from a clinical standpoint. Considering that one of the primary goals in designing this framework was to raise the standard of research by only associating DDI mechanisms with clinically proven ADEs, it was necessary to base the training data on highly reliable information from clinical sources and medical practice. This led to the use and reuse of established knowledge repositories and consequently leveraging collective information from multiple resources. Notably, the knowledge sources employed here were by no means comprehensive given the many other high-quality sources available. Rather than constituting a limit of this framework, however, the existence of such additional sources offers opportunities for its future expansion. For one, the depth, precision, and recall can be improved by way of additional training data. Similarly, incorporating additional types of information that lead to expanded annotations can extend the breadth of inferences and classifications. This framework should not be construed as an end goal; indeed, it should ideally lead to its own obsolescence if the inferences used to draw prove of significant aid in expanding the known associations of DDI mechanisms with ADRs.

4. Conclusions

This study developed a data-driven medical decision framework for identifying potential ADE mechanisms and anticipating potential ADRs in a knowledge-driven manner. The framework combines a semantic inference system and enrichment analysis and is distinct from extant efforts in approaching the problem from the perspectives of drugs and diseases. Here, the framework was employed first to rank DDI mechanisms and second to relate ADEs to DDI mechanisms based on data from commercial and publicly available resources. Its performance was further evaluated on patient health records from TWOSIDES, in which the framework demonstrated good performance at grouping ADEs with known mechanisms. Overall, the results of these tasks support this framework as being a potentially useful tool for clinicians and researchers alike.

Data Availability

The data used in the paper are available from the corresponding upon request due to requirements of permission and consent.

Conflicts of Interest

The author declares no conflicts of interest.

Supplementary Materials

The top 20 overrepresented HPO terms for each drug-drug interaction mechanism is being provided in the supplementary (1). (*Supplementary Materials*)

References

[1] D. C. Classen, S. L. Pestotnik, R. S. Evans, J. F. Lloyd, and J. P. Burke, "Adverse drug events in hospitalized PatientsExcess length of stay, extra costs, and attributable mortality," *JAMA: The Journal of the American Medical Association*, vol. 277, no. 4, pp. 301–306, 1997.

[2] D. J. Cullen, B. J. Sweitzer, D. W. Bates, E. Burdick, A. Edmondson, and L. L. Leape, "Preventable adverse drug events in hospitalized patients," *Critical Care Medicine*, vol. 25, no. 8, pp. 1289–1297, 1997.

[3] D. J. Cullen, D. W. Bates, S. D. Small, J. B. Cooper, A. R. Nemeskal, and L. L. Leape, "The incident reporting system does not detect adverse drug events: a problem for quality improvement," *Joint Commission Journal on Quality Improvement*, vol. 21, no. 10, pp. 541–548, 1995.

[4] D. W. Bates, N. Spell, D. J. Cullen et al., "The costs of adverse drug events in hospitalized patients," *JAMA: The Journal of the American Medical Association*, vol. 277, no. 4, pp. 307–311, 1997.

[5] D. W. Bates, D. J. Cullen, N. Laird et al., "Incidence of adverse drug events and potential adverse drug events," *JAMA*, vol. 274, no. 1, pp. 29–34, 1995.

[6] World Health Organization, *The Importance of Pharmacovigilance*, World Health Organization, Geneva, Switzerland, 2002.

[7] R. Leaman, L. Wojtulewicz, R. Sullivan, A. Skariah, J. Yang, and G. Gonzalez, "Towards internet-age pharmacovigilance: extracting adverse drug reactions from user posts in health-related social networks," in *Proceedings of the 2010 Workshop on Biomedical Natural Language Processing*, pp. 117–125, Sweden, 2010 July.

[8] A. Noor, "Improving bioinformatics software quality through incorporation of software engineering practices," *PeerJ Computer Science*, vol. 8, p. e839, 2022.

[9] N. P. Tatonetti, P. P. Ye, R. Daneshjou, and R. B. Altman, "Data-driven prediction of drug effects and interactions," *Science Translational Medicine*, vol. 4, no. 125, p. 125ra31, 2012.

[10] S. N. Shah, R. S. Gammal, M. G. Amato et al., "Clinical utility of pharmacogenomic data collected by a health-system Biobank to predict and prevent adverse drug events," *Drug Safety*, vol. 44, no. 5, pp. 601–607, 2021.

[11] I. Karlsson, J. Zhao, L. Asker, and H. Boström, "Predicting adverse drug events by analyzing electronic patient records," in *Proceedings of the Conference on Artificial Intelligence in Medicine in Europe*, pp. 125–129, Berlin, Heidelberg, 2013 May.

Hindawi
Journal of Healthcare Engineering
Volume 2023, Article ID 9860989, 1 page
https://doi.org/10.1155/2023/9860989

Retraction

Retracted: Effect of Transumbilical Single-Port Laparoscopic-Assisted Duhamel Operation on Serum CRP and IL-6 Levels in Children with Hirschsprung's Disease

Journal of Healthcare Engineering

Received 26 September 2023; Accepted 26 September 2023; Published 27 September 2023

This article has been retracted by Hindawi following an investigation undertaken by the publisher [1]. This investigation has uncovered evidence of one or more of the following indicators of systematic manipulation of the publication process:

(1) Discrepancies in scope
(2) Discrepancies in the description of the research reported
(3) Discrepancies between the availability of data and the research described
(4) Inappropriate citations
(5) Incoherent, meaningless and/or irrelevant content included in the article
(6) Peer-review manipulation

The presence of these indicators undermines our confidence in the integrity of the article's content and we cannot, therefore, vouch for its reliability. Please note that this notice is intended solely to alert readers that the content of this article is unreliable. We have not investigated whether authors were aware of or involved in the systematic manipulation of the publication process.

In addition, our investigation has also shown that one or more of the following human-subject reporting requirements has not been met in this article: ethical approval by an Institutional Review Board (IRB) committee or equivalent, patient/participant consent to participate, and/or agreement to publish patient/participant details (where relevant).

Wiley and Hindawi regrets that the usual quality checks did not identify these issues before publication and have since put additional measures in place to safeguard research integrity.

We wish to credit our own Research Integrity and Research Publishing teams and anonymous and named external researchers and research integrity experts for contributing to this investigation.

The corresponding author, as the representative of all authors, has been given the opportunity to register their agreement or disagreement to this retraction. We have kept a record of any response received.

References

[1] M. Wang, W. Pang, L. Zhou, J. Ma, and S. Xie, "Effect of Transumbilical Single-Port Laparoscopic-Assisted Duhamel Operation on Serum CRP and IL-6 Levels in Children with Hirschsprung's Disease," *Journal of Healthcare Engineering*, vol. 2022, Article ID 8349851, 8 pages, 2022.

Hindawi
Journal of Healthcare Engineering
Volume 2022, Article ID 8349851, 8 pages
https://doi.org/10.1155/2022/8349851

Research Article

Effect of Transumbilical Single-Port Laparoscopic-Assisted Duhamel Operation on Serum CRP and IL-6 Levels in Children with Hirschsprung's Disease

Miao Wang, Wenshuai Pang, Lixia Zhou, Jiansu Ma, and Shasha Xie

Xingtai People's Hospital, Hebei, Xingtai 054000, China

Correspondence should be addressed to Shasha Xie; xieshasha72tx@163.com

Received 5 January 2022; Revised 29 January 2022; Accepted 31 January 2022; Published 2 March 2022

Academic Editor: Liaqat Ali

Objective. To explore the clinical intervention effect of transumbilical single-port laparoscopic-assisted Duhamel operation on children with Hirschsprung's disease (HD) and to analyze the effect of treatment on children with serum C-reactive protein (CRP) and interleukin-6 (IL-6) effects. *Methods.* Retrospectively select 80 children with HD who underwent surgery in our hospital from May 2017 to May 2020 as the research subjects and they are classified as group A according to the difference of the children's surgical procedures (receiving transumbilical single-port laparoscopic-assisted Duhamel surgery, 40 cases) and group B (receiving conventional laparoscopic surgery, 40 cases), compare the perioperative period (operating time, intraoperative blood loss, surgical posthospitalization, and postoperative gastrointestinal function recovery time), early postoperative complications (perianal dermatitis, urinary retention, enterocolitis, and anastomotic leakage), and late postoperative complications (anastomotic stenosis, dirty stool, recurrence of constipation, and enterocolitis), compare the differences in the levels of CRP and IL-6 between the two groups of children before and after the operation, and conduct a 1-year follow-up of the two groups of children to compare the long-term defecation status. *Results.* The surgical time of children in group A, postoperative hospitalization time, and postoperative gastrointestinal function recovery time were significantly shorter than those of group B, and the differences between groups were statistically significant ($P < 0.05$). A group of patients: the total incidence of postearly complications was 5.00% lower than 22.50% ($P < 0.05$) in group B ($P < 0.05$), and the total incidence of previous complications after group A of patients was 10.00% lower than 27.50% of group B ($P < 0.05$). The two groups of serum CRP and IL-6 in two groups were not statistically significant ($P > 0.05$), and the serum CRP and IL-6 levels of children in group A after surgery were 3 days. It is obviously lower than those in group B, and the differences between groups have statistical significance ($P < 0.05$). At 1 month after surgery, the average bowel movement time in group A is significantly lower than those of group B ($P < 0.05$); during the 1–12 months, the difference between the defecation frequency group of the group A and group B did not have statistically significance ($P > 0.05$). *Conclusion.* Transumbilical single-port laparoscopic assistant Duhamel operation of HD has a good intervention effect, compared to traditional laparoscopic surgery, the operation time, postoperative hospitalization time, and postoperative gastrointestinal function recovery time, and also help to reduce postoperative near-long complications The incidence improves the stress reactions and long-term defecation functions in children.

1. Introduction

Hirschsprung's disease (HD) is one of the common types of pediatric digestive tract developmental deformities [1]. Its incidence ranks second among congenital malformations of the digestive system. The lesions in children are characterized by the intermuscular nerves at the end of the intestine. The lack of plexus and submucosal ganglion cells causes the intestinal tube to be in a state of spasm, loses normal peristaltic function, and makes the intestine in a narrow state [2, 3]. The clinical manifestations of children with HD are mainly refractory constipation, abdominal distension, malnutrition, and stunted growth or Hirschsprung's disease with enterocolitis. In recent years, the improvement of diagnosis and treatment technology has enabled 70–90% of cases to be diagnosed in the neonatal period, and only a few children with milder clinical symptoms are not diagnosed until adolescence or adulthood [4, 5]. Since the long-term development of this disease will cause the expansion of the proximal colon to continue to increase, the patient's constipation symptoms will continue to increase or even develop into acute intestinal obstruction, and it is recommended to carry out early active surgical treatment for such children [6].

The current surgical treatment principle of HD is to remove the intestinal segment without ganglion cells and the expanded intestinal segment [7]. Since the Swenson procedure was applied to the clinical treatment of HD in 1948, various modified procedures such as by Duhamel, Rehbein, and Sovae have continued emerging, providing medical workers with a variety of options [8]. Since the 1980s, minimally invasive techniques represented by laparoscopy have been gradually used in the radical resection of HD. In 1999, laparoscopic-assisted Soave endorectal evacuation was recognized as the gold standard for HD treatment. With the continuous improvement of laparoscopic technology and the continuous improvement of surgical instruments, scarless surgery such as single incision through the umbilical or through the natural cavity has become the mainstream treatment for HD [9, 10]. This study is currently planning to take 80 children with HD admitted to our hospital from May 2019 to May 2020 as the research object.

A comparative analysis by means of statistical measures between transumbilical single-port laparoscopic-assisted Duhamel surgery and conventional laparoscopic surgery is carried out. The pros and cons of the surgical treatment of children with HD are compared in order to provide more detailed theoretical support for improving the prognosis of children with HD.

2. Materials and Methods

2.1. General Information. We retrospectively selected 80 children with HD who underwent surgery in our hospital from May 2017 to May 2020 as the research objects and divided them into group A according to the difference of the children's surgical procedures (receiving transumbilical single-port laparoscopic-assisted Duhamel surgical treatment, 40 cases) and group B (receiving conventional laparoscopic surgery, 40 cases). The two groups of gender, age, weight, and lesion are included, and the intergroup differential comparisons were implemented. As a result, the difference between the above data groups in the two groups did not have statistically significant ($P > 0.05$), suggesting comparable (Table 1).

Inclusion criteria: those who have been diagnosed with Hirschsprung's disease, those who are ineffective in conservative treatment and have indications for surgery, and the case data are complete.

Exclusion criteria: patients with congenital malformations or organic diseases, combined with severe heart, liver, and kidney function failures, combined with malignant tumor, patients with hematological diseases, included other unfinished clinical researchers.

2.2. Intervention Methods. Children in group A underwent transumbilical single-port laparoscopic-assisted Duhamel operation, received conventional antibiotic treatment before operation, and selected general anesthesia for tracheal intubation. A longitudinal incision was made at the umbilical fossa of the children, and a trocar was placed to create an artificial pneumoperitoneum environment (8–12 mmHg); the child's lithotomy position was used to dilate the anus, and the rectal mucosa was incised obliquely at a distance of 1 cm from the dentinal line and 2 cm from the anterior wall of the rectal mucosa. Mesocolon, pull the free colon to the right lower abdomen, push the small intestine to the left upper abdomen, straighten out the mesenteric blood vessels, transfer the operation to the perineum, cut off the rectal muscle sheath through the anus, and drag the free colon out of the body and cut it off. And finally, implement the colorectal anastomosis. The preoperative operation of the children in group B was the same as that in group A. The same incision was made in the umbilical area, and a laparoscope with a 5 mm operating channel was inserted. After the situation was verified, a 5 mm trocar was placed in the left and right lower abdomen, and an ultrasonic knife edge was used. Dissociate around the pelvic cavity and rectum and process the colonic mesangium and blood vessels until the normal intestinal canal. After dissociation is completed, perform perineal operations and finally suture the edge of the colon and rectal mucosa.

2.3. Observation Indicators and Evaluation Standards. General surgical indicators of the two groups of children, including operation time, postoperative hospitalization time, intraoperative blood, and postoperative gastrointestinal function recovery time; early postoperative complications of the two groups of children include perianal dermatitis, incidence rates of urinary retention, enterocolitis, and secondary operations; the incidence of long-term postoperative complications of the two groups of children including anastomotic stenosis, feces, constipation recurrence, and enterocolitis; serum CRP and IL-6 levels of the two groups of children when they were admitted to the hospital and 3 days after the operation; the defecation function evaluation of the two groups of children after 12 months of follow-up.

2.4. Statistical Methods. The collected data are entered into the Excel form, statistical SPSS 22.0 software was used for data analysis, and a normal distribution test on the collected data was carried out, such as data compliance with normal distribution, counting data is indicated by (n (%)), differential analysis selection card foundation inspection, metrology data representation (measurement) difference analysis, and t-test was selected. Take $P < 0.05$ as a statistical significance [11].

3. Results

3.1. Comparison of Differences in Perioperative Indicators between the Two Groups of Children. In comparison, the

Table 1: Comparison of baseline data differences in two groups ($\overline{x} \pm s$)/(n (%)).

Baseline data		Group A ($n = 40$)	Group B ($n = 40$)	t/χ^2	P
Gender	Male	21	19	0.05	0.823
	Female	20	20		
Average age (years)		2.79 ± 0.22	2.81 ± 0.19	0.435	0.665
Average weight (kg)		15.19 ± 1.22	15.23 ± 1.09	0.155	0.877
Average height (cm)		0.81 ± 0.05	0.79 ± 0.07	1.47	0.146
Type of lesion	Common type	34	35	0.105	0.745
	Long section	6	5		

operation time of children in group A, postoperative hospitalization time, and postoperative gastrointestinal function recovery time were significantly shorter than those of the group B, and the difference in groups had statistically significance ($P < 0.05$), and the intraoperative blood volume is two. The difference in groups does not have statistical significance ($P > 0.05$) (Figure 1).

The comparison showed that the operation time, postoperative hospital stay, and postoperative gastrointestinal function recovery time of group A were significantly shorter than those of group B. The differences between groups are statistically significant. It is of statistical significance ($P < 0.05$); the difference between the two groups in the intraoperative blood loss did not have statistically significance ($P > 0.05$). It means that the difference between the same index group is statistically significant.

3.2. Comparison of the Incidence of Early Postoperative Complications in the Two Groups. Statistics showed that 1 case of perianal dermatitis and 1 case of enterocolitis occurred in group A. The total incidence of complications was 5.00%. In group B, there were 3 cases of perianal dermatitis, 1 case of urinary retention, and 5 cases of enterocolitis. The total incidence rate was 22.50%, and the difference between the individual complications of the individual complications was not statistically significant ($P > 0.05$), and the total incidence of complications was lower than that in group B ($P < 0.05$) (Table 2, Figure 2).

There was no statistically significant difference in the two groups in recent complications after surgery. The total incidence of recent complications in groups was significantly lower than those in group B ($P < 0.05$). The comparison between the same indicator group is statistically significant.

3.3. Comparison of the Incidence of Long-Term Complications after the Operation of the Two Groups of Children. Statistics showed that 2 children in group A had postoperative fecal contamination, 2 cases of enterocolitis, and the total complication rate was 10.00%. In group B children, postoperative anastomotic stenosis occurred in 1 case, fecal contamination was in 5 cases, constipation recurred in 1 case, and 4 cases of enterocolitis; the total incidence of complications was 27.50%. The total incidence of comparative complications in group A was lower than those in group B ($P < 0.05$) (Table 3, Figure 3).

Compared with 2 cases of fecal infection and 2 cases of enterocolitis in group A, the total incidence of postoperative complications in group B was 10.00%. The incidence of anastomotic stoma was in group B, including 1 case of stenosis, 5 cases of fecal contamination, 1 case of constipation, and 4 cases of enterocolitis. The total incidence of complications was 27.50%. It can be concluded that the incidence of complications in group A is lower than that in group B ($P < 0.05$). This means that the difference between the same finger array is statistically significant.

3.4. Differences in Serum CRP and IL-6 Levels between the Two Groups before and after Operation. At the time of admission, the two groups of children were collected in the empty stomach of the two groups, and preoperative and postoperative serum CRP and IL-6 levels were detected after surgery. Differential differences between the sexy fraternal CRP and IL-6 were not statistically significant ($P > 0.05$), and serum CRP and IL-6 levels in group A were significantly lower than those in group B, and the difference in groups was significantly lower than those in the group. It has statistically significance ($P < 0.05$), while serum CRP and IL-6 levels in two groups of children before surgery were significantly reduced ($P < 0.05$) (Table 4, Figure 4).

3.5. Differences in Long-Term Prognosis Assessment between the Two Groups. Assess the long-term prognosis of the two groups. The results show that at 1 month after surgery and 3 months follow-up, the average bowel movement of the A group is significantly lower than that of group B ($P < 0.05$); 6 months after surgery, 9 months after surgery, and 12 months after surgery, the difference in the defecation time group of group A and group B did not have statistically significance ($P > 0.05$). The difference between the two groups of patients during 1–12 months after surgery did not have statistically significance ($P > 0.05$) (Figures 5 and 6).

As shown in Figure 6, for 12 months, during 1–12 months after surgery, the difference in the defecation frequency group in group A and group B did not have a statistical significance ($P > 0.05$).

4. Discussion

Hirschsprung's disease (HD) was first formally named in 1894. At first, medical workers believed that the pathological feature of the disease was expansion of the colon and the formation of Hirschsprung's disease led to constipation [12]. It was not until 1948 that Swenson discovered that the pathological feature of HD was stenosis of the distal bowel

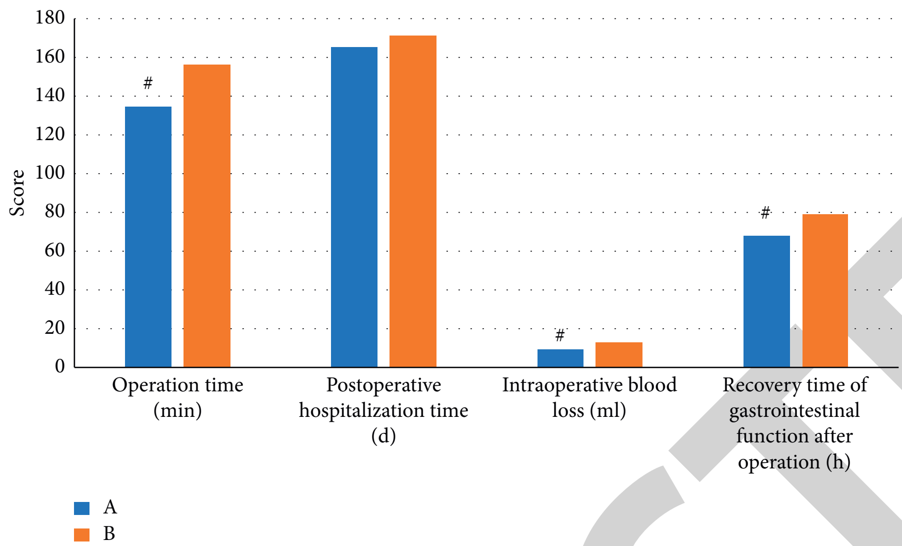

Figure 1: Comparison of perioperative index differences in children in two groups.

Table 2: Comparison of the incidence of early postoperative complications between the two groups of children (n (%)).

Group	Number of cases	Perianal dermatitis	Urinary retention	Enterocolitis	Second surgery	Total incidence
Group A	40	1 (2.50)	0 (0.00)	1 (2.50)	0 (0.00)	2 (5.00)
Group B	40	3 (7.50)	1 (2.50)	5 (12.50)	0 (0.00)	9 (22.50)
X^2	—	1.053	1.013	2.88	0.0	5.165
P	—	0.305	0.314	0.090	1.0	0.023

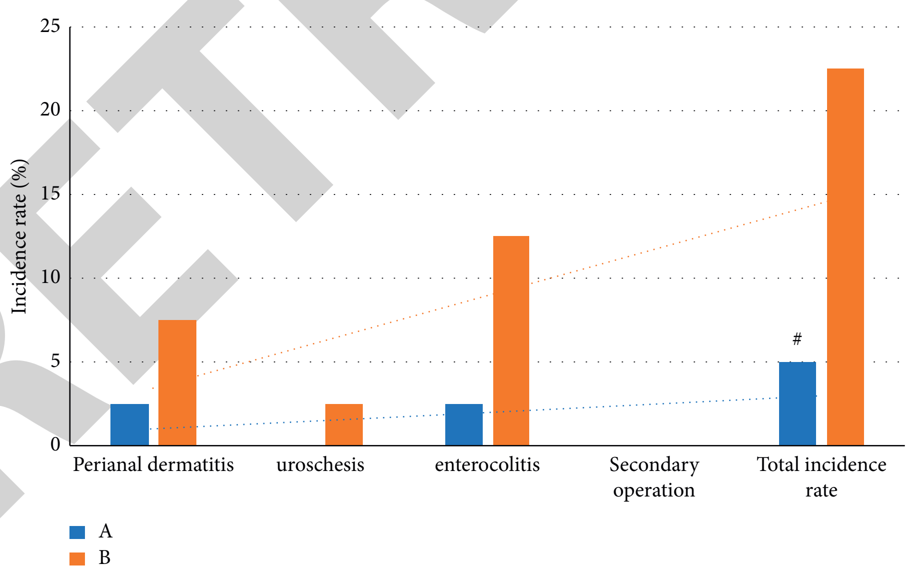

Figure 2: The incidence of early complications in the two groups.

through barium enema and finally confirmed that its pathological mechanism was the loss of ganglion cells in the stenosis of the colon, which caused the expansion of the proximal colon [13, 14]. HD is currently a relatively common gastrointestinal malformation in pediatric surgery. The incidence is relatively high in the Middle East worldwide, and the incidence in Europe is relatively low. My country is a high-risk group of HD [15, 16].

This study established a control group to demonstrate in detail the advantages and disadvantages of applying transumbilical single-port laparoscopic-assisted Duhamel surgery and traditional laparoscopic surgery in the

Table 3: Comparison of the incidence of long-term postoperative complications between the two groups of children (n (%)).

Group	Number of cases	Anastomotic stenosis	Dung	Recurrence of constipation	Enterocolitis	Total incidence
Group A	40	0 (0.00)	2 (2.50)	0 (0.00)	2 (5.00)	4 (10.00)
Group B	40	1 (2.50)	5 (12.50)	1 (2.50)	4 (10.00)	11 (27.50)
X^2	—	1.013	1.409	1.013	0.721	4.021
P	—	0.314	0.235	0.314	0.396	0.045

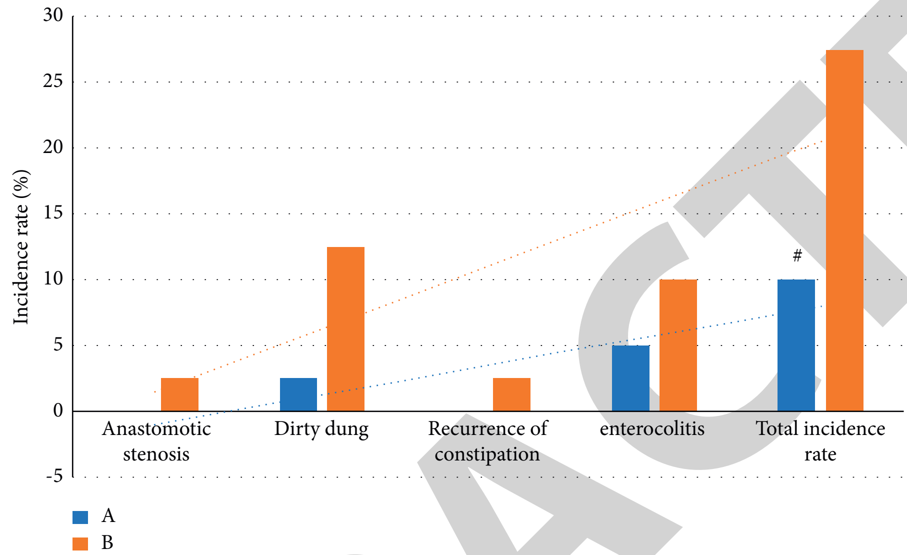

Figure 3: The incidence of postoperative complications after two groups.

Table 4: Differences in serum CRP and IL-6 levels between the two groups of children before and after surgery ($\bar{x} \pm s$).

Group	Number of cases	CRP (mg/ml)		IL-6 (pg/ml)	
		On admission	3 d after operation	On admission	3 d after operation
Group A	40	39.29 ± 5.44	$15.49 \pm 2.11^{\#}$	36.98 ± 2.11	$25.67 \pm 4.33^{\#}$
Group B	40	39.98 ± 4.98	$20.11 \pm 1.98^{\#}$	37.32 ± 1.98	$29.11 \pm 3.98^{\#}$
t	—	0.592	10.098	0.743	3.699
P	—	0.556	<0.001	0.460	0.000

Compared with admission, $^{\#}P < 0.05$.

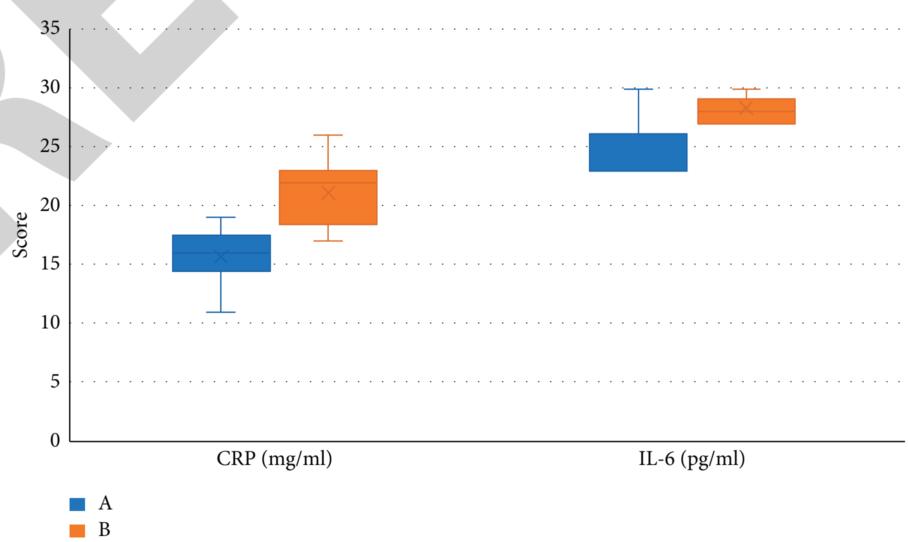

Figure 4: The serum CRP and IL-6 levels of children in two groups before and after surgery. The serum CRP and IL-6 levels of children in group A were significantly lower than those in group B, and the difference in groups was significantly lower than those of group B, and the difference in groups was statistically significant ($P < 0.05$). $^{\#}$The comparison between the same indicator group is statistically significant.

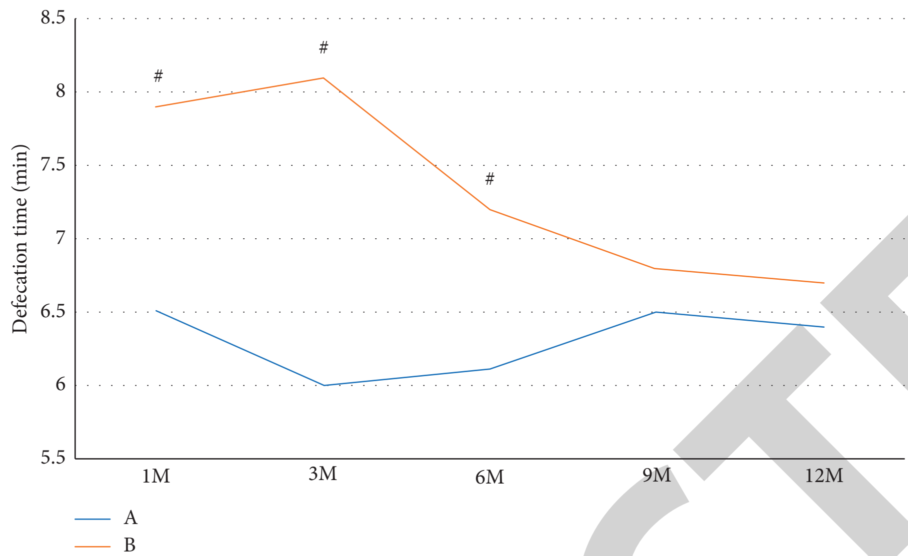

Figure 5: Postoperative defecation time follow-up for two groups of patients. For 12 months at 1 month after surgery, the average bowel movement of the A group was significantly lower than those of group B ($P < 0.05$); 6 months after surgery, 9 months after surgery, and 12 months after surgery, the difference in the blasting time group in groups A and B did not have statistically significance ($P > 0.05$). #The comparison between the same indicator group is statistically significant.

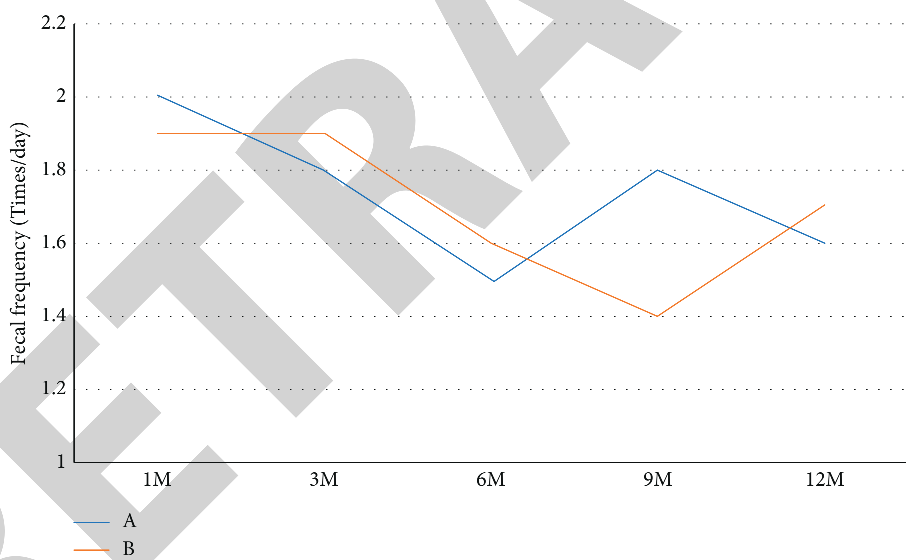

Figure 6: After the two groups of patients were followed up.

surgical treatment of children with HD. The results show that compared with traditional laparoscopic surgery in group B of children, children in group A who underwent transumbilical single-port laparoscopic-assisted Duhamel surgery had obvious advantages in terms of operation time, postoperative hospital stay, and postoperative gastrointestinal function recovery time, which are comparable to the results of other scholars [17]. The results of a comparative study conducted on 109 children with HD showed that compared with traditional laparoscopic surgery, transumbilical laparoscopic surgery has the advantages of less trauma and faster recovery after surgery, which is convenient for shortening the postoperative hospital stay [18]. The author of this article analyzes and believes that transumbilical single-port laparoscopic surgery is a modified operation that can be inserted into the umbilical laparoscopic to explore the lesions and complete the perineal rectal mucosal dissection. On the one hand, this operation only has a hidden incision in the umbilical area. It is easy for parents to accept, and on the other hand, it effectively eliminates the "chopstick effect" brought by the same direction operating equipment, which is convenient for intraoperative operation [19].

The article also analyzes the incidence of short and long-term complications in children undergoing two types of surgery. The results show that group A has obvious advantages in terms of both short-term and long-term complications. The author of this article analyzes and believes that the emergence of complications is an important reason for the poor prognosis of children. In this study, the incidence of short-term and long-term complications after surgery in group A was low. The reason may be related to the following transumbilical single-port laparoscopic-assisted Duhamel surgery advantages: comprehensive exploration of the abdominal cavity during the operation can accurately determine the diseased intestine; it can better preserve the vascular arch of the intestine edge, reduce the damage to the external anal sphincter, avoid excessive traction on the sigmoid colon, and reduce postoperative anastomotic leakage, the emergence of feces, and the rapid recovery of defecation function in children after surgery; the use of NOTES surgical instruments during surgery is avoided, and medical costs are reduced [20, 21]. In fact, this point is also reflected in the levels of serum CRP and IL-6 in the two groups of children after surgery. On the one hand, serum CRP and IL-6 can be used as indicators to reflect the postoperative inflammatory status of the children, and on the other hand, it can also reflect the degree of stress in children during operation [22, 23]. The abovementioned indicators in group A are lower than those in group B after surgery, which indicates that the stress stimulation in group A is lower during operation. The perioperative indexes of children in group A are better than those in group B.

Finally, the article also conducted a preliminary analysis of the long-term prognosis of the two groups of children. The results showed that the average defecation time of the children in group A was lower than that of group B in the early postoperative period, but the defecation function of the two groups of children was not obvious in the long-term. The difference indicates that the two types of surgery have a significant improvement effect on the long-term defecation function of children, but the difference between the groups is not obvious. It is recommended that in terms of reducing the early postoperative stress response and the incidence of complications in children, try to choose transumbilical single-port laparoscopic-assisted Duhamel surgery for children with HD [24].

In summary, transumbilical single-port laparoscopic-assisted Duhamel surgery has a better intervention effect on children with HD. Compared with traditional laparoscopic surgery, it can significantly shorten the operation time, postoperative hospital stay, and postoperative gastrointestinal function recovery time, and it also helps to reduce short and long-term postoperative complications, incidence rate and improve postoperative stress response and long-term bowel function in children.

Data Availability

The data used to support the findings of this study are available from the corresponding author upon request.

Conflicts of Interest

The authors declare that there are no conflicts of interest.

Acknowledgments

This work was supported by Xingtai People's Hospitale.

References

[1] L. Ambartsumyan, C. Smith, and R. P. Kapur, "Diagnosis of Hirschsprung disease," *Pediatric and Developmental Pathology*, vol. 23, no. 1, pp. 8–22, 2020.

[2] A. D. Harouna, I. Salahoudine, A. Mahamoudi, A. E. Madi, K. Khattala, and Y. Bouabdallah, "Perforation cæcale néonatale inaugurale du diagnostic d'un mégacôlon congénital [Neonatal caecal perforation revealing congenital megacolon]. Pan Afr," *Journal of Forests*, vol. 31, p. 216, 2018 in French.

[3] Y. Shen, Y. Fang, D. Wu, J. Bai, and Y. Lin, "Application of wc," *Journal of Paediatrics and Child Health*, vol. 56, no. 10, pp. 1551–1556, 2020.

[4] S. Chusilp, B. Li, D. Lee, C. Lee, P. Vejchapipat, and A. Pierro, "Intestinal organoids in infants and children," *Pediatric Surgery International*, vol. 36, no. 1, pp. 1–10, 2020.

[5] X. J. Wang and M. Camilleri, "Hirschsprung disease: insights on genes penetrance and prenatal diagnosis," *Neuro-Gastroenterology and Motility The Official Journal of the European Gastrointestinal Motility Society*, vol. 31, no. 11, Article ID e13732, 2019.

[6] L. V. Veras, M. Arnold, J. R. Avansino et al., "Guidelines for synoptic reporting of surgery and pathology in h," *Journal of Pediatric Surgery*, vol. 54, no. 10, pp. 2017–2023, 2019.

[7] M. Klein and I. Varga, "Hirschsprung's disease-recent understanding of embryonic aspects, etiopathogenesis and future treatment avenues," *Medicina*, vol. 56, no. 11, p. 611, 2020.

[8] R. O. Heuckeroth, "Hirschsprung disease - integrating basic science and clinical medicine to improve outcomes," *Nature Reviews Gastroenterology & Hepatology*, vol. 15, no. 3, pp. 152–167, 2018.

[9] J. M. Tilghman, A. Y. Ling, T. N. Turner et al., "Molecular genetic anatomy and risk profile of Hirschsprung's disease," *New England Journal of Medicine*, vol. 380, no. 15, pp. 1421–1432, 2019.

[10] K. Kyrklund, C. E. J. Sloots, I. de Blaauw et al., "ERNICA guidelines for the management of rectosigmoid Hirschsprung's disease," *Orphanet Journal of Rare Diseases*, vol. 15, no. 1, p. 164, 2020.

[11] R. Soret, S. Schneider, G. Bernas et al., "Glial cdn factor induces enteric neurogenesis and improves colon structure and function in mouse models of Hirschsprung disease," *Gastroenterology*, vol. 159, no. 5, pp. 1824–1838, Article ID e17, 2020.

[12] H. Nakamura, T. Lim, and P. Puri, "Inflammatory bowel disease in patients with Hirschsprung's disease: a systematic review and meta-analysis," *Pediatric Surgery International*, vol. 34, no. 2, pp. 149–154, 2018.

[13] B. B. Rogers, "Forward perspectives in pediatric pathology Hirschsprung disease," *Pediatric and Developmental Pathology*, vol. 23, no. 1, p. 3, 2020.

[14] Y. Dai, Y. Deng, Y. Lin, R. Ouyang, and L. Li, "Long-term outcomes and quality of life of patients with hirschsprung disease: a systematic review and meta-analysis," *BMC Gastroenterology*, vol. 20, no. 1, p. 67, 2020.

[15] R. J. Meinds, A. F. W. van der Steeg, C. E. J. Sloots et al., "Long-term functional outcomes and quality of life in patients

Hindawi
Journal of Healthcare Engineering
Volume 2023, Article ID 9818379, 1 page
https://doi.org/10.1155/2023/9818379

Retraction

Retracted: Serum Expression Level of MicroRNA-122 and Its Significance in Patients with Hepatitis B Virus Infection

Journal of Healthcare Engineering

Received 26 September 2023; Accepted 26 September 2023; Published 27 September 2023

This article has been retracted by Hindawi following an investigation undertaken by the publisher [1]. This investigation has uncovered evidence of one or more of the following indicators of systematic manipulation of the publication process:

(1) Discrepancies in scope
(2) Discrepancies in the description of the research reported
(3) Discrepancies between the availability of data and the research described
(4) Inappropriate citations
(5) Incoherent, meaningless and/or irrelevant content included in the article
(6) Peer-review manipulation

The presence of these indicators undermines our confidence in the integrity of the article's content and we cannot, therefore, vouch for its reliability. Please note that this notice is intended solely to alert readers that the content of this article is unreliable. We have not investigated whether authors were aware of or involved in the systematic manipulation of the publication process.

Wiley and Hindawi regrets that the usual quality checks did not identify these issues before publication and have since put additional measures in place to safeguard research integrity.

We wish to credit our own Research Integrity and Research Publishing teams and anonymous and named external researchers and research integrity experts for contributing to this investigation.

The corresponding author, as the representative of all authors, has been given the opportunity to register their agreement or disagreement to this retraction. We have kept a record of any response received.

References

[1] Q. Fang, W. Chen, Y. Jian et al., "Serum Expression Level of MicroRNA-122 and Its Significance in Patients with Hepatitis B Virus Infection," *Journal of Healthcare Engineering*, vol. 2022, Article ID 8430276, 7 pages, 2022.

Hindawi
Journal of Healthcare Engineering
Volume 2022, Article ID 8430276, 7 pages
https://doi.org/10.1155/2022/8430276

Research Article

Serum Expression Level of MicroRNA-122 and Its Significance in Patients with Hepatitis B Virus Infection

Qingqing Fang,[1] Wei Chen,[1] Yourong Jian,[1] Yu Li,[1] Wei Lian,[1] Hongyu Wan,[1] Shiyao Chen,[1,2] Feng Li,[1,2] and Ying Chen[1]

[1]*Department of Gastroenterology, Minhang Hospital, Fudan University, Shanghai 201199, China*
[2]*Department of Gastroenterology, Zhongshan Hospital, Fudan University, Shanghai 200032, China*

Correspondence should be addressed to Feng Li; 13661654285@163.com and Ying Chen; chenying_1120@fudan.edu.cn

Qingqing Fang and Wei Chen contributed equally to this work.

Received 9 January 2022; Accepted 26 January 2022; Published 24 February 2022

Academic Editor: Liaqat Ali

Objectives. To analyze the expression of miR-122 and evaluate its significance in patients with HBV infection in different phases. *Methods*. Eleven chronic hepatitis B (CHB), 26 hepatitis B virus (HBV)-induced cirrhosis, 16 HBV-associated hepatocellular carcinoma (HCC) patients and 10 healthy control cases were enrolled. The serum levels of miR-122 were detected by RT-PCR and compared between healthy individuals and CHB at different stages. *Results*. Compared with healthy control cases, serum miR-122 levels were markedly increased in HBV infection cases (AUC = 0.795, $P = 0.002$). In the CHB group, miR-122 levels were positively associated with albumin levels ($P < 0.05$) but had no significant associations with alanine aminotransferase (ALT) and aspartate aminotransferase (AST) ($P > 0.05$). In the cirrhosis group, miR-122 expression was remarkably lower in the Child C group in comparison with the Child A group ($P = 0.025$). At the same time, miR-122 amounts had a negative correlation with HVPG ($P < 0.05$). In the HCC group, miR-122 amounts were negatively associated with alkaline phosphatase (AKP) and alpha-fetoprotein (AFP) ($P < 0.05$). Serum miR-122 amounts in 3 patients who died were lower than the survival group (5.520 ± 0.522 vs. 5.860 ± 1.183, $P > 0.05$). *Conclusion*. Serum miR-122 can be leveraged to screen patients with HBV infection. In HBV sufferers, the serum miR-122 expression level is related to liver disease progression, hence making it an underlying molecular biomarker for predicting the development of CHB.

1. Introduction

More than 250 million individuals globally have chronic HBV infection [1]. Persistent HBV infection might induce hepatic damage and develop into advanced hepatic pathologies. Approximately 3%–6% hepatic sclerosis cases may progress to primary HCC [2]. Hence, HBV patients with worsening liver function and decompensating liver cirrhosis should be imperatively assessed at the disease early stage.

HBV replication is modulated by various host factors, including miRNAs. miRNAs are remarkably conserved small ncRNAs that simultaneously regulate physiological and pathological functions in the liver. Changes in the expression of miRNAs are related to hepatic metabolic disorders, hepatic damages, hepatic fibrosis, and tumor progression, which make miRNAs appealing targets for the diagnoses and treatment of hepatic diseases [3].

Research has revealed that an overall 277 miRNAs are expressed in the liver, of which microRNA-122 (miR-122) is considered one of the most potent miRNAs [4, 5]. MiR-122 was shown to decrease HBV DNA levels by downregulating cyclin G1, a negative modulator of p53 [6]. Moreover, miR-122 participates in the intricate signal transmission network in BP involved in hepatic development and differentiation, liver lipidic metabolism, stress reactions, and HCC [7–10]. In addition, miR-122 is related to the phase and seriousness of the infection. This correlation might help measure therapeutic effects [11–13].

The present work aimed to assess miR-122 expression in diverse phases of CHB infection and to examine its significance.

2. Materials and Methods

2.1. Patients. This trial enrolled CHB, hepatitis B-induced sclerosis, and hepatitis B-related HCC patients in the Department of Gastroenterology, Minhang Hospital, Fudan University, from June 2020 to June 2021.

Inclusion criteria were as follows: (1) control group, healthy subjects; (2) CHB group, meeting the diagnostic criteria for chronic hepatitis [14]; (3) hepatitis B cirrhosis group, HBV history, and meeting the diagnostic criteria of the guidelines for diagnosing and treating hepatic sclerosis [15]; and (4) HBV-associated HCC group, HBV history combined with clinical imaging, laboratory indicators, and/or liver biopsy indicating HCC.

Exclusion criteria were as follows: (1) liver damage induced by other causes, including HCV infection, drug intake, drinking quantity, and AIH; (2) severe heart, lung, kidney, and/or systemic diseases; (3) liver cirrhosis and liver cancer caused by other chronic liver diseases; and (4) combination with other malignant tumors. All eligible patients and healthy controls provided written informed consent, and all assays were accepted by the Ethical Board of Minhang Hospital affiliated to Fudan University (batch number: 006-01K).

2.2. Serum Sample Collection. Peripheral blood samples ($n = 63$) were collected and centrifuged at 3000 g for 10 minutes at ambient temperature. The resulting supernatants were further subjected to centrifugation for 10 minutes at 4°C. Then, serum was immediately kept at −80°C until utilization.

2.3. Methods

2.3.1. Determination of miRNA-122 Levels in Serum. The PerfectStart™ Green qPCR SuperMix kit was employed to assess miRNA-122 levels on a LightCycler® 480 II fluorescent quantitation PCR equipment (Roche, Switzerland). The reaction included 2× PerfectStart™ Green qPCR SuperMix (5 μl), 10 μM Universal primer (0.2 μl), 10 μM microRNA-specific primer (0.2 μl), cDNA (1 μl), and nuclease-free water (3.6 μl). Amplification was carried out at 94°C (30 s), followed by 45 cycles of 94°C (5 s) and 60°C (30 s). After the last cycle, a melting curve was utilized to detect product specificity: the temperature was increased from 60°C to 97°C, and fluorescence was recorded 5 times per centigrade. miRNA-122 expression was computed by the $2^{-\Delta\Delta Ct}$ method.

2.3.2. Blood Routine, Biochemical Function, and AFP Measurement. Automatic routine biochemical and immune analyzers were utilized to measure blood routine, liver and kidney function, and AFP.

2.3.3. HVPG Measurement. The hepatic vein wedge pressure and free pressure were measured by jugular vein catheterization, and the difference between the two was HVPG [16].

2.4. Statistics. SPSS 23.0 program was leveraged to assess the data. The data were described as $x \pm s$, and one-way ANOVA was utilized for multigroup comparisons. The t-test was performed for group pair comparisons. Categorical variables were compared by the χ^2 test. Pearson correlation analysis was utilized for classification, rank, or non-normally distributed continuous data. Spearman correlation analysis was utilized for normally distributed continuous data. $P < 0.05$ was considered statistically significant.

3. Results

3.1. Baseline Patient Characteristics. This study enrolled 10 healthy controls, 11 CHB, and 26 hepatic sclerosis cases. There were 10 Child A, 11 Child B, 5 Child C, and 16 HCC cases. No remarkable differences in gender and age were found among these four groups of patients. In terms of HGB, WBC count, Cr, TB, DB, AKP, Alb, and AFP, there were significant differences (Table 1). The data are detailed in Table 1.

3.2. Serum miR-122 Amounts in Healthy Controls and Cases with Different Stages of HBV Infection. In contrast to the healthy control cases, the expression levels of miR-122 were increased significantly in the CHB, HBV-related cirrhosis, and HCC groups (Figure 1; all $P < 0.05$). Among the infected patients, the highest miR-122 amounts were detected in the CHB group ($P < 0.05$). There were no remarkable diversities between the cirrhosis and HCC groups in terms of miR-122 levels ($P = 0.878$).

3.3. Significance of Serum miR-122 Expressing in Chronic Hepatitis B. ROC curves were generated for assessing the diagnostic efficacy of serum miR-122 in CHB. Serum miR-122 expression displayed a great diagnostic value for HBV infection (Figure 2(a); AUC = 0.795, $P = 0.002$). Therefore, serum miR-122 was expected to be effective in screening patients with HBV infection. Meanwhile, in the CHB group, serum miR-122 was significantly associated with albumin content (Figure 2(b), $P = 0.030$) but showed no associations with ALT and AST (both $P > 0.05$).

3.4. Significance of Serum miR-122 Expression in Cirrhosis. In the hepatic sclerosis group, serum miR-122 amounts in cases with distinct Child–Pugh scores were different, which were higher in Child A cases than Child C cases (Figure 3(a), $P < 0.05$). More importantly, serum miR-122 amounts were negatively associated with HVPG (Figure 3(b), $P = 0.037$). Serum miR-122 amounts in cases with HVPG ≤ 10 and HVPG > 10 were 6.741 ± 1.177 and 5.788 ± 0.838, respectively (Figure 3(c), $P = 0.062$). Therefore, miR-122 may be an effective index for predicting further decompensation of liver cirrhosis and aggravation of portal hypertension.

3.5. Significance of Serum miR-122 Expression in Hepatocellular Carcinoma. The associations of clinical indexes with miR-122 in 16 serum specimens in the HCC group were

Table 1: Clinical data of four groups in study subjects.

Clinical data	Healthy ($N = 10$)	CHB ($N = 11$)	Cirrhosis ($N = 26$)	HCC ($N = 16$)	P value
Age	61.5 ± 5.1	53.1 ± 3	59.1 ± 2.5	62.3 ± 3.5	0.447
Male (%)	60	54.5	80.8	75	0.336
Hb	$134.1 \pm 26.71^{a,b}$	$133.64 \pm 16.11^{c,d}$	$103.31 \pm 31.24^{a,c}$	$101.31 \pm 30.19^{b,d}$	0.002
WBC	5.33 ± 1.49	6.29 ± 2.71	$97.04 \pm 60.59^{a,c}$	$118.75 \pm 65.65^{b,d}$	≤0.01
PLT	$195.89 \pm 90.51^{a,b}$	$211.64 \pm 79.08^{c,d}$	4.31 ± 2.03	5.96 ± 4.25	0.158
Ur	6.41 ± 4.71	4.75 ± 1.23	5.98 ± 2.41	8.23 ± 5.29	0.092
Cr	80.44 ± 33.33	71.00 ± 17.47	71.54 ± 14.54	101.25 ± 54.27	0.032
AST	33.10 ± 26.43	163.00 ± 315.03	40.96 ± 25.22	150.86 ± 225.52	0.081
ALT	27.22 ± 25.03	211.73 ± 407.64	34.73 ± 38.92	100.38 ± 168.27	0.068
TB	14.51 ± 7.49^{a}	13.12 ± 8.15^{b}	$27.32 \pm 16.59^{a,b}$	50.28 ± 56.77	0.010
DB	5.86 ± 3.32^{a}	7.00 ± 5.23^{b}	$14.74 \pm 11.54^{a,b}$	30.68 ± 40.11	0.017
AKP	85.67 ± 52.38	73.55 ± 36.53	83.50 ± 37.63	162.56 ± 130.3	0.050
Alb	44.67 ± 4.39	36.36 ± 4.55	35.42 ± 7.08	29.50 ± 7.23	≤0.01
AFP	2.49 ± 1.51	40.96 ± 72.78	9.56 ± 15.59	610.48 ± 591.12	≤0.01

Data are mean ± SD. CHB, chronic hepatitis B; HCC, hepatocellular carcinoma; WBC, white blood cell; PLT, platelet; Ur, urea; Cr, creatinine; AST, aspartate aminotransferase; ALT, alanine aminotransferase; TB, total bilirubin; DB, direct bilirubin; AKP, alkaline phosphatase; Alb, albumin; AFP, alpha-fetoprotein; ^{a}, ^{b}, ^{c} and ^{d}: $P < 0.05$, significant between-group differences.

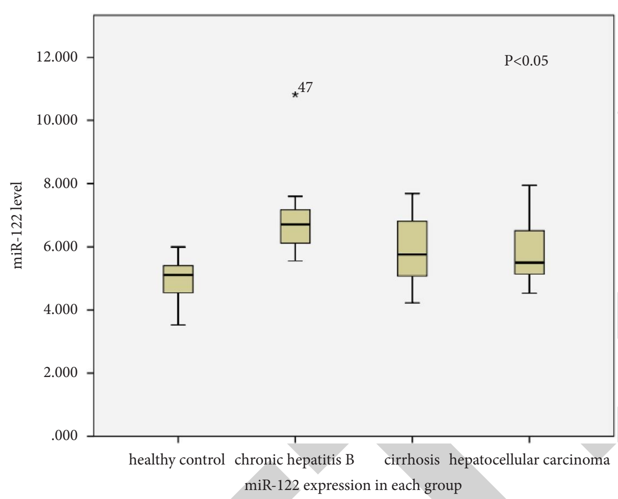

Figure 1: Serum miR-122 expression in each group.

assessed. As shown in Figures 4(a) and 4(b), serum AKP and AFP were increased, while serum miR-122 was reduced, indicating negative correlations ($P = 0.035$ and $P = 0.029$).

4. Discussion

Timely diagnosis of persistent viral hepatitis is vital for treating and preventing hepatitis, which can also help inhibit disease progression and reduce disease spread in the population to a large extent [17, 18]. In a meta-analysis [19], miR-122 was found to exhibit sensitivity and sensitivity of 0.92 and 0.84 in the diagnosis of chronic viral hepatitis, respectively; only 10% of negative results were false negatives. As shown above, miR-122 could detect CHB with an AUC of 0.795 ($P = 0.002$). Because of insufficient samples in this study, we could not verify the results in an external cohort. Consequently, the clinical significance of miR-122 application in diagnosis deserves further investigation.

A few studies [20–22] have examined the role of microRNAs in HBV infection. The correlation between HBV duplication and miR-122 has been explored as well. After exposure of hepatocytes to HBV, inflammation leads to increased cell necrosis and apoptosis, and massive miR-122 amounts are released into the circulation [23]. After released by damaged hepatocytes, the microRNAs cumulate persistently and reach a greater level. HBV DNAs, as the most direct and dependable indicator of virus duplication, is capable of straightly reflecting the virus and the infection ability in vivo. As shown above, serum miR-122 was remarkably increased in CHB cases compared with control individuals. There was a report that serum miR-122 amounts are tightly associated with HBV [24]. Serum miR-122 levels are elevated in HBV patients. Therefore, miR-122 might become a sensitive marker reflecting hepatitis activity in HBV cases.

In different phases of HBV infection, albumin indexes of patients were positively correlated with miR-122 levels in the CHB group, as shown above. Albumin from the liver has functions such as immune regulation and antioxidation. It was shown that miR-122 exerts negative modulatory effects on HBV replication [25, 26]. In terms of HBV modulation, Chen et al. [27] have revealed that miR-122 is capable of binding to the remarkably conservative area of a bicistronic mRNA referred to as HBV pregenomic RNA, which has been discovered to be capable of encoding the HBV polymerase and core protein. Hence, it eventually induces the suppression of HBV genetic expression and duplication. Therefore, the decrease of serum miR-122 weakens the inhibitory effect of HBV DNA replication, thereby aggravating the injury and causing a decrease in albumin. In the liver cancer group, the expression of miR-122 in patients was related to AKP indicators in a negative way. AKP is often associated with impaired liver functions. In two other studies [10, 28], it was found that miR-122 amounts in CHB are negatively correlated with HBV DNA, ALT, and HBsAg levels. Therefore, we speculate that miR-122 may be associated with the severity of hepatocyte damage. Briefly, the lower the miR-122 expression, the severer the hepatocyte damage and the worse the prognosis.

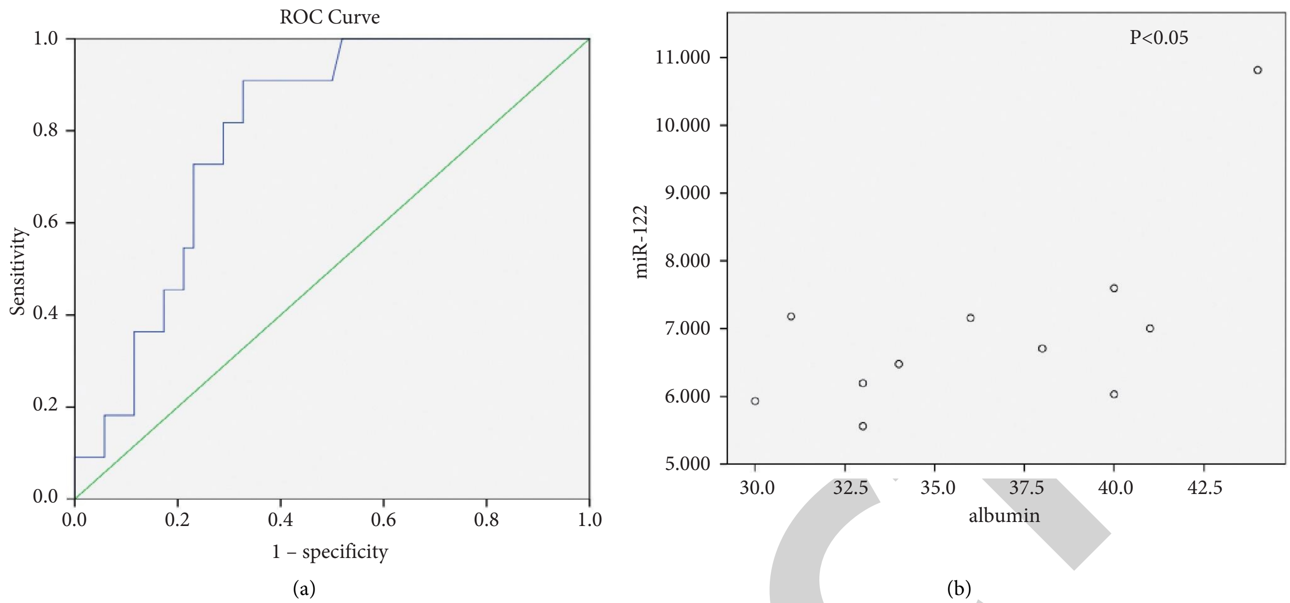

Figure 2: (a) Detection of miR-122 in CHB. (b) Correlation between miR-122 and albumin.

After hepatitis B infection, with disease progression, miR-122 levels gradually decreased. This study demonstrated miR-122 amounts were highest in the CHB group but lower in the liver cancer group in comparison with the liver cirrhosis group, although statistical significance was not reached. These lower serum miRNA levels in patients with more advanced illness may be secondary to their decreased excretion because of the absence of functional liver cells instead of their elevated releasing from damaged liver cells in earlier phases of hepatic illnesses [29–31]. Those diversities may reveal that miR-122 might be one of the stimulative factors in the development of HBV-triggered illnesses. In the cirrhosis group, we found that miR-122 expression was related to the Child–Pugh class. Cirrhosis is a progressive disease, and each stage has distinct clinical and prognostic features. Studies have shown miR-122 affects HBV replication in vitro and is remarkably related to HBV-associated hepatic sclerosis [32]. MicroRNAs participate primarily in the response to low oxygen by regulating key genes participating in apoptosis, including BCL2 and XIAP. Hypoxia is vital for the development of sclerosis because it activates revascularization, suppresses cellular proliferative factors, and induces fibrogenic activities, fostering gradual portal pressure elevation and hyperdynamic circulation [33, 34]. The antifibrotic disorders of miRNAs induce the onset of hepatic sclerosis in CHB cases [35], and the decreased expression of miR-122 weakens the inhibitory effect on liver fibrosis, thereby aggravating the occurrence of liver cirrhosis, which corroborates this study. Interestingly, in the cirrhosis group, miR-122 was negatively associated with HVPG, as shown above. The serum miR-122 of 4 patients with HVPG < 10 mmHg was higher than 21 patients with HVPG > 10 mmHg. HVPG ≥ 10 mmHg is the gold standard for the diagnosis of CSPH [36], and an independent risk factor for rebleeding in hepatic sclerosis [37]. Here, we found that the lower the miR-122 expression, the higher the portal pressure, the greater the risk of portal hypertension-related complicating diseases such as hemorrhage, and the worse the prognosis. However, HVPG can only be assessed by invasive methods that require the proficiency of doctors in major hospitals. miRNA-122 is expected to become a new noninvasive biomarker that could be used as an alternative to HVPG. Cirrhosis is a progressive disease, each stage of which exhibits distinct clinical and prognostic features. As the disease progressed, miR-122 was downregulated in this study. Therefore, we speculate that miR-122 is associated with the development of hepatic illnesses.

In addition, miR-122 has been discovered to participate in the process of hepatic cancer. One discovered the causal link beneath the progression of hepatic carcinoma is the variant of cancer inhibitor genes triggered by the overexpression of apolipoprotein B mRNA-editing enzyme catalytic subunit 2 (APOBEC2) in liver cells. The role of HBV in APOBEC2 was demonstrated through the downregulation of cellular miR-122, which promotes carcinogenesis in hepatocytes [38]. miR-122 can also regulate the activity and stability of the p53 protein by modulating regulatory proteins of the cell cycle, thereby inhibiting tumor metastasis [39]. The low expression of miR-122 can regulate the onset and progression of cancer through a variety of pathways and can be utilized as a biomarker for early hepatic carcinoma diagnoses [40]. The expression of miR-122 is high in mature hepatocytes but remarkably downregulated in HCC. This downregulation is tightly associated with liver carcinogenesis, unsatisfactory prognosis, and metastasis in HCC [41]. In the latter study, tumor-free survival time in HCC cases who exhibited high miR-122 expression was remarkably longer compared with the remaining ones, suggesting miR-122 is tightly associated with prognosis in hepatic carcinoma. In this report, serum miR-122 amounts were lowest in the liver cancer group and were correlated with AFP, whereas the ROC curve results indicated that the

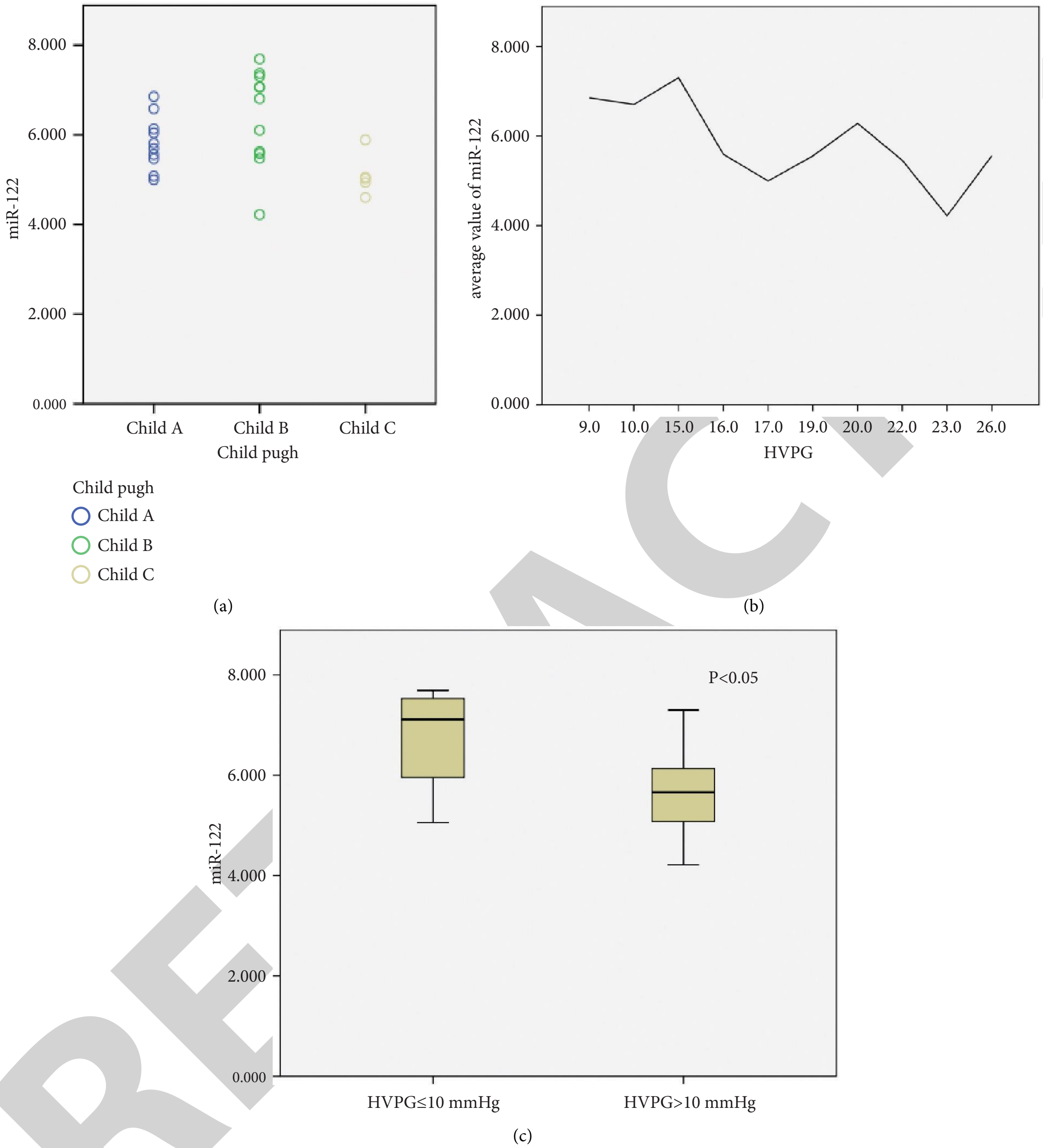

Figure 3: (a) miR-122 expression with Child-Pugh. (b) Correlation between miR-122 and HVPG. (c) miR-122 expression in HVPG ≤ 10 mmHg and HVPG > 10 mmHg.

sensitiveness and specificness of miR-122 for the diagnosis of liver cancer were not satisfactory. This might be due to the insufficient samples herein. Overall, miR-122 is expected to become an effective biomarker for the early diagnosis of liver cancer. Our team also found that 4 of the 16 patients in the liver cancer group died, due to liver cancer combined with gastrointestinal bleeding ($n = 1$), liver cancer combined with liver failure ($n = 2$), and cardiac insufficiency ($n = 1$; this patient was excluded). The serum miR-122 amounts of three patients in the death group were 5.520 ± 0.522, which were lower than 5.860 ± 1.183 detected in the 12 survival patients, although the p value was over 0.05. This may be due to insufficient samples and short follow-up. Taken together, miR-122 is expected to become an effective indicator for predicting the survival rate of liver cancer patients.

As the sample size was limited, the effects of miR-122 in chronic HBV patients have to be assessed in larger cohorts involving cases in diverse phases.

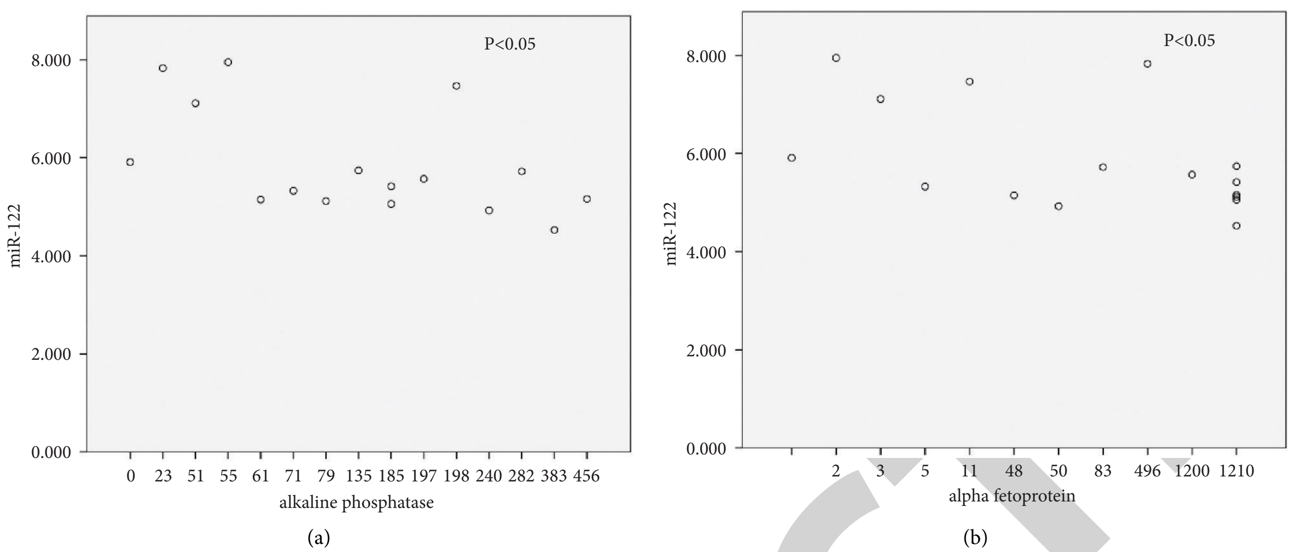

Figure 4: (a) Correlation between miR-122 and AKP. (b) Correlation between miR-122 and AFP.

5. Conclusion

This study revealed that miR-122 could be utilized to screen patients with CHB infection. The peak level of serum miR-122 was found in CHB patients, with the progression of hepatitis B and serum miR-122 levels decreased gradually, providing novel insights into the mechanism of HBV-triggered illnesses. Overall, miR-122 is associated with hepatitis B activity, liver cell damage, and liver disease progression. It participates in the whole process of CHB and is anticipated to be a molecular marker for predicting the progression of CHB.

Abbreviations

HBV: Hepatitis B virus
CHB: Chronic hepatitis B
HCC: Hepatocellular carcinoma
ALT: Alanine aminotransferase
AST: Aspartate aminotransferase
AKP: Alkaline phosphatase
miRNAs: MicroRNAs
HVPG: Hepatic venous pressure gradient
miR-122: MicroRNA-122
ncRNAs: Non-coding RNAs
BP: Biological processes
HCV: Hepatitis C virus
AIH: Autoimmune hepatitis
HGB: Hemoglobin
AFP: Alpha-fetoprotein
CSPH: Clinically significant portal hypertension.

Data Availability

The data used to support the findings of this study are available from the corresponding author upon request.

Conflicts of Interest

The authors declare that there are no conflicts of interest.

Acknowledgments

This work in this paper was supported by the Department of Gastroenterology, Minhang Hospital, Fudan University.

References

[1] World Health Organization, "Hepatitis B vaccines: WHO position paper, July 2017–Recommendations," *Vaccine*, vol. 37, no. 2, pp. 223–225, 2019.

[2] Y.-C. Chen, C.-M. Chu, C.-T. Yeh, and Y.-F. Liaw, "Natural course following the onset of cirrhosis in patients with chronic hepatitis B: a long-term follow-up study," *Hepatology International*, vol. 1, no. 1, pp. 267–273, 2007.

[3] X. Wang, Y. He, B. Mackowiak, and B. Gao, "MicroRNAs as regulators, biomarkers and therapeutic targets in liver diseases," *Gut*, vol. 70, no. 4, pp. 784–795, 2021.

[4] R. Mjelle, S. O. Dima, N. Bacalbasa et al., "Comprehensive transcriptomic analyses of tissue, serum, and serum exosomes from hepatocellular carcinoma patients," *BMC Cancer*, vol. 19, no. 1, p. 1007, 2019.

[5] M. M. Jelen and D. Glavač, "Importance of MicroRNAs in hepatitis B and C diagnostics and treatment," *Advanced Treatment of Hepatitis C and B*, vol. 3, 2017.

[6] S. Wang, L. Qiu, X. Yan et al., "Loss of microRNA 122 expression in patients with hepatitis B enhances hepatitis B virus replication through cyclin G1-modulated P53 activity," *Hepatology*, vol. 55, no. 3, pp. 730–741, 2012.

[7] I. Laudadio, I. Manfroid, Y. Achouri et al., "A feedback loop between the liver-enriched transcription factor network and miR-122 controls hepatocyte differentiation," *Gastroenterology*, vol. 142, no. 1, pp. 119–129, 2012.

[8] R. O. Benatti, A. M. Melo, F. O. Borges et al., "Maternal high-fat diet consumption modulates hepatic lipid metabolism and microRNA-122 (miR-122) and microRNA-370 (miR-370) expression in offspring," *British Journal of Nutrition*, vol. 111, no. 12, pp. 2112–2122, 2014.

Hindawi
Journal of Healthcare Engineering
Volume 2023, Article ID 9860360, 1 page
https://doi.org/10.1155/2023/9860360

Retraction

Retracted: Automated Detection of Rehabilitation Exercise by Stroke Patients Using 3-Layer CNN-LSTM Model

Journal of Healthcare Engineering

Received 23 May 2023; Accepted 23 May 2023; Published 24 May 2023

This article has been retracted by Hindawi following an investigation undertaken by the publisher [1]. This investigation has uncovered evidence of one or more of the following indicators of systematic manipulation of the publication process:

(1) Discrepancies in scope
(2) Discrepancies in the description of the research reported
(3) Discrepancies between the availability of data and the research described
(4) Inappropriate citations
(5) Incoherent, meaningless and/or irrelevant content included in the article
(6) Peer-review manipulation

The presence of these indicators undermines our confidence in the integrity of the article's content and we cannot, therefore, vouch for its reliability. Please note that this notice is intended solely to alert readers that the content of this article is unreliable. We have not investigated whether authors were aware of or involved in the systematic manipulation of the publication process. Wiley and Hindawi regrets that the usual quality checks did not identify these issues before publication and have since put additional measures in place to safeguard research integrity.

We wish to credit our own Research Integrity and Research Publishing teams and anonymous and named external researchers and research integrity experts for contributing to this investigation.

The corresponding author, as the representative of all authors, has been given the opportunity to register their agreement or disagreement to this retraction. We have kept a record of any response received.

References

[1] Z. U. Rahman, S. I. Ullah, A. Salam, T. Rahman, I. Khan, and B. Niazi, "Automated Detection of Rehabilitation Exercise by Stroke Patients Using 3-Layer CNN-LSTM Model," *Journal of Healthcare Engineering*, vol. 2022, Article ID 1563707, 12 pages, 2022.

Hindawi
Journal of Healthcare Engineering
Volume 2022, Article ID 1563707, 12 pages
https://doi.org/10.1155/2022/1563707

Research Article

Automated Detection of Rehabilitation Exercise by Stroke Patients Using 3-Layer CNN-LSTM Model

Zia Ur Rahman,[1] **Syed Irfan Ullah**,[1] **Abdus Salam**,[1] **Taj Rahman**,[2] **Inayat Khan**,[3] and **Badam Niazi**[4]

[1]*Department of Computing and Technology Abasyn University, Peshawar 25000, Pakistan*
[2]*Qurtuba University of Science and Technology Peshawar, Peshawar 25000, Pakistan*
[3]*Department of Computer Science, University of Buner, Buner 19290, Pakistan*
[4]*Department of Computer Science, University of Nangarhar, Jalalabad 2600, Afghanistan*

Correspondence should be addressed to Badam Niazi; niazi5.48@gmail.com

Received 10 December 2021; Accepted 12 January 2022; Published 4 February 2022

Academic Editor: Liaqat Ali

According to statistics, stroke is the second or third leading cause of death and adult disability. Stroke causes losing control of the motor function, paralysis of body parts, and severe back pain for which a physiotherapist employs many therapies to restore the mobility needs of everyday life. This research article presents an automated approach to detect different therapy exercises performed by stroke patients during rehabilitation. The detection of rehabilitation exercise is a complex area of human activity recognition (HAR). Due to numerous achievements and increasing popularity of deep learning (DL) techniques, in this research article a DL model that combines convolutional neural network (CNN) and long short-term memory (LSTM) is proposed and is named as 3-Layer CNN-LSTM model. The dataset is collected through RGB (red, green, and blue) camera under the supervision of a physiotherapist, which is resized in the preprocessing stage. The 3-layer CNN-LSTM model takes preprocessed data at the convolutional layer. The convolutional layer extracts useful features from input data. The extracted features are then processed by adjusting weights through fully connected (FC) layers. The FC layers are followed by the LSTM layer. The LSTM layer further processes this data to learn its spatial and temporal dynamics. For comparison, we trained CNN model over the prescribed dataset and achieved 89.9% accuracy. The conducted experimental examination shows that the 3-Layer CNN-LSTM outperforms CNN and KNN algorithm and achieved 91.3% accuracy.

1. Introduction

Stroke is a worldwide healthcare problem which causes due to heart failure or malfunctioning of blood vessels. It is a common, dangerous, and disabling health disease that affects people all around the world. Stroke is the second or third leading cause of death in most regions, as well as one of the leading causes of acquired adult disability [1]. Over the next couple of decades, the frequency of stroke-related burden is predicted to rise. Stroke causes losing control of the motor function, incoordination or paralysis of all body parts, and severe back pain. Due to stroke, patients will have muscle and neurological trauma and disorders such as cerebrum paralysis [2], trauma and paralytic injury [3], posttraumatic stiffness [4], congenital deformity [5], and Guillain–barre syndrome [6]. Injuries to the cervical spinal cord usually result in loosened leg and arms functions where hip flexors and legs are degraded by lumbar and spinal cord injuries. The survivors of a stroke have a similar condition since they must relearn the lost skills when their brain is hit by a stroke.

A physiotherapist employs many therapies, including nerve reeducation, task coaching, and muscle strengthening to restore the mobility needs of everyday life. Different physiotherapy and rehabilitation programs are needed to restore the function of the upper extremity and increase their quality of life. Some exercises such as motor training (movement exercise), mobility training (restriction-induced), motion therapy (flow therapy), and repetitive task training (workout training) are very effective for learning and taking control of the body [7]. Both for upper and lower limbs, balancing exercises are of considerable benefit to increase the balance after spinal cord injury. It is obvious that serious health problems may lead to death or acquired physical impairment due to injury to the backbone. Different neuroplastic results have shown that it can be recovered partly through adequate rehabilitation exercises [8].

Motor function controls mobility and muscle movement and is a commonly recognized impairment due to stroke. To reestablish motor function, the most important technique is to perform rehabilitation exercises under the direction of a physiotherapist. The financial requirement to receive the treatment is not easy, so the family can suffer from financial burden. The resolution of this is a new virtual reality rehabilitation problem, which uses sensor tools to capture and recognize movements. The rehabilitation program requires physiological exercises like flexion, extension, abduction, adduction, enlargement, sleeves, dorsiflexion, plantar flexion, and rotation of various joints in patients with muscular and neurological trauma and disorder. In the existing literature studies, most of the researchers have focused on the detection of human activities like standing, sitting, sleeping, walking up and down stairs, etc., but very less attention was focused on the recognition and classification of rehabilitation physiotherapy exercises which is a multifaceted area of HAR.

Hitherto, HAR has been widely used in numerous applications, like gesture recognition gait analysis, human-computer interaction, home behavior analysis, personal health system, video surveillance, and antiterrorism monitoring [9–16]. It has the ability to learn in advance from raw data around human activities. Currently, HAR is a popular research track, due to progression in the field of human-computer interaction. Generally, there are two types of HAR: sensor-based and video-based. Sensor-based HAR depends on the data learned through keen sensors. Due to the development of ubiquitous computing and sensor technology, sensor-based HAR is more frequently used. To improve recognition accuracy, researchers have developed various types of sensing technologies such as techniques based on static and dynamic sensors. The video-based HAR takes advantage of the data acquired through various kinds of cameras to determine human activities [17], which is becoming popular due to the reduced complexity and ease of availability of different kinds of cameras. In this research article, for the detection of rehabilitation physiotherapy exercise, the dataset is collected through an RGB camera, and then a 3-Layer CNN-LSTM algorithm is applied for the detection of rehabilitation physiotherapy exercise. The 3-Layer CNN-LSTM algorithm seeks to leverage the power of merging both CNN and LSTM and address the deficiencies of existing approaches, laterally with the following characteristics: (1) the model is robust enough to perform equally well or better on input data, (2) it is evaluated on our self-created complex dataset, having rehabilitation physiotherapy exercises, (3) extracting and classifying activity features automatically, (5) and having better or at least same accuracy as of the existing DL approaches laterally with fast convergence speed and good generalization ability.

The manuscript is organized as follows: in Section 2 we take a look at some current techniques for HAR which is using machine learning and deep learning approaches. Section 3 explains CNN and LSTM algorithms and data preprocessing for the proposed model. Moreover, it contains a detailed overview of the 3-Layer CNN-LSTM model and its implementation. In Section 4, the performance of the 3-Layer CNN-LSTM model is explained along with their experimental results. Section 5, concludes the research work with a brief summary.

2. Literature Review

Machine learning models are used to learn the fundamental connections in data through experience while performing some tasks and making decisions without explicit instructions [18]. For a very long time, ML models have been used widely for HAR. Different types of models which can apply for HAR depend on data type, the volume of data, number of activities, similarities among activities, and number of activity classes. The existing ML models such as hidden Markov model (HMM) [19], linear discriminant analysis (LDA) [20], random forest (RnF) [21], logistic regression [22], support vector machine (SVM) [23], decision tree (DT) [24], histogram oriented gradient (HOG) [25], and K-nearest neighbour (KNN) [26] are used for human activity classification. Nevertheless, for precision and accuracies of the abovementioned algorithms, the selection of different parameters like the method of distance calculation and the number of neighbors for KNN, choice of the kernel for SVM, the tolerance value for LDA, and the number of trees for RnF plays a significant role which should be considered carefully [27–29]. These algorithms have achieved remarkable classification accuracies, nonetheless, it requires a lot of hand-tuning to formulate the data, feature engineering, preprocessing, and domain knowledge amongst others. These methods are not suitable in scenarios like indoor environments where confidentiality is required. Some of the other approaches are highly vulnerable to illumination disparities and background changes which are restraining their practical use.

A unique biometric system for detecting human actions in 3D space is proposed in [30] in which joint skeleton angles recorded through an RGB depth sensor are used as input features. The angle information is stored using the sliding kernel method. Before lowering the data dimension, the Haar wavelet transform (HWT) is used to maintain feature information. For dimensionality reduction, an averaging technique is applied to reduce computing costs and result in faster convergence. Moreover, the system may be used for elderly care and video surveillance, but there are a few drawbacks to the suggested approach. First, improper skeletal detection leads to inaccurate angle calculations, which causes the classification to be automatically misled. As the system is trained on activities in two directions at various angles and positions, there may be some confusion when attempting to recognize an activity due to probable similarities in the positions and angles of different activities. RGB-D images are beneficial for action recognition; however, the computational complexity of the learning model grows rapidly as the number of frames grows. As a result, the system becomes more complex and slower. Thus, instead of an RGB-D camera, a simple RGB camera could be explored to broaden the applications of the HAR system. Activity sequence recording, function extraction, model implementation, and finally identification are the four essential steps in vision-based HAR [31, 32]. The Kinect-based rehabilitation training system has arisen recently, which is utilized in most research studies. Some researchers focus on skeleton data while most of the researchers use RGB-D data, which is due to the fact that Kinect is based on depth sensors and uses structured light, which is not accurate. On the basis of depth data, it obtains the skeleton data, which is of low quality and high noise. Thus, the data obtained through skeleton joints is not accurate and has outliers which are declining the model performance.

Researchers have turned towards DL techniques for the detection of complex human activities. DL techniques extract features automatically from raw data during the training phase and have produced remarkable results in many activity recognition tasks. It has tremendous applications in the field of HAR, as the process of extracting features and classification are performed simultaneously. The RNN-LSTM approach used in [33, 34] has achieved outstanding performances and shown excellent results when compared to traditional hand-crafted practices, nevertheless, it exaggerates the temporal and understates the spatial information of input data. In many tasks such as NLP and speech recognition amongst others, CNN achieved better or at least similar performance to that of recurrent neural network (RNN). Due to this trend, recently CNN is widely used in the literature to grab the HAR problems. Numerous studies showed that CNN-based approaches are far better than traditional hand-crafted approaches since CNN has the ability to learn complex motion features [35]. The presented DL models for HAR are having simple architecture and great accuracy. However, these models were tested on simple datasets like standing, sitting, sleeping, walking upstairs and downstairs, and do not have a good generalization ability.

The main goal of this research work is to design a DL-based algorithm for automated detection of rehabilitation physiotherapy exercises. In the suggested 3-Layer CNN-LSTM model, data is fed to the convolutional layer for the extraction of useful features, and for classification, it is passed to LSTM to recognize the rehabilitation exercise. Batch normalization (BN) is applied to stabilize the learning process and reduce internal covariate shift. The model automatically detects the set of rehabilitation physiotherapy exercises and classify them under certain categories.

3. Methodology

For rehabilitation of stroke patients mostly two conventional techniques are used: artificially and robot-assisted. However, due to the cost of intelligent robots and their supplementary maintenance, robot-assisted techniques are difficult to be used. Moreover, due to the shortage of healthcare providers, artificial form of rehabilitation is also hard to be accessed. As we know that rehabilitation of stroke patients is a long-lasting process due to which both robot-assisted and artificial forms of rehabilitation are not feasible. Therefore, an automated rehabilitation training method is needed to address this issue. Consequently, we designed an automated model to recognize the physiotherapy exercise while keeping in view the existing HAR approaches. The architecture of the proposed algorithm is shown in Figure 1.

The 3-Layer CNN-LSTM model seeks to leverage the power of merging both CNN and LSTM. The main approach is divided into two sections, the detection of physiotherapy exercise and its classification. The first section contains data collection, preprocessing of images, dimensionality reduction, and data augmentation. The second section is using a combination of DL models to evaluate the features and classify the physiotherapy exercises efficiently. To test the model's efficiency, various experiments were performed for the detection and classification of physiotherapy exercises. The main components of the algorithm are discussed briefly below.

3.1. Convolutional Neural Network. It is a type of deep neural network (DNN) having multiple layers. Its concept is originated from the receptive field and neural cognitive machine which is more sophisticated than a traditional neural network. In the presence of additional deep layers, the DNN model learns deeply compared to other shallow neural networks. Dealing with the problem of image classification and recognition, the CNN has high distortion tolerance due to its spatial structure and weight sharing mechanism [36]. The fundamental structures of the CNN are the amalgamation of weight sharing, subsampling, local receptive field, and dimensionality reduction during feature extraction. To reduce the complexity of the model, enhance their performance and efficiently regulate the number of weights, the weight sharing mechanism is used. CNN map input image data to an output variable i.e., it takes the input image data, processes the data, and predict the image class efficiently. Input data is in the form of a two-dimensional vector and CNN deals with it in a better way. In 3-layer CNN-LSTM model, we used CNN to extract useful features from the input image matrix. In this step, the physiotherapy exercise image is taken as input which is processed to extract features from it. In this work, the LSTM is used to classify the input data under certain categories. The process of CNN for feature extraction is described in detail in Section 3.3. The learning and classification technique of CNN is described mathematically through (1). In equation (1), Z_i is the set of inputs, W_i is the set of weights, and B is the bias operation.

$$P = f\left(\sum_{i=1}^{N} Z_i \times W_i + B\right). \tag{1}$$

3.2. Long Short-Term Memory. LSTM is used to evade the problem of gradient vanishing or gradient exploding during training. The back propagation (BP) algorithm is used to

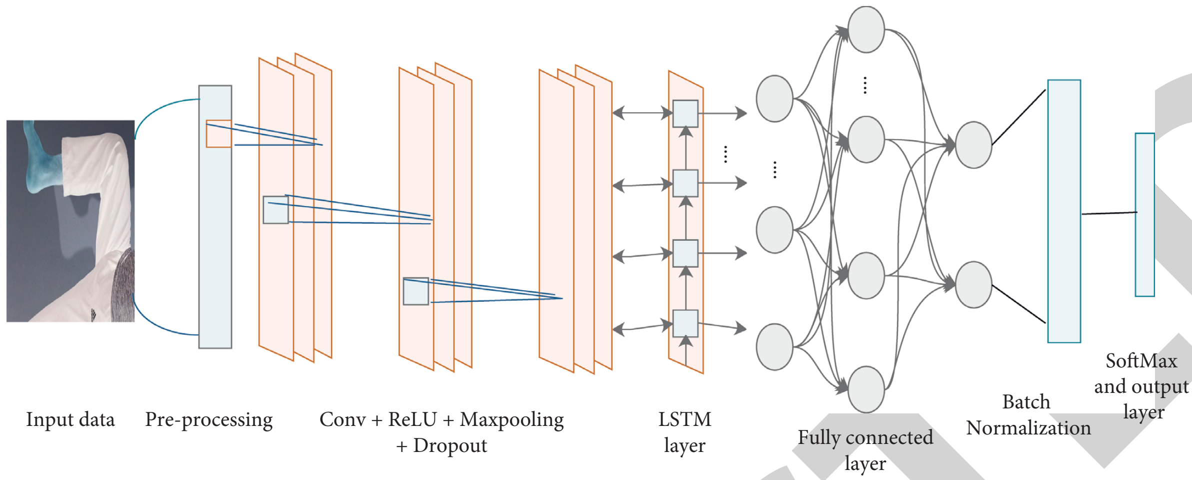

Figure 1: Architecture of 3-Layer CNN-LSTM model.

update the weights of the neural network. The BP algorithm first calculates the gradient using the chain rule and then updates the weights of the network on the base of the calculated loss. The BP starts from the output layer and the whole network is traversed towards the input layer which is facing vanishing gradient or exploding gradient problems while updating the weights in DNN. So, to avoid the said problem of gradient explosion or gradient vanishing during training traditional RNNs, an LSTM algorithm is proposed. Furthermore, RNNs are unable to memorize long sequences of data, while LSTM efficiently deals with it. LSTM is a type of RNN and the building block of artificial neural network which is having additional memory cells for time steps and remembers the past information. The process diagram of LSTM is shown in Figure 2. It is capable to remember and learn long-term sequences. LSTM consists of 4 different components: input gate (I_t), output gate (O_t), forget gate (F_t), and cell state (C_t) at time step (t) [37]. The past information is stored in the state vector of C_{t-1}. The I_t decides how to update the state vector using the current input information. The data which are added to the state from the current input is represented through L_t vector. Z_t represents input vector at time step t, H_t, and H_{t-1} is the current and previous cell output, C_t and C_{t-1} is the current and previous memory cell, (x) is elementwise multiplication, and W, U represent weights of the four gates i.e. I_t, O_t, F_t, and C_t. Due to this structure of LSTM, it is applied to learn efficiently complex sequences of data.

$$L_t = \tanh\left(Z_t \times W_L + H_{t-1} x U_L\right), \tag{2}$$

$$F_t = \sigma\left(Z_t x W_F + H_{t-1} x U_F\right), \tag{3}$$

$$I_t = \sigma\left(Z_t x W_I + H_{t-1} x U_I\right), \tag{4}$$

$$O_t = \sigma\left(Z_t x W_o + H_{t-1} x U_O\right), \tag{5}$$

$$C_t = F_t x C_{t-1} + I_t x L_t, \tag{6}$$

$$H_t = O_t x \tanh\left(C_t\right). \tag{7}$$

The σ and Tanh is a nonlinear activation function and U_{I}, W_{I}, U_{F}, W_{F}, U_{O}, W_{O}, U_{L}, and W_{L} are the respective weights which are having $M \times 2\mathrm{N}$ dimensions, where M shows the number of memory cells and N shows the dimension of the input vector. The mathematics of LSTM behind the whole process is formalized in [38] as shown in equations (2) to (7).

3.3. Data Representation and Feature Extraction. Data representation is the first section of the suggested approach which contains data collection, preprocessing, and feature extraction. Data for this research study were collected through an RGB camera, from participants performing exercises under the direction of a physiotherapist. Data augmentation is used to reduce overfitting and enlarge the dataset artificially as shown in Figure 3. After the collection of raw images, the next step is to preprocess them prior to the implementation of any proceeding functionalities. Data preprocessing involves data cleaning such as noise removal, resizing and filling, or removing null values.

Data for each rehabilitation physiotherapy exercise are combined in one file named as "Categories" and preprocessed by resizing each image to reduce complexity. This whole process is shown in Algorithm 1.

To minimize the set of features and enhance the efficiency of the classification algorithm, useful features are extracted from the data. The extraction of correct features is an exciting job for the recognition of physiotherapy exercises for which CNN is used. In feature extraction phase convolution operation, pooling operation and ReLU (rectified linear unit) activation function is applied as shown in equations (8) and (9), respectively

The physiotherapy exercise data named as, New_array is taken as input and passed through convolutional layer followed by ReLU, pooling, and dropout layer to extract useful features from it. The input is of order 2 matrix with HxW (rows, columns), H and W are indexed as (m, n), where $0 \le m \le H, 0 \le n \le W$. The final and useful feature map values i.e., $F\_y_{m,\ n}$ is obtained through convolutional operation layer 3

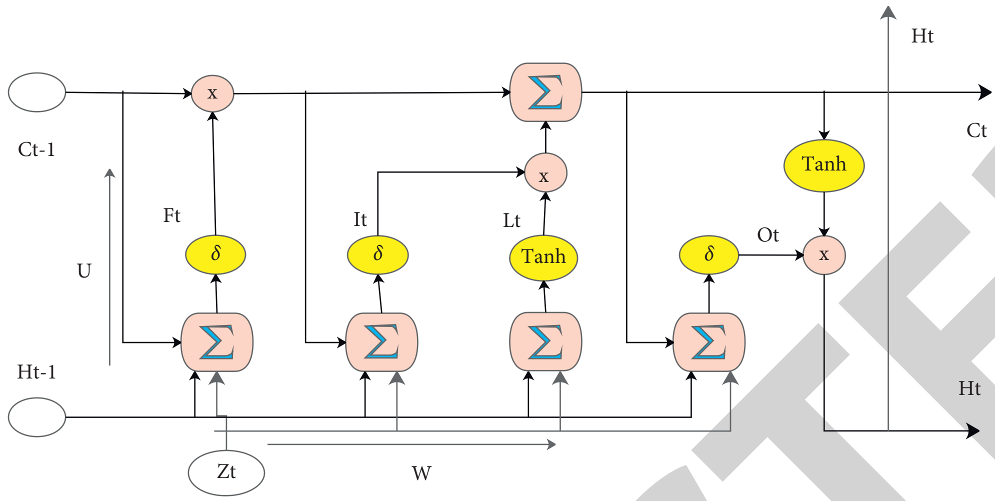

Figure 2: Process diagram of LSTM.

Figure 3: Data augmentation.

$$O_{m,n} = \sum_m \sum_n f[j,k]Z[m-j,n-k], \tag{8}$$

$$F\_Y_{m,n} = \max\left(0, F\_0_{m,n}\right). \tag{9}$$

The activation function is applied at every layer to make the model capable of solving nonlinear problems as shown in equation (9), while to minimize the computational load, max pooling and dropout technique is used.

3.4. Classification. The 3-layer CNN-LSTM is used as a learning algorithm for feature extraction and its classification. The whole process of feature extraction and its classification under certain categories are shown in Algorithm 2. For classification of rehabilitation physiotherapy exercise pretrained LSTM is applied as explained in detail in Section 3.2. The pretrained LSTM is followed by fully connected (FC) layers, batch normalization (BN) layer, and SoftMax function. The proposed algorithm makes it possible to see that during the training phase, the accuracy is much more than the testing phase, which is because of overfitting and outcome a complication in the regularization and balancing of hyperparameters.

BN is applied to stabilize the learning process and reduce internal covariate shift. During the training period, at each middle layer, the BN calculates the mean and variance as shown through equations (10) and (11). For each layer, the normalized input is gained from the previously calculated mean and variance as shown in equation (12).

$$\text{mean} = \frac{1}{m}\sum_{i=1}^{n} Z_i, \tag{10}$$

$$\text{var} = \frac{1}{m}\sum_{i=1}^{n} \left(Z_i - \text{mean}\right)^2, \tag{11}$$

$$Z_i' = \frac{\left(Z_i - \text{mean}\right)}{\sqrt{\text{var} + \varepsilon}}. \tag{12}$$

During the training of the network, γ (standard deviation) and β (mean parameter) along other parameters are learned. The final mean and variance equations for testing the model are shown in equation (13) to (15), respectively [39]. In these equations' "j" shows the number of batches where each batch has "m" samples. The final mean and variance are assessed from the previous mean, variance formulas calculated for each batch during training.

Input: rehabilitation exercise, labelled dataset categories
Preprocessing:
(1) Categories ⟵ Dataset categories
(2) Apply data augmentation on Categories
(3) for each_Image in Categories
  a: Image_array ⟵ (Image, "gray")
  b: Drop null values
  c: New_array = Resize (Image_array, (256, 256)) end for
Preparation: Training_data = [ ]
(4) For each_class in Categories
  a: class_num ⟵ Categories (each_class)
  b: Training_data ⟵ (New_array, class_num) end for
(5) Create Training_data
(6) Shuffle randomly (Training_data)

ALGORITHM 1: Data preprocessing for training.

Consequently, after all in BN, the layers are normalized through final mean and variance procedures.

$$f\_\text{mean} = \frac{1}{m}\sum_{i=1}^{j} \text{mean}_{(i)}, \tag{13}$$

$$f\_\text{var} = \frac{1}{m}\left(\frac{m}{m-1}\right)\sum_{i=1}^{j} \text{var}(i), \tag{14}$$

$$f\_y_i = \frac{\gamma}{\sqrt{f\_\text{var}+\varepsilon}}(Z) + \left(\beta + \frac{\gamma \times f\_\text{mean}}{\sqrt{f\_\text{var}+\varepsilon}}\right). \tag{15}$$

The purpose of training the model is to adjust the filter weights such that the predicted class should be as close as possible to the actual class. During training, the network runs in the forward direction to get the resultant predicted value. The loss function is calculated to evaluate how well our proposed model is working. To compare the predicted value with the corresponding target value through continuous forward pass running, the total loss at the last layer is obtained. The loss is guiding the model to update parameters to reduce the error rate. The relative probability of real values at the output layer is calculated through the SoftMax function to recognize the rehabilitation exercise. A short comparison of the proposed model to the current state-of-the-art models is given in Table 1.

4. Results and Discussion

The model is trained in a fully supervised manner, and the gradient is backpropagated from the SoftMax to CNN layer to reduce the loss. Through randomly selected values the bias and weights are initialized at each layer.

4.1. Hyperparameter Selection. During classification, the model performance is greatly affected by the selection of hyperparameters. The impact of different hyperparameters such as the number of convolution filters, batch size, learning rate, kernel size, pooling size, epochs, and type of optimizer is observed on model performance and explained as follows.

To increase the number of convolution filters, the model learns more complex features which ultimately increases the number of parameters and causes overfitting issues. So, the accurate and balanced selection of filters at each layer is important. At the first layer, we used 64 filters. In the second convolutional layer, the number of filters is doubled compared to the first convolution layer and so on, to cope with downsampling caused by the pooling layer. The selected number of filters shown in Table 2 outperforms the other combination of filters at different layers. In the start, a reduced size filter is used to learn low-level features, nevertheless, for high level and specific features, large size filters perform better. In layer 1, kernel size of (5,5) is selected, whereas in layers 2 and 3, kernel size is reduced. The idea behind selecting a large filter size at the start is that it read generic features in one value and its effect is more globally on the whole image, but missing local features. In layer 2 and layer 3, a small filter size is used to learn local and specific features. The number of filters and size of the filter are selected by the hit and trial method.

We used different batch sizes and monitor the model performance. By selecting 32 batch sizes, the highest accuracy is achieved. An optimal learning rate of 0.1 along with 36 epochs is used in the training stage to improve the fitting ability of the model. The impact of changing learning rate and the number of epochs was studied and it was concluded that by reducing the learning rate, the process takes a long time to converge while the high learning rate results in the process to converge quickly. It is observed that the learning rate and the number of epochs have an inter-relationship with each other and affect model performance. During training the 3-layer CNN-LSTM model, Adam optimizer is used which has the best fitting effect on model performance and gives the highest accuracy. For training purposes, numerous combinations of hyperparameters are used and tested by using the hit and trial method for parameters selection, and finally, the best parameters giving the highest performance results are selected. The list of selected hyperparameters is shown in Table 2.

Input: unobserved exercise image
Initialization:
(1) $Z_{m,n}$ array of image (m rows, n column) at convolution layer 1
(2) $F_{\mathrm{i},\,j}$ filter (i rows, j column)
(3) $O_{m,n}$ resultant array obtained after convolution
(4) $Y_{m,n}$ output array after removing negative values
(5) * sum of product operation
(6) FM feature map function
(7) $Q_{m,n}$ output array at 2^{nd} convolution layer
(8) $\mathrm{F}\_Y_{\mathrm{m,\,n}}$ output at 3^{rd} convolution layer
Preparation:
(1) Load CNN model
(2) Load trained LSTM model
Steps:
(3) CNN $\longleftarrow$ New_array (Z_{i})
(4) Load FM in Conv1: (convolution layer 1), filter_size (5, 5)
Number of rows and columns (m, n)
a: $O_{m,n} \longleftarrow F_{\mathrm{i},\,\mathrm{j}} \times Z_{m,n}$ No. of filters $\longleftarrow$ 64
b: $Y_{m,n} \longleftarrow \max(0, O_{m,n})$
c: Max_pooling (4, 4)
d: Dropout (0.5)
(5) Load FM in Conv2: (convolution layer 2), filter size (3, 3)
a: $P_{m,n} \longleftarrow F_{\mathrm{i},\,\mathrm{j}} \times Y_{m,n}$ No. of filters $\longleftarrow$ 128
b: $Q_{m,n} \longleftarrow \max(0, P_{m,n})$
c: Max_pooling (2, 2)
d: Dropout (0.5)
(6) : Load FM in Conv3: (convolution layer 3), filter size (3, 3)
a: $F\_O_{m,n} \longleftarrow F_{\mathrm{i},\,\mathrm{j}} \times Q_{m,n}$ No. of filters $\longleftarrow$ 256
b: $\mathrm{F}\_Y_{\mathrm{m,\,n}} \longleftarrow \max(0, \mathrm{F}\_0_{m,\,n})$
c: Max_pooling $\longleftarrow 2 \times 2$
(7) LSTM (64) $\longleftarrow$ $\mathrm{F}\_Y_{\mathrm{m,\,n}}$ after Conv3
(8) FC Layer $\longleftarrow$ Dense (64)
(9) Predicted values $\longleftarrow$ Dense (64)
(10) Pass the predicted values through the BN layer
(11) Calculate Loss $\longleftarrow$ (ground_truth_value–predicted_value)
(12) SoftMax function $\longleftarrow$ predicted exercise
Output: display and label the predicted exercise

Algorithm 2: 3-layer CNN-LSTM model for the detection of rehabilitation exercise.

Table 1: Comparison of 3-layer CNN-LSTM model with other standard models.

S. No	Other standard models	Proposed CNN-LSTM model
1	RNN-LSTM model used in [33] for HAR system and achieved great accuracy, but this model exaggerates the temporal and understates the spatial information as both of the models best fit for temporal data.	CNN is used for feature extraction and selection of useful features, while LSTM is used for exercise recognition. This model maintains a balance between spatial and temporal information.
2	In [40], LSTM-CNN model is used for activity recognition. The LSTM is used before CNN to process input data which is not efficient for the processing of spatial input data.	In the proposed model, 3-layer CNN is applied first to process spatial input data. The data is then fed to the LSTM layer to further refine the extracted data and detect the rehabilitation exercise.
3	The CNN model for exercise recognition was tested and observed that CNN learn too many complex parameters of about 2,575,753 during training.	The model learned about 392,765 parameters which conclude that CNN-LSTM model is lightweight which has reduced complexity and achieved better accuracy.
4	In [30], KNN is applied to recognize human activity which fails to address occlusion, deformation, and viewpoint variation, as KNN is using hand-crafted techniques.	The 3-layer CNN-LSTM model learns activity feature automatically and handles these issues efficiently. We used an RGB camera instead of Kinect sensors to reduce complexity and processing time.

Table 2: List of hyperparameters selected for training.

Processing stage	Hyperparameters	Values selected
Convolution_1	Filters	64
	Kernel size	5
	Stride	1
	Max pooling	4
Convolution_2	Filters	128
	Kernel size	3
	Max pooling	2
Convolution_3	Filters	256
	Kernel size	3
	Max pooling	2
Training parameters	Learning rate	0.1
	Epochs	36
	Batch size	32
	Optimizer	Adam

4.2. Dataset of Rehabilitation Exercises. A physiotherapist employs many complex exercises for the rehabilitation of stroke patients depending on the type and severity of stroke. Rehabilitation exercises include but are not limited to flexion and extension of the neck, flexion and extension of the trunk, flexion and extension of the knee joint, flexion and extension of the hip joint, flexion and extension of the wrist, abduction and adduction of the upper limb, and dorsiflexion and plantar flexion of the foot as shown in Figure 4.

In this research work, we generated our own dataset under the direction of a physiotherapist consisting of 2250 different samples. The data is recorded from participants performing different rehabilitation exercises through an RGB camera. The participants include males, females, and children having up to 40 years of age. The description of the dataset is given in Table 3.

4.3. Training. The model training is performed on a Dell laptop with an Intel Core i7 processor and 16 GB RAM equipped with 64 bits operating system The classification model is implemented in Python 2.7.0 with Jupyter notebook. The main theme of the training is to adjust the filter weights such that the predicted class should be as close as possible to the actual class. The dataset is divided into two parts. The first part is having 80% of data which is used for training purposes while the second part is having 20% of data and is used for testing the efficiency of the model. The Adam optimization algorithm is used for adjusting the weights in such a way to move from a large loss point to a small loss point using the error backpropagation method for optimization. According to the activation function, the weights are then updated.

4.4. Performance Evaluation Metrics. To scrutinize the performance of the model various evaluation metrics are used, which shows the reliability of the model in examining the rehabilitation exercise. The most common metrics used for performance evaluation are recall, f1-score, precision, and accuracy [41–44].

4.4.1. Precision. It is the ratio of true positive (TP) to TP and false positive (FP) observation, which is predicted positive and is calculated as

$$\text{Precision} = \frac{\text{TP}}{(\text{TP} + \text{FP})}. \quad (16)$$

4.4.2. Recall. The recall is the ratio of the predicted true positive observation to true positive and false negative (FN) observation, which is actually positive and is calculated as follows:

$$\text{Recall} = \frac{\text{TP}}{(\text{TP} + \text{FN})}. \quad (17)$$

4.4.3. F1-Score. F1-score is the weighted average of recall and precision and calculated as

$$F1\text{-}score = \frac{2 \times \text{recall} \times \text{precision}}{\text{recall} + \text{precision}}. \quad (18)$$

4.4.4. Accuracy. It is the ratio of correctly classified activities to the total number of classified activities.

$$\text{Accuracy} = \frac{(\text{TP} + \text{TN})}{(\text{TP} + \text{FP} + \text{TN} + \text{FN})}. \quad (19)$$

4.5. Results. The confusion matrix of rehabilitation exercises is shown in Figure 5, which shows the true label at the y-axis and the predicted label at the x-axis. The numbering from 0 to 6 shows the set of different exercises e.g. dorsiflexion, neck exercise, plantar flexion, trunk extension, trunk flexion, wrist extension, and wrist flexion, respectively. The classification report of 3-layer CNN-LSTM along with the CNN model is shown in Table 4.

The performance evaluation of the 3-layer CNN-LSTM model is obtained in terms of precision, recall, f1-score, and accuracy which is calculated according to equations (16) to (19). The performance of the model for discrete rehabilitation exercises is evaluated through Figure 6. To validate the dominance of the suggested 3-layer CNN-LSTM model, it is compared with KNN [30] and CNN models. The overall accuracy achieved by KNN, CNN, and 3-layer CNN-LSTM model is given in Table 5 while represented graphically in Figure 7. Consequently, we see from Table 5, a gradual decrease in test errors and an increase in accuracy. The model achieved the highest recall of 96%, precision of 95%, f1-score of 95% for dorsiflexion of the foot, and lowest recall of 90%, precision of 84%, and f1-score of 87% for the wrist flexion as shown in Figure 6.

The precision, recall, and f1-scores are calculated to validate the performance, in case the dataset in a class is imbalanced and accuracy may produce deceptive results.

In 3-layer CNN-LSTM model, the LSTM which is a variant of RNN is the primary learning element and

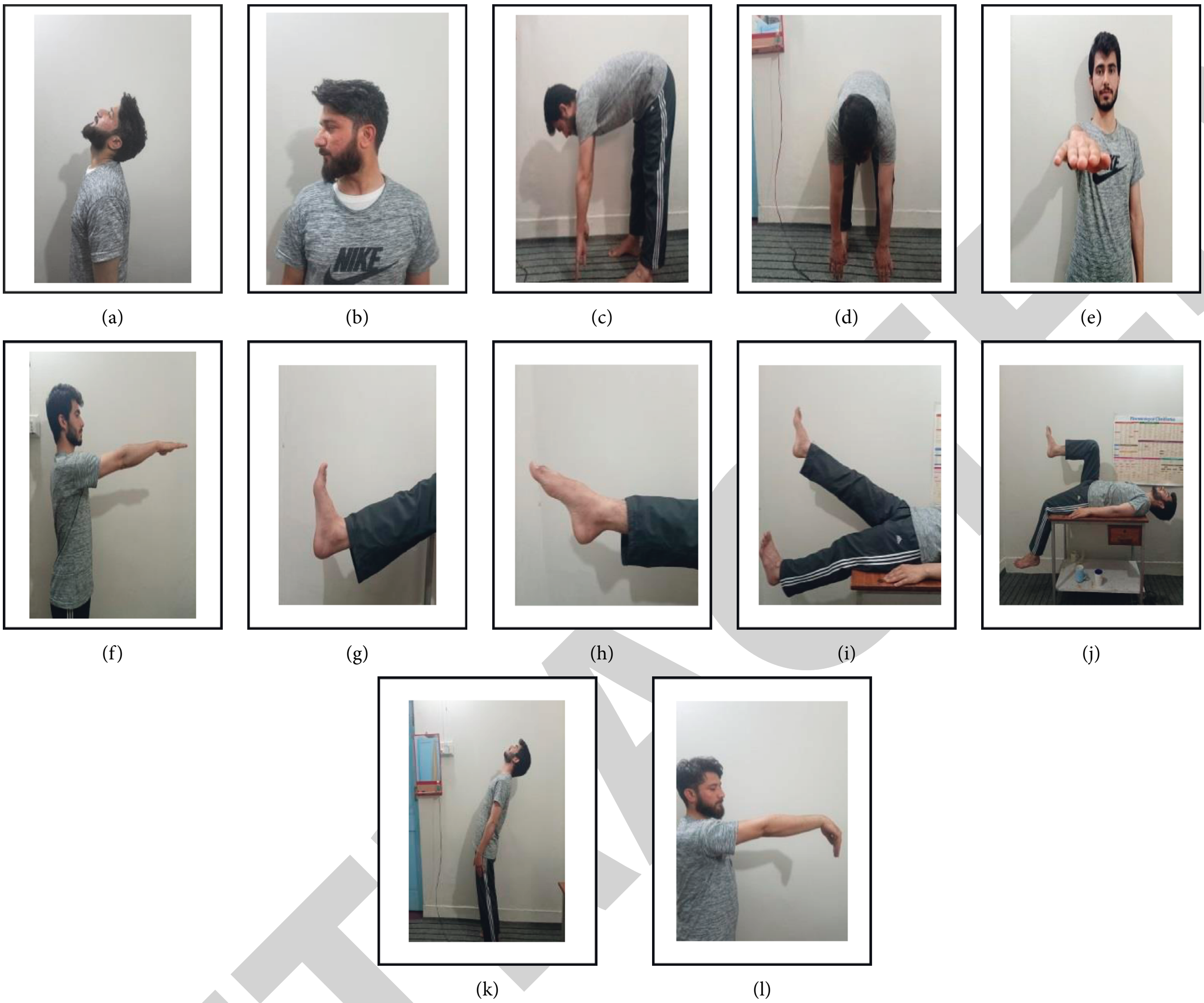

Figure 4: List of rehabilitation exercises, from left to right: (a) extension of the neck; (b) rotation of neck; (c) flexion of the trunk side view; (d) flexion of the trunk front view; (e), (f) extension of the elbow joint (front and side view); (g) dorsiflexion of the foot; (h) plantar flexion of the foot; (i), (j) extension and flexion of the knee joint; (k) extension of the trunk; and (l) flexion of the wrist.

Table 3: Description of the dataset.

Total samples of rehabilitation exercise: 2250	
Number of participants: 20	
Rehabilitation exercise	No. of samples
Flexion and extension of neck	332
Flexion and extension of trunk	328
Flexion of knee joint	348
Flexion and extension of wrist	489
Dorsiflexion and plantar flexion	419
Abduction of upper limb	334

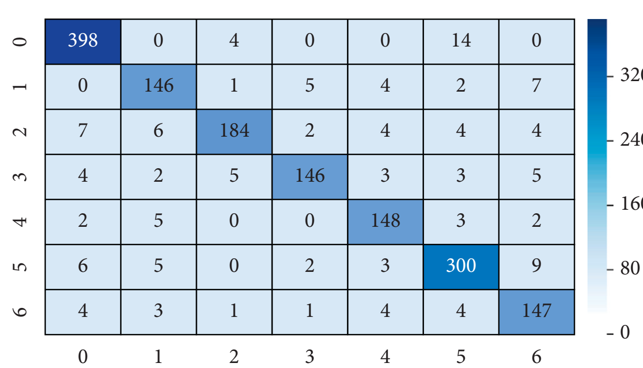

Figure 5: Confusion matrix of 3-layer CNN-LSTM model.

produced better or at least the same accuracy compared to other state-of-the-art models on the prescribed datasets. The model was tested on different types of data, which the model had not seen before, and observed that the CNN-LSTM model has the same best accuracy. It confirms that the model is not overfitted and is performing better in situations like that of occlusion, viewpoint variation, and deformation.

Table 4: Classification report of 3-layer CNN-LSTM and CNN model.

	CNN-LSTM model			CNN model		
Exercises	Precision	Recall	F1-score	Precision	Recall	F1-score
Dorsiflexion	0.95	0.96	0.95	0.93	0.99	0.96
Neck exercise	0.87	0.88	0.88	0.87	0.87	0.87
Plantar flexion	0.94	0.87	0.91	0.91	0.86	0.89
Trunk extension	0.94	0.87	0.90	0.93	0.81	0.86
Trunk flexion	0.89	0.93	0.91	0.95	0.84	0.89
Wrist extension	0.91	0.92	0.92	0.85	0.90	0.88
Wrist flexion	0.84	0.90	0.87	0.84	0.90	0.87

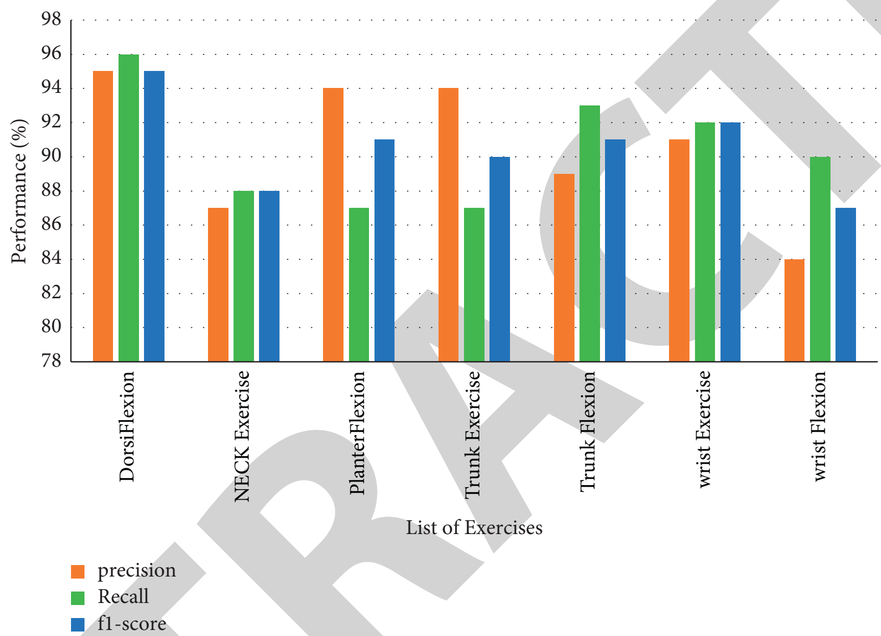

Figure 6: Performance in terms of precision, recall, and f1-score.

Table 5: Performance comparison of different models.

S. No	Model	Accuracy (%)
1	KNN [30]	86.1
2	CNN	89.9
3	3-layer CNN-LSTM	91.3

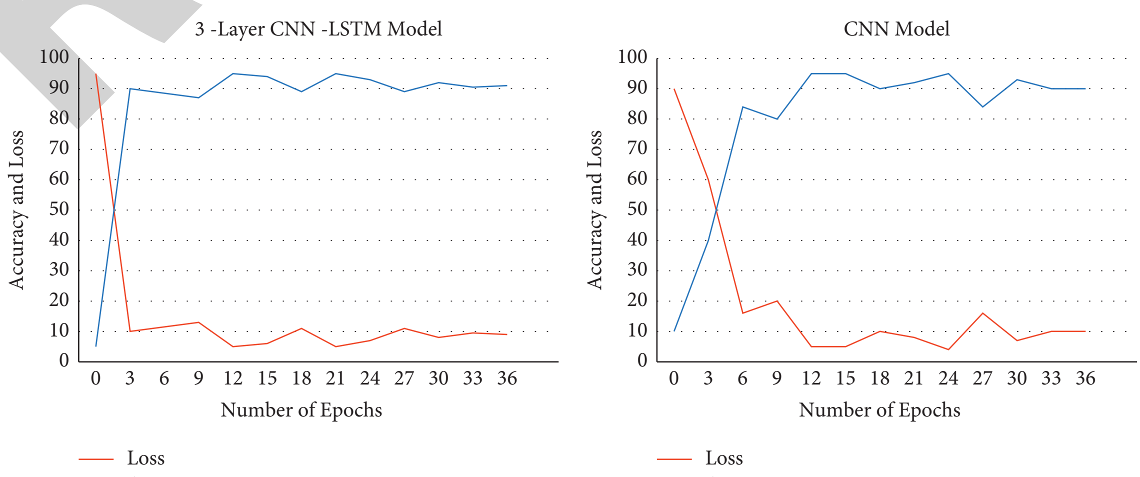

Figure 7: Line graph showing the average accuracy of CNN-LSTM and CNN model.

5. Conclusion and Future Work

Deep learning models have powerful learning abilities in dealing with deformation, viewpoint variation, occlusion, and background switches. In the suggested model, a DNN algorithm is implemented that combines CNN and LSTM as 3-layer CNN-LSTM for the detection of rehabilitation exercises. After the fully connected layer, a BN layer is added to reduce the internal covariate shift and speed up the convergence procedure of the model. In the proposed architecture, the data collected by an RGB camera under the direction of a physiotherapist is fed into a 3-layer CNN followed by an LSTM layer. The CNN along with LSTM is making the model proficient in learning the spatial and temporal dynamics at various time slots. The parameters are learned over CNNs and further classified by LSTM to attain better accuracy and preserve a high recognition rate. In the future, the model shall be trained on more complex datasets to detect complex rehabilitation physiotherapy exercises. Moreover, the algorithm will be updated in such a way that can be used at home for a patient to carry out the prescribed rehabilitation exercises without direct in-person supervision of physical therapists.

Data Availability

The data that support the findings of this study are available upon request from the first author.

Conflicts of Interest

The authors declare that they have no conflicts of interest.

References

[1] J. Bernhardt, P. Langhorne, and G. Kwakkel, "Stroke care 2 : stroke rehabilitation," *Lancet*, vol. 377, no. 9778, pp. 1693–1702, 2011.

[2] I. E. Nikityuk, G. A. Ikoeva, and O. I. Kivoenko, "The vertical balance management system is more synchronized in children with cerebral paralysis than in healthy children," *Pediatric Traumatology, Orthopaedics and Reconstructive Surgery*, vol. 5, no. 3, pp. 49–57, 2017.

[3] D. Nizamutdinov and L. A. Shapiro, "Overview of traumatic brain injury: an immunological context," *Brain Sciences*, vol. 7, no. 1, pp. 1–11, 2017.

[4] L. Adolfsson, "Post-traumatic stiff elbow," *EFORT Open Reviews*, vol. 3, no. 5, pp. 210–216, 2018.

[5] R. J. Oskouian, C. A. Sansur, and C. I. Shaffrey, "Congenital abnormalities of the thoracic and lumbar spine," *Neurosurgery Clinics of North America*, vol. 18, no. 3, pp. 479–498, 2007.

[6] S. Esposito and M. R. Longo, "Guillain-Barré syndrome," *Autoimmunity Reviews*, vol. 16, no. 1, pp. 96–101, 2017.

[7] K. N. Borschmann and K. S. Hayward, "Recovery of upper limb function is greatest early after stroke but does continue to improve during the chronic phase: a two-year, observational study," *Physiotherapy*, vol. 107, pp. 216–223, 2020.

[8] C. A. Doman, K. J. Waddell, R. R. Bailey, J. L. Moore, and C. E. Lang, "Changes in upper-extremity functional capacity and daily performance during outpatient occupational therapy for people with stroke," *American Journal of Occupational Therapy : Official Publication of the American Occupational Therapy Association*, vol. 70, no. 3, pp. 7003290040–11, 2016.

[9] S. Skaria, A. Al-Hourani, M. Lech, and R. J. Evans, "Hand-gesture recognition using two-antenna Doppler radar with deep convolutional neural networks," *IEEE Sensors Journal*, vol. 19, no. 8, pp. 3041–3048, 2019.

[10] W. Tao, T. Liu, R. Zheng, and H. Feng, "Gait analysis using wearable sensors," *Sensors*, vol. 12, no. 2, pp. 2255–2283, 2012.

[11] F. Karray, M. Alemzadeh, J. Abou Saleh, and M. Nours Arab, "Human-computer interaction: overview on state of the art," *International Journal on Smart Sensing and Intelligent Systems*, vol. 1, no. 1, pp. 137–159, 2008.

[12] J. Reyes-Campos, G. Alor-Hernández, I. Machorro-Cano, J. O. Olmedo-Aguirre, J. L. Sánchez-Cervantes, and L. Rodríguez-Mazahua, "Discovery of resident behavior patterns using machine learning techniques and IoT paradigm," *Mathematics*, vol. 9, no. 3, pp. 1–25, 2021.

[13] L. Verde, G. De Pietro, and G. Sannino, "Voice disorder identification by using machine learning techniques," *IEEE Access*, vol. 6, pp. 16246–16255, 2018.

[14] M. Elhoseny, "Multi-object detection and tracking (MODT) machine learning model for real-time video surveillance systems," *Circuits, Systems, and Signal Processing*, vol. 39, no. 2, pp. 611–630, 2020.

[15] M. Xi, N. Lingyu, and S. Jiapeng, "RETRACTED: research on urban anti-terrorism intelligence perception system from the perspective of Internet of things application," *International Journal of Electrical Engineering Education*, vol. 58, no. 2, pp. 248–257, 2021.

[16] I. Ullah, M. Jian, S. Hussain et al., "Global context-aware multi-scale feature aggregative network for salient object detection," *Neurocomputing*, vol. 455, pp. 139–153, 2021.

[17] J. P. Zhu, H. Q. Chen, and W. Bin Ye, "Classification of human activities based on radar signals using 1D-CNN and LSTM," in *Proceedings of the IEEE Int. Symp. Circuits Syst*, no. 1–5, Seville, Spain, October 2020.

[18] A. Khan, A. Sohail, U. Zahoora, and A. S. Qureshi, "A survey of the recent architectures of deep convolutional neural networks," *Artificial Intelligence Review*, vol. 53, no. 8, pp. 5455–5516, 2020.

[19] B. Schuster-Böckler and A. Bateman, "An introduction to hidden Markov models," *Curr. Protoc. Bioinforma*, vol. 18, no. 1, 2007.

[20] S. J. D. Prince and J. H. Elder, "Probabilistic linear discriminant analysis for inferences about identity," in *Proceedings of the IEEE Int. Conf. Comput. Vis.*, no. 2, pp. 1–8, Seoul, Republic of Korea, October 2007.

[21] M. Schonlau and R. Y. Zou, "The random forest algorithm for statistical learning," *STATA Journal*, vol. 20, no. 1, pp. 3–29, 2020.

[22] M. Maalouf, "Logistic regression in data analysis: an overview," *International Journal of Data Analysis Techniques and Strategies*, vol. 3, no. 3, pp. 281–299, 2011.

[23] S. Huang, C. A. I. Nianguang, P. Penzuti Pacheco, S. Narandes, Y. Wang, and X. U. Wayne, "Applications of support vector machine (SVM) learning in cancer genomics," *CANCER GENOMICS and PROTEOMICS*, vol. 15, no. 1, pp. 41–51, 2018.

[24] Y. Y. Song and Y. Lu, "Decision tree methods: applications for classification and prediction," *Shanghai Arch. Psychiatry*, vol. 27, no. 2, pp. 130–135, 2015.

[25] A. V. Vokhmintcev, I. V. Sochenkov, V. V. Kuznetsov, and D. V. Tikhonkikh, "Face recognition based on a matching algorithm with recursive calculation of oriented gradient

Hindawi
Journal of Healthcare Engineering
Volume 2023, Article ID 9845732, 1 page
https://doi.org/10.1155/2023/9845732

Retraction

Retracted: Brain Tumor Detection and Classification by MRI Using Biologically Inspired Orthogonal Wavelet Transform and Deep Learning Techniques

Journal of Healthcare Engineering

Received 23 May 2023; Accepted 23 May 2023; Published 24 May 2023

This article has been retracted by Hindawi following an investigation undertaken by the publisher [1]. This investigation has uncovered evidence of one or more of the following indicators of systematic manipulation of the publication process:

(1) Discrepancies in scope
(2) Discrepancies in the description of the research reported
(3) Discrepancies between the availability of data and the research described
(4) Inappropriate citations
(5) Incoherent, meaningless and/or irrelevant content included in the article
(6) Peer-review manipulation

The presence of these indicators undermines our confidence in the integrity of the article's content and we cannot, therefore, vouch for its reliability. Please note that this notice is intended solely to alert readers that the content of this article is unreliable. We have not investigated whether authors were aware of or involved in the systematic manipulation of the publication process. Wiley and Hindawi regrets that the usual quality checks did not identify these issues before publication and have since put additional measures in place to safeguard research integrity.

We wish to credit our own Research Integrity and Research Publishing teams and anonymous and named external researchers and research integrity experts for contributing to this investigation.

The corresponding author, as the representative of all authors, has been given the opportunity to register their agreement or disagreement to this retraction. We have kept a record of any response received.

References

[1] M. Arif, F. Ajesh, S. Shamsudheen, O. Geman, D. Izdrui, and D. Vicoveanu, "Brain Tumor Detection and Classification by MRI Using Biologically Inspired Orthogonal Wavelet Transform and Deep Learning Techniques," *Journal of Healthcare Engineering*, vol. 2022, Article ID 2693621, 18 pages, 2022.

Hindawi
Journal of Healthcare Engineering
Volume 2022, Article ID 2693621, 18 pages
https://doi.org/10.1155/2022/2693621

Research Article

Brain Tumor Detection and Classification by MRI Using Biologically Inspired Orthogonal Wavelet Transform and Deep Learning Techniques

Muhammad Arif ,[1] F. Ajesh,[2] Shermin Shamsudheen ,[3] Oana Geman ,[4,5] Diana Izdrui ,[5] and Dragos Vicoveanu[5]

[1]*Department of Computer Science and Information Technology, University of Lahore, Lahore, Pakistan*
[2]*Department of Computer Science and Engineering, Sree Buddha College of Engineering, Alappuzha, Kerala, India*
[3]*College of Computer Science and Information Technology, Jazan University, Jazan, Saudi Arabia*
[4]*Neuroaesthetics Lab, Stefan cel Mare University of Suceava, Suceava, Romania*
[5]*Faculty of Electrical Engineering and Computer Science, Stefan cel Mare University of Suceava, Suceava, Romania*

Correspondence should be addressed to Muhammad Arif; arifmuhammad36@hotmail.com and Oana Geman; oana.geman@usm.ro

Received 15 November 2021; Revised 4 December 2021; Accepted 9 December 2021; Published 10 January 2022

Academic Editor: Liaqat Ali

Radiology is a broad subject that needs more knowledge and understanding of medical science to identify tumors accurately. The need for a tumor detection program, thus, overcomes the lack of qualified radiologists. Using magnetic resonance imaging, biomedical image processing makes it easier to detect and locate brain tumors. In this study, a segmentation and detection method for brain tumors was developed using images from the MRI sequence as an input image to identify the tumor area. This process is difficult due to the wide variety of tumor tissues in the presence of different patients, and, in most cases, the similarity within normal tissues makes the task difficult. The main goal is to classify the brain in the presence of a brain tumor or a healthy brain. The proposed system has been researched based on Berkeley's wavelet transformation (BWT) and deep learning classifier to improve performance and simplify the process of medical image segmentation. Significant features are extracted from each segmented tissue using the gray-level-co-occurrence matrix (GLCM) method, followed by a feature optimization using a genetic algorithm. The innovative final result of the approach implemented was assessed based on accuracy, sensitivity, specificity, coefficient of dice, Jaccard's coefficient, spatial overlap, AVME, and FoM.

1. Introduction

Every year, more than 190,000 people in the world are diagnosed with primary or metastatic brain (secondary) tumors. Although the causes of brain tumors are not certain, there are many trends among the people who get them. Any human being, whether a child or an adult, may be affected by it. The tumor region has initially identified a reduction in the risk of mortality [1]. As a result, the radiology department has gained prominence in the study of brain tumors using imaging methods. Many studies have looked at the causes of brain tumors, but the results have not been conclusive. In [2], an effective partitioning strategy was presented using the *k*-means clustering method integrated with the FCM technique. This approach will benefit from the *k*-means clustering in terms of the minimum time of calculation FCM helps to increase accuracy. Amato et al. [3] structured PC-assisted recognition using mathematical morphological reconstruction (MMR) for the initial analysis of brain tumors. Test results show the high accuracy of the segmented images while significantly reducing the time of calculation. In [4], classification of neural deep learning systems was proposed for the identification of brain tumors. Discrete wavelet transformation (DWT), excellent extraction method, and main component analysis (PCA) were applied to the classifier here, and performance evaluation was highly acceptable across all performance measurements.

In [5], a new classifier system was developed for brain tumor detection. The proposed system achieved 92.31% of accuracy. In [6], a method was suggested for classifying the brain MRI images using an advanced machine learning approach and brain structure analytics. To identify the separated brain regions, this technique provides greater accuracy and to find the ROI of the affected area. Researchers in [7] proposed a strategy to recognize MR brain tumors using a hybrid approach incorporating DWT transform for feature extraction, a genetic algorithm to reduce the number of features, and to support the classification of brain tumors by vector machine (SVM) [8]. The results of this study show that the hybrid strategy offers better output in a similar sense and that the RMS error is state-of-the-art. Specific segmentation concepts [9–33] include region-based segmentation [10], edge-based technique [11], and thresholding technique [12] for the detection of cancer cells from normal cells. Common classification method is based on the Neural Network Classifier [13], SVM Classifier [14], and Decision Classifier [15]. In [32], a brain tumor detection method was developed using the GMDSWS-MEC model. The result shows high accuracy and less time to detect tumors.

1.1. Research Gap Identified. From the research analysis, we have identified that traditional algorithms are very effective to the initial cluster size and cluster centers. If these clusters vary with different initial inputs, then it creates problems in classifying pixels. In the existing popular fuzzy cluster mean algorithm, the cluster centroid value is taken randomly. This will increase the time to get the desired solution. Manual segmentation and evaluation of MRI brain images carried out by radiologists are tedious; the segmentation is done by using machine learning techniques whose accuracy and computation speed are less. Many neural network algorithms have been used for the classification and detection of the tumor where the accuracy is less. The detection accuracy is based on the segmentation and the detection algorithms used. So far, in an existing system, the accuracy and the quality of the image are less.

1.2. Contribution of the Proposed Research. The proposed technique is an effective technique to detect tumour from MRI images. In the proposed technique, different classifiers are used. The proposed system should be capable of processing MRI, multislice sequences, accurately bounding the tumor area from the preprocessed image via skull stripping and morphological operations. The region should be segmented by Berkeley's wavelet transformation and extract the texture features using ABCD, FOS, and GLCM features. Classifiers such as Naïve Bayes, SVM-based BoVW, and CNN algorithm should compare the classified result and must identify the tumor region with high precision and accuracy. Finally, based on the classifier result, the tumor region is classified into malignant or benign.

The rest of the article is intended to continue: section 1 presents the background to brain tumors and related work; section 2 presents the construction techniques with the measures used throughout the method used; section 3 describes the results and analysis and the comparative study; and, finally, section 4 presents the conclusions and upcoming work.

2. Methodology

In this research work, the initial image database is collected; the obtained images are enhanced by thresholding, morphological operation, and region filling. After preprocessing, the tumor region is segmented using the BWT algorithm. The features are extracted by using the GLCM algorithm. The genetic algorithm is used for selecting the features. Finally, the SVM Naïve Bayes, BOV-based SVM classifier, and CNN classify the image accurately. The flow for identifying the brain tumors is portrayed in Figure 1.

2.1. Data Acquisition. The data collected are grouped into two kinds—healthy brain images and unhealthy brain images. Among the 66 patients, 22 patients have normal MRI brain images and the rest 44 collect in the abnormal MRI brain image category from the Harvard Medical School website (http://med.harvard.edu/AANLIB/) [16]. The MRI brain image obtained from the database were in the form of an axial plane, T2-weighted, and 256×256 pixels. These images are scrutinized, and preprocessing is done before the processing of algorithms.

2.2. Preprocessing. The preprocessing step focuses on specifically removing the redundancy present in the captured image without affecting the subtleties that play a key role in the general procedure. It is done to improve the visual look and characteristics of an image. In the conventional model, MRI images [34] are often affected by impulse noise, such as salt and pepper, which degrades the performance of the tumor segmentation system to avoid the proposed skull stripping and morphological operations.

The key activities in preprocessing are thresholding, morphological operation, and region filling. In the input image, at first, mean is calculated, and thresholding operation is done. To remove holes from the input image, region filling operation is done, which is trailed by morphological activity, with the goal that it can eliminate noise as well as small objects from the background. Normally, preprocessing can be assessed visually or quantitatively.

2.3. Segmentation-Berkeley's Wavelet Transformation. Segmentation is used to identify the tumor infected area from the MR images. The Berkeley wavelet transformation uses two-dimensional triadic wavelet transformation and a complete, orthonormal basis, and hence it is very ideal for the identification of the area of interest from the MR images

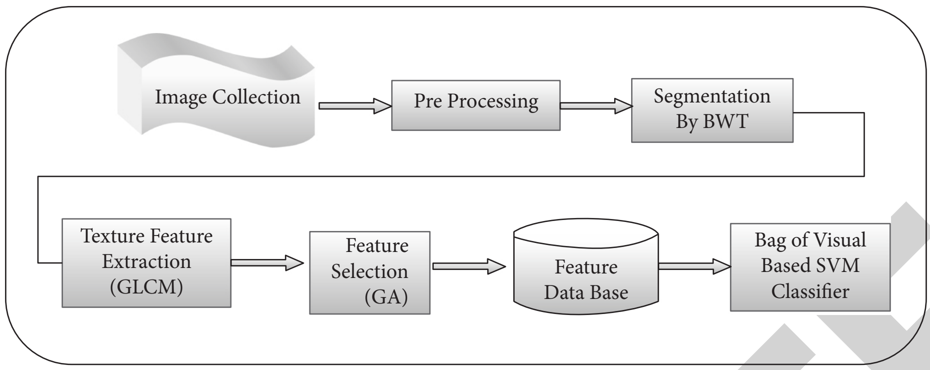

Figure 1: Basic block diagram of planned work.

[17]. The BWT converges repetitively from one level to n—number of levels—and decomposes the other part of the image at a very fast rate.

The partition of the highly contagious MR brain areas is done as follows:

(i) In the initial stage, the enhanced brain MRI image is transformed into a binary image with a cut-off level of 117. Pixels with values larger than the defined level are converted to white, whereas the remaining pixels are marked as black, resulting in the development of two distinct regions around the infected tumor tissues.

(ii) In the second stage, the morphological erosion procedure is used to remove white pixels. Finally, the region is divided into destruction and identical areas, and the area of the omitted black pixels of the erosion process is counted as the MR image mask for the brain.

This present work deals with the conversion of Berkeley's wavelets, which is used to effectively section the brain MR image. The conversion of the Berkeley wavelet (BWT) is defined as the transformation of two-dimensional triadic wavelets, which can be used to analyze the signal or image. The BWT is used in features, such as spatial position, band pass frequency, band pass orientation tuning, quadrature phase, etc. As with the conversion of the mother wavelet or other wavelet transformation communities, the BWT algorithm will also allow for an efficient transition from one spatial form to a temporal domain frequency. The BWT is an important method of image transformation and is a complete orthonormal one.

BWT consists of eight major mother wavelets grouped into four pairs, each pair having different 0, 45, 90, and 135 degrees aspects. Inside each pair of wavelet transforms, some wavelet has odd symmetry, while another wavelet also has symmetry. The BWT algorithm is an accurate, orthonormal basis and is therefore useful for computational power reduction. Here, the Berkeley wavelet transformation is used for efficient division [18]. Wavelet analysis is an efficient approach capable of revealing data aspects which are other techniques for analyzing the signal. The process, by considering the images at numerous stages, can take out the finer details from them and in effect enhance the image quality. Alternatively, wavelet analysis can compress or denoise a signal without significant degradation. The BWT algorithm steps are defined as follows:

(1) Initially calculate scaling and translation process:

$$P = \frac{1}{\sqrt{S}}\psi\left(\frac{T-\tau}{S}\right). \tag{1}$$

(2) Perform conversion of data from a spatial form to a temporal domain frequency.

(3) Simplification of image conversion calculation of the mother wavelet transformation is partly fixed:

$$\begin{aligned} \beta_\theta^\phi(\tau, S) &= \frac{1}{S^2}\beta_\theta^\phi\left(3^S(x-i), 3^S(y-j)\right), \\ \beta_0 &= \frac{1}{\sqrt{9}}\left[\mu\left(\frac{x}{3}, \frac{y}{3}\right)\right]. \end{aligned} \tag{2}$$

(4) Apply the morphological technique.

(5) Reschedule the corresponding pixel values; this process is only for binary images.

(6) Removing pixels from or to the edge area of the artifacts relies on just the streamlining element of the image selected.

2.4. Feature Extraction. The extraction procedure for the element is utilized to consequently find the lesion. There are three procedures to consider for the extraction of features: FOS, ABC, and GLCM.

2.4.1. ABC Parameter. The extracted features based on ABC are given as follows:

(i) Asymmetry index:

$$AI = \frac{A_1 + A_2}{2A_r}. \tag{3}$$

(ii) Four different border irregularity measures are

(a) Compactness index:

$$CI = (P2L) = 4AL. \tag{4}$$

(b) Fractal index: The set of fractals is calculated using the tracking of boxes. The box tracking is portrayed by $N(S)$ in the fractal dimension plot, and N symbolizes a sequence of boxes. Box track is described for the Hausdorff dimension plot with log $N(S)$, and log N signifies several columns.

(c) Edge abruptness:

$$\mathrm{EI} = \frac{(\max . \min)\%6 + 2}{100}. \tag{5}$$

(d) Gray transition: It calculates the position and velocity of an image's gradient.

(iii) Diameter: The diameter of the lesion field is calculated for smaller axis length by using the function' region props' function. The resulting value is converted to a value of the nanometer, and that value is assigned the diameter.

2.4.2. GLCM Features. This strategy obeys two measures to synthesize characteristics of the medicinal images. During the initial process, the GLCM features are computed and in the next process, the texture characteristics depending upon the GLCM are determined. The metric formula is depicted below for a few of the innovative features. Extraction of the feature is done using a co-occurrence matrix of the gray level [20]. Several texture features are available, but this study uses only four features: strength, contrast, correlation, and homogeneity.

$$\begin{aligned}
\text{Energy} &= \sum_{i=0}^{G-1}\sum_{j=0}^{G-1}[p(x,y)]^2,\\
\text{Homogenity} &= -\sum_{i=0}^{G-1} p(i)\log_2[p(x)],\\
\text{Correlation} &= \sum_{i=0}^{G-1}\sum_{i=0}^{G-1}\frac{x, y\, p(x,y) - \mu_x\mu_y}{\sigma_x\sigma_y},\\
\text{Contrast} &= \sum_{i=0}^{G-1}\sum_{j=0}^{G-1}(x-y)p(x,y).
\end{aligned} \tag{6}$$

2.4.3. Statistical Features. The descriptor Color Moment (CM) is used to derive both functions. Statistical Function Equations (FOS) are given below:

$$\begin{aligned}
\text{Mean}\,\mu &= \sum_{i=0}^{G-1} \mathrm{i}\,\mathrm{p}(x),\\
\text{Variance}\,\sigma^2 &= \sum_{i=0}^{G-1}(x-\mu)^2 p(x),\\
\text{Skewness}\,\mu_3 &= \sigma^{-3}\sum_{i=0}^{G-1}(x-\mu)^3 p(x),\\
\text{Kurtosis}\,\mu_4 &= \sigma^{-4}\sum_{i=0}^{G-1}(x-\mu)^4 p(x),\\
\text{Entropy}\,H &= -\sum_{i=0}^{G-1}\sum_{j=0}^{G-1} p(x,y)\log_2[p(x)].
\end{aligned} \tag{7}$$

Figure 2 shows 13 features that are selected for contributions to the classification system. The network consists of 4 hidden neurons, and 1 output neuron is used for the final examination of the network. At that point, the rules for choosing the component are utilized to diminish the quantity of feature input.

2.5. Features Selection Using Genetic Algorithm. Not all the features make a payment to the classification process. Feature selection is carried out to identify the most suitable feature set. We use the genetic algorithm to optimize the selected feature values for the proposed method because it offers significant advantages over typical optimization techniques, such as linear programming, heuristic, first depth, first breadth, and Praxis [21] Feature selection process is presented in Figure 3, and the procedure of GA is given in Algorithm 1.

2.5.1. Features Selection: Genetic Algorithm. Genetic algorithms play an important role in reducing the dimensionality of the feature space, thus helping to improve the performance of the classifier. In the genetic algorithm, the major stages are fitness evaluation, chromosome encoding, selection technique, genetic operators, and the condition stops iteration. In binary search space, the genetic algorithm considers chromosomes to be a bit string. Figure 4 shows the matrix representation showing the bit value of the chromosome in genetic algorithm.

Initially, a primary population is formed arbitrarily as well as by utilizing fitness function, it is assessed. In the testing, the chromosome with the bit string value "1" represents the specific feature indexed by the selected position. The ranking determines the accuracy of previously tested classification data. The chromosomes that have the highest fitness function are selected according to the ranking. The remaining chromosome has to undergo mutation and

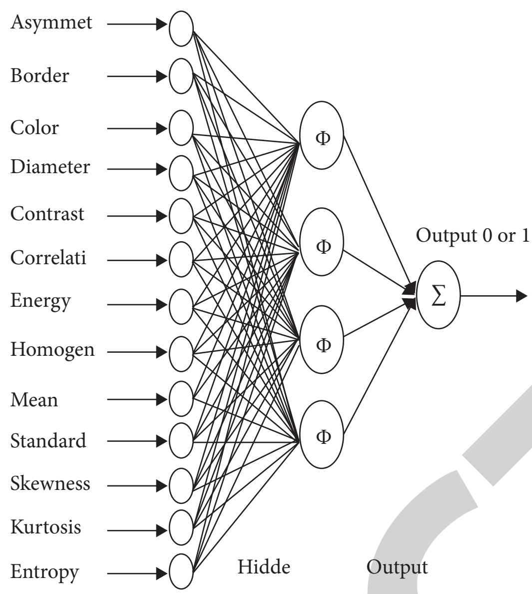

FIGURE 2: Features selected for CNN techniques.

Stage 1: Establish a randomly generated population.
Stage 2: Each chromosome, its fitness function is calculated.
Stage 3: Continue the stages below until the ‘*n*’ offspring are produced.
(1) Choose the current population parent chromosome
(2) Probably PC crossover the set to form two offspring at a randomly selected point
(3) Mute the above process with probability Pm
Stage 4: Current population is replaced by a new population.
Stage 5: repeat step 2.

ALGORITHM 1: Algorithm for genetic algorithm.

crossover to produce a greater likelihood of a new chromosome. This process is repeated until the attainment of a fitness function [22].

(1) Initial Population Selection. The initial population matrix is given by $m \times n$, where m and n represent population size and chromosome length. In the present function, the number of derived features of the picture block is equal to the length of the chromosome, and the number of chromosomes indicates the size of the population. Each bit of a chromosome in the features matrix indicates the position of the feature. A “1” in the chromosome is the selection of the matrix of the equivalent feature.

2.5.2. Fitness Evaluation. A fitness function has the original goal of assessing the discriminating capacity of each subset. Evaluating the reasonable number of the test data and the function space of the training sets solves the classification problem.

$$D(x_{test}, x_i) = \sqrt{\sum_{m-1}^{M} (x_{test} - x_i)^2}. \tag{8}$$

Since the GA iterates, dependent upon the classification error, the distinct chromosomes in the present population are assessed and the fitness is ranked as well. Iteration is mainly done to decrease the error rate and to find the smallest and best fitness value,

$$\text{fit} = \frac{\alpha}{N_f} + \text{Exp}\left(\frac{-1}{N_f}\right). \tag{9}$$

Here, N_f = cardinality of the selected features and α = represents the classification error.

(1) New Population for Generation of Children. A new generation is established after evaluating the fitness function. It mainly depends on the genetic operator such as crossover and mutation. This new population is named: Elite, crossover, and mutation.

(a) *Elite Children*. Since these new populations are the finest children containing the highest fitness value, these are pushed automatically to the successive generation. The population size gives the total elite chromosome. This infers EliteCount ≤ populationSize.

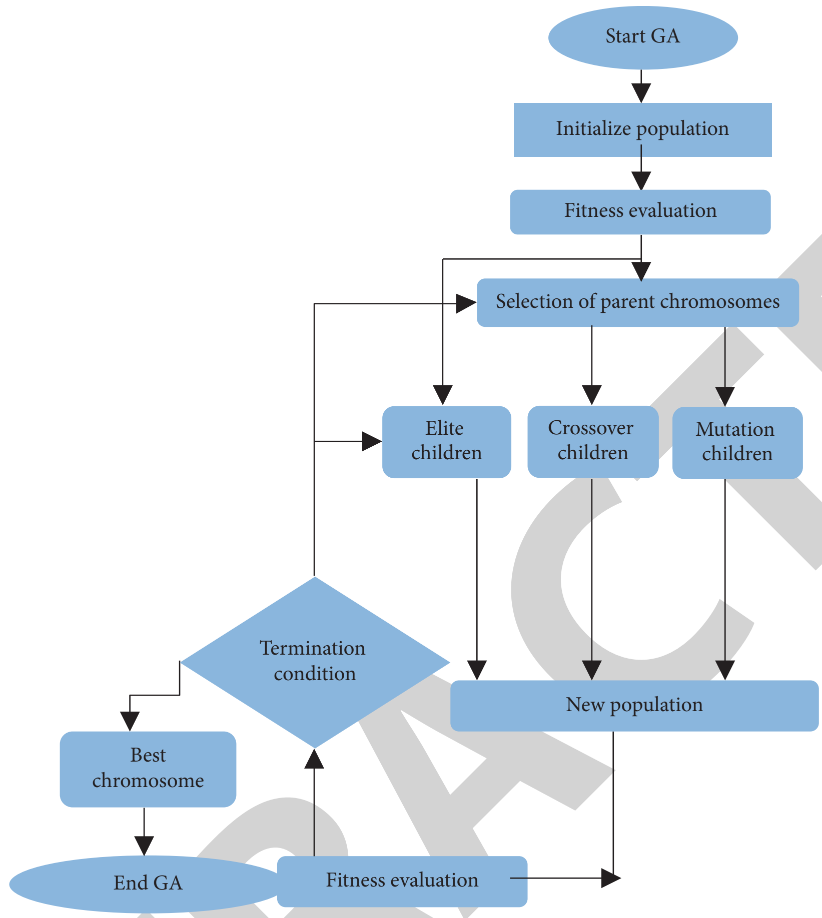

Figure 3: GA-based feature selection.

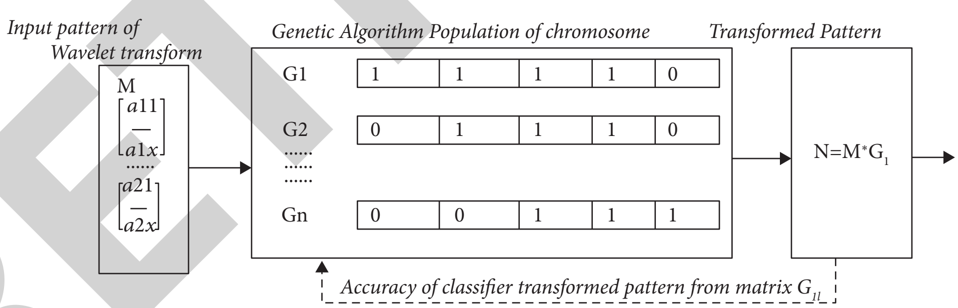

Figure 4: Matrix representation showing the bit value of chromosome in genetic algorithm.

If the size of chromosomes is 2, the genetic algorithm chooses the two finest chromosomes and pushes them to the subsequent generation.

(b) *Crossover Children*. Crossover fraction is the ratio of the following generation besides the remaining kids, which are created by crossover. There are no children with mutations when the fraction is fixed to one.

(c) New Population: Mutation Children. Lastly, the number of mutation children is $M_{\text{count}} = 100$-EliteCount-COcount $= 100-2-78 = 20$. This infers $\text{Elite}_{\text{Count}} + \text{CO}_{\text{count}} + M_{\text{count}} = 100$.

(2) Tournament. In the genetic algorithm, the goal of the selection technique is to ensure the population is being persistently enhanced with complete fitness values. This technique aids the GA in eliminating poor designs as well as maintaining simply the finest individuals. There are a lot of selection techniques, for instance, stochastic uniform. In this proposed research, the selected tournament is having a size of 2 which is used because of its easiness, speed, and efficacy. Tournament selection always ensures in the selection process that the poorest individual does not go to the subsequent generation. To carry out tournament selection, two functions are required (i.e., the players (parents) and the winners). Two chromosomes of size 2 are selected in the

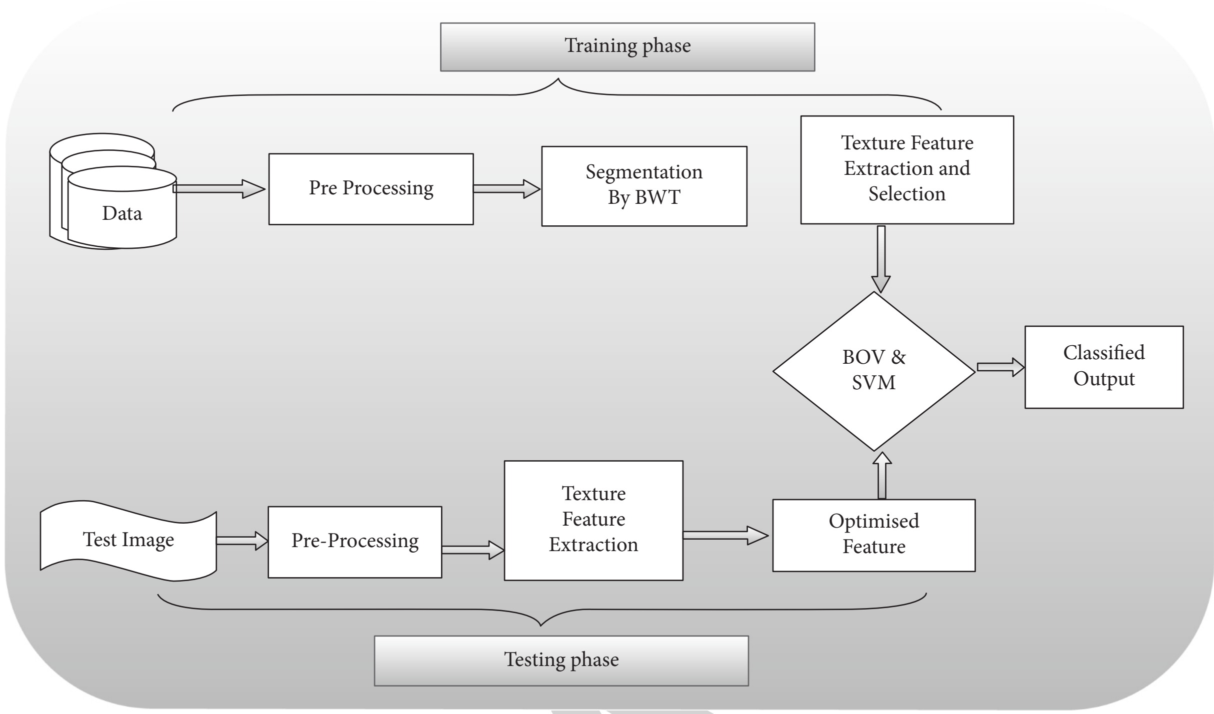

Figure 5: Block diagram showing the steps for support vector machine training and testing.

tournament selection, from the elite children's population and finest of the two chromosomes. It is carried out iteratively by filling up a freshly produced population.

(3) Crossover Function. In the GA, to produce children for the next generation, the crossover operator genetically combines two individuals called parents. After the removal of elite kids, the number of new kids formed from the new population is given by the crossover kids and it is being evaluated. The crossover fraction normally has a value between 0 and 1. The present work crossover value is 0.8. Two-parent chromosomes have binary values and an XOR operation is carried out on these chromosomes.

2.6. Classification. Within the area of computers, vision classification is a significant chore. The labeling of images hooked on one of several defined groupings is called image classification. The classification scheme contains a database that holds predefined patterns that relates to the perceived item to organize into a suitable classification. Here, various techniques like Naïve Bayes, SVM-based BoVW, and CNN algorithm are used.

2.6.1. Naïve Bayes Classifier. The classification of Naïve Bayes has played a major role in the extraction of medical data. It shows superior accuracy, performance because the attributes are independent of each other. The missing values arise continuously in the case of clinical data [35]. This naturally treats misplaced ideals as if lost by mistake. This algorithm replaces zeros with limited numerical data and zero vectors with categorical negative data. In nested columns, missing values are interpreted as being sparse. Missing values in columns with simple data types are interpreted as missing at random. Generally, when choosing to manage our data preparation, Naïve Bayes requires binning. It trusts to estimate the likelihood of accumulation of procedures [23]. To reduce the cardinality, the columns should be discarded as appropriate.

In principle, it has the base error rate in contrast with every other classifier. They give hypothetical avocation to different classifiers which do not expressly utilize the Naïve Bayes theorem. For example, it tends to be shown, based on specific presumptions, that numerous neural systems and curve-fitting calculations yield the most posterior hypothesis, as does the naïve Bayesian classifier. This classification is completed by using a probabilistic methodology that calculates the class probabilities and predicts the most likely classes. A Naïve Bayes classifier applies Bayesian statistics with strong, independent suspicions on the features that drive the classification procedure. It is the basic grouping conspires, which approximations the class conditional likelihood by expecting that the properties are restrictively autonomous, given the class name c. The conditional probability can be finally conveyed as pursues:

$$P(C|A) = c = \prod_{i=1}^{n} P\left(\frac{A_i}{C}\right) = c, \tag{10}$$

wherever both attributes set $A = \{A1, A2 \ldots. An\}$ contains the capabilities of n attributes. With the restrictive probability ratio, instead of calculating the class conditional probability for each grouping of A, just estimate the conditional probability of each A_i, given C. The last method is becoming increasingly useful as it does not

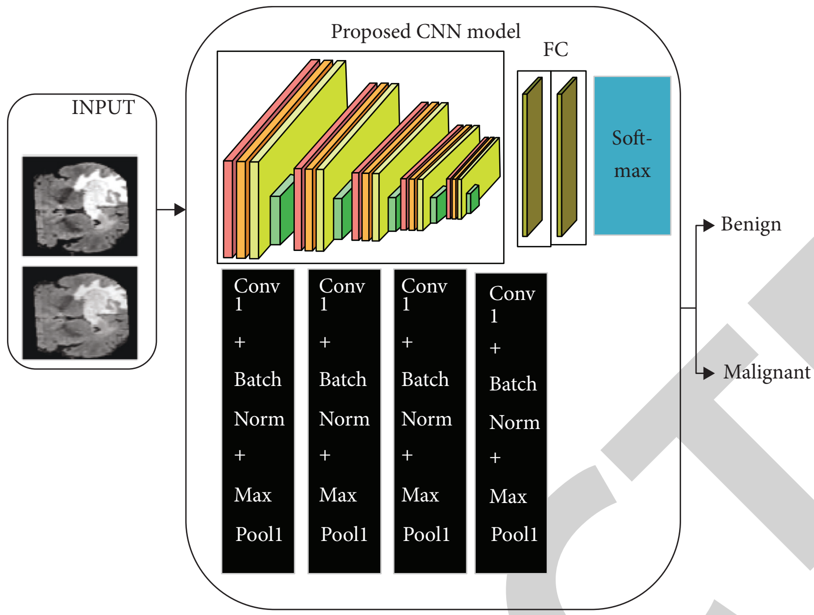

FIGURE 6: Basic diagram for the working of CNN.

entail an incredibly huge collection of preparations to get a reasonable estimate of the likelihood. Each classifier determines the posterior likelihood for each class C to be used to classify a test sample.

$$P(C|A) = P(C)\frac{\prod_{i=1}^{n} P(A_i/C)}{P(A)}. \tag{11}$$

Since $P(A)$ is fixed for each A, it is adequate to choose the class that boosts the numerator term:

$$P(C)\prod_{i=1}^{n} P\left(\frac{A_i}{C}\right). \tag{12}$$

This classifier has a few benefits. It is informal to use different classification approaches; only one time scan of the training data is compulsory. The naïve Bayesian classifier can simply hold missing characteristic qualities by essentially precluding the probability when computing the probabilities of enrolment in each class.

2.6.2. SVM Classification Based on BoV. BoVwords is a supervised model of learning and an extension to the NLP algorithm. Bag of Words is used for classification of images. It is used quite widely aside from CNN. In essence, BOV provides a vocabulary that can best describe the image in terms of extrapolating properties. By generating a bag of visual words, it uses the Computer Vision Toolbox™ functions to define the image categories. The method produces histograms of occurrences of visual words; such histograms are used to classify the images. The steps of the support vector machine are presented in Figure 5.

The steps below explain how to set up your images, develop a bag of visual words, then train and apply a classifier for the image type [24].

It follows 4 simple steps:

(i) Ability of Image features of a defined label
(ii) Development of visual vocabulary by clustering, accompanied by frequency analysis
(iii) Classification of generating vocabulary-based images
(iv) Obtain the best class for the query image.

The algorithm for the bag of visual classifier based SVM is as follows:

Level 1: Set up image type sets.
Level 2: Generate functional Bag.
Level 3: Training the image with BoVwords.
Level 4: Classification using SVM classifier.

Based on the operation of the BOV classifier, the images are processed for examination, specifically, the image is divided into two parts: (1) training and (2) testing subjects. After that, the takeout support vector machine produces a visual vocabulary from each package's representative images. The image is extracted from the training set in the process used to extract the characteristics from the image. Using the nearest neighbor algorithm, an image histogram function is constructed. The histogram converts the image into a function vector. Classification finally is done with SVM classifier assistance.

2.6.3. Convolutional Neural Network. Deep learning methodology is used for arranging the information mainly into four objective factors and to check its precision for each point. Very few investigations were conveyed utilizing different classifications from this informative collection. Deep learning is a kind of AI that manages calculations roused by brain structure and capacity, called neural artificial networks. The thing that isolates it from neural systems is the huge realizing, which is utilized to explain the advancement of new technology in an ANN to process bigger measures of information and to improve its precision of the data classification [36]. Convolution Neural Network (CNN) is an exceptional sort of neural system for preparing information in image, text, and sound structures that have worked effectively in their usage [25]. The expression "Convolution Neural Network" built up a measurable activity called convolution, to show their network. The convolution operation is the operation of a dot product between the process's input matrices. The working of the CNN is presented in Figure 6, and the basic architecture is presented in Figure 7.

Convolutional Neural Network relies upon connecting the previous layer's local territory to the following layer. Spatially, CNN sets up a neighborhood relationship by applying a progressive example of communication between neurons of adjoining layers. The one-layer units connect to the former layer subunits. Preceding layer unit number forms map width. The subsequent rendition takes motivation from the Lanet-5. This standard of forcing neighborhood, availability is portrayed, as observed in Figure 8.

Anyway, as in customary multilayer systems, CNN shares loads; the measure of accessible boundaries does not expand considerably to the input measurements. The main elements of CNN-2 layer classifiers are explained below:

(1) The Convolutional Layer. Behaviors of a 2D sifting between x-input images and w channel bank, producing an extra assortment of h images. Input-output correspondences are shown by an association table; channel reactions are consolidated straightly from the input associated with a similar output image. An association with the accompanying semiconductor is framed through the MRI column: (input Image, separated, output Image). This layer does the mapping after

$$h_j = \sum_{i,k \in CT_{i,k,j}} x_i * w_k, \tag{13}$$

where * shows true 2D convolution. A given layer's w_k the channel has a similar size, and x_i determines the size of the output image alongside the input value h_j. Likewise with standard multilayer systems, 'he is then applied to the nonlinear activation function.

(2) Pooling Layer. The pooling layer does not mean to lessen the calculation unpredictability, however, in addition to the direct decision of the feature. The input images are tiled in uncorrelated subareas, which recover just one output an incentive from. Most extreme or normal mainstream choices, ordinarily named as max-pooling and avg-pooling. The max-pooling is normally profitable given that it adds a slight invariance to interpretation and distortion, which in turn prompts quicker assembly and better speculation.

(3) Fully Connected Layer. In the layered system, a fully connected layer acts as a base layer. Either the system switches convolutional and max-pooling layers with the 1D feature vector the gotten at some stage, or the outcomes collected are redesigned for 1D structure. The base layer is directly connected to the classification process, with the same number of neurons as classes. With a softmax activation function, the outputs are normalized, and in this way gauge probabilities of the back class. Various measuring techniques such as size and number of capabilities maps bit sizes, factor skipping, and connection table are used in the convolution layer.

In the proposed system, the bit size utilized by the connected layer is 7×7, the number of feature maps compared to 6 for the main layer of convolution, and the second layer of convolution equivalent to 12. The skipping component in the network decides the horizontal and vertical pixel number by which the part will skip between ensuing convolutions. In each layer where M includes the size maps (M_x, M_y), the size part (K_x, K_y), the skipping factors (S_x, S_y) are than the size relationship of the output maps as per the above parameters:

$$\begin{aligned} Mnx &= M_{n-1x} - k_{nx}S_{nx} + 1, \\ Mny &= M_{n-1y} - k_{ny}S_{ny} + 1, \end{aligned} \tag{14}$$

where the layer is demonstrated by the record "n." In layer $Ln - 1$ at most, each map in layer Ln is associated with Mn−1 maps. Neurons of a given map share their loads yet have distinctive open fields.

The information layer has a component map compared to the size of the character's standardized image. In this exploration, masses are arbitrarily picked from a uniform dispersion inside the range [−1/fan-in, 1/fan-in] where the contributions to a hidden variable are given by fan-in. For CNN, this relies upon the quantity of feature maps input and the size of the open field. Likewise, with the CNN case, max-pooling is a nondirect down-example. The input image is partitioned into a collection of nonoverlapping rectangles by methods for max-pooling, and yields are determined as the most elevated advantage for each such sublocale [26].

For two reasons, max-pooling is useful in vision:

(a) reduces the numerical sophistication of the upper strata.

(b) It provides different types of invariance in translation.

The second layer of convolution layer comprises six component maps which are gotten by interpreting the size 5×5 pieces into the feature map of the info. The subtesting layer is shown in the third layer, and it is employed in the downexamining of the image. For a downsampling of the image, the max-pooling method is employed over the 2×2 region of the input image. The convolution layer, which is the third layer, makes the changes over the image to a partition size of 5×5 based on the feedback from the past layer. At this stage, the number of feature maps acquired equivalents 12. Again, the subinspecting is acted in the fourth layer with the procedure max-pooling in the area of size 4×4. The fifth layer is a fully associated layer that drives a classifier to give a feedforward yield.

The training part considers the elements in layers 1–4 are the extraction part of the trainable element, and the classifier

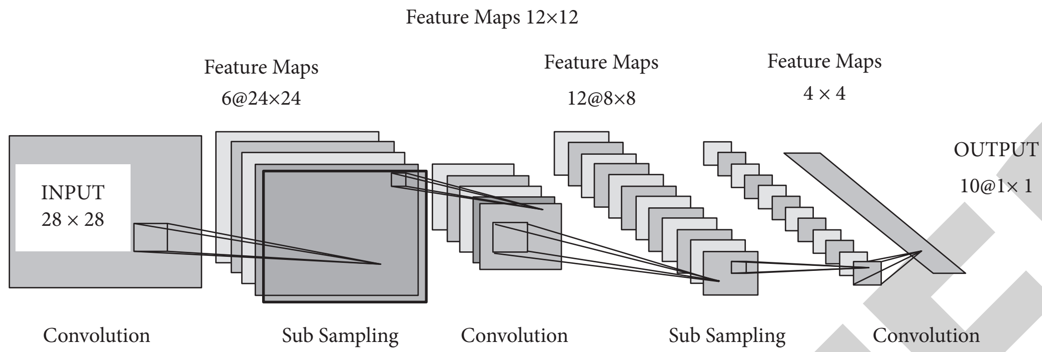

Figure 7: The Convolutional Neural Network basic architecture.

is the following replacement layer. Images are partitioned into a test set and preparing the set. Every computerized image was size-standardized and dependent on a 28 × 28-pixel fixed-scale image. In the first dataset, each pixel of the image is portrayed by an incentive somewhere within the range of 0 and 255, where 0 is dark, 255 is white, and everything in the middle is an alternate shade of dim. An image is represented as a 1-dimensional array of float esteems of 784 (28 × 28) from 0 to 1 (0 methods dark, 1 method white). At the point when we utilize the dataset, we split the preparation and test cluster into smaller than normal bunches.

2.6.4. Performance Analysis. The following performance metrics are obtained from the segmentation and classified result.

Detection part:

$$\text{Jaccard index} = J(A, B) = \frac{S(A \cap B)}{S\left(A \bigcup B\right)}.$$

$$\text{Dice overlap index (DOI)} = D(A, B) = 2X\frac{A \cap B}{A + B},$$

$$\text{Similarity index SI} = \frac{2X\text{Truepositive}}{2X\text{truepositive} + \text{falsepositive} + \text{falsenegative}}, \tag{15}$$

$$\text{Absolute volume measurement error } (AVME) = \left(\frac{V_{automatic}}{V_{manual}} - 1\right) \times 100\%,$$

$$\text{Figure of merit } (\varepsilon) = 1 - (\varepsilon) = 1 - \frac{\left|V_{\text{manual}} - V_{\text{automatic}}\right|}{V_{\text{manual}}}.$$

Classification part:

$$\text{Sensitivity} = \frac{TP}{TP + FN} \times 100\%,$$

$$\text{Specificity} = \frac{TN}{TN + FP} \times 100\%, \tag{16}$$

$$\text{Accuracy} = \frac{TP + TN}{TP + FP + FN + TN} \times 100\%.$$

3. Results and Discussion

The suggested strategy was created using MATLAB software that has a Core 2 Duo code configuration. Initially, the preprocessing technique is applied to enhance the image. Next, the segmentation is applied to extract the boundary region of the tumor. The result is shown in Figures 9 and 10.

In our approach after applying the fitness function of the GA, the optimized features considered are mean, variance, skewness, kurtosis, and energy. The result is shown in Table 1. The cycle of classification is divided into two parts (i.e., the training part and the evaluation part). First, known data (i.e., 24 features* 46 images) are given in the training part to the training classifier. Second, unknown data are provided to the classifier in the testing phase, and the classification is carried out after the training part. The classification's accuracy rate and error rate depend on the quality of the training.

Figures 11–13show the results of GA, and Figure 14 shows the visual word occurrence of the BoVW classifier. Here, the x-axis represents the visual word index, and the y-axis represents the frequency of occurrences in the images correspondingly. The obtained accuracy and confusion matrix is shown in Figures 15 and 16. The obtained accuracy

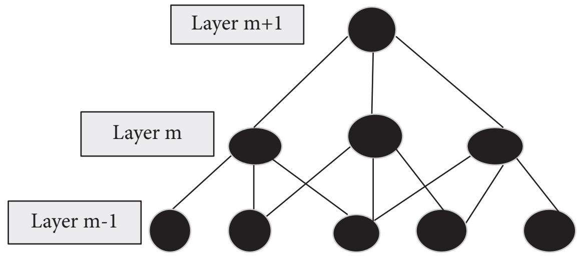

Figure 8: Local connections pattern representation.

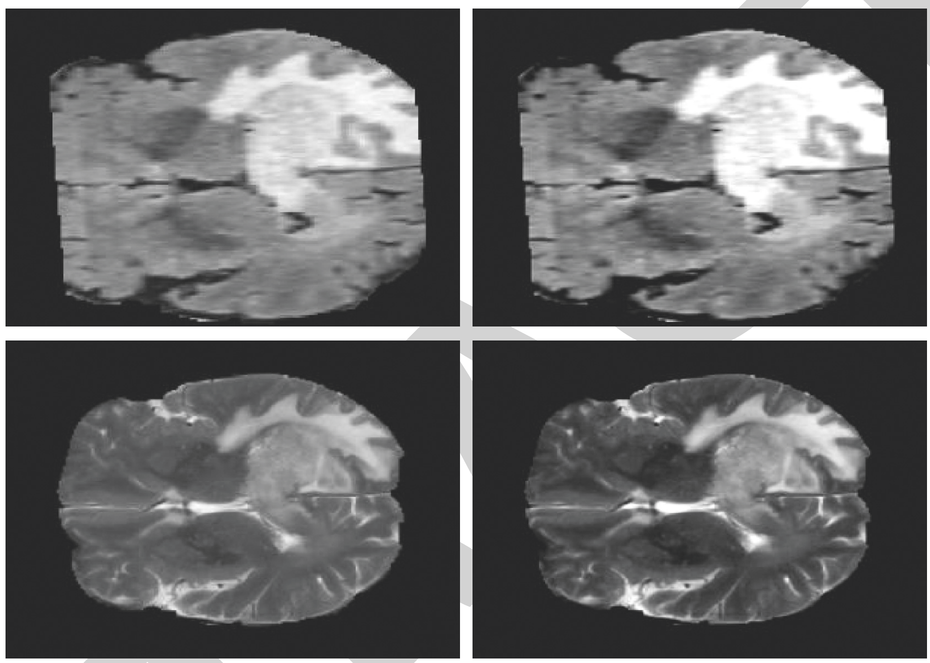

Figure 9: Preprocessing results.

of the proposed classifier is 90% and 97.3%. Table 1 shows the performance value of the suggested classifier. Table 2 presents the statistical analysis of the brain images, and Table 3 presents the performance comparisons.

Further, the findings have acquired an average index coefficient of 0.82 dice similarity, suggesting a greater comparison between the computerized tumor areas (machines) extracted by radiologists and manual tumour region extraction Our current technique results demonstrated the importance of quality parameters and accuracy compared to state-of-the-art techniques.

In CNN, the model ResNet-50 consists of 5 stages, each with a convolution block and identity block. Each block of convolution has three layers, and every block of identity has three layers of convolution too. The ResNet-50 has more than 23 million trainable parameters. Figures 17 and 18 show the first line of ResNet and First Convolution Layer Weights. A confusion matrix is a table that is sometimes used to explain the output of a classification model over a set of test data defined for true values. It enables the output of an algorithm to be visualized. In a projected class, the matrix row represents instances, while each column represents instances in a real class (or vice versa). Figure 19 shows the matrices obtained for precision and uncertainty. The accuracy obtained is 98.5 percent. Figures 20 and 21 show the plot of different classifiers for performance.

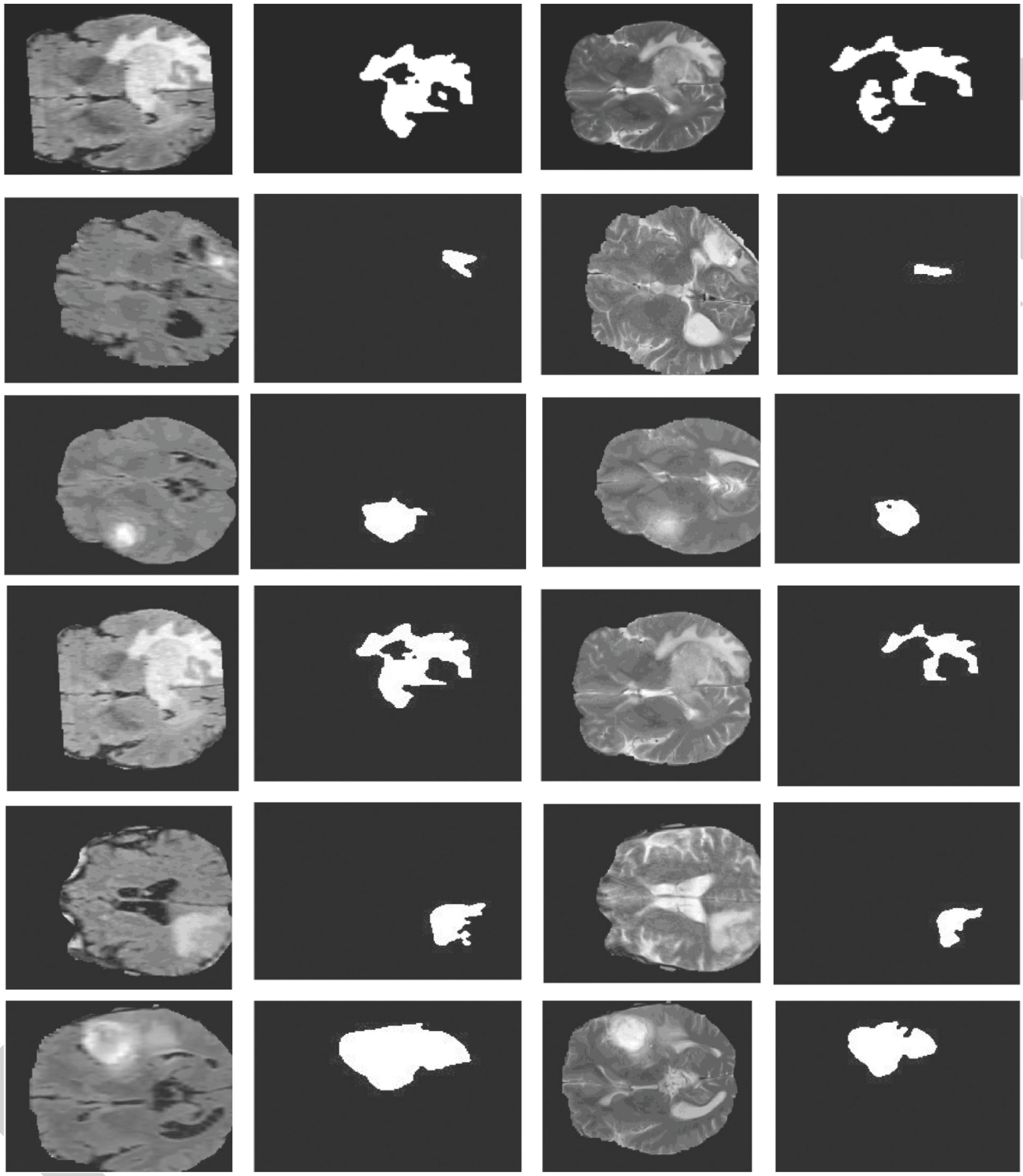

Figure 10: Result of the proposed segmentation in FLAIR and T2 images.

Table 1: Optimized feature extracted after applying genetic algorithm.

Image no.	First-order statistics (FOS) feature				
	Mean	Standard deviation	Skewness	Kurtosis	Entropy
1	0.011	0.019105	2.274177	7.10785	2.68715
2	0.006	0.010301	1.605176	4.28244	2.05357
3	0.008	0.010716	1.578003	4.13867	2.57759
4	0.010	0.01203	0.826578	2.47775	2.77483
5	0.011	0.01429	0.945757	2.65592	2.23901
6	0.010	0.008143	0.419944	2.28365	2.81441
7	0.014	0.01945	2.495946	12.0050	3.11189
8	0.012	0.01388	1.159288	3.16243	3.16398
9	0.014	0.02124	2.216729	9.24762	2.65219
10	0.008	0.010971	1.308686	4.27185	2.4252

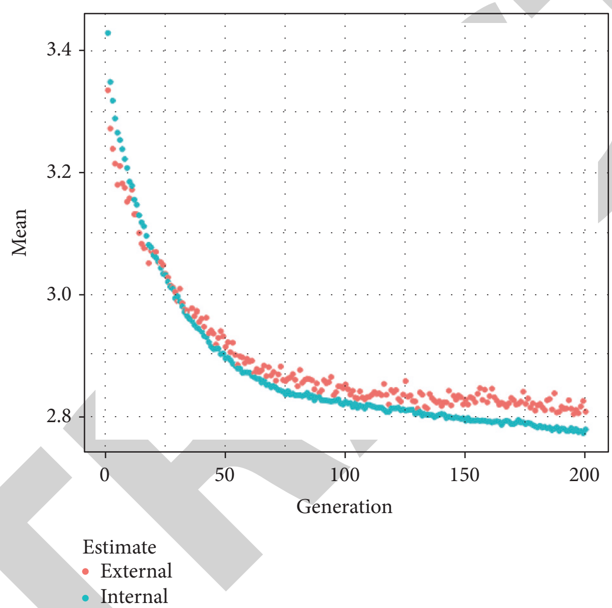

Figure 11: Feature selection result using GA.

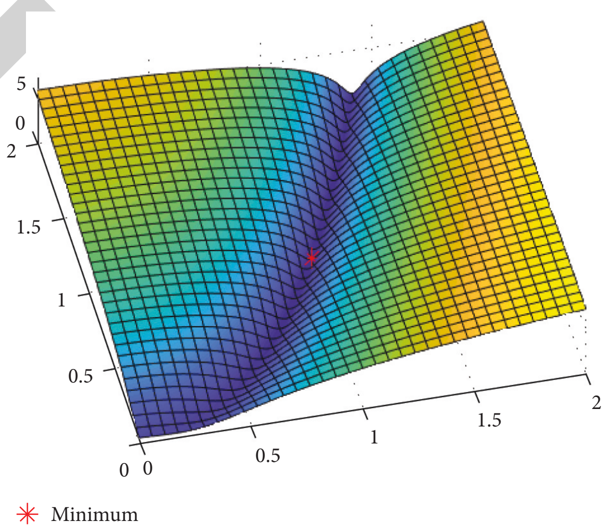

Figure 12: Fitness function using GA.

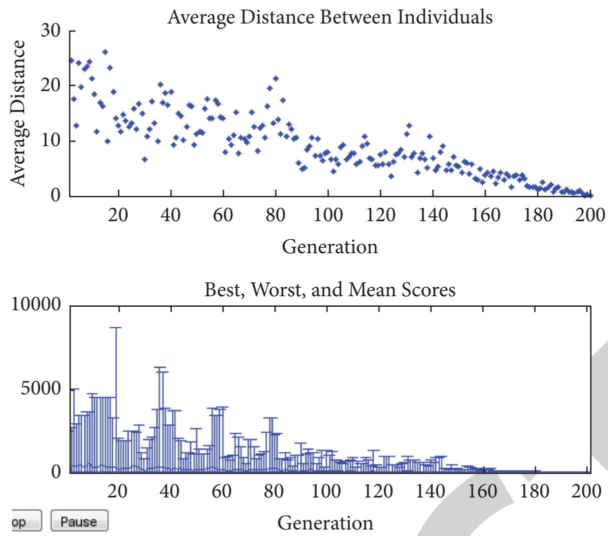

Figure 13: Crossover and mutation result.

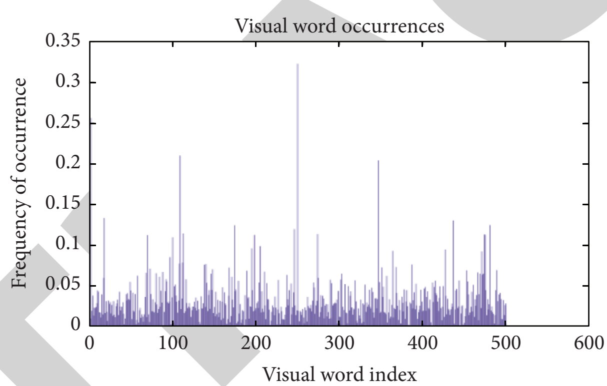

Figure 14: Visual word occurrence of the BoVW.

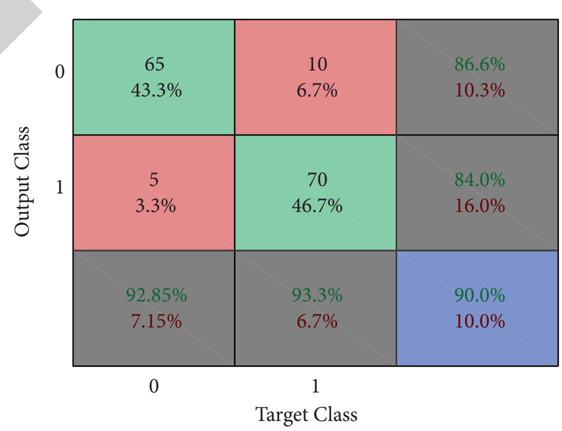

Figure 15: Confusion matrix of Naïve Bayes.

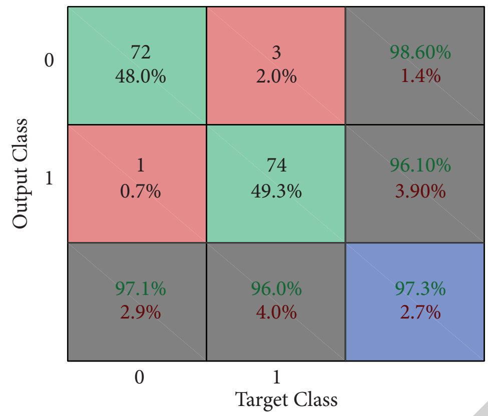

Figure 16: Confusion matrix of BOVW based SVM classifier.

Table 2: Statistical analysis of the brain images.

Image	Dice coefficient	Jaccard's coefficient	Spatial overlap	AVI	Spatial overlap	VOI of segmented ROI	Accuracy	Specificity	Time elapsed	Figure of merit
1	0.85	0.81	0.891	24.349	0.892	859	98.58	99.5838	0.687	0.826
2	0.89	0.79	0.833	−28.549	0.834	532	98.91	99.6829	0.7011	0.799
3	0.87	0.88	0.912	−19.46	0.97	577	98.88	99.6765	0.6835	0.978
4	0.79	0.81	0.888	−22.163	0.884	723	99.02	99.6969	0.6524	0.787
5	0.73	0.89	0.967	−7.889	0.961	785	99.18	99.8522	0.9601	0.232
6	0.85	0.82	0.878	29.862	0.875	935	99.16	99.8343	0.980	0.612
7	0.87	0.88	0.914	20.134	0.917	925	99.11	99.7590	0.7404	0.939
8	0.89	0.71	0.762	−39.225	0.768	444	99.06	99.8163	0.8194	0.967
9	0.85	0.89	0.938	−13.315	0.939	794	98.88	99.5867	0.677	0.653
10	0.87	0.88	0.913	−16.892	0.913	775	98.73	99.7162	0.699	0.477

Table 3: Performance comparison.

Classifier	Naïve Bayes (%)	BoVW-based SVM (%)	CNN (%)
Accuracy	90	97.3	98.5
Error	10	2.7	1.5
Sensitivity	86.6	98.6	98.6
Specificity	84	96.1	97
Precision	93.3	96	98

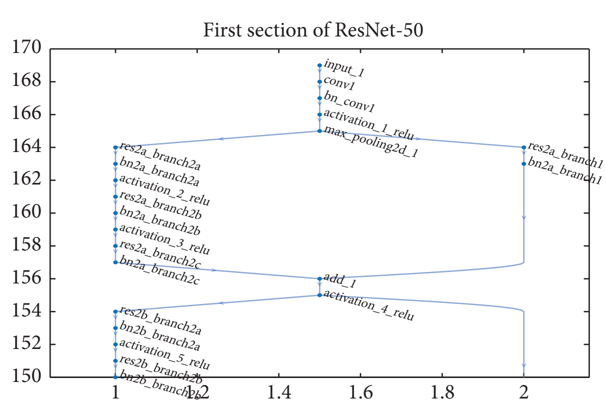

Figure 17: First section of ResNet.

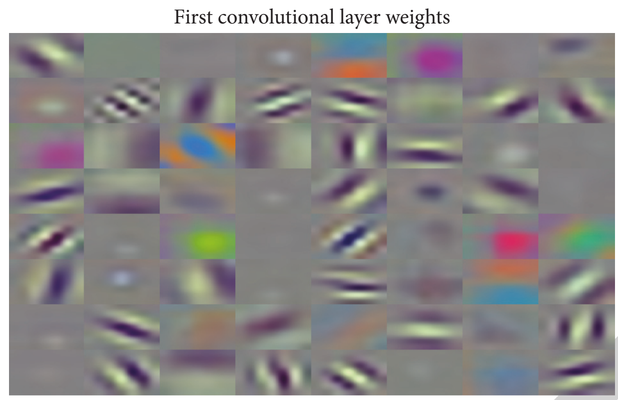

FIGURE 18: First convolution layer weights.

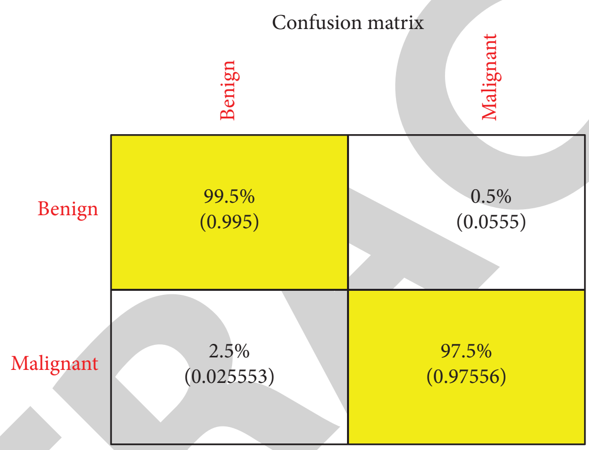

FIGURE 19: The confusion matrix of proposed CNN.

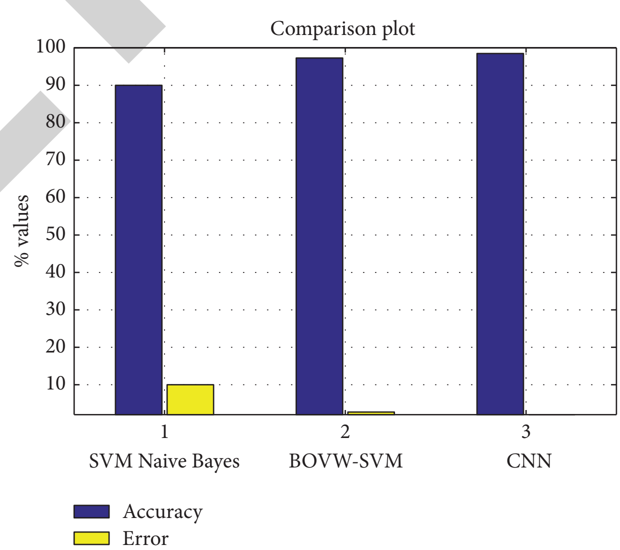

FIGURE 20: Accuracy and error plot.

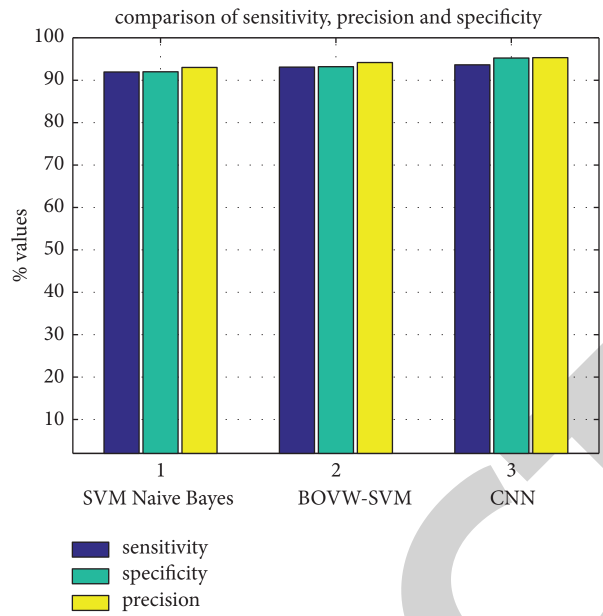

Figure 21: Accuracy, sensitivity, and precision plot.

4. Conclusion

Medical image segmentation is a challenging issue due to the complexity of the images, as well as the lack of anatomical models that fully capture the potential deformations in each structure. This proposed method works very effectively to the initial cluster size and cluster centers. The segmentation is done by using BWT techniques whose accuracy and computation speed are less. This work recommends a system that requires negligible human intrusion to partition the brain tissue. The main aim of this recommended system is to aid the human experts or neurosurgeons in identifying the patients with minimal time. The experimental results show 98.5% accuracy compared to the state-of-the-art technologies. Computational time, system complexity, and memory space requirements taken for executing the algorithms could be further reduced. The same approach can be also used to detect and analyze different pathologies found in other parts of the body (kidney, liver, lungs, etc.). Different classifiers with optimization methodology can be used in future research to improve accuracy by integrating more effective segmentation and extraction techniques with real-time images and clinical cases using a wider data set covering various scenarios.

Data Availability

Data will be available from the corresponding author upon request.

Conflicts of Interest

The authors declare that they have no conflicts of interest regarding the publication of this paper.

References

[1] M. A. Dorairangaswamy, "A novel invisible and blind watermarking scheme for copyright protection of digital images," *IJCSNS International Journal of Computer Science and Network Security*, vol. 9, no. 4, 2009.

[2] W.-J. Kim, J. K. Lee, J.-H. Kim, and K.-R. Kwon, "Block-based watermarking using random position key," *IJCSNS International Journal of Computer Science and Network Security*, vol. 9, no. 2, 2009.

[3] F. Amato, A. López, E. M. Peña-Méndez, P. Vaňhara, A. Hampl, and J. Havel, "Artificial neural networks in medical diagnosis," *Journal of Applied Biomedicine*, vol. 11, no. 2, pp. 47–58, 2013.

[4] A. Demirhan, M. Toru, and I. Guler, "Segmentation of tumor and e along with healthy tissues of brain using wavelets and neural networks," *IEEE Journal of Biomedical and Health Informatics*, vol. 19, no. 4, pp. 1451–1458, 2015.

[5] S. Madhukumar and N. Santhiyakumari, "Evaluation of k-Means and fuzzy C-means segmentation on MR images of brain," *The Egyptian Journal of Radiology and Nuclear Medicine*, vol. 46, no. 2, pp. 475–479, 2015.

[6] M. T. El-Melegy and H. M. Mokhtar, "Tumor segmentation in brain MRI using a fuzzy approach with class center priors," *EURASIP Journal on Image and Video Processing*, vol. 201421 pages, 2014.

[7] G. Coatrieux, H. Hui Huang, H. Huazhong Shu, L. Limin Luo, and C. Roux, "A watermarking-based medical image integrity control system and an image moment signature for tampering characterization," *IEEE Journal of Biomedical and Health Informatics*, vol. 17, no. 6, pp. 1057–1067, 2013.

[8] M. Arif and G. Wang, "Fast curvelet transform through genetic algorithm for multimodal medical image fusion," *Soft Computing*, vol. 24, pp. 1815–1836, 2020.

[9] S. Lal and M. Chandra, "Efficient algorithm for contrast enhancement of natural images," *The International Arab*

Hindawi
Journal of Healthcare Engineering
Volume 2023, Article ID 9812937, 1 page
https://doi.org/10.1155/2023/9812937

Retraction

Retracted: Machine Learning Techniques for Human Age and Gender Identification Based on Teeth X-Ray Images

Journal of Healthcare Engineering

Received 10 October 2023; Accepted 10 October 2023; Published 11 October 2023

This article has been retracted by Hindawi following an investigation undertaken by the publisher [1]. This investigation has uncovered evidence of one or more of the following indicators of systematic manipulation of the publication process:

(1) Discrepancies in scope
(2) Discrepancies in the description of the research reported
(3) Discrepancies between the availability of data and the research described
(4) Inappropriate citations
(5) Incoherent, meaningless and/or irrelevant content included in the article
(6) Peer-review manipulation

The presence of these indicators undermines our confidence in the integrity of the article's content and we cannot, therefore, vouch for its reliability. Please note that this notice is intended solely to alert readers that the content of this article is unreliable. We have not investigated whether authors were aware of or involved in the systematic manipulation of the publication process.

In addition, our investigation has also shown that one or more of the following human-subject reporting requirements has not been met in this article: ethical approval by an Institutional Review Board (IRB) committee or equivalent, patient/participant consent to participate, and/or agreement to publish patient/participant details (where relevant).

Wiley and Hindawi regrets that the usual quality checks did not identify these issues before publication and have since put additional measures in place to safeguard research integrity.

We wish to credit our own Research Integrity and Research Publishing teams and anonymous and named external researchers and research integrity experts for contributing to this investigation.

The corresponding author, as the representative of all authors, has been given the opportunity to register their agreement or disagreement to this retraction. We have kept a record of any response received.

References

[1] K. C. Santosh, N. Pradeep, V. Goel et al., "Machine Learning Techniques for Human Age and Gender Identification Based on Teeth X-Ray Images," *Journal of Healthcare Engineering*, vol. 2022, Article ID 8302674, 14 pages, 2022.

Hindawi
Journal of Healthcare Engineering
Volume 2022, Article ID 8302674, 14 pages
https://doi.org/10.1155/2022/8302674

Research Article

Machine Learning Techniques for Human Age and Gender Identification Based on Teeth X-Ray Images

K. C. Santosh,[1] Nijalingappa Pradeep,[1] Vikas Goel,[2] Raju Ranjan,[3] Ekta Pandey,[4] Piyush Kumar Shukla ,[5] and Stephen Jeswinde Nuagah [6]

[1]*CS&E Department, Bapuji Institute of Engineering and Technology, Davangere, Karnataka, India*
[2]*Department of Information Technology, KIET Group of Institutions, Delhi-NCR Meerut Road (NH-58), Ghaziabad 201206, Uttar Pradesh, India*
[3]*School of Computing Science and Engineering, Galgotias University, Greater Noida, Uttar Pradesh, India*
[4]*Applied Science Department, Bundelkhand Institute of Engineering and Technology, Jhansi, Uttar Pradesh, India*
[5]*Computer Science & Engineering Department, University Institute of Technology, Rajiv Gandhi Proudyogiki Vishwavidyalaya, Technological University of Madhya Pradesh, Bhopal 462033, India*
[6]*Department of Electrical Engineering, Tamale Technical University, Tamale, Ghana*

Correspondence should be addressed to Stephen Jeswinde Nuagah; jeswinde@tatu.edu.gh

Received 29 October 2021; Accepted 17 December 2021; Published 4 January 2022

Academic Editor: Liaqat Ali

The use of digital medical images is increasing with advanced computational power that has immensely contributed to developing more sophisticated machine learning techniques. Determination of age and gender of individuals was manually performed by forensic experts by their professional skills, which may take a few days to generate results. A fully automated system was developed that identifies the gender of humans and age based on digital images of teeth. Since teeth are a strong and unique part of the human body that exhibits least subject to risk in natural structure and remains unchanged for a longer duration, the process of identification of gender- and age-related information from human beings is systematically carried out by analyzing OPG (orthopantomogram) images. A total of 1142 digital X-ray images of teeth were obtained from dental colleges from the population of the middle-east part of Karnataka state in India. 80% of the digital images were considered for training purposes, and the remaining 20% of teeth images were for the testing cases. The proposed gender and age determination system finds its application widely in the forensic field to predict results quickly and accurately. The prediction system was carried out using Multiclass SVM (MSVM) classifier algorithm for age estimation and LIBSVM classifier for gender prediction, and 96% of accuracy was achieved from the system.

1. Introduction

Technological advancement in modern medicine helps medical professionals to diagnose the nature of the medical condition of a person more effectively and medicate accurately. Technical advancement in the field of medicine shows several types of evolution in radiologic technology, such as radiographic fluoroscopy, molecular imaging, and digital imaging. The present study was conducted by using digital radiographs of teeth, also known as orthopantomogram (OPG), considered as input for gender identification and age estimation of humans. However, the traditional method followed by forensic practitioners for identification is time-consuming; hence, a complete automated system was developed for personal identification, which produces results quickly and accurately.

The human body has a tendency to undergo changes in lifetime due to any external cause or internal metabolism changes. In such case, teeth are the only structure that will not be affected by any causes due to their hardness nature and low metabolism [1]. Dental X-ray images provide useful information in identification, and it is considered a good material in either living or nonliving populations for genetic study and odonatological, anthropological, and forensic investigation. Identification based on teeth images has higher accurate results than any other parts in humans. Teeth development stages and dental eruption factors depicted in a few atlases help manual investigation process in forensic dentistry. Identification of an individual in forensic medicine is most challenging and confidential in the matter of civil law and crime investigation [2, 3]. Hence, prediction based on observing anatomical features of teeth should be conducted with higher accuracy. Teeth images are publicly unavailable and have to be collected from the dental college, dental hospitals, or clinics that have X-ray imaging facilities.

Forensic odontology is a department in dentistry that is associated with the scientific study of the anatomy of teeth that should handle properly and analyze eruption of teeth as evidence of gender determination and age assessment. Various techniques exist in estimation of age like anthropological study, psychological and radiological method, and odonatological and skeletal analysis [4, 5]. The cuspids or eyeteeth mainly show the sexual difference from other teeth in humans. These teeth are rugged in nature and have resistance to disease. The main goal of this paper is to deliver a state of art evidence and trends and to fill gaps in the experiments on age and gender determination that was based on machine learning methods. In particular, medical image analysis is the trending and challenging research area in machine learning communities. Though the dental structures and features are almost the same in males and females, few changes in the size of the tooth will exhibit some clues about gender differences. Forensic experts manually identify gender and age differences by tooth dimensions and craniofacial morphologies [6, 7]. Figure 1 illustrates a standard numbering for each tooth. Panoramic image of teeth is divided into four quadrants; each quadrant has 8 sets of teeth. A number of denotation systems for teeth are available in the dentition field, but FDI (Federation Dentaire International) is a global standard labeling system used by many researchers. FDI uses a 2-digit global standard labeling system for tooth identification, where the first number represents the quadrant of the tooth and the second number represents the number of the tooth from the midline, as depicted in Figure 1.

A sample of FDI dental labeling on an adult panoramic image is depicted in Figure 1. It has four quadrants, upper jaw right (Q1), upper jaw left (Q2), lower jaw left (Q3), and lower jaw right (Q4). It can be evaluated in a clockwise direction [8]. The teeth number begins from 1 to 8 in each quadrant that starts from the middle line and moves towards the distal end. For example, an upper jaw right is a wisdom tooth that can be called tooth number "18" or a lower jaw left tooth that can be numbered as "38." A complete set (32 teeth) of an adult human is depicted in Figure 2.

Human teeth have two parts, upper jaw and lower jaw, called maxillary and mandible jaw, respectively. Each jaw has 8 teeth on the left side and 8 teeth on the right part with a universal numbering and palmer numbering system [9]. Table 1 illustrates the numbering system of each tooth.

Orthopantomogram, known as OPG, and cephalogram are two different types of X-ray images in dental analysis. OPG creates a panoramic vision of teeth, which consist of both the maxillary jaw and mandible jaw, whereas a cephalogram is an X-ray image of facial structure. Age and gender determination required a complete view of teeth rather than a partial view like cephalogram [10, 11]. Hence, OPG is used widely in individual identification. Figure 3 depicts the different types of dental X-ray imaging available.

Figure 3(a) is bitewing X-ray imaging that depicts details of lower teeth and upper teeth in a particular part of the mouth. The exposed area in bitewing X-ray imaging shows the features of teeth from the crown to the root of teeth. In Figure 3(b), periapical X-ray imaging type, one can notice minute parts inside a tooth that depicts the entire tooth with roots and soft tissues. Every periapical tooth image depicts a complete portion of a tooth, either lower jaw tooth or upper jaw tooth. Figure 3(c) is the orthopantomogram X-ray image. This type of imaging displays a complete panoramic view of teeth [12–14]. Dataset of orthopantomogram (OPG) was used in this paper for detection of gender and age estimation.

2. Literature Review

Many researchers have focused on the manual method of identification using teeth, but very few contributions were made on machine learning approaches and computer vision for automated gender and age identification based on teeth. In this section, we briefly focus on the latest articles that illustrate the methodology, technical aspects, and other significant contributions of researchers in the prediction of age and gender.

Wallraff et al. [15] in 2021 proposed a method for age determination based on panoramic digital X-ray images of teeth using deep learning. The authors used a supervised regression-based deep learning technique by considering a dataset of 14000 images.

Saloni et al. [16] in 2020 proposed a method based on digital images of teeth in the identification of teeth by analyzing morphometric means of mandible ramus of 250 OPG samples. The mandible ramus may be used as an alternate tool in determining gender based on the OPG of the selected population. The authors studied mandible ramus measurements by discriminant function analysis. This outcome indicates that mandible ramus exhibits better sexual dimorphism. In 2020, Poornima Vadla et al. [17] introduced a technique based on permanent mandible teeth of the left-sided jaw. Their study focused on estimating age with high accuracy based on the Camerier method applied from an Indian-specific formula on the left and right sides of mandibular teeth. The authors used radiographs of 50 samples (25 males and 25 females) of range 5–15 years. The outcome values were recorded based on the Camerier technique in estimation of age based on Indian-specific equations. Okkesim and Erhamza [18] in 2020 conducted a study for determination of human gender based on mandibular ramus. Mandibular teeth play a vital role in determining human gender since mandible bone is the largest,

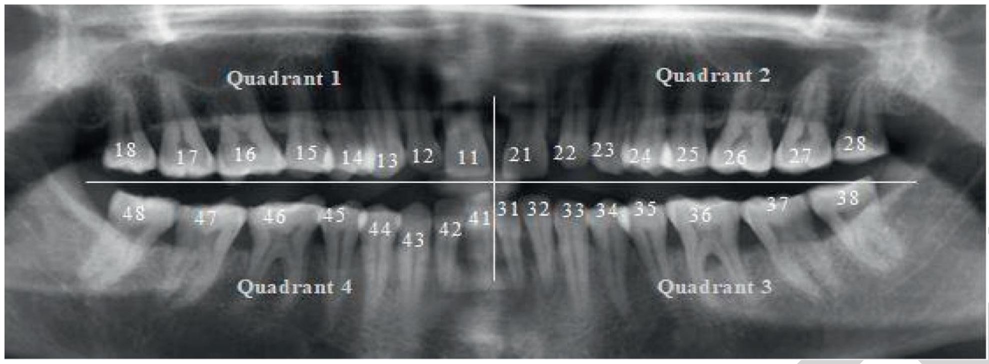

Figure 1: FDI nomenclature illustrated on a panoramic radiograph.

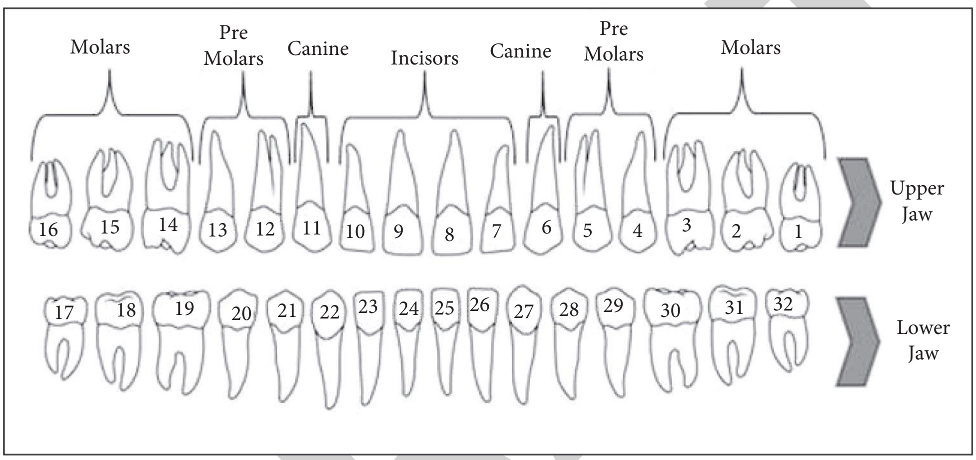

Figure 2: Anatomy of human teeth.

Table 1: Numbering system and names of teeth.

	Maxillary jaw (upper jaw)			Mandibular jaw (lower jaw)		
	Universal numbering	Palmer numbering system	Tooth name	Universal numbering	Palmer numbering system	Tooth name
	1	Up. Rt. 8	3rd molar	32	L. Rt. 1	3rd molar
	2	Up. Rt. 7	2nd molar	31	L. Rt. 2	2nd molar
	3	Up. Rt. 6	1st molar	30	L. Rt. 3	1st molar
	4	Up. Rt. 5	2nd premolar	29	L. Rt. 4	2nd premolar
Right	5	Up. Rt. 4	1st premolar	28	L. Rt. 5	1st premolar
	6	Up. Rt. 3	Canine	27	L. Rt. 6	Canine
	7	Up. Rt. 2	Lateral incisor	26	L. Rt. 7	Lateral incisor
	8	Up. Rt. 1	Central incisor	25	L. Rt. 8	Central incisor
	9	Up. Lt. 1	Central incisor	24	L. Lt. 8	Central incisor
	10	Up. Lt. 2	Lateral incisor	23	L. Lt. 7	Lateral incisor
	11	Up. Lt. 3	Canine	22	L. Lt. 6	Canine
Left	12	Up. Lt. 4	1st premolar	21	L. Lt. 5	1st premolar
	13	Up. Lt. 5	2nd premolar	20	L. Lt. 4	2nd premolar
	14	Up. Lt. 6	1st molar	19	L. Lt. 3	1st molar
	15	Up. Lt. 7	2nd molar	18	L. Lt. 2	2nd molar
	16	Up. Lt. 8	3rd molar	17	L. Lt. 1	3rd molar

dimorphic, and strongest bone in the skull. Most recent studies highlighted that CBCT (cone-beam computed tomography) is better than any traditional technique. Some of the important features in mandible teeth like-gonial angle, ramus measurement, and a few morphologic parameters are reported. Researchers studied different parameters in the

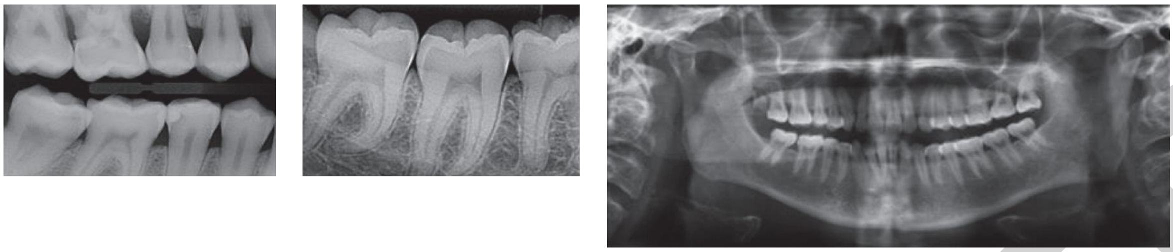

(a) (b) (c)

Figure 3: Types of dental imaging. (a) Bitewing X-ray. (b) Periapical X-ray. (c) Orthopantomogram X-ray.

mandible. Vila et al. [19] built a gender classification technique based on CNN approaches like the DASNet method and VGG-16 architecture methods. Their classification system was carried out using 3500 OPG images. Patil et al. [20] conducted a study to determine the gender of humans using discriminant analysis and logistic regression based on mandible parameters. They conducted a study using 509 panoramic images. The accuracy of their experimental results is tabulated in Table 2.

In 2020, Neves et al. [21] developed a predictive model for gender identification based on mesiodistal widths using a permanent dental cast. A total of 168 dental casts were considered for classification. Mesiodistal width of first right molar to left molar was calculated for every cast. In 2020, Dalessandri et al. [22] reviewed articles on 2D radiological method versus 3D radiological for determination of age based on teeth of 18 years old. The authors' review assesses the present trend with reliability and accuracy of OPG versus CBCT for determination of age and gender. The final outcome of their survey illustrated that CBCT was found to be accurate when compared with OPG in teeth anatomy evaluation. Stella and Thirumalai [23] developed an automation tool for estimation of age based on dental OPG images. The authors developed two methods for individual age assessment using the Demirjian and Nolla methods. This application was developed by using MS excel Visual Basic Application (VBA). This helps in the automation technique using any programming environment. Bali Behl et al. [24] proposed a method based on panoramic evaluation for mandible morphometric changes in postpubertal and prepubertal in the Turkish population. The authors measured bicondylar breadth (BB), gonial angle measurement, antegonial angle (AGA), ramus height, and ramus breadth (RHRB), which were captured from the Turkish population. They conducted this experiment on 750 digital radiographic images of ages from 5 years to 50 years. All parameters values from OPG radiographs were recorded and analyzed using the software Java Image Process. In 2019, Andrade et al. [25] developed a system for determination of gender and age estimation using pulp cavity volumes based on the CBCT method. They used 120 experimental samples of CBCT scans from the Brazilian population of both genders of ages ranging from 13 years to 70 years. Pearson's correlation evaluation methods were used in assessing the relation between pulp volume and chronological age. Higher accuracy can be achieved by using this formula when it is applied to pulp volume for one or both teeth. Good results can be fetched for samples of age more than 35 years in age estimation.

3. Feature Extraction

Feature extraction is the process of identifying key features in the dataset available. It is a part of the dimensionality reduction process in which an initial set of images were divided into many manageable groups. Determination of humans based on skeletal parts available is the most challenging task for forensic experts when only fragmented parts of the body are recovered [26]. In this situation, forensic dentistry will help in gender identification and age estimation based on the dental remaining and skull part. Some of the salient and dominant features in teeth for the identification process are illustrated in this section. In this paper, the most dominant features of teeth which help in determination of age and gender were identified. Few features identified from teeth are intercanine distance, incisor width, and canine width; they play a significant role in judging age and gender using teeth. Feature values extracted and recorded the values of these features in a feature matrix form. The next phase in the identification process is the conversion of feature matrix values to an understandable classifier format [27].

The odontometric features identified and analyzed for gender and age assessment are as follows:

(i) Incisor width: central incisors' width from both mandible and maxilla was analyzed and measured. The measurement of the incisor in the mandible differs from the maxillary jaw in males and females.

(ii) Distance measured between canine: distance between canine from maxilla and mandible jaw is noted. This intercanine distance is the measurement between teeth numbers 13 and 23 in the maxillary jaw and the distance between teeth numbers 33 and 43 in the mandible. Figures 4(a) and 4(b) represent the samples of measurement of maxillary incisor teeth and mandible intercanine distance.

4. Materials and Methods

The present experimental study for the prediction of individuals was conducted based on digital X-ray images of teeth. Dental X-ray images were publicly not available. Hence, they were collected from local dental colleges and dental clinics, which

Table 2: Literature review summary.

SN	Authors	Year	Research findings	Remark
01	Saloni, Pradhuman V, P Mahajan, Ankush, Sukhleen Kaur, and Sakshi [16]	2020	Three parameters out of five mandible ramus variables studied showed statistically ($p < 0.05$) significant differences in gender	Mandible ramus may be used as an alternate tool in determining gender based on OPG
02	Poornima V, Surekha, Venkateswara Rao, G. Deepthi, Naveen S, and Arun Kumar [17]	2020	Right and left permanent mandible teeth were evaluated in OPG using the Camerier technique	High accuracy is achieved based on the Camerier method applied from an Indian-specific formula
03	A Okkesim and S Erhamza [18]	2020	The average value in min ramus width for males is 31.7 mm and for females is 29 mm. The average projection height value of ramus in females is measured 53.9 mm and in males is 48 mm	Mandible ramus in CBCT-based model exhibits significant differences in gender determination
04	N Vila, R. R. Vilas, and M. J. Carreira [19]	2020	Gender is evaluated based on DASNet and VVG 16 architecture	Accuracy of gender classification is 83% for DASNet and 90% for VGG-16
05	Vathsala Patil, Ravindranath, Saumya, Adithya, and Namesh [20]	2020	Gender determination based on mandible parameters using a logistic regression technique	In discriminant analysis, accuracy is 69%, in logistic regression, accuracy is 70%, and ANN shows the highest accuracy of 75%
06	J Albernaz, Nathalie A, Ferreira, Vanessa, and Proença [21]	2020	Teeth cast was used for the experimental procedure. Mesiodistal width of Rt. 1st molar to Lt. 1st molar was measured on each cast	Gender determination was classified with accuracy of 75%
07	Dalessandri D, Ingrid Tonni, Laura L, Marco Migliorati, Gaetano I, LVisconti, Stefano B, and C Paganelli [22]	2020	Reliability and accuracy of OPG versus CBCT for determination of age and gender	CBCT was found to be accurate when compared with OPG images in prediction
08	Stella A and Thirumalai [23]	2020	Tooth was divided into different stages starting from A stage to H stage	Individual age assessment using the Demirjian and the Nolla methods
09	Ahima Bali Behl [24]	2020	Measurement of bicondylar breadth (BB), gonial angle measurement, antegonial angle (AGA), ramus height, and ramus breadth (RHRB)	Upper and lower breadths of ramus were calculated. Ramus condylar height and coronoid height were measured appropriately
10	Vanessa M A, Rocharles, Andreia D'Souza, Casimiro, Andrea, Francisco C, and Deborah Q Eduardo Jr. [25]	2019	Equations for prediction of age and gender using pulp volumes from upper canine and upper central incisor	High accuracy can be achieved by using this formula when it is applied to pulp volume
11	Wallraff Sarah, Vesal Sulaiman, Syben Christopher, Lutz Rainer, and Maier Andreas [15]	2021	Unisex and sex-specific approaches based on deep learning methods achieve better results on the test data set	Male gender is slightly estimated younger than female gender

have digital X-ray imaging facilities [28]. The local dataset was obtained with proper proceedings and academic agreement between two dental colleges. A total of 995 samples of teeth were collected from the College of Dental Sciences, Davangere, and 147 samples were collected from Bapuji Dental College and Hospital, Davangere, Karnataka, India. In total, we have 1142 datasets available for research analysis.

Figure 5(a) depicts the distribution of datasets based on the age of 5-year interval, segregating male and female count per group. The age distributions of available 1142 datasets of teeth were divided into 11 groups of 5 years of range per group except the first and last groups since the first group is datasets of the age group of 1–10 years and the last group is for the age group of 60 years and above. Figure 5(b) illustrates the total samples of males and females (total 632 male and 510 female samples).

4.1. Methodology. The proposed system for age assessment and determination of gender has a systematic methodology depicted in Figure 6. Basic blocks in methodology are data collection, preprocessing of input image [29], features extraction, feature matrix, conversion of feature matrix into understandable classifier format, and classification. Out of 1142 local samples, 80 percent of dataset samples (913 samples) were used as the training dataset, and 20 percent of dataset samples (229 samples) were used as the unseen testing dataset. Subjects that came under the decayed tooth, missing tooth, or broken tooth were excluded from the experimental study. A normal healthy state and caries-free teeth were considered for the study. An OPG of teeth was provided as input for the model. The initial stage of the identification system was preprocessing the image. This input sample was preprocessed by removing unwanted labels and noise present in the sample. The outcome of preprocessing stage was an enhanced image, which was essential for better accuracy in prediction. The most important and dominant features in teeth that helped in the identification process were extracted. Feature values of teeth like incisor width and intercanine distance were extracted from an input OPG image. Feature matrix was constructed,

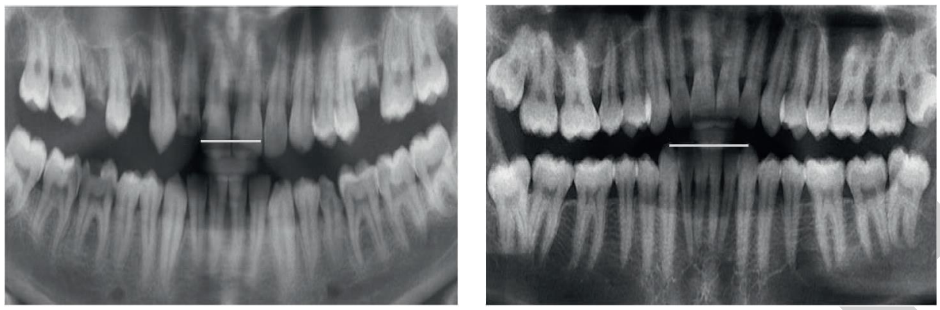

(a) (b)

Figure 4: (a) Central incisor teeth measurement. (b) Intercanine measurement.

and feature matrix values were converted to classifier understandable format. Figure 6 depicts the methodology for age and gender identification. Finally, the model classified age and gender from an input OPG image. The age and gender identification system were implemented using a Support Vector Machine (SVM) classifier.

Gender identification based on teeth was carried out using the LIBSVM classifier tool and training with several kernels and with different values of hyperparameters [29]. Since gender determination required two classes, the age estimation process was carried out using the Multiclass SVM (MSVM) classifier tool, and images were trained with several kernels and with different hyperparameter values. Age estimation required multiple classes. Hence, the LIBSVM classifier and MSVM classifier were used for gender and age identification [30], respectively.

Few samples of teeth datasets collected from College of Dental Sciences, Davangere, and Bapuji Dental College and Hospital, Davangere, are shown in Figures 7 and 8, respectively. These images were received in Tagged Image File Format (TIFF) format.

5. Experimental Results and Discussion

The human age and gender classification model is a fully automated system that predicts the gender of humans with an estimation of age. The model displays the result by taking only the input of an OPG of teeth. It produces results in less than a minute with higher accuracy. Classification techniques used and outputs obtained from classifiers with various kernels and hyperparameters are highlighted in this section. Age estimation and gender determination are carried out by MSVM and LIBSVM, respectively. The initial stage in the prediction model is to preprocess the input image by removing image noises, which may be adjoined while capturing images. The subsequent task of image preprocessing is to enhance the brightness and quality of the image [31].

5.1. Pixel Brightness Transformation. Brightness transformations modify pixel brightness, and the transformation depends on the properties of a pixel. Contrast enhancement is an important area in image processing. It is widely used for medical image processing. The function used is *cv2.cvtColor (img, cv2.COLOR_BGR2GRAY)*. The outcome of this stage is an enhanced version of the original image. The result after the preprocessed image is depicted in Figure 9.

5.1.1. Edge Detection Using Canny Edge Detection Algorithm. Image segmentation is a technique of partitioning the images into multiple segments. Specifically, the image segmentation method is used to locate objects and boundaries of images. The Canny detection algorithm is used to detect edges of teeth, which aids the model in predicting age and gender accurately.

The Canny edge detection technique uses five steps for the detection of edges of input images. The following steps are used in this paper to detect edges from teeth OPG. Figure 10 depicts the outcome of the Canny edge detection technique performed on an OPG image.

Steps in edge detection using the Canny edge detection algorithm are as follows:

(1) Conversion of image based on Gaussian filter.
Sigma = 1.5, G Kernel size (5×5)
(2) Gradient Calculation.
Horizontal filter K_X and Vertical filter K_Y
Ix = filters.convolve (image, *Kx*).
Iy = filters.convolve (image, *Ky*).
(3) Nonmax suppression: To achieve thin edges
$angle = A * 180/np.pi$
angle [angle <0] + = 180
(4) Double Threshold
high_Threshold = image.max( ) * highThresholdratio;
low_Threshold = high_Threshold * hlowThresholdratio;
(5) Tracking edge-based hysteresis
Low_T = Low_T * max(max(b-w))
High_T = Low_T * max(max(b-w))

5.1.2. Mathematical Modeling for Prediction Based on Teeth. Mathematical equations involved in prediction of age and gender are described in this section. Equation (1) is used in

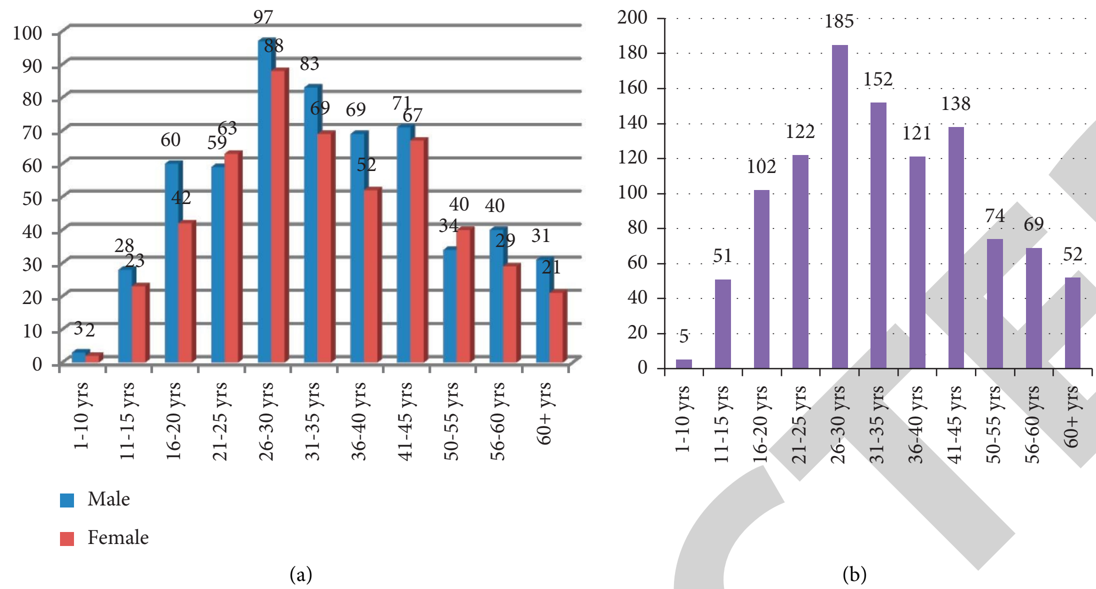

Figure 5: (a) and (b) Dataset distribution based on gender and age group.

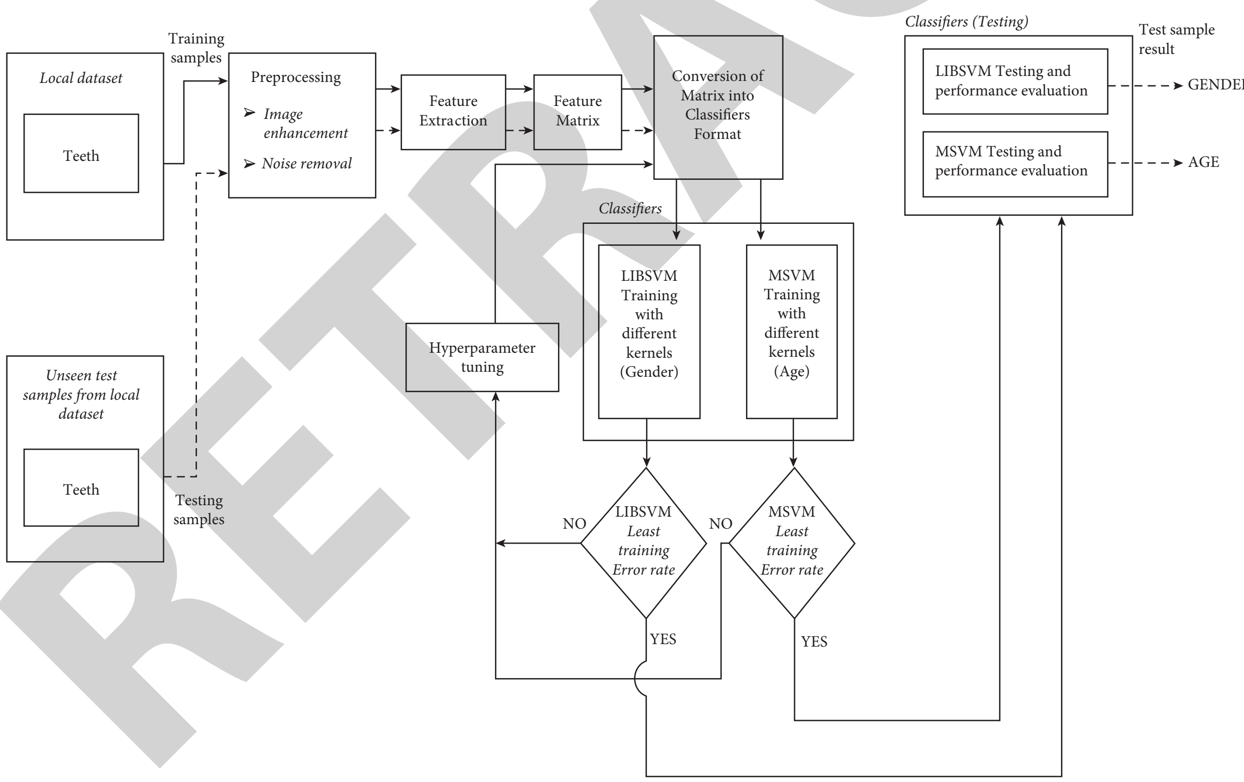

Figure 6: Methodology for gender and age assessment system using OPG of teeth.

calculation for gender differences that appeared on the left and right part of maxillary and mandible canines:

$$\text{gender difference} = \frac{(Xm/Xf - 1)}{100}, \qquad (1)$$

where Xm is the average of canine teeth width in males and Xf is the average of canine teeth width in females.

Noise removal from digital images is done by applying a Gaussian filter, as shown in equation (2). To perform this operation, the image convolution method was used by applying a Gaussian kernel of 3×3, 5×5, 7×7, and so on. Sizes of Gaussian kernel depend on image blurring effects. In the present model, a 5×5 kernel size has been used. The formula for Gaussian kernel filter $(2k+1) * (2k+1)$ is given as

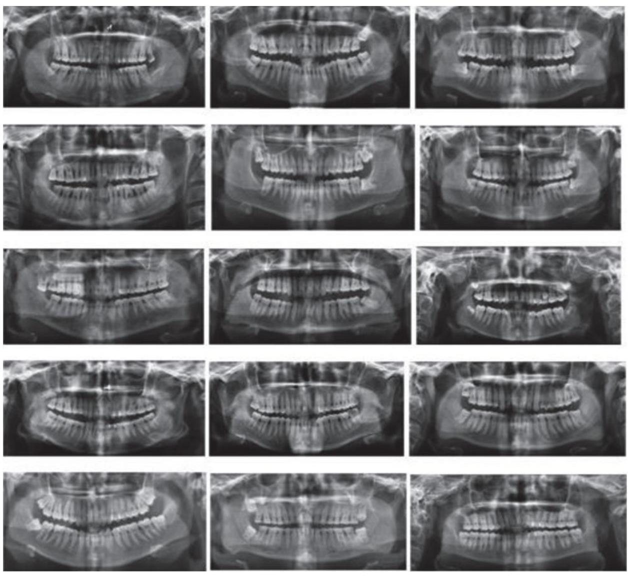

Figure 7: Dataset collected from College of Dental Science, Davangere.

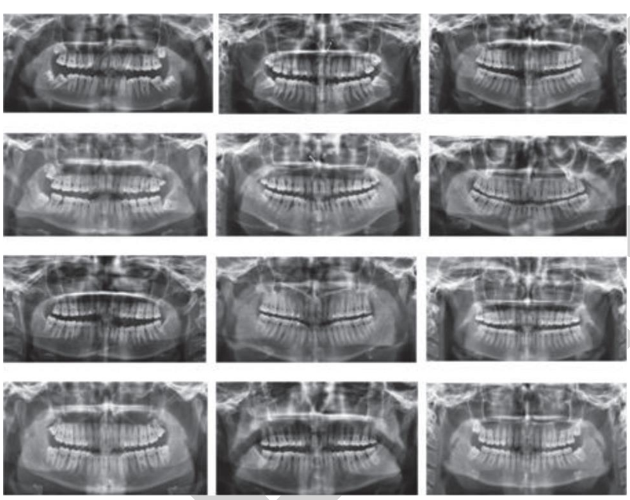

Figure 8: Dataset collected from Bapuji Dental College and Hospital, Davangere.

$$Hij = \frac{1}{2\pi\sigma}\exp\left(-\frac{(m-(k+1))^2+(n-(k+1))^2}{2\sigma^2}\right). \quad (2)$$

Some part of mathematics is involved behind the scene, mainly depending on derivatives. This mathematical-based formula was converted to equivalent python codes. Table 3 is the comparison between feature values of central incisor width and intercanine width in millimeters.

5.2. SVM Training

5.2.1. LIBSVM Training for Gender Determination. The LIBSVM classifier is used for gender determination from teeth images. LIBSVM is trained with different kernels of SVM, namely, Linear, Polynomial, Gaussian Radial Basis Function (RBF), and Sigmoid kernels. These are trained with different parameters of SVM like C, γ, and d. The LIBSVM executable *svmtrain* is employed for SVM training with various svm_type and kernel_type. Kernel parameters also have a significant effect on the decision boundary. Two features values from the teeth were extracted for age and gender determination [29]. The values of these features are extracted from the GUI from a teeth X-ray image. The training (memorization) accuracy of the SVM classification engine is calculated using the following expression:

$$\text{training accuracy} = \frac{\mathrm{Tc}}{Ts} \times 100, \quad (3)$$

where T_C represents the total number of samples correctly classified by the SVM and T_S represents the total number of samples used for testing.

Figure 11 depicts the training dataset feature matrix of teeth for gender identification. Each row in the feature matrix represents the feature of each image in the dataset [30]. The first column represents the class for gender determination, where 0 is for male and 1 indicates female. The second and third columns represent the feature values extracted from teeth.

LIBSVM classifier uses two classes for gender, and the description of the class label used in the LIBSVM classifier is depicted in Table 4, since gender determination has only two classifications.

5.2.2. MSVM Training for Age Estimation. The MSVM classifier is used for age estimation from teeth images. Different kernels of MSVM, namely, Linear, Polynomial, Gaussian Radial Basis Function (RBF), and Sigmoid kernels, are used for training teeth datasets. The training dataset feature matrix of teeth is depicted in Figure 12, where 832 indicates the number of data (images in the dataset) and 2 indicates the dimension (number of features) of the data. Each row in the feature matrix represents the feature of each teeth image in the dataset [31]. The last column represents the class of the age classification.

MSVM classifier uses multiple class labels for age estimation. The class label description used in the M-SVM classifier is depicted in Table 5, since age estimation has multiple age groups, and hence it is classified using multiple class label SVM.

5.3. SVM Testing.

For the testing phase, 20 percent of unseen data samples were used for gender and age classification system.

5.3.1. LIBSVM Testing for Gender. The LIBSVM executable command svm-predict.exe is used for testing and validating the classification results. Once the best hyperparameters are determined using the grid search technique, the training model with the best cross-validation accuracy [15] is considered for LIBSVM testing.

Accuracy from teeth unseen dataset is depicted in Table 6 and in Figure 13, respectively. From Table 6, we can notice that the RBF kernel shows the best classification results of

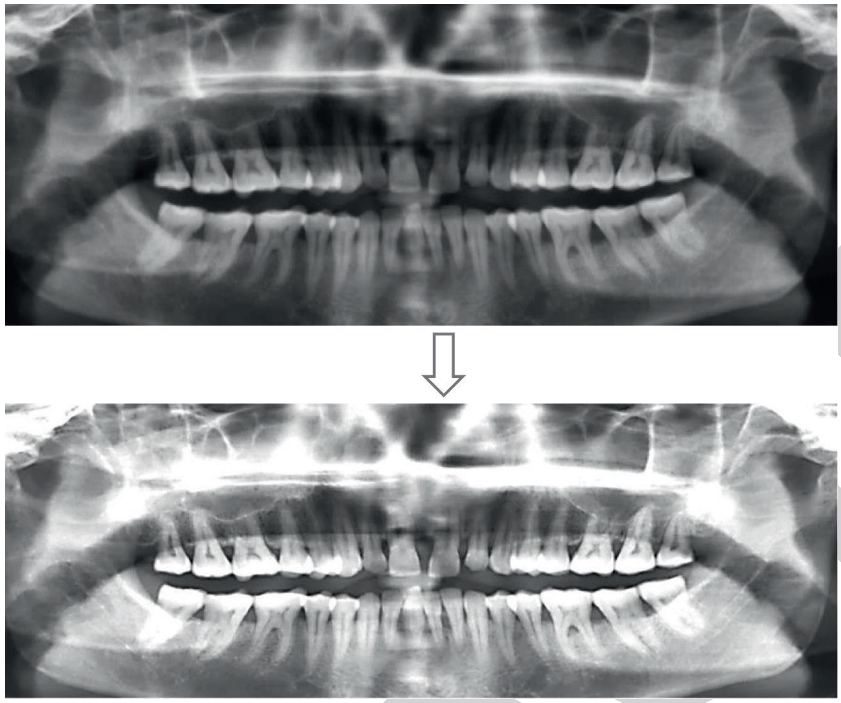

Figure 9: Result of preprocessing.

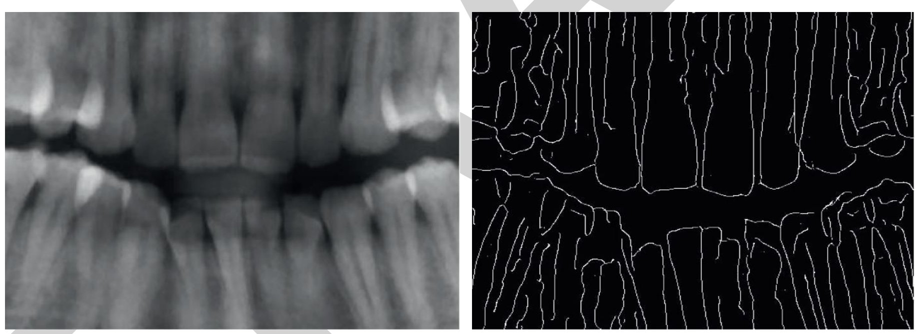

Figure 10: Detection of edge in teeth image using Canny edge detector.

Table 3: Central incisor and intercanine width (male versus female).

Sl. no.	Parameters	Gender	Mean (in mm)
01	Central incisor width	Male	9.4
		Female	8.3
02	Intercanine distance	Male	29.14
		Female	25.7

accuracy of 95.83 percent for the teeth dataset. Since the classification result is above 95 percent, the models generated for the teeth dataset using RBF kernel by LIBSVM training are acceptable. Comparisons of different LIBSVM kernels for gender determination with various hyperparameters are illustrated in Figure 14. Figures 14(a)–14(d) show the accuracy of gender classification performed by using Polynomial, Linear, RBF, and Sigmoid kernels, respectively. The highest accuracy of 95.83% is achieved for gender classification from the RBF kernel for hyperparameter values $d = 3$, $c = 28$, and $g = 0.04167$.

5.3.2. MSVM Testing for Age. The MSVM executable command *predmsvm.exe* is used for testing and validating the classification results. The best hyperparameters are selected using the grid search technique, and the training model with the best cross-validation accuracy is considered for MSVM testing. Figure 15 depicts the age classification test case results validated for unseen dataset samples of teeth. MSVM classifiers with various kernels are used to build the best model for accuracy.

RBF kernel yields best classification results of accuracy of 97.91 percent for teeth testing dataset as depicted in Table 7.

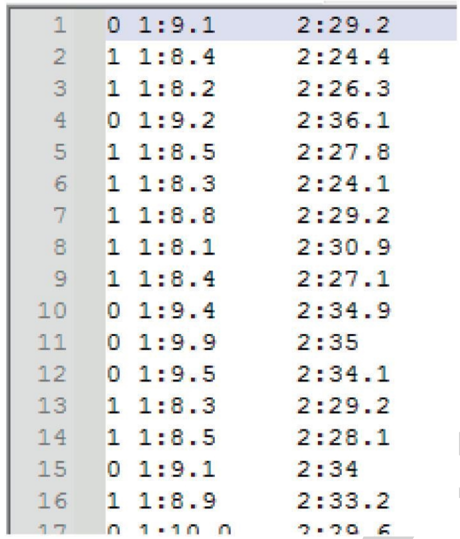

```
0 1:9.1   2:29.2
1 1:8.4   2:24.4
1 1:8.2   2:26.3
0 1:9.2   2:36.1
1 1:8.5   2:27.8
1 1:8.3   2:24.1
1 1:8.8   2:29.2
1 1:8.1   2:30.9
1 1:8.4   2:27.1
0 1:9.4   2:34.9
0 1:9.9   2:35
0 1:9.5   2:34.1
1 1:8.3   2:29.2
1 1:8.5   2:28.1
0 1:9.1   2:34
1 1:8.9   2:33.2
```

Figure 11: Feature matrix of teeth dataset for gender.

Table 4: Class label description.

Class label	Gender
Class 0	Male
Class 1	Female

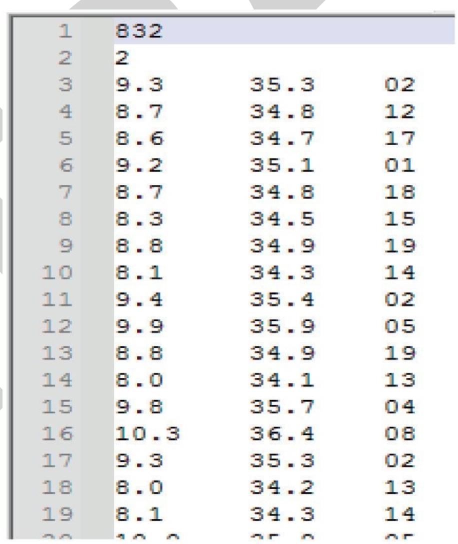

```
832
2
9.3    35.3   02
8.7    34.8   12
8.6    34.7   17
9.2    35.1   01
8.7    34.8   18
8.3    34.5   15
8.8    34.9   19
8.1    34.3   14
9.4    35.4   02
9.9    35.9   05
8.8    34.9   19
8.0    34.1   13
9.8    35.7   04
10.3   36.4   08
9.3    35.3   02
8.0    34.2   13
8.1    34.3   14
```

Figure 12: Feature matrix of teeth dataset for age.

Table 5: MSVM class label description.

Class label_M	Age_M (years)	Class label_F	Age_G (years)
Class 1	1–15	Class 11	1–15
Class 2	16–20	Class 12	16–20
Class 3	21–25	Class 13	21–25
Class 4	26–30	Class 14	26–30
Class 5	31–35	Class 15	31–35
Class 6	36–40	Class 16	36–40
Class 7	41–45	Class 17	41–45
Class 8	46–50	Class 18	46–50
Class 9	51–55	Class 19	51–55
Class 10	56+	Class 20	56+

Table 6: LIBSVM testing for Gender with different kernels.

Kernel with hyperparameters	Number of samples correctly classified	Number of samples misclassified	Accuracy (%)
Linear ($C = 256$)	43	05	89.5833
Polynomial ($d = 2$, $C = 64$, $g = 0.09153$)	42	06	85.41
RBF ($C = 16$, $g = 0.08245$)	46	02	95.8333
Sigmoid ($C = 512$, $g = 0.31626$)	40	08	83.3333

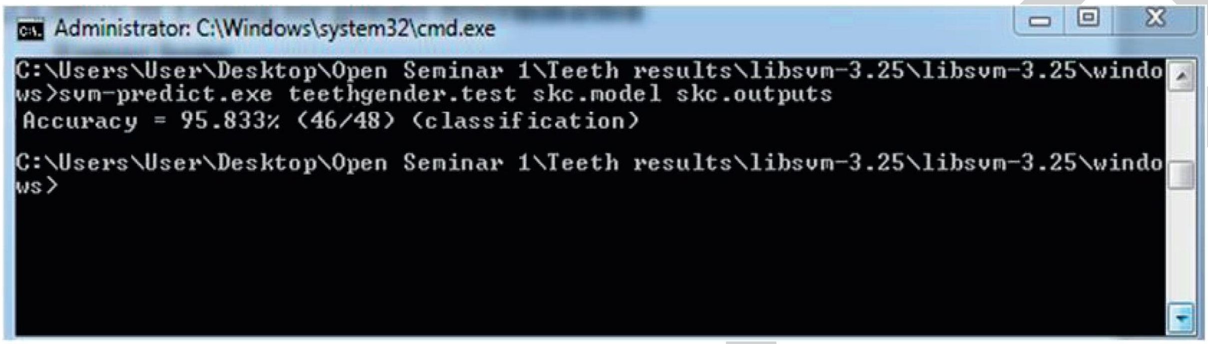

Figure 13: Gender accuracy of teeth dataset.

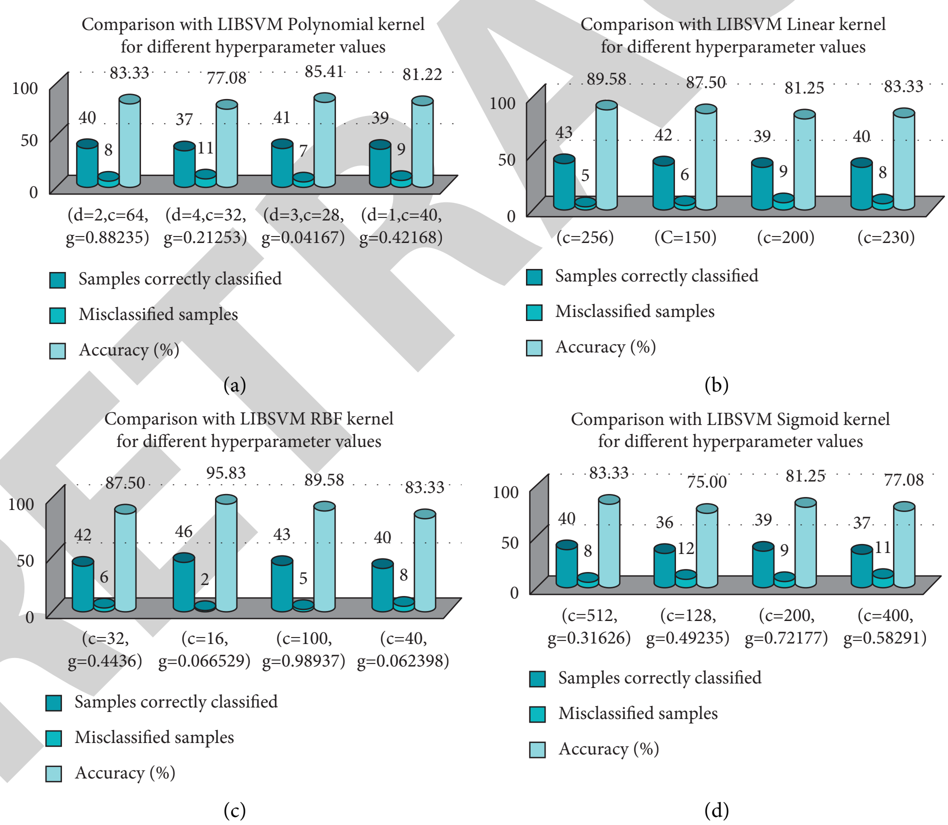

Figure 14: Comparison of different LIBSVM kernels with different hyperparameter values. (a) Polynomial kernel, highest accuracy = 85.41% ($d = 3$, $c = 28$, and $g = 0.81032$). (b) Linear kernel, accuracy = 89.58% ($c = 256$). (c) RBF kernel, accuracy = 95% ($c = 16$; $g = 0.08245$). (d) Sigmoid kernel, accuracy = 83.33% ($c = 512$; $g = 0.31626$)).

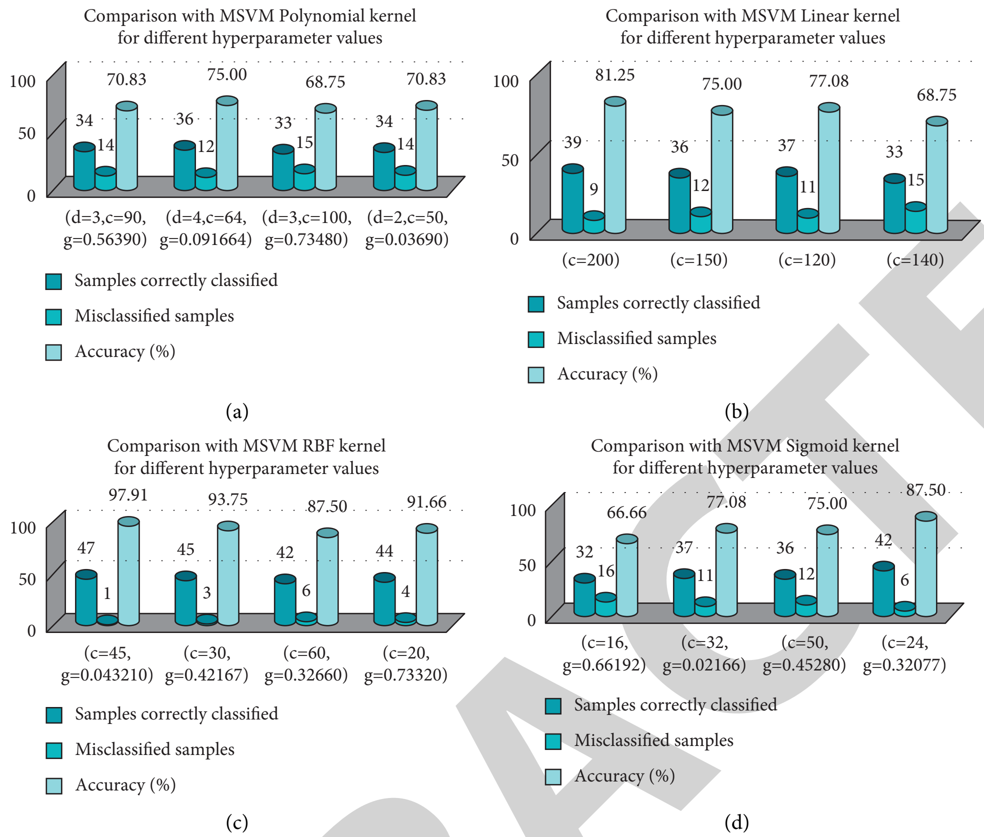

Figure 15: Comparison of different MSVM kernels with different hyperparameter values. (a) Polynomial kernel, highest accuracy = 75.41% ($d = 4$, $c = 64$, and $g = 0.09164$). (b) Linear kernel, accuracy = 81.25% ($c = 200$). (c) RBF kernel, accuracy = 97.91($c = 45$ and $g = 0.043216$). (d) Sigmoid kernel, accuracy = 87.50 ($c = 24$ and $g = 0.32077$).

Table 7: MSVM testing for age with different kernels.

Kernel with hyperparameters	Number of samples correctly classified	Number of samples misclassified	Accuracy (%)
Linear ($C = 200$)	39	09	81.25
Polynomial ($d = 4$, $C = 64$, and $g = 0.05273$)	36	12	75.0
RBF ($C = 45$ and $g = 0.04317$)	47	48	97.916
Sigmoid ($C = 256$ and $g = 0.63419$)	42	06	87.50

Since the classification result is above 97 percent, the models generated for femur and teeth dataset using RBF kernel by MSVM training can be acceptable.

6. Conclusion and Future Scope

From the present study, the morphological differences in identifying age and gender in the teeth were observed. Incisor width and intercanine distance in male teeth were found to be more compared to female teeth. The majority of all the parameters from the teeth of the male tended to be slightly more than female. The formula that was developed and used in this paper provided good and accurate results in prediction by using LIBSVM classifier and MSVM classifier. 95% of accuracy was achieved for gender determination, and 97% of accuracy was achieved for estimation of age. In conclusion of this paper, we were able to meet the goal of prediction by achieving the experimental results, which were nearly matching to ground truth values. This system may be used further as a novel model in personal identification without human intervention. It can be effectively used and applicable in the forensic science department for accurate and fast test results. In this paper, we have developed a system that makes the task easier in studying and analysing the femur digital radiographs for age and gender identification. This paper can be elaborated by identifying and extracting some more important teeth features and by standardizing those new features from the datasets. Furthermore, this research work can be elaborated on other parts of the human body, such as pelvis bone, skull, wrist, and other long bones. These digital images may also contribute to the identification of gender and age. In this paper, we have developed a system that makes the task easier in studying and analysing the femur digital radiographs for age and gender identification. This paper can be further carried out by developing a web-based application or on a smartphone-based application that can be user-friendly to access.

Data Availability

The data that support the findings of this study are available from the corresponding author upon request.

Conflicts of Interest

The authors declared that they do not have any conflicts of interest.

References

[1] N. Pandey and M. S. Ma, "Evaluation of sexual dimorphism in maxillary and mandibular canine using mesiodistal, labiolingual dimensions, and crown height," *Indian Journal of Dental Research: Official Publication of Indian Society for Dental Research*, vol. 27, pp. 473–476, 2016.

[2] E. Avuçlu and F. Bas_çiftçi, *The Determination of Age and Gender by Implementing New Image Processing Methods and Measurements to Dental X-ray Images*, pp. 0263–2241, Elsevier, Amsterdam, Netherlands, 2019.

[3] R. Srivastava, B. Jyoti, J. Prakash, M. Gupta, P. Devi, and R. Jayaram, "Gender determination from the mesiodistal dimension of permanent maxillary incisors and canines: an odontometric study," *Journal of Indian Academy of Oral Medicine and Radiology*, vol. 26, no. 3, 2014.

[4] N. Mohan and T. Aravinth Raja, "Comparasion of the position mental foramen and permanent maxillary canine width in gender determination," *IOSR Journal of Dental and Medical Science*, vol. 17, no. 5, pp. 12–18, 2018.

[5] R. Cameriere, L. Ferrante, and M. Cingolani, "Age estimation in children by measurement of open apices in teeth," *International Journal of Legal Medicine*, vol. 120, no. 1, pp. 49–52, 2006.

[6] A. Omar and S. Azab, "Applicability of determination of gender from odontometric measurements of canine teeth in a sample of adult Egyptian population," *Cairo Dent J*, vol. 25, pp. 167–180, 2009.

[7] V. K. Asrani and J. S. Shah, "Mental foramen: a predictor of age and gender and guide for various procedures," *Forensic Sci Med*, vol. 4, pp. 76–84, 2018.

[8] A. Sklavos, D. Beteramia, S. N. Delpachitra, S. N. Delpachitra, and R. Kumar, "The panoramic dental radiograph for emergency physicians," *Emergency Medicine Journal*, vol. 36, no. 9, pp. 565–571, 2019.

[9] V. Sairam, G. R. Potturi, B. Praveen, and G. Vikas, "Assessment of effect of age, gender, and dentoalveolar changes on mandibular morphology: a digital panoramic study," *Contemporary Clinical Dentistry*, vol. 9, pp. 49–54, 2018.

[10] Ch. Sai kiran, T. Khaitan, P. Ramaswamy, S. Sudhakar, B. Smitha, and G. Uday, "Role of mandibular canines in establishment of gender," *Egypt J Forensic Sci*, vol. 4, no. 3, pp. 71–74, 2014.

[11] Y. Kaeswaren and A. Z. Weinheimer, "The use of mandibular and maxillary canine teeth in establishing sexual dimorphism in the Malaysian population of selangor," *J Forensic Sci & Criminal Inves*, vol. 11, no. 3, Article ID 555815, 2019.

[12] G. Suragimath, S. R. Ashwinirani, V. Christopher, S. Bijjargi, R. Pawar, and A. Nayak, "Gender determination by radiographic analysis of mental foramen in the Maharashtra population of India," *Journal of Forensic Dental Sciences*, vol. 8, p. 176, 2016.

[13] Z.-P. Ge, Y. Pan, G. Li, J.-Z. Zhang, and X.-C. Ma, "Age estimation based on pulp cavity/chamber volume of 13 types of tooth from cone beam computed tomography images," *International Journal of Legal Medicine*, vol. 5, no. 4, pp. 2421–2425, 2016.

[14] C. Monali, P. Pritam, M. Tapan, and D. Kajal, "Gender determination: a view of forensic odontologist," *Indian Journal of Forensic Medicine and Pathology*, vol. 4, no. 4, 2011.

[15] S. Wallraff, S. Vesal, C. Syben, R. Lutz, and A. Maier, "Age estimation on panoramic dental X-ray images using deep learning," *Bildverarbeitung für die Medizin 2021*, Springer, Berlin/Heidelberg, Germany, pp. 186–191, 2021.

[16] P. V. Saloni, P. Mahajan, A. Puri, S. Kaur, and S. Mehta, "Morphometric analysis of mandibular ramus: a panoramic study," *Indian Journal of Dental Research*, vol. 31, no. 3, 2020.

[17] P. Vadla, R. Surekha, G. V. Rao, G. Deepthi, S. Naveen, and C. Arun Kumar, "Assessing the accuracy of Cameriere's Indian-specific formula for age estimation on right and left sides of orthopantomogram," *Egyptian Journal of Food Science*, vol. 10, no. 1, 2020.

[18] A. Okkesim and S. Erhamza, "Assessment of mandibular ramus for sex determination: retrospective study," *Journal of Oral Biology and Craniofacial Research*, vol. 10, no. 4, pp. 569–572, 2020.

[19] N. Vila, R. R. Vilas, and M. J. Carreria, *Towards Deep Learning Reliable Gender Estimation from Dental Panoramic Radiographs*, STAIRS, Santiago de Compostela, Spain, 2020, http://ceur-ws.org/.

[20] V. Patil, R. Vineetha, S. Vatsa et al., "Artificial neural network for gender determination using mandibular morphometric parameters: a comparative retrospective study," *Cogent Engineering*, vol. 7, no. 1, Article ID 1723783, 2020.

[21] J. A. Neves, N. Antunes-Ferreira, V. Machado et al., "Sex prediction based on MesiodistalWidth data in the Portuguese population," *Applied Sciences*, vol. 10, p. 4156, 2020.

[22] D. Dalessandri, I. Tonni, L. Laffranchi et al., "2D vs. 3D radiological methods for dental age determination around 18 Years: a systematic review," *Applied Sciences*, vol. 10, no. 9, p. 3094, 2020.

[23] A. Stella and S. Thirumalai, "Age assessment automation tool using VBA with OPG," *International Journal of Scientific & Technology Research Volume*, vol. 9, no. 1, 2020.

[24] A. Bali Behl, S. Grewal, K. Bajaj, P. S. Baweja, G. Kaur, and P. Kataria, "Mandibular ramus and gonial angle—identification tool in age estimation and sex determination: a digital panoramic radiographic study in north Indian population," *Journal of Indian Academy of Oral Medicine and Radiology*, vol. 32, no. 1, p. 31, 2020.

[25] V. M. Andrade, R. C. Fontenele, A. C. de Souza et al., "Age and sex estimation based on pulp cavity volume using cone beam computed tomography: development and validation of formulas in a Brazilian sample," *Dentomaxillofacial Radiology*, vol. 48, Article ID 20190053, 2019.

[26] E. Michael Onyema, P. Kumar Shukla, S. Dalal, M. Neeraj Mathur, M. Zakariah, and B. Tiwari, "Enhancement of patient facial recognition through deep learning algorithm: ConvNet," *Journal of Healthcare Engineering*, vol. 2021, Article ID 5196000, 8 pages, 2021.

[27] P. K. Shukla, J. Kaur Sandhu, A. Ahirwar, D. Ghai, P. Maheshwary, and P. K. Shukla, "Multiobjective genetic algorithm and convolutional neural network based COVID-19 identification in chest X-ray images," *Mathematical Problems in Engineering*, vol. 2021, Article ID 7804540, 9 pages, 2021.

[28] V. Roy, P. K. Shukla, A. K. Gupta, V. Goel, P. K. Shukla, and S. Shukla, "Taxonomy on EEG artifacts removal methods,

Hindawi
Journal of Healthcare Engineering
Volume 2023, Article ID 9876909, 1 page
https://doi.org/10.1155/2023/9876909

Retraction

Retracted: An Ensembled Spatial Enhancement Method for Image Enhancement in Healthcare

Journal of Healthcare Engineering

Received 23 May 2023; Accepted 23 May 2023; Published 24 May 2023

This article has been retracted by Hindawi following an investigation undertaken by the publisher [1]. This investigation has uncovered evidence of one or more of the following indicators of systematic manipulation of the publication process:

(1) Discrepancies in scope
(2) Discrepancies in the description of the research reported
(3) Discrepancies between the availability of data and the research described
(4) Inappropriate citations
(5) Incoherent, meaningless and/or irrelevant content included in the article
(6) Peer-review manipulation

The presence of these indicators undermines our confidence in the integrity of the article's content and we cannot, therefore, vouch for its reliability. Please note that this notice is intended solely to alert readers that the content of this article is unreliable. We have not investigated whether authors were aware of or involved in the systematic manipulation of the publication process. Wiley and Hindawi regrets that the usual quality checks did not identify these issues before publication and have since put additional measures in place to safeguard research integrity.

We wish to credit our own Research Integrity and Research Publishing teams and anonymous and named external researchers and research integrity experts for contributing to this investigation.

The corresponding author, as the representative of all authors, has been given the opportunity to register their agreement or disagreement to this retraction. We have kept a record of any response received.

References

[1] M. H. Siddiqi and A. Alsirhani, "An Ensembled Spatial Enhancement Method for Image Enhancement in Healthcare," *Journal of Healthcare Engineering*, vol. 2022, Article ID 9660820, 12 pages, 2022.

Hindawi
Journal of Healthcare Engineering
Volume 2022, Article ID 9660820, 12 pages
https://doi.org/10.1155/2022/9660820

Research Article

An Ensembled Spatial Enhancement Method for Image Enhancement in Healthcare

Muhammad Hameed Siddiqi and Amjad Alsirhani

College of Computer and Information Sciences, Jouf University, Sakaka, Aljouf,2014, Saudi Arabia

Correspondence should be addressed to Muhammad Hameed Siddiqi; mhsiddiqi@ju.edu.sa

Received 15 November 2021; Revised 13 December 2021; Accepted 20 December 2021; Published 4 January 2022

Academic Editor: Liaqat Ali

Most medical images are low in contrast because adequate details that may prove vital decisions are not visible to the naked eye. Also, due to the low-contrast nature of the image, it is not easily segmented because there is no significant change between the pixel values, which makes the gradient very small Hence, the contour cannot converge on the edges of the object. In this work, we have proposed an ensembled spatial method for image enhancement. In this ensembled approach, we first employed the Laplacian filter, which highlights the areas of fast intensity variation. This filter can determine the sufficient details of an image. The Laplacian filter will also improve those features having shrill disjointedness. Then, the gradient of the image has been determined, which utilizes the surrounding pixels for the weighted convolution operation for noise diminishing. However, in the gradient filter, there is one negative integer in the weighting. The intensity value of the middle pixel might be deducted from the surrounding pixels, to enlarge the difference between the head-to-head pixels for calculating the gradients. This is one of the reasons due to which the gradient filter is not entirely optimistic, which may be calculated in eight directions. Therefore, the averaging filter has been utilized, which is an effective filter for image enhancement. This approach does not rely on the values that are completely diverse from distinctive values in the surrounding due to which it recollects the details of the image. The proposed approach significantly showed the best performance on various images collected in dynamic environments.

1. Introduction

Nowadays, in the real-world society of artificial intelligence (AI), the images might be sensed anytime and anyplace, which are commonly based on the human visualization that intuitively direct the people to easily realize the information that the images carry to us [1]. In healthcare domains, the images comprise various noises, due to which the physicians may face a problem detecting the corresponding diseases. We might utilize the image enhancement technology to diminish the various noises and visual effects to improve the quality of the image [2].

Image enhancement is one of the significant parameters in healthcare domains. Image enhancement is commonly divided into single-point procedures and spatial procedures. The point procedures contain contrast increase, noise reduction, histogram modulation, and similar colors. Point operations are generally simple nonlinear operations. In contrast, today, linear spatial processes are often used in image processing. The reason is that local linear operations are simple and easy to implement. Though linear image enhancement techniques are frequently suitable in numerous applications, important advantages in image enhancement might be achieved if nonlinear methods are utilized. The nonlinear methods efficiently reserve the individual characteristics of the image, while the operators using the linear mode distort the image. In addition, nonlinear techniques are less sensitive to noise canceling devices. The noise is always presented because of random physical imagination [3].

There are various types of image processing and machine learning approaches proposed for the enhancement of images. One approach is to propose and realize the possibility of artificial intelligence and pattern recognition applications which categorize the images through their corresponding pictorial resources such as radiology images. These days, the main resource which is employed for such images is the electromagnetic energy spectrum such as acoustic, supersonic, and electrical microscopy. Radiology images such as X-ray, computed tomography (CT), and magnetic resonance imaging (MRI) have fascinating roles in the wellness domain that help the medical specialists to easily identify various illnesses from such radiology images.

A state-of-the-art method for image enhancement was proposed by Ma et al. [4], where they ensembled the local filters along with the global optimization approach. This method was based on global sparseness disintegration and a variable factor. Initially, the global sparse disintegration has been utilized in order to preeliminate a portion of the surface to improve the performance of smoothing. Similarly, Fang and Han [5] proposed a nonlinear incline field-guided image enhancement technique where they proved optimal value as a model factor. Moreover, the fractional order calculus is utilized to gradient ancestry along with the impetus technique in order to train the neural network. Moreover, a new type of method was designed by Deng et al. [6] for the purpose of smoothing or enhancement based on a fine-tuning parameter. This filter was based on a Laplacian-based formulation (that amalgamates the operations of smoothing and enhancement), an interpolation method (similar to that employed in the trained filter that delivers edge-consciousness ability), and the comprehensive Gamma spreading (that is utilized as the preceding for parameter approximation). However, the performances of these systems were decreased in dynamic and naturalistic domains.

Accordingly, in this work, we have proposed an ensembled spatial method for the purpose of image enhancement. In this ensembled approach, first, we utilized the Laplacian filter that highlights the regions of the fast intensity variation. This is a capable filter that determines the acceptable descriptions of an image. Moreover, those features having piercing disjointedness will be enhanced by the Laplacian filter, which has been fed to another filter that finds the gradient of the corresponding image. This filter is same as an averaging filter that utilized neighboring pixels for the weighted convolution operation for noise diminishing. However, in the gradient filter, there is one negative integer in the weighting, due to which the intensity value of the middle pixel might be deducted from the surrounding pixels, to enlarge the difference between the head-to-head pixels for calculating the gradients. This is one of the reasons due to which the gradient filter is not completely optimistic, which may be calculated in eight directions. Therefore, the averaging filter will be utilized which is an effective filter for image enhancement. This approach does not rely on the values that are completely diverse from distinctive values in the surrounding due to which it recollects the details of the image. The proposed approach significantly showed best performance on various images collected in dynamic environments. Moreover, this method also showed best performance against existing state-of-the-art works.

The rest of the paper is organized as follows: Section 2 presents some related work regarding the image enhancement method with their shortcomings. Section 3 presents the detailed description of the proposed ensembled spatial enhancement method. The performance of the proposed ensembled methods along with some discussions are presented in Section 4. Lastly, Section 5 summarizes the proposed approach along with some future directions.

2. Related Work

Image enhancement has a significant role in healthcare domains that facilitates the physicians to easily diagnose various kinds of diseases from clear images. Huge amount of works have been carried out for the purpose of image enhancement; however, most of them suffer from their own limitations.

A novel point-level method was developed by Hao et al. [7] for diminishing the illumination effects and decomposition of reflectance that was based on nonlocal Haar wavelet transform. In this method, they utilized low-level frequency coefficients for diminishing the illumination effects, while high-level frequency coefficients were utilized for the reconstruction of the image. However, Haar transform might not be utilized for image enhancement because it has a poor energy concentration for the image [8]. Similarly, a latest approach was proposed by Kirsten et al. [9] where the authors evaluated numerous state-of-the-art deep neural networks for document enhancement. They assessed their performance qualitatively and quantitatively against the matrix of image quality assessment and then compared it with existing methods. However, deep neural networks cannot be utilized in real healthcare domains because this model has huge number of operations that requires a lot of time for training and testing.

On the other hand, a novel method was developed by Wan et al. [10] in order to diminish the noise and improve the lighting effects in real domains. This method was based on the entanglement network, which completely employed the corresponding features of the noise removal and environmental effects. However, the entanglement network only reduced the noise and does not consider the illumination in real-world domains. Furthermore, a new and modified ambient light-fused equation was designed by Wang et al. [11] for image enhancement that is based on the analysis-synthesis network. This method explained the association between the ambient light of color channels, and many dependances are entrenched. They performed extensive evaluation against the underwater synthetic dataset. However, the analysis-synthesis network considered resident block consequences that required lots of calculations. Also, in this approach, the overbright effects might not be diminished. Furthermore, this method has some other shortcomings such as damage of detail and color misrepresentation [12]. Likewise, a normalized flow model was proposed by Wang et al. [13] that was based on one-to-many associations which took low-illuminated features in order to map the delivery of the normal visible images with well-enhanced images. They claimed significant performance under the realistic domains. However, normalizing flow is implied in the formalism of constant normalization which necessitates the creation of equivariant feature space—constraining their modest application to conservative advanced dimensional multiplicative demonstrating areas such as real images [14].

An underwater image enhancement method was designed recently by Yadav et al. [15] that was based on histogram equalization. Before the histogram equalization process, the image was converted from color to gray scale in order to speed up the process. Then, the histogram equalization was employed to sustain the intensities of the images in order to improve the contrast. Furthermore, the image colors were maintained by utilizing a convolutional neural network model. However, histogram equalization only emphasizes the local contrast instead of considering the entire contrast of the image. Also, histogram equalization produces artifacts during enhancement which is a common limitation. Similarly, the authors in [16–18] presented an approach which finds the optimum arrangement and strength of different image enhancement techniques through a neural network along with a new kind of layer which acquires the limitations of optimum image enhancement. However, the neural network has no specific scheme for finding the structure of neurons due to which the suitable and targeted results may not be achieved [19]. Moreover, in [20], the authors proposed an image enhancement method which was based on illumination tuning and the field variations of depth. This is attained and clustered by utilizing the principle of dark channel and spectral clustering techniques, respectively. Once the image had been divided in subimages, then, respectively, it was enhanced and fused. However, the performance of this approach degraded in real domains.

An integrated method was proposed by Moran et al. [21] that is the combination of multiple local parametric filters such as elliptical, graduated, and polynomial filters. This approach enhanced the images by the automatic estimation of the parametric filters. These filters are fast and easy to implement; however, these filters have common limitations that the entire display range might not be employed and possibly more critical, which is one of the reasons through which we may lose the performance [22]. Similarly, an alternative approach was designed by Muller [23] in order to interrupt the ration of the amount of FLOP (floating point operation per second) to the amount of parameter, which conserves the image scale. This method was expecting convolutional filters from the input image through a hypernetwork [23]. However, the convolutional filters are difficult to train when it got extensive along with dense hypernetworks [24].

Furthermore, an architecture of deep neural network has been proposed by Liang et al. [25] in order to pick up the RAW and color mapping based on a generalized nature. In this architecture, the authors utilized global subnetwork and local subnetwork. The local subnetwork emphasized on finding the mapping of illumination and color, while the global subnetwork was utilized in order to recover the image details. However, this approach cannot be utilized in naturalistic domains.

Therefore, this work proposes an ensembled spatial method for the purpose of image enhancement. In this ensembled approach, we first employed the Laplacian filter, which highlights the areas of fast intensity variation. This filter has the ability to determine the acceptable details of an image. Then, the gradient of the image has been determined, which utilizes the surrounding pixels for the weighted convolution operation for noise diminishing. After this stage, the averaging filter was utilized which is an effective filter for image enhancement. This approach does not rely on the values that are completely diverse from distinctive values in the surrounding due to which it recollects the details of the image.

3. Proposed Ensembled Spatial Method

The overall procedure of the proposed approach is presented in Figure 1. Moreover, the step-by-step procedure is described in the following sections.

3.1. Laplacian. The second-order derivative is called as the Laplacian and is an isotropic, whose response is independent of the direction of the discontinuities in the image. For an image, function $f(x, y)$ can be written as

$$\nabla^2 z \approx \frac{\partial^2 z}{\partial^2 x^2} + \frac{\partial^2 z}{\partial^2 y^2}. \tag{1}$$

The derivative has linear operations, so the Laplacian is a linear operator. Considering only the horizontal and vertical neighbor of a pixel, we can find the Laplacian in the x and y direction.

$$\begin{aligned} \frac{\partial^2 z}{\partial^2 x^2} &\approx z(x+1, y) + z(x-1, y) - 2z(x, y), \\ \frac{\partial^2 z}{\partial^2 y^2} &\approx z(x, y+1) + z(x, y-1) - 2z(x, y). \end{aligned} \tag{2}$$

The 2D Laplacian can be found by summing the abovementioned two equations.

$$\begin{aligned} \nabla^2 z \approx\ & [z(x+1, y) + z(x-1, y) + z(x, y+1) \\ & + z(x, y-1) - 4z(x, y)]. \end{aligned} \tag{3}$$

The original image data and the Laplacian filter data are, respectively, shown in Figure 2. Numerically, the data of the original image are presented in Figure 2(a). The enhanced pixels are the zero-crossings represented in Figure 2(b).

Equation (3) calculates the template coefficients of the Laplacian operator, which has a normalization function that guarantees the addition of the template coefficients is one so that the noise is not reduced in the uniform regions. This is because, in contrast, the sum of the template coefficients is zero against the previous Laplacian operator. Meanwhile, the template which is created by the aforementioned function might be used inside the template intricacy. Here, the Laplacian operator overpowers the effect of pixels far away from the middle of the template, finding the variation on those pixels closer to the middle pixel; then, the standard deviation is selected in order to make sure this act. Some of the well-known properties of the Laplacian filter are described as follows:

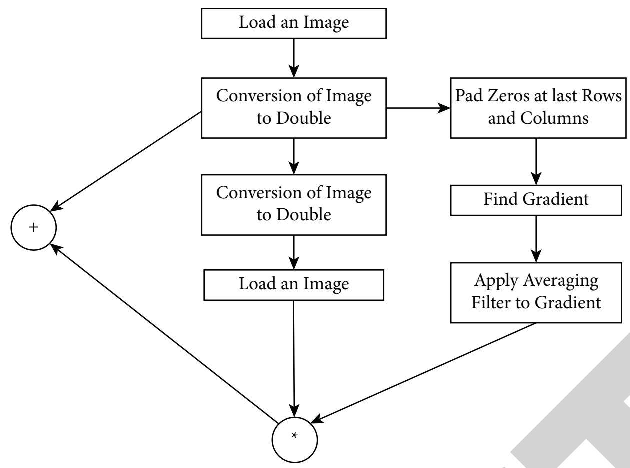

Figure 1: The overall flow of the proposed ensembled approach.

$$a = \begin{bmatrix} 1 & 2 & 3 & 4 & 1 & 1 & 2 & 1 \\ 2 & 2 & 3 & 0 & 1 & 2 & 2 & 1 \\ 3 & 0 & 38 & 39 & 37 & 26 & 3 & 0 \\ 4 & 1 & 40 & 44 & 41 & 42 & 2 & 1 \\ 1 & 2 & 43 & 44 & 40 & 39 & 1 & 3 \\ 2 & 0 & 39 & 41 & 42 & 40 & 2 & 0 \\ 1 & 2 & 0 & 2 & 2 & 3 & 1 & 1 \\ 0 & 2 & 1 & 3 & 1 & 0 & 4 & 2 \end{bmatrix}$$

(a)

$$M = \begin{bmatrix} 0 & 0 & 0 & 0 & 0 & 0 & 0 & 0 \\ 0 & 1 & -31 & -47 & -36 & -32 & 0 & 0 \\ 0 & -44 & 70 & 37 & 31 & 60 & -28 & 0 \\ 0 & -42 & 34 & 12 & 1 & 50 & -39 & 0 \\ 0 & -37 & 47 & 8 & -6 & 33 & -42 & 0 \\ 0 & -45 & 72 & 37 & 45 & 74 & -34 & 0 \\ 0 & 5 & -44 & -38 & -40 & -31 & -6 & 0 \\ 0 & 0 & 0 & 0 & 0 & 0 & 0 & 0 \end{bmatrix}$$

(b)

Figure 2: (a) The original image data; (b) the data after Laplacian.

(i) It is used to highlight the fine detail of an image
(ii) Moreover, it is also used to enhance the blur image, but the Laplacian amplifies the noise in the image
(iii) Also, the Laplacian of the image in a flat area (having the same intensity level) is zero
(iv) The Laplacian of a ramp or a step at the onset is nonzero
(v) Similarly, the Laplacian of a ramp is zero with a constant slop
(vi) The Laplacian has a stronger response to highlight the fine details
(vii) The Laplacian has a double response at the step change in a gray level
(viii) The Laplacian has a stronger response to a line than to a step and to a point than to a line

However, the Laplacian has some common limitations during implementation.

(xi) If we place the mask at the first and last row and column of the image, some elements of the mask are outside of the image, so to remove this difficulty:
    (i) Extra rows and columns are padded at the start and end of the image
    (ii) The pixel intensity of the first and last rows and columns is replicated
    (iii) The first and last row and columns are not considered, as shown in Figure 3
(x) During Laplacian calculation, the range of the pixel intensities is [0–255]
(xi) First, the minimum in the image is found
(xii) The sign is changed to minimum and added to each value of the image
(xiii) Then, the maximum in the image is found and multiplied (255/max) with each element and converted into the whole number

Therefore, in order to tackle the abovementioned limitations, we consider to utilize the gradient filter.

3.2. Gradient of the Image. The gradient of an image is simply the first-order derivative of an image. The gradient is used to enhance the edges, line, and point in an image. The edge is a group of associated points which lies on the border among various areas (as shown in Figure 4).

There are two elements associated with the gradient: the first one is the magnitude of the gradient, while the second one is the direction of the gradient and the edges as indicated in Figure 5.

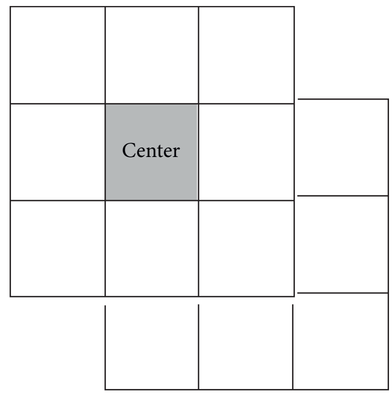

Figure 3: The implementation mask of the Laplacian.

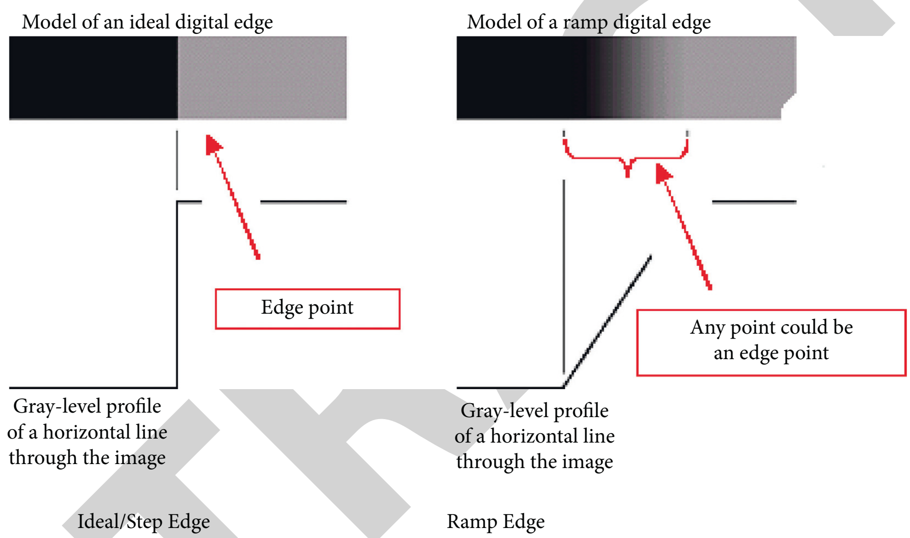

Figure 4: A model to show the group of associated points which lie on the border among two areas.

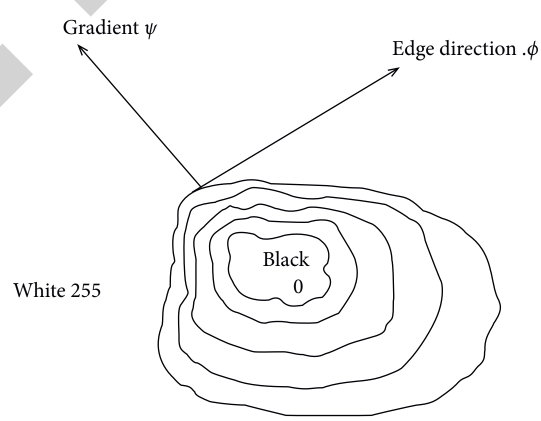

Figure 5: The direction of the gradient and edges inside an image.

The gradient of an image at the location at (x, y) is

$$\nabla z \approx \left[\frac{\partial z}{\partial x} \cdot \frac{\partial z}{\partial y}\right],$$

$$\text{mag}\,(\nabla z) \approx \sqrt{\left[\frac{\partial z}{\partial x}\right]^2 + \left[\frac{\partial z}{\partial x}\right]^2} \approx \left|\frac{\partial z}{\partial x}\right|\left|\frac{\partial z}{\partial y}\right|, \tag{4}$$

$$\cdot \arctan\left(\frac{(\partial z/\partial y)}{(\partial z/\partial x)}\right).$$

Some common shortcomings of the gradient during implementation are as follows:

(i) Using the formula $G_x = z(x+1,\ y) - z(x,\ y)$ and $G_y = z(x,\ y+1) - z(x,\ y)$, there is a problem when we are at the last row or at the last column. So, to solve it, we

 (i) Either pad extra rows and columns at the end of the image
 (ii) Replicate the pixel intensity of the last rows and columns
 (iii) Do not consider the last rows and columns

So, the smoothing filter has been considered in order to tackle the abovementioned shortcomings of the gradient.

3.3. Averaging Filter. For every pixel in the processed image, $\hat{z}\,(i, j)$ is attained from the average in a neighborhood pixel value of (i, j) in the involvement image. For instance, for a 3×3 neighborhoods window, we utilized the following mask for the surrounding pixels.

The value of the corresponding pixel is increased by 1/9 and added, and the outcome is positioned in the corresponding resultant image. The abovementioned window is continuously moved on the entire image till each pixel has been enclosed. This means, the corresponding image is convoluted along with this enhancement mask that is also represented as a spatial filter.

3.3.1. Weighted Mask. A weighted average spatial filter is one of the robust filters for the smoothing averaging filter. The term weighted averaging filter indicates that different pixels are multiplied by various factors, which gives the most significance (weight) to some points at the additional area as represented in Figure 6.

The weighted averaging filter of size $m \times n$ (m and n odd) is given by the expression

$$g\,(x, y) = \frac{\sum_{s=-a}^{a} \sum_{t=-b}^{b} w\,(s, t)\, f\,(x+s, y+t)}{\sum_{s=-a}^{a} \sum_{t=-b}^{b} w\,(s, t)}. \tag{5}$$

$\frac{1}{16} \times$

1	2	1
2	4	2
1	2	1

Figure 6: Weighted filter mask.

The strong point about the weighted filter is that it is used to diminish the noise from the corresponding image. Also, the average filter adds blur to the image. Moreover, it is a linear filter.

3.3.2. Box Mask. A form of spatial averaging filter also known as box filter is given in Figure 7.

$$R = \frac{1}{9} \sum_{i=1}^{9} z_i. \tag{6}$$

It is the average of the gray levels of the pixel in a 3×3 neighborhood defined by the mask.

4. Performance Evaluation

The proposed ensembled spatial algorithm has been assessed against various experiments. The experimental results are prescribed in the following sections.

4.1. Setup. The proposed approach has been validated as follows:

(i) The proposed algorithm has been tested and thoroughly assessed on various images in order to show the effectiveness of the proposed ensembled spatial algorithm
(ii) A subjective comparison has been provided against various recent works, which means that their corresponding average accuracies were taken based on the enhancement rate against various images

5. Results

The Laplacian of an image can be found by using the mask if we consider only the x and y coefficient the Laplacian mask is under (as shown Figures 8 in 9, respectively).

The sum of the coefficient of the Laplacian mask is zero because when we apply the Laplacian mask to a flat area that has same grayscale value, there will be no change. The image is enhanced by applying the following rules:

$$g\,(x, y) = \begin{cases} f\,(x, y) - \nabla^2 f\,(x, y) & \text{if the mask center coeff is negative} \\ f\,(x, y) + \nabla^2 f\,(x, y) & \text{if the mask center coeff is positive} \end{cases}. \tag{7}$$

$$\frac{1}{9} \times \begin{array}{|c|c|c|} \hline 1 & 1 & 1 \\ \hline 1 & 1 & 1 \\ \hline 1 & 1 & 1 \\ \hline \end{array}$$

Figure 7: Box filter mask.

0	1	0
1	-4	1
0	1	0

Center is Negative

0	-1	0
-1	4	-1
0	-1	0

Center is Positive

Figure 8: Laplacian 4×4 mask for implementation.

1	1	1
1	-8	1
1	1	1

Center is Negative

-1	-1	-1
-1	8	-1
-1	-1	-1

Center is Positive

Figure 9: Laplacian mask for implementation when we considered diagonal.

The corresponding results of the Laplacian are presented in Figure 10.

Similarly, we use different masks for enhancing the edges of an image. First, we enhance the vertical edges and then the horizontal edges, and to enhance the overall edges of an image, we add the result of the vertical and horizontal edges (as shown in Figures 11 and 12, respectively).

As can be described from Figure 10 that the Laplacian did not clearly enhance, we did not get the best results. Therefore, we applied the gradient along with averaging. The sample results are presented in Figure 13.

As illustrated in Figure 13, we still did not achieve the best enhancement results, due to which we are unable to enhance the desired features of the images. Therefore, we utilized the proposed ensembled spatial enhancement algorithm in order to get the best results that may be further utilized in the healthcare domain. The sample results of the proposed approach are presented in Figures 14(a) and 14(b), respectively.

It is significant from Figures 14(a) and 14(b) that the proposed ensembled spatial enhancement algorithm achieved significant results. The significance is because the proposed approach has the ability to enhance various kinds of images in different dynamic environments.

Lastly, we presented the subjective comparison of the proposed approach with some state-of-the-art methods. The subjective performances along with the proposed approach are presented in Table 1.

A subjective comparison has been provided against various recent works, which means that their corresponding average accuracies were taken based on the enhancement rate against various images. As presented, the proposed approach not only achieves significant performance on various images but also showed the best enhancement accuracy subjectively (shown in Table 1). This is because the proposed approach highlights the areas of fast intensity variation, through which it determines the acceptable details of an image. Moreover, the proposed method also determines the surrounding pixels for the weighted convolution operation for noise diminishing. After this stage, the averaging filter was utilized which is an effective filter for image enhancement. This approach does not rely on the values that are completely diverse from distinctive values in the surrounding due to which it recollects the details of the image.

6. Discussion

We have proposed an ensembled spatial method for the purpose of image enhancement. In the proposed approach, first, an adoptive Laplacian filter was utilized, which includes various image information due to which the effects might be a bit diverse. The middle increment of every structure might be negative, and the rest of the neighbors (that will be either four or eight) might be positive, without damaging the image information. Essentially, this is significant to guarantee that the summation of template parameters must be zero, which further signifies the edges should not be detected in the uniform brightness regions. The Laplacian operator has equal possessions in every direction; however, at present, it comprises no smoothing and will rejoin the noise again, more so than a first-order operator since it is differentiation of a higher order. But still, computation wise, the Laplacian filter is less expensive. After the Laplacian, we employed the averaging filter, where the average result is used to diminish

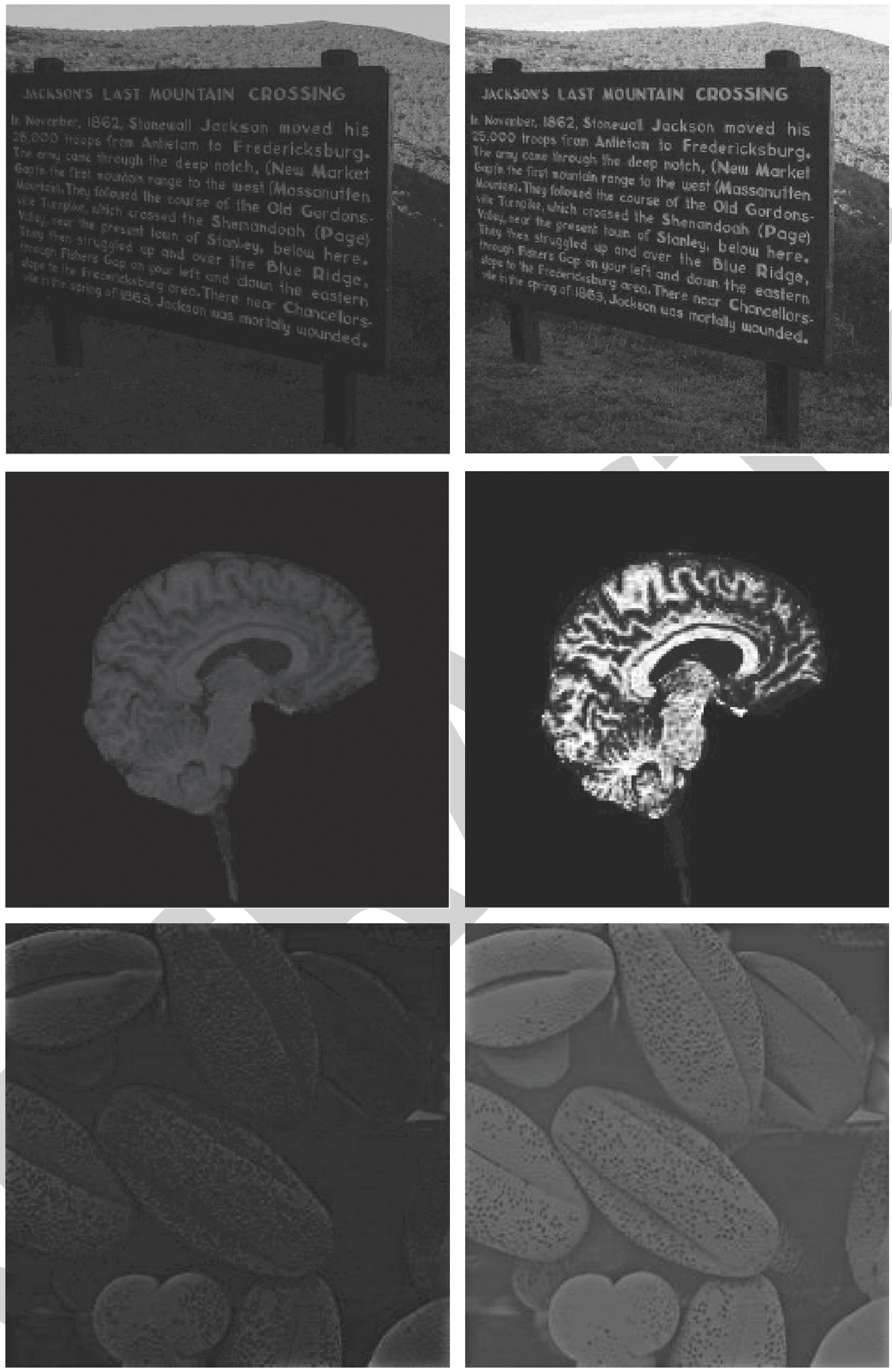

Figure 10: Sample enhancement results of the Laplacian mask (left column represents the original images, while the right column is the enhanced images).

−1	−1	−1
0	0	0
1	1	1

Prewitt

−1	−2	−1
0	0	0
1	2	1

Sobel

Figure 11: Horizontal edge detector $Gx = df/dx$.

−1	0	1
−1	0	1
−1	0	1

Prewitt

−1	0	1
−2	0	2
−1	0	1

Sobel

Figure 12: Vertical edge detector $Gy = df/dy$.

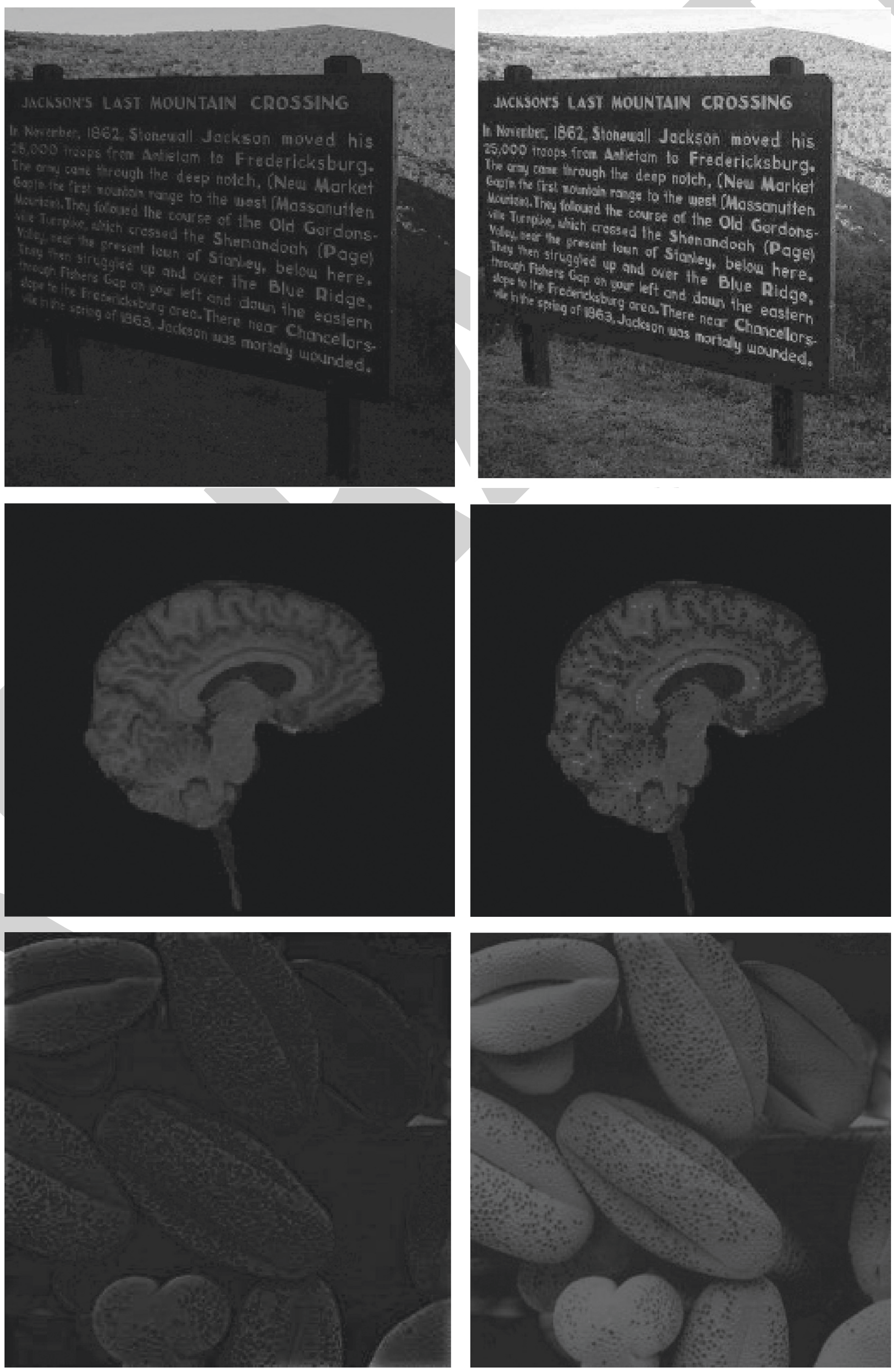

Figure 13: Sample results of the gradient along with the averaging filter.

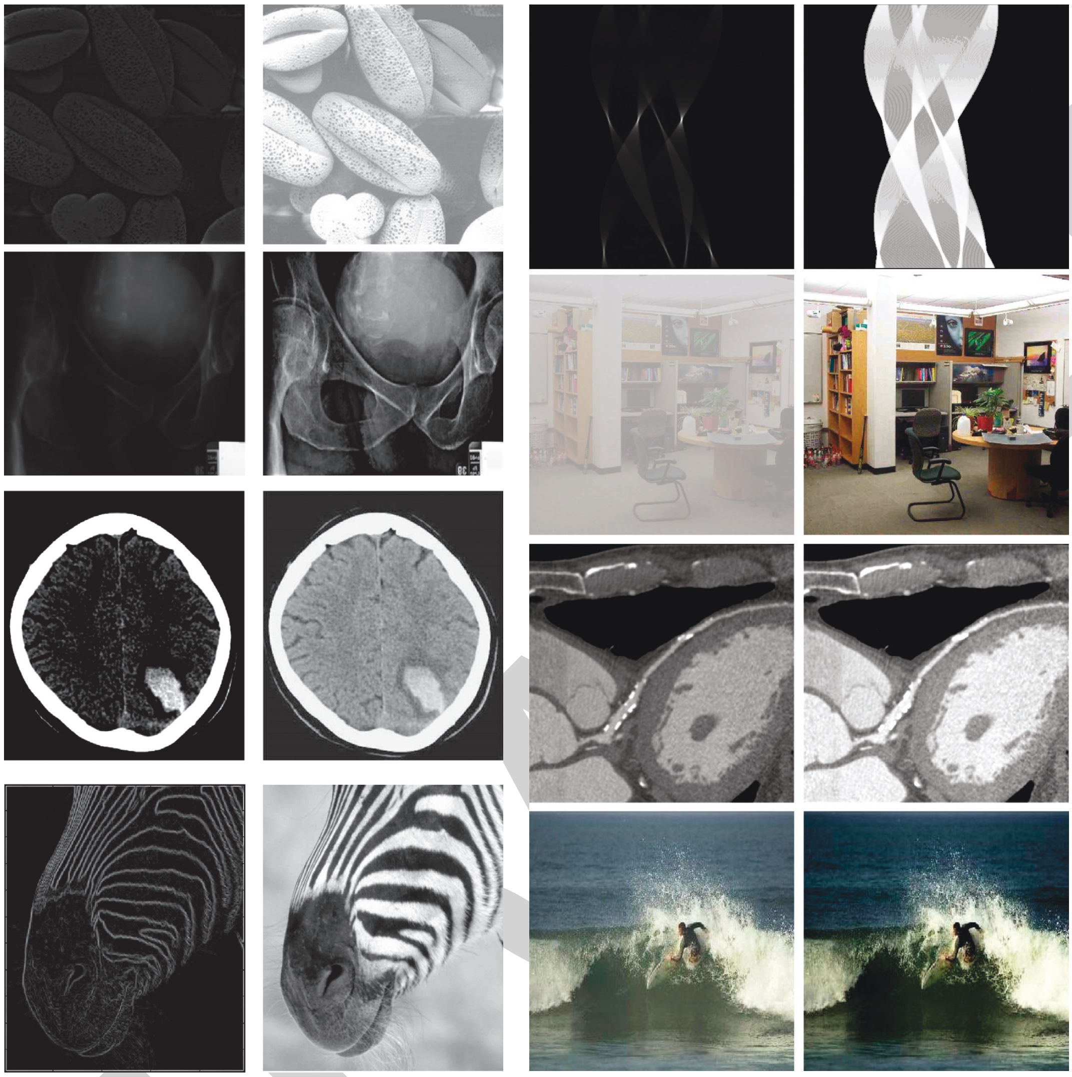

(a) (b)

Figure 14: (a), (b) The sample results of the proposed approach.

Table 1: Subjective comparison between the state-of-the-art and the proposed approach.

Existing approaches	Performance (%)
[26]	89
[27]	91
[28]	88
[29]	93
[30]	90
[31]	94
[32]	91
Proposed approach	98

the noise. This is a low-pass filter whose result is used to permit the frequencies of the low spatial to be reserved, and the high-frequency components will be overpowered. In order to diminish the noise, a 5×5 window is used, but it reduced the detailed level. Therefore, the averaging operator size is equal to the mutual of a low-pass filter. As described before, the smoothing was attained by the gradient of images, which actually gives another approach to execute the template convolution. In the gradient of images and the Laplacian operator, multiplication is the twin procedure for convolution, which means that it might be applied by reproducing the template along with the gradient of images and the Laplacian operator of the image to whom the template is employed. In order to return the domain of the image, the result must be inverse transform, for which the size of the transformed template and the size of the image must be similar. Hence, initially, the picture comprising the template is zero-expanded. The procedure begins by the estimation of the transmute of the zero-expanded template. Then, the convolution multiplies the template transform by the image transform pixel by pixel. Once the scheme is raised, it is completed along with an image transform, and the resultant transform is ordered again before the converse alteration, to make sure that the picture is represented accurately.

7. Conclusions

Over a couple of years, healthcare image processing has arisen as a significant research domain. Medical images are very subtle to the illumination and naturalistic factors. The principal goal of image enhancement is to improve the quality of the image by recovering the features of corresponding image. However, image enhancement is challenging due to some factors such as dynamic changes of ecological factors, illumination, lighting effects, and noise (made by humans or machine). Thus, in the medical domain, the correct image enhancement is necessary, before the disease diagnosis. In the literature, there are various types of image processing approaches proposed for the enhancement of images. One approach is to propose and realize the possibility of artificial intelligence and pattern recognition applications which categorize the images through their corresponding pictorial resources such as radiology images. However, most of the previous techniques produced over-enhancement, and sometimes, they produced checker board on images. Because of that, the physicians might lose the significant evidences in the X-ray, CT, and MR image. Therefore, in this work, we have proposed an ensembled spatial method for the purpose of image enhancement. In this ensembled approach, we first employed the Laplacian filter, which highlights the areas of fast intensity variation. This filter has the ability to determine the acceptable details of an image. Then, the output has been fed to another filter which utilized neighboring pixels for the weighted convolution operation for noise diminishing. Then, the averaging filter has been employed which is an effective filter for image enhancement. This approach does not rely on the values that are completely diverse from distinctive values in the surrounding due to which it recollects the details of the image. The proposed approach significantly showed the best performance on various images collected in dynamic environments.

In the future, we will try to improve the proposed model and will employ it in the healthcare, especially for the enhancement of the radiology images for the recommendation of physicians.

Data Availability

Data used for this study and simulation will be provided on demand.

Conflicts of Interest

The authors declare no conflicts of interest regarding the present study.

Acknowledgments

This work was funded by the Deanship of Scientific Research at Jouf University under grant no. DSR–2021–02–0344.

References

[1] P. Li, H. Wang, M. Yu, and Y. Li, "Overview of image smoothing algorithms," *Journal of Physics: Conference Series*, vol. 1883, no. 1, Article ID 012024, 2021.

[2] A. Vacavant, "Smoothed shock filtering: algorithm and applications," *Journal of Imaging*, vol. 7, no. 3, p. 56, 2021.

[3] G. R. Arce, J. Bacca, and J. L. Paredes, "Nonlinear filtering for image analysis and enhancement," in *The Essential Guide to Image Processing*, pp. 263–291, Academic Press, Cambridge, MA, USA, 2009.

[4] X. Ma, X. Li, Y. Zhou, and C. Zhang, "Image smoothing based on global sparsity decomposition and a variable parameter," *Computational Visual Media*, vol. 7, no. 4, pp. 483–497, 2021.

[5] Q. Fang and X. U. E. Han, "A nonlinear gradient domain-guided filter optimized by fractional-order gradient descent with momentum RBF neural network for ship image dehazing," *Journal of Sensors*, vol. 2021, Article ID 8864906, 15 pages, 2021.

[6] G. Deng, F. Galetto, M. Alnasrawi, and W. Waheed, "A guided edge-aware smoothing-sharpening filter based on patch interpolation model and generalized Gamma distribution," *IEEE Open Journal of Signal Processing*, vol. 2, pp. 119–135, 2021.

[7] H. Hao, H. Yingkun, S. Yuxuan, W. Benzheng, and X. Jun, "NLHD: a pixel-level non-local retinex model for low-light image enhancement," 2021, https://arxiv.org/abs/2106.06971.

[8] P. Porwik and A. Lisowska, "The Haar-wavelet transform in digital image processing: its status and achievements," *Machine Graphics and Vision*, vol. 13, no. 1/2, pp. 79–98, 2004.

[9] L. N. Kirsten, R. Piccoli, and R. Ribani, "Evaluating deep neural networks for image document enhancement," in *Proceedings of the 21st ACM Symposium on Document Engineering*, Limerick, Ireland, 2021, August.

[10] Y. Wan, Y. Cheng, and M. Shao, "Rain Removal and Illumination Enhancement Done in One Go," 2021, https://arxiv.org/abs/2108.03873?context=cs.

[11] Z. Wang, L. Shen, M. Yu, Y. Lin, and Q. Zhu, "Single Underwater Image Enhancement Using an Analysis-Synthesis Network," 2021, https://arxiv.org/abs/2108.09023.

[12] W. Wang, X. Wu, X. Yuan, and Z. Gao, "An experiment-based review of low-light image enhancement methods," *IEEE Access*, vol. 8, Article ID 87884, 2020.

[13] Y. Wang, R. Wan, W. Yang, H. Li, L. P. Chau, and A. C. Kot, "Low-Light Image Enhancement with Normalizing Flow," 2021, https://arxiv.org/abs/2109.05923.

[14] A. J. Bose and I. Kobyzev, "Equivariant Discrete Normalizing Flows," 2021, https://arxiv.org/abs/2110.08649.

[15] A. Yadav, M. Upadhyay, and G. Singh, "Underwater Image Enhancement Using Convolutional Neural Network," 2021, https://arxiv.org/abs/2109.08916.

[16] N. Mitschke, Y. Ji, and M. Heizmann, "Task specific image enhancement for improving the accuracy of CNNs," in *Proceedings of the 10th International Conference on Pattern Recognition Applications and Methods*, pp. 174–181, Vienna, Austria, January 2021.

[17] Y. Zhao, L. Gao, L. Xiang, Q. Zhang, and Z. Zhao, "Research on image enhancement algorithm base on convolutional neural network in scotopic vision environment," in *Proceedings of the 2020 International Conference on Pattern Recognition and Intelligent Systems*, pp. 1–5, Athens, Greece, July 2020.

[18] Y. Lu, Y. Guo, and M. Liang, "CNN-enabled visibility enhancement framework for vessel detection under haze environment," *Journal of Advanced Transportation*, vol. 2021, Article ID 5598390, 14 pages, 2021.

[19] https://www.asquero.com/article/advantages-and-disadvantages-of-artificial-neural-networks/.